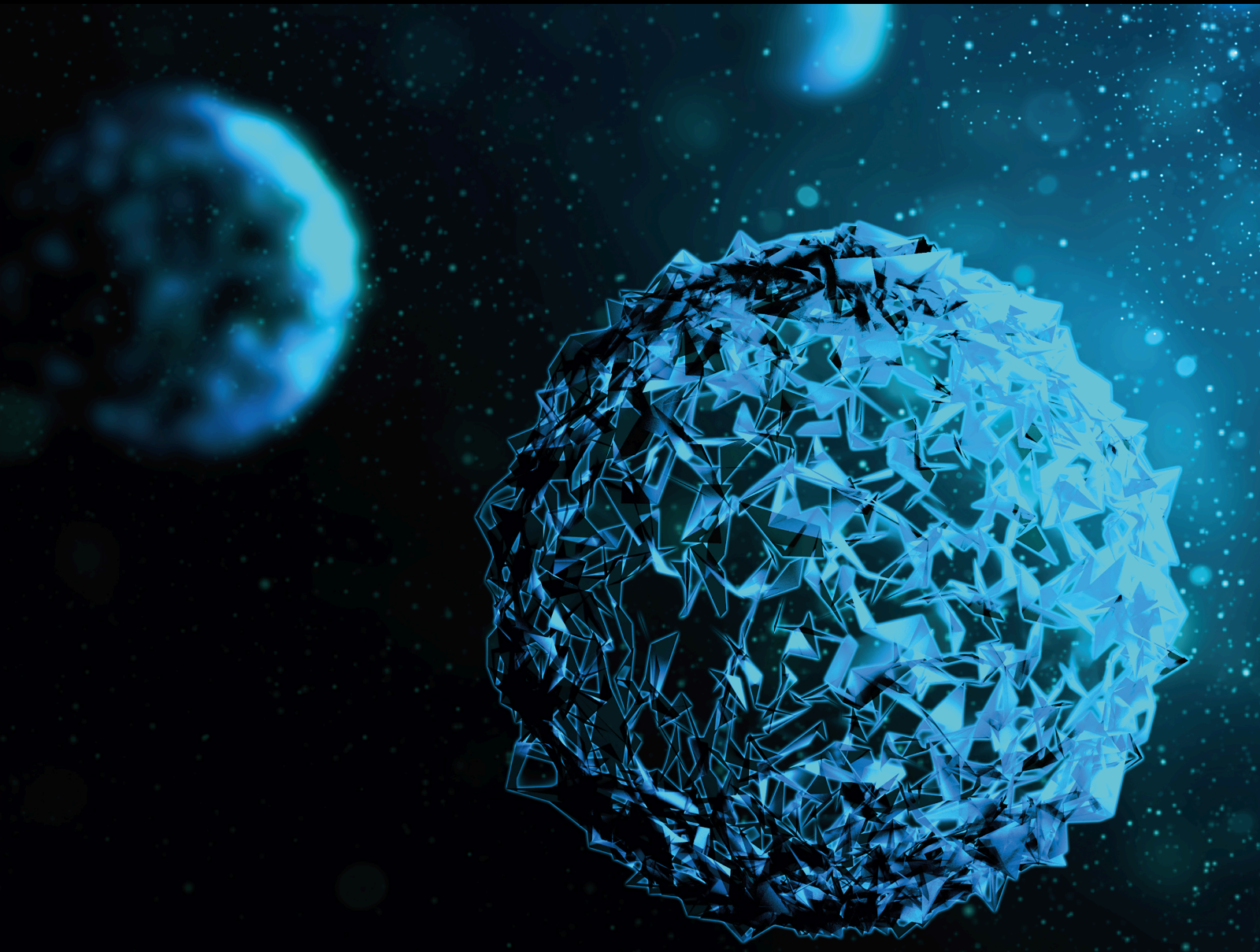# Effects of Microbiota on Cancer Immune Responses and Immunotherapy

Lead Guest Editor: Yingbin Shen
Guest Editors: Yongqiang Chen, Aly El Sheikha, and Visweswara Rao Pasupuleti

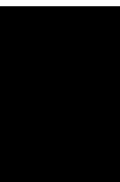# Effects of Microbiota on Cancer Immune Responses and Immunotherapy

Effects of Microbiota on Cancer Immune Responses and Immunotherapy

Lead Guest Editor: Yingbin Shen
Guest Editors: Yongqiang Chen, Aly El Sheikha, and Visweswara Rao Pasupuleti

Eugenio Zoni , Switzerland

Contents

Retracted: Identification of lncRNA Biomarkers and LINC01198 Promotes Progression of Chronic Rhinosinusitis with Nasal Polyps through Sponge miR-6776-5p
BioMed Research International
Retraction (1 page), Article ID 9854205, Volume 2024 (2024)

Retracted: Brusatol Inhibits Proliferation and Metastasis of Colorectal Cancer by Targeting and Reversing the RhoA/ROCK1 Pathway
BioMed Research International
Retraction (1 page), Article ID 9853485, Volume 2024 (2024)

Retracted: Establishment and Validation of an MTORC1 Signaling-Related Gene Signature to Predict Overall Survival in Patients with Hepatocellular Carcinoma
BioMed Research International
Retraction (1 page), Article ID 9851737, Volume 2024 (2024)

Retracted: Prokineticins as a Prognostic Biomarker for Low-Grade Gliomas: A Study Based on The Cancer Genome Atlas Data
BioMed Research International
Retraction (1 page), Article ID 9848746, Volume 2024 (2024)

Retracted: LINC00518 Promotes Cell Malignant Behaviors via Influencing EIF4A3-Mediated mRNA Stability of MITF in Melanoma
BioMed Research International
Retraction (1 page), Article ID 9846817, Volume 2024 (2024)

Retracted: The Treatment Combining Antiangiogenesis with Chemoradiotherapy Impinges on the Peripheral Circulation Vascular Endothelial Cells and Therapeutic Effect in the Patients with Locally Advanced Nasopharyngeal Carcinoma
BioMed Research International
Retraction (1 page), Article ID 9842547, Volume 2024 (2024)

Retracted: Immunotherapy Mechanism of Esophageal Squamous Cell Carcinoma with the Effect of STK11/AMPK Signaling Pathway
BioMed Research International
Retraction (1 page), Article ID 9838254, Volume 2024 (2024)

Retracted: The Expression Profile of miRNA in Glioma and the Role of miR-339-5p in Glioma
BioMed Research International
Retraction (1 page), Article ID 9837525, Volume 2024 (2024)

Retracted: Mechanism of Gegen Qinlian Decoction Regulating ABTB1 Expression in Colorectal Cancer Metastasis Based on PI3K/AKT/FOXO1 Pathway
BioMed Research International
Retraction (1 page), Article ID 9831386, Volume 2024 (2024)

Contents

Contents

Contents

Retraction

Retracted: Mechanism of RNA circHIPK3 Involved in Resistance of Lung Cancer Cells to Gefitinib

BioMed Research International

This article has been retracted by Hindawi following an investigation undertaken by the publisher [1]. This investigation has uncovered evidence of one or more of the following indicators of systematic manipulation of the publication process:

(1) Discrepancies in scope

(2) Discrepancies in the description of the research reported

(3) Discrepancies between the availability of data and the research described

(4) Inappropriate citations

(5) Incoherent, meaningless and/or irrelevant content included in the article

(6) Manipulated or compromised peer review

The presence of these indicators undermines our confidence in the integrity of the article's content and we cannot, therefore, vouch for its reliability. Please note that this notice is intended solely to alert readers that the content of this article is unreliable. We have not investigated whether authors were aware of or involved in the systematic manipulation of the publication process.

Wiley and Hindawi regrets that the usual quality checks did not identify these issues before publication and have since put additional measures in place to safeguard research integrity.

We wish to credit our own Research Integrity and Research Publishing teams and anonymous and named external researchers and research integrity experts for contributing to this investigation.

The corresponding author, as the representative of all authors, has been given the opportunity to register their agreement or disagreement to this retraction. We have kept a record of any response received.

References

[1] Y. Zhao, C. Zhang, H. Tang, X. Wu, and Q. Qi, "Mechanism of RNA circHIPK3 Involved in Resistance of Lung Cancer Cells to Gefitinib," *BioMed Research International*, vol. 2022, Article ID 4541918, 9 pages, 2022.

Retraction

Retracted: Correlation of Carotid Artery Intima-Media Thickness with Calcium and Phosphorus Metabolism, Parathyroid Hormone, Microinflammatory State, and Cardiovascular Disease

BioMed Research International

This article has been retracted by Hindawi following an investigation undertaken by the publisher [1]. This investigation has uncovered evidence of one or more of the following indicators of systematic manipulation of the publication process:

(1) Discrepancies in scope

(2) Discrepancies in the description of the research reported

(3) Discrepancies between the availability of data and the research described

(4) Inappropriate citations

(5) Incoherent, meaningless and/or irrelevant content included in the article

(6) Manipulated or compromised peer review

The presence of these indicators undermines our confidence in the integrity of the article's content and we cannot, therefore, vouch for its reliability. Please note that this notice is intended solely to alert readers that the content of this article is unreliable. We have not investigated whether authors were aware of or involved in the systematic manipulation of the publication process.

Wiley and Hindawi regrets that the usual quality checks did not identify these issues before publication and have since put additional measures in place to safeguard research integrity.

We wish to credit our own Research Integrity and Research Publishing teams and anonymous and named external researchers and research integrity experts for contributing to this investigation.

The corresponding author, as the representative of all authors, has been given the opportunity to register their agreement or disagreement to this retraction. We have kept a record of any response received.

References

[1] P. Huang, J. Tan, X. Gu et al., "Correlation of Carotid Artery Intima-Media Thickness with Calcium and Phosphorus Metabolism, Parathyroid Hormone, Microinflammatory State, and Cardiovascular Disease," *BioMed Research International*, vol. 2022, Article ID 2786147, 9 pages, 2022.

Retraction

Retracted: circZC3HAV1 Regulates TBC1D9 to Affect the Biological Behavior of Colorectal Cancer Cells

BioMed Research International

This article has been retracted by Hindawi following an investigation undertaken by the publisher [1]. This investigation has uncovered evidence of one or more of the following indicators of systematic manipulation of the publication process:

(1) Discrepancies in scope

(2) Discrepancies in the description of the research reported

(3) Discrepancies between the availability of data and the research described

(4) Inappropriate citations

(5) Incoherent, meaningless and/or irrelevant content included in the article

(6) Manipulated or compromised peer review

The presence of these indicators undermines our confidence in the integrity of the article's content and we cannot, therefore, vouch for its reliability. Please note that this notice is intended solely to alert readers that the content of this article is unreliable. We have not investigated whether authors were aware of or involved in the systematic manipulation of the publication process.

Wiley and Hindawi regrets that the usual quality checks did not identify these issues before publication and have since put additional measures in place to safeguard research integrity.

We wish to credit our own Research Integrity and Research Publishing teams and anonymous and named external researchers and research integrity experts for contributing to this investigation.

The corresponding author, as the representative of all authors, has been given the opportunity to register their agreement or disagreement to this retraction. We have kept a record of any response received.

References

[1] J. Zhang, Y. Xue, H. Gao et al., "circZC3HAV1 Regulates TBC1D9 to Affect the Biological Behavior of Colorectal Cancer Cells," *BioMed Research International*, vol. 2022, Article ID 7386946, 17 pages, 2022.

Retraction

Retracted: Understanding the Critical Role of Glycolysis-Related lncRNAs in Lung Adenocarcinoma Based on Three Molecular Subtypes

BioMed Research International

This article has been retracted by Hindawi following an investigation undertaken by the publisher [1]. This investigation has uncovered evidence of one or more of the following indicators of systematic manipulation of the publication process:

(1) Discrepancies in scope

(2) Discrepancies in the description of the research reported

(3) Discrepancies between the availability of data and the research described

(4) Inappropriate citations

(5) Incoherent, meaningless and/or irrelevant content included in the article

(6) Manipulated or compromised peer review

The presence of these indicators undermines our confidence in the integrity of the article's content and we cannot, therefore, vouch for its reliability. Please note that this notice is intended solely to alert readers that the content of this article is unreliable. We have not investigated whether authors were aware of or involved in the systematic manipulation of the publication process.

Wiley and Hindawi regrets that the usual quality checks did not identify these issues before publication and have since put additional measures in place to safeguard research integrity.

We wish to credit our own Research Integrity and Research Publishing teams and anonymous and named external researchers and research integrity experts for contributing to this investigation.

The corresponding author, as the representative of all authors, has been given the opportunity to register their agreement or disagreement to this retraction. We have kept a record of any response received.

References

[1] P. Cao, B. Zhao, Y. Xiao et al., "Understanding the Critical Role of Glycolysis-Related lncRNAs in Lung Adenocarcinoma Based on Three Molecular Subtypes," *BioMed Research International*, vol. 2022, Article ID 7587398, 36 pages, 2022.

Retraction

Retracted: Current Status of Malignant Tumors after Organ Transplantation

BioMed Research International

This article has been retracted by Hindawi following an investigation undertaken by the publisher [1]. This investigation has uncovered evidence of one or more of the following indicators of systematic manipulation of the publication process:

(1) Discrepancies in scope

(2) Discrepancies in the description of the research reported

(3) Discrepancies between the availability of data and the research described

(4) Inappropriate citations

(5) Incoherent, meaningless and/or irrelevant content included in the article

(6) Manipulated or compromised peer review

The presence of these indicators undermines our confidence in the integrity of the article's content and we cannot, therefore, vouch for its reliability. Please note that this notice is intended solely to alert readers that the content of this article is unreliable. We have not investigated whether authors were aware of or involved in the systematic manipulation of the publication process.

Wiley and Hindawi regrets that the usual quality checks did not identify these issues before publication and have since put additional measures in place to safeguard research integrity.

We wish to credit our own Research Integrity and Research Publishing teams and anonymous and named external researchers and research integrity experts for contributing to this investigation.

The corresponding author, as the representative of all authors, has been given the opportunity to register their agreement or disagreement to this retraction. We have kept a record of any response received.

References

[1] B. Shen, Z. Cen, M. Tan et al., "Current Status of Malignant Tumors after Organ Transplantation," *BioMed Research International*, vol. 2022, Article ID 5852451, 12 pages, 2022.

Retraction

Retracted: Evaluation of Liquid Biopsy in Patients with HER2-Positive Breast Cancer

BioMed Research International

This article has been retracted by Hindawi following an investigation undertaken by the publisher [1]. This investigation has uncovered evidence of one or more of the following indicators of systematic manipulation of the publication process:

(1) Discrepancies in scope

(2) Discrepancies in the description of the research reported

(3) Discrepancies between the availability of data and the research described

(4) Inappropriate citations

(5) Incoherent, meaningless and/or irrelevant content included in the article

(6) Manipulated or compromised peer review

The presence of these indicators undermines our confidence in the integrity of the article's content and we cannot, therefore, vouch for its reliability. Please note that this notice is intended solely to alert readers that the content of this article is unreliable. We have not investigated whether authors were aware of or involved in the systematic manipulation of the publication process.

Wiley and Hindawi regrets that the usual quality checks did not identify these issues before publication and have since put additional measures in place to safeguard research integrity.

We wish to credit our own Research Integrity and Research Publishing teams and anonymous and named external researchers and research integrity experts for contributing to this investigation.

The corresponding author, as the representative of all authors, has been given the opportunity to register their agreement or disagreement to this retraction. We have kept a record of any response received.

References

[1] J. Huai, M. Cao, Y. Jiang et al., "Evaluation of Liquid Biopsy in Patients with HER2-Positive Breast Cancer," *BioMed Research International*, vol. 2021, Article ID 6388492, 5 pages, 2021.

Hindawi

Retraction

Retracted: Silencing of Long Noncoding RNA HLA Complex P5 (*HCP5*) Suppresses Glioma Progression through the *HCP5*-miR-205-Vascular Endothelial Growth Factor A Feedback Loop

BioMed Research International

This article has been retracted by Hindawi following an investigation undertaken by the publisher [1]. This investigation has uncovered evidence of one or more of the following indicators of systematic manipulation of the publication process:

(1) Discrepancies in scope

(2) Discrepancies in the description of the research reported

(3) Discrepancies between the availability of data and the research described

(4) Inappropriate citations

(5) Incoherent, meaningless and/or irrelevant content included in the article

(6) Manipulated or compromised peer review

The presence of these indicators undermines our confidence in the integrity of the article's content and we cannot, therefore, vouch for its reliability. Please note that this notice is intended solely to alert readers that the content of this article is unreliable. We have not investigated whether authors were aware of or involved in the systematic manipulation of the publication process.

Wiley and Hindawi regrets that the usual quality checks did not identify these issues before publication and have since put additional measures in place to safeguard research integrity.

We wish to credit our own Research Integrity and Research Publishing teams and anonymous and named external researchers and research integrity experts for contributing to this investigation.

The corresponding author, as the representative of all authors, has been given the opportunity to register their agreement or disagreement to this retraction. We have kept a record of any response received.

References

[1] R. Cheng, L. Ji, H. Su et al., "Silencing of Long Noncoding RNA HLA Complex P5 (*HCP5*) Suppresses Glioma Progression through the *HCP5*-miR-205-Vascular Endothelial Growth Factor A Feedback Loop," *BioMed Research International*, vol. 2022, Article ID 3092063, 14 pages, 2022.

Retraction

Retracted: Mechanism of Sevoflurane Anesthesia under Hypothermic Cardiopulmonary Bypass on Postoperative Atrial Fibrillation Rhythm in Patients Undergoing Mitral Valve Replacement

BioMed Research International

This article has been retracted by Hindawi following an investigation undertaken by the publisher [1]. This investigation has uncovered evidence of one or more of the following indicators of systematic manipulation of the publication process:

(1) Discrepancies in scope

(2) Discrepancies in the description of the research reported

(3) Discrepancies between the availability of data and the research described

(4) Inappropriate citations

(5) Incoherent, meaningless and/or irrelevant content included in the article

(6) Manipulated or compromised peer review

The presence of these indicators undermines our confidence in the integrity of the article's content and we cannot, therefore, vouch for its reliability. Please note that this notice is intended solely to alert readers that the content of this article is unreliable. We have not investigated whether authors were aware of or involved in the systematic manipulation of the publication process.

Wiley and Hindawi regrets that the usual quality checks did not identify these issues before publication and have since put additional measures in place to safeguard research integrity.

We wish to credit our own Research Integrity and Research Publishing teams and anonymous and named external researchers and research integrity experts for contributing to this investigation.

The corresponding author, as the representative of all authors, has been given the opportunity to register their agreement or disagreement to this retraction. We have kept a record of any response received.

References

[1] H. Che, Y. Lv, F. Yao, F. Zhao, and L. Zhao, "Mechanism of Sevoflurane Anesthesia under Hypothermic Cardiopulmonary Bypass on Postoperative Atrial Fibrillation Rhythm in Patients Undergoing Mitral Valve Replacement," *BioMed Research International*, vol. 2022, Article ID 5312897, 8 pages, 2022.

Retraction

Retracted: Development of a 5-Gene Signature to Evaluate Lung Adenocarcinoma Prognosis Based on the Features of Cancer Stem Cells

BioMed Research International

This article has been retracted by Hindawi following an investigation undertaken by the publisher [1]. This investigation has uncovered evidence of one or more of the following indicators of systematic manipulation of the publication process:

(1) Discrepancies in scope

(2) Discrepancies in the description of the research reported

(3) Discrepancies between the availability of data and the research described

(4) Inappropriate citations

(5) Incoherent, meaningless and/or irrelevant content included in the article

(6) Manipulated or compromised peer review

The presence of these indicators undermines our confidence in the integrity of the article's content and we cannot, therefore, vouch for its reliability. Please note that this notice is intended solely to alert readers that the content of this article is unreliable. We have not investigated whether authors were aware of or involved in the systematic manipulation of the publication process.

Wiley and Hindawi regrets that the usual quality checks did not identify these issues before publication and have since put additional measures in place to safeguard research integrity.

We wish to credit our own Research Integrity and Research Publishing teams and anonymous and named external researchers and research integrity experts for contributing to this investigation.

The corresponding author, as the representative of all authors, has been given the opportunity to register their agreement or disagreement to this retraction. We have kept a record of any response received.

References

[1] R. Wan, H. Liao, J. Liu et al., "Development of a 5-Gene Signature to Evaluate Lung Adenocarcinoma Prognosis Based on the Features of Cancer Stem Cells," *BioMed Research International*, vol. 2022, Article ID 4404406, 28 pages, 2022.

Retraction

Retracted: Biomechanical Analysis of Different Internal Fixation Combined with Different Bone Grafting for Unstable Thoracolumbar Fractures in the Elderly

BioMed Research International

This article has been retracted by Hindawi following an investigation undertaken by the publisher [1]. This investigation has uncovered evidence of one or more of the following indicators of systematic manipulation of the publication process:

(1) Discrepancies in scope

(2) Discrepancies in the description of the research reported

(3) Discrepancies between the availability of data and the research described

(4) Inappropriate citations

(5) Incoherent, meaningless and/or irrelevant content included in the article

(6) Manipulated or compromised peer review

The presence of these indicators undermines our confidence in the integrity of the article's content and we cannot, therefore, vouch for its reliability. Please note that this notice is intended solely to alert readers that the content of this article is unreliable. We have not investigated whether authors were aware of or involved in the systematic manipulation of the publication process.

Wiley and Hindawi regrets that the usual quality checks did not identify these issues before publication and have since put additional measures in place to safeguard research integrity.

We wish to credit our own Research Integrity and Research Publishing teams and anonymous and named external researchers and research integrity experts for contributing to this investigation.

The corresponding author, as the representative of all authors, has been given the opportunity to register their agreement or disagreement to this retraction. We have kept a record of any response received.

References

[1] Q. Shang, Y. Jiang, W. Sheng et al., "Biomechanical Analysis of Different Internal Fixation Combined with Different Bone Grafting for Unstable Thoracolumbar Fractures in the Elderly," *BioMed Research International*, vol. 2022, Article ID 2863379, 13 pages, 2022.

Retraction

Retracted: Identification of lncRNA Biomarkers and LINC01198 Promotes Progression of Chronic Rhinosinusitis with Nasal Polyps through Sponge miR-6776-5p

BioMed Research International

This article has been retracted by Hindawi following an investigation undertaken by the publisher [1]. This investigation has uncovered evidence of one or more of the following indicators of systematic manipulation of the publication process:

(1) Discrepancies in scope

(2) Discrepancies in the description of the research reported

(3) Discrepancies between the availability of data and the research described

(4) Inappropriate citations

(5) Incoherent, meaningless and/or irrelevant content included in the article

(6) Manipulated or compromised peer review

The presence of these indicators undermines our confidence in the integrity of the article's content and we cannot, therefore, vouch for its reliability. Please note that this notice is intended solely to alert readers that the content of this article is unreliable. We have not investigated whether authors were aware of or involved in the systematic manipulation of the publication process.

Wiley and Hindawi regrets that the usual quality checks did not identify these issues before publication and have since put additional measures in place to safeguard research integrity.

We wish to credit our own Research Integrity and Research Publishing teams and anonymous and named external researchers and research integrity experts for contributing to this investigation.

The corresponding author, as the representative of all authors, has been given the opportunity to register their agreement or disagreement to this retraction. We have kept a record of any response received.

References

[1] X. Wang, X. Zhu, L. Peng, and Y. Zhao, "Identification of lncRNA Biomarkers and LINC01198 Promotes Progression of Chronic Rhinosinusitis with Nasal Polyps through Sponge miR-6776-5p," *BioMed Research International*, vol. 2022, Article ID 9469207, 27 pages, 2022.

Retraction

Retracted: Brusatol Inhibits Proliferation and Metastasis of Colorectal Cancer by Targeting and Reversing the RhoA/ROCK1 Pathway

BioMed Research International

This article has been retracted by Hindawi following an investigation undertaken by the publisher [1]. This investigation has uncovered evidence of one or more of the following indicators of systematic manipulation of the publication process:

(1) Discrepancies in scope

(2) Discrepancies in the description of the research reported

(3) Discrepancies between the availability of data and the research described

(4) Inappropriate citations

(5) Incoherent, meaningless and/or irrelevant content included in the article

(6) Manipulated or compromised peer review

The presence of these indicators undermines our confidence in the integrity of the article's content and we cannot, therefore, vouch for its reliability. Please note that this notice is intended solely to alert readers that the content of this article is unreliable. We have not investigated whether authors were aware of or involved in the systematic manipulation of the publication process.

Wiley and Hindawi regrets that the usual quality checks did not identify these issues before publication and have since put additional measures in place to safeguard research integrity.

We wish to credit our own Research Integrity and Research Publishing teams and anonymous and named external researchers and research integrity experts for contributing to this investigation.

The corresponding author, as the representative of all authors, has been given the opportunity to register their agreement or disagreement to this retraction. We have kept a record of any response received.

References

[1] R.-j. Lu, G.-z. Zhao, R. Jiang et al., "Brusatol Inhibits Proliferation and Metastasis of Colorectal Cancer by Targeting and Reversing the RhoA/ROCK1 Pathway," *BioMed Research International*, vol. 2022, Article ID 7132159, 13 pages, 2022.

Retraction

Retracted: Establishment and Validation of an MTORC1 Signaling-Related Gene Signature to Predict Overall Survival in Patients with Hepatocellular Carcinoma

BioMed Research International

This article has been retracted by Hindawi following an investigation undertaken by the publisher [1]. This investigation has uncovered evidence of one or more of the following indicators of systematic manipulation of the publication process:

(1) Discrepancies in scope

(2) Discrepancies in the description of the research reported

(3) Discrepancies between the availability of data and the research described

(4) Inappropriate citations

(5) Incoherent, meaningless and/or irrelevant content included in the article

(6) Manipulated or compromised peer review

The presence of these indicators undermines our confidence in the integrity of the article's content and we cannot, therefore, vouch for its reliability. Please note that this notice is intended solely to alert readers that the content of this article is unreliable. We have not investigated whether authors were aware of or involved in the systematic manipulation of the publication process.

Wiley and Hindawi regrets that the usual quality checks did not identify these issues before publication and have since put additional measures in place to safeguard research integrity.

We wish to credit our own Research Integrity and Research Publishing teams and anonymous and named external researchers and research integrity experts for contributing to this investigation.

The corresponding author, as the representative of all authors, has been given the opportunity to register their agreement or disagreement to this retraction. We have kept a record of any response received.

References

[1] Z. Yao, S. Wen, J. Luo, W. Hao, W. Liang, and Y. Chen, "Establishment and Validation of an MTORC1 Signaling-Related Gene Signature to Predict Overall Survival in Patients with Hepatocellular Carcinoma," *BioMed Research International*, vol. 2021, Article ID 6299472, 15 pages, 2021.

Retraction

Retracted: Prokineticins as a Prognostic Biomarker for Low-Grade Gliomas: A Study Based on The Cancer Genome Atlas Data

BioMed Research International

This article has been retracted by Hindawi following an investigation undertaken by the publisher [1]. This investigation has uncovered evidence of one or more of the following indicators of systematic manipulation of the publication process:

(1) Discrepancies in scope

(2) Discrepancies in the description of the research reported

(3) Discrepancies between the availability of data and the research described

(4) Inappropriate citations

(5) Incoherent, meaningless and/or irrelevant content included in the article

(6) Manipulated or compromised peer review

The presence of these indicators undermines our confidence in the integrity of the article's content and we cannot, therefore, vouch for its reliability. Please note that this notice is intended solely to alert readers that the content of this article is unreliable. We have not investigated whether authors were aware of or involved in the systematic manipulation of the publication process.

Wiley and Hindawi regrets that the usual quality checks did not identify these issues before publication and have since put additional measures in place to safeguard research integrity.

We wish to credit our own Research Integrity and Research Publishing teams and anonymous and named external researchers and research integrity experts for contributing to this investigation.

The corresponding author, as the representative of all authors, has been given the opportunity to register their agreement or disagreement to this retraction. We have kept a record of any response received.

References

[1] J. Zhong, D. Xiang, and X. Ma, "Prokineticins as a Prognostic Biomarker for Low-Grade Gliomas: A Study Based on The Cancer Genome Atlas Data," *BioMed Research International*, vol. 2022, Article ID 2309339, 12 pages, 2022.

Hindawi

Retraction

Retracted: LINC00518 Promotes Cell Malignant Behaviors via Influencing EIF4A3-Mediated mRNA Stability of MITF in Melanoma

BioMed Research International

This article has been retracted by Hindawi following an investigation undertaken by the publisher [1]. This investigation has uncovered evidence of one or more of the following indicators of systematic manipulation of the publication process:

(1) Discrepancies in scope

(2) Discrepancies in the description of the research reported

(3) Discrepancies between the availability of data and the research described

(4) Inappropriate citations

(5) Incoherent, meaningless and/or irrelevant content included in the article

(6) Manipulated or compromised peer review

The presence of these indicators undermines our confidence in the integrity of the article's content and we cannot, therefore, vouch for its reliability. Please note that this notice is intended solely to alert readers that the content of this article is unreliable. We have not investigated whether authors were aware of or involved in the systematic manipulation of the publication process.

Wiley and Hindawi regrets that the usual quality checks did not identify these issues before publication and have since put additional measures in place to safeguard research integrity.

We wish to credit our own Research Integrity and Research Publishing teams and anonymous and named external researchers and research integrity experts for contributing to this investigation.

The corresponding author, as the representative of all authors, has been given the opportunity to register their agreement or disagreement to this retraction. We have kept a record of any response received.

References

[1] P. Zhang, X. Liu, G. Pan et al., "LINC00518 Promotes Cell Malignant Behaviors via Influencing EIF4A3-Mediated mRNA Stability of MITF in Melanoma," *BioMed Research International*, vol. 2022, Article ID 3546795, 10 pages, 2022.

Retraction

Retracted: The Treatment Combining Antiangiogenesis with Chemoradiotherapy Impinges on the Peripheral Circulation Vascular Endothelial Cells and Therapeutic Effect in the Patients with Locally Advanced Nasopharyngeal Carcinoma

BioMed Research International

This article has been retracted by Hindawi following an investigation undertaken by the publisher [1]. This investigation has uncovered evidence of one or more of the following indicators of systematic manipulation of the publication process:

(1) Discrepancies in scope

(2) Discrepancies in the description of the research reported

(3) Discrepancies between the availability of data and the research described

(4) Inappropriate citations

(5) Incoherent, meaningless and/or irrelevant content included in the article

(6) Manipulated or compromised peer review

The presence of these indicators undermines our confidence in the integrity of the article's content and we cannot, therefore, vouch for its reliability. Please note that this notice is intended solely to alert readers that the content of this article is unreliable. We have not investigated whether authors were aware of or involved in the systematic manipulation of the publication process.

Wiley and Hindawi regrets that the usual quality checks did not identify these issues before publication and have since put additional measures in place to safeguard research integrity.

We wish to credit our own Research Integrity and Research Publishing teams and anonymous and named external researchers and research integrity experts for contributing to this investigation.

The corresponding author, as the representative of all authors, has been given the opportunity to register their agreement or disagreement to this retraction. We have kept a record of any response received.

References

[1] X. Gong, L. Wang, W. Wu et al., "The Treatment Combining Antiangiogenesis with Chemoradiotherapy Impinges on the Peripheral Circulation Vascular Endothelial Cells and Therapeutic Effect in the Patients with Locally Advanced Nasopharyngeal Carcinoma," *BioMed Research International*, vol. 2022, Article ID 1787854, 7 pages, 2022.

Retraction

Retracted: Immunotherapy Mechanism of Esophageal Squamous Cell Carcinoma with the Effect of STK11/AMPK Signaling Pathway

BioMed Research International

This article has been retracted by Hindawi following an investigation undertaken by the publisher [1]. This investigation has uncovered evidence of one or more of the following indicators of systematic manipulation of the publication process:

(1) Discrepancies in scope

(2) Discrepancies in the description of the research reported

(3) Discrepancies between the availability of data and the research described

(4) Inappropriate citations

(5) Incoherent, meaningless and/or irrelevant content included in the article

(6) Manipulated or compromised peer review

The presence of these indicators undermines our confidence in the integrity of the article's content and we cannot, therefore, vouch for its reliability. Please note that this notice is intended solely to alert readers that the content of this article is unreliable. We have not investigated whether authors were aware of or involved in the systematic manipulation of the publication process.

Wiley and Hindawi regrets that the usual quality checks did not identify these issues before publication and have since put additional measures in place to safeguard research integrity.

We wish to credit our own Research Integrity and Research Publishing teams and anonymous and named external researchers and research integrity experts for contributing to this investigation.

The corresponding author, as the representative of all authors, has been given the opportunity to register their agreement or disagreement to this retraction. We have kept a record of any response received.

References

[1] Y. Xia, P. Wang, Y. Ye et al., "Immunotherapy Mechanism of Esophageal Squamous Cell Carcinoma with the Effect of STK11/AMPK Signaling Pathway," *BioMed Research International*, vol. 2022, Article ID 8636527, 8 pages, 2022.

Retraction

Retracted: The Expression Profile of miRNA in Glioma and the Role of miR-339-5p in Glioma

BioMed Research International

This article has been retracted by Hindawi following an investigation undertaken by the publisher [1]. This investigation has uncovered evidence of one or more of the following indicators of systematic manipulation of the publication process:

(1) Discrepancies in scope

(2) Discrepancies in the description of the research reported

(3) Discrepancies between the availability of data and the research described

(4) Inappropriate citations

(5) Incoherent, meaningless and/or irrelevant content included in the article

(6) Manipulated or compromised peer review

The presence of these indicators undermines our confidence in the integrity of the article's content and we cannot, therefore, vouch for its reliability. Please note that this notice is intended solely to alert readers that the content of this article is unreliable. We have not investigated whether authors were aware of or involved in the systematic manipulation of the publication process.

Wiley and Hindawi regrets that the usual quality checks did not identify these issues before publication and have since put additional measures in place to safeguard research integrity.

We wish to credit our own Research Integrity and Research Publishing teams and anonymous and named external researchers and research integrity experts for contributing to this investigation.

The corresponding author, as the representative of all authors, has been given the opportunity to register their agreement or disagreement to this retraction. We have kept a record of any response received.

References

[1] J. Lin, S. Wang, H. Shen, and B. Zheng, "The Expression Profile of miRNA in Glioma and the Role of miR-339-5p in Glioma," *BioMed Research International*, vol. 2022, Article ID 4085039, 8 pages, 2022.

Hindawi

Retraction

Retracted: Mechanism of Gegen Qinlian Decoction Regulating ABTB1 Expression in Colorectal Cancer Metastasis Based on PI3K/AKT/FOXO1 Pathway

BioMed Research International

This article has been retracted by Hindawi following an investigation undertaken by the publisher [1]. This investigation has uncovered evidence of one or more of the following indicators of systematic manipulation of the publication process:

(1) Discrepancies in scope

(2) Discrepancies in the description of the research reported

(3) Discrepancies between the availability of data and the research described

(4) Inappropriate citations

(5) Incoherent, meaningless and/or irrelevant content included in the article

(6) Manipulated or compromised peer review

The presence of these indicators undermines our confidence in the integrity of the article's content and we cannot, therefore, vouch for its reliability. Please note that this notice is intended solely to alert readers that the content of this article is unreliable. We have not investigated whether authors were aware of or involved in the systematic manipulation of the publication process.

Wiley and Hindawi regrets that the usual quality checks did not identify these issues before publication and have since put additional measures in place to safeguard research integrity.

We wish to credit our own Research Integrity and Research Publishing teams and anonymous and named external researchers and research integrity experts for contributing to this investigation.

The corresponding author, as the representative of all authors, has been given the opportunity to register their agreement or disagreement to this retraction. We have kept a record of any response received.

References

[1] F. Li, L. Chen, J. Zheng et al., "Mechanism of Gegen Qinlian Decoction Regulating ABTB1 Expression in Colorectal Cancer Metastasis Based on PI3K/AKT/FOXO1 Pathway," *BioMed Research International*, vol. 2022, Article ID 8131531, 7 pages, 2022.

Retraction

Retracted: Efficacy of Aidi Injection and Brucea javanica Oil Emulsion Injection in Rectal Cancer during CapeOX Adjuvant Chemotherapy

BioMed Research International

This article has been retracted by Hindawi following an investigation undertaken by the publisher [1]. This investigation has uncovered evidence of one or more of the following indicators of systematic manipulation of the publication process:

(1) Discrepancies in scope

(2) Discrepancies in the description of the research reported

(3) Discrepancies between the availability of data and the research described

(4) Inappropriate citations

(5) Incoherent, meaningless and/or irrelevant content included in the article

(6) Manipulated or compromised peer review

The presence of these indicators undermines our confidence in the integrity of the article's content and we cannot, therefore, vouch for its reliability. Please note that this notice is intended solely to alert readers that the content of this article is unreliable. We have not investigated whether authors were aware of or involved in the systematic manipulation of the publication process.

Wiley and Hindawi regrets that the usual quality checks did not identify these issues before publication and have since put additional measures in place to safeguard research integrity.

We wish to credit our own Research Integrity and Research Publishing teams and anonymous and named external researchers and research integrity experts for contributing to this investigation.

The corresponding author, as the representative of all authors, has been given the opportunity to register their agreement or disagreement to this retraction. We have kept a record of any response received.

References

[1] W. Meng, X. Zeng, Y. Gao, Q. Chen, and L. Bai, "Efficacy of Aidi Injection and Brucea javanica Oil Emulsion Injection in Rectal Cancer during CapeOX Adjuvant Chemotherapy," *BioMed Research International*, vol. 2021, Article ID 2033353, 8 pages, 2021.

Retraction

Retracted: DNM1: A Prognostic Biomarker Associated with Immune Infiltration in Colon Cancer—A Study Based on TCGA Database

BioMed Research International

This article has been retracted by Hindawi following an investigation undertaken by the publisher [1]. This investigation has uncovered evidence of one or more of the following indicators of systematic manipulation of the publication process:

(1) Discrepancies in scope

(2) Discrepancies in the description of the research reported

(3) Discrepancies between the availability of data and the research described

(4) Inappropriate citations

(5) Incoherent, meaningless and/or irrelevant content included in the article

(6) Manipulated or compromised peer review

The presence of these indicators undermines our confidence in the integrity of the article's content and we cannot, therefore, vouch for its reliability. Please note that this notice is intended solely to alert readers that the content of this article is unreliable. We have not investigated whether authors were aware of or involved in the systematic manipulation of the publication process.

Wiley and Hindawi regrets that the usual quality checks did not identify these issues before publication and have since put additional measures in place to safeguard research integrity.

We wish to credit our own Research Integrity and Research Publishing teams and anonymous and named external researchers and research integrity experts for contributing to this investigation.

The corresponding author, as the representative of all authors, has been given the opportunity to register their agreement or disagreement to this retraction. We have kept a record of any response received.

References

[1] M. Hu, J. Gu, W. Su et al., "DNM1: A Prognostic Biomarker Associated with Immune Infiltration in Colon Cancer—A Study Based on TCGA Database," *BioMed Research International*, vol. 2021, Article ID 4896106, 9 pages, 2021.

Retraction

Retracted: Identification of Cigarette Smoking-Related Novel Biomarkers in Lung Adenocarcinoma

BioMed Research International

This article has been retracted by Hindawi following an investigation undertaken by the publisher [1]. This investigation has uncovered evidence of one or more of the following indicators of systematic manipulation of the publication process:

(1) Discrepancies in scope

(2) Discrepancies in the description of the research reported

(3) Discrepancies between the availability of data and the research described

(4) Inappropriate citations

(5) Incoherent, meaningless and/or irrelevant content included in the article

(6) Manipulated or compromised peer review

The presence of these indicators undermines our confidence in the integrity of the article's content and we cannot, therefore, vouch for its reliability. Please note that this notice is intended solely to alert readers that the content of this article is unreliable. We have not investigated whether authors were aware of or involved in the systematic manipulation of the publication process.

Wiley and Hindawi regrets that the usual quality checks did not identify these issues before publication and have since put additional measures in place to safeguard research integrity.

We wish to credit our own Research Integrity and Research Publishing teams and anonymous and named external researchers and research integrity experts for contributing to this investigation.

The corresponding author, as the representative of all authors, has been given the opportunity to register their agreement or disagreement to this retraction. We have kept a record of any response received.

References

[1] Y. Zhang, Q. Wang, T. Zhu, and H. Chen, "Identification of Cigarette Smoking-Related Novel Biomarkers in Lung Adenocarcinoma," *BioMed Research International*, vol. 2022, Article ID 9170722, 10 pages, 2022.

Retraction

Retracted: The Valuable Role of ARMC1 in Invasive Breast Cancer as a Novel Biomarker

BioMed Research International

This article has been retracted by Hindawi following an investigation undertaken by the publisher [1]. This investigation has uncovered evidence of one or more of the following indicators of systematic manipulation of the publication process:

(1) Discrepancies in scope

(2) Discrepancies in the description of the research reported

(3) Discrepancies between the availability of data and the research described

(4) Inappropriate citations

(5) Incoherent, meaningless and/or irrelevant content included in the article

(6) Manipulated or compromised peer review

The presence of these indicators undermines our confidence in the integrity of the article's content and we cannot, therefore, vouch for its reliability. Please note that this notice is intended solely to alert readers that the content of this article is unreliable. We have not investigated whether authors were aware of or involved in the systematic manipulation of the publication process.

Wiley and Hindawi regrets that the usual quality checks did not identify these issues before publication and have since put additional measures in place to safeguard research integrity.

We wish to credit our own Research Integrity and Research Publishing teams and anonymous and named external researchers and research integrity experts for contributing to this investigation.

The corresponding author, as the representative of all authors, has been given the opportunity to register their agreement or disagreement to this retraction. We have kept a record of any response received.

References

[1] Y. Gan, F. Zhong, H. Wang, and L. Li, "The Valuable Role of ARMC1 in Invasive Breast Cancer as a Novel Biomarker," *BioMed Research International*, vol. 2022, Article ID 1740295, 18 pages, 2022.

Hindawi

Retraction

Retracted: Study on Inflammatory Factors in Aneurysmal Perimembranous Ventricular Septal Defect in Congenital Heart Disease

BioMed Research International

This article has been retracted by Hindawi following an investigation undertaken by the publisher [1]. This investigation has uncovered evidence of one or more of the following indicators of systematic manipulation of the publication process:

(1) Discrepancies in scope

(2) Discrepancies in the description of the research reported

(3) Discrepancies between the availability of data and the research described

(4) Inappropriate citations

(5) Incoherent, meaningless and/or irrelevant content included in the article

(6) Manipulated or compromised peer review

The presence of these indicators undermines our confidence in the integrity of the article's content and we cannot, therefore, vouch for its reliability. Please note that this notice is intended solely to alert readers that the content of this article is unreliable. We have not investigated whether authors were aware of or involved in the systematic manipulation of the publication process.

Wiley and Hindawi regrets that the usual quality checks did not identify these issues before publication and have since put additional measures in place to safeguard research integrity.

We wish to credit our own Research Integrity and Research Publishing teams and anonymous and named external researchers and research integrity experts for contributing to this investigation.

The corresponding author, as the representative of all authors, has been given the opportunity to register their agreement or disagreement to this retraction. We have kept a record of any response received.

References

[1] J. Zhou, Y. Liu, J. Wang et al., "Study on Inflammatory Factors in Aneurysmal Perimembranous Ventricular Septal Defect in Congenital Heart Disease," *BioMed Research International*, vol. 2022, Article ID 8282624, 5 pages, 2022.

Retraction

Retracted: hsa_circ_0084811 Regulates Cell Proliferation and Apoptosis in Retinoblastoma through miR-18a-5p/miR-18b-5p/E2F5 Axis

BioMed Research International

This article has been retracted by Hindawi following an investigation undertaken by the publisher [1]. This investigation has uncovered evidence of one or more of the following indicators of systematic manipulation of the publication process:

(1) Discrepancies in scope

(2) Discrepancies in the description of the research reported

(3) Discrepancies between the availability of data and the research described

(4) Inappropriate citations

(5) Incoherent, meaningless and/or irrelevant content included in the article

(6) Manipulated or compromised peer review

The presence of these indicators undermines our confidence in the integrity of the article's content and we cannot, therefore, vouch for its reliability. Please note that this notice is intended solely to alert readers that the content of this article is unreliable. We have not investigated whether authors were aware of or involved in the systematic manipulation of the publication process.

Wiley and Hindawi regrets that the usual quality checks did not identify these issues before publication and have since put additional measures in place to safeguard research integrity.

We wish to credit our own Research Integrity and Research Publishing teams and anonymous and named external researchers and research integrity experts for contributing to this investigation.

The corresponding author, as the representative of all authors, has been given the opportunity to register their agreement or disagreement to this retraction. We have kept a record of any response received.

References

[1] G. Jiang, M. Qu, L. Kong, X. Song, and S. Jiang, "hsa_circ_0084811 Regulates Cell Proliferation and Apoptosis in Retinoblastoma through miR-18a-5p/miR-18b-5p/E2F5 Axis," *BioMed Research International*, vol. 2022, Article ID 6918396, 16 pages, 2022.

Retraction

Retracted: Effect of FLOT2 Gene Expression on Invasion and Metastasis of Colorectal Cancer and Its Molecular Mechanism under Nanotechnology and RNA Interference

BioMed Research International

This article has been retracted by Hindawi following an investigation undertaken by the publisher [1]. This investigation has uncovered evidence of one or more of the following indicators of systematic manipulation of the publication process:

(1) Discrepancies in scope

(2) Discrepancies in the description of the research reported

(3) Discrepancies between the availability of data and the research described

(4) Inappropriate citations

(5) Incoherent, meaningless and/or irrelevant content included in the article

(6) Manipulated or compromised peer review

The presence of these indicators undermines our confidence in the integrity of the article's content and we cannot, therefore, vouch for its reliability. Please note that this notice is intended solely to alert readers that the content of this article is unreliable. We have not investigated whether authors were aware of or involved in the systematic manipulation of the publication process.

Wiley and Hindawi regrets that the usual quality checks did not identify these issues before publication and have since put additional measures in place to safeguard research integrity.

We wish to credit our own Research Integrity and Research Publishing teams and anonymous and named external researchers and research integrity experts for contributing to this investigation.

The corresponding author, as the representative of all authors, has been given the opportunity to register their agreement or disagreement to this retraction. We have kept a record of any response received.

References

[1] C. Zhong, F. Zheng, S. Ye, G. Gao, P. He, and D. Liu, "Effect of FLOT2 Gene Expression on Invasion and Metastasis of Colorectal Cancer and Its Molecular Mechanism under Nanotechnology and RNA Interference," *BioMed Research International*, vol. 2022, Article ID 2897338, 11 pages, 2022.

Retraction

Retracted: Discovery of New Therapeutic Targets for Osteosarcoma Treatment Based on Immune-Related lncRNAs in the Tumor Microenvironment

BioMed Research International

This article has been retracted by Hindawi following an investigation undertaken by the publisher [1]. This investigation has uncovered evidence of one or more of the following indicators of systematic manipulation of the publication process:

(1) Discrepancies in scope

(2) Discrepancies in the description of the research reported

(3) Discrepancies between the availability of data and the research described

(4) Inappropriate citations

(5) Incoherent, meaningless and/or irrelevant content included in the article

(6) Manipulated or compromised peer review

The presence of these indicators undermines our confidence in the integrity of the article's content and we cannot, therefore, vouch for its reliability. Please note that this notice is intended solely to alert readers that the content of this article is unreliable. We have not investigated whether authors were aware of or involved in the systematic manipulation of the publication process.

Wiley and Hindawi regrets that the usual quality checks did not identify these issues before publication and have since put additional measures in place to safeguard research integrity.

We wish to credit our own Research Integrity and Research Publishing teams and anonymous and named external researchers and research integrity experts for contributing to this investigation.

The corresponding author, as the representative of all authors, has been given the opportunity to register their agreement or disagreement to this retraction. We have kept a record of any response received.

References

[1] R. Fu and X. Hong, "Discovery of New Therapeutic Targets for Osteosarcoma Treatment Based on Immune-Related lncRNAs in the Tumor Microenvironment," *BioMed Research International*, vol. 2022, Article ID 3113857, 13 pages, 2022.

Retraction

Retracted: lncRNA MIR4435-2HG Accelerates the Development of Bladder Cancer through Enhancing IQGAP3 and CDCA5 Expression

BioMed Research International

This article has been retracted by Hindawi following an investigation undertaken by the publisher [1]. This investigation has uncovered evidence of one or more of the following indicators of systematic manipulation of the publication process:

(1) Discrepancies in scope

(2) Discrepancies in the description of the research reported

(3) Discrepancies between the availability of data and the research described

(4) Inappropriate citations

(5) Incoherent, meaningless and/or irrelevant content included in the article

(6) Manipulated or compromised peer review

The presence of these indicators undermines our confidence in the integrity of the article's content and we cannot, therefore, vouch for its reliability. Please note that this notice is intended solely to alert readers that the content of this article is unreliable. We have not investigated whether authors were aware of or involved in the systematic manipulation of the publication process.

Wiley and Hindawi regrets that the usual quality checks did not identify these issues before publication and have since put additional measures in place to safeguard research integrity.

We wish to credit our own Research Integrity and Research Publishing teams and anonymous and named external researchers and research integrity experts for contributing to this investigation.

The corresponding author, as the representative of all authors, has been given the opportunity to register their agreement or disagreement to this retraction. We have kept a record of any response received.

References

[1] T. Yang, Y. Li, G. Wang et al., "lncRNA MIR4435-2HG Accelerates the Development of Bladder Cancer through Enhancing IQGAP3 and CDCA5 Expression," *BioMed Research International*, vol. 2022, Article ID 3858249, 17 pages, 2022.

Retraction

Retracted: LINC00707 Promotes Cell Proliferation in Cervical Cancer via the miR-374c-5p/SDC4 Axis

BioMed Research International

This article has been retracted by Hindawi following an investigation undertaken by the publisher [1]. This investigation has uncovered evidence of one or more of the following indicators of systematic manipulation of the publication process:

(1) Discrepancies in scope

(2) Discrepancies in the description of the research reported

(3) Discrepancies between the availability of data and the research described

(4) Inappropriate citations

(5) Incoherent, meaningless and/or irrelevant content included in the article

(6) Manipulated or compromised peer review

The presence of these indicators undermines our confidence in the integrity of the article's content and we cannot, therefore, vouch for its reliability. Please note that this notice is intended solely to alert readers that the content of this article is unreliable. We have not investigated whether authors were aware of or involved in the systematic manipulation of the publication process.

Wiley and Hindawi regrets that the usual quality checks did not identify these issues before publication and have since put additional measures in place to safeguard research integrity.

We wish to credit our own Research Integrity and Research Publishing teams and anonymous and named external researchers and research integrity experts for contributing to this investigation.

The corresponding author, as the representative of all authors, has been given the opportunity to register their agreement or disagreement to this retraction. We have kept a record of any response received.

References

[1] F. Fang, C. Guo, W. Zheng, and Q. Li, "LINC00707 Promotes Cell Proliferation in Cervical Cancer via the miR-374c-5p/SDC4 Axis," *BioMed Research International*, vol. 2022, Article ID 5793912, 12 pages, 2022.

Retraction

Retracted: circZC3HAV1 Regulates TBC1D9 to Affect the Biological Behavior of Colorectal Cancer Cells

BioMed Research International

This article has been retracted by Hindawi following an investigation undertaken by the publisher [1]. This investigation has uncovered evidence of one or more of the following indicators of systematic manipulation of the publication process:

(1) Discrepancies in scope

(2) Discrepancies in the description of the research reported

(3) Discrepancies between the availability of data and the research described

(4) Inappropriate citations

(5) Incoherent, meaningless and/or irrelevant content included in the article

(6) Manipulated or compromised peer review

The presence of these indicators undermines our confidence in the integrity of the article's content and we cannot, therefore, vouch for its reliability. Please note that this notice is intended solely to alert readers that the content of this article is unreliable. We have not investigated whether authors were aware of or involved in the systematic manipulation of the publication process.

Wiley and Hindawi regrets that the usual quality checks did not identify these issues before publication and have since put additional measures in place to safeguard research integrity.

We wish to credit our own Research Integrity and Research Publishing teams and anonymous and named external researchers and research integrity experts for contributing to this investigation.

The corresponding author, as the representative of all authors, has been given the opportunity to register their agreement or disagreement to this retraction. We have kept a record of any response received.

References

[1] J. Zhang, Y. Xue, H. Gao et al., "circZC3HAV1 Regulates TBC1D9 to Affect the Biological Behavior of Colorectal Cancer Cells," *BioMed Research International*, vol. 2022, Article ID 7386946, 17 pages, 2022.

Research Article

circZC3HAV1 Regulates TBC1D9 to Affect the Biological Behavior of Colorectal Cancer Cells

Jianxian Zhang,[1] Yan Xue,[2] Hengling Gao,[1] Yunxi Yu,[3] Huabin Cheng,[1] Xukun Lv,[1] and Ke Ke [4]

[1]*Department of Gastrointestinal Surgery, The Second People's Hospital of Liaocheng, Liaocheng, 252600 Shandong, China*
[2]*Department of Gastroenterology, The Second People's Hospital of Liaocheng, Liaocheng, 252600 Shandong, China*
[3]*Department of Emergency, Huangshi Hospital of Traditional Chinese Medicine (Municipal Infectious Disease Hospital),
Huangshi, China*
[4]*Puai Hospital of Huangshi Central Hospital of East Hubei Medical Group, Affiliated Hospital of Hubei Institute of Technology,
Huangshi, 435000 Hubei, China*

Correspondence should be addressed to Ke Ke; 1657218286@qq.com

Background. Colorectal cancer (CRC) is one of the most frequently diagnosed cancers all over the world, which accounts for a large proportion of cancer-associated deaths. The regulatory function of circular RNAs (circRNAs) has been affirmed in diverse cancers. circ_0082628, named circRNA zinc finger CCCH-type containing antiviral 1 (circZC3HAV1), has been discovered to be significantly downregulated in CRC tissues. Nevertheless, the function and mechanism of circZC3HAV1 in CRC remain unclear. *Purpose.* We targeted at studying the specific role and mechanism of circZC3HAV1 in CRC cells. *Methods.* The expression of the genes was detected by quantitative real-time polymerase chain reaction (qPCR). The binding relationship among different genes was verified by mechanism assays. Functional assays were carried out to reveal the role of different RNAs in CRC cell malignant behaviors. *Results.* circZC3HAV1 was significantly downregulated in CRC cells. circZC3HAV1 overexpression hampered CRC cell migratory and invasive abilities. As for the mechanism, circZC3HAV1 competitively bound with microRNA-146b-3p (miR-146b-3p) to enhance the expression of TBC1 domain family member 9 (TBC1D9). Rescue assays demonstrated circZC3HAV1 sponged miR-146b-3p and upregulated TBC1D9 to restrict migration and invasion of CRC cells. *Conclusion.* circZC3HAV1 could upregulate TBC1D9 via absorbing miR-146b-3p, consequently inhibiting migratory and invasive capabilities of CRC cells.

1. Introduction

Colorectal cancer (CRC) is a common diagnosed malignancy in both genders in the world. Although improvements have been achieved in diagnostic and therapeutic methods, CRC still leads to cancer-related deaths significantly [1]. Hence, it is important to understand the potential regulatory mechanism underlying CRC in order to develop effective treatments.

Circular RNAs (circRNAs) belong to noncoding RNAs with a covalently closed structure that are derived from back-splicing [2]. The regulatory function of circRNAs has

been affirmed in diverse cancers. For instance, circRNA_0000392 contributes to CRC development through the miR-193a-5p/PIK3R3/AKT axis [3]. Exosomal circPACRGL promotes CRC progression through the miR-142-3p/miR-506-3p/TGF-β1 pathway [4]. Moreover, circHIPK3 prompts CRC growth and metastasis via sponging miR-7 [5]. Therefore, to find out a novel circRNA and uncover its role and potential regulatory mechanism in CRC are of interest.

MicroRNAs (miRNAs) refer to small noncoding RNAs which could repress or degrade target messenger RNAs (mRNAs) [6]. mRNAs have become a promising class of drugs for all kinds of therapeutic applications in the past

few years [7]. It has been reported that the competing endogenous RNA (ceRNA) network (circRNA-miRNA-mRNA) is implicated in various cancers including squamous cell carcinoma [8], melanoma [9], and lung adenocarcinoma [10]. CRC has been reported to be regulated by ceRNA pattern as well. For example, circ_001680 influences the proliferative and migratory abilities of CRC through regulating BMI1 mRNA targeted by miR-340 [11]. circCAMSAP1 facilitates CRC tumor growth via modulation of the miR-328-5p/E2F1 pathway [12]. Furthermore, hsa_circRNA_002144 sponges miR-615-5p to upregulate LARP1, consequently promoting CRC progression [13]. Hence, whether ceRNA network is involved in the malignant behaviors of CRC cells is worthy to be unveiled.

In summary, the main focusing point of our research was to study the role and underlying mechanism of a novel circRNA in CRC, which might provide new potential biomarkers or therapeutic targets for CRC.

2. Materials and Methods

2.1. Cell Culture. Human CRC cell lines (NCI-H508, RKO, and CW-2) were procured from Cell Resource Center, Peking Union Medical College. Human colonic epithelial cell line FHC was procured from Kunming Cell Bank, Chinese Academy of Sciences. 293T cells were acquired from National Institutes for Food and Drug Control. NCI-H508 and CW-2 cells were cultivated in RPMI 1640 (w/o Hepes)+10% fetal bovine serum (FBS). RKO cells were cultured in Minimal Essential Medium-Earle's Balanced Salt Solution (MEM-EBSS) +10% FBS. FHC cells were left to grow in basic medium+10% FBS. And 293T cells were cultivated in RPMI-1640 medium+10% FBS. All the cells were cultured with 5% CO_2 at 37°C.

2.2. Plasmid Transfection. In order to overexpress circZC3HAV1, pcDNA3.1-circZC3HAV1 vectors were synthesized in advance. Empty pcDNA3.1 worked as the negative control (NC), while for the overexpression of miR-146b-3p, miR-146b-3p mimics was used. For the knockdown of lemur tyrosine kinase 2 (LMTK2), TBC1 domain family member 9 (TBC1D9), tumor protein p53 inducible nuclear protein 2 (TP53INP2), and specific short hairpin RNAs (si-RNAs) were devised and constructed with nontargeting si-RNA (si-NC) as control. In accordance with the protocols, the transfections were performed with Lipofectamine 2000 (Invitrogen).

2.3. Quantitative Real-Time Polymerase Chain Reaction (qPCR). QPCR analysis was conducted based on previous protocol [14]. Based on the guidance of TRIzol reagent (Takara, Japan), the extraction of total RNA from cells was completed. The complementary DNA (cDNA) for miRNAs was generated utilizing TaqMan™ MicroRNA Reverse Transcription Kit, while the cDNA for circRNAs and mRNAs was obtained by means of PrimeScript RT Reagent Kit. QPCR reaction was conducted with SYBR Green PCR Kit followed by $2^{-\Delta\Delta Ct}$ method. β-Actin or U6 was used as internal reference for miRNA or circRNA/mRNA.

2.4. Transwell Assay. Transwell assay was conducted as previously described [15]. To assess the migratory ability, CRC cells were fixed on the upper part of 24-well Transwell chambers without Matrigel. As for invasion assay, the top compartment was coated with Matrigel. The lower chambers were added with FBS. After 24 h, cells that successfully migrated or invaded into the lower compartment were fixed by methanol for 15 min. In the end, cells stained by crystal violet was subjected to microscope observation.

2.5. Cell Counting Kit-8 (CCK-8) Assay. Cell viability was assessed via CCK-8 analysis following previous research [14]. CW-2 and RKO cells were seeded to 96-well plates for cultivation. Next, 10 μl of CCK-8 solution (Dojindo, Kumamoto, Japan) was added for 1 h incubation. Absorbance at 450 nm was detected with the microplate reader.

2.6. Wound Healing Assay. The assay was performed as previously described [16]. CW-2 or RKO cells were plated in 24-well plates. After cell confluence reached over 80%, pipette tip was taken to scratch the surface of cell layer. Afterwards, phosphate-buffered saline (PBS) was utilized to wash the detached cells. Subsequently, the width of wound at 0 h was captured and recorded. Next, cells were cultured for another 24 h, and the wound width was photographed and recorded.

2.7. Flow Cytometry Analysis. This assay was conducted following precious description [16]. Transfected CRC cells were harvested and rinsed with PBS. Later, cells were double stained with Annexin V-FITC/PI Apoptosis kit. Apoptotic rate of the cells was evaluated by a Cytoflex flow cytometer, and the data collected were analyzed with FlowJo software.

2.8. Fluorescence In Situ Hybridization (FISH) Assay. FISH assay was carried out according to published research [17]. The FISH probe prepared for circZC3HAV1 localization was synthesized by Ribobio (Guangzhou, China). The sequence of specific FISH probe was biotin-TTAATTACT TGATAAAGAAT-biotin. FISH probes were incubated with CW-2 and RKO cells in hybridization buffer. Afterwards, nuclei were counterstained with 4′,6-diamidino-2-phenylindole (DAPI). Finally, confocal laser scanning microscope (Zeiss LSM7 DUO) was adopted to observe the subcellular localization of circZC3HAV1.

2.9. Subcellular Fractionation Assay. PARIS™ Kit was applied to carry out the experiment in CW-2 and RKO cells. After centrifugation, cells were treated with cell disruption buffer. Eventually, the level of circZC3HAV1 in the cytoplasm and nucleus was examined by qPCR. β-Actin or U6 was used as nuclear or cytoplasmic control.

2.10. RNA Pull Down Assay. The Pierce™ RNA 3′ End Desthiobiotinylation Kit was used for conducting the experiments. miR-146b-3p with wild-type (WT) or mutant (MUT) sequence was marked with biotin. Cell lysates of 1 $\times 10^6$ cells were incubated with bio-NC, bio-miR-146b-3p-WT, or bio-miR-146b-3p-MUT for 1 h. Afterwards, precipitated RNAs were purified. The enrichment of circZC3HAV1 was examined by qPCR.

(a)

(b)

(c)
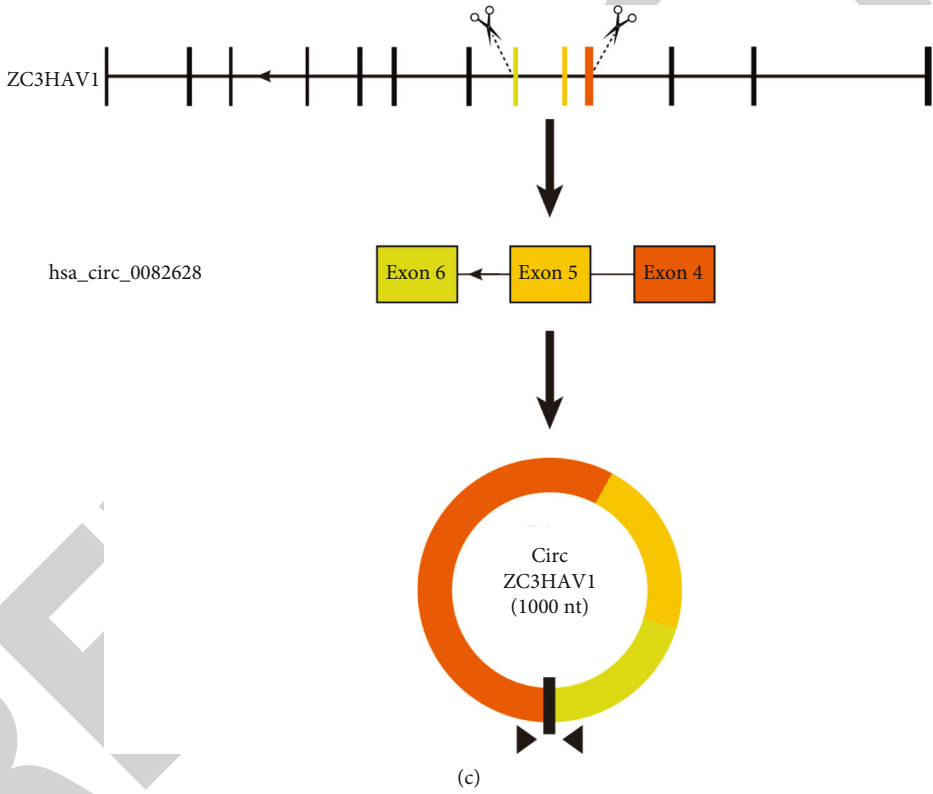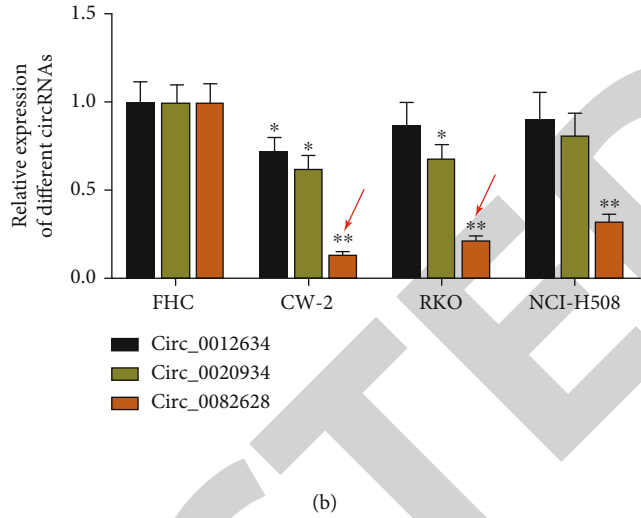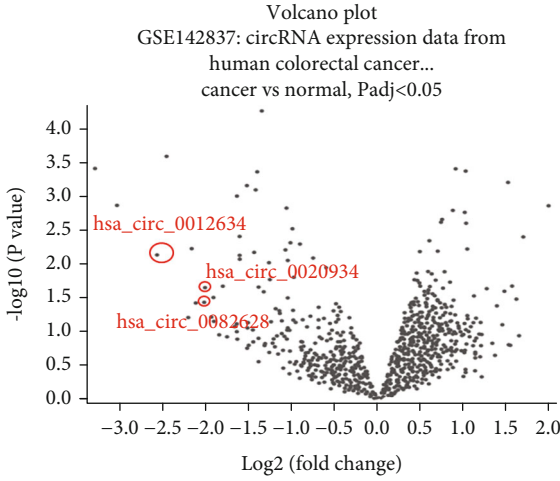
FIGURE 1: Continued.
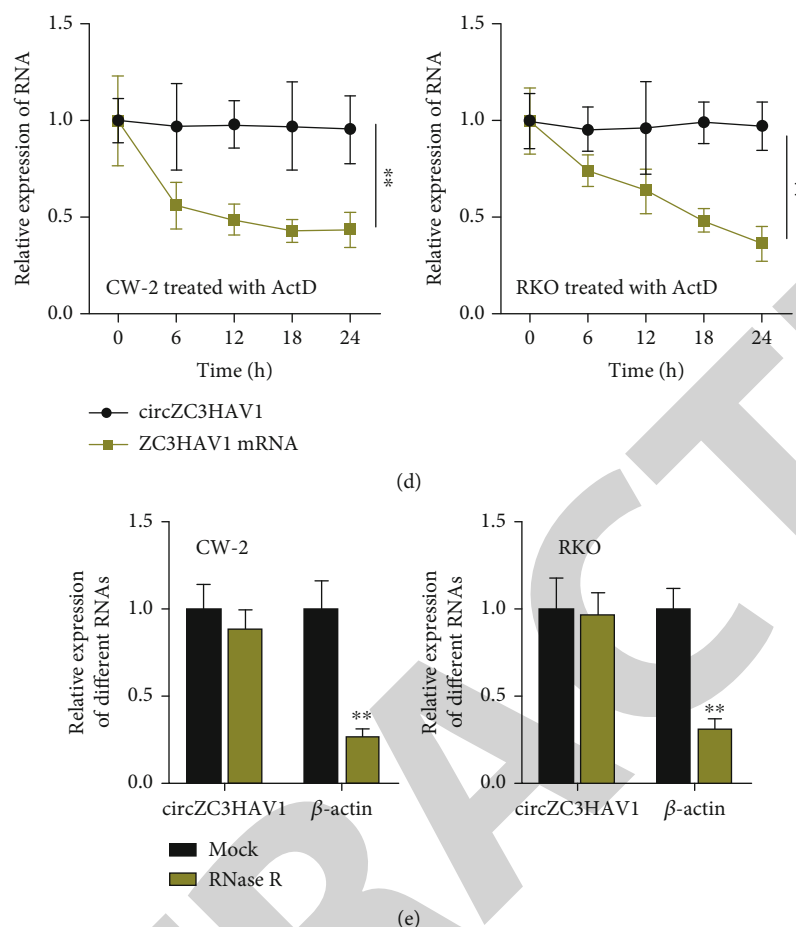
Figure 1: circZC3HAV1 has low expression level and a stable loop structure in CRC cells. (a) Three candidate circRNAs were picked from the GSE142837 dataset under specific conditions and showed in a volcano plot. (b) QPCR detected the expression of candidate circRNAs in human normal colorectal epithelial cells FHC and CRC cells (CW-2, RKO, and NCI-H508). (c) The diagram of hsa_circ_0082628 formation (ZC3HAV1 as the host gene) was demonstrated. (d) circZC3HAV1 and ZC3HAV1 expression levels were measured by qPCR in CRC cells treated with ActD. (e) circZC3HAV1 expression was measured by qPCR in CRC cells treated with RNase R. $^*P < 0.05$; $^{**}P < 0.01$.

2.11. RNA Binding Protein Immunoprecipitation (RIP). This assay was performed as previously described [18]. Using Magna RIP RNA-Binding Protein Immunoprecipitation Kit, RIP assay was carried out. CW-2 and RKO cells were lysed by RIP buffer first and then cocultured with anti-argonaute-2 (AGO2) or anti-immunoglobulin G (IgG) (NC group). Next, magnetic beads were added into cell lysates for incubation at 4°C, followed by RNA expression analysis through qPCR.

2.12. Luciferase Reporter Assay. The assay was carried out as previously described [18]. Full-length of TBC1D9 3′ untranslated regions (3′UTR) covering wild-type or mutant miR-146b-3p binding sites was inserted into pmirGLO luciferase vectors to construct pmirGLO+TBC1D9 3′UTR-WT/MUT. Similarly, pmirGLO+circZC3HAV1-WT/MUT plasmids were obtained. miR-146b-3p mimics or NC mimics was cotransfected with the abovementioned plasmids into CRC cells. After 48 h transfection, the luciferase activity was analyzed, utilizing the dual-luciferase reporter assay system.

2.13. Statistical Analyses. Each experiment was conducted in triplicate. Experimental data were subject to SPSS software analysis and shown as mean ± standard deviation (SD). The differences between two groups were compared by Student's *t*-test, while the differences among multiple groups were assessed by one-way or two-way analysis of variance (ANOVA). Statistic difference with *P* value less than 0.05 was regarded to be statistically significant.

3. Results

3.1. circZC3HAV1 Is Significantly Downregulated in CRC Cells. At first, we used the GEO database to look for the circRNAs that were remarkably downregulated in CRC tissues in comparison with normal tissues. Under the conditions of $P < 0.05$ and $|\log FC| \geq 2$, 8 circRNAs were picked. Among the 8 circRNAs, hsa_circ_0009361 and hsa_circ_0003266 have been studied in CRC [19] [20]; hsa_circ_0005927 has been studied in gastric cancer [21]; hsa_circ_0043278 has been studied in lung cancer [22]; and hsa_circ_0000775 has been studied in Alzheimer disease [23]. Therefore, hsa_circ_0012634, hsa_circ_0082628, and hsa_circ_

(a)

(b)

(c)

(d)

Figure 2: Continued.

(e)
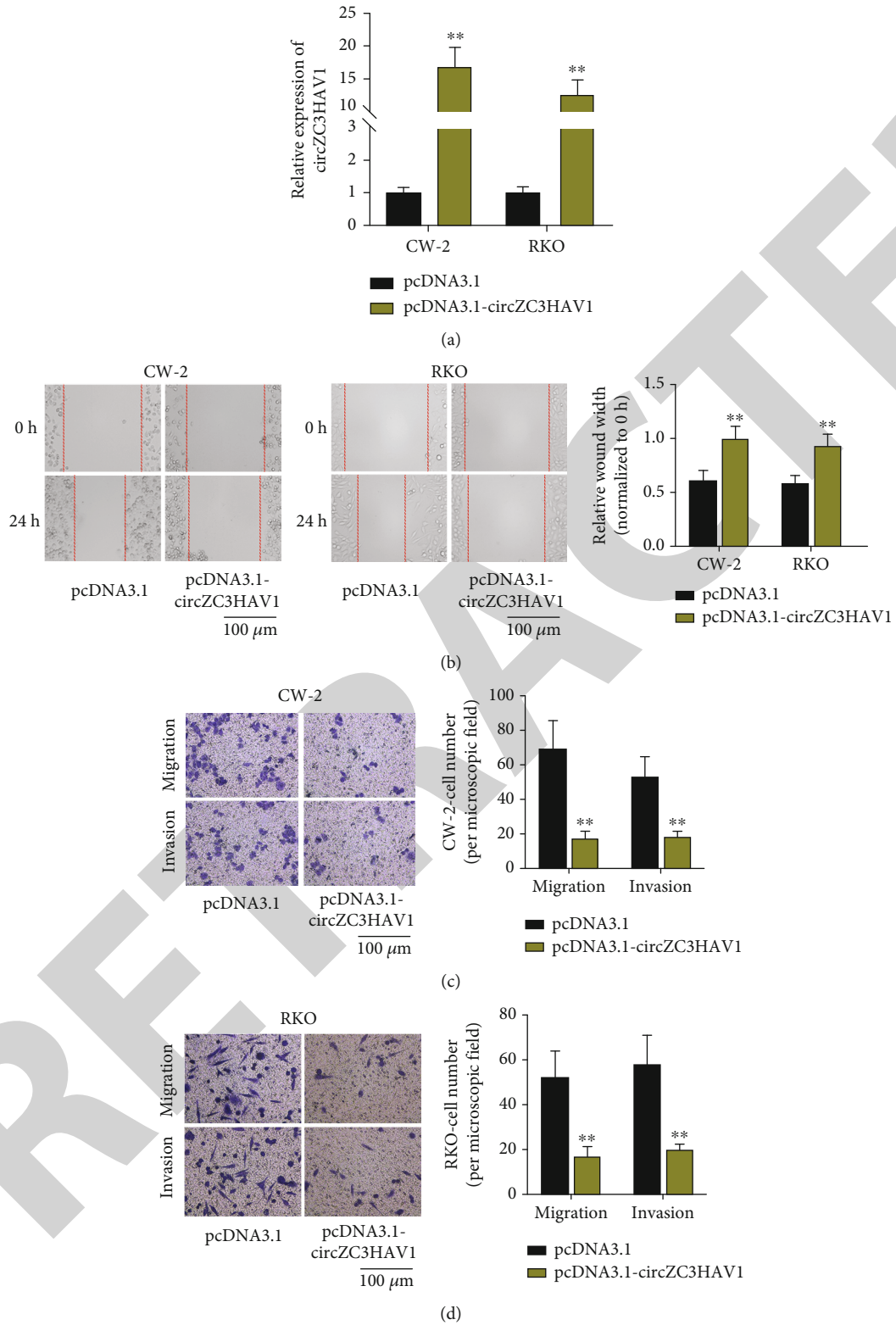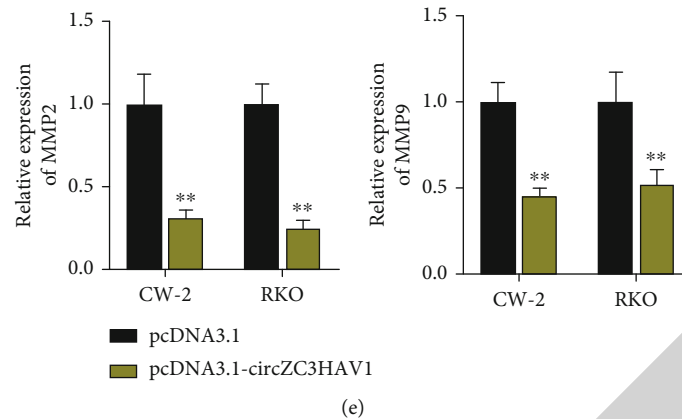
Figure 2: circZC3HAV1 upregulation contributes to the inhibition of CRC cell migration and invasion. (a) The overexpressing efficiency of pcDNA3.1-circZC3HAV1 was detected by qPCR. (b) Wound healing assay evaluated the effect of circZC3HAV1 on CRC cell migration. Scale bar: 100 μm. (c, d) Transwell assay was conducted to measure the migratory and invasive abilities of CRC cells upon circZC3HAV1 upregulation. Scale bar: 100 μm. (e) QPCR was implemented to examine the expression of MMP2 and MMP9 in CW-2 and RKO cells upon circZC3HAV1 overexpression. $^{**}P < 0.01$.

0020934 were chosen as candidates. The bioinformatics prediction of the candidate circRNA expression in CRC tissues and normal tissues was displayed (Figure 1(a) and Figure S1A–C). Then, the expression of the three circRNAs in human normal colorectal epithelial cells (FHC) and CRC cell lines (CW-2, RKO, and NCI-H508) was measured by qPCR. The result elucidated that the expression level of circ_0082628 was obviously lower in CRC cell lines than that of the other two circRNAs (Figure 1(b)). Therefore, circ_0082628 was chosen for further experiments. As its host gene is ZC3HAV1, we named it as circZC3HAV1 in our study. Loop formation diagram of circ_0082628 was shown in Figure 1(c). After CW-2 and RKO cells were treated with Actinomycin D (ActD), the expression of circZC3HAV1 and ZC3HAV1 mRNA was examined by qPCR. The outcome uncovered that the expression of ZC3HAV1 mRNA was noticeably decreased, while that of circZC3HAV1 was hardly changed (Figure 1(d)). Moreover, the expression of circZC3HAV1 and β-actin was examined by qPCR in CW-2 and RKO cells with RNase R treatment. We found that the circZC3HAV1 expression had no significant change, while β-actin expression dramatically declined (Figure 1(e)). To summarize, circZC3HAV1 has a stable loop structure and displays a significantly lower expression in CRC cells.

3.2. circZC3HAV1 Overexpression Impedes CRC Cell Migration and Invasion. In this part, we mainly delved into the specific influence of circZC3HAV1 on CRC cell malignant behaviors. At first, the high overexpression efficiency of pcDNA3.1-circZC3HAV1 was validated by qPCR in CRC cells (Figure 2(a)). Next, wound healing assay was done to reveal the migratory condition of CRC cells when circZC3HAV1 was overexpressed. We found that circZC3HAV1 overexpression inhibited cell migration (Figure 2(b)). Transwell assays were then implemented for the assessment of cell migratory and invasive abilities. The experimental results showed that overexpressing cir-

cZC3HAV1 restricted cell migration and invasion (Figures 2(c) and 2(d)). Moreover, qPCR was utilized to test the expression of invasion-linked factors (MMP2 and MMP9). We noticed expression of these factors decreased upon circZC3HAV1 augment (Figure 2(e)). CCK-8 was utilized to uncover the influence of overexpressing circZC3HAV1 on CRC cell proliferation. We found that circZC3HAV1 up-regulation had no obvious influence on cell proliferation (Figure S1D–E). Finally, flow cytometry analysis was taken to measure the apoptosis rate of the cells after overexpressing circZC3HAV1. The outcomes elucidated that there was no obvious change in cell apoptosis (Figure S1F). To conclude, circZC3HAV1 overexpression hinders migration and invasion of CRC cells.

3.3. circZC3HAV1 Sponges miR-146b-3p in CRC Cells. As revealed in Figure 2, circZC3HAV1 augment inhibited CRC cell invasive and migratory abilities in vitro. Hence, we tried to uncover the downstream regulatory mechanism of circZC3HAV1 in CRC cells. Based on the results of subcellular fractionation and FISH assays, circZC3HAV1 was mainly distributed in cytoplasm (Figures 3(a) and 3(b)). Then, RIP assay showed circZC3HAV1 was enriched in anti-AGO2 in both CW-2 and RKO cells (Figure 3(c)), indicating circZC3HAV1 might regulate the downstream genes through ceRNA pattern. circBank database (http://www.circbank.cn/) was used to predict the miRNAs which might bind to circZC3HAV1. The top 10 miRNAs (in a descending order of binding site number) were selected (Figure 3(d)). Among these miRNAs, miR-1200, miR-5587-5p, miR-6828-5p, miR-1914-5p, and miR-302b-3p have not been studied in cancers; miR-378a-5p, miR-1254, and miR-302a-3p have been proven to inhibit CRC progression [24–26]; miR-671-5p has been revealed to promote prostate cancer progression [27]; miR-146b-3p has been found to accelerate progression of liver cancer [28] and thyroid cancer [29]. Therefore, we chose miR-671-5p and miR-146b-3p as candidates. In CW-2 cells, the enrichment of the two

(a)

(b)

(c)
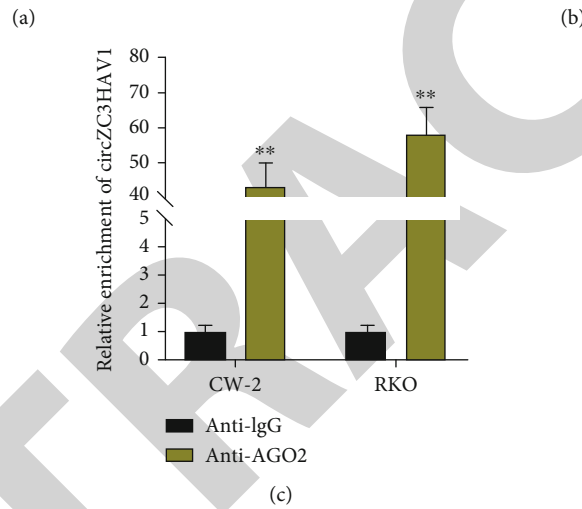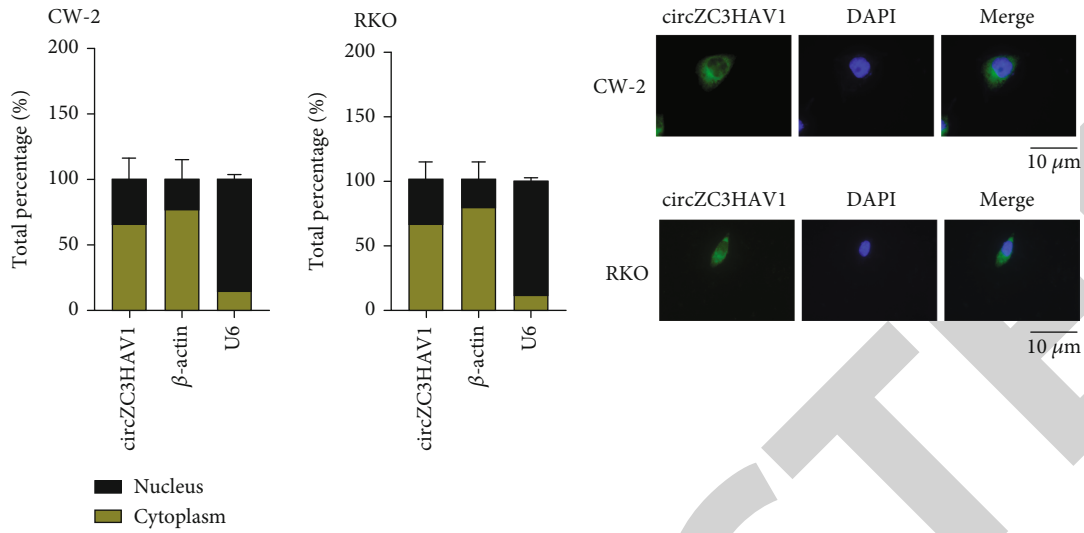
circBank ID	circbase ID	Length	miRNA ID (miR_ID)	miRanda binding site (positions)	Tragetscan binding site (positions)
hsa_circZC3HAV1...	hsa_circ_0082628	1000	hsa_miR-1200	544	209 559 689 214 565 694
hsa_circZC3HAV1...	hsa_circ_0082628	1000	hsa_miR-378a-5p	191	208 560 689 214 565 694
hsa_circZC3HAV1...	hsa_circ_0082628	1000	hsa_miR-5587a-5p	480	404 492 845 410 498 850
hsa_circZC3HAV1...	hsa_circ_0082628	1000	hsa_miR-671-5p	137	149 351 705 155 357 710
hsa_circZC3HAV1...	hsa_circ_0082628	1000	hsa_miR-6828-5p	335 687	150 350 704 155 357 710
hsa_circZC3HAV1...	hsa_circ_0082628	1000	hsa_miR-1254	699	332 718 339 724
hsa_circZC3HAV1...	hsa_circ_0082628	1000	hsa_miR-146b-3p	132	145 66 151 72
hsa_circZC3HAV1...	hsa_circ_0082628	1000	hsa_miR-1914-5p	494	144 508 149 514
hsa_circZC3HAV1...	hsa_circ_0082628	1000	hsa_miR-302a-3p	324 745	339 761 346 767
hsa_circZC3HAV1...	hsa_circ_0082628	1000	hsa_miR-302b-3p	324 745	339 761 346 767

(d)

Figure 3: Continued.

(e)

(f)

(g)

(h)

(i)
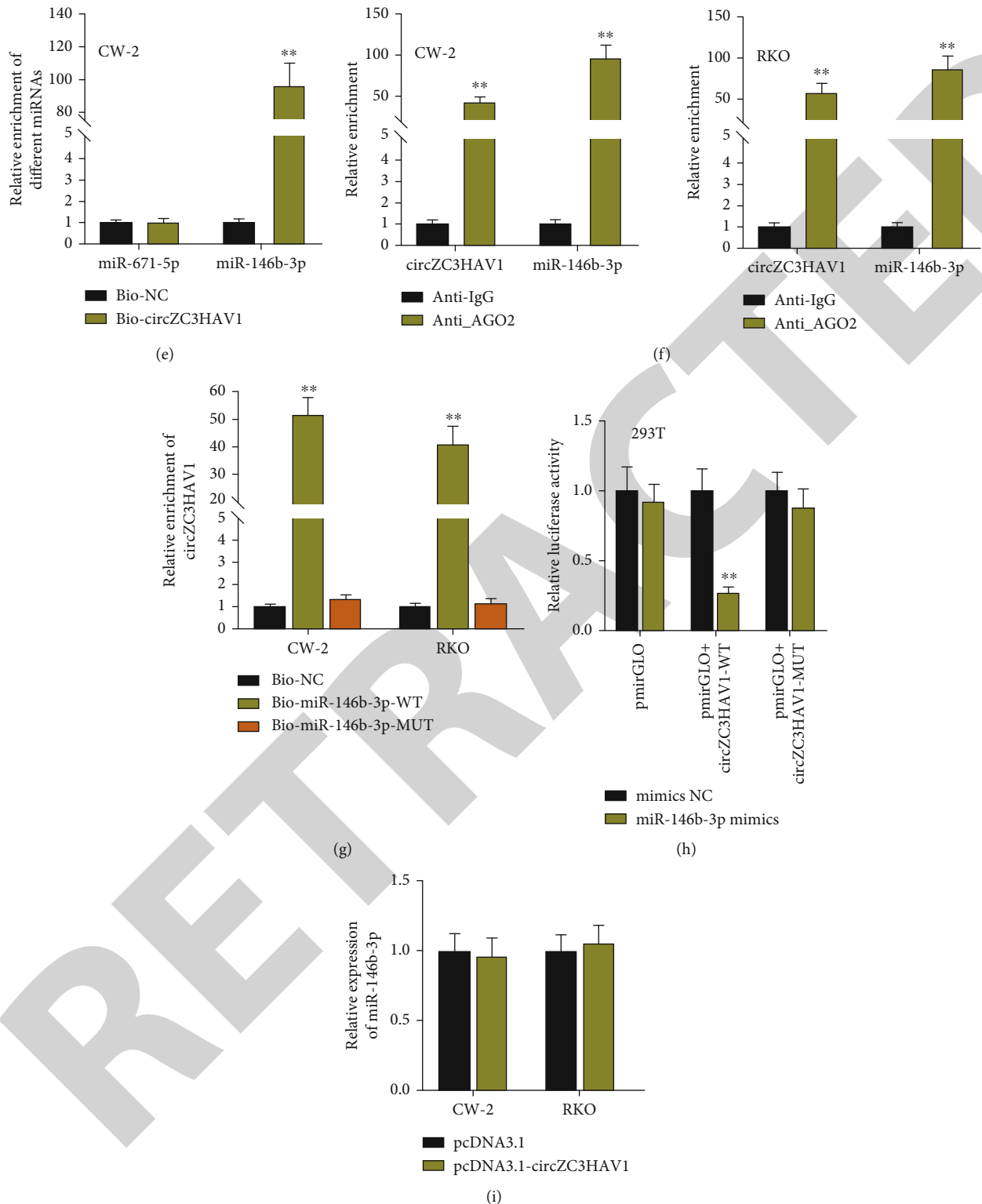
Figure 3: circZC3HAV1 competitively binds to miR-146b-3p in CRC cells. (a,b) The localization of circZC3HAV1 in CRC cells was detected through subcellular fractionation and FISH assays. Scale bar: $10\,\mu$m. (c) RIP assay was conducted to detect the enrichment of circZC3HAV1 in anti-AGO2. (d) circBank database was used to project the potential miRNAs which might bind to circZC3HAV1. (e) The binding affinities between circZC3HAV1 and candidate miRNAs were evaluated by RNA pull down assay. (f) RIP assay was performed to detect the enrichment of circZC3HAV1 and miR-146b-3p in anti-AGO2 by RIP assay. (g) The binding of circZC3HAV1 and miR-146b-3p was tested by RNA pull down assay. (h) In 293T cells, luciferase reporter assay was implemented to examine the luciferase activity of circZC3HAV1 when miR-146b-3p was upregulated. (i) The miR-146b-3p expression was examined by qPCR before and after the overexpression of circZC3HAV1 in CRC cells. $^{**}P < 0.01$.

(a)

(b)

(c)

(d)

Figure 4: Continued.

(e)

(f)

(g)

(h)
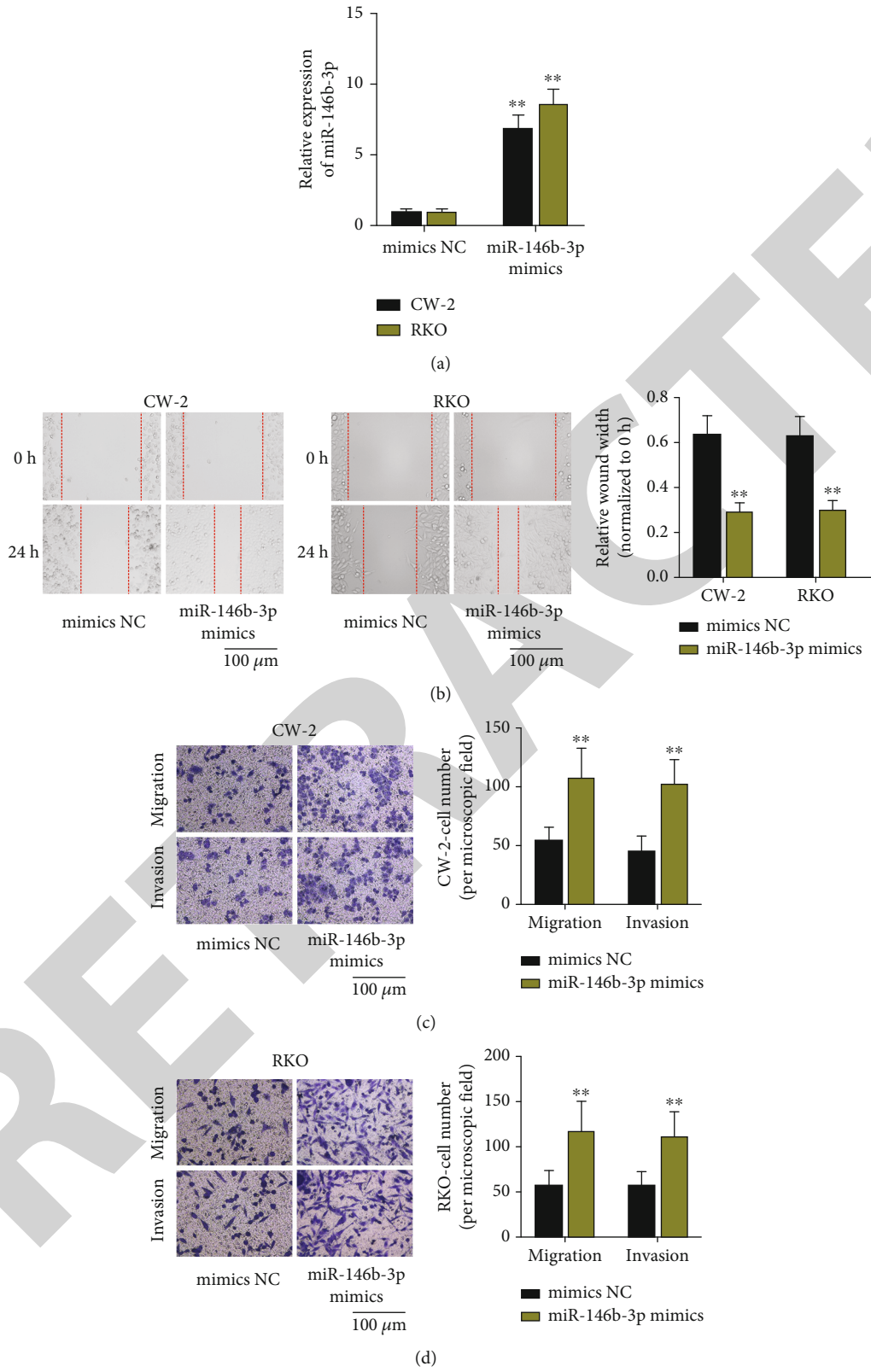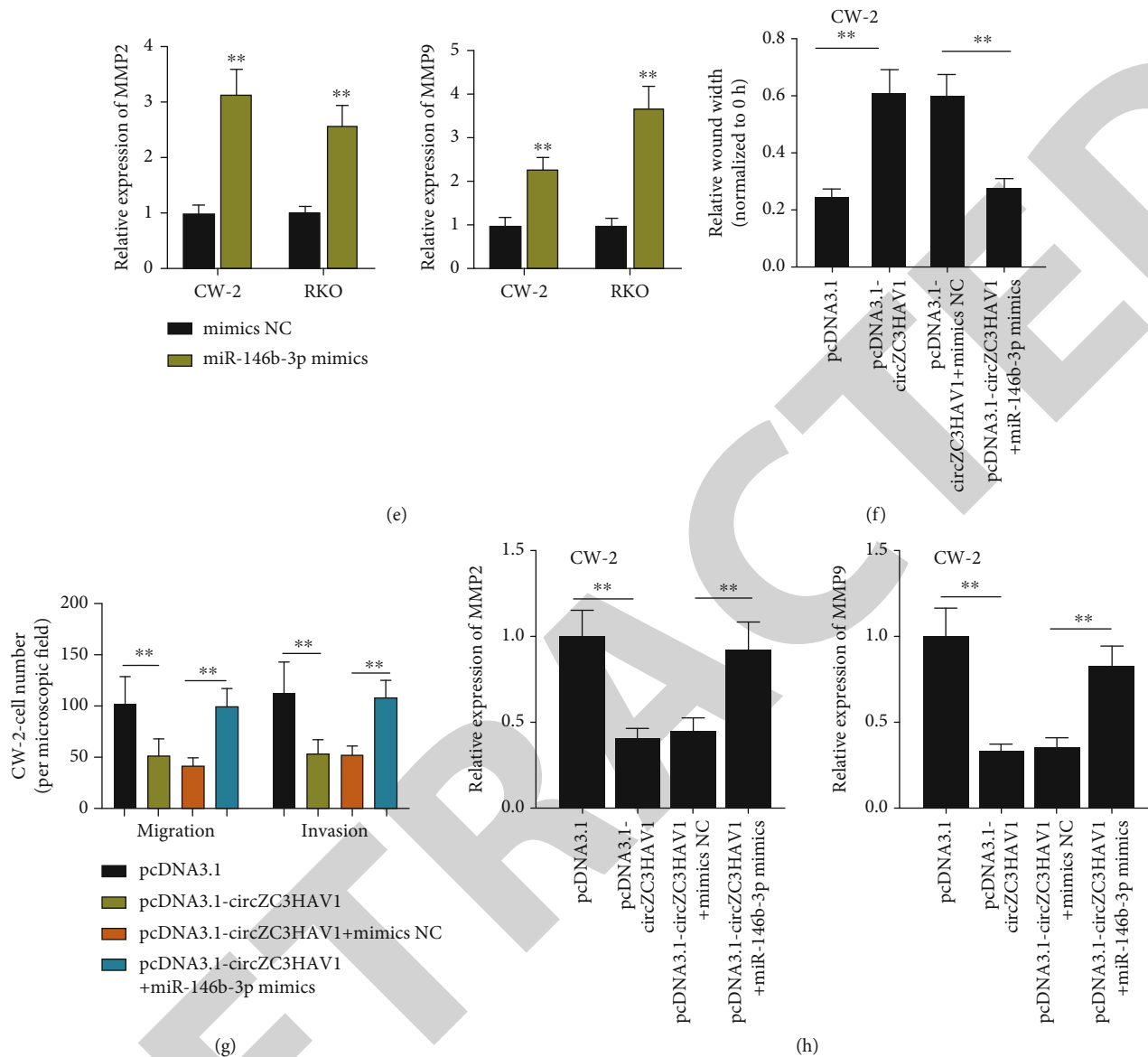
Figure 4: circZC3HAV1 regulates CRC cell migration and invasion by sponging miR-146b-3p. (a) The overexpression efficacy of miR-146b-3p mimics was measured by qPCR in CRC cells. (b) Wound healing assay was utilized for detecting the migratory capability of CRC cells in response to miR-146b-3p mimics. Scale bar: 100 μm. (c, d) The migratory and invasive abilities of CRC cells were detected by Ttranswell assays after overexpressing miR-146b-3p. Scale bar: 100 μm. (e) After the overexpression of miR-146b-3p, qPCR was utilized to detect the expression of MMP2 and MMP9. (f) Wound healing assay was performed to detect CRC cell migration under different conditions. (g) Migratory and invasive processes of CRC cells were evaluated by Transwell assays upon indicated conditions. (h) The expression of MMP2 and MMP9 in CRC cells transfected with different plasmids was detected by qPCR. $^{**}P < 0.01$.

miRNAs in Bio-circZC3HAV1 was detected after RNA pull down assay. The outcomes indicated that miR-146b-3p had the better binding ability with circZC3HAV1 (Figure 3(e)). Therefore, miR-146b-3p was chosen for the following experiments. Subsequently, we learned from the RIP result that circZC3HAV1 could bind to miR-146b-3p (Figure 3(f)). Moreover, RNA pull down assay outcome further proved the finding above that circZC3HAV1 could bind to miR-146b-3p (Figure 3(g)). In 293T cells, luciferase reporter assay was implemented to evaluate the circZC3HAV1 luciferase activity when miR-146b-3p was overexpressed. The data revealed that circZC3HAV1 could interact with miR-146b-

3p as the luciferase activity declined upon miR-146b-3p augment (Figure 3(h)). Finally, the expression of miR-146b-3p was tested via qPCR before and after the overexpression of circZC3HAV1. It turned out the expression of miR-146b-3p had no obvious change (Figure 3(i)). To sum up, circZC3HAV1 competitively adsorbs miR-146b-3p in CRC cells.

3.4. circZC3HAV1 Competitively Binds with miR-146b-3p to Restrain CRC Cell Migration and Invasion. The overexpression efficacy of miR-146b-3p mimics was tested by qPCR in CRC cells at first (Figure 4(a)). Then, in CW-2 and

(a)

(b)

(c)

(d)

(e)

Figure 5: Continued.

(f)

(g)

(h)

Figure 5: Continued.

(i)

(j)

(k)

Figure 5: Continued.

(l)

(m)

(n)

(o)

Figure 5: circZC3HAV1 regulates TBC1D9 expression via competitively adsorbing miR-146b-3p. (a) DIANA tools database was used to detect candidate mRNA that might bind to miR-146b-3p. (b, d) The interference efficiency of target mRNAs was measured by qPCR in CRC cells. (e) After LMTK2 downregulation, the migration of CRC cells was monitored in wound healing assays. Scale bar: 100 μm. (f) After LMTK2 knockdown, MMP2 and MMP9 expressions in CRC cells were detected by qPCR. (g) After TBC1D9 deficiency, the migration of CRC cells was tested by wound healing assays. Scale bar: 100 μm. (h) Upon TBC1D9 depletion, MMP2 and MMP9 expressions in CRC cells were detected by qPCR. (i) After downregulation of TP53INP2, the migration of CRC cells was examined via wound healing assays. Scale bar: 100 μm. (j) After knockdown of TP53INP2, the expression of MMP2 and MMP9 in CRC cells was detected by qPCR. (k) The enrichment of circZC3HAV1, miR-146b-3p, and TBC1D9 were detected by RIP assay in CRC cells. (l) Luciferase reporter assay was carried out to detect the influence of circZC3HAV1 overexpression on the binding of TBC1D9 and miR-146b-3p in 293T cells. (m) CRC cell migration was detected by wound healing assay under different conditions. (n) Transwell assay was applied for assessing migration and invasion of CRC cells transfected with different plasmids. (o) MMP2 and MMP9 expressions were detected by qPCR in CW-2 cells transfected with indicated plasmids. $^{**}P < 0.01$.

RKO cells with transfection of miR-146b-3p mimics, wound healing assay was done for assessing the cell migratory condition. It turned out miR-146b-3p overexpression promoted CRC cell migration (Figure 4(b)). The migratory and invasive abilities of CRC cells were analyzed by Transwell assays after overexpressing miR-146b-3p. The experimental outcomes proved that overexpressing miR-146b-3p could accel-erate the migration and invasion of CRC cells (Figures 4(c) and 4(d)). After the upregulation of miR-146b-3p, qPCR was employed to test the expression of MMP2 and MMP9. The expression of the genes increased, which indicated that overexpressing miR-146b-3p accelerated CRC cell invasion (Figure 4(e)). Wound healing assay was implemented to monitor the CRC cell migration under diverse conditions.

When circZC3HAV1 was overexpressed, the cell migration was inhibited, while the cotransfection of miR-146b-3p mimics offset its influence (Figure 4(f)). In addition, Transwell assays demonstrated the suppressive impact of circZC3HAV1 overexpression on cell migration and invasion was counteracted by miR-146b-3p augment (Figure 4(g)). The expression of MMP2 and MMP9 in CRC cells was detected by qPCR. The inhibited expression of MMP2 and MMP9 caused by pcDNA3.1-circZC3HAV1 was recovered by overexpressing miR-146b-3p (Figure 4(h)). In summary, circZC3HAV1 restricts CRC cell migration and invasion via competitively binds with miR-146b-3p.

3.5. circZC3HAV1 Regulates TBC1D9 Expression via Competitively Adsorbing miR-146b-3p. DIANA database (http://diana.imis.athena-innovation.gr/) was used to project the mRNAs that might bind to miR-146b-3p, and 15 mRNA candidates were projected (Figure 5(a)). Afterwards, we utilized UALCAN (http://ualcan.path.uab.edu/index.html) to search for the expression of 15 candidate mRNAs in colon adenocarcinoma (COAD) tissues and normal tissues (Figure S2A–O). As only LMTK2, TBC1D9, and TP53INP2 were significantly downregulated in COAD tissues, they were involved in the following research. The interference efficiency of candidate mRNAs was measured by qPCR in CRC cells. The results were shown in Figures 5(b)–5(d). After interfering LMTK2, the migration of CRC cells was detected through wound healing assays, and MMP2 and MMP9 expressions in CRC cells were detected by qPCR. Through the results above, we could conclude that LMTK2 interference had no significant influence on cell migration and invasion (Figures 5(e) and 5(f)). Next, the influence of TBC1D9 knockdown on the migration and invasion of CRC cells was detected via wound healing assays and qPCR. We found that interfering TBC1D9 could promote cell migration and invasion (Figures 5(g) and 5(h)). Moreover, results of wound healing and qPCR assays manifested TP53INP2 depletion had no obvious influence on cell migration and invasion (Figures 5(i) and 5(j)). Hence, we finally chose TBC1D9 as the target gene. In CRC cells, RIP assay result showed that circZC3HAV1, miR-146b-3p, and TBC1D9 were all enriched in anti-AGO2 (Figure 5(k)). Luciferase reporter assay was done to measure the luciferase activity in 293T cells. We found after transfection of miR-146b-3p mimics, the luciferase activity of TBC1D9 3′UTR was decreased, while cotransfection of pcDNA3.1-circZC3HAV1 totally recovered the luciferase activity (Figure 5(l)). In CW-2 cells, wound healing assay was carried out to detect the CRC cell migration. We noticed suppressed cell migration caused by circZC3HAV1 overexpression was reversed totally by inhibiting TBC1D9 (Figure 5(m)). Transwell assay was conducted to detect CRC cell migratory and invasive capabilities. When circZC3HAV1 was overexpressed, CRC cell migratory and invasive abilities were inhibited, while TBC1D9 inhibition could totally abrogate the suppressive impact (Figure 5(n)). Furthermore, based on qPCR analysis, decreased MMP2 and MMP9 expression caused by pcDNA3.1-circZC3HAV1 was restored by inhibiting TBC1D9 (Figure 5(o)). Taken together, circZC3HAV1 sponges miR-146b-3p to upregulate TBC1D9, thus impeding CRC cell migration and invasion.

4. Discussion

CRC is the third commonest cancer globally and causes cancer-linked death in both genders [30]. There exist multiple conventional treatment options for CRC ranging from simple endoscopic polypectomy, radio-chemotherapy, to complex chemotherapeutical regimen combined with drugs, but these treatments all have some disadvantages and side effects [31] [1]. During the past years, the management of CRC has been advanced. However, metastatic CRC is still difficult to treat. A deeper understanding of the pathways involved in the malignant processes of cancer cells has driven the development of targeted therapies [32]. Therefore, it is in an urgent need to explore more potential targets for CRC to improve its treatment.

circRNAs are noncoding RNA family members that have a close structure. The function of circRNAs has been affirmed in diverse diseases [33]. In the recent five years, the studies on the features and roles of circRNAs in CRC are on the rise. For instance, circRNA_0000392 accelerates CRC progression via miR-193a-5p/PIK3R3/AKT axis [3]. Moreover, it has been validated that circDDX17 functions as a tumor suppressor in CRC [34]. As a newly found circRNA, circZC3HAV1 was found to be evidently downregulated in CRC cells, and circZC3HAV1 overexpression inhibited CRC cell migration and invasion.

circRNAs can act as ceRNAs to indirectly modulate gene expression via shared miRNAs [35]. The existence of circRNA-associated ceRNA network (circRNA-miRNA-mRNA) has been identified in various cancers, including CRC. For example, circ3823 has been uncovered to act as a ceRNA of miR-30c-5p to restrain the inhibiting impact of miR-30c-5p on its target TCF7 mRNA, which eventually promotes CRC progression [36]. In the present research, we first found that circZC3HAV1 could bind to miR-146b-3p in a ceRNA manner. As reported, elevated expression of miR-146b-3p in CRC tissues and cells is linked to unfavorable overall survival [37]. Consistent with this literature, our study confirmed miR-146b-3p overexpression facilitated CRC cell migratory and invasive processes. Subsequently, we discovered that TBC1D9 was the downstream mRNA of miR-146b-3p. After a series of mechanism and rescue assays, it was unveiled that circZC3HAV1 could restrict the malignant behaviors of CRC cells via regulating the miR-146b-3p-TBC1D9 pathway.

Due to the limited time and experimental materials, *in vivo* assays and clinical samples are not involved in this research. However, there are still some innovative points in our study. Our study is the first to verify that circZC3HAV1 plays an oncogenic part in CRC cells. Moreover, the finding that circZC3HAV1 influences invasion and migration of CRC cells through regulating the miR-146b-3p/TBC1D9 axis is also new. We hope our study might provide useful information for relevant research on CRC.

Data Availability

The data used to support the findings of this study are included within the article.

Conflicts of Interest

The authors declare that they have no conflicts of interest.

Authors' Contributions

Jianxian Zhang and Yan Xue are co-first authors.

Supplementary Materials

Supplementary 1. Figure S1. (A–C) The expression of candidate circRNAs was analyzed in adjacent normal and CRC tissues based on the GEO database (GSE142837). (D, E) CCK-8 assay was conducted to measure the influence of circZC3HAV1 augment on CRC cell proliferation. (F) Flow cytometry analysis was done to measure the apoptosis rate of CRC cells after overexpressing circZC3HAV1.

Supplementary 2. Figure S2. (A–O) UALCAN database was applied to project the expression of candidate target mRNAs in normal and CRC tissues.

References

[1] G. Lech, R. Słotwiński, M. Słodkowski, and I. W. Krasnodębski, "Colorectal cancer tumour markers and biomarkers: recent therapeutic advances," *World Journal of Gastroenterology*, vol. 22, no. 5, pp. 1745–1755, 2016.

[2] J. Jin, H. Sun, C. Shi et al., "Circular RNA in renal diseases," *Journal 0f Cellular and Molecular Medicine*, vol. 24, no. 12, pp. 6523–6533, 2020.

[3] H. Xu, Y. Liu, P. Cheng et al., "CircRNA_0000392 promotes colorectal cancer progression through the miR-193a-5p/PIK3R3/AKT axis," *Journal of Experimental & Clinical Cancer Research*, vol. 39, no. 1, pp. 1–17, 2020.

[4] A. Shang, C. Gu, W. Wang et al., "Exosomal circPACRGL promotes progression of colorectal cancer via the miR-142-3p/miR-506-3p- TGF-β1 axis," *Molecular Cancer*, vol. 19, no. 1, pp. 1–15, 2020.

[5] K. Zeng, X. Chen, M. U. Xu et al., "CircHIPK3 promotes colorectal cancer growth and metastasis by sponging miR-7," *Cell Death & Disease*, vol. 9, no. 4, pp. 1–15, 2018.

[6] X. Du, J. Zhang, J. Wang, X. Lin, and F. Ding, "Role of miRNA in lung cancer-potential biomarkers and therapies," *Current Pharmaceutical Design*, vol. 23, no. 39, pp. 5997–6010, 2018.

[7] B. Li, X. Zhang, and Y. Dong, "Nanoscale platforms for messenger RNA delivery," *Wiley Interdisciplinary Reviews Nanomedicine and Nanobiotechnology*, vol. 11, no. 2, article e1530, 2019.

[8] R. S. Zhou, E. X. Zhang, Q. F. Sun et al., "Integrated analysis of lncRNA-miRNA-mRNA ceRNA network in squamous cell carcinoma of tongue," *BMC Cancer*, vol. 19, no. 1, pp. 1–10, 2019.

[9] L. X. Wang, C. Wan, Z. B. Dong, B. H. Wang, H. Y. Liu, and Y. Li, "Integrative analysis of long noncoding RNA (lncRNA), microRNA (miRNA) and mRNA expression and construction of a competing endogenous RNA (ceRNA) network in metastatic melanoma," *Medical Science Monitor: International Medical Journal of Experimental and Clinical Research*, vol. 25, pp. 2896–2907, 2019.

[10] X. Wu, Z. Sui, H. Zhang, Y. Wang, and Z. Yu, "Integrated analysis of lncRNA-mediated ceRNA network in lung adenocarcinoma," *Frontiers in Oncology*, vol. 10, article 554759, 2020.

[11] X. Jian, H. He, J. Zhu et al., "hsa_circ_001680 affects the proliferation and migration of CRC and mediates its chemoresistance by regulating BMI1 through miR-340," *Molecular Cancer*, vol. 19, no. 1, pp. 1–16, 2020.

[12] C. Zhou, H. S. Liu, F. W. Wang et al., "circCAMSAP1 promotes tumor growth in colorectal cancer via the miR-328-5p/E2F1 axis," *Molecular Therapy: The Journal of the American Society of Gene Therapy*, vol. 28, no. 3, pp. 914–928, 2020.

[13] M. Wu, C. Kong, M. Cai et al., "Hsa_circRNA_002144 promotes growth and metastasis of colorectal cancer through regulating miR-615-5p/LARP1/mTOR pathway," *Carcinogenesis*, vol. 42, no. 4, pp. 601–610, 2021.

[14] C. Han, F. Tang, J. Chen et al., "Knockdown of lncRNA-UCA1 inhibits the proliferation and migration of melanoma cells through modulating the miR-28-5p/HOXB3 axis," *Experimental and Therapeutic Medicine*, vol. 17, no. 5, pp. 4294–4302, 2019.

[15] P. Wang, L. Hu, G. Fu et al., "LncRNA MALAT1 promotes the proliferation, migration, and invasion of melanoma cells by downregulating miR-23a," *Cancer Management and Research*, vol. 12, pp. 6553–6562, 2020.

[16] G. Huang, M. Liang, H. Liu et al., "CircRNA hsa_circRNA_104348 promotes hepatocellular carcinoma progression through modulating miR-187-3p/RTKN2 axis and activating Wnt/β-catenin pathway," *Cell Death & Disease*, vol. 11, no. 12, pp. 1–14, 2020.

[17] Y. Yang, W. Xu, Z. Zheng, and Z. Cao, "LINC00459 sponging miR-218 to elevate DKK3 inhibits proliferation and invasion in melanoma," *Scientific Reports*, vol. 9, no. 1, pp. 1–12, 2019.

[18] J. Fan, X. Kang, L. Zhao, Y. Zheng, J. Yang, and R. N. A. Noncoding, "CCAT1 functions as a competing endogenous RNA to upregulate ITGA9 by sponging miR-296-3p in melanoma," *Cancer Management and Research*, vol. 12, pp. 4699–4714, 2020.

[19] Y. Geng, X. Zheng, W. Hu et al., "Hsa_circ_0009361 acts as the sponge of miR-582 to suppress colorectal cancer progression by regulating APC2 expression," *Clinical Science*, vol. 133, no. 10, pp. 1197–1213, 2019.

[20] C. Wen, X. Feng, H. Yuan, Y. Gong, and G. Wang, "Circ_0003266 sponges miR-503-5p to suppress colorectal cancer progression via regulating PDCD4 expression," *BMC Cancer*, vol. 21, no. 1, pp. 1–11, 2021.

[21] H. X. Ding, Q. Xu, B. G. Wang, Z. Lv, and Y. Yuan, "MetaDE-based analysis of circRNA expression profiles involved in gastric cancer," *Digestive Diseases and Sciences*, vol. 65, no. 10, pp. 2884–2895, 2020.

[22] J. Cui, W. Li, G. Liu et al., "A novel circular RNA, hsa_circ_0043278, acts as a potential biomarker and promotes non-small cell lung cancer cell proliferation and migration by regulating miR-520f," *Artificial Cells, Nanomedicine, and Biotechnology.*, vol. 47, no. 1, pp. 810–821, 2019.

[23] Y. Li, H. Fan, J. Sun et al., "Circular RNA expression profile of Alzheimer's disease and its clinical significance as biomarkers for the disease risk and progression," *The International Journal of Biochemistry & Cell Biology*, vol. 123, article 105747, 2020.

Retraction

Retracted: lncRNA MIR4435-2HG Accelerates the Development of Bladder Cancer through Enhancing IQGAP3 and CDCA5 Expression

BioMed Research International

This article has been retracted by Hindawi following an investigation undertaken by the publisher [1]. This investigation has uncovered evidence of one or more of the following indicators of systematic manipulation of the publication process:

(1) Discrepancies in scope

(2) Discrepancies in the description of the research reported

(3) Discrepancies between the availability of data and the research described

(4) Inappropriate citations

(5) Incoherent, meaningless and/or irrelevant content included in the article

(6) Manipulated or compromised peer review

The presence of these indicators undermines our confidence in the integrity of the article's content and we cannot, therefore, vouch for its reliability. Please note that this notice is intended solely to alert readers that the content of this article is unreliable. We have not investigated whether authors were aware of or involved in the systematic manipulation of the publication process.

Wiley and Hindawi regrets that the usual quality checks did not identify these issues before publication and have since put additional measures in place to safeguard research integrity.

We wish to credit our own Research Integrity and Research Publishing teams and anonymous and named external researchers and research integrity experts for contributing to this investigation.

The corresponding author, as the representative of all authors, has been given the opportunity to register their agreement or disagreement to this retraction. We have kept a record of any response received.

References

[1] T. Yang, Y. Li, G. Wang et al., "lncRNA MIR4435-2HG Accelerates the Development of Bladder Cancer through Enhancing IQGAP3 and CDCA5 Expression," *BioMed Research International*, vol. 2022, Article ID 3858249, 17 pages, 2022.

Research Article

lncRNA MIR4435-2HG Accelerates the Development of Bladder Cancer through Enhancing IQGAP3 and CDCA5 Expression

Tao Yang,[1] Yan Li,[2] Gang Wang,[1] Liuxiong Guo,[1] Fuzhen Sun,[1] Shoubin Li,[1] Xinna Deng,[3] and Junjiang Liu [1]

[1]*Department of Urology, Hebei Provincial People's Hospital, Shijiazhuang, 050000 Hebei, China*
[2]*Department of Hematology, Hebei Provincial People's Hospital, Shijiazhuang, 050000 Hebei, China*
[3]*Fourth Department of Oncology, Hebei Provincial People's Hospital, Shijiazhuang, 050000 Hebei, China*

Correspondence should be addressed to Junjiang Liu; liu_junjiang@outlook.com

Background. Bladder cancer (BCa) is one of the most prevalent cancers occurring in the urinary system. Long noncoding RNAs (lncRNAs), in recent years, have emerged as crucial regulators in various biological processes of tumors. *Aim.* To identify the role of MIR4435-2 host gene (MIR4435-2HG) and uncover its molecular mechanism in BCa. *Methods.* Firstly, quantitative real-time PCR (RT-qPCR) analysis was used to examine MIR4435-2HG expression in BCa cells. Cell Counting Kit-8 (CCK-8), 5-ethynyl-2′-deoxyuridine (EdU), wound healing, and transwell assays were implemented to identify the role of MIR4435-2HG in BCa. RNA-binding protein immunoprecipitation (RIP), RNA pull down, and luciferase reporter assays were applied to explore the potential mechanism of MIR4435-2HG in BCa. *Results.* MIR4435-2HG was highly expressed in BCa. Moreover, MIR4435-2HG silencing abrogated BCa cell proliferation, migration, and invasion. In terms of underlying mechanism, MIR44352HG acted as a microRNA-2467-3p (miR-2467-3p) sponge to control the expression of IQ motif containing GTPase activating protein 3 (IQGAP3) and cell division cycle associated 5 (CDCA5), resulting in activation of the rat sarcoma virus (Ras)/rapidly accelerated fibrosarcoma (Raf)/mitogen-activated protein kinase (MEK)/extracellular signal-regulated kinase (ERK) and PI3K/AKT/mTOR signaling pathways. *Conclusion.* MIR4435-2HG involves in the progression of BCa, which might provide novel insights for BCa treatment.

1. Introduction

Bladder cancer (BCa) is defined as a type of malignancy in which certain cells become abnormal and multiple without control in the bladder. It is one of the most common cancers of the genitourinary tract and a leading cause of morbidity and mortality [1]. Epidemiologic studies have indicated that cigarette smoking and occupational exposures are major risk factors for the occurrence of BCa [2]. Up to date, the management of BCa remains challenging and complicated due to its heterogeneity [3]. Therefore, surgery, radiation, and chemotherapy are still considered as main therapeutic strategies [4]. Accumulating evidence has demonstrated that emerging biomarkers may help to promote the early detection and diagnosis of BCa [5]. Hence, it is urgent to explore novel molecular markers to improve the therapeutic effect for BCa patients.

It is widely acknowledged that long noncoding RNAs (lncRNAs) occupy a vital position in regulating a variety of cellular processes of cancers through various mechanisms [6]. For example, Shang et al. have manifested that PVT1 plays an oncogenic role in colorectal cancer through interaction with miR-214-3p [7]. Wang et al. have demonstrated that UCA1 hampers tumor growth in esophageal squamous cell carcinoma via modulation of the Wnt signaling pathway [8]. Ding et al. have revealed that MIF-AS1 suppresses breast cancer progression via competing endogenous RNA (ceRNA) mode [9]. Previous studies have reported that ceRNA refers to a class of RNA functioning as miRNA sponges to regulate messenger (mRNA) expression, which affects tumor development [10]. Moreover, dysregulation of lncRNAs has also been suggested to be associated with the pathogenesis of BCa [11]. For example, Zhan et al. have illustrated that SOX2OT

enhances cell stemness in BCa through upregulating SOX2 [12]. Li et al. have proved that MAFG-AS1 accelerates BCa development via the miR-143-3p/COX-2 axis [13]. Wu et al. have declared that ZEB2-AS1 induces the occurrence of BCa by serving as a sponge for miR-27b [14].

MIR4435-2 host gene (MIR4435-2HG) is affiliated with the lncRNA class. lncRNA MIR4435-2HG has been reported to affect multiple cancers, including gastric cancer, hepatocellular carcinoma, and ovarian carcinoma [15–17], and all findings testify the oncogenic role of MIR4435-2HG in tumors. But its function in BCa remains to be unearthed. Some reports have uncovered the downstream molecular mechanism of MIR4435-2HG. For instance, MIR4435-2HG triggers tumor progression via targeting miR-128-3p to modulate CKD14 expression in ovarian cancer [18]. MIR4435-2HG facilitates tumor progression of cervical cancer cells via the miR-128-3p/MSI2 axis [19]. In addition, MIR4435-2HG promotes the aggressiveness of liver cancer cells via the miR-136-5p/B3GNT5 axis. Here, we intended to explore the MIR4435-2HG-mediated ceRNA network in BCa.

In this research, we intended to explore the investigation into the role and regulation mechanism of MIR4435-2HG in BCa.

2. Materials and Methods

2.1. Cell Culture. BCa cell lines (T24, HT-1197, HT-1376, and 5637) and normal cell line (SV-HUC-1) were all provided by American Type Culture Collection (Manassas, VA). T24 cell line was cultured in McCoy's 5a Medium, HT-1197 and HT-1376 cell lines both in Eagle's Minimum Essential Medium, 5637 cell line in RPMI-1640 Medium, and SV-HUC-1 in F-12K Medium. All mediums were added with 10% fetal bovine serum (Gibco) for cell culture at 37°C in 5% CO_2.

2.2. Plasmid Transfection. Short hairpin RNAs (shRNAs) against MIR4435-2HG, IQGAP3, or CDCA5, as well as their respective controls, were all generated by Genechem (Shanghai, China) and used for gene silencing. IQGAP3 or CDCA5 was overexpressed by inserting the sequence of IQGAP3 or CDCA5 into pcDNA3.1 vectors (Invitrogen, Carlsbad, CA). miR-2467-3p mimics/inhibitor and corresponding negative controls were all supplied by RiboBio (Shanghai, China). Transfection of $2\,\mu L$ plasmids (knockdown or overexpression vectors: $0.8\,\mu g/50\,\mu L$; miR-2467-3p mimics/inhibitor: a final concentration of $100\,nM$) into BCa cells in a 24-well format was conducted utilizing $1\,\mu L$ Lipofectamine 3000 (Invitrogen).

2.3. Quantitative Real-Time PCR (RT-qPCR) Analysis. RT-qPCR was performed as previously described [20]. Using TRIzol Reagent (Invitrogen), total RNA was extracted and complementary DNA (cDNA) was synthesized by RevertAid First Strand cDNA Synthesis Kit (Thermo Fisher Scientific, Rockford, IL). To evaluate the expression of genes, PCR was conducted utilizing SYBR Green PCR Master Mix (Applied Biosystems, Foster City, CA). Gene expression level was calculated as per the $2^{-\Delta\Delta Ct}$ method, normalized to the expression of endogenous control (GAPDH or U6). The experiment was independently done in triplicate. Primers used for RT-qPCR are reported in Supplementary Table 1.

2.4. Cell Counting Kit-8 (CCK-8) Assay. BCa cells were placed into 96-well plates at a density of 5×10^3 cells per well. This assay was performed as previously described. After 24 h, 48 h, and 72 h of transfection, each well was added with CCK-8 reagent. Subsequent to 2 h of incubation, the absorbance at 450 nm was measured. The experiment was independently conducted in triplicate.

2.5. 5-Ethynyl-2′-deoxyuridine (EdU) Staining Assay. EdU staining assay was implemented as previously described [21]. BCa cells were placed on sterile coverslips in 96-well plates (5×10^4 cells per well). Cells were incubated with EdU staining kit (RiboBio) and treated in DAPI staining solution for 5 min. Cell proliferation was observed under an Olympus fluorescence microscope (Tokyo, Japan). The assay was independently carried out in triplicate.

2.6. Wound Healing Assay. Wound healing assay was done as previously described [22]. A total of 3×10^3 cells were inoculated into 6-well plates and cultured in medium with no serum for 24 h at 37°C. A pipette tip was used to make a straight scratch when cells reached 80% confluence. Afterwards, BCa cells were subjected to another 24 h of incubation. The scratches were monitored and recorded at 0 and 24 h. The assay was performed in triplicate. Wound areas were analyzed by ImageJ software.

2.7. Transwell Assay. Transwell migration or invasion assay was carried out by using a 24-well transwell chamber (Corning), with Matrigel (BD Bioscience) precoating only for invasion assay. Transfected BCa cells ($8 \times 10^3 \sim 3.6 \times 10^4$) were placed into the upper chamber with addition of serum-free medium. Complete culture medium was put into the lower chamber. Subsequent to 24 h of incubation, cells were fixed in methanol. Subsequently, 0.1% crystal violet was used to stain the migrated or invaded cells for counting. The experiment was independently executed in triplicate. Transwell migration and Matrigel invasion assays were performed as previously described [23].

2.8. Subcellular Fractionation. Isolation of cytoplasmic-nuclear RNA was conducted as previously described [24]. Utilizing PARIS™ Kit (Ambion, Austin, TX), cytoplasmic and nuclear fractions were separated followed by RNA quantification by RT-qPCR. In this assay, GAPDH or U6 was regarded as cytoplasmic or nuclear control individually. The assay was independently carried out in triplicate.

2.9. Fluorescent In Situ Hybridization (FISH). MIR4435-2HG-specific RNA FISH probe was procured from RiboBio for cellular analysis, in light of the instruction of supplier. BCa cells went through incubation with FISH probe in hybridization buffer, then treated with DAPI staining reagent. Images were acquired using an Olympus fluorescent microscope. The assay was independently carried out in triplicate.

2.10. RNA Pull-Down Assay. RNA pull-down assay was executed as previously described [25]. In a word, BCa cells (1×10^7) were treated with biotinylated MIR4435-2HG probe (Sigma-Aldrich, St. Louis, MO), followed by addition of

magnetic beads (Millipore, Bedford, MA). The pull downs collected by magnetic beads were purified for PCR analysis. The experiment was performed in triplicate.

2.11. RNA-Binding Protein Immunoprecipitation (RIP).

RIP assay was conducted as previously described [26]. In accordance with the user guide, Magna RIP RNA-Binding Protein Immunoprecipitation Kit (Millipore) was employed for RIP assay. Cell lysates were incubated with Anti-Ago2 antibody (~1.5 mg/mL; Sigma-Aldrich) and anti-IgG antibody (2.38 mg/mL; Invitrogen) which were used for immunoprecipitation. Subsequently, the RNA was extracted from immunoprecipitates for RT-qPCR. The experiment was performed in triplicate.

2.12. Luciferase Reporter Assay.

The wild-type (Wt) or mutant-type (Mut) sequence of MIR4435-2HG full-length, IQGAP3, or CDCA5 fragments covering miR-2467-3p binding sites was inserted into pmirGLO dual-luciferase vector for the construction of pmirGLO-MIR4435-2HG-Wt/Mut, pmirGLO-IQGAP3 3′-UTR-Wt/Mut, and pmirGLO-CDCA5 3′-UTR-Wt/Mut individually. After that, the reporter construct was cotransfected with control mimics or miR-2467-3p mimics (a final concentration: 100 nM) into BCa cells. Eventually, dual-luciferase reporter assay system (Promega) was applied to detect the luciferase activity. Luciferase reporter assay was conducted and analyzed as previously described [25]. The experiment was executed in triplicate.

2.13. Western Blot Analysis.

Western blot was performed as previously described [20]. Firstly, protein samples were separated and shifted onto PVDF membranes (Millipore, Billerica, MA). Subsequent to sealing with nonfat milk, the membranes were subjected to overnight incubation at 4°C with the following primary antibodies against IQGAP3 (1.7 mg/mL, Invitrogen), CDCA5 (0.5 mg/mL, Invitrogen), EGFR (1 mg/mL, Sigma-Aldrich), K-Ras (1 mg/mL, Thermo Fisher Scientific), p-B-Raf (1 mg/mL, Sigma-Aldrich), p-MEK (~1 mg/mL, Invitrogen), MEK (~1 mg/mL, Invitrogen), p-ERK (0.5 mg/mL, Invitrogen), ERK (0.5 mg/mL, Invitrogen), p-mTOR (0.5 mg/mL, Invitrogen), mTOR (1 mg/mL, Thermo Fisher Scientific), p-PI3K (1 mg/mL, Invitrogen), PI3K (1 mg/mL, Thermo Fisher Scientific), p-AKT (1 mg/mL, Invitrogen), AKT (0.1 mg/mL, Invitrogen), and GAPDH (0.5 mg/mL, Merck, Darmstadt, Germany). Then, the blots went through incubation with secondary antibody (~2 mg/mL, Sigma-Aldrich). At length, chemiluminescence system supplied by GE Healthcare (Chicago) was utilized for protein detection. The experiment was performed in triplicate.

2.14. Statistical Analysis.

All the experiments were performed in triplicate. Statistical analysis of experimental data was processed by SPSS software (V22.0). All data were shown as mean ± standard deviation (SD). In addition, Student's t-test or one-way ANOVA was applied for comparison of group difference between two or more groups. A P value < 0.05 was considered as statistically significant.

3. Results

3.1. MIR4435-2HG Expression Is Upregulated in BCa and Associated with Poor Survival Outcome.

With the application of GEPIA database (http://gepia2.cancer-pku.cn/#index), we found that MIR4435-2HG expression was overtly increased in BCa tissues versus normal tissues (Figure 1(a)). Through RT-qPCR, we examined the expression of MIR4435-2GH in normal cell line SV-HUC-1 and BCa cell lines (T24, HT-1197, HT-1376, and 5637). It was found that MIR4425-2HG was highly expressed in BCa cell lines versus normal cell line (Figure 1(b)). At the same time, survival analysis indicated that high expression of MIR4435-2HG was related to an unfavorable overall survival in patients with BCa (Figure 1(c)). Overall, lncRNA MIR4435-2HG expression is prominently elevated in BCa.

3.2. MIR4435-2HG Insufficiency Blocks Cell Proliferation, Migration, and Invasion in BCa.

To unearth the impact of MIR4435-2HG on BCa progression, we carried out a series of functional experiments. Firstly, MIR4435-2HG was knocked down in T24 and 5637 cells (Figure 2(a)). CCK-8 assay demonstrated that when MIR4435-2HG was silenced, the viability of BCa cells was accordingly inhibited (Figure 2(b)). Also, EdU-positive cells were largely reduced in BCa cells under MIR4435-2HG silencing, which confirmed that MIR4435-2HG depletion hinders cell proliferation (Figure 2(c)). Besides, wound healing and transwell assays were implemented to assess the migratory capacity of BCa cells. MIR4435-2HG deficiency inhibited wound closure and led to the decreased number of migrated cells (Figures 2(d) and 2(e)). The results turned out that silencing of MIR4435-2HG markedly attenuated the migratory capacity of T24 and 5637 cells. Similarly, we found a distinct decrease in number of invaded cells caused by deficiency of MIR4435-2HG (Figure 2(f)). To summarize, MIR4435-2HG aggravates cell proliferation, migration, and invasion in BCa.

3.3. miR-2467-3p Is Sequestered by MIR4435-2HG.

We next explored the molecular mechanism underlying MIR4435-2HG-mediated BCa progression. Firstly, we conducted cytoplasmic-nuclear fractionation and FISH assays to detect the distribution of MIR4435-2HG in BCa cells. The results presented that MIR4435-2HG was primarily accumulated in the cytoplasm (Figures 3(a) and 3(b)), which suggested that MIR4435-2HG might exert function at the posttranscriptional level in BCa cells. RIP assay proved that MIR4435-2HG was highly abundant in Ago2-bound complex (Figure 3(c)), which suggested that MIR4435-2HG might serve as a miRNA sponge in an Ago2-dependent manner. With the help of starBase website (http://starbase.sysu.edu.cn/index.php) (CLIP Data ≥ 5), we predicted 17 potential miRNAs. RNA pull-down assay further verified that only miR-2467-3p was observably enriched in the complexes pulled down by biotinylated MIR4435-2HG probe (Figure 3(d)). As demonstrated in Figure 3(e), miR-2467-3p expression was prominently downregulated in BCa cell lines versus normal cell line. The predicted binding

(a)

(b)

(c)
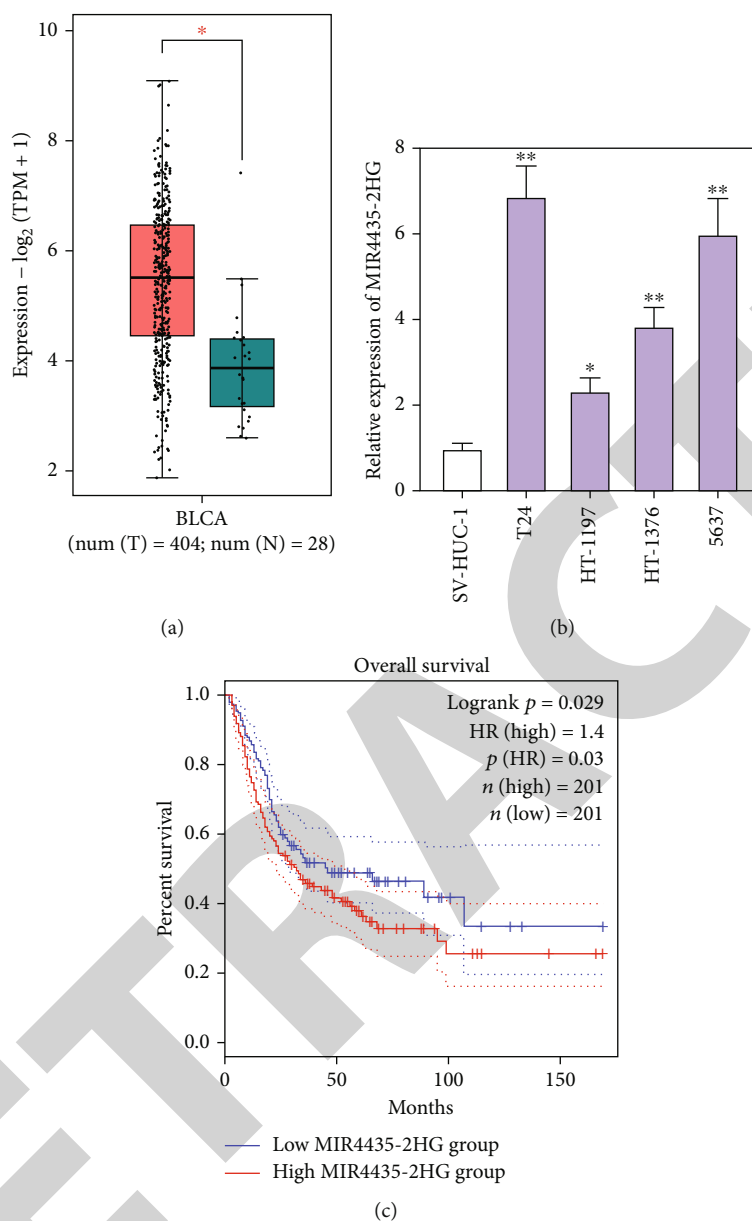
FIGURE 1: MIR4435-2HG expression is upregulated in BCa and associated with poor survival outcome. (a) GEPIA of MIR4435-2HG expression in BCa samples ($n = 404$) and normal samples ($n = 28$). (b) RT-qPCR detected MIR4435-2HG expression in normal cell line (SV-HUC-1) and BCa cell lines (T24, HT-1197, HT-1376, and 5637). (c) GEPIA correlation analysis of MIR4435-2HG expression and overall survival rate of BCa patients. $^*P < 0.05$; $^{**}P < 0.01$.

sequences between MIR4435-2HG and miR-2467-3p are displayed in Figure 3(f). Subsequently, miR-2467-3p expression was enhanced in BCa cells after transfection of miR-2467-3p mimics (Figure 3(g)). Then, luciferase reporter assay was performed to detect the binding between MIR4435-2HG and miR-2467-3p. We found that miR-2467-3p upregulation significantly reduced the luciferase activity of MIR4435-2HG-Wt versus the control group (Figure 3(h)). In a word, MIR4435-2HG functions as a ceRNA against miR-2467-3p.

3.4. IQGAP3 and CDCA5 Are Downstream Genes of miR-2467-3p. Further, we investigated the downstream target of

miR-2467-3p. By means of GEPIA and starBase, overlap of Venn diagram exhibited 2 potential mRNAs (Figure 4(a)). RT-qPCR analysis revealed that IQGAP3 and CDCA5 levels were both decreased in BCa cells under miR-2467-3p overexpression (Figure 4(b)). Hence, we speculated that IQGAP3 and CDCA5 were downstream targets of miR-2467-3p. The binding sites between miR-2467-3p and IQGAP3 or CDCA5 are exhibited in Figure 4(c). RIP assay manifested that MIR4435-2HG, miR-2467-3p, IQGAP3, and CDCA5 were highly abundant in the complex bound with Ago2 antibody (Figure 4(d)), verifying that miR-2467-3p binds to IQGAP3 and CDCA5. Luciferase reporter assays also validated the binding between miR-2467-3p and IQGAP3 or CDCA5

(a)

(b)

(c)

FIGURE 2: Continued.

(d)

(e)
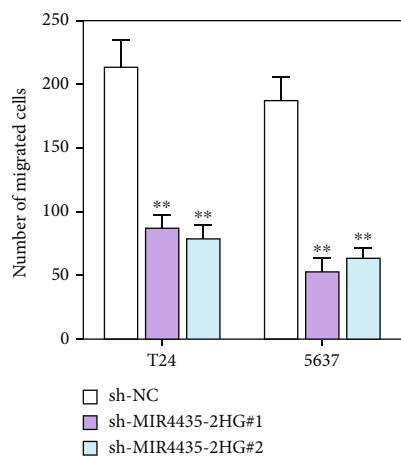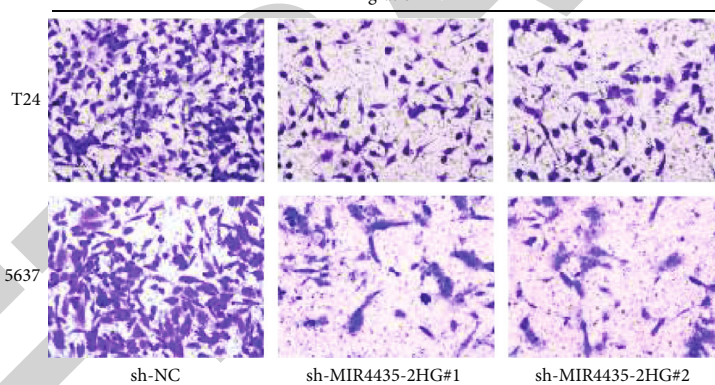
Figure 2: Continued.
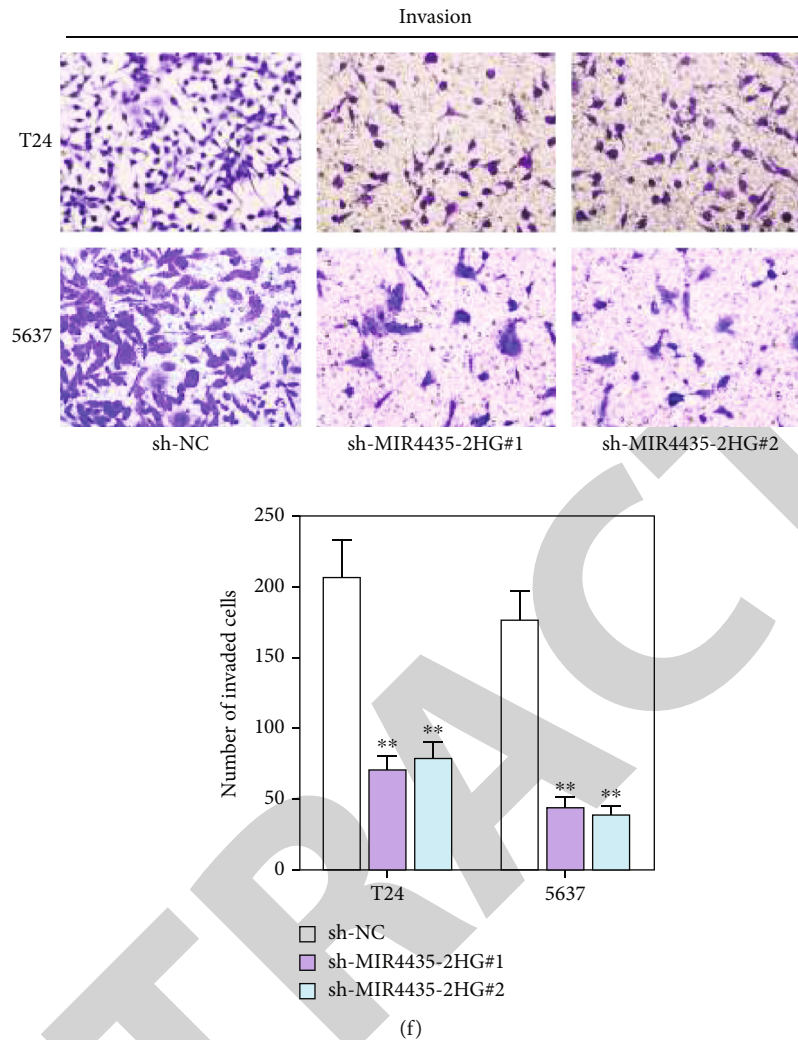
Figure 2: MIR4435-2HG insufficiency blocks cell proliferation, migration, and invasion in BCa. (a) Gene ablation of MIR4435-2HG in MIR4435-2HG-deficient T24 and 5637 cells was tested via RT-qPCR. (b, c) CCK-8 and EdU assays (magnification × 100) were used to evaluate cell proliferation. (d–f) Wound healing (magnification × 100) and transwell assays (magnification × 100) were used to determine the migratory and invasive capacities of BCa cells. $^{**}P < 0.01$.

(Figure 4(e)). The level of miR-2467-3p was reduced in miR-2467-3p-deficient T24 and 5637 cells (Figure 4(f)). In addition, MIR4435-2HG deficiency caused a distinct reduction in the expression of IQGAP3 and CDCA5 at mRNA level and protein level while this effect was fully restored by miR-2467-3p silencing (Figures 4(g) and 4(h)). Taken together, miR-2467-3p targets IQGAP3 and CDCA5 and negatively regulates their expression.

3.5. IQGAP3 Activates the Ras/Raf/MEK/ERK Signaling Pathway and CDCA5 Stimulates the PI3K/AKT/mTOR Signaling Pathway. IQGAP3 and CDCA5 have been reported to be involved in the Ras/Raf/MEK/ERK and PI3K/AKT/mTOR pathways, respectively, [27, 28]. Thereafter, we conducted western blot analysis to validate whether IQGAP3 and CDCA5 influence key factors in the related signaling pathways. First of all, IQGAP3 expression was decreased in T24 and 5637 cells (Figure 5(a)). Western blot

analyzed that EGFR, k-Ras, p-B-Raf, p-MEK, and p-ERK protein levels were all lessened in IQGAP3-inhibited BCa cells (Figure 5(b)). Meanwhile, CDCA5 was also knocked down in T24 and 5637 cells (Figure 5(c)). Likewise, the expression of p-mTOR, p-PI3K, and p-AKT at protein level was also decreased in BCa cells on account of CDCA5 abrogation (Figure 5(d)). Altogether, IQGAP3 and CDCA5 are important activators of the Ras/Raf/MEK/ERK and PI3K/AKT/mTOR pathways, respectively.

3.6. MIR4435-2HG Contributes to BCa Progression via Modulation of the miR-2467-3p/IQGAP3/CDCA5 Axis. To verify the role of the MIR4435-2HG/miR-2467-3p/IQGAP3/CDCA5 axis in BCa, we performed a list of rescue experiments. The expression levels of IQGAP3 and CDCA5 were greatly elevated in T24 cells after transfection of pcDNA3.1/IQGAP3 and pcDNA3.1/CDCA5 (Figure 6(a)). As shown in CCK-8 and EdU assays, MIR4435-2HG

(a)

(b)

(c)

(d)

Figure 3: Continued.

MIR4435-2HG-Wt: 5' acUGUGGACUCUGAGGCCUCUGCa 3'

miR-2467-3p: 3' ggAC--UCGGAGA--GACGGAGACGa 5'

MIR4435-2HG-Mut: 5' acACUGCAGAGAGAGCGGAGACGa 3'

(e)

(f)

(g)

(h)
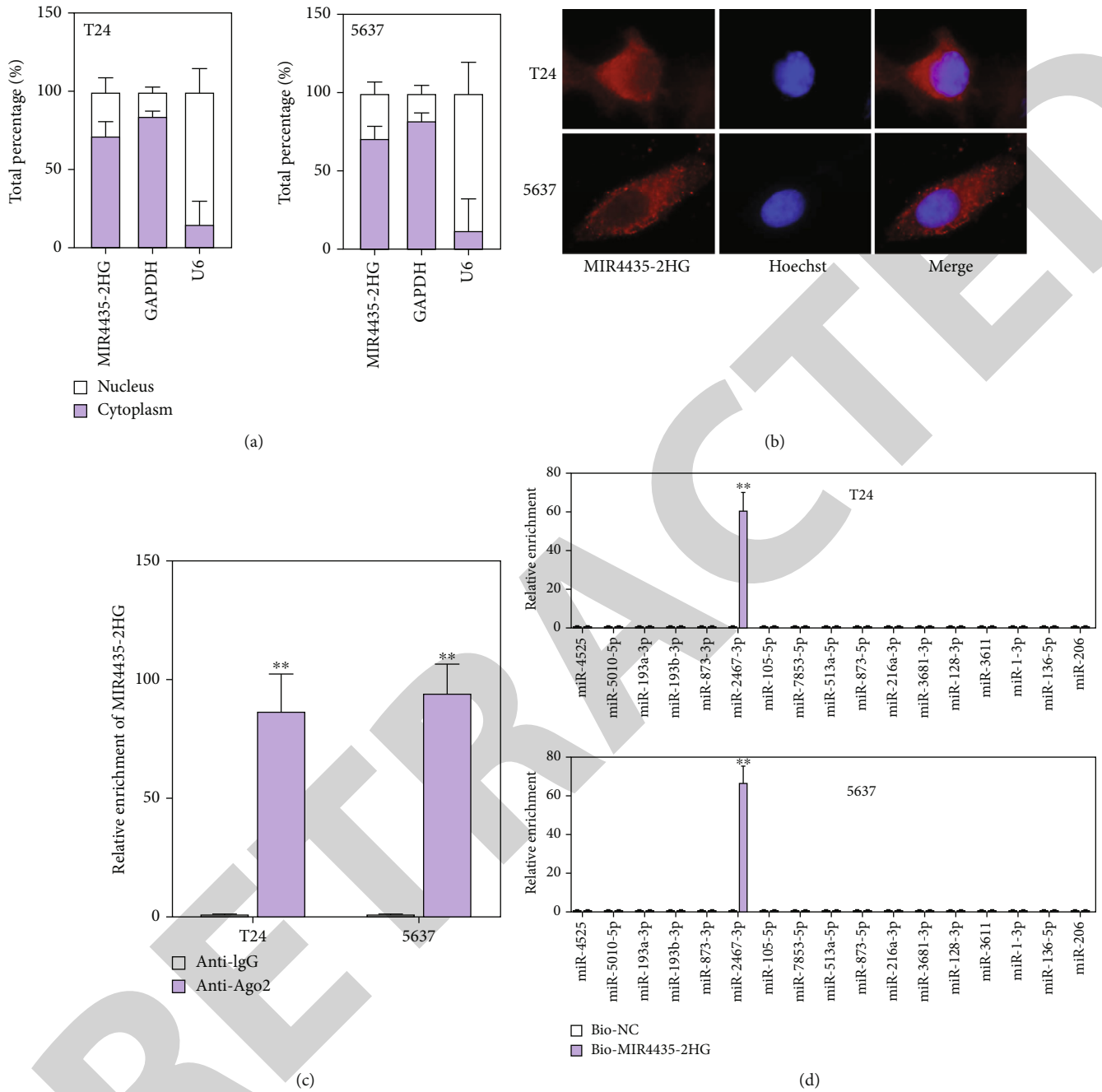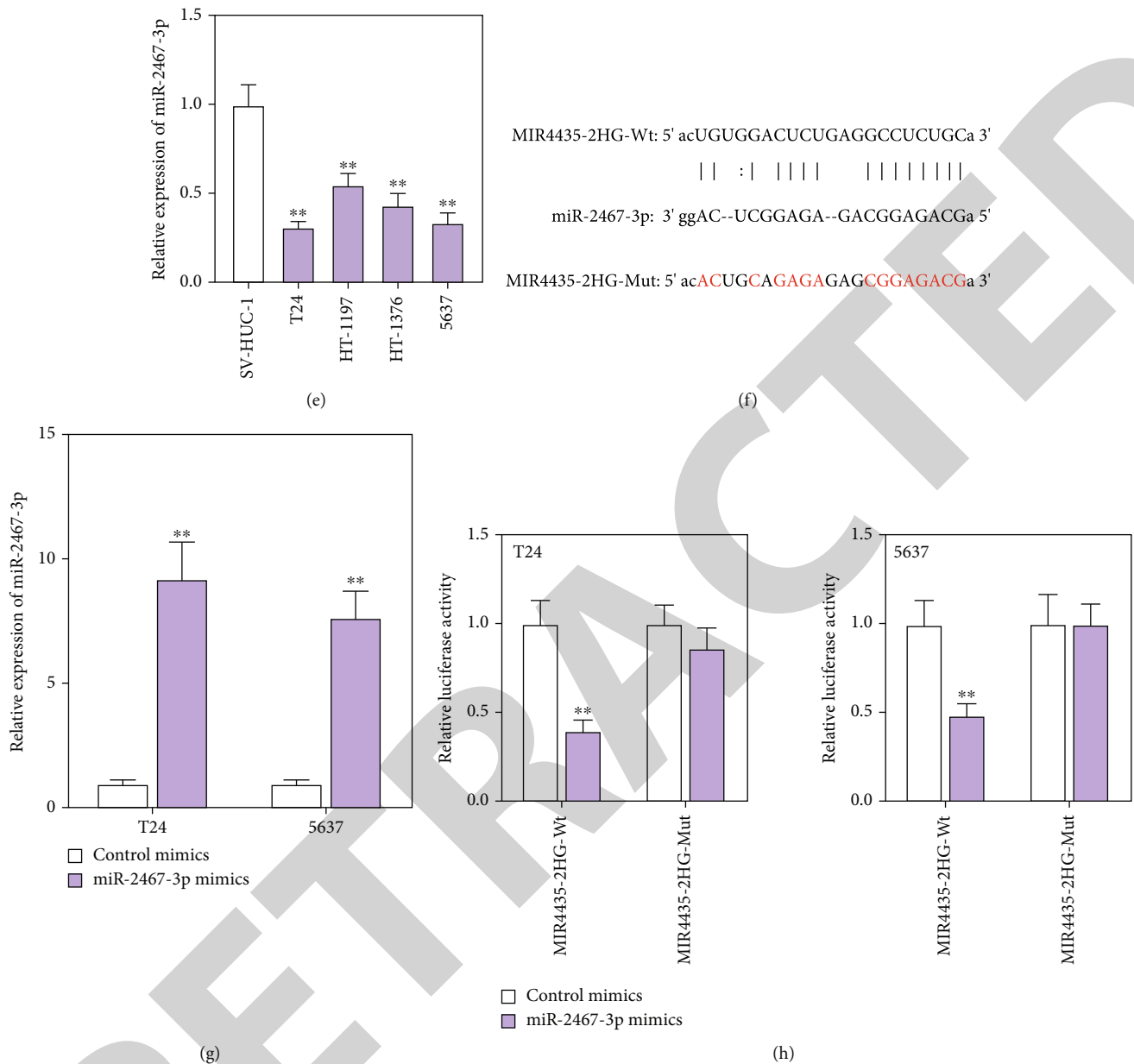
Figure 3: miR-2467-3p is sequestered by MIR4435-2HG. (a, b) Subcellular fractionation and FISH assays (magnification × 1,000) were conducted to explore the distribution of MIR4435-2HG in BCa cells. (c) RIP assay examined the enrichment of MIR4435-2HG in Ago2-RISC. (d) The enrichment of predicted 17 miRNAs in the complexes pulled down by biotinylated MIR4435-2HG probe was measured by RNA pull-down assay. (e) RT-qPCR examined the expression of miR-2467-3p in BCa cell lines and SV-HUC-1. (f) The starBase website was applied to predict the binding sites between MIR4435-2HG and miR-2467-3p. (g) Gene overexpression efficiency of miR-2467-3p was verified by RT-qPCR. (h) The physical interaction between MIR4435-2HG and miR-2467-3p was detected by luciferase reporter assay. $^*P < 0.05$; $^{**}P < 0.01$.

interference resulted in a decrease on cell proliferation while this suppression effect was thoroughly restored by miR-2467-3p silencing and partially altered by overexpression of either IQGAP3 or CDCA5 (Figures 6(b) and 6(c)). In like manner, wound healing and transwell assays elucidated that miR-2467-3p inhibition completely offset the suppressive effect of MIR4435-2HG inhibition on cell migration and invasion, whereas either IQGAP3 overexpression or CDCA5 overexpression partially countervailed the impaired cell migration and invasion imposed by deletion of MIR4435-2HG (Figures 6(d)–6(f)). All in all, MIR4435-2HG stimulates the progression of BCa via targeting the miR-2467-3p/IQGAP3 or miR-2467-3p/CDCA5 axis.

4. Discussion

Emerging evidence has highlighted that lncRNA MIR4435-2HG influences the malignant phenotypes of cancer cells.

Up-regulated
(Log2 fold change ≥ 2)

152   2   487

MicroT and miRmap

(a)

(b)

IQGAP3-Wt: 5′   gaucuGCAGUCCUGCCUCUGCc   3′

                          | | : | | | | | | | | | |

miR-2467-3p: 3′   ggacuCGGAGAGACGGAGACGa   5′

IQGAP3-Mut: 5′   gaucuCGAGUCGACGGAGACGc   3′

CDCA5-Wt: 5′   ggcccuaauaaaacCCUCUGCc   3′

                          | | | | | | |

miR-2467-3p: 3′   ggacucggagagacGGAGACGa   5′

CDCA5-Mut: 5′   ggcccuaauaaaacGGAGACGc   3′

(c)

Anti-IgG
Anti-Ago2

(d)

Control mimics
miR-2467-3p mimics

(e)
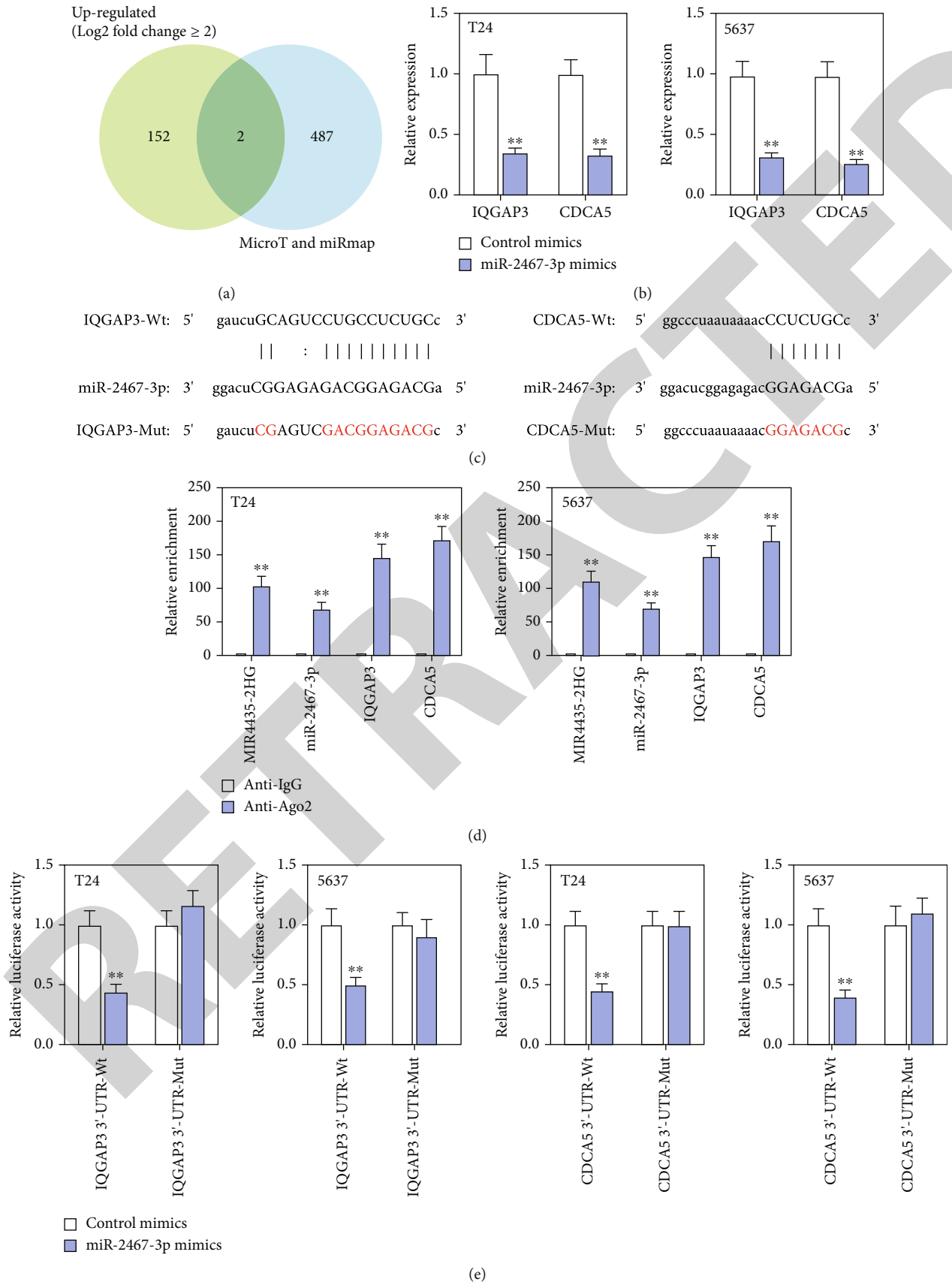
Figure 4: Continued.
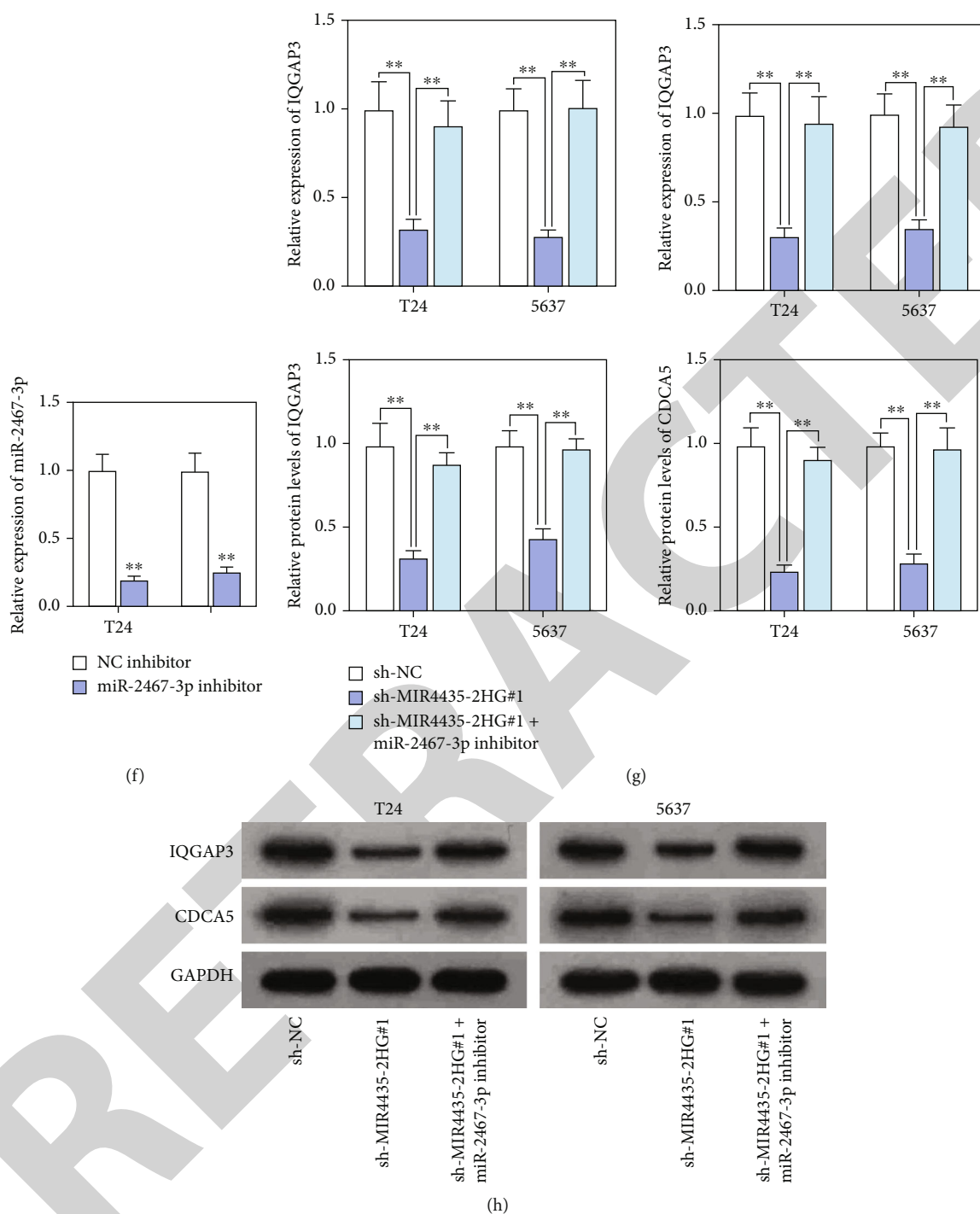
Figure 4: IQGAP3 and CDCA5 are downstream genes of miR-2467-3p. (a) Overlap of Venn diagram exhibited 2 predicted mRNAs. (b) IQGAP3 and CDCA5 levels were detected in miR-2467-3p-overexpressing BCa cells. (c) The predicted binding regions between miR-2467-3p and IQGAP3 or CDCA5. (d) The relationship among MIR4435-2HG, miR-2467-3p, IQGAP3, and CDCA5 was detected by RIP assay. (e) Luciferase activity in the IQGAP3 3$'$UTR-Wt group, IQGAP3 3$'$UTR-Mut group, CDCA5 3$'$UTR-Wt group, and CDCA5 3$'$UTR-Mut group in BCa cells cotransfected with miR-2467-3pmimics was detected. (f) Transfection of miR-2467-3p inhibitor into BCa cells was performed for miR-2467-3p silencing. (g, h) The expression of IQGAP3 and CDCA5 at mRNA level and protein level was detected in different groups. $^{**}P < 0.01$.

For example, Kong et al. have unmasked that MIR4435-2HG boosts cell proliferation in hepatocellular carcinoma through enhancing miR-487a expression [16]. Yang et al. have manifested that MIR4435-2HG targets the miR-206/YAP1 axis to advance colorectal cancer cell proliferation and metastasis [29]. Liu et al. have disclosed that MIR4435-2HG suppresses the process of osteoarthritis via binding to miR-510-3p [30]. In this research, we demonstrated that MIR4435-2HG
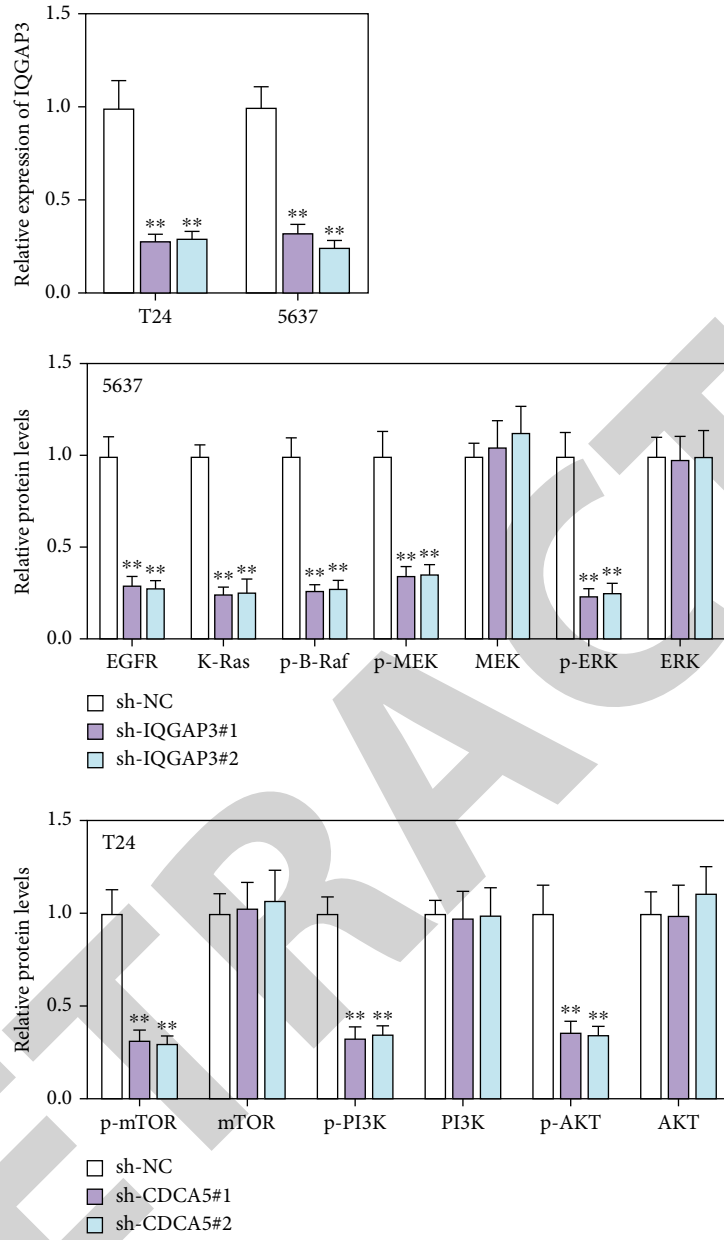
(a)

Figure 5: Continued.
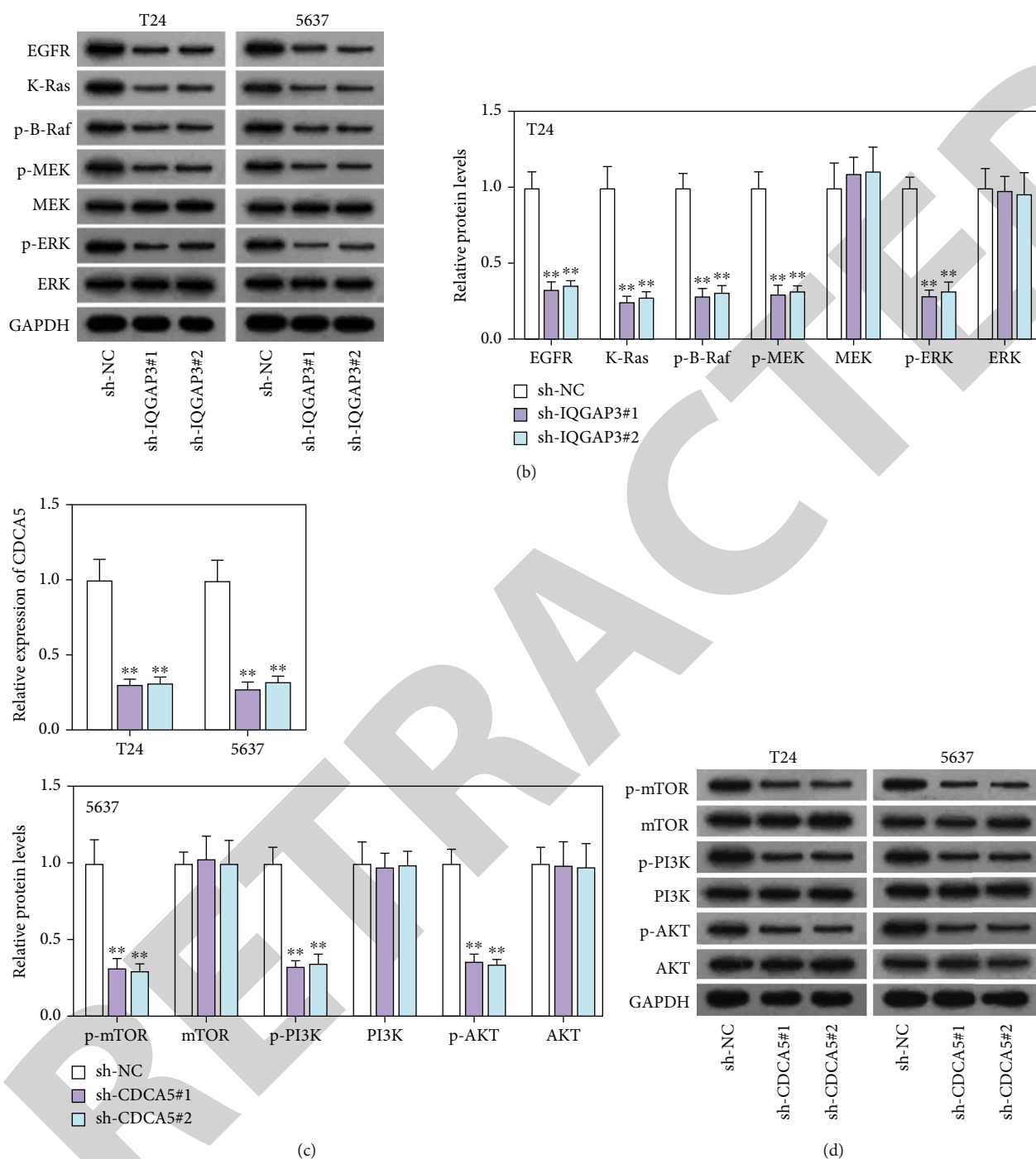
Figure 5: IQGAP3 activates the Ras/Raf/MEK/ERK signaling pathway, and CDCA5 stimulates the PI3K/AKT/mTOR signaling pathway. (a) Gene deletion efficiency of IQGAP3 in T24 and 5637 cells was examined by RT-qPCR. (b) Western blot analyzed the protein levels of EGFR, K-Ras, p-B-Raf, p-MEK, MEK, p-ERK, and ERK in IQGAP3-deficient BCa cells. (c) Gene deletion efficiency of CDCA5 in BCa cells was assessed via RT-qPCR. (d) The levels of PI3K/AKT/mTOR signaling pathway-associated proteins in CDCA5-silenced BCa cells were analyzed via western blot. $**P < 0.01$.

expression was obviously high in BCa cells and associated with poor survival in BCa patients. Moreover, our study firstly identified the oncogenic role and molecular mechanism of MIR4435-2HG in BCa. Specifically, we found that downregulation of MIR4435-2HG impairs the proliferative, migratory, and invasive abilities of BCa cells.

The lncRNA-miRNA-mRNA ceRNA network has been regarded to be critical in BCa pathogenesis [31, 32]. Here, the present study indicated that MIR4435-2HG might serve as a ceRNA to participate in posttranscriptional events. Importantly, miR-2467-3p was validated to be a downstream target of MIR4435-2HG.

(a)

(b)

a: ☐ sh-NC
b: ☐ sh-MIR4435-2HG#1
c: ☐ sh-MIR4435-2HG#1 + miR-2467-3p inhibitor
d: ☐ sh-MIR4435-2HG#1 + pcDNA3.1/IQGAP3
e: ☐ sh-MIR4435-2HG#1 + pcDNA3.1/CDCA5

(c)

☐ sh-NC
☐ sh-MIR4435-2HG#1
☐ sh-MIR4435-2HG#1 + miR-2467-3p inhibitor
☐ sh-MIR4435-2HG#1 + pcDNA3.1/IQGAP3
☐ sh-MIR4435-2HG#1 + pcDNA3.1/CDCA5

(d)

Figure 6: Continued.

(e)

(f)
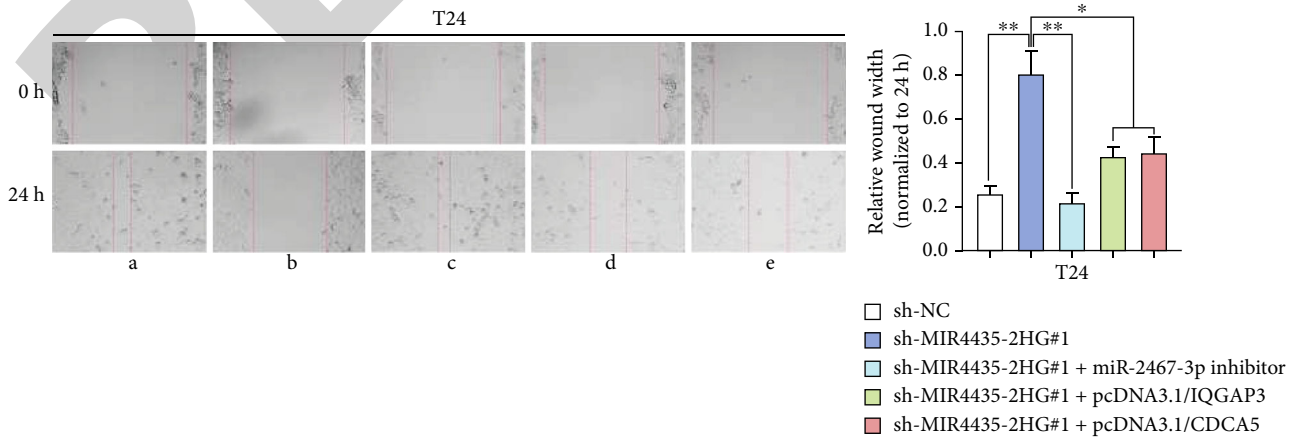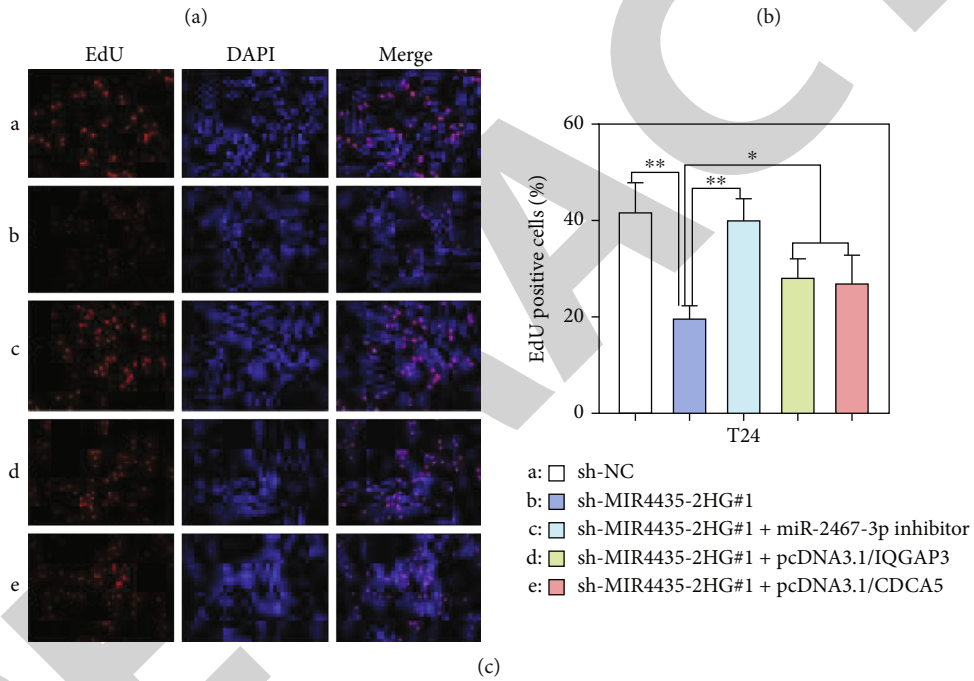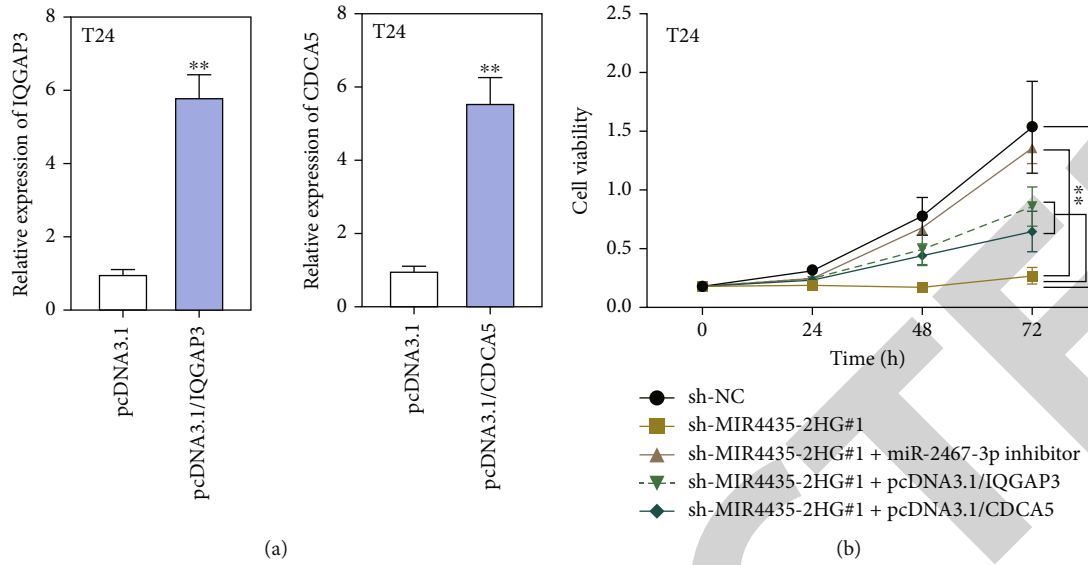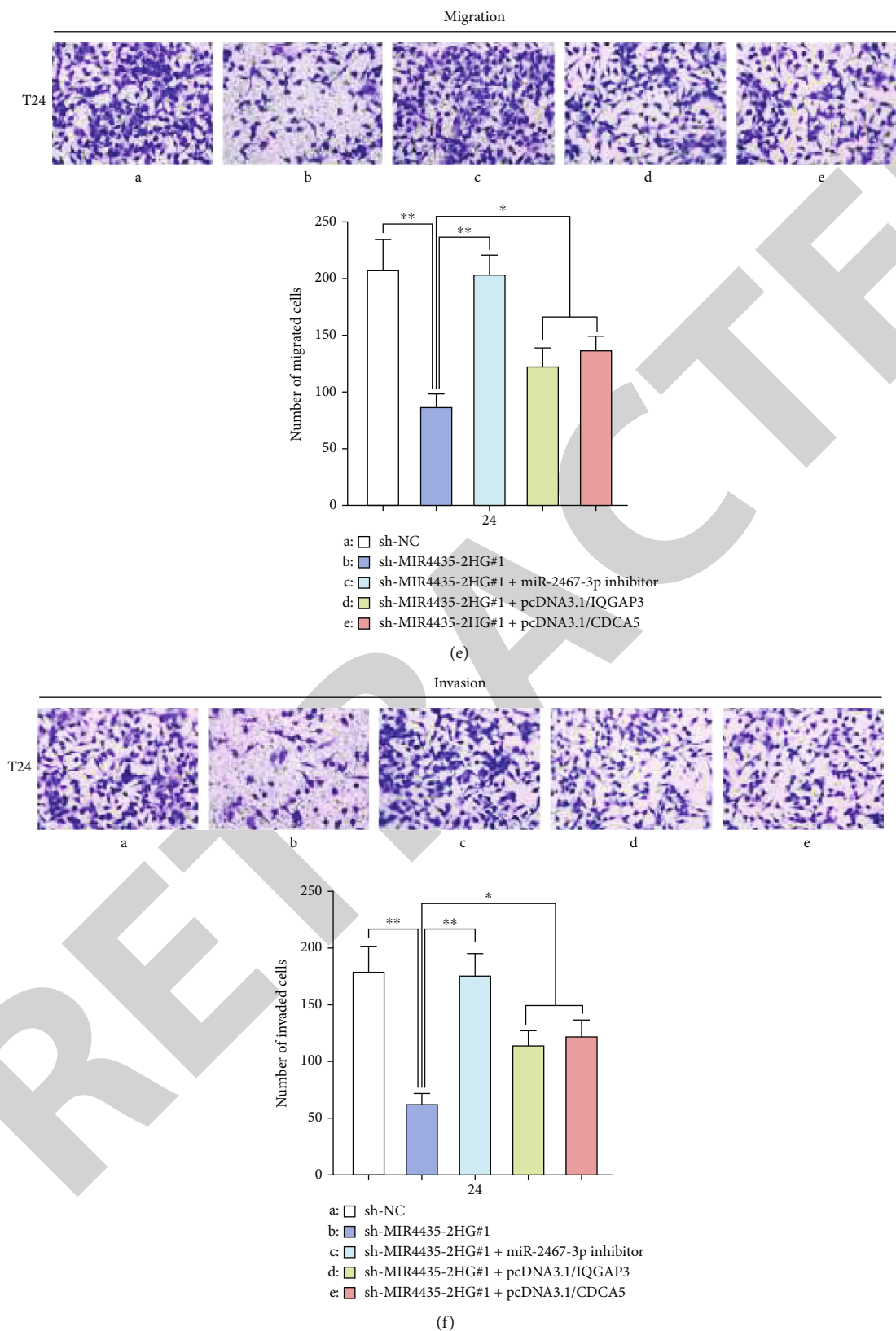
Figure 6: MIR4435-2HG contributes to BCa progression via modulation of the miR-2467-3p/IQGAP3/CDCA5 axis. (a) Gene upregulation efficiency of IQGAP3 and CDCA5 in T24 cells was tested via RT-qPCR. (b, c) CCK-8 and EdU assays (magnification × 100) were conducted to detect the proliferation of T24 cells under different transfections. (d–f) The migration and invasion capacities of BCa cells under different transfections were assessed by wound healing (magnification × 100) and transwell assays (magnification × 100). $^*P < 0.05$; $^{**}P < 0.01$.

Besides, miR-2467-3p suppresses the progression of colorectal cancer, cervical cancer, and non-small-cell lung cancer [33–35]. Consistent with these findings, our study manifested that miR-2467-3p expression was downregulated in BCa cells. More importantly, miR-2467-3p was verified to participate in the regulation of BCa progression.

IQGAP3 has been shown to govern cell proliferation and migration [36] and has been certified to exhibit high expression in some cancers, such as breast cancer, lung cancer, prostate cancer, kidney cancer, liver cancer, and colorectal cancer [37]. Also, previous studies have demonstrated the oncogenic functions of IQGAP3 in cancers, such as ovarian cancer [38] and gastric cancer [39]. Besides, IQGAP3 urinary cell-free NA may be utilized as a new noninvasive bladder cancer diagnostic marker [40]. Additionally, IQGAP3 can interact with ERK1 to modulate the Ras/Raf/MEK/ERK signaling pathway [27]. Moreover, CDCA5 has been confirmed to aggravate cell cycle and inhibit cell apoptosis in BCa via activation of the PI3K/AKT/mTOR signaling pathway [28]. Through our investigation, IQGAP3 and CDCA5 were found to be targeted by miR-2467-3p and negatively regulated by miR-2467-3p in BCa. More interestingly, downregulation of IQGAP3 or CDCA5 inactivates the MEK/ERK pathway and PI3K/AKT/mTOR pathway, respectively. In this research, we found that the MIR4435-2HG/miR-2467-3p/IQGAP3/CDCA5 axis enhances BCa progression.

All in all, MIR4435-2HG was demonstrated to be an oncogene in BCa and predicted poor survival outcome. Deficiency of MIR4435-2HG repressed BCa cell proliferation, migration, and invasion. As for the underlying mechanism, MIR4435-2HG sequestered miR-2467-3p to modulate the expression of IQGAP3 and CDCA5 via ceRNA mode, leading to activation of the MEK/ERK and PI3K/AKT/mTOR pathways. All the findings might provide novel insights for BCa treatment.

Data Availability

The data used to support the findings of this study are included within the article.

Conflicts of Interest

No conflicts of interest exist.

Authors' Contributions

Tao Yang was responsible for the research design; Yan Li, Gang Wang, and Liuxiong Guo carried out the experiment; Fuzhen Sun, Shoubin Li, and Xinna Deng completed the figures. Junjiang Liu wrote the paper.

Acknowledgments

Supplementary Materials

Supplementary Table 1: specific primers used for RT-qPCR. F: forward; R: reverse. *(Supplementary Materials)*

References

[1] L. S. Borden Jr., P. E. Clark, and M. C. Hall, "Bladder cancer," *Current Opinion in Oncology*, vol. 17, no. 3, pp. 275–280, 2005.

[2] P. W. Kantoff, "Bladder cancer," *Current Problems in Cancer*, vol. 14, no. 5, pp. 237–292, 1990.

[3] J. Zhang, S. Gerst, R. A. Lefkowitz, and A. Bach, "Imaging of bladder cancer," *Radiologic clinics of North America*, vol. 45, no. 1, pp. 183–205, 2007.

[4] J. Sakatoku and N. Yamamoto, "Bladder cancer," *Gan to Kagaku Ryoho Cancer & Chemotherapy*, vol. 10, no. 5, pp. 1225–1234, 1983.

[5] X. Zhang, C. Han, and J. He, "Recent advances in the diagnosis and management of bladder cancer," *Cell Biochemistry and Biophysics*, vol. 73, no. 1, pp. 11–15, 2015.

[6] L. Bolha, M. Ravnik-Glavač, and D. Glavač, "Long noncoding RNAs as biomarkers in cancer," *Disease Markers*, vol. 2017, 7243919 pages, 2017.

[7] A. Q. Shang, W. W. Wang, Y. B. Yang et al., "Knockdown of long noncoding RNA PVT1 suppresses cell proliferation and invasion of colorectal cancer via upregulation of *microRNA-214-3p*," *American Journal of Physiology-Gastrointestinal and Liver Physiology*, vol. 317, no. 2, pp. G222–g232, 2019.

[8] X. Wang, Z. Gao, J. Liao et al., "lncRNA UCA1 inhibits esophageal squamous-cell carcinoma growth by regulating the Wnt signaling pathway," *Journal of Toxicology and Environmental Health Part A*, vol. 79, no. 9-10, pp. 407–418, 2016.

[9] J. Ding, W. Wu, J. Yang, and M. Wu, "Long non-coding RNA MIF-AS1 promotes breast cancer cell proliferation, migration and EMT process through regulating miR-1249-3p/HOXB8 axis," *Pathology, Research and Practice*, vol. 215, no. 7, article 152376, 2019.

[10] N. Yang, K. Liu, M. Yang, and X. Gao, "ceRNAs in cancer: mechanism and functions in a comprehensive regulatory network," *Journal of Oncology*, vol. 2021, Article ID 4279039, 12 pages, 2021.

[11] S. Chandra Gupta and T. Y. Nandan, "*Potential of long non-coding RNAs in cancer patients: from biomarkers to therapeutic targets*," *International Journal of Cancer*, vol. 140, no. 9, pp. 1955–1967, 2017.

[12] Y. Zhan, Z. Chen, S. He et al., "Long non-coding RNA SOX2OT promotes the stemness phenotype of bladder cancer cells by modulating *SOX2*," *Molecular Cancer*, vol. 19, no. 1, 2020.

[13] D. Li, S. Zhong, Z. Zhu et al., "LncRNA MAFG-AS1 promotes the progression of bladder cancer by targeting the miR-143-3p/COX-2 Axis," *Pathobiology*, vol. 87, no. 6, pp. 345–355, 2020.

[14] X. Wu, T. Yan, Z. Wang, X. Wu, G. Cao, and C. Zhang, "*LncRNA ZEB2-AS1 promotes bladder cancer cell proliferation and inhibits apoptosis by regulating miR-27b*," *Biomedicine & Pharmacotherapy*, vol. 96, pp. 299–304, 2017.

[15] H. Wang, M. Wu, Y. Lu et al., "LncRNA MIR4435-2HG targets desmoplakin and promotes growth and metastasis of gastric cancer by activating Wnt/β-catenin signaling," *Aging*, vol. 11, no. 17, pp. 6657–6673, 2019.

Retraction

Retracted: LINC00707 Promotes Cell Proliferation in Cervical Cancer via the miR-374c-5p/SDC4 Axis

BioMed Research International

This article has been retracted by Hindawi following an investigation undertaken by the publisher [1]. This investigation has uncovered evidence of one or more of the following indicators of systematic manipulation of the publication process:

(1) Discrepancies in scope

(2) Discrepancies in the description of the research reported

(3) Discrepancies between the availability of data and the research described

(4) Inappropriate citations

(5) Incoherent, meaningless and/or irrelevant content included in the article

(6) Manipulated or compromised peer review

The presence of these indicators undermines our confidence in the integrity of the article's content and we cannot, therefore, vouch for its reliability. Please note that this notice is intended solely to alert readers that the content of this article is unreliable. We have not investigated whether authors were aware of or involved in the systematic manipulation of the publication process.

Wiley and Hindawi regrets that the usual quality checks did not identify these issues before publication and have since put additional measures in place to safeguard research integrity.

We wish to credit our own Research Integrity and Research Publishing teams and anonymous and named external researchers and research integrity experts for contributing to this investigation.

The corresponding author, as the representative of all authors, has been given the opportunity to register their agreement or disagreement to this retraction. We have kept a record of any response received.

References

[1] F. Fang, C. Guo, W. Zheng, and Q. Li, "LINC00707 Promotes Cell Proliferation in Cervical Cancer via the miR-374c-5p/SDC4 Axis," *BioMed Research International*, vol. 2022, Article ID 5793912, 12 pages, 2022.

Hindawi

Research Article

LINC00707 Promotes Cell Proliferation in Cervical Cancer via the miR-374c-5p/SDC4 Axis

Fang Fang [ID],[1] Chunfeng Guo,[2] Weinan Zheng,[3] and Qingyang Li[4]

[1]*Department of Obstetric and Gynecology, Renmin Hospital of Wuhan University, Wuhan 430000, China*
[2]*Department of Gynecology, The First Affiliated Hospital of Xinjiang Medical University, Urumchi 830001, China*
[3]*Department of Human Anatomy and Embryology, Chengdu Medical College, Chengdu 610000, China*
[4]*Department of Gynecology and Obstetrics, Xinjiang Production and Construction Corps 13 Division Red Star Hospital, Hami City 839000, China*

Correspondence should be addressed to Fang Fang; haomeike45909784@163.com

Cervical cancer (CC) is the second main reason of cancer-related deaths in women around the world. Long intergenic nonprotein coding RNA 707, which is known as LINC00707, has been elucidated to facilitate the progression of multifarious tumors, but how it may exert functions in CC has not been elucidated yet. By using quantitative real-time RT-PCR (RT-qPCR), we identified the expression pattern LINC00707 may possess in CC. Loss-of-function assays including Cell Counting Kit-8 (CCK-8), colony formation, and transferase-mediated dUTP nick-end labeling (TUNEL) assays were taken to verify the effects of LINC00707 inhibition on CC cell proliferation and apoptosis. The downstream RNAs were selected through bioinformatics prediction, and their interaction with LINC00707 was verified through mechanism assays including the luciferase reporter assay, RNA pull-down assay, and RNA immunoprecipitation (RIP) assay. According to results, LINC00707 was upregulated in CC cells, and LINC00707 insufficiency inhibited cell proliferation while facilitating cell apoptosis. MicroRNA (miRNA) miR-374c-5p interacted with LINC00707, and syndecan-4 (SDC4) was verified to be the downstream target gene. Data of rescue assays proved that LINC00707 could promote CC cell malignancy via the miR-374c-5p/SDC4 axis, which revealed a potential treatment option for CC.

1. Introduction

Cervical cancer (CC) is one of the most familiar malignant tumors in the female genital system, resulting in a great deal of cancer-related deaths globally, especially in underdeveloped and developing countries [1]. In spite of great progress made in methods of diagnosis and treatment for CC [2], the overall outcomes remain unsatisfying. Hence, it is of necessity to clarify the molecular mechanism beneath CC progression so as to recognize and offer more effective diagnostic biomarkers and therapeutic targets for medical treatment of CC.

As crucial regulators, long noncoding RNAs (lncRNAs) exert considerable roles in numerous cancers by influencing many cellular processes, regulating gene expression during different stages of cancer development [3]. lncRNA-Hh promotes the generation of cancer stem cells in breast cancer by activating the hedgehog signaling pathway [4]. lncRNA LINC01207 facilitates cell proliferation in lung adenocarcinoma [5]. lncRNA MALAT1 with its upregulation in esophageal squamous cell carcinoma aggravates cell growth [6]. LINC00707 has been illustrated to possess carcinogenic property in cancers. It accelerates the proliferation along with metastasis of lung adenocarcinoma by upregulating Cdc42 [7]. It is determined to accelerate breast cancer via the modulation of the miR-30c/CTHRC1 loop [8]. Combined with these considerations, we are interested in LINC00707 and we try to verify how LINC00707 may exert certain impacts on CC.

In this study, we planned to figure out what specific impacts LINC00707 may exert on CC progression, and we found that LINC00707 promoted cell proliferation in CC

via the miR-374c-5p/SDC4 axis, which may provide new thoughts for treating CC.

2. Materials and Methods

2.1. Cell Culture.
Human cervical epithelial immortalized cell line (H8), along with CC cell lines (SiHa, HeLa, CaSki, and C-33A), was purchased from the Chinese Academy of Sciences (Beijing, China). They were incubated in Dulbecco's modified Eagle medium (DMEM) (Gibco-BRL, Grand Island, NY, USA) which contained 10% fetal bovine serum (FBS) (Gibco-BRL) plus 100 mg/mL penicillin and streptomycin (Invitrogen, Carlsbad, CA, USA). The condition for cell cultivation was set as 5% CO_2 at 37°C in a humid atmosphere.

2.2. Cell Transfection.
After transfection of 48 h, SiHa and HeLa cells were put into 6-well plates at a cell density of 70%-80%. shRNAs against LINC00707 (sh-LINC00707#1/2) and SDC4 (sh-SDC4#1/2), along with their negative controls (shNCs), were constructed to knock down LINC00707 or SDC4 expression. The miR-374c-5p mimics, NC mimics, miR-374c-5p inhibitor, and NC inhibitor were all obtained from GeneChem (Shanghai, China) for the overexpression or silencing of miR-374c-5p in CC cells. The above control plasmids were transfected with Lipofectamine (Invitrogen, Carlsbad, CA, USA).

2.3. Quantitative Real-Time RT-PCR.
By using the TRIzol reagent (Invitrogen, Carlsbad, USA), we supplemented the extraction of total RNA from CC cells, which were then reversely transcribed into cDNA by using the Reverse Transcription Kit (Invitrogen). RT-qPCR was processed on the Bio-Rad CFX96 system using the SYBR-Green Real-Time PCR Kit (Takara Bio Inc., Tokyo, Japan). The normalization was set as GAPDH or U6, with expression fold changes calculated by $2^{-\Delta\Delta Ct}$ methods. Each experiment went through three repeats.

2.4. Cell Viability Assay.
SiHa and HeLa cells were planted in 96-well plates (Corning Costar, Corning, NY, USA), with a density of 1×10^3 cells in each well, and then, they were cultured at five time points over 0, 24, 48, 72, and 96 h. 10 μl of CCK-8 solution was added, and the cells were cultured for another 4 h. The absorbance at 450 nm was finally detected using the ELX-800 spectrometer reader (Bio-Tek Instruments Inc., Waltham, MA, USA).

2.5. TUNEL (Terminal Deoxynucleotidyl Transferase-Mediated Nick-End Labeling) Assay.
In Situ Cell Death Detection Kit (Roche, Mannheim, Germany) was applied to evaluate cell apoptosis by the TUNEL staining assay based upon the standardized guidelines. DAPI (Haoran Biotechnology, Shanghai, China) or merge (Gene-denovo, Guangzhou, Guangdong, China) was employed for dyeing SiHa and HeLa cells. By using an EVOS FL microscope (Thermo Fisher Scientific, Massachusetts), relative fluorescence intensity was measured, and the calculation for cells was made using ImageJ software.

2.6. Western Bolt.
Protein extraction reagent (Pierce, IL, USA) was used to obtain total protein. Proteins were isolated by 10% SDS-PAGE (Boster Biological Technology, LA, CA, USA) and then transferred to PVDF (East Fluorine Chemical Technology, Shanghai, China) after separation and blocked with milk. The membranes were incubated with specific antibodies: anti-Bcl-2 (ab32124, Abcam, Cambridge, UK), anti-Bax (ab32503, Abcam), anti-SDC4 (ab213830, Abcam), or GAPDH (ab8245, Abcam) which served as the internal reference. The amount of protein was detected by the chemiluminescence system (GE Healthcare, Chicago, IL, USA).

2.7. Luciferase Reporter Assay.
The LINC00707 sequences or 3′-UTR fragments of SDC4 containing corresponding binding sites of miR-374c-5p were subcloned into the pmirGLO dual-luciferase vector (Promega), thereby constructing LINC00707/SDC4-WT, together with the corresponding mutant-type vector LINC00707/SDC4-MUT. Then, the plasmids were subjected to cotransfection with NC mimics or miR-374c-5p mimics into SiHa or HeLa cells. After 48 h of transfection, the luciferase activity was measured via the dual-luciferase reporter assay kit (Promega, USA) as per the guides of the manufacturer.

2.8. Colony Formation Assay.
After transfection, 800-1000 cells were planted in 6-well plates. The medium was changed every 3 days, as required. Two weeks later, the cells were washed with PBS (Solibao Technology, Beijing, China) for two times. Methanol (Solarbio) was used for cell fixation for 15 minutes, and crystal violet (Beyotime Biotechnology, Nantong, China) was applied to dye the cells. Later, the visible colony numbers were counted using ImageJ software.

2.9. Subcellular Fractionation.
The extracts of the cytoplasmic and nuclear component were gained from SiHa and HeLa cells with NE-PER Nuclear and Cytoplasmic Extraction Reagents (Thermo Scientific, Waltham, MA, USA). The cell cytoplasm was isolated by adding the cell fractionation buffer, and cell disruption buffer was used to collect the cell nucleus. At last, the content of LINC00707, as well as the cytoplasmic control GAPDH and the nucleus control U6, was presented.

2.10. RNA Pull-Down Assay.
LINC00707-WT/Mut and miR-374c-5p-WT/Mut, along with the negative control NC, were biotinylated into Bio-LINC00707-WT/Mut, Bio-miR-374c-5p-WT/Mut, and Bio-NC. Then, the biotinylated RNA was cultured with cell lysate overnight. RNA-bound beads were cocultivated for 48 h, and finally, the purified RNA complexes were evaluated by RT-qPCR.

2.11. RIP Assay.
This assay was conducted using Magna RNA-binding protein immunoprecipitation kit (Millipore, Billerica, MA, USA). Lysates of CC cells (SiHa and HeLa) were cultured in RIP buffer containing magnetic beads which were combined with the Ago2 antibody, with normal IgG regarded as the control. Finally, RNAs after purification were analyzed by RT-qPCR.

(a)

(b)

(c)
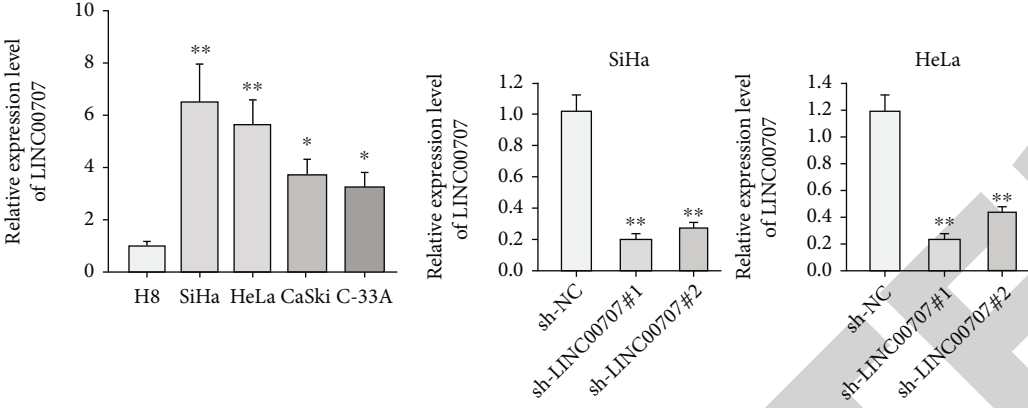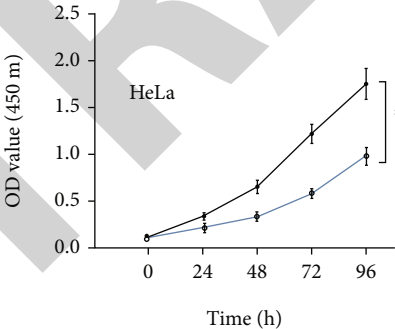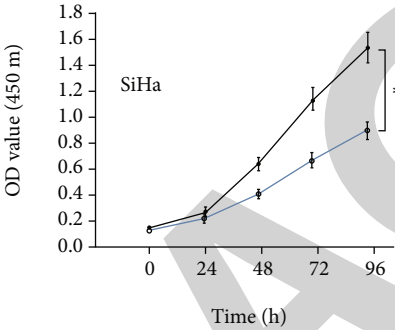
Figure 1: Continued.
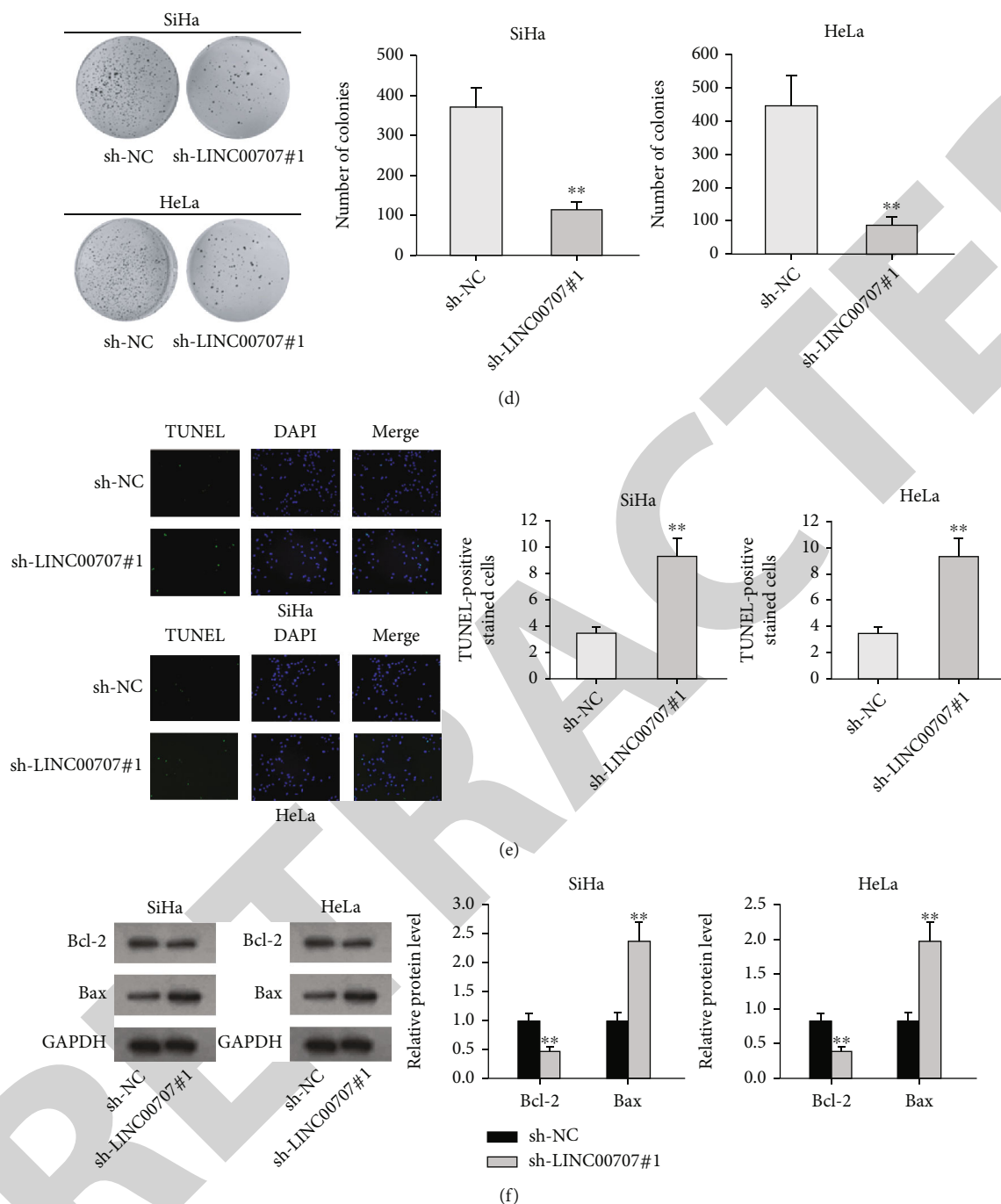
Figure 1: LINC00707 knockdown inhibits CC cell proliferation. (a) LINC00707 expression in four CC cell lines (SiHa, HeLa, CaSki, and C-33A) and normal H8 cell line. (b) LINC00707 expression was knocked down in CC cells. (c, d) The effects of LINC00707#1 depletion on cell proliferation were validated by CCK-8 and colony formation assays. (e, f) The effects of LINC00707#1 depletion on cell apoptosis level were measured by TUNEL assay and western blot, with GAPDH as an internal control. Error bars represent the mean ± SD of at least three independent experiments. $^*P < 0.05$, $^{**}P < 0.01$.

2.12. Statistical Analysis. For this study, every experiment went through three repeats. Represented as means ± standard deviation (SD), related data were subjected to analyses by the GraphPad Prism 7 software package (GraphPad Software, Inc., La Jolla, CA, USA). ANOVA and Student's *t*-test were applied to compare the difference of multiple groups and two groups. Data with statistical significance was set as *P* value below 0.05.

3. Results

3.1. Knockdown of LINC00707 Inhibits CC Cell Proliferation. At first, LINC00707 was examined to be with higher expression in CC cell lines (SiHa, HeLa, CaSki, and C-33A) than in the normal cell line (H8) (Figure 1(a)). Sh-LINC00707#1/2 was transfected into SiHa and HeLa cell lines that contained the highest LINC00707 expression to knock down its

(a)

(b)

(c)

(d)

(e)
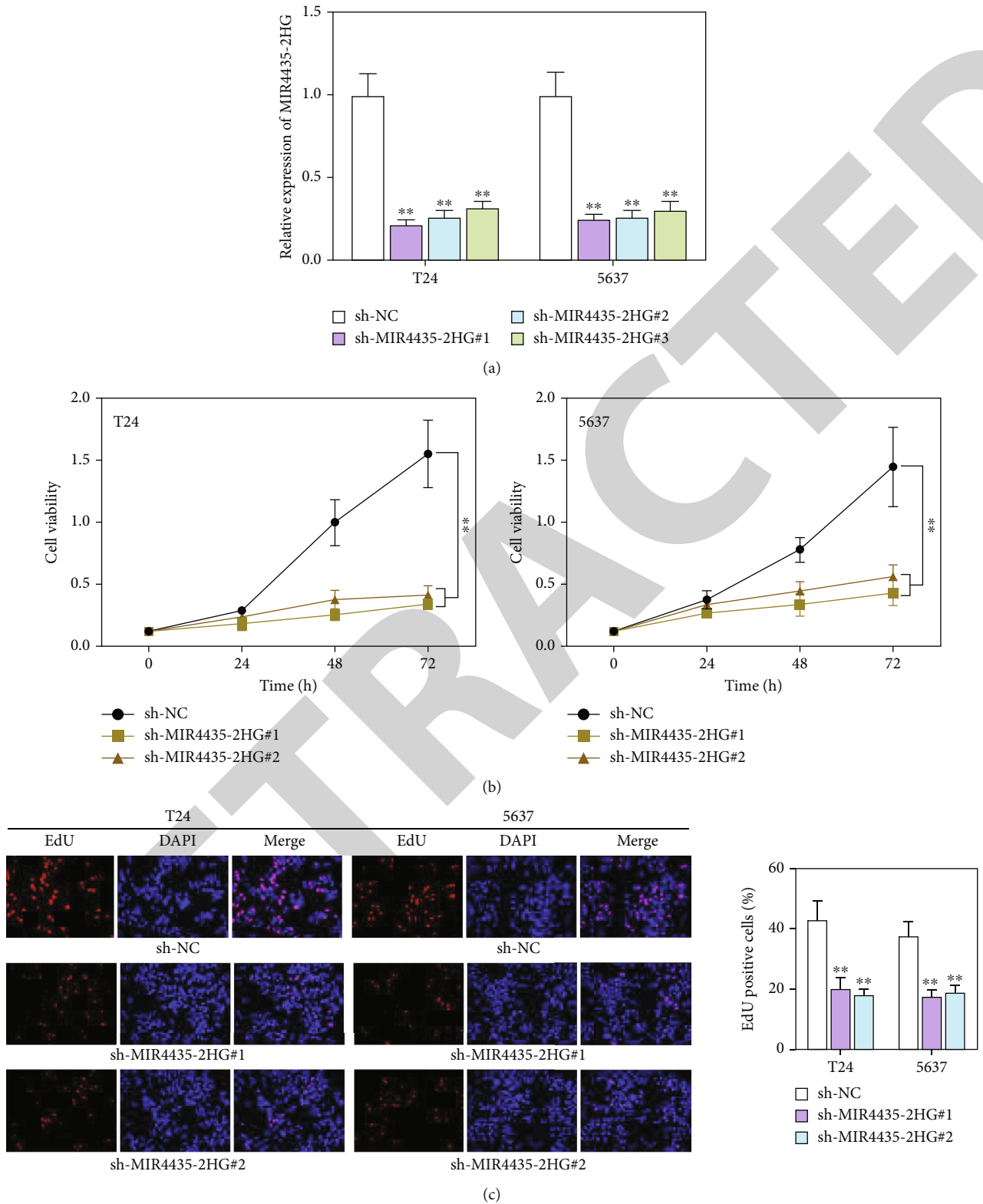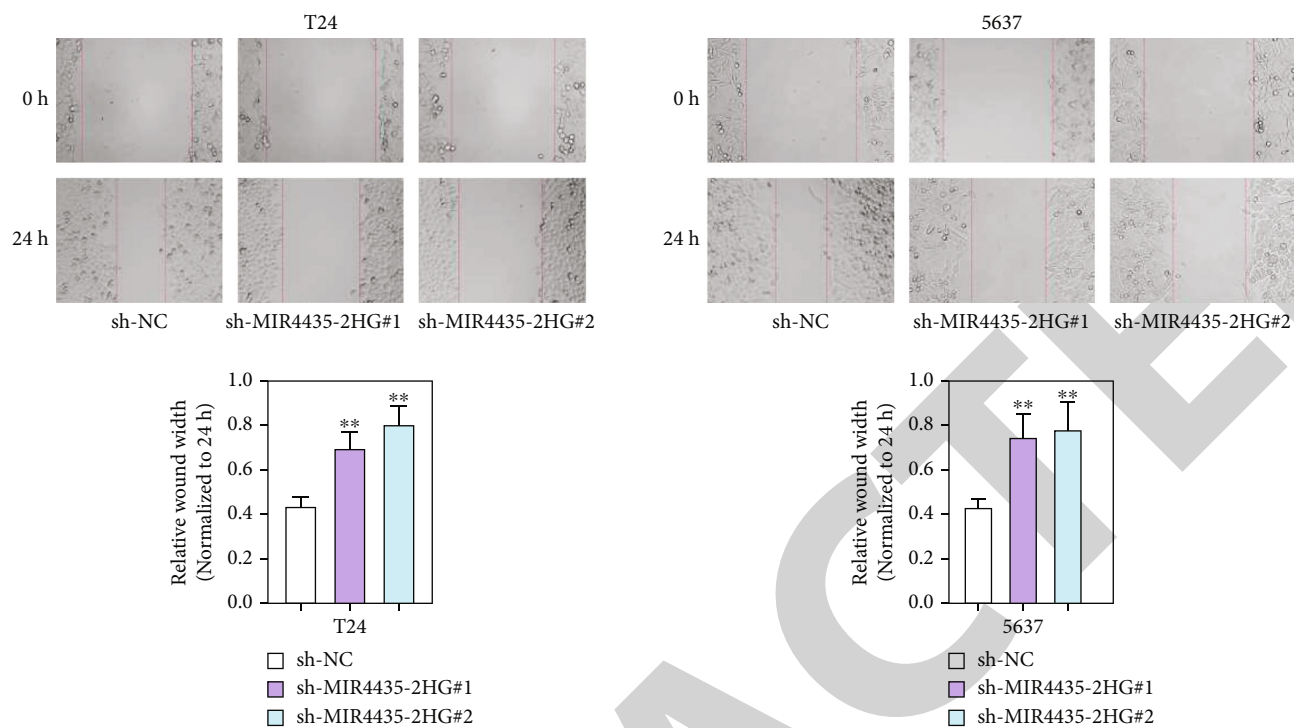
Figure 2: Continued.

(f)   (g)

FIGURE 2: LINC00707 sponges miR-374c-5p in CC cells. (a) LINC00707 localization identified by subcellular fractionation detection, with GAPDH and U6 as internal controls. (b) Potential miRNAs of LINC00707 predicted through starBase. (c) RNA pull-down assay was taken to detect the enrichment of the selected miRNA candidates in the Bio-LINC00707-WT group. (d) miR-374c-5p expression in CC cell lines was verified. (e) The binding sites between LINC00707 and miR-374c-5p were exhibited. (f) The luciferase activity of CC cells in LINC00707-WT and LINC00707-Mut groups upon miR-374c-5p mimic transfection. (g) miR-374c-5p expression in sh-LINC00707#1-transfected CC cells. Error bars represent the mean ± SD of at least three independent experiments. $^{*}P < 0.05$, $^{**}P < 0.01$.

expression (Figure 1(b)), and LINC00707#1 with better efficiency was used for the next-step loss-of-function assays. After LINC00707 inhibition, SiHa and HeLa cells displayed weakened viability (Figure 1(c)). Validated by the reduced number of colonies in LINC00707-downregulated SiHa and HeLa cells, we could say that LINC00707#1 knockdown repressed cell proliferation (Figure 1(d)). Next, TUNEL data exhibited that absence of LINC00707 enhanced the apoptosis of CC cells (Figure 1(e)). Additionally, Bcl-2 protein expression was declined while Bax expression was elevated by LINC00707#1 shortage, indicating that LINC00707 inhibition facilitated cell apoptosis (Figure 1(f)).

3.2. LINC00707 Sponges miR-374c-5p in CC Cells. We carried out subcellular fractionation analysis to identify the cellular localization of LINC00707 in CC cells, and the majority cytoplasmic existence of LINC00707 was seen (Figure 2(a)). Cytoplasmic lncRNAs are well known as competing endogenous RNAs, namely, ceRNAs in cancer progression [9]. By using the online software program miRBase, we screened out 8 miRNAs (miR-376c-3p, miR-30c-5p, miR-30a-5p, miR-30d-5p, miR-30b-5p, miR-30e-5p, miR-374c-5p, and miR-338-3p) that have complementary base pairing with LINC00707 (Figure 2(b)). As shown by RNA pull-down data, miR-374c-5p presented the highest enrichment in the Bio-LINC00707-WT group (Figure 2(c)), so it was chosen for further investigations. The low expression of miR-374c-5p was verified in CC cell lines via RT-qPCR (Figure 2(d)). The binding sites between LINC00707 and miR-374c-5p were predicted by using a bioinformatics tool (Figure 2(e)). After miR-374c-5p overexpression, the LINC00707-WT group exhibited declined luciferase activity, with bare variation in the mutant group (Figure 2(f)). Finally, RT-qPCR

data manifested that LINC00707 knockdown led to elevated miR-374c-5p expression (Figure 2(g)).

3.3. SDC4 Is Targeted by miR-374c-5p. As shown in Figure 3(a), SDC4 and ARID4A were predicted to combine with miR-374c-5p by starBase, making them potential downstream targets of miR-374c-5p. It was then verified through the RNA pull-down assay that SDC4 and ARID4A were both enriched in the Bio-miR-374c-5p-Wt group, while the enrichment of SDC4 was greater than that of ARID4A (Figure 3(b)). It was found by RT-qPCR analysis that SDC4 possessed a high expression pattern in CC cell lines (Figure 3(c)). What is more, LINC00707, SDC4, and miR-374c-5p exhibited high enrichment in the Ago2 antibody, which indicated their coexistence in RISC (RNA-induced silencing complex) (Figure 3(d)). To probe the interactions between miR-374c-5p and SDC4, we upregulated miR-374c-5p expression in the SiHa cell line via miR-374c-5p mimic transfection and inhibited its expression in C-33A cells by miR-374c-5p inhibitor transfection (Figure 3(e)). SDC4 was negatively regulated by miR-374c-5p, as evidenced via RT-qPCR along with western blot (Figure 3(f)). Furthermore, the binding sites of miR-374c-5p and SDC4 were conjectured by bioinformatics, and it was verified that the SDC4-WT group presented declined luciferase activity in miR-374c-5p mimic-transfected CC cells (Figure 3(g)). Furthermore, RT-qPCR data validated that SDC4 expression was declined by LINC00707 inhibition in CC cells (Figure 3(h)).

3.4. LINC00707 Promotes CC Cell Proliferation via the miR-374c-5p/SDC4 Axis. SDC4 expression was silenced in SiHa cells via sh-SDC4#1/#2 transfection (Figure 4(a)) for the

miRNA	↑↓	GeneName	↑↓	RNA22	↑↓	miRmap	↑↓	AgoExpNum	↑↓	Pan-Cancer	↑↓
hsa-miR-374c-3p ↑		ARID4A	↑	1 (6,0)	↑	1 (5,0)	↑	7	↑	1	↑
hsa-miR-374c-3p		SDC4		1 (6,0)		1 (3,0)		6		1	

(a)

(b)

Bio-NC
Bio-miR-374c-5p-WT
Bio-miR-374c-5p-Mut

(c)

(d)

Anti-IgG
Anti-Ago2

(e)

(f)

Figure 3: Continued.

SDC4-WT 5`-cauuucc**ACA**GC**ACC**UG**CUAAGU**u-3`

|| ||||||||||

miR-374c-5p 3`-uauauua**UGU**--**UGGACGAUUCA**c-5`

SDC4-Mut 5`-cauuucc**UGUGCUGGACGAUUCA**u-3`

(g)

(h)
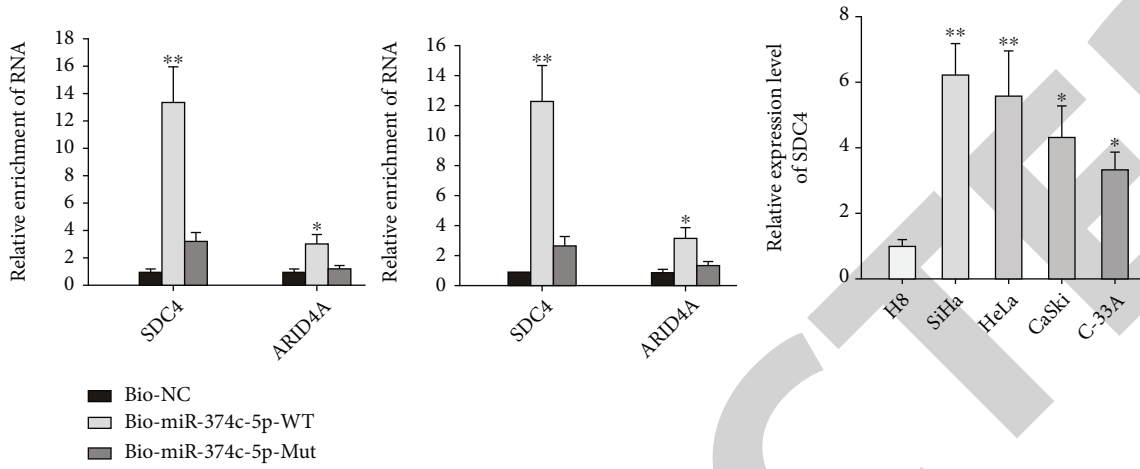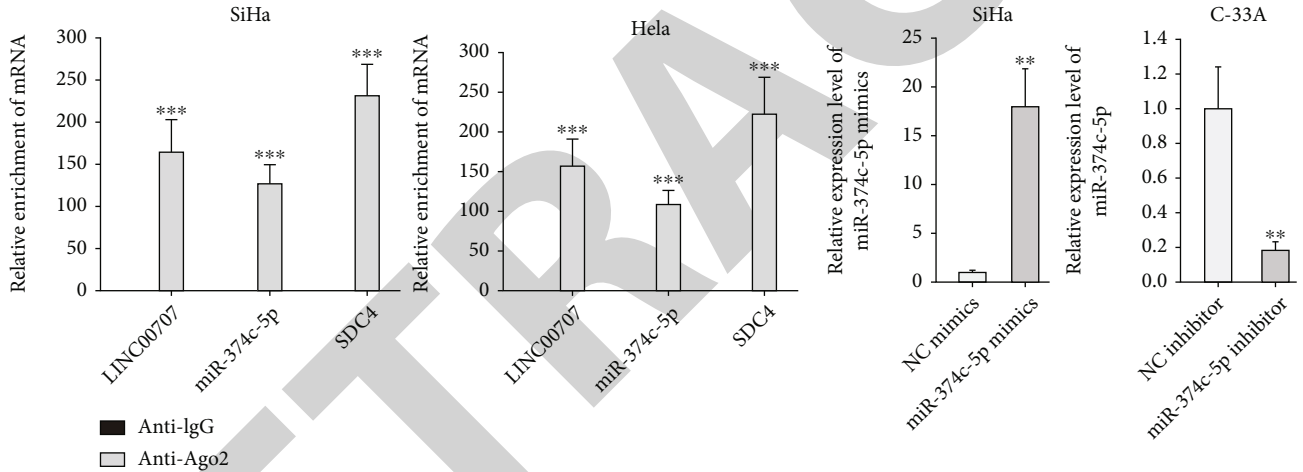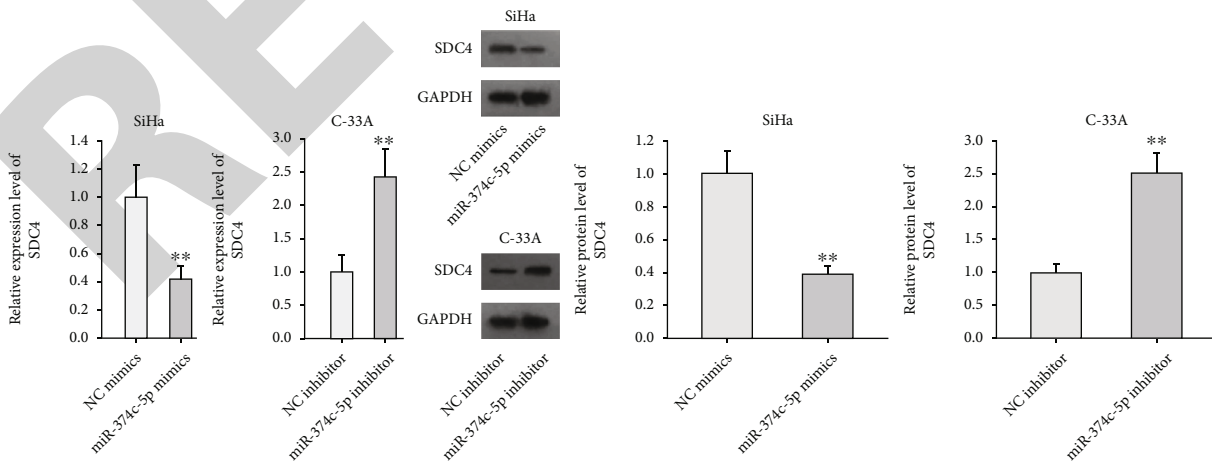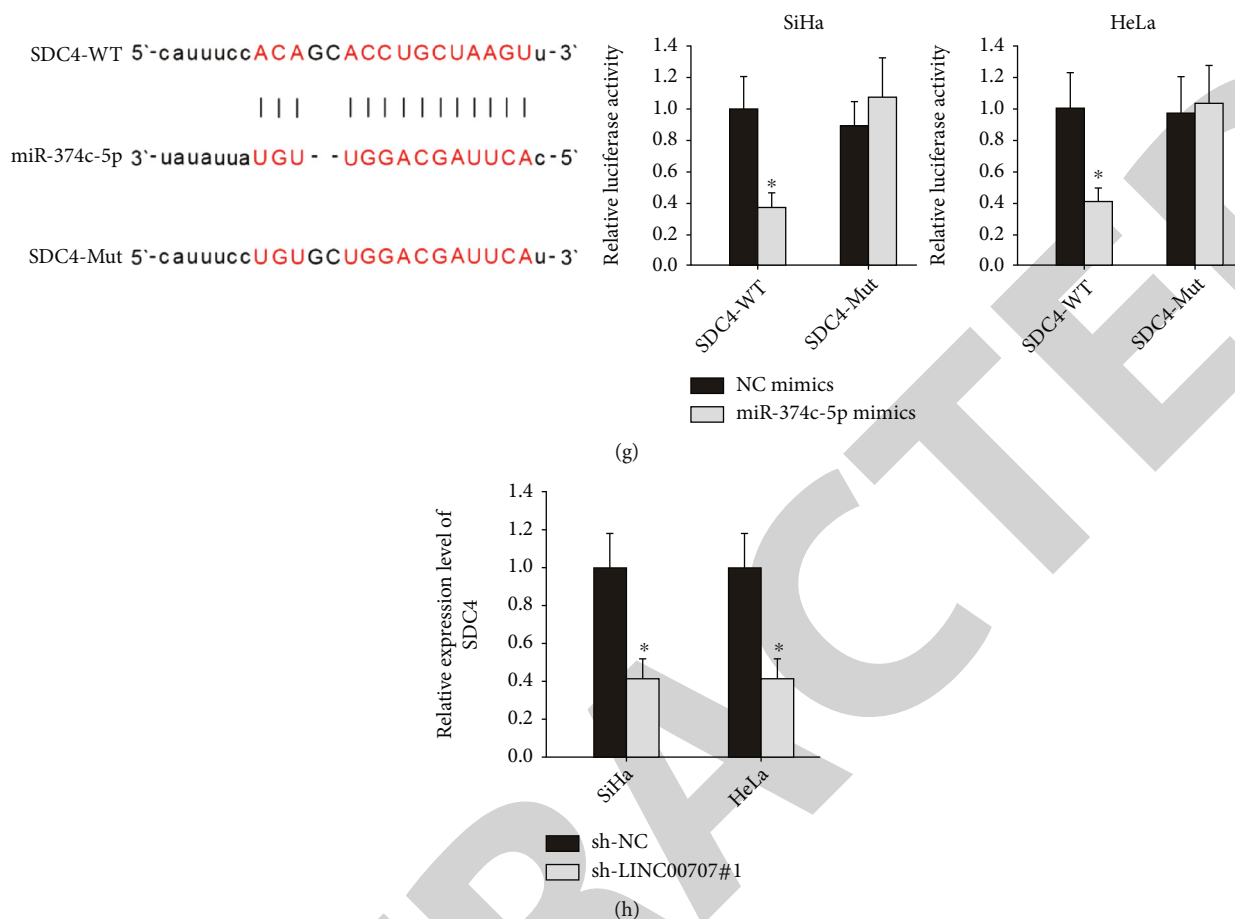
Figure 3: SDC4 is the target gene of miR-374c-5p in CC cells. (a) Potential mRNAs that may bind to miR-374c-5p were selected using starBase. (b) RNA pull-down assay was taken to measure the enrichment of selected two mRNAs (SDC4 and ARID4A) in Bio-miR-374c-5p-WT/Mut groups. (c) The identified SDC4 expression in CC cell lines. (d) RIP assay was performed to test the enrichment of LINC00707, miR-374c-5p, and SDC4 in the anti-Ago2 group and the control IgG group. (e) miR-374c-5p expression was elevated in the SiHa cell line via miR-374c-5p mimic transfection while it was reduced via miR-374c-5p inhibitor transfection in C-33A cells. (f) The relative expression along with protein level of SDC4 upon miR-374c-5p overexpression or inhibition. (g) The binding sites between miR-374c-5p and SDC4 were evidenced by the luciferase reporter assay. (h) SDC4 expression in sh-LINC00707#1-transfected CC cells. Error bars represent the mean ± SD of at least three independent experiments. $^{*}P < 0.05$, $^{**}P < 0.01$, and $^{***}P < 0.001$.

follow-up rescue assays. The viability and proliferation of SiHa cells were suppressed by LINC00707 knockdown, while they were promoted upon the cotransfection of the miR-374c-5p inhibitor. Such effect was normalized again by the cotransfection of sh-SDC4#1 (Figures 4(b) and 4(c)). As for CC cell apoptosis, it was verified through the TUNEL assay that miR-374c-5p downregulation reversed the promoting effects of sh-LINC00707#1 on cell apoptosis, while this impact was normalized again by knockdown of SDC4 (Figure 4(d)). Same results were observed through western blot analysis (Figure 4(e)). In conclusion, LINC00707 promotes CC cell proliferation via the miR-374c-5p/SDC4 axis.

4. Discussion

Cervical cancer (CC) is one of the most common malignant cancers in females [10, 11]. Referring to concerned statistics, nearly 530,000 new cases are diagnosed universally each year [12], and the number of CC-caused mortality in low- and

middle-income countries is remarkably higher than that in high-income countries [13]. Long noncoding RNAs (lncRNAs) are extensively linked with all kinds of cancer-related biological activities [14, 15]. Dysregulation of lncRNAs, together with their various impacts in CC, has been well elucidated [16, 17]. For example, lncRNA PVT1 accelerates cervical cancer progression by downregulating miR-424 [18]. lncRNA HOXA11 antisense aggravates tumor development and stemness maintenance in cervical cancer [19]. lncRNA HOXD-AS1 modulates cell proliferation in cervical cancer by motivating the Ras/ERK signaling pathway [20]. It has been documented that LINC00707 aggravates the development of many cancers, including colorectal cancer [21], osteosarcoma [22], and gliomas [23]. We verified the high expression of LINC00707 in CC for the first time, and we further validated that LINC00707 inhibition suppressed the malignant cell behaviors in CC.

lncRNAs are extensively affirmed to be the "sponge" or "ceRNA (competing endogenous RNA)" in the regulatory

(a)

(b)

(c)

FIGURE 4: Continued.

(d)

(e)
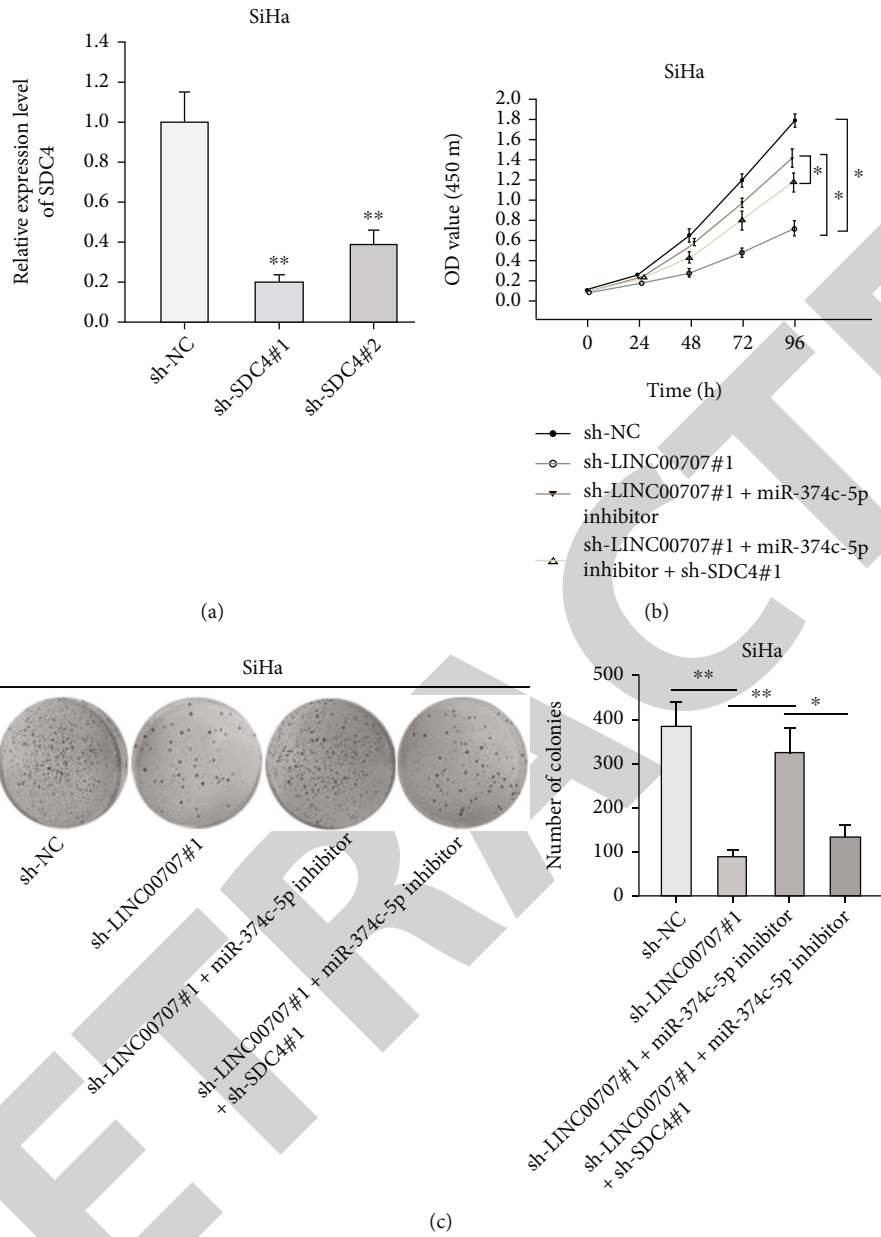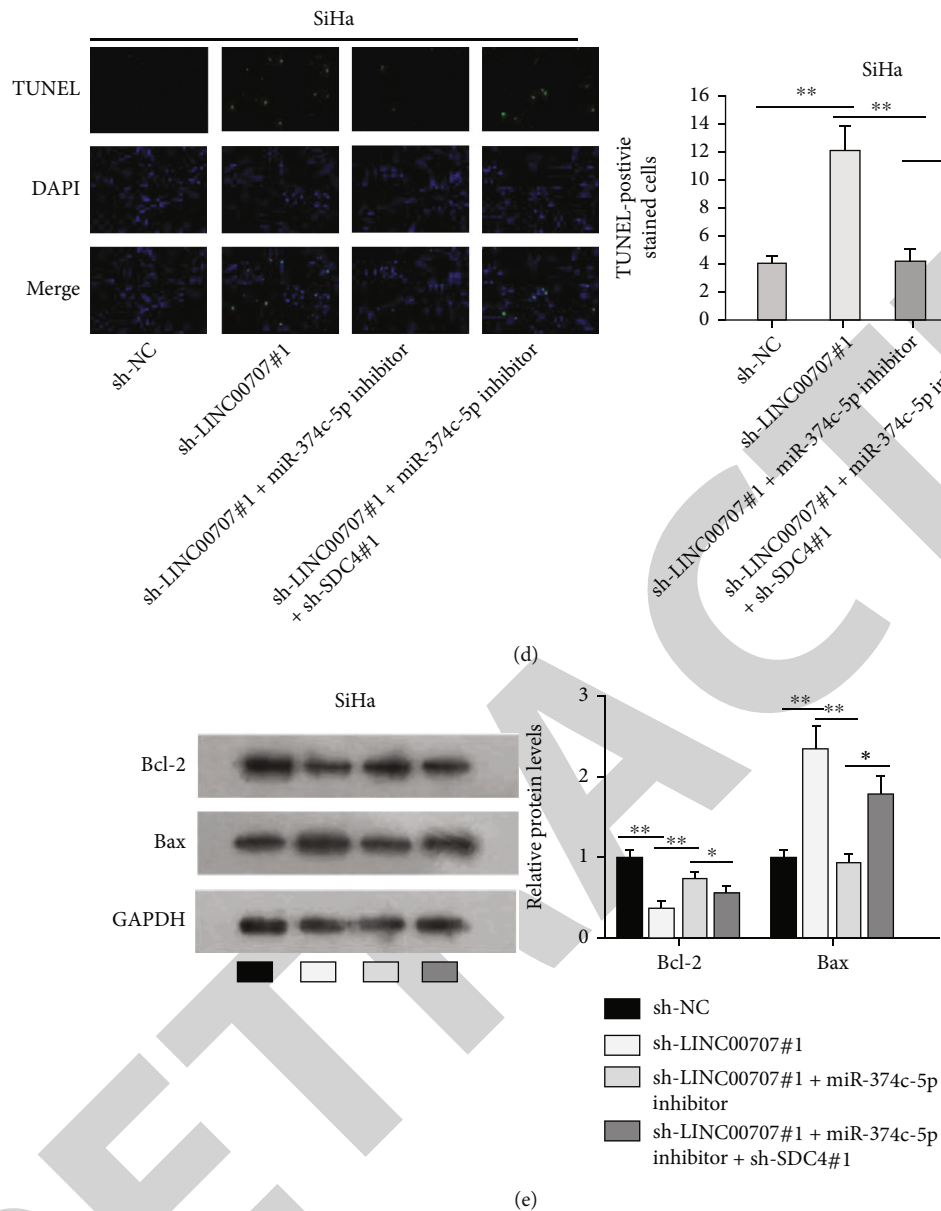
Figure 4: LINC00707 promotes CC cell proliferation via the miR-374c-5p/SDC4 axis. (a) Sh-SDC4#1/#2 transfection in the SiHa cell line to knock down gene expression. (b, c) The viability and proliferation of CC cells were measured by CCK-8 along with colony formation assay in different groups (sh-NC, sh-LINC00707#1, sh-LINC00707#1+miR-374c-5p inhibitor, and sh-LINC00707#1+miR-374c-5p inhibitor+sh-SDC4#1). (d, e) Cell apoptosis change was measured by TUNEL and western blot assays. GAPDH was an internal control. Error bars represent the mean ± SD of at least three independent experiments. $^*P < 0.05$, $^{**}P < 0.01$.

network involving with lncRNA, miRNA, and target genes [24]. For illustration, lncRNA HOTAIR exerts accelerating impact in gastric cancer malignancy via effectively becoming a sink for miR-331-3p and thus regulating the depression of HER2 [25]. lncRNA LINC00511 promotes tumorigenesis and stemness of breast cancer through regulating the signaling composed of miR-185-3p, E2F1, and Nanog [26]. lncRNA 00152 acts as a ceRNA to regulate NRP1 expression via sponging miRNA-206 in colorectal cancer [27]. By conducting subcellular localization analysis, the majority of LINC00707 in the cytoplasm of CC cells was observed, which suggested the potential ceRNA model. Through bioinformat-

ics prediction along with related mechanism assays, miR-374c-5p was identified as the target of LINC00707, and SDC4 was further confirmed to be the downstream gene, which constituted a ceRNA model in CC cells. Results of rescue assays testified that LINC00707 could promote the malignant development of CC cells via sponging miR-374c-5p to elevate SDC4 expression. LINC00707 has been demonstrated to be involved in the ceRNA network to affect cancer progression such as hepatocellular carcinoma and colorectal cancer [21, 28], but it was the first time that we revealed a ceRNA pathway of LINC00707/miR-374c-5p/SDC4 in the regulation of CC cells. miR-374c-5p has been illustrated to

regulate the invasion and migration of CC [29], and what we had discovered about miR-374c-5p in CC cell malignancy may help to provide more therapeutic strategies for CC treatment in the future.

To sum up, we confirmed through this research that LINC00707 promoted CC malignancy cells via the miR-374c-5p/SDC4 axis. Though the clinical significance of LINC00707 along with its regulatory mechanism remains to be verified in the future researches, we hope that our experimental outcomes can help shed some light on the future treatment for CC.

Data Availability

The data used to support the findings of this study are included within the article.

Conflicts of Interest

The authors declare no conflicts of interest in this study.

Acknowledgments

References

[1] S. Pimple, G. Mishra, and S. Shastri, "Global strategies for cervical cancer prevention," *Current Opinion in Obstetrics & Gynecology*, vol. 28, no. 1, pp. 4–10, 2016.

[2] P. Petignat and M. Roy, "Diagnosis and management of cervical cancer," *BMJ*, vol. 335, no. 7623, pp. 765–768, 2007.

[3] J. D. Ransohoff, Y. Wei, and P. A. Khavari, "The functions and unique features of long intergenic non-coding RNA," *Nature Reviews. Molecular Cell Biology*, vol. 19, no. 3, pp. 143–157, 2018.

[4] M. Zhou, Y. Hou, G. Yang et al., "LncRNA-Hh strengthen cancer stem cells generation in twist-positive breast cancer via activation of hedgehog signaling pathway," *Stem Cells*, vol. 34, no. 1, pp. 55–66, 2016.

[5] G. Wang, H. Chen, and J. Liu, "The long noncoding RNA LINC01207 promotes proliferation of lung adenocarcinoma," *American Journal of Cancer Research*, vol. 5, no. 10, pp. 3162–3173, 2015.

[6] L. Hu, Y. Wu, D. Tan et al., "Up-regulation of long noncoding RNA MALAT1 contributes to proliferation and metastasis in esophageal squamous cell carcinoma," *Journal of Experimental & Clinical Cancer Research*, vol. 34, no. 1, pp. 1–13, 2015.

[7] T. Ma, H. Ma, Z. Zou et al., "The long intergenic noncoding RNA 00707 promotes lung adenocarcinoma cell proliferation and migration by regulating Cdc42," *Cellular Physiology and Biochemistry*, vol. 45, no. 4, pp. 1566–1580, 2018.

[8] R. X. Yuan, D. Bao, and Y. Zhang, "Linc00707 promotes cell proliferation, invasion, and migration via the miR-30c/CTHRC1 regulatory loop in breast cancer," *European Review for Medical and Pharmacological Sciences*, vol. 24, no. 9, pp. 4863–4872, 2020.

[9] J. H. Noh, K. M. Kim, W. McClusky, K. Abdelmohsen, and M. Gorospe, "Cytoplasmic functions of long noncoding RNAs," *Wiley Interdisciplinary Reviews: RNA*, vol. 9, no. 3, article e1471, 2018.

[10] E. Morris and M. A. Roett, "Genital cancers in women: cervical cancer," *FP Essentials*, vol. 438, pp. 18–23, 2015.

[11] R. Siegel, D. Naishadham, and A. Jemal, "Cancer statistics, 2013," *CA: a Cancer Journal for Clinicians*, vol. 63, no. 1, pp. 11–30, 2013.

[12] B. J. Lahue, E. Baginska, S. S. Li, and M. Parisi, "Health technology assessment on cervical cancer screening, 2000-2014," *International Journal of Technology Assessment in Health Care*, vol. 31, no. 3, pp. 171–180, 2015.

[13] M. Vu, J. Yu, O. A. Awolude, and L. Chuang, "Cervical cancer worldwide," *Current Problems in Cancer*, vol. 42, no. 5, pp. 457–465, 2018.

[14] J. Dong, M. Su, W. Chang, K. Zhang, S. Wu, and T. Xu, "Long non-coding RNAs on the stage of cervical cancer," *Oncology Reports*, vol. 38, no. 4, pp. 1923–1931, 2017.

[15] C. Han Li and Y. Chen, "Small and long non-coding RNAs: novel targets in perspective cancer therapy," *Current Genomics*, vol. 16, no. 5, pp. 319–326, 2015.

[16] E. S. Hosseini, M. Meryet-Figuiere, H. Sabzalipoor, H. H. Kashani, H. Nikzad, and Z. Asemi, "Dysregulated expression of long noncoding RNAs in gynecologic cancers," *Molecular Cancer*, vol. 16, no. 1, pp. 1–13, 2017.

[17] H. Aalijahan and S. Ghorbian, "Long non-coding RNAs and cervical cancer," *Experimental and Molecular Pathology*, vol. 106, pp. 7–16, 2019.

[18] Y. L. Gao, Z. S. Zhao, M. Y. Zhang, L. J. Han, Y. J. Dong, and B. Xu, "Long noncoding RNA PVT1 facilitates cervical cancer progression via negative regulating of miR-424," *Oncology Research*, vol. 25, no. 8, pp. 1391–1398, 2017.

[19] H. J. Kim, K. J. Eoh, L. K. Kim et al., "The long noncoding RNA HOXA11 antisense induces tumor progression and stemness maintenance in cervical cancer," *Oncotarget*, vol. 7, no. 50, pp. 83001–83016, 2016.

[20] Y. C. Hu, A. M. Wang, J. K. Lu, R. Cen, and L. L. Liu, "Long noncoding RNA HOXD-AS1 regulates proliferation of cervical cancer cells by activating Ras/ERK signaling pathway," *European Review for Medical and Pharmacological Sciences*, vol. 21, no. 22, pp. 5049–5055, 2017.

[21] H. J. Shao, Q. Li, T. Shi, G. Z. Zhang, and F. Shao, "LINC00707 promotes cell proliferation and invasion of colorectal cancer via miR-206/FMNL2 axis," *European Review for Medical and Pharmacological Sciences*, vol. 23, no. 9, pp. 3749–3759, 2019.

[22] X. R. Zhang, J. L. Shao, H. Li, and L. Wang, "Silencing of LINC00707 suppresses cell proliferation, migration, and invasion of osteosarcoma cells by modulating miR-338-3p/AHSA1 axis," *Open Life Sciences*, vol. 16, no. 1, pp. 728–736, 2021.

[23] H. Liu and K. Hu, "The long intergenic noncoding RNA 00707 sponges microRNA-613 (miR-613) to promote proliferation and invasion of gliomas," *Technology in Cancer Research & Treatment*, vol. 19, article 1533033820962092, 2020.

[24] Y. Tay, J. Rinn, and P. P. Pandolfi, "The multilayered complexity of ceRNA crosstalk and competition," *Nature*, vol. 505, no. 7483, pp. 344–352, 2014.

[25] X. H. Liu, M. Sun, F. Q. Nie et al., "Lnc RNA HOTAIR functions as a competing endogenous RNA to regulate HER2 expression by sponging miR-331-3p in gastric cancer," *Molecular Cancer*, vol. 13, no. 1, article 92, 2014.

[26] G. Lu, Y. Li, Y. Ma et al., "Long noncoding RNA LINC00511 contributes to breast cancer tumourigenesis and stemness by

Retraction

Retracted: hsa_circ_0084811 Regulates Cell Proliferation and Apoptosis in Retinoblastoma through miR-18a-5p/miR-18b-5p/E2F5 Axis

BioMed Research International

This article has been retracted by Hindawi following an investigation undertaken by the publisher [1]. This investigation has uncovered evidence of one or more of the following indicators of systematic manipulation of the publication process:

(1) Discrepancies in scope

(2) Discrepancies in the description of the research reported

(3) Discrepancies between the availability of data and the research described

(4) Inappropriate citations

(5) Incoherent, meaningless and/or irrelevant content included in the article

(6) Manipulated or compromised peer review

The presence of these indicators undermines our confidence in the integrity of the article's content and we cannot, therefore, vouch for its reliability. Please note that this notice is intended solely to alert readers that the content of this article is unreliable. We have not investigated whether authors were aware of or involved in the systematic manipulation of the publication process.

Wiley and Hindawi regrets that the usual quality checks did not identify these issues before publication and have since put additional measures in place to safeguard research integrity.

We wish to credit our own Research Integrity and Research Publishing teams and anonymous and named external researchers and research integrity experts for contributing to this investigation.

The corresponding author, as the representative of all authors, has been given the opportunity to register their agreement or disagreement to this retraction. We have kept a record of any response received.

References

[1] G. Jiang, M. Qu, L. Kong, X. Song, and S. Jiang, "hsa_circ_0084811 Regulates Cell Proliferation and Apoptosis in Retinoblastoma through miR-18a-5p/miR-18b-5p/E2F5 Axis," *BioMed Research International*, vol. 2022, Article ID 6918396, 16 pages, 2022.

Research Article

hsa_circ_0084811 Regulates Cell Proliferation and Apoptosis in Retinoblastoma through miR-18a-5p/miR-18b-5p/E2F5 Axis

Guangwei Jiang,[1] Mingxuan Qu,[2] Lili Kong,[3] Xiaoming Song,[3] and Shanhao Jiang [1]

[1]*Department of Ophthalmology, Yantai Affiliated Hospital of Binzhou Medical University, Yantai City,*
Shandong Province 264100, China
[2]*Hemodialysis Room, Yantai Affiliated Hospital of Binzhou Medical University, Yantai City, Shandong Province 264100, China*
[3]*Endocrinology & Metabolic Diseases, Yantai Affiliated Hospital of Binzhou Medical University, Yantai City,*
Shandong Province 264100, China

Correspondence should be addressed to Shanhao Jiang; jiangshanhao09@outlook.com

Background. Retinoblastoma (RB) is the commonest primary intraocular malignancy during childhood. Circular RNAs (circRNAs) act as regulators in RB development, and hsa_circ_E2F5 (circ_0084811 in this study) was found to be highly expressed in RB cells, so we wanted to identify its detailed molecular mechanism. *Methods*. The expression level of circ_0084811 in RB cells was tested by RT-qPCR and its effects on RB cells were evaluated through functional assays. The regulatory mechanism that circ_0084811 may exert in RB progression was testified through mechanism experiments. *Results*. High circ_0084811 expression in RB cells facilitated cell proliferation but inhibited cell apoptosis. The enrichment of acetylation of histone 3 lysine 27 (H3K27ac) in circ_0084811 promoter induced circ_0084811 upregulation. Moreover, circ_0084811 regulated E2F transcription factor 5 (E2F5) expression via sponging microRNA-18a-5p (miR-18a-5p) and microRNA-18b-5p (miR-18b-5p). *Conclusion*. circ_0084811 modulated RB progression via the miR-18a-5p/miR-18b-5p/E2F5 axis.

1. Background

Retinoblastoma (RB) is defined as a malignant tumor which derives from the developing retina, and it accounts for 3% of all childhood cancers [1, 2]. The commonest signs of RB include white eye reflex and strabismus [3]. Although RB is a rare cancer among children, it is widely considered to be the most frequent primary intraocular malignancy during childhood [4]. According to statistics, the survival rate of RB patients has been improved a lot in developed countries but remains low in developing countries [5]. In this regard, exploring the development of RB from the perspective of molecular mechanism may be of great value to the treatment of RB [6].

Noncoding RNAs (ncRNAs) are defined as a heterogeneous class of RNAs which is limited in coding proteins. As a common type of ncRNAs, circular RNAs (circRNAs) are defined as covalently closed RNA molecules produced by back-splicing. Growing evidence has identified the great importance of circRNAs in tumors [7]. For instance, Liu et al. have proposed that hsa_circ_001783 accelerates the development of breast cancer through sequestering miR-200c-3p [8]. Lu et al. have proved that circSLC8A1 plays a suppressive role in bladder cancer via the crosstalk with the miR-130b/miR-494/PTEN axis [9]. Yu et al. have mentioned that circRNA_100876 exacerbates the proliferation and metastasis of gastric cancer via enhancing MIEN1 expression [10]. Moreover, circRNAs have been reported to participate in ocular diseases including RB [11]. For example, Jiang et al. have disclosed that circ_0000034 exacerbates the malignant development of RB through the miR-361-3p/ADAM19 axis [12]. Zhao et al. have uncovered that circ_0075804 boosts cell proliferation in RB through recruiting HNRNPK protein and stabilizing E2F3 mRNA [13]. Xing et al. have implied that hsa_circ_0001649

(a)

(b)

(c)

Figure 1: Continued.

Figure 1: circ_0084811 was highly expressed in RB cells, and its loop structure was confirmed. (a) Potential circRNAs whose gene symbol was E2F5 were selected via the circBank database. Their expression in RB cell lines and normal cell line was tested via RT-qPCR. (b) The schematic diagram of the genomic location of circ_0084811. (c) circ_0084811 and linear E2F5 expression in RB cells treated with RNase R. (d) The loop structure of circ_0084811 confirmed through gel electrophoresis. (e) Relative RNA level of circ_0084811 and linear-E2F5 in RB cells treated with actinomycin D. Each assay went through three biological replicates. The sample number $(n) = 3$. $^*P < 0.05$ and $^{**}P < 0.01$.

modulates RB malignancy through modulation of the AKT/mTOR signaling pathway [14].

The E2F family of transcription factors has been illustrated as a key regulator related to the proliferation, differentiation, and apoptosis of a variety of tissues [15]. E2F transcription factor 5 (E2F5), a member of E2F family, has been characterized as a transcriptional repressor which can regulate cell proliferation through its interaction with the RB protein for inhibition of target gene transcription. In addition, it has been documented to play critical roles in cancer development, including RB [16, 17]. Since circRNAs can be transcribed together with their parental genes and, in turn, they can regulate the transcription of the parental gene or related genes [18], we explored whether circ_0084811 may regulate its host gene E2F5 in RB.

2. Methods

2.1. Cell Culture.
RB cells (HXO-Rb44, Y79, SO-Rb50, and WERI-Rb-1) and human retinal pigment epithelial ARPE-19 cell line were selected for this study. Y79, WERI-Rb-1, and ARPE-19 cells were bought from ATCC (Manassas, VA, USA). HXO-Rb44 cell line was obtained from Zishi Biotechnology Co., Ltd. (Shanghai, China) while SO-Rb50 cell line was bought from Huatuo Biotechnology Co., Ltd. (Shenzhen, China). The four RB cell lines were cultivated in RPMI-1640 medium while ARPE-19 cell line was cultured in DMEM: F12 medium. All the above mediums were treated with 10% FBS in humidified air, with the culture condition set as 37°C, 5% CO_2.

2.2. Cell Transfection.
The shRNAs targeting CBP (sh-CBP#1/2), circ_0084811 (sh-circ_0084811#1/2/3), or E2F5 (sh-E2F5#1/2) were designed and synthesized by RiboBio (Guangzhou, China). For the overexpression of E2F5, the sequence was subcloned into pcDNA 3.1 vectors with empty pcDNA3.1 vector as the negative control. Besides, miR-18a-5p mimics/inhibitor, miR-18b-5p mimics/inhibitor, and their respective negative controls (control mimics/NC inhibitor) were also constructed by RiboBio. Transfection

(a)

(b)

(c)

(d)

(e)

(f)

(g)

Figure 2: Continued.

(h)

(i)
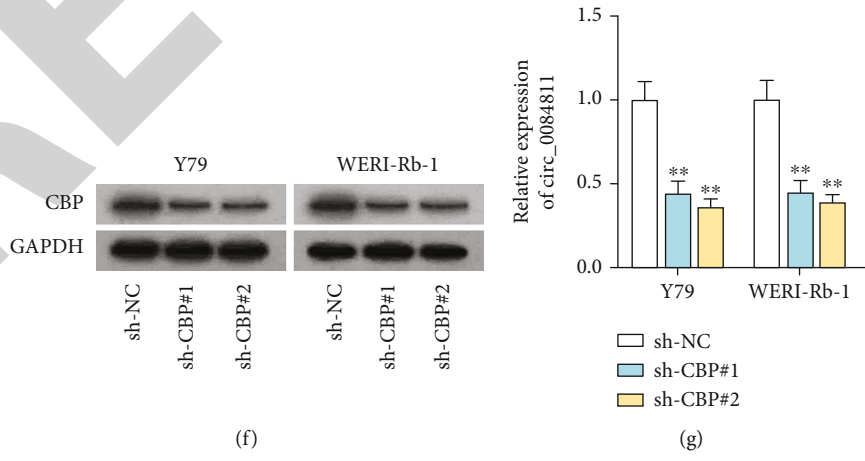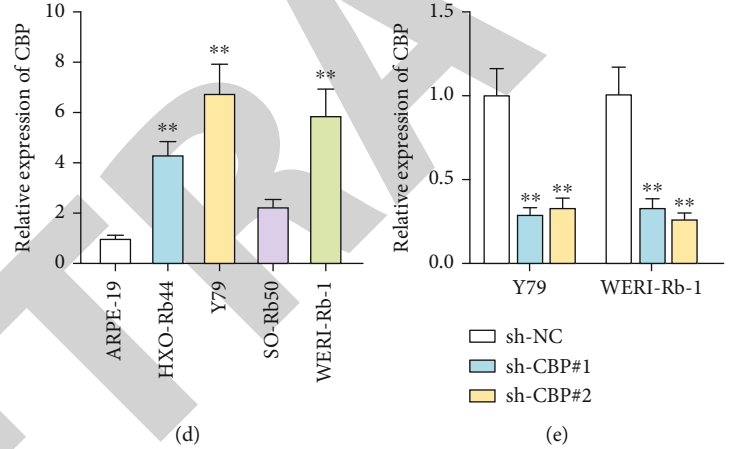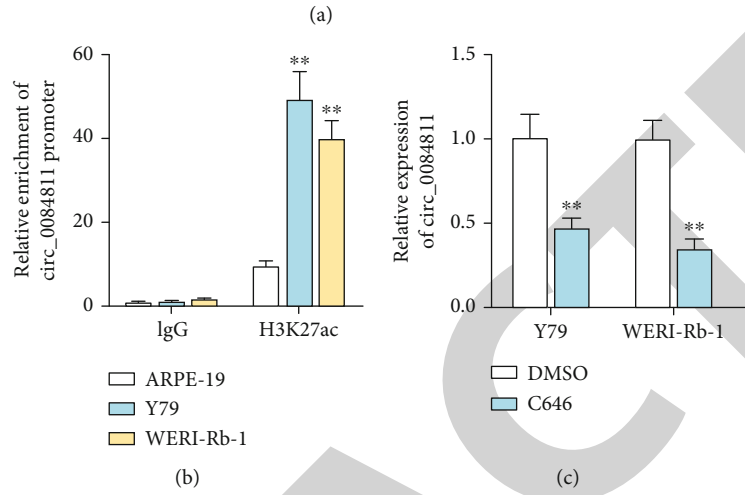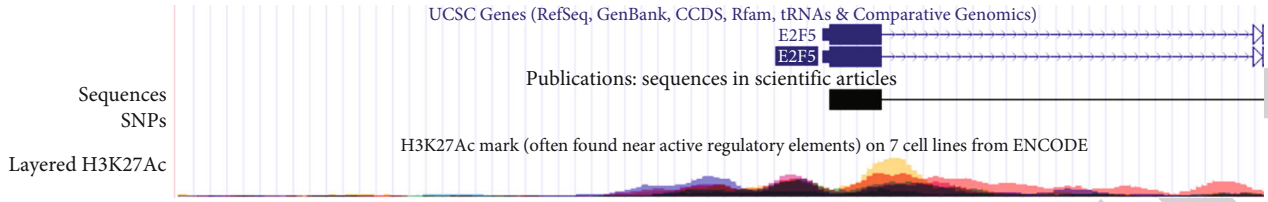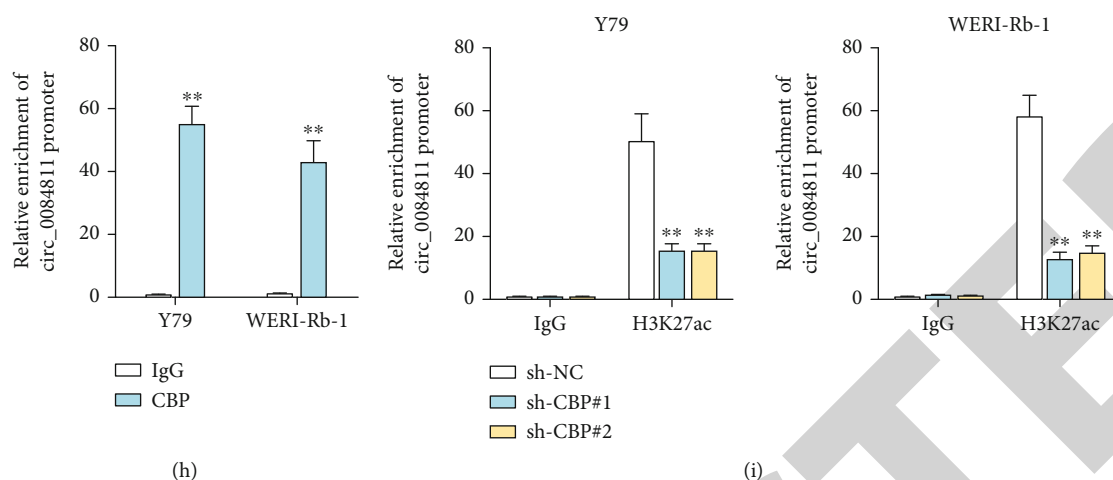
Figure 2: H3K27ac activated the expression of circ_0084811 in RB cells. (a) H3K27ac level in the circ_0084811 promoter region was measured through the UCSC database. (b) The interaction between H3K27ac and the circ_0084811 promoter in RB cells was confirmed through ChIP analysis. (c) circ_0084811 expression in cells treated with C646. (d) CBP expression in RB cell lines and normal cell line. (e, f) CBP expression and protein level were decreased by sh-CBP transfection. (g) circ_0084811 expression was measured after CBP was silenced. (h) The binding ability between circ_0084811 promoter and CBP in RB cells was verified by ChIP assay. (i) The enrichment of circ_0084811 promoter in H3K27ac antibody when CBP was downregulated. Each assay went through three biological replicates. The sample number $(n) = 3$. $^{**}P < 0.01$.

was performed by using Lipofectamine 3000 (Invitrogen) for 48 h.

2.3. Total RNA Extraction and Quantitative Real-Time Polymerase Chain Reaction (RT-qPCR) Analysis.
In line with the instruction of TRIzol reagent (Invitrogen), the isolation of total RNA samples was extracted in RB cells. RNA concentration was detected by NanoDrop 2000 (Thermo Scientific, USA). Synthesis of complementary DNA (cDNA) was carried out using the PrimeScript™ RT master mix (Takara, Japan). RT-qPCR reaction was achieved with SYBR Green PCR Master Mix (Applied Biosystems) followed by the $2^{-\Delta\Delta CT}$ method. GAPDH and U6 were used as internal controls. The experimental procedure was independently carried out in triplicate. Detailed sequences are provided in Supplementary Table 1.

2.4. MTT Assay.
Transfected cells were seeded in 96-well plates (200 μL, 3×10^3 cells/well) added with 10 μL MTT (5 mg/mL) in each well. After incubation for 4 h, the precipitates were dissolved in dimethyl sulfoxide (DMSO, 100 μL). The absorbance was measured at 490 nm under a microplate spectrophotometer. Experiments were independently carried out in triplicate.

2.5. Soft Agar Assay.
After transfection, RB cells were plated in 6-well plates. After 2-4 weeks, cells were maintained in an upper layer of 0.35% agarose (Lonza Rockland) in DMEM added with 10% FBS. With the utilization of 0.5% basal agar and 10% FBS, suspend cells were overlaid and kept under room temperature until the solidification of agarose. Finally, images of cell colonies were taken. The experiment went through three independent repeats.

2.6. Subcellular Fractionation.
PARIS™ Kit (Ambion, Austin, TX) was used to separate cytoplasmic and nuclear elements

in accordance with the user guide. Cell cytoplasm was isolated by adding the cell fractionation buffer, and cell disruption buffer was used to collect cell nucleus. GAPDH was the cytoplasmic control and U6 was the nuclear control. The assay went through three independent repeats.

2.7. Fluorescent In Situ Hybridization (FISH) Assay.
The circ_0084811-specific RNA FISH probe (CTGAAGATATC ACCTGTAAG-biotin) was procured from RiboBio for cellular analysis according to the instruction of the provider. The fixed cell samples were rinsed in PBS and then dehydrated. After that, the air-dried cells were hybridized with FISH probe in hybridization buffer and then treated with DAPI staining reagent. Nuclei were counterstained with DAPI, and finally, an Olympus fluorescent microscope was applied for image observation. The assay went through three independent repeats.

2.8. RNA Pull-Down Assay.
RB cells were treated with a biotinylated circ_0084811 probe. Magnetic beads were then added into cells. The precipitated product collected by beads was purified for RT-qPCR analysis. The biotin-labeled circ_0084811 probe with Bio-NC was designed and synthesized by RiboBio (Guangzhou, Guangdong, China). Cells were lysed with lysis buffer, and then, the lysates were incubated with specific biotin-labeled probes for 2 h. Then, the mixtures were incubated with the streptavidin beads to pull down the biotin-labeled RNA complex for another 4 h. After washing, the RNA complex was extracted with TRIzol and the enrichment of miR-654-3p, miR-18b-5p, and miR-18a-5p was examined via RT-qPCR assay. The experiment was subject to three independent repeats.

2.9. RNA Immunoprecipitation (RIP) Assay.
In accordance with the user guide, Magna RIP RNA-Binding Protein

(a)

(b)

(c)
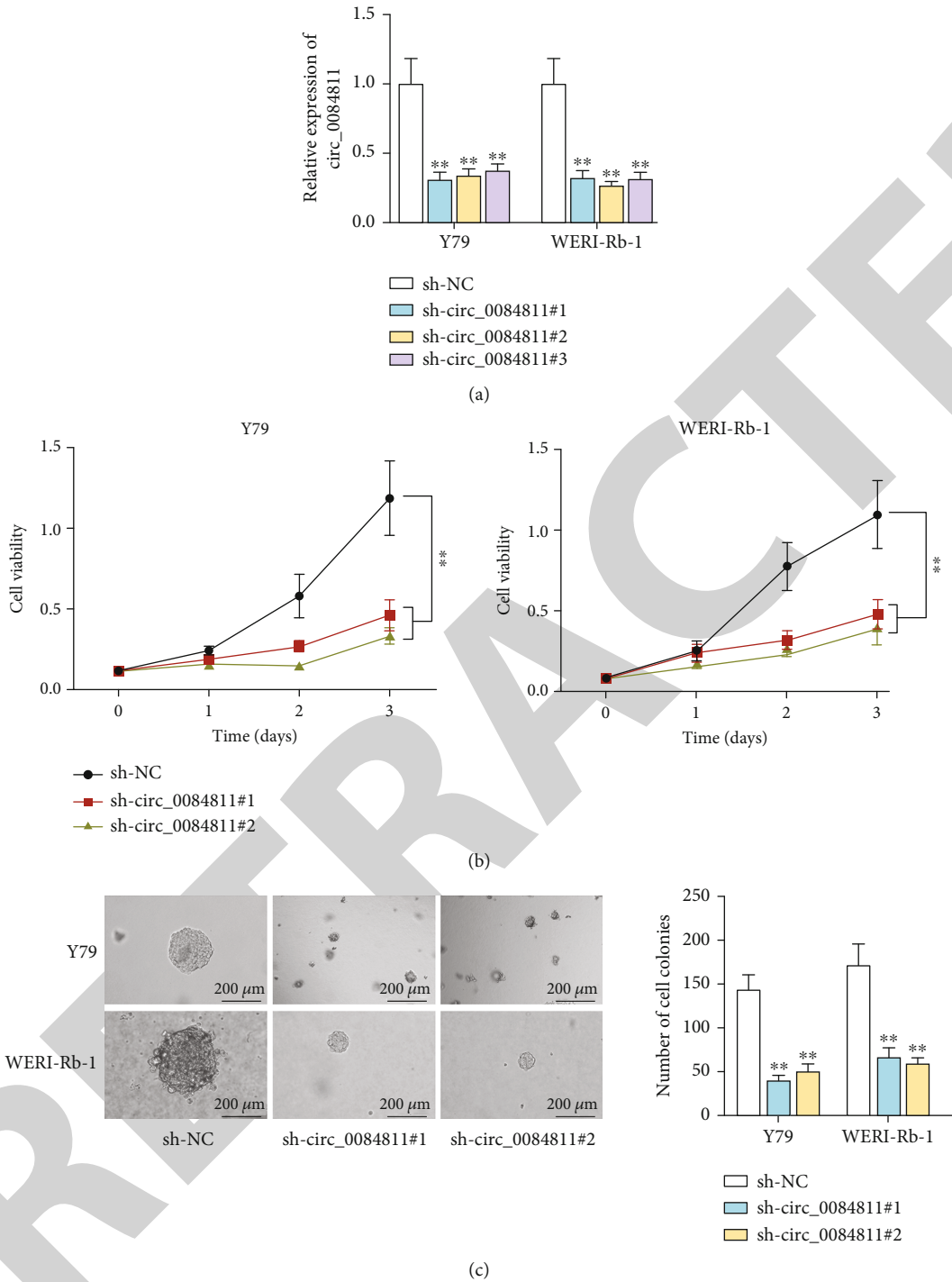
Figure 3: Continued.

(d)
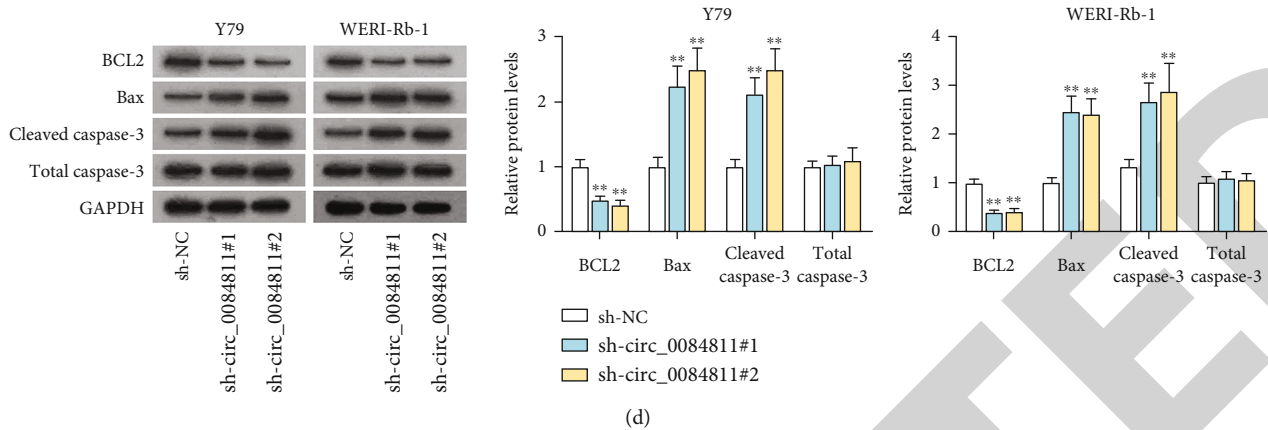
FIGURE 3: circ_0084811 knockdown hampered the proliferation and induced the apoptosis of RB cells. (a) circ_0084811 expression was decreased in RB cells by sh-circ_0084811 transfection. (b, c) MTT assay, together with soft agar assay (scale bar: 200 μm), was conducted to observe cell proliferation upon circ_0084811 knockdown in RB. (d) The protein levels of apoptosis-related factors after circ_0084811 was depleted. Each assay went through three biological replicates. The sample number (n) = 3. $^{**}P < 0.01$.

Immunoprecipitation Kit (Millipore, Bedford, MA) was used for RIP assay. Cells were lysed with RNA lysis buffer, and then, Ago2 antibody (Abcam, ab186733; 1/30-1/50) and IgG antibody (Abcam, ab172730; 1-2 μg/mL) were used to immunoprecipitate cell lysates. Finally, the RNA complexes were extracted for RT-qPCR analysis. The experiment was subject to three independent repeats.

2.10. Chromatin Immunoprecipitation (ChIP) Assay. ChIP assay was implemented utilizing ChIP Assay Kit (Beyotime, Shanghai, China). In short, BC cell lysates were sonicated to be fragments and immunoprecipitated using anti-H3K27AC (BioVision, 6869-25, 1-2 μL) or anti-CBP (Abcam, ab154532; 1/500-1/3000) with immunoglobulin G (IgG) antibody (Abcam; ab172730; 1-2 μg/mL) as a negative control. The immunoprecipitated DNA was extracted for RT-qPCR analysis. The experiment went through three independent repeats.

2.11. Luciferase Reporter Assay. The fragments of circ_0084811 or E2F5 mRNA covering wild-type (Wt) and mutant-type (Mut) miR-18a-5p or miR-18b-5p binding sites were inserted into pmirGLO dual-luciferase vector to construct pmirGLO-circ_0084811-Wt/Mut and pmirGLO-E2F5 3′UTR-Wt/Mut, respectively. Later, the reporter gene went through the cotransfection with control mimics and miR-18a-5p or miR-18b-5p mimics into RB cells for 48 h. Dual-luciferase reporter assay system (Promega) was eventually applied to measure the luciferase activity. The assay was subject to three independent repeats.

2.12. Western Blot Assay. Total cell lysates were extracted using RIPA lysis buffer (Thermo Fisher, USA), followed by using a BCA protein assay reagent (Beyotime) to confirm the protein concentration. After being separated through SDS-PAGE (sodium dodecyl sulfate polyacrylamide gel electrophoresis), proteins were transferred to polyvinylidene fluoride (PVDF) membranes and cultured in 5% skim milk. The membrane was incubated with the primary antibodies, including CBP (ab119488, Abcam; 1/500-1/3000), BCL2

(ab196495, Abcam; 1/1000), Bax (ab32503, Abcam; 1/1000-1/10000), Cleaved caspase-3 (ab2302, Abcam; 1/500), total caspase-3 (EPX01A-12012-901, Thermo Fisher; 1/5000), E2F5 (ab59769, Abcam; 1/5000-1/20000), β-actin (ab6276, Abcam; 1/5000-1/16000), and GAPDH (ab8245, Abcam; 1/500-1/10000) overnight at 4°C. Subsequently, the membranes were incubated with horseradish peroxidase-labeled secondary antibodies. By using Clarity Max Western ECL Substrate (Bio-Rad), we confirmed the protein bands. The experiment was subject to three independent repeats.

2.13. Statistical Analysis. All the experiments went through three independent repeats. The analysis of data was conducted by SPSS 22.0 statistical software package. All data were exhibited as mean ± standard deviation (SD). The group differences between two or more groups were analyzed using Student's t-test or one-way ANOVA. The significance of statistics was set at $P < 0.05$ (∗) or $P < 0.01$ (∗∗).

3. Results

3.1. circ_0084811 Was Highly Expressed in RB Cells, and Its Loop Structure Was Confirmed. As we have illustrated before, we have known that E2F5 is associated with RB, and we wanted to find the potential circRNA which was cyclized from E2F5 and their interaction in RB, so we performed experiments with the aim to verify the target circRNA whose host gene is E2F5 in RB cells and to further verify their regulatory mechanism. Through the circBank database (http://www.circbank.cn/index.html), we found four circRNAs whose gene symbol was E2F5, which were hsa_circ_E2F5_001 (circBase_id: circ_0084811), hsa_circ_E2F5_002 (circBase_id: circ_0137212), hsa_circ_E2F5_003 (circBase_id: circ_0137213), and hsa_circ_E2F5_004 (circBase_id: circ_0137214) (Figure 1(a), left). Then, we examined their expression in RB cell lines (HXO-Rb44, Y79, SO-Rb50, and WERI-Rb-1) and normal ARPE-19 cell line and found that only circ_0084811 was with obviously high expression in RB cell lines (Figure 1(a), right). The schematic

(a)

(b)

(c)

(d)
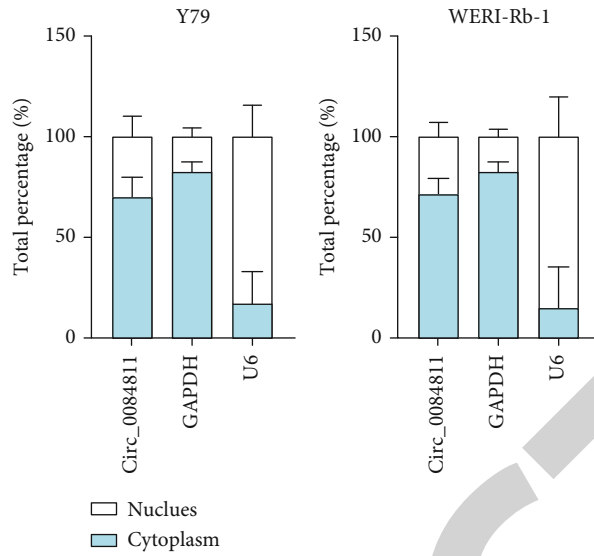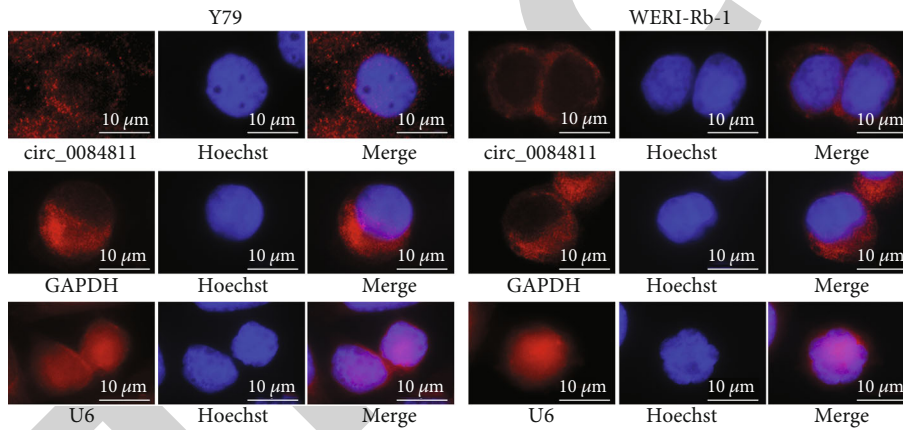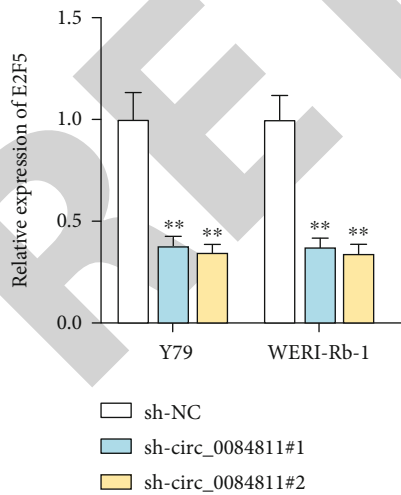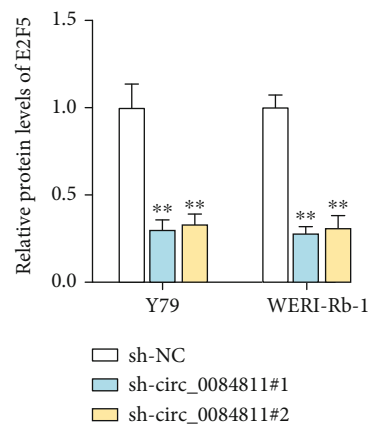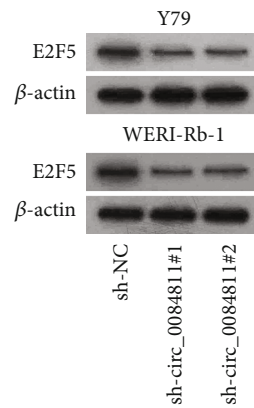
Figure 4: Continued.
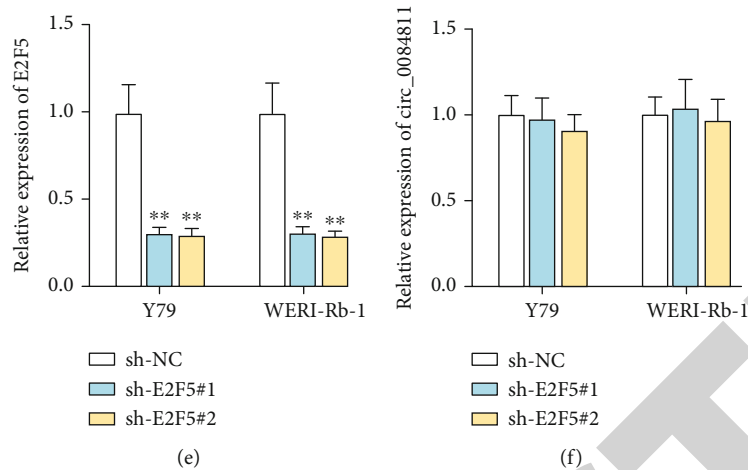
Figure 4: circ_0084811 modulated E2F5 expression. (a, b) The location of circ_0084811 in RB cells determined by subcellular fractionation along with FISH assay (scale bar: 10 μm). (c, d E2F5 expression as well as protein level after circ_0084811 was silenced. (e) E2F5 expression was cut down in RB cells by the sh-E2F5 transfection. (f) circ_0084811 expression was tested when E2F5 was downregulated. Each assay went through three biological replicates. The sample number (n) = 3. **$P < 0.01$.

diagram of the genomic location of circ_0084811 is demonstrated in Figure 1(b). After RNase R treatment, linear-E2F5 level was observably reduced while circ_0084811 level had no variation, which verified the loop structure of circ_0084811 (Figure 1(c)). The specific convergent and divergent primers were, respectively, designed to amplify the linear and back-splicing forms of E2F5, and circ_0084811 was only amplified by cDNA templates instead of genomic DNA (gDNA) templates (Figure 1(d)). After adding actinomycin D (Act D), circ_0084811 displayed a longer half-life in comparison with linear E2F5, indicating its stable form (Figure 1(e)).

3.2. H3K27ac Activated circ_0084811 Expression in RB Cells. Increasing studies have elaborated the critical role of histone acetylation in gene expression [19]. Moreover, many reports have illustrated that RNAs are upregulated by H3K27ac modification at promoter region to transcriptionally activate the expression of these RNAs, which suggests the crucial role of H3K27ac in cancer progression [20–23]. Therefore, we wanted to explore the H3K27ac level in the promoter region of circ_0084811. According to the search results of UCSC (http://genome.ucsc.edu/), H3K27ac was enriched in the promoter of circ_0084811 (Figure 2(a)). The result of ChIP assay also suggested that H3K27ac was highly enriched in the promoter region of circ_0084811 in RB cells (Figure 2(b)). Additionally, we observed that after the treatment of C646, the histone acetyltransferase inhibitor, circ_0084811 expression decreased (Figure 2(c)). CBP is a crucial factor in chromatin acetylation, so we made a conjecture that CBP might also contribute to the acetylation. CBP was tested to be with high expression in RB cells (Figure 2(d)), and circ_0084811 expression was reduced after sh-CRP#1/2 transfection was made in RB cells (Figures 2(e)–2(g)). Next, the considerable enrichment of CBP in the circ_0084811 promoter showed the binding ability between them, as exhibited by ChIP assay (Figure 2(h)). We found that CBP deficiency impeded the binding between circ_0084811 promoter and

H3K27ac (Figure 2(i)). In a word, the upregulation of circ_0084811 in RB cells was mediated by H3K27ac acetylation.

3.3. circ_0084811 Knockdown Hampered the Proliferation and Induced the Apoptosis of RB Cells. We tried to evaluate the impact circ_0084811 may exert on RB progression through a series of functional assays. First of all, we transfected sh-circ_0084811#1/2/3 in RB cells, and a favorable interference efficiency was observed (Figure 3(a)). It was confirmed from MTT assay and soft agar assay that cell viability as well as proliferation was declined by circ_0084811 depletion (Figures 3(b) and 3(c)). Moreover, the protein levels of apoptosis-related factors (BCL2, Bax, and Cleaved caspase-3) were confirmed via western blot, and results suggested that circ_0084811 downregulation decreased BCL2 protein level while Bax along with Cleaved caspase-3 displayed increased protein expression (Figure 3(d)). Overall, circ_0084811 promoted cell proliferation while it inhibited cell apoptosis in RB.

3.4. circ_0084811 Modulated E2F5 Expression. According to subcellular fractionation detection as well as FISH assay, the majority of circ_0084811 was in the cytoplasm of transfected cells (Figures 4(a) and 4(b)). It was then verified that E2F5 expression and protein level were lessened upon circ_0084811 silencing (Figures 4(c) and 4(d)). In view of the fact that E2F5 functions as a common transcription factor, we conducted RT-qPCR assay to verify whether E2F5 may influence the expression of circ_0084811. The expression of E2F5 was firstly knocked down by the transfection of sh-E2F5#1/2 plasmids, and then, we found that circ_0084811 expression was not influenced by E2F5 (Figures 4(e) and 4(f)). To conclude, E2F5 was positively regulated by circ_0084811 while E2F5 could not regulate the expression of circ_0084811.

3.5. circ_0084811 Sponged miR-18a-5p and miR-18b-5p to Regulate E2F5 Expression. With the application of starBase (http://starbase.sysu.edu.cn/), we could see that there were

(a)

(b)

Circ_0084811-Wt: 5'   acuUUUGGCCAUU-CAGGCACCUUc 3'
                         | : | | | | : | | | | | | | | |
miR-18a-5p: 3'   gauAGAC---GUGAUCUACGUGGAAu 5'

circ_0084811-Mut: 5'   acuAUACGCGUUA-CUGCGUGGAAc 3'

E2F5-Wt: 5'   aaaauaaugaauguaaCACCUUu 3'
                                        | | | | | |
miR-18a-5p: 3'   gauagacgugaucuacGUGGAAu 5'

E2F5-Mut: 5'   aaaauaaugaauguaaGUGGAAu 3'

Circ_0084811-Wt: 5'   uuuuggcCAUU--CAGGCACCUUc 3'
                         | | : | | | | | | | | |
miR-18a-5p: 3'   gauugacGUGAUCUACGUGGAAu 5'

circ_0084811-Mut: 5'   uuuuggcGUUA--CUGCGUGGAAc 3'

E2F5-Wt: 5'   aaaauaaugaauguaaCACCUUu 3'
                                        | | | | | |
miR-18b-5p: 3'   gauugacgugaucuacGUGGAAu 5'

E2F5-Mut: 5'   aaaauaaugaauguaaGUGGAAu 3'

(c)

(d)

(e)

Figure 5: Continued.

Figure 5: Continued.

(i)
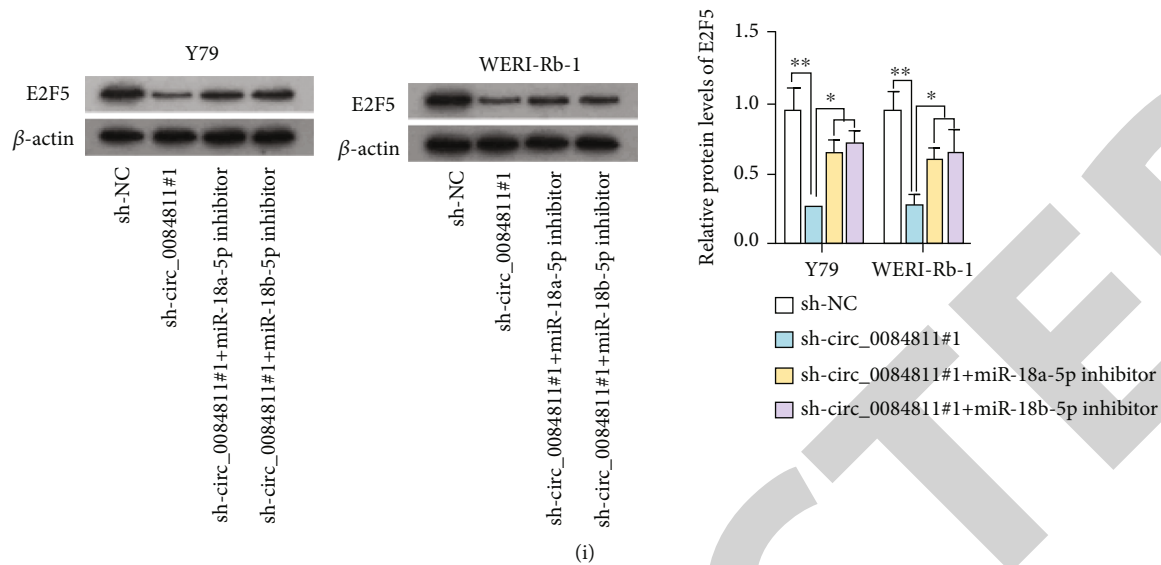
FIGURE 5: circ_0084811 sponged miR-18a-5p and miR-18b-5p to regulate E2F5 expression. (a) Potential miRNAs of circ_0084811 and E2F5 forecasted through starBase. (b) miR-654-3p, miR-18a-5p ,and miR-18b-5p enrichment in bio-circ_0084811 probe was confirmed via RNA pull-down assay. (c) Predicted binding sites between circ_0084811 and miR-18a-5p or miR-18b-5p, E2F5, and miR-18a-5p or miR-18b-5p. (d) The relationship among circ_0084811, miR-18a-5p, miR-18b-5p, and E2F5 was confirmed through RIP assay. (e) miR-18a-5p mimics and miR-18b-5p mimics were utilized to elevate their expression in RB cells. (f) The affinity of miR-18a-5p or miR-18b-5p with circ_0084811 or E2F5 was testified by luciferase reporter assays. (g) miR-18a-5p and miR-18b-5p were, respectively, silenced in RB cells by inhibitor transfection. (h, i) E2F5 expression in RB cells transfected with sh-NC, sh-circ_0084811#1, sh-circ_0084811#1+miR-18a-5p inhibitor, and sh-circ_0084811#1+miR-18b-5p inhibitor plasmids. Each assay went through three biological replicates. The sample number (n) = 3. $^*P < 0.05$ and $^{**}P < 0.01$.

3 potential miRNAs (miR-654-3p, miR-18b-5p, and miR-18a-5p) which had binding possibility to circ_0084811 and E2F5 (Figure 5(a)). We found through RNA pull-down assay that miR-18a-5p and miR-18b-5p were dramatically accumulated in the biotin-labeled circ_0084811 probe while no change could be seen in the miR-654-3p group (Figure 5(b)). Figure 5(c) exhibited related binding sequences between these RNAs. After that, RIP assay was carried out, and it was observed that circ_0084811, miR-18a-5p, miR-18b-5p, and E2F5 were all enriched in Ago2 antibody rather than IgG antibody (Figure 5(d)). The expression of these two miRNAs was elevated in RB cells, and it was then observed that after their overexpression, the wild type of the circ_0084811 group and E2F5 3'UTR group both exhibited declined luciferase activity, while the according mutant groups were barely affected (Figures 5(e) and 5(f)). After that, miR-18a-5p and miR-18b-5p expression was reduced in RB cells (Figure 5(g)), and then, the expression of E2F5 in different transfection groups was analyzed. As shown by the results, decreased E2F5 expression after circ_0084811 silencing was partially restored by miR-18a-5p inhibitor or miR-18b-5p inhibitor (Figures 5(h) and 5(i)). Taken together, circ_0084811 targeted E2F5 via sequestering miR-18a-5p and miR-18b-5p.

3.6. circ_0084811 Promoted RB Progression via Modulating the miR-18a-5p/miR-18b-5p/E2F5 Axis. E2F5 was overexpressed in Y79 cells via using the pcDNA3.1/E2F5 vector for later rescue experiments (Figure 6(a)). At first, we found through MTT assay that circ_0084811 downregulation inhibited cell viability, but this impact was partially counter-

acted by the treatment of miR-18a-5p inhibitor or miR-18b-5p inhibitor, while E2F5 overexpression could fully reverse this effect (Figure 6(b)). The similar result was also seen in the soft agar assay (Figure 6(c)), which indicated that RB cell proliferation upon circ_0084811 silencing was regulated by the miR-18a-5p/miR-18b-5p/E2F5 axis. Subsequently, we adopted RT-qPCR as well as western blot assays to analyze RB cell apoptosis under different conditions, and it was shown that the declined BCL2 expression and protein levels caused by circ_0084811 silencing was partially counteracted by miR-18a-5p inhibition or miR-18b-5p inhibition while it was greatly recovered by E2F5 overexpression. Besides, the expression and protein levels of Bax and Cleaved caspase-3 showed opposite results (Figure 6(d)). The above results indicated that promoted cell apoptosis induced by circ_0084811 deficiency could be partially countervailed by the knockdown of miR-18a-5p or miR-18b-5p while it could be greatly counteracted by E2F5 upregulation. To sum up, the circ_0084811/miR-18a-5p/miR-18b-5p/E2F5 axis contributed to the progression of RB.

4. Discussion

In recent years, the significance of circRNAs in RB has been highlighted [24]. E2F5 has been commonly considered to act as an oncogene in cancers, which include prostate cancer, non-small-cell lung cancer, and ovarian cancer [25–27]. Moreover, it has been confirmed that E2F5 can boost RB progression by affecting cell proliferation, invasion, and tumor formation [17]. More importantly, it has been

(a)

(b)

(c)
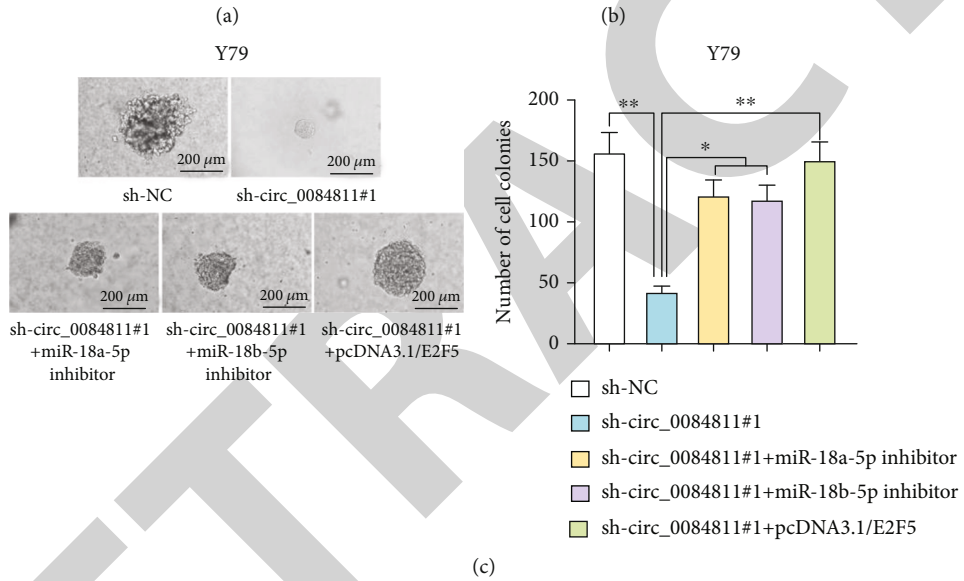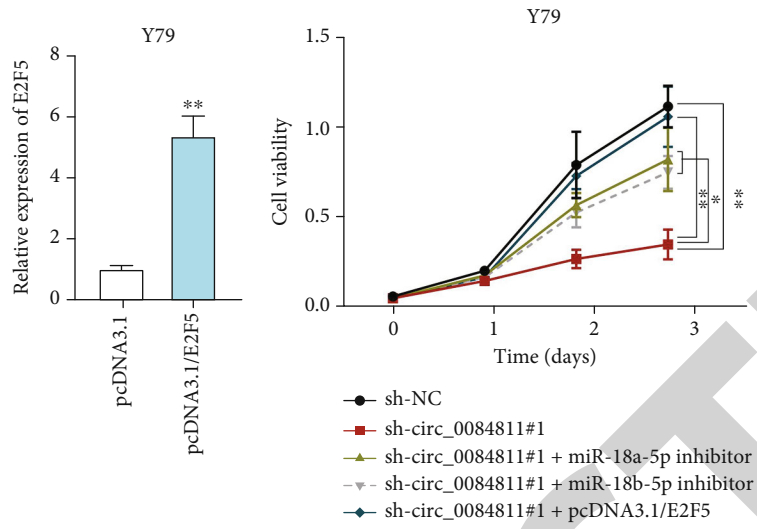
Figure 6: Continued.

(d)
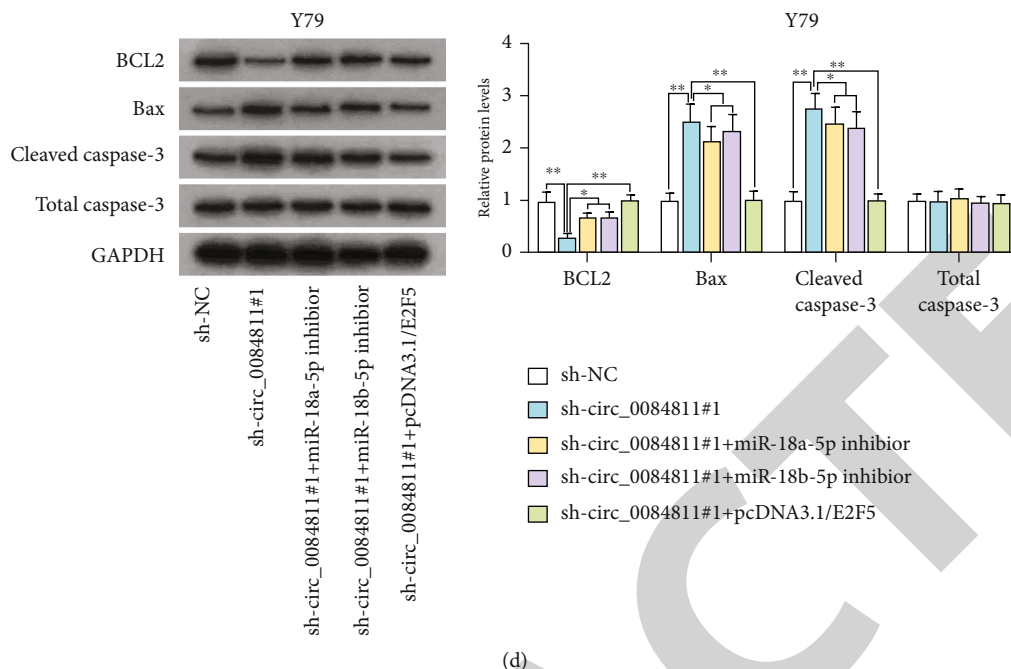
Figure 6: circ_0084811 promoted RB progression via the miR-18a-5p/miR-18b-5p/E2F5 axis. (a) E2F5 expression in pcDNA3.1/E2F5-transfected cells. (b–d) The proliferative capacity of Y79 cells (b, c) as well as cell apoptosis in RB (d) was assessed in different transfection groups (scale bar for soft agar assay: 200 μm). Each assay went through three biological replicates. The sample number (n) = 3. $^{*}P < 0.05$ and $^{**}P < 0.01$.

reported that some circRNAs can be transcribed together with their parental genes and in turn regulate the transcription of the parental gene or related genes [18], so we speculated that circRNAs which were cyclized from E2F5 might also exert certain impact on RB progression. In our study, circ_0084811 was discovered to be distinctly overexpressed in RB cells, and it was verified through mechanism experiments that the upregulation of circ_0084811 in RB cells was induced by the enrichment of H3K27ac in the circ_0084811 promoter. Functionally, inhibition of circ_0084811 diminished RB cell proliferation and stimulated cell apoptosis.

circRNAs functioning as miRNA sponges to influence mRNA translation or stability, thereby participating in the cellular activities in human cancers, have been widely documented [28]. Through our investigation, the cytoplasmic distribution of circ_0084811 in RB cells was identified, and we discovered that circ_0084811 also positively regulated the expression of E2F5. Hence, we speculated that circ_0084811 might sequester certain miRNAs to modulate E2F5 expression. With the application of the starBase database, 3 potential miRNAs were predicted. At the same time, miR-18a-5p and miR-18b-5p were selected to be the downstream target genes, which contributed to the malignant progression of RB. miR-18a-5p has been proven to inhibit the malignancy of ovarian cancer and hepatocellular carcinoma [29, 30]. Besides, miR-18b-5p has been demonstrated to repress lung adenocarcinoma, ovarian cancer, and liver cancer [31–33]. Through our investigations, we revealed the interaction of circ_0084811, miR-18b-5p, and E2F5 in RB and demonstrated that circ_0084811 had the further value to be studied as a competing endogenous RNA (ceRNA).

Circular RNAs (circRNAs) sponging miRNAs (microRNAs) to further regulate the downstream gene expression have been well-elucidated by many researches [34]. In RB, the ceRNA model of circRNA_100782 sponging miR-574-3p to further modulate Rb expression is confirmed [35] and circ-E2F3 sponges miR-204-5p and positively regulates ROCK1 expression to promote cancer progression [36]. circ_0000527 functioning as a ceRNA to directly target miR-646 and positively regulate LRP6 expression in RB cells has also been elucidated [37]. What we have demonstrated about the ceRNA network in RB cells may help to enrich the current exploration of this regulatory mechanism in the regulation of RB malignancy.

5. Conclusion

All in all, circ_0084811 was demonstrated to be mediated by H3K27ac acetylation, and high circ_0084811 expression in RB cells hindered the malignant cell behaviors in RB. Furthermore, circ_0084811 aggravated the progression of RB through the miR-18a-5p/miR-18b-5p/E2F5 axis. Lack of clinical investigation is a main limitation of the current study. We will collect clinical samples to elaborate the clinical significance of the circ_0084811/miR-18a-5p/miR-18b-5p/E2F5 axis in RB in our future study.

Abbreviations

RB: Retinoblastoma
circRNAs: Circular RNAs
E2F5:   E2F transcription factor 5

miR-18a-5p: MicroRNA-18a-5p
miR-18b-5p: MicroRNA-18b-5p
ncRNAs: Noncoding RNAs
ceRNA: Competing endogenous RNA
ATCC: American Type Culture Collection
RT-qPCR: Quantitative reverse transcription real-time polymerase chain reaction
FISH: Fluorescent in situ hybridization
RIP: RNA immunoprecipitation
ChIP: Chromatin immunoprecipitation
IgG: Immunoglobulin G
Wt: Wild type
Mut: Mutant type
SD: Standard deviation
gDNA: Genomic DNA
Act D: Actinomycin D.

Data Availability

The data used to support the findings of this study are included within the article.

Conflicts of Interest

The authors have no conflicts of interest to declare.

Authors' Contributions

Guangwei Jiang and Mingxuan Qu are co-first authors.

Acknowledgments

We sincerely thank all lab personnel for the help provided in this research.

Supplementary Materials

Supplementary Table 1: related sequences utilized in this study. (Supplementary Materials)

References

[1] C. Rodriguez-Galindo, D. B. Orbach, and D. VanderVeen, "Retinoblastoma," *Pediatric Clinics of North America*, vol. 62, no. 1, pp. 201–223, 2015.

[2] P. R. Mendoza and H. E. Grossniklaus, "The biology of retinoblastoma," *Progress in Molecular Biology and Translational Science*, vol. 134, pp. 503–516, 2015.

[3] R. Rao and S. G. Honavar, "Retinoblastoma," *Indian Journal of Pediatrics*, vol. 84, no. 12, pp. 937–944, 2017.

[4] I. D. Fabian, Z. Onadim, E. Karaa et al., "The management of retinoblastoma," *Oncogene*, vol. 37, no. 12, pp. 1551–1560, 2018.

[5] R. L. Lumbroso-Le, "Retinoblastoma," *La Revue du praticien*, vol. 67, no. 8, pp. 888–891, 2017.

[6] M. Jagadeesan, V. Khetan, and A. Mallipatna, "Genetic perspective of retinoblastoma: from present to future," *Indian Journal of Ophthalmology*, vol. 64, no. 5, pp. 332–336, 2016.

[7] I. L. Patop and S. Kadener, "circRNAs in cancer," *Current Opinion in Genetics & Development*, vol. 48, pp. 121–127, 2018.

[8] Z. Liu, Y. Zhou, G. Liang et al., "Circular RNA hsa_circ_001783 regulates breast cancer progression via sponging miR-200c-3p," *Cell Death & Disease*, vol. 10, no. 2, p. 55, 2019.

[9] Q. Lu, T. Liu, H. Feng et al., "Circular RNA circSLC8A1 acts as a sponge of miR-130b/miR-494 in suppressing bladder cancer progression via regulating PTEN," *Molecular Cancer*, vol. 18, no. 1, p. 111, 2019.

[10] X. Yu, W. Xiao, H. Song, Y. Jin, J. Xu, and X. Liu, "CircRNA_100876 sponges miR-136 to promote proliferation and metastasis of gastric cancer by upregulating MIEN1 expression," *Gene*, vol. 748, article 144678, 2020.

[11] Y. Y. Qu, R. Zhao, H. L. Zhang et al., "Inactivation of the AMPK-GATA3-ECHS1 pathway induces fatty acid synthesis that promotes clear cell renal cell carcinoma growth," *Cancer Research*, vol. 80, no. 2, pp. 319–333, 2020.

[12] Y. Jiang, F. Xiao, L. Wang, T. Wang, and L. Chen, "Circular RNA has_circ_0000034 accelerates retinoblastoma advancement through the miR-361-3p/ADAM19 axis," *Molecular and Cellular Biochemistry*, vol. 476, no. 1, pp. 69–80, 2021.

[13] W. Zhao, S. Wang, T. Qin, and W. Wang, "Circular RNA (circ-0075804) promotes the proliferation of retinoblastoma via combining heterogeneous nuclear ribonucleoprotein K (HNRNPK) to improve the stability of E2F transcription factor 3 E2F3," *Journal of Cellular Biochemistry*, vol. 121, no. 7, pp. 3516–3525, 2020.

[14] L. Xing, L. Zhang, Y. Feng, Z. Cui, and L. Ding, "Downregulation of circular RNA hsa_circ_0001649 indicates poor prognosis for retinoblastoma and regulates cell proliferation and apoptosis *via* AKT/mTOR signaling pathway," *Biomedicine & Pharmacotherapy*, vol. 105, pp. 326–333, 2018.

[15] J. C. Kusek, R. M. Greene, and M. M. Pisano, "Expression of the E2F and retinoblastoma families of proteins during neural differentiation," *Brain Research Bulletin*, vol. 54, no. 2, pp. 187–198, 2001.

[16] H. Xie, Y. Kang, S. Wang et al., "E2f5 is a versatile transcriptional activator required for spermatogenesis and multiciliated cell differentiation in zebrafish," *PLoS Genetics*, vol. 16, no. 3, article e1008655, 2020.

[17] Y. Zhang, X. Zhu, X. Zhu et al., "MiR-613 suppresses retinoblastoma cell proliferation, invasion, and tumor formation by targeting E2F5," *Tumour Biology*, vol. 39, no. 3, 2017.

[18] J. C. Qi, Z. Yang, T. Lin et al., "CDK13 upregulation-induced formation of the positive feedback loop among circCDK13, miR-212-5p/miR-449a and E2F5 contributes to prostate carcinogenesis," *Journal of Experimental & Clinical Cancer Research*, vol. 40, no. 1, p. 2, 2021.

[19] H. Fukuda, N. Sano, S. Muto, and M. Horikoshi, "Simple histone acetylation plays a complex role in the regulation of gene expression," *Briefings in Functional Genomics & Proteomics*, vol. 5, no. 3, pp. 190–208, 2006.

[20] H. Dong, J. Hu, K. Zou et al., "Activation of LncRNA TINCR by H3K27 acetylation promotes Trastuzumab resistance and epithelial-mesenchymal transition by targeting MicroRNA-125b in breast cancer," *Molecular Cancer*, vol. 18, no. 1, p. 3, 2019.

[21] M. Han, Y. Gu, P. Lu et al., "Exosome-mediated lncRNA AFAP1-AS1 promotes trastuzumab resistance through binding with AUF1 and activating ERBB2 translation," *Molecular Cancer*, vol. 19, no. 1, p. 26, 2020.

[22] X. Meng, Y. Zhao, B. Han et al., "Dual functionalized brain-targeting nanoinhibitors restrain temozolomide- resistant

Retraction

Retracted: Study on Inflammatory Factors in Aneurysmal Perimembranous Ventricular Septal Defect in Congenital Heart Disease

BioMed Research International

This article has been retracted by Hindawi following an investigation undertaken by the publisher [1]. This investigation has uncovered evidence of one or more of the following indicators of systematic manipulation of the publication process:

(1) Discrepancies in scope

(2) Discrepancies in the description of the research reported

(3) Discrepancies between the availability of data and the research described

(4) Inappropriate citations

(5) Incoherent, meaningless and/or irrelevant content included in the article

(6) Manipulated or compromised peer review

The presence of these indicators undermines our confidence in the integrity of the article's content and we cannot, therefore, vouch for its reliability. Please note that this notice is intended solely to alert readers that the content of this article is unreliable. We have not investigated whether authors were aware of or involved in the systematic manipulation of the publication process.

Wiley and Hindawi regrets that the usual quality checks did not identify these issues before publication and have since put additional measures in place to safeguard research integrity.

We wish to credit our own Research Integrity and Research Publishing teams and anonymous and named external researchers and research integrity experts for contributing to this investigation.

The corresponding author, as the representative of all authors, has been given the opportunity to register their agreement or disagreement to this retraction. We have kept a record of any response received.

References

[1] J. Zhou, Y. Liu, J. Wang et al., "Study on Inflammatory Factors in Aneurysmal Perimembranous Ventricular Septal Defect in Congenital Heart Disease," *BioMed Research International*, vol. 2022, Article ID 8282624, 5 pages, 2022.

Research Article

Study on Inflammatory Factors in Aneurysmal Perimembranous Ventricular Septal Defect in Congenital Heart Disease

Jin Zhou,[1] **Ying Liu,**[2] **Jing Wang** ●,[1] **Wei Yan,**[1] **Yongjian Liu,**[1] **Litao Chen,**[1] **Zhixing Du,**[1] **and Qilian Xie**[3]

[1]*The First Hospital of Hebei Medical University, Shijiazhuang 050031, China*
[2]*The Fourth Hospital of Shijiazhuang, Shijiazhuang 050000, China*
[3]*Anhui Provincial Children's Hospital, Hefei 230000, China*

Correspondence should be addressed to Jing Wang; iamjane@126.com

Jin Zhou and Ying Liu contributed equally to this work.

To detect the expression of inflammatory factors such as interleukin-1β (IL-1β), interleukin-6 (IL-6), transforming growth factor (TGF-β), and tumor necrosis factor (TNF-α) in the tumor tissue of ventricular septal defect (VSD) in congenital heart disease and to explore the role of inflammatory response in the formation of aneurysmal perimembranous VSD(APVSD). Children with APVSD of congenital heart disease treated by surgery were selected and divided into true aneurysmal perimembranous group (TAP group) and pseudoaneurysmal perimembranous group (PAP group) according to echocardiography and surgical findings. There were 15 children in the TAP group and 31 in the PAP group. The aneurysmal perimembranous tissue of the two groups of children was collected during the operation. IL-1β, IL-6, TGF-β, and TNF-α were positively expressed in the aneurysmal perimembranous tissue of the two groups, and the expression levels of all inflammatory factors in the PAP group were higher than those in the TAP group, and the difference was statistically significant ($P < 0.05$). The expression levels of IL-1β, IL-6, TGF-β, and TNF-α in the aneurysmal perimembranous tissue of the two groups were negatively correlated with the width of the APVSD breach. IL-1β, IL-6, TGF-β, and TNF-α may be involved in the occurrence and development of APVSD through inflammatory mechanism.

1. Introduction

VSD is a common congenital heart disease, and most children with APVSD will have perimembranous aneurysm at birth or shortly after birth [1]. The self-healing rate of APVSD was high, but its mechanism is still unclear. Study had shown that inflammatory responses may be involved in this process [2–4]. In this study, in order to study the role of IL-1β, IL-6, TGF-β, and TNF-α in the formation of APVSD, children with APVSD who were surgically treated in the First Hospital of Hebei Medical University and Anhui Children's Hospital were selected. The expression levels of inflammatory factors in the perimembranous tissue of aneurysm were detected by enzyme-linked immunosorbent assay

(ELISA) to explore the role of inflammatory response in the formation of APVSD and the possible mechanism of VSD self-healing.

2. Subjects and Methods

2.1. Subjects. From July 2009 to June 2013, a total of 46 children with APVSD who received surgical treatment in the First Hospital of Hebei Medical University and Anhui Children's Hospital were selected. The children were divided into TAP group and PAP group. There were 15 children in the TAP group, including 9 men and 6 women, with an average age of 9.3 ± 3.8 years. There were 31 children in the

PAP, including 17 men and 14 women, with an average age of 9.3 ± 3.5 years.

Diagnostic criteria for TAP VSD: according to the findings during the operation, the ventricular septum tissue was weak and elongated, forming a pouch-like, protruding to the right ventricular cavity. The pouch had no adhesion to the tricuspid valve and aortic valve, and the periphery of the VSD was composed of membranous tissue and fibrous connective tissue.

Diagnostic criteria for PAP VSD [5, 6]: the shunting orifice of the ventricular defect was adhered to part of the septal valve tissue, local fibrous tissue proliferated, and the right cardiac chamber bulged. There was no real rightward protruding pouch wall.

Exclusion criteria: patients with complex congenital heart disease such as tetralogy of Fallot and other congenital malformations; no heart valve prolapse, pulmonary hypertension; no other heart malformations; no systemic inflammation and immune connective tissue disease.

2.2. Methods

(1) Philips IEElite advanced cardiac color Doppler ultrasound and Philips IE33 advanced cardiac color Doppler ultrasound systems were used for VSD diagnosis. The frequency of the probe was 3-5 MHz, and they could display the location, size, and the base, width, depth of the perimembranous aneurysm, and the width of the breach in multiple sections, angles, and directions. If there were multiple breaches, it was calculated by the sum of all breach widths

(2) Determination of inflammatory factors in aneurysmal perimembranous tissue: aneurysmal perimembranous tissue with a size of $3 \, \text{mm} \times 3 \, \text{mm}$ was taken from the breaches from all children with APVSD during the operation. The tissue was minced and ground sufficiently, and the suspension was collected by centrifugation. The levels of IL-1β, IL-6, TGF-β, and TNF-α were determined by ELISA.

2.3. Statistical Analysis.

SPSS23.0 was used to process and analyze the data. The measurement data were shown as mean $\pm$ standard deviation ($\bar{x} \pm s$), and t test was used to compare the means of the two groups, and Spearman correlation analysis was used for correlation. $P < 0.05$ was considered to be statistically significant.

3. Results

3.1. Clinical Characteristics.
There were no significant differences in age, gender, height, weight, body mass index (BMI), and other indicators between the two groups ($P > 0.05$) (Table 1).

3.2. Comparison of Inflammatory Factors and Tumor Characteristics between the Two Groups.
The expression levels of IL-1β, IL-6, TGF-β, and TNF-α in tissue of PAP group were 10.2 ± 1.5 pg/mL, 31.4 ± 3.4 pg/mL, 64.7 ± 5.8

TABLE 1: Clinical characteristics of children in the two groups.

Groups	Age (years)	Gender (men/women)	Height (cm)	Weight (KG)	BMI (kg/m²)
TAP	9.3 ± 3.8	9/6	134.7 ± 18.7	31.3 ± 13.0	16.4 ± 2.1
PAP	9.3 ± 3.5	17/14	135.7 ± 17.7	32.5 ± 12.9	16.9 ± 2.1

pg/mL, and 220.3 ± 17.2, which were significantly higher than those in TAP group (9.3 ± 1.4 pg/mL, 29.0 ± 3.4 pg/mL, 58.4 ± 5.2 pg/mL, 197.5 ± 17.5) ($P < 0.05$) (Table 2). However, tumor depth and breach width of TAP group and PAP group were similar.

3.3. Correlation of Tumor Depth and Breach Width with the Levels of IL-1β, IL-6, TGF-β, and TNF-α in All APVSD.
Correlation analysis showed that the levels of IL-1β, IL-6, TGF-β, and TNF-α in tumor tissue were negatively correlated with the tumor depth ($P < 0.05$), but had no correlation with the breach width ($P > 0.05$) (Table 3).

4. Discussion

According to the source and anatomical structure, APVSD of congenital heart disease is divided into true perimembranous aneurysm VSD and pseudoperimembranous aneurysm VSD. The formation of true perimembranous aneurysm is due to the failure to close the fetal membranous ventricular septum in time after birth, the closure of the membranous portion is delayed after birth, and part of the generated membranous portion is continuously pressed under the left ventricular high pressure to form perimembranous aneurysm, leaving the top of the tumor, and the breach causes a left-to-right shunt at the ventricular level. Another common perimembranous aneurysm VSD is the so-called pseudoperimembranous aneurysm, which is a relatively immature fibrous tissue formed by the continuous proliferation and adhesion of the tricuspid valve septum, chordae tendineae, or surrounding tissue [7–9]. Previous study has shown that under the condition of left-to-right shunting of intraventricular blood at the level of VSD chamber, long-term high pressure impacted the inferior membrane defect, causing damage to the perimembranous tissue and the gap of the true perimembranous aneurysm. The damage will stimulate the self-repair of the body tissue. However, the specific repair mechanism is not yet clear. Previous study suggested that the formation of perimembranous aneurysm was related to the remodeling of connective tissue involving metallomatrix proteases (MMPS) [10, 11].

As one of the important members of the IL-1 cytokine family, L-1β is an important hyperresponsive proinflammatory cell factor secreted and released mainly by monocytes and macrophages activated under inflammatory conditions, cell damage, or immune responses. It is a key factor in the body's regulation of inflammatory response. On the one hand, it has the function of promoting the repair of damaged tissues; on the other hand, IL-1β can play a key role in various acute and chronic inflammatory responses by inducing

TABLE 2: Comparison of inflammatory factors and tumor characteristics between the two groups.

Groups	IL-1β (pg/mL)	IL-6 (pg/mL)	TNF-α (pg/mL)	TGF-β (pg/mL)	Tumor depth (mm)	Breach width (mm)
TAP	9.3 ± 1.4	29.0 ± 3.4	58.4 ± 5.2	197.5 ± 17.5	6.8 ± 1.0	7.0 ± 1.5
PAP	10.2 ± 1.5	31.4 ± 3.4	64.7 ± 5.8	220.3 ± 17.2	6.9 ± 1.0	6.9 ± 1.5
t	2.142	2.681	3.706	4.166	0.285	0.246
P	0.046	0.038	0.001	<0.001	0.778	0.807

TABLE 3: Correlation of inflammatory factor levels with tumor depth and breach width in children with APVSD.

Tumor characteristics	IL-1β (ng/L)		IL-6 (ng/L)		TGF-β (pg/mL)		TNF-α (pg/mL)	
	R value	P value	R value	P value	R value	P value	R value	P value
Tumor depth	0.053	0.727	0.149	0.323	0.118	0.434	0.113	0.454
Breach width	-0.595	<0.001	-0.620	<0.001	-0.427	0.003	-0.467	0.001

the release of other inflammatory mediators, proinflammatory cytokines, and chemokines. TNF-α is a monokine mainly produced by monocytes and macrophages, which can improve the phagocytic ability of neutrophils and stimulate the secretion of IL-1 and IL-6 by endothelial cells and promote the adhesion of neutrophils and endothelial cells [12, 13]. IL-6 is secreted by activated macrophages, lymphocytes, and epithelial cells and can be induced by IL-1 and TNF-α. It is an important mediator of inflammatory response and has both proinflammatory and inhibitory effects. Transforming growth factor-β (TGF-β) is an important cytokine that regulates cell growth and differentiation and has the effect of regulating the proliferation of fibroblasts, smooth muscle cells, and endothelial cells [14, 15]. Various cells in the body can secrete TGF-β in an inactive state, and the cleavage of the protein itself can turn the TGF-β complex into an activated TGF-β.

Generally, tissues with active cell differentiation often contain high levels of TGF-β. TGF-β is an important factor regulating cell proliferation and differentiation. It can promote the proliferation and phenotypic transformation of vascular smooth muscle cells, fibroblasts, and other cells and promote the synthesis and secretion of extracellular matrix leading to the thickening of the cardiovascular intima, which is closely related to the occurrence of various cardiovascular diseases. TGF-β plays an important role in the occurrence and development of various diseases by inducing the expression of VEGF, promoting endothelial cell proliferation, tissue remodeling, and fibrosis formation [16, 17]. In the early stage of VSD, the contraction of the left ventricle produces a huge pressure to divert blood from the left ventricle to the right ventricle, resulting in an increase in right ventricular preload. Under the impact of high-pressure blood flow, aneurysmal perimembranous tissue will cause myocardial cell damage such as aneurysmal perimembranous tissue, right ventricular endocardium, and chordae tendineae and activate these inflammatory cytokines. TNF-α and IL-1β further activate MMPS and increase its expression, which are involved in inflammation and tissue proliferation [18, 19]. Our study showed that both the true perimembranous aneurysm VSD and the pseudoperimem-

branous aneurysm VSD, the above-mentioned inflammatory factors, were expressed in aneurysmal perimembranous tissue, and these inflammatory factors were jointly involved in the proliferation of aneurysmal perimembranous tissue. The persistent proliferative aneurysmal perimembranous tissue eventually closed the gap in the ventricular septum. Therefore, this study may be a more reliable evidence to explain that the perimembranous aneurysm formation was the self-healing tendency of VSD children.

In this study, inflammatory factors were detected in the aneurysmal perimembranous tissue of the TAP and PAP groups. However, by comparison, it was found that the expression intensity of inflammatory factors in the aneurysmal perimembranous tissue of children in PAP group was significantly higher than that of the TAP group. The reason may be related to the histology and location of perimembranous aneurysm in the two groups. The pseudoperimembranous aneurysm is a relatively immature fibrous tissue formed by the continuous proliferation and adhesion of the tricuspid valve septum, chordae tendineae, or surrounding tissue [20]. The left-to-right shunt at the ventricular level had a larger impact force and wider damage area, so the inflammatory response was more severe [21]. Our study also found that the expression levels of inflammatory factors were negatively correlated with the breach width of the perimembranous aneurysm in the TAP and PAP groups. The smaller the breach of the perimembranous aneurysm, the greater the corresponding blood flow resistance and the heavier the tumor tissue damage. This was essentially a reflection of the severity of the injury and the severity of the inflammatory response, which just proved that the pseudoperimembranous aneurysm was an active tissue that can proliferate continuously. The aneurysmal perimembranous tissue was continuously damaged by the impact of blood flow, and the continuous inflammatory response made the aneurysmal perimembranous tissue continue to proliferate [22]. This ability to proliferate allowed the larger defects of the VSD to shrink or even close.

This study confirmed that IL-1β, IL-6, TGF-β, and TNF-α were positively expressed in both the TAP and PAP groups, and the expression levels of all inflammatory factors

in the PAP group were higher than those in the TAP group. The expression levels of IL-1β, IL-6, TGF-β, and TNF-α in the perimembranous tissue of aneurysm in both groups were negatively correlated with the width of the APVSD breach IL-1β, IL-6, TGF-β, and TNF-α may be involved in the occurrence and development of APVSD through inflammatory mechanisms. However, due to the small sample size and the large time span of sample selection, the results may be biased. In the future, research will be conducted from the perspective of pathology. In future studies, we will further expand the sample size and do further follow-up work. In addition, we also plan to further examine the regulation of these inflammatory factors in animal models or at the cellular level, and look for the possibility of early diagnosis and targeted therapy.

5. Conclusion

IL-1β, IL-6, TGF-β, and TNF-α were positively expressed in the aneurysmal perimembranous tissue of children with APVSD, and their expression levels were negatively correlated with the width and number of APVSD breach. IL-1β, IL-6, TGF-β, and TNF-α may be involved in the occurrence and development of APVSD through inflammatory mechanism.

Data Availability

The data used to support the findings of this study are included within the article.

Conflicts of Interest

The authors declare that they have no competing interest.

Acknowledgments

References

[1] H. Li, Y. Shi, S. Zhang et al., "Short- and medium-term follow-up of transcatheter closure of perimembranous ventricular septal defects," *BMC Cardiovascular Disorders*, vol. 19, no. 1, p. 222, 2019.

[2] T. Shi, R. Liu, C. Zhang, and S. Guo, "Repair of traumatic ventricular septal defect and left ventricular aneurysm after blunt chest trauma," *Interactive Cardiovascular and Thoracic Surgery*, vol. 32, no. 1, pp. 156–158, 2021.

[3] A. Milovancev, M. Kovacevic, A. Lazarevic, A. Ilic, S. Maja, and A. Stojsic-Milosavljevic, "Left ventricular diverticulum vs. ventricular septal defect vs. ventricular aneurysm," *The International Journal of Cardiovascular Imaging*, vol. 37, no. 2, pp. 741-742, 2021.

[4] K. Wrobel, K. Zbikowska, R. Wojdyga, E. Pirsztuk, M. Zygier, and K. Kurnicka, "The role of temporary mechanical circulatory support in an effective surgical treatment of a left ventricular aneurysm and a ventricular septal defect in a patient after anterior wall myocardial infarction," *Kardiologia Polska*, vol. 79, no. 6, pp. 718-719, 2021.

[5] A. M. Belyaev, A. S. Popov, and M. D. Alshibaya, "Postmyocardial infarction ventricular septal defect and ventricular aneurysm repair with a "double-patch frame" technique," *Journal of Cardiac Surgery*, vol. 37, no. 3, pp. 515–523, 2022.

[6] J. D. Vossler, A. Fontes, R. Moza, S. C. Menon, V. L. Wong, and S. A. Husain, "Traumatic left ventricular aneurysm and ventricular septal defect in a child," *World Journal for Pediatric and Congenital Heart Surgery*, vol. 13, no. 1, pp. 116–119, 2022.

[7] S. Okugi, M. Koide, Y. Kunii, M. Tateishi, R. Shimbori, and H. Moriuchi, "Repair of a unique sinus of Valsalva defect in an infant," *Journal of Cardiac Surgery*, vol. 36, no. 6, pp. 2133–2135, 2021.

[8] A. Assaf, R. Berry, Y. Mantha, M. Zughaib, and S. Saba, "Isolated ventricular septal aneurysm: a differential diagnosis for a right sinus of Valsalva aneurysm," *The American Journal of Case Reports*, vol. 22, article e930930, 2021.

[9] A. Muhyieddeen, A. Sadhale, S. Kunchakarra, and A. Rathod, "Supracristal ventricular septal defect complicated by formation of an aorto-right ventricular outflow tract fistula: a rare cause of biventricular enlargement," *Methodist DeBakey Cardiovascular Journal*, vol. 17, no. 2, pp. 157–160, 2021.

[10] S. Yamada, S. Kainuma, K. Toda, and Y. Sawa, "Giant left ventricular pseudoaneurysm 10 years after post-infarct ventricular septal defect repair," *Circulation Journal*, vol. 86, no. 5, p. 877, 2022.

[11] M. Kawashima, H. Murakami, Y. Nomura, and H. Tanaka, "Giant pseudoaneurysm that developed seven years after surgical repair of a postinfarction ventricular septal defect," *General Thoracic and Cardiovascular Surgery*, vol. 69, no. 8, pp. 1240–1242, 2021.

[12] C. E. Tomasulo, C. Ravishankar, S. Natarajan, C. E. Mascio, and A. C. Glatz, "Large aneurysms and pseudoaneurysms of surgically reconstructed right ventricular outflow tracts," *Cardiology in the Young*, vol. 31, no. 9, pp. 1522–1524, 2021.

[13] S. H. Taha, A. A. Wahid, S. A. Haleem, S. Anilkumar, A. Elmaghraby, and P. C. Sivadasan, "Ruptured sinus of Valsalva into the right ventricle a new management strategy," *Revista Portuguesa de Cirurgia Cardio-Torácica e Vascular*, vol. 27, no. 3, pp. 209–211, 2020.

[14] J. Piche, P. P. Van Vliet, M. Puceat, and G. Andelfinger, "The expanding phenotypes of cohesinopathies: one ring to rule them all!," *Cell Cycle*, vol. 18, no. 21, pp. 2828–2848, 2019.

[15] T. R. Caulfield, J. J. Richter, E. E. Brown, A. N. Mohammad, D. P. Judge, and P. S. Atwal, "Protein molecular modeling techniques investigating novel TAB2 variant R347X causing cardiomyopathy and congenital heart defects in multigenerational family," *Molecular Genetics & Genomic Medicine*, vol. 6, no. 4, pp. 666–672, 2018.

[16] K. P. Wijnands, J. Chen, L. Liang et al., "Genome-wide methylation analysis identifies novel CpG loci for perimembranous ventricular septal defects in human," *Epigenomics-Uk*, vol. 9, no. 3, pp. 241–251, 2017.

[17] S. A. Sadom, H. Hashim, S. Maran et al., "Screening of SMAD7 in Malay patients with ventricular septal defect," *American Journal of Cardiovascular Disease*, vol. 6, no. 4, pp. 138–145, 2016.

[18] J. P. Ackerman, J. A. Smestad, D. J. Tester et al., "Whole exome sequencing, familial genomic triangulation, and systems

Retraction

Retracted: The Treatment Combining Antiangiogenesis with Chemoradiotherapy Impinges on the Peripheral Circulation Vascular Endothelial Cells and Therapeutic Effect in the Patients with Locally Advanced Nasopharyngeal Carcinoma

BioMed Research International

This article has been retracted by Hindawi following an investigation undertaken by the publisher [1]. This investigation has uncovered evidence of one or more of the following indicators of systematic manipulation of the publication process:

(1) Discrepancies in scope

(2) Discrepancies in the description of the research reported

(3) Discrepancies between the availability of data and the research described

(4) Inappropriate citations

(5) Incoherent, meaningless and/or irrelevant content included in the article

(6) Manipulated or compromised peer review

The presence of these indicators undermines our confidence in the integrity of the article's content and we cannot, therefore, vouch for its reliability. Please note that this notice is intended solely to alert readers that the content of this article is unreliable. We have not investigated whether authors were aware of or involved in the systematic manipulation of the publication process.

Wiley and Hindawi regrets that the usual quality checks did not identify these issues before publication and have since put additional measures in place to safeguard research integrity.

We wish to credit our own Research Integrity and Research Publishing teams and anonymous and named external researchers and research integrity experts for contributing to this investigation.

The corresponding author, as the representative of all authors, has been given the opportunity to register their agreement or disagreement to this retraction. We have kept a record of any response received.

References

[1] X. Gong, L. Wang, W. Wu et al., "The Treatment Combining Antiangiogenesis with Chemoradiotherapy Impinges on the Peripheral Circulation Vascular Endothelial Cells and Therapeutic Effect in the Patients with Locally Advanced Nasopharyngeal Carcinoma," *BioMed Research International*, vol. 2022, Article ID 1787854, 7 pages, 2022.

Research Article

The Treatment Combining Antiangiogenesis with Chemoradiotherapy Impinges on the Peripheral Circulation Vascular Endothelial Cells and Therapeutic Effect in the Patients with Locally Advanced Nasopharyngeal Carcinoma

Xiuyun Gong,[1] Limin Wang,[2] Weili Wu,[1] Yuanyuan Li,[1] Jinhua Long,[1] Xiaoxiao Chen,[1] Xiuling Luo,[1] Qianyong He,[1] Ting Bi,[1] Zhuoling Li,[1] Yanan Luomeng,[3] and Feng Jin ![ORCID][1]

[1]*Head and Neck Oncology, The Affiliated Cancer Hospital of Guizhou Medical University, The Affiliated Hospital of Guizhou Medical University, Guiyang 550004, China*
[2]*Guiyang First People's Hospital, Guiyang 550002, China*
[3]*Department of Oncology, Hainan Province Nongken General Hospital, Haikou 570100, China*

Correspondence should be addressed to Feng Jin; jinf8865@yeah.net

Xiuyun Gong and Limin Wang contributed equally to this work.

This study was implemented for the evaluation on the circulating endothelial cells' (CECs) clinical significance in the locally advanced nasopharyngeal carcinoma treatment with endostatin-combined chemoradiotherapy. This study enrolled 47 patients with locally advanced nasopharyngeal carcinoma who were hospitalized from May 9, 2012 to March 10, 2013. These patients were split up into the observation group (25 patients) and control group (22 patients). Patients in the observation group received the endostatin combined with induction chemotherapy and subsequently with concurrent chemoradiotherapy with endostatin. Patients in the control group were treated with inductive chemotherapy followed by concurrent chemoradiotherapy. CECs in peripheral blood were conducted separately before or after inductive chemotherapy and additionally in the end of concurrent chemoradiotherapy. The CEC values of the observation group showed significant statistical differences ($p < 0.05$) before or after different therapies, whereas those data in the control group were not statistically different. And, the mostly importantly, the CEC values in the observation group and control group turned out a statistical difference. The combination of endostatin and chemoradiotherapy significantly reduced parameters of peripheral blood CECs in these patients. According to the CEC parameters' variety that we observed in the combined therapies, this study demonstrated that the CECs might be a clinical clue to evaluate this antiangiogenic chemoradiotherapy. And the clinical value of CECs will be further determined along with increasing comparative studies and clinical long-term efficacy observation.

1. Introduction

Nasopharyngeal carcinoma (NPC) is a sort of epithelial malignancy that occurs frequently in Southeast Asia and North Africa (1). Studies indicate that genetic, ethnic, and environmental factors may jointly influence the pathogenesis of NPC (1–3). The current treatment for nasopharyngeal carcinoma is mainly radiotherapy. However, a large proportion of patients will experience local recurrence or distant metastasis after treatment (3). The Chinese Society of Clinical Oncology (CSCO) clinical guidelines for the diagnosis and treatment of nasopharyngeal carcinoma (2021) adds grade I recommendations in first-line treatment for recurrent/metastatic nasopharyngeal cancer: cisplatin +5-fluorouracil (5-FU) + local radiotherapy and new recommendation for grade III: cisplatin + gemcitabine + endostatin (recombinant human endostatin) (4). Folkman

proposed the theory that tumor growth and metastasis are reliant on angiogenesis in 1971 (5). This theory suggested that curbing tumor angiogenesis is the key factor to inhibit tumor growth and metastasis (5). Recombinant human endostatin has the functions of inducing apoptosis of vascular endothelial cells, inhibiting tumor angiogenesis and inhibiting cell proliferation and migration (4).

Peripheral blood is a convenient biopsy sample that can be obtained without trauma. Peripheral blood is used for biomarker detection. CECs are a kind of vascular endothelial cells free in peripheral blood. These cells are associated with angiogenesis and the growth and metastasis of tumor, deemed as the target of angiogenesis inhibitors and the biomarker to appraise therapeutic efficiency. Moreover, numeric alteration of CECs is also a biomarker to estimate the damage of vascular endothelium. An essential process in tumorigenesis and metastasis is angiogenesis (6, 7). The numeric alteration of CECs is a favorable predictive factor to appraise angiogenesis and prognosis (8). Recombinant human vascular endostatin is currently a widely applied injection in clinical, but its treatment outcome is hard to trace. Numeric increasement of the CECs in human lymphoma xenograft mouse models was positively correlative with tumor load, and it also implied its relationship with tumorous occurrence and development (9). On the basis of the both comparison and observation into the CEC alteration in patients' peripheral blood samples during our combined treatment, we elucidated the clinical significance of peripheral blood CEC detection in antiangiogenic chemoradiotherapy.

2. Patients and Methods

2.1. The Patients and Their General Information. Our subjects were the patients who were treated in the Head and Neck Oncology Department of Guizhou Province Cancer Hospital, dating from May 9, 2012 to March 10, 2013. Here is the clinical trial registration: Chi CRT-ONRC-12002394.

The trial was approved by the ethics committee at Guizhou Province Cancer Hospital. Inclusion criteria were as follows: male or female, the ones aged from 18 to 70 who were volunteered and offered a written consents for medical treatment; the one whose carcinoma was diagnosed as differentiated or undifferentiated type of nonkeratinizing nasopharyngeal carcinoma; their clinical stages were about at III-IVa and IVb (basing on 2010 UICC); KPS > 70, life expectancy ≥ 6 months; and whose white blood cell, hemoglobin, platelet, and liver and kidney function values were within the normal reference value range. No serious complication was demanded, such as hypertension, diabetes, coronary heart disease, and mental illness; this treatment was the first course of treatment (no history of head and neck radiotherapy, no history of concurrent radiotherapy and chemotherapy, no history of chemotherapy within 3 months). Exclusion criteria were as follows: the ones were with serious and uncontrolled medical illness or suffering major organ failure. All patients in this study were not randomly divided, and another 47 cases of the patients were enrolled as Clinical study control.

2.2. Inductive Chemotherapy. Both the control group and observation group were commenced with a two-cycle (with a cycle of 21 days) inductive chemotherapy TP (docetaxel, Jiangsu Aosaikang Pharmaceutical, E1203012) + cisplatin (Shandong Qilu Pharmaceutical, 2A1A1202011A): a one-day intravenous drip of 75 mg/m^2 docetaxel, and the subsequent intravenous drip of 80 mg/m^2 cisplatin over the next three days was conducted.

Eight days after inductive chemotherapy, the observation group was additionally treated with an intravenous drip of 7.5 mg/m^2/day recombinant human endostatin (Endostar Jiangsu Mr. Pharmaceutical, 201201001), and this treatment lasted for 14 days (a cycle of the treatment).

2.3. Concurrent Chemoradiotherapy. Both the control group and observation group were given a cisplatin (intravenous drip of 80 mg/m^2 cisplatin was given on the first day and second day of the therapy) concurrent chemotherapy after first-day radiotherapy. The observation group was treated with an additional recombinant human endostatin intravenous drip with the dose of Endostar 7.5 mg/m^2/day two weeks after the concurrent chemoradiotherapy, and this treatment lasted for a cycle of 14 days.

2.4. Radiotherapy. Both the control group and observation group were given intensity modulated radiation therapy (IMRT) (TOSHIBA Atlas, Japan) targets, and therapeutic dose was shown in report (10).

2.5. Flow Cytometry Detection of CECs. The isotype control of each sample was performed to eliminate the interruptions from background and cell immunofluorescence. Two clean sterile test tubes were tagged as control tube and experimental tube. The tube tagged as control was added with 100 mL whole blood and 20 μL isotype antibody, prepared as the control. The tube tagged as experimental was added with 100 μL whole blood and 20 μL CECs detection antibody. Both the tubes were kept at room temperature in the dark for 15 min, which were subsequently added with 800 μL 1× hemolysin and subjected to a room-temperature 5 min incubation in the dark. Then, these tubes were incubated in a water bath at 37°C for 5 min and centrifuged at 1000/min. The leftovers in these tubes were rinsed with PBS twice and resuspended. The on-machine processing was carried out on a flow cytometer (BD, USA). 1×10^4 mononuclear cells were collected in each sample, whose data were analyzed with BD FACSDIVA analysis software. FITC-anti-human CD3ε monoclonal antibody, PE-anti-human CD146 monoclonal antibody, FITC-anti-human IgG1 antibody, and PE-anti-human IgG2a antibody were purchased from BD PharMingen, USA. Three independent replicates were performed.

These white blood cells varied in size and complexity within the nucleus, which were categorized into three populations basing on FSC/SSC collection chart, from left to right: lymphocyte population, monocyte population, and granulocyte population. A circle gate analysis was performed on lymphocytes and monocyte populations (i.e., mononuclear cell populations). FITC-anti-human IgG1 and PE-

anti-human IgG2a were deemed as isotype controls and adjusted the voltage and compensate: the number of CECs = CD3 − CD146 + per 10,000 mononuclear cells.

2.6. Observation Indicators and the Follow-Up. Peripheral blood CEC values of patients in the observation group and treatment group were obtained and recorded as above. In the observation group, one case (4%) of patients with cardiac adverse reactions occurred. The remaining adverse reactions were mainly nausea and vomiting (16%) associated with chemotherapy. The content of the follow-up included the curative efficacy at 3 months, 1 - and 3-year progression-free survival, and overall survival. We also followed up patients by phone every 3 to 6 months and notified them to return to the hospital for review.

2.7. Statistical Methods. SPSS 22.0 was applied for the data statistical analysis in this experiment. Measurement data were expressed in form of mean ± standard deviation or median (upper and lower quartile), and count data were expressed in the number of cases (percentage). Chi-square test was applied for the comparison onto T stage, N stage, gender, age, pathological type, and effective rate between groups. The changes of CECs in the control group and the observation group before and after treatment were compared by paired t-test. The cumulative overall survival (OS), disease free survival (DFS), progression-free survival (PFS), and distant metastasis-free survival (DMFS) at 1, 3, and 5 years were calculated by the Kaplan-Meier method to evaluate progression-free survival and overall survival. Log-rank test was used for comparison between groups to draw survival curves.

3. Result

3.1. Clinical Characteristics of the Patient. There were 25 patients, aged from 31 to 70, in our treatment group, made up of 7 female and 18 males with a median age of 52 years old. Pathological types were made up of 5 cases of the non-keratinized differentiation and 20 cases of the nonkeratinized undifferentiation. The control group was made up of 6 female and 16 males, with 22 cases of patients aged from 30 to 70 in total with a median age of 47 years old. Pathological types were made up of 3 cases of the nonkeratinized differentiation and 19 cases of the nonkeratinized undifferentiation. There were no significant differences in age, gender, pathological type, and clinical stage between the two groups (Table 1).

3.2. The Numeric Alteration of CECs in the Observation Group. There was a declining trend of the CECs in the observation group. The alteration of the treatment group was shown in Figure 1. The value of CECs before induction was 14.96 ± 7.62, and after induction was 10.16 ± 5.14, resulting in their difference statistically significant ($t = 2.61$, $p = 0.037$). The value of CECs before induction was 14.96 ± 7.62, and after radiotherapy was 5.84 ± 6.76, having their difference statistically significant. The value of CECs after induction was 10.16 ± 5.14, and that after radiotherapy was 5.84 ± 6.76, making a statistical significance ($t = 2.54$, $p = 0.004$).

Table 1: The clinical characteristics of 47 nasopharyngeal patients.

Characteristic	Treatment group	Control group	p value
Gender			0.956
Male	18	16	
Female	7	6	
Age*			0.196
Range	31-70	30-70	
Median	52	47	
Pathological type**			0.849
Undifferentiated type	20	19	
Differentiated type	5	3	
Clinical stages△			1.000
III stage	2	2	
IV stage	23	20	

Note: * in age, △ 2010UICC stage, ** nonkeratinizing cancer.

3.3. The Numeric Alteration of CECs in the Control Group. There were no significant alterations in CEC values revealed in the observation group (Figure 1). In the control group, the value of CECs before induction was 13.77 ± 6.60, and after induction was 12.59 ± 6.24, showing no statistical significance ($t = 0.09$, $p = 0.515$). The value of CECs before induction was 13.77 ± 6.60, and the value after radiotherapy was 10.27 ± 5.02, representing no statistical significance ($T = 0.31$, $p = 0.057$). The value of CECs after induction was 12.59 ± 6.24, and after radiotherapy was 10.27 ± 5.02, turning out a statistical insignificance ($t = 0.21$, $p = 0.204$). CEC value of the observation group and in the control group after radiotherapy was 5.84 ± 6.76 and 10.27 ± 5.02, showing a statistical significance ($t = 2.57$, $p = 0.001$). It demonstrated that endostatin combined with inductive chemotherapy and concurrent radiotherapy significantly reduces the number of CECs in the blood of patients.

3.4. Follow-Up Results. The effective rate of treatment in the whole group reached 100%, and the CR rates (3 months after concurrent radiotherapy and chemotherapy) of the observation group and the control group were 60% and 50%, respectively ($t = -1.725$, $p = 0.091$). There was no statistical distinction within groups; the CR rates of the observation group and the control group after 1 year were 100% and 95.45%, respectively ($t = 1.000$, $p = 0.332$), having no statistical significance. The last follow-up was on July 30, 2018, with a median follow-up of 70 months, and the follow-up was 100% completed. Our results turned out that there were 11 deaths from various causes: 5 deaths in the observation group and 6 deaths in the control group; 1-, 3-, and 5-year OS, DFS, PFS, and DMFS in the observation group had survival advantages over those in the control group, but there was no statistical significance in the two groups (Table 2). The survival curve was shown in Figure 2.
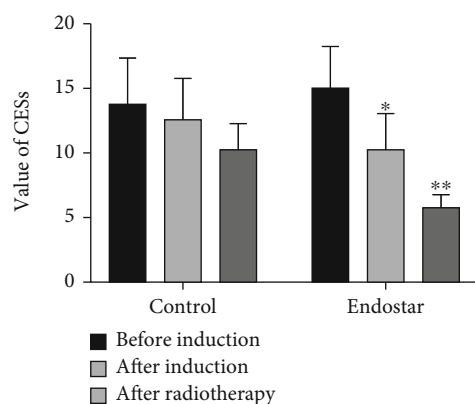
Figure 1: The changes of CECs during the treatment. $^{*}p < 0.05$, $^{**}p < 0.01$.

Table 2: The survival comparison between the two groups.

Items	Treatment group	Control group	χ^2/Z value	p value
N	25	22		
OS			0.291	0.589
1 year	92%	90.9%		
3 years	88%	77.3%		
5 years	76%	72.7%		
DFS			0.203	0.653
1 year	92%	90.9%		
3 years	76%	77.3%		
5 years	68%	67.7%		
PFS			0.046	0.830
1 year	92%	90.9%		
3 years	80%	81.8%		
5 years	68%	72.7%		
DMFS				
1 year	92%	90.9%	0.136	0.712
3 years	84%	77.3%		
5 years	76%	68.2%		

4. Discussion

The mainstream treatment for advanced local nasopharyngeal carcinoma patients is a comprehensive treatment combining with radiotherapy, chemotherapy, and targeted therapy, which greatly improves patients' five-year survival rate and especially has that of the advanced local nasopharyngeal carcinoma (stages III and IVa) which reach nearly 80%. Failure of nasopharyngeal carcinoma IMRT mainly attributes to the distant metastasis of this cancer (11–14). Therefore, controlling local recurrence and distant metastasis might ensure the long-term survival of patients.

Short-term effective rate of recombinant human endostatin combined with induction chemotherapy and sequential concurrent chemoradiotherapy in the treatment of advanced local nasopharyngeal carcinoma was higher than that of induction chemotherapy and sequential concurrent chemoradiotherapy (10). Antiangiogenesis therapy normalizes tumor angiogenesis and alleviates tumor hypoxia, thereby elevating tumor radiotherapy and chemotherapy sensitivity (15, 16).

Antitumor neovascularization is an important aspect of targeted therapy, but the evaluation standard for tumor efficacy is mainly the evaluation to chemotherapy drugs' efficacy (17–19). Antiangiogenic drugs act on the blood vessels of tumors, and most of them cannot quickly shrink tumors, because tumorous volume change often comes later than blood supply inhibition. Therefore, the mere evaluation to tumor volume is not objective enough, which makes the current evaluation to antiangiogenic drugs still limited. The evaluation to antiangiogenesis effect mainly includes imaging examination, biomarker detection, morphological examination, and clinical symptoms.

In addition to vascular endothelial growth factor, the related biomarkers also include peripheral blood circulating endothelial cells. It has been found that the binding of vascular endothelial cell-specific heparin to growth factors can promote the formation of new blood vessels in vivo (20, 21). The high expression of VEGF is regarded as one of the potential markers of early metastasis of nasopharyngeal carcinoma, which often indicates lymph node metastasis, recurrence, and poor prognosis of nasopharyngeal

carcinoma. The CECs in lung cancer patients reflected lung cancer angiogenesis and were used to judge the prognosis (11). The number of CECs in the blood of patients with head and neck tumors was also increased, which is associated with VEGF (22). Goon et al. compared the number of CECs detected through magnetic separation and flow cytometry, and they found that in the case of specific CEC phenotype, flow cytometry was more accurate in detecting the number of CECs (23).

This study was implement via the added recombinant human endostatin to the usual treatment of patients with advanced local nasopharyngeal cancer, and our results turned out that the CEC value in the observation group before the inductive chemotherapy was 14.96 ± 7.62, and after concurrent chemoradiotherapy was 5.84 ± 6.76, showing a notable numeric alteration that the difference is statistically significant; however, the value of CECs in the control group was 13.77 ± 6.60 before induction chemotherapy and 10.27 ± 5.02 after concurrent radiotherapy and chemotherapy, and there was no obvious difference between the pre and the post, where the difference was statistically insignificant ($p = 0.057$). By comparing the values of CECs at the end of treatment, we found that the CEC value in the observation group was notably lower than the control group with the difference statistically significant (5.84 ± 6.76, 10.27 ± 5.02, $t = 2.57$, $p = 0.001$). Our results are consistent with those reported by Lee et al. (3), and it shows that endostatin combined with inductive chemotherapy and concurrent radiotherapy significantly reduces the number of CECs in the patient's blood, indirectly illustrating potential efficacy of recombinant human endostatin in the treatment of nasopharyngeal carcinoma. Previous research reported that CECs are increased in the blood of cancer patients and correlate with angiogenesis, therefore potentially serving as a biomarker to determine progressive disease, prognosis,
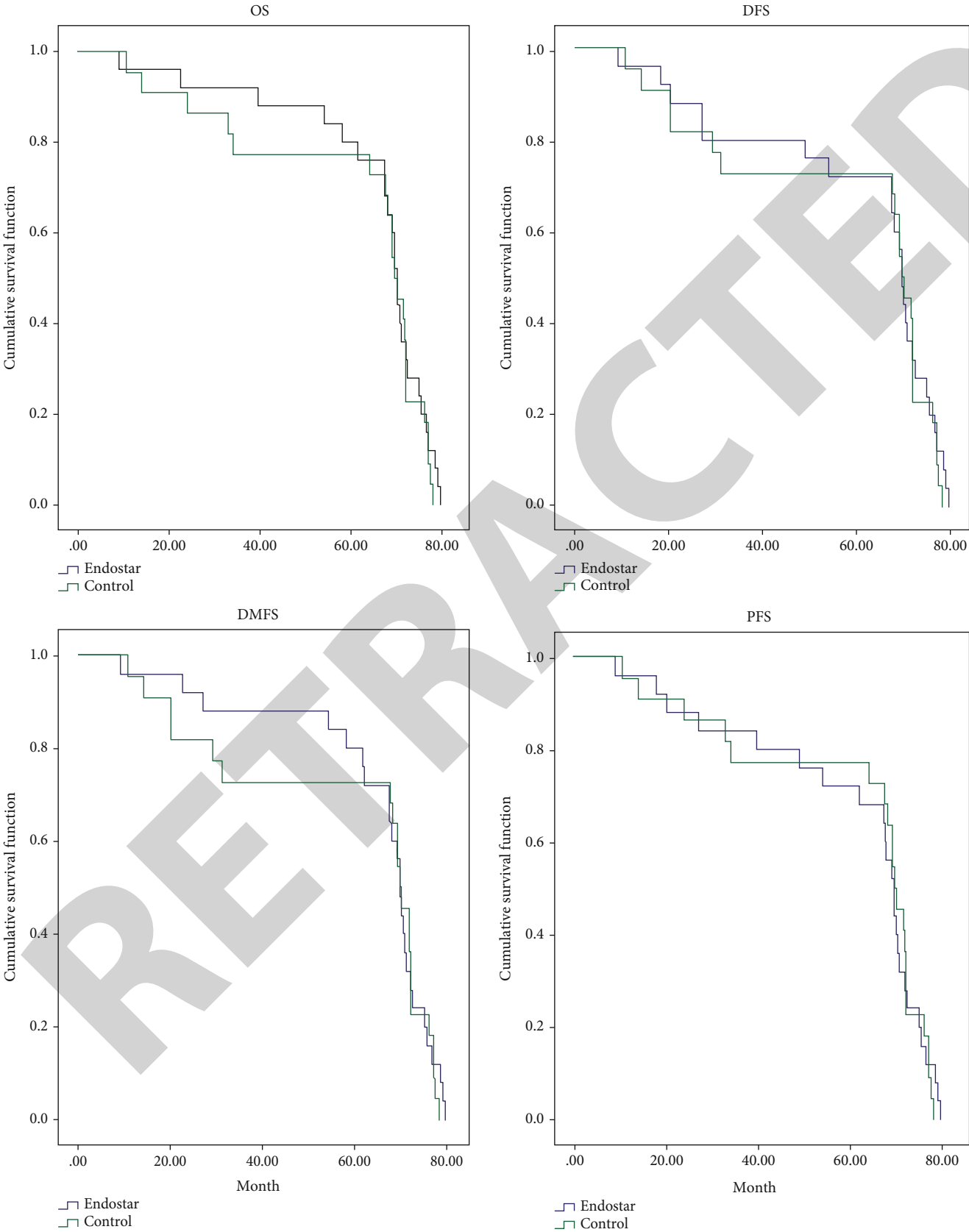
Figure 2: The survival curve of OS, DFS, PFS, and DMFS.

and response to therapy (24, 25). In the long-term follow-up, we found that the observation group showed a slight survival advantage trend of OS and PFS, but there was no statistical difference. Guan et al. confirmed that the CR rate of recombinant Endostar and radiotherapy for advanced, locally recurrent nasopharyngeal carcinoma could reach 90.9% (26).

The combination of endostatin and chemoradiotherapy reduced parameters of peripheral blood CECs in these patients. This study demonstrated that the CECs might be a clinical clue to evaluate this antiangiogenic chemoradiotherapy. The limitation of this study was the number of cases that is relatively small. There were 11 deaths from various causes: 5 deaths in the observation group and 6 deaths in the control group in our study. This may be why CR reached 100% after 1 year. Considering that the number of patients in the group may be less, no statistical difference was shown. The shortcomings of this study lie in the nonrandomized comparative study to single-center small samples, and the number of cases is relatively small. Further clinical application of this study needs to be confirmed in a large multicenter phase III clinical study.

5. Conclusion

In this study, we found that concurrent chemoradiotherapy combined with endostatin effectively decreases the CEC number in peripheral blood of patients with advanced local nasopharyngeal carcinoma versus the control group. Through long-term follow-up of patients, we can see the trend of survival benefits. We believe that the detection to CEC numeric alteration in peripheral blood is potentially significant clinical measures to evaluate the efficacy of antiangiogenesis combined radiotherapy and chemotherapy.

Data Availability

The data used to support the findings of this study are included within the article.

Ethical Approval

The experiment was approved by the ethics committee of Guizhou Province Cancer Hospital.

Conflicts of Interest

The authors declare that there are no conflicts of interest.

Authors' Contributions

XYG and LMW collected the data, performed the experiments, and wrote the manuscript. WLW, YYL, JHL, XXC, XLL, QYH, TB, ZLL, and YNLM contributed to collecting data and reviewing the manuscript. FJ and LMW conceived the study and contributed to reviewing/editing the manuscript. All authors have read and approved the final manuscript. Xiuyun Gong and Limin Wang contributed equally to this work.

References

[1] Y. P. Chen, A. T. C. Chan, Q. T. Le, P. Blanchard, Y. Sun, and J. Ma, "Nasopharyngeal carcinoma," *Lancet*, vol. 394, no. 10192, pp. 64–80, 2019.

[2] F. Bray, J. Ferlay, I. Soerjomataram, R. L. Siegel, L. A. Torre, and A. Jemal, "Global cancer statistics 2018: GLOBOCAN estimates of incidence and mortality worldwide for 36 cancers in 185 countries," *CA: a Cancer Journal for Clinicians*, vol. 68, no. 6, pp. 394–424, 2018.

[3] H. M. Lee, K. S. Okuda, F. E. González, and V. Patel, "Current perspectives on nasopharyngeal carcinoma," *Advances in Experimental Medicine and Biology*, vol. 1164, pp. 11–34, 2019.

[4] L. L. Tang, Y. P. Chen, C. B. Chen et al., "The Chinese Society of Clinical Oncology (CSCO) clinical guidelines for the diagnosis and treatment of nasopharyngeal carcinoma," *Cancer Commun (Lond)*, vol. 41, no. 11, pp. 1195–1227, 2021.

[5] J. Folkman, "Tumor angiogenesis: therapeutic implications," *The New England Journal of Medicine*, vol. 285, no. 21, pp. 1182–1186, 1971.

[6] S. Takizawa, E. Nagata, T. Nakayama, H. Masuda, and T. Asahara, "Recent progress in endothelial progenitor cell culture systems: potential for stroke therapy," *Neurologia Medico-Chirurgica (Tokyo)*, vol. 56, no. 6, pp. 302–309, 2016.

[7] E. S. de Bont, J. E. Guikema, F. Scherpen et al., "Mobilized human CD34+ hematopoietic stem cells enhance tumor growth in a nonobese diabetic/severe combined immunodeficient mouse model of human non-Hodgkin's lymphoma," *Cancer Research*, vol. 61, no. 20, pp. 7654–7659, 2001.

[8] K. Bogos, F. Renyi-Vamos, J. Dobos et al., "High VEGFR-3-positive circulating lymphatic/vascular endothelial progenitor cell level is associated with poor prognosis in human small cell lung cancer," *Clinical Cancer Research*, vol. 15, no. 5, pp. 1741–1746, 2009.

[9] S. Monestiroli, P. Mancuso, A. Burlini et al., "Kinetics and viability of circulating endothelial cells as surrogate angiogenesis marker in an animal model of human lymphoma," *Cancer Research*, vol. 61, no. 11, pp. 4341–4344, 2001.

[10] Y. Li, F. Jin, W. Wu et al., "Clinical results of recombinant human endostatin combined with chemoradiotherapy for locally advanced nasopharyngeal carcinoma," *Zhonghua Zhong Liu Za Zhi*, vol. 37, no. 2, pp. 128–132, 2015.

[11] X. Sun, S. Su, C. Chen et al., "Long-term outcomes of intensity-modulated radiotherapy for 868 patients with nasopharyngeal carcinoma: an analysis of survival and treatment toxicities," *Radiotherapy and Oncology*, vol. 110, no. 3, pp. 398–403, 2014.

[12] B. B. Chen, S. Y. Lu, H. Peng et al., "Comparison of long-term outcomes and sequelae between children and adult nasopharyngeal carcinoma treated with intensity modulated radiation therapy," *International Journal of Radiation Oncology • Biology • Physics*, vol. 106, no. 4, pp. 848–856, 2020.

[13] S. Fox-Alvarez, K. Shiomitsu, A. T. Lejeune, A. Szivek, and L. Kubicek, "Outcome of intensity-modulated radiation therapy-based stereotactic radiation therapy for treatment of canine nasal carcinomas," *Veterinary Radiology & Ultrasound*, vol. 61, no. 3, pp. 370–378, 2020.

Retraction

Retracted: Prokineticins as a Prognostic Biomarker for Low-Grade Gliomas: A Study Based on The Cancer Genome Atlas Data

BioMed Research International

This article has been retracted by Hindawi following an investigation undertaken by the publisher [1]. This investigation has uncovered evidence of one or more of the following indicators of systematic manipulation of the publication process:

(1) Discrepancies in scope

(2) Discrepancies in the description of the research reported

(3) Discrepancies between the availability of data and the research described

(4) Inappropriate citations

(5) Incoherent, meaningless and/or irrelevant content included in the article

(6) Manipulated or compromised peer review

The presence of these indicators undermines our confidence in the integrity of the article's content and we cannot, therefore, vouch for its reliability. Please note that this notice is intended solely to alert readers that the content of this article is unreliable. We have not investigated whether authors were aware of or involved in the systematic manipulation of the publication process.

Wiley and Hindawi regrets that the usual quality checks did not identify these issues before publication and have since put additional measures in place to safeguard research integrity.

We wish to credit our own Research Integrity and Research Publishing teams and anonymous and named external researchers and research integrity experts for contributing to this investigation.

The corresponding author, as the representative of all authors, has been given the opportunity to register their agreement or disagreement to this retraction. We have kept a record of any response received.

References

[1] J. Zhong, D. Xiang, and X. Ma, "Prokineticins as a Prognostic Biomarker for Low-Grade Gliomas: A Study Based on The Cancer Genome Atlas Data," *BioMed Research International*, vol. 2022, Article ID 2309339, 12 pages, 2022.

Research Article

Prokineticins as a Prognostic Biomarker for Low-Grade Gliomas: A Study Based on The Cancer Genome Atlas Data

Junqing Zhong [iD],[1] Ding Xiang,[1] and Xinlong Ma [iD][2]

[1]Department of Rehabilitation, Tianjin Hospital, Tianjin, China
[2]Department of Orthopedics, Tianjin Hospital, Tianjin, China

Correspondence should be addressed to Xinlong Ma; maxinlong8686@sina.com

Lower-grade glioma (LGG) is a crucial pathological type of glioma. Prokineticins have not been reported in LGG. Prokineticins as a member of the multifunctional chemokine-like peptide family are divided into two ligands: PROK1 and PROK2. We evaluated the role of PROK1 and PROK2 in LGG using TCGA database. We downloaded the datasets of LGG from TCGA and evaluated the influence of prokineticins on LGG survival by survival module. Correlations between clinical information and prokineticins expression were analyzed using logistic regression. Univariable survival and multivariate Cox analysis was used to compare several clinical characteristics with survival. Correlation between prokineticins and cancer immune infiltrates was explored using CIBERSORT and correlation module of GEPIA. We analyzed genes of PROK1 and PROK2 affecting LGG, screened differentially expressed genes (DEGs), interacted protein-protein with DEGs through the STRING website, then imported the results into the Cytospace software, and calculated the hub genes. To analyze whether hub genes and prokineticins are related, the relationship between PROK1 and PROK2 and hub genes was assessed and shown by heat map. In addition, gene set enrichment analysis (GSEA) was performed using the TCGA dataset. The univariate analysis using logistic regression and PROK1 and PROK2 showed opposite expression differences between tumor and normal tissues ($p < 0.05$). PRO1 and PROK2 expressions showed significant differences in tumor grade, age, Iiscitrate DeHydrogenase (IDH) status, histological type, and 1P/19q codeletion. Multivariate analysis revealed that the up-regulated PROK1 and PROK2 expression is an independent prognostic factor for bad prognosis. Specifically, prokineticin expression level has significant correlations with infiltrating levels of Th1 cells, NK CD 56bright cells, and Mast cells in LGG. We screened 21 DEGs and obtained 5 hub genes (*HOXC10*, *HOXD13*, *SOX4*, *GATA4*, *HOXA9*). GSEA-identified FCMR activation, creation of C4 and C2 activators, and CD22-mediated BCR regulation in gene ontology (GO) were differentially enriched in high PROK1 and PROK2 expression phenotype pathway, cytoplasmic ribosomal proteins, and ribosome and were differentially enriched in the low PROK1 and PROK2 expression phenotype pathway. Prokineticins are a prognostic biomarker and the correlation between hub genes and LGG requires further attention.

1. Introduction

Low-grade gliomas (LGG), also known as grade I and grade II gliomas, originate from the glial cells of the primary slow-growing brain tumors and account for approximately15% of all primary brain tumors [1]. LGG is the most common invasive tumor in the adult cerebral hemisphere, including astrocytoma, oligodendrocyte, and astrocytoma, and is most common in young people under 50 [2]. Because of its highly diffuse nature, complete neurosurgical resection is challenging, and residual tumors can lead to recurrence and higher levels of progression [3]. At present, WHO's histologic classification is still used in LGG classification, but the clinical treatment plan is influenced by image examination, histological classification, and WHO classification.

There has been considerable debate about the best treatment strategy for LGG [4], such as surgery, chemotherapy, and radiation therapy. However, recent studies have found

that the prognosis of LGG is inconsistent with WHO classi-fication, and clinical decision-making may be better guided by genetic classification. Clinicians and scientists have delved into identifying molecular markers associated with gliomas and pathology that influences a patient's individual-ized treatment [5]. We aim to accurately predict patient sur-vival or response to individualized therapy; new biomarkers were identified in patients with gliomas.

Prokineticins belong to a family of multifunctional chemokine-like peptides and were identified forty years ago [6]. The researchers identified two phenotypes, PROK1 and PROK2 [7], based on the homology of human protein codes (proteins isolated from the dendroaspis polylepis venom [8] and skin secretions of bomtina variegat [6]). Numerous studies have found that prokineticins and their receptors are found in various human tissues, such as the brain, heart, bone marrow, and peripheral blood. Since they are distributed in different cells and tissues and exhibit a wide range of tissue-specific biological activities, they coor-dinate complex behaviors, such as feeding, circadian rhythms, and hyperalgesia [9]. They are further involved in neuronal migration [10], survival, angiogenesis, hematopoi-esis, and inflammation.

Prokineticins have been detected in the central nervous system [11], anterior horn of the spinal cord [12], and other nerve tissues for 20 years. Prokineticins can be tissue-specific cell survival factors regulating LGG, and their ability to induce angiogenesis and coordinate inflammatory immune responses has got our attention. Therefore, we used LGG-related data from The Cancer Genome Atlas (TCGA) to determine the correlation between prokineticins and LGG using R and Gene Expression Profiling Interactive Analysis (GEPIA). In addition, we detected the correlation between the expression of kinetin and density of tumor infiltrating immune cells (TIICs) in different tumor microenviron-ments. We screened the differentially expressed genes (DEGs) in LGG for up- and down-regulated hub genes that may be relevant targets or biomarkers and contribute to the potential positive role of prokineticins in LGG.

2. Materials and Methods

2.1. Data Acquisition. Level 3 HTSeq-FPKM RNAseq data-sets from the LGG project were selected from the Open TCGA database (https://portal.gdc.cancer.gov/) [13]. The RNAseq data obtained in the fragments per kilobase per mil-lion (FPKM) format was converted to Transcripts Per Mil-lion reads (TPM) format and Log2 converted to eliminate the control/normal missing entries. Based on the expression of PROK1 and PROK2, the tumor tissues were divided into two groups: low expression group, 0–50%; high expression group, 50–100%.

2.2. Expression and Survival Analysis of PROK1 and PROK2. The correlation between the expression of PROKR1 and PROK2 in LGG and the clinicopathological information was confirmed online from the GEPIA database (http://GEPIA.cancer-pku.cn/index.html) [14]. A box map was constructed according to the disease status (tumor or nor-

mal), and the differential expression of PROK1 and PROK2 was calculated. GEPIA database integrates TCGA big data, for cancerous tissue, and GTEx big data, for normal tissue, and uses bioinformatics to answer important questions in cancer pathophysiology; reveal cancer subtypes; drive the expression of genes, alleles, and differentially expressed or carcinogenic factors; and explore new cancer targets and markers.

The main clinical parameters of PROK1 and PROK2, expression, grade, gender, age, IDH status, histological type, and 1p/19q were statistically analyzed using R (3.6.3); ggplot2 was used for visual rendering [15].

2.3. Detection of TIICs Immune Response in LGG. CIBER-SORT (http://cibersort.stanford.edu/) is a deconvolution algorithm based on gene expression used to evaluate the rel-ative changes in the expression of a group of genes in a sam-ple [16]. We used CIBERSORT to measure the immune responses of 21 kinds of TIICs in LGG and evaluated the correlation between survival rate and molecular subsets. By establishing the gene expression dataset using standard annotation files, the algorithm is uploaded to the CIBER-SORT website, and the algorithm runs with a default signa-ture matrix of 1000 permutations. CIBERSORT estimated the P value of deconvolution by Monte Carlo sampling and determined the confidence of the results. We used 529 LGG samples from TCGA, and low expression and high expression groups each accounted for 50% of the samples; furthermore, we used the GSVA package in R (3.6.3) for vioplot [17].

2.4. Differential Expression Analysis of PROK1 and PROK2 in Pan Cancer. We analyzed the expression differences of PROK1 and PROK2 using the Level 3HTSeq-FPKM data of the Universal Cancer Project in TCGA database, the RNAseq data in FPKM format is converted to log2, and the result is visualized.

2.5. Analysis of Differentially Expressed Genes(DEGs). Using R, we analyzed the RNAseq data of PROK1 and PROK2 for LGG obtained from the TCGA database and found that the screening criteria met | log2(FC) |>1.5 and p. adj<0.05, and Venn set, PROK1 and PROK2 common DEGs were obtained. The results (DEGs) were imported into the STRING online site [18], where protein-protein interactions (PPI) were used to obtain the intergenic network of DEGs and then imported into Cytospace [19]. The DEGs were cal-culated from node to node using the cytoHubba plug-in on the Cytospace [20]; the top 5 hub genes were selected according to "Degree." The selected hub gene and PROK1 and PROK2 were analyzed and validated the correlation by the molecular heat map. The groups were classified accord-ing to 50% of the low- and high-expression groups.

2.6. Gene Enrichment Analysis. For gene enrichment analy-sis, we used the gene set enrichment analysis (GSEA) method [21], which uses a predefined set of genes and sorts them according to their expression in the two types of sam-ples. In this study, GSEA generated an initial list of gene classifications based on its association with the expression

Table 1: Clinical baseline data of different concentrations of PROK1 and PROK2.

Characteristic	Low expression of PROK1	High expression of PROK1	P	Low expression of PROK2	High expression of PROK2	P
N	264	264		264	264	
WHO grade			**0.047**			0.974
G2	123 (26.3%)	101 (21.6%)		111 (23.8%)	113 (24.2%)	
G3	110 (23.6%)	133 (28.5%)		119 (25.5%)	124 (26.6%)	
Gender			1			0.08
Female	119 (22.5%)	120 (22.7%)		109 (20.6%)	130 (24.6%)	
Male	145 (27.5%)	144 (27.3%)		155 (29.4%)	134 (25.4%)	
Age, meidan (IQR)	38 (31, 48)	43.5 (33, 55)	< **0.001**	41 (33, 50)	39 (31.75, 55.25)	0.613
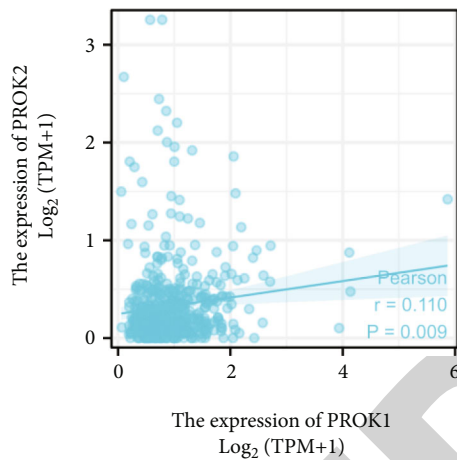
Figure 1: PROK1 and PROK2 correlation analysis. Pearson correlation coefficient r =0.110, P =0.009, indicating that there is a positive correlation between PROK1 and PROK2.

of PROK1 and PROK2. This calculation illustrates the differences between the high and low expression of PROK1 and PROK2 groups. For each analysis, we performed 1000 repeated gene set permutations and presented the phenotypic labels for the expression of PROK1 and PROK2. In addition, we used the P values, normalized enrichment score (NES), and false discovery rate (FDR) <0.05, as criteria for selecting and classifying significant enrichment outcomes in each phenotype [22].

2.7. Statistical Analysis. The data obtained from TCGA were analyzed using R (3.6.3). The Shapiro-Wilk normality test was used to analyze PROK1 and PROK2 data, and the Pearson correlation coefficient was used to transform the unsatisfied variables [23]. The Wilcoxon rank sum test was used to compare the expression of PROK1 and PROK2 between variations in clinical parameters (tumor, grade, gender, age, IDH status, and histological type) [24]. Using the Shapiro-Wilk normality test for 21 kinds of TIICs, the Wilcoxon sum test or analysis of variance was used to determine whether it was in accordance with the normal distribution (the results showed significant difference if P < 0.05. Marked by: ns, P ≥ 0.05; *, P < 0.05; **, P < 0.01; ***, P < 0.001).

PROK1 (ACU = 0.766)
PROK2 (ACU = 0.738)
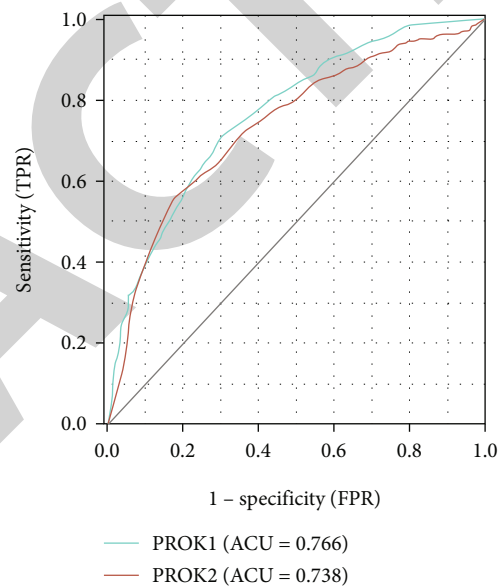
Figure 2: ROC of PROK1 and PROK2. The area under the ROC curve of PROK1 and PROK2 is 0.766 and 0.738, respectively. The cut-off value, sensitivity, specificity, positive predictive value, negative predictive value, and Yoden index of PROK1 were 0.328, 0.711, 0.694, 0.514, 0.841 and PROK2 were 0.104, 0.558, 0.824, 0.590, 0.804, and 0.382, respectively.

3. Results

3.1. Characteristics and Multifactorial Analysis of Patients. In October 2021, clinical and gene expression data of 529 patients with LGG were obtained on the TCGA website, excluding the cases with insufficient or missing data on age and total survival time. We analyzed the effect of low and high expression of PROK1 and PROK2 on the median sex and age of WHO Grade and Gender, respectively, as shown in Table 1. In addition, the Pearson correlation analysis was used to determine the correlation between PROK1 and PROK2. The results showed that there was a positive correlation between PROK1 and PROK2 (R =0.11, 95% CI =0.029-0.197, P = 0.009), as shown in Figure 1. The area of PROK1 and Prok2 was close to each other. The sensitivity of PROK1 and PROK2 was 0.711 (cut-off 0.328) and 0.824,
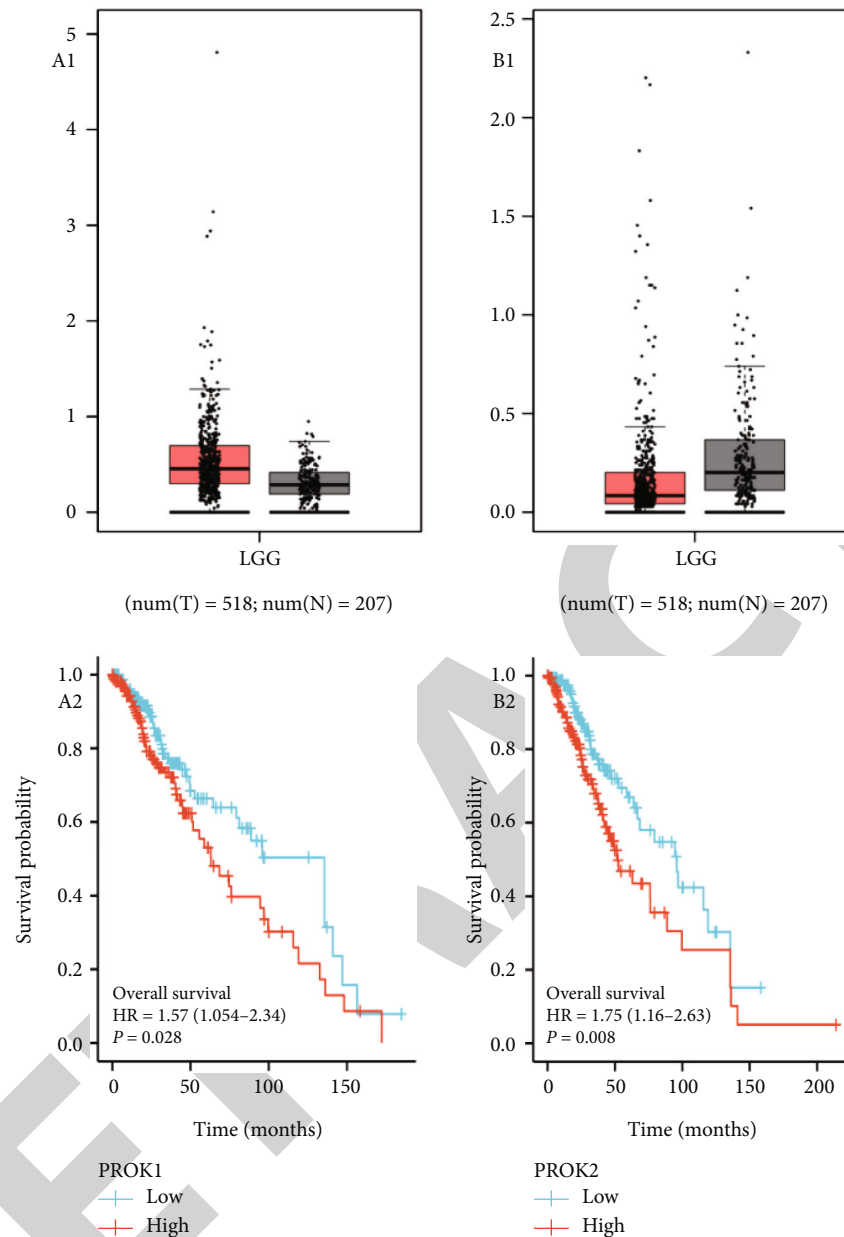
FIGURE 3: The survival curve and expression boxmap of normal and tumor tissues were constructed using GEPIA analysis. (a1) Comparison of PROK1 expression between normal and tumor tissues. (b1) Comparison of PROK2 expression between normal and tumor tissue. In PROK1, tumor group was higher than normal group; the difference was statistically significant ($P < 0.05$). In PROK2, tumor group was lower than normal group; the difference was statistically significant ($P < 0.01$). (a2) The survival curve of low and high concentration PROK1 was compared ($P = 0.028$). (b2) The survival curve of low and high concentration PROK2 was compared ($P = 0.008$). The concentrations of PROK1 and PROK2 had significant difference for survival.

respectively. The negative predictive value for both PROK1 and PROK2 was more than 0.8, as shown in Figure 2.

3.2. Survival Analysis and Clinical Multifactorial Expression of PROK1 and PROK2. The survival curve and expression boxmap of normal and tumor tissues were constructed using GEPIA analysis, as shown in Figure 3. The results showed that PROK1 and PROK2 were significantly correlated with overall survival in different states ($P < 0.01$). In addition, the expression of PROK1 in tumor tissue samples was significantly higher than that in normal tissue samples ($P < 0.05$),

as shown in Figure 3(a1); the expression of PROK2 in tumor tissue samples was significantly lower than that in normal tissue samples (P <0.01), as shown in Figure 3(b1). The median survival time of low and high expressions of PROK1 was 135.6 and 63, respectively (P =0.028), as shown in Figure 3(a2), and the median survival time of low and high concentrations of PROK2 was 95.8 and 51.6, respectively (P =0.008), as shown in Figure 3(b2).

According to Figure 4(a), the expression of PROK1 is more significant than that of PROK2 (median 0.847 : 0.184). With the progression of grade, although the
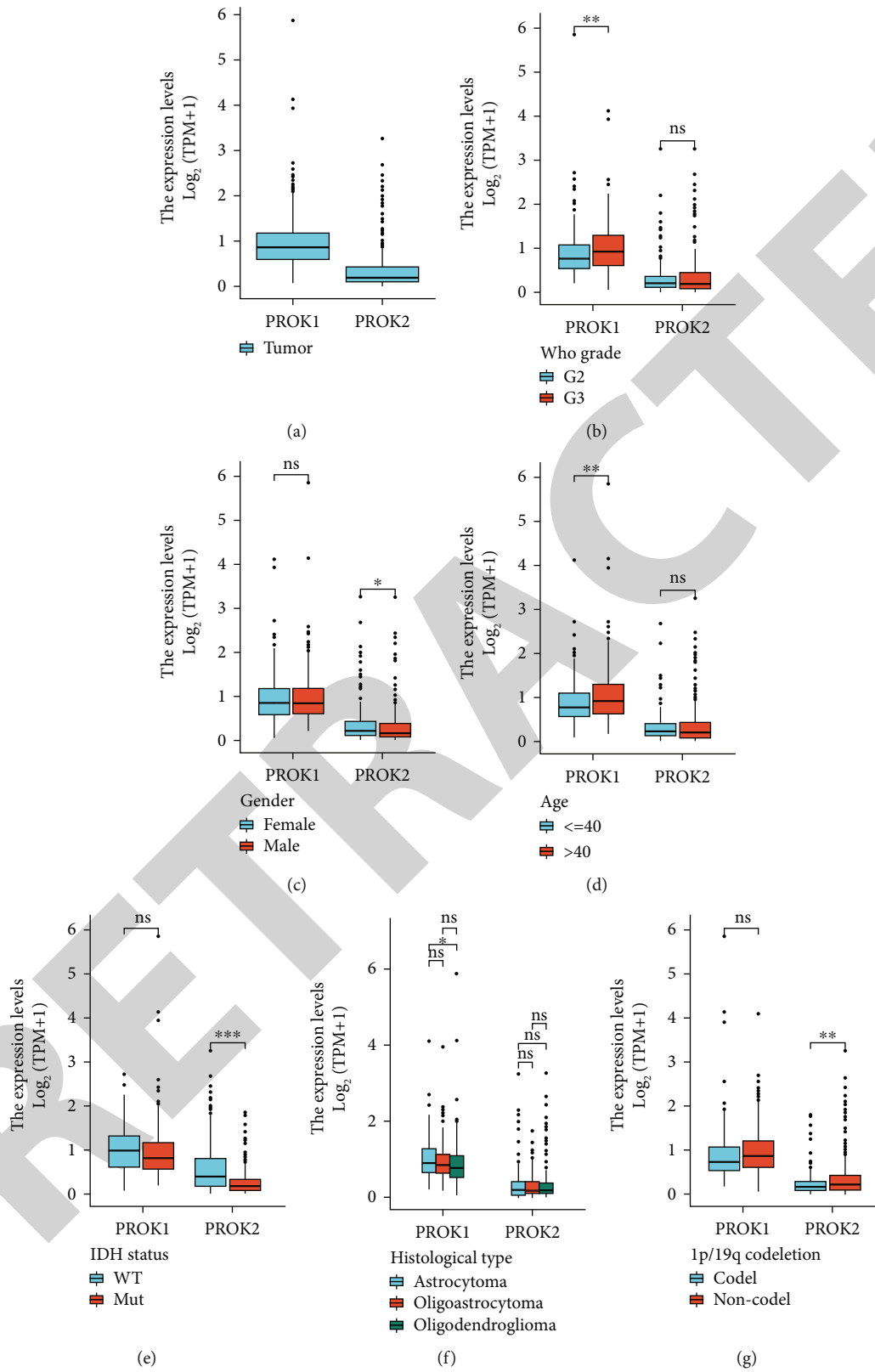
Figure 4: Clinical multifactorial expression of PROK1 and PROK2. (a) Expression of PROK1 and PROK2 in tumor tissue. (b) Expression of low and high concentrations of PROK1 and PROK2 in WHO grade. (c) Expression of low and high concentrations of PROK1 and PROK2 in gender. (d) Expression of low and high concentrations of PROK1 and PROK2 in age. (e) Expression of low and high concentrations of PROK1 and PROK2 in IDH status. (f) Expression of low and high concentrations of PROK1 and PROK2 in histological type. (g) Expression of low and high concentrations of PROK1 and PROK2 in 1p/19q codeletion.

Characteristics	Total (N)	HR (95% CI) multivariate analysis	P value multivariate analysis
Who grade	466		
G2	223		
G3	243	2.078 (1.350–3.198)	<0.001
Age	527		
<=40	264		
>40	263	2.928 (1.901–4.510)	<0.001
Gender	527		
Female	238		
Male	289		
IDH status	524		
WT	97		
Mut	427	0.298 (0.184–0.485)	<0.001
1p/19q codeletion	527		
Codel	170		
Non−codel	357	1.892 (1.128–3.176)	0.016
PROK1	527	1.259 (0.944–1.678)	0.117
PROK2	527	0.971 (0.709–1.330)	0.854

FIGURE 5: PROK1 and PROK2 multivariate Cox analysis of forest plot. As tumor grade, age, IDH status, 1p/19q codeletion, and PROK1 and PROK2 expression are independent prognostic factors.

expression of PROK1 significantly increased ($P = 0.003$), the expression of PROK2 was not significantly different ($P = 0.989$), as shown in Figure 4(b). We compared the variation in high and low expressions as per sex, age, IDH status, histological type, and 1p/19q co-deletion; the results are shown in Figures 4(c)–4(g). The expression of PROK1 in grade ($P = 0.003$) and age ($P = 0.005$) was significant, while the expression of PROK2 in IDH status ($P < 0.001$) and 1p/19q co-deletion ($P = 0.007$) was significant. Multivariate Cox analysis showed that tumor grade, age, IDH status, 1p/19q co-deletion, and PROK1 and PROK2 were multivariate Cox analysis of forest plot for LGG, as shown in Figure 5.

3.3. Expression of PROK1 and PROK2 in TIICs. Azimi et al. have shown that lymphocyte is an independent predictor of sentinel lymph node status and survival in cancer patients [25]. Based on this theory, we hypothesized that the expression of PROK1 and PROK2 was related to the immunologic invasion of LGG. A total of 529 tumor specimens were divided into two groups based on PROK1 and PROK2 expression. Figure 6 shows the proportion of 21 immune cell subsets in which Th1 cells, CD56 bright NK cells, and mast cells were the main immune cells affected by the expression of PROK1 and PROK2. Interestingly, the high and low expression of PROK1 and PROK2 had the opposite effect on Th1 cells ($P^{PROK1}0.001$: $P^{PROK2}0.000$). Except for the immune cells affected by Th1 cells, CD56 dim NK cells, neutrophils, macrophages, eosinophils, cytotoxic cells, and B cells, there were significant differences in the expression of PROK2 ($P < 0.001$), while the expression of PROK1 had relatively little effect on immune cells (TFH).

3.4. Differential Analysis of Pan Cancer. A total of 11,093 samples (para 730: tumor 10363) were obtained from the TCGA database. The expressions of PROK1 and PROK2 in 33 kinds of Pan cancer were analyzed. In addition to LGG, the expressions of PROK1 in BLCA, BRCA, COAD, HNSC, KICH, KIRP, and PRAD in tumor group were significantly lower than those in normal group ($P < 0.001$). The expression of PROK2 in BRCA, LIHC, LUAD, LUSC, and UCEC in tumor group was significantly lower than that in para-cancer group ($P < 0.001$) (Figure 7).

3.5. Comparison of DEGs of PROK1 and PROK2 in LGG and Screening of Hub Genes. The screening condition for the differential genes was to satisfy the $|\log2(FC)| > 1.5$ and p. adj<0.05 criteria. Among those that satisfied the criteria, 50 differentially expressed genes were obtained from PROK1, 45 were up-regulated and 5 were down-regulated, and 348 were obtained from PROK2, 345 were up-regulated and 3 were down-regulated. A Venn map was constructed by crossing the PROK1 and PROK2, and a total of 21 DEGs were obtained (Figure 8(a)), which were imported into the STRING protein-protein interaction database. The results were screened for hub genes using the cytoHubba plug-in in Cytospace; *HOXC10*, *HOXD13*, and *SOX4* were selected according to "Degree"; *GATA4* and *HOXA9* are the hub genes of PROK1 and PROK2, in which *SOX4* is the down-regulated gene and the rest is the up-regulated gene (Figure 8(b)).

To verify whether there were significant differences among the five hub genes screened by Cytospace, we performed a Pearson coefficient analysis of them, as shown in Table 2. We found that, except for the nonsignificant correlation between GATA4 and PROK1, the remaining hub genes were significantly different for PROK1 (Figure 9(a)) and PROK2 (Figure 9(b)) and were visualized with heat map.

3.6. Enrichment Analysis of Prokineticins. Based on the GSEA signal pathway to identify correlations between different expression datasets of PROK1 and PROK2 in LGG, five high and low expression enrichment pathways of PROK1 (Figures 10(a) and 10(b)) and PROK2 (Figures 10(c) and (d)) have been listed, respectively, by NRS. Activation of FCGR, creation of C4 and C2 activators, and regulation of CD22-mediated BCR were observed in PROK1 and PROK2. Further, cytoplasmic ribosomal proteins and ribosome were detected in PROK1 and PROK2.

4. Discussion

Little is known about the role of prokineticins in human cancer, and current research is only related to the pathogenesis of a few cancers [26, 27]. Studies revealed that prokineticins have similar affinity to two homologous 7-transmembrane g protein-coupled receptors (PROKR1 and PROKR2).
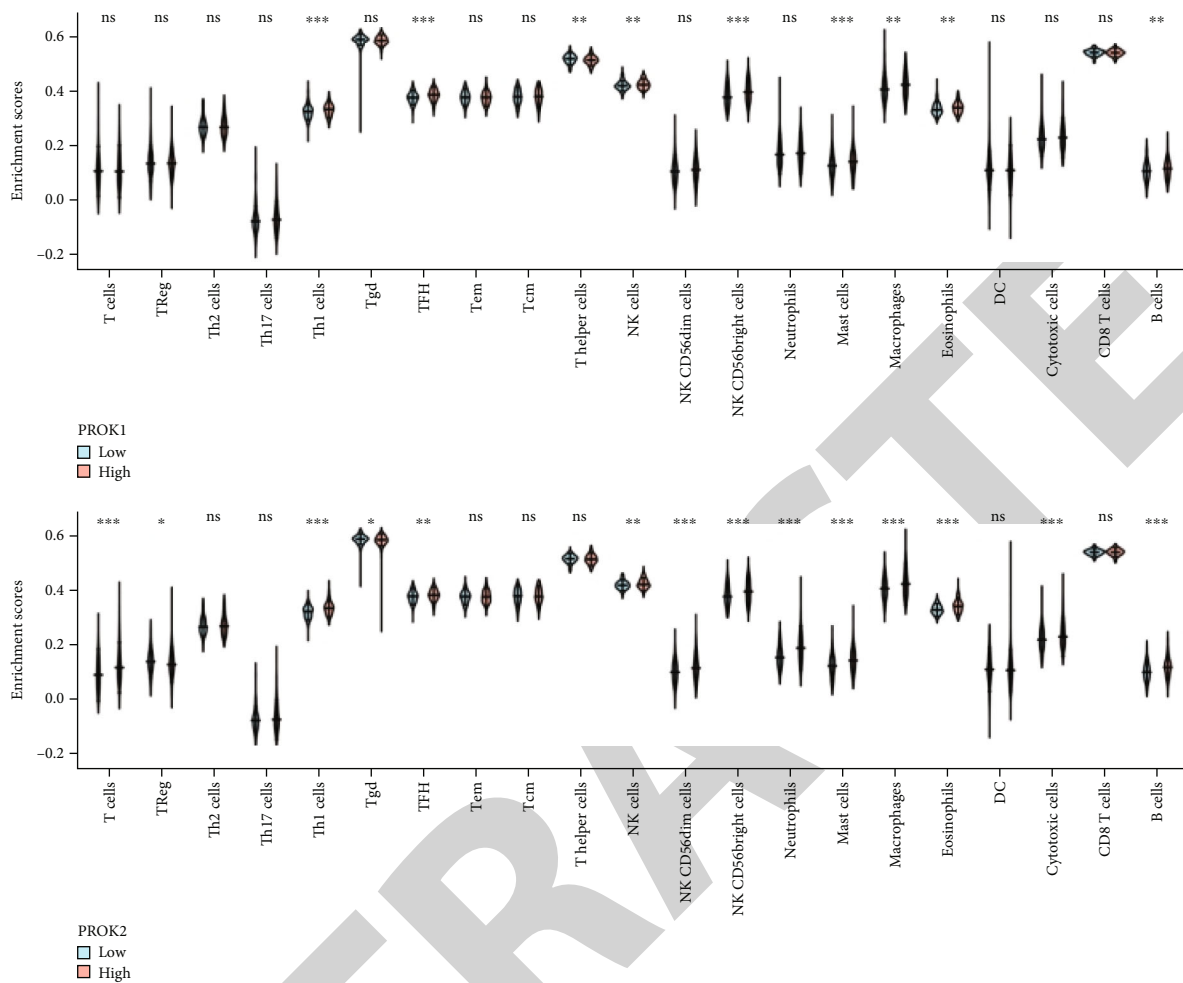
Figure 6: The proportion of 21 immune cells affected by the expression of PROK1 and PROK2. PROK1 and PROK2 had 21 TIICs (Th1 cells, NK CD 56bright cells, and Mast cells had significant difference in PROK1 and PROK2).

Prokineticins are highly conserved among species and are characterized by N-terminal AVIT consensus sequence and 5-disulfide bonds [28]. Prokineticins and their receptors are distributed in various human tissues, such as the ovaries, testes, adrenal glands, brain, heart, and bone marrow. They show a wide range of tissue-specific biological activities [9]. They coordinate complex behaviors, such as eating, drinking, circadian rhythm, and hyperalgesia, and also participate in neuron migration and survival, angiogenesis, hematopoiesis, and inflammation [29]. This diversity stems from the difference in their distribution in tissues. Their receptors can activate a variety of signaling events. In different tissues, the expression of PROK1 is significantly different from that of human multiple myeloma cells. In hepatocellular carcinoma, the expression of PROK2 is inversely proportional to the degree of malignancy; although the two have similar homology, their differences exist in a wide range of tissue-specific biological activities. In view of their role in tumor pathophysiology, as survival factors of some tissue-specific cells, their ability to induce angiogenesis and coordinate proinflammatory immune response may be one of the major causes of cancer.

We found that changes in the expression of PROK1 and PROK2 were closely related to the prognosis of LGG; their expression is inversely proportional to the prognosis. Downregulation of their expression is an independent prognostic factor indicating a positive prognosis. Xiao et al. [30] showed that PROK1 was overexpressed in human glioma, but not in normal human brain tissue, and the expression was proportional to WHO grade, which was consistent with our study. Therefore, the prognosis of high expression of PROK1 with a value of LGG was poor. In addition, our research showed that different immune marker sets and immune infiltration levels were related to the expression of PROK1 and PROK2 in LGG. Therefore, PROK1 and PROK2 may influence tumor immunology and be potential tumor biomarkers. In this study, we observed that there were significant differences in the expression of PROK1 and PROK2 in normal and LGG tissues. To further study the potential mechanism underlying the expression of prokineticins in cancer, we downloaded the dataset from TCGA. TCGA analysis using R(3.6.3) showed that the expression of PROK1 and PROK2 was related to tumor grade. Multivariate analysis showed that the expression of PROK1 and PROK2 was an

(a)

(b)
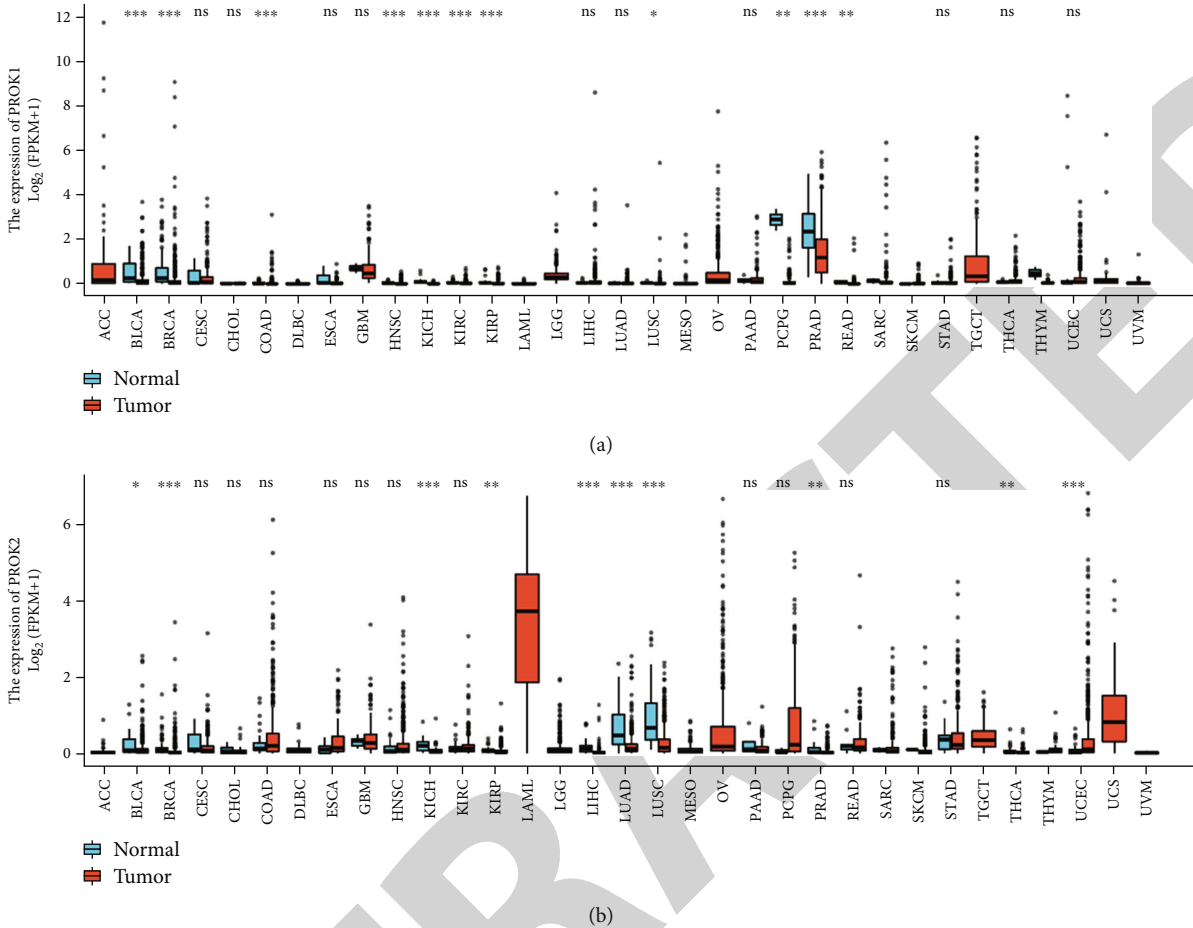
FIGURE 7: Expression difference of Pan cancer between PROK1 and PROK2. (a) The expression of PROK1 was significantly different in BLCA, BRCA, COAD, HNSC, KICH, KIRP, and PRAD ($P < 0.001$). (b) The expression of PROK2 was significantly different in BRCA, LIHC, LUAD, LUSC, and UCEC ($P < 0.001$).

(a)

(b)
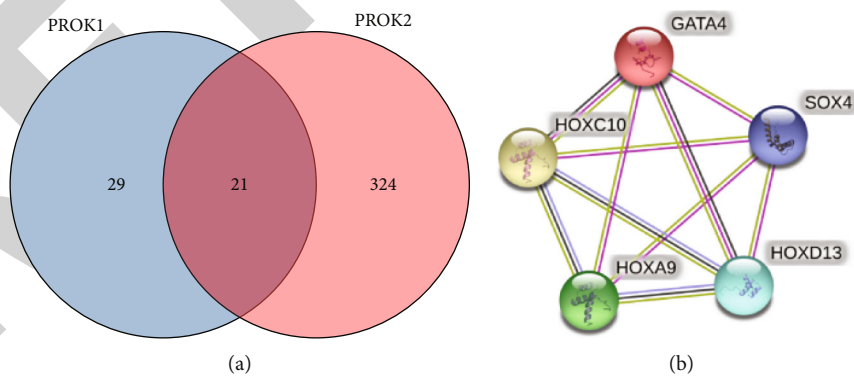
FIGURE 8: Venn of prokineticins and hub genes. (a) The Venn intersection of PROK1 and PROK2 yields 21 DEGs. (b) Protein-protein interaction network of hub genes (enrichment $P = 6.82$e-09).

independent factor influencing the prognosis of a patient with LGG. Clinical data showed that PROK1 was closely related to age; PROK2 was significantly different from IDH status, and its expression was higher in WT. In addition to comparing the expression of LGG, we also performed extended analysis of the expression of Pan in order to find

out whether PROK1 and PROK2 are similar to LGG in other cancers, and we found that there were significant differences in the expression of Pan cancer and adjacent tissues, which confirmed that there were co-expression in different tissues, but there were significant differences in expression pattern [31]. The high and low expression of PROK2 was

TABLE 2: PROK1 and PROK2 are associated with hub genes, Pearson's coefficient, and P values.

Hub genes	PROK1		PROK2	
	Pearson	P	Pearson	P
HOXC10	0.130	0.003	0.277	<0.001
HOXD13	0.104	0.017	0.184	<0.001
SOX4	-0.093	0.033	-0.264	<0.001
GATA4	0.061	0.158	0.235	<0.001
HOXA9	0.128	0.003	0.203	<0.001

(a)

(b)
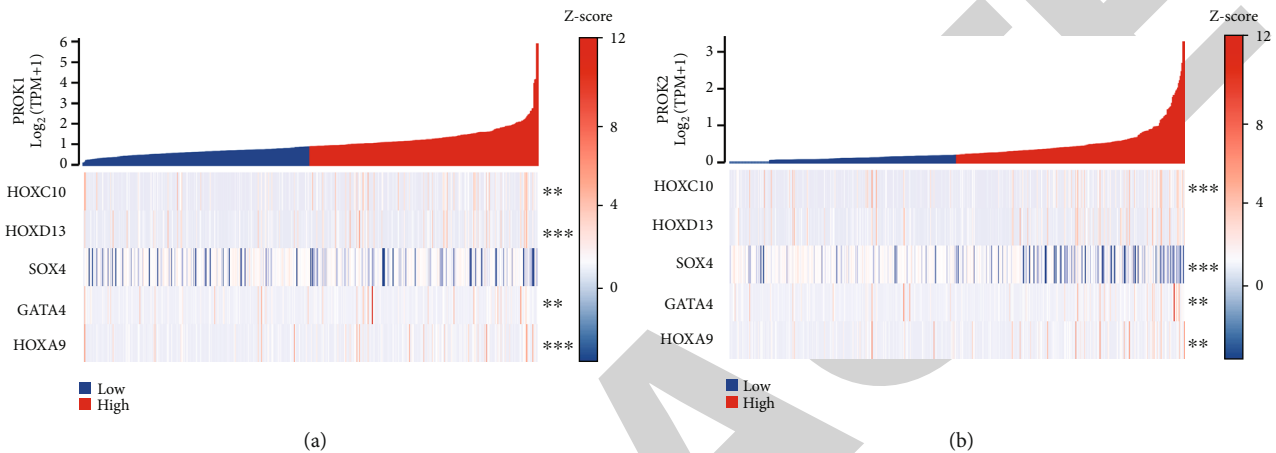
FIGURE 9: Heat map of correlation analysis between PROK1 and PROK2 and hub genes. Except for the nonsignificant correlation between GATA4 and PROK1, the remaining hub genes were significantly different for PROK1 (a) and PROK2 (b).

significantly different in the analysis of immunologic infiltration (Th1, NK CD56dim, NK CD56bright, Neutrophil, Mast, Macrophages, Eosinophils, Cytotoxic, and B-cells); previous studies have also shown that PROK2 limited the expression of natural immune cells, such as neutrophil, monocytes, and macrophages. Zhong et al. [32] studied that PROK2 promotes the mobilization of hematopoietic cells and neutrophil chemotaxis and triggers the release of proinflammatory cytokine from bone marrow cells, whereas PROK1 is less expressed in immune cells, but it can regulate the differentiation and activation of monocytes [27]. Our analysis showed that the expression of PROK1 and PROK2 is significantly related to TH1 cells, NK CD56 bright cells, and master cells in LGG, suggesting PROK1 and PROK2 are of great significance in regulating the immune microenvironment in LGG tumors. We found that the high expression of PROK1 and low expression of PROK2 were significantly different for Th1 cells. Therefore, there may be a correlation between the changes in expression of the two ligands in LGG. According to Montfort et al., the expression of immune characteristics among different immune cell types is closely related, indicating diverse, predictable, and consistent immune infiltration in tumor conditions. Therefore, the influence of PROK1 and PROK2 on LGG may be related to T cells, NK cells, and B cells. Central nervous system tumors show a strong dependence on glycolysis [33], so a ketosomal diet has become an important tool in the treatment of brain gliomas; the mechanism may be through enhancing antitumor immunity and changing gene expression to improve the

sensitivity of weight-bearing chemotherapy and then affect the growth of tumor.

To understand the differential gene expression of PROK1 and PROK2 in LGG, we imported the screened differential genes into Cytospace, based on the results of online PPI analysis using data from STRING, obtained the five most significant hub genes through "Degree," and verified the five hub genes by the Pearson correlation analysis. Except for GATA4, there was no significant difference in PROK1. Among them, HOXC10, HOXD13, and HOXA9 are homeobox family of genes, which play an important role in the morphogenesis of multicellular organisms [34]. HOXC10 is closely related to EGFR (Epidermal Growth Factor Receptor). EGFR is closely related to tumor cell proliferation, invasion, and angiogenesis, EGFR may also be involved in tumor angiogenesis, and in the highly vascularized LGG, the EGFR promoter may be involved in inducing angiogenesis and thus accelerating tumor cell proliferation and invasion. Curtis et al. [35] used an antagonist called PROK2 to reduce the branching of endothelial cells. Interestingly, in previous studies, a protein called endocrine gland-derived vascular endothelial growth factor (EGVE GF) was highly homologous to PROK1 [31]. EGVEFG and EGFR are of the same vascular endothelial growth factor, both of which promote angiogenesis, which may be one of the reasons that PROK1 expression is proportional to the malignant degree of LGG. SOX4, a member of the SOX family and no introns, combines with other proteins to form a complex and can be a transcription regulatory factor, which mediates the apoptosis of cells and tumors. The study found

(a)

(b)

(c)

(d)
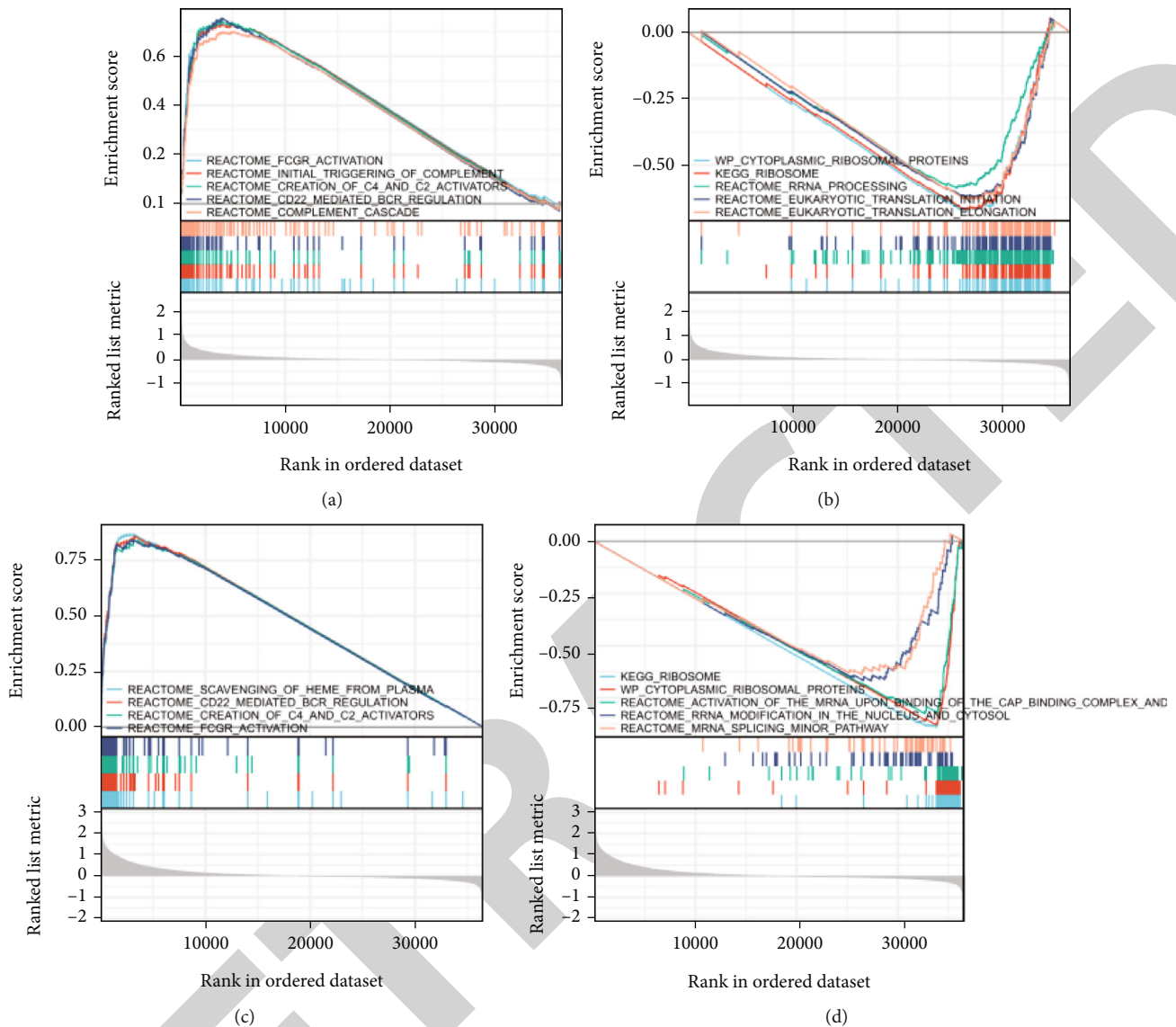
Figure 10: Enrichment plots from gene set enrichment analysis (GSEA). (a) GSEA results showing differential enrichment of genes with high PROK1 expression. (FCMR activation, initial triggering of complement, creation of C4 and C2 activators, CD22-mediated BCR regulation, and complement cascade). (b) GSEA results showing differential enrichment of genes with low PROK1 expression (cytoplasmic ribosomal proteins, ribosome, rRNA processing, eukaryotic translation initiation, and eukaryotic translation elongation). (c) GSEA results showing differential enrichment of genes with high PROK2 expression (scavenging of heme from plasma, CD22-mediated BCR regulation, creation of C4 and C2 activators, FCGR activation, and role of LAT2 NTAL lab on calcium mobilization). (d) GSEA results showing differential enrichment of genes with low PROK2 expression (ribosome, cytoplasmic ribosomal proteins, activation of the mRNA upon binding of the cap binding complex and eifs and subsequent binding to 43 s, rRNA modification in the nucleus and cytosol, and mRNA splicing minor pathway).

that SOX4 is closely related to the invasion and specialization of various tumors [36, 37], and Lin et al. [38] have previously found that SOX4 is more expressed in gliomas, which may be related to its role in the central nervous system development. PROK1 and PROK2 not only affect LGG through immune cells but also indirectly affect the expression of genes of LGG and the occurrence and development of this tumor through multiple genes [39].

To further study the functions of prokineticins in LGG, we used TCGA data to conduct GSEA, which showed CD22-mediated BCR regulation. Creation of C4

and C2 activators and activation of FCGR are differentially enriched in PROK1 and PROK2 high expression phenotypes and in ribozyme and cytogenetic fundamental proteins in PROK1 and PROK2 low expression phenotypes. The concentration changes of PROK1 and PROK2 can activate FCGR, which acts on complement and B cells and cell ribosomes. The participation and signal activity of FCGR can further stimulate different types of immune cells, such as DC, macrophages, or neutrophils, and further change the adaptive immune response through antigen presentation, cytokine production, and chemotaxis.

Therefore, prokineticins can be potential indicators of LGG prognosis and act as therapeutic targets.

5. Conclusion

Prokineticins may be potential molecular markers that will aid in predicting the prognosis of patients with LGG. In addition, the possible key pathway underlying prognosis is regulated by PROK1 and PROK2 through ribosomes and by activating FCGR. We suggest further research on this topic, especially on hub genes, to improve the evidence on the biological effects of prokineticins.

Data Availability

The datasets used and/or analyzed during the current study are available from the corresponding author on reasonable request.

Conflicts of Interest

The authors declare no potential conflicts of interest.

References

[1] M. J. McGirt, K. L. Chaichana, F. J. Attenello et al., "Extent of surgical resection is independently associated with survival in patients with hemispheric infiltrating low-grade gliomas," Neurosurgery, vol. 63, no. 4, pp. 700–708, 2008, author reply 7-8.

[2] E. S. Murphy, C. M. Leyrer, M. Parsons et al., "Risk factors for malignant transformation of low-grade glioma," International Journal of Radiation Oncology • Biology • Physics, vol. 100, no. 4, pp. 965–971, 2018.

[3] H. Xia, Y. Qi, S. S. Ng et al., "microRNA-146b inhibits glioma cell migration and invasion by targeting MMPs," Brain Research, vol. 1269, pp. 158–165, 2009.

[4] J. G. Cairncross and N. J. Laperriere, "Low-grade glioma," Archives of Neurology, vol. 46, no. 11, pp. 1238-1239, 1989.

[5] J. Chen, Z. Wang, W. Wang et al., "SYT16 is a prognostic biomarker and correlated with immune infiltrates in glioma: a study based on TCGA data," International Immunopharmacology, vol. 84, article 106490, 2020.

[6] C. Mollay, C. Wechselberger, G. Mignogna et al., "Bv8, a small protein from frog skin and its homologue from snake venom induce hyperalgesia in rats," European Journal of Pharmacology, vol. 374, no. 2, pp. 189–196, 1999.

[7] M. Li, C. M. Bullock, D. J. Knauer, F. J. Ehlert, and Q. Y. Zhou, "Identification of two prokineticin cDNAs: recombinant proteins potently contract gastrointestinal smooth muscle," Molecular Pharmacology, vol. 59, no. 4, pp. 692–698, 2001.

[8] D. J. Strydom, "Snake venom toxins," European Journal of Biochemistry, vol. 69, no. 1, pp. 169–176, 1976.

[9] E. S. Ngan and P. K. Tam, "Prokineticin-signaling pathway," The International Journal of Biochemistry & Cell Biology, vol. 40, no. 9, pp. 1679–1684, 2008.

[10] Z. Bao, Y. Liu, B. Chen et al., "Prokineticin-2 prevents neuronal cell deaths in a model of traumatic brain injury," Nature Communications, vol. 12, no. 1, p. 4220, 2021.

[11] D. Melchiorri, V. Bruno, G. Besong et al., "The mammalian homologue of the novel peptide Bv8 is expressed in the central nervous system and supports neuronal survival by activating the MAP kinase/PI-3-kinase pathways," The European Journal of Neuroscience, vol. 13, no. 9, pp. 1694–1702, 2001.

[12] D. Maftei, V. Marconi, F. Florenzano et al., "Controlling the activation of the Bv8/prokineticin system reduces neuroinflammation and abolishes thermal and tactile hyperalgesia in neuropathic animals," British Journal of Pharmacology, vol. 171, no. 21, pp. 4850–4865, 2014.

[13] A. Blum, P. Wang, and J. C. Zenklusen, "SnapShot: TCGA-analyzed tumors," Cell, vol. 173, no. 2, p. 530, 2018.

[14] Z. Tang, C. Li, B. Kang, G. Gao, C. Li, and Z. Zhang, "GEPIA: a web server for cancer and normal gene expression profiling and interactive analyses," Nucleic Acids Research, vol. 45, no. W1, pp. W98–W102, 2017.

[15] M. Ceccarelli, F. P. Barthel, T. M. Malta et al., "Molecular profiling reveals biologically discrete subsets and pathways of progression in diffuse glioma," Cell, vol. 164, no. 3, pp. 550–563, 2016.

[16] A. J. Gentles, A. M. Newman, C. L. Liu et al., "The prognostic landscape of genes and infiltrating immune cells across human cancers," Nature Medicine, vol. 21, no. 8, pp. 938–945, 2015.

[17] S. Hanzelmann, R. Castelo, and J. Guinney, "GSVA: gene set variation analysis for microarray and RNA-seq data," BMC Bioinformatics, vol. 14, no. 1, p. 7, 2013.

[18] B. Snel, G. Lehmann, P. Bork, and M. A. Huynen, "STRING: a web-server to retrieve and display the repeatedly occurring neighbourhood of a gene," Nucleic Acids Research, vol. 28, no. 18, pp. 3442–3444, 2000.

[19] P. Shannon, A. Markiel, O. Ozier et al., "Cytoscape: a software environment for integrated models of biomolecular interaction networks," Genome Research, vol. 13, no. 11, pp. 2498–2504, 2003.

[20] C. H. Chin, S. H. Chen, H. H. Wu, C. W. Ho, M. T. Ko, and C. Y. Lin, "cytoHubba: identifying hub objects and subnetworks from complex interactome," BMC Systems Biology, vol. 8, Suppl 4, p. S11, 2014.

[21] A. Subramanian, P. Tamayo, V. K. Mootha et al., "Gene set enrichment analysis: a knowledge-based approach for interpreting genome-wide expression profiles," Proceedings of the National Academy of Sciences of the United States of America, vol. 102, no. 43, pp. 15545–15550, 2005.

[22] M. Ackermann and K. Strimmer, "A general modular framework for gene set enrichment analysis," BMC Bioinformatics, vol. 10, no. 1, p. 47, 2009.

[23] M. R. Flynn, "Analysis of censored exposure data by constrained maximization of the Shapiro-Wilk W statistic," The Annals of Occupational Hygiene, vol. 54, no. 3, pp. 263–271, 2010.

[24] Z. Fang, R. Du, and X. Cui, "Uniform approximation is more appropriate for Wilcoxon Rank-Sum Test in gene set analysis," PLoS One, vol. 7, no. 2, article e31505, 2012.

[25] F. Azimi, R. A. Scolyer, P. Rumcheva et al., "Tumor-infiltrating lymphocyte grade is an independent predictor of sentinel lymph node status and survival in patients with cutaneous melanoma," Journal of Clinical Oncology, vol. 30, no. 21, pp. 2678–2683, 2012.

[26] M. H. Wu, P. R. Wu, Y. H. Hsieh, C. L. Lin, C. J. Liu, and T. H. Ying, "Silencing PROK2 inhibits invasion of human cervical cancer cells by targeting MMP15 expression," International Journal of Molecular Sciences, vol. 21, no. 17, p. 6391, 2020.

Hindawi

Retraction

Retracted: LINC00518 Promotes Cell Malignant Behaviors via Influencing EIF4A3-Mediated mRNA Stability of MITF in Melanoma

BioMed Research International

This article has been retracted by Hindawi following an investigation undertaken by the publisher [1]. This investigation has uncovered evidence of one or more of the following indicators of systematic manipulation of the publication process:

(1) Discrepancies in scope

(2) Discrepancies in the description of the research reported

(3) Discrepancies between the availability of data and the research described

(4) Inappropriate citations

(5) Incoherent, meaningless and/or irrelevant content included in the article

(6) Manipulated or compromised peer review

The presence of these indicators undermines our confidence in the integrity of the article's content and we cannot, therefore, vouch for its reliability. Please note that this notice is intended solely to alert readers that the content of this article is unreliable. We have not investigated whether authors were aware of or involved in the systematic manipulation of the publication process.

Wiley and Hindawi regrets that the usual quality checks did not identify these issues before publication and have since put additional measures in place to safeguard research integrity.

We wish to credit our own Research Integrity and Research Publishing teams and anonymous and named external researchers and research integrity experts for contributing to this investigation.

The corresponding author, as the representative of all authors, has been given the opportunity to register their agreement or disagreement to this retraction. We have kept a record of any response received.

References

[1] P. Zhang, X. Liu, G. Pan et al., "LINC00518 Promotes Cell Malignant Behaviors via Influencing EIF4A3-Mediated mRNA Stability of MITF in Melanoma," *BioMed Research International*, vol. 2022, Article ID 3546795, 10 pages, 2022.

Research Article

LINC00518 Promotes Cell Malignant Behaviors via Influencing EIF4A3-Mediated mRNA Stability of MITF in Melanoma

Ping Zhang,[1] Xuefeng Liu,[1] Guangtao Pan [iD],[2] Jing Xu,[1] Bin Shen,[3] Xin Ding,[4] and Wenliang Lv [iD][1]

[1]*Clinical College of TCM, Hubei University of Chinese Medicine, Wuhan, 410063 Hubei Province, China*
[2]*Dermatology, Yancheng TCM Hospital Affiliated to Nanjing University of Chinese Medicine, Yancheng, 224000 Jiangsu Province, China*
[3]*Department of Rehabilitation of Traditional Chinese Medicine, Jiangsu Vocational College of Medicine, Yancheng, 224000 Jiangsu Province, China*
[4]*School of Pharmacy, Hubei University of Chinese Medicine, Wuhan, 410063 Hubei Province, China*

Correspondence should be addressed to Guangtao Pan; panguangtaowuhan@foxmail.com and Wenliang Lv; 1306@hbtcm.edu.cn

Melanoma has become the most severe sort of skin cancer, deriving from the pigment-producing melanocytes. Existing research has validated that long noncoding RNAs (lncRNAs) have critical function in the progression of cancers. LINC00518 has been studied in cutaneous melanoma; however, the molecular mechanism of LINC00518 in melanoma needs in-depth investigation. In our study, LINC00518 was revealed to be upregulated in melanoma tissues and cells, and melanoma patients in high LINC00518 expression group had poorer prognosis as depicted in GEPIA database. Functional assays revealed that LINC00518 depletion inhibited cell proliferation, migration, invasion, and epithelial-mesenchymal transition (EMT). Furthermore, MITF was confirmed to be upregulated in melanoma tissues and cells, and melanoma patients in high MITF expression group had poorer prognosis as displayed in GEPIA database. MITF expression was positively connected to LINC00518 expression. Additionally, results of mechanism assays uncovered EIF4A3 could bind with LINC00518 and MITF, and LINC00518 recruited EIF4A3 to stabilize MITF mRNA. Finally, it was demonstrated that upregulation of MITF could partially abrogate the inhibitory impact of LINC00518 knockdown on melanoma cell malignant behaviors. To summarize, LINC00518 promotes the malignant processes of melanoma cells through targeting EIF4A3/MITF axis, which might provide novel potential biomarkers for melanoma prognosis.

1. Introduction

Melanoma has become the most severe sort of skin cancer, deriving from the pigment-producing melanocytes [1, 2]. Distinct genetic alterations as well as sun exposure have been deemed as major risk factors [3]. Occurrence rate of melanoma is increasing, and melanoma in advanced stage is highly resistant to therapies [4, 5]. Given that melanoma is resistant to normal anticancer therapies [6], it is important to find out more novel potential biomarkers and develop targeted therapies for melanoma.

Long noncoding RNAs (lncRNAs) are a subtype of noncoding RNAs with limited protein-coding capability [7, 8].

Extensive research has evidenced that lncRNAs have indispensable function in the development and progression of varied cancers. According to published research work, lncRNA HEIH serves as a malignancy promoter in colorectal cancer via countervailing miR-939-mediated transcriptional suppression of Bcl-xL [9]. lncRNA H19 impedes the progression of thyroid cancer via downregulation of IRS-1 [10]. Data from previous work also suggest that lncRNAs actively engage in the melanoma development. For instance, the lncRNA CCAT1 prompts cell proliferation and invasion through inhibition of miR-33a in melanoma [11]. lncRNA HEIH acts as an oncogenic molecule in melanoma via suppressing miR-200b/a/429 [12]. lncRNA MEG3 restrains the

progression of melanoma via sequestering miR-499-5p to regulate CYLD expression [13]. Despite that LINC00518 has been testified to promote various cancers [14–16] and its expression has been measured in cutaneous melanoma [17, 18], the molecular mechanism of LINC00518 in melanoma has not been investigated in depth.

Microphthalmia-associated transcription factor (MITF) has been confirmed to exert crucial effects on melanoma cell growth, differentiation, and invasion [19]. Eukaryotic translation initiation factor 4A3 (EIF4A3) has been pointed out to participate in cell cycle regulation and apoptosis via modulating messenger RNA (mRNA) decay, and it might function as an essential regulatory factor implicated in the occurrence and progression of various diseases [20]. Moreover, previous studies have shown that EIF4A3 could be recruited by lncRNAs to affect the translation of target genes in tumors [21]. Hence, the interaction among LINC00518, EIF4A3, and MITF, as well as their roles in melanoma, attracted our interest.

This research was conducted to evaluate the role of LINC00518 in melanoma. Our study provided new insights into the underlying regulatory mechanism of LINC00518 in melanoma and tried to figure out whether LINC00518 exerted an oncogenic effect on melanoma via affecting EIF4A3-mediated mRNA stability of MITF, which might provide novel promising biomarkers for melanoma.

2. Materials and Methods

2.1. Cell Line and Cell Culture.
Human melanoma cell lines (B16, A2058, and A375) and human epidermal melanocytes (HEMn) were provided by the American Type Culture Collection (ATCC; VA, USA). The aforementioned cells were incubated in Dulbecco's modified Eagle's medium (DMEM; HyClone, Logan, USA) blended with 10% fetal bovine serum (FBS; Gibco, Australia) and 1% penicillin-streptomycin solution. The culture plates were maintained at 37°C with 5% CO_2.

2.2. Plasmids and Cell Transient Transfection.
The plasmids, including short hairpin-negative control (sh-NC), sh-LINC00518#1/2, sh-EIF4A3, pcDNA3.1, and pcDNA3.1/MITF, were produced by Genechem (Shanghai, China). A2058 and A375 cells were seeded into six-well plates and cultured with plasmids prepared in advance. The transfection procedure was completed by Lipofectamine 2000 (Invitrogen, CA, USA) based on the manufacturer's guidelines.

2.3. Quantitative Reverse Transcription Polymerase Chain Reaction (RT-qPCR).
The experiments were performed as previously described [22] Total RNA was isolated from melanoma cells utilizing TRIzol (Invitrogen) following the user's manual. The complementary DNA (cDNA) was obtained by applying the reverse transcription kit (TaKaRa, Shanghai, China) as per the supplier's guideline. Subsequently, PCR amplification was completed via the SYBR-Green PCR system (TaKaRa). GAPDH functioned as internal control. Expression fold-change of LINC00518, MITF, and EIF4A3 was calculated following the $2^{-\Delta\Delta Ct}$ method.

2.4. Cell Counting Kit-8 (CCK-8) Assay.
The viability of melanoma cells was measured through the application of CCK-8 following previous description [22]. A2058 or A375 cells were added into 96-well plates and then incubated for different time. Next, CCK-8 reagent (KeyGEN, Jiangsu, China) was added to the culture plate and cultured for another 2 h under the guidance of the manufacturer. The optical density at 450 nm was examined under the spectrophotometer (GloMax Multi Detection System, Promega, USA).

2.5. Colony Formation Assay.
The experiment was carried out as previously described [11]. To begin with, 1×10^3 cells were seeded into 6-well plates containing DMEM. Subsequently, cells were incubated for 14 days. Afterward, these colonies were subjected to 15 min methanol fixation and 10 min crystal violet staining. The quantity of colonies was eventually measured manually.

2.6. Transwell Assay.
Transwell chambers (Corning, 8 μm, NY, USA) were applied to evaluate melanoma cell migration following previous protocol [23]. The lower compartment was added with DMEM blended with 20% FBS. After cell transfection, A2058 and A375 cells were placed onto the upper chambers containing serum-free medium for incubation, allowing cells to migrate for 24 h. Then, migrated cells were treated with 4% paraformaldehyde for 15 min fixation and crystal violet staining. Finally, cells successfully migrated to the lower part were photographed and counted with the help of a microscope (Olympus, Tokyo, Japan).

2.7. Western Blot.
The experiment was conducted as previously described [22]. The cells were lysed in Radioimmunoprecipitation Assay (RIPA) lysis buffer (Beyotime Biotechnology, Shanghai, China). After the total protein was collected, bicinchoninic acid (BCA) protein reagent kit (ThermoFisher) was employed for the measurement of protein concentration. The samples electrophoresed through the employment of 10% sodium dodecyl sulfate–polycrylamide gel electrophoresis (SDS-PAGE) were shifted to polyvinylindene difluoride (PVDF) membranes. Subsequently, the membranes were sealed with 5% defatted milk for 1 h and cultured with specific primary antibodies to MITF, MMP2, MMP7, MMP9, E-cadherin, N-cadherin, and GAPDH. Antibodies were obtained from Abcam (Cambridge, UK) overnight at 4°C. Subsequently, the secondary antibodies were incubated with these membranes for 2 h. The western blots were captured and scanned via BioImaging Systems (BIO-RAD, CA, USA).

2.8. RNA Pull Down Assay.
The experiment was conducted as previously described [24]. RNA pull down assay was employed to evaluate the possible binding affinity between LINC00518 and EIF4A3. LINC00518-wide-type (Wt) and LINC00518-mutant (Mut) were transcribed by using Transcript Aid T7 High Yield Transcription Kit (ThermoFisher). Bio-LINC00518-Wt and Bio-LINC00518-Mut were produced utilizing Biotin RNA labeling mix (Roche Diagnostics, Indianapolis, IN, USA). Biotin-labeled RNAs were incubated with A2058 or A375 cell lysates overnight at 4°C. Next, streptavidin-Dyna beads (11205D, Invitrogen) were added

for precipitation. After the beads were rinsed for 4 times and boiled, enriched proteins were examined by western blot.

2.9. RNA Binding Protein Immunoprecipitation (RIP) Assay.
The experiment was conducted as previously described [24]. RIP was applied to testify the binding ability between LINC00518 and EIF4A3, as well as EIF4A3 and MITF. An EZ-Magna RIP kit (Millipore) was employed to investigate the abovementioned relationship. A2058 and A375 cells were dissolved, and then, the extracts were cultured with RIP buffer which contains magnetic beads conjugating with antibodies that recognized EIF4A3 protein. IgG was used to be internal control. To continue, the beads were rinsed and incubated with Proteinase K. Ultimately, RT-qPCR was conducted to quantify purified RNA.

2.10. Statistical Analysis.
Each of the assays involved in this study was carried out in triplicate. The data was processed with the SPSS 21.0 software (IBM, Armonk, NY, USA). The quantitative results were displayed as the mean ± standard deviation (SD). The statistical analysis was conducted employing Student's t-test (data comparison between two groups) or the one-way analysis of variance (ANOVA) (data comparison among multiple groups with one variable). The statistical significance of P value was computed. When it was below 0.05, data difference was deemed as statistically significant.

3. Results

3.1. LINC00518 Is Upregulated in Melanoma and Expedites Multiple Malignant Phenotype of Melanoma Cells.
To unravel the potential function of LINC00518 in melanoma, we first searched the GEPIA database for LINC00518 expression and found that LINC00518 displayed the high expression in melanoma tissues (Figure 1(a)). It was also revealed in the GEPIA database that melanoma patients in the high LINC00518 expression group had shorter overall survival time than patients in the low LINC00518 expression group (Figure 1(b)). Moreover, LINC00518 was observed to be significantly upregulated in melanoma cell lines (B16, A2058, and A375) than in human epidermal melanocytes (HEMn) (Figure 1(c)). As depicted in Figure 1(d), sh-LINC00518#1/2 was verified to be able to induce a notable decrease in LINC00518 expression in A2058 and A375 cells compared with the scramble control. CCK-8 assays represented that sh-LINC00518#1/2 inhibited proliferation of melanoma cells, and sh-LINC00518#1 possessed stronger inhibitive effect on cell proliferation (Figure 1(e)). Based on colony formation assay, the number of cell colonies decreased after melanoma cells were transfected with sh-LINC00518#1 (Figure 1(f)). Transwell assay confirmed that LINC00518 deficiency suppressed the migration of melanoma cells (Figure 1(g)). Western blot assay revealed that the expression of proteins (MMP2, MMP7, MMP9, E-cadherin, and N-cadherin) associated with migration, invasion, and epithelial-mesenchymal transition (EMT) was diminished by LINC00518 knockdown (Figure 1(h)). In brief,

LINC00518 is upregulated in melanoma tissues and cells, prompting cell proliferation, migration, invasion, and EMT.

3.2. MITF Is Upregulated in Melanoma, and Its Expression Positively Correlates with LINC00518 Expression.
The existing studies on MITF have suggested that MITF serves as a regulator in melanoma [25–27]. To dig into the molecular mechanism of MITF in melanoma, we firstly searched the GEPIA database for information concerning MITF, noticing that MITF presented the high expression in melanoma tissues (Figure 2(a)). The GEPIA database also manifested that melanoma patients in the high MITF expression group had more unfavorable prognosis than those in the low MITF expression group (Figure 2(b)). Furthermore, MITF expression was found to be positively correlated with that of LINC00518 via the GEPIA database (Figure 2(c)). Moreover, it was found that MITF was conspicuously upregulated in melanoma cell lines (B16, A2058, and A375) compared with human epidermal melanocytes (HEMn) (Figure 2(d)). The data from RT-qPCR illustrated that the mRNA level of MITF was lessened by LINC00518 knockdown (Figure 2(e)). Western blot assay manifested that LINC00518 silencing inhibited MITF protein expression (Figure 2(f)). In summary, MITF is expressed at a high level in melanoma tissues and cells, and its expression is positively regulated by LINC00518.

3.3. LINC00518 Enhances MITF mRNA Stability via Binding to EIF4A3.
StarBase and UCSC websites predicted that EIF4A3 had potential binding sites with LINC00518 at chr6:10430479-10430530 (Fig. S1A). Moreover, prediction on StarBase website demonstrated that the expression of EIF4A3 was positively connected to that of LINC00518 (Fig. S1B). To further explore the relationship between EIF4A3 and LINC00518, we conducted RNA pull down assay and the obtained data suggested that EIF4A3 could bind with LINC00518 (Figure 3(a)). The subsequent RIP assay also showed LINC00518 was greatly enriched in the anti-EIF4A3 group (Figure 3(b)). Moreover, data on StarBase website manifested that EIF4A3 expression was positively linked to MITF expression (Fig. S1C). In order to form a more comprehensive understanding of the interaction between EIF4A3 and MITF, RIP assays were done, and the outcome elucidated that EIF4A3 and MITF were conspicuously more enriched in the anti-EIF4A3 group than in the anti-IgG group (Figure 3(c)). As shown by Figure 3(d), EIF4A3 silencing caused the downregulation of EIF4A3. Additionally, knockdown of EIF4A3 induced a reduction in MITF expression, which was validated in RT-qPCR assay and western blot assay (Figure 3(e)). RT-qPCR analysis implied that the transfection of sh-LINC00518#1 or sh-EIF4A3 reduced the mRNA level of MITF in cells treated with actinomycin D (ActD) (Figures 3(f) and 3(g)), which meant the mRNA stability of MITF was decreased in LINC00518-depleted melanoma cells and EIF4A3-depleted melanoma cells. Last but not least, we found that EIF4A3 knockdown resulted in a decline of MITF expression, whereas LINC00518 upregulation could not abrogate the former effect (Figure 3(h)). The abovementioned
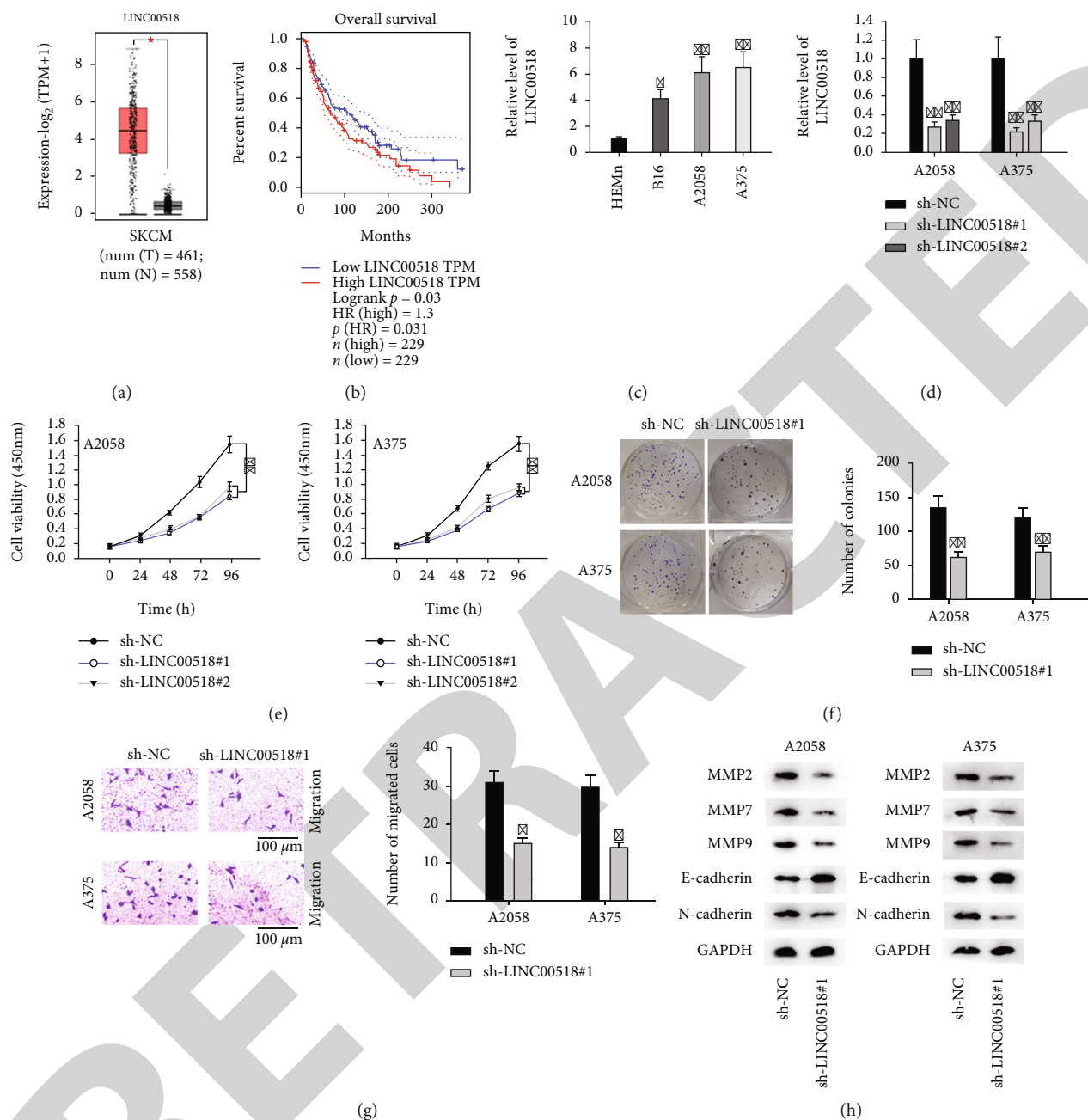
Figure 1: LINC00518 is upregulated in melanoma, and LINC00518 inhibits multiple malignant behaviors of melanoma cells. (a) The level of LINC00518 in melanoma tumor tissues and noncancerous tissues was projected on the GEPIA database. (b) The GEPIA database demonstrated the overall survival of patients in the high/low LINC00518 group. (c) The level of LINC00518 in melanoma cell lines (B16, A2058, and A375) and the human epidermal melanocytes (HEMn) was examined by RT-qPCR. (d) RT-qPCR assays measured knockdown efficiency of sh-LINC00518#1/2. (e) CCK-8 assays were done to examine proliferative ability of cells upon LINC00518 knockdown. (f) Number of formed colonies was detected by colony formation assays after LINC00518 deficiency. (g) Transwell assays evaluated the migration of melanoma cells upon LINC00518 depletion. (h) The influences of LINC00518 knockdown on the expression of key proteins related to invasion, migration, and EMT were assessed in western blot assays. $^{*}P < 0.05$; $^{**}P < 0.01$.

findings jointly proved that LINC00518 had to recruit EIF4A3 to stabilize MITF mRNA. To conclude, LINC00518 strengthens MITF mRNA stability via binding to EIF4A3.

3.4. Overexpression of MITF Partially Counteracts the Inhibiting Impact of LINC00518 Knockdown on the Malignant Behaviors of Melanoma Cells. To further explore whether LINC00518 promoted the malignant processes of melanoma cells through regulating MITF, rescue assays were conducted. The quantitative data of RT-qPCR illustrated that transfection of pcDNA3.1/MITF upregulated the expression of MITF (Figure 4(a)). The outcome of CCK-8 assay manifested that MITF augment partly reversed the LINC00518 silencing-mediated inhibition on cell proliferation (Figure 4(b)). In

(a)

(b)

(c)

(d)

(e)

(f)
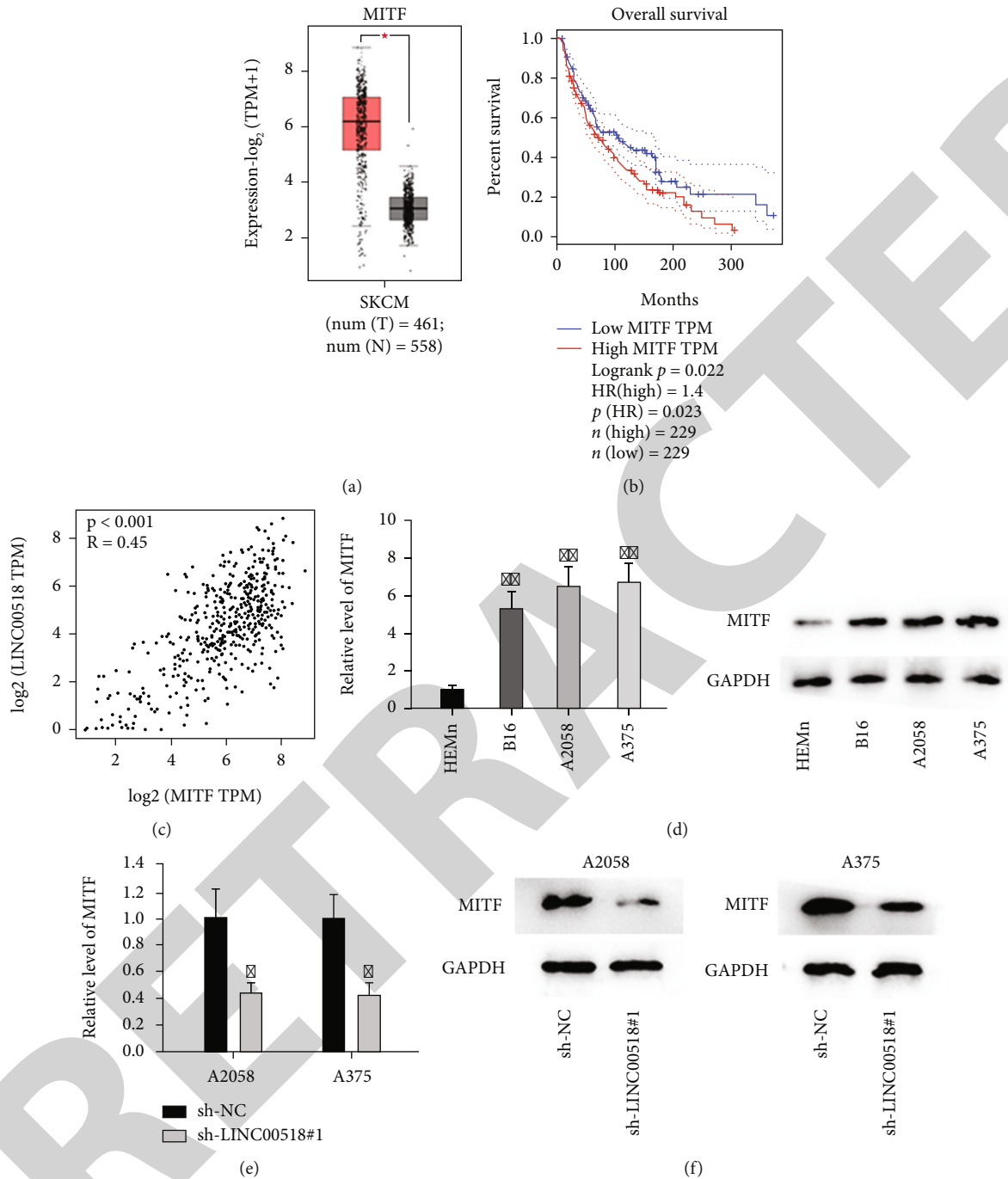
Figure 2: MITF has a significantly high expression in melanoma tissues and cells, and its expression positively correlates with LINC00518 expression. (a) MITF expression in melanoma tissues and adjacent noncancer tissues was projected on the GEPIA database. (b) The relationship between patients in the high MITF group and their overall survival was obtained from the GEPIA database. (c) The GEPIA database provided the correlation between LINC00518 expression and MITF expression. (d) The expression of MITF in melanoma cell lines (B16, A2058, and A375) and the human epidermal melanocytes (HEMn) was quantified by RT-qPCR and western blot. (e) RT-qPCR analysis measured the effect of LINC00518 knockdown on MITF mRNA expression. (f) Western blot assay examined the impact of LINC00518 knockdown on MITF protein level. $^{*}P < 0.05$; $^{**}P < 0.01$.

addition, colony formation assay suggested that the sh-LINC00518#1-mediated reduction of colony number was partially recovered by MITF overexpression (Figure 4(c)). Moreover, according to transwell assay results, the suppressive influence of LINC00518 depletion on cell migration was counteracted by MITF augment (Figure 4(d)). Eventually, western blot assay confirmed that the suppressive influence of LINC00518 silencing on the levels of proteins linked to migration, invasion, and EMT was weakened by MITF overexpression (Figure 4(e)). To conclude, overexpression of MITF
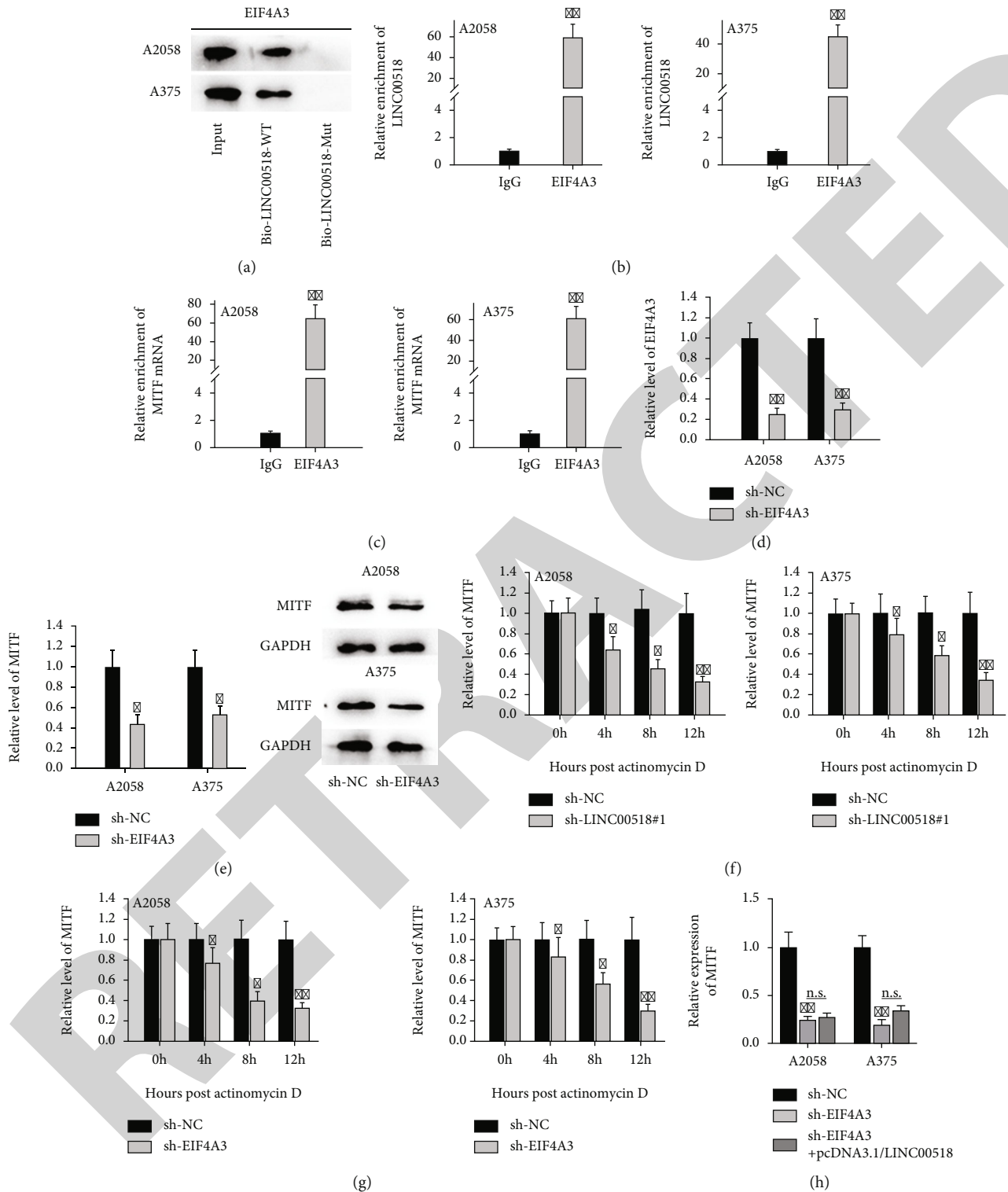
Figure 3: LINC00518 maintains MITF mRNA stability via binding to EIF4A3. (a) RNA pull down assays detected if LINC00518 could bind to EIF4A3 in melanoma cells. (b) RIP assay further assessed the binding ability between LINC00518 and EIF4A3. (c) The binding ability between MITF and EIF4A3 was testified by RIP assay. (d) RT-qPCR assays measured the efficacy of EIF4A3 knockdown. (e) The impact of EIF4A3 depletion on MITF expression levels was evaluated by RT-qPCR and western blot assays. (f) Degradation rate of MITF mRNA in sh-LINC00518#1-transfected melanoma cells was assessed via RT-qPCR. (g) Degradation rate of MITF mRNA in sh-EIF4A3-transfected melanoma cells was evaluated in RT-qPCR assay. (h) RT-qPCR assay detected the expression of MITF in melanoma cells under different conditions. $^{*}P < 0.05$; $^{**}P < 0.01$.
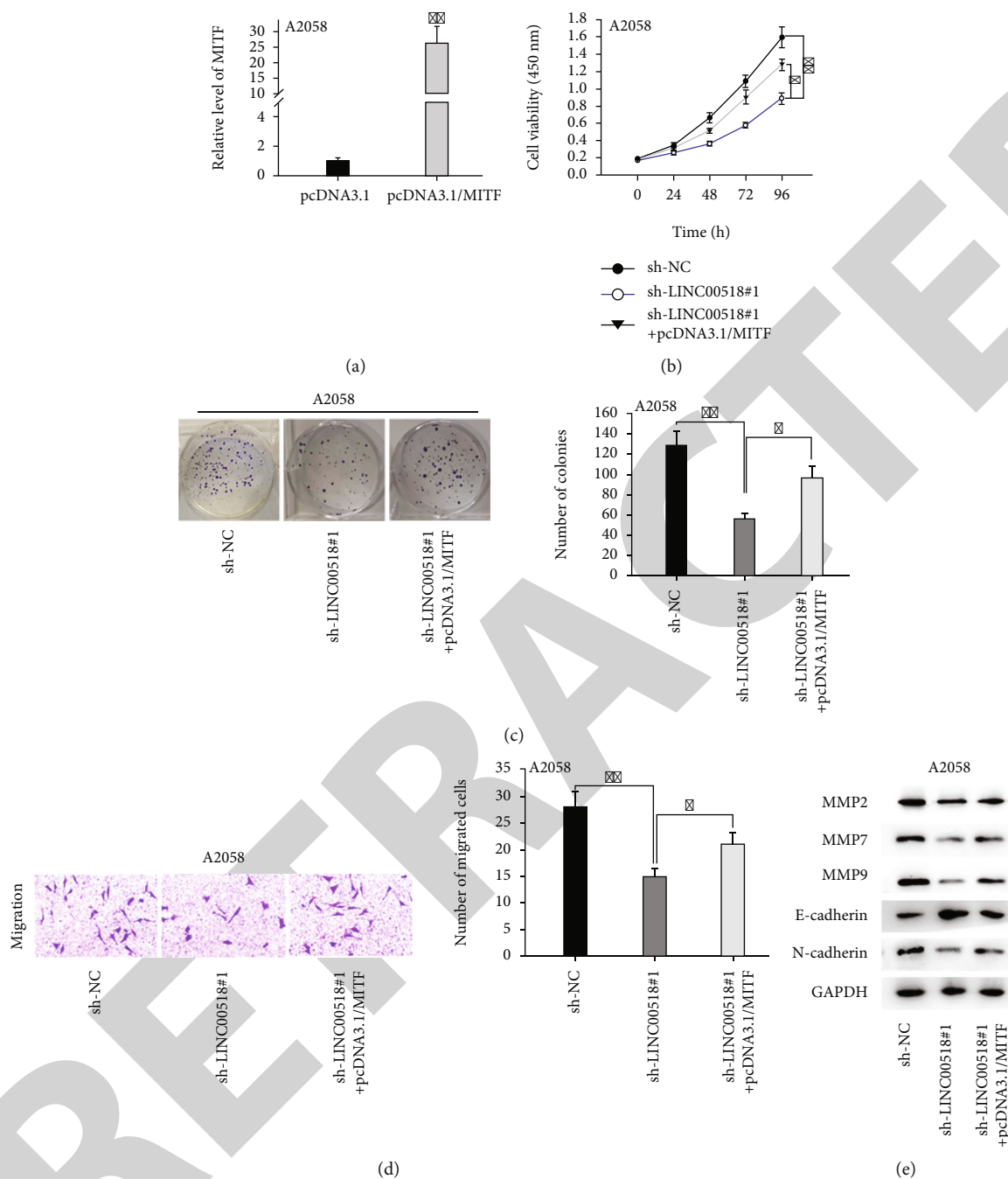
FIGURE 4: MITF overexpression partly countervails the inhibiting influence of LINC00518 knockdown on melanoma progression. (a) The efficacy of MITF overexpression in transfected melanoma cells was tested via RT-qPCR. (b) CCK-8 assay was conducted to evaluate viability of melanoma cells under different conditions. (c) Number of formed colonies was measured by colony formation assay. (d) Transwell assay assessed the changes of melanoma cell migration under the indicated conditions. (e) The protein levels of MMP2, MMP7, MMP9, E-cadherin, and N-cadherin in melanoma cells transfected with different plasmids were detected via western blot assay. $^*P < 0.05$; $^{**}P < 0.01$.

partially counteracts the inhibitory impact of LINC00518 knockdown on melanoma cell malignant behaviors.

3.5. Discussion. The published literature on lncRNAs suggests that abnormal expression of lncRNAs affects the development of various cancers, for instance, pancreatic cancer, ovarian

cancer, and bladder cancer [28–30]. LINC00518 has been discovered to work as a cancer promoter in varied cancers, and its expression has been detected in several studies [14–18]. Similar to these findings, our study also confirmed that LINC00518 was upregulated in melanoma tissues and cells, and knockdown of LINC00518 suppressed melanoma

cell proliferation, migration, and invasion, which signified that LINC00518 played an oncogenic part in melanoma.

mRNAs have also been recognized to have crucial roles in the tumorigenesis of cancers. For instance, Smad4 mRNA suppresses cell metastasis in prostate cancer [31]. CDK2AP1 mRNA acts as an anticancer gene in the progression of human breast cancer [32]. The mRNA expression of MITF has been detected to be upregulated in melanoma [33, 34]. Consistent with former literature, the current study also uncovered that MITF was upregulated in melanoma tissues and cells. Moreover, some regulatory mechanisms concerning MITF in melanoma have also been studied. For example, inhibition of MITF enhances cell sensitivity to BRAF inhibitor in melanoma [35]. SOX5 suppresses the expression of MITF to inhibit the progression of melanoma [36]. Knockdown of NAT10 inhibits melanogenesis and melanoma growth via reducing MITF expression [25]. Herein, we found LINC00518 positively regulated MITF expression to promote melanoma cell malignant processes, which was similar to the former studies.

RNA-binding proteins (RBPs) can affect the modulation of RNA-mediated genes via taking part in the posttranscriptional regulation [37, 38]. Researchers have unraveled that RBPs play a pivotal part in the development of melanoma. For instance, the RBP UNR/CSDE1 promotes cell invasion and metastasis in melanoma [39]. RBP NOVA1 functions as a malignancy promoter in melanoma via modulating FOXO3a expression [40, 41]. Previous research has identified that EIF4A3 influences the development of certain cancers via acting as a RBP [42]. It was revealed in our study that EIF4A3 could bind with LINC00518 and MITF, and the expression of EIF4A3 had a positive relationship with that of LINC00518 and MITF. Furthermore, silencing of LINC00518 or EIF4A3 weakened the stability of MITF mRNA. Taken together, LINC00518 maintained MITF mRNA stability via binding to EIF4A3. In the end, rescue assays validated that MITF augment could partly counteract the inhibiting effect of LINC00518 knockdown on melanoma cell malignant behaviors. Referring to a published report, LINC00667 stabilizes VEGFA mRNA via recruiting EIF4A3, consequently promoting cell proliferation and migration in non-small-cell lung cancer [43]. Our study also confirmed LINC00518 recruited EIF4A3 to enhance the stability of MITF mRNA, which finally facilitated melanoma cell proliferation, migration, and invasion.

In summary, LINC00518 promoted melanoma cell proliferation, migration, and invasion through regulating EIF4A3-mediated mRNA stability of MITF. Considering MITF overexpression could only partially offset the inhibiting influence of LINC00518 knockdown on melanoma cell malignant behaviors, there might exist other mechanisms or pathways for LINC00518 to regulate the biological behaviors of melanoma cells, which will be our research focus in the future. Moreover, due to the limitation of time and resources, clinical samples and in vivo assay were not involved in this study, and we will try to explore the clinical associations in our future research. Based on our current findings, LINC00518 might serve as a potential biomarker for melanoma.

Data Availability

The data used to support the findings of this study are included within the article.

Conflicts of Interest

The authors declare that no competing interest exists in this study.

Authors' Contributions

Guangtao Pan and Wenliang Lv contributed equally to this work as cocorresponding author.

Acknowledgments

Supplementary Materials

Figure S1: (A) the potential binding sequence of LINC00518 and EIF4A3 was projected on StarBase and UCSC websites. (B) StarBase website demonstrated the correlation between LINC00518 expression and EIF4A3 expression. (C) StarBase website provided the correlation between MITF expression and EIF4A3 expression. (*Supplementary Materials*)

References

[1] D. U. Ekwueme, Guy GP Jr, C. Li, S. H. Rim, P. Parelkar, and S. C. Chen, "The health burden and economic costs of cutaneous melanoma mortality by race/ethnicity-United States, 2000 to 2006," *Journal of the American Academy of Dermatology*, vol. 65, no. 5, pp. S133–S143, 2011.

[2] Z. Ali, N. Yousaf, and J. Larkin, "Melanoma epidemiology, biology and prognosis," *EJC Supplements*, vol. 11, no. 2, pp. 81–91, 2013.

[3] D. Schadendorf, D. E. Fisher, C. Garbe et al., "Melanoma," *Nature Reviews Disease Primers*, vol. 1, no. 1, p. 15003, 2015.

[4] G. P. Guy Jr., C. C. Thomas, T. Thompson, M. Watson, G. M. Massetti, and L. C. Richardson, "Vital signs: melanoma incidence and mortality trends and projections - United States, 1982-2030," *MMWR Morbidity and Mortality Weekly Report*, vol. 64, no. 21, pp. 591–596, 2015.

[5] H. Kupcova Skalnikova, J. Cizkova, J. Cervenka, and P. Vodicka, "Advances in proteomic techniques for cytokine analysis: focus on melanoma research," *International Journal of Molecular Sciences*, vol. 18, no. 12, p. 2697, 2017.

[6] M. S. Soengas and S. W. Lowe, "Apoptosis and melanoma chemoresistance," *Oncogene*, vol. 22, no. 20, pp. 3138–3151, 2003.

[7] Y. Zheng, L. Liu, and G. C. Shukla, "A comprehensive review of web-based non-coding RNA resources for cancer research," *Cancer Letters*, vol. 407, pp. 1–8, 2017.

[8] M. Huarte, "The emerging role of lncRNAs in cancer," *Nature Medicine*, vol. 21, no. 11, pp. 1253–1261, 2015.

[9] C. Cui, D. Zhai, L. Cai, Q. Duan, L. Xie, and J. Yu, "Long non-coding RNA HEIH promotes colorectal cancer tumorigenesis via counteracting miR-939–mediated transcriptional repression of Bcl-xL," *Cancer Research and Treatment*, vol. 50, no. 3, pp. 992–1008, 2018.

[10] P. Wang, G. Liu, W. Xu, H. Liu, Q. Bu, and D. Sun, "Long non-coding RNA H19 inhibits cell viability, migration, and invasion via downregulation of IRS-1 in thyroid cancer cells," *Technology in Cancer Research & Treatment*, vol. 16, no. 6, pp. 1102–1112, 2017.

[11] L. Lv, J. Q. Jia, and J. Chen, "The lncRNA CCAT1 upregulates proliferation and invasion in melanoma cells via suppressing miR-33a," *Oncology Research*, vol. 26, no. 2, pp. 201–208, 2018.

[12] H. Zhao, G. Xing, Y. Wang, Z. Luo, G. Liu, and H. Meng, "Long noncoding RNA HEIH promotes melanoma cell proliferation, migration and invasion via inhibition of miR-200b/a/429," *Bioscience Reports*, vol. 37, no. 3, 2017.

[13] J. Long and X. Pi, "lncRNA-MEG3 suppresses the proliferation and invasion of melanoma by regulating CYLD expression mediated by sponging miR-499-5p," *BioMed Research International*, vol. 2018, Article ID 2086564, 15 pages, 2018.

[14] H. B. Wang, H. Wei, J. S. Wang, L. Li, A. Y. Chen, and Z. G. Li, "Down-regulated expression of LINC00518 prevents epithelial cell growth and metastasis in breast cancer through the inhibition of CDX2 methylation and the Wnt signaling pathway," *Biochimica et Biophysica Acta - Molecular Basis of Disease*, vol. 1865, no. 3, pp. 708–723, 2019.

[15] J. He, M. Sun, H. Geng, and S. Tian, "Long non-coding RNA Linc00518 promotes paclitaxel resistance of the human prostate cancer by sequestering miR-216b-5p," *Biology of the Cell*, vol. 111, no. 2, pp. 39–50, 2019.

[16] D. W. Wang, D. You, J. Dong, and T. F. Liu, "Knockdown of long non-coding RNA LINC00518 inhibits cervical cancer proliferation and metastasis by modulating JAK/STAT3 signaling," *European Review for Medical and Pharmacological Sciences*, vol. 23, no. 2, pp. 496–506, 2019.

[17] L. K. Ferris, B. Jansen, J. Ho et al., "Utility of a noninvasive 2-gene molecular assay for cutaneous melanoma and effect on the decision to biopsy," *JAMA Dermatology*, vol. 153, no. 7, pp. 675–680, 2017.

[18] P. Gerami, Z. Yao, D. Polsky et al., "Development and validation of a noninvasive 2-gene molecular assay for cutaneous melanoma," *Journal of the American Academy of Dermatology*, vol. 76, no. 1, pp. 114–120.e2, 2017.

[19] C. Abrahamian and C. Grimm, "Endolysosomal cation channels and MITF in melanocytes and melanoma," *Biomolecules*, vol. 11, no. 7, p. 1021, 2021.

[20] Y. Zhu, C. Ren, and L. Yang, "Effect of eukaryotic translation initiation factor 4A3 in malignant tumors," *Oncology Letters*, vol. 21, no. 5, p. 358, 2021.

[21] J. Ye, X. She, Z. Liu et al., "Eukaryotic initiation factor 4A-3: a review of its physiological role and involvement in oncogenesis," *Frontiers in Oncology*, vol. 11, article 712045, 2021.

[22] C. Han, F. Tang, J. Chen et al., "Knockdown of lncRNA-UCA1 inhibits the proliferation and migration of melanoma cells through modulating the miR-28-5p/HOXB3 axis," *Experimental and Therapeutic Medicine*, vol. 17, no. 5, pp. 4294–4302, 2019.

[23] P. Wang, L. Hu, G. Fu et al., "LncRNA MALAT1 promotes the proliferation, migration, and invasion of melanoma cells by downregulating miR-23a," *Cancer Management and Research*, vol. Volume 12, pp. 6553–6562, 2020.

[24] T. Huang, Y. J. Wang, M. T. Huang et al., "LINC00470 accelerates the proliferation and metastasis of melanoma through promoting APEX1 expression," *Cell Death & Disease*, vol. 12, no. 5, p. 410, 2021.

[25] T. I. Oh, Y. M. Lee, B. O. Lim, and J. H. Lim, "Inhibition of NAT10 suppresses melanogenesis and melanoma growth by attenuating microphthalmia-associated transcription factor (MITF) expression," *International Journal of Molecular Sciences*, vol. 18, no. 9, article 1924, 2017.

[26] J. Vachtenheim and L. Ondrusova, "Microphthalmia-associated transcription factor expression levels in melanoma cells contribute to cell invasion and proliferation," *Experimental Dermatology*, vol. 24, no. 7, pp. 481–484, 2015.

[27] R. B. Mokhamatam, B. K. Sahoo, and S. K. Manna, "Suppression of microphthalmia-associated transcription factor, but not NF-kappa B sensitizes melanoma specific cell death," *Apoptosis*, vol. 21, no. 8, pp. 928–940, 2016.

[28] X. Huang, X. Zhi, Y. Gao, N. Ta, H. Jiang, and J. Zheng, "LncRNAs in pancreatic cancer," *Oncotarget*, vol. 7, no. 35, pp. 57379–57390, 2016.

[29] T. Worku, D. Bhattarai, D. Ayers et al., "Long non-coding RNAs: the new horizon of gene regulation in ovarian cancer," *Cellular Physiology and Biochemistry*, vol. 44, no. 3, pp. 948–966, 2017.

[30] E. S. Martens-Uzunova, R. Böttcher, C. M. Croce, G. Jenster, T. Visakorpi, and G. A. Calin, "Long noncoding RNA in prostate, bladder, and kidney cancer," *European Urology*, vol. 65, no. 6, pp. 1140–1151, 2014.

[31] D. T. Zhang, J. G. Shi, Y. Liu, and H. M. Jiang, "The prognostic value of Smad4 mRNA in patients with prostate cancer," *Tumour Biology*, vol. 35, no. 4, pp. 3333–3337, 2014.

[32] R. Gera, L. Mokbel, W. G. Jiang, and K. Mokbel, "mRNA expression of CDK2AP1 in human breast cancer: correlation with clinical and pathological parameters," *Cancer Genomics Proteomics*, vol. 15, no. 6, pp. 447–452, 2018.

[33] M. L. Hartman and M. Czyz, "MITF in melanoma: mechanisms behind its expression and activity," *Cellular and Molecular Life Sciences*, vol. 72, no. 7, pp. 1249–1260, 2015.

[34] M. L. Hartman and M. Czyz, "Pro-survival role of MITF in melanoma," *The Journal of Investigative Dermatology*, vol. 135, no. 2, pp. 352–358, 2015.

[35] S. Aida, Y. Sonobe, H. Tanimura et al., "MITF suppression improves the sensitivity of melanoma cells to a BRAF inhibitor," *Cancer Letters*, vol. 409, pp. 116–124, 2017.

[36] T. Kordaß, C. E. M. Weber, M. Oswald et al., "SOX5 is involved in balanced MITF regulation in human melanoma cells," *BMC Medical Genomics*, vol. 9, no. 1, p. 10, 2016.

[37] S. C. Kwon, H. Yi, K. Eichelbaum et al., "The RNA-binding protein repertoire of embryonic stem cells," *Nature Structural & Molecular Biology*, vol. 20, no. 9, pp. 1122–1130, 2013.

[38] L. Wurth and F. Gebauer, "RNA-binding proteins, multifaceted translational regulators in cancer," *Biochimica et Biophysica Acta*, vol. 1849, no. 7, pp. 881–886, 2015.

Retraction

Retracted: Mechanism of Sevoflurane Anesthesia under Hypothermic Cardiopulmonary Bypass on Postoperative Atrial Fibrillation Rhythm in Patients Undergoing Mitral Valve Replacement

BioMed Research International

This article has been retracted by Hindawi following an investigation undertaken by the publisher [1]. This investigation has uncovered evidence of one or more of the following indicators of systematic manipulation of the publication process:

(1) Discrepancies in scope

(2) Discrepancies in the description of the research reported

(3) Discrepancies between the availability of data and the research described

(4) Inappropriate citations

(5) Incoherent, meaningless and/or irrelevant content included in the article

(6) Manipulated or compromised peer review

The presence of these indicators undermines our confidence in the integrity of the article's content and we cannot, therefore, vouch for its reliability. Please note that this notice is intended solely to alert readers that the content of this article is unreliable. We have not investigated whether authors were aware of or involved in the systematic manipulation of the publication process.

Wiley and Hindawi regrets that the usual quality checks did not identify these issues before publication and have since put additional measures in place to safeguard research integrity.

We wish to credit our own Research Integrity and Research Publishing teams and anonymous and named external researchers and research integrity experts for contributing to this investigation.

The corresponding author, as the representative of all authors, has been given the opportunity to register their agreement or disagreement to this retraction. We have kept a record of any response received.

References

[1] H. Che, Y. Lv, F. Yao, F. Zhao, and L. Zhao, "Mechanism of Sevoflurane Anesthesia under Hypothermic Cardiopulmonary Bypass on Postoperative Atrial Fibrillation Rhythm in Patients Undergoing Mitral Valve Replacement," *BioMed Research International*, vol. 2022, Article ID 5312897, 8 pages, 2022.

Research Article

Mechanism of Sevoflurane Anesthesia under Hypothermic Cardiopulmonary Bypass on Postoperative Atrial Fibrillation Rhythm in Patients Undergoing Mitral Valve Replacement

Hao Che,[1] Yufang Lv,[1] Fang Yao,[2] Fang Zhao,[1] and Liyun Zhao [1]

[1]*Department of Anesthesiology, Beijing Anzhen Hospital of Capital Medical University, Beijing 100029, China*
[2]*Department of Anesthesiology, Chaoyang City Second Hospital, Chaoyang, 122000 Liaoning Province, China*

Correspondence should be addressed to Liyun Zhao; zhaoliyun100700@163.com

Objective. It was to investigate the mechanism of atrial fibrillation after mitral valve replacement under extracorporeal circulation in patients with rheumatic heart disease under sevoflurane anesthesia maintenance and to provide scientific and effective basis for clinical treatment. *Methods*. Forty patients with rheumatic heart disease who underwent mitral valve replacement were randomly rolled into group I (sinus rhythm of propofol anesthesia, $n = 10$), group II (atrial fibrillation rhythm of propofol anesthesia, $n = 10$), group III (sinus rhythm of sevoflurane anesthesia, $n = 10$), and group IV (atrial fibrillation rhythm of sevoflurane anesthesia, $n = 10$). Inflammatory factors, free tissue of right atrium, and incidence of postoperative atrial fibrillation were compared among all groups. *Results*. (i) The serum levels of NT-proBNP, CRP, sST-2, IL-6, TNF-α, and TGF-β1 in group II were higher than those in group I, group III, and group IV, and the indexes in group III were higher than those in group IV ($P < 0.05$). (ii) The relative expression levels of PLB, CaMK II, Bax, and TP53 in the free tissue of right atrium in group II were higher than those in group I, III, and IV, and the index levels in group IV were higher than those in group III ($P < 0.05$). (iii) The incidence of postoperative atrial fibrillation in group III (0.00%) was significantly lower than that in group I (30%), group II (50%), and group IV (40.0%), and group II (50%) was the highest ($P < 0.05$). *Conclusion*. The maintenance of sevoflurane anesthesia can improve the inflammatory response and myocardial tissue autophagy in patients with sinus rhythm and atrial fibrillation rhythm and can reduce the incidence of postoperative atrial fibrillation in patients.

1. Introduction

Atrial fibrillation is the most common arrhythmia in clinical practice, and its incidence tends to increase with age [1]. The incidence of atrial fibrillation is high in patients with rheumatic heart disease, and when severe, it can evidently affect the quality of life of patients [2]. At present, the only radical treatment for rheumatic heart disease is mitral valve replacement, which has good clinical application effect [3]. However, mitral valve replacement has high surgical risk, slow prognosis, and heart failure. When the optimal surgical opportunity is missed, patients' atrial fibrillation and left atrial enlargement are difficult to be effectively alleviated [4]. In addition, during the onset of atrial fibrillation, patients are prone to thrombosis in the atria, which leads to severe and concurrent occurrence

of cerebral embolism and systemic circulation embolism, thus, having a high disability rate and fatality rate [5]. Therefore, it is very important to alleviate the onset of atrial fibrillation in patients. Atrial fibrillation is maintained by drug therapy to maintain sinus rhythm, and the probability of embolization after atrial fibrillation is reduced by ablative therapy, anticoagulation therapy, and other methods [6]. In recent years, studies suggested that electrical remodeling of the atria can lead to shortening, prolonging, or incongruity of the effective refractory period. Remodeling can trigger the delay of electrical signal conduction in the atria and then cause the dysfunction of atrial contraction function [7, 8]. In addition, myocardial fibrosis also plays an important role in atrial remodeling [9]. The main forms of myocardial fibrosis are the deposition of fibrous tissue in the interstitium of cardiomyocytes and

replacement/repair fibrosis after apoptosis of cardiomyocytes. In summary, atrial remodeling plays an important role in the occurrence of atrial fibrillation.

Recent studies confirmed that inflammatory response is also associated with the occurrence and maintenance of atrial fibrillation [10, 11]. In surgery, sevoflurane inhalation anesthesia can effectively reduce the incidence of atrial fibrillation and other rapid heart rate disorders in patients during or after surgery, so it has a certain effect of drug defibrillation [12]. Sevoflurane does not stimulate the respiratory tract and does not increase airway secretions, but can easily cause respiratory depression and reduce the levels of insulin and glucagon [13]. Propofol, a short-acting intravenous anesthetic, is administered intravenously to put patients to sleep quickly and smoothly. However, the analgesic effect of this drug is weak and will cause adverse reactions such as respiratory depression, decreased blood pressure, and decreased intracranial pressure [14]. At present, there is a lack of clinical comparison on the application effect of the two anesthetics.

Therefore, this study is aimed at exploring the effects of sevoflurane and propofol anesthesia on the incidence of atrial fibrillation in patients undergoing mitral valve replacement under hypothermia cardiopulmonary bypass and at exploring the changes of sevoflurane on the inflammatory response and myocardial cell apoptosis in patients. The mechanism of action of sevoflurane on myocardial protection of patients undergoing mitral valve replacement under CPB was explored, to provide effective research basis for improving surgical effect and prognosis of patients.

2. Materials and Methods

2.1. General Information. Forty patients with rheumatic heart disease who underwent mitral valve replacement in X Hospital from June 2017 to June 2020 were selected as the study subjects. Patients were randomly rolled into group I (sinus rhythm group under propofol anesthesia ($n = 10$)), group II (atrial fibrillation group under propofol anesthesia ($n = 10$)), group III (sinus rhythm group under sevoflurane anesthesia ($n = 10$)), and group IV (atrial fibrillation group under sevoflurane anesthesia ($n = 10$)) according to random number table method. General data, cardiac function grades, valve regurgitation before and after surgery, cardiac function indicators, and the incidence of atrial fibrillation one day after surgery were collected. Inclusion criteria: (i) patients diagnosed with chronic rheumatic heart disease and mitral stenosis by clinical signs, medical history, and imaging examination; (ii) patients with a history of atrial fibrillation heart rhythm at least six months; (iii) there was no severe mitral regurgitation. Exclusion criteria: (i) patients with complicated infective endocarditis; (ii) patients with diabetes, hypertension, coronary heart disease, or severe organ insufficiency; (iii) patients with preoperative treatment history of calcium channel blockers; (iv) patients with aortic stenosis; (v) patients with mitral valve severe regurgitation; (vi) women with active liver disease, pregnancy, or lactation; (vii) patients with malignant tumors or immune system diseases.

This study had been reviewed and approved by the medical ethics committee, and all patients included in the study had been aware of the trial process and signed the informed consent.

2.2. Treatment Methods. All patients underwent surgical treatment under general anesthesia and hypothermia external circulation. In addition, the surgical incision was located at the midline of the sternum, and cardiopulmonary bypass was established. Routine monitoring of pulse oxygen saturation and noninvasive blood pressure was required from the time the patient entered the operating room. Invasive blood pressure monitoring was implemented via radial artery puncture and a five-lead electrocardiogram. After endotracheal intubation, end-tidal carbon dioxide partial pressure and nasopharyngeal temperature were monitored. The central venous pressure was monitored by internal jugular vein puncture and catheterization. All patients received 0.1 mg/kg midazolam + 0.3 mg/kg etomidate + 0.005 mg/kg fentanyl + 0.15 mg/kg vecuronium for induction of anesthesia. Patients in groups I and II were then given 2% propofol to maintain anesthesia. Patients in groups III and IV received 2% sevoflurane for maintenance anesthesia. All patients in each group needed intermittent infusion of fentanyl and vecuronium during maintenance anesthesia. The bispectral index (BIS) was used to detect the depth of anesthesia, and the BIS was maintained at about 40 ± 5.

After an incision was made in the middle of the sternum, the pericardium was opened, and 300 IU/kg heparin was administered. Catheterization of the aorta and vena cava and cardiopulmonary bypass was performed after the coagulation time of the whole blood exceeded 480 s. The central venous pressure was required to be maintained during surgery. If the patient appeared hypotension, it was necessary to timely supplement deoxyadrenalin for pressor treatment. After surgery, twelve-lead electrocardiogram was used to diagnose atrial fibrillation rhythm.

2.3. Detection of Serum Biochemical Indexes. Fasting cubital vein blood was collected and placed in a refrigerator at -20°C for 60 min after anticoagulation treatment, followed by centrifugation at 3,000 rpm for 10 min, and supernatant was taken. The electrochemiluminescence double antibody sandwich immunoassay was adopted to determine the level of serum midbrain natriuretic peptide N-terminal precursor hormone (NT-probNP), and the kit was purchased from Roche. Enzyme-linked immunosorbent assay (ELISA) (Thermo, USA, MultiskanFC microplate analyzer) was used to detect C-reactive protein (CRP), somatostatin subtype receptor 2 (SST-2), interleukin (IL) -6, tumor necrosis factor (TNF-α), and transforming growth factor (TGF-β1) in serum of patients, following the instructions.

2.4. Real-Time Quantitative PCR Detection. When mitral valve replacement was performed and cardiopulmonary bypass was established, a small amount of free wall tissue of the right atrium was taken, rinsed with phosphoric acid buffer, and stored in liquid nitrogen. After grinding of the tissues, an appropriate amount of Trizol reagent was added

Table 1: Quantitative primers of target genes.

Gene	Primer (5′ →3′)	Product (bp)
PLB	F: AGAGTGGATGCAGGAAGAGAT R: AGAGCCCAGAGAAGGTTTGAT	235
CaMK II	F: ACTGGCGTCACGTTGTACTG R: CCTCGCTGATTTCTGGCTCC	127
Bax	F: CCCGAGAGGTCTTTTTCCGAG R: CCAGCCCATGATGGTTCTGAT	155
TP53	F: ACTTGTCGCTCTTGAAGCTAC R: GATGCGGAGAATCTTTGGAACA	113
GAPDH	F: TGTGGGCATCAATGGATTTGG R: ACACCATGTATTCCGGGTCAAT	116

Table 2: Comparison of general information of patients in each group.

Item	Group I ($n = 10$)	Group II ($n = 10$)	Group III ($n = 10$)	Group IV ($n = 10$)
Age (years old)	60.17 ± 5.33	61.20 ± 6.18	62.07 ± 5.74	61.58 ± 4.39
Male (n/%)	4/40.0	5/50.0	5/50.0	5/50.0
TC (mmol/L)	4.77 ± 0.43	4.78 ± 0.41	4.77 ± 0.50	4.80 ± 0.49
Cr (mg/dL)	85.09 ± 0.67	85.36 ± 1.88	86.05 ± 1.52	86.11 ± 2.13
UA (mg/dL)	323.25 ± 91.25	330.62 ± 97.14	331.29 ± 89.13	328.43 ± 86.47
LADd (mm)	46.31 ± 5.28	50.33 ± 8.97	47.05 ± 9.03	50.84 ± 10.26
RADd (mm)	36.07 ± 5.15	40.12 ± 6.36	37.11 ± 6.17	40.97 ± 6.05
LVDd (mm)	51.36 ± 8.02	52.11 ± 8.93	51.02 ± 7.11	52.03 ± 8.21
RVDd (mm)	36.85 ± 6.07	38.54 ± 6.17	36.90 ± 5.22	38.46 ± 6.28
LVEF (%)	64.72 ± 8.36	60.14 ± 11.07	62.08 ± 8.14	59.08 ± 10.36
Heart function (n/%)				
Grade I	1/10.0	0/0.0	1/10.0	0/0.0
Grade II	4/40.0	4/40.0	3/30.0	4/40.0
Grade III	5/50.0	6/60.0	6/60.0	5/50.0
Grade IV	0/0.0	0/0.0	0/0.0	0/0.0

TC: total cholesterol; Cr: creatinine; UA: uric acid; LADd: left atrial end-diastolic diameter; RADd: right atrial end-diastolic diameter; LVDd: left ventricular end-diastolic diameter; RVDd: right ventricular end-diastolic diameter; LVEF: left ventricular ejection fraction.

to extract total RNA, and the concentration, purity, and integrity were detected. Reverse transcription of cDNA was performed according to the instructions of the cDNA reverse transcription kit (Takara, Japan). Phospholamban (PLB), calmodulin-dependent protein kinase II (CaMK-II), Bax, and tumor protein 53 (TP53) quantitative detection primers were designed and synthesized, as shown in Table 1. The target gene expression was detected according to the instructions of the TB Green® Premix Ex Taq™ test kit (Takara, Japan). The PCR products were detected by 2% agarose gel electrophoresis imaging. 2% agarose gel with a thickness of 3 mm was taken, 5-10 μL PCR reaction solution containing 3 μL bromophenollan solution was added, medium voltage electrophoresis apparatus was applied, and 0.5 × TBE working solution was given under the power supply. Then, the electrophoresis lasted for 50 min under the voltage of 80 V. The test was carried out on the quartz glass table of the UV transmittance instrument. Using GAPDH gene as internal reference, 2-$^{\triangle\triangle Ct}$ was used to detect the relative expression level of target gene.

2.5. Statistical Treatment. SPSS 19.0 was employed to arrange the experimental data. The dichotomous variables were represented by frequency (%), and the continuous variables were represented by means ± SD, whose differences were compared by chi-square test and one-way ANOVA, respectively. When $P < 0.05$, there was a significant difference between the two groups.

3. Results

3.1. Comparison of General Information. Before surgery, the differences among the general information of the four groups of patients were compared in Table 2. It was found

(a)

(b)

(c)

(d)

(e)

(f)
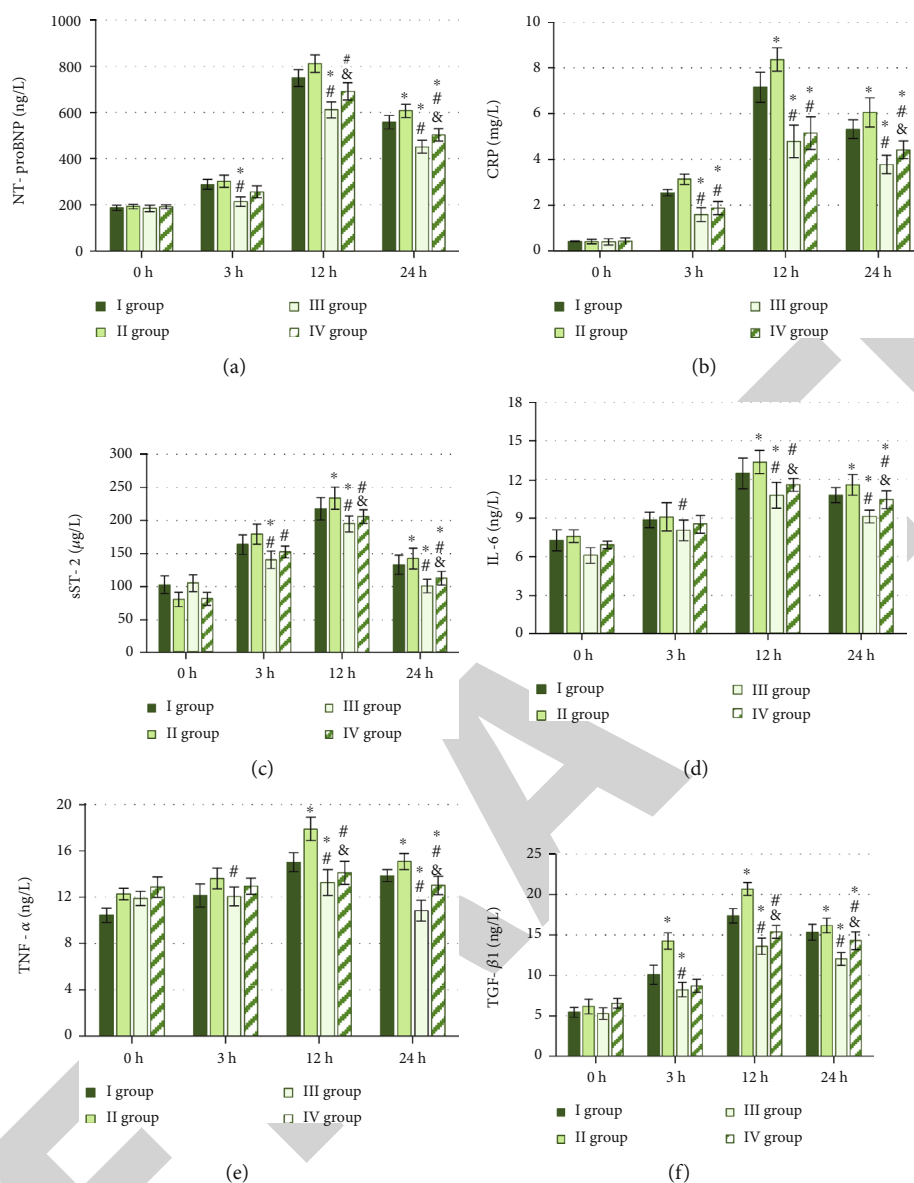
Figure 1: Comparison of differences in serum biochemical index levels of patients in each group. Note: (a) NT-proBNP level; (b) CRP level; (c) sST-2 level; (d) IL-6 level; (e) TNF-α level; (f) TGF-β1 level. Compared to group I, $^*P < 0.05$; compared with group II, $^{\#}P < 0.05$; compared with group III, $^{\&}P < 0.05$.

that the average age, sex ratio, TC, Cr, UA, LADd, RADd, LVDd, RVDd, LVEF, and cardiac function classification of the patients in each group had no significant difference ($P > 0.05$).

3.2. The Effect of Sevoflurane on the Level of Serum Biochemical Indexes in Patients.

The differences in serum levels of NT-proBNP, CRP, sST-2, IL-6, TNF-α, and TGF-β1 in each group of patients were compared before operation (0 h), 3 h after operation, 12 h after operation, and 24 h after operation. The results were shown in Figure 1. With the prolongation of the operation, the serum levels of NT-proBNP, CRP, sST-2, IL-6, TNF-α, and TGF-β1 in each group reached the highest at 12 h after surgery, and they were all reduced at 24 h after surgery. The differences in serum biochemical index levels of patients in each group at
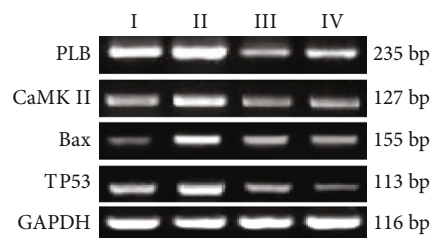
Figure 2: PCR diagram of the detection of the expression level of each target gene.

each time point were compared. With 24 hours after operation as an example, compared with group I, the levels of serum indexes of patients in group II were dramatically
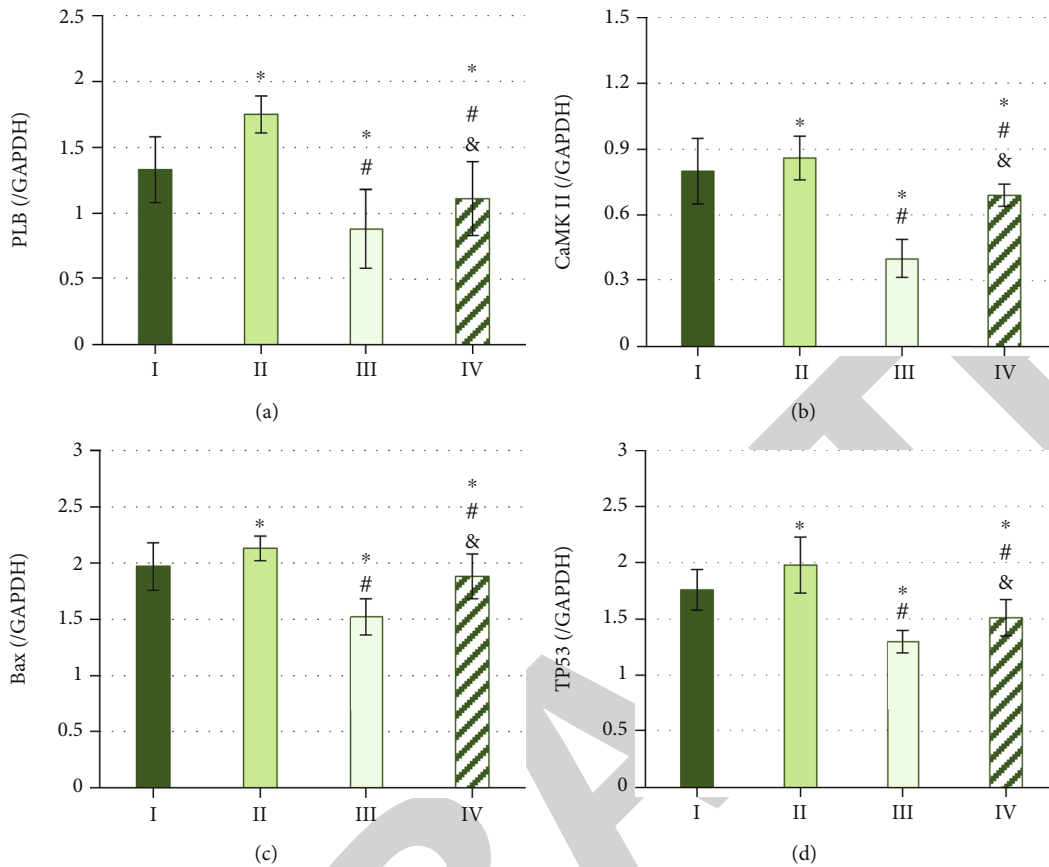
Figure 3: Statistics of the relative expression level of each target gene. Note: (a) the relative expression level of PLB; (b) the relative expression level of CaMK II; (c) the relative expression level of Bax; (d) the relative expression level of TP53. Compared to group I, $^*P <$ 0.05; compared with group II, $^\#P < 0.05$; compared with group III, $^\&P < 0.05$.
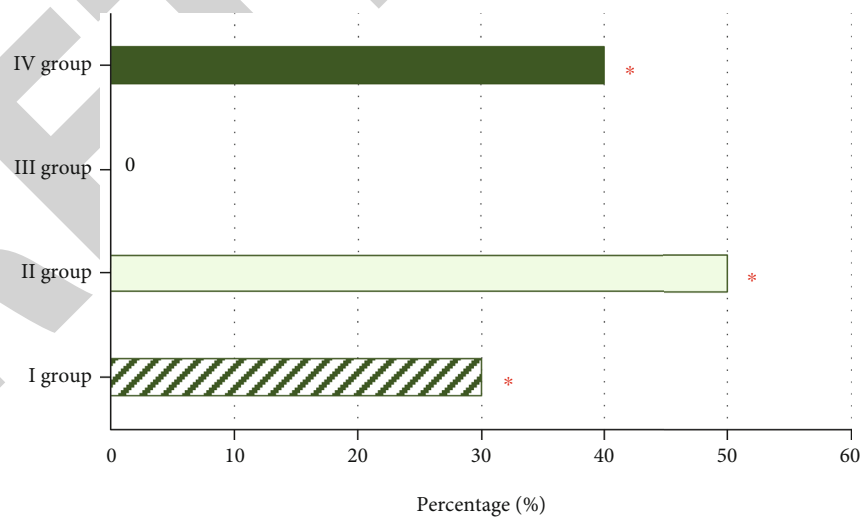
Figure 4: Statistics of the incidence of atrial fibrillation in each group of patients. ("∗" meant that compared with group III, the incidence of atrial fibrillation in group I, II, and IV was higher, and there was a statistical difference ($P < 0.05$).)

increased ($P < 0.05$), and the levels of serum indexes of patients in groups III and IV were greatly decreased ($P < 0.05$). Compared with group II, serum levels of patients in group III and group IV were obviously lower ($P < 0.05$). The serum levels of patients in group IV were notably superior to those of group III ($P < 0.05$).

3.3. The Effect of Sevoflurane on the Expression of PLB, CaMK II, Bax, and TP53 in Patients. Real-time fluorescence quantitative PCR was used to detect the relative expression levels of PLB, CaMK II, Bax, and TP53 in the right atrium free tissues of each group of patients. The detection bands were shown in Figure 2. The expression levels of PLB, CaMK II, Bax, and TP53 in the tissues of group II were the highest, while the expression levels of PLB, CaMK II, Bax, and TP53 were the lowest in the tissues of group III.

Subsequently, GAPDH was used as an internal reference gene to calculate the relative expression levels of PLB, CaMK II, Bax, and TP53, and the results were shown in Figure 3. Compared with group I, the expression levels of PLB, CaMK II, Bax, and TP53 in the tissues of group II patients were dramatically increased ($P < 0.05$). The expression levels of PLB, CaMK II, Bax, and TP53 in the tissues of patients in groups III and IV were substantially reduced ($P < 0.05$). In addition, the expression levels of PLB, CaMK II, Bax, and TP53 in the tissues of patients in groups III and IV were obviously lower than those in group II ($P < 0.05$). The expression levels of PLB, CaMK II, Bax, and TP53 in the tissues of the group IV were notably superior to those in the group III ($P < 0.05$).

3.4. Comparison of Incidence of Atrial Fibrillation. The difference between the probability of atrial fibrillation in each group of patients was compared during the operation to 24 hours after the end of the operation, and the results were shown in Figure 4. The probability of atrial fibrillation in group I, group II, group III, and group IV was 30.0%, 50.0%, 0.0%, and 40.0%, respectively. Compared with group I ($P < 0.05$), the incidence of atrial fibrillation in group II was dramatically increased, but the incidence of atrial fibrillation in group III was substantially reduced ($P < 0.05$). In addition, the incidence of atrial fibrillation in group III was also substantially reduced compared with group II and group IV ($P < 0.05$).

4. Discussion

Atrial fibrillation affects about 2% of the general population, and there are many factors to induce atrial fibrillation [15]. Studies revealed that for every additional ten years of age, the risk of atrial fibrillation increases two times. The incidence of atrial fibrillation in males is 1.5 times higher than that in females [16]. At present, a number of studies concluded that there are many factors triggering atrial fibrillation, mainly including inflammatory response, oxidative stress, and autonomic nervous system imbalance [7, 17]. The underlying mechanism of atrial fibrillation may be related to the abnormality of focal potential and arrhythmia, but the specific mechanism remains unclear and uncertain. Studies confirmed that sevoflurane inhalation anesthesia can effectively reduce the incidence of atrial fibrillation in patients, with certain drug defibrillation effect [18]. Therefore, the effects of sevoflurane and propofol anesthesia maintenance on serum NT-proBNP, CRP, sST-2, IL-6, TNF-α, and TGF-β1 levels in patients undergoing mitral valve replacement surgery were analyzed. NT-proBNP is a type of peptide hormone. When atrial pressure tension increases, the level of NT-proBNP will also increase [19]. IL-6 is mainly produced by T cells and macrophages, which can induce the expression of inflammatory response proteins in the acute phase, such as TNF-α. CRP, TNF-α, and TGF-β1 all belong to a class of inflammatory mediators [20]. Studies pointed out that there will be more obvious inflammation in the myocardial tissue of patients with atrial fibrillation [21]. SST-2 belongs to the family of interleukins, which can help the immune response of T cells after binding to IL-33 and inhibit the fibrosis and apoptosis of myocardial tissue [22]. The results showed that compared with patients with sinus rhythm, postoperative serum NT-proBNP, CRP, sST-2, IL-6, TNF-α, and TGF-β1 levels in patients with atrial fibrillation all increased to varying degrees, which confirmed the relationship between the occurrence of atrial fibrillation and the body's inflammatory response, indicating that the inflammatory response can promote the occurrence of postoperative atrial fibrillation in patients [23]. Compared with the maintenance of propofol anesthesia, sevoflurane used for maintenance of anesthesia in patients with atrial fibrillation substantially reduced serum NT-proBNP, CRP, sST-2, IL-6, TNF-α, and TGF-β1 levels after maintenance. Sevoflurane is a kind of volatile anesthetic, and its effect on myocardial protection is evidently better than that of intravenous anesthetics [24]. The results confirmed that sevoflurane anesthesia can greatly reduce the postoperative inflammatory response in patients.

Real-time fluorescence quantitative PCR technology was used to detect the changes in the expression levels of PLB, CaMK II, Bax, and TP53 mRNA in the free tissues of the patient's right atrium. In myocardial tissue, PLB can inhibit the activity of the sarcoplasmic reticulum calcium pump, thereby inhibiting the entry of calcium ions into the sarcoplasmic reticulum [25]. CaMK II phosphorylation can form pentamers with PLB, and the two factors can mutually regulate the release of calcium ions during myocardial diastole and systole and then participate in the occurrence of arrhythmia such as atrial fibrillation [26]. Moreover, there is also a close relationship between atrial fibrillation and the apoptosis of cardiomyocytes. Bax is an important factor regulating cell apoptosis, which can promote cell apoptosis [27]. TP53 can cause cell apoptosis and cardiac dysfunction [28]. It was found that compared with patients with sinus rhythm, the expression levels of PLB, CaMK II, Bax, and TP53 mRNA in the free tissues of the right atrium in patients with atrial fibrillation were dramatically increased after surgery. It was revealed that there were phenomena such as increased release of calcium ions from cardiomyocytes and cardiomyocyte apoptosis in patients with atrial fibrillation [29]. Compared with the propofol anesthesia group, the expression levels of PLB, CaMK II, Bax, and TP53 mRNA in the atrial free tissues of patients with atrial fibrillation after sevoflurane anesthesia were substantially reduced. It was also found that after sevoflurane anesthesia, the probability of atrial fibrillation recurrence in patients with atrial fibrillation was 0.0%. Therefore, sevoflurane anesthesia can evidently improve postoperative atrial fibrillation and inflammation in patients undergoing mitral valve replacement under hypothermic cardiopulmonary bypass, and the effect was better than propofol anesthesia.

5. Conclusion

The effects of sevoflurane and propofol anesthesia on atrial fibrillation in patients undergoing mitral valve replacement were investigated. The results showed that sevoflurane anesthesia could significantly reduce the postoperative inflammatory response, the release of calcium ions, and apoptosis of cardiomyocytes in patients with atrial fibrillation, and significantly reduce the incidence of postoperative atrial fibrillation. However, only clinical data were used to analyze the mechanism of sevoflurane in patients with atrial fibrillation after mitral valve replacement. The underlying regulatory mechanism is still unclear; therefore, the relationship between sevoflurane and postoperative atrial fibrillation will be further explored through animal or cell studies. However, through this study, it is concluded that sevoflurane has a good development prospect in clinical surgical anesthesia for patients with atrial fibrillation, and it is worthy of further study.

Data Availability

The data used to support the findings of this study are included within the article.

Conflicts of Interest

The authors declare that they have no competing interests.

References

[1] N. A. Bosch, J. Cimini, and A. J. Walkey, "Atrial fibrillation in the ICU," *Chest*, vol. 154, no. 6, pp. 1424–1434, 2018.

[2] G. Karthikeyan, S. J. Connolly, M. Ntsekhe et al., "The INVICTUS rheumatic heart disease research program: rationale, design and baseline characteristics of a randomized trial of rivaroxaban compared to vitamin K antagonists in rheumatic valvular disease and atrial fibrillation," *American Heart Journal*, vol. 225, pp. 69–77, 2020.

[3] G. Fu, Z. Zhou, S. Huang et al., "Mitral valve surgery in patients with rheumatic heart disease: repair vs. replacement," *Frontiers in Cardiovascular Medicine*, vol. 8, no. 8, article 685746, 2021.

[4] J. Fu, Y. Li, H. Zhang et al., "Outcomes of mitral valve repair compared with replacement for patients with rheumatic heart disease," *The Journal of Thoracic and Cardiovascular Surgery*, vol. 162, no. 1, pp. 72–82.e7, 2021.

[5] V. Reddy, W. Taha, S. Kundumadam, and M. Khan, "Atrial fibrillation and hyperthyroidism: a literature review," *Indian Heart Journal*, vol. 69, no. 4, pp. 545–550, 2017.

[6] C. Gutierrez and D. G. Blanchard, "Diagnosis and treatment of atrial fibrillation," *American Family Physician*, vol. 94, no. 6, pp. 442–452, 2016.

[7] J. Jalife and K. Kaur, "Atrial remodeling, fibrosis, and atrial fibrillation," *Trends in Cardiovascular Medicine*, vol. 25, no. 6, pp. 475–484, 2015.

[8] D. H. Lau, D. Linz, and P. Sanders, "New findings in atrial fibrillation mechanisms," *Cardiac Electrophysiology Clinics*, vol. 11, no. 4, pp. 563–571, 2019.

[9] C. Sohns and N. F. Marrouche, "Atrial fibrillation and cardiac fibrosis," *European Heart Journal*, vol. 41, no. 10, pp. 1123–1131, 2020.

[10] B. S. Karam, A. Chavez-Moreno, W. Koh, J. G. Akar, and F. G. Akar, "Oxidative stress and inflammation as central mediators of atrial fibrillation in obesity and diabetes," *Cardiovascular Diabetology*, vol. 16, no. 1, p. 120, 2017.

[11] Y. F. Hu, Y. J. Chen, Y. J. Lin, and S. A. Chen, "Inflammation and the pathogenesis of atrial fibrillation," *Nature Reviews. Cardiology*, vol. 12, no. 4, pp. 230–243, 2015.

[12] P. M. Jones, D. Bainbridge, M. W. Chu et al., "Comparison of isoflurane and sevoflurane in cardiac surgery: a randomized non-inferiority comparative effectiveness trial," *Canadian Journal of Anesthesia/Journal canadien d'anesthésie*, vol. 63, no. 10, pp. 1128–1139, 2016.

[13] Y. Zhang, G. J. Shan, Y. X. Zhang et al., "Propofol compared with sevoflurane general anaesthesia is associated with decreased delayed neurocognitive recovery in older adults," *British Journal of Anaesthesia*, vol. 121, no. 3, pp. 595–604, 2018.

[14] S. Hemphill, L. McMenamin, M. C. Bellamy, and P. M. Hopkins, "Propofol infusion syndrome: a structured literature review and analysis of published case reports," *British Journal of Anaesthesia*, vol. 122, no. 4, pp. 448–459, 2019.

[15] P. Zimetbaum, "Atrial fibrillation," *Annals of Internal Medicine*, vol. 166, no. 5, pp. ITC33–ITC48, 2017.

[16] M. S. Kallistratos, L. E. Poulimenos, and A. J. Manolis, "Atrial fibrillation and arterial hypertension," *Pharmacological Research*, vol. 128, pp. 322–326, 2018.

[17] V. Vyas, R. J. Hunter, M. P. Longhi, and M. C. Finlay, "Inflammation and adiposity: new frontiers in atrial fibrillation," *Europace*, vol. 22, no. 11, pp. 1609–1618, 2020.

[18] E. Hamaguchi, H. Kawano, S. Kawahito, H. Kitahata, and S. Oshita, "Torsade de pointes associated with severe bradycardia after induction of general anesthesia," *Masui. The Japanese Journal of Anesthesiology*, vol. 60, no. 9, pp. 1097–1100, 2011.

[19] J. Pagola, J. Juega, J. Francisco-Pascual et al., "Crypto-AF study group. Predicting atrial fibrillation with high risk of embolization with atrial strain and NT-proBNP," *ranslational Stroke Research*, vol. 12, no. 5, pp. 735–741, 2021.

[20] Q. Wu, H. Liu, J. Liao et al., "Colchicine prevents atrial fibrillation promotion by inhibiting IL-1β-induced IL-6 release and atrial fibrosis in the rat sterile pericarditis model," *Biomedicine & Pharmacotherapy*, vol. 129, article 110384, 2020.

[21] Y. Liu, F. Wu, Y. Wu et al., "Mechanism of IL-6-related spontaneous atrial fibrillation after coronary artery grafting surgery: IL-6 knockout mouse study and human observation," *Translational Research*, vol. 233, pp. 16–31, 2021.

[22] P. Wałek, I. Gorczyca, U. Grabowska, M. Spałek, and B. Wożakowska-Kapłon, "The prognostic value of soluble suppression of tumourigenicity 2 and galectin-3 for sinus rhythm maintenance after cardioversion due to persistent atrial fibrillation in patients with normal left ventricular systolic function," *Europace*, vol. 22, no. 10, pp. 1470–1479, 2020.

[23] C. J. Boos, "Infection and atrial fibrillation: inflammation begets AF," *European Heart Journal*, vol. 41, no. 10, pp. 1120–1122, 2020.

[24] Y. J. Cho, K. Nam, T. K. Kim et al., "Sevoflurane, propofol and carvedilol block myocardial protection by limb remote ischemic preconditioning," *International Journal of Molecular Sciences*, vol. 20, no. 2, p. 269, 2019.

Retraction

Retracted: The Expression Profile of miRNA in Glioma and the Role of miR-339-5p in Glioma

BioMed Research International

This article has been retracted by Hindawi following an investigation undertaken by the publisher [1]. This investigation has uncovered evidence of one or more of the following indicators of systematic manipulation of the publication process:

(1) Discrepancies in scope

(2) Discrepancies in the description of the research reported

(3) Discrepancies between the availability of data and the research described

(4) Inappropriate citations

(5) Incoherent, meaningless and/or irrelevant content included in the article

(6) Manipulated or compromised peer review

The presence of these indicators undermines our confidence in the integrity of the article's content and we cannot, therefore, vouch for its reliability. Please note that this notice is intended solely to alert readers that the content of this article is unreliable. We have not investigated whether authors were aware of or involved in the systematic manipulation of the publication process.

Wiley and Hindawi regrets that the usual quality checks did not identify these issues before publication and have since put additional measures in place to safeguard research integrity.

We wish to credit our own Research Integrity and Research Publishing teams and anonymous and named external researchers and research integrity experts for contributing to this investigation.

The corresponding author, as the representative of all authors, has been given the opportunity to register their agreement or disagreement to this retraction. We have kept a record of any response received.

References

[1] J. Lin, S. Wang, H. Shen, and B. Zheng, "The Expression Profile of miRNA in Glioma and the Role of miR-339-5p in Glioma," *BioMed Research International*, vol. 2022, Article ID 4085039, 8 pages, 2022.

Research Article

The Expression Profile of miRNA in Glioma and the Role of miR-339-5p in Glioma

Jie Lin [iD],[1] **Shouyi Wang** [iD],[2] **Huanan Shen** [iD],[3] **and Buyi Zheng** [iD][1]

[1]*Department of Neurosurgery, Wenzhou People's Hospital, Wenzhou, Zhejiang Province, China 325000*
[2]*Department of Vascular & Interventional Radiology, Wenzhou People's Hospital, Wenzhou, Zhejiang Province, China 325000*
[3]*Department of Neonatology, Wenzhou People's Hospital, Wenzhou, Zhejiang Province, China 325000*

Correspondence should be addressed to Buyi Zheng; zhengbuyi800@126.com

Objective. To reveal the expression profile of miRNA in glioma and the effects of microRNA-339-5p (miR-339-5p) on glioma. *Methods.* The glioma and normal tissues were randomly selected for miRNA gene chip detection and qRT-PCR verification. The U87 cells were separated into miR-NC, miR-339-5p mimic, and miR-339-5p suppressor group. Clonogenesis test, flow cell technique, Transwell, and cell scratch assay were utilized to verify the roles of miR-339-5p in cell proliferation, cell apoptosis, cell invasion, and cell migration. The epithelial-meso-transformation-associated proteins was verified by Western blot. *Results.* A total of 49 miRNAs (16 upregulated and 33 downregulated) were differentially expressed in glioma tissues, and miR-339-5p was the most downregulated. The clone number, invasion number, and healing rate of cells in miR-339-5p mimic group were decreased compared with miR-NC group ($P < 0.05$); the clone quantity, invasion number, and healing rate of cells in miR-339-5p inhibitor group were increased compared with miR-NC group ($P < 0.05$). The apoptosis rate of human glioma U87 cells in miR-339-5P mimic group was compared with miR-NC group ($P < 0.05$); the apoptosis rate of human glioma U87 cells in miR-339-5p suppressor group decreased compared with miR-NC group ($P < 0.05$). Compared with miR-NC group, the protein expression of Twist, Snsnail, N-cadherin, and Vimentin in miR-339-5p mimic group was considerably decreased, whereas E-cadherin was elevated ($P < 0.05$). Compared with miR-NC group, the protein expression of Twist, Snsnail, N-cadherin, and Vimentin in miR-339-5p suppressor group was considerably increased, whereas E-cadherin was considerably decreased ($P < 0.05$). *Conclusion.* Forty-nine glioma-related miRNAs were screened out, and miRNA expression was significantly different between glioma and normal tissues. The downregulated miR-339-5p in glioma can regulate the proliferative, apoptotic, invasive, and migratory abilities of glioma U87 cells and might suppress the occurrence and development of glioma.

1. Introduction

Tumors originating from neuroepithelium are collectively referred to as glioma, which is caused by the canceration of glial cells in the cerebrum and spinal cord and is featured by obvious invasiveness, high morbidity, and high death rate [1]. The pathogenic factors of this disease are relatively complex. Under the interaction of congenital genetic factors and environmental carcinogenic factors, the level of genetic and epigenetic material of cells has undergone cancer mutation [2]. These mutations drive cells to continuously enter the cell cycle, avoid immune suppression, apoptosis, and mitosis, and contact suppression of cell growth, etc., and abnormal

energy metabolism, hypoxia, and necrosis corresponding to continuous cell growth also induce changes in tumor angiogenesis [3]. Low-grade gliomas develop slowly and have a good clinical prognosis, while high-grade gliomas develop rapidly and have a poor clinical prognosis [4]. Due to the rapid growth rate and high infiltration of glioma, the blood-brain barrier restriction cannot allow anticancer drugs to enter the central nervous system [5], and the effect of surgery combined with radiotherapy and chemotherapy is not satisfactory. Hence, it is imperative to identify the etiopathogenesis of glioma, search for biomarkers for diagnosis and treatment, and screen therapeutic targets for prolonging the survival of patients. miRNAs are highly conserved and

are pivotal for gene expression, translation, and posttranscriptional regulation of biological processes [6]. MicroRNAs (miRNAs) have drawn much attention because of their diagnostic value in diverse cancers, including glioma. The exchange of miRNAs through gap junctions has been reported between glioma cells and from mesenchymal stem cells to glioma cells. It extensively participates in physiopathological process like tissue differentiation, neural development, synaptic formation, and cell apoptosis [7]. Current studies have shown that miRNA is tightly associated with the onset and developmental process of glioma. However, the role of miR-339-5p in glioma remains unknown. In the present study, we first detected the expression of miR-339-5p in glioma. The regulatory effect of miR-339-5p on glioma was further explored. In this paper, our team identified the expression profile of miRNA in the brain tissue of glioma patients and investigated the roles of miR-339-5p in the pathogenesis of glioma. The specific report is as follows.

2. Materials and Methods

2.1. Total RNA Extraction. Overall RNA was abstracted from tissues via TRIzol (Qiagen, Valencia, CA). Glioma tissues and normal tissues were ground into powder in liquid nitrogen, mixed with TRIzol, and centrifuged at 4°C at $12000 \times g$ for 5 min, then the supernate was moved to a novel EP tube of chloroform and isoamyl alcohol, and the centrifugation was continued. After centrifugation, the upper RNA was taken and washed with ethanol, the ethanol was removed, and the RNA was dissolved in DEPC water. The total RNA was identified and quantified by NanoDrop and Agilent 2100 bioanalyzer.

2.2. miRNA Gene Chip Detection and Analysis. A total of 50 patients with glioma (age range, 39-80 years; mean age, 59 years) were diagnosed between January 2021 and June 2022 at Wenzhou People's Hospital. Ten glioma tissues and 10 normal tissues were randomly selected for miRNA chip detection. After total RNA extraction, miRNA was labeled; total RNA, CIP buffer, and CIP enzyme were mixed with a centrifuge tube without RNA enzyme; PCR cycle was conducted; and CIP was added. The reaction was performed after 5 step: labeling buffer, fluorescent label (Hy3 TM), DMSO, labeling enzyme, and mixing; PCR cycle was conducted once; and miRNA chip hybridization was performed 24 h later. Exiqon miRCURY™ LNA Array (V.18.0) chip was used to detect miRNA expression in the tissues of the above two groups.

2.3. qRT-PCR Was Used to Verify miRNAs. After total RNA extraction, total RNA absorbance was determined, and cDNA was retrotranscribed as per the specification of the miRcute miRNA fluorescent quantitation identification tool. PCR reaction system was 25 μL, TB Green Premix Ex Taq II 12.5 μL (Bio-Rad), PCR Forward Primer 1 μL (Bio-Rad), PCR Reverse Primer 1 μL (Bio-Rad), cDNA 2 μL (Bio-Rad), and RNase Free dH2O 8.5 μL; reactive conditions are as follows: predenaturation under 95°C for 0.5 min, denaturized under 95°C for 5 s, and annealing and extension under 60°C for 0.5 min, an overall 40. The CT value of 2-ΔΔCT was calculated as the comparative expression value of the gene according to the CT result of the targeted gene in each specimen. The following primer pairs were used for the qPCR: miR-339-5p forward: 5′-GCCGAGTCCCT GTCCTCCAGG-3′ and reverse: 5′-CTCAACTGGTGTCG TGGA-3′ and U6 forward: 5′-GCTTCGGCAGCACATA TACTAAAAT-3′ and reverse: 5′-CGCTTCACGAATTT GCGTGTCAT-3′.

2.4. Cell Culture and Grouping. Human glioma U87 cells were cultivated with RPMI 1640 intermediary involving 10% FBS and 1×105 U/L penicillin/streptomycin dual antibody solution in a constant temperature incubator. Follow-up experiments were carried out when the cells were in log-growth phase. U87 cells were separated into miR-NC group, miR-339-5p mimic group, and miR-339-5p suppressor group. The cells in every group were inoculated into 6-well dishes, and Lipofectamine 3000 was transfected, and strict operations were completed as per the supplier's specification. miR-nc was introduced into U87 cells via transfection as miR-NC group. miR-339-5p mimic was introduced into U87 cells via transfection, and miR-339-5p suppressor was introduced into U87 cells via transfection and miR-339-5p suppressor was introduced into U87 cells via transfection. Transfection efficiency values were obtained through measurements after cell-lysis activity assay and were compared to efficiencies obtained in parallel with a commercially available liposome-preparation (Lipofectamine).

2.5. The Proliferative Ability of U87 Cells Was Detected by Clonal Formation Assay. U87 cells in every group at log-growth phase were subjected to digestion via trypsin to produce cellular suspension, and the cellular density was adjusted to 2.0×10^3 cells/cell. The culture medium was discarded, the culture medium was cleaned with PBS, methanol was added and fixed for 15 min, PBS was cleaned, crystal violet staining was performed for 20 min, PBS was rinsed, and photography was counted.

2.6. Apoptosis of U87 Cells Was Identified by Flow Cell Technique. Posterior to the 48 h transfectional process, the cells were cleaned in PBS and prepared into suspension. Annexin V-FITC 5 μL and 5 μL PI (Thermo Fisher Scientific) were supplemented into the suspension under dark conditions. The cells were cultivated for 15 min and analyzed by flow cell technique to identify apoptosis rate of U87 cells in every group.

2.7. U87 Cell Invasion Was Detected by Transwell. An appropriate amount of diluted Matrigel was supplemented into Transwell chamber (Beckman Coulter, Fullerton, CA) and cultivated with 5% CO_2 and 37°C culture phase until the matrix gelated. The cells were prepared into suspension and seeded into a 24-well dish with 5×10^4 cells per well, incubated at room temperature for 24 h, subjected to fixation in methyl alcohol for 0.5 h, dyed in 0.1% gentian violet for 20 min, washed with water, and removed the cells that did

not penetrate the membrane. The cells were observed under microscope in 5 fields and photographed for counting.

2.8. Cell Scratch Test U87 Cell Migration. U87 cells in each group were transfected with liposome (Millipore) for 48 h, and the cellular content was modified to 1×10^6 cells/dish. The cells were seeded in a 35 mm Petri dish, added to the medium, and cultivated in a 5% CO_2 incubating device under 37°C. After discarding the intermediary, PBS was used for cleaning, 200 μL spear tip was used to uniformly make linear scratches in the Petri dish, and the scratches in each group were roughly the same in thickness. PBS was used to wash the scratch healing area, then intermediary without serum was added, and pictures were captured via a microscopic device, which was marked as 0 h. Culture and incubation were continued, and images were taken under the microscope at 48 h.

2.9. The Expression of Epithelial-Mesenchymal (E-M) Transformational Proteins Was Identified via Western Blot. All reagents were obtained from Sigma-Aldrich (St. Louis, MO). The transfected U87 cells of each group were used for ice lysis with cell lysate containing PMSF, and protein was collected. Protein levels were identified via BCA approach and SDS-PAGE polyacrylamide gel electrophoresis, closed, incubation Twist (1:500), snq-2 (1:1000), N-cadherin (1:500), Vimentin (1:1000), E-cadherin (1:500) primary antibody, 4°C shaking bed overnight. HRP labeled second antibody (1:10,000) was cultivated for 120 min, the membrane was removed and cleaned with TBST, and ECL luminescent solution was added for exposure, and pictures were taken.

2.10. Statistical Treatment. GraphPad Prism 9 was utilized for statistic assay, and data was represented by $\bar{x} \pm s$. T-test was utilized for pair-to-group contrast, and ANOVA was utilized for multigroup contrast. $P < 0.05$ had significance on statistics.

3. Results

3.1. Analysis of Quality and Quantity of RNA Samples. The A260/A280 of the extracted RNA was in the range of 1.8~2.1, with good RNA purity and no obvious degradation, and no protein contamination during the extraction process, which can be used for subsequent experiments.

3.2. Microarray Expression Profile of miRNA in Glioma. The microarray hybridization results were analyzed, and the analysis standards were set as follows: multiple of change ≥2 and $P \leq 0.05$ were considered as differential expression. Compared with normal tissues, 49 miRNAs were differentially expressed in glioma tissues, of which 16 miRNAs were upregulated, 33 miRNAs were significantly downregulated, and the downregulation of miR-339-5p was the most remarkable in the differential expression spectrum. miR-339-5p was chosen as the object of subsequent research. The heat map results of the 49 differentially expressed miRNA are shown in Figure 1 and Table 1.

3.3. Validation of miRNAs by qRT-PCR. Based on miRNA chip screening, miR-339-5p with low expression was selected as research objects, and qRT-PCR was utilized to detect 8 miRNAs. The outcomes revealed that the expression of miR-339-5p, miR-185, and miR-539 in glioma was lower than those in healthy samples, and the diversities displayed significance on statistics ($P < 0.05$); qRT-PCR outcomes reveal that the chip results can be trusted, as shown in Figure 2.

3.4. Role of miR-339-5p in the Proliferative Ability of Human Glioma U87 Cells. The outcomes revealed that the number of human glioma U87 cells cloned in miR-339-5p mimic group was considerably smaller vs. miR-NC group, and the diversities displayed significance on statistics ($P < 0.05$), the clone quantity of human glioma U87 cells in miR-339-5p suppressor group was considerably greater vs. miR-NC group, and the diversities displayed significance on statistics ($P < 0.05$), as presented by Figure 3.

3.5. Role of miR-339-5p in the Programmed Cell Death of Human Glioma U87 Cells. Flow cell technique revealed that the apoptotic rate of HUMAN glioma U87 cells in miR-339-5p mimic group was considerably greater vs. miR-NC group, and the diversity displayed significance on statistics ($P < 0.05$), the apoptotic rate of human glioma U87 cells in miR-339-5p suppressor group was considerably lower vs. miR-NC group, and the diversity displayed significance on statistics ($P < 0.05$), as presented by Figure 4.

3.6. Roles of miR-339-5P in Invasion of Human Glioma U87 Cells. Transwell outcomes revealed that the invasion quantity of mankind glioma U87 cells in miR-339-5p mimic group was considerably smaller vs. miR-NC group, and the diversity displayed significance on statistics ($P < 0.05$), the invasion quantity of human glioma U87 cells in miR-339-5p suppressor group was considerably greater vs. miR-NC group, and the diversity displayed significance on statistics ($P < 0.05$), as presented by Figure 5.

3.7. Roles of miR-339-5P in Human Glioma U87 Cell Migration. The outcomes of cell scratch assay revealed that the healing rate of human glioma U87 cells in miR-339-5p mimic group was significantly lower vs. miR-NC group, the difference had significance on statistics ($P < 0.05$), the healing rate of human glioma U87 cells in miR-339-5p suppressor group was considerably greater vs. miR-NC group, and the difference had significance on statistics ($P < 0.05$), as presented by Figure 6.

3.8. Role of miR-339-5P in E-M Transformation-Associated Proteins in Human Glioma U87 Cells. Western blot revealed that miR-339-5p was considerably higher vs. the miR-nc group, and the protein expression levels of Twist, Snake-2, N-cadherin, and Vimentin were reduced considerably in mimic group, whereas the protein expression level of E-cadherin increased considerably ($P < 0.05$). In contrast to miR-NC group, the protein expression levels of Twist, Snsnail, N-cadherin, and Vimentin in miR-339-5p suppressor group was considerably increased, whereas the protein
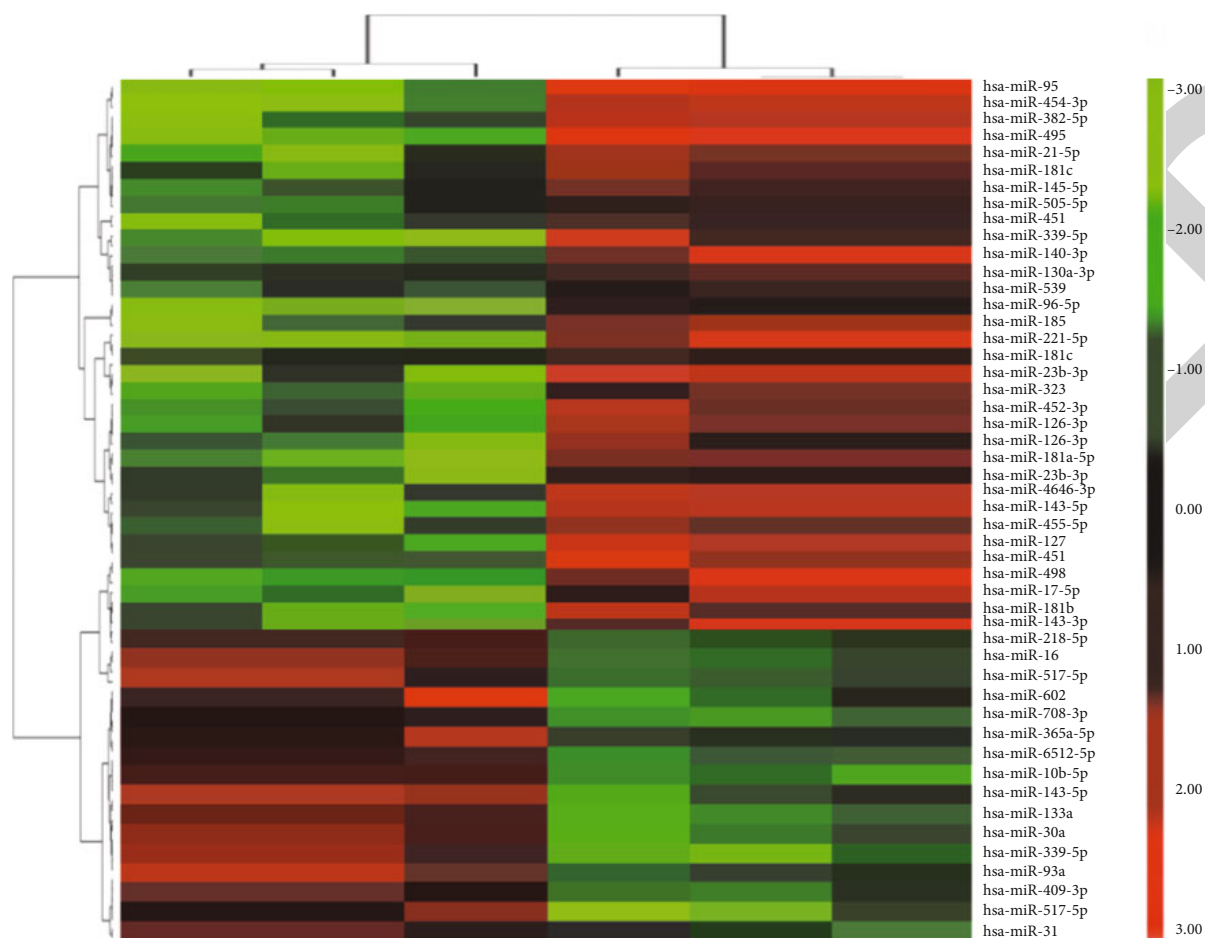
Figure 1: Heat map of miRNA microarray results in glioma brain tissue and normal tissue. Note: green denotes low expression level of miRNA, and red denotes high expression level of miRNA.

Table 1: Differential expression of miRNAs in glioma brain tissue.

Upregulated miRNA ($n = 16$)	Downregulated miRNA ($n = 33$)	
hsa-miR-10b-5p	hsa-miR-339-5p	hsa-miR-143-5p
hsa-miR-143-5p	hsa-miR-185	hsa-miR-23b-3p
hsa-miR-218-5p	hsa-miR-539	hsa-miR-455-5p
hsa-miR-133a	hsa-miR-454-3p	hsa-miR-140-3p
hsa-miR-93a	hsa-miR-323	hsa-miR-127
hsa-miR-16	hsa-miR-452-3p	hsa-miR-130a-3p
hsa-miR-30a	hsa-miR-95	hsa-miR-451
hsa-miR-517-5p	hsa-miR-126-3p	hsa-miR-96-5p
hsa-miR-339-5p	hsa-miR-382-5p	hsa-miR-498
hsa-miR-602	hsa-miR-126-3p	hsa-miR-505-5p
hsa-miR-409-3p	hsa-miR-495	hsa-miR-17-5p
hsa-miR-708-3p	hsa-miR-181a-5p	hsa-miR-221-5p
hsa-miR-517-5p	hsa-miR-21-5p	hsa-miR-181b
hsa-miR-365a-5p	hsa-miR-23b-3p	hsa-miR-181b
hsa-miR-6512-5p	hsa-miR-143-3p	hsa-miR-181c
hsa-miR-31	hsa-miR-4646-3p	hsa-miR-143-3p
	hsa-miR-145-5p	

expression level of E-cadherin was considerably reduced ($P < 0.05$), as presented by Figure 7.

4. Discussion

miRNA is an endogenetic noncoding RNA with regulatory function, which is widely involved in various physiological processes of cells, organogenesis, and the development of organisms [8]. Many research has revealed that miRNAs can modulate the onset, progression, and metastases of cancers and become markers and therapeutic targets of related tumors [9], thus providing possibilities for tumor diagnosis and treatment. Related studies have analyzed miRNA expression profiles in cancer and healthy samples at different stages and found that miRNA can distinguish between cancer and healthy samples [10]. miRNA is widely found in gliomas, but the expression levels of each miRNA are different in gliomas [11]. Relevant studies used real-time fluorescent quantification PCR reaction to identify the expression levels of 10 miRNAs in malignant tumors of different degrees and found that the higher the malignant degree of glioma, the lower the expression levels of miR-137 and miR-7, and miR-21, miR-17, miR-9, miR-26a, miR-23a, and miR-20a were subsequently increased [12]. Piwecka et al. demonstrated that miRNA differential expression may be an
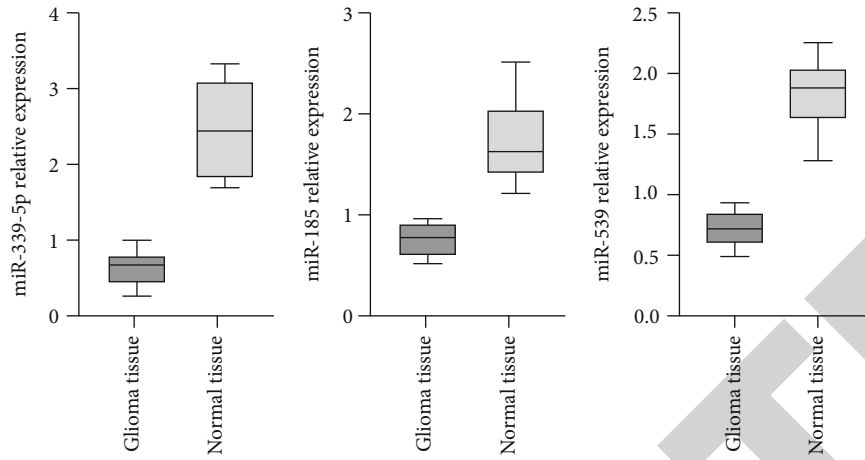
Figure 2: Expression of miRNAs in healthy and glioma samples.
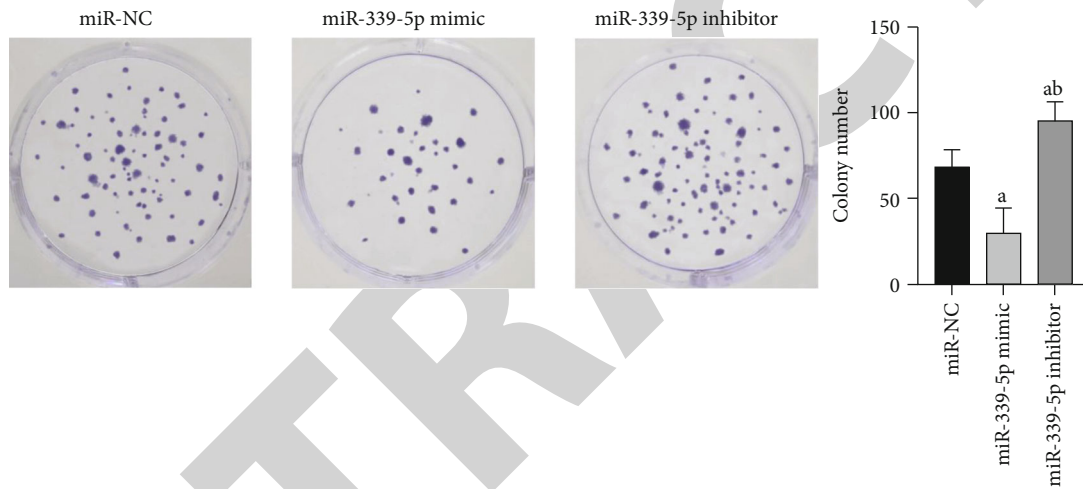
Figure 3: Comparison of proliferation capability of human glioma U87 cells in each group. Note: in contrast to miR-NC group, [a]$P < 0.05$ and [b]$P < 0.05$ vs. mir-339-5p mimic group.
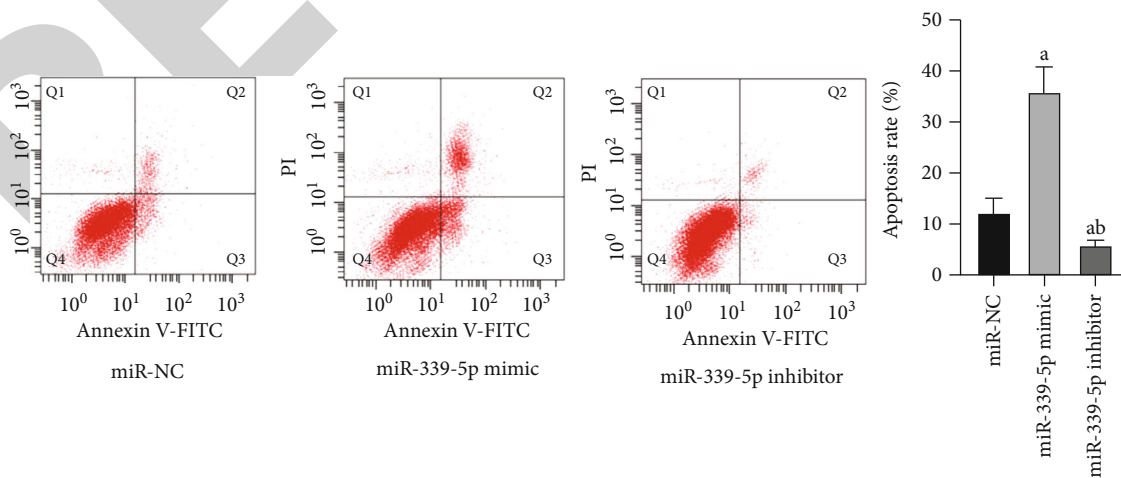
Figure 4: Apoptosis of human glioma U87 cells in all groups. Note: in contrast to miR-NC group, [a]$P < 0.05$ and [b]$P < 0.05$ vs. miR-339-5p mimic group.
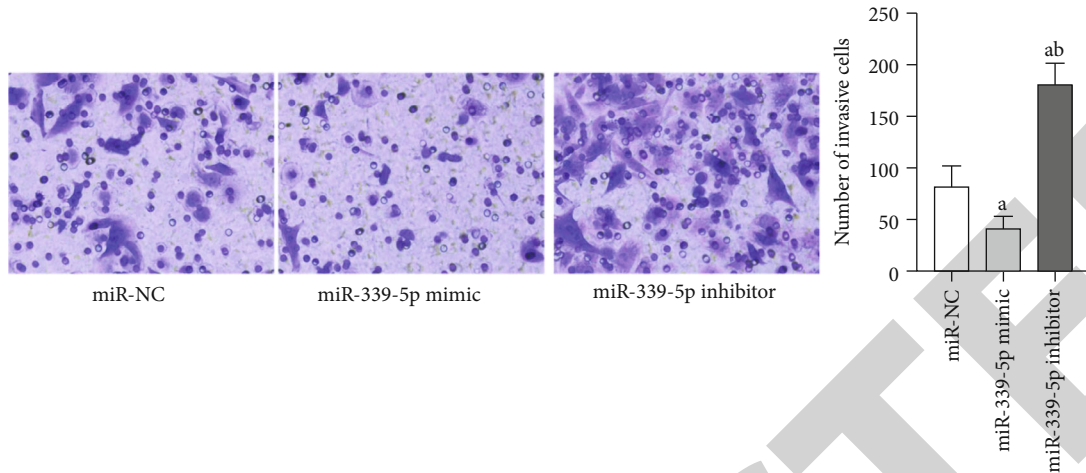
FIGURE 5: Comparison of invasion capability of human glioma U87 cells in each group. Note: in contrast to miR-NC group, [a]$P < 0.05$ and [b]$P < 0.05$ vs. miR-339-5p mimic group.
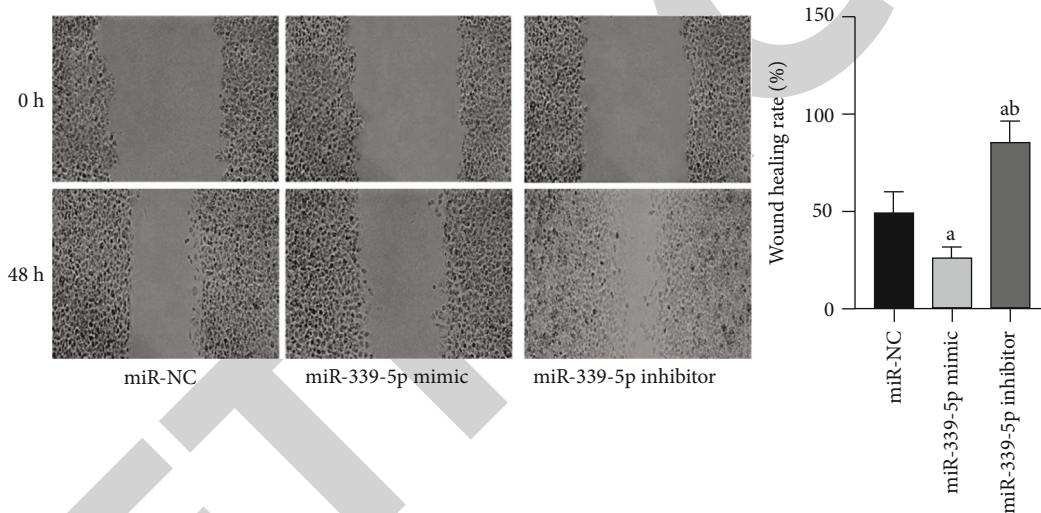
FIGURE 6: Comparison of migration ability of human glioma U87 cells in each group. Note: in contrast to miR-NC group, [a]$P < 0.05$ and [b]$P < 0.05$ vs. miR-339-5p mimic group.
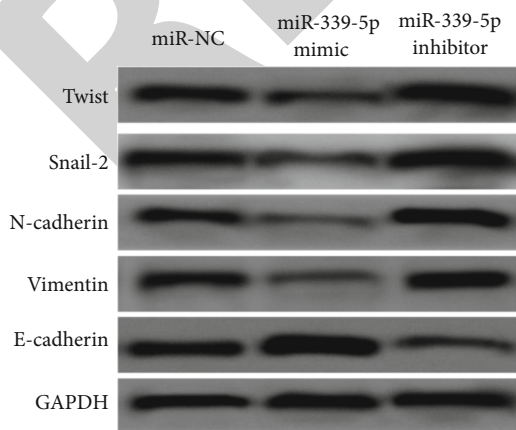
FIGURE 7: Expression of E-M transformation-related proteins in human glioma U87 cells of each group.

important molecular biomarker for gliomas and has potential research value in gene expression regulation [13]. Therefore, some miRNAs with abnormal expression in glioma tissues are pivotal for the etiopathogenesis of glioma.

Herein, gene chip technology was used to detect miRNAs, and a total of 49 miRNAs displayed different expression in glioma tissues, 16. The expression levels of 33 miRNAs were considerably upregulated, and the expression of 33 miRNAs was significantly downregulated. qRT-PCR was completed to verify the differentially sequenced miRNAs, and the outcomes revealed that the expression of miR-339-5p, miR-185, and miR-539 in glioma was lower than that in normal samples, and miR-339-5p was regulated downward most obviously. There are few reports about miR-339-5p in gliomas, and recent researchers have found that miR-339-5p is abnormally expressed in many solid tumors. Relevant research has revealed that miR-339-5p is regulated downward in pulmonary carcinoma lineage cells

[14], and miR-339-5p is regulated downward in colonic carcinoma tissular specimens and colonic carcinoma lineage cells [15]. In the present paper, the role of miR-339-5p in the proliferative, apoptotic, invasive, and migratory abilities of human glioma U87 cells was demonstrated. The outcomes revealed that the number of clones, invasion, and healing rate of human glioma U87 cells subjected to miR-339-5p mimic transfection were considerably smaller vs. cells subjected to miR-NC and miR-339-5P transfection. The cloning quantity, invasive quantity, and healing rate of human glioma U87 cells in the suppressor group were considerably greater vs. cells in the miR-NC transfection group. The apoptosis rate of human glioma U87 cells subjected to miR-339-5p mimic transfection was evidently smaller in contrast to cells subjected to miR-NC transfection, and the apoptosis rate of human glioma U87 cells subjected to miR-339-5p suppressor transfection was considerably smaller in contrast to cells subjected to miR-NC transfection. Those outcomes reveal that overly expressed miR-339-5p can suppress the proliferative, invasive, and migratory abilities of human glioma U87 cells and facilitate programmed cell death and suppress the expression of miR-339-5p on the contrary. Relevant research has revealed that miR-339-5P suppresses the migratory and invasive abilities of non-small-cell oncocytes and is closely related to cancer lymphatic metastases phase and lymphonodus metastases [16]. Other studies have shown that suppression of miR-339-5p expression elevated the migratory and invasive abilities of OVCAR5 cells, whereas in SKOV3 cells, upregulated miR-339-5P weakened the migratory and invasive abilities [17], like the results of this study.

Epithelial mesenchymal transformation denotes the conversion of epithelium cells into mesenchyme cells under normal or special physiologic conditions [18]. Studies have shown that epithelial-mesenchymal transformation is vital for the modulation of malignancies, and Twist, Snsnail, N-cadherin, Vimentin, and E-cadherin are pivotal transcriptional factors that regulate the process of epithelial-mesenchymal transformation and are vital for embryo development and tissue genesis [19] Zhang Y, Zhang Y, Zhang Y, et al. Epithelial-mesenchymal transformation is an early marker of tumor invasion and metastases [20]. Herein, our team finally verified the roles of miR-339-5p in E-M transformation in human glioma U87 cells. The outcomes revealed that overly expressed miR-339-5p repressed the protein expression levels of Twist, Snsnail, N-cadherin, and Vimentin, facilitated the expression level of E-cadherin, suppressed the expression level of miR-339-5p, elevated the protein expression levels of Twist, Snail-2, N-cadherin, and Vimentin, but reduced the protein expression level of E-cadherin. Related research has unveiled that the transfection process of miR-339-5P mimics reduced the proliferative, migratory, invasive abilities, and other abilities of prostate carcinoma cells, increased apoptosis rate, increased E-cadherin in epithelial mesenchymal transformation, and decreased snell-2 and N-cadherin expression [21]. Other research has unveiled that miR-339-5P suppresses metastases of non-small-cell carcinoma via modulating E-M transformation [22], like the results of this study.

In summary, 49 gliomas were preliminarily screened out in this study. The expression of miRNAs is significantly different between glioma and healthy samples. The low expression level of miR-339-5p in glioma can modulate the proliferative, apoptotic, invasive, and migratory of glioma U87 cells and might exert an effect on tumor suppression during the occurrence and development of glioma.

Data Availability

The data used to support the findings of this study are available from the corresponding author upon request.

Conflicts of Interest

The authors declare that they have no competing interest.

Acknowledgments

References

[1] Z. Zhang, S.-Z. Yang, Y.-F. Qi, and Y. Yin, "Identification of miR-21-5p/TET1-negative regulation pair in the aggressiveness of glioma cells," *Folia Neuropathologica*, vol. 59, no. 3, pp. 239–248, 2021.

[2] A. A. Campbell, R. D. Gartrell-Corrado, M. Mansukhani et al., "*SETD2* Mutation in an Aggressive Optic Nerve Glioma," *JAMA Ophthalmology*, vol. 138, no. 1, pp. 102–104, 2020.

[3] B. Luo and J. Zhang, "MicroRNA-16 inhibits the migration and invasion of glioma cell by targeting Bcl-2 gene," *Tropical Journal of Pharmaceutical Research*, vol. 19, no. 12, pp. 2499–2504, 2021.

[4] C. Cao, J. Zhang, Z. Zhang, Y. Feng, and Z. Wang, "Knockdown circular RNA circGFRA1 inhibits glioma cell proliferation and migration by upregulating microRNA-99a," *Neuroreport*, vol. 32, no. 9, pp. 748–756, 2021.

[5] Y. Zhou, Y. Peng, M. Liu, and Y. Jiang, "MicroRNA-181b inhibits cellular proliferation and invasion of glioma cells via targeting Sal-like protein 4," *Oncology Research*, vol. 25, no. 6, pp. 947–957, 2017.

[6] L. M. Moore, V. Kivinen, Y. Liu et al., "Transcriptome and small RNA deep sequencing reveals deregulation of miRNA biogenesis in human glioma," *Journal of Pathology*, vol. 229, no. 3, pp. 449–459, 2013.

[7] A. Pushkin, O. I. Kit, E. E. Rostorguev, D. H. Porksheyan, N. S. Kuznetsova, and S. E. Kavitskiy, "Aberrant miRNA expression in glioma," *Journal of Clinical Oncology*, vol. 37, article e13506, Supplement 15, 2019.

[8] L. Zhao, A. M. Bode, Y. Cao, and Z. Dong, "Regulatory mechanisms and clinical perspectives of miRNA in tumor radiosensitivity," *Carcinogenesis*, vol. 33, no. 11, pp. 2220–2227, 2012.

[9] H. Deng, Y. Guo, H. Song et al., "MicroRNA-195 and microRNA-378 mediate tumor growth suppression by epigenetical regulation in gastric cancer," *Gene*, vol. 518, no. 2, pp. 351–359, 2013.

Retraction

Retracted: Silencing of Long Noncoding RNA HLA Complex P5 (*HCP5*) Suppresses Glioma Progression through the *HCP5*-miR-205-Vascular Endothelial Growth Factor A Feedback Loop

BioMed Research International

This article has been retracted by Hindawi following an investigation undertaken by the publisher [1]. This investigation has uncovered evidence of one or more of the following indicators of systematic manipulation of the publication process:

(1) Discrepancies in scope

(2) Discrepancies in the description of the research reported

(3) Discrepancies between the availability of data and the research described

(4) Inappropriate citations

(5) Incoherent, meaningless and/or irrelevant content included in the article

(6) Manipulated or compromised peer review

The presence of these indicators undermines our confidence in the integrity of the article's content and we cannot, therefore, vouch for its reliability. Please note that this notice is intended solely to alert readers that the content of this article is unreliable. We have not investigated whether authors were aware of or involved in the systematic manipulation of the publication process.

Wiley and Hindawi regrets that the usual quality checks did not identify these issues before publication and have since put additional measures in place to safeguard research integrity.

We wish to credit our own Research Integrity and Research Publishing teams and anonymous and named external researchers and research integrity experts for contributing to this investigation.

The corresponding author, as the representative of all authors, has been given the opportunity to register their agreement or disagreement to this retraction. We have kept a record of any response received.

References

[1] R. Cheng, L. Ji, H. Su et al., "Silencing of Long Noncoding RNA HLA Complex P5 (*HCP5*) Suppresses Glioma Progression through the *HCP5*-miR-205-Vascular Endothelial Growth Factor A Feedback Loop," *BioMed Research International*, vol. 2022, Article ID 3092063, 14 pages, 2022.

Research Article

Silencing of Long Noncoding RNA HLA Complex P5 (*HCP5*) Suppresses Glioma Progression through the *HCP5*-miR-205-Vascular Endothelial Growth Factor A Feedback Loop

Rui Cheng, Lei Ji, Haiyang Su, Lijun Wang, Ding Jia, Xiaohui Yao, and Hongming Ji

Department of Neurosurgery, Shanxi Provincial People's Hospital, Taiyuan, 030012 Shanxi, China

Correspondence should be addressed to Hongming Ji; jihongmingedu@126.com

Long noncoding RNA (lncRNA) HLA complex P5 (*HCP5*) is correlated with multiple diseases, especially cancers. However, it remains to be further studied whether *HCP5* is involved in the malignant behaviors of gliomas. This study is aimed at investigating the role and regulation mechanisms of *HCP5* in gliomas. *HCP5* expression in glioma tumor tissues and its association with glioma patients' survival were analyzed based on RNA-sequencing data. The expression of *HCP5* was also examined in glioma cells. Then, *HCP5* was downregulated in U251 cells and/or primary glioblastoma cells to explore its effects on cell proliferation and migration. The influence of *HCP5* downregulation on tumor growth was confirmed in xenograft mice. About the mechanism, we investigated whether *HCP5* functioned via interacting with microRNA- (miR-) 205 and regulating vascular endothelial growth factor A (*VEGF-A*) expression in gliomas. Results showed that *HCP5* upregulation was found in glioma tissues and cell lines. Patients with high *HCP5* expression showed lower survival probability and shorter survival time. *HCP5* downregulation inhibited cell proliferation and migration and mitigated tumor growth. miR-205 was downregulated in glioma cells. Knockdown of *HCP5* led to miR-205 upregulation and *VEGF-A* downregulation. miR-205 overexpression exhibited the similar effects as *HCP5* downregulation on cell viability and proliferation. And *VEGF-A* overexpression could reverse the effects of *HCP5* downregulation on cell viability and proliferation, as well as tumor growth. In conclusion, *HCP5* silencing suppressed glioma progression through the *HCP5*-miR-205-*VEGF-A* feedback loop.

1. Introduction

Gliomas are the type of primary neoplasias that occur in the brain, accounting for over eighty percent of primary brain tumors [1, 2]. Glioblastomas (GBMs), the most lethal primary gliomas, are grade IV gliomas classified by the World Health Organization [3, 4]. Currently, multiple therapeutic strategies have been applied in gliomas, such as surgical resection, chemotherapy, and radiotherapy; however, the prognosis is still very poor. The median survival is only 15 months in GBM patients, and 5-year survival rate postdiagnosis is proven to be 5.1% [5, 6]. Hence, the underlying mechanisms of glioma progression need further studies [4].

Long noncoding RNAs (lncRNAs), the transcripts exceeding 200 nucleotides in length, play important roles in cancers [7]. Increasing evidence reveals that many lncRNAs are dysregulated and implicated in the progression of many cancers, including gliomas, and they might act as therapeutic targets [8–13]. lncRNA HLA complex P5 (*HCP5*), firstly discovered in 1993, is correlated with a large majority of diseases, especially cancers [14]. *HCP5* was revealed to be a carcinogenic RNA contributing to the proliferation, migration, invasiveness, and angiogenic ability of follicular thyroid carcinoma cells [15]. *HCP5* promoted prostate cancer cell proliferation via interaction with microRNA- (miR-) 4656 [16]. Considering the reported malignant

effects of *HCP5*, it is uncertain whether *HCP5* has a similar role in gliomas. Up to now, only one study reported that *HCP5* was upregulated in gliomas and its downregulation mitigated the malignant biological behavior of glioma cells [17].

miRs are endogenous short noncoding RNA strands with ~22 nucleotides that are responsible for 40%-60% of posttranscriptional regulation of gene expression [18]. Current thinking holds that lncRNAs function in cancers through serving as sponges for miRs. For example, *HCP5* contributed to the epithelial-mesenchymal transition (EMT) of colorectal cancer via interacting with miR-139-5p [19]. In anaplastic thyroid cancer, *HCP5* knockdown showed a tumor-suppressive function, which was proven to be correlated with the upregulation of miR-128-3p [20]. For gliomas, *HCP5* has been demonstrated to affect the malignant behavior of glioma cells via interacting with a tumor suppressor, miR-139, along with the alteration of Runt-related transcription factor 1 [17]. miR-205 is a highly conserved miRNA in many species. Studies have demonstrated that miR-205 could act as tumor promotor or suppressor in different cancers [21]. It has been demonstrated to be downregulated and functioned as a tumor suppressor in gliomas [22]. However, whether other miRs including miR-205 lie downstream of *HCP5* in gliomas still needs to be further studied.

This study is aimed at evaluating the role *HCP5* in gliomas both *in vitro* and *in vivo*. Moreover, the molecular mechanism of *HCP5* in the progression of gliomas was analyzed mainly focusing on the miR-205/vascular endothelial growth factor A (*VEGF-A*) axis.

2. Material and Methods

2.1. RNA-Sequencing Data Processing and Analysis. Based on the RNA-sequencing data ($n = 9,736$ for tumor samples; $n = 8,587$ for normal samples) from The Cancer Genome Atlas (TCGA) and Genotype-Tissue Expression (GTEx) projects, a web-based tool named Gene Expression Profiling Interactive Analysis (GEPIA: http://gepia.cancer-pku.cn/) was used to analyze gene expression [23]. The differential expression analyses of *HCP5* were performed via GEPIA in several cancer types, including cervical squamous cell carcinoma and endocervical adenocarcinoma (CESE; tumor: $n = 306$; normal: $n = 13$), cholangiocarcinoma (CHOL; tumor: $n = 36$; normal: $n = 9$), colon adenocarcinoma (COAD; tumor: $n = 275$; normal: $n = 349$), esophageal carcinoma (ESCA; tumor: $n = 182$; normal: $n = 286$), kidney chromophobe (KICH; tumor: $n = 66$; normal: $n = 53$), acute myeloid leukemia (LAML; tumor: $n = 173$; normal: $n = 70$), stomach adenocarcinoma (STAD; tumor: $n = 408$; normal: $n = 211$), and GBM (tumor: $n = 163$; normal: $n = 207$). Survival analysis of 224 glioma patients was also analyzed by GEPIA. These patients were assigned into two groups according to the median value of *HCP5* expression.

2.2. Cell Culture. Commercially available human GBM cell lines, including U87 MG (ATCC® HTB-14™) and A172 (ATCC® CRL-1620™), were purchased from the American

Type Culture Collection (ATCC; Rockville, MD, USA). Normal human astrocytes (NHA) and human GBM cell line U251 were both obtained from the China Academia Sinica Cell Repository (Shanghai, China). GBM cells were cultured in Dulbecco's modified Eagle's medium (DMEM; Gibco, Carlsbad, CA, USA) containing 10% fetal bovine serum (FBS; Gibco), while NHA cells were grown in MCDB-131 medium (Sigma; St. Louis, MO, USA) containing 3% FBS and 10× G-5 Supplement (Gibco). Primary glioblastoma cell line was established as previously described [24]. Briefly, tumor tissue was obtained from one GBM patient. After removing the vessels, clotted blood, and charred tissue, sample was dissociated by Collagenase Type IVa (250 U/mL) and Pronase E (2.5 U/mL) for 1 h at 37°C. Then, cells were centrifuged at $300 \times g$ for 5 min at 4°C, resuspended in DMEM containing 10% FBS, and put in a cell culture flask. The cell culture medium was changed every 2 days. Cells were all maintained in a humidified incubator with an atmosphere of 5% CO_2 at 37°C.

2.3. Cell Transfection. Small interfering RNAs (siRNAs) against *HCP5* (si-HCP5#1, si-HCP5#2, and si-HCP5#3), their negative control (si-NC), miR-205 mimics, and scrambled miRs (NC mimics) were synthesized by GenePharma Co., Ltd. (Shanghai, China). Short hairpin RNA (shRNA) targeting *HCP5* (sh-HCP5) and its negative control (sh-NC) were cloned into pGPU6/GFP/Neo plasmid by Gene-Pharma Co., Ltd. Full-length human *VEGF-A* gene was ligated into pcDNA3.1 plasmid (Invitrogen, Carlsbad, CA, USA), with empty pcDNA3.1 vector as a control (pcDNA3.1). These vectors were transfected into U251 cells using Lipofectamine 2000 (Invitrogen) following the manufacturer's instructions. Transfected cells were collected at 48 h after transfection to do the downstream experiments.

2.4. Cell Viability Assay. U251 or primary glioblastoma cells (2×10^3 cells per well) were seeded in 96-well plates. After transfection, 20 μL 3-(4,5-dimethylthiazol-2-yl)-5-(3-carboxymethoxyphenyl)-2-(4-sulfophenyl)-2H-tetrazolium (MTS) (Promega, Madison, WI, USA) per well was added on days 0, 1, 2, 3, 4, and 5, respectively. After 2 h incubation at 37°C, the absorbance value was measured by a plate reader at a test wavelength of 490 nm.

2.5. Scratch Wound-Healing Assay. U251 or primary glioblastoma cells (4×10^5 cells per well) were seeded in 6-well culture plates. Cells were transfected with siRNA against *HCP5* (si-HCP5) or control siRNA (si-NC). 48 h after transfection, a linear scratch was created by a 200 μL pipette tip, and cellular debris were removed by washing with phosphate buffer saline for three times. After culturing for another 48 h in serum-free medium, images of the scratched region were photographed by a microscope equipped with a camera (Nikon, Tokyo, Japan).

2.6. Proliferation Assay. Cell proliferative ability was determined by 5-ethynyl-2′-deoxyuridine (EdU) cell proliferation assay kit (RiboBio, Guangzhou, China) as previously described [25]. Firstly, transfected cells were seeded into

96-well plates. Following adhesion of the cells, 50 μM EdU was added into each well, and cells were incubated at 37°C for 4 h, followed by fixation and permeabilization. Then, the cell nuclei were stained with 4,6-diamidino-2-phenylindole, dihydrochloride (DAPI). A fluorescence microscopy (Olympus, Tokyo, Japan) was employed to obtain the images. For each group, EdU-positive cells were counted as the average number in five random fields.

2.7. *In Vivo Xenograft Experiments.* Eight-week-old male C57BL/6 nude mice, obtained from the Guangdong Medical Laboratory Animal Center (Guangzhou, China), were divided into sh-HCP5 and sh-NC groups, or divided into pcDNA3.1-VEGF-A, pcDNA31, pcDNA31+sh-HCP5, and pcDNA3.1-VEGF-A+sh-HCP5 groups ($n = 10$ per group). After transfection with indicated plasmid, U251 cells (5×10^6 cells per mouse) were subcutaneously injected into mice. Tumor volumes were recorded every 5 days from day 8 after injection according to the following formula: volume $(\text{mm}^3) = \text{length} \times \text{width}^2/2$. All mice were euthanized by intraperitoneal injection of 100 mg/kg pentobarbital at 4 weeks postinjection, and tumor tissues were excised for further experiments. The animal experiments were carried out according to the Guide for the Care and Use of Experimental Animals of the National Institutes of Health, and the experimental protocol was approved by the Ethics Committee of the Shanxi Provincial People's Hospital (Shanxi, China).

2.8. *Dual-Luciferase Reporter Assay.* The binding sequence of miR-205 and *HCP5* was predicted by IntaRNA 2.0 online software (http:/http://rna.informatik.uni-freiburg.de/). The wild-type or mutant sequence of *HCP5* was cloned into pmirGLO dual-luciferase vector to construct luciferase reporter vectors, named HCP5 WT or HCP5 MT, respectively, and dual-luciferase reporter assay was carried out according to a previous study [26]. HEK293T cells were seeded into 96-well plates, followed by cotransfection with luciferase reporter vectors (HCP5 WT or HCP5 MT) and miRs (NC mimics or miR-205 mimics). After transfection for 48 h, the luciferase activity of transfected cells was determined by a Dual-Luciferase Reporter Assay System (Promega, Madison, WI, USA), as suggested by the manufacturer's instructions. Renilla luciferase was an internal reference.

2.9. *Quantitative Reverse Transcription PCR (qRT-PCR).* Total RNA extracted by TRIzol reagent (Invitrogen) was used as a template for the synthesis of first-strand cDNA with the SuperScript® VILO™ cDNA Synthesis Kit (Invitrogen), and all steps were performed as the manufacturer's instructions. *HCP5* expression levels were obtained using a One Step SYBR® PrimeScript™ PLUS RT-RNA PCR Kit (TaKaRa Biotechnology, Dalian, China). The expression level of miR-205 was assessed using an All-in-One™ miRNA qRT-PCR reagent kit (GeneCopoeia Inc., Rockville, MD, USA). Besides, *VEGF-A* mRNA expression levels were measured by the PrimeScript™ 1st Strand cDNA Synthesis kit (TaKaRa) and the TB Green™ Premix Ex Taq™ II (TaKaRa)

TABLE 1: The primers used for real-time PCR.

Name	Primer sequences (5′ to 3′)
miR-205	Forward: GGGTCCTTCATTCCACCGG
	Reverse: CAGTGCGTGTCGTGGAGT
U6	Forward: GCTTCGGCAGCACATATACTAAAAT
	Reverse: CGCTTCACGAATTTGCGTGTCAT
HCP5	Forward: GACTCTCCTACTGGTGCTTGGT
	Reverse: CACTGCCTGGTGAGCCTGTT
VEGF-A	Forward: TCTTGGGTGCATTGGAGCCT
	Reverse: AGCTCATCTCTCCTATGTGC
GAPDH	Forward: CAATGACCCCTTCATTGACC
	Reverse: GACAAGCTTCCCGTTCTCAG

for reverse transcription and qRT-PCR, respectively. Primers used in this study are shown in Table 1, and the relative quantification of genes was calculated by the $2^{-\Delta\Delta Ct}$ method [16]. GAPDH was chosen as the housekeeping gene for *HCP5* and *VEGF-A*, whereas U6 was used as that for miR-205.

2.10. *Western Blot Analysis.* Proteins in U251 cells and tumor tissues were extracted using radioimmunoprecipitation assay (RIPA) lysis buffer containing 1 mM phenylmethanesulfonyl fluoride (PMSF) (both from Beyotime Biotechnology, Shanghai, China). After centrifugation, proteins in the supernatant were quantified using the BCA™ Protein Assay Kit (Pierce, Appleton, WI, USA). Then, extracted proteins were loaded (50 μg/lane) and separated by dodecyl sulfate, sodium salt-polyacrylamide gel electrophoresis. Subsequently, proteins were transferred from the gel to the polyvinylidene difluoride membranes. Protein-bound transfer membranes were blocked by 5% nonfat milk for 1 h at room temperature, and then, membranes were successively incubated with respective primary antibodies (VEGF-A (ab214424) or GAPDH (ab181602), both were from Abcam (Cambridge, UK)) and HRP-conjugated secondary antibody (goat anti-rabbit, ab205718, Abcam, Cambridge, UK). Specific protein bands were visualized by using an ECL detection reagent (GE Healthcare, Braunschweig, Germany). Band intensity of VEGF-A was quantified using the ImageJ software (National Institutes of Health, Bethesda, MA, USA), with normalization to GAPDH.

2.11. *Statistical Analysis.* All experiments were repeated three times. Data are presented as the mean ± standard deviation (SD). Statistical analysis was carried out with GraphPad Prism 6 software (GraphPad, San Diego, CA, USA). The differences between two groups were analyzed by Student's t test. The differences among groups were compared by one-way analysis of variance (ANOVA) with Bonferroni post hoc test. Survival analysis was performed by the Kaplan-Meier method. $P < 0.05$ was considered as statistically significant.

(a)

(b)

(c)

(d)
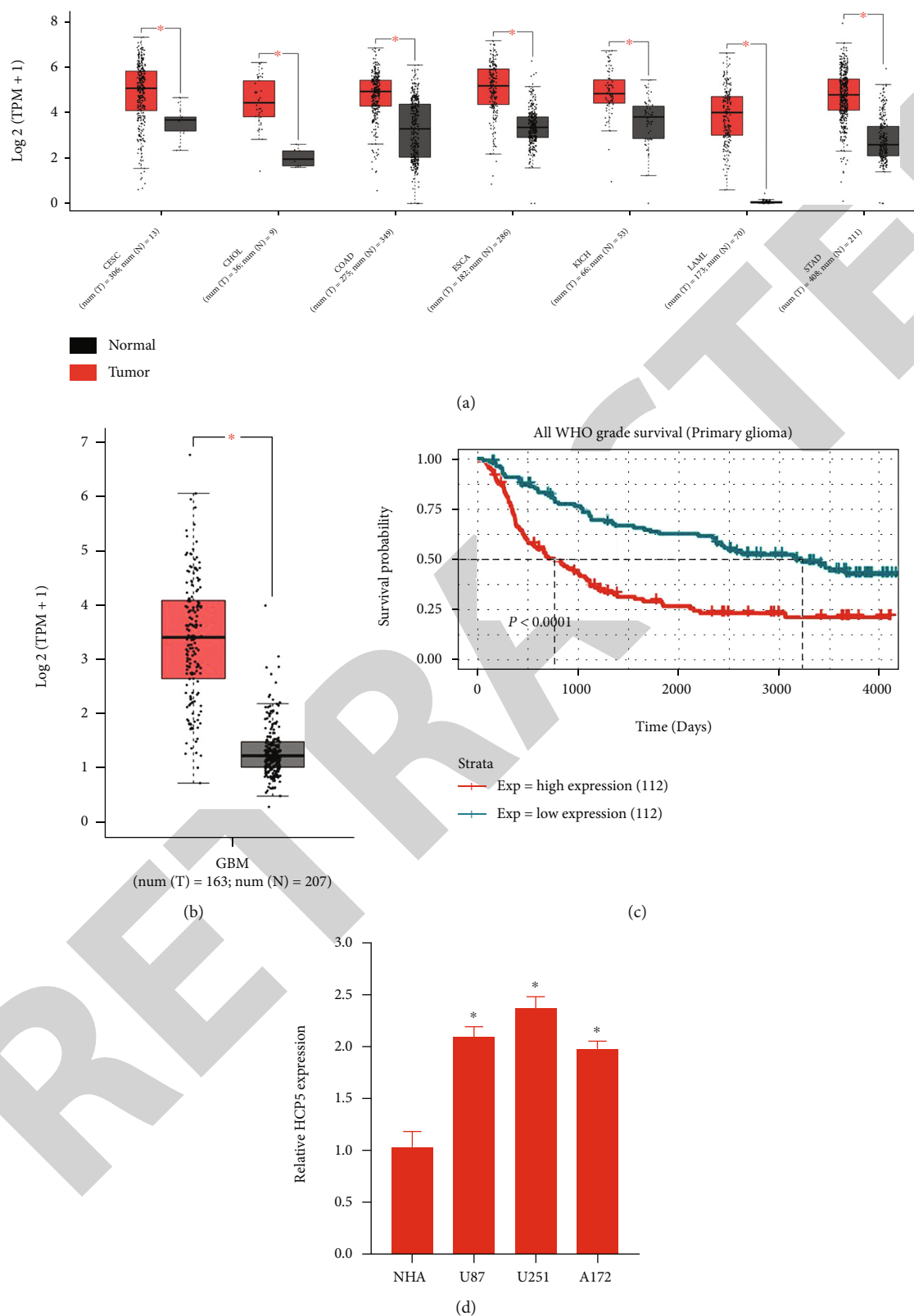
Figure 1: Potential correlation between *HCP5* overexpression and glioma. (a) The expression of *HCP5* in diverse cancer types, which was analyzed by GEPIA. (b) *HCP5* expression was assayed in GBM using GEPIA software. The boxes show the median and interquartile range, and the whiskers show the minimum and maximum values. (c) Prognostic value of *HCP5* in glioma patients detected by GEPIA. (d) The expression of *HCP5* in GMB cell lines and normal NHA cells, analyzed by qRT-PCR. Data are presented as the mean ± SD. *$P < 0.05$. TPM: transcripts per million.

(a)

(b)

(c)

(d)

Figure 2: Continued.

(e)

(f)

(g)

(h)

Figure 2: Continued.

(i)

(j)

(k)

(l)
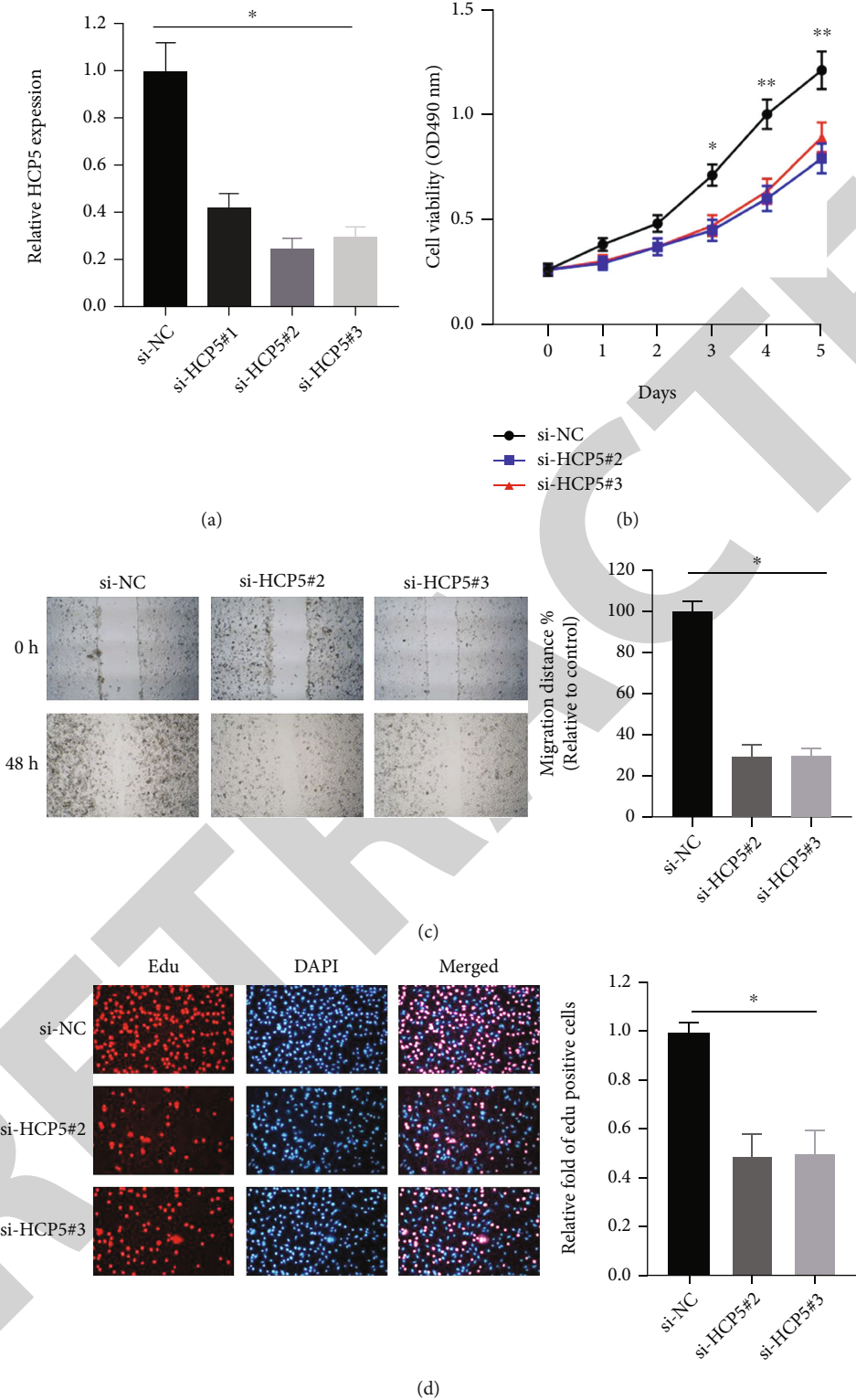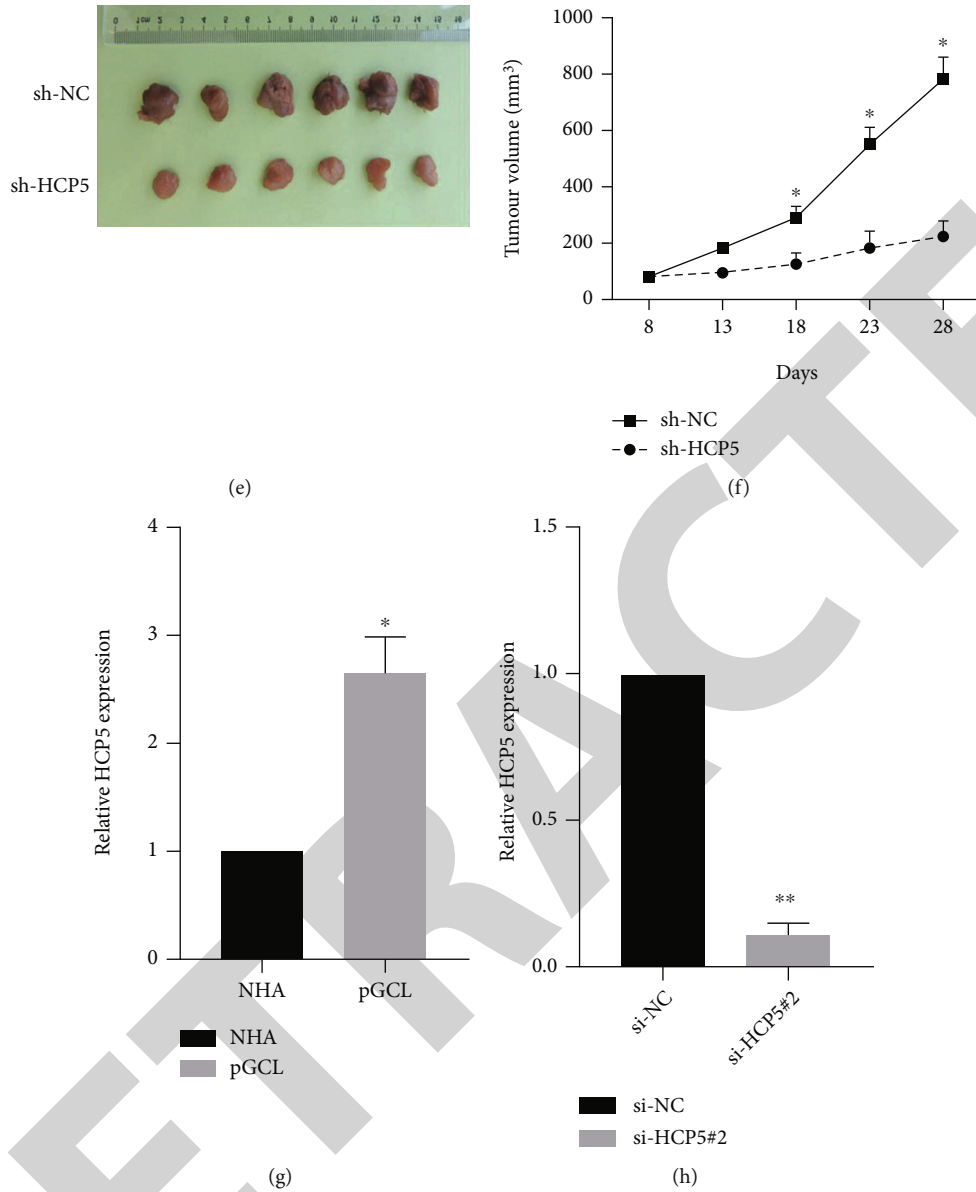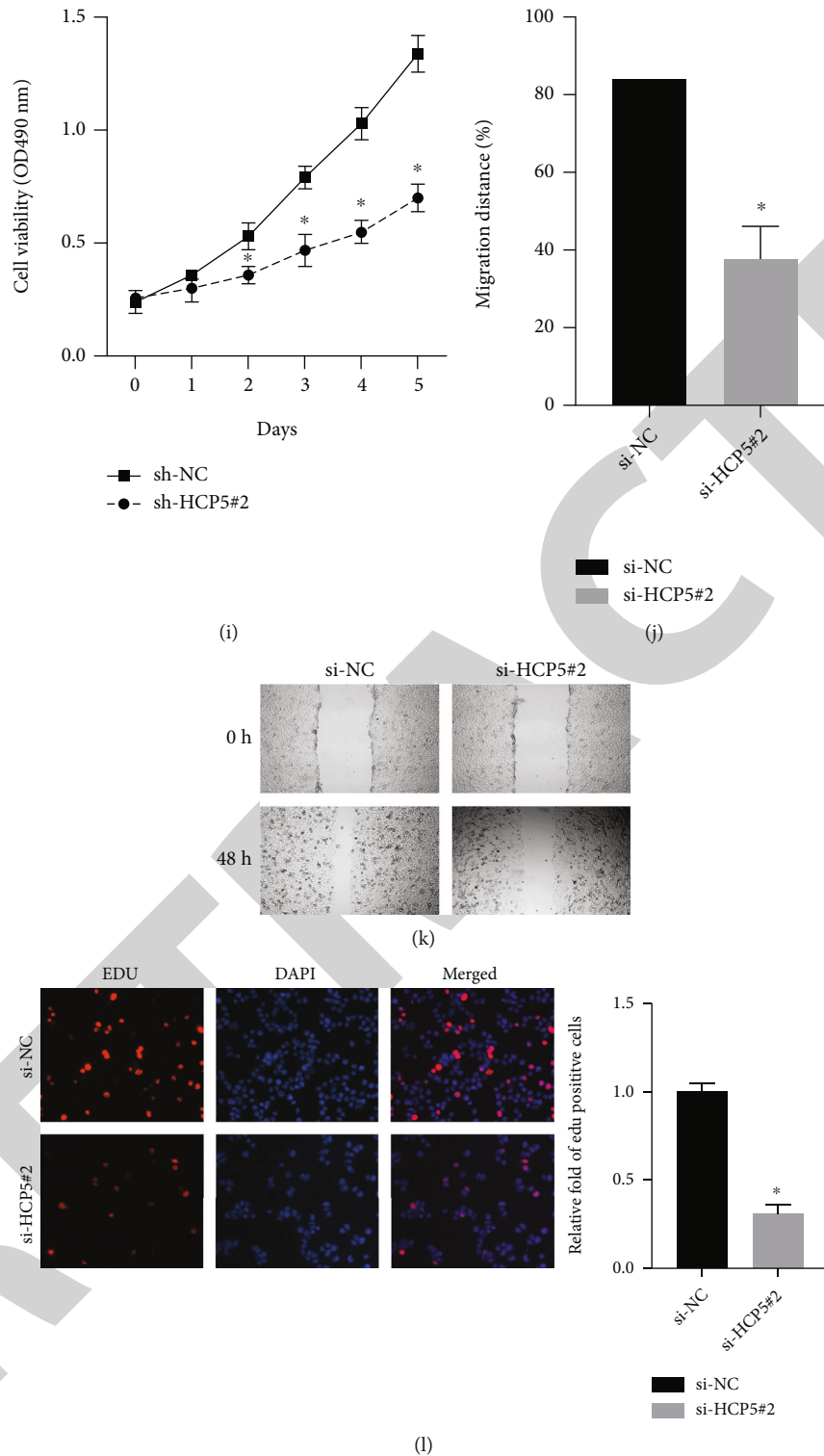
FIGURE 2: *HCP5* downregulation inhibited cell viability and migration and mitigated tumor growth. U251 cells were transfected with si-NC, si-HCP5#1, si-HCP5#2, or si-HCP5#3. (a) *HCP5* expression was determined by qRT-PCR. (b) Cell viability was assessed by MTS assay. (c) Cell migration was examined by scratch wound-healing assay. (d) Proliferation was determined by EdU incorporation proliferation assay. U251 cells were transfected with sh-NC or sh-HCP5 and then injected into nude mice. (e) Tumors isolated from nude mice. (f) Tumor volume was recorded every 5 days from day 8 after injection. (g) *HCP5* expression in primary glioblastoma cells (pGCL) and NHA cells was measured by qRT-PCR. pGCL cells were transfected with si-HCP5#2. (h) *HCP5* expression level was analyzed. (i) Cell viability was assessed by MTS assay. (j, k) The migration of U251 cells was examined by scratch wound-healing assay after transfection with si-HCP5#2 and si-NC. And the wound-healing rate was measured. (l) EdU was used to examine the proliferation of pGCL cells. Data are presented as the mean ± SD. *$P < 0.05$; **$P < 0.01$.

(a)

(b)

miR-2O5   5'-   TTC   GGAGTCTG-3'
                      TCCTTCA   CACC
                      | | | | | | | | | | |
                      AGGAAGT   GTGG
HCP5   3'-TTC..GGGTA   TGA   ACAGC..CAG-5'
                            | |
                          873   860
HCP5
Mutated Type   3'- … GGGTATCCTTCATGACACCACAGC…-5'

(c)

(d)

Control
NC mimics
miR-205 mimics

(e)

mimics NC
miR-205 mimics
mimics NC + si-HC5#2
mimics mimics + si-HC5#2

(f)

Figure 3: Continued.

(g)
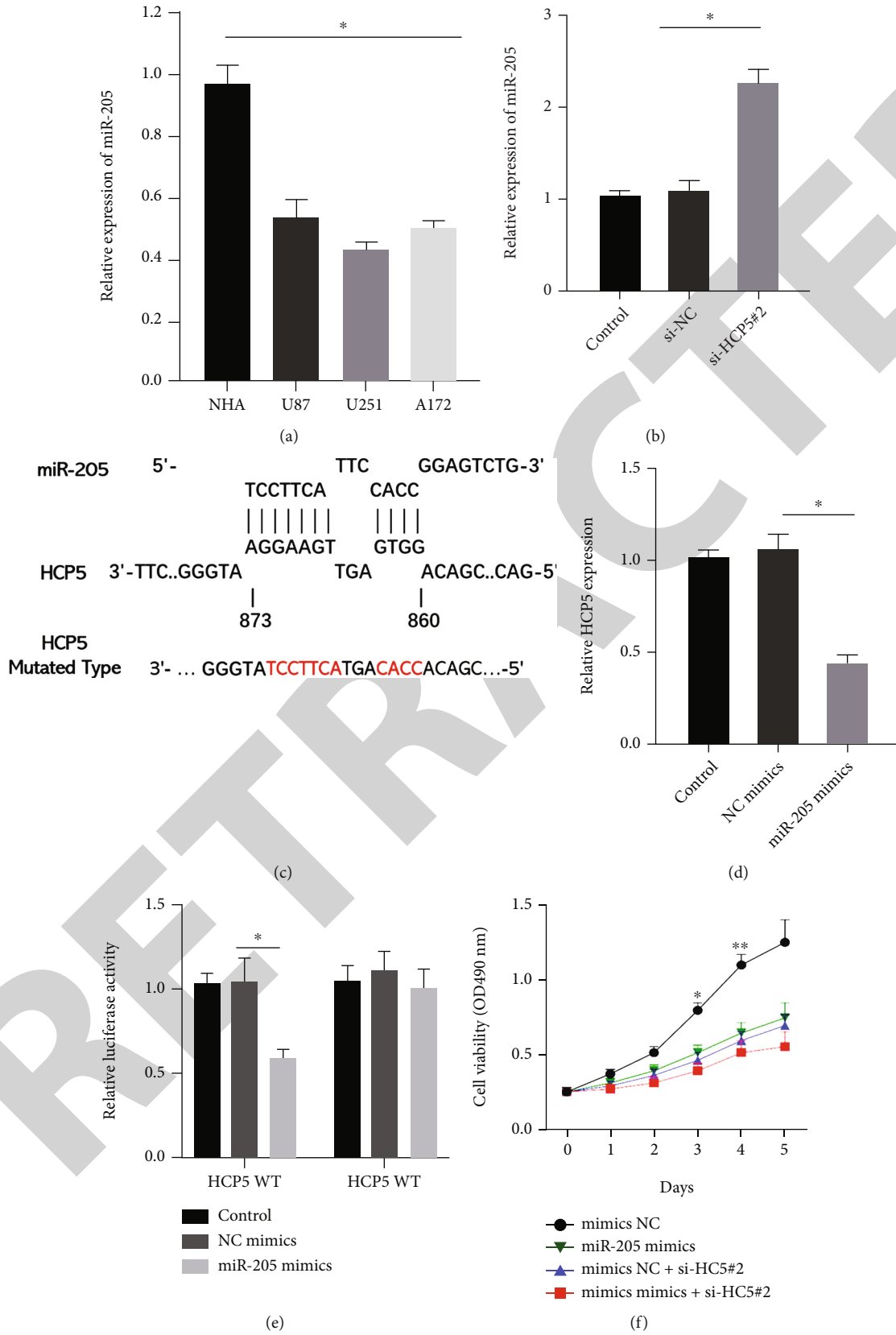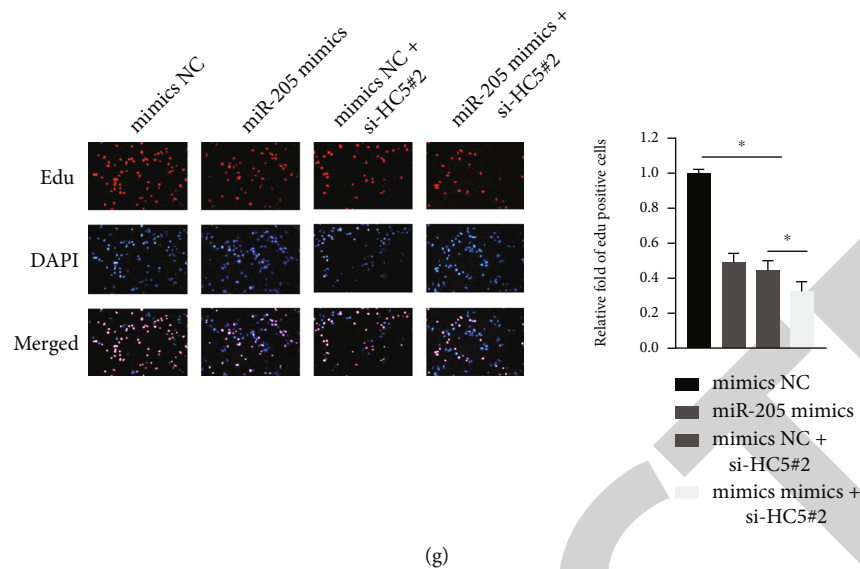
Figure 3: *HCP5* downregulation repressed cell proliferation via interaction with miR-205. (a) miR-205 expression was assessed by qRT-PCR. U251 cells were transfected with si-NC or si-HCP5#2. Untransfected U251 cells acted as a control. (b) miR-205 expression was determined by qRT-PCR. (c) The binding sites between *HCP5* and miR-205 were predicted by IntaRNA 2.0. U251 cells were transfected with NC mimics or miR-205 mimics. Untransfected U251 cells acted as a control. (d) *HCP5* expression was assessed by qRT-PCR. (e) Relative luciferase activity was performed by dual-luciferase reporter assay. (f) Cell viability was evaluated by MTS assay in transfected U251 cells. (g) Proliferation was determined by EdU incorporation proliferation assay in transfected U251 cells. Data are presented as the mean ± SD. $^*P < 0.05$; $^{**}P < 0.01$.

3. Results

3.1. HCP5 Was Aberrantly Upregulated in Glioma Specimens and Commercial Glioma Cells.

We firstly compared *HCP5* expression in cancer tissue samples and healthy control samples. Results in Figure 1(a) showed that *HCP5* levels in CESC, CHOL, COAD, ESCA, KICH, LAML, and STAD were all prominently higher than those in normal samples (all $P < 0.05$). Similarly, *HCP5* expression was significantly upregulated in GBM samples when compared to normal samples ($P < 0.05$, Figure 1(b)). Using the RNA-sequencing data from the Chinese Glioma Genome Atlas, the relationship between *HCP5* expression and the prognosis of 224 glioma patients was analyzed. Results revealed that patients with high *HCP5* expression had lower survival probability and shorter survival times than those with low *HCP5* expression (both $P < 0.0001$, Figure 1(c)). Moreover, the expression of *HCP5* in GBM cell lines (i.e., U87 MG, U251, and A172) was notably higher than that in normal NHA cells (all $P < 0.05$, Figure 1(d)). These results implied that *HCP5* overexpression might be correlated with GBM progression.

3.2. HCP5 Downregulation Inhibited Cell Proliferation and Migration and Mitigated Tumor Growth.

The influences of *HCP5* on the malignant behaviors of GBM were analyzed via silencing *HCP5* both *in vitro* and *in vivo*. In this study, we designed three siRNAs against *HCP5*. *HCP5* levels in cells transfected with the three siRNAs against *HCP5* were significantly lower than those in cells with si-NC ($P < 0.05$, Figure 2(a)), and si-HCP5#2 and si-HCP5#3 showed higher knockdown efficiency than si-HCP5#1. Figure 2(b) shows that cell viability was apparently mitigated after *HCP5* downregulation. Wound-healing assay in Figure 2(c) showed that knockdown of *HCP5* decreased cell migration, as the migration distance was obviously reduced following *HCP5* downregulation ($P < 0.05$). As depicted in Figure 2(d), compared with the si-NC group, the percentage of EdU-positive cells was decreased by *HCP5* downregulation (both $P < 0.01$). Furthermore, the effects of *HCP5* on GBM were investigated in nude mice. Tumor growth was slower in mice injected with *HCP5*-silenced U251 cells compared to those injected with U251 cells transfected with sh-NC (all $P < 0.05$, Figures 2(e) and 2(f)). Additionally, the effects of *HCP5* on GBM were also evaluated in primary glioblastoma cell line. We found that *HCP5* expression was higher in primary glioblastoma cells than in NHA cells ($P < 0.05$, Figure 2(g)). Downregulation of *HCP5* in primary glioblastoma cells significantly suppressed cell viability, migration, and the percentage of EdU-positive cells (all $P < 0.05$, Figures 2(h)–2(l)). These data suggested that *HCP5* was involved in tumorigenesis, as silencing of *HCP5* suppressed cell proliferation and migration *in vitro*, and repressed tumor growth *in vivo*.

3.3. HCP5 Downregulation Repressed Cell Proliferation via Interaction with miR-205.

The regulatory mechanism of *HCP5* in GBM was further studied. miR-205 expression was found to be apparently downregulated in GBM cell lines including U87 MG, U251, and A172 cells relative to NHA cells (all $P < 0.05$, Figure 3(a)). We also found that miR-205 level was obviously higher in *HCP5*-silenced U251 cells than the si-NC group ($P < 0.05$, Figure 3(b)), which indicated that there might be a negative correlation between miR-205 and *HCP5* in GBM. The potential binding sites

(a)

(b)

(c)

(d)

Figure 4: Continued.

(e)

(f)

(g)
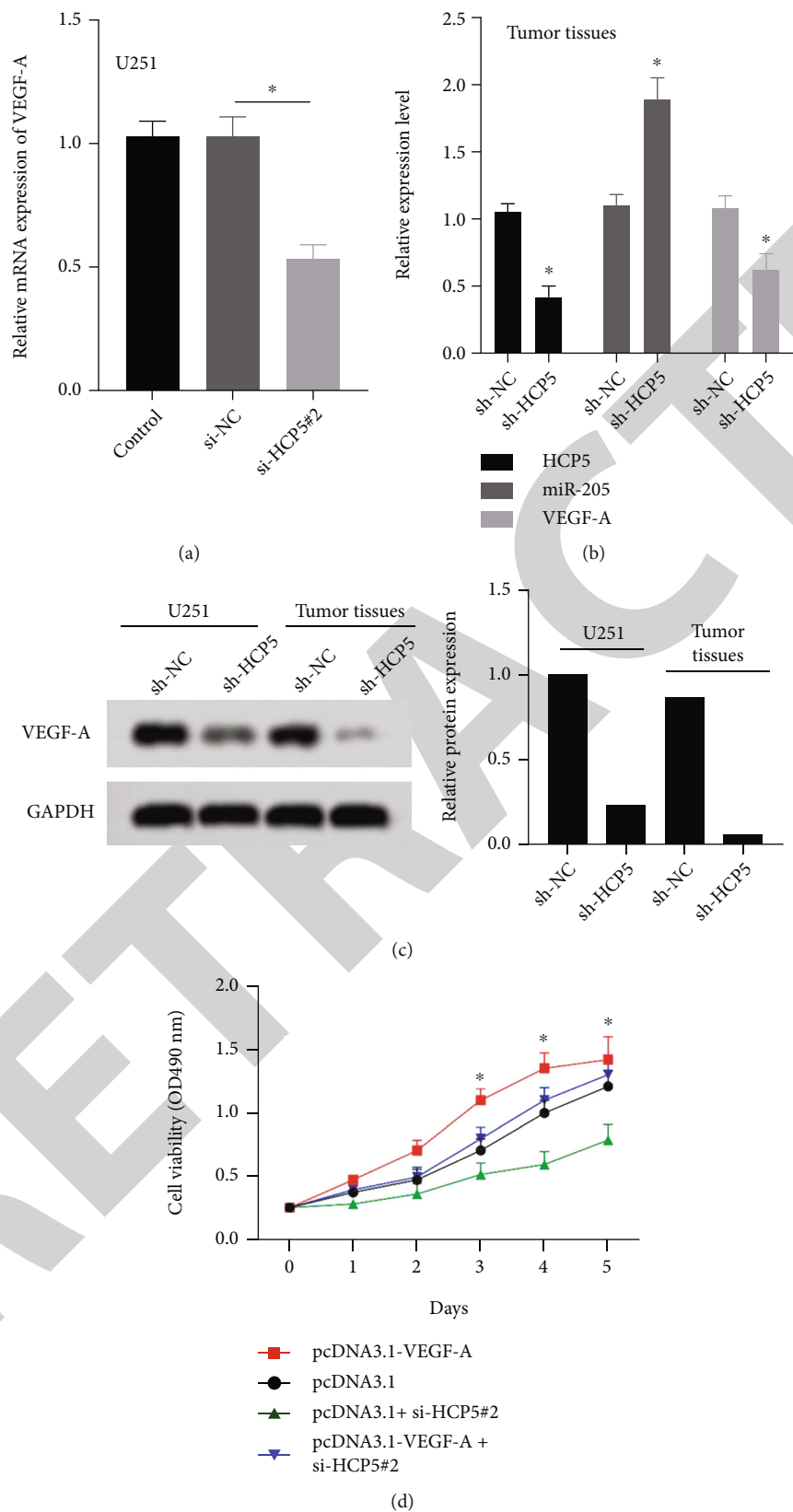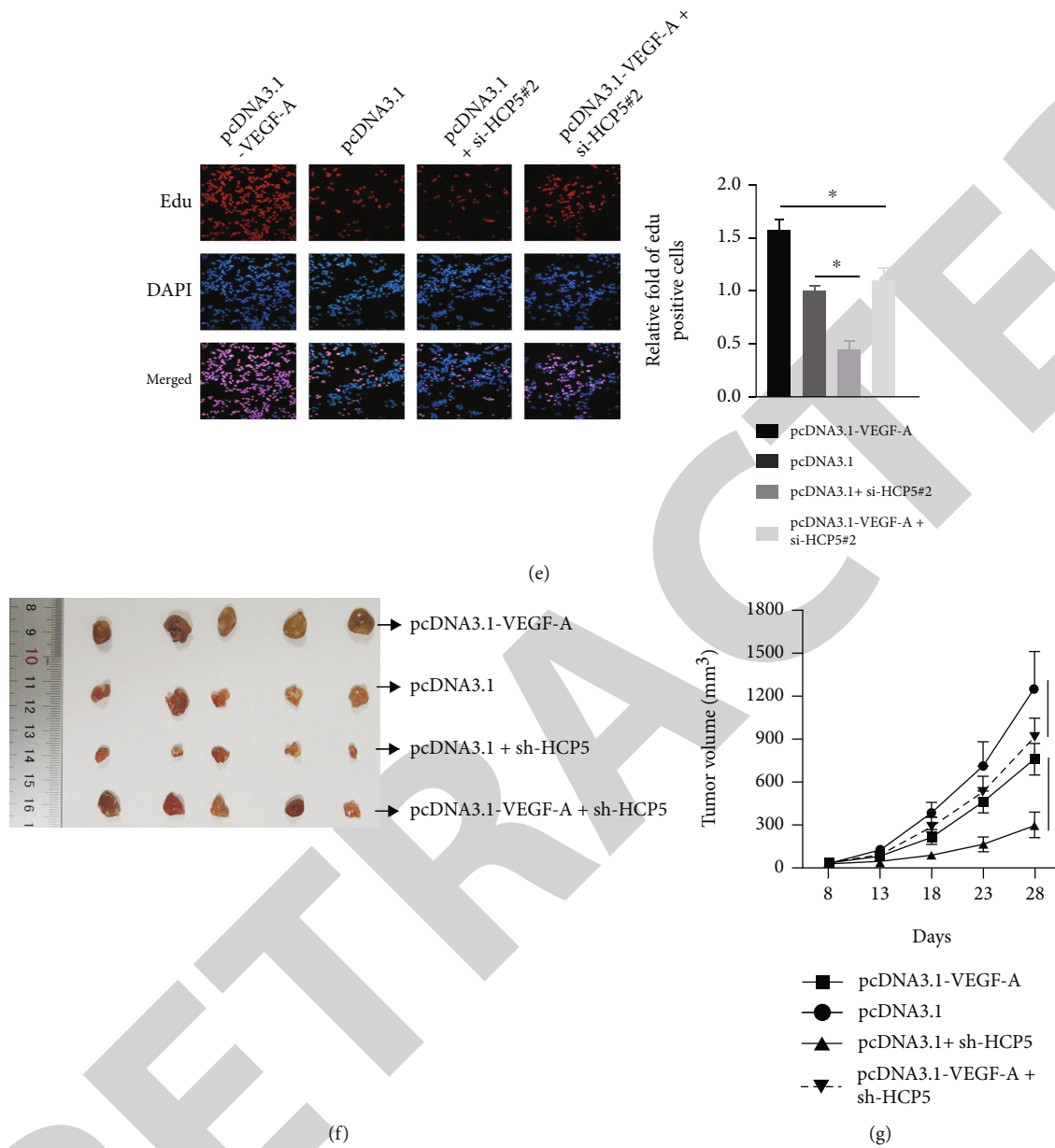
FIGURE 4: Silencing of *HCP5* repressed GBM proliferation through downregulating VEGF-A. U251 cells were transfected with si-NC or si-HCP5#2. Untransfected U251 cells acted as a control. (a) *VEGF-A* mRNA expression was determined by qRT-PCR. U251 cells were transfected with sh-NC or sh-HCP5 and then injected into nude mice. (b) The expression levels of *HCP5*, miR-205, and *VEGF-A* mRNA in tumor tissues were examined by qRT-PCR. (c) VEGF-A protein levels in U251 cells and tumor tissues were determined by western blot analysis. (d) Cell viability was evaluated by MTS assay in transfected U251 cells. (e) Proliferation was detected by EdU incorporation proliferation assay in transfected U251 cells. U251 cells were transfected with pcDNA3.1-VEGF-A/pcDNA3.1 or cotransfected with sh-HCP5 and pcDNA3.1-VEGF-A/pcDNA3.1 and then injected into nude mice. (f) Tumors isolated from nude mice. (g) Tumor volume was recorded every 5 days from day 8 after injection. Data are presented as the mean ± SD. $^{*}P < 0.05$.

between *HCP5* and miR-205 were graphically marked in Figure 3(c). *HCP5* expression was prominently downregulated after miR-205 overexpression ($P < 0.05$, Figure 3(d)). Results in Figure 3(e) illustrated that the luciferase activity was markedly reduced in HEK293T cells that were cotransfected with HCP5 WT and miR-205 ($P < 0.05$), but a similar phenomenon was not found in cells with HCP5 MT. Moreover, both cell viability and the proportion of EdU-positive cells were dramatically lowered by miR-205 or si-HCP5.

And compared with the si-HCP5 or miR-205 mimic group, cell viability and proliferation were further decreased in the si-HCP5+miR-205 mimic group (all $P < 0.05$, Figures 3(f) and 3(g)). These results confirmed that *HCP5* might act as a sponge of miR-205 in U251 cells.

3.4. *HCP5 Downregulation Repressed GBM Proliferation through Downregulating VEGF-A*. Finally, we investigated whether *HCP5* regulated GBM progression by modulating

VEGF-A through miR-205. qRT-PCR assay showed that compared with the si-NC group, *VEGF-A* mRNA expression was significantly repressed in *HCP5*-silenced cells ($P < 0.05$, Figure 4(a)). Moreover, *HCP5* and *VEGF-A* mRNA levels were strikingly decreased while miR-205 expression was markedly increased in *HCP5*-silenced tumor tissues, compared to the sh-NC group (all $P < 0.05$, Figure 4(b)). Unsurprisingly, western blot results in Figure 4(c) indicated that VEGF-A protein expression levels were reduced both in *HCP5*-silenced U251 cells and tumor tissues. Additionally, a rescue experiment was used to further confirm whether *HCP5* functioned via regulating *VEGF-A*. Figure S1 illustrates that VEGF-A was successfully overexpressed in U251 cells transfected with pcDNA3.1-VEGF-A. In U251 cells, we found that *VEGF-A* overexpression not only increased cell viability and the proportion of EdU-positive cells but also reversed the influence of *HCP5* downregulation on these malignant behaviors (all $P < 0.05$, Figures 4(d) and 4(e)). Similarly, upregulation of *VEGF-A* promoted tumor growth and abrogated the effect of sh-HCP5 on tumor growth *in vivo* (all $P < 0.05$, Figures 4(f) and 4(g)). These data proved that *HCP5* downregulation functioned in GBM through downregulating *VEGF-A*.

4. Discussion

GBM is a devastating disease that is related to the dysregulation of multiple lncRNAs. In this study, we found that *HCP5* was aberrantly upregulated in GBM patients and cell lines. Patients with high *HCP5* expression showed shorter survival time. *In vitro* experiments proved that *HCP5* downregulation could suppress cell viability, migration, and proliferation in U251 cells. *HCP5* knockdown also repressed tumor growth in xenograft mice. Further experiments demonstrated that *HCP5* functioned via sponging miR-205 to positively regulate *VEGF-A* in gliomas.

Accumulating evidence has proven that *HCP5* was involved in the tumorigenesis of many cancers [27, 28]. Recently, researchers come to realize the importance of RNA sequencing in exploration for genetic mechanisms underlying human diseases [29]. RNA-sequencing data from TCGA and GTEx illustrated that *HCP5* was upregulated in many types of cancers including gliomas, which implied that *HCP5* possessed oncogenic potential in gliomas. In addition, lower survival probability and shorter survival time were shown in patients with high *HCP5* expression. *In vitro* experiments showed the increase of *HCP5* in GBM cells. The upregulation of *HCP5* in gliomas was consistent with a previous study [17]. Taken together, we hypothesized that *HCP5* might be an oncogenic gene in gliomas.

Two main distinguishing features of gliomas are rapid proliferation and angiogenesis [30]. Migration contributes to the high mortality of gliomas, and blocking cancer cell metastasis is considered to be a promising avenue for the treatment of this disease [31]. Studies have confirmed that *HCP5* promoted the proliferation and migration in clear cell renal cell carcinoma and gastric cancer [32, 33]. A previous study has pointed out that *HCP5* downregulation decreased cell viability and migration in U87 and U251 cells [17]. In

line with these studies described above, this study found that *HCP5* knockdown inhibited the migration and proliferation of U251 and primary glioblastoma cells and prevented tumor growth in xenograft mice, which suggested that *HCP5* exerted a tumor-promotor role in gliomas.

Studying the molecular mechanisms of *HCP5* may provide innovative strategies for glioma therapy. The importance of miR-205 in gliomas has been evidenced in recent studies. For example, miR-205 was downregulated not only in glioma tissues but also in glioma cell lines, and it could inhibit EMT and tumor growth of gliomas [22]. miR-205 has been reported to be a target of many lncRNAs in gliomas [34, 35]. Hence, our study explored whether miR-205 was a target of *HCP5* in gliomas. We found that there was a negative correlation between miR-205 and *HCP5*, and *HCP5* could directly bind to miR-205 in GBM cells. Furthermore, miR-205 overexpression showed the similar effects as *HCP5* downregulation on GBM cell viability and proliferation. These results confirmed that *HCP5* functioned via targeting miR-205.

Many features of cancers such as migration, angiogenesis, and permeabilization of blood vessels are commonly correlated with *VEGF-A* [36]. Vascularization plays an important role in tumor progression, and aberrant angiogenesis is a hallmark of GBM [37]. Many studies indicated that there were binding sequences between miR-205 and *VEGF-A*, and miR-205 could target *VEGF-A* to inhibit the progression of multiple cancers [38–40]. Thus, we selected the *VEGF-A* as the downstream target gene of miR-205 and further analyzed whether *VEGF-A* was a downstream factor of *HCP5*. In this study, we found that *VEGF-A* was downregulated in *HCP5*-silenced U251 cells and tumor tissues. Moreover, the viability and proliferation of GBM cells as well as tumor growth could be enhanced by *VEGF-A* overexpression, and the upregulation of *VEGF-A* reversed the impacts of *HCP5* downregulation on these features. Our results, combined with previous studies, suggested that *HCP5* might affect glioma progression through the miR-205/*VEGF-A* axis.

5. Conclusions

Upregulation of *HCP5* was found in glioma tissues and cell lines. *HCP5* knockdown induced miR-205 upregulation, followed by the downregulation of *VEGF-A*, resulting in the repression of tumor cell proliferation and migration as well as tumor growth in gliomas. To our knowledge, this is the first time to report the correlation between *HCP5* and miR-205 in gliomas. Targeting *HCP5* and miR-205 might provide insight into a new strategy for glioma therapy.

Abbreviations

lncRNA: Long noncoding RNA
HCP5:   HLA complex P5
VEGF-A: Vascular endothelial growth factor A
GBM: Glioblastoma
miR: MicroRNA
EMT: Epithelial-mesenchymal transition

TCGA: The Cancer Genome Atlas
GTEx: Genotype-Tissue Expression
GEPIA: Gene Expression Profiling Interactive Analysis
CESE: Cervical squamous cell carcinoma and endocervical adenocarcinoma
CHOL: Cholangiocarcinoma
COAD: Colon adenocarcinoma
ESCA: Esophageal carcinoma
KICH: Kidney chromophobe
LAML: Acute myeloid leukemia
STAD: Stomach adenocarcinoma
ATCC: American Type Culture Collection
NHA: Normal human astrocytes
DMEM: Dulbecco's modified Eagle's medium
FBS: Fetal bovine serum
siRNAs: Small interfering RNAs
NC: Negative control
shRNA: Short hairpin RNA
MTS: 3-(4,5-Dimethylthiazol-2-yl)-5-(3-carboxymethoxyphenyl)-2-(4-sulfophenyl)-2H-tetrazolium
DAPI: 4,6-Diamidino-2-phenylindole, dihydrochloride
EdU: 5-Ethynyl-2′-deoxyuridine
qRT-PCR: Quantitative reverse transcription PCR
RIPA: Radioimmunoprecipitation assay
PMSF: Phenylmethanesulfonyl fluoride
SD: Standard deviation
ANOVA: One-way analysis of variance.

Data Availability

The data used to support the findings of this study are included within the article.

Additional Points

Highlights. (i) *HCP5* was aberrantly upregulated in glioma samples and cells. (ii) *HCP5* silencing inhibited cell proliferation and migration and reduced tumor growth. (iii) *HCP5* downregulation repressed cell proliferation via interaction with miR-205. (iv) *HCP5* functioned via the miR-205/*VEGF-A* pathway.

Conflicts of Interest

The authors declare that they have no competing interest.

Supplementary Materials

Figure S1: VEGF-A was overexpressed in U251 cells transfected with pcDNA3.1-VEGF-A. U251 cells were transfected with pcDNA3.1 or pcDNA3.1-VEGF-A, and untransfected cells acted as a control. VEGF-A protein expression was determined by western blot analysis. *(Supplementary Materials)*

References

[1] L. Zhang, Z. Liu, J. Li et al., "Genomic analysis of primary and recurrent gliomas reveals clinical outcome related molecular features," *Scientific Reports*, vol. 9, no. 1, p. 16058, 2019.

[2] Q. T. Ostrom, H. Gittleman, G. Truitt, A. Boscia, C. Kruchko, and J. S. Barnholtz-Sloan, "CBTRUS statistical report: primary brain and other central nervous system tumors diagnosed in the United States in 2011-2015," *Neuro-Oncology*, vol. 20, Supplement_4, pp. iv1–iv86, 2018.

[3] S. Y. L. Ang, L. Lee, A. A. Q. See, T. Y. Ang, B. T. Ang, and N. K. K. King, "Incidence of biomarkers in high-grade gliomas and their impact on survival in a diverse SouthEast Asian cohort - a population-based study," *BMC Cancer*, vol. 20, no. 1, p. 79, 2020.

[4] M. Lara-Velazquez, R. Al-Kharboosh, S. Jeanneret et al., "Advances in brain tumor surgery for glioblastoma in adults," *Brain Sciences*, vol. 7, no. 12, p. 166, 2017.

[5] K. A. McNeill, "Epidemiology of brain tumors," *Neurologic Clinics*, vol. 34, no. 4, pp. 981–998, 2016.

[6] J. Liang, X. Lv, C. Lu et al., "Prognostic factors of patients with gliomas – an analysis on 335 patients with glioblastoma and other forms of gliomas," *BMC Cancer*, vol. 20, no. 1, p. 35, 2020.

[7] M. Huarte, "The emerging role of lncRNAs in cancer," *Nature Medicine*, vol. 21, no. 11, pp. 1253–1261, 2015.

[8] M. Matsui and D. R. Corey, "Non-coding RNAs as drug targets," *Nature Reviews Drug Discovery*, vol. 16, no. 3, pp. 167–179, 2017.

[9] F. Corrà, C. Agnoletto, L. Minotti, F. Baldassari, and S. Volinia, "The network of non-coding RNAs in cancer drug resistance," *Frontiers in Oncology*, vol. 8, p. 327, 2018.

[10] J. Shen, T. R. Hodges, R. Song et al., "Serum HOTAIR and GAS5 levels as predictors of survival in patients with glioblastoma," *Molecular Carcinogenesis*, vol. 57, no. 1, pp. 137–141, 2018.

[11] J. X. Yang, B. Liu, B. Y. Yang, and Q. Meng, "Long non-coding RNA homeobox (HOX) A11-AS promotes malignant progression of glioma by targeting miR-124-3p," *Neoplasma*, vol. 65, no. 4, pp. 505–514, 2018.

[12] J. Li, Y. Zhu, H. Wang, and X. Ji, "Targeting long noncoding RNA in glioma: a pathway perspective," *Molecular Therapy-Nucleic Acids*, vol. 13, pp. 431–441, 2018.

[13] Y. Sun, Y. Shen, and X. Li, "Knockdown of long non-coding RNA AGAP2-AS1 suppresses the proliferation and metastasis of glioma by targeting microRNA-497-5p," *Bioengineered*, 2021.

[14] C. Vernet, M. T. Ribouchon, G. Chimini, A. M. Jouanolle, I. Sidibé, and P. Pontarotti, "A novel coding sequence belonging to a new multicopy gene family mapping within the human MHC class I region," *Immunogenetics*, vol. 38, no. 1, pp. 47–53, 1993.

[15] L. Liang, J. Xu, M. Wang et al., "LncRNA HCP5 promotes follicular thyroid carcinoma progression via miRNAs sponge," *Cell Death & Disease*, vol. 9, no. 3, p. 372, 2018.

[16] R. Hu and Z. Lu, "Long non-coding RNA HCP5 promotes prostate cancer cell proliferation by acting as the sponge of miR-4656 to modulate CEMIP expression," *Oncology Reports*, vol. 43, no. 1, pp. 328–336, 2020.

[17] H. Teng, P. Wang, Y. Xue et al., "Role of HCP5-miR-139-RUNX1 feedback loop in regulating malignant behavior of glioma cells," *Molecular Therapy: The Journal of the American Society of Gene Therapy*, vol. 24, no. 10, pp. 1806–1822, 2016.

[18] A. Benmoussa and P. Provost, "Milk microRNAs in health and disease," *Comprehensive Reviews in Food Science and Food Safety*, vol. 18, no. 3, pp. 703–722, 2019.

Retraction

Retracted: Identification of Cigarette Smoking-Related Novel Biomarkers in Lung Adenocarcinoma

BioMed Research International

This article has been retracted by Hindawi following an investigation undertaken by the publisher [1]. This investigation has uncovered evidence of one or more of the following indicators of systematic manipulation of the publication process:

(1) Discrepancies in scope

(2) Discrepancies in the description of the research reported

(3) Discrepancies between the availability of data and the research described

(4) Inappropriate citations

(5) Incoherent, meaningless and/or irrelevant content included in the article

(6) Manipulated or compromised peer review

The presence of these indicators undermines our confidence in the integrity of the article's content and we cannot, therefore, vouch for its reliability. Please note that this notice is intended solely to alert readers that the content of this article is unreliable. We have not investigated whether authors were aware of or involved in the systematic manipulation of the publication process.

Wiley and Hindawi regrets that the usual quality checks did not identify these issues before publication and have since put additional measures in place to safeguard research integrity.

We wish to credit our own Research Integrity and Research Publishing teams and anonymous and named external researchers and research integrity experts for contributing to this investigation.

The corresponding author, as the representative of all authors, has been given the opportunity to register their agreement or disagreement to this retraction. We have kept a record of any response received.

References

[1] Y. Zhang, Q. Wang, T. Zhu, and H. Chen, "Identification of Cigarette Smoking-Related Novel Biomarkers in Lung Adenocarcinoma," *BioMed Research International*, vol. 2022, Article ID 9170722, 10 pages, 2022.

Research Article

Identification of Cigarette Smoking-Related Novel Biomarkers in Lung Adenocarcinoma

Yuan Zhang,[1] Qiong Wang,[1] Ting Zhu,[1] and Hui Chen [2]

[1]*Department of Respiratory Medicine, Zhenhai Hospital of Traditional Chinese Medicine, Ningbo, 315000 Zhejiang, China*
[2]*Department of Preventive Medicine of Traditional Chinese medicine, Jiangnan Hospital Affiliated to Zhejiang Chinese Medical University (Hangzhou Xiaoshan Hospital of Traditional Chinese Medicine), Hangzhou 310000, Zhejiang, China*

Correspondence should be addressed to Hui Chen; huichen26@outlook.com

Objective. The aims of this study were to screen the gene mutations that are able to predict the risk of cigarette smoking-related lung adenocarcinoma (LUAD) and to evaluate its prognostic significance. *Methods*. Clinical data and genetic information were retrieved from the TCGA database, and the patients with LUAD were divided into three groups including never smoking, light smoking, and heavy smoking according to cigarette smoking dose. Differentially mutated genes (DMGs) of each group were analyzed. At the same time, the function of DMGs in three smoking groups was evaluated by GO function and KEGG pathway analysis. The driver genes and protein variation effect of DMGs were performed to further screen key genes. The survival characteristics of the gene expression and mutation of those genes were analyzed and plotted to visualize by the Kaplan-Meier model. *Result*. The DMGs for different smoking doses were identified. The driver and deleterious mutation in the DMGs were screened and gene interaction network was constructed. The DMGs with driver mutations and deleterious mutations that were associated with the overall survival in the heavy smoking patients were considered as the candidate genes for novel markers of smoking-related LUAD. The final novel risk factor gene was identified as MYH7 and the high express of MYH7 in LUAD correlation with patients' gender, lymph node metastasis, T stage, and clinical stage. *Conclusions*. In summary, it can be concluded that MYH7 is a novel biomarker for heavy smoking-related LUAD and it is significantly correlated with the prognosis of lung cancer and is related to the clinical characteristics of lung cancer.

1. Introduction

Lung cancer is the most common malignancy in humans which leads to high cancer-related deaths worldwide. Lung adenocarcinoma (LUAD) is the main histological type, including more than 40% of lung cancer [1, 2]. The 5-year survival rate of patients with LUAD is less than 10%, and 90% of them die of complications related to tumor metastasis [3, 4]. Most patients with LUAD are diagnosed at advanced stages, thus miss best opportunities for surgical treatments. To make matters worse, LUAD is not sensitive to radiotherapy and chemotherapy, and the prognosis of patients with LUAD remains poor. In recent years, the incidence and mortality of lung cancer have been increasing year by year, which has caused serious negative effects on patients and society [5].

Many studies have shown that cigarette smoking is the main cause of lung cancer [6–8]. Tobacco smoke contains polycyclic aromatic hydrocarbons and the nicotine-derived nitrosamines, which induce gene mutations in known oncogenes such as *KRAS* and *TP53* [9]. Moreover, it is reported that tobacco aldehydes inhibit the DNA repair [10]. Smoking increases the risk for development of the lung cancer via these mechanisms, and thus, smoking-associated LUAD has its specific gene mutations compared with general LUAD. In the current context of precision treatment of cancer, it is necessary to explore biomarkers or molecular targets for cigarette smoking-associated LUAD. Understanding the mechanism of the occurrence and development of cigarette smoking-associated LUAD contributes to identifying therapeutic targets and approaches for the prevention and management.

TABLE 1: Clinical characteristics of patients with different smoking degrees.

Clinical	Never smoker	Light smoker	Heavy smoker	p value
Smoking amount	0	1-10	11-128	
Age	67.59 (43-87)	59.25 (42-78)	65.69 (38-84)	0.205
Gender				0.015
Men	7	7	66	
Women	20	10	52	
TNM stage				0.567
I	16	13	60	
II	5	1	24	
III	4	3	15	
IV	1	0	8	
Overall survival (OS)	21.69	19.86	14.13	0.023

In this study, data of gene mutation for lung adenocarcinoma patients were downloaded from The Cancer Genome Atlas (TCGA), and the differentially mutated genes (DMGs) among three groups including never smoking, light smoking, and heavy smoking groups were screened. We analyzed the gene function enrichment of the specific DMGs for heavy smoking patients and identified the oncogenic drivers in them. We also analyzed gene-gene interaction of the specific DMGs and their association with prognosis for overall survival. Combining the above results, we found a novel biomarker, *MYH7*, with high occurrence of mutation in heavy smoking patients. There are to date few reports for *MYH7* in lung cancer. Therefore, *MYH7* can be used as a novel target for the diagnosis of smoking-associated lung cancer or for targeted precision therapy targeting *MYH7*.

2. Materials and Methods

2.1. Datasets. The clinical data and gene expression information of lung cancer patients were downloaded from the American Cancer Genome Atlas Database (TCGA), and lung adenocarcinoma (Broad, Cell 2012) dataset was used to obtain lung cancer patients' information. A total of 184 samples were included in this study. A total of 65,768 somatic mutations were detected.

2.2. Identification of Differentially Mutated Genes. Differentially mutated gene analysis for the never smoker, light smoker, and heavy smoker groups in the LUAD dataset was performed by using the clinical enrichment function of the maftools package in R software. p value < 0.05 was defined as the significant difference.

2.3. Functional Annotation. As for the obtained different genes, Gene Ontology (GO) and Kyoto Encyclopedia of Genes and Genomes (KEGG) pathway annotation were performed with the R package (clusterProfiler). GO annotation was carried out from the aspects of biological process (BP), molecular function (MF), and cellular component (CC). Fisher's test was used to calculate the p value of significance level, so as to screen the GO with significant enrichment of different genes. The p value < 0.01 was marked with red as

the significant enrichment item and the blue as the nonsignificant item. KEGG database was used to explore the signal pathway of significantly differentially expressed gene enrichment, with p value < 0.05 as the threshold.

2.4. Driver Gene Analysis Based on Mutation Location Clustering. Oncogene mutations usually gather at specific locations of proteins (also known as mutation hot spots), and the mutations in these domains are beneficial to the growth or proliferation of cancer cells. We used OncodriveCLUST algorithm to cluster the mutation sites of gene bases to identify cancer genes. The key information calculated included the number of mutation hot spots, the number of mutations clustering in the hot spots, the length of amino acids corresponding to the protein, the proportion of clustering mutations in all mutations of the gene, and the p value and FDR values. The smaller the value, the stronger the driving force.

2.5. Mutation Damaging Was Assessed Based on PROVEAN and SIFT Software. Homologous proteins were found in the database, and protein sequences with high similarity and consistent function were selected for multisequence PSI-BLAST alignment to evaluate the conserved protein sites, and the risk was evaluated by PROVEAN/SIFT database score.

2.6. Interacting Network Analysis. The STRING database (https://string-db.org/) is used to explore the interactions between proteins and genes. The SRING database contains experimental data, direct interactions, and indirect functional correlations between proteins and obtains the PPI interaction network diagram.

2.7. Statistical Analysis. The gene expression information and overall survival (OS) data were obtained from TCGA database. The Kaplan-Meier analysis was used to calculate the hazard ratio (HR), and the survival curve was drawn. $p < 0.05$ was considered to be significantly related to the prognosis of lung cancer patients.
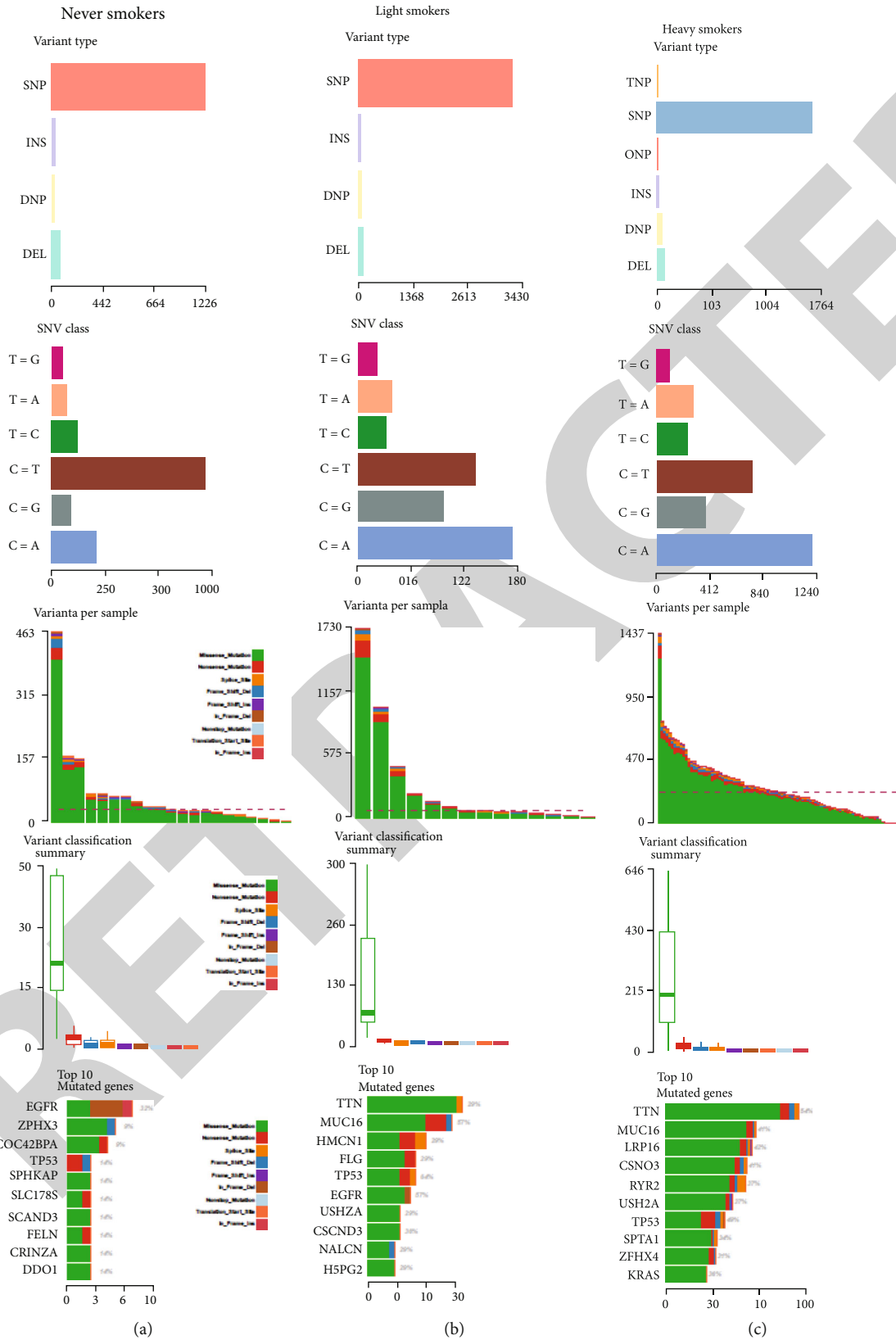
FIGURE 1: The profile of somatic mutations for never smokers (a), light smokers (b), and heavy smokers (c) in LUAD, respectively. From top to bottom, each row is the statistics of mutation types, the type and number of mutation bases (vertical axis is classified; horizontal axis scale is counted), and the count box diagram of mutation number and mutation species in each sample.
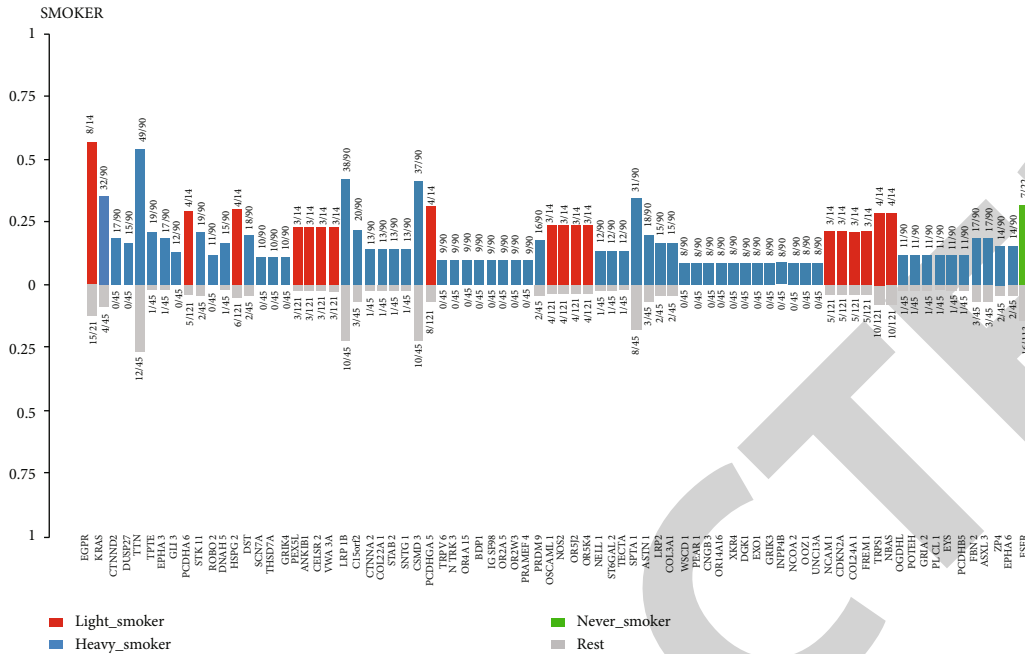
FIGURE 2: Genes with *p* value < 0.05 for differential mutation significance in a given group are shown, sorted from left to right by significance of difference in different subgroups. The horizontal axis shows the gene names, the vertical axis shows the proportion of mutations in different subgroups, and the bar chart colors show the subgroups, corresponding to the figure notes on the right.

3. Results

3.1. Screening of Differential Mutation Genes in Lung Cancer Patients with Different Smoking Levels.
The somatic gene mutation profiles and clinical data were acquired from the TCGA database, which included 184 patients. The result of the survival analysis showed that the smoking situation significantly associated with patient's OS (Table 1, $p = 0.023$). Lung adenocarcinoma patients were divided into nonsmoking group, light smoking group, and heavy smoking group based on their total amount of smoking (the product of the number of packs smoked and the number of years) up to the time of tumor diagnosis: heavy (>10), light (>0 and<10), and never (=0). The mutation status of patients in each group was statistically analyzed, and the results are shown in Figure 1. As can be seen from the figure, the single nucleotide missense mutation was the dominant mutation in the three types of patients with different smoking levels. Patients in the nonsmoking group mutated the base type to replace thymine cytosine nucleotide with cytosine nucleotide (C>T), followed by cytosine nucleotide substitution for adenine nucleotide substitution (C>A), while cytosine nucleotide substitution for adenine nucleotide substitution in light and heavy smoking groups (C>A) is the most common, followed by cytosine nucleotide instead of thymine (C>T). The top 10 mutant genes in the nonsmoking group were *EGFR*, *ZFHX3*, *CDC42BPA*, *TP53*, *SPHKAP*, *SLC17A6*, *Scand3*, *RelN*, *GRTN2A*, and *DIDO1*. The top 10 mutant genes in light smoking group were *TTN*, *MUC16*, *HMCN1*, *FLG*, *TP53*, *EGFR*, *USH2A*, *CSMD3*, *NALCN*, and *HSPG2*. The top 10 mutant genes in the heavy smoking group were *TTN*, *MUC16*, *LRP1B*, *CSMD3*, *RyR2*, *USH2A*, *TP53*, *SPTA1*, *ZFHX4*, and *KRAS*. The 1122 DMGs were identified in heavy smoking, 432 DMGs were identified in light smoking, and 327 DMGs were identified in never smoking, and the significant genes are shown in Figure 2.

3.2. GO and KEGG Pathway Analysis of Mutated Differential Genes.
Using GO analysis, the difference of gene has been studied, and the results are shown in Figure 3; the difference of gene biological pathways is mainly related to cell adhesion, involving the main molecular function of the ion channels combining exercise, calcium ion, and extracellular matrix structure; these genes mainly located in the plasma membrane and organelle membrane, which are involved in cell information exchange, may be related to the spread of cancer cells to metastasize. KEGG pathway results are shown in Figure 3. These genes were significantly correlated with adhesion, ECM receptor interaction, olfaction transduction, and other signaling pathways.

3.3. Protein Variation Effect of Mutated Genes and Candidate Marker Genes.
In order to validate the protein variation effect of mutation genes between never smoking, light smoking, and heavy smoking patients, boxplots of model genes were drawn, and both PROVEN and SIFT programs showed that the variation effect scores for the protein functions between never, light, and heavy smoking groups were significantly different ($p < 0.05$, Figure 4), while PROVEN and SIFT scores were conflicting in light smoking group. Mutations in light smokers were more deleterious in the SIFT scores while contrary in the PROVEN scores.
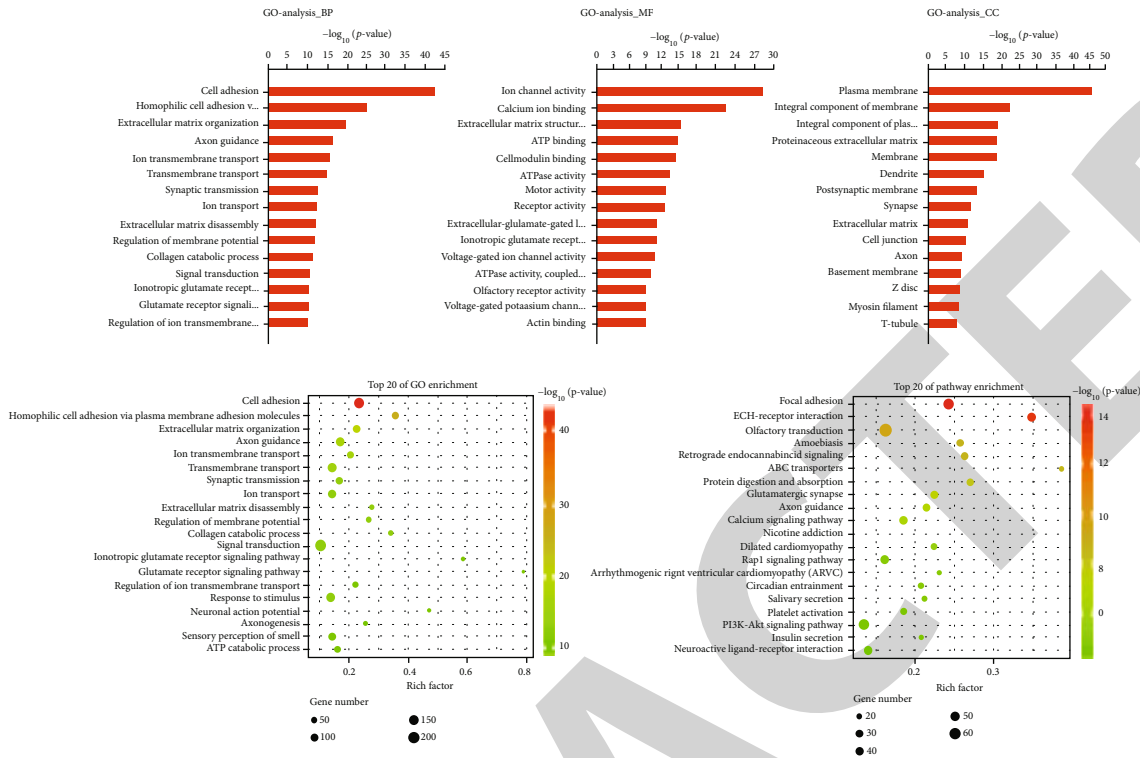
FIGURE 3: GO and KEGG pathway enrichment analysis of differentially mutated genes.
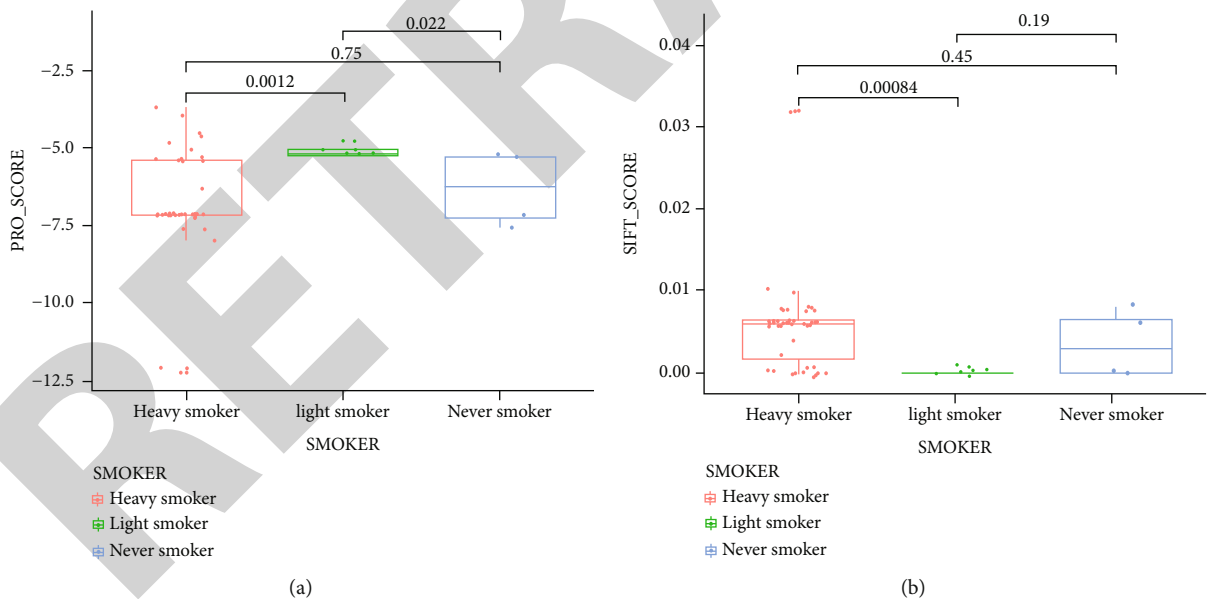
FIGURE 4: The box chart showing the harmfulness of mutations in patients with different smoking conditions (harmless and neutral mutation data have been screened out). (a) The result predicted by the PROVEAN and (b) the result predicted by the SIFT.

Driver gene analysis was performed on the mutation data of lung cancer dataset based on mutation location clustering. The results of cancer driver genes with p value less than 0.05 are shown in Table 2. The oncogenes significantly associated with lung cancer were KRAS, NR4A2, CDKN2A, EGFR, OR5AS1, OR5D14, DOCK11, TFEB, and ZNF335.

Based on the results of differential mutation, cancer driving gene analysis, and mutation harmfulness analysis, the genes were intersected. Differential mutations that may be cancer drivers in the never smoker, light smoker, and heavy smoker groups were obtained (p value < 0.1), and damaging and deleterious genes are considered as key candidate genes

Table 2: Genes in driver and deleterious mutation obtained from the DMGs for different smoking conditions. Genes were arranged by mutation frequency.

Hugo_ Symbol	Total mutated	Mutated samples	Hugo_ Symbol	Total mutated	Mutated samples	Hugo_ Symbol	Total mutated	Mutated samples
TP53	67	63	CNTNAP5	21	17	SCN11A	11	9
TTN	144	61	CTNND2	20	17	ARAP2	10	9
MUC16	95	51	KIF2B	20	17	MYO10	10	9
LRP1B	85	48	LRP2	20	17	OR10AG1	10	9
SPTA1	49	39	MYO18B	20	17	PCDHA9	10	9
ZFHX4	51	36	EPHA5	20	16	GABRA5	9	9
KRAS	36	36	SORCS3	18	15	OR4M2	9	9
PCLO	48	34	POTEC	16	15	WSCD1	11	8
XIRP2	47	34	KEAP1	15	15	THBS2	10	8
PCDH15	36	29	PCDH10	18	14	MKRN3	9	8
CSMD1	40	26	TRPS1	17	14	AGBL1	8	8
LPHN3	30	26	CMYA5	15	14	CDKN2A	8	8
RP1L1	31	25	LRRC4C	15	14	GP2	8	8
RELN	29	24	MYH7	15	14	OR5D14	8	8
DNAH9	34	23	CDH7	13	13	SLC6A2	8	8
EGFR	26	23	KCNT2	15	12	LPA	8	7
ZNF804A	26	22	KIAA1211	15	12	ADCY5	7	7
ZNF536	30	21	LRRTM4	13	12	OR5B17	7	7
CUBN	27	21	MYH8	14	11	PKP2	7	7
FAM5C	27	21	BRAF	12	11	SAGE1	7	7
STK11	21	21	FAM71B	12	11	TSHR	7	7
BAI3	24	20	TLR4	12	11	VSTM2A	7	7
MXRA5	22	20	CNTN5	11	11	ADAM21	7	6
TPTE	22	20	POM121L12	11	11	FCRLA	7	6
CDH10	24	19	TGIF2LX	11	11	OR5AS1	7	6
FLG2	21	18	SLC17A6	13	10	C7orf10	6	6
DNAH3	20	18	MMP16	12	10	CLCNKA	6	6
EPHA3	20	18	OR2M2	11	10	NR4A2	6	6
PRDM9	20	18	TRHDE	11	10	OR10A4	6	6
CSMD2	19	18	KCNJ3	10	10	OR10Z1	6	6
PKHD1L1	26	17	RAG1	10	10	TRIM48	6	6

in PROBEAN/SIFT prediction, which are arranged by mutation frequency, as shown in Table 2.

3.4. Interacting Networks of Important Differential Mutants.
The interaction between proteins of cancer-driving genes was explored based on the STRING database, which included experimental data, results mined from PubMed abstracts and integrated data from other databases, as well as results predicted by bioinformatics methods. The PPI interaction network diagram is shown in Figure 5. It can be seen from the diagram that CDKN2A, KRAS, EGFR, TLR4, and TP53 with high-grade index are the core genes, followed by STK11, SPTA1, MYH8, MYH7, and MYO10, and most of the core genes have been reported. Literature mining was performed for searching the association of those genes to the smoking lung cancer. The results showed that

only MYH7 and MYH8 genes had not been reported yet, and they were candidate genes related to lung cancer of new types of smoking. Although there is an enrichment of MYH7 mutation in heavy smoking patients, the mutation loci varied in the patients (Supplementary Table 1).

3.5. Novel Biomarkers of Smoking-Related LUAD.
PubMed was used to search for papers related to the key node genes of result 2.4 and cancer caused by smoking. The results showed that only *MYH7* and *MYH8* genes had not been reported yet and were candidate genes related to lung cancer caused by heavy smoking. Survival curve analysis was conducted on these two genes using the prognosis data from lung adenocarcinoma (TCGA, provisional) database, and the results are shown in Figure 6. As can be seen from the figure, high expression of *MYH7* gene significantly reduced
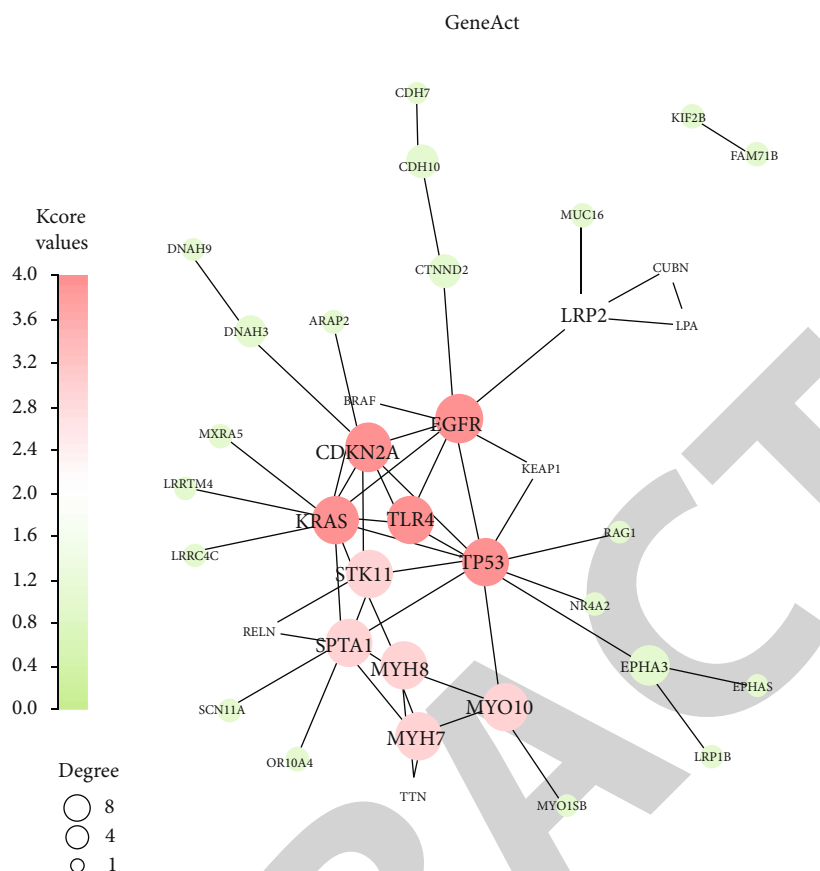
FIGURE 5: Gene-gene interaction of specific DMGs in driver and deleterious mutations. The circular nodes represent genes and the straight lines represent the reciprocal relationships that exist in genes. The size of the node represents the degree value, and the color shade represents the *k*-core value size.

the prognostic survival rate of patients. The high expression of *MYH8* gene had no significant effect on the prognostic survival rate. Therefore, *MYH7* was screened as a new smoking-induced lung cancer target gene.

4. Discussion

In this study, we focused on the analysis of mutated genes associated with tobacco smoking in LUAD. We identified specific mutations in LUAD patients with heavy smoking that were distinct from the nonsmoking group. Among these mutations, we screened the genes with driver mutations and those with deleterious mutations. Considering that these mutated genes have regulatory relationships and affect the occurrence of LUAD through common pathways, we subsequently performed gene interaction analysis for these mutated genes and constructed a gene network for smoking-related LUAD centered on genes known to be high frequency mutated in LUAD, such as *KRAS* and *TP53*. Based on the results of the literature search, most of these smoking-related core genes (*CDKN2A*, *EGFR*, *KRAS*, *TLR4*, *TP53*, *SPTA1*, and *STK11*) we identified have been reported in many studies for their association with lung cancer. However, *MYH7* has not been studied to elaborate

its association with lung cancer. In LUAD, *MYH7* has a high mutation frequency (11 of 90), so *MYH7* can be used as a novel diagnostic biomarker. Meanwhile, the gene expression of *MYH7* correlated with the overall survival of LUAD patients and the tumor stage and lymph node metastasis of patients, suggesting that *MYH7* is associated with the progression of LUAD, and thus precise targeted therapies targeting MYH7 can be carried out in the future.

Current research on *MYH7* has focused on studies in cardiomyopathies, as it is predominantly expressed in the normal human ventricle. Mutations in this gene are associated with familial hypertrophic cardiomyopathy, myosin storage myopathy, dilated cardiomyopathy, and Laing early-onset distal myopathy [11–14]. In our results, *MYH7* was shown to be highly expressed in LUAD tumor tissue. In addition, only a small number of studies have shown that *MYH7* is associated with tumorigenesis. Sun et al. reported that *MYH7* is one of the top ten hub genes in *PTEN* mutation prostate cancer [15]. Huang et al. reported that mutations in MYH7 occur in Epstein-Barr virus-associated intrahepatic cholangiocarcinoma [16]. This paper is the first to propose that the lack of function of *MYH7* is one of the causes of LUAD, especially for smoking-associated LUAD.

(a)

(b)

Expression of MYH7 in LUAD based on sample types

(c)

Expression of MYH7 in LUAD based on individual cancer stages

(d)

Expression of MYH7 in LUAD based on patient's race

(e)

Expression of MYH7 in LUAD based on patient's geneder

(f)
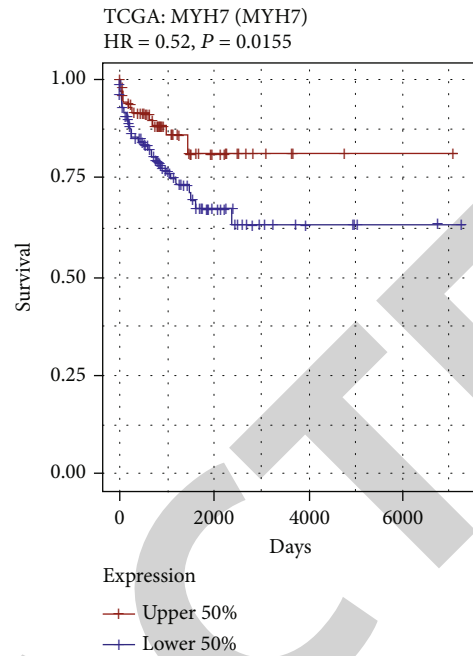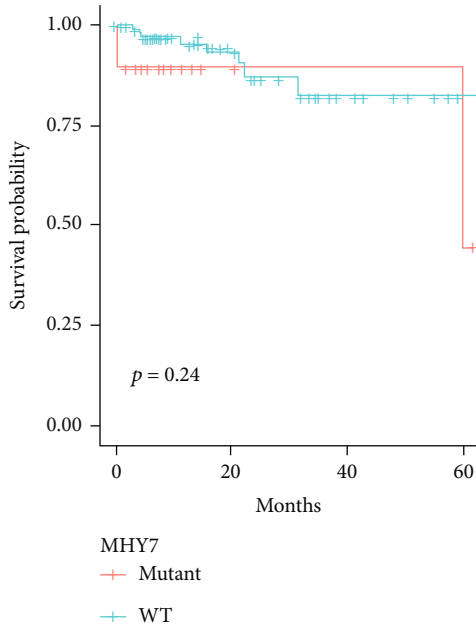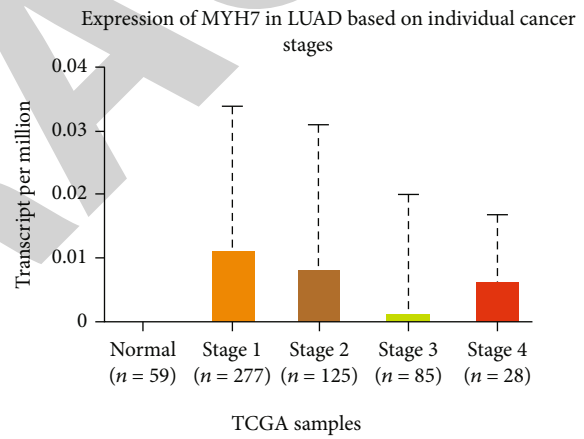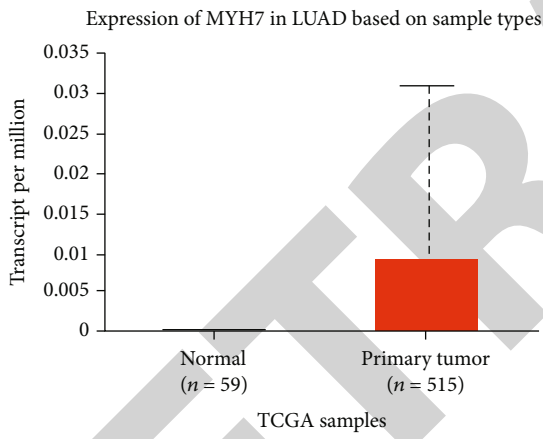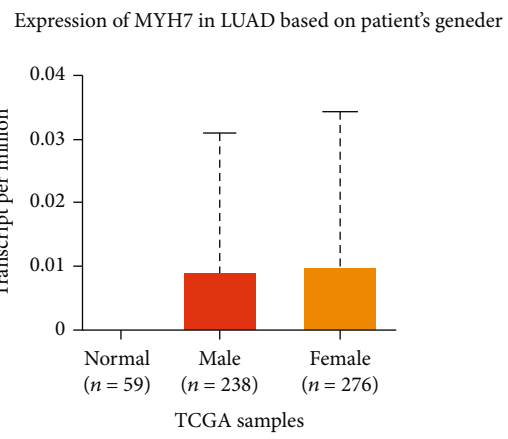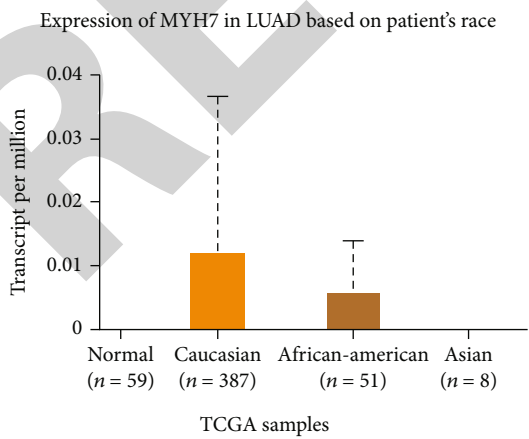
Figure 6: Continued.
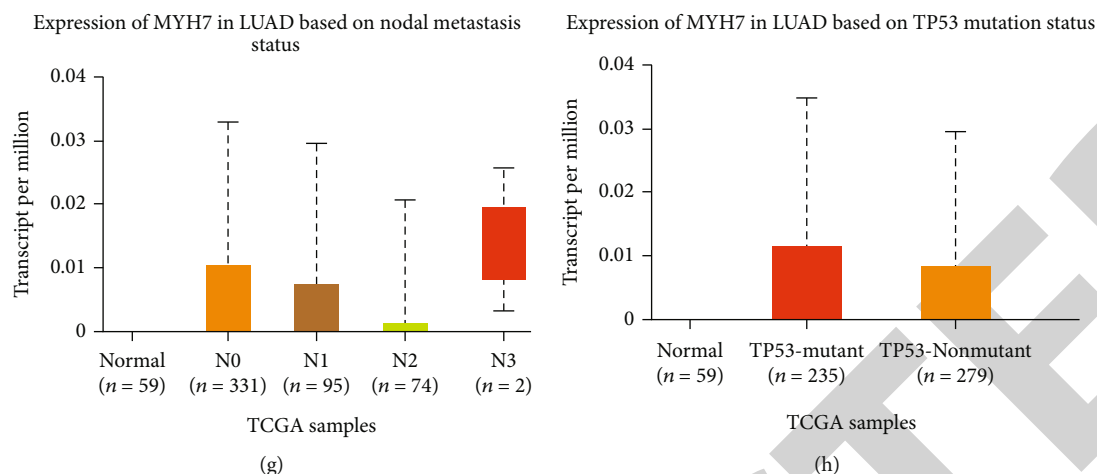
Figure 6: The association of *MYH7* mutation with overall survival ($p = 0.24$) (a) and the association of *MYH7* expression with overall survival ($p = 0.02$) (b) of LUAD patients and with the sample type ($p = 0.001$) (c), tumor stages ($p = 0.004$) (d), race ($p = 0.02$) (e), gender ($p = 0.61$) (f), nodal metastasis ($p = 0.03$) (g), and *TP53* mutation ($p = 0.23$) (h) in LUAD.

Although cigarette smoking is the main cause of lung cancer, the incidence of lung cancer is increasing among nonsmokers. It is estimated that about 25% of lung cancer cases are observed in nonsmokers, and some studies have observed that 40% of nonsmoking men and 31.2% of nonsmoking women have no known exposure history to major carcinogens [17, 18]. If lung cancer in nonsmokers were considered as a single cancer, it would be the seventh leading cancer death in the world [17]. If the current growth rate of nonsmoking lung cancer continues, it is predicted that nonsmoking lung cancer will be the main type of lung cancer in the next 10 years [19]. Current evidence shows that nonsmoking lung cancer shows a different pattern from smokers' lung cancer, and there are essential differences between nonsmoking lung cancer and smoking-related lung cancer in terms of gender, clinical characteristics, and molecular genetic changes [20, 21]. Heavy smokers were found to have many specific gene mutations in this study, while never smokers did not seem to have specific gene mutations, compared to other smoking patients. Therefore, the results of the present study cannot explain the etiology of non-smoking-related LUAD. Considering the high rate of non-smoking-related lung cancer as well, more studies are still needed for non-smoking-related LUAD, but we suggest that studies can be conducted at levels other than gene mutations.

Data Availability

The data used to support the findings of this study are included within the article.

Conflicts of Interest

The authors declare that they have no competing interest.

Supplementary Materials

Supplementary Table 1: the mutated sites of MYH7 in the heavy smoking patients. *(Supplementary Materials)*

References

[1] M. Noguchi, A. Morikawa, M. Kawasaki et al., "Small adenocarcinoma of the lung. Histologic characteristics and prognosis," *Cancer*, vol. 75, no. 12, pp. 2844–2852, 1995.

[2] C. Zappa and S. A. Mousa, "Non-small cell lung cancer: current treatment and future advances," *Translational lung cancer research*, vol. 5, no. 3, pp. 288–300, 2016.

[3] B. Y. Wang, J. Y. Huang, H. C. Chen et al., "The comparison between adenocarcinoma and squamous cell carcinoma in lung cancer patients," *Journal of Cancer Research and Clinical Oncology*, vol. 146, no. 1, pp. 43–52, 2020.

[4] D. Zhang, Q. Jiang, X. Ge et al., "RHOV promotes lung adenocarcinoma cell growth and metastasis through JNK/c-Jun pathway," *International Journal of Biological Sciences*, vol. 17, no. 10, pp. 2622–2632, 2021.

[5] R. L. Siegel, K. D. Miller, H. E. Fuchs, and A. Jemal, "Cancer statistics, 2021," *CA: a Cancer Journal for Clinicians*, vol. 71, no. 1, pp. 7–33, 2021.

[6] I. Petersen, "The morphological and molecular diagnosis of lung cancer," *Deutsches Ärzteblatt International*, vol. 108, no. 31-32, pp. 525–531, 2011.

[7] H. M. Schuller, "The impact of smoking and the influence of other factors on lung cancer," *Expert Review of Respiratory Medicine*, vol. 13, no. 8, pp. 761–769, 2019.

[8] G. Siasos, V. Tsigkou, E. Kokkou et al., "Smoking and atherosclerosis: mechanisms of disease and new therapeutic approaches," *Current Medicinal Chemistry*, vol. 21, no. 34, pp. 3936–3948, 2014.

[9] S. S. Hecht, "Progress and challenges in selected areas of tobacco carcinogenesis," *Chemical Research in Toxicology*, vol. 21, no. 1, pp. 160–171, 2008.

[10] M. W. Weng, H. W. Lee, S. H. Park et al., "Aldehydes are the predominant forces inducing DNA damage and inhibiting DNA repair in tobacco smoke carcinogenesis," *Proceedings of the National Academy of Sciences of the United States of America*, vol. 115, no. 27, pp. E6152–E6161, 2018.

[11] S. Klaassen, S. Probst, E. Oechslin et al., "Mutations in sarcomere protein genes in left ventricular noncompaction," *Circulation*, vol. 117, no. 22, pp. 2893–2901, 2008.

Retraction

Retracted: Brusatol Inhibits Proliferation and Metastasis of Colorectal Cancer by Targeting and Reversing the RhoA/ROCK1 Pathway

BioMed Research International

This article has been retracted by Hindawi following an investigation undertaken by the publisher [1]. This investigation has uncovered evidence of one or more of the following indicators of systematic manipulation of the publication process:

(1) Discrepancies in scope

(2) Discrepancies in the description of the research reported

(3) Discrepancies between the availability of data and the research described

(4) Inappropriate citations

(5) Incoherent, meaningless and/or irrelevant content included in the article

(6) Manipulated or compromised peer review

The presence of these indicators undermines our confidence in the integrity of the article's content and we cannot, therefore, vouch for its reliability. Please note that this notice is intended solely to alert readers that the content of this article is unreliable. We have not investigated whether authors were aware of or involved in the systematic manipulation of the publication process.

Wiley and Hindawi regrets that the usual quality checks did not identify these issues before publication and have since put additional measures in place to safeguard research integrity.

We wish to credit our own Research Integrity and Research Publishing teams and anonymous and named external researchers and research integrity experts for contributing to this investigation.

The corresponding author, as the representative of all authors, has been given the opportunity to register their agreement or disagreement to this retraction. We have kept a record of any response received.

References

[1] R.-j. Lu, G.-z. Zhao, R. Jiang et al., "Brusatol Inhibits Proliferation and Metastasis of Colorectal Cancer by Targeting and Reversing the RhoA/ROCK1 Pathway," *BioMed Research International*, vol. 2022, Article ID 7132159, 13 pages, 2022.

Research Article

Brusatol Inhibits Proliferation and Metastasis of Colorectal Cancer by Targeting and Reversing the RhoA/ROCK1 Pathway

Rui-jin Lu,[1] Guo-zhi Zhao,[2] Rong Jiang,[1] Shuang He,[1] Hang Xu,[3] Jia-ming He,[1] Yue Sun,[1] Meng-na Wu,[3] Jian-hua Ran,[3] Di-long Chen,[4] and Jing Li [1]

[1]*Lab of Stem Cell and Tissue Engineering, Department of Histology and Embryology, Chongqing Medical University, Chongqing, China*
[2]*Department of Urology, The First Affiliated Hospital of Chongqing Medical University, Chongqing, China*
[3]*Neuroscience Research Center, College of Basic Medicine, Chongqing Medical University, Chongqing, China*
[4]*Chongqing Key Laboratory of Development and Utilization of Genuine Medicinal Materials in Three Gorges Reservoir Area, Chongqing, China*

Correspondence should be addressed to Jing Li; 100392@cqmu.edu.cn

Brusatol (BRU) is an important compound extracted from Brucea javanica oil, whose pharmacological effects are able to induce a series of biological effects, including inhibition of tumor cell growth, anti-inflammatory, antiviral, and antitumor. Currently, there are so few studies about the brusatol effects on colorectal cancer that its anticancer mechanism has not been clearly defined. In this study, we made an in-depth investigation into the brusatol effect towards the proliferation and metastasis of colon cancer and the possible mechanism. The inhibitory effect of BRU on the proliferation of colorectal cancer cells was unveiled via CCK-8 method and colony formation assay, while the inhibitory effect of BRU on migration and invasion of colorectal cancer cells was revealed by scratch assay and transwell assay. In addition, Western blot results also revealed that BRU inhibited not only the expressions of RhoA and ROCK1 but also the protein expressions of EMT-related markers e-cadherin, N-cadherin, Vimentin, MMP2, and MMP9 in colon cancer cells. Through the xenotransplantation model, our in vivo experiment further verified the antitumor effect of BRU on colon cancer cells in vitro, and the results were consistent with the protein expression trend. In conclusion, BRU may inhibit the proliferation and metastasis of colorectal cancer by influencing EMT through RhoA/ROCK1 pathway.

1. Introduction

Colorectal cancer (CRC) is one of the most common gastrointestinal malignancies, causing nearly 700,000 deaths every year, and is the fourth fatal cancer in the world. The incidence of colorectal cancer has increased over the past decade, and while the use of many emerging chemotherapy drugs has increased the average survival time for patients with advanced colorectal cancer, patients usually die within three years [1]. The five-year survival rate for patients with advanced colon cancer is reported to be less than 10%[2], and there are about 20% and 30% of CRC patients diagnosed with remote metastases on their first visit [3, 4]. Metastasis is

the primary cause of death in solid tumors [5], as is colorectal cancer. At present, the treatment of colorectal cancer is mainly surgery-based comprehensive treatment, but postoperative recurrence and metastasis are still the main cause of death of colorectal cancer patients. In the treatment of metastatic colorectal cancer, cetuximab and other drugs have achieved good clinical efficacy but are prone to drug resistance [6, 7]. Poor treatment outcomes highlight the need for a better understanding of the mechanisms that contribute to the onset, development, metastasis, and spread of colorectal cancer.

Metastasis is a multifactorial and multicellular process involving the dynamic formation and breakdown of actin

structures [8]. Rho GTplase is one of the most important protein families regulating cell migration, playing a crucial role in regulating cell morphology, motility, cell-cell, and cell-matrix adhesion [9].

Rho kinase (ROCK) is a key serine/threonine kinase downstream of Rho, and the activated RhoA activates ROCK1, leading to the inactivation of myosin phosphatase due to phosphorylation and then resulting in the failure of dephosphorylation of phosphorylated myosin, which would ultimately increase the content of the phosphorylated myosin in cytoplasm and incur more interaction between actin and myosin, thereby the cell adhesion, invasion, and migration are brought about [10, 11]. ROCK is deemed as an anticancer target for its role in promoting the invasion and migration of various cancers [12–14].

Brusatol (BRU) is a bioactive triterpenoid extracted from Brucea javanica oil. It also has a variety of biological effects, including inhibiting tumor cell growth, reducing malaria site replication, reducing inflammation, and resisting virus invasion [15, 16].

At present, BRU has been recognized as an effective antitumor agent for a wide range of tumor cells [15]. Previous studies have shown that BRU would inhibit c-myC synthesis and effectively cripple down tumor cell metabolism and lymphocytic leukemia cell proliferation [17]. Subsequent studies have found that BRU causes rapid and even instantaneous depletion of Nrf2 protein through the posttranscriptional mechanism, thus playing a significant inhibitory effect on the proliferation of HCC cells [18]. At present, it has been pointed out that brusatol, the traditional Chinese medicine, has inhibitory effects on a variety of tumors like liver cancer [19], pancreatic cancer [20], nasopharyngeal carcinoma [21], and melanoma [22]. However, there are few reports about brusatol on colorectal cancer, and its mechanism of action has not been clearly described. Therefore, we made an investigation in this paper into the effects of brusatol on proliferation, migration, and invasion of colorectal cancer cells and then elucidated its role in RhoA/ROCK1 pathway.

2. Materials and Methods

2.1. Reagents and Antibodies. BRU (14907-98-3, purity > 98 %) was fetched from Shanghai Yuanye Biotechnology Co., Ltd. (Shanghai, China), which was dissolved with dimethyl sulfoxide (DMSO) and stored at -80°C. In our subsequent experiments, the BRU was diluted with fresh Dulbecco's Modified Eagle's medium (DMEM, C11995500BT, Gibco) until the final concentration of DMSO was less than 0.1%. MMP2 (40994S), MMP9 (13667S), and E-cadherin (14472S) were purchased from Cell Signaling Technology, USA. Vimentin (AF0318), N-cadherin (AF0243), RhoA (AF2179), ROCK1 (AF1795), and the ROCK inhibitor (Y37632) were brought from Shanghai Biyuntian Biotechnology Co., Ltd.

2.2. Cell Culture and Culture Condition. Human colon cancer cell lines HCT-116 and SW480 were provided by Zhongqiao Xinzhou Biotechnology Company (Shanghai, China). NCM460 human normal colonic epithelial cells were stored in the human tissue embryonic stem cell labora-

tory of Chongqing Medical University. Those cells were cultured with the 10%-fetal-bovine-serum DMEM medium supplemented (10270-106, Gibco) with 1% penicillin and streptomycin (Beyotime, China) and grown at 5% CO_2 and 37°C.

2.3. Cell Viability Assay. In this experiment, Cell Counting Kit-8 (CCK-8, MedChemExpress, USA, HY-K0301) was used to estimate cell viability. NCM460, HCT-116, and SW480 cells at logarithmic phase were taken, and the cell number was adjusted to 5×10^3/well; the cells were laid in a 96-well cell culture plate; then, $100 \mu L$ of medium was added to each well. After the cellular adherence, the cells were treated with 0-160 nM BRU for 24, 48, and 72 h, respectively. Then, we added $10 \mu L$ of CCK-8 to each well and incubated the cells for 2 hours. The absorbance of each well was measured at 450 nm by a microplate reader (Bio-Rad, CA, USA). Finally, we used the GraphPad Prism 8 software to reckon the BRU's effects at different concentrations on the IC50 of HCT-116 and SW480 cells. The experiment was repeated three times.

2.4. Cell Colony Formation Assay. HCT-116 and SW480 cells of logarithmic growth stage were inoculated into 6-well plates with 2×10^2 cells per well. After the cellular adherence, the cells were treated with or without BRU for 24 h. After that, the culture medium was replaced with fresh DMEM, and the cells were continued to be cultured for another two weeks. The cells were then fixed with 4% paraformaldehyde for 20 min at room temperature, then washed with PBS, and stained with 1% crystal violet solution (Beyotime, China). Finally, the ImageJ software was used to take photos and reckon the data. The experiment was repeated three times.

2.5. Wound-Healing Assay. HCT-116 and SW480 cells were inoculated into 6-well plates at a density of 5×10^4/mL. After the cells were fully grown, a straight line was scratched in the central area of cell monolayers with sterilized $200 \mu L$ head. Subsequently, the cells were washed by PBS and incubated in serum-free DEME with or without BRU. Then, a random plate of cells was taken from each group and observed and photographed under an inverted microscope immediately after the scratches. The remaining cells were incubated in a 5% CO_2 incubator at 37°C for 24 h and observed under an inverted microscope. Five fields were randomly selected to be taken photos of. The ImageJ software was used to calculate the areas of the scar and the relative mobility of each group. The experiment was repeated three times.

2.6. Transwell Assay. Matrigel (Corning, USA, 356234) gel was diluted with serum-free DEME medium in the ratio of 8 : 1 and thoroughly mixed. The mixture was evenly spread over a Transwell upper chamber with pore diameter of 8.0 μm (Corning, USA, 3422), $100 \mu L$ per well. The plates were placed at 37°C for 4 h until the gel was solidified. Each well of the Transwell upper chamber was inoculated with 5×10^4 HCT-116 and SW480 cells with the serum-free DMEM medium containing different final concentrations of BRU added into. $500 \mu L$ DMEM medium (containing

20% fetal bovine serum) was added to the lower chamber of each well; then, the plates were incubated in incubators for 24 h. After that, noninvasive cells in the upper chamber were gently wiped with cotton. The bottom of the chamber was fixed with 4% paraformaldehyde at room temperature for 15 min. After washing with PBS, the cells stained with 1% crystal violet solution, and 5 fields of view were randomly selected from each group under the microscope to observe and taken pictures of. The experiment was repeated three times.

2.7. Western Blot Assay. Tumor samples from tumor cells or homogenates were cleaned with PBS and suspended again in a lysate containing 1% phenyl-methane-sulfonyl fluoride (Beyotime, China) before use. After standing on ice for 30 min, the supernatant was collected after centrifugation at 12 000 rpm at 4°C for 15 min, and the protein concentration was determined using BCA protein detection kit (Beyotime, China). After SDS-PAGE treatment, the isolated proteins were transferred onto polyvinylidene fluoride (PVDF) membrane. The membranes were blocked with rapid blocking solution (New Cell&Molecu biotech, China) at room temperature for 15 min, incubated with corresponding primary antibody overnight at 4°C, washed in Tris-buffered saline with Tween 20 (TBST) for 30 min, and incubated with corresponding secondary antibody for 1 h at room temperature. Bound immune-complexes were detected by hypersensitive enhanced chemiluminescence (ECL) solution (Biosharp, China) and visualized them by luminescence image analyzer (Bio-Rad, CA, USA). The experiment was repeated three times.

2.8. Immunofluorescence Staining. The cells were treated with BRU for 24 h and then fixed with 4% paraformaldehyde at room temperature, permeabilization with 0.5% Triton X-100 in PBS for 20 min and then incubated with 1% goat serum albumin blocking solution. Finally, corresponding primary antibodies were added in the cells and incubated overnight at 4°C. After being washed thrice with PBS, the cells were incubated with FITC-conjugated secondary antibodies at 37°C for 1 h. At the last 5 min, the nuclei were stained with DAPI. Images were captured by fluorescence microscope (Olympus, Japan). The experiment was repeated three times.

2.9. Q-PCR (Quantitative Real-Time PCR) Assay. HCT-116 cells were collected after treated with or without 6 nM BRU for 24 h. Total RNA was extracted with TRIzol reagent (Invitrogen, Carlsbad, CA). RNAs were converted to cDNAs using a reverse transcription kit (Takara, Japan), SYBR® Select Master Mix (2X) (ABI, USA) to measure mRNA expressions, and the mRNAs were quantified through -$\Delta\Delta$Ct method. Primer sequences used in this experiment were as follows:

    RhoA (forward): GGAAAGCAGGTAGAGTTGGCT
    RhoA (reverse): GGCTGTCGATGGAAAAACACAT
    ROCK1 (forward): AAGTGAGGTTAGGGCGAAATG
    ROCK1 (reverse): AAGGTAGTTGATTGCCAACGAA

2.10. Xenograft Models in Nude Mice. BALB/C nude mice (female, 5 weeks old) were purchased from Beijing Vital River Laboratory Animal Technology Co., Ltd. After being fed for 1 week in animal Experiment Center of Chongqing Medical University, the nude mice were randomly divided into two groups. And 0.2 mL HCT-116 cell suspension (1×10^7 cells/mL) was subcutaneously injected into the right axilla of nude mice. When the tumors grew to 0.5 cm in diameter, the mice were randomly divided into two groups. Mice in the treatment group were intraperitoneally injected with 2 mg/kg BRU, and mice in the control group were intraperitoneally injected with normal saline once every two days for 28 consecutive days. Parameters of animal weights and tumor sizes were recorded before each administration. After treatment, the animals were sacrificed; all tumors were isolated and weighed. The tumor volume was calculated through the formula (length $\times$ width^2/2). Nude mice were injected with 0.2 mL HCT-116 cell suspension (1×10^7 cells/mL) through tail vein and randomly divided into two groups: BRU group was injected intraperitoneally with 2 mg/kg BRU once every two days, and the control group was injected intraperitoneally with normal saline. After 28 days of treatment, the mice were sacrificed, and the metastatic nodules in lung and intestine were counted. All animal experiments were approved by the Animal Experiment Center of Chongqing Medical University and carried out in accordance with the principles of animal care.

2.11. HE Staining. Xenograft tumor tissues from different groups were fixed with 10% neutral buffer formalin, embedded in paraffin, and sectioned with the thickness of 8 μm. The sections were then stained with a HE assay kit (Solarbio, China) according to the manufacturer instructions. Histological observation was conducted with light microscope (×200 and ×400; Nikon).

2.12. Statistical Analysis. Data in this paper were displayed in a manner of mean ± SD (standard deviation). Statistical analysis was performed with the GraphPad Prism 8.0 software (San Diego, CA, USA), and the data significance was analyzed via either *t*-test or bidirectional analysis of variance (ANOVA).

3. Results

3.1. BRU Inhibited Both the Proliferation of HCT-116 and SW480 Cells. The chemical structure formula of BRU ($C_{26}H_{32}O_{11}$) was shown in Figure 1(a). HCT-116 cells and SW480 cells were treated with different concentrations of BRU for 24, 48, and 72 h, and the cell viability was detected by CCK-8 method, so that we could determine the effects of BRU on the proliferation of colorectal cancer cells in vitro. And it turned out that BRU significantly inhibited the proliferation of HCT-116 cells and SW480 cells in a dose-dependent and time-dependent manner (Figures 1(c) and 1(d)). Normal colonic epithelial cell line NCM460 was treated with BRU at the same low concentration, and no toxicity of BRU to NCM460 cells was detected by cell viability tests (Figure 1(b)). The IC$_{50}$ of HCT-116 and SW480 cells was 16.63 nM and 76.07 nM, respectively, after treated with BRU for 24 h, while the survival rate of the two cells was

(a)

(b)

(c)

(d)

(e)

(f)

(g)

(h)
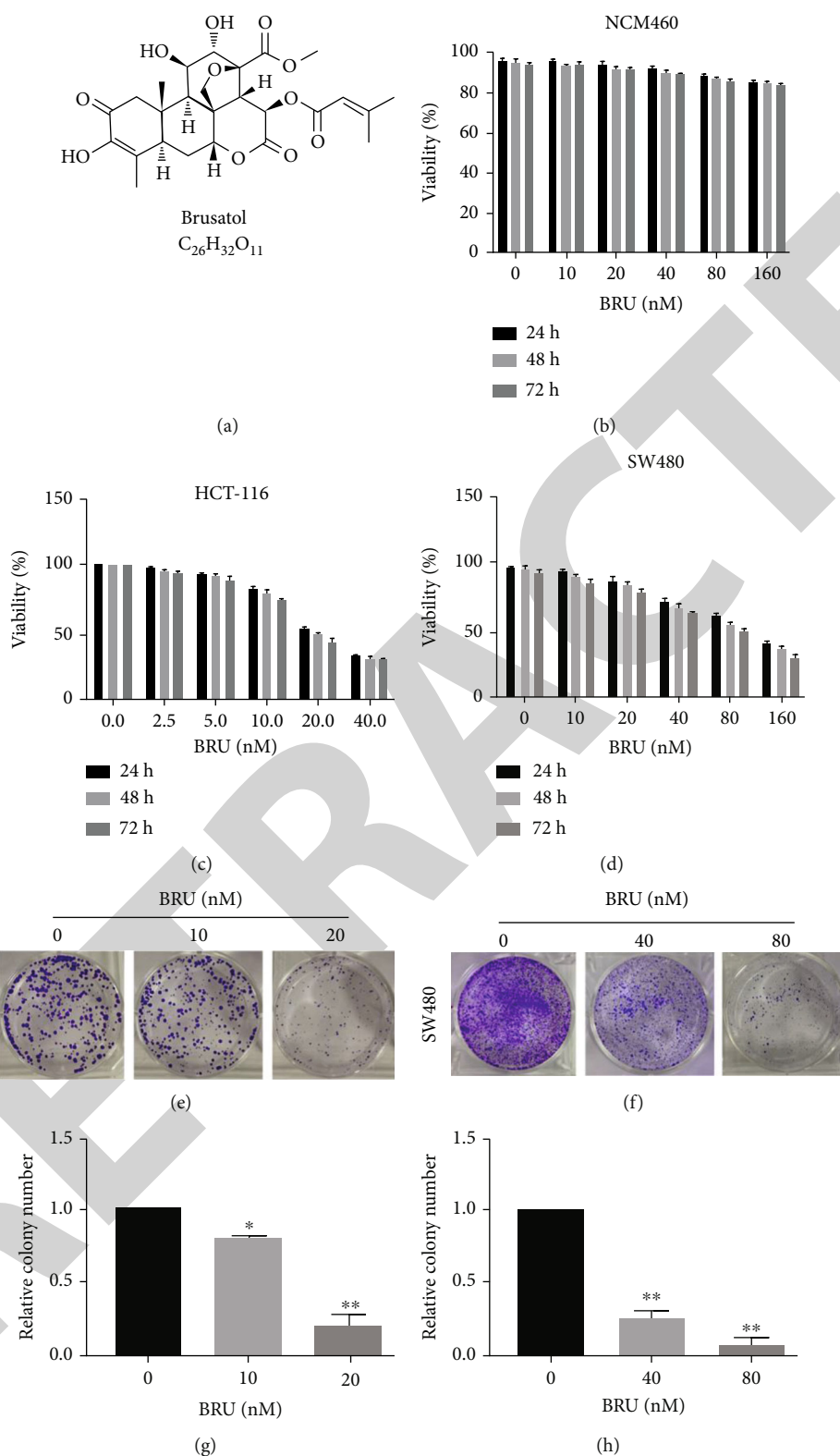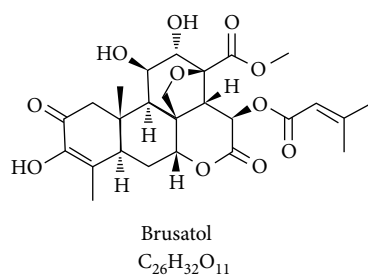
Figure 1: BRU inhibited the proliferation of HCT-116 and SW480 cells in vitro. Chemical structures of BRU (a), NCM 460 (b), HCT-116 (c), and SW480 (d) cells were treated with various specified concentrations of BRU (0-160 nM) for 24, 48, and 72 h, respectively, and cell viability was measured by CCK-8 assay. Images were formed of representative colonies of HCT-116 cells (e) and SW480 cells (f) treated with different concentrations of BRU. (g, h) Statistical analysis of cell colony formation of HCT-116 and SW480. All data were shown as mean ± SD from three independent trials ($^*P < 0.05$, $^{**}P < 0.01$ vs. control).

more than 90% when treated with 20 nM and 80 nM BRU for 24 h. Therefore, unless otherwise specified, we continued to treat HCT-116 and SW480 cells with 20 nM and 80 nM BRU as the maximum concentration, and 24 h was the treatment duration.

In the colony formation experiment, we selected the concentration of IC$_{50}$ and 1/2 IC$_{50}$ about 24 h after BRU acted on HCT-116 and SW480 cells to treat the cells, so as to explore the effect of BRU on the proliferation of CRC cells. The results showed that BRU significantly reduced the colony-forming ability of colorectal cancer cells, and the inhibition effect was most significant in the highest concentration group (Figures 1(e)–1(h)). These results all confirmed the inhibitory effect of BRU on the proliferation of CRC cells in vitro.

3.2. BRU Inhibited Both the Migration and Invasion of HCT-116 and SW480 Cells In Vitro.

This section investigated the effects of BRU on migration and invasion of HCT-116 and SW480 cells. We treated HCT-116 and SW480 cells with increasing concentrations of BRU for 24 h and found that BRU significantly inhibited the migration and invasion of HCT-116 (Figures 2(a) and 2(e)) and SW480 (Figures 2(c) and 2(g)) cells. In HCT-116 cells, the relative mobility of each group was $(28.9 \pm 0.8)\%$, $(17.7 \pm 1.6)\%$, and $(10.3 \pm 3.1)\%$ (Figure 2(b)); through calculation, we learned that the number of invaded membrane cells in each group was 760 ± 27, 532 ± 57, and 353 ± 8 under each field (Figure 2(f)). In SW480 cells, the relative mobility of each group were $(59.1 \pm 3.8)\%$, $(22.8 \pm 2.3)\%$, and $(7.4 \pm 3.1)\%$ (Figure 2(d)); after calculation, the number of invaded membrane cells per field of vision in each group was 926 ± 99, 676 ± 19, and 608 ± 8 (Figure 2(h)).

3.3. BRU Reversed the Epithelial-Mesenchymal Transformation (EMT) of HCT-116 and SW480 Cells.

EMT is involved in the migration and invasion of most malignant tumor cells [23]. We treated HCT-116 and SW480 cells with BRU (0, 3, and 6 nM) and BRU (0, 10, and 20 nM) for 24 h, respectively, and detected EMT-related proteins expression by western blot. The results showed that compared with the control group, the expression of E-cadherin protein was upregulated in both HCT-116 and SW480 cells treated with BRU, while the expressions of Vimentin, N-cadherin, MMP2, and MMP9 protein were downregulated (Figures 3(a)–3(d)).

3.4. BRU Inhibited Colorectal Cancer Cellular Invasion by Blocking the RhoA/ROCK1 Pathway.

HCT-116 and SW480 cells were treated with BRU (0, 3, and 6 nM) and BRU (0, 10, and 20 nM), respectively, to verify the antitumor mechanism of BRU on colorectal cancer cells. After 24 h treatment, the expressions of RhoA/ROCK1 pathway protein were assessed by western blot assay. Western blot results showed that compared with the control group, protein expressions of RhoA and ROCK1 in both HCT-116 (Figures 4(a) and 4(c)) and SW480 (Figures 4(b) and 4(d)) cells were significantly reduced in a concentration-dependent manner after BRU treatment. In addition, the immunofluorescence results of HCT-116 cells after 6 nM BRU treatment showed that the protein expressions of RhoA and ROCK1 in the BRU treatment group were greatly decreased in contrast to the control group (Figures 4(e) and 4(f)). Likewise, q-PCR results unveiled that the mRNA expressions of RhoA and ROCK1 were also decreased after BRU treatment (Figure 4(g)).

3.5. BRU Reversed the EMT Process of HCT-116 and SW480 Cells by Blocking RhoA/ROCK1 Signaling Pathway.

Subsequent experiments verified that BRU affects the EMT process of colorectal cancer cells through RhoA/ROCK1 signaling pathway: we treated HCT116 and SW480 cells with BRU, Y27632 (inhibitors of ROCK), and BRU + Y27632. The protein expression levels of RhoA, ROCK1, E-cadherin, Vimentin, N-cadherin, MMP2, and MMP9 were detected by western blot. The results showed that BRU inhibited the expressions of RhoA and ROCK1 proteins in both HCT-116 and SW480 cells. In addition, Y27632 also downregulated the levels of these proteins, and BRU enhanced the downregulation of these proteins by Y27632 (Figures 5(a)–5(d)). In Figures 5(e)–5(h), HCT-116 and SW480 were treated in the same way, and the results showed that both BRU and Y27632 could enhance the protein expression of E-cadherin and inhibit the protein expressions of Vimentin, N-cadherin, MMP2, and MMP9. Moreover, the BRU + Y27632 treatment group enhanced or inhibited the expression of these proteins more significantly. Together, these results implied that BRU reverses EMT in colorectal cancer cells by blocking the RhoA/ROCK1 pathway.

3.6. BRU Inhibited Tumor Growth and Metastasis in HCT-116 Xenograft Mice.

The mouse HCT-116 xenotransplantation model was used to study the antitumor effect of BRU in vivo. In order to investigate whether BRU inhibits tumor growth in vivo, the HCT-116 cells were inoculated subcutaneously into nude mice to construct mouse models. These mice were divided into control group and BRU group. It was seen that the tumor volume in the BRU group was significantly smaller than that in the control group (Figure 6(a)), and its weight was also significantly lighter (Figure 6(e)). In addition, our outcomes of measurements showed that at the beginning of administration, the tumor volume of the control group and the BRU group was almost the same. With the increase of administration time, the tumor volume of the control group increased, while that of the BRU group did not change much (Figure 6(d)). There was no significant difference in mouse body weight between control and BRU groups, suggesting that BRU has no toxic side effects (Figure 6(b)).

In addition, paraffin-embedded sections of tumor tissues were analyzed by HE staining, and it was observed under ×200 and ×400 microscopes that tumor tissue necrosis, nuclear fragmentation, and dissolution were evident in the BRU group versus the control group (Figure 6(c)). Western blot analysis of tumor tissue showed that the expressions of RhoA, ROCK1, Vimentin, N-cadherin, MMP2, and MMP9 protein decreased, and the expressions of E-cadherin protein increased (Figures 6(f) and 6(g)), which was consistent with the results of in vitro experiment.

(a)

(b)

(c)

(d)

(e)

(f)

(g)

(h)
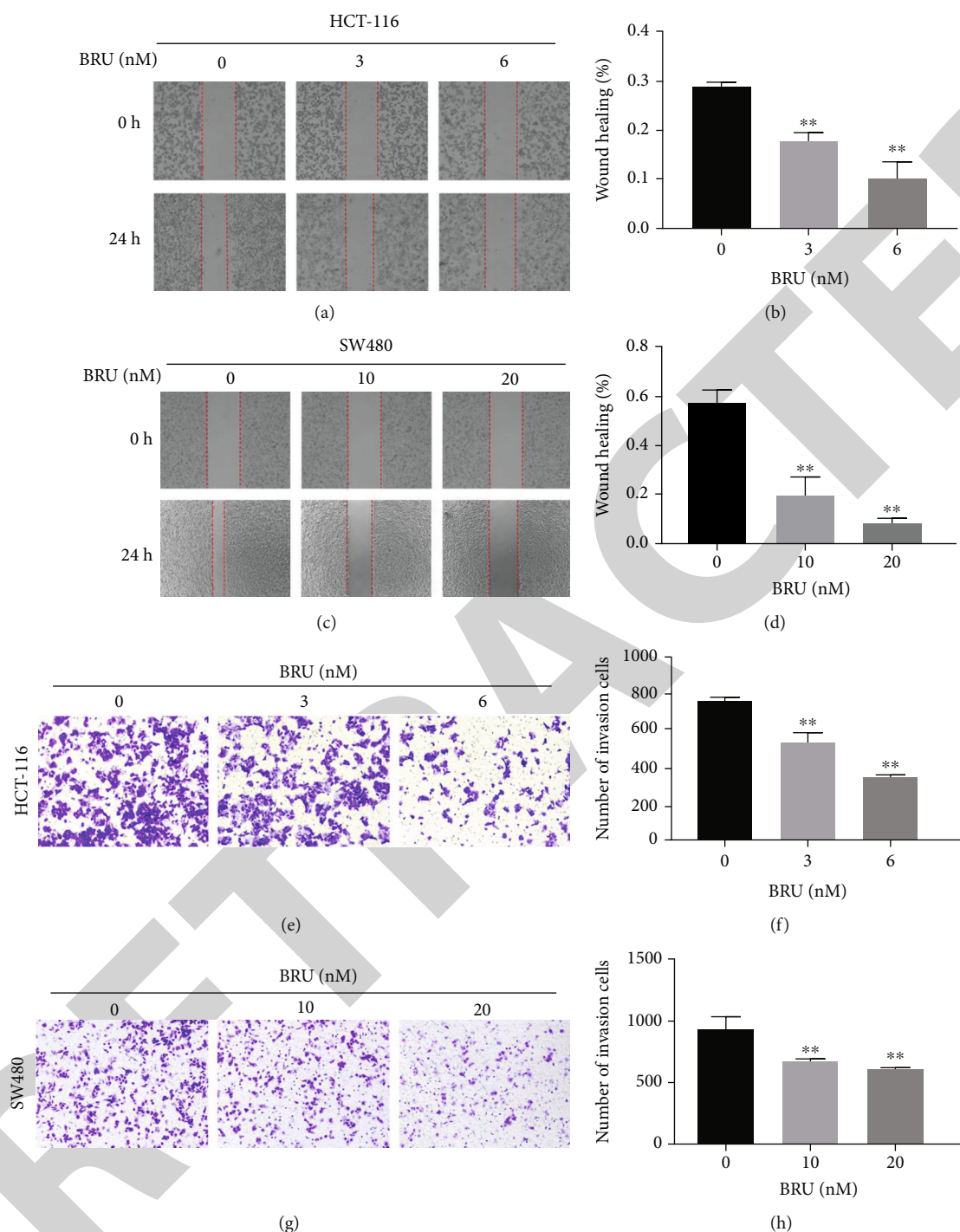
Figure 2: BRU inhibited the migration and invasion of HCT-116 and SW480 cells. Wound healing experiments were performed to detect representative images (a, c) and statistical analysis of cell mobility (b, d) of HCT-116 and SW480 cells treated with different concentrations of BRU for 24 h. Representative images (e, g) of the invasion results of HCT-116 and SW480 cells treated with BRU at different concentrations were detected by transwell assay. Statistical plots of invaded cells (f, h). All data were shown as mean ± SD from three independent trials ($^*P < 0.05$, $^{**}P < 0.01$ vs. control).

In the early stage of treatment, the weight of mice in each group was not significantly different; but in the late stage of treatment, that is, three weeks after the drug was administered, due to the massive proliferation and metastasis of tumor cells, the body weight of the mice in the control group decreased significantly. The body weight of the mice in the

two groups was almost unchanged, and the body weight of the two groups of mice was significantly different, and the difference was statistically significant (Figure 6(h)). We then counted metastatic nodules in the lung and intestine, and the results showed that the number of metastatic nodules in the lung and intestine was significantly reduced by more than

(a)

(b)

(c)

(d)
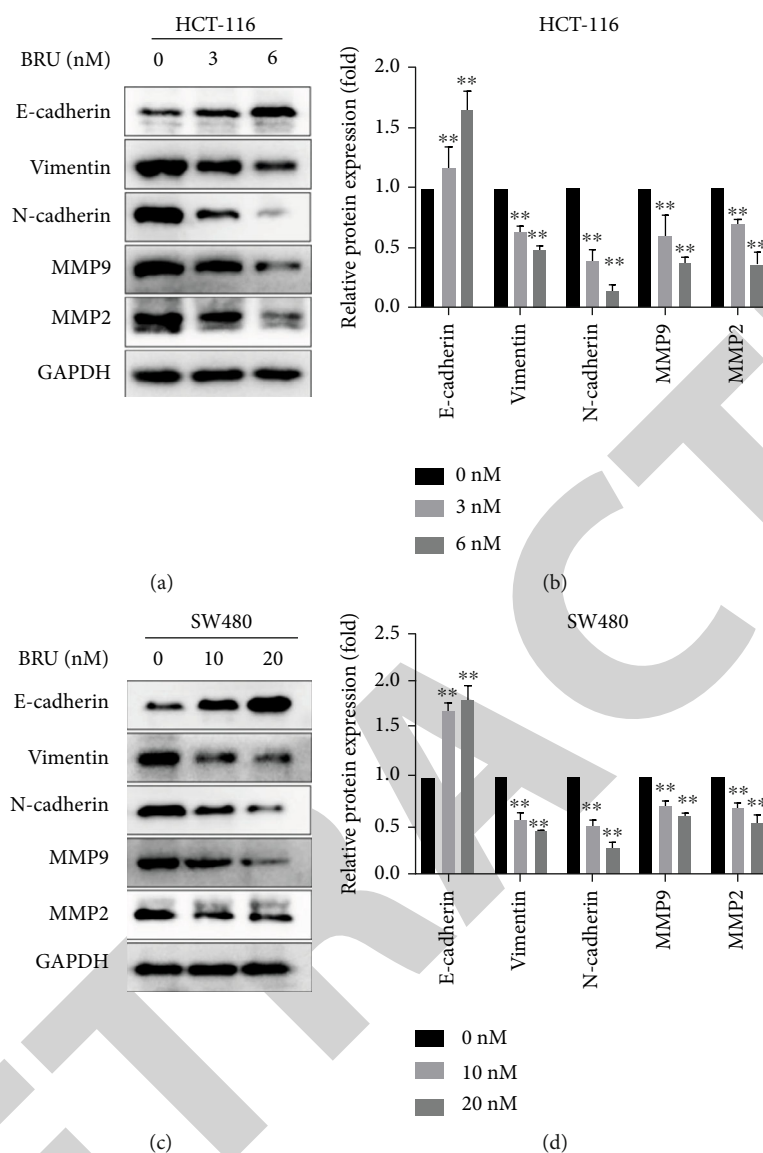
Figure 3: BRU reversed protein expressions of EMT-related markers in both HCT-116 and SW480 cells. Western blotting was performed to analyze the protein level of E-cadherin, Vimentin, N-cadherin, MMP9, and MMP2 in HCT-116 cells (a, b) and SW480 cells (c, d), and quantitative analysis was performed by the Image Lab software. All data were shown as mean ± SD from three independent trials ($^{*}P < 0.05$, $^{**}P < 0.01$ vs. control).

60.8% and 57.1% compared with the control group (Figures 6(i) and 6(j)). These results suggest that BRU is capable of inhibiting the growth and metastasis of colorectal cancer cells in vivo.

4. Discussion

One of the merits of Chinese herbal medicine is less toxic and side effects, which has been coming to be concerned last decades, especially in antitumor realm. Brusatol, one of the herbal extracts, has been widely recognized for its remarkable efficacy in the treatment of many cancer diseases [24, 25]. Our studies found that BRU has a significant inhibitory effect on the growth of colorectal cancer cells in both vivo and vitro, which also indicates that BRU has potential clinical application value in the development of new remedies for CRC.

The proliferation ability of tumor cells is the basis of tumor growth and development, and all tumors have the distinctive characteristic of uncontrolled proliferation [26]. Our study verified the effective inhibitory effect of BRU on the proliferation of HCT-116 cells and SW480 cells. We conducted CCK-8 analysis and colony formation test successively and found that BRU reduced the growth capacity of HCT-116 cells and SW480 cells in a time-dependent and dose-dependent manner. In addition, the number of cell colonies formed in treatment group was significantly less than that in the control group. The results above all reflected the inhibitory effect of BRU on CRC cellular proliferation in vitro.

The process of tumorous metastasis is not only complex but also a malignant behavior in the occurrence and development of tumor. Migration and invasion are two essential
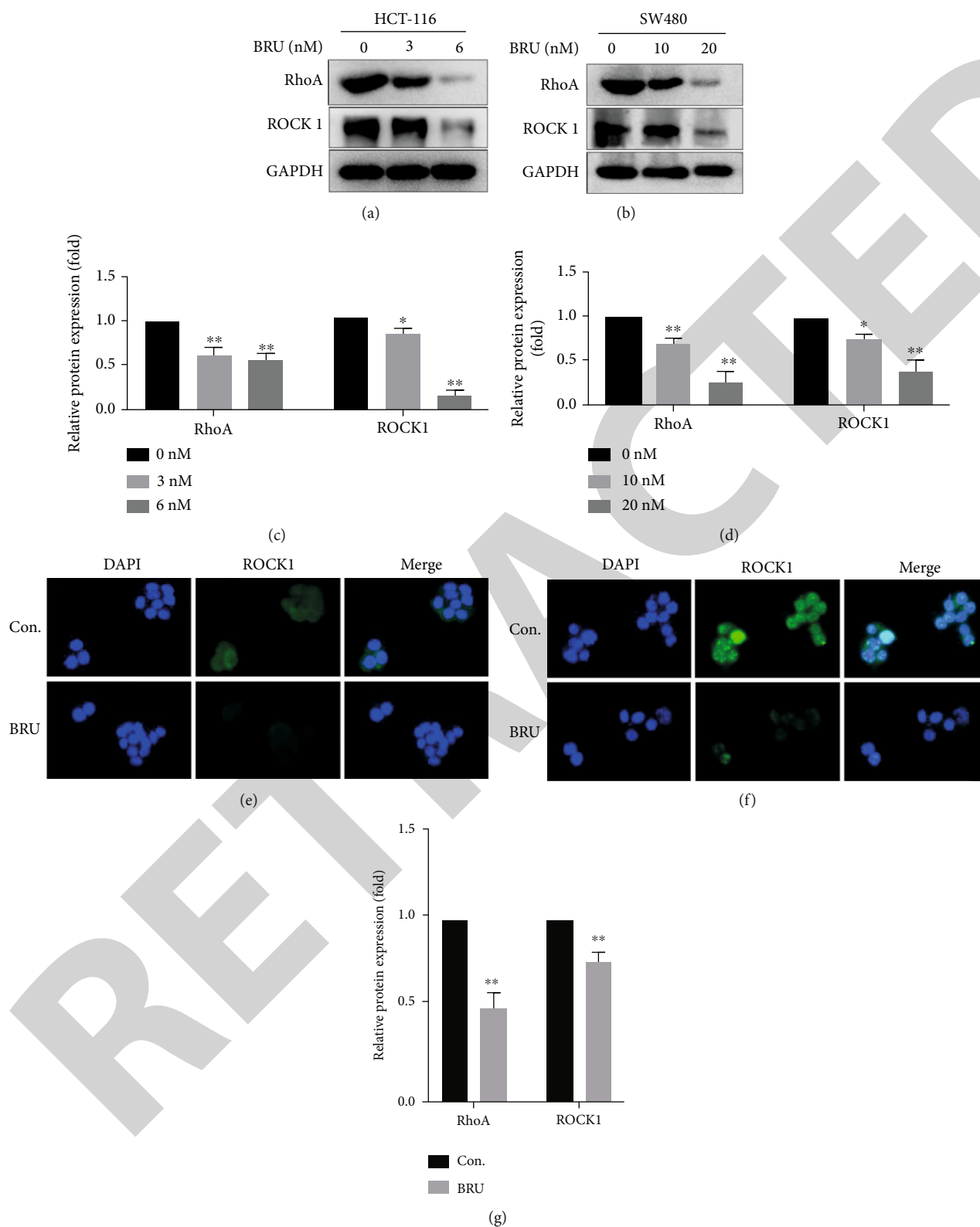
FIGURE 4: BRU downregulates RhoA/ROCK1 pathway protein expressions in colorectal cancer cells. After the respective treatment concentrations were added into HCT-116 and SW480 cells, the expressions of RhoA and ROCK1 in the treated and the untreated groups were detected by western blot (a, b), and the results of quantitative analysis by the Image Lab software (c, d). Representative immunofluorescence images of HCT-116 cells treated with or without 6 nM BRU for 24 h (e, f). The mRNA expressions of RhoA and ROCK1 in HCT-116 cells were determined by RT-QPCR (g). All data were shown as mean ± SD from three independent trials ($^{*}P < 0.05$, $^{**}P < 0.01$ vs. control).
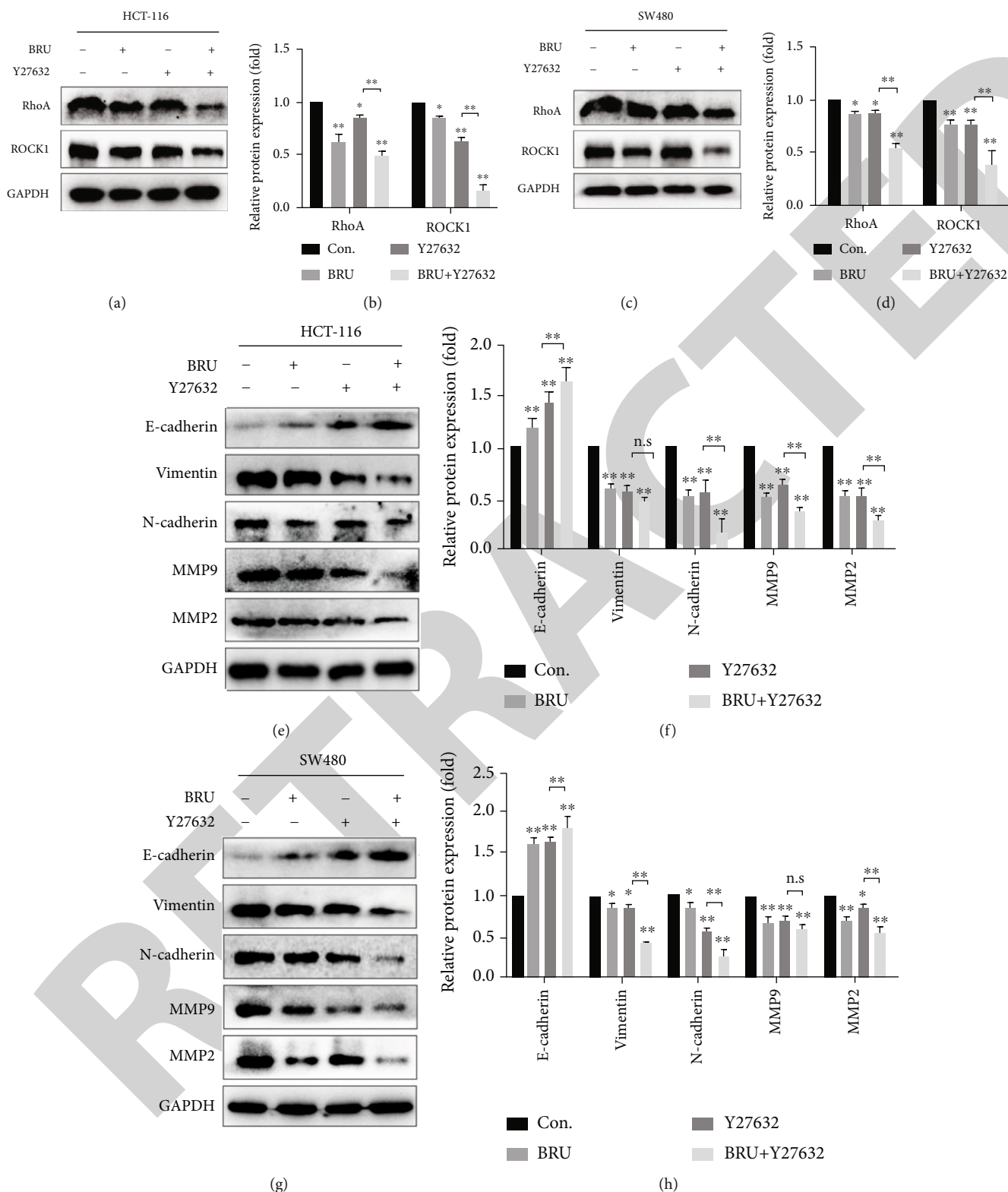
Figure 5: Possible mechanism of BRU reversal of EMT process in colorectal cancer cells. After HCT-116 and SW480 cells were treated with or without BRU, Y27632 and BRU + Y27632, RhoA and ROCK1 in cells were analyzed by western blot (a, c) and quantitative analysis by the Image Lab software (b, d); after HCT-116 and SW480 cells were treated with or without BRU, Y27632, BRU + Y27632, western blot analysis of E-cadherin, Vimentin, N-cadherin, MMP2, MMP9 in cells (e, g) and quantitative analysis of the Image Lab software (f, h). All data were shown as mean ± SD from three independent trials ($^*P < 0.05$, $^{**}P < 0.01$ vs. control).

(a)

(b)

(c)

(d)

(e)

(f)

Figure 6: Continued.

(g)

(h)

(i)

(j)
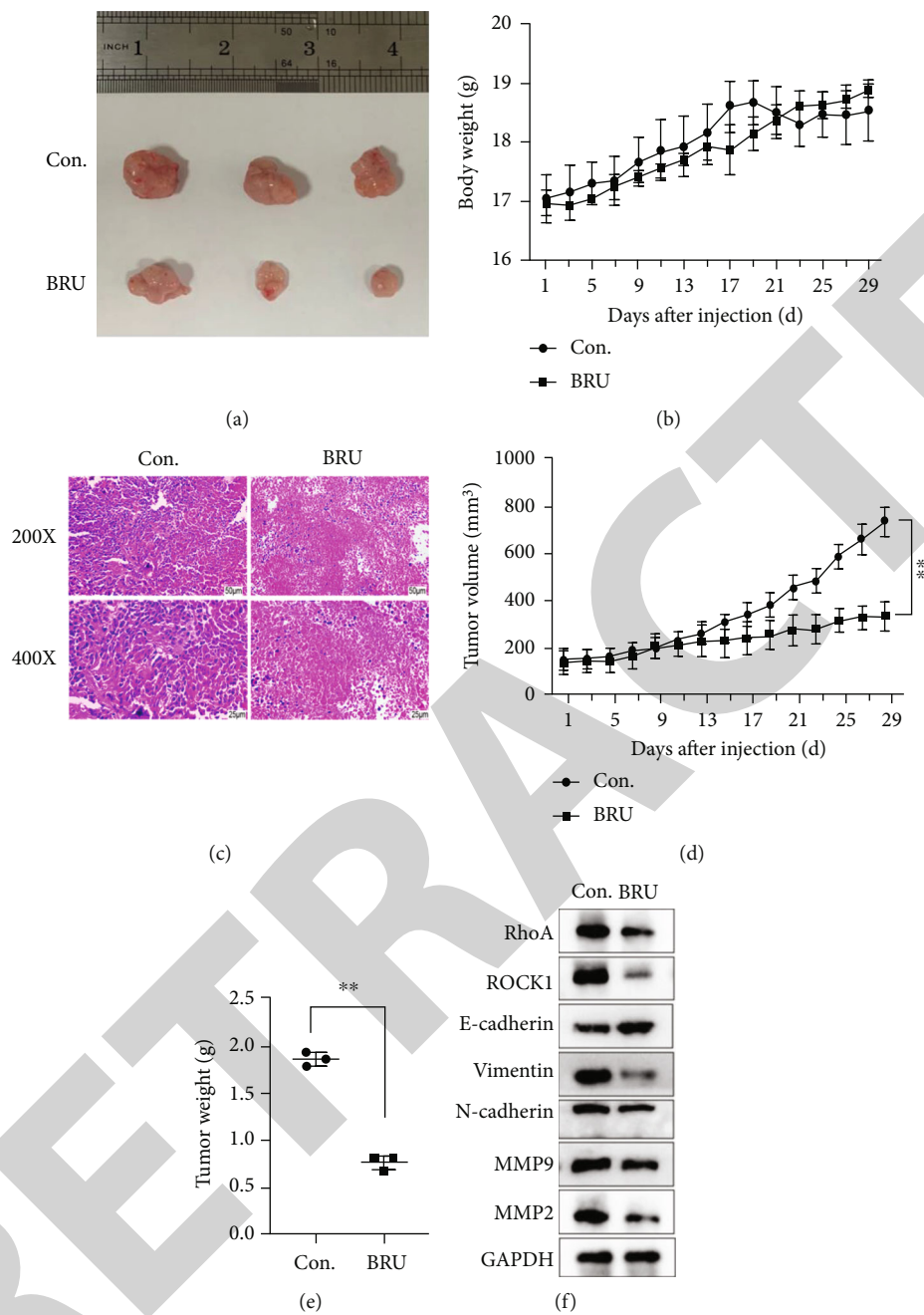
Figure 6: BRU inhibits the tumorous growth and metastasis in nude mice. Representative image of nude mouse tumor in subcutaneous tumor-forming model of the control group (normal saline) and BRU (2 mg/kg) group (a). Changes in body weight of mice in the control group and BRU group during treatment (b). Representative image of HE staining in tumor tissue (c). Changes in tumor volume and weight were compared between the control group and the BRU group during treatment (d, f). The protein levels of RhoA, ROCK1, E-cadherin, Vimentin, N-cadherin, MMP2, and MMP9 in tumor tissues were analyzed by western blotting (g, h). Body weight changes of the control group and BRU group in the nude mouse model after tail vein injection (h). Metastatic nodules in lung and bowel (i, j). All data were shown as mean ± SD from three independent trials ($^*P < 0.05$, $^{**}P < 0.01$ vs. control).

cellular processions in tumor metastasis [27]. Both scratch assay and Transwell assay results showed that BRU effectively inhibited the migration and invasion of HCT-116 and SW480 cells in a dose-dependent manner, which was sufficient to demonstrate the effective inhibitory effect of BRU on the migration and invasion of CRC cells.

EMT is a morphogenetic process, which also occurs in cancer, triggering loss of cell polarity, disruption of cell-cell adhesion, actin cytoskeletal recombination, and cell migration. The transformation of cells with an epithelial phenotype into cells with a mesenchymal phenotype is called epithelial-mesenchymal transformation, a normal process required for embryonic development and one of the pathologic features associated with tumor metastasis [28]. EMT plays a crucial role in early tumor metastasis, enabling tumor cells to migrate and invade and at the same time giving tumor cells the properties of stem cells [29, 30]. Among the markers of EMT, high expression of N-cadherin is positively correlated with HCC and colon cancer tissue metastasis, suggesting a low survival rate in patients [31]. Vimentin is commonly expressed in nondiseased mesenchymal cells

and overexpressed in a wide range of epithelial cancers, which are also positively associated with tumor proliferation, metastasis, and reduced patient survival [32]. Reduction of E-cadherin is associated with invasion of CRC cells, and it would also increase the tumor cellular resistance to standard chemotherapy drugs [33, 34]. MMP2 enhances fibronectin mediated tumor cell adhesion by regulating the migration of various tumor cells in the extracellular matrix through integrin [35]. MMP9 is able to effectively affect the vascularization and growth rate of tumor cells, leading to the formation and degradation of cell-matrix [36]. Therefore, reversing the procession of EMT is considered as a potential strategy to improve the migration and aggressiveness of malignant tumors. Western blot assay revealed that BRU inhibits the EMT of cancer cells by upregulating the expression of E-cadherin and downregulating the protein levels of Vimentin, N-cadherin, MMP2, and MMP9, thus hindering the metastasis of colon cancer cells.

Cancer cell migration is a multistep dynamic process involving cell-cell adhesion, cell-matrix adhesion, and biochemical and biophysical reorganization of cell shape or

polarity [37, 38], and one of the key requirements of tumor metastasis is the recombination of actin cytoskeleton. Actin is the critical component of cytoskeleton, the main mediator of intercellular force generation, and it is also the key component of cell diffusion and adhesion. Cytoskeletal recombination of actin is also essential for the transition of adequately characterized epithelial-mesenchymal transition (EMT) to mesenchymal like cells [39]. Studies have shown that RhoA-ROCK1 signaling pathway is related to cytoskeleton regulation, which has an important impact on cancer metastasis [40]. Studies have also justified that targeting RhoA-ROCK1 signaling pathway is one of the feasible methods to inhibit CRC metastasis [41]. A study on colon cancer cells showed that expression and subsequent activation of RhoC protein, accompanied with the downregulation of E-cadherin and a significant reduction in RhoA activation, are associated with EMT development [42]. Therefore, we have reason to believe that BRU would inhibit EMT through RhoA/ROCK1 pathway, thus inhibiting the proliferation and metastasis of colorectal cancer. In this study, we found that the protein and mRNA expressions of RhoA and ROCK1 were decreased in BRU-treated colorectal cancer cells. After the addition of ROCK1 inhibitor (Y27632) to inhibit ROCK1 expression, BRU would further enhance the inhibitory effect of Y27632 on colorectal cancer cells.

In addition, our in vivo experiments further confirmed the antitumor effect of BRU. These findings suggested the antiproliferation and antimetastasis effects of BRU towards CRC, which may be related to the reversal of EMT by targeting the RhoA/ROCK1 pathway.

5. Conclusion

In summary, this study for the first time clarified the anticolorectal cancer role of BRU: BRU inhibits tumor growth and metastasis in vivo and in vitro by blocking the RhoA/ROCK1 signaling pathway-mediated EMT process. These findings provide solid evidence that BRU may be an attractive candidate for the treatment of CRC in the future. However, tumor metastasis is a complex process, and whether BRU regulates this process through other mechanisms is worthy of our further exploration.

Data Availability

The data used to support the findings of this study are included within the article.

Conflicts of Interest

The authors declare that they have no competing interest.

References

[1] H. Brody, "Colorectal cancer," *Nature*, vol. 521, no. 7551, p. S1, 2015.

[2] J. Lin, M. A. Piper, L. A. Perdue et al., "Screening for colorectal cancer," *JAMA*, vol. 315, no. 23, pp. 2576–2594, 2016.

[3] S. Bruin, C. Klijn, G. J. Liefers et al., "Specific genomic aberrations in primary colorectal cancer are associated with liver metastases," *BMC Cancer*, vol. 10, no. 1, p. 662, 2010.

[4] Y. Kawaguchi, H. A. Lillemoe, E. Panettieri et al., "Conditional recurrence-free survival after resection of colorectal liver metastases: persistent deleterious association with RAS and TP53 co-mutation," *Journal of the American College of Surgeons*, vol. 229, no. 3, pp. 286–294.e1, 2019.

[5] S. Friberg and A. Nyström, "Cancer metastases: early dissemination and late recurrences," *Cancer growth and metastasis*, vol. 8, pp. 43–49, 2015.

[6] R. Silva-Oliveira, V. A. O. Silva, O. Martinho et al., "Cytotoxicity of allitinib, an irreversible anti-EGFR agent, in a large panel of human cancer-derived cell lines: KRAS mutation status as a predictive biomarker," *Cellular Oncology (Dordrecht)*, vol. 39, no. 3, pp. 253–263, 2016.

[7] L. A. Diaz Jr., R. T. Williams, J. Wu et al., "The molecular evolution of acquired resistance to targeted EGFR blockade in colorectal cancers," *Nature*, vol. 486, no. 7404, pp. 537–540, 2012.

[8] E. Ko, D. Kim, D. W. Min, S. H. Kwon, and J. Y. Lee, "Nrf2 regulates cell motility through RhoA-ROCK1 signalling in non-small-cell lung cancer cells," *Scientific Reports*, vol. 11, no. 1, p. 1247, 2021.

[9] S. Ellenbroek and J. Collard, "Rho GTPases: functions and association with cancer," *Clinical & Experimental Metastasis*, vol. 24, no. 8, pp. 657–672, 2007.

[10] Y. Bai, Y. H. Zhao, J. Y. Xu, X. Z. Yu, Y. X. Hu, and Z. Q. Zhao, "Atractylodin induces myosin light chain phosphorylation and promotes gastric emptying through ghrelin receptor," *Evidence-based Complementary and Alternative Medicine: Ecam*, vol. 2017, p. 2186798, 2017.

[11] Z. Xu, H. Liang, M. Zhang et al., "Ardipusilloside-I stimulates gastrointestinal motility and phosphorylation of smooth muscle myosin by myosin light chain kinase," *The Korean journal of physiology & pharmacology: official journal of the Korean Physiological Society and the Korean Society of Pharmacology*, vol. 21, no. 6, pp. 609–616, 2017.

[12] M. Amano, M. Nakayama, and K. Kaibuchi, "Rho-kinase/ROCK: a key regulator of the cytoskeleton and cell polarity," *Cytoskeleton (Hoboken, N.J.)*, vol. 67, no. 9, pp. 545–554, 2010.

[13] H. Campbell, N. Fleming, I. Roth et al., "Δ133p53 isoform promotes tumour invasion and metastasis via interleukin-6 activation of JAK-STAT and Rho A-ROCK signalling," *Nature Communications*, vol. 9, no. 1, p. 254, 2018.

[14] G. Mu, Q. Ding, H. Li et al., "Gastrin stimulates pancreatic cancer cell directional migration by activating the Gα12/13-RhoA-ROCK signaling pathway," *Experimental & Molecular Medicine*, vol. 50, no. 5, pp. 1–14, 2018.

[15] S. Cai, Y. Liu, S. Han, and C. Yang, "Brusatol, an NRF2 inhibitor for future cancer therapeutic," *Cell & Bioscience*, vol. 9, no. 1, p. 45, 2019.

[16] W. Tang, J. Xie, S. Xu et al., "Novel nitric oxide-releasing derivatives of brusatol as anti-inflammatory agents: design, synthesis, biological evaluation, and nitric oxide release studies," *Journal of Medicinal Chemistry*, vol. 57, no. 18, pp. 7600–7612, 2014.

[17] I. Hall, K. H. Lee, S. A. Elgebaly, Y. Imakura, Y. Sumida, and R. Y. Wu, "Antitumor agents XXXIV: mechanism of action of bruceoside A and brusatol on nucleic acid metabolism of P-388 lymphocytic leukemia cells," *Journal of Pharmaceutical Sciences*, vol. 68, p. 883, 1979.

Retraction

Retracted: Identification of lncRNA Biomarkers and LINC01198 Promotes Progression of Chronic Rhinosinusitis with Nasal Polyps through Sponge miR-6776-5p

BioMed Research International

This article has been retracted by Hindawi following an investigation undertaken by the publisher [1]. This investigation has uncovered evidence of one or more of the following indicators of systematic manipulation of the publication process:

(1) Discrepancies in scope

(2) Discrepancies in the description of the research reported

(3) Discrepancies between the availability of data and the research described

(4) Inappropriate citations

(5) Incoherent, meaningless and/or irrelevant content included in the article

(6) Manipulated or compromised peer review

The presence of these indicators undermines our confidence in the integrity of the article's content and we cannot, therefore, vouch for its reliability. Please note that this notice is intended solely to alert readers that the content of this article is unreliable. We have not investigated whether authors were aware of or involved in the systematic manipulation of the publication process.

Wiley and Hindawi regrets that the usual quality checks did not identify these issues before publication and have since put additional measures in place to safeguard research integrity.

We wish to credit our own Research Integrity and Research Publishing teams and anonymous and named external researchers and research integrity experts for contributing to this investigation.

The corresponding author, as the representative of all authors, has been given the opportunity to register their agreement or disagreement to this retraction. We have kept a record of any response received.

References

[1] X. Wang, X. Zhu, L. Peng, and Y. Zhao, "Identification of lncRNA Biomarkers and LINC01198 Promotes Progression of Chronic Rhinosinusitis with Nasal Polyps through Sponge miR-6776-5p," *BioMed Research International*, vol. 2022, Article ID 9469207, 27 pages, 2022.

Research Article

Identification of lncRNA Biomarkers and LINC01198 Promotes Progression of Chronic Rhinosinusitis with Nasal Polyps through Sponge miR-6776-5p

Xueping Wang [iD],[1] Xiaoyuan Zhu,[1] Li Peng,[2] and Yulin Zhao[1]

[1]*Department of Otolaryngology Head and Neck Surgery, The First Affiliated Hospital of Zhengzhou University, Zhengzhou, Henan, China 410000*
[2]*Department of Obstetrics and Gynecology, The First People's Hospital of Nanyang, Nanyang, Henan, China 473000*

Correspondence should be addressed to Xueping Wang; fccwangxp@zzu.edu.cn

Background. Chronic sinusitis (CRS) was a chronic inflammation that originated in the nasal mucosa and affected the health of most people around the world. Chronic rhinosinusitis with nasal polyps (CRSwNP) was one kind of chronic sinusitis. Emerging research had suggested that long noncoding RNAs (lncRNAs) played vital parts in inflammatories and inflammation development. *Methods*. We acquired GEO data to analyze the differential expression between the miRNA, immune genes, TF, and lncRNA data in CRSWNP and the corresponding control tissues. Bioinformatic analysis by coexpression of endogenous RNA network and competitive way enrichment, analysis, and forecasting functions of these noncoding RNA. The different pathway expressions in CRSwNP patients were confirmed using GSVA to analyze the differentially expressed immune genes and TF data sets in CRSwNP patients. The differential immune gene and transcription factor data set in CRSwNP perform functional notes and protein-protein interaction (PPI) network structure. We predicted the potential genes and RNAs related to CRSWNP by constructing a ceRNA network. In addition, we also used 19 hub immune genes to predict the potential drugs of CRSWNP. lncRNA biomarkers in CRSwNP were identified by lncRNAs LASSO regression. The CIBERSORT algorithm was used to contrast the divergence in immune infiltrations between CRSwNP and usual inferior turbinate organizations in 22 immunocyte subgroups. *Results*. We identified a total of 48 miRNAs, 304 lncRNAs, 92 TFs, and 525 immune genes as CRSwNP-specific RNAs. GO and KEGG pathways both analyzed differentially expressed immune genes and transcription factor data sets. We predicted the potential genes GNG7, TUSC8, LINC01198, and has-miR-6776-5p by constructing ceRNA and PPI networks. At the same time, we found that the above genes were involved in two important pathways: chemokine signal path and PI3K/AKT signal path. In addition, we predicted 5 small molecule drugs to treat CRSwNP by analyzing 19 central immune genes, namely, danazol, ikarugamycin, semustine, cefamandole, and molindone. Finally, we identified 5 biomarkers in CRSwNP, namely, LINC01198, LINC01094, LINC01798, LINC01829, and LINC01320. *Conclusions*. We had identified CRSwNP-related miRNAs, lncRNAs, TFs, and immune genes, which may be making use of latent therapeutic target for CRSwNP. At the same time, we identified 5 lncRNA biomarkers in CRSwNP. The results of this study showed that LINC01198 promoted the progression of CRSwNPs through spongy miR-6776-5p. Our studies provide a new way for further analyses of the pathogenesis of CRSwNP.

1. Background

Chronic sinusitis (CRS) was a chronic inflammation that comes of the mucosa of the sneezers and affects the physique of many person on a global scale [1, 2]. On the basis of epi-demiological datas, CRS affected 10.9% and 7. 0% of the number of people in Europe and South Korea, separately [3, 4]. Chronic rhinosinusitis with nasal polyps (CRSwNP) was a clinical manifestation of chronic sinusitis. CRS patients mainly had the following symptoms: nasal

congestion, hyposmia, olfactory asthenia, encephalalgias, facial pain, or pressure, of which CRSwNP and nasal congestion and anosmia are related [5–7]. According to clinical data, CRSwNP patients were prone to drug resistance during treatment, so patients with CRSwNP were often difficult to cure. At the same time, the studies had found that the incidence of CRSwNP had nothing to do with whether the patient had undergone repeated sinus surgery and the expression level of local corticosteroids or long-term systemic glucocorticoids [8, 9]. To make a long story short, pursuing the latent mechanism of CRSwNP is significant for the cure of CRSwNP.

Long noncoding RNAs (lncRNAs) were long, exceed 200 nucleotides, and referred to RNA that could not encode protein [10]. More and more studies had proved that lncRNAs participated in almost all parts of gene control, consisting of epigenetic developmental control, nucleocytoplasmic transship, and transcription [11]. Therefore, lncRNAs affect most cell biological proceeding consisting of cell growth, proliferation, metastasis, invasion, and divergence [11, 12]. Abnormal lncRNA expression was a common feature of many diseases [13]. However, there were few studies on CRSwNP and lncRNAs. As a specific differentiated lncRNA, LINC01198, a contraction of long intergenic nonprotein coding RNA 1198, was located on chromosome 13 and initially captured in a glioma study where LINC01198 was predicted to be remarkably associated with tumor grade and overall prognosis on clinical tissue level by virtue of bioinformatic data analysis, preliminarily implying the oncogenic nature of it. The latest research has suggested that the abnormal expression of LINC01198 was related to glioma and rectal cancer. It was relevant to the incidence and progression of bladder cancer [14–16]. However, the role of LNC01198 in other inflammatory diseases was not reported.

MicroRNAs (miRNAs) were small, 20-24 nucleotides, and were newly discovered type of noncoding RNAs that mediated protein levels by binding target mRNAs. It belongs to endogenous RNA. At present, some studies had demonstrated that miRNAs played a crucial role in the occurrence and progression of cancer [17]. Studies had found that some miRNAs were differentially expressed in CRSwNP and affected its development [8, 18]. The effect of miR-6776-5p has already been evidenced by current studies, such as promoting the occurrence of renal cancer development by inhibiting the degradation of oncogene TRPM3 [19]. Both microRNAs and lncRNAs played important roles in regulating gene expression and involved a variety of biological processes. Salmena et al. proposed a hypothesis about competitive endogenous RNA (Cerna) in 2011 and proved it [20–22]. The ceRNA referred to the existence of certain RNAs (herein referred to as ceRNAs) and targeted miRNAs that had a common binding site and a competitive activity, thereby affecting the function of the target miRNA. The ceRNAs could interact with the target miRNA to control transcription group expression [23].

In this study, we identified 5 lncRNA biomarkers in CRSwNP (LINC01198, LINC01094, LINC01798, LINC01829, and LINC01320). We found that compared with the control group, LINC01198 was downregulated in CRSwNP. We established a ceRNA network and found that LINC01198, TUSC8, miR-6776-5p, and GNG7 had a mutual regulatory relationship. At the same time, they were related to the PI3K/AKT signaling pathway. We speculated that LINC01198 could regulate miR-6776-5p through ceRNA and might promote the proceeding of CRSwNPs through the PI3K/AKT signaling pathway. Therefore, LINC01198 may be a latent target for the cure of CRSwNP. In addition, we also enriched the immune gene GNG7 in CRSwNP with GSEA and predicted the results of the small molecule drug treatment of 19 hub immune genes for CRSwNP. Finally, we found that the M2 macrophages between the resting dendritic cells in CRSwNP may be synergistic by immunopermeation analysis. The research results obtained from this article are very important and can supply a novel thinking model for prevention, cure, and prognosis of CRSwNP.

2. Materials and Methods

2.1. GEO Data Set Collection. We retrieved the microarray data sets (mRNA and lncRNA) from the GEO database (http://www.ncbi.nlm.nih.gov/geo) through R GEOquery package. The data set accession numbers used are GSE136825, GSE36830, and GSE169376.

2.2. Record Pretreatment and Abnormal Expression Analysis. The crude TXT data gathered from the GEO database was pretreated using the microarray data (limma) R package. Batch effects were adjusted by the combat function of sva package of R software using empirical Bayes frameworks after merging all microarray data. Finally, the expression values were normalized according to the normalizeBetweenArrays function of the package of limma in R software so that the expression values have similar distribution across a set of arrays. For the obtained limma, the explored sequence was downloaded from the explanatory note platform and justified with the human-genome to obtain the expression level of miRNA. We used the R limma package to detect differential expression of the miRNA data set GSE169376. We used |logFC | >1 and FDR < 0.05 as the filter strip to the final differentially expressed miRNA, immune gene, TF (transcription factors), and lncRNA. They were named as DmiRNA, DimGene, DTFgene, and DlncRNA data sets. As a result, R ggplot2 package was used to paint the volcano map and the heat map.

2.3. Target Prediction and Functional Enrichment. All predicted targets were subjected to Gene Ontology (https://www.kegg.jp/) analysis and genome KEGG (https://www.kegg.jp) type pathway enrichment analysis, which was implemented by the R package clusterProfilter [24, 25] ($P < 0.01$).

2.4. GSVA Analysis. Gene set variation analysis (GSVA), a functional enrichment analysis method similar to gene set enrichment analysis (GSEA), allowed the assessment of underlying pathway activity variation in each sample by pre-inputting a selected gene set. It can draw such a conclusion that as an uncommon method, GSVA may have amazing latent capacity in related research of signal path.
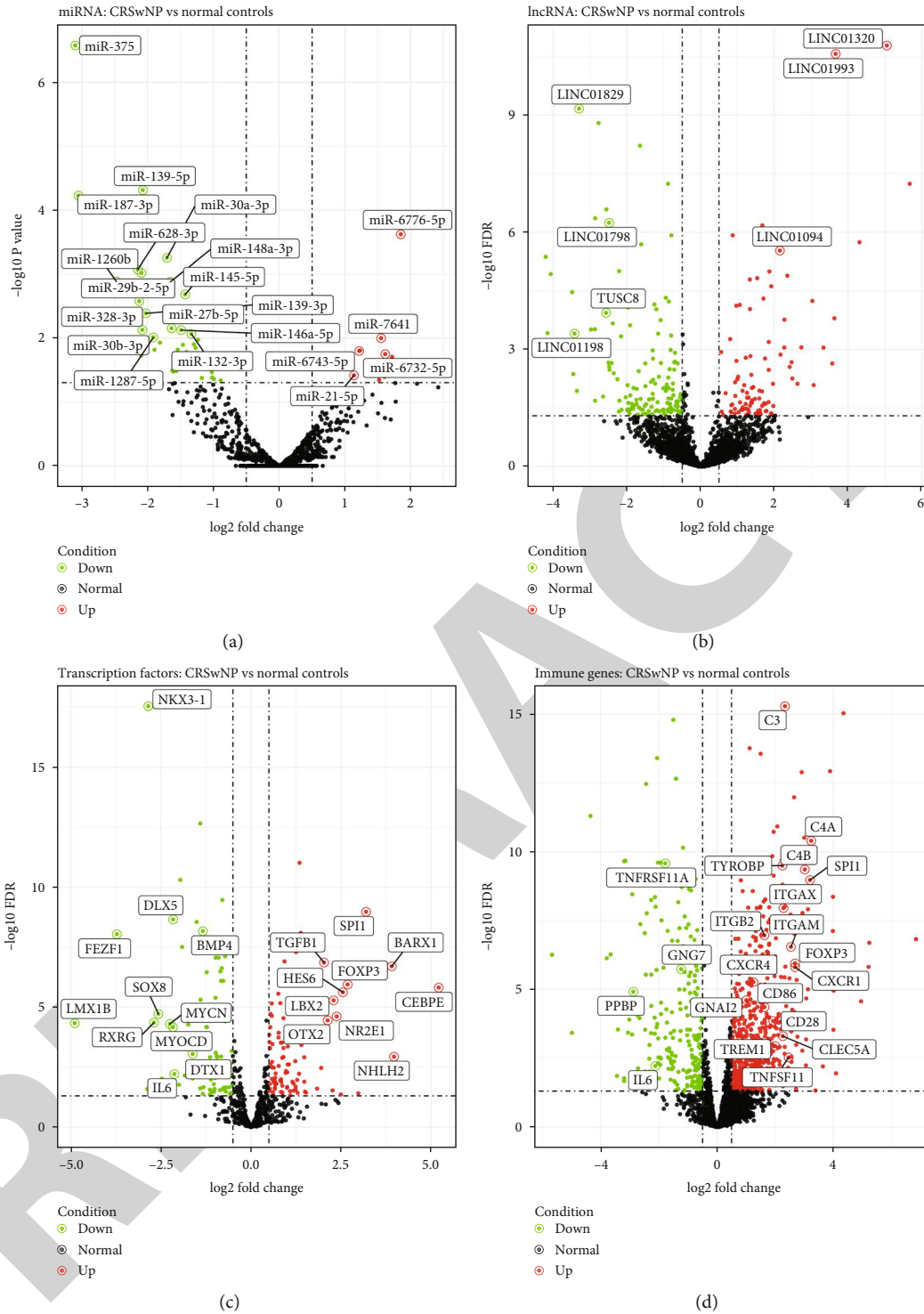
FIGURE 1: Volcano plots of abnormally expressed miRNA, immune genes, TF, and lncRNA in CRSwNP. Volcano plots of abnormally expressed miRNA (a), immune genes (b), TF, and lncRNA in CRSwNP and normal. Red and green points correspond to log2FC (|log 2FC| >0.5) up/down, respectively, and indicate FDR < 0.05. (a–d). Volcano plot of differential expression of miRNA (a), immune genes (b), transcription factors (c), and lncRNA (d) with log (fold change) as the abscissa and -log10 (P value) as the ordinate. Red and green splashes represent the genes that were significantly up- or downregulated in CRSwNP, respectively. Green splashes mean genes without significantly different expression. FDR < 0.05 and |logFC| >0.5.
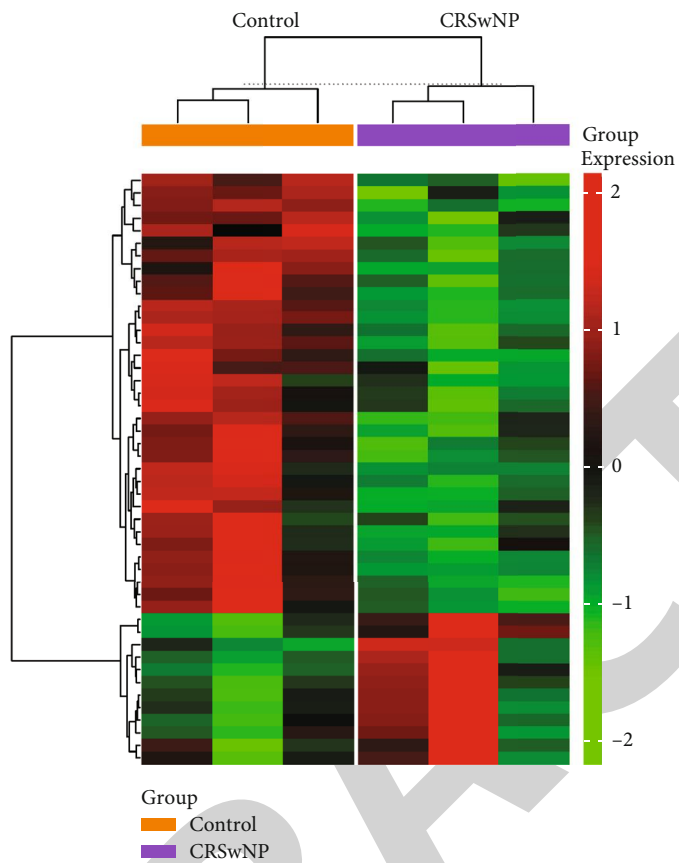
(a) miRNA

Figure 2: Continued.
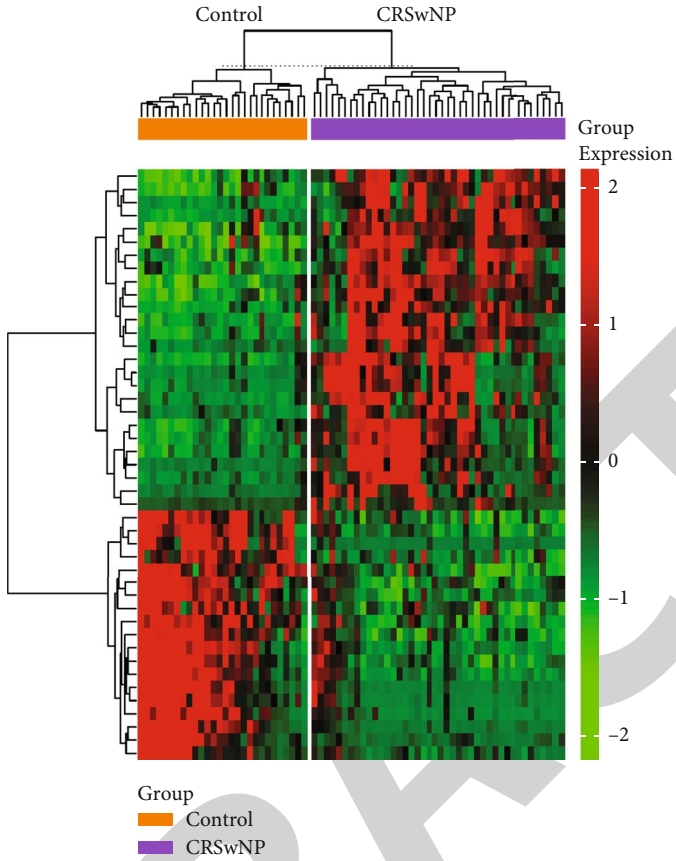
(b) Immune gene

Figure 2: Continued.
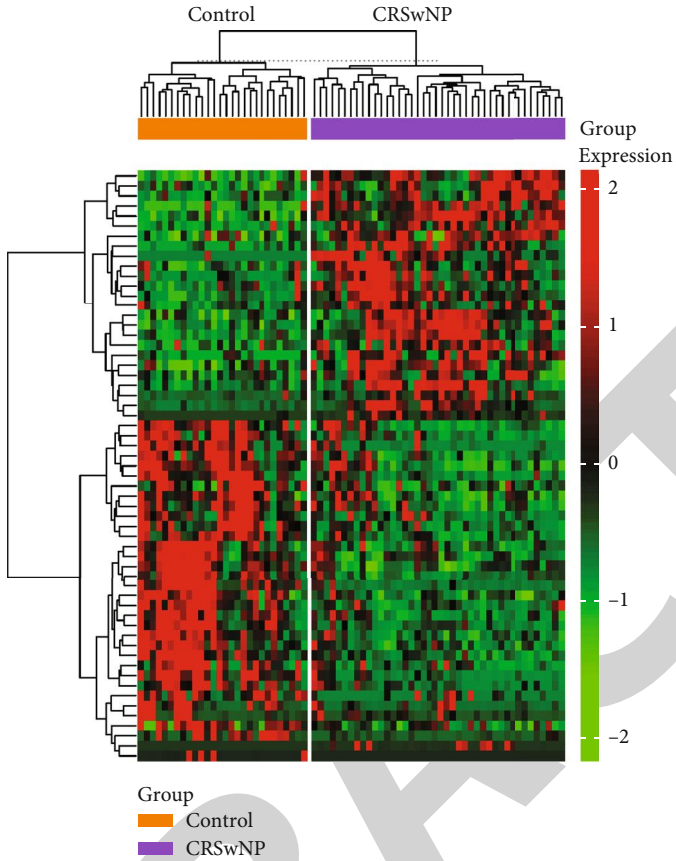
(c) TF

Figure 2: Continued.
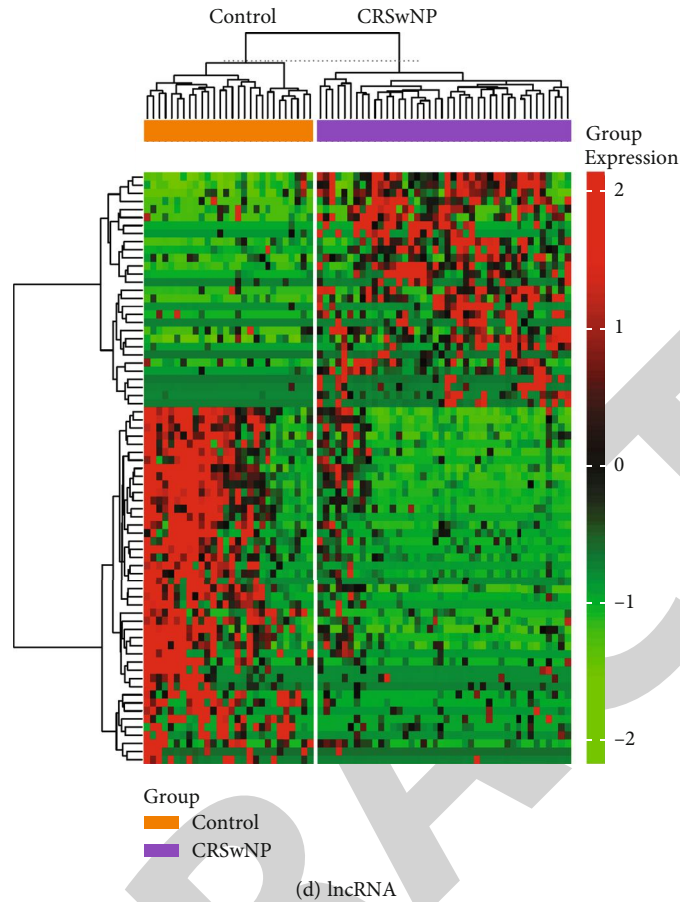
Figure 2: The heat map of abnormally expressed miRNA, immune genes, TF, and lncRNA in normal and CRSwNP. The heat map of abnormally expressed miRNA, immune genes, TF, and lncRNA in normal and CRSwNP hierarchically clustered. Each list indicates a sample and every line indicates an miRNA (a), immune gene (b), transcription factors (c), and lncRNA (d). The expression value for each line was normalized by the z-score. Red indicates high relative expression and green indicates low relative expression ($|logFC| > 1$ and FDR < 0.05).

Table 1: GEO data set.

GEO accession	Platforms	Normal	Case	Organism	Experiment type
GSE136825	GPL20301	28	42	Homo sapiens	Expression profiling by array
GSE36830	GPL570	6	12	Homo sapiens	Expression profiling by array
GSE169376	GPL21572	3	3	Homo sapiens	Noncoding RNA profiling by array

GSVA was used to distinguish signal path levels among CRSwNP patients. GSVA had a capacity to compute enrichment scores of selected gene sets for every patient. Therefore, through GSVA, the patients' gene set matrix including path enrichment score was obtained.

2.5. PPI Network Construction. The PPI network was drawn from the String database (https://www.string-db.org/) against the differential immune gene and transcription factor data set in CRSwNP, and the parameter setting was confidence > 0.9. We used the clusterProfiler gene to enrich the KEGG pathway and combined with PPI network to draw TF-immune genes-pathway network through Cytoscape 3.8.0.

We used the online database search tool String to build the PPI network and DTFgene network and score the fusion ≥ 0.9 as the critical point ≥ 0.9 and removed the protein nodes that cannot interacted with the other. In addition, we used Cytoscape (version: 3.8.0) to analyze the PPI network to screen the caused modules and hub genes. The MCODE (version: 2.0.0) plug-in was used to choose the significant clustering module according to the standard MCODE score > 10 and the amount of nodes > 20 and used the cluster preliquid to carry out the path enrichment analysis package of the genes in these modules. Then, using the apoptosis (version: 0.1) insert to show the PPI network, genes with a degree > 10 were identified as hub genes in CRSwNP.
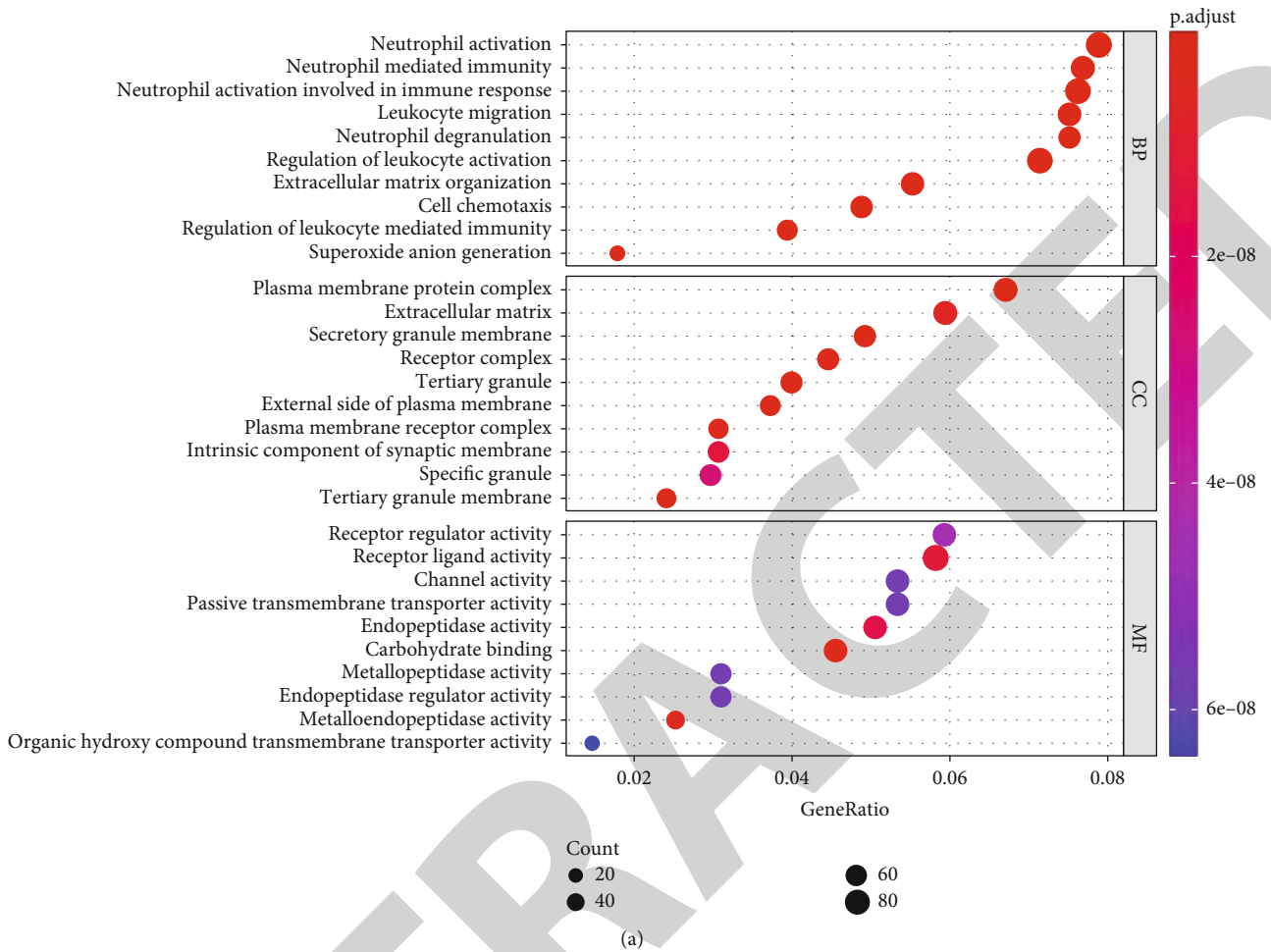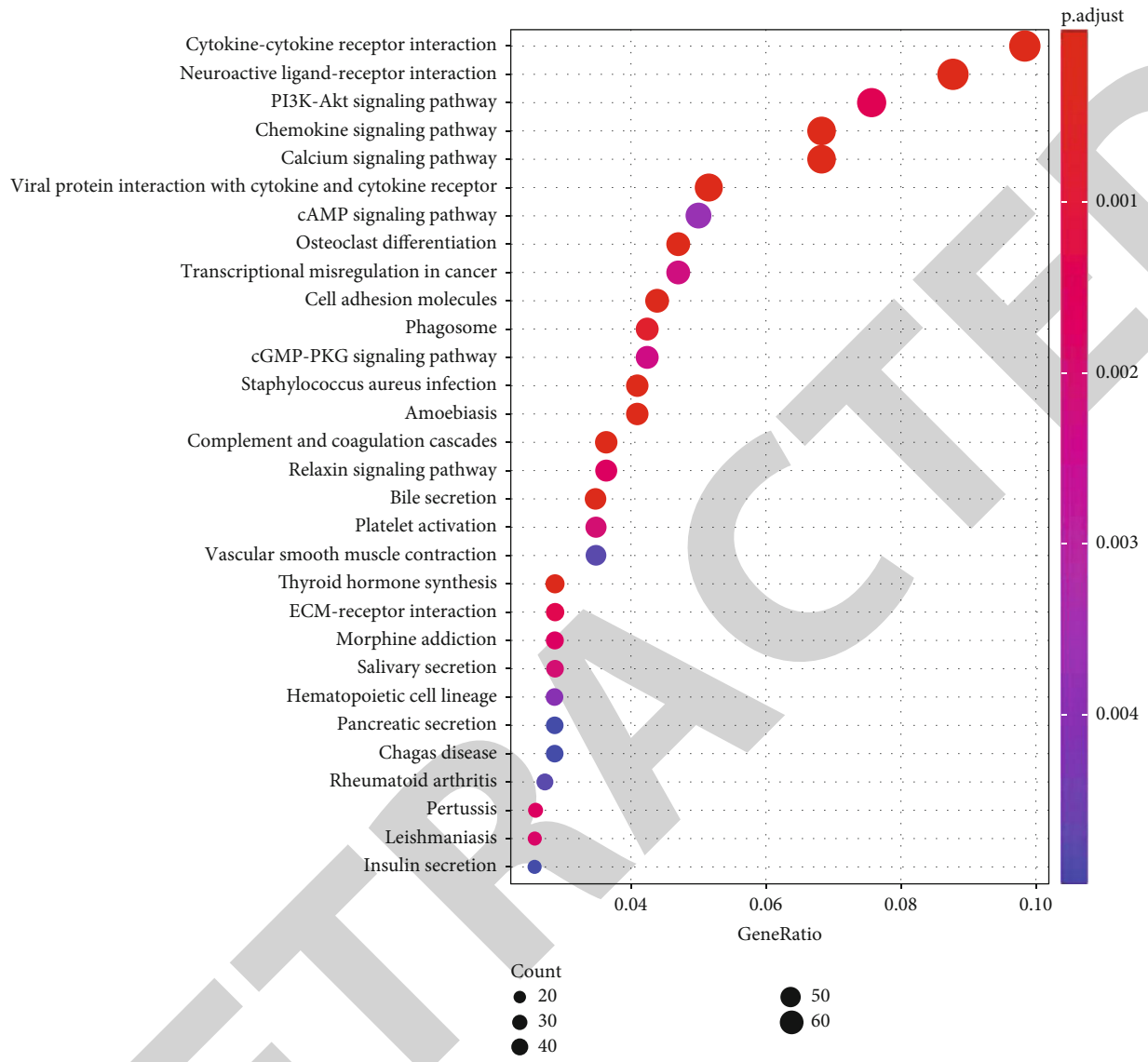
(b)

FIGURE 3: Continued.

(c)
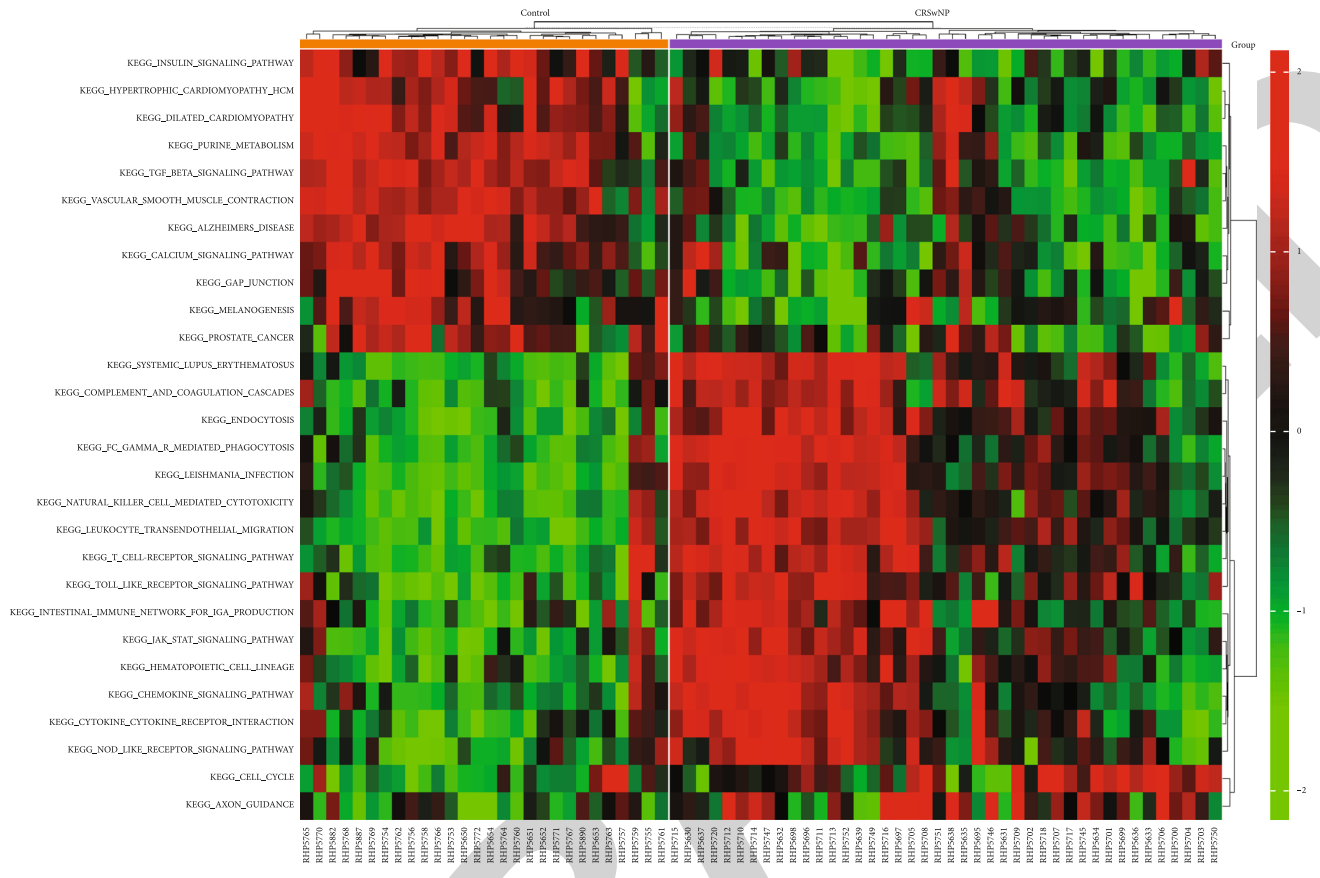
Figure 3: Continued.

(d)
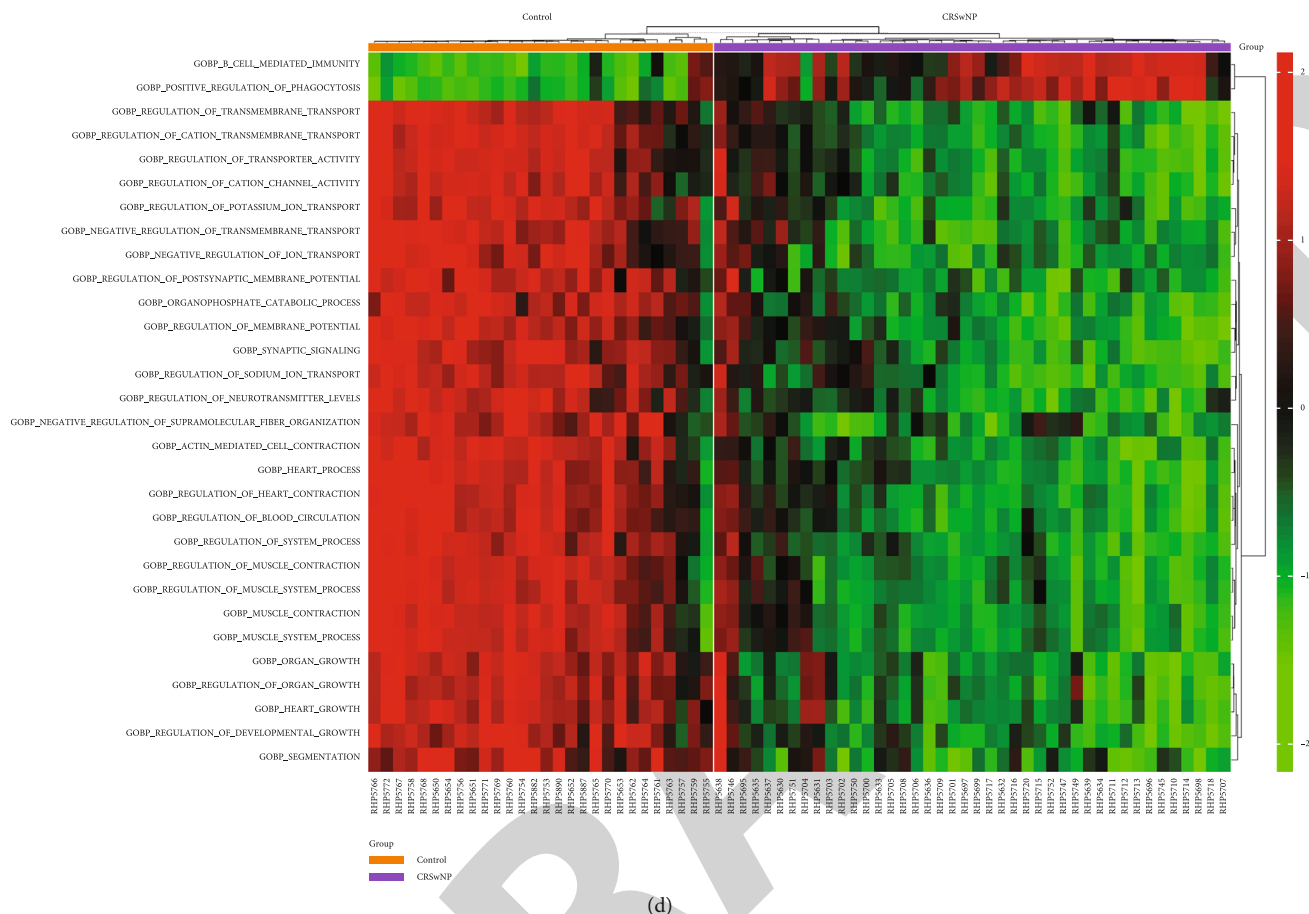
Figure 3: The enrichment of differentially expressed immune genes and transcription factors predicted targets in CRSwNP. Used to visualize the enrichment of differentially expressed immune genes and transcription factor prediction targets in CRSwNP. Detailed GO enrichment and KEGG information are presented in the bubble map. Gene Ontology (GO) Kyoto Encyclopedia of Genes and Genomes (KEGG) pathological analysis of immune and TF genes. Significantly enriched pathways featured $P < 0.001$. The analysis was conducted using R clusterProfilter. (a) GO enrichment analyses of TF and immune genes. y-axis represents GO terms, and x-axis represents GeneRatio. The number of genes enriched in the enrichment term is indicated by the size of the node. The importance of the GO term is indicated by the color, and the red indicates the highest significance. (b) KEGG pathway enrichment analyses of TF and immune genes. The y-axis represents the KEGG term. The x-axis represents GeneRatio. The number of genes enriched in the enrichment term is represented by the size of the node. The importance of the KEGG term is represented by color, and red represents the highest significance. (c) The heat map of differentially expressed immune genes for KEGG pathway horizontally represents KEGG terminology; longitudinal direction means sample, red means upregulation, and green means downregulation. (d) The heat map of differentially expressed immune genes for GO; horizontal means GO term, longitudinal means sample, red means upregulation, and green means downregulation.

2.6. ceRNA Network Construction. We used TargetScan, miRDB, and miRanda online tools to reversely predict miRNA for 9 hub immune genes, took the intersection to obtain miRNA, and then took the intersection with DmiRNA. We used lncbase (https://diana.e-ce.uth. gr/lncba-sev3/) and MiRcode (http://www.mircode.org/) to forecast the relationship between lncRNAs and miRNAs and obtain miRNA target lncRNA by taking the intersection and then took the intersection with DlncRNA. According to the lncRNA-miRNA-mRNA ceRNA regulation principle, lncRNA and miRNA were negatively correlated, lncRNA and mRNA were positively correlated, and miRNAs and mRNAs were negatively correlated. lncRNA-miRNA-mRNA ceRNA regulation relationship Tab. was screened out. Finally, we merged the hub TF-immune genes-

pathway network to carry out the lncRNA-miRNA-TF-immune gene-pathway ceRNA network, visualized the network through Cytoscape, and constructed the key immune gene lncRNA-miRNA-Hub gene-pathway ceRNA network.

2.7. Statistical Analysis. Statistical analysis was implemented using R 3.6.3. digital datas, which were certified to obey a normal distribution shown as the mean ± standard, and the differences between means were analyzed using Student's t-test. ANOVA analysis was used to predict lncRNA, immune genes, TF, and miRNA abnormal expression among diverse groups. The considerably lncRNA, immune genes, TF, and miRNA were inquired into limma R package. A threshold value of $|\log 2FC| \geq 1$ and FDR < 0.05, the heat mapping were showed form ggplot 2, ComplexHeatmap.

Table 2: Kyoto Encyclopedia of Genes and Genomes (KEGG) pathway.

#term ID	Term description	False discovery rate
hsa04060	Cytokine-cytokine receptor interaction	3.30E-28
hsa05150	Staphylococcus aureus infection	7.73E-15
hsa04062	Chemokine signaling pathway	9.22E-15
hsa04380	Osteoclast differentiation	2.36E-10
hsa04610	Complement and coagulation cascades	1.91E-09
hsa04630	Jak-STAT signaling pathway	2.83E-09
hsa04659	Th17 cell differentiation	6.15E-08
hsa05200	Pathways in cancer	1.43E-07
hsa05202	Transcriptional misregulation in cancer	1.43E-07
hsa05133	Pertussis	1.93E-07
hsa04145	Phagosome	2.19E-07
hsa04657	IL-17 signaling pathway	3.48E-07
hsa04640	Hematopoietic cell lineage	2.41E-06
hsa05152	Tuberculosis	2.41E-06
hsa04151	PI3K-Akt signaling pathway	2.84E-06
hsa05140	Leishmaniasis	2.97E-06
hsa05323	Rheumatoid arthritis	3.09E-06
hsa05322	Systematic lupus erythematosus	9.88-06
hsa04668	TNF signaling pathway	4.13E-05
hsa05221	Acute myeloid leukemia	5.32E-05
hsa04650	Natural killer cell mediated cytotoxicity	0.00016
hsa05321	Inflammatory bowel disease (IBD)	0.00017
hsa04015	Rap1 signaling pathway	0.00019
hsa04621	NOD-like receptor signaling pathway	0.00021
hsa05142	Chagas disease (American trypanosomiasis)	0.00035
hsa04658	Th1 and Th2 cell differentiation	0.00047
hsa04672	Intestinal immune network for IgA production	0.00047
hsa05167	Kaposi's sarcoma-associated herpesvirus infection	0.00054
hsa05215	Prostate cancer	0.00091
hsa05418	Fluid shear stress and atherosclerosis	0.00091

3. Results

3.1. Identification of Differentially Expressed miRNA, Immune Genes, TF, and lncRNA in CRSWNP. We used the GEO database to analyze differential expression of the substance of miRNA, lncRNA, TF (transcription factors), and immune gene in CRSwNP, and the results were displayed in a volcano graph. Compared with the control group, a total of 48 lower miRNAs were abnormally expressed in CRSwNP. 12 raised miRNAs and 36 miRNAs were appraised between CRSwNP and control (Figure 1(a)). There were 304 abnormally expressed lncRNAs, 141 were upregulated and 163 reduced, that were identified between CRSwNP and control (Figure 1(b)). There were 92 abnormally expressed TFs, among 44 were raised and 48 were downregulated (Figure 1(c)). There were 525 abnormally expressed immune genes, of which 394 were upregulated and 131 downregulated (Figure 1(d)). We performed a 2D hierarchical clustering analysis on the above data. The results are shown in Figure 2, revealing the differences in

the expression profiles of CRSwNP miRNA, lncRNA, TF (transcription factors), and immune gene (|logFC| >1 and FDR < 0.05). The specific data set is shown in Table 1.

3.2. Functional Annotation of Gene Enrichment and Prediction Targets. We implemented functional enrichment of the abnormally expressed immune genes and transcription factor data sets in CRSwNP. Through KEGG and GO enrichment analysis, we discovered that the above genes are significantly enriched in the following three types of functions, including biological processes (BP), cellular fraction (CC), and molecular function (MF). The top 10 enrichment terms in BP, CC, and MF are provided in Figure 3(a). In Figure 3(b), KEGG analysis appraised 30 paths in total, several of which interact with cytokine-cytokine receptors, neuroactive ligand-receptor interaction, PI3K-Akt signal path, chemokine signal path, and calcium. The above results revealed that these pathways are involved in the pathological progress of CRSwNP. We used the GSVA method to calculate the standardized pathway enrichment scores of 658

Table 3: GSVA analysis of KEGG pathway.

ID	logFC	P value	Adj. P value
KEGG_PURINE_METABOLISM	-0.68	1.50E-15	6.46E-14
KEGG_TGF_BETA_SIGNALING_PATHWAY	-0.63	7.20E-14	2.81E-12
KEGG_VASCULAR_SMOOTH_MUSCLE_CONTRACTION	0.57	8.01E-16	3.52E-14
KEGG_ALZHEIMERS_DISEASE	-0.56	1.36E-13	5.17E-12
KEGG_DILATED_CARDIOMYOPATHY	-0.40	1.70E-09	5.10E-08
KEGG_INSULIN_SIGNALING_PATHWAY	-0.36	2.04E-10	7.35E-09
KEGG_HYPERTROPHIC_CARDIOMYOPATHY_HCM	-0.33	1.68E-06	4.20E-05
KEGG_GAP_JUNCTION	-0.28	2.80E-08	7.83E-07
KEGG_CALCIUM_SIGNALING_PATHWAY	-0.27	1.36E-07	3.67E-06
KEGG_MELANOGENESIS	-0.24	3.21E-06	7.70E-05
KEGG_PROSTATE_CANCER	-0.21	0.000136386	0.002591328
KEGG_CHEMOKINE_SIGNALING_PATHWAY	0.22	0.000230059	0.003910995
KEGG_CYTOKINE_CYTOKINE_RECEPTOR_INTERACTION	0.23	1.19E-05	0.000261605
KEGG_AXON_GUIDANCE	0.26	7.29E-05	0.001457423
KEGG_INTESTINAL_IMMUNE_NETWORK_FOR_IGA_PRODUCTION	0.32	2.82E-05	0.000591205
KEGG_NOD_LIKE_RECEPTOR_SIGNALING_PATHWAY	0.37	6.28E-06	0.000144332
KEGG_HEMATOPOIETIC_CELL_LINEAGE	0.38	1.88E-07	4.90E-06
KEGG_JAK_STAT_SIGNALING_PATHWAY	0.39	8.90E-09	2.58E-07
KEGG_CELL_CYCLE	0.39	0.000147908	0.002662341
KEGG_ENDOCYTOSIS	0.43	1.63E-15	6.85E-14
KEGG_COMPLEMENT_AND_COAGULATION_CASCADES	0.46	6.72E-10	2.15E-08
KEGG_TOLL_LIKE_RECEPTOR_SIGNALING PATHWAY	0.52	2.06E-10	7.35E-09
KEGG_LEUKOCYTE_TRANSENDOTHELIAL_MIGRATION	0.55	1.12E-14	4.59E-13
KEGG_SYSTEMATIC_LUPUS_ERYTHEMATOSUS	0.57	2.20E-10	7.49E-09
KEGG_NATURAL_KILLER_CELL_MEDIATED_CYTOTOXICITY	0.63	1.67E-12	6.18E-11
KEGG_T_CELL_RECEPTOR_SIGNALING_PATHWAY	0.63	1.29E-09	3.99E-08
KEGG_LEISHMANIA_INFECTION	0.64	1.29E-14	5.16E-13
KEGG_FC_GAMMA_R_MEDIATED_PHAGOCYTOSIS	0.67	2.35E-10	7.77E-09

immune gene set-based pathways for each CRSwNP patient using the CRSwNP immunization and TF data sets, shown in the heat map (Figures 3(c) and 3(d)). We found that in some CRSwNP patients, the pathway enrichment scores based on CRSwNP immunization and TF collection seemed to be partially aggregated. Many patients had dependently high path enrichment fractions, while others could not spread higher expression models. This indicated that CRSwNP patients had different pathway expression profiles, which was consistent with some published studies. Table 2 is the description of the related terms of the KEGG pathway. Table 3 is the specific data of the KEGG pathway GSVA analysis.

3.3. PPI Network Establisher and Hub Gene Authentication.

We are grateful for the suggestion. To be more clear and in accordance with the reviewer concerns, we have revised the manuscript accordingly. "We used the clusterProfiler gene to enrich the KEGG pathway and combined it with the PPI network and used Cytoscape version 3.8.0 to draw the TF-immune genes-pathway network (Figure 4(b)). We used Cytoscape MCODE plug-in (version: 2.0.0) and CytoHubba

plug-in (version: 0.1) to screen out hub network and hub genes (Figures 4(c) and 4(d)).

3.4. Construction of ceRNA Network on Account of Differential DmiRNA, DimGene, DTFgene, and DlncRNA.

We established ceRNA network on account of expression profiles of DmiRNA, DimGene, DTFgene, DlncRNA, and CRSwNP patients. We used hub immune genes to reversely predict miRNAs, then intersected with differentially expressed miRNAs, and obtained 14 miRNA nodes (8 upregulation and 6 downregulation). We used lncbase and MiRcode to forecast the relationship between lncRNAs and miRNAs and took the intersection to obtain 38 lncRNA nodes (20 upregulated and 18 downregulated). The result is shown in Figure 5(a) (|logFC| >1 and FDR < 0.05). According to the establishment of the lncRNA-miRNA-mRNA ceRNA regulatory relationship list in CRSwNP (Table 4). We merged the hub TF-immune genes-pathway network to carry out the lncRNA-miRNA-TF-immune gene-pathway ceRNA network, visualized the network through Cytoscape, and constructed the key immune gene lncRNA-miRNA-Hub gene-pathway ceRNA network, and

(a)
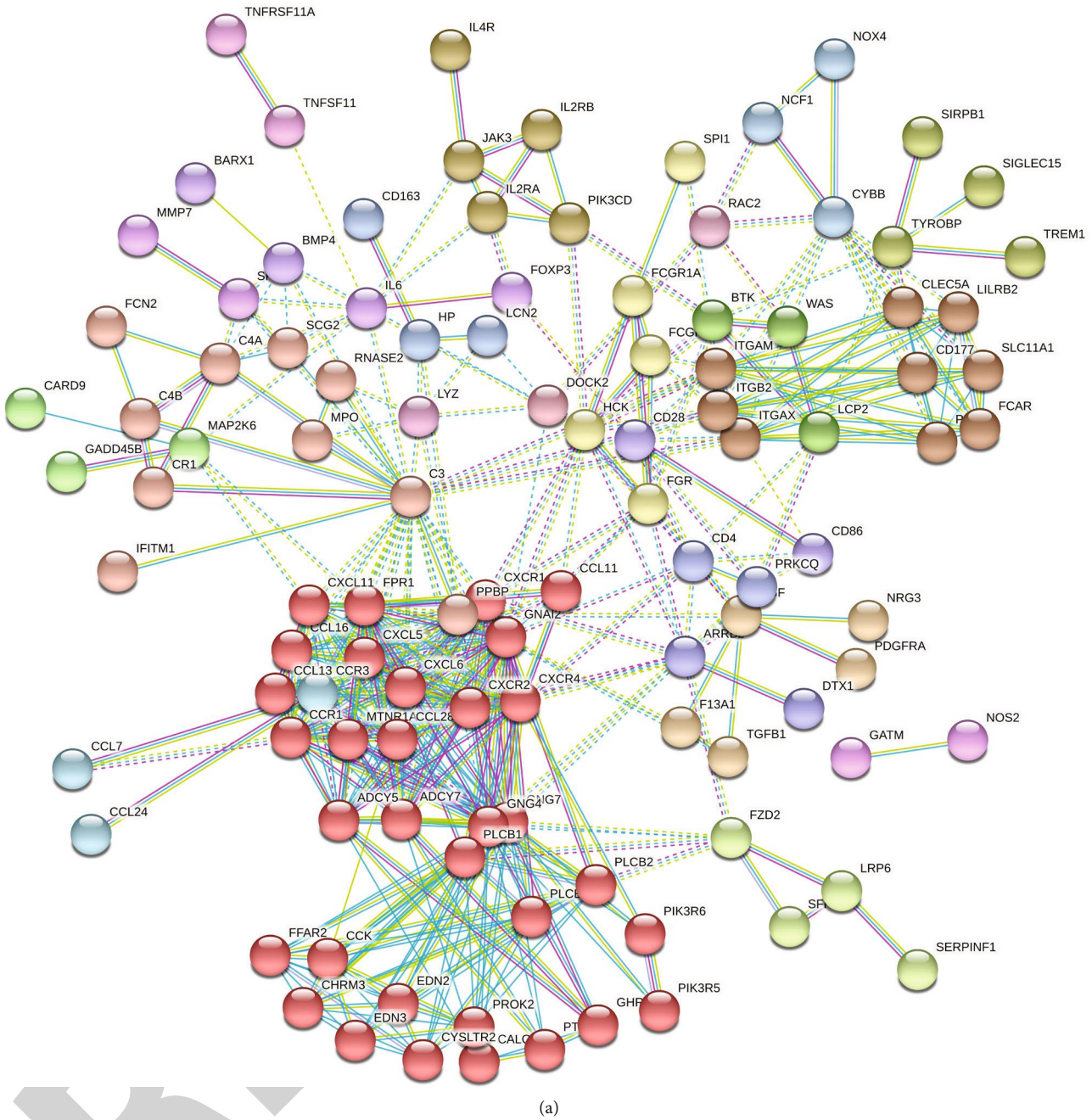
Figure 4: Continued.
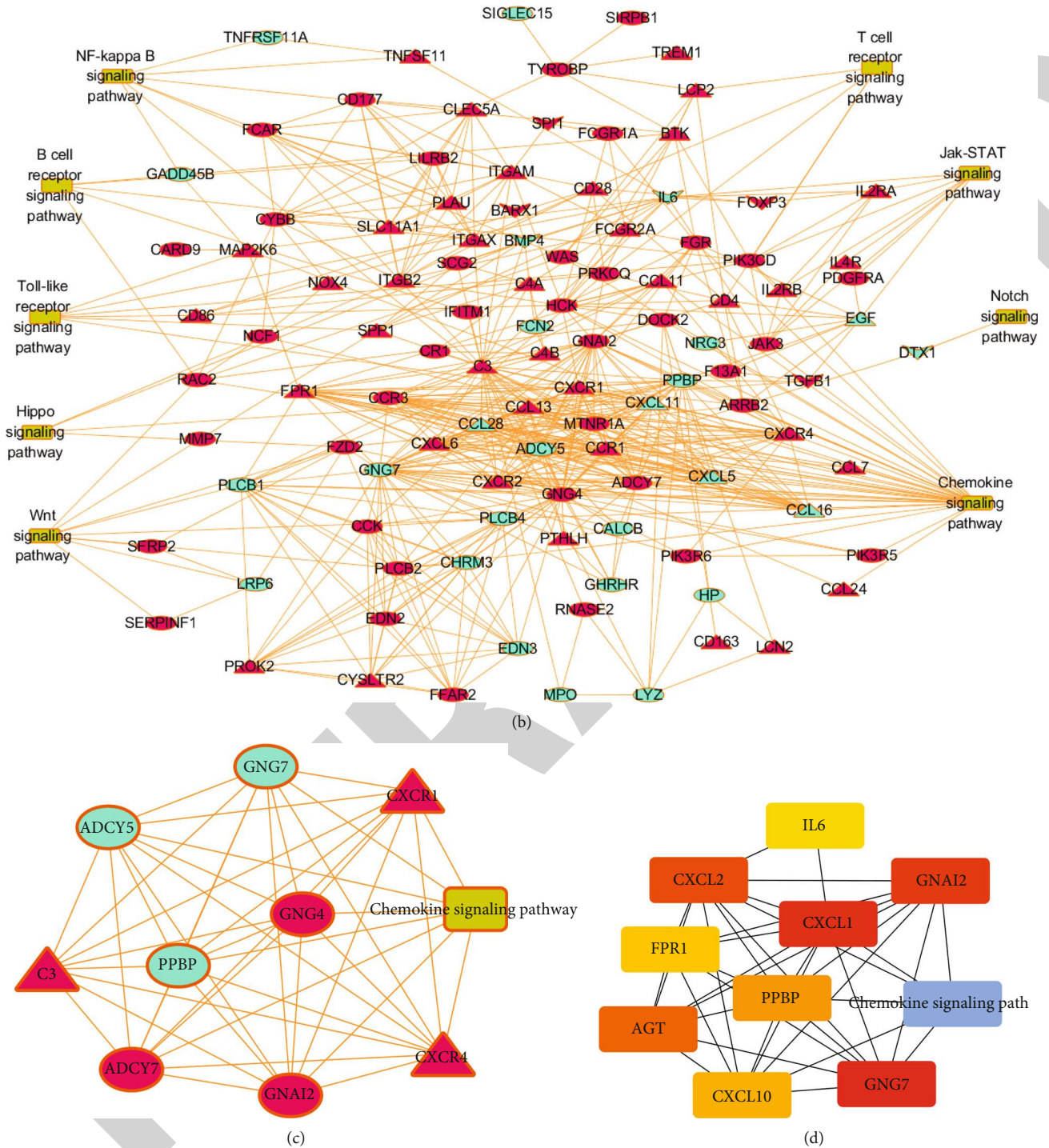
Figure 4: Construction of TF-immune genes-pathway networks. (a) The protein-protein interaction (PPI) network. (b) TF-immune genes-pathway network. (c) The hub network by MCODE. (d) The hub network by CytoHubba.

the obtained two important pathways are shown in Figure 5(b).

3.5. CMAP: Small Molecule Therapeutic Drugs. The enrichment outcomes of PIK3R1 revealed that it was significantly enriched in the JAK-STAT signal path, T Toll-like receptor signal path, TNF signal path, fluid shear pressure, and atheromatosis AGE-RAGE signal path in diabetes mellitus diffi-

cult problem and chemokine signaling pathway (Figure 6 (a)). Using the CMAP database, we used 19 hub immune genes (KMT2A, PTPN1, TFAP2C, TLR7, SMARCE1, KLRD1, LIFR, FZD1, FST, TGFB2, KLRC4, CYSLTR1, PIK3R1, BCAR1, TRIM36, CCR9, THBS1, NOD2, and C7) to forecast latent therapeutic medicines for CRSWNP. Five drugs in total, called danazol, ikarugamycin, semustine, cefamandole, and molindone, were identified (Figures 6(b) and 6

(a)

(b)
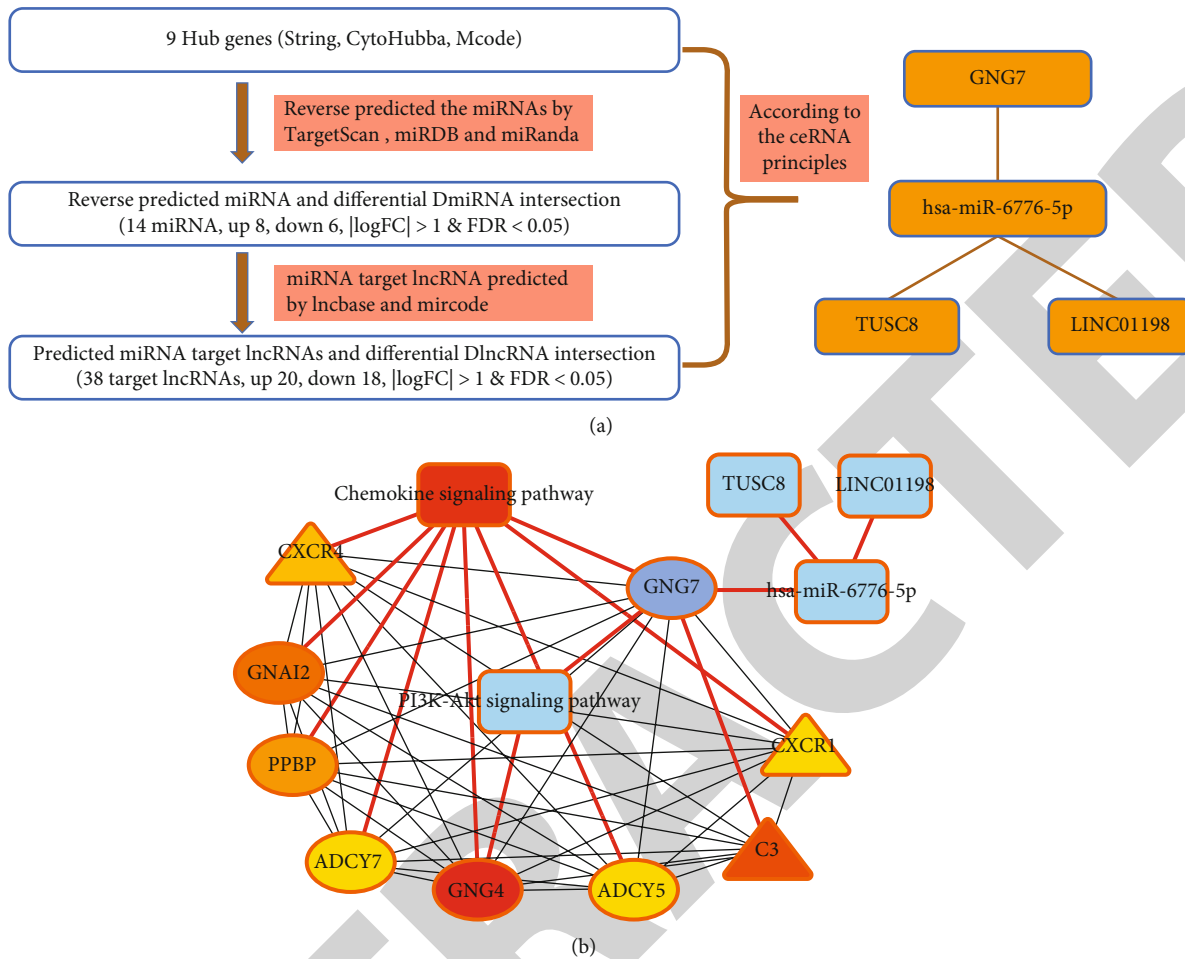
FIGURE 5: The results of using mRNA to stepwise reverse predict miRNA and lncRNA and constructing a ceRNA network. (a) The flow chart of predicted miRNA target gene and network construction. (b) The hub lncRNA-miRNA-mRNA ceRNA pathway.

TABLE 4: lncRNA-miRNA-mRNA ceRNA regulatory relationship list.

lncRNA	logFC	Mature miRNA	logFC	Immune gene	logFC
TUSC8	-2.566634992	hsa-miR-6776-5p	1.849653653	GNG7	-1.236759067
LINC01198	-3.423148908	hsa-miR-6776-5p	1.849653653	GNG7	-1.236759067

(c)). Hub immune genes were used to forecast latent medicines for the cure of CRSwNP .

3.6. Construction of CRSWNP Diagnostic Model Based on Immune-Related Genes.

LASSO coefficient profiles of 42 lncRNAs are displayed in Figure 7(a), and the line of dashes make known the selected value by tenfold cross-validation. Tenfold cross-proving for harmonious parameter choice in the LASSO pattern is displayed in Figure 7(b). In Figures 7 (a) and 7(b), the quantity above the chart delegates the quantity of paths related in the LASSO pattern. Through the LASSO regression process, 5 of 42 lncRNA set were filtered for subsequent analysis (Table 5). ROC were painted and their AUCs decided to appraise the diagnostic value of the key lncRNAs using the pROC package in R 3.6.3. DlncRNAs have an AUC of >0.85 and were differentially regulated. Data sets were used to establish one binomial

LASSO pattern deal with R. In the training and validation set, 50% of specimens in the GSE169376 data set was stochastic choice by the caret package in R 3.6.3 (Figures 7(c) and 7(d)). As λ raises, LASSO prefers decrease the regression coefficient to zero. lncRNA with AUC > 0.85 in the GSE169376 data sets was defined as biomark lncRNAs (Figure 7(e)). The expression levels of 5 lncRNA biomarkers in CRSwNP patients and normal controls are shown (Figures 7(f)–7(j)).

3.7. Immune Infiltration Analyses.

Due to technical limitations, CRSwNP immune penetration has not been fully revealed, especially in subgroups with low cell numbers. Using the CIBERSORT algorithm, we first investigated the differences in immune infiltration between 42 CRSwNP and 28 normal inferior turbinate tissues in 22 immune cell parts. Figure 8(a) reveals the scale of immune cells in 28

(a)

KEGG_ABC_TRANSPORTERS
KEGG_B_CELL_RECEPTOR_SIGNALING_PATHWAY
KEGG_CELL_CYCLE
KEGG_CHEMOKINE_SIGNALING_PATHWAY
KEGG_GLYCINE_SERINE_AND_THREONINE_METABOLISM
KEGG_GLYCOLYSIS_GLUCONEOGENESIS
KEGG_JAK-STAT_SIGNALING_PATHWAY
KEGG_NITROGEN_METABOLISM
KEGG_NON_HOMOLOGOUS_END_JOINING
KEGG_P53_SIGNALING_PATHWAY
KEGG_PATHOGENIC_ESCHERICHIA_COLI_INFECTION
KEGG_PRIMARY_BILE_ACID_BIOSYNTHESIS
KEGG_PROTEIN_EXPORT
KEGG_RETINOL_METABOLISM
KEGG_T_CELL_RECEPTOR_SIGNALING_PATHWAY
KEGG_TAURINE_AND_HYPOTAURINE_METABOLISM
KEGG_TRYPTOPHAN_METABOLISM
KEGG_VALINE_LEUCINE_AND_ISOLEUCINE_DEGRADATION
KEGG_VASCULAR_SMOOTH_MUSCLE_CONTRACTION

(b)

Figure 6: Continued.

| Benzbromarone | Cefsulodine | CID2333 | CID445643 |

| Diethylstilbestrol | Dydrogesterone | Hydrocortisone | Levobunolol |

| Benzbromarone | Benzbromarone |

(c)

Figure 6: Predictive results of small molecule drug therapy for CRSwNP. Single-gene GSEA enrichment results of GNG7 gene and prediction results of potential small molecule drugs for the treatment of CRSwNP based on 19 hub immune genes. (a) lncRNA-miRNA-pathway ceRNA network. (b) Single-gene enrichment analysis of GNG7 gene (GSEA, gene set enrichment analysis). (c) Prediction results of targeted drugs.

normal controls and 42 CRSwNP patients. Obviously, plasma cells and B cell naive were explained for the most permeating cells, notably in 28 normal control tissues, but M2 macrophages were increased in CRSwNP tissue. The abnormal expression ratio of immune permeating cells in CRSwNP is displayed in Figure 8(b). Only M2 macrophages, T cell CD8, and plasma cells were abnormally expressed, and M2 macrophages were increased in CRSwNP tissue (P values, 0.001). Plasma cells and T cell CD8 were downregulated in CRSwNP tissue, and the P values of the two types of immune cells were 0.048 and 0.044. From CRSwNPA (Figure 8(c)), the ratio of immune cells in 42 CRSwNP and 28 normal controls did not show significant population bias aggregation but individual differences. Figure 8(d) shows the relevance between abnormally expression forms of immune cells. M2 macrophages were actively bound up with dendritic cells resting ($r = 0.33$) and passively bound up with B cell naive. Macrophages M0, Macrophages M1, T cells, CD4 memory resting, Plasma cells ($r = −0.4, r = −0.32, r = −0.21, r = −0.22$ and $r = −0.39$, respectively). M2 macrophages between dendritic cell resting in CRSwNP may be synergistic. However, it is indicated that the function of B cell naive, macrophage M0, macrophage M1, T cell CD4 memory resting, and plasma cells in CRSwNP was antagonistic (Figures 8(e)–8(j)).

The overall design idea of the experiment is shown in Figure 9.

4. Discussion

In our research, we found a ceRNA regulatory network and a PPI network in CRSwNP and identified five lncRNA biomarkers. Among them, LINC01094 and LINC01320 were upregulated in CRSwNP, while LINC01798, LINC01198, and LINC01829 were downregulated. We combined the ceRNA network and the PPI network to find that TUSC8 and LINC01198 coregulate miR-6776-5p and then regulated

the chemokine signal path and PI3K/Akt signal path through GNG7 to act a major part in the development of CRSwNP.

CRSwNP was a clinical manifestation of chronic sinusitis [26]. CRSwNP involved the mucosa of the sinuses, which was a common chronic inflammatory disease. The molecular mechanism of its pathogenicity remained unclear. Therefore, identifying new biomarkers, strengthening predictions, and understanding the underlying mechanisms were essential for the treatment of CRSwNP. The causes and progression of CRSwNP were the combined results of many factors, such as genetic disorders and pathological factors. In European and American Caucasians, more than 80% of CRSwNP have characteristic eosinophil infiltration, dominated by T helper 2 cell (Th2 cell) type inflammation [27, 28]. However, in yellow Asians, there is more infiltration of neutrophils and other inflammatory cells, with T helper 1 cell (Th1 cell) or T Helper 17 cell (Th L7 cell) as the dominant type of inflammation. So, we have reason to believe that eosinophils and helper T cells are the key cells in its pathogenesis [27, 28]. At the molecular level, CRSwNP may be caused by abnormalities in multiple noncoding RNAs, transcription factors, and immune genes [29–32]. As new noncoding RNAs, lncRNAs played vital parts in the progress of CRSwNP. For instance, lncRNA XLOC_010280 came to light to affect the development of eosinophilic inflammation by influencing CCL18 [33]. There were many pathological features of CRSwNP, including infiltration of inflammatory cells and interstitial edema [34]. Both this research and previous studies indicated that the pathogenic factors of CRSwNP may be related to abnormal expression of noncoding RNAs and immune dysregulation, despite the mechanisms were still unknown [35]. For instance, Ma et al. found that the inflammatory response regulator LRRK2 was highly expressed in patients with CRSwNP and was positively correlated with CD3 expression. At the same time, they also found that IL-17A can raise

Figure 7: Continued.

(g)

(h)

(i)

(j)
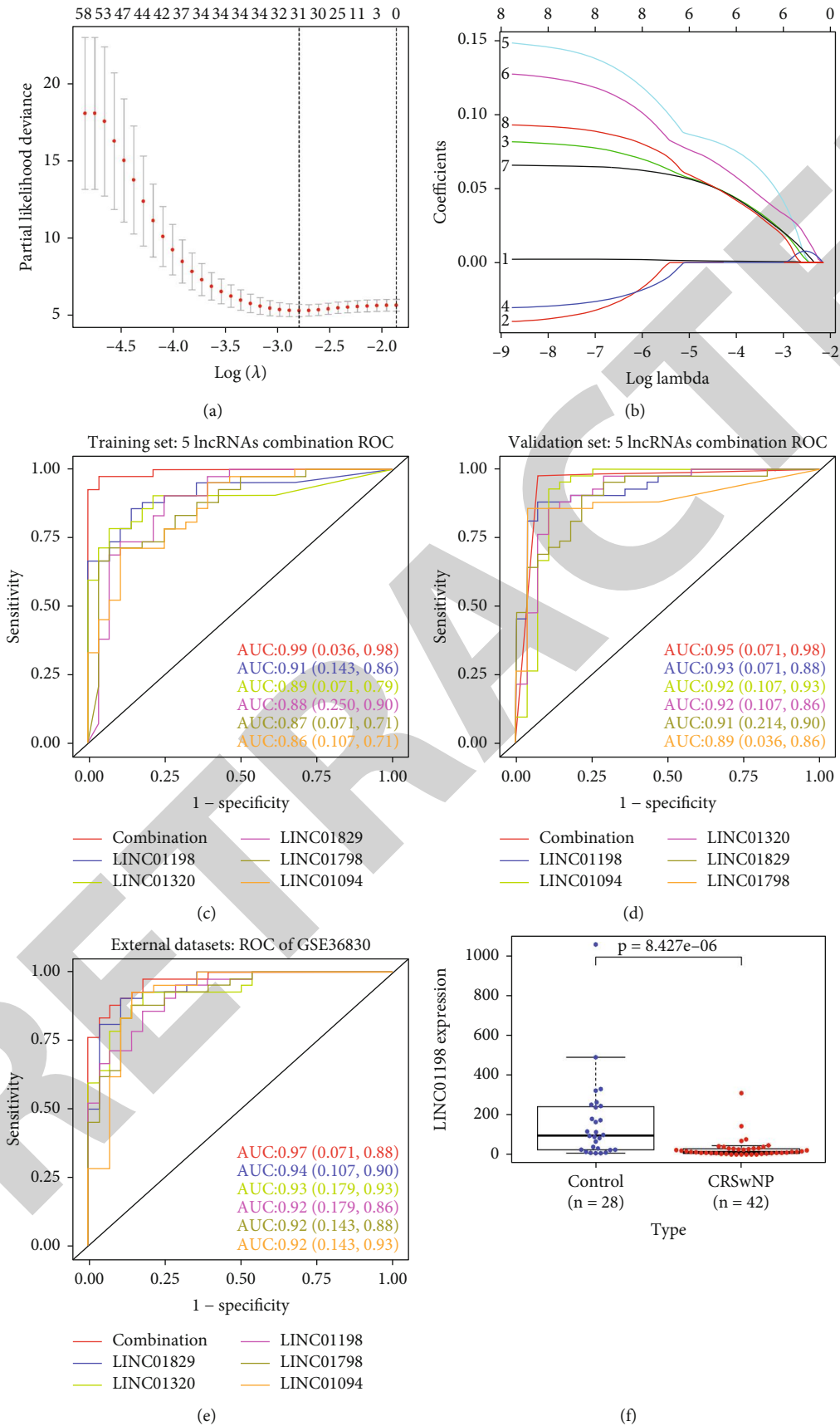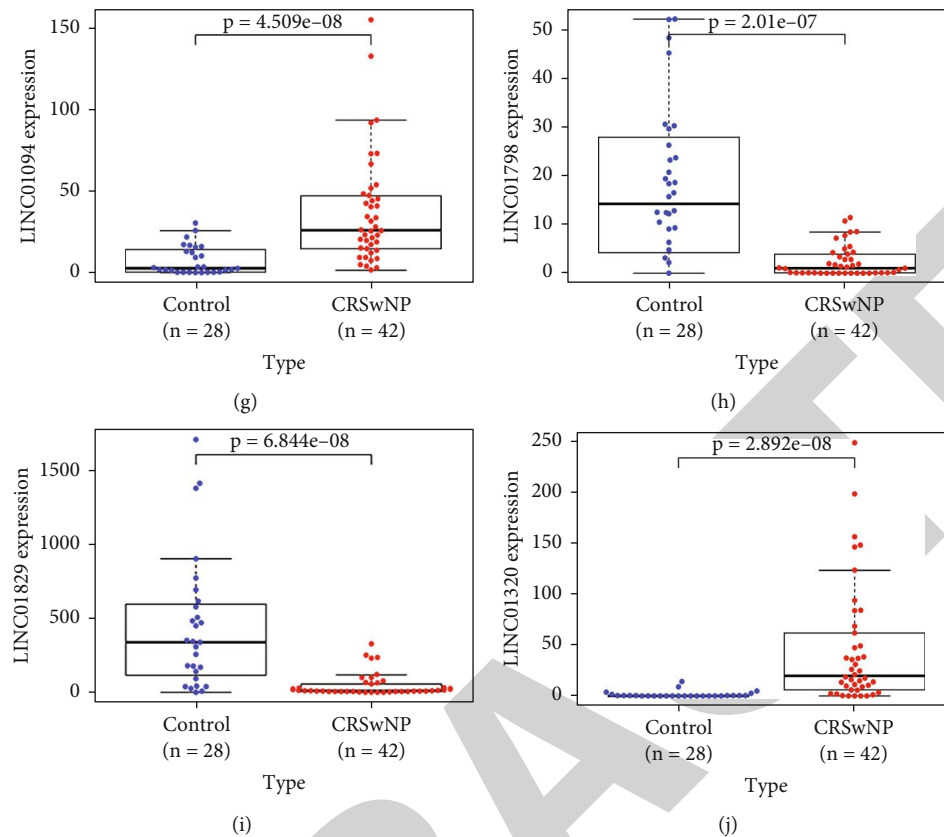
FIGURE 7: Development and validation of lncRNA biomarkers. (a) The LASSO regression. (b) LASSO coefficient profiles of the 5 lncRNAs. (c) Receiver operating characteristic (ROC) curve of the CRSWNP for the training set (GSE136825). (d) Receiver operating characteristic (ROC) curve of the CRSWNP for validation set (GSE136825). (e) Receiver operating characteristic (ROC) curve of the CRSWNP for external data set (GSE36830). The x-axis represents the 1-specificity and y-axis represents the sensitivity. AUC: area under the curve. (f) Gene expression levels of LINC01198. (g) Gene expression levels of LINC01094. (h) Gene expression levels of LINC01798. (i) Gene expression levels of LINC01829. (j) Gene expression levels of LINC01320.

TABLE 5: Multi-Cox analysis of lncRNA showed 5 lncRNA with a biomark.

lncRNA	Coef	HR	HR. 95L	HR. 95H	Cox P value
LINC01094	0.001471451	1.001472534	1.000057684	1.002889385	0.041357096
LINC01798	0.079829794	1.83102701	1.017376455	1.53075104	0.12443396
LINC01829	0.126665257	1.35037009	1.009532575	1.276144072	0.034119673
LINC01320	0.063348029	1.065397564	0.992187746	1.144009261	0.081152175
LINC01998	0.186665257	0.977302291	0.947132838	1.008432744	0.002443396

LRRK2 and inhibit the level of noncoding RNA NRON, thereby promoting the development of CRSwNP [36]. Interestingly, relative evidence suggested that both increased mucus secretion and macrophage activation were related to the pathogenesis of CRSwNP, indicating that immune infiltration analysis could be used to determine the risk of CRSwNP [35]. However, the pathogenesis of CRSwNP was affected by environmental factors and the underlying mechanism was still largely unknown. Therefore, our investigation of abnormally altered genes will help to understand the pathogenesis of CRSwNP.

At present, large-scale RNA sequencing had determined more than 10,000 lncRNAs in mammalian genomes including humans. More and more researches had affirmed that lncRNAs and miRNAs acted a vital part in most cell biological proceedings containing cell growth, proliferation, invasion, invasion, and cytodifferentiation [37, 38]. Abnormal expression of lncRNAs and miRNAs was a common feature of the pathogenesis of many diseases [39, 40]. For example, the study by Wang et al. showed that by constructing a ceRNA network of miRNAs and lncRNAs, it came to light that the etiopathogenesis of CRSwNP was related to AGR2, FAM3D, PIP, TMC, and DSE [29, 33]. In addition, the study found that lncRNA was related to the pathological development of CRSwNP-sinusitis with rhinopolyps and asthma type 2 hyperinflammation, and determined the expression profile of lncRNA in CRSwNP [29, 33]. Zhang et al. [41] have found that lncRNA GATA3-AS1 is specifically

(a)

(b)
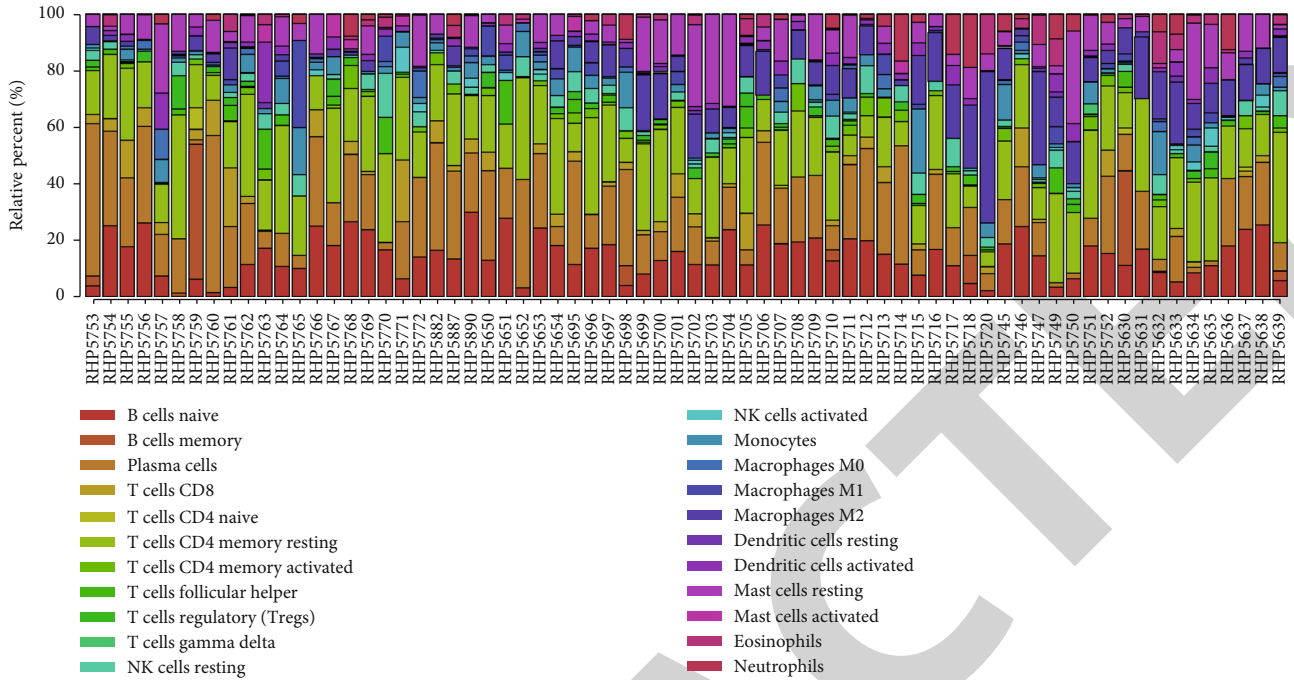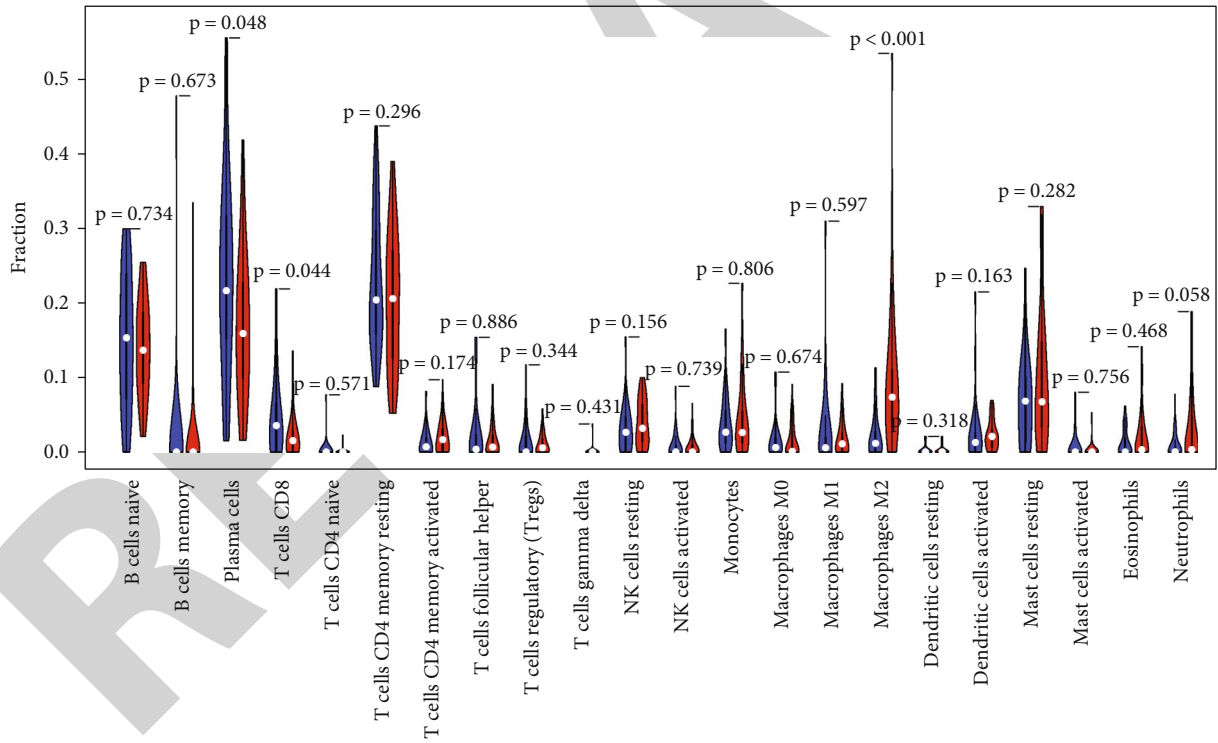
Figure 8: Continued.
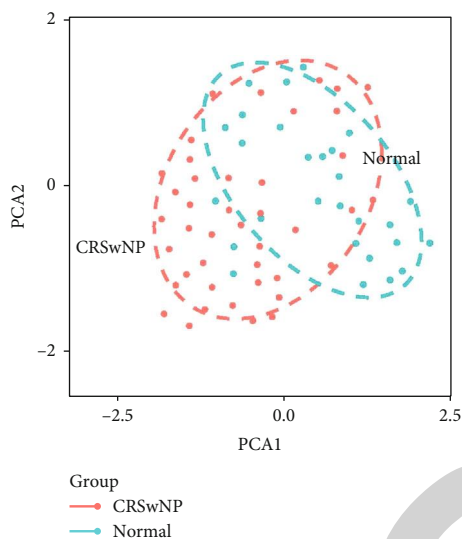
(c)
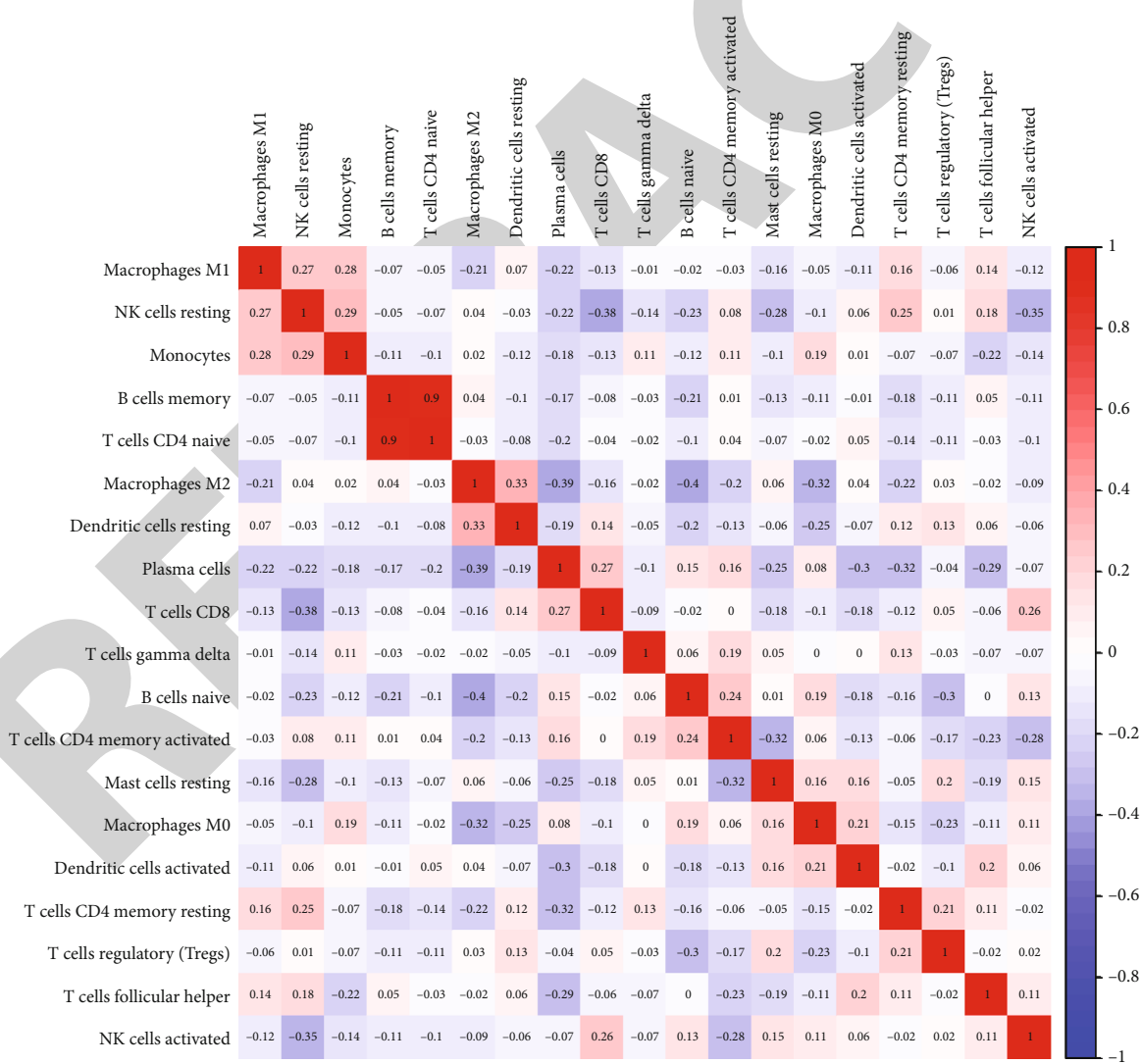
(d)

FIGURE 8: Continued.
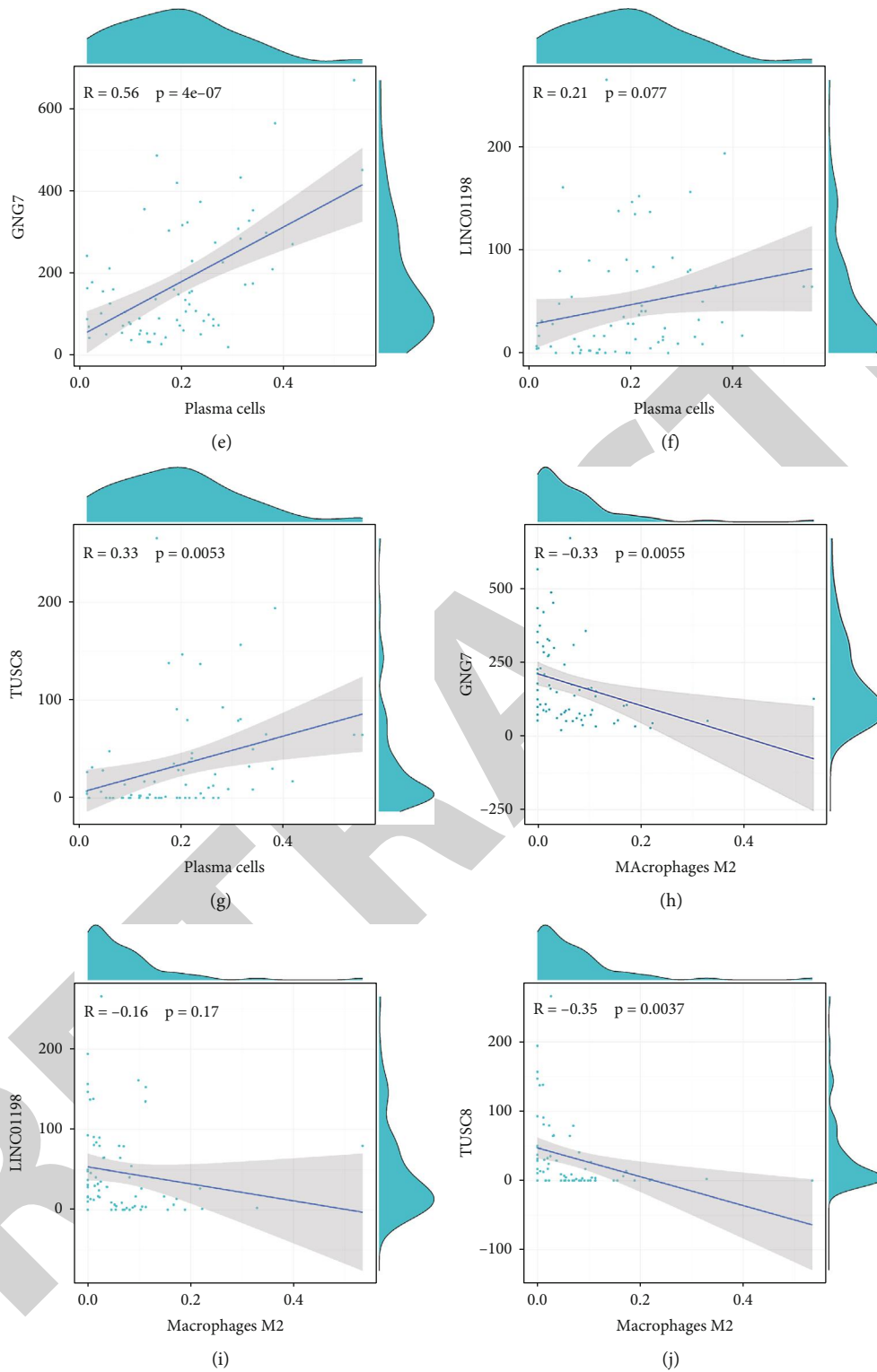
Figure 8: Visualization of immune cell infiltration and correlation between GNG7, TUSC8, and LINC01198 expressions and infiltrating immune cells. (a) The composition of infiltrating immune cells. (b) Violin plot of differences of immune cell infiltration. (c) Principal component analysis cluster plot of immune cell infiltration. (d) Correlation matrix of proportions of 22 types of infiltrating immune cells. (e) Correlation between GNG7 expression and plasma cells ($R = 0.56$, $p = 4e - 07$). (f) Correlation between LINC01198 expression and plasma cells ($R = 0.21$, $p = 0.077$). (g) Correlation between TUSC8 expression and plasma cells ($R = 0.33$, $p = 0.0053$). (h) Correlation between GNG7 expression and macrophage M2 ($R = -0.33$, $p = 0.0055$). (i) Correlation between LINC01198 expression and macrophage M2 ($R = -0.16$, $p = 0.17$). (j) Correlation between TUSC8 expression and macrophage M2 ($R = -0.35$, $p = 0.0037$).
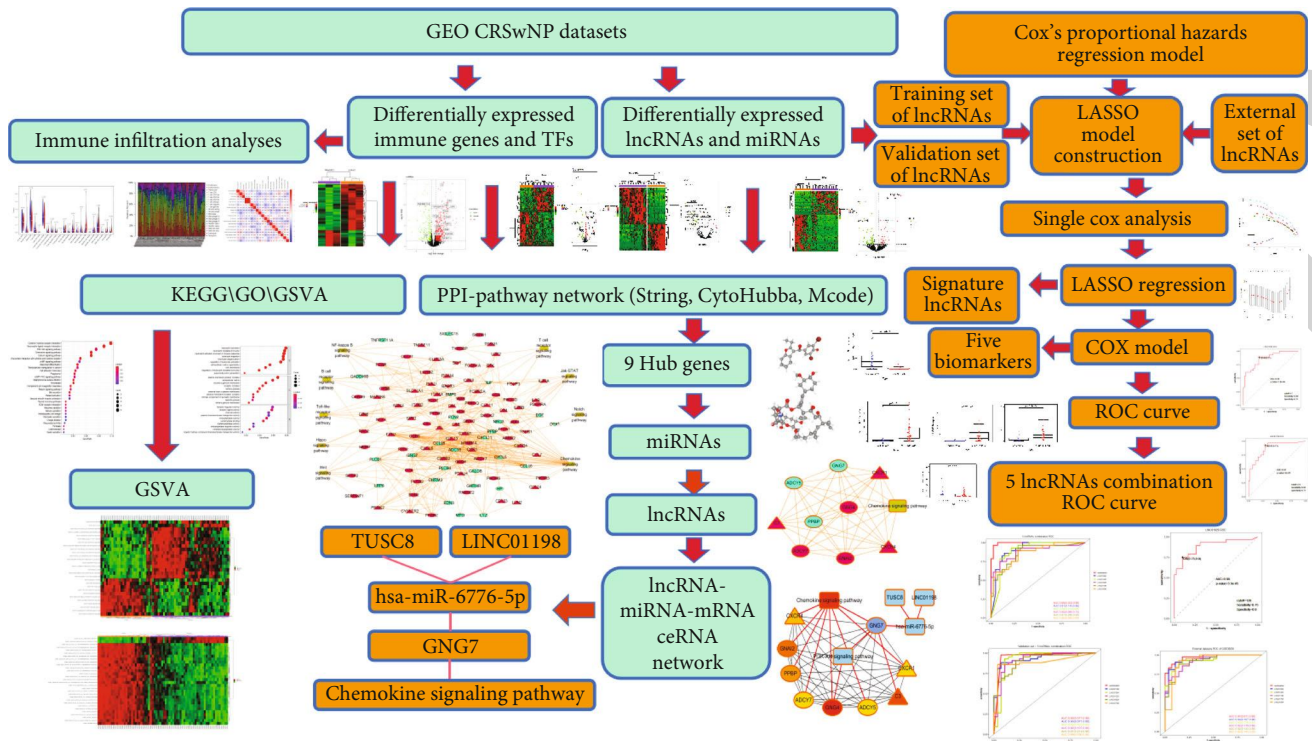
FIGURE 9: Flow chart.

expressed in Th2 cells and lncRNA GATA3-AS1 and GATA3 genes are regulated by the same transcriptional regulatory element, which may play an important role in Th2L-type immune response. Zhu et al. [42] showed that the expression of LNC-GAS5 was upregulated in exosomes in nasal mucus of patients with allergic rhinitis and in exosomes of human nasal epithelial cells stimulated by ovalbumin. LNC-GAS5 inhibits the differentiation of Th1 cells by downregulating T-BET and EZH2 and promotes the differentiation of Th2 cells by upregulating GATA-3, suggesting that LNC-GAS5 is a key mediator of Th1/Th2 differentiation. In addition, Yue et al. [43] found that LNC-000632 expression was downregulated in nasal mucosal samples from patients with allergic rhinitis and IL-13-stimulated nasal epithelial cells. LNC-000632 targets MIR-498 and inhibits IL-13-induced production of granulocyte-macrophage colony stimulating factor, eosinophil chemokine, and MUAC5AC. But the above study results were confined only to the relevance between miRNAs and lncRNAs in CRSwNP. In our research, we carried on a genome expression profile both in CRSwNP and homologous control groups. We appraised and analyzed abnormally expressed miRNA, immune genes, TF, and lncRNA to illustrate the etiopathogenesis of CRSwNP. Our research found that a gross of 48 miRNAs, 304 lncRNAs, 92 TFs, and 525 immune genes was unusually expressed in CRSwNP. As far as we know, this is the first to systematically identify and analyze noncoding RNA, TFs, and immune genes related to CRSwNP.

Our research found that the pathological progress of CRSwNP was related to cytokine-cytokine receptor interaction, neuroactive ligand-receptor interaction, PI3K-Akt signal path, chemokine signal path, and calcium. In addition,

we found that in some CRSwNP patients, immune genes were based on abnormal expression of CRSwNP and pathway enrichment collected by TF overlap, which was the same as previous studies. Therefore, we judged that cell proliferation and immune regulation were also involved in the pathogenesis of CRSwNP. Based on the above analysis, we further used the String database to draw a PPI network for the differential immune gene and transcription factor data set in CRSwNP. We established a ceRNA network on account of the expression profiles of DmiRNA, DimGene, DTFgene, DlncRNA, and CRSwNP patients. We got 14 miRNA nodes (8 upregulated and 6 downregulated) and 38 lncRNA nodes (20 upregulated and 18 downregulated). Based on the above analysis, we further selected a pair of Cernas: TUSC8/LINC01198/has-miR-6776-5p/GNG7.

As a member of lncRNA family, LINC01198 was identified in tumor cells. In latest studies, it had been put forward that LINC01198-originated chromosome 13 could affect many biological functions. For instance, LINC01198 adjusted multiplication in various diseases and cancers [44, 45]. In the light of S. Chen et al., LINC01198 was bound up with cell apoptosis [15]. Sun et al. suggested that LINC01198 played a regulatory role in the biological function of bladder cancer [16]. Base on the above, it could be verdicted that LINC01198 had to do with the effect of pathological process in CRSwNP. To verify that the effect of LINC01198 on CRSwNP may be adjusted by expression, we quantified the expression of LINC01198 in CRSwNP and control and proved that LINC01198 was downregulated in CRSwNP, which indicated that the low expression of LINC01198 promoted the pathogenesis of CRSwNP. miRNA imbalance was bound up with diversified inflammations and unusual immune responses,

such as pulmonary fibrosis and asthma. Fundamentally, present studies had confirmed that assorted miRNAs were abnormally expressed in CRSwNP and impacted the progress of CRSwNP inflammation [46, 47]. Zhong et al. identified that miR-6776-5p was linked to calcification of vascular smooth muscle cells induced by high glucose/senescence [48]. On the basis of Li et al., miR-6776-5p was bound up with the invasions of renal cell cancer via restraining TRPM3 [19]. Our study corroborated that miR-6776-5p was upregulated in CRSwNP patients. Its high expression in CRSwNP tissue makes it clear that it may be relevant to the occurrence of CRSwNP. We discovered that LINC01198 promoted CRSwNP by meditating miR-6776-5p, but this still requires test verification.

A variety of lncRNAs were abnormally expressed in CRSwNP and were related to the occurrence of CRSwNP. Despite these lncRNAs were not proposed in this research, they may be related to the differences between different detection platforms [30, 49–51]. For example, it had been reported that AKT1, CDH1, PIK3R1, CBL, LRP1, MALAT1, and XIST had been shown to be involved in the pathogenesis of CRSWNP [52]. Draw ROC map according to LASSO model, and choose DlncRNA with AUC > 0.85 and differentially expressed as lncRNA biomarkers. From this, we identified LINC01198, LINC01094, LINC01798, LINC01829, and LINC01320 as CRSWNP biomarkers. The above evidence indicated that our results provided new data for CRSwNP biomarkers. However, these data still need to be experimentally verified.

According to the literature, the inflammatory mechanism in CRSwNP may be related to TH2 polarization and tissue eosinophils [53, 54]. We collected data on 22 immune cell subsets in 42 CRSwNP and 28 normal inferior turbinate tissues. Through immune penetration analysis, we found that there was a positive correlation between M2 macrophages and resting dendritic cells in CRSwNP. However, a negative correlation with B cell naiveness, macrophage M0, macrophage M1, T cells, and plasma cells. This indicated that there may be a synergistic effect between M2 macrophages and dendritic cells in CRSwNP, while CRSwNP had antagonistic effects on B cell naiveness, macrophage M0, macrophage M1, T cell CD4 memory cessation, and plasma cell function. These results indicated that immune disorders were related to the pathogenesis of CRSwNP, but this result had individual differences. In addition, in order to find effective medicines for the remedy of CRSwNP, we used the CMAP database to detect 19 immune genes and identified 5 drugs, namely, danazol, idarubicin, semustine, cephalosporin, and morpholinone.

Importantly, known, abnormally expressed lncRNAs and miRNAs can regulate the pathological process of many diseases including CRSwNP. According to the establishment of a ceRNA network, we found that there may be mutual regulation between LINC01198, TUSC8, miR-6776-5p, and GNG7 that were abnormally expressed in CRSwNP. In addition, they were related to the PI3K/AKT signal path. This may involve a critical mechanism in CRSwNP. Further research on these RNAs may announce more significant message about the pathogenesis of CRSwNP.

5. Conclusion

We constructed a ceRNA network specific to CRSwNP related to immune gene, TF, miRNA, and lncRNA and identified 5 lncRNA biomarkers. We found that LINC01198, TUSC8, miR-6776-5p, and GNG7 were among the ceRNA networks. There was a mutual regulatory relationship related to the PI3K/AKT signal path. This research may provide a new idea for further understanding of the pathogenesis of this disease.

Data Availability

The data used to support the findings of this study are included within the article.

Conflicts of Interest

The authors declare that they have no competing interest.

Acknowledgments

References

[1] W. J. Fokkens, V. J. Lund, J. Mullol et al., "EPOS 2012: European position paper on rhinosinusitis and nasal polyps 2012. A summary for otorhinolaryngologists," *Rhinology*, vol. 50, no. 1, pp. 1–12, 2012.

[2] A. S. DeConde and Z. M. Soler, "Chronic rhinosinusitis: epidemiology and burden of disease," *American Journal of Rhinology & Allergy*, vol. 30, no. 2, pp. 134–139, 2016.

[3] D. Jarvis, R. Newson, J. Lotvall et al., "Asthma in adults and its association with chronic rhinosinusitis: the GA2LEN survey in Europe," *Allergy*, vol. 67, no. 1, pp. 91–98, 2012.

[4] Y. S. Kim, N. H. Kim, S. Y. Seong, K. R. Kim, G. B. Lee, and K. S. Kim, "Prevalence and risk factors of chronic rhinosinusitis in Korea," *American Journal of Rhinology & Allergy*, vol. 25, no. 3, pp. 117–121, 2011.

[5] W. W. Stevens, R. P. Schleimer, and R. C. Kern, "Chronic rhinosinusitis with nasal polyps," *The Journal of Allergy and Clinical Immunology. In Practice*, vol. 4, no. 4, pp. 565–572, 2016.

[6] E. O. Meltzer, D. L. Hamilos, J. A. Hadley et al., "Rhinosinusitis: Establishing definitions for clinical research and patient care," *Otolaryngology and Head and Neck Surgery*, vol. 131, no. 6, pp. 1–62, 2004.

[7] M. S. Benninger et al., "Adult chronic rhinosinusitis: definitions, diagnosis, epidemiology, and pathophysiology," *Otolaryngology and Head and Neck Surgery*, vol. 129, 3_suppl, pp. S1–32, 2003.

[8] K. Avdeeva and W. Fokkens, "Precision medicine in chronic rhinosinusitis with nasal polyps," *Current Allergy and Asthma Reports*, vol. 18, no. 4, p. 25, 2018.

[9] E. O. Meltzer and D. L. Hamilos, "Rhinosinusitis diagnosis and management for the clinician: a synopsis of recent consensus guidelines," *Mayo Clinic Proceedings*, vol. 86, no. 5, pp. 427–443, 2011.

[10] J. Y. Ip and S. Nakagawa, "Long non-coding RNAs in nuclear bodies," *Development, Growth & Differentiation*, vol. 54, no. 1, pp. 44–54, 2012.

[11] Y. He, X. M. Meng, C. Huang et al., "Long noncoding RNAs: novel insights into hepatocelluar carcinoma," *Cancer Letters*, vol. 344, no. 1, pp. 20–27, 2014.

[12] F. Di Gesualdo, S. Capaccioli, and M. Lulli, "A pathophysiological view of the long non-coding RNA world," *Oncotarget*, vol. 5, no. 22, pp. 10976–10996, 2014.

[13] K. Liao, J. Xu, W. Yang, X. You, Q. Zhong, and X. Wang, "The research progress of LncRNA involved in the regulation of inflammatory diseases," *Molecular Immunology*, vol. 101, pp. 182–188, 2018.

[14] Y. Xie and Y. Cheng, "LINC01198 facilitates gliomagenesis through activating PI3K/AKT pathway," *RNA Biology*, vol. 17, no. 7, pp. 1040–1052, 2020.

[15] S. Chen, H. Yuan, B. C. Chen, Z. A. Wan, S. L. Tu, and X. Y. Hu, "LINC01198 promotes colorectal cancer cell proliferation and inhibits apoptosis via Notch signaling pathway," *European Review for Medical and Pharmacological Sciences*, vol. 24, no. 16, pp. 8439–8446, 2020.

[16] Y. Sun, D. Y. Zhu, H. J. Xing, Y. Hou, and Y. Liu, "Screening of characteristic biomolecules related to bladder cancer based on construction of ceRNA regulation network," *World Journal of Urology*, vol. 38, no. 11, pp. 2835–2847, 2020.

[17] T. X. Lu and M. E. Rothenberg, "MicroRNA," *The Journal of Allergy and Clinical Immunology*, vol. 141, no. 4, pp. 1202–1207, 2018.

[18] T. Liu, Y. Sun, and W. Bai, "The role of epigenetics in the chronic sinusitis with nasal polyp," *Current Allergy and Asthma Reports*, vol. 21, no. 1, p. 1, 2020.

[19] W. Li, F. Q. Yang, C. M. Sun et al., "circPRRC2A promotes angiogenesis and metastasis through epithelial-mesenchymal transition and upregulates TRPM3 in renal cell carcinoma," *Theranostics*, vol. 10, no. 10, pp. 4395–4409, 2020.

[20] L. Salmena, L. Poliseno, Y. Tay, L. Kats, and P. P. Pandolfi, "A ceRNA hypothesis: the Rosetta Stone of a hidden RNA language," *Cell*, vol. 146, no. 3, pp. 353–358, 2011.

[21] M. S. Ebert, J. R. Neilson, and P. A. Sharp, "MicroRNA sponges: competitive inhibitors of small RNAs in mammalian cells," *Nature Methods*, vol. 4, no. 9, pp. 721–726, 2007.

[22] D. Y. Lee, Z. Jeyapalan, L. Fang et al., "Expression of versican 3'-untranslated region modulates endogenous microRNA functions," *PLoS One*, vol. 5, no. 10, article e13599, 2010.

[23] Y. Tay, J. Rinn, and P. P. Pandolfi, "The multilayered complexity of ceRNA crosstalk and competition," *Nature*, vol. 505, no. 7483, pp. 344–352, 2014.

[24] Gene Ontology Consortium, "Expansion of the Gene Ontology knowledgebase and resources," *Nucleic Acids Research*, vol. 45, no. D1, pp. D331–D338, 2017.

[25] M. Kanehisa and S. Goto, "KEGG: Kyoto Encyclopedia of Genes and Genomes," *Nucleic Acids Research*, vol. 28, no. 1, pp. 27–30, 2000.

[26] D. Lal, J. M. Scianna, and J. A. Stankiewicz, "Efficacy of targeted medical therapy in chronic rhinosinusitis, and predictors of failure," *American Journal of Rhinology & Allergy*, vol. 23, no. 4, pp. 396–400, 2009.

[27] W. J. Fokkens, V. J. Lund, J. Mullol et al., "European position paper on rhinosinusitis and nasal polyps 2012," *Rhinology. Supplement*, vol. 23, pp. 3–298, 2012.

[28] N. Zhang, T. Van Zele, C. Perez-Novo et al., "Different types of T-effector cells orchestrate mucosal inflammation in chronic sinus disease," *The Journal of Allergy and Clinical Immunology*, vol. 122, no. 5, pp. 961–968, 2008.

[29] M. Wang, X. Bu, G. Luan et al., "Distinct type 2-high inflammation associated molecular signatures of chronic rhinosinusitis with nasal polyps with comorbid asthma," *Clinical and Translational Allergy*, vol. 10, no. 1, p. 26, 2020.

[30] B. Callejas-Díaz, G. Fernandez, M. Fuentes et al., "Integrated mRNA and microRNA transcriptome profiling during differentiation of human nasal polyp epithelium reveals an altered ciliogenesis," *Allergy*, vol. 75, no. 10, pp. 2548–2561, 2020.

[31] T. K. Soklic, M. Rijavec, M. Silar et al., "Transcription factors gene expression in chronic rhinosinusitis with and without nasal polyps," *Radiology and Oncology*, vol. 53, no. 3, pp. 323–330, 2019.

[32] H. Wang, D. Q. Hu, Q. Xiao et al., "Defective STING expression potentiates IL-13 signaling in epithelial cells in eosinophilic chronic rhinosinusitis with nasal polyps," *The Journal of Allergy and Clinical Immunology*, vol. 147, no. 5, pp. 1692–1703, 2021.

[33] W. Wang, Z. Gao, H. Wang et al., "Transcriptome analysis reveals distinct gene expression profiles in eosinophilic and noneosinophilic chronic rhinosinusitis with nasal polyps," *Scientific Reports*, vol. 6, no. 1, pp. 1–14, 2016.

[34] W. J. Fokkens, "EPOS2020: a major step forward," *Rhinology*, vol. 58, no. 1, p. 1, 2020.

[35] S. H. Cho, D. W. Kim, and P. Gevaert, "Chronic rhinosinusitis without nasal polyps," *The Journal of Allergy and Clinical Immunology. In Practice*, vol. 4, no. 4, pp. 575–582, 2016.

[36] Y. Ma, C. Zheng, and L. Shi, "The kinase LRRK2 is differently expressed in chronic rhinosinusitis with and without nasal polyps," *Clin Transl Allergy*, vol. 8, no. 1, p. 8, 2018.

[37] W. Zhao, D. Geng, S. Li, Z. Chen, and M. Sun, "LncRNA HOTAIR influences cell growth, migration, invasion, and apoptosis via the miR-20a-5p/HMGA2 axis in breast cancer," *Cancer Medicine*, vol. 7, no. 3, pp. 842–855, 2018.

[38] X. Zhang, W. Wang, W. Zhu et al., "Mechanisms and functions of long non-coding RNAs at multiple regulatory levels," *International Journal of Molecular Sciences*, vol. 20, no. 22, p. 5573, 2019.

[39] F. Kopp and J. T. Mendell, "Functional classification and experimental dissection of long noncoding RNAs," *Cell*, vol. 172, no. 3, pp. 393–407, 2018.

[40] M. Hou, W. Li, Z. Xie, J. Ai, B. Sun, and G. Tan, "Effects of anticholinergic agent on miRNA profiles and transcriptomes in a murine model of allergic rhinitis," *Molecular Medicine Reports*, vol. 16, no. 5, pp. 6558–6569, 2017.

[41] H. Zhang, C. E. Nestor, S. Zhao et al., "Profiling of human CD4 + T-cell subsets identifies the TH2-specific noncoding RNA GATA3-AS1," *Journal of Allergy and Clinical Immunology*, vol. 132, no. 4, pp. 1005–1008, 2013.

[42] X. Zhu, X. Wang, Y. Wang, and Y. Zhao, "Exosomal long non-coding RNA GAS5 suppresses Th1 differentiation and promotes Th2 differentiation via downregulating EZH2 and T-bet in allergic rhinitis," *Molecular Immunology*, vol. 118, pp. 30–39, 2020.

Retraction

Retracted: Discovery of New Therapeutic Targets for Osteosarcoma Treatment Based on Immune-Related lncRNAs in the Tumor Microenvironment

BioMed Research International

This article has been retracted by Hindawi following an investigation undertaken by the publisher [1]. This investigation has uncovered evidence of one or more of the following indicators of systematic manipulation of the publication process:

(1) Discrepancies in scope

(2) Discrepancies in the description of the research reported

(3) Discrepancies between the availability of data and the research described

(4) Inappropriate citations

(5) Incoherent, meaningless and/or irrelevant content included in the article

(6) Manipulated or compromised peer review

The presence of these indicators undermines our confidence in the integrity of the article's content and we cannot, therefore, vouch for its reliability. Please note that this notice is intended solely to alert readers that the content of this article is unreliable. We have not investigated whether authors were aware of or involved in the systematic manipulation of the publication process.

Wiley and Hindawi regrets that the usual quality checks did not identify these issues before publication and have since put additional measures in place to safeguard research integrity.

We wish to credit our own Research Integrity and Research Publishing teams and anonymous and named external researchers and research integrity experts for contributing to this investigation.

The corresponding author, as the representative of all authors, has been given the opportunity to register their agreement or disagreement to this retraction. We have kept a record of any response received.

References

[1] R. Fu and X. Hong, "Discovery of New Therapeutic Targets for Osteosarcoma Treatment Based on Immune-Related lncRNAs in the Tumor Microenvironment," *BioMed Research International*, vol. 2022, Article ID 3113857, 13 pages, 2022.

Research Article

Discovery of New Therapeutic Targets for Osteosarcoma Treatment Based on Immune-Related lncRNAs in the Tumor Microenvironment

Ribin Fu [1] **and Xiaofang Hong** [2]

[1]*Department of Joint Surgery and Sports Medicine, Zhongshan Hospital, Xiamen University, Xiamen 361004, China*
[2]*Department of Stomatology, Zhongshan Hospital, Xiamen University, Xiamen 361004, China*

Correspondence should be addressed to Ribin Fu; 13799786280@163.com

Ribin Fu and Xiaofang Hong contributed equally to this work.

Background. Long noncoding RNAs (lncRNAs) play an important role in osteosarcoma development, but their role in the tumor microenvironment (TME) is not fully understood. This study associated lncRNAs with immune-related genes and explored the mechanism of lncRNAs in osteosarcoma progression. *Methods*. Unsupervised consensus clustering was applied to construct immune subtypes based on immune-related lncRNAs identified by Pearson's correlation analysis. A series of functional analysis was performed to reveal the links among lncRNAs, immune subtypes, TME, and osteosarcoma prognosis. *Results*. We identified two immune subtypes C1 and C2 showing distinct overall survival. ECM-receptor interaction pathway was more activated in C2 subtype, while immune response pathways were more enriched in C2 subtype. Differential TME and response to chemotherapeutic drugs were observed between the two subtypes. Four metagenes of costimulation, cytolytic activity (CYT), immune score, and STAT1 were differentially enriched in the two subtypes. Based on 26-paired lncRNAs, we constructed a 4-paired lncRNA prognostic signature for predicting prognosis of osteosarcoma prognosis. *Conclusions*. This study focused on immune-related lncRNAs and TME, showing the possible role and mechanisms of lncRNAs in tumor growth and metastasis. ECM may be the new therapeutic target for treating osteosarcoma, and 26-paired lncRNAs could serve as a basis for further studying the mechanisms of CYT and STAT1 in immune response, cancer cell proliferation, and migration. The two subtypes and prognostic signature could promote the design of personalized osteosarcoma treatment.

1. Introduction

Osteosarcoma, which is the most common bone malignancy derived from mesenchymal cells, frequently occurs in children and young adults. About 20% osteosarcoma patients will develop metastasis of which pulmonary metastasis accounts for nearly 80% of all metastatic cases [1, 2]. 5-year overall survival of metastatic osteosarcoma patients and recurrent patients greatly varies but is still lower than 30% [2]. Although adjuvant and neoadjuvant chemotherapy and aggressive surgery are currently employed as the standard for treating osteosarcoma, approximately 30-40% patients still suffer from relapse [1, 3].

In recent years, immunotherapy, especially immune checkpoint inhibitors, has emerged as a new approach to treating various cancers, and a series of clinical trials show favorable outcomes [4, 5]. However, the results of clinical trials using immune checkpoint inhibitors such as ipilimumab and pembrolizumab for treating osteosarcoma are disappointing [6, 7], which may be due to suppressed immune response generated by tumor microenvironment or a lack of neoantigens. Wu et al. compared the level of immune infiltration among different cancer types and found that a majority of osteosarcoma patients show less immune infiltration than other cancer types, which could explain a
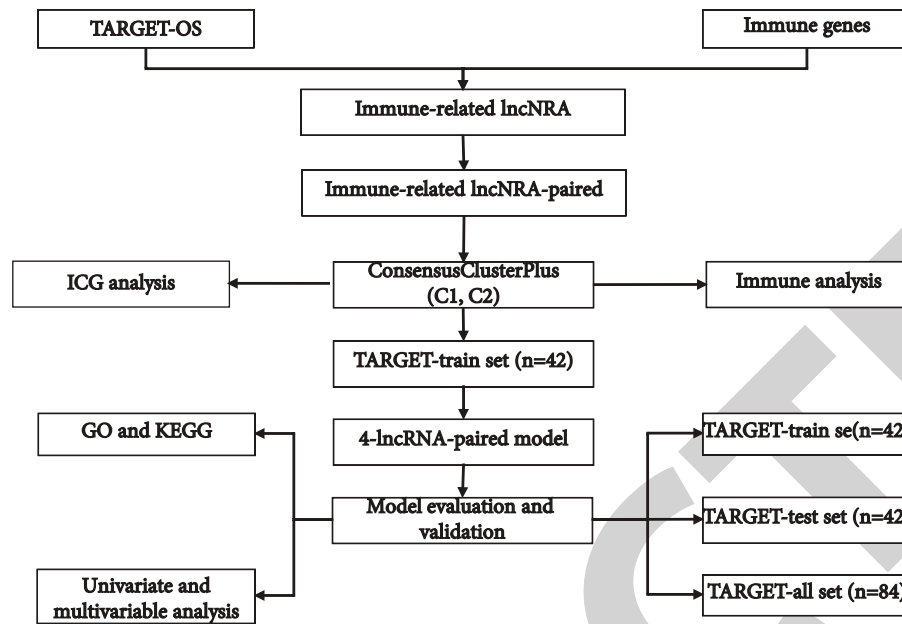
Figure 1: The workflow of constructing a prognostic model based on immune-related lncRNAs.

low response to immune checkpoint inhibitors [8]. In addition, three immune subsets of osteosarcoma with different levels of immune infiltration were defined, and close correlation between genomic alternations and immune suppression was found [8]. However, to fulfill an effective targeted therapy, the mechanism of osteosarcoma development and progression should be further understood.

It has been previously demonstrated that aberrant expression or regulation of long noncoding RNAs (lncRNAs) are associated with cancer development [9]. For example, DANCR and TUG1 upregulated in osteosarcoma tissues can enhance migratory potential and invasion of osteosarcoma cells [10, 11]. LINC00588 is a tumor suppressor that hinders tumor cell proliferation, migration, angiogenesis, and epithelial-mesenchymal transition (EMT) through acting as a ceRNA for miRNA-1972 in osteosarcoma [12]. In oncogenic pathways such as PI3K/AKT and WNT signaling pathways, lncRNAs play a modulatory role in the activity of these pathways [13–16]. Moreover, lncRNAs secreted from tumor cells are critical molecules for mediating cell-cell communications in tumor microenvironment (TME), thereby providing a tumor-supportive microenvironment [17, 18]. T. Zhang et al. constructed a signature of 12 immune-related lncRNAs and 3 immune-related genes for predicting osteosarcoma prognosis [19]. Therefore, lncRNAs can serve as predictable biomarkers for indicating prognosis or promising targets for personalized therapies.

In this study, we applied a paired lncRNA strategy to identify two immune subtypes and constructed a 4-paired lncRNA prognostic signature for osteosarcoma. Further integrative analysis discovered the pivotal role of lncRNAs in TME and osteosarcoma development. The findings paved an important step for searching new lncRNA-based targeted therapies and allowed an early identification for osteosarcoma patients with high-risk metastasis.

2. Materials and Methods

2.1. Data Information and Preprocessing. RNA-seq data and clinical information of osteosarcoma samples were downloaded from TARGET database (https://ocg.cancer.gov/programs/target/data-matrix). The samples without clinical information, survival time, or survival status were excluded. We use R software package hgu133plus2.db to convert Ensembl ID into gene symbol. Median expression level was selected when one gene had multiple gene symbols. After data preprocessing, 84 osteosarcoma samples (55 alive status and 29 dead) were retained, including 47 male samples and 37 female samples. The workflow of this study was shown in Figure 1.

2.2. Identification of Immune-Related lncRNAs. Immune-related genes were obtained from ImmPort database (http://www.immport.org, Release 42, January 2022). Latest gene transfer format (GTF) file came from GENCODE (https://www.gencodegenes.org/, GRCh38.p13). mRNA and lncRNA expression profiles of osteosarcoma were distinguished by GTF file. Then, Spearman's correlation coefficients were calculated between each immune-related gene and each lncRNA. Finally, 42 immune-related lncRNAs were screened under the conditions of correlation coefficient > 0.4 and false discovery rate (FDR) < 0.05.

2.3. Pairing of Immune-Related lncRNAs. Loop pairing was implemented to pair immune-related lncRNAs. Zero or one matrix was constructed based on the assumption defined as follows: lncRNA A and lncRNA B were paired, and their expression difference was defined as C; C was defined as 0 when lncRNA A expression was lower than lncRNA B; otherwise, C = 1. In this way, 375-paired lncRNAs were included with the condition that the proportion of C = 1 was 40%-80%.

(a)

(b)

(c)
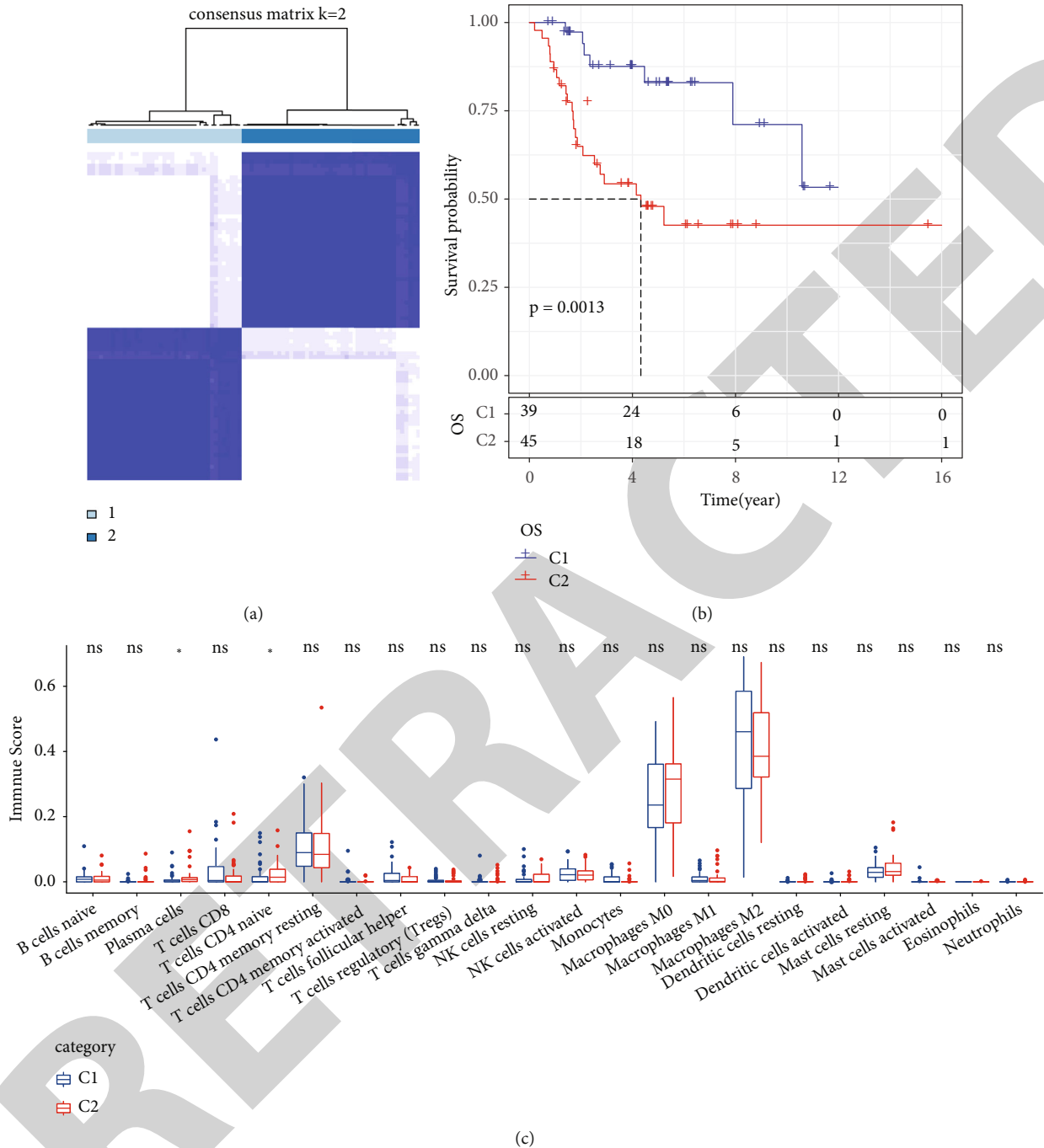
Figure 2: Consensus clustering for identifying two molecular subtypes. (a) Consensus matrix when cluster number $k = 2$. (b) The Kaplan-Meier survival curve of C1 and C2 subtypes. Log-rank test was performed. (c) Distribution difference of immune infiltrating cells in 22 of C1 and C2 subtypes.

2.4. Consensus Clustering for Identifying Molecular Subtypes. Paired lncRNAs related to osteosarcoma prognosis were identified by univariate Cox regression analysis using coxph function in survival R package. Consensus clustering in ConsensusClusterPlus (v1.48.0) R package was conducted under parameters of reps = 100, pItem = 0.8, pFeature = 1, distance = "spearman", and clusterAlg = "pam" [20].

2.5. Immune Analysis of Molecular Subtypes. GSVA R package was used to perform single sample gene set enrichment analysis (ssGSEA) for calculating enrichment score of 22 immune cells and 13 immune metagenes [21, 22]. Each immune metagene contained a series of immune-related genes. Immune score was calculated by ESTIMATE method [23]. 47 immune checkpoints obtained from the previous

(a)

(b)

(c)

(d)
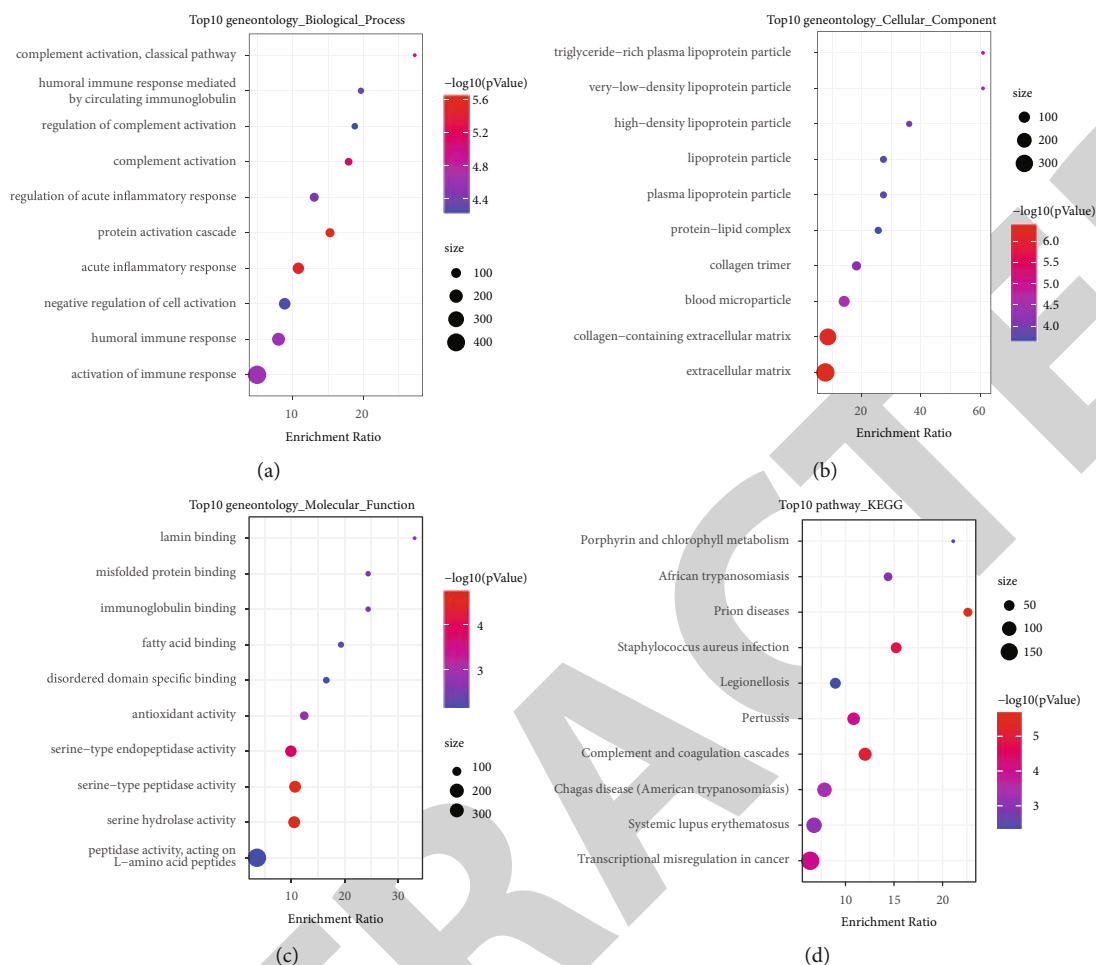
FIGURE 3: Enrichment analysis of biological process (a), cellular component (b), molecular function (c), and KEGG pathways (d) in upregulated genes. The top 10 enriched terms were displayed. Vertical axis displays the annotated terms. Dot represents the counts of enriched genes in one term.

study were included to further assess tumor microenvironment [24]. Log2 (gene expression + 1) was defined to analyze the expression level of the 47 immune checkpoints.

2.6. Analysis of KEGG Pathways and GO Function.
In function analysis of molecular subtypes, we first identified differentially expressed genes (DEGs) with $|$fold change $(FC)| > 1.5$ and $p < 0.05$ by limma R package [25]. Then, WebGestalt R package was performed to annotate Kyoto Encyclopedia of Genes and Genomes (KEGG) pathways and Gene Ontology (GO) terms [26].

Spearman's correlation analysis was conducted to calculate each correlation coefficient between each paired lncRNA and each mRNA. Correlation coefficient > 0.3 and $p < 0.05$ were the criteria to screen genes significantly associated with paired lncRNAs. Then, WebGestalt R package was used to annotate KEGG pathways and GO terms.

2.7. Construction of a Prognostic Model.
A total of 84 osteosarcoma samples were divided into training cohort and test cohort with a ratio of 1 : 1 for 100 times of random sampling. coxph function in survival R package was applied to perform univariate Cox regression analysis for detecting immune-

related paired lncRNAs associated with prognosis ($p < 0.05$). Least absolute shrinkage and selection operator (LASSO) Cox regression analysis in glmnet R package was employed to reduce the number of variables (paired lncRNAs) [27], and 10-fold cross validation was used to construct models. Next, step Akaike information criterion (stepAIC) in MASS package was used to further optimize the model [28]. The least number of variables was remained to acquire enough fitting degree. The coefficient of finally remained paired lncRNAs was calculated by multiple Cox regression analysis. The prognostic model was defined as follows: risk score = coefficient 1 ∗ expression of paired lncRNA 1 + ⋯ + coefficient n ∗ expression of paired lncRNA n. Risk score was transformed to z-score, and $z-score = 0$ was set as a cut-off to classify samples into high-risk and low-risk groups. Finally, receiver operating characteristic (ROC) curve in timeROC R package was used to analyze the effectiveness of the prognostic model.

3. Results

3.1. Identification of Two Molecular Subtypes Based on Immune-Related Paired lncRNAs.
Immune-related lncRNAs
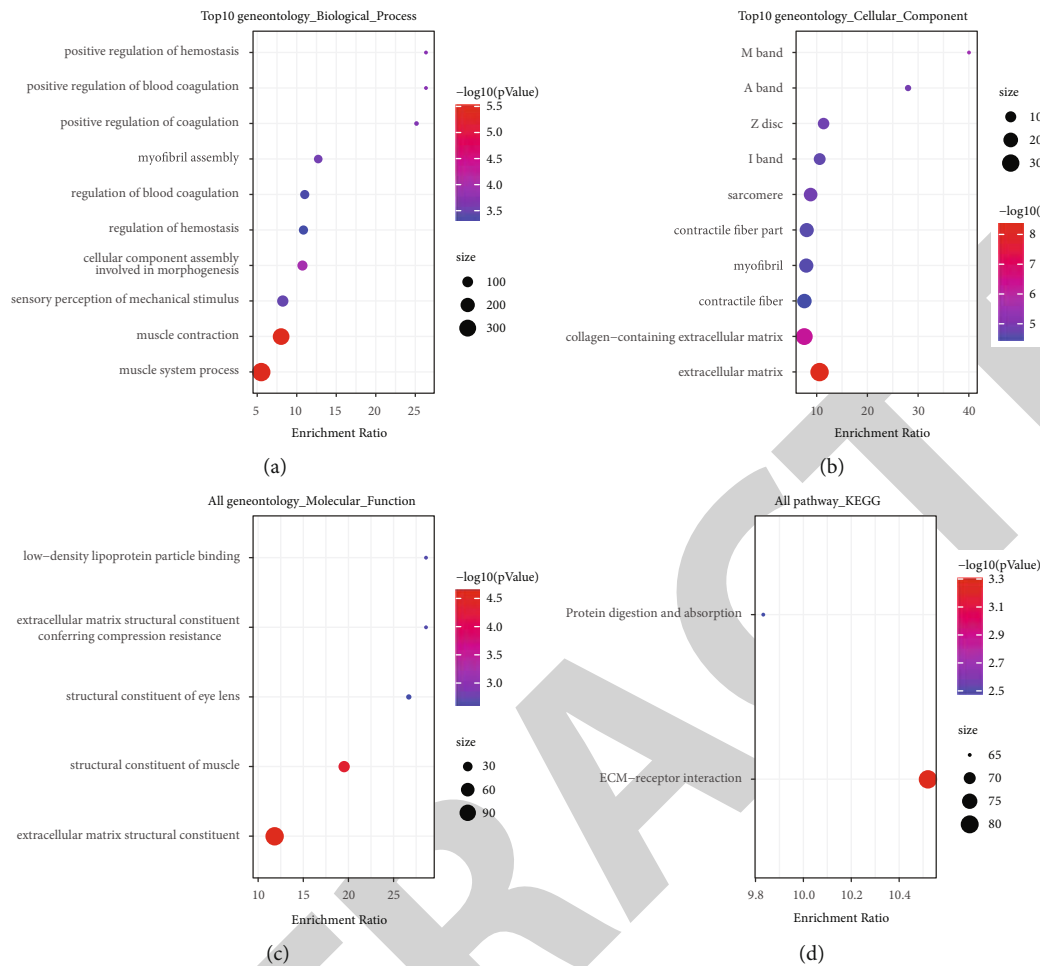
Figure 4: Enrichment analysis of biological process (a), cellular component (b), molecular function (c), and KEGG pathways (d) in downregulated genes. The top 10 enriched terms were displayed. Vertical axis displays the annotated terms. Dot represents the counts of enriched genes in one term.

were screened by the Pearson correlation analysis between expression of immune-related genes and lncRNAs. 42 immune-related lncRNAs and 332 immune-related genes were identified when correlation coefficient > 0.4 and FDR < 0.05. Then, 42 immune-related lncRNAs were loop-paired and 375-paired lncRNAs were generated. Using univariate Cox regression analysis in TARGET dataset, we obtained 26-paired lncRNAs correlated with osteosarcoma prognosis ($p < 0.05$). Based on the expression of 26-paired lncRNAs, consensus clustering was applied to cluster 84 osteosarcoma samples (Supplementary Table 1). The samples were neatly classified into two clusters when $k = 2$ (Figure 2(a)), with C1 group showing a more favorable overall survival than C2 group ($p = 0.0013$, Figure 2(b)). We observed higher T cell CD4 naive and plasma cell infiltration in the C2 subtype (Figure 2(c)).

3.2. Enrichment Analysis of KEGG Pathways and GO Function for DEGs of C1 and C2.
As significantly differential prognosis was observed between C1 and C2, we examined the difference of expression feature between the two subtypes. 213 DEGs were screened between C1 and C2 when | FC| > 1.5 and $p < 0.05$. Specifically, 99 DEGs were downreg-

ulated and 114 DEGs were upregulated in C1 group. Enrichment analysis of KEGG pathways and GO function identified 240 terms of biological process, 15 terms of cellular component, 14 terms of molecular function, and 14 terms of functional pathways from the upregulated genes ($p < 0.05$). The top 10 terms of each column were visualized in Figure 3. Of the downregulated genes, 39 terms of biological process, 30 terms of cellular component, 5 terms of molecular function, and 2 KEGG pathways were annotated ($p < 0.05$, Figure 4). Terms of complement activation, inflammatory response, and immune response were greatly enriched in upregulated genes, suggesting an active immune response in C1 group (Figure 3(a)). Meanwhile, ECM-receptor interaction pathway potentially involved in cancer development was highly enriched in the downregulated genes that were highly expressed in C2 group (Figure 4(d)). These functional annotations validated the differential prognosis of two molecular subtypes.

3.3. The Difference of Tumor Microenvironment between the Two Molecular Subtypes.
TME is consisted of various immune cells, tumor cells, stromal cells, cytokines, chemokines, and so on and can decide the progression of tumor
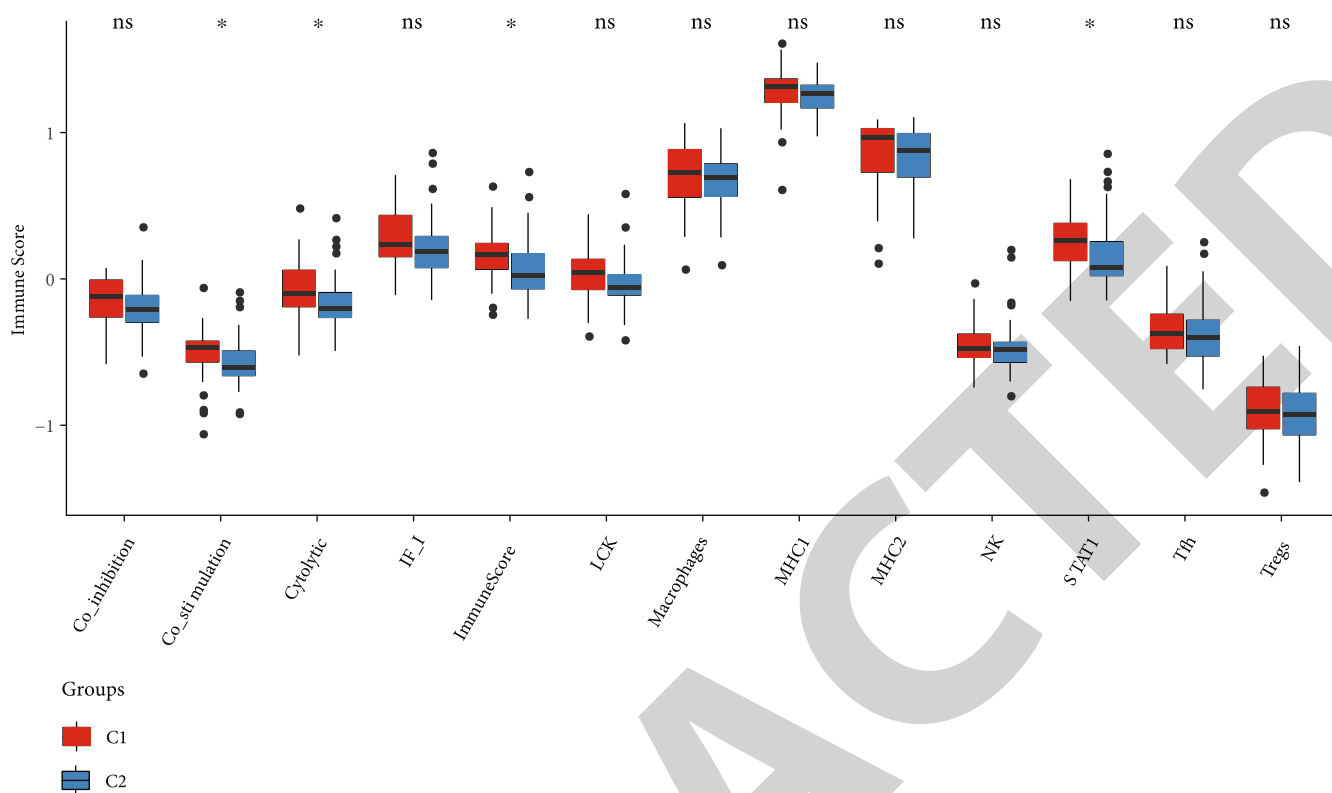
(a)
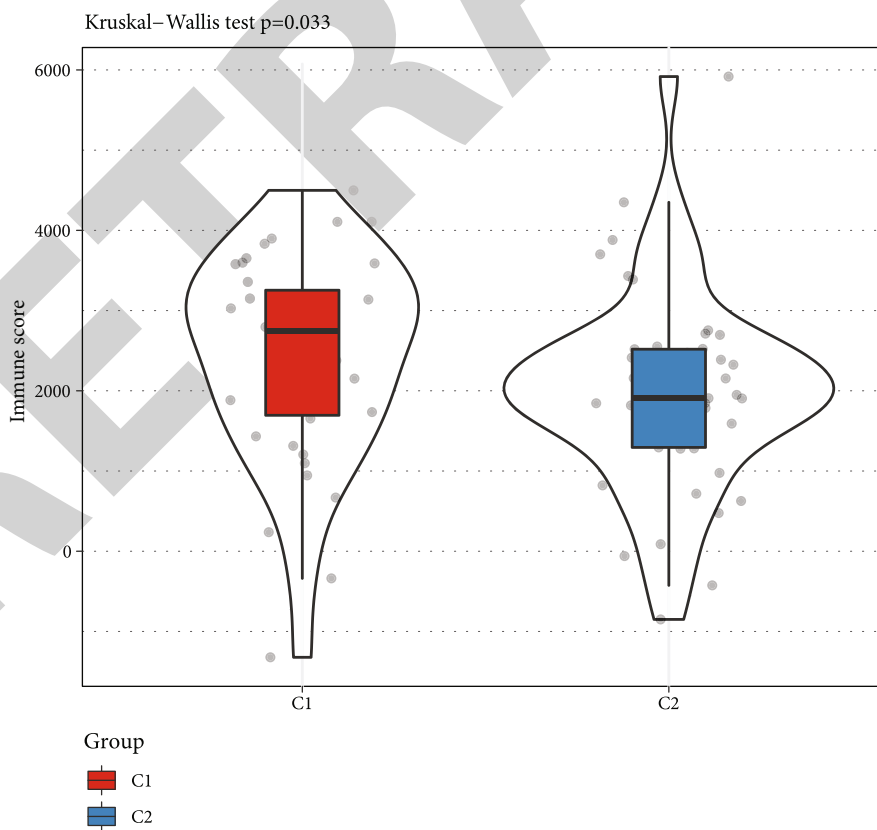
(b)

FIGURE 5: The enrichment score of two molecular subtypes in 13 immune metagenes (a) and immune score (b). Student's t test was performed in 13 immune metagenes. The Kruskal-Wallis test was performed in immune score. $*p < 0.05$. ns: no significance.
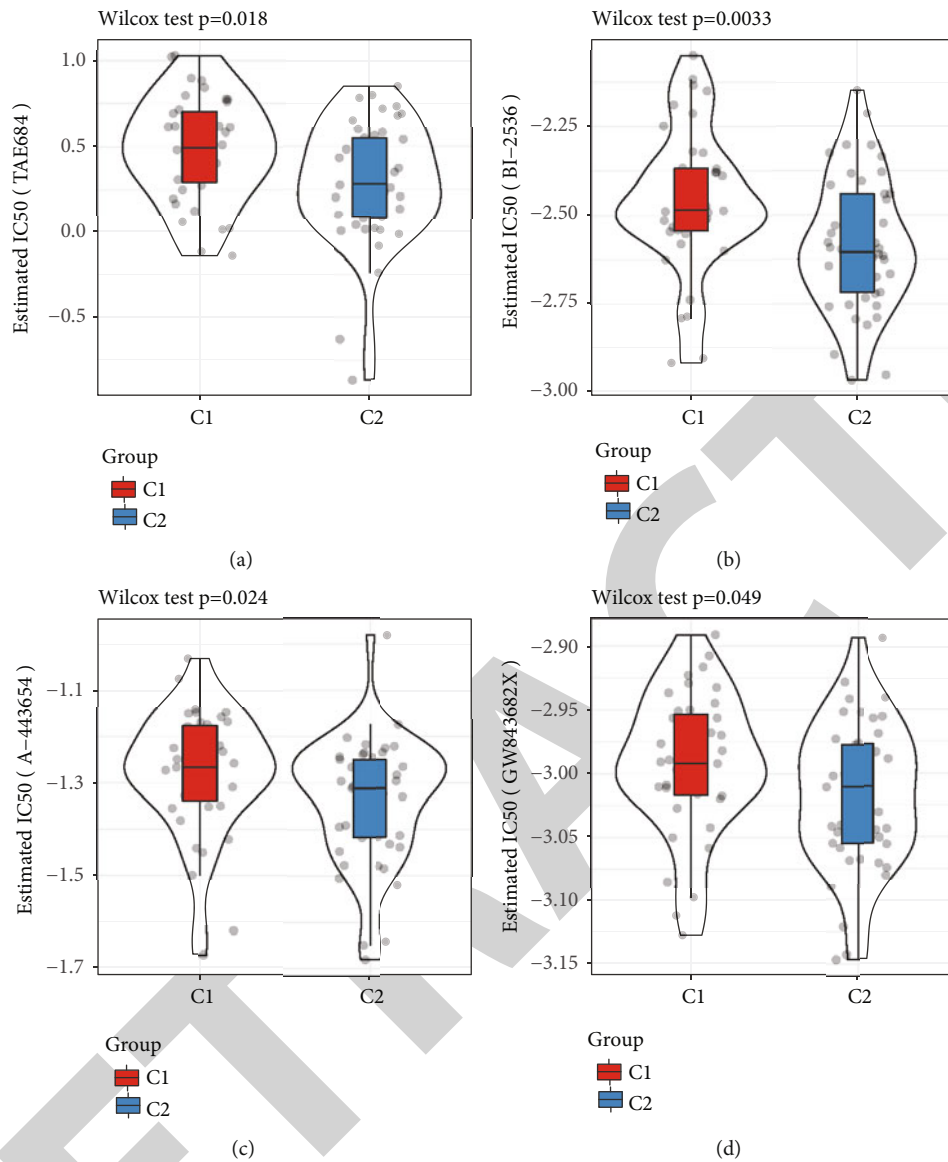
FIGURE 6: The estimated IC50 of TAE684 (a), BI-2536 (b), A-443654 (c), and GW843682X (d) in C1 and C2 subtypes. The Wilcoxon test was performed.

cells. To understand the difference of TME between the two subtypes, ssGSEA was conducted to calculate the score of 22 immune cells of each sample, and we found an obviously higher enrichment of activated CD8 T cells, immature B cells, macrophages, myeloid derived suppressor cells (MDSCs), and regulator T cells in C1 group (Supplementary Figure S1A). In addition, we analyzed the expression of 13 immune metagenes identified by previous studies through ssGSEA [22, 29]. Each of the immune metagene contained a series genes related to immune response. The majority of metagenes were found to be highly expressed in C1 group, especially costimulation, cytolytic, immune score, and STAT1 ($p < 0.05$, Figure5(a)), which indicated higher immune response of C1 group. Similarly, ESTIMATE analysis also revealed higher immune score in C1 group ($p = 0.033$, Figure 5(b)). Furthermore, we included 47 immune checkpoints and compared their expression level between C1 and C2 groups. Only 7 immune checkpoints, including CD40, CD40LG, CD48, HAVCR2, LAG3, LAIR1, and TNFRSF4, presented significant difference between them ($p < 0.05$, Supplementary Figure S1B).

3.4. Sensitivity to Four Chemotherapeutic Drugs. We also assessed whether two molecular subtypes had different sensitivities to chemotherapeutic drugs. Four drugs of TAE684, BI-2536, A-443654, and GW843682X were used. The result exhibited that C2 group had lower estimated IC50 of four drugs than C1 group, indicating that C2 group was more sensitive to these drugs ($p < 0.05$, Figure 6). The finding suggested that patients with C2 subtype could benefit much from chemotherapy.

3.5. Construction of a 4-Paired lncRNA Prognostic Model. A sum of 84 osteosarcoma samples were divided into

(a)

(b)
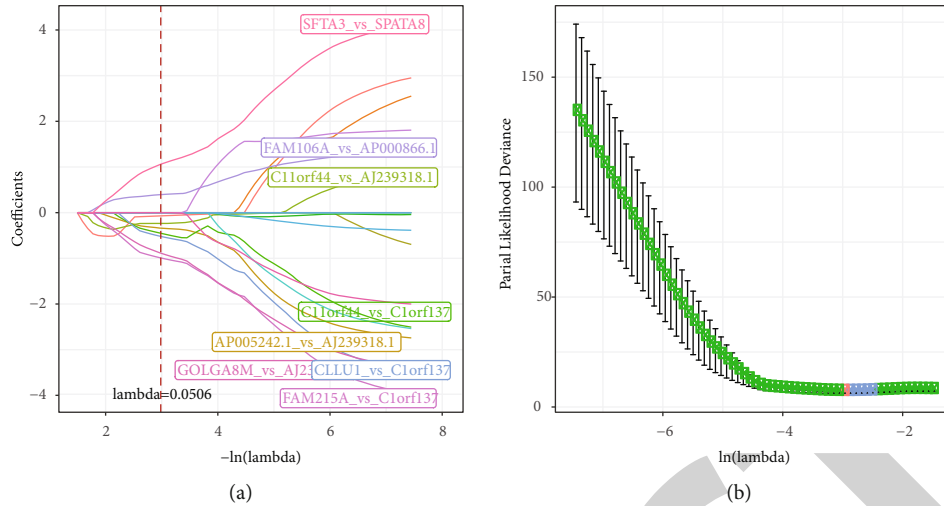
FIGURE 7: LASSO Cox regression for 21-paired lncRNAs. (a) The track plot of 21-paired lncRNAs changing with the lambda value. Different colors of curves represent different paired lncRNAs. Red-dotted line represents the site of lambda = 0.0506. (b) The confidence interval of partial likelihood deviance changing with the lambda value. The orange dot represents the site of lambda = 0.0506.

(a)

(b)
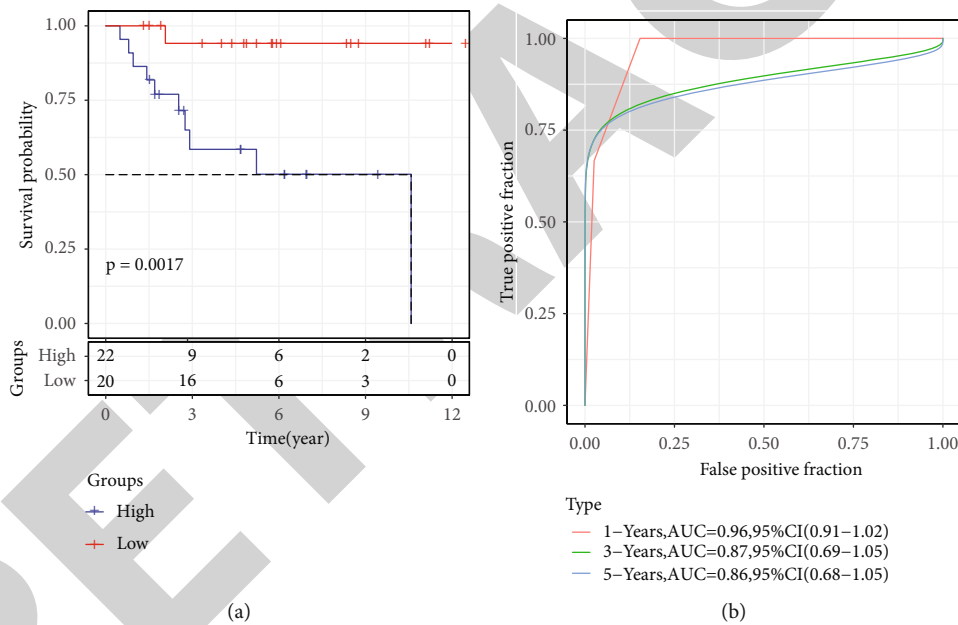
FIGURE 8: The performance of 4-paired lncRNA prognostic model in the training cohort. (a) The Kaplan-Meier survival plot of high-risk and low-risk groups. Red curve represents high-risk group and dark blue represents low-risk group. Log-rank test was performed. (b) ROC curve of 1-year (red), 3-year (green), and 5-year (blue) overall survival.

training cohort and test cohort with ratio 1 : 1 through random sampling. In the training cohort, 21-paired lncRNAs associated with prognosis were screened from 375-paired lncRNAs by univariate Cox regression analysis ($p < 0.05$). As a 21-paired lncRNA prognostic model was complex to apply in clinical practice, therefore, we performed LASSO and AIC to further simplify the model. LASSO regression analysis can reduce variables by introducing the lambda value. When lambda = 0.0506, the optimal model containing 8-paired lncRNAs was generated (Figure 7). Through utilizing stepAIC, a minimum number of variables can be obtained with considerable fitting degree. Finally, 4-paired lncRNAs were remained, and the prognostic model was defined as follows:

$$
\begin{aligned}
\text{Risk score} = &-1.431 * (\text{GOLGA8M vs.AJ239318.1}) \\
&- 1.699 * (\text{C11orf44 vs.C1orf137}) \\
&- 1.593 * (\text{FAM215A vs.C1orf137}) \\
&+ 1.755 * (\text{SFTA3 vs.SPATA8}).
\end{aligned}
\tag{1}
$$

Risk score was converted to z-score, and $z-\text{score} = 0$ was defined as a cut-off for classifying samples into high-risk ($z-\text{score} > 0$) and low-risk ($z-\text{score} < 0$) groups. In
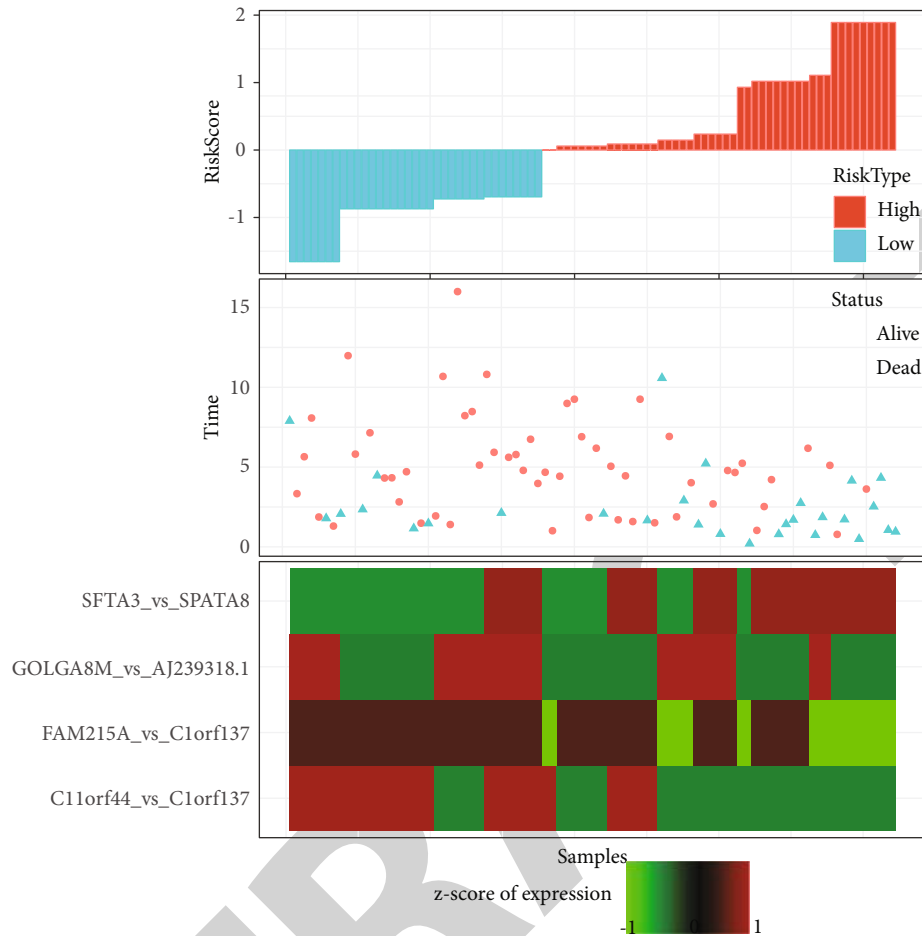
FIGURE 9: The distribution of survival status and expression of four-paired lncRNAs corresponding with the risk score.

the training cohort, 22 samples were classified into high-risk group, and 20 samples were classified into low-risk group, with a distinct overall survival ($p = 0.0017$, Figure 8(a)). ROC analysis showed the effectiveness of the model in predicting 1-year, 3-year, and 5-year overall survival (Figure 8(b)). The robustness of the prognostic model was validated in the test cohort. Consistently, 42 samples were classified into high-risk and low-risk groups that were significantly with differential prognosis ($p = 0.044$, Supplementary Figure S2). Moreover, the tendency of survival status and expression of 4-paired lncRNAs changed consistently with the variation of risk score (Figure 9). The samples of dead status were more concentrated in the high-risk group. The expression level of FAM215A vs. C1orf137 and C11orf44 vs. C1orf137 paired lncRNAs were higher in the low-risk group.

In the relation of risk score to clinical features and molecular subtypes, we assessed their distribution in the high-risk and low-risk groups. The dead samples showed significant higher risk score than samples of alive status (Supplementary Figure S3A). The female and male samples had a similar distribution of risk score (Supplementary Figure S3B). Two molecular subtypes identified by the previous section displayed a significant difference in risk

score (Supplementary Figure S3C). C2 subtype had higher risk score than C1 subtype, which was consistent with the poor survival of C2 subtype.

We systematically compared the relationship between the expression of GOLGA8M, AJ239318.1, C11orf44, C1orf137, FAM215A, SFTA3, and SPATA8 in paired lncRNAs and disease. We observed that GOLGA8M, C1orf137, and SFTA3 in these lncRNAs were significantly overexpressed in tumor samples (Supplementary Figure S4A). In addition, C11orf44 was significantly overexpressed in C1 subgroup, and C1orf137 was significantly overexpressed in C2 subgroup (Supplementary Figure S4B). Univariate and multivariate survival analyses showed that AJ239318.1 high expression was significantly correlated with poor prognosis (Supplementary Figure S4C-D). The scores of the 22 immune cells in each sample were calculated by CIBERSORT algorithm, and then, the correlation between the expression of these 7 lncRNAs and immune infiltration score was calculated by Pearson's method. It can be observed that T cell CD4 naïve, T cell CD4 memory resting, and T cell CD4 memory activated showed a significant positive correlation with C11orf44, C1orf137, FAM215A, and SFTA3 (Supplementary Figure S4E).

(a)

(b)

(c)

(d)
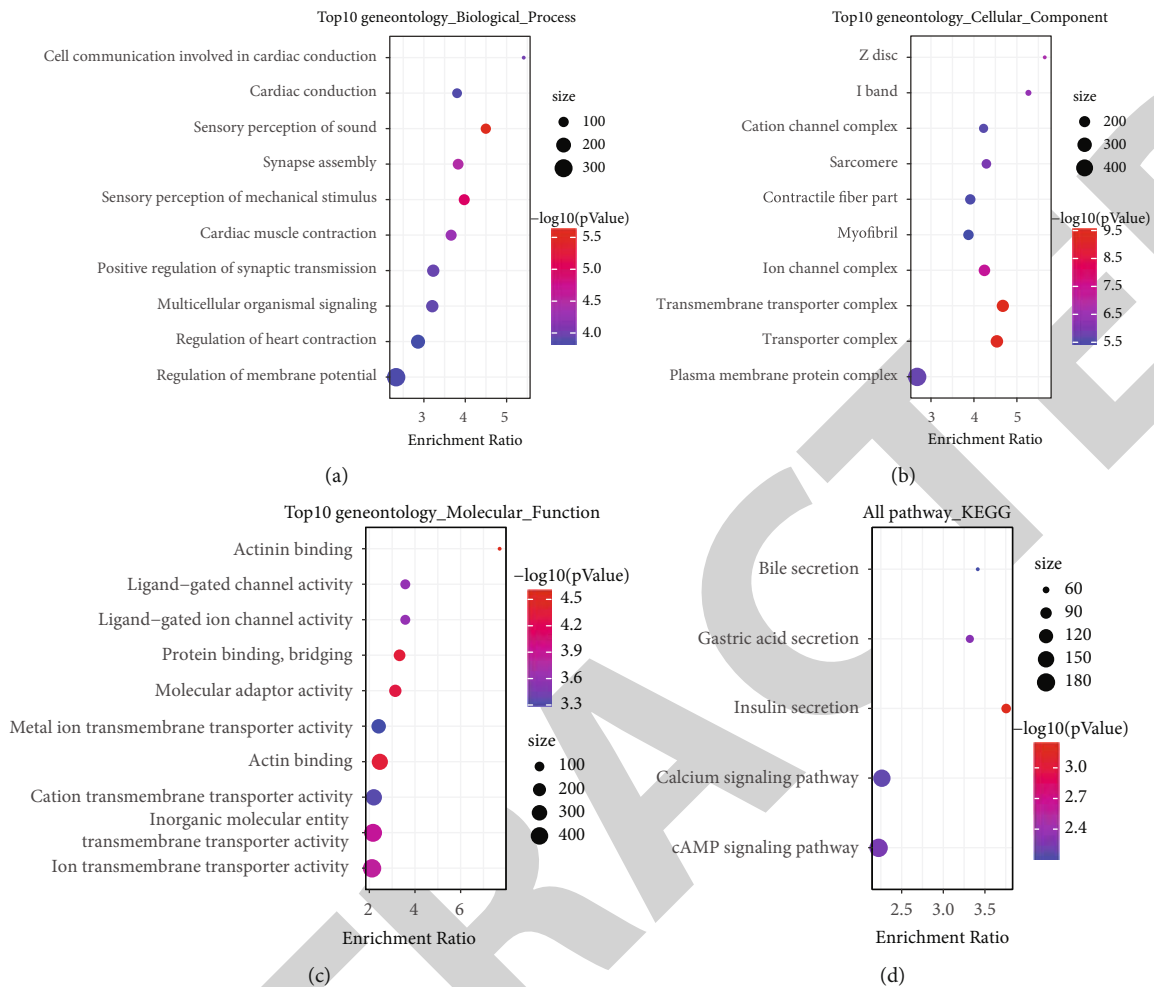
FIGURE 10: Enrichment analysis of biological process (a), cellular component (b), molecular function (c), and KEGG pathways (d) for 661 genes. The top 10 enriched terms were displayed. Vertical axis displays the annotated terms. Dot represents the counts of enriched genes in one term.

3.6. Identification and Functional Analysis of Genes Related to Four Prognostic Paired lncRNAs. To assess the possible function of these four-paired lncRNAs, Spearman's correlation analysis was performed to analyze the relation between lncRNAs and mRNAs. 661 genes were identified with a condition of correlation coefficient > 0.3 and $p < 0.05$. Then, we applied WebGestalt R package to annotate KEGG pathways and GO function significantly associated with 661 genes. The analysis showed 109 terms of biological process, 120 terms of cellular component, and 70 terms of molecular function (Figures 10(a)–10(c)). Calcium signaling pathway and cAMP signaling pathway involved in cancer development were annotated (Figure 10(d)).

4. Discussion

Previous studies have confirmed the essential role of lncRNAs in cancer cell proliferation, invasion, and metastasis. Aberrantly expressed lncRNAs secreted from cancer cells can help the cells escape from immune capture and create tumor-supportive immune microenvironment through the

interactions with oncogenic pathways [18]. In osteosarcoma, low immune infiltration is shown in TME compared with other cancers, which may be the major reason leading to unsatisfactory results of immunotherapy [6–8]. The role of lncRNAs in shaping TME beneficial and facilitating tumor growth has not been completely understood. This study systematically examined and interpreted the close correlations among lncRNAs, TME, and prognosis, according to the transcriptional data of osteosarcoma samples and integrated bioinformatics analysis.

Compared with the absolute quantification based on gene expression profile, the relative ranking method has the advantages of independent standardization method and cross platform comparison. In this study, a new data matrix is established by using the relative rank of lncRNA. Using a paired lncRNA strategy and unsupervised consensus clustering, we identified two immune subtypes (C1 and C2) significantly associated with prognosis. Between the two subtypes, 213 differentially expressed immune-related genes contained 114 upregulated genes and 99 downregulated genes in C1. The functional analysis of these genes

showed that the upregulated genes were enriched in the processes of immune response and inflammatory response and downregulated genes were enriched in ECM-receptor interaction pathway (Figures 3 and 4). Active immune response creates a condition for impeding the proliferation of cancer cells, which was consistent with the favorable prognosis of C1 subtype.

Extracellular matrix (ECM) can be deformed by proliferation of cancer cells and activation of fibroblasts in tumor, thereby resulting in vessel compression [30, 31]. Compressed vessels can hinder the transportation of immune cells to tumor site, hence promoting tumor growth and invasion [30]. ECM-receptor interaction pathway is more active in C2 subtype, which corresponds to its poorer overall survival. Studies have also demonstrated that ECM-related genes are upregulated in other cancer types such as prostate cancer and gastric cancer [32, 33]. In addition, ECM can interact with tumor-associated macrophages (TAMs) to regulate tumor angiogenesis and foster immunosuppressive microenvironment [34]. In an anti-VEGF therapy of colorectal cancer, ECM is remodeled and treatment efficacy is improved in mouse models [35]. Therefore, 26-paired lncRNAs significantly related to osteosarcoma prognosis may serve as key regulators for up- or downregulated expression of DEGs. ECM and ECM-receptor interaction pathway may be potential targets for cancer therapies of osteosarcoma.

In the relation between immune subtypes and TME, we observed higher immune infiltration in C1 subtype, which was majorly resulted from the higher enrichment of CD56 bright natural kill cells, immature B cells, macrophages, MDSCs, and regulatory T cells (Supplementary Figure S1). Analysis on immune-related genes also revealed a higher immune score in C1 subtype, especially metagenes of cytolytic activity (CYT) and STAT1 (Figure 5(a)). Perforin 1 (PRF1) and oxins granzyme A (GZMA) released by cytotoxic T cells and NK cells were used to calculate CYT score and reflect antitumor immunity in cancers [36]. High CYT score has been considered as a protective factor of the prognosis in many cancer types, such as hepatocellular carcinoma [37] and gastric cancer [38]. Moreover, the CYT score was positively associated with the expression of immune checkpoint molecules in prostate cancer [39] and colorectal cancer [40]. Higher expression of immune checkpoint molecules, particularly CD40, CD48, HAVCR2, LAG3, LGALS9, and TNFRSF4, was also found in C1 subtype (Supplementary Figure S1B), indicating that C1 could benefit much from immune checkpoint blockade. J. Zhang et al. found that anti-CD40 mAb treatment could enhance the efficacy of anti-PD-1 treatment through converting PD-1^{hi} T cells to PD-1^{lo} T cells [41]. It provides a possibility that these differentially expressed immune checkpoint molecules may be the therapeutic target for combined immunotherapies in osteosarcoma, especially C1 subtype.

Signal transducer and activator of transcription-1 (STAT1), which is regulated by lncRNA NEAT1, are involved in osteosarcoma metastasis [42]. The inhibition of STAT1 expression can activate EMT process of osteosarcoma sites [42]. In other cancer types, upregulated expression of STAT1 is also associated with favorable outcome [43, 44]. In our results, C1 subtype has a higher enrichment score of STAT1 and a better prognosis than C2 subtype, which was consistent with other studies. A number of lncRNAs such as PSMB8-AS1 [45], LINC01123 [46], and LINC00174 [47] interacting with STAT1 have been found to contribute tumor progression. The 26-paired lncRNAs identified in this study may also be involved in the interactions with STAT1 expression, which can serve as a basis to further examine STAT1 mechanism in cancer metastasis in the future study.

Two immune subtypes classified by different expression patterns of lncRNAs manifested differences in prognosis and TME and therefore further supported the critical role of lncRNAs in suppressing or promoting tumor growth and metastasis. Furthermore, the two subtypes provided a direction for developing new targeted immunotherapies and guiding the personalized application of four chemotherapeutic drugs.

Based on the 26-paired lncRNAs, we constructed a prognostic model with robust performance to predict prognosis of osteosarcoma patients. Patients were clearly stratified into high-risk and low-risk groups according to the expression of four-paired lncRNAs (GOLGA8M vs. AJ239318.1, C11orf44 vs. C1orf137, FAM215A vs. C1orf137, and SFTA3 vs. SPATA8). This 4-paired lncRNA signature enables a quick identification of patients with poor prognosis and promotes earlier treatment to avoid unfavorable outcomes. However, before the application of immune subtypes and prognostic signature, more clinical objects should be included to validate our results.

5. Conclusion

In conclusion, this study established an association among immune-related lncRNAs, TME, and osteosarcoma prognosis through identifying two immune subtypes and four-paired prognostic lncRNAs. We revealed that the ECM-receptor interaction pathway was a new therapeutic target for treating osteosarcoma patients. A possible relation was identified between CYT and immune checkpoints that could direct the personalized immunotherapy but requires further validation. The current findings showed the mechanism and role of lncRNAs in osteosarcoma progression such as the involvement of STAT1 interacting with lncRNAs. Importantly, the immune subtypes and 4-paired lncRNA signature could be useful tools in clinical practice.

Data Availability

The data used to support the findings of this study are included within the article.

Conflicts of Interest

The authors declare that they have no competing interest.

Authors' Contributions

R Fu and X Hong were responsible for the conception and design. R Fu was responsible for the administrative support. R Fu and X Hong were responsible for the provision of study materials or patients. R Fu and X Hong were responsible for the collection and assembly of data. R Fu and X Hong were responsible for the data analysis and interpretation. All authors wrote the manuscript. All authors approved the final manuscript. Ribin Fu and Xiaofang Hong are the first authors and contributed equally to this work.

Supplementary Materials

Supplementary 1. Supplementary Figure S1: the enrichment score of 22 immune cells (A) and the log2 (gene expression+1) of 47 immune checkpoints (B) in two molecular subtypes.

Supplementary 2. Supplementary Figure S2: the performance of 4-paired lncRNA prognostic model in the test cohort. (A) The Kaplan-Meier survival plot of high-risk and low-risk groups. Red curve represents high-risk group and dark blue represents low-risk group. Log-rank test was performed. (B) ROC curve of 1-year (red), 3-year (green), and 5-year (blue) overall survival.

Supplementary 3. Supplementary Figure S3: the distribution of high-risk and low-risk samples in different survival status (A), genders (B), and molecular subtypes (C).

Supplementary 4. Supplementary Figure S4: the relationship between the expression of seven lncRNAs in paired lncRNAs and diseases. (A) The expression of seven lncRNAs was different between tumor and normal samples. (B) The expression differences of seven lncRNAs in C1 and C2 subtypes. (C) Univariate survival analysis showed the relationship between the expression of seven lncRNAs and prognosis. (D) Multivariate survival analysis showed the relationship between the expression of seven lncRNAs and prognosis. (E) Pearson correlation heatmap between the expression of 7 lncRNAs and 22 immune cell infiltration scores.

Supplementary 5. Supplementary Table 1: molecular subtype information of each sample.

References

[1] B. Otoukesh, B. Boddouhi, M. Moghtadaei, P. Kaghazian, and M. Kaghazian, "Novel molecular insights and new therapeutic strategies in osteosarcoma," *Cancer Cell International*, vol. 18, no. 1, p. 158, 2018.

[2] B. A. Lindsey, J. E. Markel, and E. S. Kleinerman, "Osteosarcoma Overview," *Rheumatology and Therapy*, vol. 4, no. 1, pp. 25–43, 2017.

[3] D. J. Harrison, D. S. Geller, J. D. Gill, V. O. Lewis, and R. Gorlick, "Current and future therapeutic approaches for osteosarcoma," *Expert Review of Anticancer Therapy*, vol. 18, no. 1, pp. 39–50, 2018.

[4] M. F. Wedekind, L. M. Wagner, and T. P. Cripe, "Immunotherapy for osteosarcoma: where do we go from here?," *Pediatric Blood & Cancer*, vol. 65, no. 9, article e27227, 2018.

[5] S. Kruger, M. Ilmer, S. Kobold et al., "Advances in cancer immunotherapy 2019- latest trends," *Journal of Experimental & Clinical Cancer Research*, vol. 38, no. 1, p. 268, 2019.

[6] M. S. Merchant, M. Wright, K. Baird et al., "Phase I clinical trial of ipilimumab in pediatric patients with advanced solid tumors," *Clinical Cancer Research: An Official Journal of the American Association for Cancer Research*, vol. 22, no. 6, pp. 1364–1370, 2016.

[7] H. A. Tawbi, M. Burgess, V. Bolejack et al., "Pembrolizumab in advanced soft-tissue sarcoma and bone sarcoma (SARC028): a multicentre, two-cohort, single-arm, open-label, phase 2 trial," *The Lancet Oncology*, vol. 18, no. 11, pp. 1493–1501, 2017.

[8] C. C. Wu, H. C. Beird, J. Andrew Livingston et al., "Immunogenomic landscape of osteosarcoma," *Nature Communications*, vol. 11, no. 1, p. 1008, 2020.

[9] M. C. Jiang, J. J. Ni, W. Y. Cui, B. Y. Wang, and W. Zhuo, "Emerging roles of lncRNA in cancer and therapeutic opportunities," *American Journal of Cancer Research*, vol. 9, no. 7, pp. 1354–1366, 2019.

[10] Z. Pan, C. Wu, Y. Li et al., "LncRNA DANCR silence inhibits SOX5-mediacted progression and autophagy in osteosarcoma via regulating miR-216a-5p," *Biomedicine & Pharmacotherapy*, vol. 122, article 109707, 2020.

[11] K. Sheng and Y. Li, "LncRNA TUG1 promotes the development of osteosarcoma through RUNX2," *Experimental and Therapeutic Medicine*, vol. 18, no. 4, pp. 3002–3008, 2019.

[12] F. C. Zhou, Y. H. Zhang, H. T. Liu, J. Song, and J. Shao, "LncRNA LINC00588 suppresses the progression of osteosarcoma by acting as a ceRNA for miRNA-1972," *Frontiers in Pharmacology*, vol. 11, p. 255, 2020.

[13] N. Jiang, X. Wang, X. Xie et al., "lncRNA DANCR promotes tumor progression and cancer stemness features in osteosarcoma by upregulating AXL via miR-33a-5p inhibition," *Cancer Letters*, vol. 405, pp. 46–55, 2017.

[14] G. Yu, G. Liu, D. Yuan, J. Dai, Y. Cui, and X. Tang, "Long noncoding RNA ANRIL is associated with a poor prognosis of osteosarcoma and promotes tumorigenesis via PI3K/Akt pathway," *Journal of Bone Oncology*, vol. 11, pp. 51–55, 2018.

[15] C. Li, F. Wang, B. Wei, L. Wang, and D. Kong, "LncRNA AWPPH promotes osteosarcoma progression via activation of Wnt/β-catenin pathway through modulating miR-93-3p/FZD7 axis," *Biochemical and Biophysical Research Communications*, vol. 514, no. 3, pp. 1017–1022, 2019.

[16] Y. Chen, W. Huang, W. Sun et al., "LncRNA MALAT1 promotes cancer metastasis in osteosarcoma via activation of the PI3K-Akt signaling pathway," *Cellular Physiology and Biochemistry: International Journal of Experimental Cellular Physiology, Biochemistry, and Pharmacology*, vol. 51, no. 3, pp. 1313–1326, 2018.

[17] D. Chen, T. Lu, J. Tan, H. Li, Q. Wang, and L. Wei, "Long noncoding RNAs as communicators and mediators between the tumor microenvironment and cancer cells," *Frontiers in Oncology*, vol. 9, p. 739, 2019.

[18] A. S. Pathania and K. B. Challagundla, "Exosomal long noncoding RNAs: emerging players in the tumor microenvironment," *Molecular Therapy–Nucleic Acids*, vol. 23, pp. 1371–1383, 2021.

[19] T. Zhang, Y. Nie, H. Xia et al., "Identification of immune-related prognostic genes and LncRNAs biomarkers associated with osteosarcoma microenvironment," *Frontiers in Oncology*, vol. 10, p. 1109, 2020.

Retraction

Retracted: Biomechanical Analysis of Different Internal Fixation Combined with Different Bone Grafting for Unstable Thoracolumbar Fractures in the Elderly

BioMed Research International

This article has been retracted by Hindawi following an investigation undertaken by the publisher [1]. This investigation has uncovered evidence of one or more of the following indicators of systematic manipulation of the publication process:

(1) Discrepancies in scope

(2) Discrepancies in the description of the research reported

(3) Discrepancies between the availability of data and the research described

(4) Inappropriate citations

(5) Incoherent, meaningless and/or irrelevant content included in the article

(6) Manipulated or compromised peer review

The presence of these indicators undermines our confidence in the integrity of the article's content and we cannot, therefore, vouch for its reliability. Please note that this notice is intended solely to alert readers that the content of this article is unreliable. We have not investigated whether authors were aware of or involved in the systematic manipulation of the publication process.

Wiley and Hindawi regrets that the usual quality checks did not identify these issues before publication and have since put additional measures in place to safeguard research integrity.

We wish to credit our own Research Integrity and Research Publishing teams and anonymous and named external researchers and research integrity experts for contributing to this investigation.

The corresponding author, as the representative of all authors, has been given the opportunity to register their agreement or disagreement to this retraction. We have kept a record of any response received.

References

[1] Q. Shang, Y. Jiang, W. Sheng et al., "Biomechanical Analysis of Different Internal Fixation Combined with Different Bone Grafting for Unstable Thoracolumbar Fractures in the Elderly," *BioMed Research International*, vol. 2022, Article ID 2863379, 13 pages, 2022.

Research Article

Biomechanical Analysis of Different Internal Fixation Combined with Different Bone Grafting for Unstable Thoracolumbar Fractures in the Elderly

Qisong Shang,[1] Yuqing Jiang,[2] Wenhui Sheng,[1] Pengyuan Han,[1] Junru Zheng,[1] Xing Wang,[1] and Bing Wu [1]

[1]*Department of Spinal Surgery, The Third Affiliated Hospital of Shihezi University Medical College, Shihezi, 832000 Xinjiang Uygur Autonomous Region, China*
[2]*Department of Spinal Surgery, Changzhou Second People's Hospital Affiliated to Nanjing Medical University, Changzhou, 213000 Jiangsu Province, China*

Correspondence should be addressed to Bing Wu; wonder8182@163.com

This research was developed to accurately evaluate the unstable fractures of thoracolumbar before and after surgery and discuss the treatment timing and methods. Three-dimensional (3D) finite element method was adopted to construct the T_{12}-L_5 segment model of human body. The efficiency of percutaneous kyphoplasty (PKP) and percutaneous vertebroplasty (PVP), two commonly used internal fixation procedures, was retrospectively compared. A total of 150 patients with chest fracture who received PKP or PVP surgery in our hospital, and 104 patients with the same symptoms who received conservative treatment were collected and randomly rolled into PVP group (75 cases), PKP group (75 cases), and control group (104 cases). Visual analog scale (VAS) score and Oswestry disability index (ODI) of patients were collected before and after surgery and 2, 12, and 24 months after surgery. Then, the anterior and central height of the patient's cone and the kyphosis angle were calculated by X-ray. Lumbar minimally invasive fusion system and lumbar pedicle screw rod system were established by computer-aided design (CAD), and the biomechanical characteristics were analyzed. The results showed that there was no substantial difference in VAS score and ODI score between PKP and PVP ($P > 0.05$), but they were higher than those of the control group ($P < 0.05$). The anterior edge and middle height of vertebra in the two groups were higher than those in control group ($P < 0.05$), and the increase in PKP group was more substantial ($P < 0.05$). The kyphosis of the two groups was smaller than that of the control group ($P < 0.05$), and the decrease of the kyphosis of the PKP group was more substantial ($P < 0.05$). In summary, the thoracolumbar segment model established by 3D finite element method was an effective model, and it was verified on patients that both PKP and PVP could achieve relatively satisfactory efficacy. The implantation of the new internal fixation system had no obvious effect on the lumbar movement. This work provided a novel idea and method for the treatment of senile thoracolumbar unstable fracture, as well as experimental data of biomechanics for the operation of senile unstable fracture.

1. Introduction

China has entered the aging society since 2002. According to relevant data estimation, there are 44.49 million patients with osteoporotic vertebral compressive fracture (OVCF) in China at present, with a high growth rate of 1.81 million cases per year. For which, the social medical expenditure is as high as 9.45 billion yuan [1]. According to the corre-

sponding model study, by 2020, the number of new OVFC patients over 50 years old will reach 1.49 million [2]. For OVCF, more than 45% of spinal injuries occurred between lumbar T_{11}-L_1 [3]. Unstable fracture of thoracolumbar refers to thoracolumbar fractures, which are prone to displacement or re-displacement after reduction, accounting for half of thoracolumbar fractures. Unstable fracture is an important culprit of anatomical structure injury and deformity. Of

TABLE 1: Model material properties.

	Possion's ratio (μ)	Young's modulus (MPa)	Material model
Compact bone	0.3	12000	Anisotropy
Cancellous bone	0.2	100	Isotropy
Fiber ring	0.45	92	Isotropy
Nucleus pulposus	0.499	1.0	Viscoelasticity
Annulus matrix	0.51	3.36	Isotropy

which, 20-40% of thoracolumbar fractures are associated with nerve injury, which will lead to persistent nerve function impairment and even paralysis in patients [4–6].

As a common spinal disease in elderly patients, spinal fracture is often associated with osteoporosis. Elderly patients with spinal fracture and long-term bed rest will not only cause a variety of diseases or even death, but also bring numerous burdens to the family and society [7]. Therefore, the treatment of acute symptomatic osteoporotic thoracolumbar compression fracture patients is imperative for the prevention of osteoporosis in the general healthy elderly. Helping patients get out of bed as soon as possible and become independent is the primary goal of osteoporosis research. At present, percutaneous vertebroplasty (PVP) and percutaneous kyphoplasty (PKP) are the mainstream surgical methods for the clinical treatment of elderly thoracolumbar unstable fractures [8], whose efficacy has been fully affirmed by spine surgeons [9]. Although there are many trials comparing the efficacy of PVP and PKP, and the two vertebral amplification methods have their advantages and disadvantages, the choice of the two surgical methods is still partly controversial [10].

In terms of spinal internal fixation for osteoporosis patients, China published in 2019 *Chinese Expert Consensus on Spinal Internal Fixation for Elderly Osteoporosis* and *Clinical Guidelines for Vertebrae Enhancement for Acute Symptomatic Osteoporotic Thoracolumbar Compression Fractures*. In the *Clinical Guidelines for Vertebrae Enhancement for Acute Symptomatic Osteoporotic Thoracolumbar Compression Fractures*, PVP is recommended at level I for acute symptomatic OVCF, and PKP is recommended at level II. However, if the injured vertebra height needs to be restored, PKP (level I recommendation) is performed [11, 12].

However, the bone density of elderly patients is different from that of ordinary young and middle-aged patients. They have low bone density and poor physical quality, and some of them are accompanied by other diseases of aging. Therefore, the choice of appropriate internal fixation system and effective surgical method plays a decisive role in the solution of internal fixation failure in elderly patients. According to the clinical follow-up of elderly patients with thoracolumbar instability fracture after surgery, most of them will develop new vertebral fractures after surgery, which are often located

near the cone at the treatment site. Therefore, the pyramidal biomechanical data analysis and its performance evaluation in elderly patients with fractures are the primary issues to be addressed [13, 14].

Finite element analysis is an emerging biomechanical research method, which divides the target structure that is difficult to analyze into a finite number of unit aggregates, and it is used to accurately simulate the structure of the spine and internal fixation. By applying different loads, the biomechanical responses of the spine and internal fixation were obtained qualitatively and quantitatively, and targeted prevention methods were proposed to guide the surgical design [15–18].

At first, electrical measurement and photoelastic methods were used to study the spine. However, these methods were limited by the anatomical structure of the spine and the complexity of various material parameters and stress distribution, so it was often difficult to obtain the overall dynamic information. With the emergence of finite element analysis, all the relevant data of the spine can be reflected in mathematical form, and the internal stress and strain of the structure can be reflected as much as possible. By changing any parameter, the change information of the whole structure can be obtained, which is the most important advantage of finite element analysis.

In summary, the 3D finite element model of human cone was established to simulate the force of thoracolumbar vertebra and analyze the stress distribution of spinal functional units. The biomechanics of thoracolumbar fracture and internal fixation were studied. A total of 150 patients treated by convex plasty and 104 patients treated conservatively at the same time in our hospital were selected as the research objects, among which 75 patients in the surgery group were treated with PKP and 75 patients in the surgery group were treated with PVP. The control group was treated with conservative therapy. Follow-up was conducted before and after treatment and at 2, 12, and 24 months. Visual analog scale (VAS), Oswestry disability index (ODI), and X-ray were employed to calculate the changes of the anterior and central height of the cone, as well as the kyphosis angle of the patients to evaluate the therapeutic effect of the two surgeries. Moreover, the finite element models of lumbar minimally invasive fusion system and lumbar pedicle screw rod system were established by using CAD technology to conduct quantitative biomechanical evaluation and accurate repair of early thoracolumbar fracture.

2. Materials and Methods

2.1. Research Objects. A total of 150 patients treated with vertebroplasty in our hospital and 104 patients of the same type treated with conservative treatment were recruited as the study subjects. Of the 150 vertebroplasty patients, 75 patients in the surgery group were treated with PKP, and 75 patients in the surgery group were treated with PVP.

Inclusion criteria are as follows: (i) the patient was identified with osteoporotic vertebral fracture; (ii) the patient had indications for surgery; (iii) the bone mineral density of the patient was less than or equal to -2.5; and (iv) patients

TABLE 2: Material properties of ligaments.

	Density (ton/mm³)	Possion's ratio (μ)	Modulus of elasticity (MPa)	Cross-sectional area (mm²)	Unit number
Anterior longitudinal ligament	1.1×10^{-9}	0.4	30	6.1	5
Posterior longitudinal ligament	1.1×10^{-9}	0.4	20	5.4	5
Ligament flavum	1.1×10^{-9}	0.4	10	50.1	3
Supraspinous ligament	1.1×10^{-9}	0.4	1.5	13.1	2
Interspinous ligament	1.1×10^{-9}	0.4	10	13.1	5
Capsular ligament	1.1×10^{-9}	0.4	10	46.6	7
Intertransverse ligament	1.1×10^{-9}	0.4	11	40	2

TABLE 3: Elements and nodes of finite element model of cone implant.

Site	Element type	Element number	Node number
Cortical bone	Three-dimensional	496,000	57,000
Cancellous bone	Three-dimensional	277,000	41,000
Screw system	Three-dimensional	128,000	30,000
Cage (rectangle)	Three-dimensional	21,000	4,700
Cage (cylindrical)	Three-dimensional	28,000	5,500

with conservative treatment that cannot achieve better efficacy.

Exclusion criteria are as follows: (i) patients with malignant or metastatic tumor in the cone; (ii) the patient had chronic disease and cannot receive surgery; (iii) the patient also had hemorrhagic disease; (iv) patients with neurological symptoms or spinal canal accounted for more than one-third; and (v) the patient had local systemic or spinal infection.

There were 75 patients in PVP group, including 12 males and 63 females, aged 52-89 (67.42 ± 8.62) years. Fracture cone distributions were T_{12} of 32 cases, L_1 of 29 cases, and L_2 of 14 cases.

There were 75 patients in the PKP group, including 17 males and 58 females, ranging from 54 to 86 (65.28 ± 9.71) years old. Fracture cone distributions were T_{12} of 29 cases, L_1 of 36 cases, and L_2 of 10 cases.

A total of 104 patients in the control group received conservative treatment, including 20 males and 84 females, aged 51~88 (66.36 ± 10.32) years. As for the fracture cone distributions, there were 46 cases of T_{12}, 39 cases of L_1, and 19 cases of L_2.

Before and after treatment, X-ray images were used to calculate the height of the anterior and central cone, and the kyphosis angle of patients in the two groups, and the data were compared. Follow-up was conducted at 2, 12, and 24 months. VAS and ODI were used to evaluate the treatment effect of the two groups.

The clinical data of the two groups were comparable.

2.2. Complete Spine T_{12}-L_5 Section Data Acquisition. Siemens SENSATION 16-slice multi-spiral CT was employed to perform continuous parallel scans of the spine of a healthy male volunteer. The generated cross-sectional file was imported into the MIMICS 10.0 of Materlise, Belgium. Threshold was set as 226-2,976. The parts that did not conform to the selection of T_{12}-L_5 vertebrae were removed, and the missing gaps were filled. A 3D model was generated, and mesh smoothing was performed.

2.3. Computer-Aided Design (CAD) Post-Processing. The data was imported into ANSYS12.0 for preprocessing to generate 3D volume. Then, the 3D body was imported into the CAD software SolidWoeks2010. The generated model was processed in detail, and the cone was polished, filled, and assembled. Finally, a complete 3D model was established.

2.4. Finite Element Model Establishment. The model was imported into ANSYS Workbeach for finite element analysis preprocessing. Material parameters of the model were mainly selected according to literature [19].

Possion's ratio and Young's modulus are commonly used data for material properties. The values were assigned to the materials of each part of the model according to Table 1. Each docking unit was automatically identified as fully bound by Workbeach, and the contact surface was derived as a connecting surface.

According to the literature [20], the material properties of ligaments are shown in Table 2.

Ligaments were divided by T3D2 (Truss-3D-2node) unit, and the specific anatomical data and related material parameter settings are shown in Table 2. A facet joint capsule was added, and the facet joint was used as a contact model.

2.5. Validity Verification of Lumbar Three-Dimensional Finite Element Model. The effectiveness of thoracolumbar finite element model was verified regarding the stress and boundary constraints under normal physiological conditions
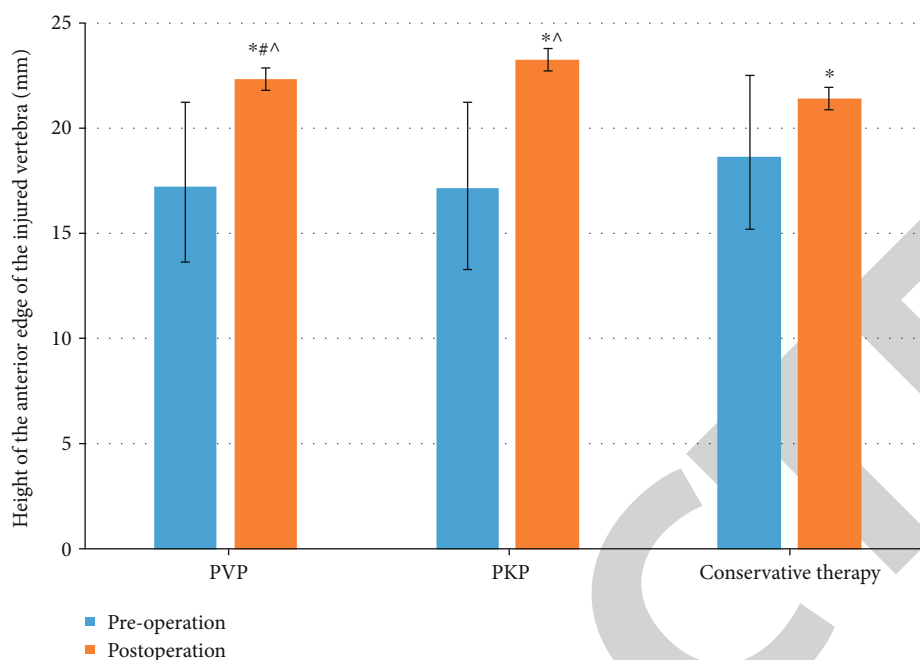
Figure 1: Comparison of the height of the front edge of the cone before and after the operation ($*P < 0.05$ compared with that before operation; $^P < 0.05$ compared with the control group; $\#P < 0.05$ compared with PKP).
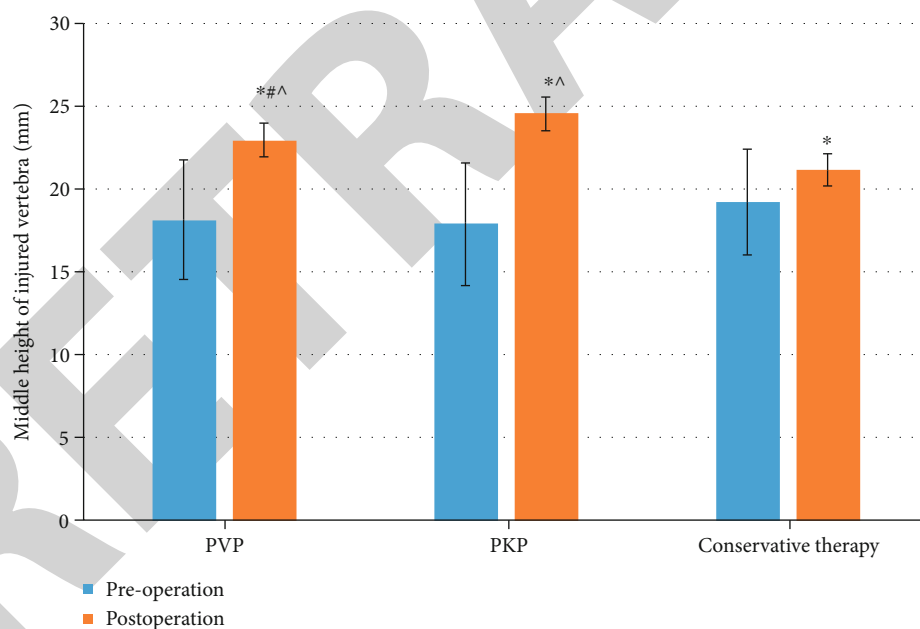
Figure 2: Comparison of the height of the injured vertebrae before and after the operation ($*P < 0.05$ compared with that before operation; $^P < 0.05$ compared with the control group; $\#P < 0.05$ compared with PKP).

of thoracolumbar. A torque load of 15 N·m was applied to a point on the upper surface of T12, and the bottom surface of T1 was fixed. The kinematic forces in six directions of forward bending, backward extension, left rotation, right rotation, left flexion, and right flexion were verified. The validation results were compared with those of Tencer A F to verify its validity [20].

2.6. Force Analysis of Finite Element Model. On the finite element model, the lower endplate of L_2 cone was fixed, and two different forces were applied to simulate a variety of different stress states. The first method was applied perpendicular to the T12 cone surface 200 n, 400 n, and 600 n force of different motion state of stress changes. The second method was applying 16 Nm torque uniformly to each surface node
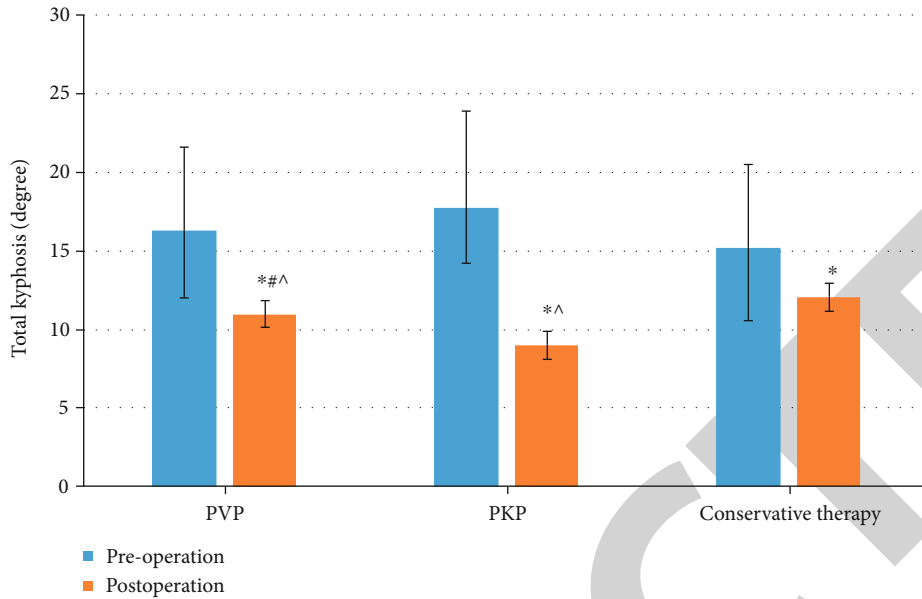
FIGURE 3: Comparison of kyphotic angle before and after surgery ($*P < 0.05$ compared with that before operation; $^\wedge P < 0.05$ compared with the control group; $\#P < 0.05$ compared with PKP).
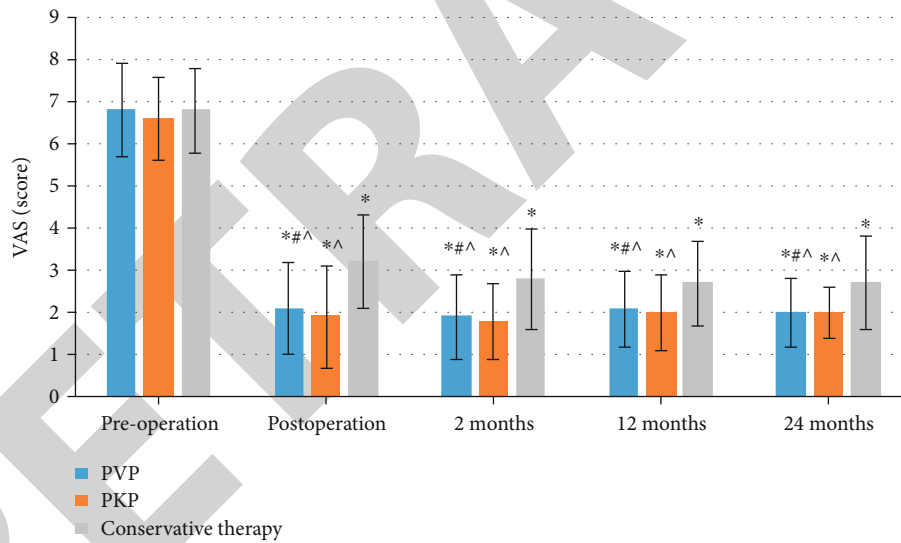
FIGURE 4: Comparison of VAS scores before and after surgery ($*P < 0.05$ compared with that before operation; $^\wedge P < 0.05$ compared with the control group; $\#P < 0.05$ compared with PKP.)

of T_{12} under different conditions, such as forward bending, left- and right-side bending, extension, and torsion.

The model was loaded to obtain the displacement and stress of the model under different stress states.

The angular displacements of functional spinal unit (FSU) were measured as follows:

(i) A point X on the leading edge of T_{12} cone was taken, and the point was displaced to X_1 after the vertical force was applied. The distance between two points was the displacement caused by the vertical force

(ii) When the neutral position was taken, the two points X and Y on the front and rear edges of the T_{12} cone surface were connected to the two points XY. The cone was displaced to X_1 and Y_1 by the buckling or elongation moment, and the two points were connected to the two points X_1Y_1. The angle β between the two lines XY and X_1Y_1 was the rotation angle of the cone when it buckled or was subjected to the extensional moment

(iii) The left and right points X and Y in the coronal position of T_{12} cone were taken, which were
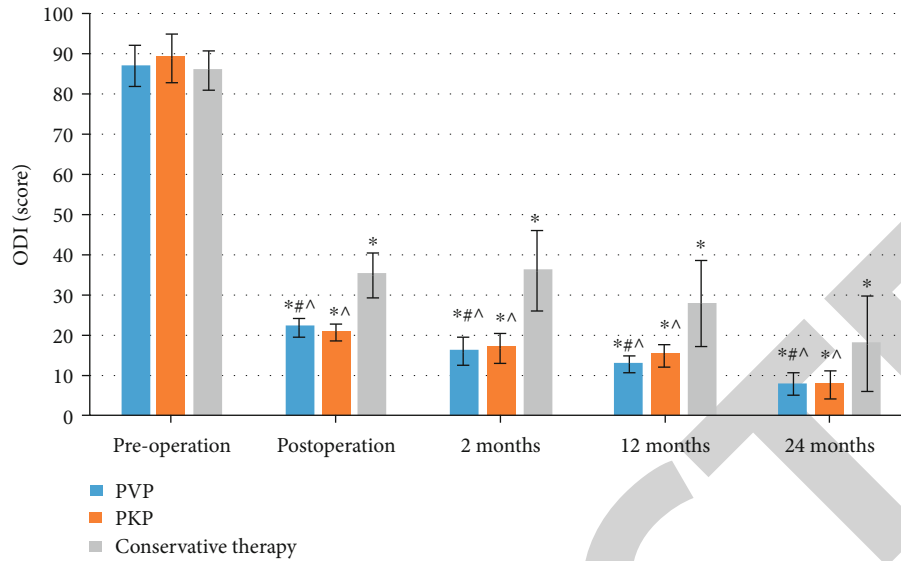
Figure 5: Comparison of ODI scores before and after surgery ($*P < 0.05$ compared with that before operation; $^P < 0.05$ compared with the control group; $\#P < 0.05$ compared with PKP).
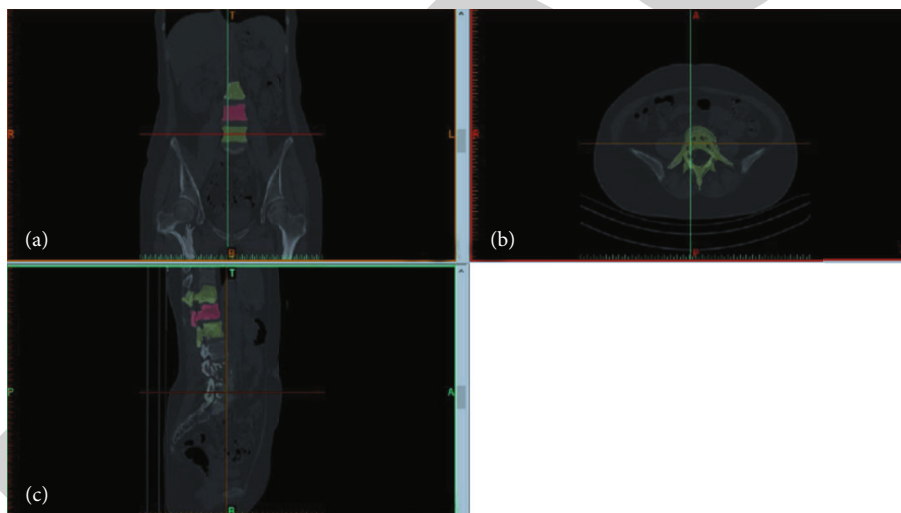
Figure 6: CT imaging of the spine of a healthy male ((a) the coronal plane, (b) the cross section, and (c) the sagittal plane).

connected as line XY. The lateral bending or torsion torque was shifted to X_1 and Y_1, and the two points were connected as X_1Y_1. The angle β between the two lines XY and X_1Y_1 was the rotation angle of the cone under lateral bending or torsion moment

The average stiffness K of FSU are calculated:

$$
\begin{aligned}
K &= \frac{F}{L}, \\
K &= \frac{F_X}{\beta}.
\end{aligned}
\tag{1}
$$

In the above equations, F is the force on the cone, L is the displacement caused by the cone, F_X is the moment when the cone is loaded, and β is the rotation angle when the moment is exerted. The unit is (Nm/degree) under compression (100 N/mm).

2.7. Establishment of a Three-Dimensional Finite Element Model of Minimally Invasive Fusion of Lumbar Spine and Its Force Analysis.

DePuy spine model interbody fusion cage (Johnson & Johnson) was used, and the corresponding data was imported into ANSYS. The corresponding data is shown in Table 3. The fusion cage was inserted into the intervertebral space from the right oblique at 45° to the bottom surface. The specific construction method was that proposed in literature [20, 21]. The lower surface of L_5 vertebral body was fixed, and a surface load of 400 N was applied uniformly perpendicular to the upper surface of L_3 vertebral body, with an additional movement torque of 6 N·m. In ANSYS, the following operations were executed after loading of the model.
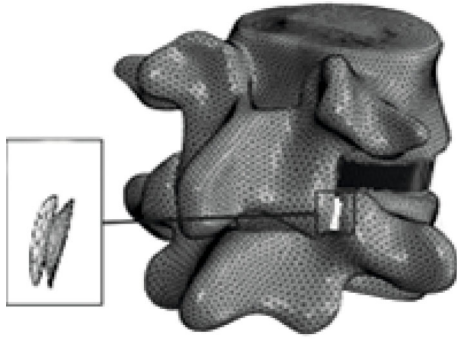
Figure 7: 3D finite element diagram of the spine (the enlarged part was the interosseous ligament model).

Figure 9: T_{12}-L_2 segment finite element model.
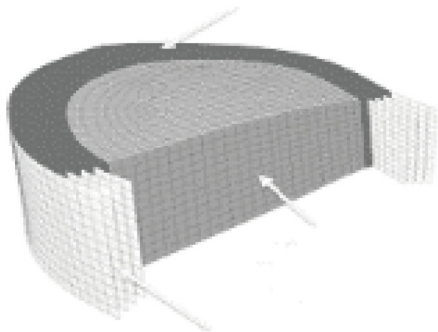
Figure 8: Schematic diagram of the intervertebral disc model.

(I) The spatial position coordinates of the anterior, posterior, and left and right four points on the L_4-L_5 surface were connected into lines, and the included angles between the lines represented the included angles between the upper surfaces of two adjacent vertebral bodies. The absolute value of the difference of the included angles before and after loading, α, was its angular displacement. (II) The angular displacement from L_3 to L_4 was recorded in the same way. (III) The stress change of each part was recorded.

2.8. Establishment of a 3D Finite Element Model of the Lumbar Pedicle Screw and Rod System. The UPASS2 pedicle screw rod system from WEGO, Shandong, was used. The interbody fusion cage was DePuy spine from Johnson & Johnson, and the corresponding data was imported into ANSYS. The intervertebral disc was divided into four zones on the front and back, and only annulus fibrosus, nucleus pulposus, and cartilage were retained in the first and forth zones. The fusion cage was inserted oblique from left to right into the $L_{4/5}$ intervertebral space to assist bilateral pedicle screw rod fixation, and the point and direction of the Wiltsc approach was simulated. The specific construction method was that proposed in literature [22]. The lower surface of the S_1 vertebral body was fixed, and a surface load of 500 N

was applied uniformly perpendicular to the upper surface of the L_3 vertebral body, with an additional movement torque of 10 N·m. In ANSYS, the following operations were executed after loading of the model. (I) The spatial position coordinates of the anterior, posterior, and left and right four points on the L_4-L_5 surface were connected into lines, and the included angles between the lines represented the included angles between the upper surfaces of two adjacent vertebral bodies. The absolute value of the difference of the included angles before and after loading, α, was its angular displacement. (II) The angular displacement from L_3 to L_4 was recorded in the same way. (III) The stress change of each part was recorded according to the software.

2.9. Statistical Methods. SPSS 19.0 was employed for data statistics and analysis. Mean ± standard deviation ($x \pm s$) was how measurement data were expressed, and percentage (%) was how count data were expressed. The pairwise comparison was performed by one factor analysis of variance. The difference was statistically considerable with $P < 0.05$.

3. Results

3.1. Comparison of the Efficacy of PVP and PKP. A total of 150 patients were analyzed. The height of the anterior edge and the middle of the wound cone after the operation in the two groups was remarkably higher than that before the operation ($P < 0.05$), and both were higher than those in the control group ($P < 0.05$). The PKP group had remarkably greater changes than the PVP group ($P < 0.05$, Figures 1 and 2). The postoperative kyphotic angle of the two groups was remarkably lower than that before the operation ($P < 0.05$), and the kyphotic angle of the two groups was smaller than that of the control group ($P < 0.05$), while the PKP group was more remarkably reduced than the PVP group ($P < 0.05$) (Figure 3). The postoperative VAS
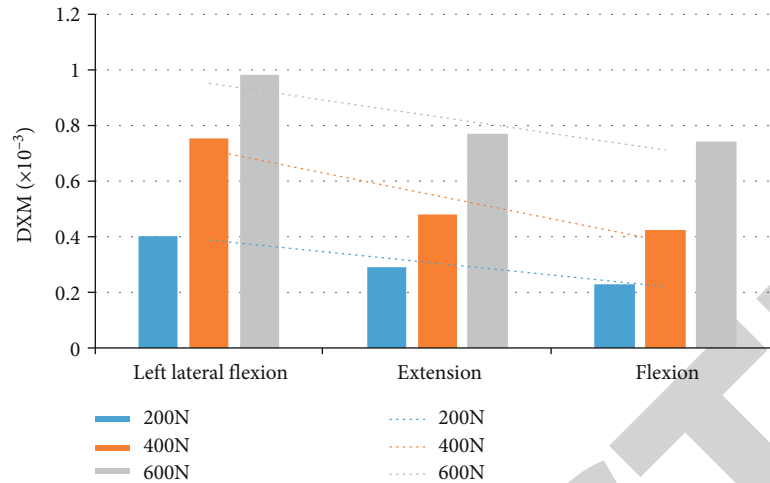
FIGURE 10: The relationship between maximum displacement (DMX) and force (the dotted line represented the trend line of the maximum displacement under the three forces).
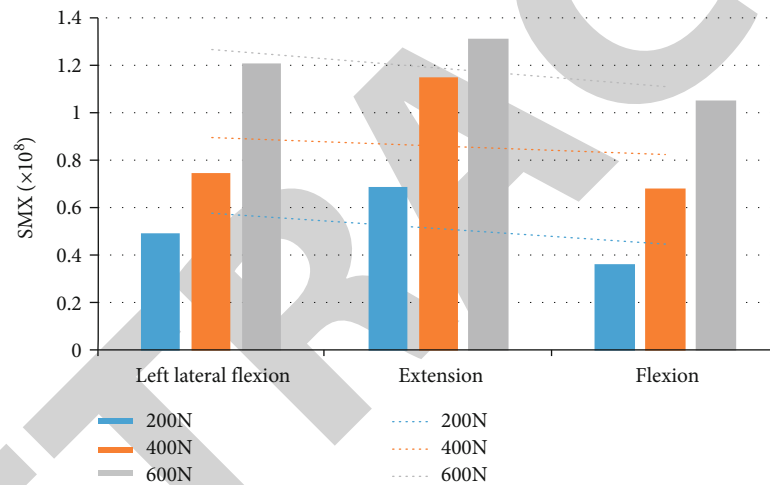
FIGURE 11: The relationship between stress maximum (SMX) and force (trend line of maximum stress under three kinds of stress).

and ODI scores of the two groups were lower than those before the operation ($P < 0.05$), but there was no statistical difference between the two groups ($P > 0.05$), and both were higher than the control group ($P < 0.05$). Moreover, within 2 to 24 months after surgery, neither the VAS score nor the ODI score was statistically substantial ($P > 0.05$, Figures 4 and 5).

3.2. Establishment of 3D Finite Element Model of Cone. The human spine obtained by the CT scan is shown in Figure 6.

The CT image-based 3D finite element models are shown in Figures 7 and 8.

All the data was imported into ANSYS to generate the finite element model of the human spine T_{12}-L_2 according to the material parameters (Figure 9).

3.3. Force Analysis of Finite Element Model of Normal T_{12}-L_2 Segment. The source of force and boundary conditions on the spine were kept unchanged, and the magnitude of the force was changed to obtain the ultimate relationship

between the displacement, stress, and force of the spine under different motion states. The details are shown in Figures 10 and 11.

From Figures 10 and 11, the vertebral body had the largest displacement when bending and flexing on the left side, and the stress was the largest when extending backward. Moreover, the changes in the spine force and the maximum displacement and the maximum stress basically conformed to the linear change law, which was also consistent with the linear elastic material of the model material of each part of the spine. These changes were consistent with clinical data.

The results of the lumbar finite element model in the three symbolic states of forward flexion, dextral flexion, and left flexion are analyzed in Figure 12; the two results were consistent with each other.

3.4. The Force Analysis of 3D Finite Element Model of the Lumbar Minimally Invasive Fusion System. The 3D finite element model of minimally invasive lumbar spine fusion

A

(a)

(b)

(c)
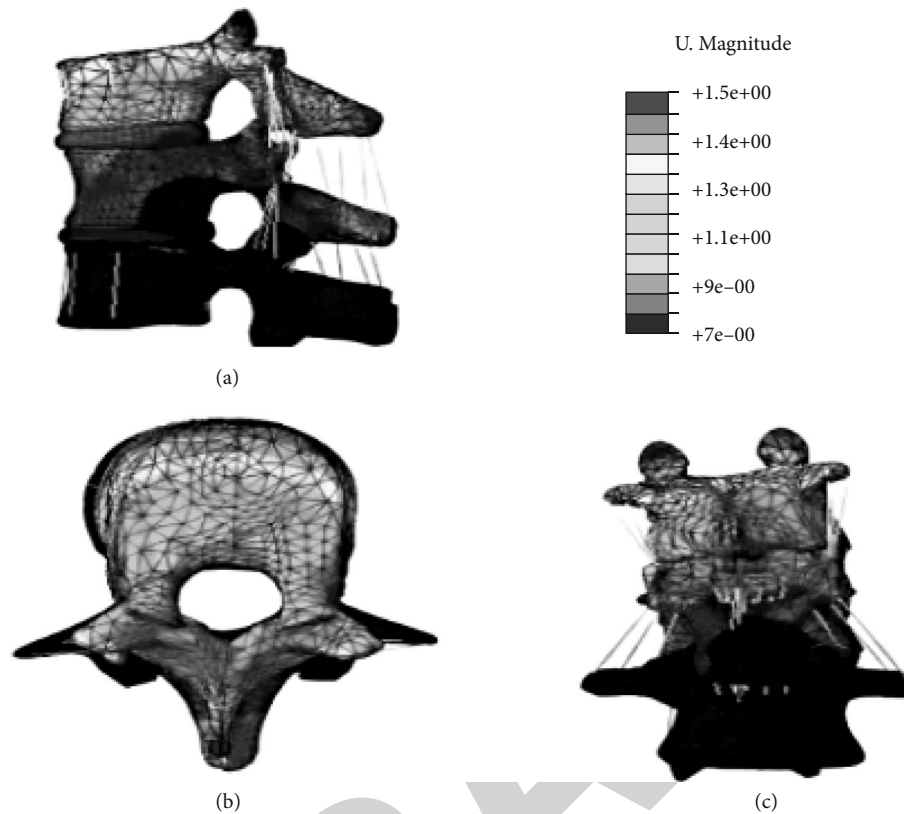
FIGURE 12: Stress distribution of T_{12}-L_2 bone finite element model ((a) was the state of vertebral flexion; (a) was dextral vertebrae; (c) was left flexion of vertebrae).

was established by ANSYS, and the specific diagram is shown in Figure 13.

The force analysis of the finite element model was also carried out, and the angular displacement occurring in the L_4~L_5 section and the angular displacement occurring in the L_3~L_4 section are shown in Figure 14.

According to Figure 13, after the pedicle screw was added, the range of motion of the spine segment did not change remarkably, that is, the pedicle screw will not cause a substantial impact on the spine.

3.5. The Force Analysis of 3D Finite Element Model of the Lumbar Pedicle Screw and Rod System. The 3D finite element model of the lumbar pedicle screw and rod system was established by ANSYS. The specific diagram is shown in Figure 15.

The force analysis of the finite element model was performed, and the angular displacement and stress changes in the $L_{4/5}$ section are shown in Figure 16.

4. Discussion

Due to the lack of methods and quantitative indicators for the accurate evaluation of thoracolumbar unstable fractures in elderly patients before and after surgery, the specific relationship between the damage degree and the mechanical harm is not clear, and the selection of treatment timing and methods is not accurate in clinical practice. Therefore, this research was developed to carry out in-depth mechani-

cal studies for the elderly thoracolumbar unstable fractures before and after surgery, and fine analysis of the changes in the unstable fractures before and after surgery was implemented. It was hoped to provide scientific evidence to improve the above theory and improve the treatment effect.

In this research, 150 patients were studied, among which 75 patients in the surgery group were treated with PKP and 75 patients in the surgery group were treated with PVP. The results showed that the height of the anterior edge and the middle of the injured cone were remarkably higher after surgery than before surgery ($P < 0.05$), and the PKP group had greater changes than the PVP group ($P < 0.05$). At 2 to 24 months after surgery, the kyphosis of both groups was remarkably lower than that of the preoperative group ($P < 0.05$), and the decrease of PKP group was more substantial than that of PVP group ($P < 0.05$). VAS and ODI scores after surgery were lower than those before surgery ($P<0.05$), but there was no statistical difference between the two groups ($P > 0.05$). There was no statistical significance in VAS score and ODI score within 2 to 24 months after operation ($P > 0.05$), which indicated that both PVP and PKP can achieve satisfactory therapeutic effect, but PKP had a slightly better therapeutic effect than PVP. Zhang et al. (2017) [23] conducted an online meta-analysis of 32 studies involving 2,852 patients to compare the VAS score, ODI, kyphotic angle correction, and refracture occurrence. It was believed that both PKP and PVP performed well in treating OVCF. However, PKP had better pain relief and improved ODI score, while PVP had advantages in kyphotic
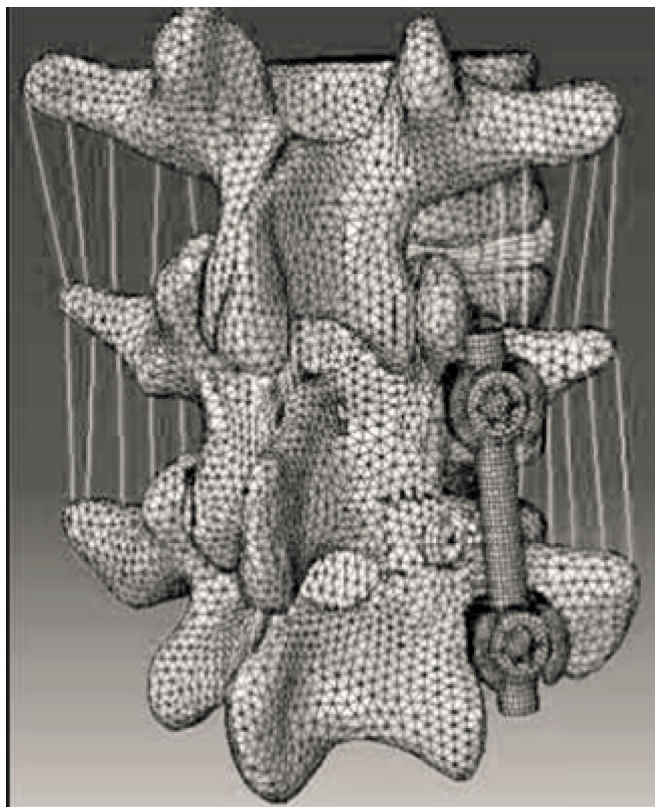
FIGURE 13: Illustration of the 3D finite element model of the lumbar spine minimally invasive fusion.
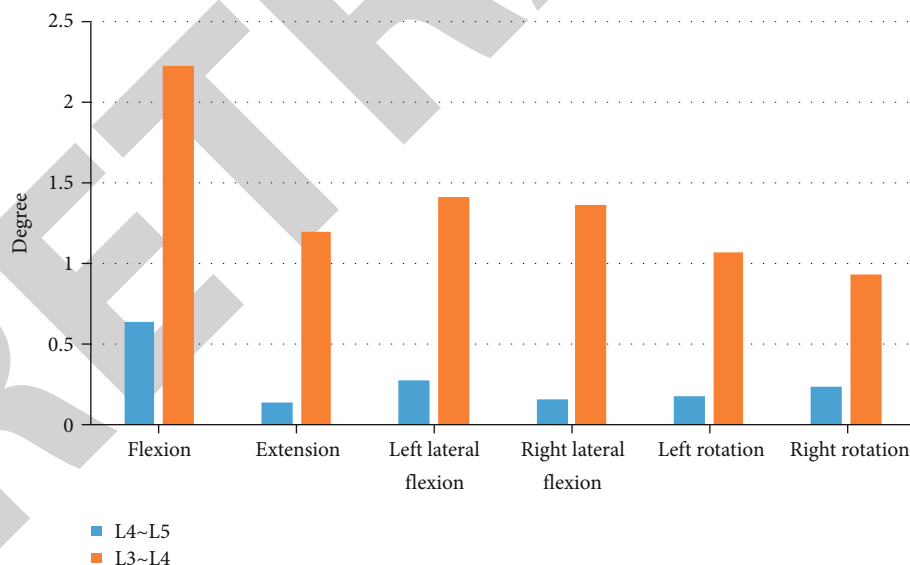
FIGURE 14: The angular displacement of each segment of the model under different forces.

angle and reduced fracture incidence. Chang et al. (2015) [24] concluded that PVP required less surgical time through a meta-analysis of prospective randomized trials. Moreover, compared with PKP, there was no substantial statistical difference in postoperative VAS and ODI scores, and PVP was still a safe and reliable treatment of first choice. This was basically consistent with the results of this research.

A finite element model ($Th_{12}L_2$) based on 3D images was constructed using CT digital imaging and medical communication in healthy controls or patients, and then motion pressure was simulated on the spinal model. For two spinal models, loads on the 12th thoracic vertebra (Th_{12}) due to compression, flexion, extension, transverse bending, and axial rotation were examined in virtual space. Then,

Figure 15: 3D finite element diagram of the pedicle screw rod system.

regarding the application of equivalent vertebrae stress, the 3D finite element analysis of the vertebral body was carried out to collect the movement state change data of the vertebral body under different stresses. Yan et al. (2016) [25] used aluminum-free glass polyacrylate cement (GPC) with an elastic modulus close to that of natural bone to establish a

finite element model and analyzed it. It was found that GPC can produce low stiffness and stress in cancellous bone. The stress at the junction of the GPC and the cortical bone of the vertebral body was closer to the stress value of the natural vertebral body, so it showed good adaptability, mechanical, and biocompatibility. GPC is a material that may
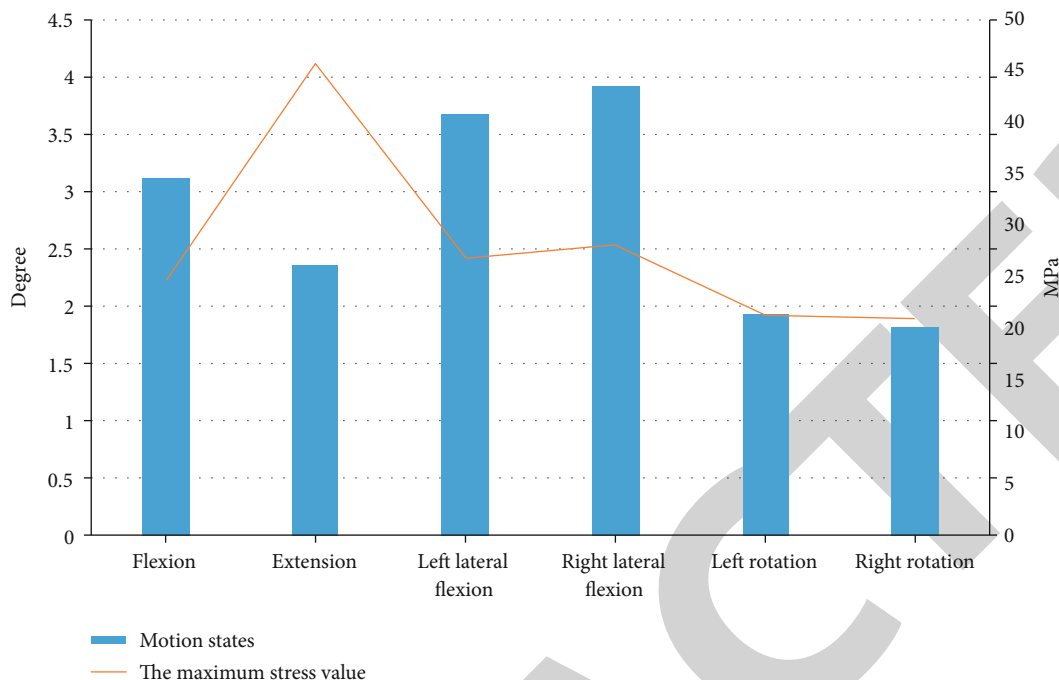
FIGURE 16: The maximum value of the range of motion and stress between the $L_{4/5}$ segments of the model.

replace traditional polymethyl methacrylate cement to treat OVCF. The simulation results were compared with those obtained in this research, which proved the validity of the simulation results of this research.

After the effectiveness of the model was verified, the models of the minimally invasive intervertebral fusion system and the intervertebral pedicle screw rod system were established. In addition, the motion and stress analysis of the two were performed, and the effectiveness was verified. Compared with previous experiments, the validity of the two models was verified. After the collection of motion and stress data, it was concluded that the use of the two different internal fixation methods did not have a substantial effect on the movement of the vertebral body.

5. Conclusion

Both PVP and PKP can achieve satisfactory treatment results, and PKP had a slightly improved effect than PVP. Massive motion data of 3D finite element models of vertebral bodies were collected through verification experiments, and 3D finite element models of two different fixation methods of minimally invasive intervertebral fusion system and intervertebral pedicle screw rod system were established. Through the collection of the movement data of the two, it was proved that the two had no substantial effect on the normal intervertebral movement. Through this experiment, data proof and confirmatory experiments can provide data support for the selection of clinical treatment means and timing and provide ideas for the construction of new therapeutic instruments. However, only some basic data was collected, and the therapeutic effect was not analyzed, which has certain limitations for the choice of therapeutic means.

However, with the development of new technologies and materials, there will be more choices of internal fixation and bone grafting for elderly thoracolumbar unstable fractures. In short, this experiment provides certain reference value for the validation of 3D finite element and biomechanical data of thoracolumbar vertebra.

Data Availability

The data used to support the findings of this study are included within the article.

Conflicts of Interest

The authors declare that they have no competing interest.

Authors' Contributions

Qisong Shang and Yuqing Jiang contributed equally to this work as co-first authors.

References

[1] S. Lou, X. Shi, X. Zhang, H. Lyu, Z. Li, and Y. Wang, "Percutaneous vertebroplasty versus non-operative treatment for osteoporotic vertebral compression fractures: a meta-analysis of randomized controlled trials," *Osteoporosis International*, vol. 30, no. 12, pp. 2369–2380, 2019.

[2] L. Zhang and P. Zhai, "A comparison of percutaneous vertebroplasty versus conservative treatment in terms of treatment effect for osteoporotic vertebral compression fractures: a meta-analysis," *Surgical Innovation*, vol. 27, no. 1, pp. 19–25, 2020.

Retraction

Retracted: Mechanism of RNA circHIPK3 Involved in Resistance of Lung Cancer Cells to Gefitinib

BioMed Research International

This article has been retracted by Hindawi following an investigation undertaken by the publisher [1]. This investigation has uncovered evidence of one or more of the following indicators of systematic manipulation of the publication process:

(1) Discrepancies in scope

(2) Discrepancies in the description of the research reported

(3) Discrepancies between the availability of data and the research described

(4) Inappropriate citations

(5) Incoherent, meaningless and/or irrelevant content included in the article

(6) Manipulated or compromised peer review

The presence of these indicators undermines our confidence in the integrity of the article's content and we cannot, therefore, vouch for its reliability. Please note that this notice is intended solely to alert readers that the content of this article is unreliable. We have not investigated whether authors were aware of or involved in the systematic manipulation of the publication process.

Wiley and Hindawi regrets that the usual quality checks did not identify these issues before publication and have since put additional measures in place to safeguard research integrity.

We wish to credit our own Research Integrity and Research Publishing teams and anonymous and named external researchers and research integrity experts for contributing to this investigation.

The corresponding author, as the representative of all authors, has been given the opportunity to register their agreement or disagreement to this retraction. We have kept a record of any response received.

References

[1] Y. Zhao, C. Zhang, H. Tang, X. Wu, and Q. Qi, "Mechanism of RNA circHIPK3 Involved in Resistance of Lung Cancer Cells to Gefitinib," *BioMed Research International*, vol. 2022, Article ID 4541918, 9 pages, 2022.

Research Article

Mechanism of RNA circHIPK3 Involved in Resistance of Lung Cancer Cells to Gefitinib

Yi Zhao, Caiming Zhang, Haibo Tang, Xiaomin Wu, and Qiugan Qi [ID]

Department of Cancer Center, Integrated Hospital of Traditional Chinese Medicine, Southern Medical University, Guangzhou 510315, China

Correspondence should be addressed to Qiugan Qi; qiqiugan@163.com

To study the mechanism of circular ribonucleic acid (RNA) circHIPK3 involved in the resistance of lung cancer cells to gefitinib, 110 patients with lung cancer were recruited as the research objects, and the tumor tissue and para-cancerous tissue of each patient's surgical specimens were collected and paraffinized to detect the expression of circHIPK3 in different tissues. Gefitinib drug-resistant cell line of lung cancer was constructed with gefitinib to detect cell apoptosis under different conditions. As a result, the relative expression of circHIPK3 in patients with tumor diameter no less than 3 cm was dramatically inferior to that in patients with tumor diameter less than 3 cm ($P < 0.05$). The relative expression of circHIPK3 in patients with TNM stage II/ III was dramatically inferior to that in patients with tumor, node, and metastasis (TNM) stage I ($P < 0.05$). Expression of circHIPK3 in patients with lymph node metastasis was dramatically inferior to that in patients without lymph node metastasis ($P < 0.05$). Of the lung cancer tissues of patients with different TNM stages, only six patients had high expression, and the remaining 104 patients had low expression. Moreover, electrophoresis revealed that circHIPK3 can only be amplified in cDNA, but not in gDNA. Gefitinib-mediated apoptosis rate of lung cancer drug-resistant cell lines decreased notably. In summary, the circular RNA circHIPK3 may have a notably low expression in lung cancer tissues, whose low expression had a certain enhancement effect on the drug resistance of lung adenocarcinoma cells to gefitinib.

1. Introduction

Lung cancer is a malignant tumor, mainly originated from the mucosal epithelium of the bronchus, which is classified into small cell carcinoma and nonsmall cell carcinoma according to the histological changes. In recent years, with the serious air pollution and the gradual deterioration of the environment, the global mortality rate of lung cancer is on the rise, seriously threatening people's health [1]. According to the report, global cancer statistics in 2018 showed that lung cancer is the malignant tumor with the highest morbidity and mortality. The incidence of lung cancer in China accounts for one-third of the total, and it is increasing [2]. Some workers in special work environments have been exposed to polycyclic aromatic hydrocarbons for long periods of time. Incomplete combustion of these mixed pollutants at 400-800°C produces benzopyrene and 1, 7-

dimethylbenzanthracene. These substances can be inhaled and further oxidized to produce free radicals and lipid peroxides that act on the membrane and endoplasmic reticulum of unsaturated fatty acids, and then peroxidation leads to cell membrane damage. Cells with damaged cell membrane will mutate into cancerous cells, leading to the occurrence of cancer [3, 4]. Data from national Cancer Center showed that in 2020, the number of new lung cancer cases in China would reach 816,000, accounting for 17.9% of all cancers [5]. That is an average of 16 people getting sick every 10 minutes. 719,000 deaths occurred, accounting for 23.8% of all cancers [6]. Gefitinib (Iressa) is an oral epidermal growth factor receptor tyrosine kinase inhibitor (EGFR-TKI), a small molecule compound. It is the world's first marketed drug for targeted and precise treatment of lung cancer [7]. Inhibition of EGFR-TK can hinder tumor growth, metastasis, and angiogenesis, and increase tumor cell apoptosis.
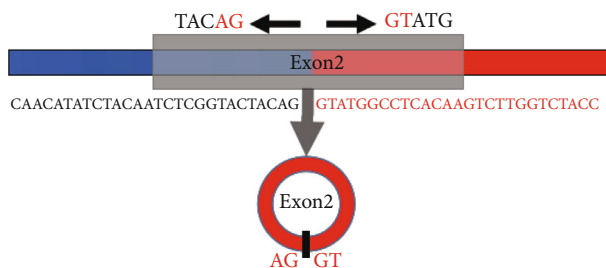
FIGURE 1: circHIPK3 reverse splicing site sequence.

Gefitinib is used to treat patients with metastatic NSCLC (NSCLC) whose tumors have specific types of epidermal growth factor receptor (EGFR) gene mutations [8, 9].

circRNA is a new type of RNA molecule that is characterized by a covalent closed loop and widely exists in eukaryotes [10]. circRNA is derived from the exon or intron regions of genes and is abundant in mammalian cells. Studies found that most circRNAs are conserved among different species [11, 12]. Because of its ring structure, it can resist the degradation of RNase R, which is relatively stable [13]. circRNA has attracted more and more attention due to its specificity of expression and complexity of regulation, as well as its important role in disease occurrence [14, 15]. Just like miRNA and long noncoding RNA, circRNA has become a new research hotspot in the RNA field [16]. Since circRNA is usually produced by special variable splicing, more than 80% of circRNAs contain protein-encoding exons, have many identical sequences with homologous mRNAs, can be ceRNAs with each other, and act as sponges to adsorb microRNAs [17, 18]. The circular RNA HIPK3 (circHOPK3) is highly expressed in the liver, brain, and lung, mainly originating from the second exon of the gene HIPK3 [19, 20].

In recent years, related studies found that using siRNA to knockdown circHIPK3 can inhibit cell proliferation. In addition, circHIPK3 can adsorb miR-124 in liver cancer and promote the proliferation of liver cancer cells by regulating the expression of target genes. However, its regulation and expression mechanism in lung cancer is still unclear. Therefore, this study was developed to explore the mechanism of the circular RNA circHIPK3 involved in the resistance of lung cancer cells to gefitinib.

2. Materials and Methods

2.1. Sample Collection. In this study, 110 lung cancer patients admitted to X Hospital from September 2019 to September 2020 were collected as the research objects. Paraffin specimens were collected from 58 male patients and 52 female patients. The study has been approved by the Medical Ethics Committee. Patients and their families understood the study content and methods of specimen acquisition and agreed to sign corresponding informed consent forms.

Inclusion criteria: (i) patients diagnosed with lung cancer by pathology and imaging; (ii) patients aged between 45 and 75 years; (iii) there was no metastasis of lung lesions, mediastinal lymph node enlargement, or pleural hypertrophy; (iv) patients who were not recently treated with other drugs or antibiotics in the study; (v) patients with normal coagulation function and platelets.

Exclusion criteria: (i) patients with diseases of other systems or organs; (ii) patients who had not received cooperative treatment due to personal or other factors; (iii) patients with incomplete clinical data and history information (tumor size, clinicopathological stage (TNM), etc.).

Paraffin sections of tumor tissue and para-cancer tissue (normal lung tissue no less than 5 cm from tumor edge and confirmed by pathological examination) from surgical specimens of each included subject were collected. The collected paraffin samples were sliced with uniform thickness ($10\,\mu$m/slice) and stored in an enzyme-free centrifuge tube (Shanghai Macklin Biochemical Technology Co., Ltd.) containing xylene (Yantai Ruiteng Intelligent Technology Co., Ltd.).

2.2. RNA Extraction from Lung Cancer Tissue Sections. Sectioning: the collected paraffin specimens were sectionalized with a thickness of $10\,\mu$m/slice and placed quickly in a 1.5 mL tube. Dewaxing: $1,200\,\mu$L xylene was added, shaken quickly to mix, centrifuged at 8,600 rpm for 10 min, which was repeated three times, then supernatant was discarded. The lower layer was added with $1,200\,\mu$L anhydrous ethanol, mixed by shaking, centrifuged at 8,600 rpm for 5 min at room temperature, and repeated twice. The supernatant was discarded, and the lower layer was dried in an oven at 37°C for half an hour. Then, $200\,\mu$L lysate and $5\,\mu$L Proteinase K (20 mg/mL) were added. After the tissue was dissolved, it was bathed in water at 95°C for 10 min and centrifuged at 8,600 rpm at room temperature for 5 min. The supernatant was absorbed and transferred to a new Rnase-free centrifuge tube. $220\,\mu$L buffer RB was added, shaken, and mixed, then added with anhydrous ethanol, and mixed again.

$700\,\mu$L solution and precipitate were absorbed and added to the adsorption column, centrifuged at high speed for 1 min. The waste solution was filtered and repeated several times until the solution and precipitate passed through the adsorption column. $80\,\mu$L DNase I working solution was added to the center of the adsorption column and left for 15 min at room temperature. $500\,\mu$L protein-free RW1 was added and centrifuged, then added with rinse solution, centrifuged again, and the waste solution was discarded. After drying, the adsorption column was transferred to a new RNase-free centrifuge tube. $35\,\mu$L RNase-free ddH$_2$O was added and centrifuged at 8,600 rpm for 5 min to obtain RNA solution. RNase R was used to process the extracted total RNA to avoid artifacts. RNase R processing reaction system: $2\,\mu$g RNA, $1\,\mu$L RiboLock, $2\,\mu$L 10x RNase R reaction buffer, and $1\,\mu$L RNase R, with sterile water supplementing the system to $20\,\mu$L [21]. The instructions were followed, and random primers were used for reverse transcription to synthesize cDNA. $2\,\mu$L $5\times$ PrimeScript Buffer, $0.5\,\mu$L enzyme mix I, $0.5\,\mu$L random 6 mers, and $7\,\mu$L total RNA were added to a 0.2 mL enzyme-free EP tube to configure a $10\,\mu$L system. The EP tube was closed and shaken for 15 s to mix, centrifuged, and put in the reverse transcription machine. The reverse transcription conditions: 37°C for 15 min, 85°C for 5 sec. After the reaction, the synthesized cDNA was transferred to -20°C refrigerator for storage.
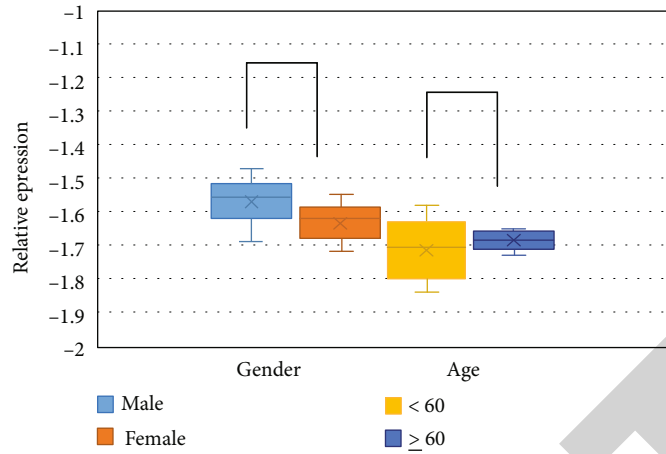
Figure 2: The expression of circHIPK3 in different lung cancer patients.

(a)

(b)
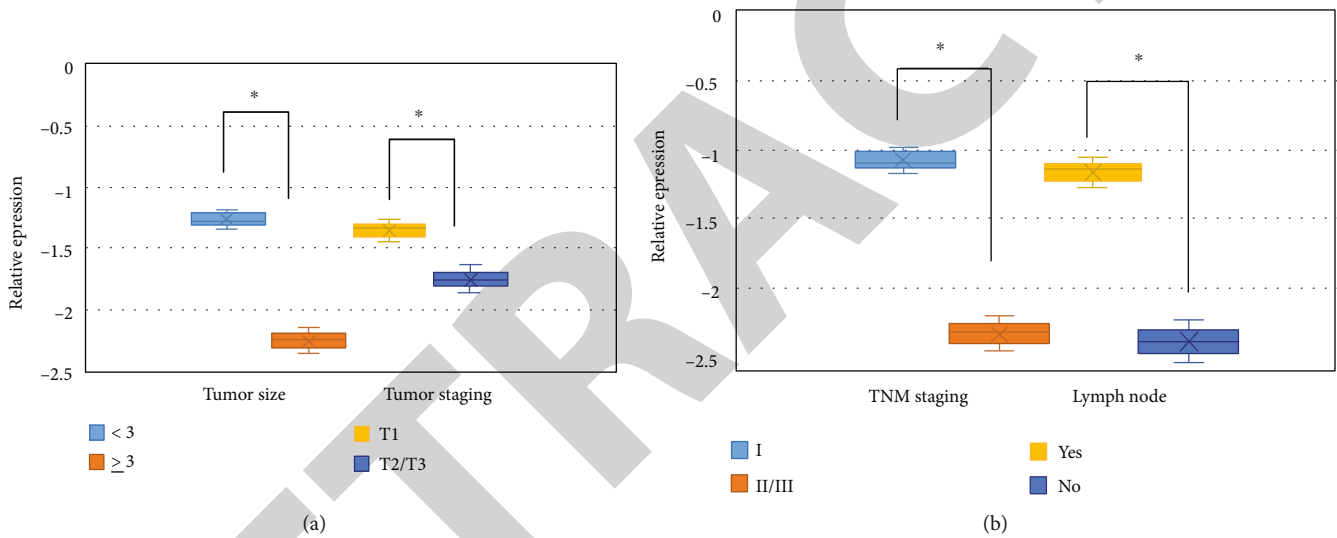
Figure 3: The expression of circHIPK3 in different tumor types. Note: (a) was tumor size and T stage; (b) was TNM stage and lymph node metastasis. ∗ indicated that the difference was considerable ($P < 0.05$).
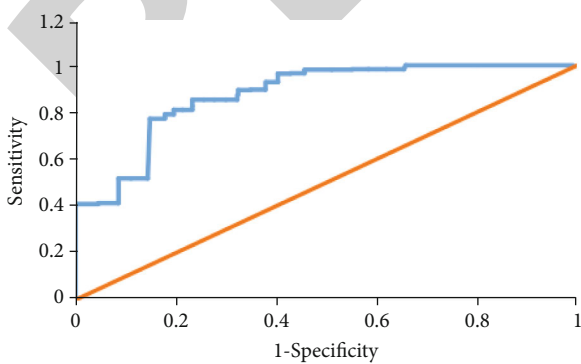
Figure 4: ROC curve of circHIPK3 for the diagnosis of lung cancer.

The length of circHIPK3 searched on NCBI was 1,099 bp, and the specific base sequence was as follows: GTATGGCCTCA CAAGTCTTGGTCTACCCACCATATGTTTATCAAACTC AGTCAAGTGCCTTTTGTAGTGTGAAGAAACTCAAAG TAGAGCCAAGCAGTTGTGTATTCCAGGAAAGAAACT ATCCACGGACCTATGTGAATGGTAGAAACTTTGGAA ATTCTCATCCTCCCACTAAGGGTAGTGCTTTTCAGAC AAAGATACCATTTAATAGACCTCGAGGACACAACTT TTCATTGCGACAAGTGCTGTTGTTTTGAAAAACACT GCAGGTGCTACAAAGGTCATAGCAGCTCAGGCACAG CAAGCTCACGTGCAGGCACCTCAGATTGGGGCGTGG CGAAACAGATTGCATTTCCTAGAAGGCCCCCAGCGA TGTGGATTGAAGCGCAAGAGTGAGGAGTTGGATAAT CATAGCAGCGCAATGCAGATTGTCGATGAATTGTCC ATACTTCCTGCAATGTTGCAAACCAACATGGGAAAT CCAGTGACAGTTGTGACAGCTACCACAGGATCAAAA CAGAATTGTACCACTGGAGAAGGTGACTATCAGTTA

(a)

(b)

(c)
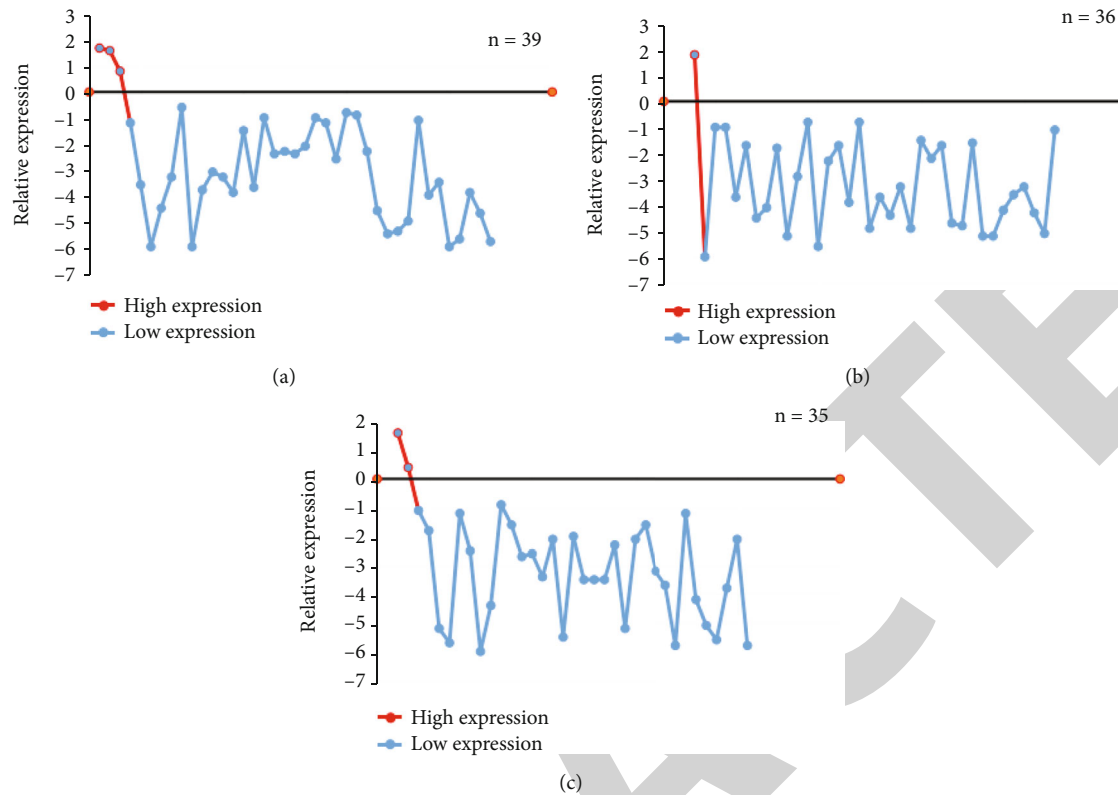
Figure 5: Relative expression analysis of circHIPK3 in patients with different stages of lung cancer. Note: (a) was TNM stage I; (b) was TNM stage I; (c) was TNM stage III.
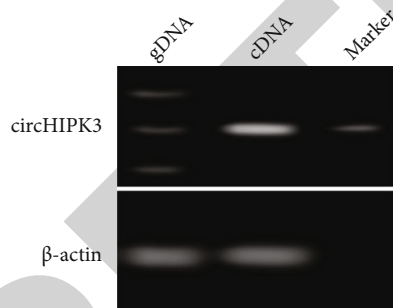
Figure 6: circHIPK3 electrophoresis diagram.

GTACAGCATGAAGTCTTATGCTCCATGAAAAATACT
TACGAAGTCCTTGATTTTCTTGGTCGAGGCACGTTT
GGCCAGGTAGTTAAATGCTGGAAAAGAGGGACAAA
TGAAATTGTAGCAATCAAAATTTTGAAGAATCATCCT
TCTTATGCCCGTCAAGGTCAAATAGAAGTGAGCATAT
TAGCAAGGCTCAGTACTGAAAATGCTGATGAATATA
ACTTTGTACGAGCTTATGAATGCTTTCAGCACCGTAA
CCATACTTGTTTAGTCTTTGAGATGCTGGAACAAAAC
TTGTATGACTTTCTGAAACAAAATAAATTTAGTCCCC
TGCCACTAAAAGTGATTCGGCCCATTCTTCAACAAGT
GGCCACTGCACTGAAAAAATTGAAAGTCTTGGTTTA
ATTCATGCTGATCTCAAGCCAGAGAATATTATGTTGG
TGGATCCTGTTCGGCAGCCTTACAGGGTTAAAGTAAT
AGACTTTGGGTCGGCCAGTCATGTATCAAAGACTGTT
TGT TCAACATATCTACAATCTCGGTACTACAG.

The designed upstream and downstream primers were as follows: circHIPK3-F: TAGACTTTGGGTCGGCCAGT; circHIPK3-R: TGGAATACACAACTGCTTGGC.

The expression of circHIPK3 was detected by real-time fluorescence quantitative polymerase chain reaction (PCR). circHIPK3 is derived from the HIPK3 gene and consists of exon 2 (1,099 bp) head-to-tail splicing. Head-to-tail splicing can be generated by trans-splicing or genome rearrangement. The sequence is a circular sequence, which is assembled from the first position of the corresponding linear RNA, and a new unique sequence is generated at the reverse splicing site. The circRNA specific primers were designed with this as the target sequence, so as to specifically recognize circRNA and distinguish circular sequence from linear RNA. The identification and location of circHIPK3 was shown in Figure 1.

2.3. Cell Culture and Passage. Serum-free cell freezing medium (RPMI) 1640 cell culture medium consisted of 10% fetal bovine serum (FBS) (Gibco BRL, USA), 100 U/mL penicillin (Hubei Yangxin Pharmaceutical Technology Co., Ltd.) and 100 mg/mL streptomycin (Shanghai Yuanye Biological Technology Co., Ltd.). The cell cryopreservation tube was taken out of the liquid nitrogen and quickly melted in a constant temperature water bath at 37°C. The thawed cell cryopreservation solution was transferred to a centrifuge tube containing cell culture medium and centrifuged at high speed for 5 min. Then, after cell culture medium was added to the lower sediment to resuspend the cells, they were transferred to RPMI medium and
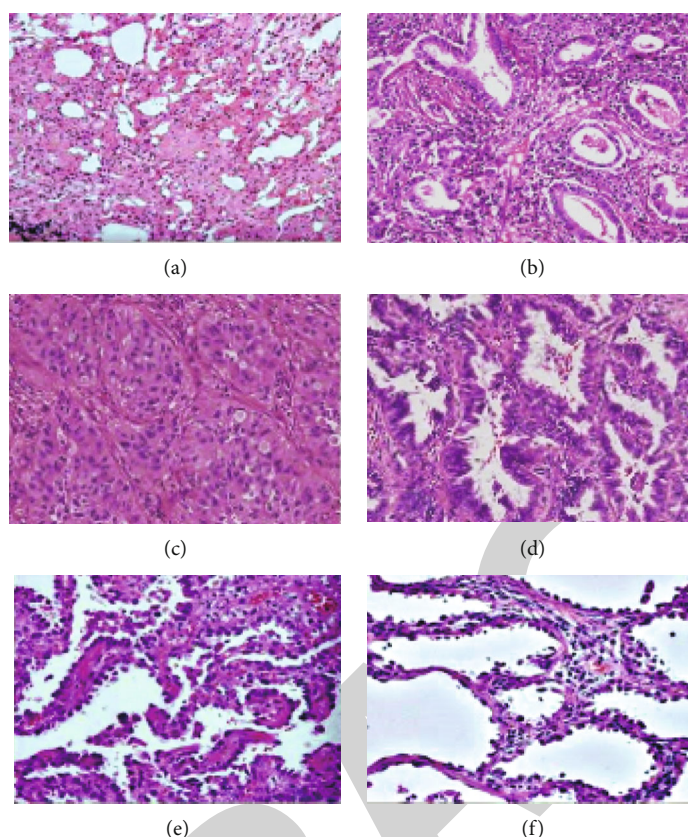
FIGURE 7: Histopathological characteristics of lung cancer. Note: (a)–(c) were 40× images; (d)–(f) were 100× images.

incubated at constant temperature. The medium was changed once the cells grew adherently.

After the cell coverage in the culture dish reached more than 80%, passaging began. After the cell culture solution was aspirated, trypsin digestion solution was added, and cells were observed under a microscope. After culturing until the cells became round, culture medium was added to stop the digestion, and the cells were resuspended and passed to a culture dish.

2.4. Construction of Gefitinib-Resistant Cell Lines. Gefitinib was dissolved in dimethyl sulfoxide (DMSO) (Abis (Shanghai) Biotechnology Co., Ltd.). The methyl tetrazolium (MTT) assay was used to determine the median lethal concentration of gefitinib on lung cancer cells (the concentration of the poison that caused half of the tested animals or cells to die in an acute toxicity test). In this study, human lung adenocarcinoma cell line A549 was used to induce gefitinib-resistant cell lines. Resistant cells were induced by a combination of high-dose shocks and gradually increased doses. MTT assay was used to determine the 50% inhibitory concentration (IC_{50}) of gefitinib on sensitive cells was 1.78 mol/L. Then, the culture medium containing 17.5 μmol/L gefitinib was used for 24 h, and the medium containing half of the inhibitory concentration gefitinib was immediately replaced for 5-10 d, until the cells grew steadily and were subcultured for 3 times. IC_{50} was determined again. The medium containing 17.5 μmol/L gefitinib was cultured for 24 h, and the medium with gradually increased inhibitory con-

centration of gefitinib was replaced until the cells grew statically in the medium containing 17.5 μmol/L gefitinib and were continuously passed for 3 times. Then, the IC_{50} of gefitinib was 34.5 μmol/L and was named A549/GR.

2.5. MTT Colorimetric Detection. Single cell suspension was prepared with culture medium containing 10% fetal bovine serum and inoculated into 96-well plates with 1,000-10,000 cells per well, and volume of each well was 200 μL. The cells were routinely cultured for 3 to 5 days, 20 μL of MTT solution (5 mg/mL, prepared by PBS) was added to each well for 4 h, and the culture was terminated. The supernatant cultured in the hole should be carefully sucked and discarded. For suspended cells, the supernatant should be discarded after centrifugation. 150 μL dimethyl sulfoxide (DMSO) was added to each well and shaken to dissolve completely. At 490 nm, the light absorption value (OD) of each hole was measured by enzyme-linked immunosorbent assay (ELISA) and recorded. The cell growth curve was plotted with time as abscissa and light absorption value as ordinate.

2.6. Statistical Methods. SPSS 19.0 was employed for data statistics and analysis. Mean ± standard deviation ($\bar{x} \pm s$) was how measurement data were expressed, and percentage (%) was how count data were expressed. Analysis of variance was used for pairwise comparison. The difference was statistically considerable with $P < 0.05$.

(a)

(b)

(c)

(d)

(e)

(f)

(g)

(h)
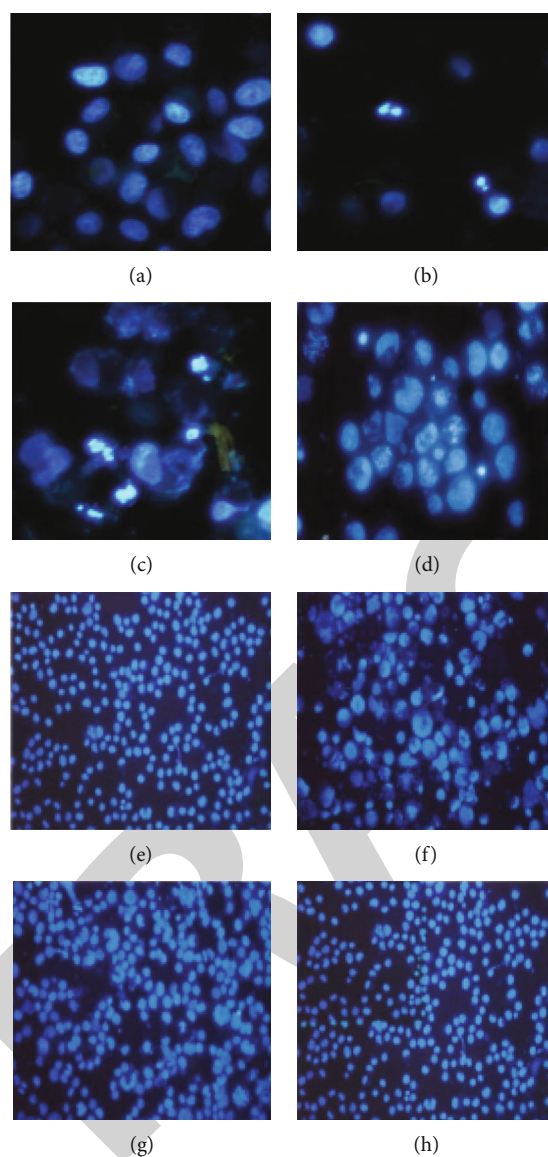
FIGURE 8: Fluorescent staining microscopic image of the constructed gefitinib drug-resistant lung cancer cell line A549/GR. Note: the multiples of (a)–(d) were 200×; the multiples of (e)–(h) were 200×.

3. Results

3.1. circHIPK3 Expression in Different Patients. Figure 2 showed the comparison of the relative expression levels of circHIPK3 in male and female patients and patients of different ages. Among the patients included in the study, there was no considerable difference in the relative expression of circHIPK3 between male patients and female patients ($P > 0.05$). There was also no considerable difference in the relative expression of circHIPK3 between patients less than 60 years old and patients no less than 60 years old ($P > 0.05$).

3.2. Expression of circHIPK3 in Different Tumor Types. Figure 3(a) showed the comparison of the relative expression levels of circHIPK3 in patients with tumor diameters less than 3 cm and tumor diameters no less than 3 cm, as well

as patients with tumor T staging of stage I and II/III. The relative expression of circHIPK3 in patients with tumor diameter no less than 3 cm was dramatically inferior to that in patients with tumor diameter less than 3 cm ($P < 0.05$). The relative expression of circHIPK3 in patients with T stage II/III tumors was dramatically inferior to that in patients with T stage I ($P < 0.05$).

Figure 3(b) showed the comparison of the relative expression levels of circHIPK3 in patients with lung cancer patients whose TNM staging was stage I and stage II/III, as well as those with and without lymph node metastasis. The relative expression of circHIPK3 in patients with TNM stage II/III was dramatically inferior to that in patients with TNM stage I ($P < 0.05$). The relative expression of circHIPK3 in patients with lymph node metastasis was dramatically inferior to that in patients without lymph node metastasis ($P < 0.05$).

3.3. Expression of circHIPK3 in Different Tumor Types.
The circular RNA circHIPK3 is widely and highly expressed in lung cancer cells, mainly located in the cytoplasm, but also in the nucleus. The expression of circHIPK3 in cancer tissues and normal lung tissues adjacent to cancer is notably different, so it is used for the diagnosis of lung cancer. With pathological and imaging findings as diagnostic criteria, Figure 4 showed the receiver operating characteristic (ROC) curve drawn from the diagnosis of lung cancer through circHIPK3. circHIPK3 had high sensitivity and specificity for the diagnosis of lung cancer, can identify tumor tissues, and had high diagnostic value.

3.4. Relative Expression Analysis of circHIPK3.
The 110 lung cancer patients included in this study were graded into stage I, stage II, and stage III according to the TNM staging. Among them, 39 patients were in TNM stage I, 36 were in stage II, and 35 were in stage III. Figure 5 showed the measurement results of the relative expression of circHIPK3 in lung cancer tissues of patients with different TNM stages. Among them, the relative expression level of circHIPK3 ($\log 2$) > 0 meant high expression, and $\log 2 < 0$ meant low expression [22]. Among the lung cancer tissues of patients with different TNM stages, only 6 patients had high expression, and the remaining 104 patients had low expression.

3.5. circHIPK3 Amplification and Electrophoresis.
The circular RNA circHIPK3 was amplified by designing primers and then electrophoresed on agarose gel plate to get the electrophoresis, as shown in Figure 6. circHIPK3 can only be amplified in cDNA, but not in gDNA.

3.6. Analysis of Histopathological Characteristics of Lung Cancer.
Figure 7 was a microscopic image of the tumor tissue of a lung cancer patient. There was inflammatory interstitial thickening, edema, fibrosis, and partial alveolar collapse. Tumor cells extended along the alveolar wall, and atypical alveolar wall cubic cells extended along the thickened alveolar interval. Focal fibers were accompanied by atelectasis, and inflammatory cell infiltration was seen.

3.7. Fluorescence Staining of Lung Cancer Cells.
Figure 8 was a fluorescent staining microscopic image of the constructed gefitinib drug-resistant lung cancer cell line. The apoptotic body cells marked in red also included dividing cells (the nucleus had been separated but the two cells had not been completely separated) and cells containing apoptotic bodies. At 200 multiples, there were many circular or other shaped intact stained bodies.

3.8. Apoptosis Detection.
The surface of normal cells is composed of lipids distributed asymmetrically on the inner and outer lobes of the plasma membrane. Phosphatidylserine is mostly distributed in the inner lobes of the plasma membrane and exposed to the cytoplasm [23]. However, in the process of apoptosis, lipid asymmetry disappears, and phosphatidylserine is exposed on the outer lobules of the plasma membrane. Annexin V is a 36 KDa calcium-dependent phospholipid-binding protein that can bind to phosphatidylserine [24]. Therefore, the fluorescently labeled Annexin
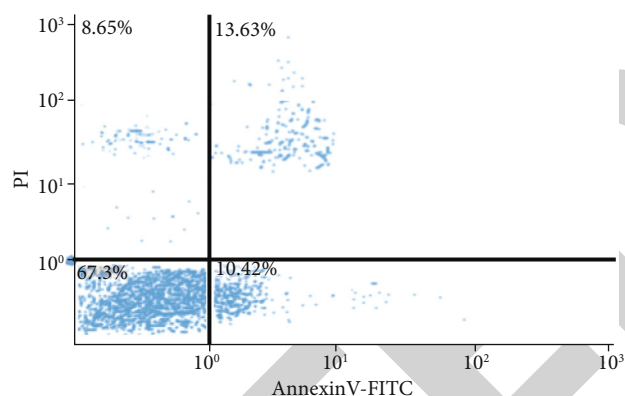
FIGURE 9: Apoptosis results of gefitinib-resistant lung cancer cell line A549.

V can be used to detect phosphatidylserine exposed to the outside of early apoptotic cells, and it can also stain necrotic cells (midlate apoptotic cells). By costaining with propidium iodide (PI), apoptotic cells were distinguished from necrotic cells. Figure 9 showed the results of flow cytometry. The upper right quadrant was the midlate apoptotic cells, and the lower right quadrant was the early apoptotic cells. Gefitinib-mediated apoptosis rate of lung cancer drug-resistant cell lines decreased notably.

4. Discussion

Gefitinib can specifically block a certain pathway of lung cancer cells, block the conduction, infiltration, and metastasis of lung cancer cells, locate and kill cancer cells, and cause little damage to normal human cells [25, 26]. It is mainly used to treat locally advanced or metastatic NSCLC that is sensitive to EGFR gene. Local NSCLC that has received chemotherapy before can also be used, but the EGFR gene must be tested before using the drug [27]. Wang et al. (2019) [28] first used AGO2 immunopurification to analyze the possibility of circHIPK3 binding to microRNA. AGO2 is the core component of RISC, connecting miRNAs and their mRNA target sites. Therefore, immunopurification of AGO2 under suitable conditions can obtain miRNA and mRNA that bind to each other, thereby identifying the target site of miRNA. Immunofluorescence can also be performed to detect the intracellular localization of the three complexes. Luciferase reporter gene experiment was combined with PCR for verification. The results showed that circHIPK3-related microRNAs can indeed resist luciferase activity, so there was an interaction between microRNAs and circHIPK3. Zhang et al. (2020) [29] identified 71 differentially expressed circRNAs in osteoarthritis and normal cartilage tissues. Coexpression analysis of circRNA and mRNA combined with transcriptome data was implemented to predict their interaction relationship. It was found that the expression of circRNA and interleukin-1 and tumor necrosis factor increased simultaneously. In addition, it was found that circRNA was involved in the degradation of extracellular matrix, and circRNA played an important regulatory role in human cells.

In this study, the tumor tissues and para-cancerous tissues from surgical specimens of 110 study subjects were collected to detect differences in the expression of circHIPK3 in different tissues. Moreover, a lung cancer gefitinib drug-resistant cell line was constructed, and cell apoptosis was detected under different conditions, to study the mechanism of circRNA involved in the resistance of lung cancer cells to gefitinib. As a result, the relative expression of circHIPK3 in patients with tumor diameter no less than 3 cm was dramatically inferior to that in patients with tumor diameter less than 3 cm ($P < 0.05$). The relative expression of circHIPK3 in patients with TNM stage II/III was dramatically inferior to that in patients with TNM stage I ($P < 0.05$). In addition, the relative expression of circHIPK3 in patients with lymph node metastasis was dramatically inferior to that in patients without lymph node metastasis ($P < 0.05$). The results indicated that the relative expression of circHIPK3 in the tumor tissues of patients with lung cancer was closely related to the diameter of the patient's tumor, the TNM stage, and the occurrence of lymph node metastasis. However, there was no high correlation with the patient's age, gender, and other information. Among lung cancer tissues of patients with different TNM stages, only 6 patients had high expression, and the remaining 104 patients had low expression. Therefore, circHIPK3 may have a notably low expression in lung cancer tissues and related cell lines, which had a high correlation with the tumor stage of patients. Flow cytometry apoptosis detection results found that gefitinib-mediated apoptosis rate of lung cancer drug-resistant cell lines decreased notably, which was similar to Zhou et al.'s (2020) [30] research, indicating that circHIPK3 had a certain effect on the drug resistance of lung adenocarcinoma cells gefitinib and can enhance its drug resistance.

5. Conclusion

In this study, tumor tissues and adjacent tissues were collected from surgical specimens of lung cancer patients to detect differences in the expression of circHIPK3 in different patients and different tumor tissues. In addition, a lung cancer gefitinib drug-resistant cell line was constructed to detect cell apoptosis under different conditions. The results showed that the circular RNA circHIPK3 may have a considerably low expression in lung cancer tissues, and its low expression had a certain enhancement effect on the drug resistance of lung adenocarcinoma cells to gefitinib. However, the sample size selected in this study is small, and the representativeness is low. Therefore, the selection of test sample size will be increased in subsequent experiments. Further study is required to clarify the mechanism of circRNA involved in the resistance of lung cancer cells to gefitinib. In short, this study provides a certain theoretical basis and data support for the drug treatment of lung cancer.

Data Availability

The data used to support the findings of this study are included within the article.

Conflicts of Interest

The authors declare that they have no competing interest.

Acknowledgments

References

[1] D. Chen, W. Ma, Z. Ke, and F. Xie, "circRNA hsa_circ_100395 regulates miR-1228/TCF21 pathway to inhibit lung cancer progression," *Cell Cycle*, vol. 17, no. 16, pp. 2080–2090, 2018.

[2] Z. Z. Liang, C. Guo, M. M. Zou, P. Meng, and T. T. Zhang, "circRNA-miRNA-mRNA regulatory network in human lung cancer: an update," *Cancer Cell International*, vol. 20, no. 1, p. 173, 2020.

[3] L. Zong, Q. Sun, H. Zhang et al., "Increased expression of circRNA_102231 in lung cancer and its clinical significance," *Biomedicine & Pharmacotherapy*, vol. 102, pp. 639–644, 2018.

[4] N. Zhang, A. Nan, L. Chen et al., "Circular RNA circSATB2 promotes progression of non-small cell lung cancer cells," *Molecular Cancer*, vol. 19, no. 1, p. 101, 2020.

[5] B. Li, L. Zhu, C. Lu et al., "*circNDUFB2* inhibits non-small cell lung cancer progression via destabilizing IGF2BPs and activating anti-tumor immunity," *Nature Communications*, vol. 12, no. 1, p. 295, 2021.

[6] Z. Fan, Y. Bai, Q. Zhang, and P. Qian, "circRNA circ_POLA2 promotes lung cancer cell stemness via regulating the miR-326/GNB1 axis," *Environmental Toxicology*, vol. 35, no. 10, pp. 1146–1156, 2020.

[7] J. Wang, X. Zhao, Y. Wang et al., "circRNA-002178 act as a ceRNA to promote PDL1/PD1 expression in lung adenocarcinoma," *Cell Death & Disease*, vol. 11, no. 1, p. 32, 2020.

[8] L. Chen, A. Nan, N. Zhang et al., "Circular RNA 100146 functions as an oncogene through direct binding to miR-361-3p and miR-615-5p in non-small cell lung cancer," *Molecular Cancer*, vol. 18, no. 1, p. 13, 2019.

[9] X. Chen, R. Mao, W. Su et al., "Circular RNAcircHIPK3modulates autophagy viaMIR124-3p-STAT3-PRKAA/AMPKα signaling in STK11 mutant lung cancer," *Autophagy*, vol. 16, no. 4, pp. 659–671, 2020.

[10] Y. Zhao, R. Zheng, J. Chen, and D. Ning, "circRNA CDR1as/miR-641/HOXA9 pathway regulated stemness contributes to cisplatin resistance in non-small cell lung cancer (NSCLC)," *Cancer Cell International*, vol. 20, no. 1, p. 289, 2020.

[11] L. Wang, X. Tong, Z. Zhou et al., "Circular RNA hsa circ 0008305 (circPTK2) inhibits TGF-β-induced epithelial-mesenchymal transition and metastasis by controlling TIF1γ in non-small cell lung cancer," *Molecular Cancer*, vol. 17, no. 1, p. 140, 2018.

[12] W. Hong, M. Xue, J. Jiang, Y. Zhang, and X. Gao, "Circular RNA circ-CPA4/ let-7 miRNA/PD-L1 axis regulates cell growth, stemness, drug resistance and immune evasion in non-small cell lung cancer (NSCLC)," *Journal of Experimental & Clinical Cancer Research*, vol. 39, no. 1, p. 149, 2020.

[13] A. Nan, L. Chen, N. Zhang et al., "Circular RNA circNOL10 inhibits lung cancer development by promoting SCLM1-mediated transcriptional regulation of the humanin polypeptide family," *Advanced Science*, vol. 6, no. 2, p. 1800654, 2019.

Retraction

Retracted: Development of a 5-Gene Signature to Evaluate Lung Adenocarcinoma Prognosis Based on the Features of Cancer Stem Cells

BioMed Research International

This article has been retracted by Hindawi following an investigation undertaken by the publisher [1]. This investigation has uncovered evidence of one or more of the following indicators of systematic manipulation of the publication process:

(1) Discrepancies in scope

(2) Discrepancies in the description of the research reported

(3) Discrepancies between the availability of data and the research described

(4) Inappropriate citations

(5) Incoherent, meaningless and/or irrelevant content included in the article

(6) Manipulated or compromised peer review

The presence of these indicators undermines our confidence in the integrity of the article's content and we cannot, therefore, vouch for its reliability. Please note that this notice is intended solely to alert readers that the content of this article is unreliable. We have not investigated whether authors were aware of or involved in the systematic manipulation of the publication process.

Wiley and Hindawi regrets that the usual quality checks did not identify these issues before publication and have since put additional measures in place to safeguard research integrity.

We wish to credit our own Research Integrity and Research Publishing teams and anonymous and named external researchers and research integrity experts for contributing to this investigation.

The corresponding author, as the representative of all authors, has been given the opportunity to register their agreement or disagreement to this retraction. We have kept a record of any response received.

References

[1] R. Wan, H. Liao, J. Liu et al., "Development of a 5-Gene Signature to Evaluate Lung Adenocarcinoma Prognosis Based on the Features of Cancer Stem Cells," *BioMed Research International*, vol. 2022, Article ID 4404406, 28 pages, 2022.

Hindawi

Research Article

Development of a 5-Gene Signature to Evaluate Lung Adenocarcinoma Prognosis Based on the Features of Cancer Stem Cells

Renping Wan,[1] Hongliang Liao,[1] Jingting Liu,[1] Lin Zhou,[1] Yingqiu Yin,[2] Tianhao Mu [ID],[3,4] and Jie Wei [ID][2]

[1]Department of Thoracic Surgery, Yuebei People's Hospital, 133 Huimin South Road, Wujiang District, Shaoguan City, Guangdong Province, China 440200

[2]Department of Respiratory Medicine, Yuebei People's Hospital, 133 Huimin South Road, Wujiang District, Shaoguan City Guangdong Province, China 440200

[3]Department of Oncology, HaploX Biotechnology, 8/F, Aotexin Power Building, No. 1, Songpingshan Road, High Tech North District, Nanshan District, Shenzhen City, Guangdong Province, China 440300

[4]Department of Biomedical and Health Engineering, Shenzhen Institute of Advanced Technology, Chinese Academy of Sciences, 1068 Xueyuan Avenue University Town, Nanshan District, Shenzhen City, Guangdong Province, China 440300

Correspondence should be addressed to Tianhao Mu; muth@haplox.com and Jie Wei; weijieybhospital@outlook.com

Cancer stem cells (CSCs) can induce recurrence and chemotherapy resistance of lung adenocarcinoma (LUAD). Reliable markers identified based on CSC characteristic of LUAD may improve patients' chemotherapy response and prognosis. OCLR was used to calculate mRNA expression-based stemness index (mRNAsi) of LUAD patients' data in TCGA. Association analysis of mRNAsi was performed with clinical features, somatic mutation, and tumor immunity. A prognostic prediction model was established with LASSO Cox regression. Kaplan-Meier Plotter (KM-plotter) and time-dependent ROC were applied to assess signature performance. For LUAD, univariate and multivariate Cox analysis was performed to identify independent prognostic factors. LUAD tissues showed a noticeably higher mRNAsi in than nontumor tissues, and it showed significant differences in T, N, M, AJCC stages, and smoking history. The most frequently mutated gene was TP53, with a higher mRNAsi relating to more frequent mutation of TP53. The mRNAsi was significantly negatively correlated with immune score, stromal score, and ESTIMATE score in LUAD. The blue module was associated with mRNAsi. The 5-gene signature was confirmed as an independent indicator of LUAD prognosis that could promote personalized treatment of LUAD and accurately predict overall survival (OS) of LUAD patients.

1. Introduction

Lung adenocarcinoma (LUAD) originates from small airway epithelial type II alveolar cells [1, 2]. Most LUAD patients are diagnosed at advanced cancer stages; conventional treatments for those patients are chemotherapy and radiation, to which LUAD is highly resistant. Thus, LUAD shows a high mortality, the five-year survival chance of which is about 15% [3, 4]. This also demands better improvement of early

diagnosis, survival prediction, and relapse monitoring of LUAD patients to prolong their survival.

A study found cancer stem cells (CSCs) as a small subgroup of cancer cells with stemness. The self-renewing of CSCs and their production of differentiated cells could facilitate the formation of tumor heterogeneity [5]. The latest evidence indicated that CSC-mediated stem-like phenotypes of cancer cells are the major factor responsible for cancer recurrence and chemical resistance [6]. This also points to
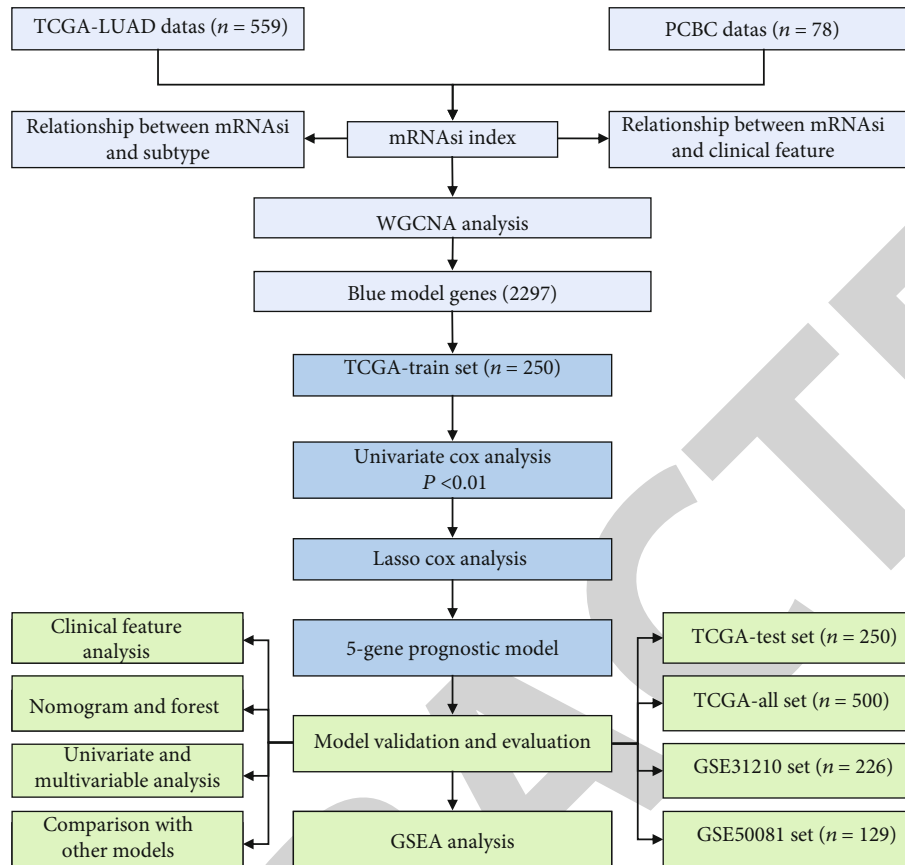
Figure 1: Flowchart of research design.

the need to accurately identify CSC population. However, due to the quiescent nature of lung epithelial cells, distinguishing normal lung epithelial cells from lung CSCs is still a great challenge [7]. A study showed that identifying CSC markers may help characterize CSCs [8]. In LUAD, several CSC markers, including CD44 [9], CD90 [10], and SOX2, have been discovered [11], but clinical application of CSC-specific biomarkers is less popular. Furthermore, the fact that most markers could mark heterogeneous stem cell populations suggests that their isolation and characterization should be developed using a combination of surface markers or a combination of intracellular or extracellular markers [12]. Malta et al. [13] developed a new indicator to reflect stem cell features of mRNAsi calculated by OCLR. Their results proved that a higher value of mRNAsi is indicative of stronger characteristics of CSCs.

At present, there are several system biology methods to identify biomarkers related to the prognosis of LUAD and construct mRNA features. Li et al. [14] identified a 7-gene signature by a nonnegative matrix factorization (NMF) method using gene expression profile related to lipid metabolism, Shi et al. [15] established three TKI-related gene expression profiles to predict the chemosensitivity of lung cancer patients. Zhang et al. [16] identified seven gene markers to predict the prognosis of lung cancer patients by using multiomics data integration analysis. The authors of the three groups tested their gene signatures in internal and external data sets but did not conduct clinical verifica-

tion. This means that identifying robust gene signatures is still a challenge, and more queues are needed to verify signatures. In conclusion, it is very important to identify the gene characteristics related to the prognosis of LUAD by bioinformatics analysis of its biological function. In this study, clinical LUAD data were derived from TCGA database, and mRNAsi was calculated based on OCLR to investigate the relationship of mRNAsi and clinical LUA characteristics and mutations of LUAD. The weighted gene coexpression network analysis (WGCNA) was constructed for screening modules associated with mRNAsi, according to which genes showing a significance of prognostic relevance to LUAD were filtered. Finally, a 5-gene independent prognostic signature was established that may be beneficial for optimizing survival risk assessment and personalized management of patients with LUAD.

2. Materials and Methods

2.1. Data Acquisition and Research Design. From the PCBC website, RNA-Seq data for pluripotent stem cell samples were acquired using the R package synapser (v 0.6.61). The data of induced pluripotent stem cells (IPSC) samples and embryonic stem cell (ESC) were retained. The Ensembl IDs of ESC and IPSC samples were reserved and converted into gene symbol to retain only protein-encoding genes. The data of 78 samples were obtained. From TCGA database, clinical LUAD data containing RNA-Seq profilation information of

Table 1: Data statistics of TCGA training set and validation set.

Clinical features	TCGA-train	TCGA-test	P
OS			
0	156	162	
1	94	88	0.6421
Gender			
Female	122	148	
Male	128	102	0.02488
T stage			
T1	82	85	
T2	143	124	
T3	17	28	0.1201
T4	8	10	
TX	0	3	
N stage			
N0	160	164	
N1	52	42	
N2	35	34	0.2326
N3	1	1	
NX	2	9	
M stage			
M0	165	167	
M1	15	9	0.4442
MX	70	74	
Stage			
I	131	137	
II	61	58	
III	39	41	0.8681
IV	15	10	
X	4	4	
Age			
≤65	111	126	
>65	133	120	0.3647
NA	6	4	

594 samples were acquired. The microarray GSE31210 ($n = 246$) and GSE50081 ($n = 181$) were downloaded from GEO website (Table S1). Each LUAD sample had expression profile information and survival data. The median expression value of multiple gene symbols was taken, whereas probes corresponding to multiple genes were excluded. The comprehensive gene annotation is obtained from the GENCODE database (GRCh38.p13), and the information is used to map the Ensembl ID to the gene symbol, and only the protein-encoding genes were reserved. Figure 1 summarizes our study design.

2.2. Correlation between mRNAsi and Clinical Features. mRNAsi was calculated according to the OCLR method provided by Malta et al. [13]. mRNAsi differences between tumor samples and normal samples were analyzed by an unpaired t-test. We used one-way ANOVA in mRNAsi dif-

ference comparison between groups of patients in terms of gender, age, clinical stage, TNM stage, and smoking history.

2.3. Relational Analysis between mRNAsi and Molecular Subtypes. MuTect [17] detection on TCGA-LUAD was performed using TCGAbiolinks [18] (V2.14.0), and differences in mRNAsi of different molecular mutant subtypes were analyzed. In addition, molecular subtype of TCGA-LUAD samples was also extracted using R package TCGA biolinks. mRNAsi differences between samples classified by the CIMP or iCluster were compared.

2.4. Weighted Gene Coexpression Network Analysis (WGCNA). For constructing a coexpression network [19], the WGCNA algorithm was performed. After removing outlier samples, Pearson's correlation coefficients were determined between groups of genes. The optimal efficacy value β was chosen to construct proximity matrix, which was transformed into topological overlap matrix (TOM). For gene cluster according to TOM (in each gene network module, the minimum number of genes was 80), an average-linkage hierarchical clustering method was applied. The pruning algorithm was applied to divide gene modules and integrate those close modules. The most relevant modules with mRNAsi were screened by correlation analysis.

2.5. Functional Enrichment Analysis. The R software (https://www.R-project.org/,version 4.0.2) packageWebGestaltR [20] (v0.4.2) was employed to perform KEGG and GO functional enrichment analyses for analyzing potential biological functions of the most relevant modules of mRNAsi obtained from WGCNA. GO categories were cellular component (CC), molecular function (MF), and biological process (BP). A statistical significance was defined when FDR < 0.05 and $P < 0.05$.

2.6. Construction and Verification of Prognostic Signature. Genes of mRNAsi-related modules were separated into verification and training sets based on the principle of the same sample size (Table 1). To analyze the relevance between genes and OS (statistical significance was $P < 0.01$), Univariate Cox analysis was used here. Glmnet software (doi:10 .18637/jss.v039.i05, version 4.1-2) package was used for LASSO Cox regression analysis. Here, those genes of a $P < 0.05$ were further refined according to the Akaike Information Criterion (AIC). The risk score was determined for each patient by multiplying risk factor obtained by Lasso Cox with gene expression extracted. After standardization, with 0 as the threshold, the samples were grouped by the risk scores into two risk groups (low and high). For OS comparisons between risk groups, we plotted Kaplan-Meier (KM) survival curve. ROC curves were used for prediction evaluation of the signature. In addition, previous LUAD prognostic models were compared with the current risk model.

2.7. The Construction of a Nomogram. To precisely determine independent LUAD prognostic factors, clinical parameters, including gender, age, AJCC stage, T stage, and risk score were subjected to univariate and multivariate Cox

(a)

(b)

(c)

(d)
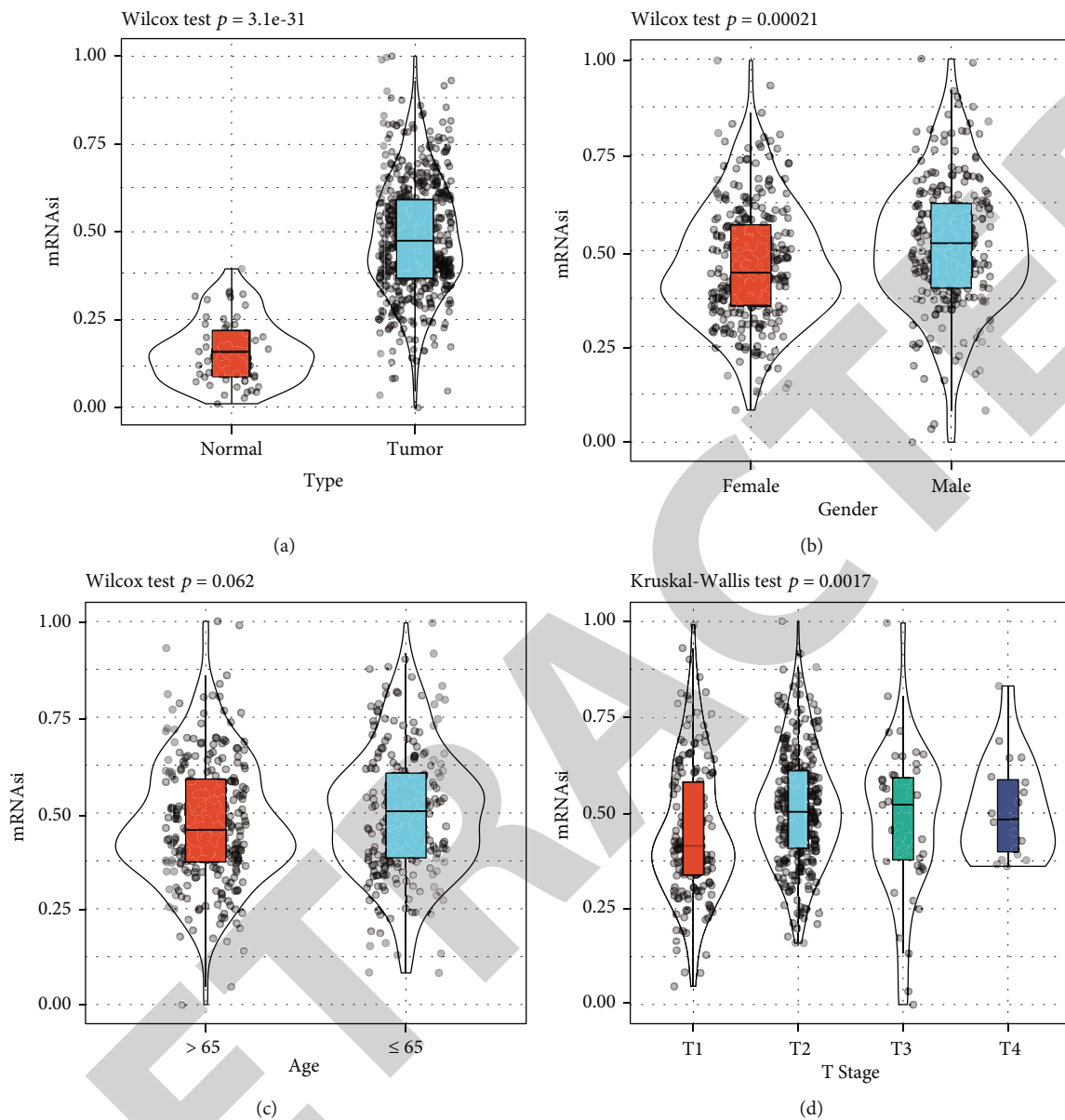
Figure 2: Continued.
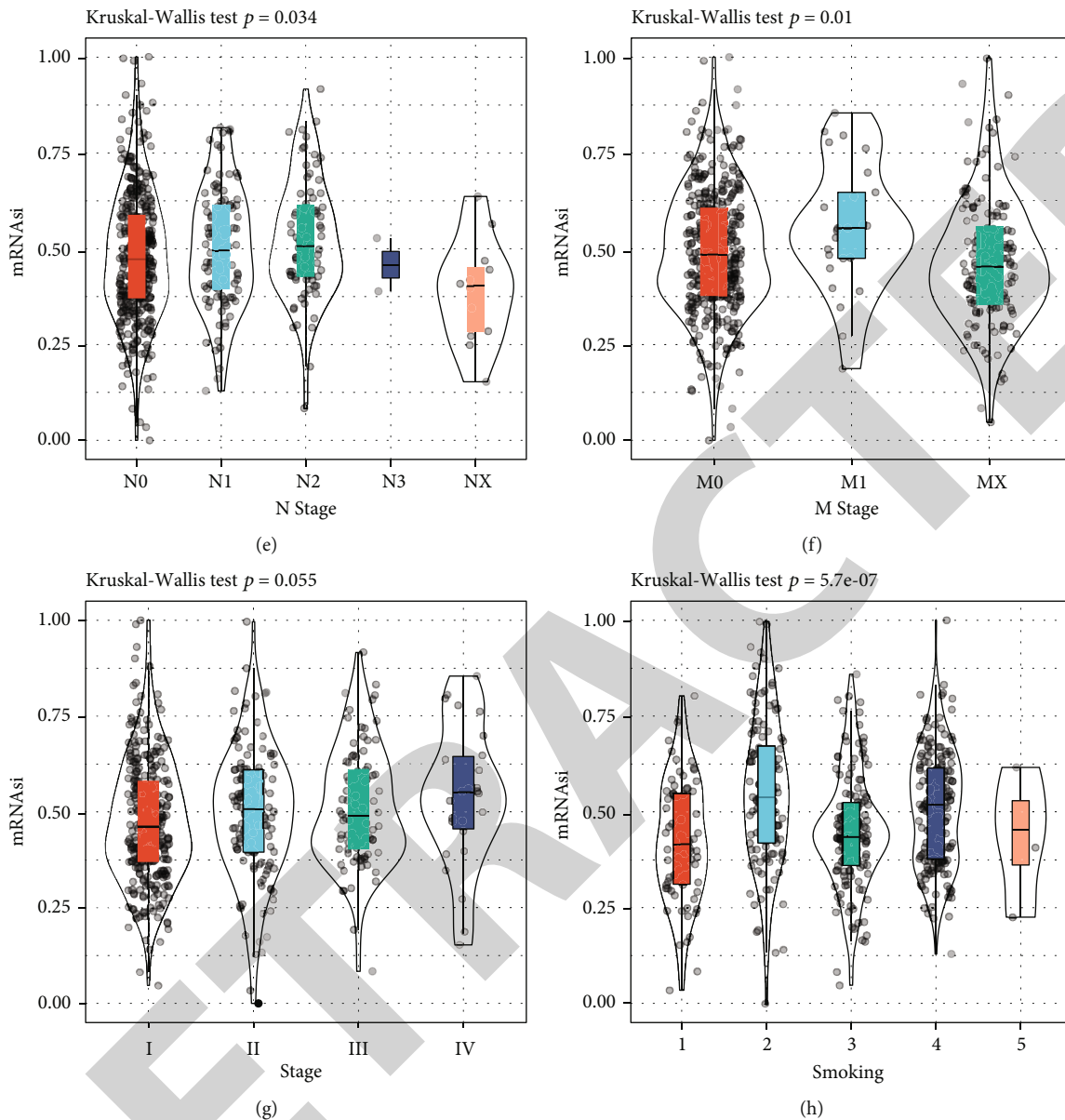
Figure 2: mRNAsi and clinical characteristics of LUAD. (a) mRNAsi differences between neoplastic and normal tissues. (b) Differences in mRNAsi between female and male LUAD patients. (c) mRNAsi difference in LUAD patients with ge > 65 and age ≤ 65. (d) mRNAsi differences between LUAD patients at different T stages. (e) mRNAsi differences between LUAD patients at different N stage. (f) mRNAsi analysis of M1 stage, M2 stage, and M3 stage patients. (g) mRNAsi differences among the four AJCC stage. (h) Differences in mRNAsi among grouped patients according to smoking.1 stands for life-long nonsmokers (fewer than 100 cigarettes during lifetime), 2 stands for current smokers (includes daily smokers and nondaily smokers or occasional smokers), 3 stands for current reformed smokers for >15 years, 4 stands for current reformed smokers for ≤15 years, and 5 stands for current reformed smokers; duration not specified = 5.

regression analyses. Using these clinical factors, a nomogram for OS analysis in 1, 3, and 5 year(s) was built.

3. Results

3.1. mRNAsi and Clinical Characteristics of LUAD. See Figure 1 for the work flow of the current work. mRNAsi, which is a new stemness index for dedifferentiation potential evaluation of tumor cells, has been regarded as a CSC marker [21]. mRNAsi was noticeably higher in LUAD tis-

sues than nontumor ones (Figure 2(a)). The clinical features of mRNAsi in LUAD were examined. The divisions of LUAD patients were divided into two groups according to gender, and age showed no significant difference in mRNAsi between age > 65 and age ≤ 65 (Figure 2(c)), but mRNAsi significant differences in N stage (Figure 2(e)), gender (Figure 2(b)), AJCC stage (Figure 2(g)), and smoking (Figure 2(h)), T stage (Figure 2(d)), and M stage (Figure 2(f)) were observed. Hence, mRNAsi was associated with TNM stage, AJCC stage, and smoking.

(a)

(b)

(c)

FIGURE 3: Continued.

(d)

(e)

(f)

(g)

(h)

(i)

Figure 3: Continued.

(j)
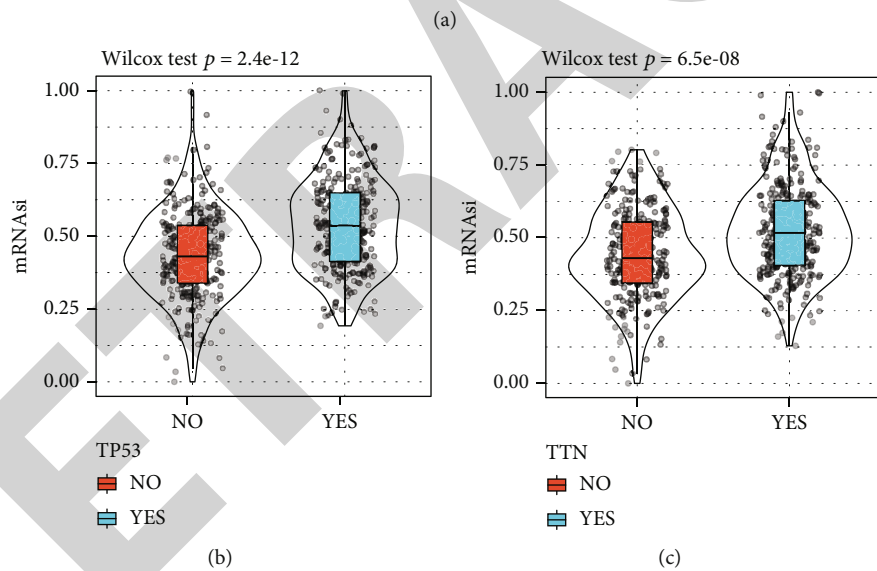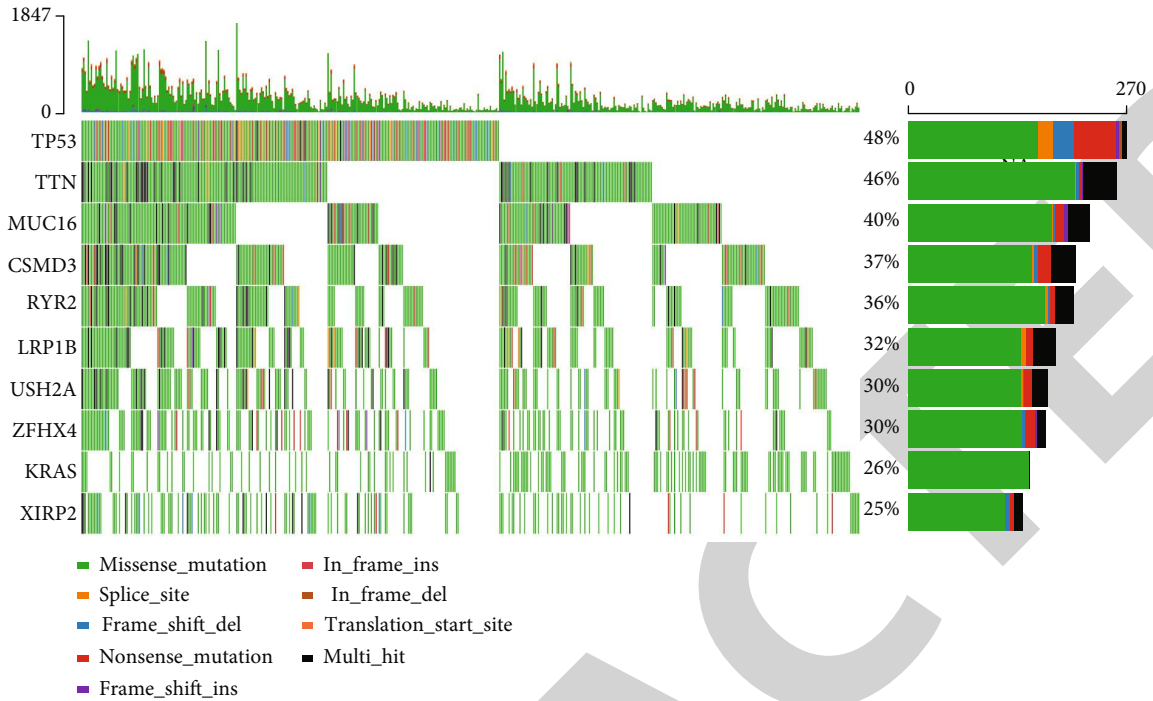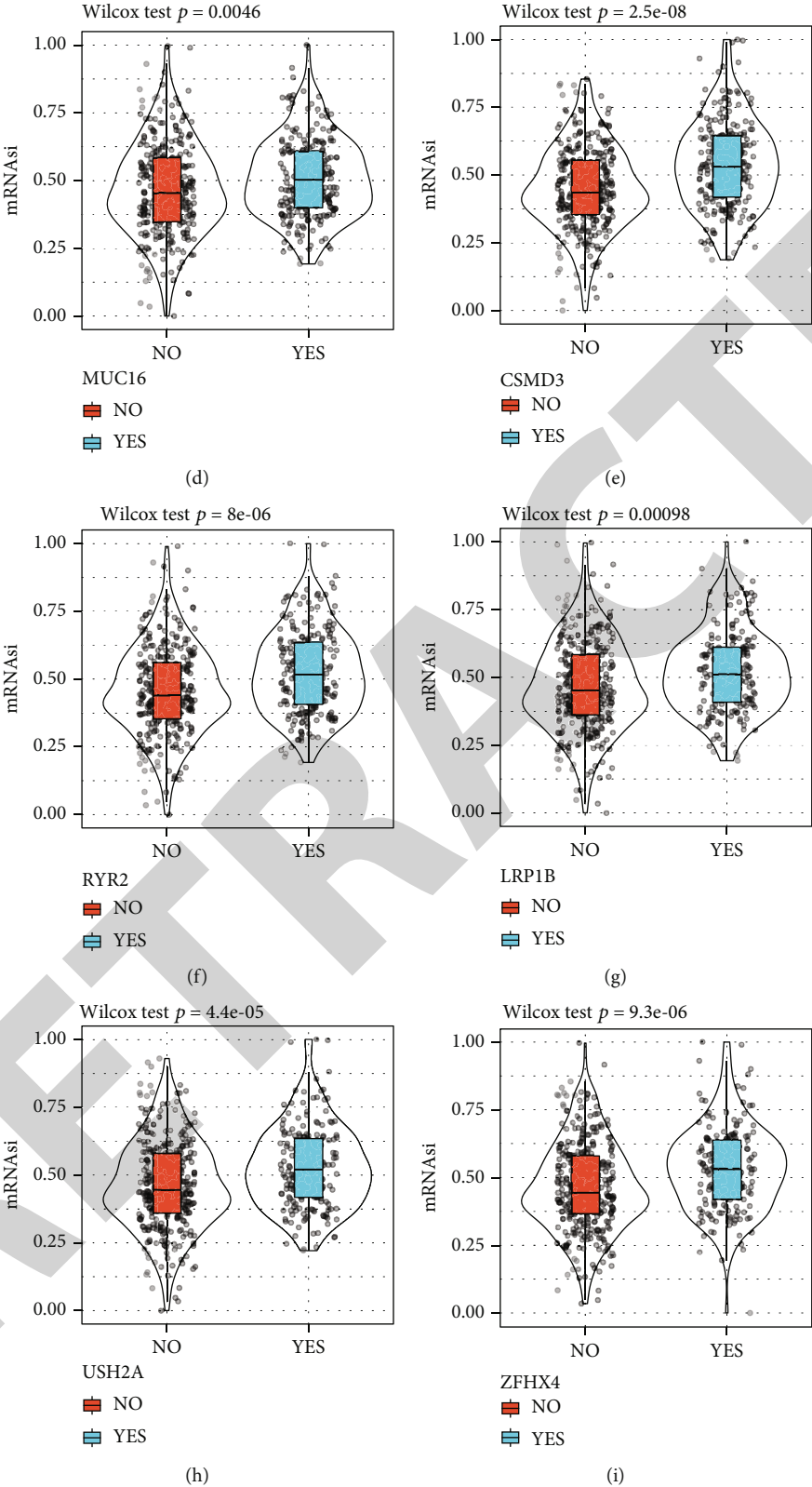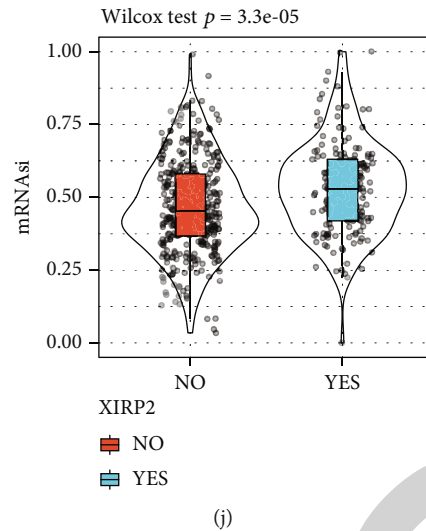
FIGURE 3: Associations of mRNAsi with mutations. (a) An overview of the mutant map in LUAD; only the 10 genes with the highest mutation frequency are shown here. (b) mRNAsi differences between TP53 mutant (MT) and TP53 wild-type (WT) samples. (c) Differences in mRNAsi between TTN mutant LUAD samples and TTN wild-type LUAD samples. (d) mRNAsi differences between MU16 mutant LUAD samples and MU16 wild-type LUAD samples. (e) mRNAsi difference in patients with CSMD3 mutant and CSMD3 wild-type. (f) mRNAsi was compared between RYR2 mutant LUAD and RYR2 wild-type LUAD patients. (g) mRNAsi in LUAD patients with mutant LRP1B was compared with that in LUAD patients without mutant LRP1B. (h) Difference analysis was used to compare the difference in mRNAsi between samples with and without mutations in USH2A. (i) Violin plots showed mRNAsi between LUAD samples with and without LRP1B mutations. (j) Differences between XIRP2 wild-type samples and XIRP2 mutant samples Violin diagram of mRNAsi.
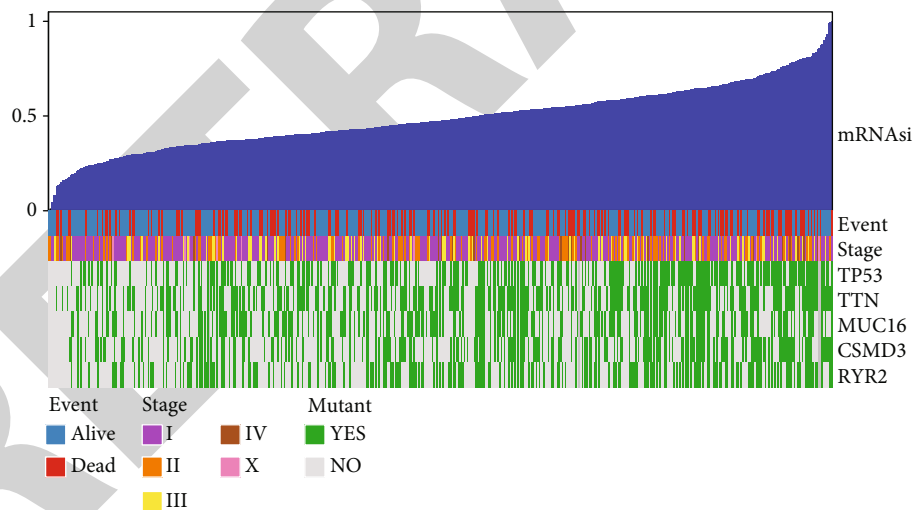
FIGURE 4: Clinical data and mutation trends for LUAD samples with different mRNAsi.

3.2. Associations of mRNAsi with Mutations. The somatic mutation spectrum of LUAD patients was analyzed by maf-tools. Figure 3(a) shows the top 10 most frequently genes (KRAS, TTN, TP53, MU16, ZFHX4, Ush2a, CSMD3, LRP1b, RyR2, and XIRP2); here, the gene showing the most frequent mutation was TP53. The mRNAsi differences of each gene between the mutated and nonmutated samples were further analyzed, and the mRNAsi of TTN-, LRP1B-, TP53-, CSMD3-, ZFHX4-, MU16-, USH2A-, XIRP2-, and RyR2-mutated samples were greatly higher than that of non-

mutated samples (Figures 3(b)–3(j))3. To further examine the relationship between mRNAsi of tumor samples and clinical features and molecular mutations, tumor samples were arranged according to mRNAsi from low to high, and the clinical data and mutation trends of different samples with mRNAsi were compared. The results demonstrated that the mortality and AJCC stage of patients were increased with the increase of mRNAsi. In addition, a higher mRNAsi was indicative of more frequent mutations of CSMD3, TTN, MU16, RyR2, and TP53 (Figure 4).

(a)

(b)
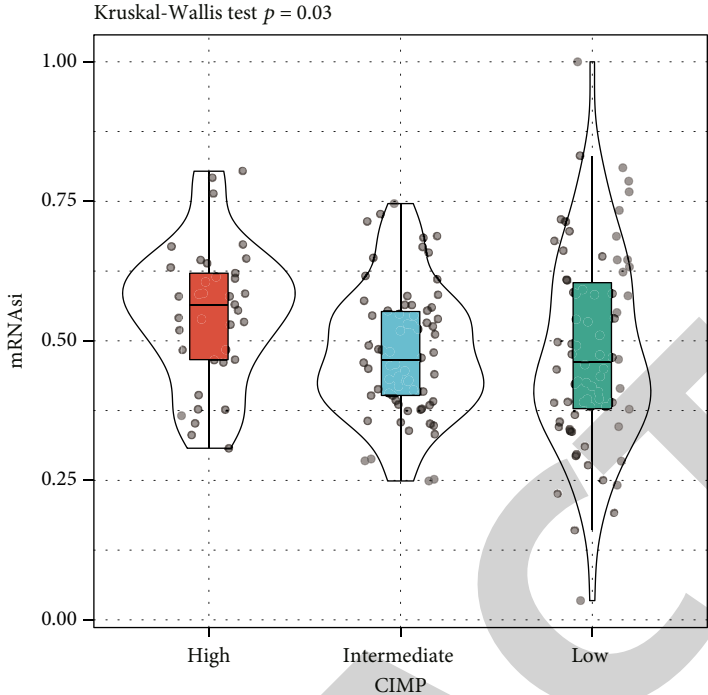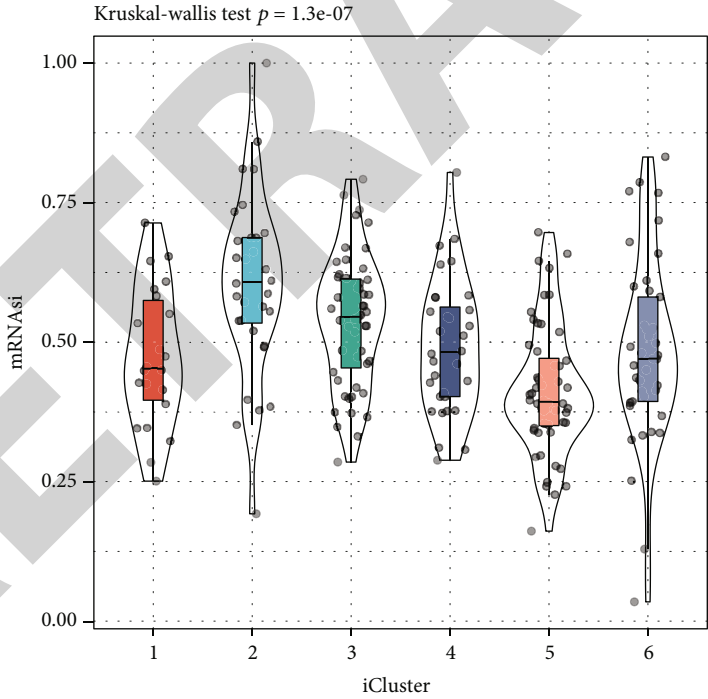
Figure 5: Continued.

(c)

(d)

Figure 5: Continued.

$R = -0.518$
$P = 1.49e-36$

(e)
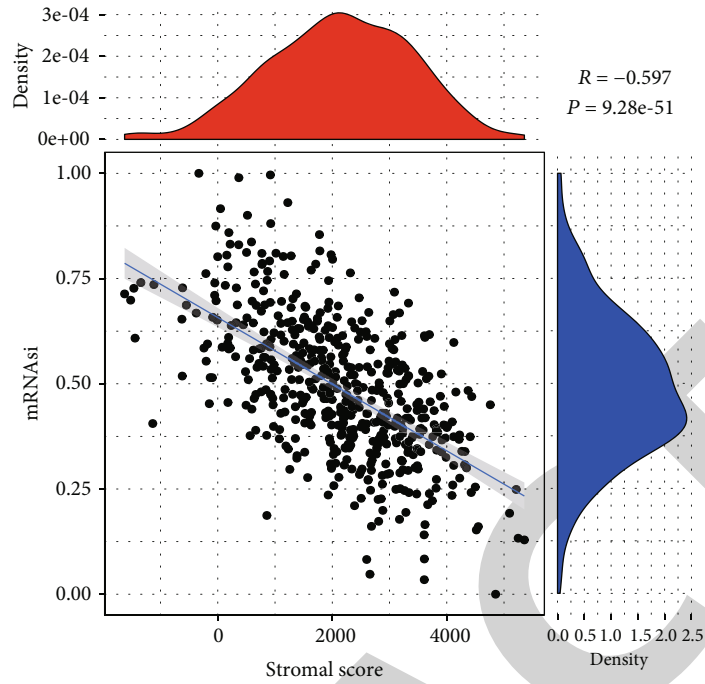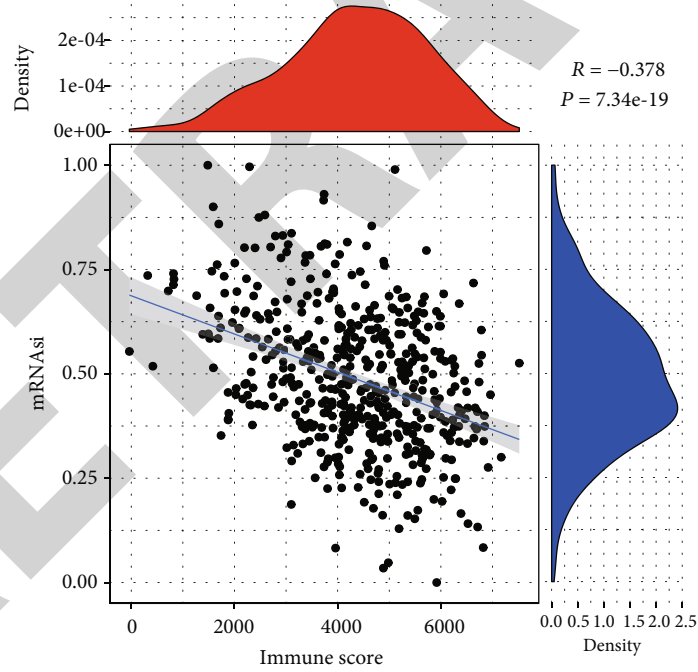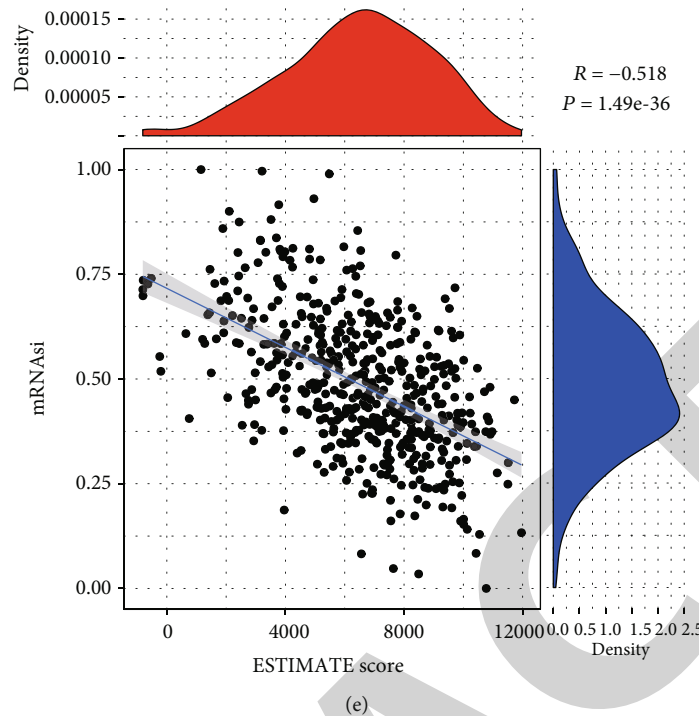
Figure 5: Correlation of mRNAsi with molecular subtypes and tumor immunity. (a) mRNAsi differences between LUAD samples classified according to CIMP. (b) mRNAsi differences among molecular subtypes identified by iCluster. (c) Correlativity between mRNAsi and stromal score of LUAD samples in TCGA. (d) Pertinent analysis between mRNAsi and immune score of LUAD samples in TCGA. (e) Correlation analysis between mRNAsi and ESTIMATE score of LUAD samples in TCGA.

3.3. Correlation of mRNAsi with Molecular Subtypes and Tumor Immunity. To understand the mRNAsi differences between subtype groupings, LUAD samples were grouped according to CpG Island methylator phenotype (CIMP) or iCluster [22]. According to CIMP, the LUAD samples were divided into three subtypes, and significant differences in mRNAsi among the three subtypes were observed (Figure 5(a)). iCluster analysis detected six clusters in LUAD, with significant differences in mRNAsi among them (Figure 5(b)). We also investigated the association of mRNAsi with tumor immunity. ESTIMATE software (https://sourceforge.net/projects/estimateproject/) package was employing for immune and matrix score determination of LUAD samples, and Pearson's correlation analysis showed that in LUAD, ESTIMATE score, immune score, and stromal score were significantly negatively linked to mRNAsi (Figures 5(c)–5(e)), indicating that mRNAsi was involved in tumor immunity.

3.4. Filtering mRNAsi-Related Gene Modules and Their Functions. WGCNA developed the coexpression network for identifying mRNAsi-related modules. Correlation coefficient in this study was >0.85 when $\beta = 6$ (Figure 6(a)). Therefore, a soft threshold of 6 was employed to establish a scale-free network; here, we obtained 14 gene modules (Figure 6(b)). The correlation of each module to LUAD patients' age, T stage, gender, smoking, N stage, AJCC stage, M stage, mRNAsi was analyzed; here, the blue module is the most associated with mRNAsi (Figure 6(c)). The biological processes involved in the blue module were explored using Gene Ontology (GO) and Kyoto Encyclopedia of Genes and Genomes (KEGG). The blue module was found to be largely implicated in cell mitogen-related pathways, including organelle fission, ribonucleoprotein complex biogenesis, and ncRNA metabolic process (Figure 6(d)). From KEGG analysis, the blue module was mainly concentrated with DNA replication, homologous recombination, base excision repair, etc. (Figure 6(e)).

3.5. Construction of the 5-Gene Signature Based on mRNAsi-Related Genes. A total of 2297 genes were extracted from the blue module by univariate Cox analysis, and 268 survival-related genes in LUAD were retained (Table S2). Nine prognosis-associated genes for LUAD patients were identified with LASSO Cox. According to AIC, 4 genes were eliminated, while the remaining 5 genes were used to build prognostic signature: Risk score = 0.117 ∗ PKP2 + 0.340 ∗ GNPNAT1 + 0.299 ∗ H2AFX + 0.263 ∗ TLE1 + 0.459 ∗ AVEN (Figure S1). TCGA training set samples were classified into two risk groups (low and high) through calculating each sample's risk score using the 5-gene signature (Figure 7(a)). Survival analysis revealed a better prognosis of low-risk LUAD patient group (Figure 7(b)). For 1-year, 3-year, and 5-year OS, the AUC of the risk score was 0.7, 0.76, and 0.65, respectively (Figure 7(c)).

3.6. Internal and External Verification of the 5-Gene Signature. To assess the prediction of the 5-gene signature,

(a)

(b)

FIGURE 6: Continued.

Module−trait relationships

	Gender	Age	T Stage	N Stage	M Stage	Stage	Smoking	mRNAsi
Green	−0.063 (0.2)	0.053 (0.2)	0.054 (0.2)	0.081 (0.07)	0.026 (0.6)	0.049 (0.3)	−0.045 (0.3)	−0.47 (2e−28)
Magenta	−0.11 (0.01)	0.11 (0.02)	−0.072 (0.1)	0.02 (0.7)	0.064 (0.2)	−0.022 (0.6)	−0.046 (0.3)	−0.64 (4e−58)
Red	−0.089 (0.05)	0.16 (6e−04)	−0.019 (0.7)	−0.0017 (1)	−0.00053 (1)	−0.043 (0.3)	−0.021 (0.6)	−0.32 (2e−13)
Black	−0.12 (0.009)	0.15 (6e−04)	−0.15 (9e−04)	−0.063 (0.2)	0.049 (0.3)	−0.14 (0.002)	0.014 (0.8)	−0.28 (4e−10)
Yellow	0.027 (0.5)	−0.049 (0.3)	0.093 (0.04)	0.03 (0.5)	−0.21 (3e−06)	0.12 (0.006)	−0.008 (0.9)	0.41 (4e−21)
Tan	0.019 (0.7)	−0.11 (0.01)	0.15 (6e−04)	0.12 (0.01)	−0.049 (0.3)	0.14 (0.002)	−0.025 (0.6)	0.31 (4e−12)
Purple	−0.044 (0.3)	0.017 (0.7)	−0.12 (0.01)	−0.021 (0.6)	0.09 (0.05)	−0.072 (0.1)	−0.093 (0.04)	−0.3 (2e−11)
Pink	−0.02 (0.7)	−0.066 (0.1)	0.025 (0.6)	0.014 (0.8)	0.015 (0.7)	0.033 (0.5)	−0.082 (0.07)	0.066 (0.1)
Brown	−0.024 (0.6)	−0.06 (0.2)	−0.098 (0.03)	−0.069 (0.1)	0.092 (0.04)	−0.075 (0.1)	−0.13 (0.005)	−0.12 (0.006)
Greenyellow	−0.048 (0.3)	0.00052 (1)	−0.12 (0.006)	−0.075 (0.1)	0.18 (8e−05)	−0.13 (0.005)	−0.12 (0.01)	−0.078 (0.08)
Salmon	0.03 (0.5)	−0.076 (0.09)	0.07 (0.1)	0.018 (0.7)	−0.041 (0.4)	0.031 (0.5)	−0.0038 (0.9)	0.35 (1e−15)
Turquoise	−0.02 (0.7)	0.022 (0.6)	0.019 (0.7)	0.03 (0.5)	0.077 (0.09)	−0.039 (0.4)	−0.055 (0.2)	0.094 (0.04)
Blue	0.1 (0.03)	−0.097 (0.03)	0.12 (0.009)	0.055 (0.2)	−0.054 (0.2)	0.13 (0.006)	−0.059 (0.2)	0.66 (1e−62)
Grey	−0.051 (0.3)	0.048 (0.3)	0.049 (0.3)	0.033 (0.5)	−0.04 (0.4)	0.025 (0.6)	−0.12 (0.009)	0.00066 (1)

(c)

FIGURE 6: Continued.

(d)

Figure 6: Continued.

(e)
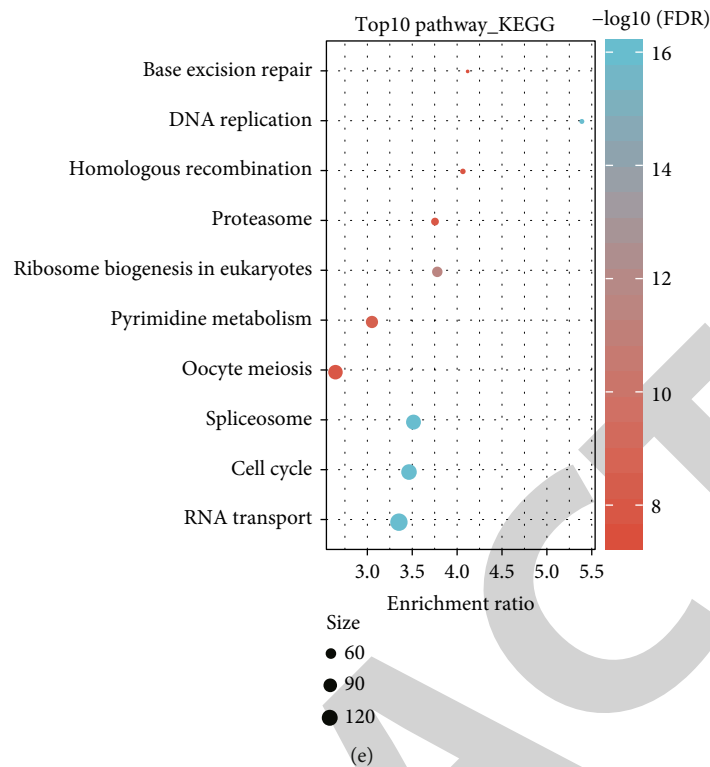
Figure 6: Identification of gene module associated with mRNAsi. (a) Analysis of network topology for various soft-thresholding powers. (b) Hierarchical clustering tree bases on the topological overlap dissimilarity. (c) Correlation between 14 gene modules and gender, age, T stage, N stage, M stage, AJCC stage, smoking, and mRNAsi. (d) Go analysis of the blue modules. (e) KEGG analysis of blue module.

further validation was performed in four queues (TCGA validation set, complete TCGA-LUAD data set, GSE31210, and GSE50081). According to the risk score, cohort samples were categorized into two groups (low and high) (Figure 8(a)). We found that in TCGA validation set, complete TCGA-LUAD dataset, GSE31210, and GSE50081, prognosis of LUAD patients with a low risk was greatly better than high-risk ones with significant differences (Figure 8(b)). From the ROC analysis on the AUCs of long-term survival, we found that the 5-year survival was higher than 0.6 in the four cohorts (Figure 8(c)). These results confirmed that the 5-gene signature predicted LUAD survival accurately.

3.7. Independent Prediction of the 5-Gene Signature in LUAD Prognosis. We explored the relationship of risk score to clinical characteristics, such as M stage, gender, T stage, AJCC, age, N stage, and smoking. As shown in Figure 9, all of these clinical characteristics showed a close relation to the risk score. For verifying the effectiveness of 5-gene signature, stratified analysis was conducted on age (age > 65 and age ≤ 65), AJCC stage (stage III-IV, stage I-II), gender (male and female), M stage (N2-N3 and N0-N1), T stage (T3-T4, T1, and T2), and N stage (M0). The results verified an effective OS prediction of the risk model in almost all subgroups apart from N2-N3 stage patients (Figure 10). Next, a nomogram was established through combining gender, age, risk score, AJCC stage, and T stage. Here, the risk score showed the greatest impact on the pre-

diction of OS (Figure S2A). Moreover, AJCC stage and risk score were independent prognostic factors for LUAD, as verified by the data from univariate and multivariate Cox analysis (Table 2).

3.8. The 5-Gene Signature Outperformed the Other Three Signatures in Predicting the Performance of the OS. We also compared the 5-gene signature with three previously developed signatures [23–29]. TCGA samples' risk score were, respectively, determined using the seven signatures, and accordingly, all patients were divided to two risk groups (low and high). The survival analysis revealed a significant prognosis difference in the two groups (Figures 11(a), 11(c), 11(e), 11111111). ROC curve of the seven signatures showed that the AUCs for the survival in 1, 3, and 5 year(s) were both lower than 0.75 and the average AUC of OS predicted by our 5-gene signature (Figures 11(b), 11(d)11(f), 11111111), which indicated a high accuracy and performance of our signature.

3.9. Functional Analysis and Immune Correlation Analysis of 5-Gene Signature. In order to clarify the potential regulatory mechanism of 5-gene signature, we used ssGSEA method to calculate the KEGG pathway enrichment score of each patient and further calculated the correlation between 5-gene signature and each pathway. We can observe the relationship between 5-gene signature and p53_SIGNALING_ PATHWAY, MISMATCH_REPAIR, DNA_REPLICA-TION, and CELL_Cycle, and other pathways were

(a)

(b)

(c)
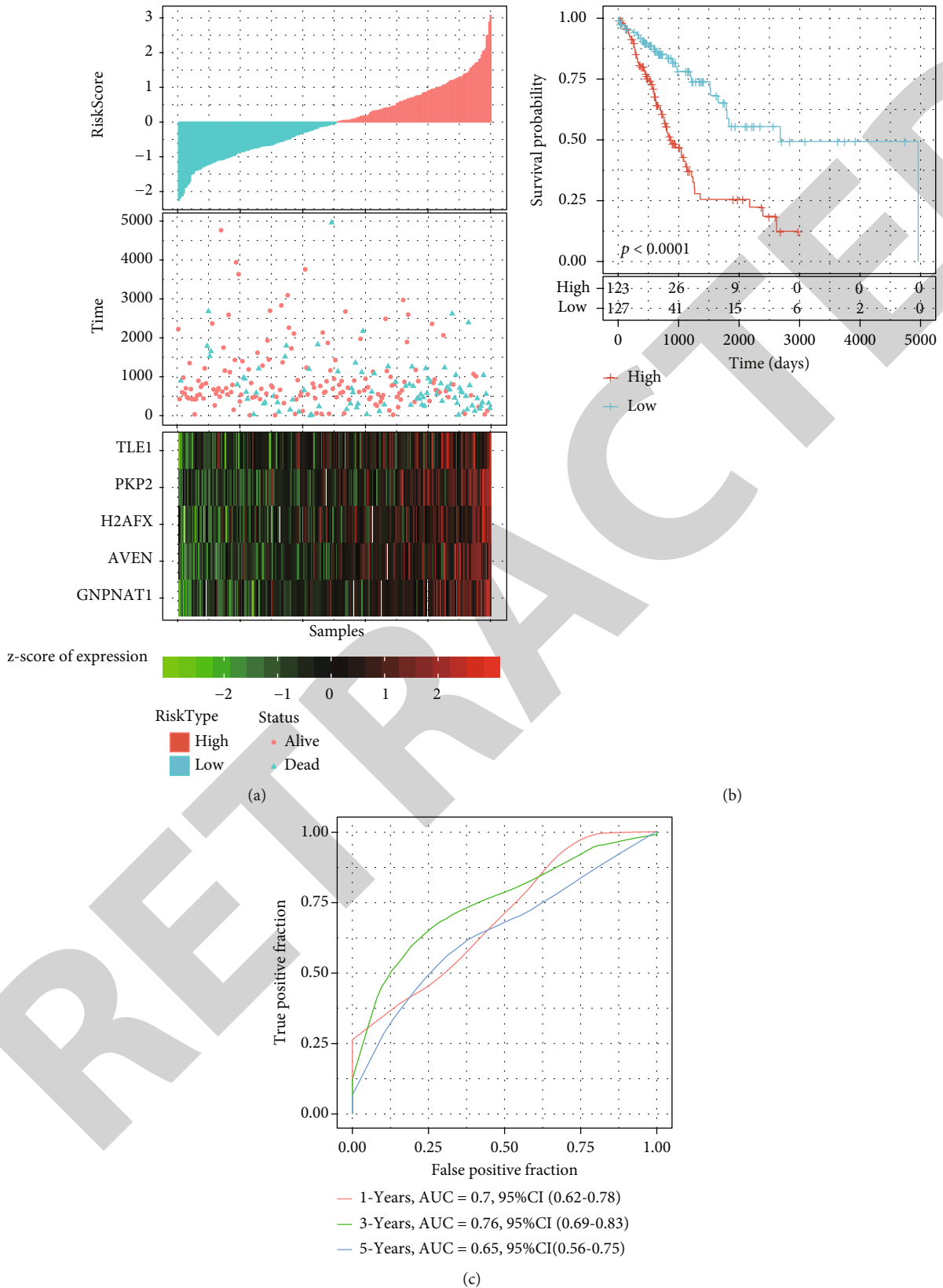
Figure 7: Construction of 5-gene signature on account of mRNAsi-related genes. (a) In TCGA training set, distribution of the risk score, survival data, and the mRNA expression of prognosis signature. (b) Survival curves of LUAD patients in a TCGA training set. (c) ROC analysis for OS prediction in TCGA training set.
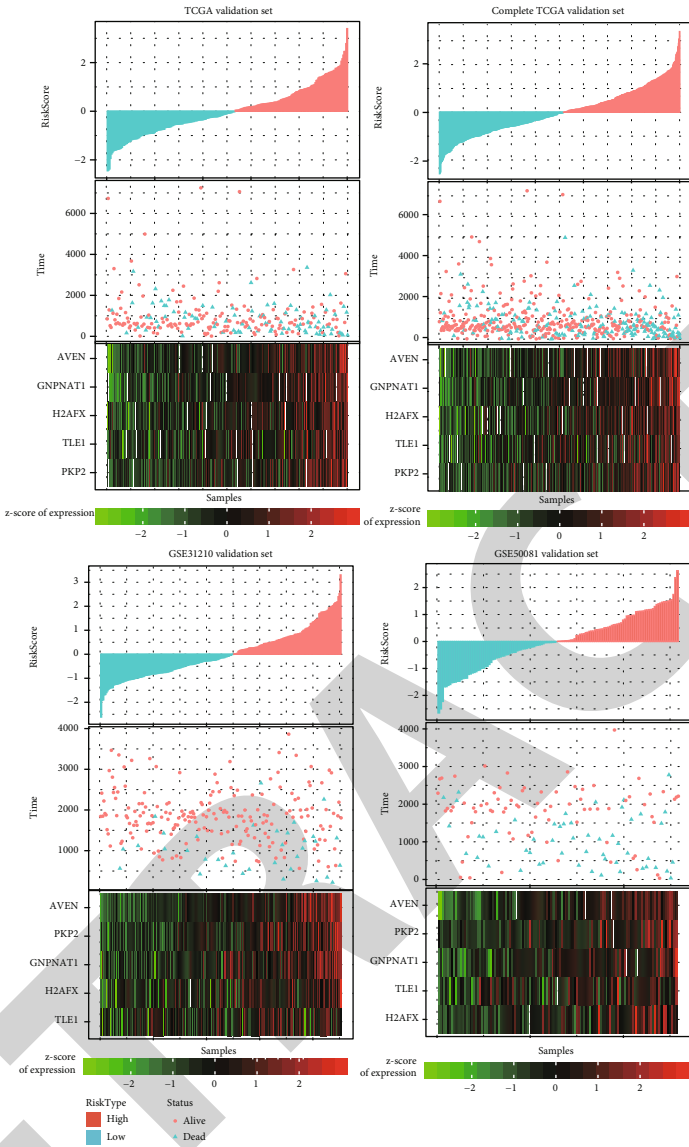
(a)

FIGURE 8: Continued.

(b)

Figure 8: Continued.

(c)
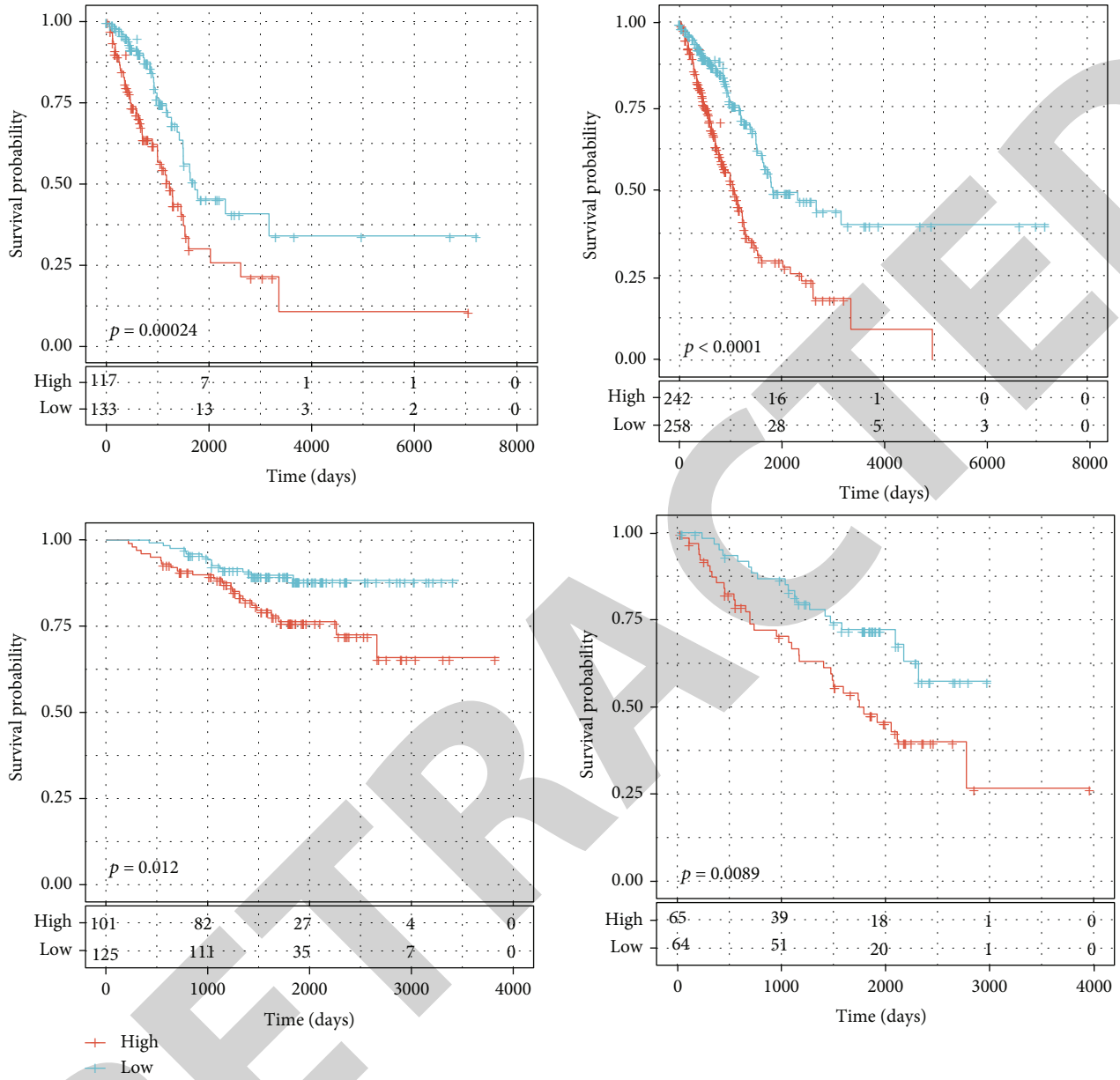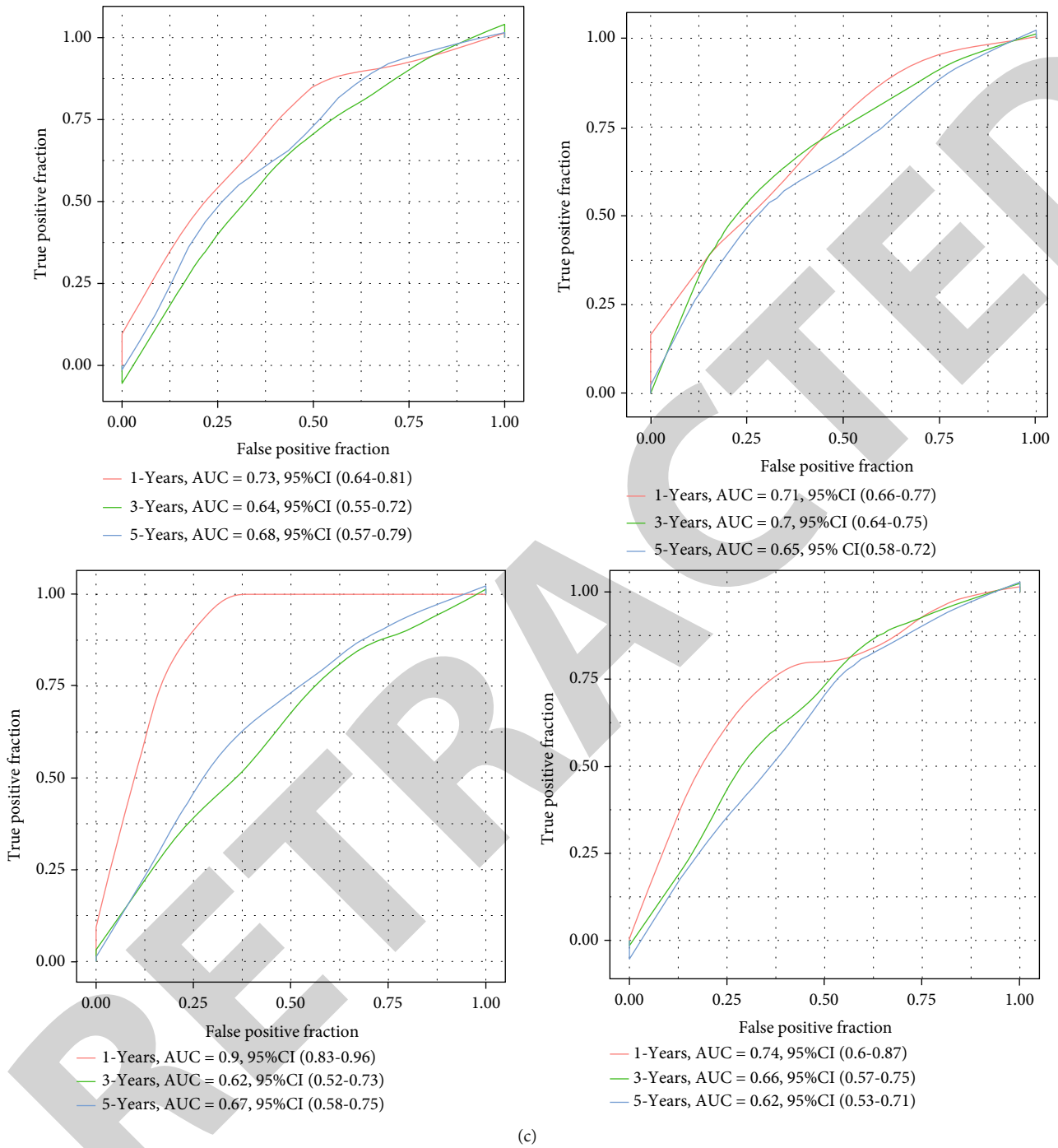
Figure 8: Internal and external verification of 5-gene signature. (a) Distribution of the risk score, survival data, and the mRNA expression of prognosis signature in different cohorts. (b) Survival curves of patients with LUAD in different cohorts in the high-risk and low-risk groups. (c) Time-dependent ROC analysis for OS prediction in four cohorts.

significantly positively correlated with Fatty_ACID_ METABOLISM and ARACHIDONIC_ACID_Metabolism, and other metabolic pathways were significantly negatively correlated (Figure S3A). In addition, we also observed a significant positive correlation between 5-gene signature and mRNAsi (Figure S3B) and a significant negative correlation between 5-gene signature and immune infiltration (Figure S3C-E). The five genes contained in 5-gene signature were significantly overexpressed in tumor samples (Figure S3F). We also analyzed the correlation between the expression of five genes contained in 5-gene signature and mRNAsi. It can be observed that except TLE1 gene, the other four genes showed significant positive correlation with mRNAsi (Figure S3J-K).
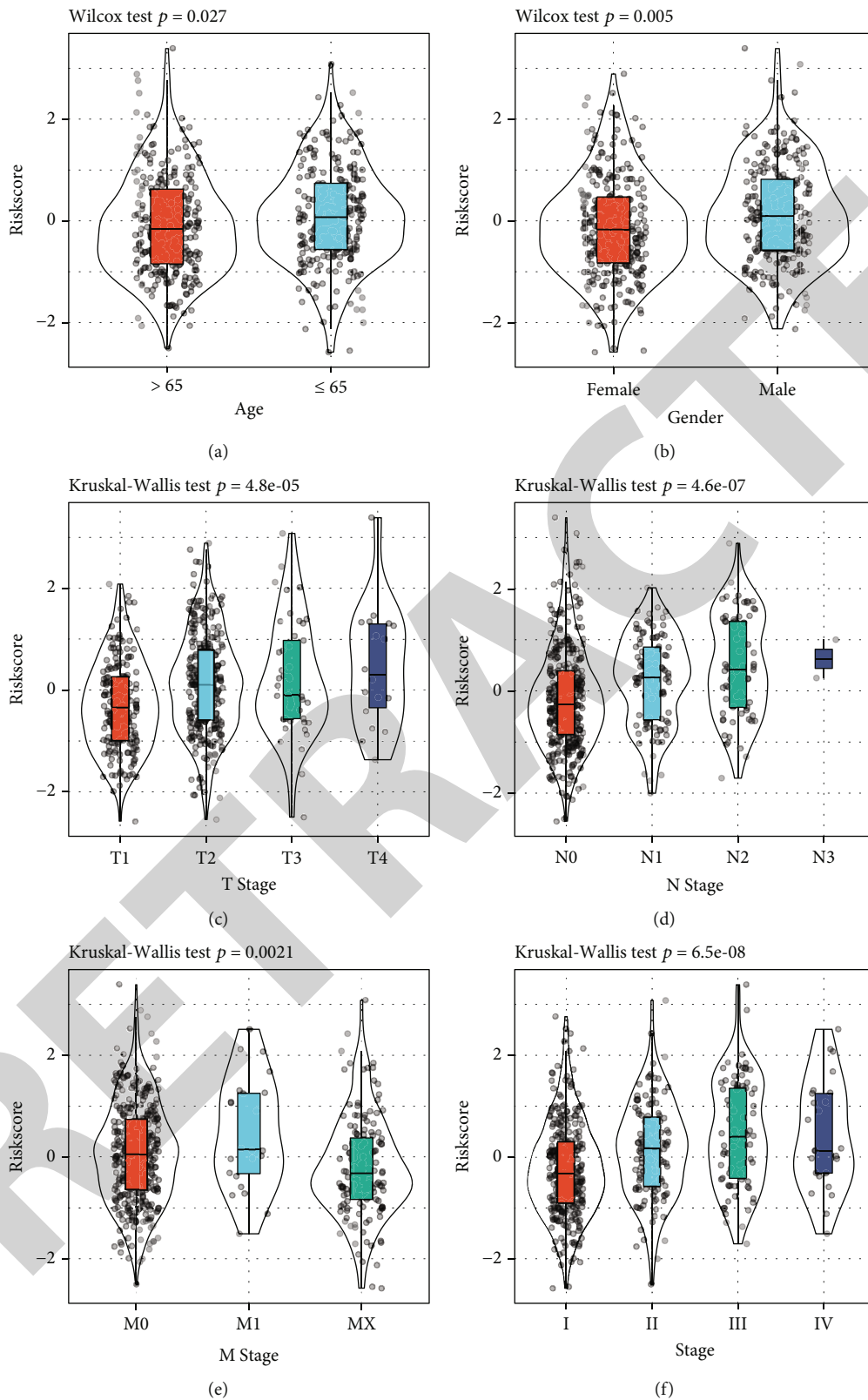
Figure 9: Continued.
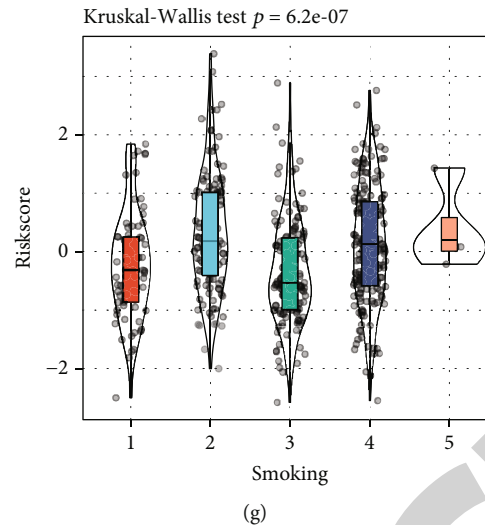
Figure 9: Correlation between risk score and each clinicopathologic feature. A t-test or one-way ANOVA determined the correlation between risk score and age (a), gender (b), T stage (c), N (d), M stage (e), AJCC stage (f), and smoking (g), respectively.

4. Discussion

Local and/or systemic treatment of LUAD has been greatly improved, but posttreatment recurrence is still relatively frequent [30]. The regrowth of such tumors after treatment is now thought to be dependent on a few CSCs [31]. Ongoing trials demonstrated that anti-CSC therapy can increase tumor response to chemotherapy and improve patient outcomes [8]. As CSCs consist of a variety of heterogeneous phenotypes rather than a single cell type, predicting the effectiveness of a specific therapy to target CSC could be difficult. Therefore, CSC-specific regulatory pathways or markers that are characteristic of LUAD should be developed along with anti-CSC therapies [32]. Here, we evaluated the CSC characteristics of LUAD samples based on mRNAsi and calculated mRNAsi for each sample in TCGA database using OCLR. Previous studies have shown that compared with normal tissue, mRNAsi is significantly higher in tumor tissues such as breast cancer tissue [33], gastric cancer tissue [34], liver cancer tissues [35], and lung squamous cell carcinoma [36]. At this point, the analytical data revealed a significantly lower mRNAsi in nontumor tissues than LUAD tissues and that mRNAsi showed great differences in M stage, N stage, smoking, AJCC stage, and T stage. Multiple studies demonstrated that LUAD had a high rate of somatic mutation and genome rearrangement [22]. In recent years, a number of somatic mutations occurring in LUAD, including TP53, KRAS, PIK3CA, and MET, have been discovered [37]. Our work found that TP53 was the gene with the highest mutation frequency in LUAD, which was also consistent with previous studies. It is reported that TP53 mutation had a negative impact on cancer prognosis and is associated with a shorter survival time [38]. The status of TTN mutation can be applied to independently evaluate immunotherapy prognosis of LUAD patients [39]. Loss of CSMD3 function resulted from somatic mutations can stimulate the oncogenic transformation of airway epithelial cells [40]. RYR2 has been considered a mutated driver of lung cancer

[41]. Somatic mutations of LRP1B are linked to lung tumor mutation load [42]. Here, a higher mRNAsi was correlated with more frequent mutations of XIRP2, MU16, ZFHX4, CSMD3, TTN, USH2A, TP53, RyR2, and LRP1B, without significant mRNAsi difference in mutant KRAS or wild-type KRAS.

A study found that CSCs can shape immune microenvironment of tumors, and in turn, the functional and phenotypic characteristics of tumor-infiltrating immune cells could affect the phenotype and differentiation of tumor cells [43]. This study then explored the association of tumor immunity to mRNAsi and confirmed that mRNAsi was closely correlated with ESTIMATE score, immune score, and stromal score of LUAD. Then, WGCNA showed that blue module was found to have the strongest correlation with mRNAsi; moreover, the module was mainly involved in pathways related to cell division. The accumulation of cell division of stem cells will lead to cancer development [44].

Based on the blue module, we developed a 5-gene signature and verified its reliability and independence in four cohorts. Previous studies reported the role of five genes in LUAD. It has been found that high-expressed PKP2 could result in a poor LUAD prognosis. Functionally, PKP2 knockdown inhibits the invasion, proliferation of lung cancer cells *in vitro*, and xenograft lung tumor growth *in vivo* [45]. GNPNAT1 has been detected to be significantly higher in LUAD in comparison with normal ones and is linked to tumor size, lymphatic metastasis status, and clinical stage of the patients [46]. GNPNAT1 is associated with prognosis and immune infiltration in LUAD [47]. H2AFX, which is considered one of the key genes related to mRNAsi, is also associated with the prognosis and cell cycle of LUAD [48]. TLE1 is identified as a lung-specific oncogene that regulates the EMT of A549 cells through inhibiting E-cadherin [49]. Aven has critical functions in cancer cell response to radiation therapy [50]. However, heterogeneity of LUAD will reduce the reliability of a single gene than the use of a combination of multiple genes.

(a)

(b)

(c)

(d)
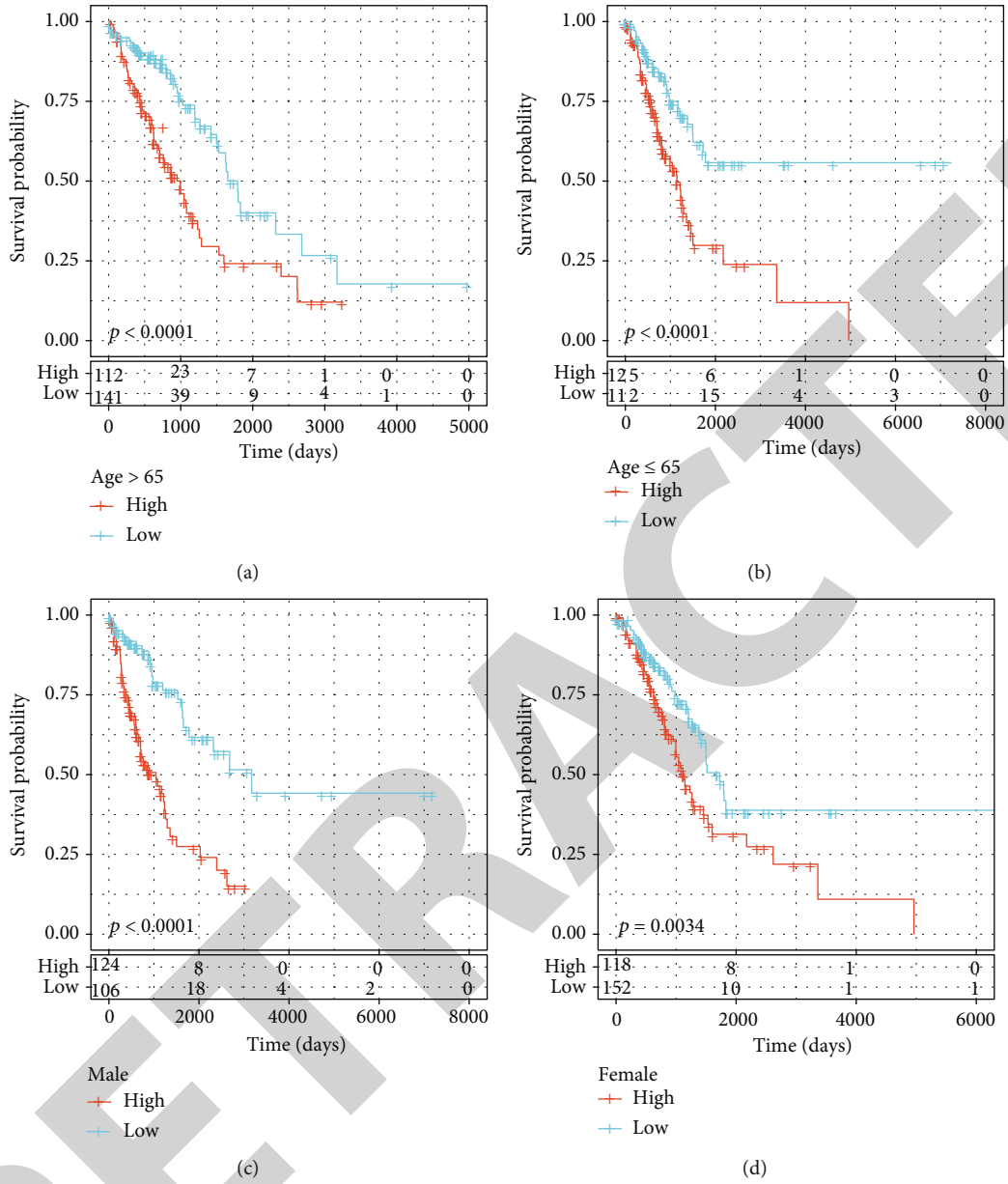
Figure 10: Continued.
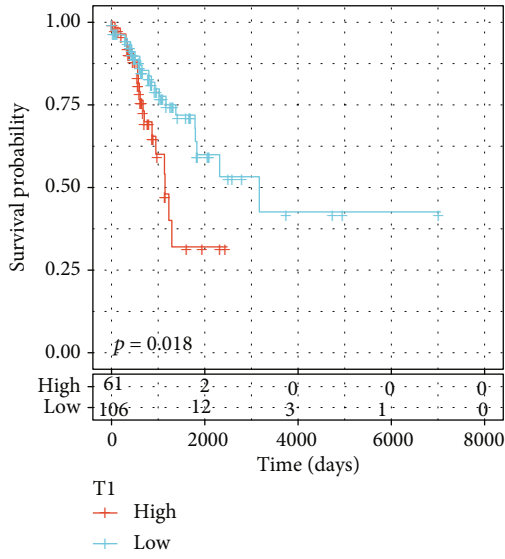
(e)
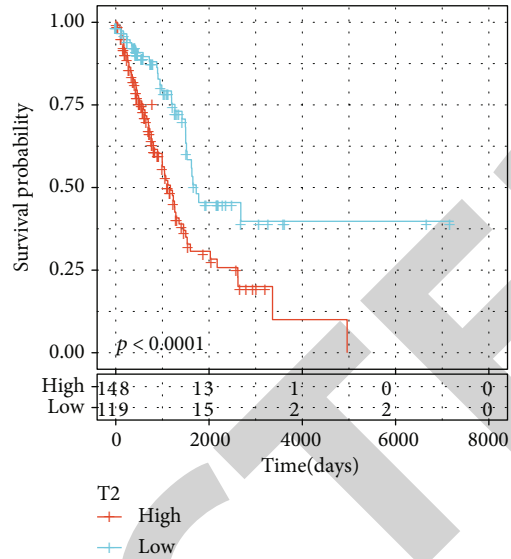
(f)
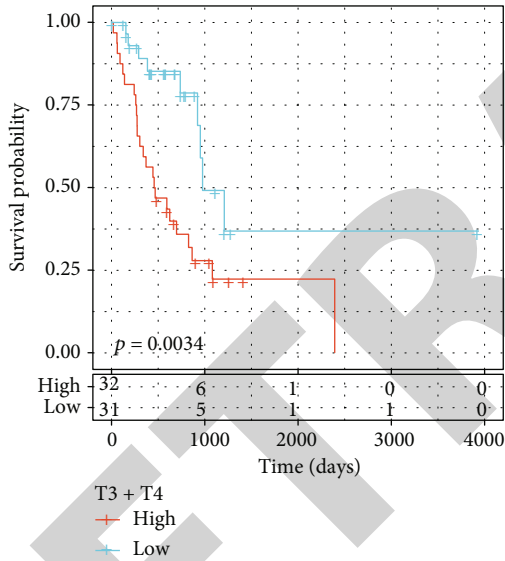
(g)
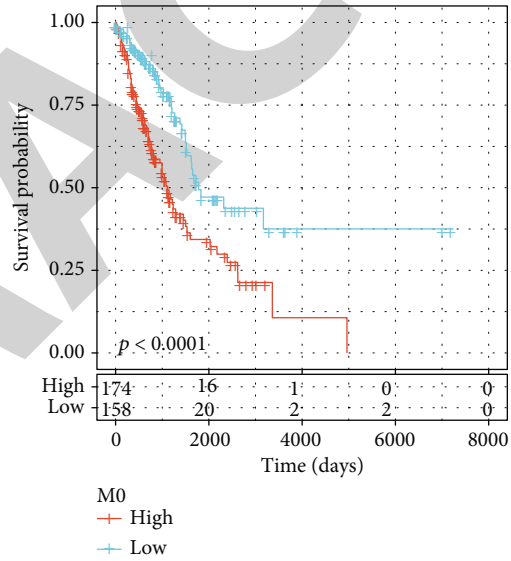
(h)

Figure 10: Continued.

(i)

(j)

(k)

(l)
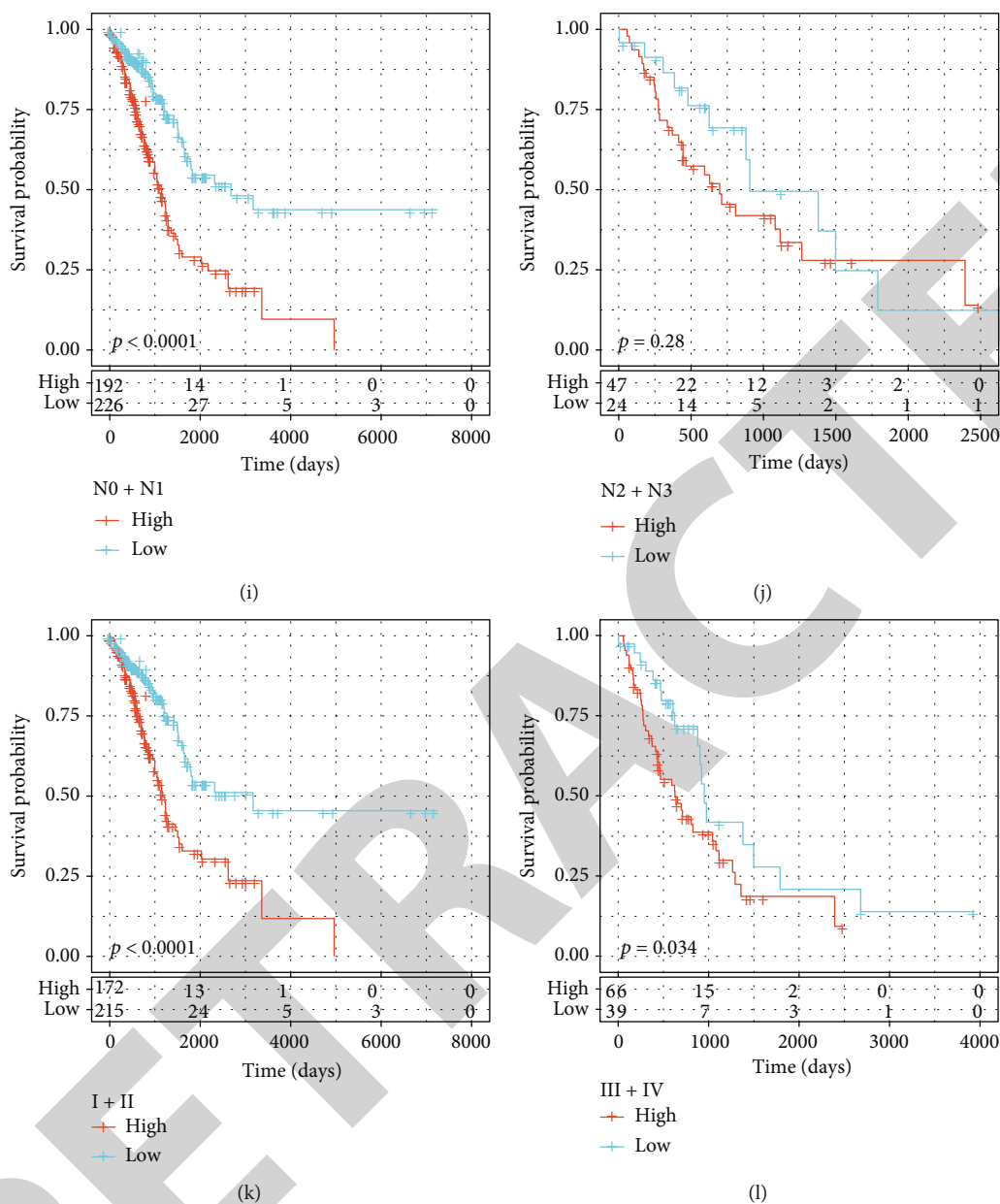
Figure 10: Kaplan-Meier stratification survival analyses in TCGA-LUAD data set, including age $\geq$ 65 (a), age $\leq$ 65 (b), male (c), female (d), T1 (e), T2 (f), T3-T4 (g), M0 (h), N0-N1 (i), N2-N3 (j), stage I-II (k), and stage III-IV (l).

Table 2: Univariate and multivariate Cox analysis of all LUAD samples in TCGA dataset.

| Variables | Univariable analysis | | | | Multivariable analysis | | | |
| | HR | 95% CI of HR | | P | HR | 95% CI of HR | | P |
		Lower	Upper			Lower	Upper	
Age	1.008	0.993	1.024	0.299	1.014	0.999	1.030	0.065
Gender	1.048	0.783	1.403	0.753	0.978	0.727	1.317	0.884
T stage	1.514	1.275	1.797	$2.3E - 06$	1.180	0.979	1.421	0.082
Stage	1.437	1.277	1.617	$1.7E - 09$	1.289	1.122	1.480	$3.3E - 04$
Risk score	1.739	1.509	2.004	$2.2E - 14$	1.737	1.489	2.025	$2.0E - 12$

(a)

- 1-Years, AUC = 0.71, 95%CI (0.65-0.77)
- 3-Years, AUC = 0.66, 95%CI (0.61-0.72)
- 5-Years, AUC = 0.65, 95%CI (0.58-0.73)

(b)

(c)

- 1-Years, AUC = 0.68, 95%CI (0.62-0.74)
- 3-Years, AUC = 0.65, 95%CI (0.6-0.71)
- 5-Years, AUC = 0.63, 95%CI (0.55-0.7)
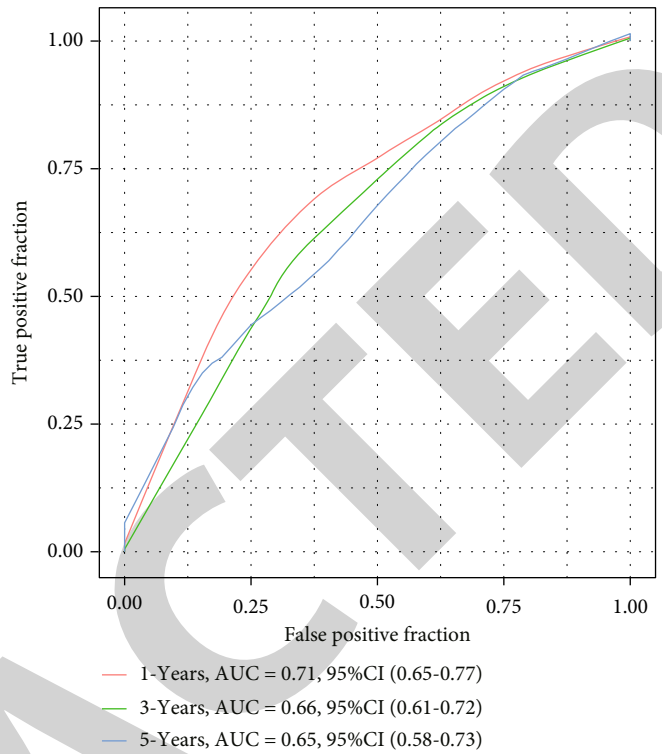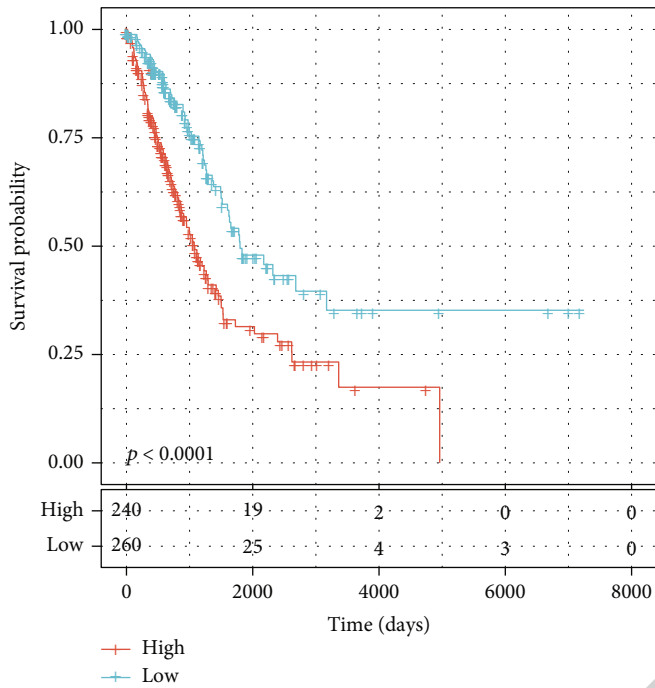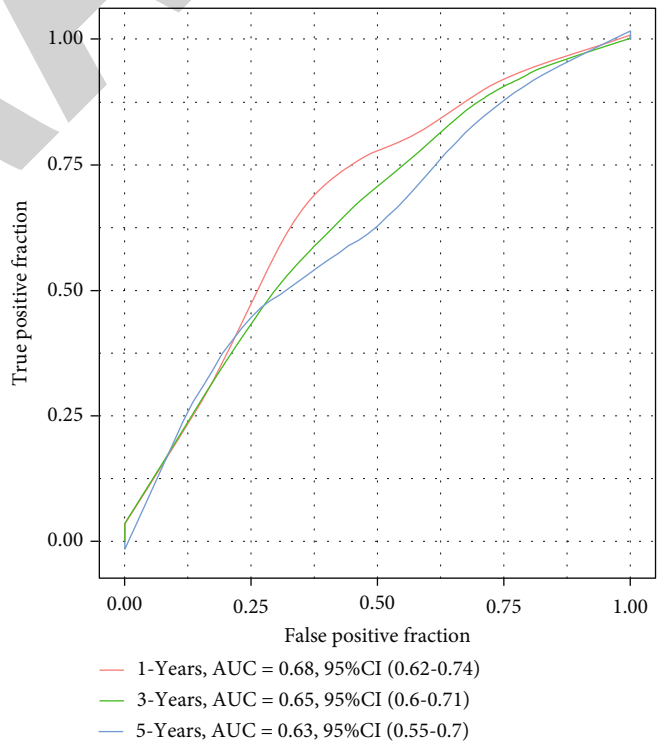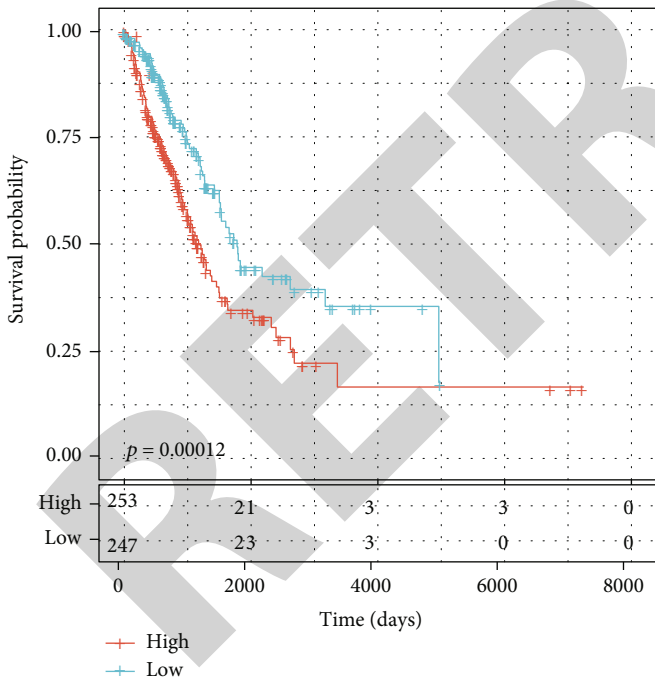
(d)

Figure 11: Continued.

(e)

(f)
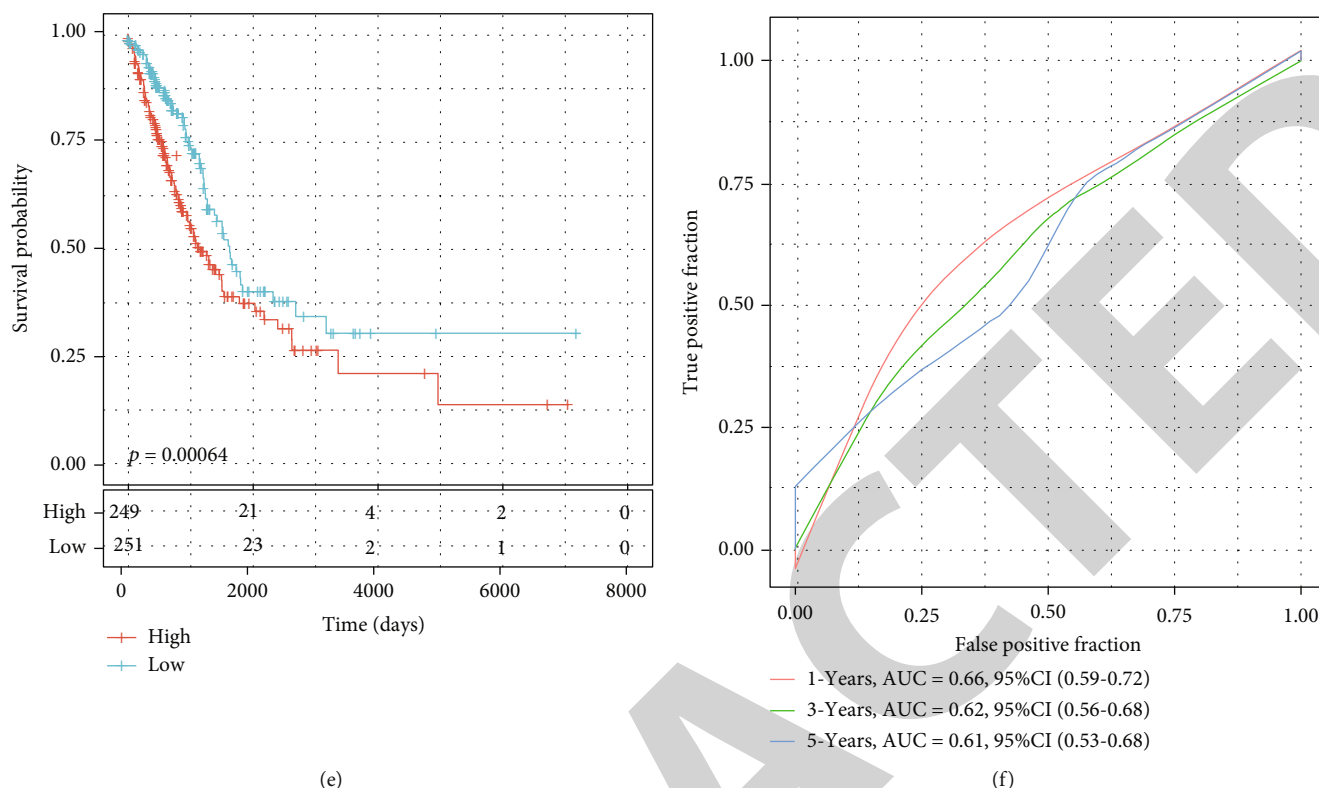
FIGURE 11: Five-gene signature outperformed the other three signatures in predicting the performance of the OS. (a) Kaplan-Meier curve of prognosis in patients with TCGA-LUAD predicted by 8-gene signature. (b) ROC curve of the 8-gene signature for 1-, 3-, and 5-year OS. (c) Kaplan-Meier curve of prognosis in patients with TCGA-LUAD predicted by 3-gene signature. (d) ROC curve of the 3-gene signature for 1-, 3-, and 5-year OS. (e) Kaplan-Meier curve of 3-gene signature developed by Cheng Yue et al. for predicting prognosis of patients with TCGA-LUAD.(f) ROC curve of the 3-gene signature developed by Yue et al. for 1-, 3-, and 5-year OS. (g) Kaplan-Meier curve for predicting the OS of TCGA-LUAD patients based on the 6-gene risk model developed by Wang et al. (h) ROC curve analysis showing the prognostic prediction efficiency of the risk model. (i) Kaplan-Meier curve for predicting the OS of TCGA-LUAD patients based on the 7-gene risk model developed by Al-Dherasi et al. (j) ROC curve analysis showing the prognostic prediction efficiency of the 7-gene risk model.

The present work performed a comprehensive study of LUAD patients based on mRNAsi, screened the blue modules most associated with mRNAsi by WGCNA, and developed 5-gene signature for OS prediction of LUAD. The 5-gene signature showed a higher AUC in short-term OS prediction in both validation and training sets but was much lower in long-term prediction, suggesting that 5-gene signature is more suitable for predicting short-term survival of LUAD. Another limitation of this study was that all our data came from TCGA database, which lacked comprehensiveness. Moreover, biological experiments (*in vitro* and *in vivo*) should be conducted for result verification and further exploration, which will be conducted in our future study with systematic biological studies.

Data Availability

The datasets used in this study were openly available at GSE31210 (https://www.ncbi.nlm.nih.gov/geo/query/acc .cgi?acc=GSE31210) and GSE50081 (https://www.ncbi.nlm .nih.gov/geo/query/acc.cgi).

Conflicts of Interest

The authors declare no conflict of interests.

Authors' Contributions

JW and THM designed the study. RPW and HLL contributed to the literature research. JTL analyzed and interpreted the data. LZ wrote the initial manuscript. YQY reviewed and edited the paper. All authors read and approved the manuscript. Renping Wan and Jie Wei contributed equally to this work.

Supplementary Materials

Supplementary 1. Figure S1: screening of genes associated with the prognosis of LUAD; A, B: Lasso Cox analysis. C: survival curves of LUAD samples with high and low expression of PKP2. D: GNPNAT1 expression was associated with LUAD survival. E: survival analysis of patients with high and low expression of H2AFX. F: survival analysis of patients with high and low expression of TLE1. G: Kaplan-Meier curves of patients with high and low expressed AVEN.

Supplementary 2. Figure S2: nomogram based on age, gender, T stage, and AJCC stage combined with risk score.

Supplementary 3. Figure S3: functional analysis and immune correlation analysis of 5-gene signature; A: KEGG pathway significantly related to 5-gene signature; B: scatter plot of correlation between 5-gene signature and mRNAsi; C-E: correlation between 5-gene signature and immune infiltration score; F: the expression and distribution of five genes in 5-gene signature were different between cancer and adjacent cancer; G-K: scatter plot of correlation between five genes in 5-gene signature and mRNAsi.

Supplementary 4. Table S1: clinical information of samples in different cohorts.

Supplementary 5. Table S2: univariate Cox analysis of 2297 genes.

References

[1] B. D. Hutchinson, G. S. Shroff, M. T. Truong, and J. P. Ko, "Spectrum of lung adenocarcinoma," *Seminars in Ultrasound, CT, and MR*, vol. 40, no. 3, pp. 255–264, 2019.

[2] C. Zappa and S. A. Mousa, "Non-small cell lung cancer: current treatment and future advances," *Translational Lung Cancer Research*, vol. 5, no. 3, pp. 288–300, 2016.

[3] T. V. Denisenko, I. N. Budkevich, and B. Zhivotovsky, "Cell death-based treatment of lung adenocarcinoma," *Cell Death & Disease*, vol. 9, no. 2, p. 117, 2018.

[4] M. Spella and G. T. Stathopoulos, "Immune resistance in lung adenocarcinoma," *Cancers*, vol. 13, no. 3, p. 384, 2021.

[5] L. Barbato, M. Bocchetti, A. Di Biase, and T. Regad, "Cancer stem cells and targeting strategies," *Cell*, vol. 8, no. 8, p. 926, 2019.

[6] Y. Garcia-Mayea, C. Mir, F. Masson, R. Paciucci, and M. E. LLeonart, "Insights into new mechanisms and models of cancer stem cell multidrug resistance," *Seminars in Cancer Biology*, vol. 60, pp. 166–180, 2020.

[7] S. Shukla, S. Khan, S. Sinha, and S. M. Meeran, "Lung cancer stem cells: an epigenetic perspective," *Current Cancer Drug Targets*, vol. 18, no. 1, pp. 16–31, 2018.

[8] L. Roy and K. D. Cowden Dahl, "Can stemness and chemoresistance be therapeutically targeted via signaling pathways in ovarian cancer?," *Cancers*, vol. 10, no. 8, p. 241, 2018.

[9] C. Zhang, H. Wang, X. Wang, C. Zhao, and H. Wang, "CD44, a marker of cancer stem cells, is positively correlated with PD-L1 expression and immune cells infiltration in lung adenocarcinoma," *Cancer Cell International*, vol. 20, no. 1, p. 583, 2020.

[10] X. Yan, H. Luo, X. Zhou, B. Zhu, Y. Wang, and X. Bian, "Identification of CD90 as a marker for lung cancer stem cells in A549 and H446 cell lines," *Oncology Reports*, vol. 30, no. 6, pp. 2733–2740, 2013.

[11] M. Nakatsugawa, A. Takahashi, Y. Hirohashi et al., "SOX2 is overexpressed in stem-like cells of human lung adenocarcinoma and augments the tumorigenicity," *Laboratory Investigation*, vol. 91, no. 12, pp. 1796–1804, 2011.

[12] L. Walcher, A. K. Kistenmacher, H. Suo et al., "Cancer stem cells-origins and biomarkers: perspectives for targeted personalized therapies," *Frontiers in Immunology*, vol. 11, p. 1280, 2020.

[13] T. M. Malta, A. Sokolov, A. J. Gentles et al., "Machine learning identifies stemness features associated with oncogenic dedifferentiation," *Cell*, vol. 173, no. 2, pp. 338–354.e15, 2018.

[14] T. Li, J. Chen, J. Liu, Q. Chen, W. Nie, and M. D. Xu, "A lipid metabolism-based seven-gene signature correlates with the clinical outcome of lung adenocarcinoma," *Journal of Oncology*, vol. 2022, Article ID 9913206, 18 pages, 2022.

[15] Y. Shi, Y. Xu, Z. Xu et al., "TKI resistant-based prognostic immune related gene signature in LUAD, in which FSCN1 contributes to tumor progression," *Cancer Letters*, vol. 532, article 215583, 2022.

[16] S. Zhang, X. Zeng, S. Lin, M. Liang, and H. Huang, "Identification of seven-gene marker to predict the survival of patients with lung adenocarcinoma using integrated multi-omics data analysis," *Journal of Clinical Laboratory Analysis*, vol. 36, no. 2, article e24190, 2022.

[17] I. F. do Valle, E. Giampieri, G. Simonetti et al., "Optimized pipeline of MuTect and GATK tools to improve the detection of somatic single nucleotide polymorphisms in whole-exome sequencing data," *BMC Bioinformatics*, vol. 17, Supplement 12, p. 341, 2016.

[18] A. Colaprico, T. C. Silva, C. Olsen et al., "TCGAbiolinks: an R/Bioconductor package for integrative analysis of TCGA data," *Nucleic Acids Research*, vol. 44, no. 8, article e71, 2016.

[19] P. Langfelder and S. Horvath, "WGCNA: an R package for weighted correlation network analysis," *BMC Bioinformatics*, vol. 9, no. 1, p. 559, 2008.

[20] J. Wang, S. Vasaikar, Z. Shi, M. Greer, and B. Zhang, "WebGestalt 2017: a more comprehensive, powerful, flexible and interactive gene set enrichment analysis toolkit," *Nucleic Acids Research*, vol. 45, no. W1, pp. W130–W137, 2017.

[21] J. Pei, Y. Wang, and Y. Li, "Identification of key genes controlling breast cancer stem cell characteristics via stemness indices analysis," *Journal of Translational Medicine*, vol. 18, no. 1, p. 74, 2020.

[22] "Comprehensive molecular profiling of lung adenocarcinoma," *Nature*, vol. 511, no. 7511, pp. 543–550, 2014.

[23] S. Li, Y. Xuan, B. Gao et al., "Identification of an eight-gene prognostic signature for lung adenocarcinoma," *Cancer Management and Research*, vol. 10, pp. 3383–3392, 2018.

[24] W. T. Liu, Y. Wang, J. Zhang et al., "A novel strategy of integrated microarray analysis identifies CENPA, CDK1 and CDC20 as a cluster of diagnostic biomarkers in lung adenocarcinoma," *Cancer Letters*, vol. 425, pp. 43–53, 2018.

[25] C. Yue, H. Ma, and Y. Zhou, "Identification of prognostic gene signature associated with microenvironment of lung adenocarcinoma," *PeerJ*, vol. 7, article e8128, 2019.

[26] Z. Wang, K. S. Embaye, Q. Yang et al., "Establishment and validation of a prognostic signature for lung adenocarcinoma based on metabolism-related genes," *Cancer Cell International*, vol. 21, no. 1, p. 219, 2021.

[27] A. Al-Dherasi, Q. T. Huang, Y. Liao et al., "A seven-gene prognostic signature predicts overall survival of patients with lung adenocarcinoma (LUAD)," *Cancer Cell International*, vol. 21, no. 1, p. 294, 2021.

[28] L. He, J. Chen, F. Xu, J. Li, and J. Li, "Prognostic implication of a metabolism-associated gene signature in lung adenocarcinoma," *Molecular Therapy - Oncolytics*, vol. 19, pp. 265–277, 2020.

[29] J. Jin, C. Liu, S. Yu et al., "A novel ferroptosis-related gene signature for prognostic prediction of patients with lung adenocarcinoma," *Aging*, vol. 13, no. 12, pp. 16144–16164, 2021.

[30] G. Hardavella, R. George, and T. Sethi, "Lung cancer stem cells-characteristics, phenotype," *Translational Lung Cancer Research*, vol. 5, no. 3, pp. 272–279, 2016.

Retraction

Retracted: Immunotherapy Mechanism of Esophageal Squamous Cell Carcinoma with the Effect of STK11/AMPK Signaling Pathway

BioMed Research International

This article has been retracted by Hindawi following an investigation undertaken by the publisher [1]. This investigation has uncovered evidence of one or more of the following indicators of systematic manipulation of the publication process:

(1) Discrepancies in scope

(2) Discrepancies in the description of the research reported

(3) Discrepancies between the availability of data and the research described

(4) Inappropriate citations

(5) Incoherent, meaningless and/or irrelevant content included in the article

(6) Manipulated or compromised peer review

The presence of these indicators undermines our confidence in the integrity of the article's content and we cannot, therefore, vouch for its reliability. Please note that this notice is intended solely to alert readers that the content of this article is unreliable. We have not investigated whether authors were aware of or involved in the systematic manipulation of the publication process.

Wiley and Hindawi regrets that the usual quality checks did not identify these issues before publication and have since put additional measures in place to safeguard research integrity.

We wish to credit our own Research Integrity and Research Publishing teams and anonymous and named external researchers and research integrity experts for contributing to this investigation.

The corresponding author, as the representative of all authors, has been given the opportunity to register their agreement or disagreement to this retraction. We have kept a record of any response received.

References

[1] Y. Xia, P. Wang, Y. Ye et al., "Immunotherapy Mechanism of Esophageal Squamous Cell Carcinoma with the Effect of STK11/AMPK Signaling Pathway," *BioMed Research International*, vol. 2022, Article ID 8636527, 8 pages, 2022.

Research Article

Immunotherapy Mechanism of Esophageal Squamous Cell Carcinoma with the Effect of STK11/AMPK Signaling Pathway

Yang Xia, Peng Wang, Yunyao Ye, Sihui Zhang, Guangzhi Sun, Jie Xu, and Gaohua Han [ID]

Department of Oncology, Taizhou People's Hospital, Taizhou, 225300 Jiangsu Province, China

Correspondence should be addressed to Gaohua Han; danny_75@njmu.edu.cn

This study was aimed at exploring the mechanism of serine threonine protein kinase 11 (STK11)/Adenosine $5'$-monophosphate-activated protein kinase (AMPK) signaling pathway after immunotherapy for esophageal squamous cell carcinoma (ESCC), providing basic information for the clinical treatment of ESCC. In this study, tissue specimens from 100 patients with ESCC who underwent surgical treatment in Taizhou People's Hospital (group A) and 20 patients with recurrent or metastatic ESCC who received second-line immunotherapy (group B) were collected. The real-time fluorescent quantitative polymerase chain reaction (PCR) (RT-qPCR) technology was used to detect the expression levels of STK11, interferon-γ (IFN-γ), interleukin 6 (IL-6), and vascular endothelial growth factor (VEGF) in the tissues. The immunohistochemical staining was used to detect the positive expression levels (PELs) of STK11 and AMPKα in the tissues, and immunofluorescence staining was used to detect the PELs Teff cells (CD3 and CD8), Treg cells (CD4 and FOXP3), and neutrophils (CD68 and CD163). RT-qPCR results showed that the expression levels of STK11 and IFN-γ in group A were obviously lower, and those of IL-6 and VEGF were much higher in contrast to group B ($P < 0.05$). The results of immunohistochemical staining showed that the number of STK11- and AMPKα-positive staining cells in group A was dramatically less than that in group B ($P < 0.05$). The results of immunofluorescence staining revealed that the number of positive staining cells for Teff cells, Treg cells, and neutrophils in group A was also less dramatically than that in group B ($P < 0.05$). In summary, immunotherapy can play a therapeutic effect on ESCC by regulating STK11/AMPK pathway and immune cell infiltration.

1. Introduction

The chest is the location with a high incidence of malignant tumors. The most common malignant tumors are esophageal cancer, lung cancer, and mediastinal tumors, and esophageal cancer is the most important breast malignant tumor [1]. Clinical data show that esophageal cancer is mainly divided into two types: esophageal squamous cell carcinoma (ESCC) and adenocarcinoma. It is more common in men, and the cause is still unclear [2]. Statistics show that the mortality rate of esophageal cancer in China has ranked fourth in the world, and the incidence of ESCC accounts for more than 90% of all esophageal cancer patients [3]. Since the early symptoms of esophageal cancer are not very obvious, gastroscopy and endoscopic biopsy are commonly used methods for screening for esophageal cancer. Nowadays, the main clinical treatment for esophageal cancer is comprehen-

sive treatment [4]. For resectable esophageal cancer lesions, surgical treatment is mainly adopted [5]. However, surgical resection alone cannot achieve satisfactory treatment results. Data shows that patients have a higher probability of local recurrence and distant metastasis after surgical treatment, and the survival rate in the past 5 years after surgery is only about 30% [6].

With the deepening of tumor immunology research, immunotherapy has become an effective means to reduce the overall mortality of esophageal cancer patients. Immunotherapy shows the advantages of strong specificity and low toxic and side effects. It can play a role in eliminating the spread or metastasis of tumor cells by regulating the specific antitumor immune response ability of the body [7]. At the same time, finding immunotherapy targets for esophageal cancer is of great significance for improving the treatment effect and increasing the survival rate. Recent studies

have shown that the mutation and inactivation of serine threonine protein kinase 11 (STK11) are closely related to the occurrence of malignant tumors, especially playing an important role in the pathogenesis and outcome of a variety of adenocarcinomas [8, 9]. Studies have shown that the mutation rate of STK11 in sporadic gastrointestinal tumors is about 10% [10]. STK11 is the upstream kinase of Adenosine 5′-monophosphate-activated protein kinase (AMPK). STK11 can activate the AMPK pathway by phosphorylating AMPK and then negatively regulate the activity of mammalian target of rapamycin (mTOR) [11]. AMPK is widely present in eukaryotic cells. It is a ternary complex composed of three subunits of α, β, and γ, and it participates in the processes of cell growth, proliferation, apoptosis, and cell polarity to regulate the tumor growth [12]. This suggests that STK11 may be able to regulate cell polarity and energy metabolism by activating the AMPK signaling pathway.

This study was aimed at exploring the specific role of STK11/AMPK pathway in immunotherapy for ESCC. In this study, ESCC tissues of patients with ESCC and receiving immunotherapy were collected, and the expression levels of related molecules in the STK11/AMPK signaling pathway in the tissues were detected. In addition, the expression changes of immune cells in the tissues of the two groups of patients were explored. This study was to provide a theoretical basis for the mechanism of STK11/AMPK pathway in ESCC and the search for new targeted therapies for ESCC.

2. Materials and Methods

2.1. Materials. TRIzol reagent was purchased from Sigma, USA; PrimeScript™ RT reagent Kit with gDNA Eraser (Perfect Real Time), TB Green® Premix Ex Taq™ (Tli RNaseH Plus), and diaminobenzidine (DBA) staining solution were purchased from Takara in Japan; hydrogen peroxide blocking endogenous peroxidase;,STK11 and AMPKα immunohistochemical primary antibodies; secondary antibodies; and Teff cells, Treg cells, and neutrophil immunofluorescence staining primary and secondary antibodies were purchased from ThermoFisher, USA.

2.2. Methods

2.2.1. Sample Collection. Tissue specimens of 100 patients with ESCC who were surgically treated in Taizhou People's Hospital (group A) and those of 20 patients with recurrent/metastatic ESCC who received second-line immunotherapy (group B) were collected. Inclusion criteria were described as follows. (I) Patients were diagnosed with ESCC at the first diagnosis. (II) Patients had complete follow-up treatment. (III) Patients undergoing surgery had received radiotherapy, chemotherapy, or other antitumor treatment before treatment. (IV) Patients with recurrent/metastatic ESCC were diagnosed as recurrence or metastasis by ultrasound endoscopy after receiving immunotherapy. (V) Patients and their family members had signed the treatment consent forms. (VI) PS score of patient was less than or equal to 2 minutes. Exclusion criteria were defined as follows: (I) patients with other malignant tumors; (II) patients

with serious diseases of the heart, kidney, liver, and other major organs; (III) patients with expected survival period shorter than 3 months; and (IV) patients with incomplete clinical data. The basic information of the two groups of patients is shown in Table 1, which showed that there was no difference between the basic data of the patients ($P > 0.05$). After all specimens were washed with phosphate buffer solution (PBS), they were divided into two parts. Some tissues were stored in liquid nitrogen for subsequent detection of the mRNA level of the target gene, and the left tissues were embedded in paraffin and made into paraffin sections with a thickness of $4\,\mu$m for subsequent immunohistochemistry and immunofluorescence staining.

2.2.2. RT-qPCR. The tissues were placed in a centrifuge tube, added with an appropriate amount of TRIzol reagent and mixed well, and lysed at room temperature for 5 minutes. After 1/5 volume of chloroform solution was added, they were shaken vigorously and then allowed to stand at room temperature for 5 minutes and then centrifuged at 12,000 rpm at 4°C for 15 minutes. After the supernatant was removed, an equal volume of isopropanol should be added to mix well and allowed to stand on ice for 20 minutes and centrifuged at 4°C at 12,000 rpm for 10 minutes to discard the supernatant. Next, the tissues were added with an appropriate amount of precooled 75% ethanol solution to wash the precipitate and centrifuged at 4°C at 12,000 rpm for 5 minutes, which was repeated 3 times. After the precipitate was dried, it was added with RNase-free ultrapure water to dissolve. The appropriate amount of RNA was removed, and the reverse transcription of complementary deoxyribonucleic acid (cDNA) was performed according to the instructions of the cDNA reverse transcription kit. The quantitative primer sequences of STK11 interferon-γ (IFN-γ), interleukin 6 (IL-6), and vascular endothelial growth factor (VEGF) and U6 were designed and synthesized by Sangon Biotech in Shanghai. The primer information is shown in Table 2. U6 was undertaken as the internal reference gene, and the relative expression of the target gene was calculated according to the equation $2^{-\Delta\Delta CT}$.

2.2.3. Immunohistochemical Staining. The prepared tissue paraffin sections were soaked in xylene solution for 10 minutes, and the tissues were dehydrated by soaking in 100%, 95%, 80%, and 70% ethanol solutions for 2 minutes and then rinsed with distilled water for 5 minutes. After the hydrogen peroxide was added to block the endogenous peroxidase, the tissues were incubated at room temperature for 10 minutes in the dark, rinsed with distilled water for 5 minutes, and then performed with the antigen retrieval treatment. Next, after rinsing with PBS for 5 minutes, the tissues were added with serum homologous to the secondary antibody and then placed in a 37°C environment for enclosed treatment for 15 minutes. After adding with the primary antibody dropwise, the tissues were placed in a refrigerator at 4°C overnight and rinsed with PBS for 5 minutes. At this time, the tissues were added with the chelate containing the secondary antibody and labeled with horseradish peroxidase at the end, incubated at 37°C for 40

Table 1: Basic information of patients.

Item	Group A ($n = 100$)	Group B ($n = 20$)	Statistical value	P value
Age (years old)	57.28 ± 8.36	58.21 ± 7.69	0.211	0.893
Males (%)	87 (87.0)	17 (85.0)	-1.092	1.221
History of smoking (%)	53 (53.0)	14 (70.0)	0.109	0.937
History of drinking (%)	76 (76.0)	15 (75.0)	0.188	0.820
Differentiation (%)			0.779	0.421
Low	4 (4.0)	1 (5.0)		
Medium	94 (94.0)	18 (90.0)		
High	2 (2.0)	1 (5.0)		
Staging (%)			-0.927	0.885
I A	0 (0.0)	0 (0.0)		
I B	9 (9.0)	1 (5.0)		
II A	15 (15.0)	3 (15.0)		
II B	20 (20.0)	4 (20.0)		
III A	33 (33.0)	7 (35.0)		
III B	7 (7.0)	1 (5.0)		
III C	16 (16.0)	4 (20.0)		

Table 2: Primer information for quantitative detection of target gene.

Gene name	Primer sequence ($5' \rightarrow 3'$)	Product size (bp)
STK11	F: GTCTGGCTGTAGCACCCTG R: GCAGCACATCGAAGAGAAACT	173
IFN-γ	F: AGCGATTCCAGTATCCTCACT R: CCAGGCTAAGCACTAGAAAGAGT	185
IL-6	F: AACAGAGACGGATGCTTCAAAA R: CCCCAGTAAAGTGGTCAAGGAT	395
VEGF	F: ATGTGTGTCCGTCTACAGATGT R: GGAAGTGTGATTGGCAAAACTGA	160
U6	F: GCCAGCTCCTACATCTCAGC R: AGCCTGACTTGCTAGTGGATTAT	211

Figure 1: Agarose gel electrophoresis detection image of the target gene. Note: 1, 2, and 3 represented three parallel samples in the same group.

minutes, and then rinsed again with PBS for 5 minutes. Finally, they were added with DAB staining solution for color development. The staining results were observed under an optical microscope.

If the cell membrane or cell nucleus was brownish yellow, the staining was positive. The pathologist performed a double-blind reading of the slides and randomly counted each section. 10 high-power fields (400x) containing positive cell staining were selected randomly for each section to count the number of positive cells, and the average value was calculated and recorded.

2.2.4. Immunofluorescence Staining. The paraffin sections were deparaffinized as in step 2.2.3, using CD36 and CD163 cells labeled with M2 macrophages for the target protein located in the cytoplasm. After 0.5% Triton X-100 reagent was added, the paraffin sections were performed with permeate treatment at room temperature for 20

minutes, washed with PBS (3 min × 3), added with goat serum, and blocked at room temperature for 30 minutes. Then, it could add diluted primary antibodies (Teff cells: anti-CD3 and CD8 antibodies; Treg cells: anti-CD4 and FOXP3 antibodies; and M2 type macrophages: anti-CD68 and CD163 antibodies), and the sections were placed in a humidified box, which was put in a 4°C refrigerator to incubate overnight in medium. After washing, the sections were added with diluted secondary antibody containing fluorescent label and incubated in a humid box at 37°C for 1 hour. Then, after the phenyl indole (DAPI) reagent was added after washing, the sections were incubated again for 5 minutes in the dark. After washing, the sections were mounted using a quencher containing antifluorescence to observe the staining results under a fluorescence microscope.

2.3. Statistical Analysis. All test data were expressed as mean ± standard deviation, and SPSS 22.0 software was used to analyze and process statistical differences. Differences between groups were compared using independent sample
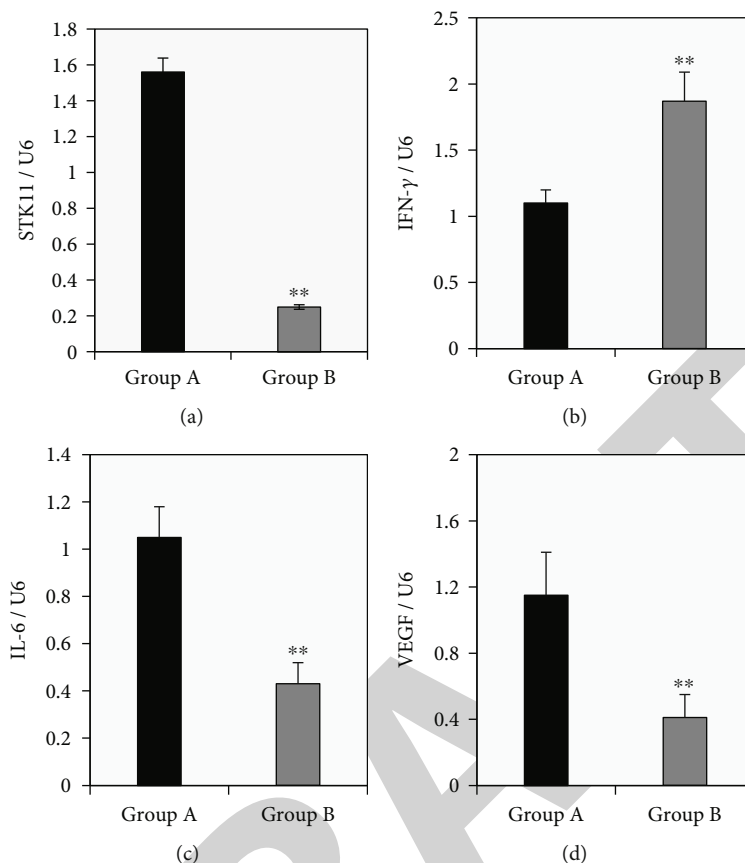
Figure 2: Differences in the expression levels of STK11, IFN-γ, IL-6, and VEGF mRNA in ESCC tissues between the two groups. Note: Panels (a~d) showed the relative expression level of STK11, IFN-γ, IL-6, and VEGF, respectively; ** suggested that there was a very significant difference compared to group A ($P < 0.01$).

t test. When $P < 0.05$, the difference showed a significantly statistical difference, while when $P < 0.01$, the difference was extremely statistically significant.

3. Results

3.1. RT-qPCR Detection Results of STK11, IFN-γ, IL-6, and VEGF in ESCC Tissues. The differences in the expression levels of STK11, IFN-γ, IL-6, and VEGF mRNA in ESCC tissues of group A and group B were compared. As can be observed from Figure 1, the expression of IFN-γ in esophageal squamous cell carcinoma of group A was significantly lower than that of group B, while the expressions of STK11, IL-6, and VEGF were significantly higher than those of group B. The expression of the internal reference gene U6 in the ESCC tissues of group A and group B was almost the same. U6 was undertaken as the internal reference gene to calculate the relative expression level of each target gene and perform statistical analysis. As revealed in Figure 2, compared with group A, the expression level of IFN-γ mRNA in ESCC tissue of group B was extremely significantly increased ($P < 0.01$), while the expression levels of STK11, IL-6, and VEGF mRNA were extremely significantly reduced ($P < 0.01$).

3.2. Immunohistochemical Staining to Detect the Positive Expression of STK11 and AMPKα in ESCC Tissues. The difference between the number of STK11 and AMPKα-positive staining cells in the ESCC tissues of group A and group B was compared, and the results are given in Figure 3. The results shown in Figure 3(a) illustrated that the number of AMPKα-positive staining cells in group B was significantly more than that in group A, while the number of STK11-positive staining cells was significantly less than that in group A. 10 staining fields were randomly selected to count the positive staining cells, the average was calculated, and the statistical comparisons were performed. As given in Figures 3(b) and 3(c), compared with group A, the average number of AMPKα-positive staining cells in ESCC tissue of group B was extremely significantly reduced ($P < 0.01$), while the average number of STK11-positive staining cells was extremely significantly increased ($P < 0.01$).

3.3. Immunofluorescence Staining to Detect the Infiltration of Teff Cells, Treg Cells, and Neutrophils in ESCC Tissue. The differences in Teff cells (CD3 and CD8), Treg cells (CD4 and FOXP3), and neutrophil (CD68 and CD163) immunofluorescence staining in ESCC tissues of group A and group B were compared. It can be clearly seen from Figure 4(a) that the numbers of Teff cells (CD3 and CD8), Treg cells (CD4
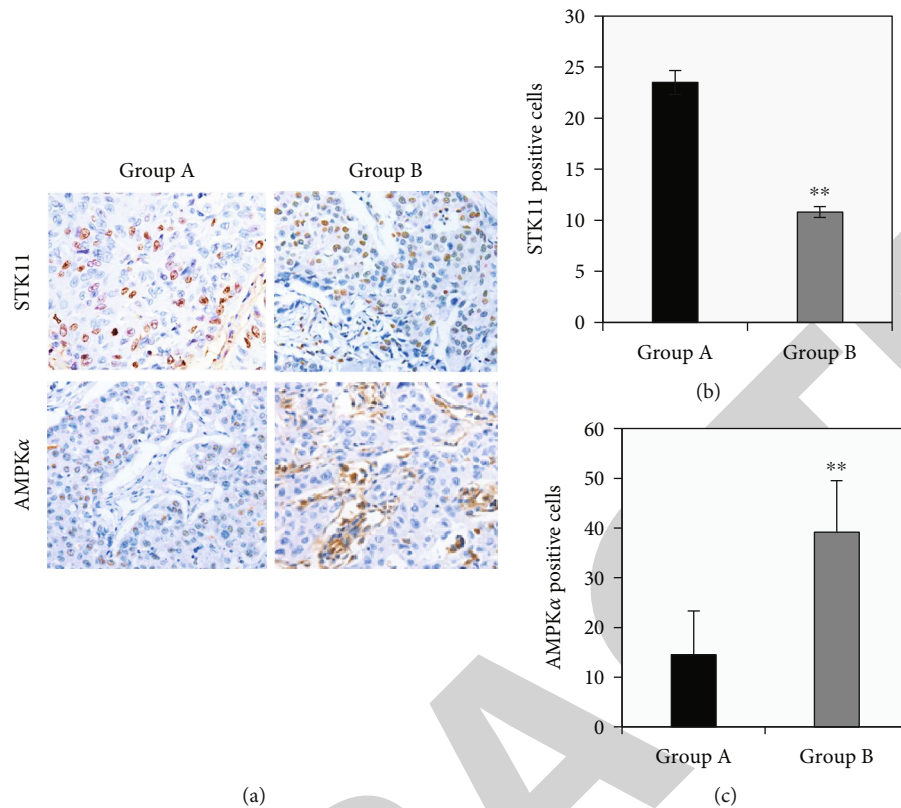
Figure 3: Immunohistochemical staining results of STK11 and AMPKα in ESCC tissues of two groups of patients. Note: Panel (a) showed the microscopic observation of STK11 and AMPKα immunohistochemical staining (magnification 400x); panel (b) was the average number of STK11-positive staining cells; panel (c) showed the average number of AMPKα-positive staining cells; ** suggested $P < 0.01$ compared with group A.

and FOXP3), and neutrophils (CD68 and CD163) positive immunofluorescence staining (yellow) cells in group B ESCC tissue were greatly more than those in group A. Therefore, 10 staining fields were randomly selected to count the positive staining cells, and the average was calculated and statistically compared. The results in Figures 4(b), 4(c), and 4(d) suggested that compared with group A, the numbers of positive immunofluorescence cells in Teff cells (CD3 and CD8), Treg cells (CD4 and FOXP3), and neutrophils (CD68 and CD163) creased dramatically in group B patients in ESCC tissues ($P < 0.01$).

4. Discussion

Esophageal cancer has gradually become one of the malignant tumors with a high mortality rate in China. Most patients are in the middle and advanced stages when they are diagnosed, and the survival rate of middle and advanced patients in the past 2 years is less than 15% [13, 14]. At present, surgical treatment of esophageal cancer has certain limitations, and the metastasis, recurrence, and mortality in the past 5 years are relatively high [15]. The survival rate of radiotherapy for early esophageal cancer can reach 80%, but due to the high degree of malignancy of the disease, problems such as recurrence and metastasis are prone to occur [16]. Therefore, finding effective treatment methods

or treatment targets is of great significance for improving the survival rate of patients with esophageal cancer.

In recent years, STK11, as a newly discovered tumor suppressor gene, has received widespread attention. STK11 germline mutation is the main pathogenic gene of Peutz-Jeghers syndrome (PJS), and the incidence of tumors in PJS patients is 10-18 times that of the general population [17, 18]. Studies have shown that STK11 is involved in the occurrence, development, and differentiation of lung cancer and other cancers [19]. It mainly activates threonine at position 172 on the ring by phosphorylation of AMPKα subunit and then plays the role of activating the AMPK pathway [20]. It is not known whether the STK11/AMPK pathway can participate in the treatment effect of ESCC. Based on this, this study adopted ESCC patient tissue as a research sample to analyze the expression of related molecules in the STK11/AMPK pathway and the role of immune cells infiltrating tumors after receiving immunotherapy.

IFN-γ plays an important role in tumorigenesis and tumor immunity. Its main antitumor activity is manifested in inhibiting tumor cell proliferation, prolonging cell cycle, inhibiting oncogene expression, activating immune cells (macrophages and NK cells, etc.), and inducing tumor necrosis factor expression and other directions [21, 22]. Wang et al. [23] confirmed that the expression level of IFN-γ was significantly increased in patients with esophageal cancer. IL-6 is

(a)

(b)

(c)

(d)
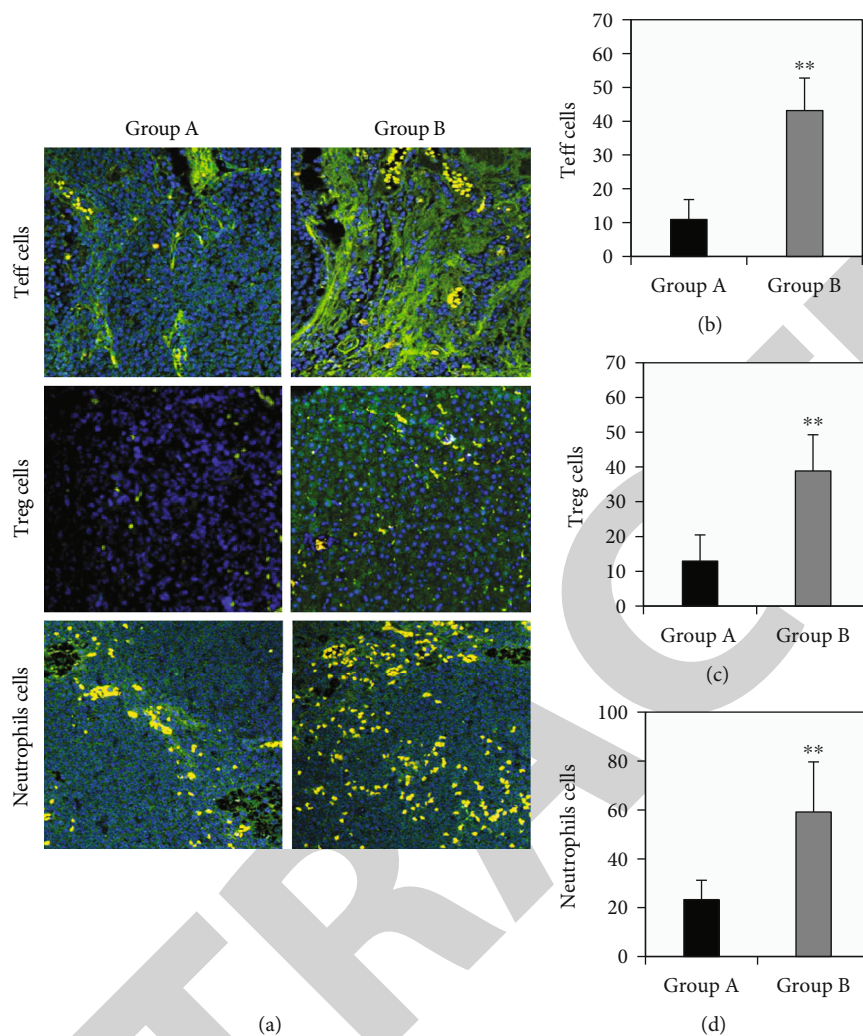
Figure 4: The immunofluorescence staining results of Teff cells, Treg cells, and neutrophils in ESCC tissues of two groups of patients. Note: Panel (a) showed the fluorescence microscopic observation of Teff cells, Treg cells, and neutrophil immunofluorescence staining (magnification 400x); panels (b), (c), and (d) were the average number of positive staining cells of Teff cells, Treg cells, and neutrophils, respectively (different immune cells in the figure were coexpressed as yellow fluorescence). ** suggested that compared with group A, there was a very significant difference ($P < 0.01$).

a kind of cytokine with multiple potency, which can activate the tumor regulation-related protein state on the cell surface by forming a complex and then exert the ability to regulate cell proliferation, migration, and invasion [24]. Research by Qiu et al. [25] showed that the level of IL-6 mRNA in esophageal cancer tissues was significantly higher than that in normal tissues. VEGF is a type of cytokine secreted by vascular endothelial cells that promotes cell division. Many studies have shown that the expression level of this gene in tumor tissues is significantly higher than that in normal tissues [26, 27]. And studies have confirmed that VEGF can be used as an independent prognostic factor for esophageal cancer, which is closely related to tumor burden, lymph node metastasis, and recurrence [28]. The results of this study showed that IFN-γ levels in ESCC tissue increased after immunotherapy, while the levels of STK11, IL-6, and VEGF decreased ($P < 0.05$). This may be because immunotherapy regulates the collective

immunomodulatory activity, enhances the ability of T cells, improves the phagocytic activity of macrophages, promotes the formation of antibodies, and ultimately enhances the immune ability of the body [29]. In addition, this study used immunohistochemistry to detect the positive expression levels of STK11 and AMPKα in ESCC tissues. The results showed that the positive expression levels of AMPKα in ESCC tissues increased significantly after immunotherapy, while the positive expression levels of STK11 decreased significantly ($P < 0.05$). It shows that immunotherapy can inhibit the process of ESCC by activating the STK11/AMPK signaling pathway.

Studies have shown that immune cell infiltration in tumor tissue is closely related to the prognosis of patients [30]. The results of tumor immunology research show that the occurrence and development of tumors are related to the disorder or loss of the immune system of the body

[31]. Teff cells, Treg cells, and neutrophils are all important immune cell subgroups, which play important roles in maintaining the homeostasis of the body's environment and tumor immune surveillance and resisting autoimmune system diseases [32]. Studies have shown that the levels of Treg and other cells in the peripheral blood or tissues of patients with esophageal cancer are significantly higher than those in healthy people [33]. This may be because when tumors appear in the body, tumor cells can release tumor-related antigens, which in turn induces the proliferation and activation of immune cells. The results of this study showed that Teff cells, Treg cells, and neutrophils PEL in ESCC tissues after immunotherapy were obviously higher than those in normal ESCC tissues ($P < 0.05$). Such results suggest that immunotherapy can inhibit tumor cells by enhancing the immune response of the body, so the levels of Teff cells, Treg cells, and neutrophils in the body have increased.

5. Conclusion

This study was aimed at exploring the effects of immunotherapy on the STK11/AMPK pathway, tumor-related cytokines, and immune cell levels in ESCC patients. The results showed that immunotherapy can significantly affect the expression level of tumor-related factors, inhibit the activation of STK11/AMPK signaling pathway, and increase the level of immune cells in the body. However, the results of this study still had some limitations. For example, it only explored the effects of immunotherapy on the levels of related factors and immune cells in patients with ESCC, but it could not prove that the STK11/AMPK signaling pathway can directly participate in the immunotherapy effect of ESCC. In future research, it will prepare corresponding animal or cell models to explore the effect of inhibiting or promoting the expression of STK11/AMPK on the effect of immunotherapy for ESCC. In summary, the results of this study could provide a theoretical reference for understanding the mechanism of action of the STK11/AMPK pathway on ESCC.

Data Availability

The data used to support the findings of this study are included within the article.

Conflicts of Interest

The authors declare that they have no competing interest.

Authors' Contributions

Yang Xia and Peng Wang contributed equally to this work as co-first author.

Acknowledgments

References

[1] F. L. Huang and S. J. Yu, "Esophageal cancer: risk factors, genetic association, and treatment," *Asian Journal of Surgery*, vol. 41, no. 3, pp. 210–215, 2018.

[2] M. W. Short, K. G. Burgers, and V. T. Fry, "Esophageal cancer," *American Family Physician*, vol. 95, no. 1, pp. 22–28, 2017.

[3] X. Hou, J. Wen, Z. Ren, and G. Zhang, "Non-coding RNAs: new biomarkers and therapeutic targets for esophageal cancer," *Oncotarget*, vol. 8, no. 26, pp. 43571–43578, 2017.

[4] E. Bollschweiler, P. Plum, S. P. Mönig, and A. H. Hölscher, "Current and future treatment options for esophageal cancer in the elderly," *Expert Opinion on Pharmacotherapy*, vol. 18, no. 10, pp. 1001–1010, 2017.

[5] A. S. Borggreve, B. F. Kingma, S. A. Domrachev et al., "Surgical treatment of esophageal cancer in the era of multimodality management," *Annals of the New York Academy of Sciences*, vol. 1434, no. 1, pp. 192–209, 2018.

[6] R. Park, S. Williamson, A. Kasi, and A. Saeed, "Immune therapeutics in the treatment of advanced gastric and esophageal cancer," *Anticancer Research*, vol. 38, no. 10, pp. 5569–5580, 2018.

[7] P. Zimmermann and N. Curtis, "Factors that influence the immune response to vaccination," *Clinical Microbiology Reviews*, vol. 32, no. 2, p. e00084, 2019.

[8] X. Chen, R. Mao, W. Su et al., "Circular RNAcircHIPK3modulates autophagy viaMIR124-3p-STAT3-PRKAA/AMPKα signaling in STK11 mutant lung cancer," *Autophagy*, vol. 16, no. 4, pp. 659–671, 2020.

[9] S. J. Chung, G. P. Nagaraju, A. Nagalingam et al., "ADIPOQ/adiponectin induces cytotoxic autophagy in breast cancer cells through STK11/LKB1-mediated activation of the AMPK-ULK1 axis," *Autophagy*, vol. 13, no. 8, pp. 1386–1403, 2017.

[10] A. M. Jelsig, B. Bertelsen, I. Forss, and J. G. Karstensen, "Two cases of somatic STK11 mosaicism in Danish patients with Peutz-Jeghers syndrome," *Familial Cancer*, vol. 20, no. 1, pp. 55–59, 2021.

[11] F. Ciccarese, E. Zulato, and S. Indraccolo, "LKB1/AMPK pathway and drug response in cancer: a therapeutic perspective," *Oxidative Medicine and Cellular Longevity*, vol. 2019, Article ID 8730816, 16 pages, 2019.

[12] Z. Wang, N. Wang, P. Liu, and X. Xie, "AMPK and cancer," *AMP-activated Protein Kinase*, vol. 107, pp. 203–226, 2016.

[13] P. D. Siersema, "Esophageal cancer," *Gastroenterology Clinics of North America*, vol. 37, no. 4, pp. 943–964, 2008.

[14] H. Kato and M. Nakajima, "Treatments for esophageal cancer: a review," *General Thoracic and Cardiovascular Surgery*, vol. 61, no. 6, pp. 330–335, 2013.

[15] A. Ashok, D. Niyogi, P. Ranganathan et al., "The enhanced recovery after surgery (ERAS) protocol to promote recovery

Research Article

Correlation between Vaginal Microecological Status and Prognosis of CIN Patients with High-Risk HPV Infection

Huizhen Zhang [ID],[1] Shuangling Jin,[1] Aifang Ji,[2] Chunyan Zhang,[1] and Shujing Shi[1]

[1]*Department of Gynecology, Heping Hospital, Changzhi Medical College, Changzhi 046000, China*
[2]*Department of Laboratory Medicine, Heping Hospital, Changzhi Medical College, Changzhi 046000, China*

Correspondence should be addressed to Huizhen Zhang; zhz@stu.czmc.edu.cn

Many microorganisms live in the vagina of healthy women. They interact with and compete with the microenvironment in the female vagina to form a dynamic balance of the microenvironment in the female vagina. However, imbalanced vaginal microecology can lead to vaginal resistance to pathogenic microorganisms. Poor capacity can cause women to develop infections of the reproductive tract. This article analyzes the vaginal microecological status of women with high-risk HPV infection for more than 6 months and healthy women and explores the risk factors that cause long-term high-risk HPV infection for timely detection and regulation of possible vaginal microecological imbalance in women with high-risk HPV infection for more than 6 months to prevent further development of cervical lesions in such patients. This article covers women with a sexual life history who attended the gynecology department of a hospital from January 2020 to September 2021. There were 280 patients in the experimental group: positive high-risk HPV; and there were 140 patients in the control group: negative high-risk HPV test. The correlation between vaginal microecology of CIN patients and patient prognosis according to the subject's vaginal microecology test results and prognosis of various levels of cervical lesions was analyzed. The experiment proved that the detection rate of normal vaginal microecology in the experimental group was 12.14% (34/280) compared with the detection rate of 29.29% (41/140) in the control group, and there was a trend of decrease, and the difference was statistically significant ($\chi^2 = 17.23, P < 0.05$). The detection rate of vaginal BV in the experimental group was 10.36% (29/280) compared with the detection rate of 5.0% (7/140) in the control group, and the difference was statistically significant ($\chi^2 = 5.19, P < 0.05$). This indicates that women with high-risk HPV infections for 6 months or longer have a higher incidence of vaginal microecological imbalances than healthy individuals and aggressive vaginal microecological screening. It is necessary to carry out the program. Detect and treat possible abnormal conditions in time to prevent the further onset of the disease.

1. Introduction

HPV is the main pathogenic factor of cervical cancer. Studying its carcinogenic mechanism and factors affecting the occurrence and development of cervical cancer plays an important role in the prevention and treatment of cervical cancer. Multiple HPV infections can increase the risk of cervical lesions in patients, accelerate the progression of cervical lesions, and affect the sensitivity of cervical cancer patients to treatment and affect the prognosis of patients. This effect is associated with accelerated HPV recombination during multiple HPV infections, the formation of new types of

HPV with greater pathogenicity and invasiveness, faster disease progression, and increased disease malignancy. Therefore, it is of particular importance to study the correlation between the various clinical features of cervical lesions caused by multiple HPV infections and whether multiple HPV infections promote HPV recombination and its mechanism.

High-risk HPV infections are mainly transmitted through sex. Cervicitis and CIN caused by infection are the most common cervical problems in clinical practice. If they are not treated in time, they may progress to cervical malignant tumors. Although the health departments around the

world attach great importance to high-risk HPV infection and invest a lot of resources in the prevention, screening, and vaccine development of high-risk HPV, the detection rate and mortality of cervical cancer are still on the rise. The virus in most infected people does not last for more than 6 months. Most women can quickly get rid of high-risk HPV by relying on the self-cleansing capacity of the vaginal microecosystem and the self-repair of cervical epithelial cells. However, some women are still unable to get rid of high-risk HPV infections in their bodies. The continued action of high-risk HPV ultimately leads to the development of CIN and cancer.

The cervix is always surrounded by the vaginal microecological environment. The cervix and vagina infected with high-risk HPV are inextricably linked to the vaginal microecological environment. Whether there is a clear difference between the vaginal microecological status of people with high-risk HPV long-term infection and healthy people, domestic and foreign scholars have not yet reached a consensus. In order to assess the vaginal microecological status of high-risk HPV infection cervical intraepithelial neoplasia, 241 high-risk HPV-infected CIN patients diagnosed and treated by the Cervical Disease Center were selected as the experimental group, and 168 women who underwent physical examination in the outpatient clinic were studied. The HPV-negative and normal cytological examination results were used as a control group to compare the differences in the vaginal microecological status between the two groups. However, the lack of experimental data in his study led to small differences in the sample set, resulting in inaccurate results [1]. There is an indirect connection between multiple sex partners (MSP) and cervical intraepithelial neoplasia (CIN) and even cervical cancer (CC). MSP can also cause bacterial vaginosis (BV). The relationship between MSP, BV, human papillomavirus (HPV) infection, and CIN/CC development in Chinese women remains unclear. Rabaan et al. retrospectively analyzed 549 female patients who had been to the physical examination center. MSP information was obtained, and vaginal microecology, HPV, and cervical conization pathology (CCP) tests were performed when necessary. In patients with different severity of BV, MSP status is different. In addition, as the severity of BV increases, the HPV-positive rate increases. At the same time, MSP is significantly related to HPV-positive results, including HPV16, HPV18, and other high-risk HPV infections. The percentage of positive CCP results in the MSP group was significantly higher. Similarly, higher severity of BV means that CIN/CC is progressing more severely. However, its overall study lacks data support, and more data is needed to support its conclusions [2]. Pan et al. investigated the role of HPV16 DNA integration in cervical lesions in Han and Uyghur women and explored the relationship between virus integration and high cervical cancer incidence and low HPV infection rates. DNA was extracted from cervical lesion biopsy specimens of 379 Uyghur and 464 Han patients, and multiple quantitative polymerase chain reaction (qPCR) analyses were performed to determine the copy numbers of HPV16E2 and E6 genes. The copy number of HPV16DNA was evaluated based on the E2/E6 ratio. Among these cases,

122 Uyghur and 121 Han specimens were found to be HPV16-positive. In these two populations, the percentage of HPV16 integrated cases increased with the degree of cervical lesions ($P < 0.05$), but the testing equipment was immature at the time of the study, resulting in insufficient accuracy [3].

In the past, clinical studies on patients with high-risk HPV infections mostly focused on the relationship between HPV infection and simple vaginal inflammation. Few studies were conducted on the overall status of vaginal microecology in women with high-risk HPV infections over 6 months. This article focuses on the relationship between HPV multiple infections in cervical cancer patients and the clinical manifestations of cervical cancer, revealing the effects of multiple HPV infections on the clinical features of cervical cancer. By investigating the mechanism of this effect and discovering and controlling potential imbalances in the vaginal microeconomics in time, further development of cervical lesions and multiple HPVs in the future can be prevented. It may provide a more theoretical basis for the prevention, evaluation, and follow-up of patients with infectious diseases.

2. Correlation between High-Risk HPV Infection and Patient Prognosis

2.1. Vaginal Microecological Status of CIN Patients with High-Risk HPV Infection

2.1.1. High-Risk HPV Infection and Normal Vaginal Microbiota. It is generally believed that a healthy vaginal microecological status is the following: the density of the colonizing bacteria in the vagina is between level II and level III, the diversity of the flora is between level II and level III, and lactobacilli occupy an absolutely dominant position in terms of quantity. No infection of pathogenic microorganisms such as BV, candidal vaginitis (VVC), and trichomonal vaginitis (TV) was found in the vagina, the number of white blood cells is less than 10/high-powered field of view, the pH value in the vagina is ≤4.5, which reflects that lactic acid Bacillus functions are positive for hydrogen peroxide; sialidase, which reflects BV infection; leukocyte esterase, which reflects the massive destruction of vaginal white blood cells due to inflammation; β-glucuronidase, which reflects the overgrowth of aerobic bacteria in the vagina and indicates possible VVC infection; or TV acetylglucosaminidase, etc., which are all negative. A healthy vaginal microecological environment has a protective function for the human body [4, 5], and an unbalanced vaginal microecological environment can easily cause the female reproductive tract to be attacked by various pathogens. Pathogens that invade the female reproductive tract can further aggravate the imbalance of vaginal microecology and form a vicious circle.

2.1.2. High-Risk HPV Infection and Vaginal Lactobacillus and pH Value. Lactobacillus is the dominant bacteria that colonize the vagina of healthy women, and it is also the main force to maintain the vaginal microecological balance. It accounts for more than 95% of the total vaginal microbes,

and 80 to 90% of women can isolate the bacteria in the vagina. The decrease in the number of lactobacilli reduces the resistance of the vagina to pathogenic microorganisms, resulting in the persistence of high-risk HPV infections. The specific mechanism of action still needs more in-depth research [6, 7]. It is ideal for women's vagina to maintain a pH value between 3.8 and 4.5. This acidic environment has a strong killing effect on most pathogens that invade the vagina. When internal or external changes cause the vaginal microecological balance to be disrupted, it will lead to changes in the vaginal pH value, and the abnormal pH value will aggravate the imbalance of the vaginal microecology, forming a vicious circle [8].

2.1.3. Current Status of Clinical Application of Vaginal Microecological Testing.

The concept of vaginal microecology was first proposed by the Obstetrics and Gynecology Infectious Diseases Cooperation Group of the Chinese Medical Association of our country and has been popularized and used for more than 10 years. Traditional vaginal secretion testing methods can only diagnose vaginitis with a clear pathogenic infection and are limited by the time of specimen collection, the quality of specimens, and the inspector's testing experience. The accuracy of the test results is not high, and the efficiency is low. In recent years, the female vaginal microecological detection system has the advantages of fast, simple, multiple results, clear morphological staining, comprehensive functional detection, etc., and the detection rate of pathogenic microorganisms is higher than that of traditional microscope detection methods, and it can be combined with the morphological and functional characteristics of the test samples to obtain more accurate and comprehensive inspection results [6, 9]. The application of the vaginal microecological assessment system, on the one hand, modifies the concept of reproductive tract infections, which diagnoses "vaginal disease" only after the discovery of pathogenic microorganisms. On the other hand, it goes beyond the existing concept of treating vaginal infections. It kills pathogens. The main purpose of improving diagnosis and treatment is to increase beneficial bacteria in the vagina and restore a healthy microecological condition of the vagina as a standard new concept that is a major advance in the diagnosis and treatment of vaginal infections. Therefore, if we want to fully understand the interaction between HPV infection and the human body, we need to use the accuracy and comprehensiveness of the vaginal microecological testing system to compare and analyze the vaginal microecological status of high-risk HPV-infected persons and healthy people [10, 11].

2.2. Artificial Neural Networks

2.2.1. Single Neuron.

In order to imitate the working mechanism of biological nerve cells, scientists have designed artificial neurons. Assuming that a neuron has three input data x_1, x_2, x_3, the intensity of the neuron's action can be expressed as w_1, w_2, w_3 by weight, plus a bias term b, which is sent into the cell for processing together [12, 13]. Thus, the input value of the neuron can be

$$\sum_{i=1}^{3} w_i x_i. \tag{1}$$

The output value can be expressed as

$$Z = f\left(\sum_{i=1}^{3} w_i x_i + b\right). \tag{2}$$

The symbol f represents the neuron function. According to the difference in solving the problem, the activation function is usually different; otherwise, it will affect the convergence of the algorithm. The commonly used activation functions are as follows, one is the Sigmoid activation function, the other is the Tanh activation function, the third is the ReLU activation function, and the fourth is the Maxout activation function. The mathematical formulas of Sigmoid function and Tanh function are shown in

$$f(h) = \frac{1}{1 + e^{(-h)}},$$
$$f(h) = \tanh(h) = \frac{e^h - e^{-h}}{e^h + e^{-h}}. \tag{3}$$

There are many similarities between the Sigmoid curve and the Tanh curve: Regardless of whether the input value is large or small, the Sigmoid function can control the value between 0 and 1; for extremely large negative numbers, the output value is 0, and for extremely large positive numbers, the output value is 1. Tanh is derived from Sigmoid, and its output value is between -1 and 1, with an average value of 0 [14, 15]. The calculation of the ReLU function is relatively simple: when the input value is less than 0, the output is 0; when the input value is greater than 0, the output is equal to the input. The formula is as follows:

$$f(h) = \max(0, h). \tag{4}$$

The advantage of this activation function is that it can process data quickly and only needs to set a threshold. However, the ReLU function also has a relatively large drawback—the ReLU neuron processes large gradients and updates the parameters, which may easily cause the neuron to not activate the data [16]. The core idea of Maxout calculation is to take the maximum value of the corresponding position of the feature map of the previous layer as the output of the Maxout unit. The formula is shown in formula (5), where k is the number of feature maps output by Maxout:

$$\begin{cases} f_i(h) = \max(Z_{ij}), & j \in [1, k], \\ Z_{ij} = h^T w_{ij} + b_{ij}. \end{cases} \tag{5}$$

Maxout does not have a fixed curve and can fit any convex function, so the fitting ability is relatively good, and it contains the advantages of the ReLU function while avoiding its defects. Other activation functions include threshold

functions and linear functions. Different functions have different characteristics, which constitute a neural network with different functions nowadays [17, 18].

2.2.2. Neural Network. Similar to brain tissue being composed of countless nerve cells, ANN is also composed of many artificial neurons. Figure 1 is a typical feedforward neural network. The small circle in the figure represents a neural processing unit, and some neurons form a layer of the network [19, 20]. The order of each layer is determined according to the sequence of information transmission. For example, the third layer only accepts the information output by the second layer. There is no feedback signal between each neural processing unit, and there is no feedback information between layers.

The input layer of a feedforward neural network structure contains multiple input neural nodes that represent the input values, and the input layer transfers data to the hidden layer for further processing. The processed values of the hidden layer cannot be directly observed during the operation of the neural network. The neuron has multiple inputs, but there is only one output value that can be sent to multiple neurons as input [21, 22]. The last layer is the output layer, which can have one or more output nodes. Multioutput neural networks can be applied to issues such as multiple results, such as computer performance evaluation. The input data of the network can use various computer hardware configurations. After processing, the output has either high performance, medium performance, or low performance. Suppose a forward neural network contains 3 network layers, the first layer is the input layer, the second layer is the hidden layer, and the third layer is the output layer. The input layer has 3 values $\{x_1, x_2, x_3\}$, the weights corresponding to the hidden layer are $\{w_{11}^{(1)}, w_{12}^{(1)}, w_{13}^{(1)}\}$, $\{w_{21}^{(1)}, w_{22}^{(1)}, w_{23}^{(1)}\}$, $\{w_{31}^{(1)}, w_{32}^{(1)}, w_{33}^{(1)}\}$, and the bias value is $\{b_1^{(1)}, b_2^{(1)}, b_3^{(1)}\}$. The hidden layer has 3 output values $\{c_1^{(2)}, c_2^{(2)}, c_3^{(2)}\}$, the weight corresponding to the output layer is $\{w_{11}^{(2)}, w_{12}^{(2)}, w_{13}^{(2)}\}$, and the bias value is $b_1^{(2)}$. The output result is represented by Z, $f(h)$ represents the activation function, and the mathematical formula to express this neural network is

$$\begin{cases} c_1^{(2)} = f\left(w_{11}^{(1)}x_1 + w_{12}^{(1)}x_2 + w_{13}^{(1)}x_3 + b_1^{(1)}\right), \\ c_2^{(2)} = f\left(w_{21}^{(1)}x_1 + w_{22}^{(1)}x_2 + w_{23}^{(1)}x_3 + b_2^{(1)}\right), \\ c_3^{(2)} = f\left(w_{31}^{(1)}x_1 + w_{32}^{(1)}x_2 + w_{33}^{(1)}x_3 + b_3^{(1)}\right), \\ Z = f\left(w_{11}^{(2)}c_1^{(2)} + w_{12}^{(2)}c_2^{(2)} + w_{13}^{(2)}c_3^{(2)} + b_1^{(2)}\right). \end{cases} \quad (6)$$

In the same way, the calculation steps of extending this model to a neural network with l layers are roughly similar. Taking c_i^l to represent the output value of the i neuron of the l layer and $w_{ij}^{(l-1)}$ and $b_i^{(l-1)}$ the weight and bias
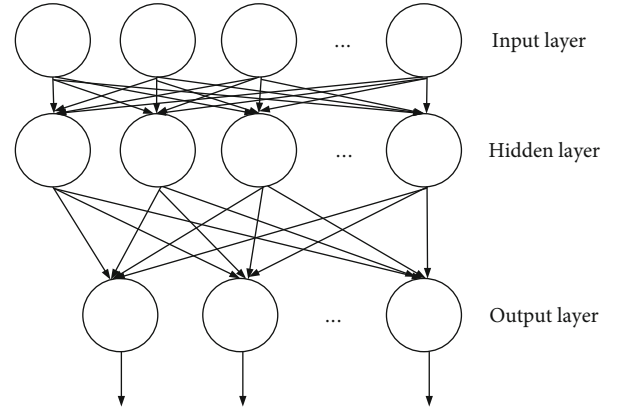
Figure 1: Feedforward neural network structure.

values of the corresponding layer, then formula (7) can be obtained:

$$\begin{cases} h_i^l = \sum_{j=1}^{n} w_{ij}^{(l-1)}x_j + b_i^{(l-1)}, \\ c_i^l = f\left(h_i^l\right). \end{cases} \quad (7)$$

BP networks are typical feedforward neural networks, and there are other radial basis function neural networks. A seemingly complex neural network is actually relatively easy to solve. From the first single neuron to two-layer, three-layer, and even multilayer neural networks, you can quickly find the output of your neuron as long as you master the solution, matrix the parameters, and use the fast computing power of your computer.

2.2.3. Reverse Conduction Algorithm. The reverse conduction algorithm can continuously optimize the connection weights and biases between each artificial neuron according to the expected output information; that is, the algorithm can propagate the difference between the expected value and the network output to the input layer layer-by-layer, to modify the weight of the connection. When the error signal is transmitted back to a certain layer, the signal will be allocated to the processing unit of this layer as the basis for modifying the weight of the unit. Backpropagation will continue until the number of iterations or learning times set by the network, or the output error is reduced to the range that the network designer can accept [23–26]. The reverse conduction algorithm is an important part of the neural network. The input layer contains two neurons x_1, x_2 with a bias of b_1; the hidden layer contains two neurons c_1, c_2 with a bias of b_2; the output layer has two values z_1, z_2. There is a weight w_i between each neuron; let the activation function be $f(h)$. Suppose the total error is E, the error of z_i is e_i,

and the expected output is t_i. Then the total error can be obtained by

$$
\begin{cases}
e_1 = \dfrac{1}{2}(t_1 - z_1)^2, \\[2mm]
e_2 = \dfrac{1}{2}(t_2 - z_2)^2, \\[2mm]
E = (e_1 + e_2) = \sum \dfrac{1}{2}(t_i - z_i)^2.
\end{cases} \tag{8}
$$

Regarding the update of the weight from the hidden layer to the output layer, the w_5 weight in the network can be used for illustration. The calculation formula is shown in Equation (9), and the partial derivative of the total error to w_5 can be obtained:

$$
\begin{cases}
h_5 = w_5 * c_1 + w_6 * c_2 + b_2 * 1, \\[2mm]
\dfrac{\partial E}{\partial w_5} = \dfrac{\partial E}{\partial z_1} * \dfrac{\partial z_1}{\partial h_5} * \dfrac{\partial h_5}{\partial w_5}.
\end{cases} \tag{9}
$$

Bringing Equation (8) into Equation (9) can get

$$
\begin{cases}
h_1 = w_1 * x_1 + w_2 * x_2 + b_1 * 1, \\[2mm]
\dfrac{\partial E}{\partial w_5} = -(t_1 - z_1) * z_1(1 - z_1) * f(h_1).
\end{cases} \tag{10}
$$

Let η be the learning rate, the updated value of weight w_5 can be obtained, expressed as gw_5, and the formula is shown in

$$
gw_5 = w_5 - \eta * \frac{\partial E}{\partial w_5}. \tag{11}
$$

For the weight update from the hidden layer to the hidden layer, the errors of e_1 and e_2 must be counted, because the neurons of the hidden layer are fully connected with the output layer. The following takes the weight update of w_1 for explanation. Before calculating the influence of w_1 on the total error E, the partial derivatives of e_1 and e_2 with respect to w_1 need to be calculated separately, as shown in

$$
\begin{cases}
\dfrac{\partial E}{\partial f(h_1)} = \dfrac{\partial e_1}{\partial f(h_1)} + \dfrac{\partial e_2}{\partial f(h_1)}, \\[2mm]
\dfrac{\partial E}{\partial w_1} = \dfrac{\partial E}{\partial f(h_1)} * \dfrac{\partial f(h_1)}{\partial h_1} * \dfrac{\partial h_1}{\partial w_1}, \\[2mm]
\dfrac{\partial E}{\partial w_1} = \left(\dfrac{\partial e_1}{\partial f(h_1)} + \dfrac{\partial e_2}{\partial f(h_1)}\right) * \dfrac{\partial f(h_1)}{\partial h_1} * \dfrac{\partial h_1}{\partial w_1}.
\end{cases} \tag{12}
$$

Finally, from Equations (12) and (11), the updated weight of w_1 can be obtained, expressed as gw_1, and the equation is shown in

$$
gw_1 = w_1 - \eta * \frac{\partial E}{\partial w_1}. \tag{13}
$$

By analogy, the update method of other weights w_2, w_3, w_4 is similar. Since then, according to the chain calculation rule, the partial derivatives of weights w_1 and b_1 are calculated as shown in

$$
\begin{cases}
\delta_i^{(l)} = \left(\displaystyle\sum_{j=1}^{S_{l+1}} w_{ij}^{(l)} \delta_j^{(l+1)}\right) f'\left(h_i^{(l)}\right), \\[3mm]
\dfrac{\partial J(w, b, x, y)}{\partial w_{ij}^{(l)}} = c_j^{(l)} \delta_i^{(l+1)}, \\[3mm]
\dfrac{\partial J(w, b, x, y)}{\partial b_i^{(l)}} = \delta_i^{(l+1)}.
\end{cases} \tag{14}
$$

Among them, (w, b) is the weight parameter of the neural network, (x, y) represents the data set $\{(x^{(1)}, y^{(2)}) \cdots (x^{(m)}, y^{(m)})\}$ to be trained by the network and contains m training samples, $J(w, b, x, y)$ is the corresponding loss function of a single training sample (x, y), and $\delta_i^{(l+1)}$ is the error of the i neural processing unit of the $l + 1$ layer. The reverse conduction algorithm can be summarized as the following: first, calculate the activation value of all neural processing units in each layer of the feedforward transmission process, then calculate the error value of the output results and samples of the network, and then return to the hidden layer to find the error of each node value, and finally, calculate the partial derivative value of the weight. In this way, the calculation method of reverse conduction is completed, and the weights are continuously updated after continuous iteration, so that the output result of the network and the expected value are constantly approaching.

3. Experimental Design of the Correlation between Vaginal Microecological Status and Prognosis of CIN Patients

3.1. Test Subject

3.1.1. Inclusion Criteria. The case selection criteria were married women who attended a gynecological outpatient clinic of a hospital from January 2020 to September 2021 and had abnormal cervical cancer and precancerous lesion screening. All patients underwent high-risk HPV testing and vaginal microbiology with informed consent and ecological testing.

3.1.2. Elimination Criteria. The elimination criteria are the following: incomplete case data, being treated with immunosuppressive agents, vaginal washing and medication 3 days before specimen collection, and a history of high-risk HPV infection in the past, who turned negative during this examination.

3.1.3. Grouping Standard. There are 280 cases in the experimental group: the first high-risk HPV test results were found to be positive 6 months ago; this time, the high-risk HPV test was still positive. There are 140 cases in the control group: all were healthy people, and no high-risk HPV

infection was found before. The second-high-risk HPV test was negative. Follow-up was performed 3, 6, 9, 12, 18, and 24 months after standard treatment. Among them, 240 high-risk HPV-positive patients underwent regular cytology and high-risk HPV testing until they turned negative. The results of vaginal microecological testing and high-risk HPV load and cervical lesions of various grades were analyzed.

3.2. Method of Obtaining Vaginal Secretions. Candidates lie on the gynecological examination table and take the bladder lithotomy position; the sterilized speculum was lubricated with a small amount of sterilized normal physiological saline and placed in the candidate's vagina to completely expose the cervix. And in particular, during the vaginal microecological examination, use a sterile cotton swab to remove vaginal secretions from the upper third of the vaginal sidewall, rotate the cotton swab, and stay on the vaginal sidewall for 15-20 seconds. After the swab is completely immersed in the specimen, carefully place it in a dry, sterile test tube and avoid contact with the vagina or vulva during this period to prevent contamination of the specimen. Then gently insert the high-risk HPV sample collection brush into the cervix and rotate the sample collection brush 5 times clockwise. After brushing enough cervical epithelial cells, carefully place the specimen sampling brush on the high-risk specimen. A special sterile sampling tube used for HPV storage reagents breaks the brush handle and closes the mouth of the sampling tube tightly. During this period, avoid touching the vagina or vulva to prevent contamination of the specimen. The above samples were collected by two obstetricians and a gynecologist and sent to the laboratory for examination by a professional inspector within 1 hour of the sample being taken. Professional inspectors strictly follow the operating procedures of the bPR-2014A Vaginal Microecological Evaluation System for cytological and functional examination of vaginal discharge.

3.3. High-Risk HPV Detection and Criteria. For the standard high-risk HPV test result determination, the content of high-risk HPV is determined by the ratio of relative light unit to the standard positive control, relative light unit/standard positive control < 1 is judged as negative, relative light unit/standard positive control ≥ 1 is judged as positive, and the larger the relative light unit/standard positive control value, the higher the load value of the high-risk HPV virus.

3.4. Follow-Up Method. With informed consent of all patients, the knowledge about cervical cancer and its precancerous lesions shall be promoted and popularized one by one, and basic information such as the patient's name, age, contact number, home address, pregnancy times, parity, and interroom bleeding shall be collected. The pathological diagnosis of biopsy means that standard treatment is given, and patients are instructed to strictly follow the doctor's instructions. Follow-ups will be conducted at 3, 6, 9, 12, 18, and 24 months after treatment. Cervical cytology and high-risk HPV testing will be performed at each follow-up. If necessary, a biopsy can be taken again.

3.5. Statistical Processing. Statistical analysis was performed with SPSS 13.0 statistical software. The significance test of the difference was performed by one-way analysis of variance. The difference between the two groups was performed by the LSD t-test. The statistics of the vaginal microecological status of CIN patients with high-risk HPV infection were performed by a group t-test. $P < 0.05$ is considered to be significant and statistically significant.

4. Experimental Correlation between Vaginal Microecological Status and Prognosis of CIN Patients

4.1. Morphological Test Results of Vaginal Microecology in Experimental Group and Control Group

4.1.1. Test Results of Vaginal Cluster Density. The 280 cases of the experimental group and 140 cases of the control group were tested for the concentration of vaginal clusters. The results are shown in Figure 2.

It can be seen from Figure 2 that the concentration of vaginal secretion flora between 0 and I indicates that the flora is inhibited. The detection rate of vaginal secretion flora in the experimental group between 0 and I is 2.50% (7/280); the detection rate of the control group was 2.14% (3/140). Compared with the two, the detection rate of vaginal flora suppression in the experimental group was lower than that of the control group. The density of normal vaginal microecological flora should be between II and III, the detection rate of the experimental group's flora density is between II and III 96.43% (270/280), and the detection rate of the control group is 97.86% (137/140). Comparing the two, the normal rate of vaginal flora density in the experimental group was lower than that in the control group. Vaginal flora density grade IV indicates the excessive proliferation of vaginal flora. The detection rate of bacterial flora density grade IV in the experimental group was 1.07% (3/280), and the detection rate in the control group was 0. Comparing the two, the experiment detection rate of vaginal flora hyperproliferation in the group was higher than that in the control group. There was no statistically significant difference in the overall composition of the two groups ($\chi^2 = 2.733$, $P > 0.05$).

4.1.2. Test Results of Vaginal Flora Diversity. The 280 cases of the experimental group and 140 cases of the control group were tested for the diversity of vaginal flora. The results are shown in Figure 3.

It can be seen from Figure 3 that the density of vaginal flora between 0 and I indicates that the diversity of flora is reduced, and the detection rate of the experimental group's flora diversity between 0 and I is 6.07% (17/280). The detection rate of the control group was 4.29% (6/140); comparing the two, the detection rate of decreased vaginal flora diversity in the experimental group was higher than that in the control group. The diversity of the normal vaginal microecological flora should be between II and III. The detection rate of the experimental group's flora diversity is between II and III 92.86% (260/280), and the detection rate of the control group is 95.71% (134/140). Comparing the two, the normal
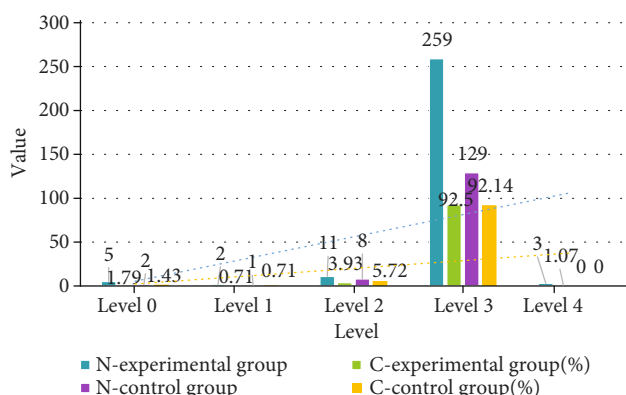
FIGURE 2: The density of vaginal microecological flora in the two groups of research subjects.
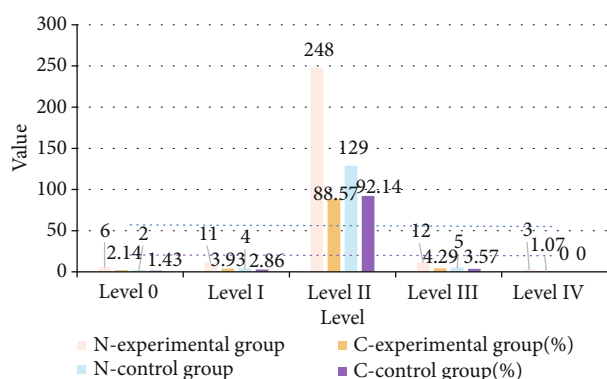
FIGURE 3: Diversity of vaginal flora in the two groups of subjects.

FIGURE 4: The status of dominant vaginal bacteria in the two groups of subjects.

TABLE 1: Vaginal secretion white blood cell count/high-powered visual field of the two groups of research subjects.

White blood cell count	Experiment group		Control group	
	Number of cases	Composition ratio (%)	Number of cases	Composition ratio (%)
≤10	183	65.36	85	60.71
>10	97	34.64	55	39.29

TABLE 2: The measurement of vaginal pH value of the two groups of research subjects.

Vagina pH	Experiment group		Control group	
	Number of cases	Composition ratio (%)	Number of cases	Composition ratio (%)
3.8~4.5	31	11.07	37	26.43
>4.6	249	88.93	103	73.57

rate of vaginal flora diversity in the experimental group was lower than that in the control group. The level of vaginal flora diversity indicates that the diversity of flora is too high. The detection rate of level IV of the experimental group's flora diversity is 1.07% (3/280), and the detection rate of the control group is 0. Comparing the two, the detection rate of excessive vaginal flora in the experimental group was higher than that in the control group. There was no statistically significant difference in the overall composition ratio between the two groups ($\chi^2 = 1.176$, $P > 0.05$).

4.1.3. Test Results of Dominant Vaginal Bacteria. 280 cases of the experimental group and 140 cases of the control group were tested for vaginal dominant bacteria; the results are shown in Figure 4.

It can be seen from Figure 4 that nondominant bacteria represent the inhibition of vaginal flora. The detection rate of nondominant bacteria in the vaginal flora in the experimental group was 2.14% (6/280), and the detection rate in the control group was 1.43% (2/140). Comparing the two, the detection rate of bacterial colony inhibition in the experimental group has a rising trend, and the difference is not statistically significant. The dominant bacteria in healthy vaginal microecology are Lactobacillus, which is Gram-positive bacteria; the detection rate of Gram-positive bacteria in the experimental group is

74.64% (209/280), and the detection rate in the control group is 90.0% (126/140). Comparing the two, the normal detection rate of dominant bacteria in the experimental group has a decreasing trend. The detection rate of the non-Gram-positive large bacterium as the dominant bacteria in the experimental group was 23.21% (65/280), and the detection rate in the control group was 8.57% (12/140); comparing the two, the detection rate of the dominant bacteria in the experimental group was out of balance; the rate has an upward trend. There was no statistically significant difference in the overall composition ratio between the two groups ($\chi^2 = 0.62$, $P > 0.05$).

4.1.4. Vaginal Secretion White Blood Cell Count/High-Powered Visual Field Results. 280 cases of the experimental group and 140 cases of the control group were tested for vaginal secretion white blood cell count. The results are shown in Table 1.

It can be seen from Table 1 that the number of white blood cells in normal vaginal secretions is ≤10/high-power field, and the white blood cell count > 10/high-power field indicates that there may be vaginal inflammation. In the

TABLE 3: The vaginal microecological enzymes of the two groups of research subjects.

Functional indicators	Experiment group		Control group		χ^2	P
	Number of cases	Composition ratio (%)	Number of cases	Composition ratio (%)		
Hydrogen peroxide is normal	186	66.43	107	76.43	5.182	<0.05
Hydrogen peroxide deficiency	94	33.57	33	23.57		
Sialidase positive	82	29.29	20	14.29	8.233	<0.05
Sialidase negative	198	70.71	120	85.71		
Leukocyte esterase positive	201	71.79	77	55.00	9.349	<0.05
Leukocyte esterase negative	79	28.21	63	45.00		
β-Glucuronidase positive	6	2.14	1	0.71	0.325	>0.05
β-Glucuronidase negative	274	97.86	139	99.29		
Acetylglucosaminidase positive	14	5.00	6	4.29	0.074	>0.05
Acetylglucosaminidase negative	266	95.00	134	95.71		
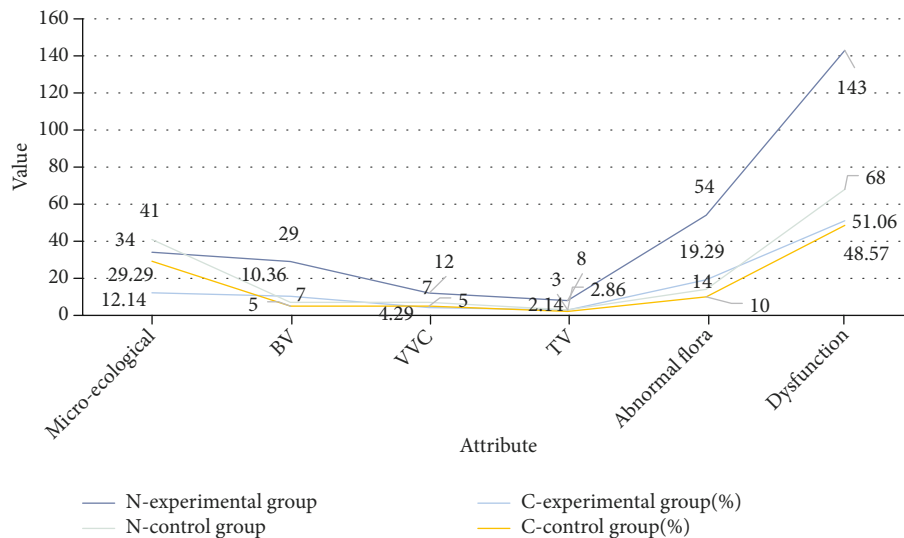
FIGURE 5: Comprehensive evaluation of vaginal microecology in the two groups of subjects.
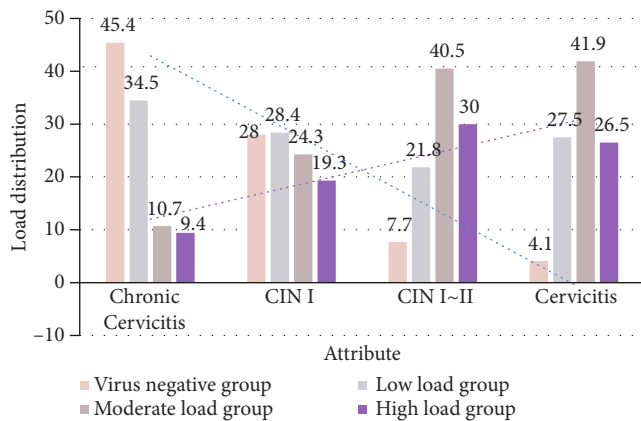
FIGURE 6: Schematic diagram of the distribution of high-risk HPV load of various levels of cervical lesions.

experimental group, the detection rate of vaginal secretion white blood cell count > 10/high-powered visual field was 34.64% (97/280). In the control group, the detection rate of vaginal secretion white blood cell count > 10/high-powered visual field was 39.29% (55/140); comparing the two, the detection rate of inflammation in the experimental group was higher than that in the control group. Calculating the comparison of the overall composition of the two groups, the difference between the two was not statistically significant ($\chi^2 = 0.004$, $P > 0.05$).

4.1.5. Measurement Results of Vaginal pH. The 280 cases of the experimental group and 140 cases of the control group were tested for vaginal pH. The results are shown in Table 2.

It can be seen from Table 2 that the normal vaginal pH value is between 3.8 and 4.5, and the pH value is higher than 4.6 abnormally. The detection rate of pH value > 4.6 in the experimental group was 88.93% (249/280), and the detection rate in the control group was 73.57% (103/140). Compared

TABLE 4: Comparison of HR-HPV load of various cervical lesions.

Year	Chronic cervicitis		CINI		CINII~III		Cervicitis		Statistics	P
	M	Q	M	Q	M	Q	M	Q		
≤35	2.700	0.588	3.450	2.311	8.965	6.968	1.440	3.572	4.200	<0.05
36~	1.173	0.510	7.335	0.783	5.290	8.020	0.398	4.826	14.759	<0.05
>50	1.294	0.460	1.782	0.545	5.525	2.983	6.150	7.938	4.656	<0.05
Statistics	2.411		4.416		1.892		0.436		—	—
P	>0.05		<0.05		>0.05		>0.05		—	—

with the control group, the detection rate of pH value > 4.6 in the experimental group has a rising trend, and the difference in the overall composition ratio between the two groups is statistically significant ($\chi^2 = 5.372, P < 0.05$).

4.1.6. Test Results of Vaginal Microecological Enzymes. 280 cases of the experimental group and 140 cases of the control group were tested for vaginal microecological enzymes. The results are shown in Table 3.

Table 3 shows that the normal detection rate of hydrogen peroxide in vaginal discharge in the experimental group was 66.43% (186/280), and the detection rate in the control group was 76.43% (107/40). The normal detection rate of hydrogen peroxide in secretions tends to decrease, and the difference is statistically significant ($\chi^2 = 5.182, P < 0.05$). The detection rate of sialidase positive in the vaginal discharge of the experimental group was 29.29% (82/280), while the detection rate of the control group was 14.29% (20/140), and the difference was statistically significant. It was $\chi^2 = 8.233, P < 0.05$. The detection rate of positive leukocyte esterase in vaginal discharge in the experimental group was 71.79% (201/280) compared to the detection rate of 55.0% (77/140) in the control group, and the difference was statistically significant ($\chi^2 = 9.349, P < 0.05$). Compared with the control group, the vaginal discharge in the experimental group had a higher detection rate of β-glucuronidase and acetylglucosaminidase, but the difference was not statistically significant.

4.1.7. Comprehensive Evaluation Results of Vaginal Microecological Status. The 280 cases of the experimental group and 140 cases of the control group were comprehensively evaluated for the vaginal microecological status, and the results are shown in Figure 5 and 6.

It can be seen from Figure 5 that the detection rate of normal vaginal microecology in the experimental group was 12.14% (34/280) compared with the detection rate of 29.29% (41/140) in the control group, and the difference was statistically significant (significance ($\chi^2 = 17.23, P < 0.05$)). The detection rate of vaginal BV in the experimental group was 10.36% (29/280) compared with the detection rate of 5.0% (7/140) in the control group, and the difference was statistically significant ($\chi^2 = 5.19, P < 0.05$). The detection rate of VVC, TV, vaginal flora abnormality, and dysfunction in the experimental group was higher than that of the corresponding control group, but the difference was not statistically significant.

4.2. Relevant Results for Patient Prognosis. The age composition of cervical lesions of each grade is different. Therefore, by comparing the relationship between high-risk HPV and cervical lesions of each grade, the age factor should be controlled. The 280 high-risk HPV-positive patients were divided into three groups: ≤35 years old, 36 years old~, and >50 years old. The results are shown in Table 4.

It can be seen from Table 4 that, stratified by age, the high-risk HPV load of each level of cervical lesions was compared by the rank sum test of multiple samples, and the differences were statistically significant ($P < 0.05$). It shows that there are significant differences in the high-risk HPV load of different grades of cervical lesions. And as the level of cervical lesions increases, the load of high-risk HPV also increases significantly. In addition, in patients with chronic cervicitis, CINII~III, and cervical cancer, there was no significant difference in the high-risk HPV load of each age group ($P > 0.05$), indicating that there is no correlation between age and high-risk HPV load. Only in CINI patients, there was a statistically significant difference in the load of high-risk HPV in each age group ($P < 0.05$). With the increase of age, the load of high-risk HPV decreased.

In the chronic cervicitis group, 45.4% of high-risk HPV cases were negative, and the remaining 54.5% of high-risk HPV-positive cases were 34.5%, 10.7%, and 9.4%, respectively. In the CINI group, 28.0% of cases were high-risk HPV-negative, and 72.0% of high-risk HPV-positive cases were 28.4%, 24.3%, and 19.3%, respectively. 7.7% of CINII-III cases were high-risk HPV-negative, and 92.3% of high-risk HPV-positive cases were 30.0%, 40.5%, and 21.8 with low-, moderate-, and high-level loads, respectively. In the cervical cancer group, 4.1% of cases were high-risk HPV-negative, and 95.9% of high-risk HPV-positive cases were 27.5%, 41.9%, and 26.5%, respectively. The load distribution of high-risk HPV in each grade of cervical lesions was compared by multiple sample rate χ^2 tests, and the difference was statistically significant ($\chi^2 = 231.119, P < 0.05$). This indicates that the high-risk HPV infection rates for different grades of cervical lesions differ significantly and that the high-risk HPV infection rates increase significantly with the level of cervical lesions.

5. Conclusions

Multiple HPV infections can increase the risk of cervical lesions. On the one hand, it may be related to the interaction between HPV subtypes. On the other hand, more and more

reports about HPV recombination suggest that multiple HPV infections may increase the risk of HPV recombination, producing HPV that is carcinogenic. This article analyzes the correlation between the vaginal microecological status of high-risk HPV-infected CIN patients and the patients' prognosis. Compared with healthy women, women with high-risk HPV infection for more than 6 months have the vaginal flora density of women with high-risk HPV infection for more than 6 months. The detection rates of abnormalities, abnormal flora diversity, dominant bacteria, vaginal secretion white blood cell count > 10/high-powered field of view, and β-glucuronidase-positive and acetylglucosaminidase-positive detection rates are all higher than those of the control group. There is no statistical significance ($P > 0.05$). The shortcomings of this article are the following: Because vaginal microecological testing is a new type of testing method, most medical institutions have not introduced the testing equipment, and the patients' acceptance of this testing method is not high, resulting in the failure of this study to be carried out on a large scale and many times. Center clinical trials can lead to inaccurate statistical results. Although there is a certain relationship between changes in female vaginal microecological status and long-term high-risk HPV infection, the specific mechanism remains unclear, and further studies are needed. Functional vaginal microecosystems play an important role in combating high-risk HPV infections. In the future, it will be used to increase the quantity and quality of lactic acid bacteria in the vagina, restore normal levels of hydrogen peroxide, and regulate vaginal pH when diagnosing and treating high-risk HPV infections. I can do it. And methods of killing pathogenic microorganisms improve the cure rate of high-risk HPV infections in many ways.

Data Availability

The data used to support the findings of this study are included within the article.

Conflicts of Interest

The authors declare that they have no competing interests.

Acknowledgments

References

[1] A. A. Rabaan, D. R. Taylor, M. F. Dawamneh, and J. A. al-Tawfiq, "Comparison of Xpert ® HPV and Hybrid Capture ® 2 DNA Test™ for detection of high-risk HPV infection in cervical atypical squamous cells of undetermined significance," *Journal of Infection and Public Health*, vol. 10, no. 2, pp. 219–223, 2017.

[2] A. Rabaan, S. A. Alfaraj, and M. A. Alkhalifah, "Comparison of the Cepheid Xpert HPV test and the HC2 High-Risk HPV DNA Test for detection of high-risk HPV infection in cervical smear samples in SurePath preservative fluid," *Journal of Medical Microbiology*, vol. 67, no. 5, pp. 676–680, 2018.

[3] H. X. Pan, J. Y. Zhu, J. H. Li, C. Song, and W. Liu, "5-Aminolevulinic acid photodynamic therapy for condyloma acuminata with high-risk HPV infection and local cellular immunoactivity of the patient," *National Journal of Andrology*, vol. 25, no. 1, pp. 50–54, 2019.

[4] Q. F. Ma, Y. L. Guo, H. Gao et al., "Prevalence and determinants of high-risk HPV infection among 11549 women from an opportunistic screening in Hubei Province," *Current Medical Science*, vol. 39, no. 4, pp. 622–630, 2019.

[5] S. N. Adebamowo, A. A. Adeyemo, and ACCME Research Group as part of the H3Africa Consortium, "Classical HLA alleles are associated with prevalent and persistent cervical high-risk HPV infection in African women," *Human Immunology*, vol. 80, no. 9, pp. 723–730, 2019.

[6] J. Zhao, L. Wang, H. Lin et al., "Association of HLA-DRB1/DQB1 polymorphism with high-risk HPV infection and cervical intraepithelial neoplasia women from Shanghai," *International Journal of Clinical and Experimental Pathology*, vol. 11, no. 2, pp. 748–756, 2018.

[7] I. Gustavsson, R. Aarnio, M. Berggrund et al., "Randomised study of HPV prevalence and detection of CIN2+ in vaginal self-sampling compared to cervical specimens collected by medical personnel," *International Journal of Cancer*, vol. 144, no. 1, pp. 89–97, 2019.

[8] W. Cheng, F. Xu, L. Gao, and J. Liu, "The correlation between the determination of vaginal micro-ecological composition and the outcome of HPV infection by High-Throughput Metagene Sequencing Information Technology on the Illumina Platform," *Journal of Infection and Public Health*, vol. 13, no. 12, pp. 1961–1966, 2020.

[9] F. Qiu, C. Yuan, J. Xu et al., "Role of B7-H4 in the progression and prognosis of cervical inflammation to cancer after human papilloma virus infection," *Journal of Biomedical Nanotechnology*, vol. 15, no. 5, pp. 1043–1051, 2019.

[10] J. Shen, L. L. Gao, Y. Zhang, L. L. Han, and J. D. Wang, "Prevalence of high-risk HPV and its distribution in cervical precancerous lesions among 35-64 years old women who received cervical cancer screening in Beijing," *Zhonghua yu fang yi xue za zhi [Chinese journal of preventive medicine]*, vol. 52, no. 5, pp. 493–497, 2018.

[11] Y. Chen, Y. R. Wang, Y. Shi, and G. H. Dai, "Prognostic value of chemotherapy-induced neutropenia in metastatic colon cancer patients undergoing first-line chemotherapy with FOLFOX," *Journal of Peking University*, vol. 49, no. 4, pp. 669–684, 2017.

[12] A. Cotoia, L. Mirabella, S. Altamura et al., "Circulating stem cells, HIF-1, and SDF-1 in septic abdominal surgical patients: randomized controlled study protocol," *Trials*, vol. 19, no. 1, pp. 179–181, 2018.

[13] O. Oral, M. Toprak, F. Uysal, O. M. Bostan, and E. Cil, "The frequency of asymptomatic urinary system abnormalities in children detected with cineurography imaging during angiocardiography," *Cardiology in the Young*, vol. 29, no. 2, pp. 119–122, 2019.

[14] A. M. Wielandt, C. Villarroel, C. Hurtado et al., "Abstract 3943: determination of the molecular profile of Chilean patients with sporadic colorectal cancer," *Cancer Research*, vol. 77, 13 Supplement, pp. 3943–3943, 2017.

[15] Y. Yamamoto, N. Yamamoto, Y. Kanematsu et al., "High white blood cell count is a risk factor for contrast-induced nephropathy following mechanical thrombectomy for acute ischemic stroke," *Cerebrovascular Diseases Extra*, vol. 10, no. 2, pp. 59–65, 2020.

[16] L. Curto-Barredo, L. Archilla, G. Vives, R. M. Pujol, and A. M. Giménez-Arnau, "Clinical features of chronic spontaneous urticaria that predict disease prognosis and refractoriness to standard treatment," *Acta Dermato Venereologica*, vol. 98, no. 7, pp. 641–647, 2018.

[17] L. Curto-Barredo, R. M. Pujol, G. Roura-Vives, and A. M. Gimenez-Arnau, "Chronic urticaria phenotypes: clinical differences regarding triggers, activity, prognosis and therapeutic response," *European journal of dermatology: EJD*, vol. 29, no. 6, pp. 627–635, 2019.

[18] B. H. Sohn, J. E. Hwang, H. J. Jang et al., "Clinical significance of four molecular subtypes of gastric cancer identified by The Cancer Genome Atlas project," *Clinical Cancer Research*, vol. 23, no. 15, pp. 4441–4449, 2017.

[19] Z. Kun-Peng, M. Xiao-Long, and Z. Chun-Lin, "lncRNA FENDRR sensitizes doxorubicin-resistance of osteosarcoma cells through down-regulating ABCB1 and ABCC1," *Oncotarget*, vol. 8, no. 42, pp. 71881–71893, 2017.

[20] A. Ogden, P. Rida, and R. Aneja, "Prognostic value of CA20, a score based on centrosome amplification- associated genes, in breast tumors," *Scientific Reports*, vol. 7, no. 1, pp. 262–294, 2017.

[21] C. Ticona-Huaroto, L. Astocondor-Salazar, J. Montenegro-Idrogo, G. Valencia-Mesias, and J. Soria, "Infección por el complejo Mycobacterium aviumintracellulare en pacientes con VIH/SIDA en un hospital peruano: una serie de casos," *Revista Peruana de Medicina Experimental y Salud Pública*, vol. 34, no. 2, pp. 323–327, 2017.

[22] S. Shiba, A. Miki, H. Ohzawa et al., "Abstract 3140: MUC1 expression as a prognosis marker and a new therapeutic target in patient with duodenal adenocarcinoma," *Cancer Research*, vol. 77, 13 Supplement, pp. 3140–3140, 2017.

[23] B. W. Kim, H. Cho, K. Ylaya et al., "Bcl-2-like protein 11 (BIM) expression is associated with favorable prognosis for patients with cervical cancer," *Anticancer Research*, vol. 37, no. 9, pp. 4873–4879, 2017.

[24] P. U. Thangavelu, C. Y. Lin, S. Vaidyanathan, T. H. M. Nguyen, E. Dray, and P. H. G. Duijf, "Overexpression of the E2F target geneCENPIpromotes chromosome instability and predicts poor prognosis in estrogen receptor-positive breast cancer," *Oncotarget*, vol. 8, no. 37, pp. 62167–62182, 2017.

Hindawi

Retraction

Retracted: Effect of FLOT2 Gene Expression on Invasion and Metastasis of Colorectal Cancer and Its Molecular Mechanism under Nanotechnology and RNA Interference

BioMed Research International

This article has been retracted by Hindawi following an investigation undertaken by the publisher [1]. This investigation has uncovered evidence of one or more of the following indicators of systematic manipulation of the publication process:

(1) Discrepancies in scope

(2) Discrepancies in the description of the research reported

(3) Discrepancies between the availability of data and the research described

(4) Inappropriate citations

(5) Incoherent, meaningless and/or irrelevant content included in the article

(6) Manipulated or compromised peer review

The presence of these indicators undermines our confidence in the integrity of the article's content and we cannot, therefore, vouch for its reliability. Please note that this notice is intended solely to alert readers that the content of this article is unreliable. We have not investigated whether authors were aware of or involved in the systematic manipulation of the publication process.

Wiley and Hindawi regrets that the usual quality checks did not identify these issues before publication and have since put additional measures in place to safeguard research integrity.

We wish to credit our own Research Integrity and Research Publishing teams and anonymous and named external researchers and research integrity experts for contributing to this investigation.

The corresponding author, as the representative of all authors, has been given the opportunity to register their agreement or disagreement to this retraction. We have kept a record of any response received.

References

[1] C. Zhong, F. Zheng, S. Ye, G. Gao, P. He, and D. Liu, "Effect of FLOT2 Gene Expression on Invasion and Metastasis of Colorectal Cancer and Its Molecular Mechanism under Nanotechnology and RNA Interference," *BioMed Research International*, vol. 2022, Article ID 2897338, 11 pages, 2022.

Research Article

Effect of FLOT2 Gene Expression on Invasion and Metastasis of Colorectal Cancer and Its Molecular Mechanism under Nanotechnology and RNA Interference

Chonghan Zhong,[1] Fangfang Zheng,[2] Shanping Ye,[1] Gengmei Gao,[1] Penghui He,[1] and Dongning Liu [1]

[1]*Department of Gastrointestinal Surgery, The First Affiliated Hospital of Nanchang University, Nanchang 330006, China*
[2]*Second Department of Cardiology, The Third Hospital of Nanchang, Nanchang 330009, China*

Correspondence should be addressed to Dongning Liu; ldn13576982921@163.com

The study is aimed at investigating the effect of the FLOT2 gene on invasion and metastasis of colorectal cancer (CRC) cells and the corresponding molecular mechanism by preparing polylysine-silicon nanoparticles. Specifically, polylysine was used to modify the silica nanoparticles prepared by the emulsification method to obtain polylysine-silicon nanoparticles. The characterization of polylysine-silicon nanoparticles was completed by nanoparticle size analyzer, laser particle size potentiometer, and transmission microscope. The influence of polylysine-silicon nanoparticles on the survival rate of CRC cell line HT-29 was detected using the method of 3-(4,5-dimethylthiazol-2-yl)-2, 5-diphenyltetrazolium bromide (MTT). The FLOT2-siRNA expression vector was constructed and transfected with HT-29. The HT-29 transfected with empty plasmid was used as the negative control (NC). Western Blot (WB) and reverse transcription-polymerase chain reaction (RT-PCR) were used to detect expression levels of FLOT2 gene and epithelial-mesenchymal transition- (EMT-) related genes. Transwell invasion assay, Transwell migration assay, and CCK8 assay were used to detect the cell invasion, migration, and proliferation. The results showed that the average particle size of polylysine-silicon nanoparticles was 30 nm, the potential was 19.65 mV, the particle size was 65.8 nm, and the dispersion coefficient was 0.103. At the same concentration, the toxicity of silicon nanoparticles to HT-29 was significantly lower than that of liposome reagent, and the transfection efficiency was 60%, higher than that of liposome reagent (40%). The mRNA level and protein expression of the FLOT2 gene in the FLOT2-siRNA group were significantly lower than those in the NC group ($P < 0.01$). The optical density (OD) value of the NC group and the blank control (CK) group were significantly higher than that of FLOT2-siRNA cells ($P < 0.01$). The OD value of FLOT2-siRNA cells was lower than that of NC cells at 48 h, 72 h, and 96 h ($P < 0.01$). The mRNA levels and protein expressions of MMP2 and vimentin in the FLOT2-siRNA group were significantly lower than those in the NC group and CK group ($P < 0.01$). The mRNA level and protein expression of the E-cadherin gene in the FLOT2-siRNA group were significantly higher than those in the NC group and CK group ($P < 0.01$). In conclusion, an RNA interference plasmid with high transfection efficiency and low cytotoxicity was established based on nanotechnology. siRNA-mediated FLOT2 protein inhibits the invasion, migration, and proliferation of CRC cells by regulating the expression changes of EMT-related genes, which provides a scientific basis for clinical treatment of CRC.

1. Introduction

As a targeted technology, RNA interference plays a key role in gene function verification, immune disease pathogenesis research, and prevention of infectious diseases [1]. The transfection systems commonly used in traditional RNA interfer- ence technology mainly include virus vector-mediated system and nonvirus-mediated DNA plasmid vector. Of them, the RNA interference transfection efficiency of virus vector-mediated system is high, but there is still a phenome- non of a small amount of virus protein expression after infec- tion of target cells, which leads to the body's specific immune

response. Moreover, vector assembly of the viral vector-mediated RNA interference system is difficult and costly [2]. A nonviral vector is obviously safer and more reliable than the viral vector, but it has the defects of low transfection efficiency and even ineffective expression of target genes when transfecting cells [3]. It is found that traditional RNA interference technologies all have the problem of gene vector selection, and a safe and effective gene vector is the key to the application of gene therapy in clinical treatment. The ideal gene vector should have the advantages of nontoxicity, high efficiency, good targeting, easy preparation, and low price. Therefore, it is of great significance to seek nontoxic gene vectors with high transfection efficiency, simple preparation, and low price. The development of nanotechnology provides new opportunities for the application of RNA interference technology. A nanoparticle-based gene carrier system has the characteristics of safety, high efficiency, and good biocompatibility, and thus, it becomes a new gene carrier [4]. Silicon is a low-toxicity biocompatible nanogene carrier material with easy surface modification. Silicon nanoparticles have been found to be a promising new gene carrier with good cell uptake effect. However, silicon nanoparticles alone cannot mediate DNA transfer, and their surface must be modified by ions or positive groups before they can be used as gene carriers [5]. Strongly positive poly-L-lysine-modified silicon nanoparticles can shield high-density positive charge, thus reducing the cytotoxicity, which has the advantages of good biocompatibility, noncytotoxicity, and easy surface modification, making it possible to become a good gene carrier [6].

Colorectal cancer (CRC) is one of the common malignant tumors of the digestive tract. According to related statistics, the incidence and mortality of CRC ranks the third among digestive tract tumors [7]. The onset of CRC is insidious, and most of the patients are in the middle or late stage when they go to see the doctor. About 55% of the patients have had distant metastases at the time of diagnosis. Although the current methods of surgery, radiotherapy, and chemotherapy have reduced the overall mortality of CRC, the prognostic effect of patients with local and remote metastasis is still not ideal. The current research results believe that invasion and metastasis are the main causes of death in CRC patients [8]. FLOT2 is highly expressed in a variety of tumor tissues and has an obvious correlation with the occurrence and development of tumors [9]. Moreover, FLOT2 expression is positively correlated with the tumor stage and lymphatic metastasis, and it is found that the proliferation of kidney cancer and breast cancer cells can be effectively inhibited after interference with FLOT2 gene [10]; in addition, FLOT2 gene expression is closely related to the invasion and metastasis of gastric cancer [11]. Studies have shown that the decrease of the expression level of FLOT2 protein mediated by siRNA can obviously inhibit the activity of Src tyrosine kinase, thus slowing down the epithelial-mesenchymal transition (EMT) process of human nasopharyngeal carcinoma cell line induced by TGF-β [12]. FLOT2 siRNA can reduce the growth and invasion of esophageal squamous cell carcinoma [13]. siRNA-mediated downregulation of FLOT2 expression can inhibit the proliferation, invasion, and migration of gastric cancer cells [14]. Mean-

while, studies have shown that FLOT2 can inhibit the proliferation of breast cancer cells by regulating Akt/FOXO signal transduction and that FLOT2 deficiency can lead to reduced cell metastasis in mouse breast cancer models [15]. These results indicate that the expression of FLOT2 gene is associated with invasion and metastasis of various tumors and is related to the activation of EMT, NF-κB, and Akt/FOXO signaling pathways. CRC metastasis is a very complex process involving multiple factors and steps, in which multiple signal transduction pathways are cross-linked and interact with each other. However, there are few studies on the effect of FLOT2 gene expression on the invasion and metastasis of CRC, and the mechanism is still unclear.

In summary, silicon nanoparticle modified with PLL is a DNA transfection carrier with high biological safety and high TE. There are few studies on the correlation between FLOT2 gene expression and CRC cell invasion and metastasis. In this study, an interference carrier of FLOT2 was constructed with RNA interference technology to explore the expression of siRNA carried by PLL-modified silicon nanoparticles in CRC cells, so as to explore the influence of FLOT2 gene on the invasion and metastasis of CRC and its corresponding molecular mechanism and provide a certain scientific basis for the clinical treatment and prognosis analysis of CRC.

2. Materials and Methods

2.1. Preparation of Silicon Nanoparticles and Modification of Polylysine. Similar to the hydrolysis method of ethyl orthosilicate in a water-in-oil microemulsion system, the silica nanoparticles were prepared by the emulsification method. The specific operation method was given as follows. After 4.0 g of nonylphenol polyoxyethylene ether, 50 mL of cyclohexane, and 0.6 mL of double distilled water were mixed and stirred completely, hexyl alcohol was added in dropwise to form a stable water/oil (W/O) microemulsion system; ethyl orthosilicate and an appropriate amount of ammonia were added and then stirred at the room temperature for 24 hours; after an appropriate amount of acetone was added, the mixture was centrifuged at 12,000 rpm/min for around 10 minutes to collect the sediment; the sediment was freeze-dried in a freeze drier, grinded into powder, added with 1.0 mL of Na$_2$CO$_3$ solution, sonicated for 15 minutes on an ice-water bath, and then centrifuged at 12,000 rpm/min for another 10 minutes to collect the sediment again; a 1.0 mL of resuspension liquid was added; the sediment was sonicated for another 20 minutes, added with 3.0 mg of polylysine powder, stirred at 4°C for 24 hours, and then centrifuged again for sediment collection; it was added with appropriate amount of sterile water for ultrasonic dispersion for around 2 hours and then autoclaved to sterilize for later use.

2.2. Property Characterization of Silicon Nanoparticle and Its Impact on Cell Viability. The PLL-modified silicon nanoparticles were prepared into 1 mg/mL suspension, and the particle size and potential of the nanoparticles were analyzed with a laser particle size potentiometer. At the same time, the

optical microscope and transmission microscope were utilized to observe its morphology. The cell survival rate was detected by MTT method, and the specific operation method was as follows. CRC cell lines HT29 and SW480 were inoculated at 5×10^3 cell/well into 96-well plates, added with different concentrations of PLL-modified silicon nano-suspension (10, 20, 30, 40, 50, 60, 70, 80, 90, and 100 μg/mL) prepared with Dulbecco's modified Eagle medium (DMEM); the liposome transfection reagent (Invitrogen Lipofectamine ™ 2000) was used as a control; after 24 hours of incubation, 100 μL of 0.5 mg/mL MTT solution was added to each well to cultivate for 4 hours, and 100 μL of dimethylsulfoxide (DMSO) was added to each well. The OD was detected at a wavelength of 490 nm, and the cell survival rate was calculated.

2.3. Design and Transfection of Interference Fragments of FLOT2 Gene.
According to the FLOT2 gene sequence information in Genbank and the principle of siRNA design, the siRN sequence of FLOT2 was designed. The siRNA sequence of FLOT2 was 5′-GCCuguccCuucUG-GuaaADTDT-3′, and NCBI showed no homology with other genes. Oligonucleotide fragments were synthesized in Shanghai and annealed after dilution to form double strands. The annealed double-stranded RNA fragments of FLOT2 were linked to linear plasmid Pgenesil-1 and named FLOT2-siRNA. Empty plasmid was used as a negative control (NC).

2.4. Cell Transfection and Transfection Efficiency Detection of FLOT2 Gene Interference Fragments.
One day before transfection, the human CRC cell strain HT29 was seeded in a 6-well plate at 5×10^4 cells/well, and the cell density during transfection should be guaranteed as about 90%. Before transfection, polylysine-silicon nanoparticles were dispersed in ice-water bath by ultrasonic for 20 min. Then, polylysine-silicon nanoparticles were mixed with FLOT2-siRNA and NC plasmids, respectively, at a mass ratio of 30 : 1. At 2 μg plasmid per well, the suspension of 15 μL polylysine-silicon nanoparticles (4 mg/mL) was mixed with 10 μL FLOT2-siRNA or NC plasmids (0.218 μg/L). After standing at room temperature for 40 min, the suspension was added to HT29 cells. After 5 h culture at 37°C in 5%CO$_2$ incubator, the culture medium was changed to DMEM complete medium containing serum. HT29 cells without plasmid transfection were used as a blank control (CK).

Using liposome transfection method as the control, the transfection was carried out according to the instruction of Invitrogen Lipofectamine TM 2000.The specific method of liposome transfection was as follows: transfection ratio was 1 : 3 (1 μg plasmid:3 μL liposome) and 2 μg plasmid was transferred to each well. 10 μL FLOT2-siRNA plasmid was mixed with 240 μL serum-free DMEM. At the same time, 6 μL liposome was mixed with 244 μL serum-free DMEM culture medium and the mixture was let still at room temperature for 5 min. The medium containing plasmid and the medium containing liposome were mixed evenly and then let still at room temperature for 20 min. When cells grew to 60-80%, the culture medium was removed, and the cells were rinsed with serum-free DMEM twice and then transferred to plasmid DNA/liposome complex medium to culture at 37°C, 5%CO$_2$, and saturated humidity for 6 h. Subsequently, the culture medium was changed to complete medium containing 10% calf serum, followed by culture for 24 h. The transfection efficiency was observed under the fluorescence microscope.

2.5. RT-PCR to Detect mRNA Expression Levels of FLOT2 and EMT-Related Molecules.
The total RNA of HT29 cells was extracted by TRIzol method. After the total RNA was detected by agarose gel electrophoresis, the cDNA was synthesized by reverse transcription kit (Takara Company) at 37°C for 15 min, and 85°C for 5 s in sequence. RT-PCR primer for FLOT2 gene: FLOT2-F: 5′-CCGTGGCT GTGA GCAGTT-3′, FLOT2-R: 5′- TGTCATACACGTCCTT GATGGT -3′; RT-PCR primer for MMP-2: MMP2-F: 5′-ATTCTGGAG-ATACAATGAGGT-3′, MMP2-R: 5′-TTCACGCTCTTCAGACTT-3′; RT-PCR primer for MMP-9: MMP9-F: 5′- GAAGATGCTGCTGTTCAG-3′, MMP9-R: 5′- AAAT AGGCTTTCTCTCGGTA-3′; RT-PCR primer for E-cadherin: E-cadherin-F: 5′-GACCAA GTGA CCACCTTA-3′, E-cadherin-R: 5′-AGAGCAGCA GAATCAGAAT-3′; and RT-PCR primer for vimentin: Vimentin-F: 5′-CATTGAGATTGCCACCTAC-3′, Vimentin-R: 5′-ATCGTTGATAACCTGTCCAT-3′. With β-actin as an internal reference, primer Actin-F of β-actin: 5′-AGGGGCCGGACTCGTCATACT-3′, Actin-R: 5′- GGCG GCACCACCATGTA CCCT-3′. Each sample was amplified with the above two pairs of primers, and a 20 μL reaction system was established. Three replicates were performed for each reaction in the Applied Biosystems StepOne real-time fluorescence quantitative PCR instrument. Annealing temperature was 60°C, and annealing time was 30 seconds, 30 cycles. The $2^{-\Delta\Delta ct}$ method [16] was used to calculate the relative expression.

2.6. WB to Detect the Expression Levels of FLOT2 and EMT-Related Protein.
After incubating in DMEM complete medium containing serum for 48 hours, the cells were collected. The total protein of liposome and HT29 cells transfected with silicon nanoparticle transfection interference plasmid were extracted, and the content of total protein extracted was determined with bicinchoninic acid (BCA). Cellular proteins were separated by sodium dodecyl sulfate polyacrylamide gel electrophoresis (SDS-PAGE), and the proteins were transferred to polyvinylidene fluoride (PVDF) membrane by wet transfer method and then sealed with 5% skimmed milk. FLOT2 and glyceraldehyde-phosphate dehydrogenase (GAPDH) antibodies diluted at a ratio of 1 : 1000 were added separately and incubated overnight at 4°C; after it was washed thoroughly with Tris-Buffered Saline Tween (TBST) for 3 times (with 10 min/time a time), horseradish peroxidase-conjugated secondary antibody was added and incubated at the room temperature for 2 h, rinsed thoroughly with TBST for another 3 times with 10 min/time each time, and then added with color developing solution for automatic exposure in development instrument. Required

photos were taken and greyscale scanning was implemented. ImageJ software was used to measure the grey values of each target protein band, and the ratio of the grey value of the target protein to that of the internal reference GAPDH protein band represented the relative expression level of the target protein.

2.7. Experiments for Transwell Invasion and Migration. The specific operation procedures of Transwell invasion were defined as below. Under sterile conditions, the Matrigel was diluted with serum-free DMEM at a ratio of 4 : 1 to generate the membrane surface coating. $40\,\mu$L of the diluted membrane surface coating was added to the upper chamber of Transwell rapidly, which should be distributed evenly on the upper compartment membrane. The cells were incubated at the $37°$C for 6 h and then inoculated. Cells in the log phase were collected, the cell suspension was prepared with serum-free DMEM after digestion, and the cell concentration was adjusted to 5×10^4 cells/mL. The cell suspension was poured to the upper layer of the Transwell chamber, $750\,\mu$L of DMEM complete medium was added to the lower chamber of the Transwell, and then, the solution was incubated at a temperature of $37°$C for 24 hours. Transwell chamber was taken out, flushed with 0.1% crystal violet lasting for 20 minutes, and rinsed with water for 3 times. Then, the photos were taken under the microscope after drying. $500\,\mu$L/well of 10% acetic acid was added to dissolve the dye on the polycarbonate membrane, and the value of each hole was measured when the wavelength was 570 nm. During the operation of the Transwell migration test, the coated filter did not contain Matrigel, the rest steps were the same as the Transwell invasion test, and the OD of every well was detected at a wavelength of 570 nm.

2.8. CCK8 Test. The cells were collected when they grew to 70%-80% and then suspend them in 3 mL of DMEM containing 10% FBS, 100 U/mL penicillin, and streptomycin, respectively; they were added with $200\,\mu$L/well cell suspension to incubate in a plate for 24, 48, and 72 h, respectively. After the CCK8 solution was mixed with DMEM containing 10% FBS, 100 U/mL penicillin, and streptomycin in a ratio of 1 : 10, respectively, $100\,\mu$L of the above mixed solution was added to each well of cells, and the culture plate was placed into the incubator for another 3 hours. The OD of every well was measured with a microplate reader at 450 nm at different incubation periods.

2.9. Statistical Analysis. SPSS 19.0 was used for data statistics and analysis. Measurement data were indicated as mean ± standard deviation ($\bar{x} \pm s$), and counting data were indicated with percentages. The measurement data obeying the normal distribution was compared by using the t-test, and measurement data not obeying the normal distribution was compared using the Wilcoxon Test. $P < 0.05$ indicated statistically meaningful difference.

3. Results

3.1. Analysis on Property Characteristics of Silicon Nanoparticles. After the silicon nanoparticles synthesized by the W/O emulsification method were modified with PLL, the electron microscope revealed that they were approximately spherical silicon nanoparticles (Figure 1(a)) with the regular morphology and uniform size (Figure 1(b)). The particle size was 5-55 nm, and the APS was 30 nm (Figure 1(c)). The analysis of particle size and potential of the nanoparticles by using the laser particle size potentiometer found that the PLL-modified silicon nanoparticles had the potential of 19.65 mV, the particle size of 65.8 nm, and the dispersion coefficient of 0.103.

3.2. Impacts of Silicon Nanoparticles on Cell Activity. Figure 2 showed the effects of polylysine-silicon nanoparticles and liposome reagents on the HT-29 cell activity. With the increasing concentration, the effects of polylysine-silicon nanoparticles and liposome reagents on the cell activity of HT-29 cell line showed a downward trend. At the same concentration, the survival rate of polylysine-silicon nanoparticle-treated cells was significantly higher than that of liposome transfection reagent-treated cells. When the concentration of polylysine-silicon nanoparticles and liposomes ranged from $50\,\mu$g/mL to $80\,\mu$g/mL, the activity of cells treated by liposomes was significantly different from that of polylysine-silicon nanoparticles ($P < 0.05$). When the concentration of polylysine-silicon nanoparticles and liposome reagent was greater than $80\,\mu$g/mL, the cell activity of transfection reagent was significantly different from that of polylysine-silicon nanoparticles ($P < 0.01$).

Figure 3 showed the effects of polylysine-silicon nanoparticles and liposome reagent on the SW480 cell activity. With the increasing concentration, the effect of polylysine-silicon nanoparticles and liposome reagent on the cell activity of SW480 cell line showed a downward trend. At the same concentration, the survival rate of polylysine-silicon nanoparticle-treated cells was significantly higher than that of liposome transfection reagent-treated cells. When the concentration of polylysine-silicon nanoparticles and liposomes ranged from $70\,\mu$g/mL to $90\,\mu$g/mL, the activity of cells treated by liposomes was significantly different from that treated by polylysine-silicon nanoparticles ($P < 0.05$). When the concentration of polylysine-silicon nanoparticles and liposomes was $100\,\mu$g/mL, the cell activity treated by liposomes was significantly different from that treated by polylysine-silicon nanoparticles ($P < 0.01$).

3.3. Detection on Transfection Efficiency of Silicon Nanoparticles. The plasmids were transfected with liposomes and nanoparticles to compare their TEs under a fluorescence microscope (Figure 4) so as to verify the TE of silicon nanoparticles in HT29 cells. It suggested that the fluorescence of plasmid transfected with nanoparticles was remarkably more than that of liposome transfection. At the same time, the average transfection efficiency of different methods was calculated in 5 fields. It was found that the transfection efficiency of nanoparticles was $60.58 \pm 2.15\%$ and that of liposomes was $40.29 \pm 1.79\%$ ($P < 0.05$).

3.4. Detection on FLOT2 Gene Expression. WB was used to detect the expression level of FLOT2 gene in HT-29 cell lines

(a)

(b)

(c)
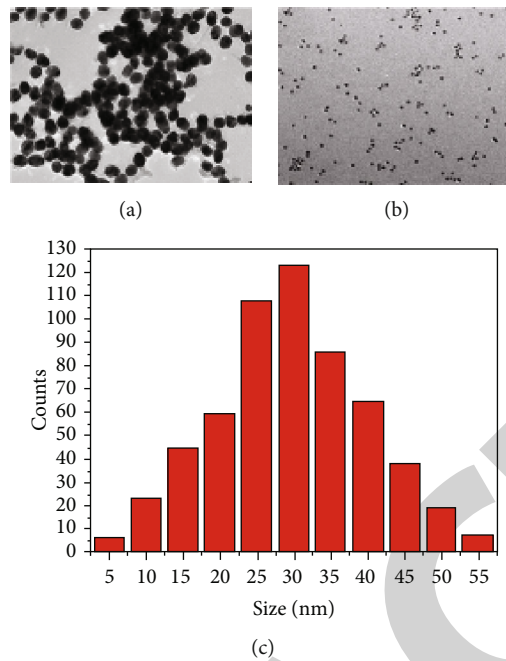
Figure 1: Analysis on property characteristics of silicon nanoparticles. (a, b) The morphology of silicon nanoparticles under transmission microscope and optical microscope, respectively. (c) The range of particle size.
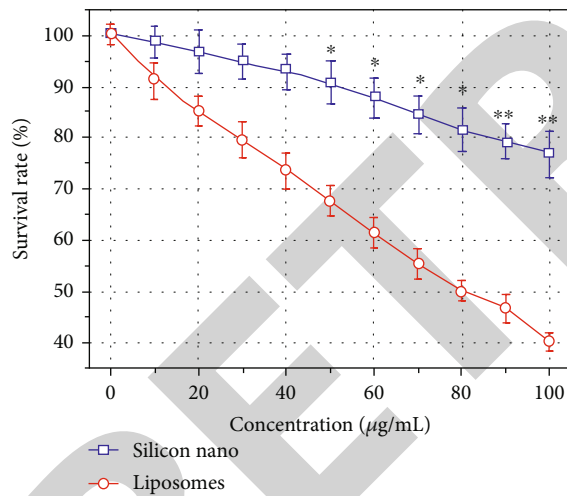
Figure 2: Effect of silicon nanoparticles on cell viability of HT29 cells. ($^*P < 0.05$ indicates a statistical difference compared with liposome-transfected cells; $^{**}P < 0.01$ indicates a significant difference compared with liposome-transfected cells).

Figure 3: Effect of silicon nanoparticles on SW480 cell activity ($^*P < 0.05$ indicates a statistical difference compared with liposome-transfected cells; $^{**}P < 0.01$ indicates a significant difference compared with liposome-transfected cells).

transfected with liposomes and nanoparticles. As shown in Figure 5, the FLOT2 gene expression bands were significantly weaker in FLOT2-siRNA in HT-29 cell lines transfected with liposomes and nanoparticles than those in NC and CK (Figure 5(a)). In HT-29 cell lines transfected with liposomes and nanoparticles, the expression of FLOT2 protein was significantly lower than that in NC and CK groups (Figures 5(b) and 5(c)) ($P < 0.01$).

RT-PCR was further used to detect the expression level of the FLOT2 gene. As shown in Figure 6, in the HT-29 cell line transfected with liposomes and nanoparticles, the mRNA expression of FLOT2 gene was significantly lower than the NC and CK groups ($P < 0.01$).

3.5. Analysis on Experiment Results of Transwell Invasion. Figure 7 showed the invasion results of the NC, CK, and FLOT2-siRNA groups. The number of invaded cells in the FLOT2-siRNA group was significantly less than that in the NC group and CK group (Figure 7(a)), and the OD value of FLOT2-siRNA group was significantly lower than that of the NC group and CK group, with significant differences ($P < 0.01$).

(a)

(b)

(c)

(d)
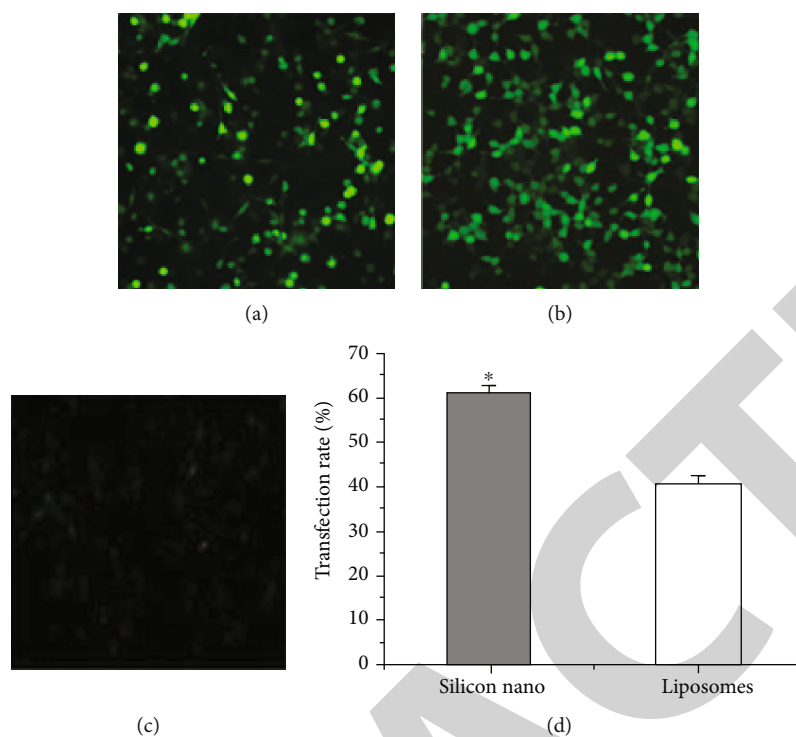
Figure 4: Fluorescence images of plasmid transfected with nanoparticles and liposome. (a, b) The fluorescence images of plasmid HT29 transfected with liposome and nanoparticles, respectively. (c) The fluorescence image of not transfected plasmid HT29. (d) The transfection efficiency of the two transfection methods ($^*P < 0.05$ indicates a statistical difference compared with liposome-transfected cells).

(a)

(b)

(c)
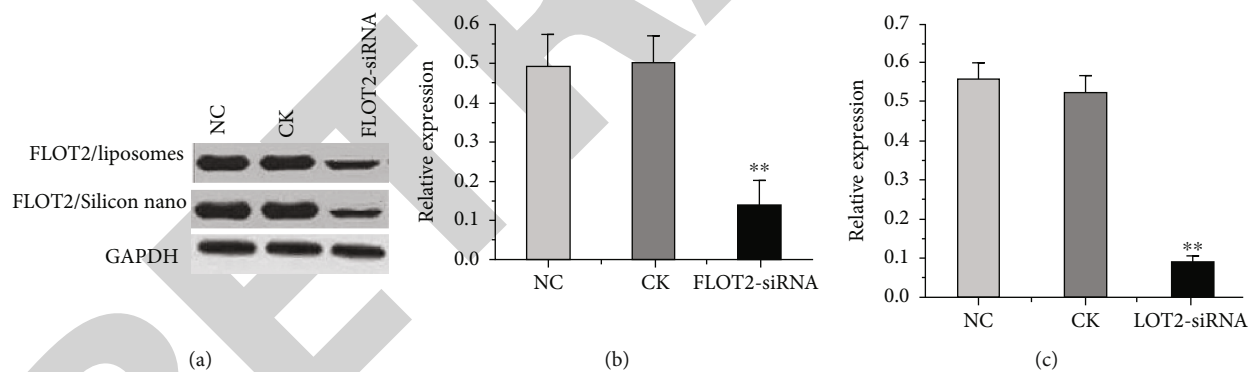
Figure 5: FLOT2 gene expression detected by WB. (a) WB development of HT-29 cells transfected with FLOT2-siRNA. (b) FLOT2 protein expression in HT-29 cells transfected with liposomes. (c) FLOT2 protein expression in HT-29 cells transfected with nanoparticles ($^{**}P < 0.01$ indicates an extremely significant difference compared with the NC group).

3.6. Analysis on Experiment Results of Transwell Migration. Figure 8 showed the migration results of the NC, CK, and FLOT2-siRNA groups. The number of migration cells in the FLOT2-siRNA group was significantly less than that in the NC group and CK group (Figure 8(a)), and the OD value of FLOT2-siRNA migration cells was significantly lower than that of NC group and CK group, with significant differences ($P < 0.01$).

3.7. Analysis on CCK8 Experiment Results. The results of the CCK8 experiment were shown in Figure 9. It suggested that the ODs of cells in NC and FLOT2-siRNA had rising trends

over time, and the ODs in two groups were not statistically different at the 0th and 24th hour ($P > 0.05$). Starting from the 48th hour, the ODs of cells in the two groups increased rapidly with time. The OD in FLOT2-siRNA was lower than that in NC at the 48th, 72nd, and 90th hour, and the two had extremely observable difference ($P < 0.01$).

3.8. Expression of EMT-Related Genes in Different Groups. The mRNA levels of EMT-related genes, namely, MMP9, MMP2, E-cadherin, and vimentin, in different groups were analyzed. As shown in Figure 10, there was no statistical difference in the expression levels of MMP9 gene in the
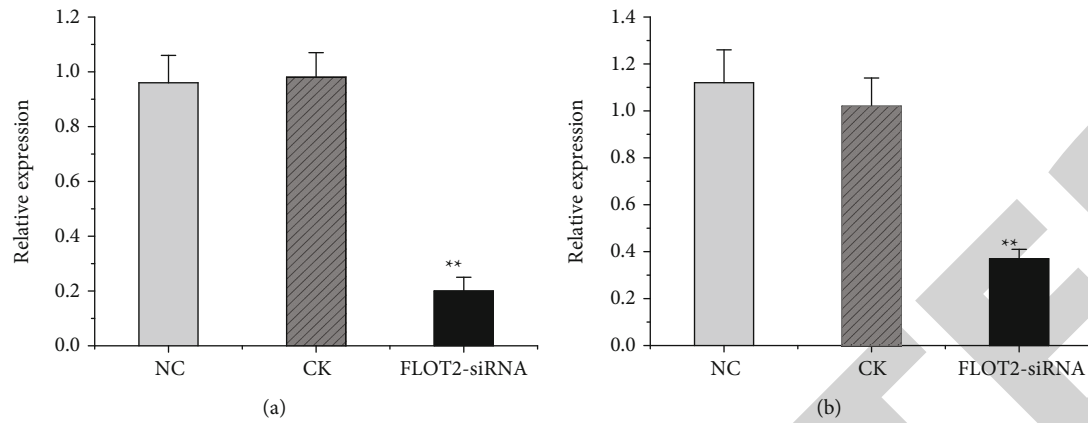
Figure 6: Comparison in mRNA level of FLOT2 gene. (a) FLOT2 mRNA level in HT-29 cells transfected with liposome plasmid. (b) FLOT2 gene mRNA level in HT-29 cells transfected with nanoparticles. ($**P < 0.01$ indicates an extremely significant difference compared with the NC group).
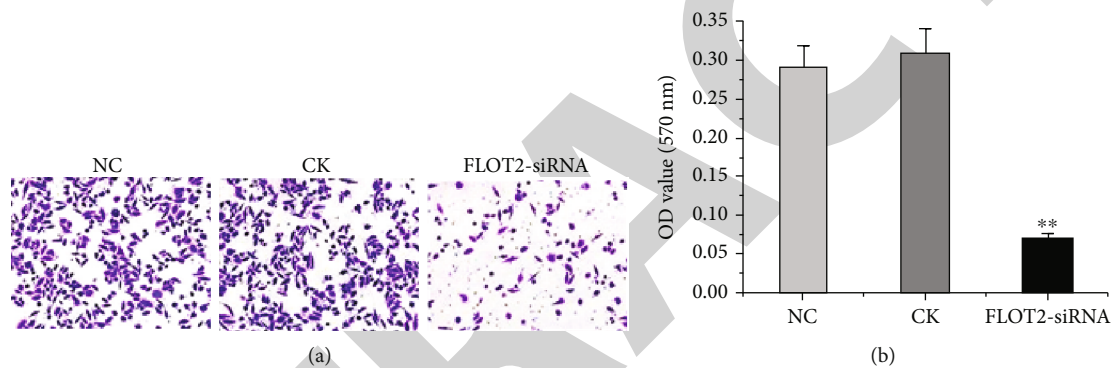
Figure 7: Experiment results of Transwell invasion in different groups. (a) The images of Transwell invasion in two groups. (b) The comparison in ODs of Transwell invasion in two groups.
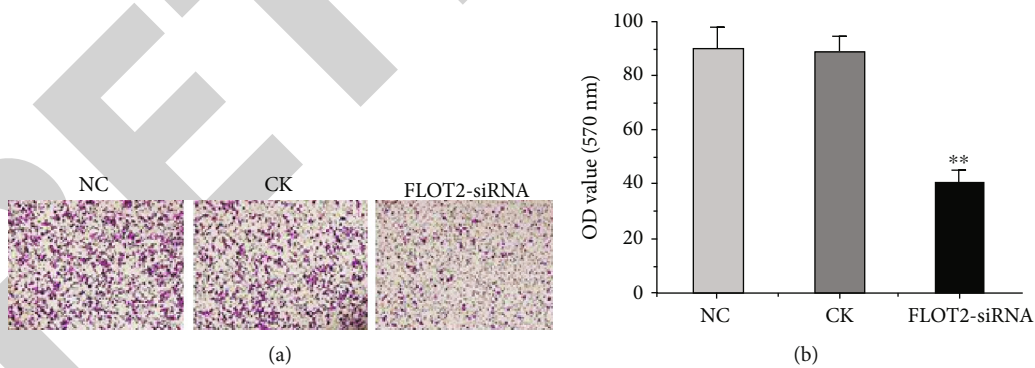
Figure 8: Analysis on experiment results of Transwell migration in different groups (a) The images of Transwell migration of cells in each group (b) The ODs of Transwell migration in each group. Note: $**P < 0.01$ suggested the difference with the NC group was extremely obvious.

NC group, CK group, and FLOT2-siRNA group ($P > 0.05$). The mRNA levels of MMP2 and vimentin in the FLOT2-siRNA group were significantly lower than those in the NC group and CK group ($P < 0.01$). The mRNA level of E-cadherin in the FLOT2-siRNA group was significantly higher than that in the NC group and CK group, with significant differences ($P < 0.01$).

Figure 11 showed the expression levels of EMT-related gene protein in different groups. There was no statistical difference in the expression levels of MMP9 protein in the NC group, CK group, and FLOT2-siRNA group ($P > 0.05$). The protein expression levels of MMP2 and vimentin in the FLOT2-siRNA group were significantly lower than those in the NC group and CK group ($P < 0.01$). The expression of
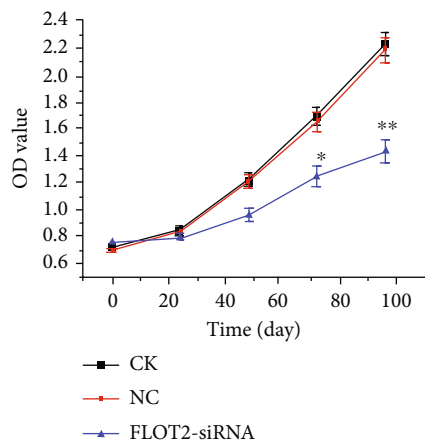
Figure 9: Comparison in CCK8 experiment results of different groups Note: $**P < 0.01$ suggests extremely obvious differences versus NC group, and $*P < 0.05$ represents a statistical difference compared with the NC group.
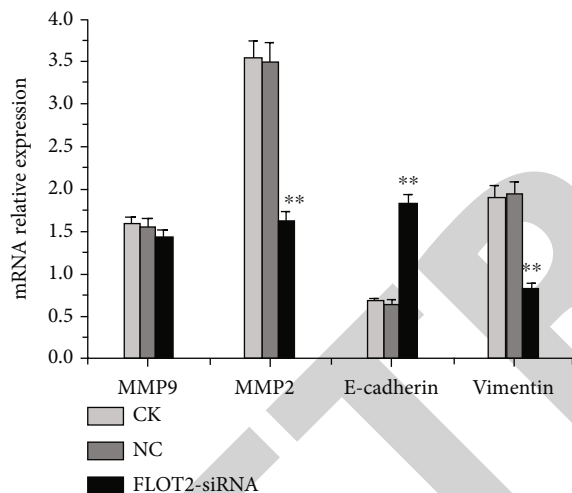
Figure 10: Expression levels of EMT-related genes in different groups. $**P < 0.01$ represents significant differences compared with NC group.

E-cadherin protein in the FLOT2-siRNA group was significantly higher than that in the NC group and CK group, with significant differences ($P < 0.01$).

4. Discussion

As a targeted technology, RNA interference technology plays a critical role in gene function verification, research on the pathogenesis of immune diseases, and prevention and treatment of infectious diseases. However, the current transfection systems commonly used in RNA interference technology have certain defects [17]. Therefore, seeking gene carriers with high TE, simple preparation, low price, and no toxicity is of important research significance. The development of nanotechnology provides a new opportunity for the application of RNA interference technology. Current studies have found that silicon nanoparticles have a better

cell uptake effect. They can adhere to the cell surface and enter the cell after binding with the target gene. They are relatively less toxic to cells. Nanoparticles can also protect foreign DNA fragments from degradation of DNA enzymes in the body [18, 19]. In this study, nonylphenol polyoxyethylene ether was undertaken as a surfactant to prepare the silicon nanoparticles by the emulsification method, the nanoparticles were modified with PLL, and their properties were analyzed. The results showed that the nanoparticles had regular morphology and uniform size under an electron microscope, with an APS of 30 nm, a potential of 19.65 mV, a particle size of 65.8 nm, and a dispersion coefficient of 0.103. Appropriate surfactants were generally adsorbed on the surface of the particles, which could protect the stability of the particles to a certain extent [20]. Studies have pointed out that the smaller the nanoparticle, the greater the density of modified substance bound per unit area [21]. Moreover, the PLL used in this study was positively charged, and the surface had a large amount of positive charges after modifying the silicon nanoparticles, which enhanced the binding capacity of plasmid DNA. To verify the effect of silicon nanoparticles prepared in this article on cell activity, differences between the two groups were compared by taking liposome transfection reagent as a control. It was found that the cell survival rate of silicon nanoparticles was observably higher than that of the liposome transfection reagent at the same concentration. It indicated that the toxicity of silicon nanoparticles to cells was greatly lower than that of liposome transfection reagents. A large number of research results have shown that cationic liposome transfection reagent as a nonviral carrier has poor stability and cytotoxicity [22]. Moreover, the results of this study found that TE of the nanoparticle and liposome was 60% and 40%, respectively, which were much different from each other. The above results indicated that the silicon nanoparticles prepared had the characteristics of low impact on cell activity and high TE, so they could be widely and extensively applied in the transfection of foreign genes.

FLOT2 is a member of the floating protein family and is an important lipid raft marker protein. As a signal protein, it was involved in various events such as cell proliferation, apoptosis, adhesion, cell signal transduction, and cell surface protein stability [23, 24]. FLOT2 was related to in human neuron differentiation and axon regeneration, T cell activation and its receptor complement, and the formation of lipid raft structure and endocytosis [25, 26]. In addition, a large number of research results show that FLOT2 is closely related to formation and development of tumor. It has been found that FLOT2 gene is highly expressed in various cancers, which promotes the occurrence and metastasis of tumor [27]. siRNA-mediated FLOT2 protein can greatly reduce the activity of Src tyrosine kinase and alleviate the epithelial-mesenchymal transformation process of nasopharyngeal carcinoma cell strains [14]; and siRNA-mediated FLOT2 protein can also reduce the growth and invasion of esophageal squamous cancer [28]. The results of this study found that the FLOT2 protein expression in the FLOT2-siRNA group was decreased greatly comparing with the NC group ($P < 0.01$). The mRNA level in the FLOT2 gene
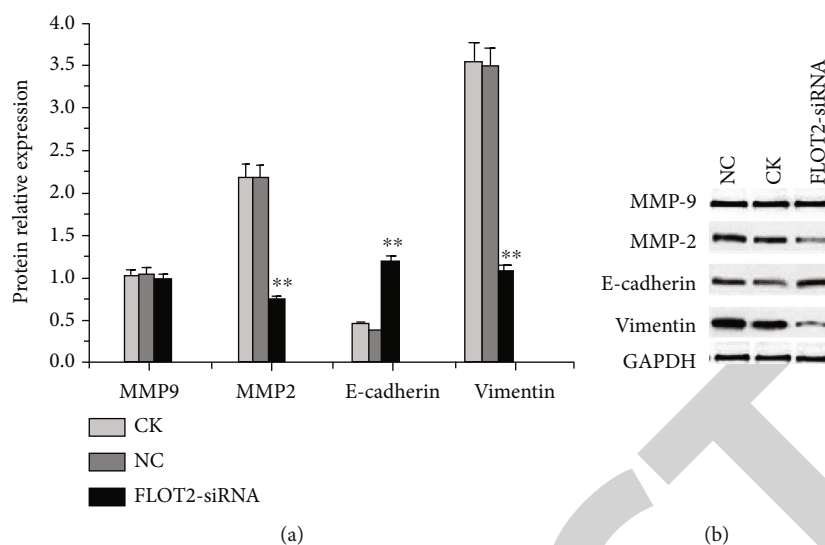
FIGURE 11: EMT-related protein expression levels in different groups. (a) Developed images of EMT-related protein in different groups. (b) EMT-related protein expression levels in different groups ($^{**}P < 0.01$ represents extremely obvious differences versus the NC group).

in the FLOT2-siRNA group was much lower than that in the NC group ($P < 0.05$), which was consistent with the current research results. This article further studied the impacts of the FLOT2 gene on the invasion and metastasis ability of CRC cells and found that the ODs of invasion cells and migration cells in NC were ncreased greatly in contrast to the FLOT2-siRNA with $P < 0.01$ and $P < 0.05$, respectively. The OD in both groups increased with time. The OD of cells in FLOT2-siRNA cells was lower than that in NC at the 48th, 72nd, and 96th hour ($P < 0.001$). Wang et al. [29] applied RNA interference technology to downregulate the expression of FLOT2 and found that the proliferation, invasion, and migration of gastric cancer cells were inhibited effectively, which was similar to the results of this article.

MMPs have been proved to be the most important proteolytic enzyme affecting matrix degradation during EMT [30]. Type IV gelatinase MMP-2 and MMP-9 are the most important MMPs [31]. Many studies have reported the role of MMP-2 and MMP-9 in the process of EMT [32, 33]. The results of this study showed that there was no statistical difference in mRNA level and protein expression of MMP9 gene in the NC group, CK group, and FLOT2-siRNA group ($P > 0.05$), and the mRNA level and protein level of MMP2 in the FLOT2-siRNA group were significantly lower than those in the NC group and CK group ($P < 0.01$). It was noted that siRNA-mediated FLOT2 protein downregulates the expression of MMP-2 and degrades the extracellular matrix in CRC cells, thus playing an important role in the EMT process of CRC cells. In addition, E-cadherin and vimentin are considered the most important epithelial cell markers and mesenchymal cell phenotypic markers during EMT [34]. Many experiments have confirmed that the decrease of E-cadherin protein activity is the first step for tumor cells to acquire the ability of dedifferentiation and invasion [35], that is, E-cadherin protein can inhibit the invasion and migration of tumor cells [36]. Meanwhile, overexpression of vimentin can promote the invasion and

migration of tumor cells [37], while blocking its expression through molecular biological methods can significantly reduce the invasion ability of tumor cells. The results showed that the mRNA level and protein expression of vimentin in the FLOT2-siRNA group were significantly lower than those in the NC group and CK group ($P < 0.01$) and that the mRNA level and protein expression of E-cadherin in the FLOT2-siRNA group were significantly higher than those in the NC group and CK group ($P < 0.01$). These results suggest that siRNA-mediated FLOT2 protein may play an important role in EMT by downregulating vimentin expression and upregulating E-cadherin expression in CRC cells. Above, this study confirmed that FLOT2 inhibits the migration and invasion of CRC cells by regulating the expression levels of MMP-2, E-cadherin, and vimentin during EMT.

5. Conclusion

Based on nanotechnology, the silicon nanoparticles were modified and applied to the construction of RNA interference plasmids. The TE of nanoparticles on the interference plasmids and their effects on cell viability were discussed. The FLOT2 gene in invasion, migration, and proliferation of CRC cell was further studied. However, there are still some shortcomings in this article. This article only studied the TE based on the FLOT2 gene fragment and did not use genes of different fragment sizes for the study. Therefore, it is unclear whether the TE of silicon nanoparticles will be affected by the gene fragment size. In the future, different fragment sizes will be added to explore whether the TE of silicon nanoparticles is related to the size of gene fragments. In the study, an RNA interference plasmid with high transfection efficiency and low cytotoxicity was established based on nanotechnology. It was found that siRNA-mediated FLOT2 protein inhibits the invasion, migration, and proliferation of CRC cells by regulating the expression of EMT-related genes, which provides a scientific basis for clinical treatment of CRC.

Data Availability

All data, models, and code generated or used during the study appear in the submitted paper.

Conflicts of Interest

No potential conflict of interest was reported by the authors.

Authors' Contributions

Chonghan Zhong and Fangfang Zheng contributed equally to this work as co-first author.

Acknowledgments

References

[1] X. Nie, Z. Zhang, C. Wang, Y. Fan, Q. Y. Meng, and Y. Z. You, "Interactions in DNA condensation: an important factor for improving the efficacy of gene transfection," *Bioconjugate Chemistry*, vol. 30, no. 2, pp. 284–292, 2019.

[2] S. R. Choudhury, E. Hudry, C. A. Maguire, M. Sena-Esteves, X. O. Breakefield, and P. Grandi, "Viral vectors for therapy of neurologic diseases," *Neuropharmacology*, vol. 120, pp. 63–80, 2017.

[3] A. Amani, T. Kabiri, S. Shafiee, and A. Hamidi, "Preparation and characterization of PLA-PEG-PLA/PEI/DNA nanoparticles for improvement of transfection efficiency and controlled release of DNA in gene delivery systems," *Iranian Journal of Pharmaceutical Research*, vol. 18, no. 1, pp. 125–141, 2019.

[4] Z. Ge, Q. Li, and C. Fan, "Framework nucleic acids for cell imaging and therapy," *Chemical Research in Chinese Universities*, vol. 36, no. 1, pp. 1–9, 2020.

[5] X. Li, D. Yao, J. Zhou et al., "Cascaded DNA circuits-programmed self-assembly of spherical nucleic acids for high signal amplification," *Science China. Chemistry*, vol. 63, no. 1, pp. 92–98, 2020.

[6] T. Suzuki, N. Miura, R. Hojo et al., "Genotoxicity assessment of intravenously injected titanium dioxide nanoparticles in _gpt_ delta transgenic mice," *Mutation Research, Genetic Toxicology and Environmental Mutagenesis*, vol. 802, pp. 30–37, 2016.

[7] A. Sveen, S. Kopetz, and R. A. Lothe, "Biomarker-guided therapy for colorectal cancer: strength in complexity," *Nature Reviews. Clinical Oncology*, vol. 17, no. 1, pp. 11–32, 2020.

[8] X. Deng, H. Ruan, X. Zhang et al., "Long noncoding RNA CCAL transferred from fibroblasts by exosomes promotes chemoresistance of colorectal cancer cells," *International Journal of Cancer*, vol. 146, no. 6, pp. 1700–1716, 2020.

[9] X. Mou and S. Liu, "MiR-485 inhibits metastasis and EMT of lung adenocarcinoma by targeting Flot2," *Biochemical and Biophysical Research Communications*, vol. 477, no. 4, pp. 521–526, 2016.

[10] R. Liu, H. Xie, C. Luo et al., "Identification of FLOT2 as a novel target for microRNA-34a in melanoma," *Journal of Cancer Research and Clinical Oncology*, vol. 141, no. 6, pp. 993–1006, 2015.

[11] T. Li, C. Cao, Q. Xiong, and D. Liu, "FLOT2 overexpression is associated with the progression and prognosis of human colorectal cancer," *Oncology Letters*, vol. 17, no. 3, pp. 2802–2808, 2019.

[12] L. Zhao, L. Lin, C. Pan et al., "Flotillin-2 promotes nasopharyngeal carcinoma metastasis and is necessary for the epithelial-mesenchymal transition induced by transforming growth factor-β," *Oncotarget*, vol. 6, no. 12, pp. 9781–9793, 2015.

[13] H. Gong, L. Song, C. Lin et al., "Downregulation of miR-138 sustains NF-κB activation and promotes lipid raft formation in esophageal squamous cell carcinoma," *Clinical Cancer Research*, vol. 19, no. 5, pp. 1083–1093, 2013.

[14] Q. Li, J. Peng, X. Li, A. Leng, and T. Liu, "miR-449a targets Flot2 and inhibits gastric cancer invasion by inhibiting TGF-β-mediated EMT," *Diagnostic Pathology*, vol. 10, no. 1, p. 202, 2015.

[15] G. Xie, J. Li, and J. Chen, "Knockdown of flotillin-2 impairs the proliferation of breast cancer cells through modulation of Akt/FOXO signaling," *Oncology Reports*, vol. 33, no. 5, pp. 2285–2290, 2015.

[16] E. Rishi, P. Rishi, and K. L. Therese, "Culture and reverse transcriptase polymerase chain reaction (RT-PCR) proven mycobacterium tuberculosis endophthalmitis: a case series," *Ocular Immunology and Inflammation*, vol. 26, no. 2, pp. 1–8, 2018.

[17] P. R. Brandao, S. S. Titzedealmeida, and R. Titzedealmeida, "Leading RNA interference therapeutics part 2: silencing delta-aminolevulinic acid synthase 1, with a focus on givosiran," *Molecular Diagnosis & Therapy*, vol. 24, no. 1, pp. 61–68, 2020.

[18] A. M. Flores, N. Hosseininassab, and K. Jarr, "Pro-efferocytic nanoparticles are specifically taken up by lesional macrophages and prevent atherosclerosis," *Nature Nanotechnology*, vol. 15, no. 2, pp. 154–161, 2020.

[19] C. Zhou, X. Hu, C. Tang et al., "CasRx-mediated RNA targeting prevents choroidal neovascularization in a mouse model of age-related macular degeneration," *National Science Review*, vol. 7, no. 5, pp. 835–837, 2020.

[20] X. Liang, L. Li, J. Tang, M. Komiyama, and K. Ariga, "Dynamism of supramolecular DNA/RNA nanoarchitectonics: from interlocked structures to molecular machines," *Bulletin of the Chemical Society of Japan*, vol. 93, no. 4, pp. 581–603, 2020.

[21] S. Hassan, F. U. Hassan, and M. S. Rehman, "Nano-particles of trace minerals in poultry nutrition: potential applications and future prospects," *Biological Trace Element Research*, vol. 195, no. 2, pp. 591–612, 2020.

[22] S. E. Samani, D. Chang, and E. M. Mcconnell, "Highly sensitive RNA-cleaving DNAzyme sensors from surface-to-surface product enrichment," *ChemBioChem*, vol. 21, no. 5, pp. 632–637, 2020.

[23] F. Gao, H. Wu, and R. Wang, "Micro RNA-485-5p suppresses the proliferation, migration and invasion of small cell lung cancer cells by targeting flotillin-2," *Bioengineered*, vol. 10, no. 1, pp. 1–12, 2019.

[24] E. Drozd, J. Krzysztoń-Russjan, and B. Gruber, "Doxorubicin treatment of cancer cells impairs reverse transcription and affects the interpretation of RT-qPCR results," *Cancer Genomics & Proteomics*, vol. 13, no. 2, pp. 161–170, 2016.

[25] M. Y. Park, N. Kim, L. L. Wu, G. Y. Yu, and K. Park, "Role of flotillins in the endocytosis of GPCR in salivary gland

Retraction

Retracted: The Valuable Role of ARMC1 in Invasive Breast Cancer as a Novel Biomarker

BioMed Research International

This article has been retracted by Hindawi following an investigation undertaken by the publisher [1]. This investigation has uncovered evidence of one or more of the following indicators of systematic manipulation of the publication process:

(1) Discrepancies in scope

(2) Discrepancies in the description of the research reported

(3) Discrepancies between the availability of data and the research described

(4) Inappropriate citations

(5) Incoherent, meaningless and/or irrelevant content included in the article

(6) Manipulated or compromised peer review

The presence of these indicators undermines our confidence in the integrity of the article's content and we cannot, therefore, vouch for its reliability. Please note that this notice is intended solely to alert readers that the content of this article is unreliable. We have not investigated whether authors were aware of or involved in the systematic manipulation of the publication process.

Wiley and Hindawi regrets that the usual quality checks did not identify these issues before publication and have since put additional measures in place to safeguard research integrity.

We wish to credit our own Research Integrity and Research Publishing teams and anonymous and named external researchers and research integrity experts for contributing to this investigation.

The corresponding author, as the representative of all authors, has been given the opportunity to register their agreement or disagreement to this retraction. We have kept a record of any response received.

References

[1] Y. Gan, F. Zhong, H. Wang, and L. Li, "The Valuable Role of ARMC1 in Invasive Breast Cancer as a Novel Biomarker," *BioMed Research International*, vol. 2022, Article ID 1740295, 18 pages, 2022.

Hindawi

Research Article

The Valuable Role of ARMC1 in Invasive Breast Cancer as a Novel Biomarker

Yunhao Gan [iD],[1] Fuxin Zhong [iD],[2] Hao Wang [iD],[3] and Lingyu Li [iD][4]

[1]*Institute of Neuroscience, Department of Pathology, Chongqing Medical University, China*
[2]*Institute of Neuroscience, Department of Human Anatomy, Chongqing Medical University, China*
[3]*Department of Breast Surgery, People's Hospital of Yubei District of Chongqing, China*
[4]*Department of Pathology, Chongqing Medical University, China*

Correspondence should be addressed to Hao Wang; wanghao123202105@163.com and Lingyu Li; 102815@cqmu.edu.cn

Yunhao Gan and Fuxin Zhong contributed equally to this work.

Background. Invasive breast carcinoma (BRCA) is a common type of breast cancer with a high clinical incidence. Thus, it is significant to find effective biomarkers for BRCA diagnosis and treatment. Although some members of armadillo (ARM) repeat family of proteins are confirmed to be biomarkers in cancers, the role of armadillo repeat-containing 1 (ARMC1) in BRCA remains unknown. *Methods*. We firstly analyzed the ARMC1 expression in normal breast tissues and BRCA samples and its association with overall survival by the public database. Next, the χ^2 test was used to evaluate the prognostic significance of ARMC1 expression in TCGA-BRCA patient samples. The ARMC1 mutations in BRCA were explored in the cBioportal database. Besides, the Gene Ontology (GO) and Kyoto Encyclopedia of Genes and Genomes (KEGG) enrichment analyses were used to explore the biological functions of ARMC1 in BRCA. Finally, immunohistochemistry and immunofluorescence staining were performed to validate the ARMC1 expression in BRCA. *Results*. ARMC1 expression in tumor samples was significantly higher than that in normal tissues, and higher expression of ARMC1 was related to lower survival. Moreover, the tumor stage and histology of BRCA patients were associated with ARMC1 expression. ARMC1 genetic mutations occurred in 32% of BRCA patients, and the amplification and high expression of ARMC1 accounted for most of them. Furthermore, functional enrichment analysis suggested that ARMC1 might be involved in the cell cycle in BRCA. Ultimately, increased ARMC1 expression was found in clinical breast carcinoma tissues by our confirmatory experiments. *Conclusions*. ARMC1 may play a significant role in BRCA and act as a biomarker, which provides valuable clues for the treatment and diagnosis of BRCA.

1. Introduction

Breast cancer is one of the most prevalent female malignancy, and it is also the main cause of cancer death in women [1, 2]. Currently, mammography and magnetic resonance imaging are the primary approaches for diagnosing breast cancer in clinical practice [3]. In terms of treatment, radical mastectomy, radiotherapy, and chemotherapy were the preferred methods for breast cancer [4]. With the improvement of screening ability and detection technology, the diagnosis and therapy for invasive breast carcinoma

(BRCA) have made ideal progress in recent years [5]. However, a large number of patients are still diagnosed with BRCA each year, and it is also the second common cause of cancer death in women [6]. Therefore, exploring novel biomarkers remains to be crucial for BRCA.

In searching potential biomarkers for BRCA, we discovered that the armadillo (ARM) repeat proteins family is widely involved in cancer progression. Recent researches have revealed that ARM repeat proteins have diverse works in many eukaryotes through their ARM repeat structure [7]. Several ARM repeat proteins have been demonstrated

(a)

(b)

(c)

Figure 1: Continued.

(d)

(e)

(f)
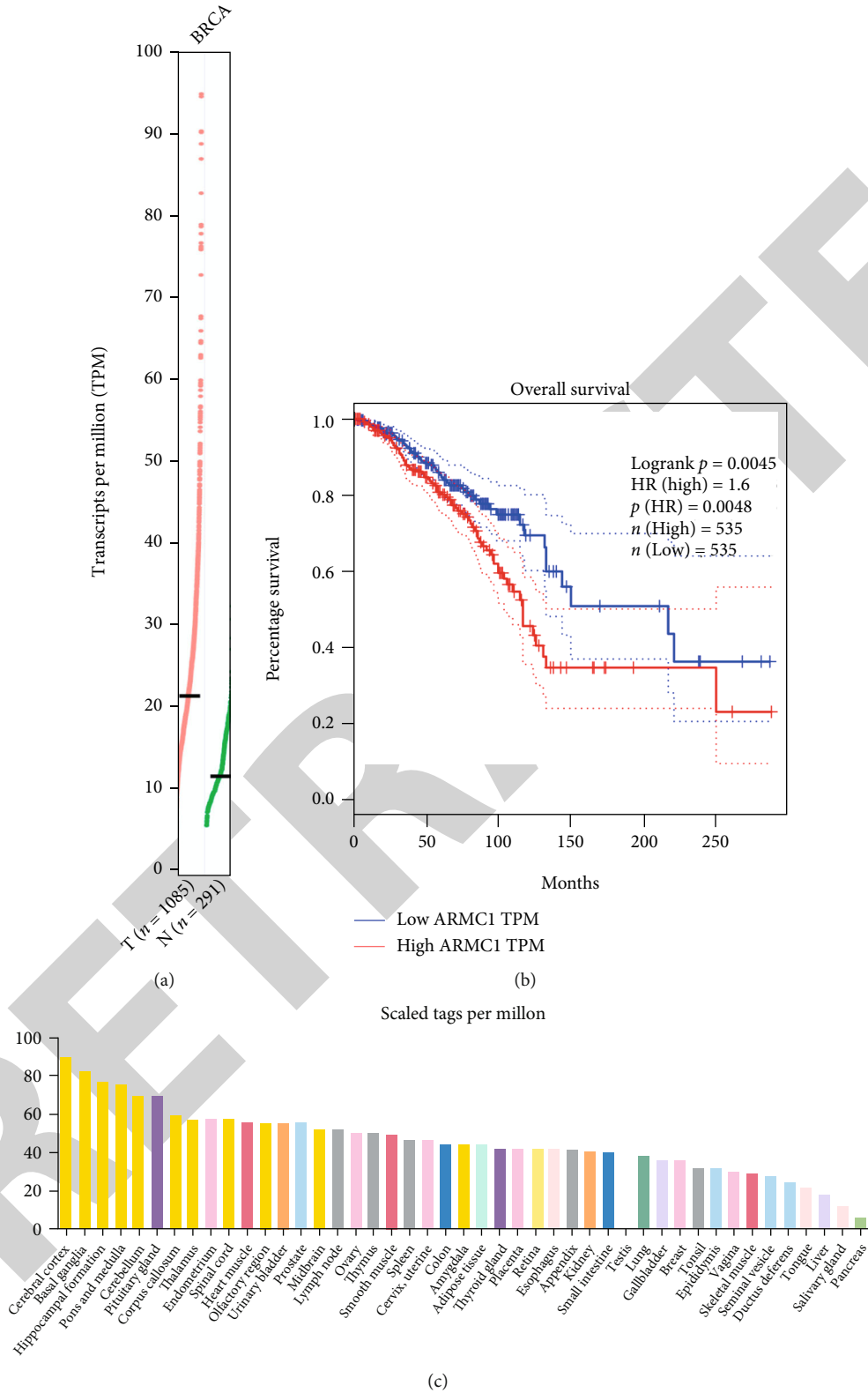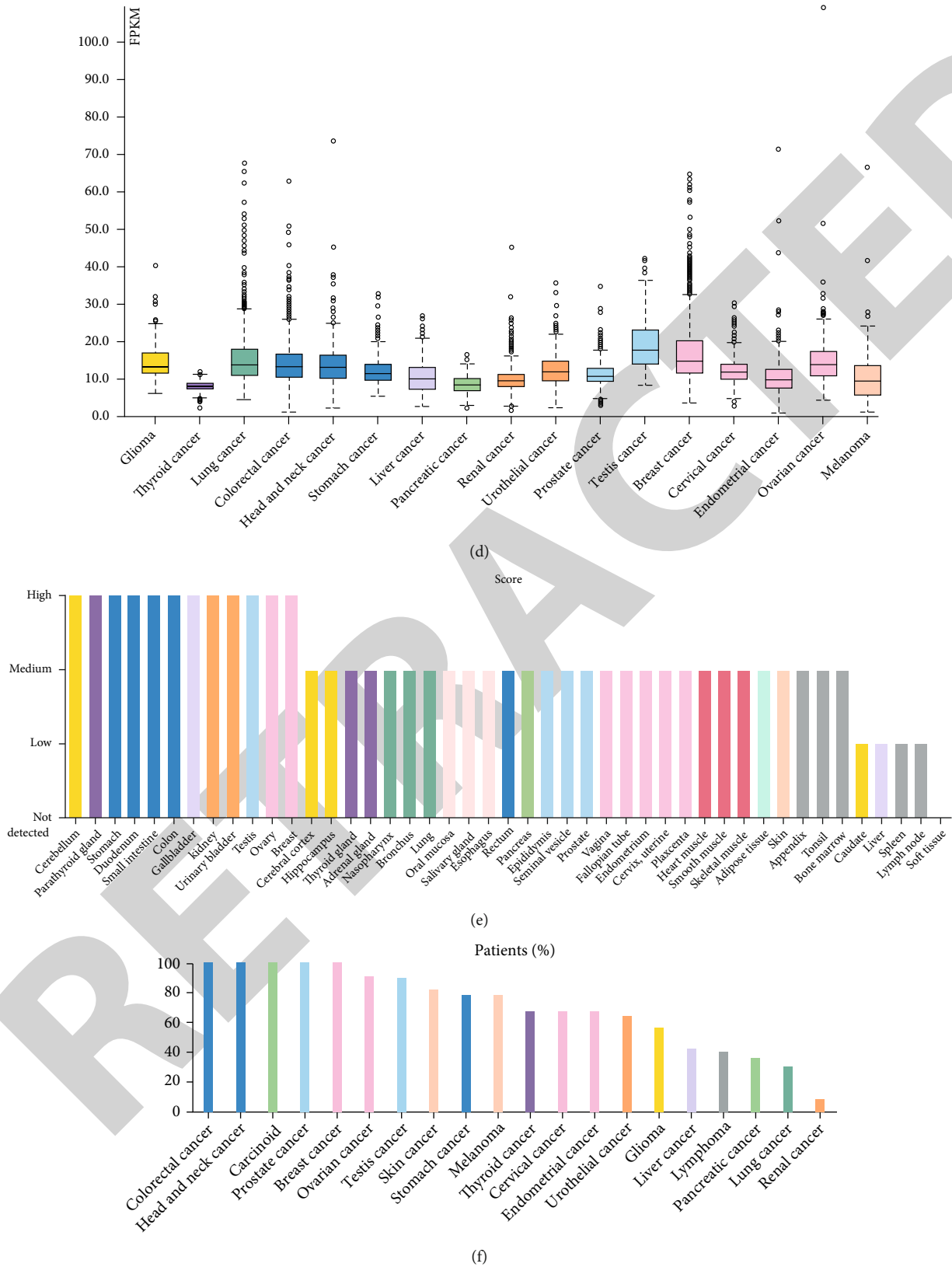
FIGURE 1: The ARMC1 expression profiles in normal and tumor samples. (a) The ARMC1 expression profile and boxplot in normal samples and BRCA samples. (b) The overall survival associated with ARMC1 expression. (c) The ARMC1 mRNA expression in normal breast tissue. (d) The ARMC1 mRNA expression in tumor samples. (e) The ARMC1 protein expression in normal samples. (f) The ARMC1 protein expression in tumor samples. ARMC1: armadillo repeat-containing 1.

(a)

(b)

(c)
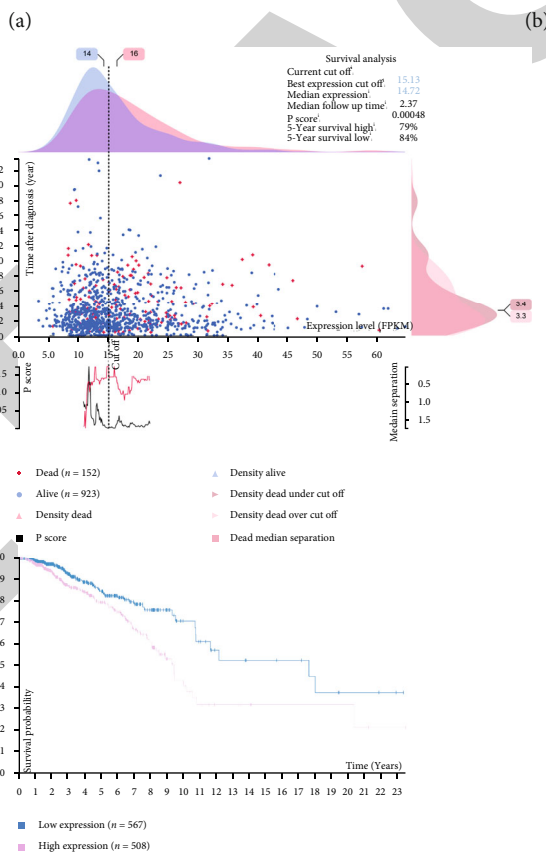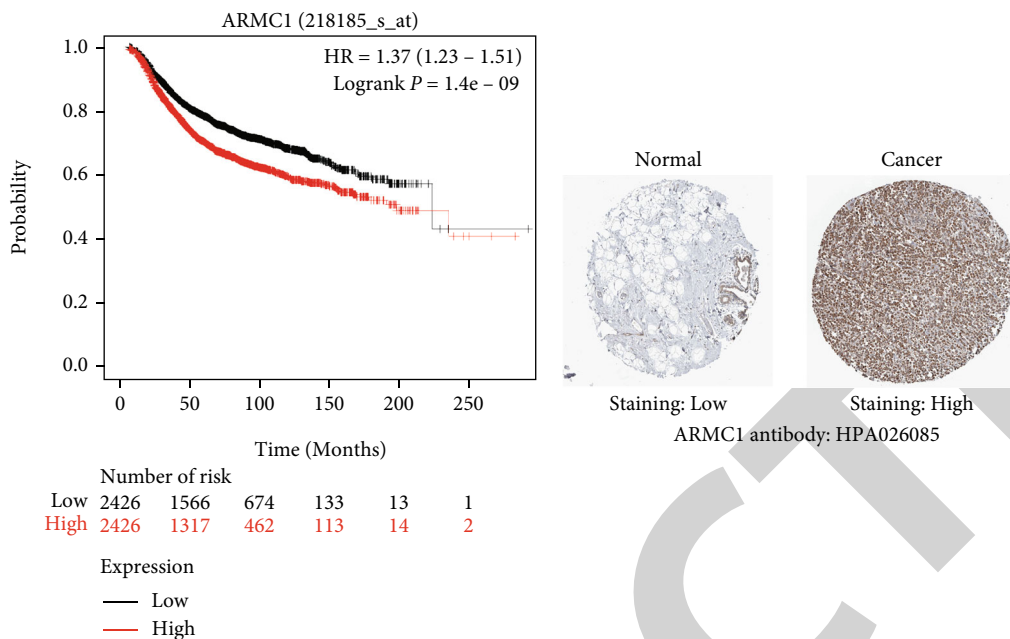
FIGURE 2: ARMC1 expression and prognostic evaluation in BRCA samples. (a) High ARMC1 level was associated with lower survival. (b) Immunohistochemistry images display that ARMC1 expression in tumor tissue was higher than that in the normal tissue. (c) Survival analysis in the HPA database showed increased ARMC1 expression associated with poor survival. HR: hazard ratio; ARMC1: armadillo repeat-containing 1; HPA: Human Protein Atlas.

TABLE 1: Clinicopathological characteristics of BRCA samples.

	No. (%)
Location	
Left site	443 (51)
Right site	419 (48.2)
Unknown	7 (0.8)
Histology	
Ductal carcinoma	608 (70)
Lobular carcinoma	215 (24.7)
Other types of carcinoma	45 (5.2)
Unknown	1 (0.1)
Nathologic tumor stage	
Stage I	156 (18)
Stage II	498 (57.3)
Stage III	189 (21.7)
Stage IV	12 (1.4)
Unknown	14 (1.6)
Nodal status	
N+	442 (50.9)
N-	408 (47)
Unknown	19 (2.1)
Nodal status, nr. of +	
0	367 (42.2)
1-3	249 (28.6)
4-9	85 (9.8)
≥10	50 (5.8)
Unknown	118 (13.6)
Lymphovascular invasion	
Present	442 (50.9)
Absent	408 (47)
Unknown	19 (2.1)
T stage	
T1	240 (27.6)
T2	493 (56.7)
T3	98 (11.3)
T4	28 (3.2)
Unknown	10 (1.2)
N stage	
N0	408 (46.9)
N1	296 (34.1)
N2	88 (10.1)
N3	58 (6.7)
Unknown	19 (2.2)

N+: lymph node positive; N-: lymph node negative; BRCA: invasive breast carcinoma.

to be involved in tumor development and metastasis. As a famous member of the ARM repeat protein family, β-catenin expression in the cytoplasm and nuclear transfer can promote prooncogene transcription such as c-Myc and CyclinD-1 by the Wnt/β-catenin signaling pathway [8, 9].

In addition, the interaction between ARMC12 and retinoblastoma binding protein 4 can promote neuroblastoma progression by inhibiting the transcription of tumor suppressor genes [10]. However, some members of ARM repeat protein family can also inhibit the development cancer. For example, adenoma polyposis coli (APC) can degrade the β-catenin through glycogen synthase kinase 3β (GSK3β), thereby blocking Wnt/β-catenin cancer signaling in colorectal cancer [11]. Armadillo repeat-containing 1 (ARMC1) was originally found in mitochondrion as a structural subunit [12]. Its coding gene locates at position 8q13.1 of the human chromosome. Similar 42 amino acid repeats define it as a member of the ARM family. However, the role of ARMC1 in BRCA remains unclear, so it is of great significance to study the role of ARMC1 in breast cancer.

This study is aimed at exploring whether ARMC1 acts as a valuable biomarker of BRCA. Therefore, we firstly investigated the expression of ARMC1 and evaluated the prognostic significance of ARMC1 in TCGA-BRCA patients. Moreover, we also explored ARMC1 genetic mutations in BRCA and the role of ARMC1 coexpressed genes in cell cycle regulation. Eventually, we validated the ARMC1 expression level in clinical breast tissues. Thus, this study may contribute to the clinical treatment of BRCA.

2. Methods

2.1. Gene Expression Profiling Interactive Analysis. The Gene Expression Profiling Interactive Analysis (GEPIA, http://gepia.cancer-pku.cn/) is a web-analysis tool based on TCGA and GTEx data, which provide interactive and customizable functions including differential expression analysis, profiling plotting, correlation analysis, and patient survival analysis [13]. Thus, GEPIA database was used to explore ARMC1 expression and its overall survival in BRCA samples.

2.2. Kaplan-Meier Plotter. Kaplan-Meier plotter (http://kmplot.com/analysis/) is a widely used online-analysis tool for prognostic value with plentiful gene expression data and relevant clinical data [14]. Kaplan-Meier plotter was performed to analyze the prognostic value of ARMC1 in BRCA.

2.3. Human Protein Atlas. Human Protein Atlas (HPA) database (https://www.proteinatlas.org) is a tool for validating immunohistochemistry-based protein expression patterns and extending the map of protein expression patterns in cancer research projects [15]. HPA was used to search the mRNA and protein expression levels of ARMC1 and analyze the prognostic evaluation of ARMC1 in BRCA.

2.4. The Cancer Genome Atlas. The Cancer Genome Atlas (TCGA, https://portal.gdc.cancer.gov/) is a public database that provides large cancer genomic profiles of over 30 human tumors; its primary purpose is to research individual cancer types through large-scale genome sequencing and integrated multidimensional analyses [16]. TCGA database was used to collect the BRCA cases with ARMC1 differentially expression for prognostic evaluation and risk factor analysis. The TCGA RNA-seq data and corresponding

Parameter	AUC	95% CI	Sensitivity	Specificity	Cutoff value	Youden index	*p* value
FPKM	0.803	0.753-0.853	0.761	0.293	16.05	0.467	<0.001

AUC: area under the ROC curve; CI: confidence interval; ROC: receiver operating characteristic curve; ARMC1: armadillo repeat-containing 1. *Statistically significant ($p < 0.05$).

clinical information of 869 BRCA samples were downloaded from TCGA.

2.5. *cBio Cancer Genomics Portal.* The cBio Cancer Genomics Portal (http://cbioportal.org) is an open-access database, which provides more than 5,000 tumor samples from 20 cancer studies to explore multidimensional cancer genomics data sets [17]. The cBio Cancer Genomics Portal database was used to find the genetic mutations of ARMC1 in BRCA and coexpressed genes associated with ARMC1.

2.6. *Metascape.* Metascape (http://metascape.org/gp/) is a web-based portal that combines works including functional enrichment, interactome analysis, gene annotation, and membership search [18]. Metascape was used to analyze the signaling pathways based on the coexpressed genes related to ARMC1 expression.

2.7. *DAVID Functional Annotation Tool.* DAVID Bioinformatics Resources (DAVID/https://david.ncifcrf.gov/) is a functional annotation tool with public bioinformatics resources. It provides over 40 available annotation categories at the gene and protein level [19]. DAVID was used to perform GO and KEGG analysis based on the coexpressed genes associate with ARMC1.

2.8. *Patient Selection.* According to the situation that ARMC1 is mainly mutated in invasive ductal carcinoma and invasive lobular carcinoma, recent clinically relevant BRCA cases (10 of invasive ductal carcinoma, 5 of invasive lobular carcinoma) that recently appeared in clinical practice were randomly selected. Fifteen pairs of paraffin sections including BRCA tissues and corresponding para-carcinoma tissues were obtained from the Pathological Diagnosis Center of Chongqing Medical University (Chongqing, China). All samples for the confirmatory experiment were selected female patients, and their ages range from 33 to 66 years old. Pathological diagnosis of breast cancer types included invasive ductal carcinoma cases and invasive lobular carcinoma. More characteristics about participants were shown in Supplement Table 1.

2.9. *Cell Line and Their Extraction.* Human breast carcinoma cell lines (MCF-7) and human normal breast cells (MCF-10A) were used for in vitro experiments, which were purchased from Procell Life Science&Technology (Wuhan, China). MCF-7 cells were maintained in Dulbecco's Modified Eagle Medium (DMEM; Gibco, Carlsbad, USA) supplemented with 10% fetal bovine serum (FBS) and 10μ/ml penicillin G/streptomycin, and MCF-10A were maintained in 10A cell-specific culture medium (Procell Life Science&-

Technology). Both cell lines were maintained at 37°C in a humidified atmosphere containing 5% CO2.

Get rid of the culture medium from the petri dish and wash it three times with phosphate-buffered saline (PBS). Cells were collected by scraping off after the addition of cell lysis buffer (Beyotime, Shanghai) and then mixed and place at a standstill for 30 minutes. Collect cell sample by extracting supernatant after centrifugation.

2.10. *Quantitative Reverse Transcription-Polymerase Chain Reaction (qRT-PCR).* Total RNA of all samples in our experiment was extracted using the M5 Universal RNA Mini Kit (Mei5bio, Beijing). Cells were collected by scraping with phosphate-buffered saline (PBS) and extracting the supernatant after mixing well with 500μl lysis solution. The supernatant was added with an equal volume of 70% ethanol and transferred to an adsorption column for centrifugation. Add protein solution RW and repeat centrifugation. Next, add rinse solution to the adsorption column and centrifuge (twice). Lastly, add 50μl RNase-Free H2O to the adsorbed membrane according to the expected RNA yield. The measured RNA concentration is $429 \, \text{ng}/\mu$l (MCF-7) and $459 \, \text{ng}/\mu$l (10A). Then, we conducted reverse transcription assays using the M5 Sprint qPCR RT kit with gDNA remover (Mei5bio, Beijing). The total volume of the cDNA reaction system was 10μl. The quantitative polymerase chain reaction (q-PCR) analysis was performed using CFX Connect Real-Time System (Bio-Rad, USA). Predenaturation was performed at 95°C for 30 s and cycled once. PCR reaction was performed at 95°C for 5 s and 60°C for 20 s, cycled 40 times. Fusion curve analysis at 95°C for 0 s and 65°C for 15 s. The following primer sequences for this assay were used: armadillo repeat-containing 1 (ARMC1): (forward): 5′-AACTACAAACAAACGTGCCAAAA-3′; (reverse): 5′-ACACACCTTTGAACACACCTATT-3′; glyceraldehyde-3-phosphate dehydrogenase (GAPDH): (forward): 5′-GGACACTGAGCAAGAGAGGC-3′; (reverse): 5′-TTATGGGGGTCTGGGATGGAA-3′. All the primer sequences came from Tsingke Biotechnology (Beijing, China).

2.11. *Enzyme-Linked Immunosorbent Assay.* This experiment was completed by using the ARMC1 enzyme-linked immunosorbent assay kit (Jiangsu Jingmei Biological Technology, China). Dilute the standard according to concentration size order, and then incubate the test plate for 30 minutes at 37°C after adding the standard, sample, and distilled water to programmed standard holes, sample holes, and blank. Put the prepared cleaning solution in each hole and shake it for washing the plate, and then tap the plate gently to get rid of the cleaning solution. Repeat this clean

(a)

(b)

(c)

(d)

Figure 3: Continued.

(e)
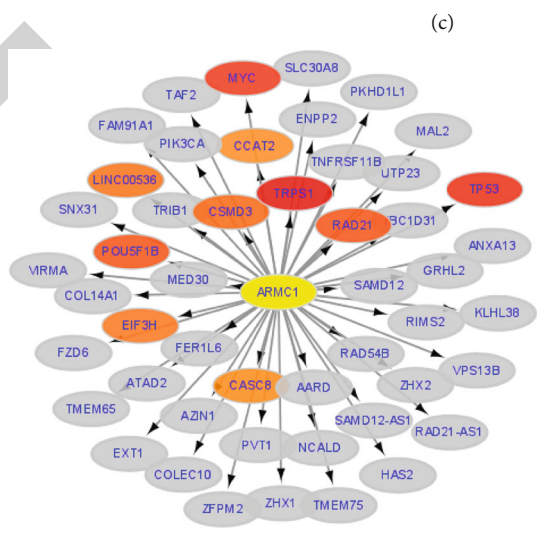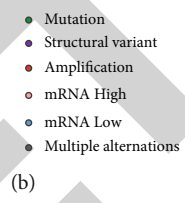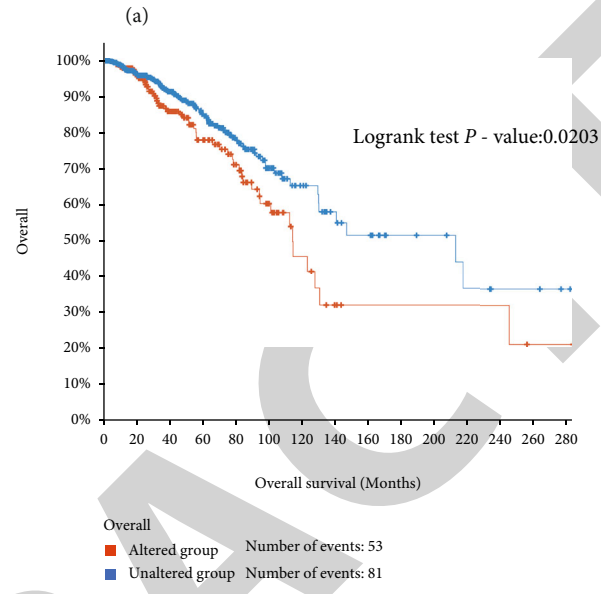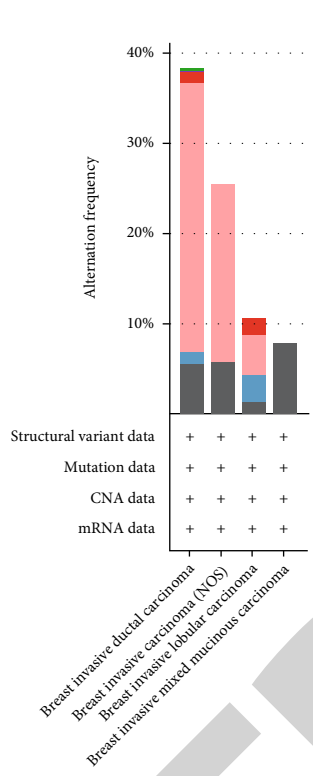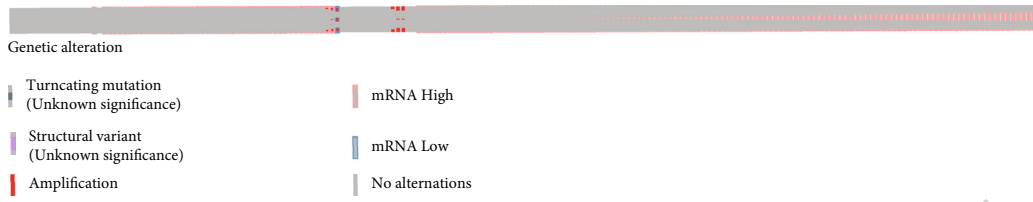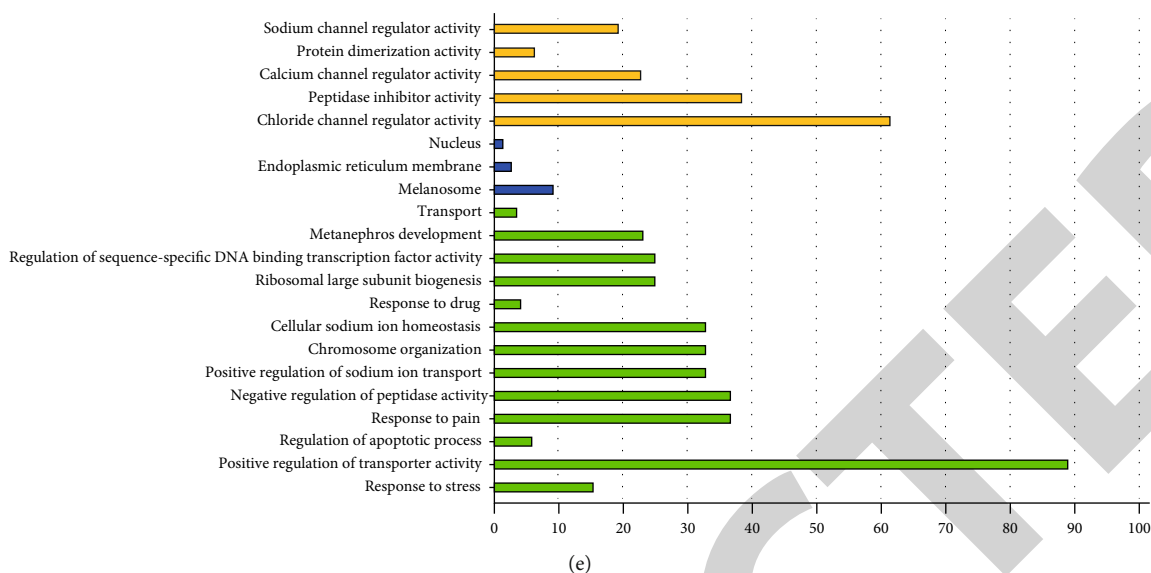
Figure 3: The mutations of ARMC1 in BRCA and its neighboring genes enriched analysis. (a) The genetic mutations of ARMC1 in BRCA. (b) The cancer types with frequent ARMC1 mutations. (c) The overall survival status associated with ARMC1 mutations. (d) Neighborhood gene network diagram of ARMC1 mutations. (e) Biological function analysis of neighboring genes with ARMC1 mutation. ARMC1: armadillo repeat-containing 1; BRCA: invasive breast carcinoma.

step after the addition of the enzyme-labeled reagent except for the blank. The developing color solution was added to each hole and placed statically at 37°C for 15 minutes in the dark. Lastly, read the results after the addition of the stop solution. The Prime 8 software was used to analyze the results of ELISA.

2.12. Immunohistochemistry (IHC) Analysis. This experiment was performed by mouse/rabbit streptavidin-biotin assay system (ZSGB-BIO, Beijing). IHC assays were performed using formalin-fixed BRCA tissue samples which were embedded in 4 μm thick paraffin sections. Paraffin sections were deparaffinized by graded alcohol and then incubated by endogenous peroxidase blockers for 20 minutes. The sections were incubated with antibodies against ARMC1 (Novus Biologicals, USA) overnight at 4°C after Goat Serum Blocking Solution incubation. Incubate slides with the secondary antibody for 15 minutes at room temperature, and then incubate the slides with horseradish enzyme-labeled streptavidin for 10 minutes after clearing the secondary antibody. The Image-Pro Plus 6.0 software was used to perform semiquantitative scoring of the images.

2.13. Immunofluorescence Staining. Tissue sections were deparaffinized by graded alcohol and then washed three times with phosphate-buffered saline (PBS), permeabilized with 0.4% Triton X-100 for 30 min, and blocked with goat serum working liquid (Wuhan Boster Biological Technology, Wuhan, China) for 2 hours after antigen retrieval. The sections were then incubated overnight with mixed primary antibodies at 4°C, washed in PBS to remove unbound primary antibodies, and incubated with secondary antibodies in the dark at room temperature (RT) for 1 hour. The sections were counterstained with $4'$, 6 diamidino-2-phenylindole (Sigma-Aldrich) for 5 minutes and washed

with PBS. The primary antibodies included mouse anti-ARMC1 (1 : 50; Novus Biologicals, USA), outer mitochondrial membrane marker-rabbit anti-TOM20 (the outer mitochondrial membrane 20) antibody (1 : 200; Wuhan Proteintech, Wuhan, China), and inner mitochondrial membrane marker-rabbit anti-TIM23 (the inner mitochondrial membrane 23) antibody (1 : 200; Wuhan Proteintech, Wuhan, China). The fluorophore-conjugated secondary antibodies used were goat anti-rabbit Alexa Fluor 488 (1 : 500; Abbkine, Wuhan, China) and goat anti-mouse Alexa Fluor 549 (1 : 500; Abbkine, Wuhan, China). Images were captured by confocal laser scanning microscopy (Nikon A1 + R, Japan). The fluorescence intensity was analyzed by using the ImageJ software.

2.14. Quantification of Staining Expression. The Image-Pro Plus (Version 6.0.0.260) was used to evaluate the ArmC1 expression in immunohistochemistry. Measure the AOI (area of interest) including average radius, perimeter, and optical density of staining position. After statistics, the IOD (integrated optical density) was calculated by density (mean)∗area density. The expression level was judged from the ratio of SUM value of IOD to SUM value of area.

2.15. Statistical Analysis. Receiver operating characteristic (ROC) curve analysis was used to settle the optimal cutoff value of the ARMC1. The optimal cutoff value of the ARMC1 was determined by the maximization of the Youden's index (Sensitivity-(1-Specificity)). Relations of the ARMC1 to other variables were evaluated using the χ^2 test or Spearman's rank correlation coefficient. All statistical analyses were performed using the SPSS version 23.0 software. $p < 0.05$ was considered to indicate a significant difference.

(a)

(b)
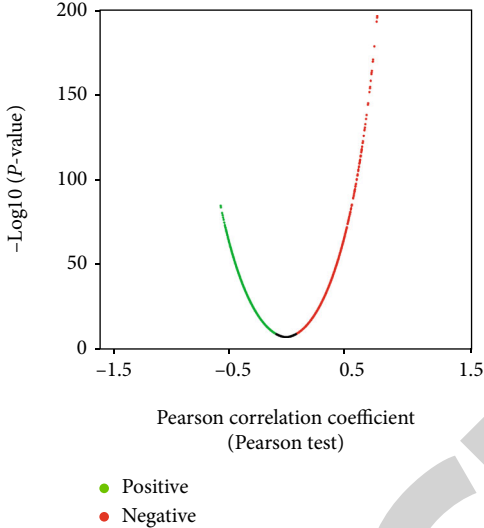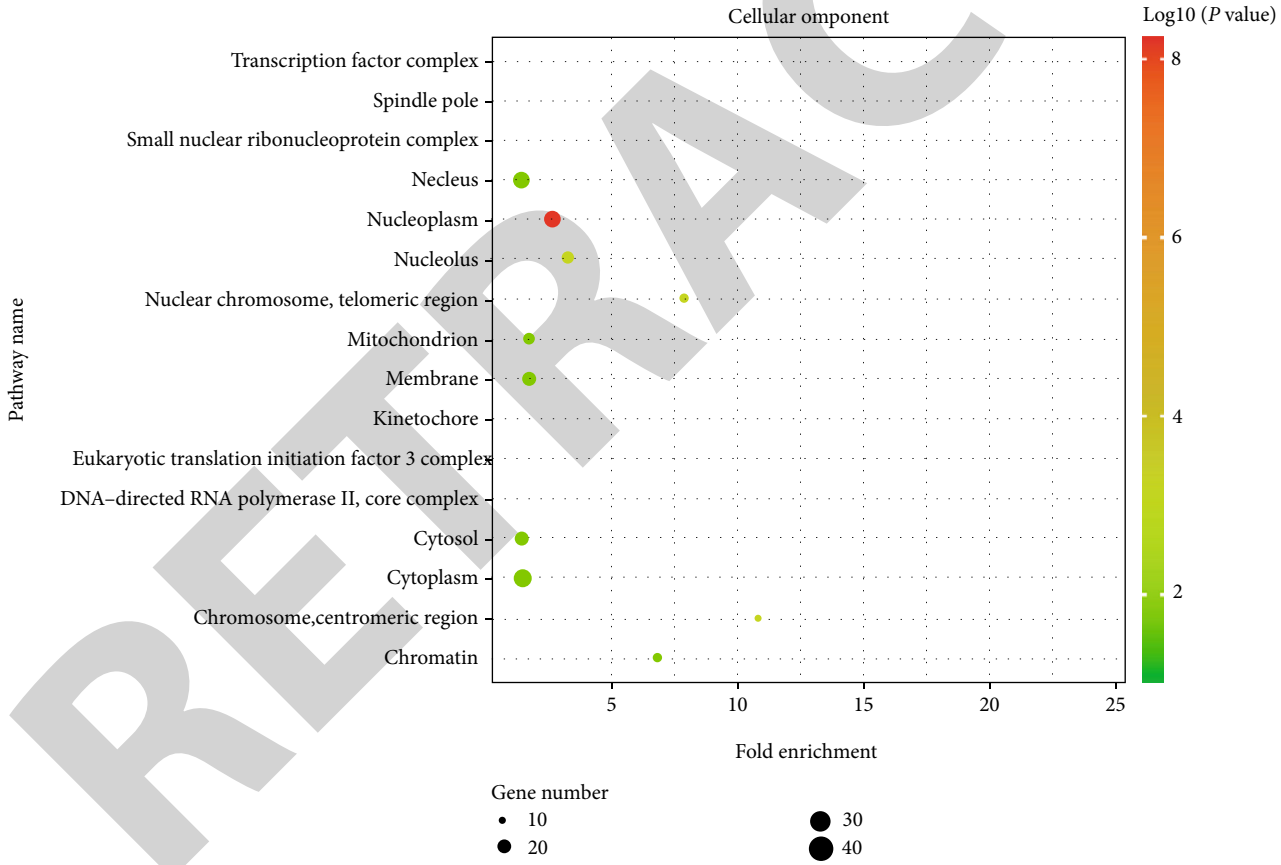
FIGURE 4: Continued.

(c)
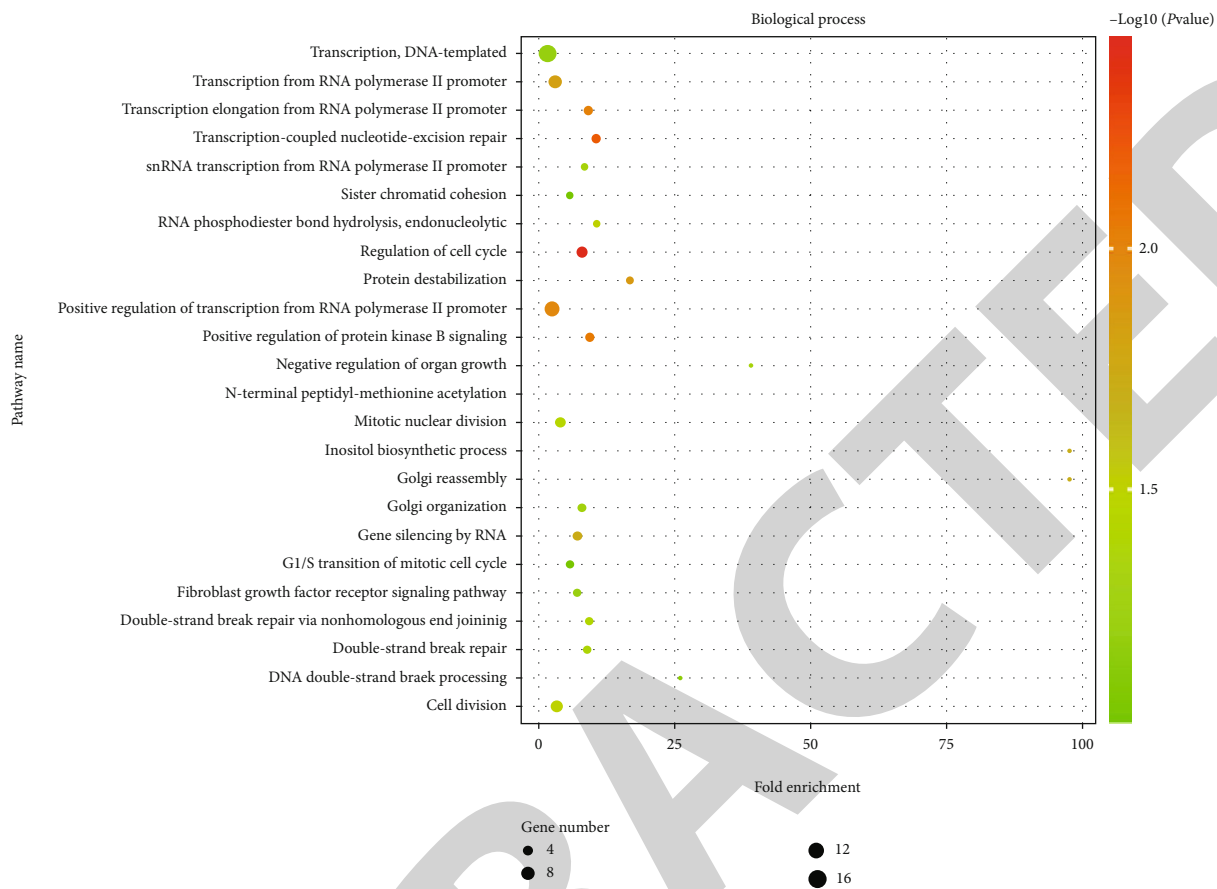
Figure 4: Continued.

(d)
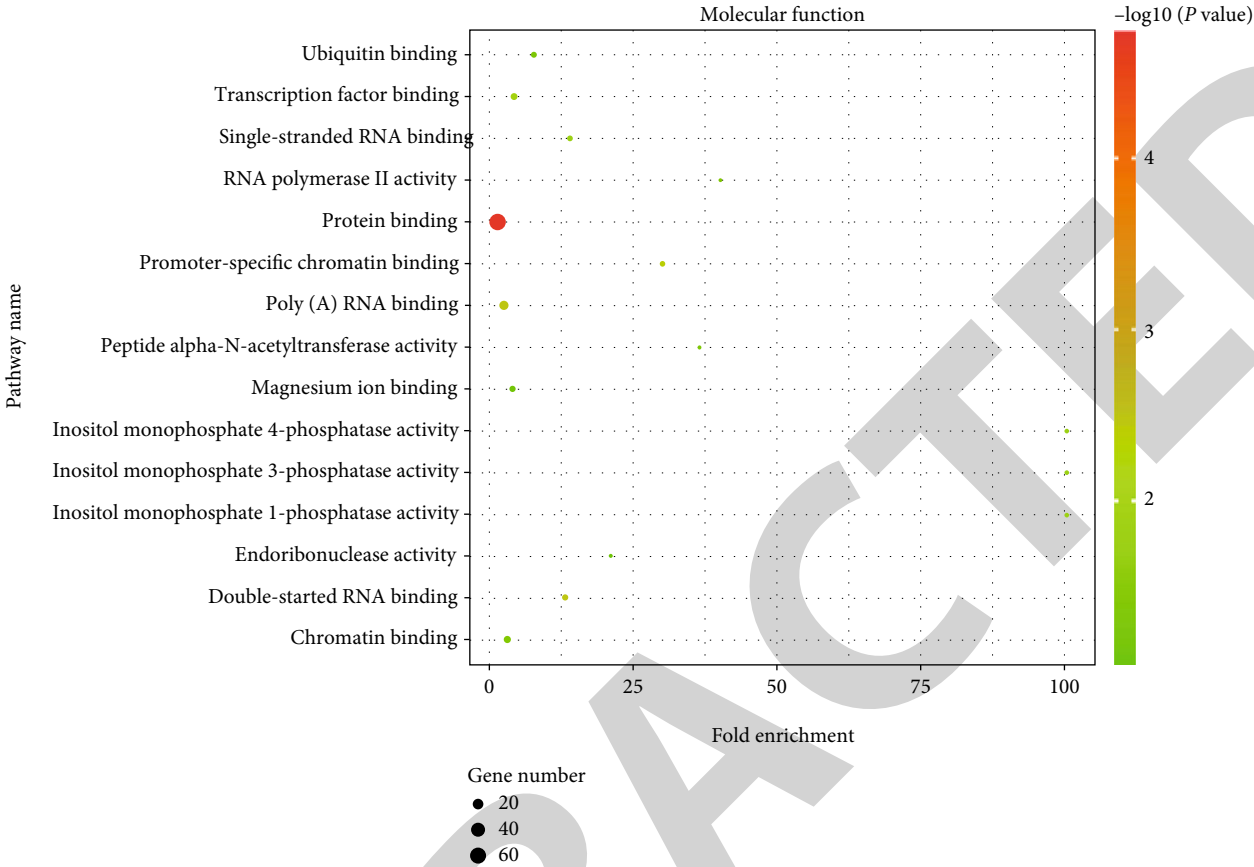
Figure 4: Continued.
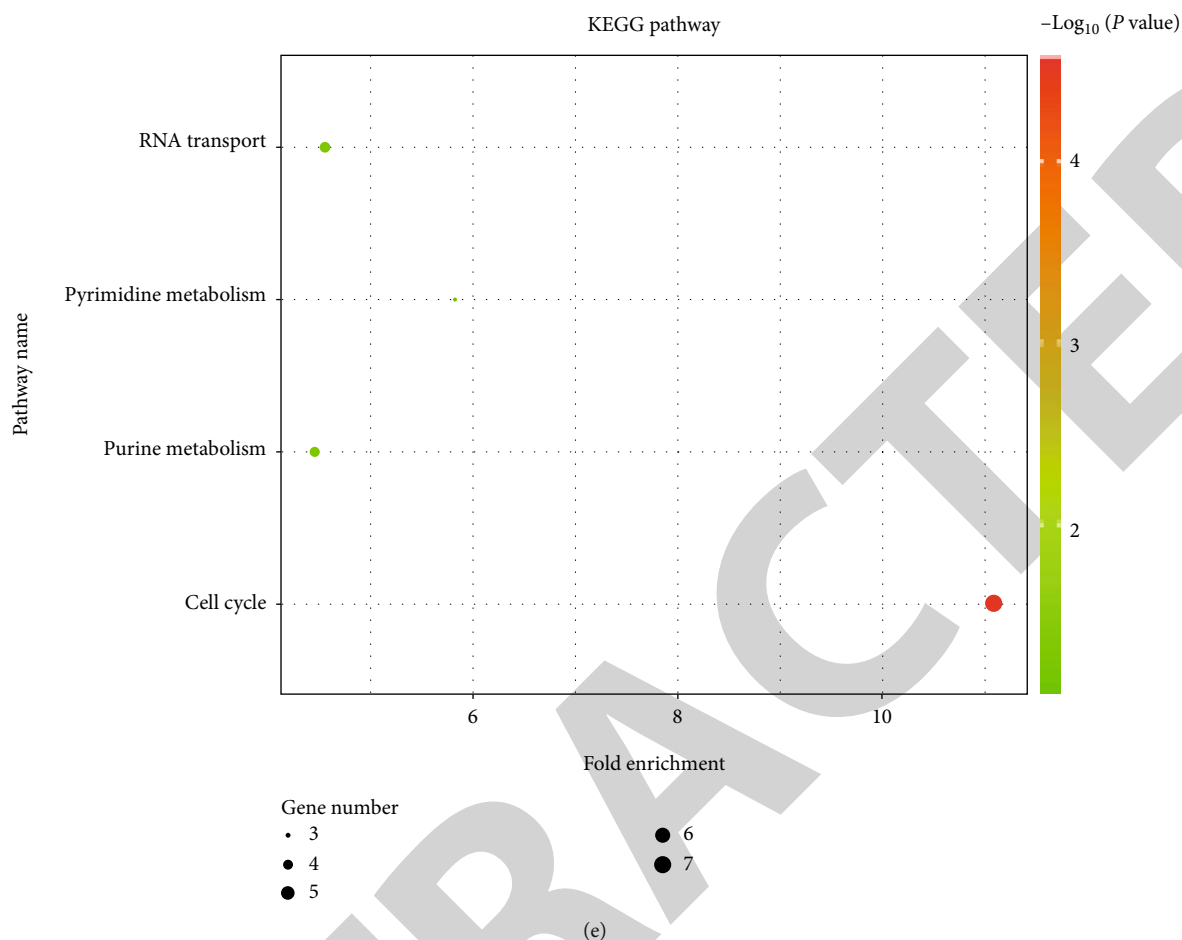
FIGURE 4: Coexpressed genes with ARMC1 and their enrichment analysis: (a) volcano plot showing coexpressed genes associated with ARMC1; (b) cellular components; (c) biological processes; (d) molecular functions; (e) KEGG pathways. ARMC1: armadillo repeat-containing 1; KEGG: Kyoto Encyclopedia of Genes and Genomes.

3. Result

3.1. The Expression Profiles of ARMC1 in BRCA Samples. The expression analysis from the GEPIA database showed that ARMC1 expression in breast tumor samples is higher than that in normal samples ($T = 1085$, $N = 291$) (Figure 1 (a)). In addition, a higher ARMC1 expression level was significantly associated with a lower overall survival ($p < 0.05$) (Figure 1(b)). Furthermore, HPA database was used to investigate the mRNA and protein expression of ARMC1 in BRCA. Interestingly, ARMC1 mRNA expression in normal breast tissue was also lower than that in other tissues (Figure 1(c)). On the other hand, we found that ARMC1 mRNA expression in BCRA samples was relatively higher than that in other types of carcinoma (Figure 1(d)). More importantly, ARMC1 protein in breast tissue was significantly higher than that in other tissues (Figures 1(e) and 1 (f)).

3.2. Prognostic Evaluation of ARMC1 Level in BRCA Patients. The Kaplan-Meier plotter tool was used to detect the correlation between ARMC1 expression and overall survival in BRCA. Consistent with the results of GEPIA, high

expression of ARMC1 was presented poor prognosis in BRCA (Figure 2(a), hazard ratio (HR) = 1.37, 95% confidence interval (CI):1.23–1.51, $p = 1.4E$-09). In addition, IHC images from the HPA database showed that the intensity and staining in tumor samples were stronger than that in normal samples (Figure 2(b)). Next, the survival analysis in the HPA database confirmed that increased ARMC1 level was associated with poor survival (Figure 2(c)). Furthermore, we explored the risk factors associated with ARMC1 expression in TCGA-BRCA patients. The TCGA-BRCA clinical parameters were collected from the HPA database. Fragments per kilobase per million (FPKM) was used to measure ARMC1 genetic expression. We included 869 patients with seven clinical parameters for this analysis. The average age of the patients was 58 (interquartile range: 48-67). The more specific information of patients is shown in Table 1. The χ^2 test showed that tumor stage ($p < 0.001$), histology ($p < 0.001$), pathological T stage ($p < 0.001$), and pathological N stage ($p < 0.001$) were associated with AMRC1 expression (Supplement Table 2). ROC analysis identified 16.05 as the best cutoff value of ARMC1 by the Youden's index (Sensitivity-(1-Specificity)) (Table 2). Curve area is shown in Supplement Figure 1.

(a)

(b)

(c)

(d)

Figure 5: Continued.

(e)
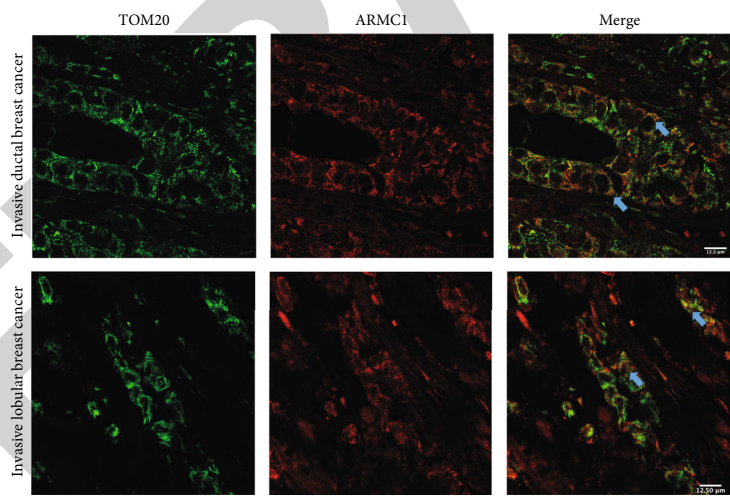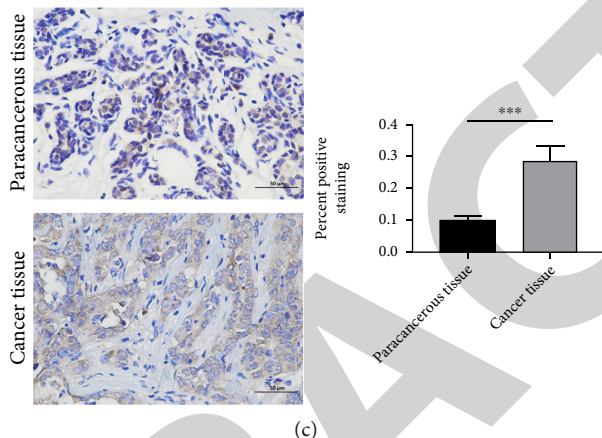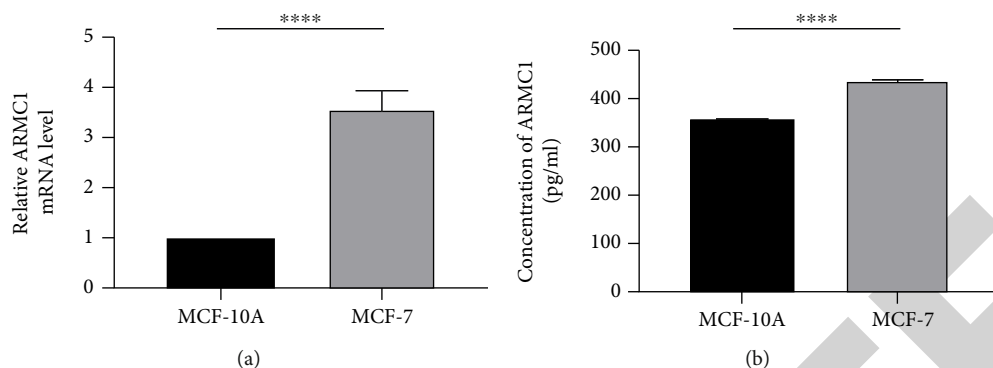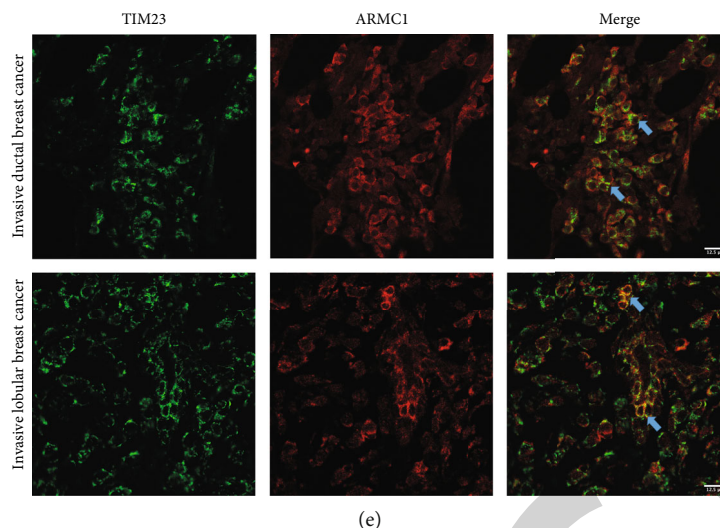
FIGURE 5: Validation of ARMC1 expression in BRCA tissues. (a) ARMC1 mRNA level was higher in MCF-7 cell lines compared with MCF-10A ($n = 10$ in each group; $****p < 0.0001$ versus controls, Student's t-test). (b) ARMC1 was higher expressed in MCF-7 cell lines compared with MCF-10A ($n = 15$ in each group; $****p < 0.0001$ versus controls, Student's t-test). C ARMC1 was higher expressed in BRCA tissues than that in para-carcinoma tissues ($n = 10$ in each group; $***p < 0.001$ versus controls, Student's t-test). Scale bar: 50 μm. (d) ARMC1 was colocalizes with TOM20 in BRCA tissues. (e) ARMC1 was colocalizes with TIM23 in BRCA tissues. Scale bar: 12.5 μm. ARMC1: armadillo repeat-containing 1; BRCA: invasive breast carcinoma; TOM20: the outer mitochondrial membrane 20; TIM23: the inner mitochondrial membrane 23; MCF-7: human breast carcinoma cell lines; MCF-10A: human normal breast cells.

3.3. The Genomic Mutations of ARMC1 and Its Biological Pathways in BRCA. The data from the cBioPortal database indicates that ARMC1 mutations occurred in 332 (32%) of 994 samples. Most of them were amplified samples; few of them were mutations of fusion and truncating (Figure 3 (a)). As shown in Figure 3(b), breast invasive ductal carcinoma was majorly associated with ARMC1 mutations, which were mainly manifested by high mRNA expression and amplification. Besides, the overall survival of the mutated samples was significantly lower than that of patients without mutation (Figure 3(c); altered group = 322, unaltered group = 672, $p = 0.0203$).

In the neighboring genes related to ARMC1 mutation, TP53 (51.24%), TRPS1 (31.99%), and RAD21 (30.75%) were identified as the top three mutant genes (Figure 3(d)). Next, we used these neighboring genes associated with ARMC1 mutations to analyze the biological networks by the DAVID Functional Annotation Tool (Figure 3(e)). In the cellular component, the endoplasmic reticulum membrane and nucleus were significantly related to ARMC1 mutations, and these mutations affect the activity of various important ion channel modulators including chloride, calcium, and sodium. Mitochondrial permeability regulation and cell death were also identified be involved in these mutations. In biological processes, some vital functions include positive regulation of transporter activity, chromosome organization, sodium ion transportation, homeostasis, and regulating DNA binding transcription factor activity were significantly related to ARMC1 mutations.

3.4. Enrichment Analysis of Coexpressed Genes Relating to ARMC1 in BRCA. We discover the coexpressed genes positively or negatively associated with ARMC1 in BRCA. As shown in Figure 4(a), most of these genes were positively correlated with ARMC1. Moreover, GO and KEGG GO and KEGG analyses were performed to explore the biological functions of these genes. Interestingly, these genes were mainly related to nucleoplasm, and the protein binding and poly (A) RNA binding were their primary molecular function. More importantly, biological processes involved in these genes included the cell cycle and positive regulation of transcription from RNA polymerase II promoter, etc. (Figures 4(b)–4(d)). Furthermore, the KEGG analysis also showed the potential effect of these genes in the cell cycle (Figure 4(e)).

3.5. ARMC1 Was Highly Expressed in Breast Tumor Tissues and Was Mainly Located in the Mitochondrial Membrane. The qRT-PCR assay showed that the ARMC1 mRNA level in MCF-7 cell lines was higher than that in the MCF-10A cell lines (Figure 5(a), $p < 0.01$). For further quantitative analysis of ARMC1 expression, we performed the enzyme-linked immunosorbent assay in two types of cell lines; the results showed that ARMC1 expression in MCF-7 cell lines was higher than in the MCF-10A cell lines (Figure 5(b), $p < 0.01$). Besides, it was obviously found that in the immunohistochemistry that staining intensity and depth of ARMC1 in BRCA tissues were higher than para-carcinoma tissue (Figure 5(c), $p < 0.01$). According to the previous studies that ARMC1 is mainly localized to the mitochondrial, it could be seen in the results of immunofluorescence that ARMC1 in invasive ductal breast carcinoma and lobular breast carcinoma were localized at the both inner mitochondrial membrane and outer mitochondrial membrane (Figures 5(d)–5(e)).

4. Discussion

Invasive breast carcinoma (BRCA) is one of the most common diseases in female patients, and various targeted treatments have been applied to BRCA. However, the heterogeneity and wide invasion make BRCA difficult to be cured completely [20]. In our study, we noticed that the expression of ARMC1 was upregulated in BRCA and upregulation of ARMC1 was associated with poor survival. Next, clinical features including tumor stage, histology, pathological T stage, and pathological N stage were found to be related to ARMC1 expression based on the TCGA-BRCA patient cohort. In addition, we found high mutations of ARMC1 in BRCA patients in public databases, as well as associations between ARMC1 and cell proliferation genes by GO and KEGG analyses, suggesting that ARMC1 may be involved in BRCA development. Thus, this study firstly revealed the role of ARMC1 as a novel biomarker in BRCA and provides a regulatory target for the diagnosis and treatment of BRCA.

ARM repeat proteins are initially found in drosophila segment polarity protein as multifunctional protein families [21]. The tandem ARM repeat structure composed of 42 repetitive amino acids enables ARM repeat proteins to participate in intracellular signaling and cytoskeletal regulation [22]. Numerous studies have verified the association of the ARM repeat protein family with tumor development [23, 24]. However, the role of ARMC1 in BRCA remains unclear. In this study, we have found that the ARMC1 mRNA expression in tumor samples was higher than that in normal samples. This differential expression highlights the significance of AMRC1 in BRCA. Next, we further explored the prognostic value of ARMC1 in the TCGA-BRCA cohort. Interestingly, the Kaplan-Meier analysis indicated that upregulation of ARMC1 was significantly associated with poor survival, and the same results were verified in TCGA-BRCA cohort. It could be found that factors such as tumor stage and histology were significantly associated with the prognosis of BRCA by χ^2 test of 869 clinical patient information in the TCGA database. Similarly, recent study also found that the higher stage in breast cancer is usually associated with distant metastasis [25]. Thus, the correlation between ARMC1 and stage may be one of the factors inducing metastasis in BRCA.

Numerous analyses of cancer genomes have proven that tumor development is usually accompanied by genetic mutations [26]. The genetic mutations are also recognized as "drivers" for tumorigenesis because of their ability to induce abnormal cell proliferation [27]. Therefore, we attempted to explore the carcinogenesis mechanism of ARMC1 in BRCA from the perspective of gene mutation. The cBio Cancer Genomics Portal database data indicated that 32% of gene mutations were found in BRCA, and amplification and high transcription accounted for most of these mutations. The genetic mutations of ARMC1 were also significantly related to poor survival. Especially, TP53 is one of the highly correlated genes in ARMC1 mutations. The frequent mutations of exon 4 and intron 3 for ARMC1 were reported in breast cancer, which can directly or indirectly cause DNA repair disorders and abnormal cell cycles [28].

Besides, the biological function enrichment showed that ARMC1 and neighboring genes were involved in the positive regulation of transporter activity and regulation of various essential ion channels. It is reported that calcium-activated chloride channels activate EGFR/STAT3 signaling, which can lead to abnormal proliferation of breast cancer cells [29]. Therefore, we speculated that this abnormal ion channel activity caused by ARMC1 mutation may be involved in this signal transduction.

Finally, we identified the coexpressed genes associated with ARMC1 and then performed the GO and KEGG analysis of them to explore the regulatory mechanisms of ARMC1 in BRCA. Notably, GO analysis showed that nucleoplasm is majorly associated with ARMC1, and the primary molecular function of them is protein binding. More importantly, KEGG analysis showed that coexpressed genes of ARMC1 were mainly involved in the cell cycle. It has been revealed that cell cycle dysregulation is abnormal cell proliferation [30]. The genes associated with cell cycle regulation such as PRKDC and E2F transcription factor 5 (E2F5) were found in our study. It has been reported that overexpression of PRKDC in breast cancer leads to cell proliferation by accelerating the G2/M cell cycle [31]. In addition, overexpression of E2F5 in breast cancer is also related to cell proliferation [32]. Thus, there are many coexpressed genes associated with ARMC1 that were identified to be involved in cell cycle regulation. ARMC1 may be directly or indirectly involved in breast carcinogenesis by affecting these regulators associated with cell proliferation. However, more studies are required to prove the relationship between ARMC1 and these coexpressed genes in BRCA.

Numerous experiments have found dysregulated ARMC1 in BRCA, which provides concrete evidence that ARMC1 may work as a crucial target in BRCA development and provides a starting point for further study of the ARMC1 mechanism in BRCA. Mitochondria serve as a regulatory center of cellular metabolism; its dysfunction can lead to activation of potential oncogenic pathways [33]. Recently, an increasing number of studies have found that mitochondria can be used as an effective target in breast cancer therapy [34]. It is well-known that mitochondria are an important hub for various ion transport and signal transduction, and ion channels and transporters on mitochondrial bilayer membranes maintain normal cellular homeostasis [35, 36]. There are various ion channels located in the outer or inner mitochondrial membrane that were identified as associated with cancer development. For instance, the overexpression of voltage-dependent anion channels 1 (VDAC1) has been found in cancer cells; it increases the glycolytic rate by the direct mitochondrial ATP transport. This abnormal glucose metabolism promotes the proliferation and migration of tumor cells (the Warburg effect) [37]. Surprisingly, we found that ARMC1 is mainly localized on both the inner and outer mitochondrial membranes in the tissues of the ductal and lobular breast carcinoma. Besides, the ARMC1 mutations may affect various ion channel activities including calcium ions in our result. Thus, ARMC1 may affect BRCA development by mitochondrial ionic homeostasis. Although ARMC1 acts as a molecule on the mitochondrial membrane,

the mechanism of ARMC1 in BRCA remains unknown. Therefore, we expect more studies in the future to explore the possible regulatory mechanism of ARMC1 in BRCA through mitochondrial energy metabolism.

5. Conclusion

Our results suggest that ARMC1 could be a potential biomarker in invasive breast cancer; it provides valuable clues for the treatment and diagnosis of invasive breast cancer. However, this experiment has some limits. Reliable prognostic model analysis cannot be performed due to the limited information of the TCGA-BRCA patient cohort. Thus, more attempts are needed to demonstrate the effect of ARMC1 on the prognosis of BRCA from other pathways.

Abbreviations

BRCA: Invasive breast carcinoma
ARMC1:   Armadillo repeat-containing 1
GO: Gene Ontology
KEGG: Kyoto Encyclopedia of Genes and Genomes
ARMC12:   Armadillo repeat-containing 12
APC: Adenoma polyposis coli
GSK3β: Glycogen synthase kinase 3β
GEPIA: Gene Expression Profiling Interactive Analysis
GTEx: Genotype-tissue expression
HPA: Human Protein Atlas
TCGA: The Cancer Genome Atlas
MCF-7:   Human breast carcinoma cell lines
MCF-10A: Human normal breast cells
DMEM: Dulbecco's Modified Eagle Medium
FBS: Fetal bovine serum
PBS: Phosphate-buffered saline
AOI: Area of interest
IOD: Integrated optical density
ELISA: Enzyme-linked immunosorbent assay
IHC: Immunohistochemistry
ROC: Receiver operator characteristic curve
mRNA: Messenger RNA
HR: Hazard ratio
CI: Confidence interval
FPKM: Fragments per kilobase per million
TRPS1:   Tricho-rhino-phalangeal syndrome 1
GESA: Gene set enrichment analysis
Arm: Armadillo
EGFR: Epidermal growth factor receptor
STAT3:   Signal transducer and activator of transcription 3
PRKDC: Protein kinase DNA-activated, catalytic subunit
E2F5:   E2F transcription factor 5
VDAC1:   Voltage-dependent anion channels 1
ATP: Adenosine triphosphate
RT: Room temperature.

Data Availability

The data used to support the findings of this study are included within the article.

Ethical Approval

The Ethics Committee approved the study of the Chongqing Medical University. All procedures performed in research involving human subjects were in accordance with the ethical standards of the institutional and/or national research committees, the 1964 Declaration of Helsinki and its subsequent amendments, or similar ethical standards.

Consent

All subjects obtained informed consent.

Disclosure

This manuscript was submitted as a preprint in the link "https://www.researchsquare.com/article/rs-1185959/v1" [38].

Conflicts of Interest

No author has financial or other contractual agreements that might cause conflict of interests.

Authors' Contributions

YG and FZ contributed equally to this article. YG performed the cell culture as well as the collection and analysis of the data and was a major contributor in writing the manuscript. FZ carried out the operation of tissue collection and related experiments. HW and LL designed the study and revised the manuscript. All authors read and approved the final manuscript. Yunhao Gan and Fuxin Zhong contibuted equally to this work. All authors have approved this manuscript.

Acknowledgments

Supplementary Materials

Supplementary Table 1: clinicopathological characteristics of 15 BRCA patients in validated experiments. Supplementary Table 2: correlation of ARMC1 level with clinicopathological characteristics. Supplementary Figure 1: ROC curve indicating the diagnostic significance of ARMC1. (*Supplementary Materials*)

References

[1] R. A. Vieira, A. M. da Costa, J. L. de Souza et al., "Risk factors for arm lymphedema in a cohort of breast cancer patients followed up for 10 years," *Breast Care (Basel)*, vol. 11, no. 1, pp. 45–50, 2016.

[2] L. A. Torre, F. Bray, R. L. Siegel, J. Ferlay, J. Lortet-Tieulent, and A. Jemal, "Global cancer statistics, 2012," *CA: a Cancer Journal for Clinicians*, vol. 65, no. 2, pp. 87–108, 2015.

[3] S. H. Jafari, Z. Saadatpour, A. Salmaninejad et al., "Breast cancer diagnosis: imaging techniques and biochemical markers," *Journal of Cellular Physiology*, vol. 233, no. 7, pp. 5200–5213, 2018.

[4] O. Peart, "Breast intervention and breast cancer treatment options," *Radiologic Technology*, vol. 86, no. 5, pp. 535M–558M, 2015.

[5] C. E. DeSantis, J. Ma, A. Goding Sauer, L. A. Newman, and A. Jemal, "Breast cancer statistics, 2017, racial disparity in mortality by state," *CA: a Cancer Journal for Clinicians*, vol. 67, no. 6, pp. 439–448, 2017.

[6] E. J. Watkins, "Overview of breast cancer," *Journal of the American Academy of PAs*, vol. 32, no. 10, pp. 13–17, 2019.

[7] R. Tewari, E. Bailes, K. A. Bunting, and J. C. Coates, "Armadillo-repeat protein functions: questions for little creatures," *Trends in Cell Biology*, vol. 20, no. 8, pp. 470–481, 2010.

[8] K. C. Valkenburg, C. R. Graveel, C. R. Zylstra-Diegel, Z. Zhong, and B. O. Williams, "Wnt/β-catenin signaling in normal and cancer stem cells," *Cancers (Basel)*, vol. 3, no. 2, pp. 2050–2079, 2011.

[9] A. I. Khramtsov, G. F. Khramtsova, M. Tretiakova, D. Huo, O. I. Olopade, and K. H. Goss, "Wnt/β-catenin pathway activation is enriched in basal-like breast cancers and predicts poor outcome," *The American Journal of Pathology*, vol. 176, no. 6, pp. 2911–2920, 2010.

[10] D. Li, H. Song, H. Mei et al., "Armadillo repeat containing 12 promotes neuroblastoma progression through interaction with retinoblastoma binding protein 4," *Nature Communications*, vol. 9, no. 1, p. 2829, 2018.

[11] S. Munemitsu, I. Albert, B. Souza, B. Rubinfeld, and P. Polakis, "Regulation of intracellular beta-catenin levels by the adenomatous polyposis coli (APC) tumor-suppressor protein," *Proceedings of the National Academy of Sciences of the United States of America*, vol. 92, no. 7, pp. 3046–3050, 1995.

[12] F. Wagner, T. C. Kunz, S. R. Chowdhury et al., "Armadillo repeat-containing protein 1 is a dual localization protein associated with mitochondrial intermembrane space bridging complex," *PLoS One*, vol. 14, no. 10, article e0218303, 2019.

[13] Z. Tang, C. Li, B. Kang, G. Gao, C. Li, and Z. Zhang, "GEPIA: a web server for cancer and normal gene expression profiling and interactive analyses," *Nucleic Acids Research*, vol. 45, no. W1, pp. W98–w102, 2017.

[14] G. X. Hou, P. Liu, J. Yang, and S. Wen, "Mining expression and prognosis of topoisomerase isoforms in non-small-cell lung cancer by using Oncomine and Kaplan-Meier plotter," *PLoS One*, vol. 12, no. 3, article e0174515, 2017.

[15] A. Asplund, P. H. Edqvist, J. M. Schwenk, and F. Pontén, "Antibodies for profiling the human proteome—the Human Protein Atlas as a resource for cancer research," *Proteomics*, vol. 12, no. 13, pp. 2067–2077, 2012.

[16] K. Tomczak, P. Czerwińska, and M. Wiznerowicz, "The Cancer Genome Atlas (TCGA): an immeasurable source of knowledge," *Contemporary Oncology*, vol. 19, no. 1a, pp. A68–A77, 2015.

[17] E. Cerami, J. Gao, U. Dogrusoz et al., "The cBio cancer genomics portal: an open platform for exploring multidimensional cancer genomics data," *Cancer Discovery*, vol. 2, no. 5, pp. 401–404, 2012.

[18] Y. Zhou, B. Zhou, L. Pache et al., "Metascape provides a biologist-oriented resource for the analysis of systems-level datasets," *Nature Communications*, vol. 10, no. 1, p. 1523, 2019.

[19] D. W. Huang, B. T. Sherman, Q. Tan et al., "DAVID Bioinformatics Resources: expanded annotation database and novel algorithms to better extract biology from large gene lists," *Nucleic Acids Research*, vol. 35, suppl_2, pp. W169–W175, 2007.

[20] Z. Anastasiadi, G. D. Lianos, E. Ignatiadou, H. V. Harissis, and M. Mitsis, "Breast cancer in young women: an overview," *Updates in Surgery*, vol. 69, no. 3, pp. 313–317, 2017.

[21] M. Peifer, S. Berg, and A. B. Reynolds, "A repeating amino acid motif shared by proteins with diverse cellular roles," *Cell*, vol. 76, no. 5, pp. 789–791, 1994.

[22] J. C. Coates, "Armadillo repeat proteins: beyond the animal kingdom," *Trends in Cell Biology*, vol. 13, no. 9, pp. 463–471, 2003.

[23] B. T. MacDonald, K. Tamai, and X. He, "Wnt/beta-catenin signaling: components, mechanisms, and diseases," *Developmental Cell*, vol. 17, no. 1, pp. 9–26, 2009.

[24] W. Xu and D. Kimelman, "Mechanistic insights from structural studies of beta-catenin and its binding partners," *Journal of Cell Science*, vol. 120, Part 19, pp. 3337–3344, 2007.

[25] D. H. Nguyen and P. T. Truong, "A debate on locoregional treatment of the primary tumor in patients presenting with stage IV breast cancer," *Expert Review of Anticancer Therapy*, vol. 11, no. 12, pp. 1913–1922, 2011.

[26] M. S. Lawrence, P. Stojanov, C. H. Mermel et al., "Discovery and saturation analysis of cancer genes across 21 tumour types," *Nature*, vol. 505, no. 7484, pp. 495–501, 2014.

[27] M. R. Stratton, P. J. Campbell, and P. A. Futreal, "The cancer genome," *Nature*, vol. 458, no. 7239, pp. 719–724, 2009.

[28] R. P. Kaur, K. Vasudeva, R. Kumar, and A. Munshi, "Role of p53 gene in breast cancer: focus on mutation spectrum and therapeutic strategies," *Current Pharmaceutical Design*, vol. 24, no. 30, pp. 3566–3575, 2018.

[29] H. Wang, F. Yao, S. Luo et al., "A mutual activation loop between the Ca^{2+}-activated chloride channel TMEM16A and EGFR/STAT3 signaling promotes breast cancer tumorigenesis," *Cancer Letters*, vol. 455, pp. 48–59, 2019.

[30] T. G. Phan and P. I. Croucher, "The dormant cancer cell life cycle," *Nature Reviews. Cancer*, vol. 20, no. 7, pp. 398–411, 2020.

[31] Y. Zhang, W. K. Yang, G. M. Wen et al., "High expression of *PRKDC* promotes breast cancer cell growth via *p38 MAPK* signaling and is associated with poor survival," *Molecular Genetics & Genomic Medicine*, vol. 7, no. 11, article e908, 2019.

[32] Y. Inagaki, D. Wu, K. Fujiwara et al., "Knockdown of E2F5 induces cell death via the TP53-dependent pathway in breast cancer cells carrying wild-type TP53," *Oncology Reports*, vol. 44, no. 5, pp. 2241–2252, 2020.

[33] P. E. Porporato, N. Filigheddu, J. M. B. Pedro, G. Kroemer, and L. Galluzzi, "Mitochondrial metabolism and cancer," *Cell Research*, vol. 28, no. 3, pp. 265–280, 2018.

[34] J. Lee, A. E. Yesilkanal, J. P. Wynne et al., "Effective breast cancer combination therapy targeting BACH1 and mitochondrial metabolism," *Nature*, vol. 568, no. 7751, pp. 254–258, 2019.

[35] B. O'Rourke, "Mitochondrial ion channels," *Annual Review of Physiology*, vol. 69, pp. 19–49, 2007.

[36] X. Wang, P. An, Z. Gu, Y. Luo, and J. Luo, "Mitochondrial metal ion transport in cell metabolism and disease," *International Journal of Molecular Sciences*, vol. 22, no. 14, 2021.

Hindawi

Retraction

Retracted: Correlation of Carotid Artery Intima-Media Thickness with Calcium and Phosphorus Metabolism, Parathyroid Hormone, Microinflammatory State, and Cardiovascular Disease

BioMed Research International

This article has been retracted by Hindawi following an investigation undertaken by the publisher [1]. This investigation has uncovered evidence of one or more of the following indicators of systematic manipulation of the publication process:

(1) Discrepancies in scope

(2) Discrepancies in the description of the research reported

(3) Discrepancies between the availability of data and the research described

(4) Inappropriate citations

(5) Incoherent, meaningless and/or irrelevant content included in the article

(6) Manipulated or compromised peer review

The presence of these indicators undermines our confidence in the integrity of the article's content and we cannot, therefore, vouch for its reliability. Please note that this notice is intended solely to alert readers that the content of this article is unreliable. We have not investigated whether authors were aware of or involved in the systematic manipulation of the publication process.

Wiley and Hindawi regrets that the usual quality checks did not identify these issues before publication and have since put additional measures in place to safeguard research integrity.

We wish to credit our own Research Integrity and Research Publishing teams and anonymous and named external researchers and research integrity experts for contributing to this investigation.

The corresponding author, as the representative of all authors, has been given the opportunity to register their agreement or disagreement to this retraction. We have kept a record of any response received.

References

[1] P. Huang, J. Tan, X. Gu et al., "Correlation of Carotid Artery Intima-Media Thickness with Calcium and Phosphorus Metabolism, Parathyroid Hormone, Microinflammatory State, and Cardiovascular Disease," *BioMed Research International*, vol. 2022, Article ID 2786147, 9 pages, 2022.

Research Article

Correlation of Carotid Artery Intima-Media Thickness with Calcium and Phosphorus Metabolism, Parathyroid Hormone, Microinflammatory State, and Cardiovascular Disease

Peng Huang, Junhua Tan, Xianjun Gu, Meiying Huang, Feifan Huang, Ruiying Ma, and Jie Wang [ID]

Department of Nephrology, The Affiliated Hospital of Youjiang Medical University for Nationalities, Baise, 533000 Guangxi, Guangxi Zhuang Autonomous Region, China

Correspondence should be addressed to Jie Wang; yyfywjj@126.com

The internal thickness of the carotid artery is the vertical distance between the intima of the carotid artery and the middle mold. Its normal thickness is less than 1 mm. It can be used to judge the degree of arteriosclerosis. Under normal circumstances, the change of the internal thickness of the carotid artery is caused by cardiovascular disease. The purpose of this article is to study the relationship between the thickness of the carotid artery and the metabolism of calcium and phosphorus, parathyroid hormone, microinflammatory state, and cardiovascular disease. This article uses ultrasound measurement to measure the IMT of ESRD patients and carotid arteries with normal renal function. The analysis includes blood pressure, blood phosphorus, blood calcium, blood creatinine, blood urea nitrogen, blood sugar, glycosylated hemoglobin, blood lipids, parathyroid hormone, and C reaction. The correlation between clinical indicators includes protein and carotid IMT in ESRD patients which can be used in designing a diagnostic plan for patients through correlation research. The results showed that the carotid artery IMT of ESRD nondialysis patients was 13% thicker than that of those with normal renal function, and it was significantly positively correlated with age, blood pressure, blood phosphorus, glycosylated hemoglobin, and C-reactive protein. The correlation ratio with calcium and phosphorus was about 0.1.

1. Introduction

Insufficient carotid artery thickness can easily lead to disorders of calcium and phosphorus metabolism, abnormal secretion of bone metabolism indicators such as window hormones, leading to fibroosteitis, bone dysplasia, osteomalacia, and other bone diseases with poor prognosis. Abnormal bone metabolism refers to a series of diseases such as osteoporosis and osteomalacia that are caused by a series of pathological factors that lead to problems in bone metabolism. Changes in CIMT are often considered to be associated with cardiovascular disease risk, but very few studies have reported this correlation. The aim of this paper is to investigate the correlation of carotid intima-media thickness with calcium and phosphorus metabolism, parathyroid hormone, microinflammatory status, and cardiovascular disease

in patients. The KDIGO guidelines define CKD-MBD caused bone disease induced by disorder of mineral metabolism [1]. Due to renal failure, patients with Maintenance Hemodialysis(MHD) have higher iPTH (Immunoreactive parathyroid hormone), resulting in less bone formation than bone resorption, increased bone loss of cortical bone and carcinogenic bone, and a significant increase in the risk of vertebral body and local fractures [2]. Since iPTH has a good histological connection with ROD, it has been widely used in the diagnosis of bone and kidney diseases in the past [3]. However, for patients with low vitamin D3 levels (and other patients with low iPTH levels), the result of the iPTH test is the sum of 1-84PTH and 7-84PTH. The latter causes a decrease in blood calcium and competes with 1-84PTH. Comparing the biological activity of PTH1-84 and iPTH can better clarify bone transport in MHD patients [4].
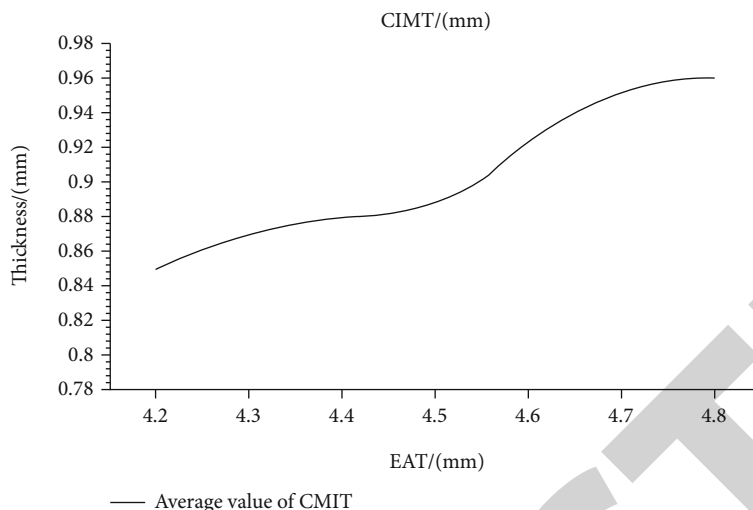
CIMT/(mm)

Figure 1: Variation of CIMT mean value with EAT.

Therefore, if the indicators with strong specificity and high sensitivity to CKD-MBD can be found from the detection indicators, the combination of iPTH is of great significance for the timely prevention and diagnosis of CKD-MBD [5].

The carotid intima-media thickness (CIMT) is a reliable marker of subclinical atherosclerosis and cardiovascular events [6]. Until today, no studies have investigated whether epicardial adipose tissue (EAT) is more important for CIMT and atherosclerotic plaques, and epicardial adipose tissue is a substitute for lipid accumulation or circulating lipids in special visceral tissues [7]. The Kocaman SA study used a cross-sectional and prospective observational design and included 252 hospitalized patients, Figure 1 shows the variation of CIMT mean value with EAT [8]. EAT is determined as an anechoic space under the pericardium on two-dimensional echocardiography and is measured perpendicular to the front of the free wall of the right ventricle at the end of systole [9, 10]. EAT is significantly correlated with CIMT. With the increase of EAT thickness, CIMT increases significantly (for patients with EAT is less than 5 mm) [11]. Multiple linear regression analysis showed that age (Beta: 0.406), male (Beta: 0.244), and EAT (Beta: 0.450) were independent related factors of CIMT [12]. However, such experiments are not stable, and the result data obtained will not be very accurate [13, 14].

The occurrence of cardiovascular disease is related to the consumption of vegetables. Epidemiological studies have shown that the risk of eating vegetables is inversely proportional to the risk of cardiovascular disease [15]. Guo-Yi et al. have studied the ingredients of vegetables. Vegetables have great potential for preventing and treating cardiovascular diseases [16]; vitamins, essential ingredients, dietary fiber, plant protein, and phytochemicals are biologically active ingredients. The cardioprotective effects of vegetables may involve antioxidant effects [17]. Anti-inflammatory, anti-platelet properties regulate blood pressure, blood sugar, and blood lipid levels; reduces myocardial damage; and regulates related enzyme activities, gene expression, and signal transduction pathways, and other biomarkers related to cardiovascular disease [18, 19]. In addition, several vegetables and their biologically active ingredients have been proven to prevent cardiovascular disease in clinical trials [20]. However, the composition of vegetables is variable, which reduces the accuracy of the results [21].

The innovation of this article lies in the domestic and foreign research on the correlation between CIMT and acyclic plaque formation and coronary heart disease [22], comparing the correlation and difference between bilateral CIMT and coronary artery disease [23]. CIMT can not only reflect the occurrence and severity of coronary artery disease but also reflect the number of blood vessels in coronary artery disease, and it can also reflect the degree of vascular stenosis. The degree of effect of the intervention on CIMT progression predicts the degree of CVD risk reduction. These data support the use of descending CIMT progression as a surrogate marker of CVD risk. CIMT has specific reference value for the diagnosis of coronary heart disease [24]. Combining the patient's baseline condition and carotid artery, Doppler ultrasound can improve the diagnostic accuracy of coronary heart disease, but due to the limitations of Doppler ultrasound itself, it is necessary to find a more objective and accurate diagnosis method; the degree of sensitivity, specificity, and accuracy of Doppler ultrasound in the diagnosis of occupying thyroid lesions is significantly higher than that produced by conventional, but in the clinic, ultrasound elastography discrimination is experienced and technology needs to be improved to further improve the accuracy [25].

2. Materials and Methods

2.1. Experimental Materials. 83 cases of ESRD nondialysis patients were selected for long-term treatment in the Department of Neurology of our hospital, 45 males and 38 females, including 52 cases of chronic seminogenic nephritis, 18 cases of diabetic renal failure, 8 cases of ischemic renal failure, Langchuang 3 cases of nephritis, 2 cases of polycystic kidney disease.

Inclusion criteria are as follows: 18 years of age or older, diagnosed with chronic renal failure (uremia); without renal replacement therapy, no infection, surgery, blood transfusion, and heart failure. Within a short period of time, there was no pregnancy, breastfeeding, severe malnutrition or other serious diseases. All selected patients have been informed of their consent and voluntarily participate in this study.

Exclusion criteria are as follows: age less than or equal to 18 years old, primary hyperthyroidism, acute renal failure, window edema, poisoning, combined malignant tumors, active immune tissue diseases, liver failure such as hepatitis and cirrhosis, blood system diseases, congenital heart disease, and abnormal blood coagulation mechanism.

At the same time, 50 patients with normal renal function treated in our hospital from December 2016 to April 2020 were randomly selected, including 24 males and 26 females, including 31 cases of renal syndrome, 9 cases of chronic spirochetal nephritis, and IgA with renal function. There were 5 cases of failure, 3 cases of diabetic renal failure, and 2 cases of purple kidney.

2.2. Data Collection Method. To further investigate the factors influencing carotid intima-media thickness, the carotid IMT measurement is as follows: The patient is placed in a supine position with the neck completely exposed. Siemens S3000 ultrasonic diagnostic instrument was used, the probe frequency is 4-8 MHz, starting from the proximal end of the bilateral joint carotid artery, measuring the vertical distance between the hospitals without obvious points, the internal connection of the block, the average value and the risk interface, and the average value after three measurements. The average bilateral IMT thickness is the IMT value of the patient's carotid artery. The blood count was collected the next morning the patient was admitted to the hospital. Blood calcium (Ca), blood phosphorus (P), blood creatinine (Cr), fasting venous blood, blood urea nitrogen, blood glucose (GLU), glycosylated hemoglobin (HbA1c), protein C (CRP), total cholesterol (TCH), and high-density lipoprotein (HDL) levels are detected by an automatic biochemical analyzer. Electrochemical photometric determination of serum parathyroid hormone (PTH) level. After a 15-minute break in the morning, all patients used a standard mercury pulse monitor to measure blood pressure in their right arm.

2.3. Ultrasound Inspection Methods. To find out the carotid intima-media thickness of patients, use cervical ultrasound to evaluate carotid artery calcification. All the patients were checked by a permanent ultrasound recorder in our hospital, but he did not know the patient's condition. The subject was asked to place his position and detector on the outside of the trachea in front of the neck. Measure the thickness of the center of the carotid artery 1 cm below the artery and vagina, and observe the longitude and lateral two-dimensional images in real time.

ITM refers to the subsonic gray area not shown on the arterial column, the vertical distance from the middle of the material yard to the interface between the middle and the outer mold. The average value of the bilateral ITM is used as the patient's ITM value. The judging criteria are as follows: the common carotid artery IMT is greater than or equal to 1.0 mm, that is, the carotid artery calcification plate is formed. Thickening of the median carotid artery, or the absence of carotid plate and carotid plate. This is the so-called carotid artery calcification process. If the artery wall extends into the official cavity, the longitudinal and lateral images and thickness of the same part become thicker than others. Half of the neighboring area is called atheroma.

2.4. Carotid Artery Intima-Media Thickness Measurement Experiment. The CIMT measurement site is the left and right common carotid arteries, 10 mm from the carotid sinus, left and right common carotid arteries. During the measurement, the subject was asked to turn the head of the No. 45 ship to the other side and place it underwater. Each subject underwent the same experienced ultrasound examination and repeated the measurement three times. The instrument used is the same ultrasound system, which is equipped with an L9-3mhz ultrasonic sensor and standard image settings. In epidemiology and clinical practice, the measurement of CIMT should take into account the gender, age, and ethnic differences of subjects. Due to the lack of uniform diagnostic criteria for carotid dysplasia worldwide, China defines the common carotid artery as greater than or equal to 1.0 mm or carotid sinus greater than or equal to 1.2 mm, and the coefficient of variance is less than 2.9%.

2.5. Statistical Methods. All statistical data should use the Chinese version of the SPSS 19.0 software. The measurement data is represented by the average value and standard deviation, and the measurement data is represented by the composition ratio. The analysis of variance was used to compare the average values between multiple measurement groups, and the LSD method was used to compare the differences between the groups. The X2 test is used to compare the differences between the measured data sets. Classification and inspection shall be adopted for the grade data. Correlation analysis adopts Pearson's correlation analysis. $P < 0.05$ indicates that the difference is statistically significant.

3. Results

3.1. Correlation Analysis of Carotid Artery Intima-Media Thickness and Calcium and Phosphorus Metabolism. In general, among the 7000 health checkups, there are 4000 males and 3000 females; age 23-86 years old, with an average age of 50 years. There are 1 400 patients with phosphate and potassium metabolism disorder, including 1 200 males and 200 females. The prevalence of phosphate and potassium metabolism disorder in the study population is 20.7%; the prevalence of phosphate and potassium metabolism disorder in men (30%) is significantly higher than the prevalence of female phosphorus and potassium metabolism disorder (7%). Calcium and phosphorus metabolism refers to the entire process of calcium and phosphorus being taken up by the body in food, then synthesized and broken down in the body, and finally excreted. Calcium in the body comes
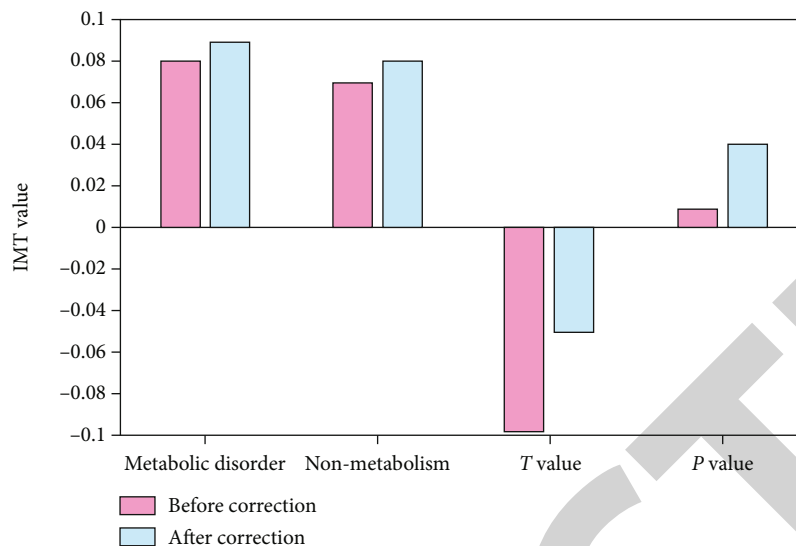
Figure 2: Comparison of carotid IMT values before and after correction.

Table 1: Comparison of the parathyroid hormone group and normal control group.

Group	OC (pg/ml)	iPTH (pg/ml)	Ca (mmol/L)	P (μmol/L)
Parathyroid hormone group	103.3	331	2.16	1.67
Normal control group	6.3	48.06	2.24	1.05
t	-7.8	-7.6	-2.4	-7.3
P	0	0	0.1	0

mainly from food and is mostly absorbed in the upper part of the small intestine. The effect of carotid artery IMT was analyzed by covariance. The carotid IMT of the phosphate and potassium metabolism disorder group before correction was significantly higher than that of the nonphosphate and potassium metabolism disorder group; Carotid IMT was higher in the corrected phosphorus and potassium metabolism disorder group than in the precorrected phosphorus and potassium metabolism disorder group. After adjusting for factors such as gender and age, the phosphorus and potassium metabolism, the carotid IMT of the disordered group was still higher than the IMT of the nonphosphate and potassium metabolism disordered group. The comparison of carotid artery IMT values before and after correction is shown in Figure 2:

Phosphorus and potassium metabolism disorder is a situation where the metabolic risk factors of a variety of cardiovascular diseases are concentrated in one person. The factors of phosphorus and potassium metabolism disorders are more complex, not only related to the environment, but also to genetics. The factors of phosphorus and potassium metabolism disorders may be due to poor nutrition and electrolyte disorders in the body caused by irregular life and diet all the time. Need to pay more attention to the diet, it is usually best to exercise properly ,have a regular diet, and promote blood flow. The barriers to phosphorus and potassium metabolism are caused by complex genetic and environmental factors. Therefore, the main problem is insulin

resistance and high insulin. Both can cause and accelerate atherosclerosis by causing hypertension and disorders of glucose and lipid metabolism.

3.2. Correlation Analysis between Carotid Artery Intima-Media Thickness and Parathyroid Hormone. Parathyroid hormone (PTH) is a basic single-chain polypeptide hormone secreted by the main cells of the parathyroid glands. Its main function is to regulate the metabolism of calcium and phosphorus in vertebrates, resulting in an increase in blood calcium levels and a decrease in blood phosphorus levels. The serum OC, iPTH, and blood phosphorus concentrations of the parathyroid group were higher than those of the control group, and there were statistical differences ($P < 0.05$). The blood calcium concentration was lower than that of the control group, and the parathyroid group was higher than the control group. As shown in Table 1:

In the parathyroid hormone group, OC and iPTH were significantly positively correlated. The specific data are shown in Figure 3:

Through analysis, it can be observed that the serum OC and iPTH levels of the parathyroid hormone group were significantly higher than those of the non-MHD group, the blood phosphorus concentration was significantly higher than that of the non-MHD group, and the Ca concentration was lower than the control group, but the difference was statistically significant. The renal function of patients with uremia was severely damaged, the filtration rate of the pellet
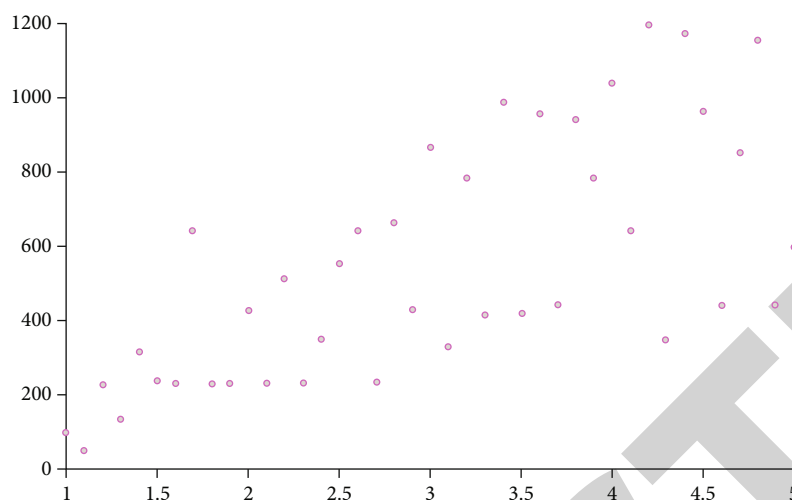
FIGURE 3: Scatter plot of OC and iPTH.

was lower than 16 ml/min, and the serum OC level was higher than that of the control group. According to research, changes in serum osteocalcin usually occur when GFR is less than 20 ml/min, and osteocalcin is mainly excreted from the kidneys. After renal dysfunction in MHD patients, the level of iPTH increases, renal clearance decreases, and iPTH deposition in the kidney decreases. The half-life is prolonged. There are high levels of iPTH in the body.

3.3. Correlation Analysis of Carotid Artery Intima-Media Thickness and Microinflammatory State. Intravascular inflammation due to the involvement of inflammatory substances is called microinflammatory state. Dialysis patients do not have systemic or local overt clinical signs of infection, but there is a low-level, persistent inflammatory state, manifested by elevated inflammatory factors. It is generally accepted that the microinflammatory response is the result of sustained activation of the monocyte/macrophage system, and that hemodialysis patients can suffer from monocyte activation due to contact between peripheral blood monocytes and contaminated endotoxin in the dialysis membrane or dialysis fluid, which can exponentially exacerbate the development of the inflammatory response. According to the CCA-IMT value measured by B-ultrasound, the study subjects were divided into 5 groups, namely, 0.60 mm group, 0.80 mm group, 0.90 group, 1.20 group, and larger than 1.20 mm group. There was no statistical difference in age, gender, height, body weight, body mass index, systolic blood pressure, diastolic blood pressure, fasting blood glucose, hemoglobin, smoking history, and drinking history among individuals in each group. Figure 4 shows the comparison of serum hsCRP, ferritin, ALB, pre-ALB, and TF between groups. It can be seen from the figure that the contents of clear hsCRP and ferritin increased with the increase of CCA.IMT value, showing a positive correlation (r is 0.84 and, respectively, 0.89); ALB, pre.ALB, and TF content decreased with the increase of CCA.IMT value,

showing a negative correlation (r is -0.62, -0.78, and -0.65, respectively).

Atherosclerosis is a chronic vascular proliferative inflammation, and inflammation plays an important role in its occurrence. Serum inflammation index occurs at different stages of atherosclerosis. C-reactive proteins are mainly acidic phase proteins produced in the liver. Usually trace amounts can be seen in normal human serum. C-reactive protein plays a regulatory role by activating complement and enhancing phagocytosis to remove invading pathogenic microorganisms and damaged, necrotic, and apoptotic tissue cells in the plasma when the body is infected or damaged by tissue (acute protein).

Specific and nonspecific inflammatory stimuli can be significantly increased. It is not only an index of clinical inflammation serum but also has the effect of inflammatory factors, directly participating in the main stages of atherosclerosis and promoting the development of atherosclerosis. On the one hand, the formation of atherosclerosis is accompanied by an increase in plasma protein C reaction; on the other hand, C-reactive protein may promote the occurrence of atherosclerosis. Inflammatory factors enter the vascular endothelium from macrophages to regulate the expression of adhesion factors and regulate the arterial wall. In cells and circulation, the role of single-cell proinflammatory factors is ancient, further promoting the formation of atherosclerosis. Therefore, C-reactive protein is actually a preinflammatory factor related to the occurrence and development of atherosclerosis.

3.4. Correlation Analysis of Carotid Artery Intima-Media Thickness and Cardiovascular Disease. Cardiovascular disease is a collective term for cardiovascular and cerebrovascular diseases and refers to ischemic or hemorrhagic diseases of the heart, brain, and systemic tissues caused by hyperlipidemia, blood viscosity, atherosclerosis, and hypertension. Comparison of CIMT and clinical indicators in CVD cardiovascular patients are as follows: the age, LDL, CRP, and
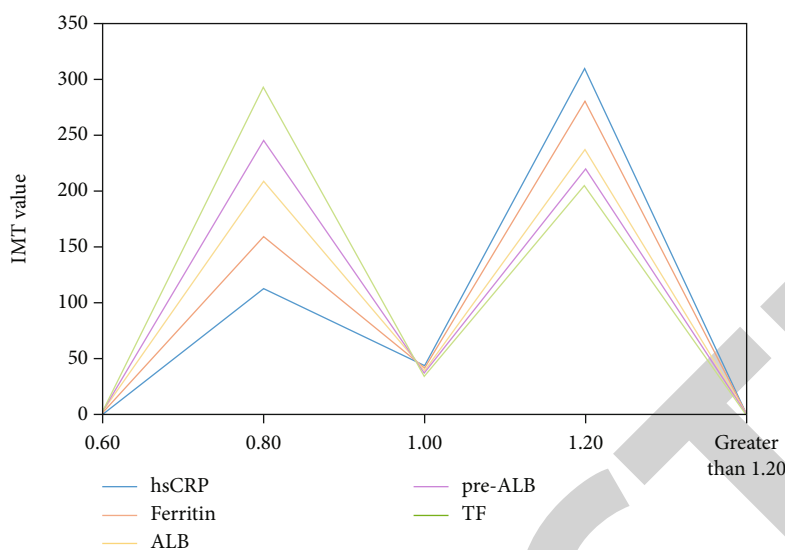
Figure 4: Comparison of serum between groups.
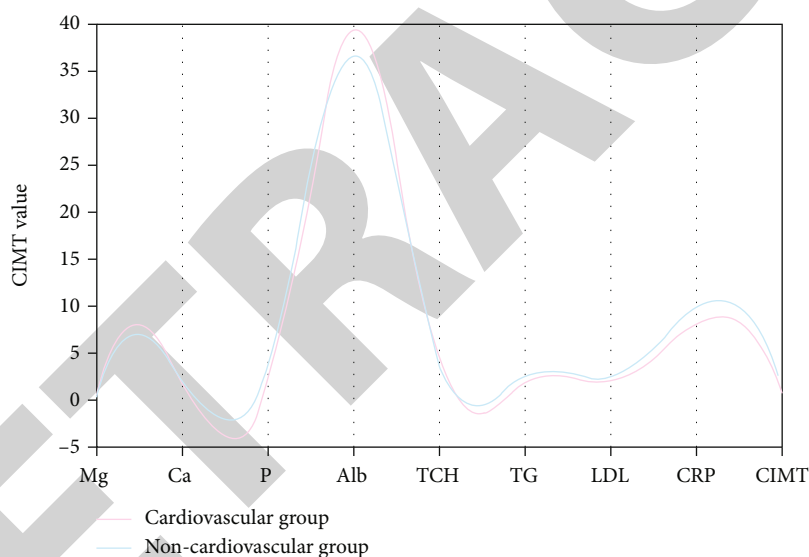
Figure 5: Comparison of CIMT between two groups of cardiovascular patients.

CIMT of CVD cardiovascular patients are significantly higher than those of patients without CVD, while the Alb and Mg of patients are significantly lower than those of HD patients without CVD, as shown in Figure 5:

According to the accounting analysis of 90 HD patients regression, the HD-related risk factor combined with cardiovascular disease is CIMT. CIMT is a powerful predictor of cardiovascular disease. CIMT and CRP are related, and both are related to cardiovascular events. The risk factor CIMT is closely related to stroke and myocardial infarction. Hypomagnesemia is a risk factor for patients with carotid atherosclerosis. Mg is closely related to vascular calcification and atrom arteriosclerosis and has an obvious negative relationship with CIMT. Hypomagnesemia can worsen the patient's arteriosclerosis. Together, they increase the incidence of

cardiovascular disease. Therefore, the LDL, CRP, and CIMT of HD patients with cardiovascular disease increased significantly, and the blood concentration of Alb and Mg decreased significantly. Risk factors for cardiovascular disease are related to CIMT and hypomagnesemia. Correcting hypomagnesemia in HD patients and improving carotid arteriosclerosis are important means to prevent cardiovascular disease in HD patients.

According to the characteristics of physical ultrasound, the distance between the two parallel rays between the inner ridge and the middle of the carotid artery is called the thickness of the middle heart artery. Fatigue is the initial stage of the carotid artery which is a sign of atherosclerosis. As a manifestation of systemic atherosclerosis, carotid atherosclerosis has a pathological basis similar to coronary arteries and

cerebral arteries. Therefore, the increase in the thickness of endothelial arteries is closely related to the occurrence of cardiovascular and cerebrovascular diseases.

3.5. Analysis of Influencing Factors of Carotid Artery Intima-Media Thickness

3.5.1. Association Analysis of Serum igG and CIMT. According to the analysis results, the serum IgG level is generally negatively correlated with the prevalence of CIMT thickening. With the increase of IgG concentration, the prevalence of CIMT thickening showed a downward trend, and there was no significant difference between men and women. As an immune disease, whether it is fungal immunity or cellular immunity, it is achieved by affecting deposition, the absorption, and peroxidation of oxidized low-density lipoprotein in the formation of atherosclerosis. Unsaturated fatty acids are fatty acids that constitute body fat and are indispensable to the human body. Insufficient unsaturated fatty acids in the diet can easily produce the following diseases: an increase in LDL and LDL cholesterol in the blood, producing atherosclerosis, and inducing cardiovascular and cerebrovascular diseases. There is evidence that the increase in serum IgG is related to the formation of lesions and the decrease in serum cholesterol levels. Low-density lipoprotein contains a large amount of multipotential unsaturated fatty acids. These fatty acids undergo peroxidation under the action of excessive free radicals and reagents and finally produce low-density lipoprotein modified by malonylurea. Studies have shown that the degree of AS is positively correlated with MDA-LDL. MDA-LDL is a clinical risk factor for AS, that is, T cells can secrete a large amount of AS and a large number of IgG anti-MDA-LDL antibodies, thereby delaying the development of AS.

3.5.2. Association Analysis of Parathyroid Glands and CIMT. The incidence of secondary hyperthyroidism in dialysis patients is higher. High levels of window-specific hormones affect the deposition of calcium and phosphorus, leading to vascular calcification, a mineral and bone disease associated with CKD. Analysis shows that high window hormones can promote the level of inflammatory factors and the proliferation of smooth muscle vascular cells. Parathyroid hormone can also directly increase the composition of FGF23 by activating the PTH-R1 receptor and indirectly stimulate the composition of potassium triol. The renal tubule 1a is hydroxylated, and the above mechanisms are involved in and accelerate the occurrence of vascular calcification. In addition, the relationship between parathyroid hormone and vascular calcification was studied using endothelial cells and detected by Western blot and ELISA methods. Western blot is a current method for semiquantification of proteins in combination with internal reference, which can reflect the information of molecular weight, and ELISA can quantify certain proteins and hormones. It was found that BMP-2 labeled osteoblasts were exposed to 10^{10} mmol/l PTH. The differentiation effect is the greatest. The expressions of osteogenic proteins BMP 2 and BMP 4 increase. Parathyroid hormone is believed to promote the differentiation of endo-thelial cell osteoblasts, mainly through protein-labeled extracellular 1/2 kinase pathway and nuclear factor kB pathway, but at present, the effects of PTH on the differentiation of endothelial cells and bone fibers and its mechanism have not been fully elucidated, and further research is needed.

3.5.3. Association Analysis between Inflammation and CIMB. Through analysis, it can be known that the main reason for the microinflammation of dialysis patients is the low immune function of dialysis patients, which may be accompanied by anemia, release of uremic toxin, and other reasons to promote the development of inflammation. These inflammatory factors mainly include C-reactive protein, tumor necrosis factor, interleukin-1, interleukin-6, and insulin growth factor. They activate the bone formation process in different ways and promote vascular calcification. Recently, in order to confirm the role of inflammation in vascular calcification, experimental rats were divided into rats with kidney damage and rats with inflammation with kidney damage. Rats were injected with adenine into the stomach and measured the level FGF23 mRNA, which confirmed that inflammation not only directly stimulates vascular calcification but also indirectly promotes the occurrence of vascular calcification in dialysis patients by increasing the level of FGF23. In addition, the exposure of macrophages to calcium phosphate mediators was also studied, and it was found that macrophages can promote inflammation-promoting release factors through protein kinase pathway C and RANKL, which may also promote macrophages to release inflammatory factors and promote vascular calcification. These confirmed related inflammation and vascular calcification.

4. Discussion

The CIMT value studied in this paper reflects not only the number of coronary artery disease but also the severity of coronary artery disease and the degree of vascular stenosis. CIMT has certain reference value for the diagnosis of coronary heart disease. Combining the basic condition of the patient's carotid artery and Doppler ultrasound can improve the accuracy of the diagnosis of coronary heart disease, but due to the limitations of Doppler ultrasound itself, it is necessary to find a more objective and accurate diagnosis method.

This article analyzes that the disease is a known risk factor for atherosclerosis and vascular disease and is associated with increased mortality. Inflammatory mediators activate blood calcification pathways, leading to upregulation of bone transformation-related factors. TNF-α, IL-6, and IL-1b can cause phenotypic changes of vascular smooth muscle cells. In CKD patients, the increase of inflammatory mediators is related to arterial calcification. In animal studies, inflammation promotes blood calcification and bone loss in mice and acts through the factor kB (NF-κB) pathway. In in vitro experiments, long noncoding RNA-ANCR reduced the expression of Runx2 and BMP-2 in vascular smooth muscle cells by inhibiting the activation of NP-KB.

This article analyzes the sporadic increase in calcium and calcium load caused by the use of active vitamin D in the

urea population, active vitamin D receptor antagonists, and calcium-phosphorus binders. The abnormal ossification of vascular smooth muscle cells on high calcium medium may be due to the secondary increase of phosphate transferred to the cells. L-type calcium channels are also involved in the process of vascular calcification. In vitro inhibition of verapamil type I calcium channels can reduce the occurrence of vascular calcification. In addition, Norin can also reduce calcification in VSMC medium. High levels of extracellular calcium are related to the release of stratigraphic cysts and may promote cell death and release, both related to the progression of calcification.

Data Availability

The data used to support the findings of this study are included within the article.

Conflicts of Interest

The authors declare that they have no conflicts of interest.

Acknowledgments

References

[1] A. Mazouri, N. Khosravi, A. Bordbar et al., "Does adding intravenous phosphorus to parenteral nutrition has any effects on calcium and phosphorus metabolism and bone mineral content in preterm neonates," *Acta Medica Iranica*, vol. 55, no. 6, pp. 395–398, 2017.

[2] S. Schmitt and B. Dobenecker, "Calcium and phosphorus metabolism in peripartal dogs," *Journal of Animal Physiology and Animal Nutrition*, vol. 104, no. 6, pp. 1–8, 2020.

[3] Z. W. Sun, Q. H. Fan, X. X. Wang, Y. M. Guo, H. J. Wang, and X. Dong, "High stocking density alters bone-related calcium and phosphorus metabolism by changing intestinal absorption in broiler chickens," *Poultry Science*, vol. 97, no. 1, pp. 219–226, 2018.

[4] J. L. Pérez Vela, "Utility of calcium and phosphorus metabolism biomarkers in the stratification of acute coronary syndrome," *Medicina Intensiva*, vol. 42, no. 2, pp. 71-72, 2018.

[5] J. Wang, L. Chen, Y. Zhang et al., "Association between serum vitamin B6 concentration and risk of osteoporosis in the middle-aged and older people in China: a cross-sectional study," *BMJ Open*, vol. 9, no. 7, article e028129, 2019.

[6] V. Chat, F. Wu, R. Demmer et al., "Association between parity and carotid intima-media thickness in Bangladesh," *Annals of Epidemiology*, vol. 27, no. 8, p. 533, 2017.

[7] Y. G. Tedla, A. D. Gepner, D. Vaidya et al., "Association between long-term blood pressure control and ten-year progression in carotid arterial stiffness among hypertensive individuals," *Journal of Hypertension*, vol. 35, no. 4, pp. 862–869, 2017.

[8] S. A. Kocaman, "An increase in epicardial adipose tissue is strongly associated with carotid intima-media thickness and atherosclerotic plaque, but LDL only with the plaque," *Anatolian Journal of Cardiology*, vol. 17, no. 1, pp. 56–63, 2017.

[9] T. Zhao, B. Chen, Y. Zhou et al., "Effect of levothyroxine on the progression of carotid intima-media thickness in subclinical hypothyroidism patients: a meta-analysis," *BMJ Open*, vol. 7, no. 10, article e016053, 2017.

[10] S. Salekzamani, A. S. Bavil, H. Mehralizadeh, M. A. Jafarabadi, A. Ghezel, and B. P. Gargari, "The effects of vitamin D supplementation on proatherogenic inflammatory markers and carotid intima media thickness in subjects with metabolic syndrome: a randomized double-blind placebo-controlled clinical trial," *Endocrine*, vol. 57, no. 1, pp. 51–59, 2017.

[11] D. M. Kusters, M. J. A. M. Braamskamp, G. Langslet et al., "Effect of Rosuvastatin on carotid intima-media thickness in children with heterozygous familial hypercholesterolemia: the CHARON study," *Circulation*, vol. 137, no. 6, pp. 641-642, 2018.

[12] H. Øygarden, "Carotid intima-media thickness and prediction of cardiovascular disease," *Journal of the American Heart Association*, vol. 6, no. 1, p. e005313, 2017.

[13] Y. Shimizu, S. Sato, J. Koyamatsu et al., "Hepatocyte growth factor and carotid intima-media thickness in relation to circulating CD34-positive cell levels," *Environmental Health & Preventive Medicine*, vol. 23, no. 1, p. 16, 2018.

[14] S. Alpaydin, Y. Turan, M. Caliskan et al., "Morning blood pressure surge is associated with carotid intima-media thickness in prehypertensive patients," *Blood Pressure Monitoring*, vol. 22, no. 3, pp. 131–136, 2017.

[15] K. Sun, J. Song, K. Liu et al., "Associations between homocysteine metabolism related SNPs and carotid intima-media thickness: a Chinese sib pair study," *Journal of Thrombosis and Thrombolysis*, vol. 43, no. 3, pp. 401–410, 2017.

[16] G. Y. Tang, X. Meng, Y. Li, C. N. Zhao, Q. Liu, and H. B. Li, "Effects of vegetables on cardiovascular diseases and related mechanisms," *Nutrients*, vol. 9, no. 8, p. 857, 2017.

[17] C. Wang, R. Qiu, Y. Cao et al., "Higher dietary and serum carotenoid levels are associated with lower carotid intima-media thickness in middle-aged and elderly people," *British Journal of Nutrition*, vol. 119, no. 5, pp. 590–598, 2018.

[18] J. R. Chauduri, K. R. Mridula, M. Umamashesh, B. Balaraju, and V. C. S. S. Bandaru, "Association of serum 25-hydroxyvitamin D in carotid intima-media thickness: a study from South India," *Annals of Indian Academy of Neurology*, vol. 20, no. 3, pp. 242–247, 2017.

[19] D. L. Jones, V. J. Rodriguez, M. L. Alcaide et al., "Subclinical atherosclerosis among young and middle-aged adults using carotid intima-media thickness measurements," *Southern Medical Journal*, vol. 110, no. 11, pp. 733–737, 2017.

[20] J. Alizargar and C. H. Bai, "Factors associated with carotid intima media thickness and carotid plaque score in community-dwelling and non-diabetic individuals," *BMC Cardiovascular Disorders*, vol. 18, no. 1, p. 21, 2018.

[21] B. Z. Leder, "Parathyroid hormone and parathyroid hormone-related protein analogs in osteoporosis therapy," *Current Osteoporosis Reports*, vol. 15, no. 2, pp. 110–119, 2017.

[22] G. A. Block, D. A. Bushinsky, S. Cheng et al., "Effect of etelcalcetide vs cinacalcet on serum parathyroid hormone in patients receiving hemodialysis with secondary hyperparathyroidism: a

Retraction

Retracted: Current Status of Malignant Tumors after Organ Transplantation

BioMed Research International

This article has been retracted by Hindawi following an investigation undertaken by the publisher [1]. This investigation has uncovered evidence of one or more of the following indicators of systematic manipulation of the publication process:

(1) Discrepancies in scope

(2) Discrepancies in the description of the research reported

(3) Discrepancies between the availability of data and the research described

(4) Inappropriate citations

(5) Incoherent, meaningless and/or irrelevant content included in the article

(6) Manipulated or compromised peer review

The presence of these indicators undermines our confidence in the integrity of the article's content and we cannot, therefore, vouch for its reliability. Please note that this notice is intended solely to alert readers that the content of this article is unreliable. We have not investigated whether authors were aware of or involved in the systematic manipulation of the publication process.

Wiley and Hindawi regrets that the usual quality checks did not identify these issues before publication and have since put additional measures in place to safeguard research integrity.

We wish to credit our own Research Integrity and Research Publishing teams and anonymous and named external researchers and research integrity experts for contributing to this investigation.

The corresponding author, as the representative of all authors, has been given the opportunity to register their agreement or disagreement to this retraction. We have kept a record of any response received.

References

[1] B. Shen, Z. Cen, M. Tan et al., "Current Status of Malignant Tumors after Organ Transplantation," *BioMed Research International*, vol. 2022, Article ID 5852451, 12 pages, 2022.

Review Article

Current Status of Malignant Tumors after Organ Transplantation

Bairu Shen [ID], Zhuofei Cen, Minghua Tan, Changshan Song, Xuhui Wu, Jiaqing Wang, and Minqian Huang

Thoracic Surgery, Foshan Clinical Medical School of Guangzhou University of Chinese Medicine, Guangdong Province, China

Correspondence should be addressed to Bairu Shen; bairushen@yeah.net

Objective. To analyze the diagnosis and treatment of patients with concomitant malignant tumors after organ transplantation by compiling data from organ transplantation patients. *Methods*. By searching CNKI and PubMed databases, we made a systematic analysis of the studies of postorgan transplantation complicating malignant tumors in the last decade. *Results*. There were 10 articles on malignant tumors after renal transplantation, 8 articles on liver transplantation, 2 articles on heart transplantation, and 1 article on lung transplantation. The incidence of malignant tumors complicating renal transplantation is 10.4% in Europe, with skin cancer and Kaposi's sarcoma being common; the incidence in the United States is 3.4%, with PTLD having the highest incidence; the incidence of malignant tumors is relatively lowest in Asia, with gastrointestinal malignancies being the main ones. The mean time to complication of malignancy after renal transplantation is 3.83 years. The incidence of concurrent malignancies after liver transplantation is 8.8% in Europe, where skin cancer and Kaposi's sarcoma are common; 5.6% in Asia, where gastrointestinal tract tumors are prevalent; and 4.5% in the United States, where gastrointestinal tract tumors, PTLD, and hematologic diseases are predominant. The mean time to complication of malignancy after liver transplantation is 4.79 years. The incidence of malignancy after heart transplantation is 6.8-10.7%. The incidence of malignancy after lung transplantation is about 10.1%. Minimization of immunosuppression or modification of immunosuppression regimens may be a key component of cancer prevention. mTOR inhibitors and phenolate (MMF) reduce the incidence of de novo malignancies in patients after solid organ transplantation. Surgical treatment improves survival in patients with early malignancies. The use of external beam radiation therapy in the treatment of hepatocellular carcinoma is limited due to the risk of radiation liver disease. *Conclusions*. The risk of concomitant malignancy needs to be guarded for 5 years of immunosuppressive therapy after organ transplantation surgery. Adjusting the immunosuppressive treatment regimen is an effective way to reduce concurrent malignancies. Systemic chemotherapy or radiotherapy requires vigilance against the toxic effects of drug metabolism kinetics on the transplanted organ.

1. Introduction

In recent years, with the advance of surgical technology and the application of immunosuppression, transplantation has merged as the best treatment for end-stage carcinoma of solid organs, which extended graft and patient survival after transplant. However, the morbidity and mortality rates of patients with recurrent malignancies after organ transplantation had increased [1]. Compared with the general population, patients with organ transplant have a higher risk of developing carcinoma by 2.6 times [2]. Over the years, tumors have become an important cause of death among solid organ transplant recipients, and it is foreseen that it would take the first place

of cardiovascular disease in mortality within the next 10 years [3, 4]. Some malignant tumors are caused by the oncogenic viruses leading to the loss of immune control, while others are not related to known infections [5]. The possible occurrence mechanism is that under medicine-induced low immune surveillance, the virus disrupts the differentiation of infected cells by disrupting cell cycle control [6]. Other causes of certain cancers may include chronic immune disorders or inflammation, potential medical conditions, or other factors such as drug toxicity. Immunosuppression has undoubtedly raised the positive outcomes in recipients after organ transplant but also increased the risk of infection. Patients are also relatively less tolerant of cancer treatment. A systematic

literature examination about the morbidity and the treatment of de novo malignancies (DNM) after different solid organ transplantation was described. Worldwide data were collected from related articles in PubMed and CNKI. Data from various experiences were reported and compared to access a clear clinical guideline.

2. Material and Methods

2.1. Search Strategy. A literature review was conducted in March 2021 through PubMed and CNKI databases to find studies pertaining to organ transplantation, malignant tumor, immunosuppression, and chemical therapy threshold. Articles published in languages other than Chinese and English were excluded. The publishing year is between 2011 and 2021. All texts were full text accessible. The keywords are (de novo malignancies after organ transplantation) AND (treatment).

2.2. Inclusion and Exclusion Criteria. Articles published in journals describing the morbidity of the malignant tumor after solid organ transplantation and its treatment were searched. Data from kidney, gastrointestinal, lung, posttransplant lymphoproliferative diseases (PTLD), and other DNM were collected and discussed from systematic reviews, randomized clinical trials, observational studies, and case-control studies. 10-year limits were applied to access the up-to-date treatments in this field. Non-English articles in PubMed and articles with no specific number of patients and the number of patients with tumors were excluded from this review. A total of 10 articles on malignant tumor after kidney transplantation, 8 articles on liver transplantation, 2 articles on heart transplantation, and 1 article on lung transplantation were screened out.

2.3. Research Method. The incidence of malignant tumors after organ transplantation and the types of malignant tumors with the highest incidence were analyzed. The types of tumors susceptible to different regions were analyzed, and the current diagnosis and treatment after various organ transplantation were summarized.

3. Results

3.1. Incidence of Concurrent Malignancies after Kidney Transplantation. Ten articles (Table 1) reported the morbidity of malignant tumors after renal transplantation in seven countries from 1966 to 2016. The incidence of posttransplant carcinoma is shown in Figure 1. Among the seven articles, Tsai et al. [7] from Taiwan, China, have reported the highest morbidity which is up to 18.8%, among which the incidence of urinary system tumor was the highest, reaching 54.3%, followed by the case data reported by Apel et al. [8] from Germany, of which the incidence of tumor was 12.3%, among which the incidence of gastrointestinal tumor was the highest, reaching 18.6%. Fröhlich et al. [9] reported that the incidence of tumor was 10.7% in the study of the UK, and the incidence of renal cancer was the highest among the reported cases, which was 31.8%. The article did not include patients with nonmelanic skin cancer. Mazzucotelli et al. [10] reported that the incidence of malignant tumors in kidney transplant patients in Italy was 10.2%, among which PTLD had the high-

est morbidity which is 34.7%. In the article reported by Zavos et al. [11] from Turkey, the incidence of tumor was 9.7%, and the highest incidence is 49.7% of skin cancer. The Italian data reported by Rossetto et al. [12] have shown the incidence of posttransplant tumor was 9.3%, and the highest morbidity was 28.8%, which is gastrointestinal tumor. Gioco et al. [13] reported that the incidence of tumors from Italy was 7.3%, and the highest incidence of skin cancer was 23.7%. Sampaio et al. [14] from the United States have reported that the incidence of posttransplant tumor was 3.4%, and the morbidity of PTLD was the highest which was 21.3%. Park et al. [15] from South Korea reported that the incidence of tumor was 2.7%, and the incidence of gastrointestinal tumor was the highest which is 34.6%. Wu et al. [16] reported that the incidence of tumor in China was 0.95%, among which the incidence of the urinary system was the highest, reaching 50%.

It can be seen that tumor viruses are prone to invade different organs among kidney transplant patients in different countries and regions and the data from different centers were quite different. Among the data reported by three centers in Italy, the highest morbidity of tumor was, respectively, skin cancer, lymphatic system, and gastrointestinal carcinoma.

Generally speaking, Europe has a higher incidence of skin cancer, which is 23.7%-49.7% in Turkey and Italy. Lymphoid tumors and gastrointestinal tumors have the morbidity of 21.3%-34.6% in North America and South Korea, and 50% of the posttransplant carcinoma in China is urinary tumor. The statistical results in our review are in conformity with domestic literature reports, the incidence of skin cancer and the proportion of which were significantly lower than the European and American countries; this may be related to skin color, the sunshine radiation, and the discrepancy in the demand of immunosuppression [17]. In China, the high risk of urology malignant tumor after renal transplantation may be due to our race, the discrepancy in type, and dosage of immunosuppression. The following reason was that when the transplanted kidney starts to work, the original kidney will not secrete urine or reduce urine secretion, which weakens the flushing effect on the urinary tract and keeps the metabolites in the urinary tract, thus continuously stimulating the urethral epithelial cells and eventually leading to renal tumor [18].

In summary, we have summarized the data on tumors after renal transplantation according to regions. The incidence of tumors after renal transplantation in Europe amounted to 10.4%, with skin cancer and Kaposi's sarcoma, and the highest incidence of gastrointestinal cancers, accounting for 16.2% of all patients with cancer. Only one country in North America has data from the United States, whose tumor incidence rate is 3.4%, with PTLD having the highest incidence rate of 21.3%. Asia has the relatively lowest tumor incidence rate of 2.9%, with the incidence of gastrointestinal tumors reaching 33.2%.

This shows that the prevalence of tumors that tend to complicate kidney transplant patients in different regions is inconsistent, with a higher incidence of skin cancer in Europe, which may be related to differences in skin color, sun exposure to radiation, and the need for immunosuppressive agents [17]. Although the incidence of gastrointestinal tumors is higher in Asia, the reason for this may be related to Asian dietary habits.

TABLE 1: Types of carcinoma in postrenal transplant patients.

Author	Year	Region	Patient in total	DNM	Renal	Gastrointestinal	Other urological cancers	Respiratory cancer	Female reproductive system	PTLD and blood t	Skin and Kaposi	Head and neck	Prostate	Breast	Others	Time of tumor diagnosis (Y)
Fröhlich et al. [9]	1995-2016	UK	1417	154	49	30	24	18	15	14	NA	NA	NA	NA	29	5.8
Park et al. [15]	2007-2015	North Korea	10085	289	58	100	13	36	17	52	45	4	14	30	72	2.9
Gioco [13]	2000-2012	Italy	535	39	5	3	1	6	NA	2	9	NA	1	2	10	3
Mazzucotelli et al. [10]	1997-2012	Italy	735	75	11	7	2	5	NA	26	12	NA	12	7	NA	1.7
Rossetto et al. [12]	1995-2010	Italy	636	59	11	17	4	3	2	NA	3	1	2	3	18	NA
Wu et al. [16]	1989-2010	China	1467	14	3	1	7	1	NA	1	NA	NA	NA	NA	2	3.6
Apel [8]	1966-2005	German	1882	231	22	43	16	14	19	7	NA	NA	5	NA	12	2.8
Tsai et al. [7]	2003-2009	Taiwan, China	186	35	NA	8	19	1	NA	4	1	NA	NA	0	1	NA
Zavos et al. [11]	1983-2013	Turkey	2054	199	5	23	2	14	9	26	99	NA	6	6	9	8
Sampaio et al. [14]	1999-2008	USA	123380	4179	431	540	158	637	93	892	55	NA	446	307	115	2.8

Note: NA: not mentioned; Y: year.
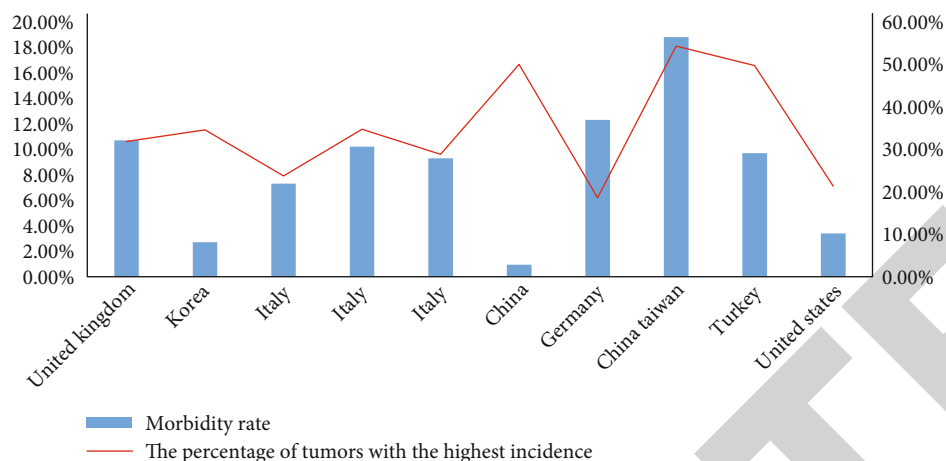
Figure 1: Tumor morbidity of postrenal transplant recipients.

However, in the Korean data by Park et al. [15], it was shown that non-Hodgkin's lymphoma, Kaposi's sarcoma, skin cancer, and leukemia (in men) were higher after transplantation compared to the general population in terms of the standardized incidence of cancer than SIR. This is similar to data from the United States, where the high prevalence of lymphatic system neoplastic disease may be related to a more sensitive lymphatic system to immunosuppression, which may lead to a higher proliferation of EBV.

3.2. Morbidity of Carcinoma of Postliver Transplantation.

It is summarized in Table 2 the data of malignant tumor after liver transplantation in eight centers in 1988-2017 years. The epidemiological data is detailed in Figure 2. We can conclude that the incidence of tumors in France and Germany is relatively high, reaching 16.5%~22.8%, followed by Japan, 11.4%, and the morbidity of tumor in Italy and Korea is 5.6% and 5.5%, respectively. The morbidity of cancer in Saudi Arabia is 3.4%, and the lowest ones are 2.2% and 0.2% reported by two Turkey centers. Specific data is shown in Figure 2. Among the cases in France and Germany, the incidence of skin cancer was the highest, reaching 29.2%~31.2%. In South Korea, the morbidity of gastrointestinal tumors was 46.9%, and the incidence of PTLD in Saudi Arabia was higher than that in Turkey, reaching 62.5%~63.1%. The incidences of gastrointestinal tumors and PTLD are both high in Japan. Youn et al. [19] concluded that colorectal malignancies are dominant in Japanese liver transplant recipients. It was consistent with the results concluded in our review.

In summary, we conclude that the incidence of postliver transplantation tumors is higher in Europe at 8.8%, with skin cancer and Kaposi's sarcoma accounting for 20.9% of all tumors and PTLD and hematologic tumors accounting for 20.7%. The incidence of new tumors in Asia is 5.6%, with a high incidence of gastrointestinal tumors, whose incidence is 44.4%. In North America, we take the United States as an example, where the incidence of tumors after transplantation is 4.5%, with 23.8% of gastrointestinal tract tumors and 23.7% of PTLD and hematologic disorders. This is basically consistent with the data after renal transplantation. In Europe, the incidence of skin cancer is higher, the reason

of which should be related to the geographical area, while the incidence of hematologic malignancies is higher, the reason of which may be related to the use of immunosuppressive drugs. Asia has the highest incidence of gastrointestinal tumors. North America has a higher incidence of PTLD and hematologic disorders, whose only independent risk factor that can be recognized is age, while patients with liver transplantation due to HCV also have a higher risk of developing hematologic tumors [24].

3.3. Morbidity of Carcinoma of Postheart Transplantation.

Youn et al. [19] analyzed 17587 patients in the International Society for Heart and Lung Transplantation (ISHLT) from January 2000 to December 2011. It was concluded that the risk of solid malignancy from the first year to the fifth year after transplantation was 10.7%. The cumulative incidence is as follows: skin cancer (7.0%), nonskin solid cancer (4.0%), and lymphoproliferative diseases (0.9%). In the United States, about 20% of heart transplant recipients will develop skin cancer within 10 years after transplantation. In all types of cancer, the survival rate of patients with new malignant tumors was significantly lower than that of patients without malignant tumors. Meiser et al. [27] reported that seven of 103 patients who received heart transplantation from April 1999 to April 2017 were suffering from malignant tumors, which morbidity is 6.8%. Among all, 3 cases were PTLD, 1 case was squamous cell carcinoma of the skin, 2 cases had colon cancer, and 1 case had bladder cancer.

3.4. Morbidity of Carcinoma of Postheart Transplantation.

There are few articles related to lung transplantation, and only one of which meets our screening conditions was selected whose title is "De Novo Malignancy after Lung Transplantation in Japan" [28]. It summarizes 179 lung transplantation operations performed in 7 institutions in Japan from 2001 to 2010, of which 18 recipients (10.1%) developed new malignancies. The higher incidence of malignancies was lymphoproliferative malignancies (12 cases, 1 of which were double neoplastic cancer after tongue cancer), followed by cervical cancer (4 cases), breast cancer (2 cases), and tongue cancer (1 case).

TABLE 2: Types of carcinoma in postliver transplant patients.

Author	Year	Region	Patients in total	DNM	Renal	Gastrointestinal	Other urological cancers	Respiratory cancer	Female reproductive system	PTLD and blood t	Skin and Kaposi	Head and neck	Prostate	Breast	Others	Time of tumor diagnosis (Y)
Egeli et al. [20]	1998-2016	Turkey	429	9	NA	NA	NA	5	NA	NA	1	2	NA	NA	1	5.3
Park et al. [15]	2007-2015	South Korea	3822	213	4	100	2	13	7	35	11	6	NA	9	26	1.9/3.0^c
Hegab et al. [21]	2001-2010	Saudi Arabia	238	8	NA	NA	1	NA	1	5	1	NA	NA	NA	NA	3.6
Ettorre et al. [22]	1990-2008	Italy	1675	98	NA	18	6	25	NA	22	6	19	NA	3	7	3.2
Carenco et al. [23]	1991-2008	France	465	106	NA	15	8^a	15	NA	13	31	17	8*	4	3	6.3 ± 4.3^d
Rademacher et al. [24]	1988-2006	German	1616	266	19*	51	19^b	59	11	NA	83	NA	9	19	15	8.1^e
Sanaei et al. [25]	1992-2012	Turkey	1700	38	NA	6	NA	NA	NA	24	3	NA	NA	NA	5	5.6
Mizuno et al. [26]	2002-2017	Japan	97	11	NA	3	1	1	NA	4	1	1	NA	NA	NA	8.3
Sampaio et al. [14]	1999-2008	USA	43106	1923	37	457	277	386	26	456	12	45	155	85	7	2.6

a: including both prostate and urogenital tumors; b: including both renal and urogenital tumors; c: 1.9 years for hematopoietic cancer; 3 years for patients with nonhematopoietic cancers; d: for solid organ cancers; e: 8.1 for solid organ tumors; NA: not mentioned; Y: year.
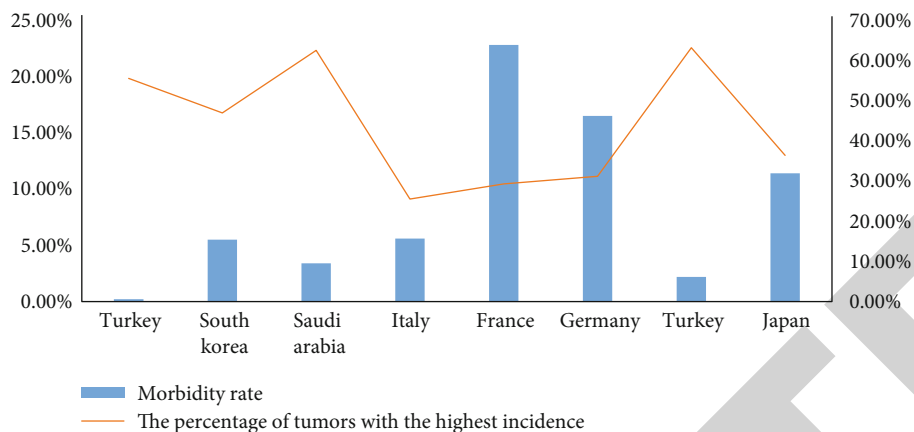
Figure 2: Tumor morbidity of postliver transplant recipients.

3.5. Immunosuppressive Therapy Analysis. The use of immunosuppression has always been heated discussed in patients after organ transplantation. Rousseau et al. [29] stated that no matter what immunosuppression regimen is adopted, post-transplant patients can benefit from the best tumor treatment, reducing the risk of death by 55%, which is acceptably safe. The article on head and neck cancer after liver transplantation reported by Graham et al. [30] also points out that induced immunosuppression does not increase the risk of carcinoma. However, in the article on concurrent tumors after liver transplantation, it is generally agreed that the minimization of calcineurin inhibitor (CNI) and the use of mTOR inhibitors can reduce the probability of recurrence or de novo tumors of hepatocellular carcinoma [31, 32].

After organ transplantation, patients will generally undergo a standardized three-drug immunosuppression regimen. In the cases of urinary system diseases reported by Karczewski et al. [33], three immunosuppressive methods were selected: tacrolimus+mycophenolate mofetil+prednisolone, cyclosporin+imidazolium thiopurine+prednisolone, and cyclosporin+mycophenolate mofetil+prednisolone.

CNI is a common immunosuppressant for immunosuppression after liver transplantation. Tacrolimus (TAC) is commonly used compared with cyclosporine because it reduces the rate of acute rejection and improves the survival of both grafts and patients [34]. However, CNI has the risk of carcinogenesis, which may be related to its mechanism of inhibiting DNA repair and apoptosis. Studies have shown that cyclosporine can accelerate tumor progression through its direct effect on cells, which especially may increase the incidence of skin cancer after transplantation [35]. It has also been reported that tacrolimus may increase the incidence of tumors in vivo after transplantation [36]. While there is still a critical controversy about the side effects of CNIs, there are increasing scholars stating not using CNI immunosuppressants. Meiser et al. [27] reported that it is possible to take no CNI immunosuppressants after heart transplantation. On the one hand, it is conducive to the survival of patients, inhibits malignant tumors, protects renal function, and resists cytomegalovirus infection and vascular diseases. On the other hand, while no CNI immunosuppression after heart transplantation (HTx) has a poor effect in preventing acute rejection, the side effects

are low. In the preliminary study of malignant tumors after renal transplantation, it is also proposed that the combined blocking of belatacept and mTOR inhibitors can achieve the same therapeutic effect as the standard treatment without CNI inhibitors and steroids after renal transplantation [37]. However, in Guethoff et al.'s report [38], it is pointed out that the reduction of CNIs does not lead to superior long-term renal function. Minimization or modification of immunosuppression may be a key component of cancer prevention, because the effect of immunosuppression on carcinogenesis seems to be dose-dependent. However, the risk of rejection and the benefits of cancer prevention need to be carefully weighed. In liver transplantation, the minimization of CNIs and the use of mTOR are associated with a significant reduction in the recurrence rate of hepatocellular carcinoma [39, 40]. There is no clear regulation on the amount of immunosuppressant. In Zhanwen's report on tumor after kidney transplantation [41], it is mentioned to reduce the dose of immunosuppressant to 1/2~2/3 of the original dose, and in Hao's study [42], it is mentioned to reduce the dose of immunosuppressant to 1/4~1/2.

3.6. Antitumor Therapy Analysis. The mammalian target of rapamycin is a serine/threonine kinase involved in cell growth, proliferation, metabolism, and angiogenesis. The mTOR pathway is upregulated in many malignant tumors, so mTOR inhibition may have chemopreventive function [43]. In the liver transplant population, a retrospective study of patients with alcoholic cirrhosis liver transplant determined that conversion to everolimus-based immunosuppression can reduce the risk of noncutaneous neomalignant tumors [44]. Rapamycin has also a good therapeutic effect on Kaposi's sarcoma [45]. In the case of Kaposi's sarcoma reported by Roy et al. [46], it is pointed out that mTOR inhibition is considered to be effective in the treatment of Kaposi's sarcoma because it inhibits angiogenesis by reducing the secretion of vascular endothelial growth factor and inhibiting the formation of tumor blood vessels.

Sirolimus and everolimus are mammalian target inhibitors of rapamycin (mTOR), which have potential antiproliferative properties and are considered to inhibit tumor growth. However, the article on their antitumor effects is not systematic [47]. More and more evidence has shown that with the introduction of mTOR inhibitors, patients with gradually reduced

CNI have a lower incidence of tumor diseases than subjects treated with standard dose CNI [48]. In addition, the introduction of mTOR inhibitors can reduce the risk of death in patients with de novo malignancies by 76% [30]. In addition, early use of everolimus can improve renal function which is a feasible choice for renal insufficiency after liver transplantation [49, 50].

Mycophenolate mofetil (MMF) is an antibiotic. As an antitumor drug for leukemia, lymphoma, and various solid tumors, it has an impact on tumor adhesion, angiogenesis, and EBV-infected cells, which reduce the incidence of new malignant tumors and long cancer-free survival after solid organ transplantation [51, 52]. MMF is commonly used along with TAC and steroids [53].

Anti-CTLA-4 and anti-PD1/PDL1 therapy can be used to treat recurrent or refractory classical Hodgkin lymphoma, metastatic melanoma, and other tumors by mobilizing the function of the autoimmune system and fighting against cancer cells [54, 55], bringing hope to patients with advanced tumors. However, in the vast majority of immunotherapy clinical trials, patients with organ transplantation complicating malignancies have not been studied because they may increase the risk of transplant organ rejection [56]. PD-1 and CTLA-4 channels are important processes in immune tolerance of transplanted organs, and alterations in these channels may lead to rejection of the transplanted organ by the recipient. The incidence of irAEs with anti-PD-1 drugs is much smaller than with anti-CTLA-4, so it has been hypothesized that anti-PD-1 drugs would be safer to use in organ transplant recipients, but this clearly does not correspond to our real-world data [57]. Blockade of the PD-1 pathway may lead to increased organ transplant rejection compared to CTLA-4 blockade, and the PD-1 pathway plays a more dominant role in allograft immune tolerance than the CTLA-4 pathway. [58]. Blazar et al. found that anti-PD-1 antibodies have a higher risk of causing graft-versus-host disease than anti-CTLA-4 and that the combination leads to more severe graft-versus-host disease [59]. None of the patients who develop graft rejection can be salvaged by immunosuppression [58], and the graft loss rate is as high as 80% [56]. However, some patients have responded or stabilized after immunotherapy [56]. Most scholars believe that there is no direct correlation between the risk of graft rejection and the time after organ transplantation [56], and we have not found that patients with long-term transplants are not prone to rejection when receiving immunotherapy [57]. However, people may be more reluctant to introduce immune checkpoint inhibitor therapy in the initial posttransplant period [60]. The rejection rate of allografts is relatively high in the early stages of the use of immunotherapy and is often accompanied by a high mortality rate [57].

Targeted therapy in driver gene-positive malignancies, particularly in patients with non-small-cell lung cancer, is currently an effective treatment modality and has shown relatively good therapeutic effects in nonorgan transplant patients. However, data on targeted therapy for organ transplantation-complicated malignancies are less available and are dominated by scattered case reports. De Pas et al. found that the use of cyclosporine was not a contraindication to treatment with erlotinib, with no associated toxicity [61]. Hecimovic et al. reported the treatment of a patient with non-small-cell lung cancer (EGFRL585R+) complicated by heart transplantation, who was treated with cyclosporine combined with erlotinib resulted in a very good treatment of the malignancy with no significant toxic side effects or rejection of the transplanted organ [62]. However, close monitoring of drug concentrations in the blood is necessary.

3.7. Surgical Treatment. After kidney transplantation, surgery will be the main treatment, before the cancer has spread. Radical tumor resection can reduce the recurrence of cancer and improve the survival rate of patients. Among the cases of urinary diseases reported by McAlister et al. [34], 13 patients with renal cancer chose nephrectomy, of which 12 survived and 1 died. Cornelis et al. [63] reported that subcutaneous radiofrequency ablation is effective for renal cell carcinoma less than 4 cm. The article reported by Kluijfhout et al. [64] pointed out that the treatment of thyroid cancer after solid organ transplantation should be similar to that of thyroid cancer patients in the general population.

Cheung et al. [65] reported the diagnosis and treatment of hepatocellular carcinoma after renal transplantation. All 15 asymptomatic patients received treatment, including 8 cases of hepatectomy, 2 cases of transcatheter arterial chemical embolization (TACE), 2 cases of radiofrequency ablation (RFA), 1 case of percutaneous ethanol injection (PEI), 1 case of operation+TACE, and 1 case of RFA+TACE. Nine of them survived, but one developed renal rejection. On the other hand, none of the 3 patients diagnosed by symptoms underwent surgery. One of them received selective internal radiation (SIT) and died 16 months later. The other 2 cases received symptomatic treatment and died only 1 month and 5 months after diagnosis. Therefore, surgical treatment can improve the survival rate of patients to a certain extent, but it is also related to the patient's physical state and tumor.

The same as patients with malignant tumors after renal transplantation, patients with new malignant tumors after liver transplantation can undergo surgical treatment, remove the cancerous area to prevent the spread of cancer cells, and perform lymph node dissection. Gastrointestinal tumors are common in Asia. Shimizu et al. [66] reported that gastric cancer was discovered 30 months after living donor liver transplantation. The patient underwent segmented gastrectomy and lymph node dissection. The histopathological examination of the resected stomach was pT2N1M0, phase II. Tacrolimus was stopped on the day of operation and recovered one day later. The patient did not receive chemotherapy after operation. He is still alive after more than four years. In the case of gastric cancer after liver transplantation for liver cancer reported by Yang et al. [67], the patient was successfully treated by radical distal gastrectomy and D2 lymph node dissection and was diagnosed as stage IIIC gastric adenocarcinoma (pT4aN3bM0) by pathological examination. The patient recovered cyclosporine and mycophenolate mofetil on the first day after operation and refused to accept postoperative adjuvant chemotherapy. Peritoneal and paraaortic lymph nodes were discovered recurrence 12 months after operation and died due to tumor progression 3 months later. This suggests that we should monitor the occurrence of gastrointestinal tumors after liver

transplantation and intervene early to obtain a higher survival rate. Chemotherapy should also be used as adjuvant treatment when necessary.

Due to the risk of radioactive liver disease, the application of external beam radiotherapy in the treatment of hepatocellular carcinoma is limited. Other treatment options for advanced liver cancer include systemic chemotherapy, chemoembolization, radiofrequency ablation, percutaneous ethanol injection, and radioembolization. Radioembolization with 90Y glass microspheres is particularly useful for patients with advanced HCC who are not suitable for resection [68].

3.8. Adjuvant Therapy. The selection of postoperative adjuvant therapy is related to the type of new tumor, the degree of malignancy, and the location of transplanted organs. Systemic chemotherapy or radiotherapy is usually limited to advanced cases and recurrent diseases [69].

The standard treatment of head and neck squamous cell carcinoma (HNSCC) includes initial surgery in the early stage of the tumor, followed by adjuvant radiotherapy (RT)/chemoradiotherapy (CRT) or initial CRT alone in patients with advanced HNSCC [26]. However, considering the results of this high-risk patient population, there is no evidence-based recommendation for the optimal treatment of patients with new HNSCC after liver transplantation.

Prostate cancer after renal transplantation is the second common malignant tumor of the urinary system. The treatment methods are radical prostatectomy, external beam radiotherapy, and androgen deprivation. The choice of treatment was based on age, comorbidity, and Gleason score. Patients undergoing surgery were younger. Patients receiving radiotherapy, with a total dose of 76 Gy, irradiated the prostate and excluded the upper pelvic area to protect the graft from potential radiation injury. Patients receiving androgen deprivation therapy died of causes unrelated to cancer several months later [70].

The treatment of PTLD after transplantation depends on its subtype. Early type and polymorphic PTLD usually respond to reduced immunosuppression and rituximab monotherapy, while monomorphic PTLD usually requires additional concurrent or sequential chemotherapy. For rare subtypes of PTLD, standard of care guidelines for neonatal lymphoma are recommended. According to the degree of disease, surgical resection or radiotherapy can be used as adjuvant treatment. Nonchemotherapy such as adoptive T cell therapy has shown promising efficacy and must be further studied [71].

Although the site of concurrent malignancy is usually not in the same area as the transplanted organ, the outlining of the radiotherapy target area is still an important step in precision radiotherapy; however, there are not many studies reported empirically on the adjustment of radiation dose.

3.9. Palliative Care. In the cases of de novo esophageal tumors after liver transplantation reported by Presser et al. [68], the corresponding treatment plan was formulated according to the patient's physical condition. A total of 5 patients (50%) received conservative treatment. The definite radiotherapy and chemotherapy included 60 Gy irradiation and cisplatin-based chemotherapy. If the esophagus is so narrow that the patient cannot eat, the patient can repeatedly receive palliative expansion or laser coagulation. The other 5 patients were generally in good condition and underwent radical lymph node dissection to achieve the purpose of treatment.

In addition, transcatheter arterial chemoembolization has also been widely used in palliative treatment of patients with large tumors, but its survival benefit is uncertain [72].

4. Discussion

Cancer, recurrence of primary diseases, cardiovascular disease, and infection are the four most common causes of long-term death after transplantation [73]. The tumors of liver transplant recipients can be divided into four types: (1) donor transmission cancer (DTC), that is, it exists in allografts at the time of transplantation; (2) donor-derived carcinoma (DDC), which develops in donor cells after transplantation; (3) new cancer, as a long-term result of transplantation, develops from recipient cells; (4) recurrent cancer refers to the recurrence of cancer treated before transplantation and after transplantation [74].

The development of cancer is a multifactorial process. The effective immune system recognizes and attempts to eliminate primary tumors via cytotoxic T lymphocytes, macrophages, and natural killer cells, which can recognize tumor cells as nonself cells (so-called immune surveillance), delay tumor progression, and prevent angiogenesis, vascular infiltration, and metastasis [75]. The immune system can also control virus infection with carcinogenic ability, but in transplant recipients, immunosuppressive drugs destroy immune function by promoting cell transformation and escaping immune recognition and directly affect the site of tumor formation [76]. The transmission of malignant tumors by donors, long-term exposure to risk factors or potential carcinogens, the growth of age, smoking, and drinking may be the inducing factors of tumors [77]. According to single factor analysis reported by Desai and Neuberger [74], age, gender, Caucasian, past malignancies, multiple organ transplantation, alcoholic liver disease, primary sclerosing cholangitis, and nonalcoholic steatohepatitis were associated with primary diseases, obesity, diabetes, age of donors, and use of mTOR inhibitors during transplantation. Donor factors (age, gender, race, and obesity) and recipient creatinine are not risk factors for malignant tumors after liver transplantation. Some studies have also shown that the survival rate after concurrent tumors is related to gender. Women could better survive after being diagnosed with malignant tumors, which is not suitable for patients with skin cancer or lymphoma [78]. The author believes that the cause of posttransplant malignant tumor is the use of immunosuppressants, which leads to systematic immunosuppression and the recipients are more vulnerable to pathogen invasion. In the meantime, the human body can not produce enough antibodies to resist the invasion of antigen, so that the cancer cells is possible to proliferate continuously. Another reason is that the body is in the state of immunosuppression for long so that the original normal flora in the body becomes pathogenic bacteria leading to carcinoma.

According to the morbidity of malignant tumor after organ transplantation, the data of different countries and

centers are different. According to the data screened in this review, the incidence of malignant tumors after organ transplantation is 0.2%~22.8%. According to the results of our review, the morbidity of malignancies after liver transplantation is relatively high. The author believes that the reasons for the high risk of tumors after liver transplantation may be related to the spread of malignant tumors by donors and the unhealthy habits like smoking and drinking by recipients. Patients who have to undergo liver transplantation usually have the habit of smoking and drinking or carry hepatitis virus, coupled with bad living habits, which are easy to induce cancer. The morbidity of skin cancer in European countries is relatively high after operation, which may be related to skin color, sunshine radiation, and immunosuppressive agents. The incidence rate of gastrointestinal cancer is higher in Korean and Japanese patients. In China, the incidence rate of urologic tumor is high, and the mechanism may be related to, which is Chinese patent medicine containing aristolochic acid [79].

The treatment of malignant tumors is generally based on surgery. Radical cancer resection can remove tumors, reduce tumor metastasis, and prolong the survival of patients. However, the patient is usually so late to found when the tumor was usually advanced and metastasized, that operation could not be performed. Patients who have no tumor metastasis and are suitable for surgery can be treated surgically [37]. The effect of the surgery is related to the type, size, and stage of the tumor; physical conditions such as there are other concurrent diseases and whether to choose the chemotherapy may also infect the survival of the patient, but there are few relevant articles. The specific treatment methods should be selected by clinicians according to the patient's condition.

The choice of postoperative adjuvant therapy should be based on the patient's age, the degree of malignancy of the tumor. For patients after organ transplantation, we had better monitor the tumor regularly, intervene in the early stage, and give adjuvant radiotherapy and chemotherapy when physical conditions permit.

A study on different forms of diagnosis and treatment of esophageal cancer patients without organ transplantation showed that patients who underwent surgical resection after neoadjuvant radiotherapy and chemotherapy had a higher survival rate than those who received radiotherapy and chemotherapy alone. The five-year survival rate of patients with radiotherapy and chemotherapy or radiotherapy alone is only 6~27%, but the five-year survival rate of patients with surgical resection after radiotherapy and chemotherapy can reach 17~49% [68].

Tacrolimus is the most common choice of immunosuppressants, and standard immune triple therapy is wildly used in clinic. However, because tacrolimus has the risk of causing cancer, it is now clinically recommended to minimize CNI or replace CNI with mTOR inhibitors, which plays the role of chemical prevention and protect renal function. Rapamycin also has a good effect on Kaposi's sarcoma. Therefore, clinicians need to decide the medication according to the specific situation of patients.

According to the current diagnosis and treatment, patients with tumors after organ transplantation should continue to take immunosuppressants. CNI can be minimized or mTOR inhibitors can be used to replace CNI. The choice of postoperative adjuvant therapy should be based on the type and spread of cancer and personal physical conditions. When the tumor is relatively limited, radiotherapy can be selected, and its side effects are relatively small. When the tumor diffusion degree is relatively high, chemotherapy should be selected to inhibit cancer cells in the whole body.

In a word, there is no clear standard in the diagnosis and treatment of this kind of patient with malignant tumors after organ transplantation. The current diagnosis and treatment method is to maintain immunosuppression and add adjuvant treatment such as surgery or radiotherapy and chemotherapy. However, there is no in-depth study on the effect of antitumor drugs on transplanted organs. The existing research results can provide limited guidance for clinical practice, and we look forward to more optimized and clear treatment strategies which bring more benefits to patients with malignant tumors after organ transplantation.

We have compiled and analyzed the development and treatment of malignancies complicating organ transplantation and summarized the treatment recommendations based on the available studies. Due to the small number of organ transplantation cases and the lack of research and data on antitumor treatment options, there are limitations in our analysis, such as the lack of research data on targeted therapy and immunotherapy, which prevents us from giving treatment recommendations for such patients. However, as the number of organ transplantation cases continues to increase, research data in this area will continue to increase and we will need to keep an eye on the treatment of this patient population.

Data Availability

The datasets used and/or analyzed during the current study are available from the corresponding author on reasonable request.

Conflicts of Interest

The authors declare that the research was conducted in the absence of any commercial or financial relationships that could be construed as a potential conflict of interest.

Acknowledgments

References

[1] A. Rana, A. Gruessner, V. G. Agopian et al., "Survival benefit of solid-organ transplant in the United States," *JAMA Surgery*, vol. 150, no. 3, pp. 252–259, 2015.

[2] A. Guillemin, B. Rousseau, C. Neuzillet et al., "Cancers solides après transplantation d'organe : épidémiologie, pronostic et

spécificités de prise en charge," *Bulletin du Cancer*, vol. 104, no. 3, pp. 245–257, 2017.

[3] S. A. Acuna, K. A. Fernandes, C. Daly et al., "Cancer mortality among recipients of solid-organ transplantation in Ontario, Canada," *JAMA Oncology*, vol. 2, no. 4, pp. 463–469, 2016.

[4] R. Na, A. E. Grulich, N. S. Meagher, G. W. McCaughan, A. M. Keogh, and C. M. Vajdic, "De novo cancer-related death in Australian liver and cardiothoracic transplant recipients," *American Journal of Transplantation*, vol. 13, no. 5, pp. 1296–1304, 2013.

[5] M. Guba, C. Graeb, K. W. Jauch, and E. K. Geissler, "Pro- and anti-cancer effects of immunosuppressive agents used in organ transplantation," *Transplantation*, vol. 77, no. 12, pp. 1777–1782, 2004.

[6] E. A. Engels, R. M. Pfeiffer, J. F. Fraumeni Jr. et al., "Spectrum of cancer risk among US solid organ transplant recipients," *JAMA*, vol. 306, no. 17, pp. 1891–1901, 2011.

[7] H. L. Tsai, J. W. Chang, T. H. Wu et al., "Outcomes of kidney transplant tourism and risk factors for de novo urothelial carcinoma," *Transplantation*, vol. 98, no. 1, pp. 79–87, 2014.

[8] H. Apel, K. Walschburger-Zorn, L. Häberle, S. Wach, D. G. Engehausen, and B. Wullich, "De novo malignancies in renal transplant recipients: experience at a single center with 1882 transplant patients over 39 yr," *Clinical Transplantation*, vol. 27, no. 1, pp. E30–E36, 2013.

[9] F. A. Fröhlich, F. Halleck, L. Lehner et al., "De-novo malignancies after kidney transplantation: a long-term observational study," *PLoS One*, vol. 15, no. 11, article e0242805, 2020.

[10] V. Mazzucotelli, P. Piselli, D. Verdirosi et al., "De novo cancer in patients on dialysis and after renal transplantation: north-western Italy, 1997–2012," *Journal of Nephrology*, vol. 30, no. 6, pp. 851–857, 2017.

[11] G. Zavos, D. Moris, I. D. Kostakis et al., "De novo visceral malignancies in renal transplant recipients: a single center experience of 2054 recipients for more than 30 years," *Experimental and Clinical Transplantation*, vol. 13, no. 4, pp. 313–318, 2015.

[12] A. Rossetto, P. Tulissi, F. De Marchi et al., "De Novo Solid Tumors After Kidney Transplantation: Is It Time for a Patient- Tailored Risk Assessment? Experience From a Single Center," *Transplantation Proceedings*, vol. 47, no. 7, pp. 2116–2120, 2015.

[13] R. Gioco, D. Corona, A. Agodi et al., "De novo cancer incidence and prognosis after kidney transplantation: a single center analysis," *Transplantation Proceedings*, vol. 51, no. 9, pp. 2927–2930, 2019.

[14] M. S. Sampaio, Y. W. Cho, Y. Qazi, S. Bunnapradist, I. V. Hutchinson, and T. Shah, "Posttransplant malignancies in solid organ adult recipients," *Transplantation*, vol. 94, no. 10, pp. 990–998, 2012.

[15] B. Park, J. Yoon, D. Choi et al., "De novo cancer incidence after kidney and liver transplantation: results from a nationwide population based data," *Scientific Reports*, vol. 9, no. 1, p. 17202, 2019.

[16] B. Wu, K. Wang, C. B. Mo, and Z. Y. Shen, "De novo malignancies in renal transplant recipients: experience at a single center in China," *International Journal of Clinical and Experimental Medicine*, vol. 8, no. 2, pp. 2911–2916, 2015.

[17] C. Wang, T. Li, J. Zhang et al., "Trend analysis of malignant tumors after renal transplantation in China," *Organ Transplantation*, vol. 6, no. 3, pp. 169–173, 2015.

[18] C. H. Liao, S. C. Chueh, M. K. Lai, and J. Chen, "Transitional cell carcinoma in renal transplant recipients," *Transplantation Proceedings*, vol. 36, no. 7, pp. 2152-2153, 2004.

[19] J. C. Youn, J. Stehlik, A. R. Wilk et al., "Temporal trends of de novo malignancy development after heart transplantation," *Journal of the American College of Cardiology*, vol. 71, no. 1, pp. 40–49, 2018.

[20] T. Egeli, T. Unek, M. Ozbilgin et al., "De novo malignancies after liver transplantation: a single institution experience," *Experimental and Clinical Transplantation*, vol. 17, no. 1, pp. 74–78, 2019.

[21] B. Hegab, H. Khalaf, N. Allam et al., "De novo malignancies after liver transplantation: a single-center experience," *Annals of Saudi Medicine*, vol. 32, no. 4, pp. 355–358, 2012.

[22] G. M. Ettorre, P. Piselli, L. Galatioto et al., "De novo malignancies following liver transplantation: results from a multicentric study in central and southern Italy, 1990–2008," *Transplantation Proceedings*, vol. 45, no. 7, pp. 2729–2732, 2013.

[23] C. Carenco, S. Faure, A. Herrero et al., "Incidence of solid organ cancers after liver transplantation: comparison with regional cancer incidence rates and risk factors," *Liver International*, vol. 35, no. 6, pp. 1748–1755, 2015.

[24] S. Rademacher, D. Seehofer, D. Eurich et al., "The 28-year incidence of de novo malignancies after liver transplantation: a single-center analysis of risk factors and mortality in 1616 patients," *Liver Transplantation*, vol. 23, no. 11, pp. 1404–1414, 2017.

[25] A. K. Sanaei, M. Aliakbarian, K. Kazemi et al., "De novo malignancy after liver transplant," *Experimental and Clinical Transplantation*, vol. 13, no. 2, pp. 163–166, 2015.

[26] S. Mizuno, A. Hayasaki, T. Ito et al., "De novo malignancy following adult-to-adult living donor liver transplantation focusing on posttransplantation lymphoproliferative disorder," *Transplantation Proceedings*, vol. 50, no. 9, pp. 2699–2704, 2018.

[27] B. Meiser, S. Buchholz, and I. Kaczmarek, "De-novo calcineurin-inhibitor-free immunosuppression with sirolimus and mycophenolate mofetil after heart transplantation," *Current Opinion in Organ Transplantation*, vol. 16, no. 5, pp. 522–528, 2011.

[28] T. Miyazaki, T. Oto, M. Okumura et al., "De novo malignancy after lung transplantation in Japan," *General Thoracic and Cardiovascular Surgery*, vol. 64, no. 9, pp. 543–548, 2016.

[29] B. Rousseau, A. Guillemin, C. Duvoux et al., "Optimal oncologic management and mTOR inhibitor introduction are safe and improve survival in kidney and liver allograft recipients withde novocarcinoma," *International Journal of Cancer*, vol. 144, no. 4, pp. 886–896, 2019.

[30] R. C. Graham, J. S. Mella, and R. S. Mangus, "De novo head and neck cancer after liver transplant with antibody-based immunosuppression induction," *Transplantation Proceedings*, vol. 50, no. 10, pp. 3661–3666, 2018.

[31] M. Rodríguez-Perálvarez, M. De la Mata, and A. K. Burroughs, "Liver transplantation," *Current Opinion in Organ Transplantation*, vol. 19, no. 3, pp. 253–260, 2014.

[32] F. Nogueras López, M. D. Espinosa Aguilar, P. Abellán Alfocea et al., "Descriptive analysis of everolimus conversion in liver transplant recipients with malignant neoplastic disease," *Transplantation Proceedings*, vol. 52, no. 2, pp. 553–555, 2020.

[33] M. Karczewski, W. Czapiewski, and J. Karczewski, "Urologic de novo malignancies after kidney transplantation: a single

center experience," *Transplantation Proceedings*, vol. 44, no. 5, pp. 1293–1297, 2012.

[34] V. C. McAlister, E. Haddad, E. Renouf, R. A. Malthaner, M. S. Kjaer, and L. L. Gluud, "Cyclosporin versus tacrolimus as primary immunosuppressant after liver transplantation: a meta-analysis," *American Journal of Transplantation*, vol. 6, no. 7, pp. 1578–1585, 2006.

[35] M. Hojo, T. Morimoto, M. Maluccio et al., "Cyclosporine induces cancer progression by a cell-autonomous mechanism," *Nature*, vol. 397, no. 6719, pp. 530–534, 1999.

[36] S. Benlloch, M. Berenguer, M. Prieto et al., "De novo internal neoplasms after liver transplantation: increased risk and aggressive behavior in recent Years?," *American Journal of Transplantation*, vol. 4, no. 4, pp. 596–604, 2004.

[37] C. Hui and Z. Wenyi, "Paying attention to the occurrence and treatment of gastrointestinal tumors after organ transplantation," *Surgical Theory and Practice*, vol. 1, pp. 15–17, 2008.

[38] S. Guethoff, K. Stroeh, C. Grininger et al., "De novo sirolimus with low-dose tacrolimus versus full-dose tacrolimus with mycophenolate mofetil after heart transplantation–8-year results," *The Journal of Heart and Lung Transplantation*, vol. 34, no. 5, pp. 634–642, 2015.

[39] H. Holdaas, P. De Simone, and A. Zuckermann, "Everolimus and malignancy after solid organ transplantation: a clinical update," *Journal of Transplantation*, vol. 2016, 4369511 pages, 2016.

[40] C. Duvoux and C. Toso, "mTOR inhibitor therapy: does it prevent HCC recurrence after liver transplantation?," *Transplantation Reviews*, vol. 29, no. 3, pp. 168–174, 2015.

[41] D. Zhanwen, *Diagnosis and Treatment of New Malignant Tumors after Renal Transplantation*, Shandong University, China, 2018.

[42] H. Xiaojun, "Meta analysis of the incidence of cancer treated with rapamycin after male renal transplantation," *Chinese Drugs and Clinic*, vol. 17, no. 1, pp. 122–124, 2017.

[43] M. Bhat and K. D. Watt, "Mammalian target of rapamycin inhibition after solid organ transplantation:canit, anddoesit, reduce cancer risk?," *Clinical Transplantation*, vol. 29, no. 7, pp. 654–663, 2015.

[44] E. Thimonier, O. Guillaud, T. Walter et al., "Conversion to everolimus dramatically improves the prognosis of de novo malignancies after liver transplantation for alcoholic liver disease," *Clinical Transplantation*, vol. 28, no. 12, pp. 1339–1348, 2014.

[45] G. Stallone, A. Schena, B. Infante et al., "Sirolimus for Kaposi's sarcoma in renal-transplant recipients," *The New England Journal of Medicine*, vol. 352, no. 13, pp. 1317–1323, 2005.

[46] D. Roy, S. H. Sin, A. Lucas et al., "mTOR inhibitors block Kaposi sarcoma growth by inhibiting essential autocrine growth factors and tumor angiogenesis," *Cancer Research*, vol. 73, no. 7, pp. 2235–2246, 2013.

[47] A. A. Pillai, "Management of de novo malignancies after liver transplantation," *Transplantation Reviews (Orlando, Fla.)*, vol. 29, no. 1, pp. 38–41, 2015.

[48] T. Mathew, H. Kreis, and P. Friend, "Two-year incidence of malignancy in sirolimus-treated renal transplant recipients: results from five multicenter studies∗," *Clinical Transplantation*, vol. 18, no. 4, pp. 446–449, 2004.

[49] C. Alegre, C. Jiménez, A. Manrique et al., "Everolimus monotherapy or combined therapy in liver transplantation: indications and results," *Transplantation Proceedings*, vol. 45, no. 5, pp. 1971–1974, 2013.

[50] I. Bilbao, M. Salcedo, M. A. Gómez et al., "Renal function improvement in liver transplant recipients after early everolimus conversion: a clinical practice cohort study in Spain," *Liver Transplantation*, vol. 21, no. 8, pp. 1056–1065, 2015.

[51] R. J. Tressler, L. J. Garvin, and D. L. Slate, "Anti-tumor activity of mycophenolate mofetil against human and mouse tumors in vivo," *International Journal of Cancer*, vol. 57, no. 4, pp. 568–573, 1994.

[52] K. Leckel, W. D. Beecken, D. Jonas et al., "The immunosuppressive drug mycophenolate mofetil impairs the adhesion capacity of gastrointestinal tumour cells," *Clinical and Experimental Immunology*, vol. 134, no. 2, pp. 238–245, 2003.

[53] R. H. Wiesner and J. J. Fung, "Present state of immunosuppressive therapy in liver transplant recipients," *Liver Transplantation*, vol. 17, Suppl 3, pp. S1–S9, 2011.

[54] J. K. Winkler, R. Gutzmer, C. Bender et al., "Safe administration of an anti-PD-1 antibody to kidney-transplant patients: 2 clinical cases and review of the literature," *Journal of Immunotherapy*, vol. 40, no. 9, pp. 341–344, 2017.

[55] S. Vardhana, K. Cicero, M. J. Velez, and C. H. Moskowitz, "Strategies for recognizing and managing immune-mediated adverse events in the treatment of Hodgkin lymphoma with checkpoint inhibitors," *The Oncologist*, vol. 24, no. 1, pp. 86–95, 2019.

[56] S. Saberianfar, L. S. Nguyen, A. Manouchehri et al., "Solid organ transplant rejection associated with immune-checkpoint inhibitors," *Annals of Oncology*, vol. 31, no. 4, pp. 543-544, 2020.

[57] N. Abdel-Wahab, H. Safa, A. Abudayyeh et al., "Checkpoint inhibitor therapy for cancer in solid organ transplantation recipients: an institutional experience and a systematic review of the literature," *Immunother Cancer*, vol. 7, no. 1, p. 106, 2019.

[58] A. S. Kittai, H. Oldham, J. Cetnar, and M. Taylor, "Immune checkpoint inhibitors in organ transplant patients," *Immunotherapy*, vol. 40, no. 7, pp. 277–281, 2017.

[59] B. R. Blazar, B. M. Carreno, A. Panoskaltsis-Mortari et al., "Blockade of programmed death-1 engagement accelerates graft-versus-host disease lethality by an IFN-γ-dependent mechanism," *The Journal of Immunology*, vol. 171, no. 3, pp. 1272–1277, 2003.

[60] T. M. Smedman, P.-D. Line, T. K. Guren, and S. Dueland, "Graft rejection after immune checkpoint inhibitor therapy in solid organ transplant recipients," *Acta Oncologica*, vol. 57, no. 10, pp. 1414–1418, 2018.

[61] T. De Pas, G. Spitaleri, G. Pelosi et al., "Erlotinib combined with cyclosporine in a liver-transplant recipient with epidermal growth factor receptor-mutated non-small cell lung cancer," *Journal of Thoracic Oncology*, vol. 4, no. 1, pp. 138-139, 2009.

[62] A. Hecimovic, A. V. Dugac, M. J. Makek, M. Cikes, M. Samarzija, and M. Jakopovic, "Treatment of EGFR positive lung adenocarcinoma in a heart transplanted patient," *Monaldi Archives for Chest Disease*, vol. 89, no. 2, 2019.

[63] F. Cornelis, X. Buy, M. André et al., "De novo renal tumors arising in kidney transplants: midterm outcome after percutaneous thermal ablation," *Radiology*, vol. 260, no. 3, pp. 900–907, 2011.

[64] W. P. Kluijfhout, F. T. Drake, J. D. Pasternak et al., "De novo thyroid cancer following solid organ transplantation-a 25-year experience at a high-volume institution with a review of the literature," *Journal of Surgical Oncology*, vol. 115, no. 2, pp. 105–108, 2017.

Retraction

Retracted: Understanding the Critical Role of Glycolysis-Related lncRNAs in Lung Adenocarcinoma Based on Three Molecular Subtypes

BioMed Research International

This article has been retracted by Hindawi following an investigation undertaken by the publisher [1]. This investigation has uncovered evidence of one or more of the following indicators of systematic manipulation of the publication process:

(1) Discrepancies in scope

(2) Discrepancies in the description of the research reported

(3) Discrepancies between the availability of data and the research described

(4) Inappropriate citations

(5) Incoherent, meaningless and/or irrelevant content included in the article

(6) Manipulated or compromised peer review

The presence of these indicators undermines our confidence in the integrity of the article's content and we cannot, therefore, vouch for its reliability. Please note that this notice is intended solely to alert readers that the content of this article is unreliable. We have not investigated whether authors were aware of or involved in the systematic manipulation of the publication process.

Wiley and Hindawi regrets that the usual quality checks did not identify these issues before publication and have since put additional measures in place to safeguard research integrity.

We wish to credit our own Research Integrity and Research Publishing teams and anonymous and named external researchers and research integrity experts for contributing to this investigation.

The corresponding author, as the representative of all authors, has been given the opportunity to register their agreement or disagreement to this retraction. We have kept a record of any response received.

References

[1] P. Cao, B. Zhao, Y. Xiao et al., "Understanding the Critical Role of Glycolysis-Related lncRNAs in Lung Adenocarcinoma Based on Three Molecular Subtypes," *BioMed Research International*, vol. 2022, Article ID 7587398, 36 pages, 2022.

Hindawi

Research Article

Understanding the Critical Role of Glycolysis-Related lncRNAs in Lung Adenocarcinoma Based on Three Molecular Subtypes

Peng Cao ,[1] Bo Zhao,[1] Yajie Xiao,[2] Shan Hu,[1] Kangle Kong,[1] Peng Han,[1] Jiaqi Yue,[1] Yu Deng,[1] Zhikun Zhao,[2] Dongfang Wu ,[2] Lu Zhang ,[3] and Fan Li [1]

[1]*Department of Thoracic Surgery, Tongji Hospital, Tongji Medical College, Huazhong University of Science and Technology, No. 1095 Jiefang Avenue, Wuhan, 43000 Hubei Province, China*

[2]*Department of Clinical Translational Medicine, Yucebio Biotechnology Co., Ltd, Yantian District, Shenzhen, Guangdong Province, 4th Floor, Phase I, Dabaihui Center, No. 2002, Shenyan Road, Haishan Street, Yantian District, Shenzhen, China*

[3]*Department of Oncology, Tongji Hospital, Tongji Medical College, Huazhong University of Science and Technology, No. 1095 Jiefang Avenue, Wuhan, 43000 Hubei Province, China*

Correspondence should be addressed to Dongfang Wu; wudongfang@yucebio.com, Lu Zhang; zhanglutjh@hotmail.com, and Fan Li; tjhtsdrli@163.com

Background. Glycolysis is closely associated with tumor progression, but the roles of lncRNAs in glycolysis have not been comprehensively investigated in lung adenocarcinoma (LUAD). This study is aimed at studying the possible mechanisms of glycolysis-related lncRNAs in tumor development and providing a guidance for targeted therapy. *Methods.* Unsupervised consensus clustering was used to identify molecular subtypes. Gene enrichment analysis was applied to screen important pathways involved in tumor progression. A series of immune analysis was performed to assess immune infiltration. Critical transcription factors (TFs) interacting with lncRNAs were selected by Pearson correlation analysis. A first-order partial correlation analysis was implemented to identify critical lncRNAs with prognostic significance. *Results.* Three molecular subtypes (C1, C2, and C3) were identified with distinct overall survival. Three subtypes showed differential immune infiltration, and C3 subtype was the optimal for immunotherapy treatment. Ten lncRNA-TF pairs among four glycolysis-related lncRNAs (FTX, LINC00472, PSMA3-AS1, and SNHG14) and six TFs (FOXP1, SP1, MYC, FOXM1, HIF1A, and FOS) were involved in tumor progression. We identified four critical glycolysis-related lncRNAs significantly associated with prognosis. *Conclusions.* This study identified three molecular subtypes that could guide personalized therapy. The four-lncRNA prognostic model can serve as an indicator for predicting prognosis or early screening of lung adenocarcinoma patients. The current results improve the understanding of the relation between lncRNAs and glycolysis.

1. Introduction

Lung cancer is a leading cause of cancer death worldwide, and lung adenocarcinoma (LUAD) is the most common primary lung cancer. Smoking, including primary or secondary exposure to tobacco smoke, is a main risk factor for developing lung cancer. The incidence and mortality showed a decline since 1980s; according to the global cancer statistics in 2020, 2,206,771 new cases (11.4% of total new cases of cancer) were diagnosed, and 1,796,144 deaths (18.0% of total cancer deaths) of lung cancer were reported [1]. 5-year sur-

vival of lung cancer is lower than 15% largely because most of the patients are already advanced at the time of diagnosis [2–4]. However, an early screening and diagnosis of lung cancer is currently a great challenged.

Lung adenocarcinoma belongs to non-small-cell lung cancer (NSCLC) and has replaced squamous cell lung cancer as the most prevalent type of NSCLC in the past two decades [5]. Advances in detecting gene mutations and genome variations have discovered genetic alternations as one of the mechanisms contributing to NSCLC development. For example, mutations in *p53* gene occur in over half of NSCLC

cases, and epidermal growth factor receptor gene (*EGFR*) and Kirsten rat sarcoma viral oncogene homolog (*KRAS*) mutations are associated with worse clinical outcome [2]. Tyrosine kinase inhibitors such as erlotinib or gefitinib could prolong 5-year survival of metastatic NSCLC patients with *EGFR* mutation to 14.6% as compared with lower than 5% of nontreated patients [6]. However, only a small number of patients can benefit from tyrosine kinase inhibitors. Therefore, mechanisms of tumorgenesis for lung cancer are needed to be explored to increase early diagnose rate and facilitate personalized therapies.

In the recent years, long noncoding RNAs (lncRNAs) have been found to play critical roles in tumorgenesis, tumor immune microenvironment, and tumor metastasis in lung adenocarcinoma as well as in many other cancer types [7]. For example, LUADT1 is high expressed in LUAD and can promote cancer cell proliferation through interacting with SUZ12 and mediating the trimethylation of H3K27 at the promoter region of p27 [8]. DGCR5 is also upregulated in LUAD, and downregulation of DGCR5 is associated with favorable prognosis [9]. Studies have discovered various lncRNA signatures for predicting prognosis of LUAD from different aspects; for example, researchers have identified prognostic lncRNAs from lncRNA-ceRNA network [10] and also developed a four-lncRNA signature with immune features [11]. These newly identified signatures provide guidance to predict prognosis and contribute to a better understanding of the mechanisms related to lncRNAs in LUAD.

In this study, we associated glycolysis with lncRNAs to further reveal the mechanisms of tumor development in LUAD. Highly active glycolysis in cancer cells produces more energy for cancer cell proliferation and could therefore serve as a target for cancer treatment [12, 13]. lncRNAs are regulators in activating or suppressing expression of genes involved in glycolysis, and a series of lncRNAs, such as LINC00857 [14], LINC01123 [15], NORAD [16], and so on, have been discovered to function to regulate glycolysis in LUAD. In the present study, we identified a number of glycolysis-related lncRNAs and explored three molecular subtypes with clinical value for guiding personalized immunotherapy. Importantly, based on a lines of bioinformatics analysis, we discovered the possible roles and mechanisms of lncRNAs for regulating glycosis in LUAD. This study developed a four-lncRNA signature related to glycolysis for predicting prognosis of LUAD. The current findings emphasized the critical role of lncRNAs and provided possibilities for discovering therapeutic drugs based on glycolysis-related lncRNAs.

2. Materials and Methods

2.1. Data Information and Preprocessing.
RNA-seq data and expression profiles of LUAD samples were obtained from The Cancer Genome Atlas (TCGA, https://portal.gdc.cancer.gov/) database and Gene Expression Omnibus (GEO, https://www.ncbi.nlm.nih.gov/geo/) database. TCGA-LUAD dataset containing RNA-seq data was downloaded from TCGA, while samples without clinical information were excluded. Ensembl ID was converted to gene

symbol. 485 samples in TCGA-LUAD dataset were finally included. GSE31210 [17] and GSE72094 [18] datasets were downloaded from GEO. Samples of GSE cohort were selected if survival time was longer than 30 days but shorter than 15 years. Probes without value or mapped to multiple genes were excluded. Median value was taken when multiple probes were mapped to one gene. Totally 226 and 386 samples from in GSE31210 and GSE72094 datasets remained data preprocessing, respectively. The workflow of the overall study is shown in Figure 1.

2.2. Acquisition of lncRNA Expression Profiles.
GSE31210 and GSE72094 datasets were used for reannotation to obtain lncRNA expression profiles. Fasta file of probe sequence was downloaded from GPL570 and GPL15048 chip platform, and that of transcription reference sequence was downloaded from GENCODE (https://www.gencodegenes.org/human/). SeqMap [19] tool was used to blast probe sequence and reference sequence under nonmismatch condition. Then, GTF (gene transfer format) file downloaded from GENCODE [20] was used to distinguish lncRNA expression profile from mRNA expression profile in TCGA-LUAD, GSE31210, and GSE72094 datasets.

2.3. Identification of Glycolysis-Related lncRNAs.
Genes related to glycolysis (hallmark glycolysis pathway) were downloaded from MSigDB database [21] (https://www.gsea-msigdb.org/gsea/msigdb/). Glycolysis score of each sample in three datasets was calculated by single sample gene set enrichment analysis (ssGSEA) using GSVA R package [22]. Pearson correlation analysis between glycolysis score and lncRNAs was conducted. Glycolysis-related lncRNAs were selected when |correlation coefficient| >0.3 and $p < 0.05$.

2.4. Unsupervised Consensus Clustering for Identifying Molecular Subtypes.
Unsupervised consensus clustering was applied to construct consensus matrix and subtyping samples based on the expression of glycolysis-related lncRNAs using ConsensusClusterPlus R package [23]. PAM algorithm was used, and distance metric of "1 - Pearson correlation coefficient" was set to perform 500 times of bootstraps. Each bootstrap contained 80% samples as training group. Cluster number $k = 2$ to 10 was used to calculate consensus matrix and cumulative distribution function (CDF) to confirm the optimal clusters.

2.5. Enrichment Analysis of Functional Pathways.
GSEA was conducted to enrich hallmark genes downloaded from Molecular Signatures Database (MSigDB, https://www.gsea-msigdb.org/gsea/msigdb/) database. To assess the function of glycolysis-related lncRNAs, ClusterProfiler R package was used to annotate functional pathways in TCGA-LUAD dataset [24].

2.6. Immune Analysis of Three Molecular Subtypes.
CIBER-SORT [25](https://cibersort.stanford.edu/) was performed to visualize the enrichment of immune cells. Estimation of Stromal and Immune cells in MAlignant Tumours using Expression data (ESTIMATE) was performed to calculate
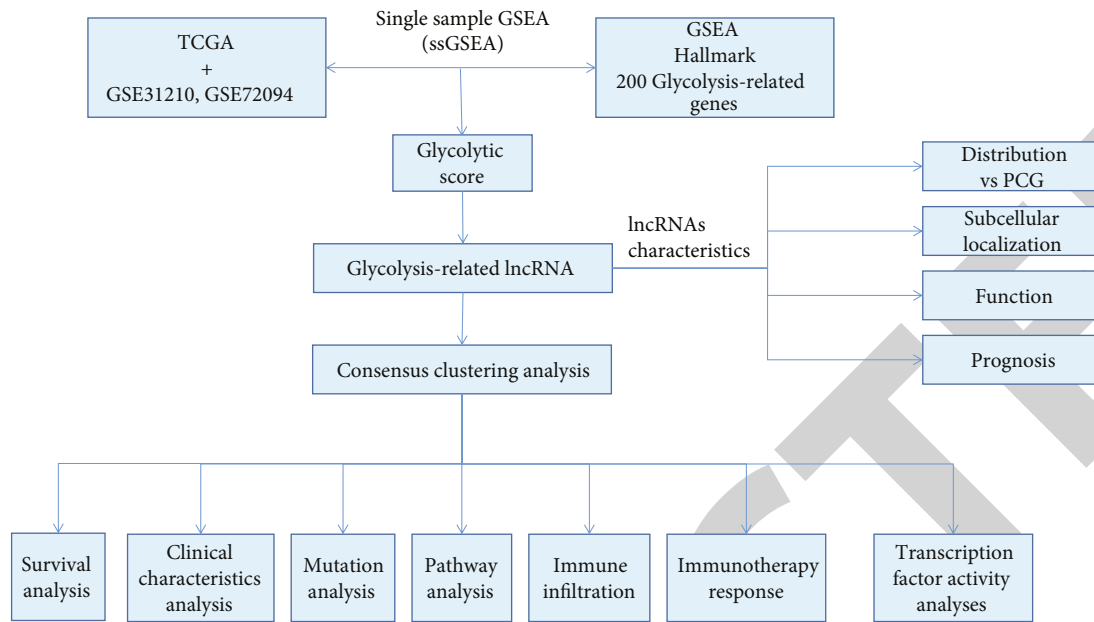
FIGURE 1: Work flow chart.

stromal score, immune score, and ESTIMATE score of the samples [26]. The TIDE [27] software (http://tide.dfci .harvard.edu/) was employed to predict the immune response of three molecular subtypes to immunotherapy.

2.7. Assessment of TF Activity. TF activity was assessed using a method from Garcia-Alonso et al. [28]. Firstly, gene expression of each sample was normalized by CDF [22]. Then, TF activity was approximated as a function of the collective mRNA levels of its targets using analytic Rank-based Enrichment Analysis (aREA) in VIPER R package [29]. Relative TF activity was estimated by normalized enrichment score (NES). NES = 0 was the cut-off to define relative high or low TF activity. ANOVA was performed to compare the TF activity among the three molecular subtypes. TFs with differential activity were screened by $p < 0.05$.

2.8. A First-Order Partial Correlation Analysis. A first-order partial correlation analysis was implemented to assess correlation among glycolysis-related lncRNAs, glycolysis score, and glycolysis-related genes. The glycolysis score was assumed to be x, and expression of glycolysis-related genes was assumed to be y. The first-order partial correlation between x and y conditioned on lncRNAs was:

$$r_{xylncRNA} = \frac{r_{xy} - r_{xlncRNA} * r_{ylncRNA}}{\sqrt{\left(1 - r_{xlncRNA}^2\right) * \left(1 - r_{ylncRNA}^2\right)}} \quad (1)$$

2.9. Construction of a Prognostic Model. Four glycolysis-related lncRNAs identified by the first-order partial correlation analysis were used to construct a prognostic model. Univariate Cox regression analysis was performed to calculate correlation coefficients between the four lncRNAs and overall survival. The prognostic model was defined as risk score = (

beta $i \times$ exp i), where i represents lncRNAs, exp i represents the expression of lncRNAs, and beta i represents the correlation coefficients. Samples were classified into high-risk and low-risk group according to the cut-off of $z - score = 0$.

2.10. Copy Number Variation (CNV) Analysis and Mutation Analysis. We downloaded from GDC (https://portal.gdc .cancer.gov/) the MuTect2 [30] software processed Simple Nucleotide Variation dataset and CNV dataset; we used the R package maftools (version 2.8.05) to evaluate mutation characteristics, compared mutations and copy number differences in different molecular subtype using chi-square tests, and visualized them using the function oncoplot in R package maftools [31].

3. Results

3.1. Constructing Molecular Subtypes of LUAD Based on Glycolysis-Related lncRNAs. Three datasets of TCGA-LUAD, GSE31210, and GSE72094 were included to screen lncRNAs related to glycolysis activity. A total of 3940 lncRNAs in TCGA-LUAD dataset, 379 in GSE31210, and 586 in GSE72094 were identified to be associated with glycolysis activity (Figure 2(a)). 37 of the lncRNAs coexisted in all three datasets, and they were selected for further analysis. In TCGA-LUAD dataset, 485 samples were included for consensus clustering using ConsensusClusterPlus R package. According to the CDF and relative change under CDF curve, cluster number $k = 3$ was determined to classify samples into three groups (Figures 2(b) and 2(c)). Therefore, a consensus matrix was visualized, and three molecular subtypes of C1, C2, and C3 were identified when $k = 3$ (Figure 2(d)).

To validate the effectiveness of the clustering, the relations between molecular subtypes and overall survival (OS), subtypes and glycolysis score were assessed in three datasets.
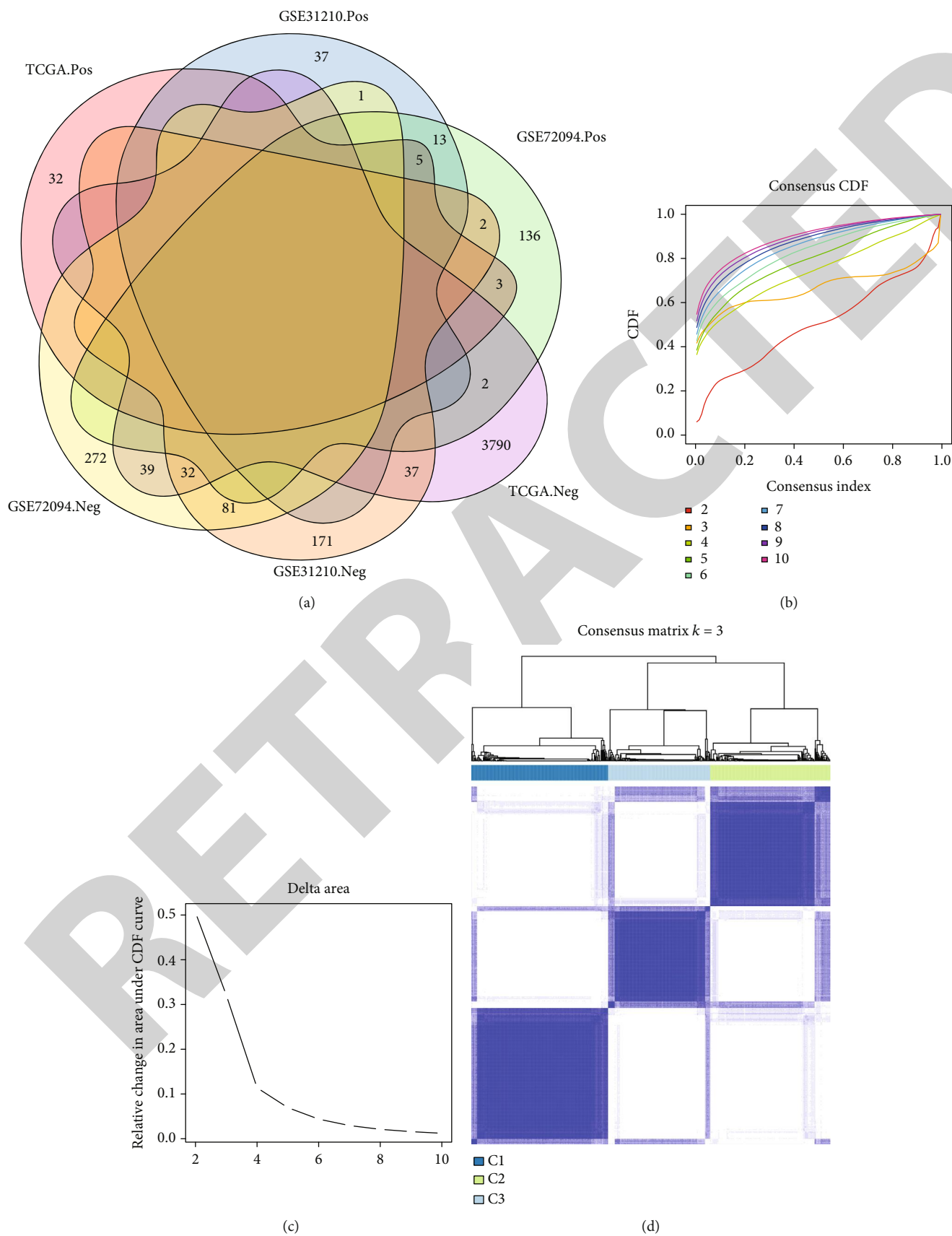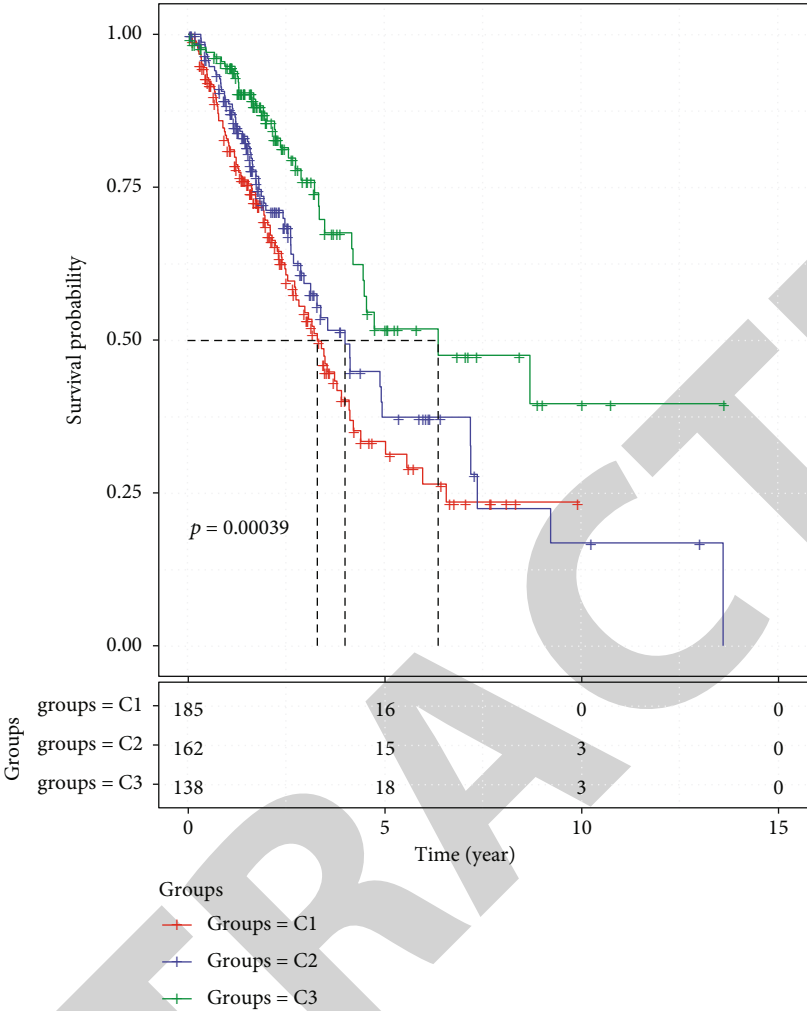
(a)

(b)

(c)

(d)

Figure 2: Continued.

(e)

FIGURE 2: Continued.

(f)
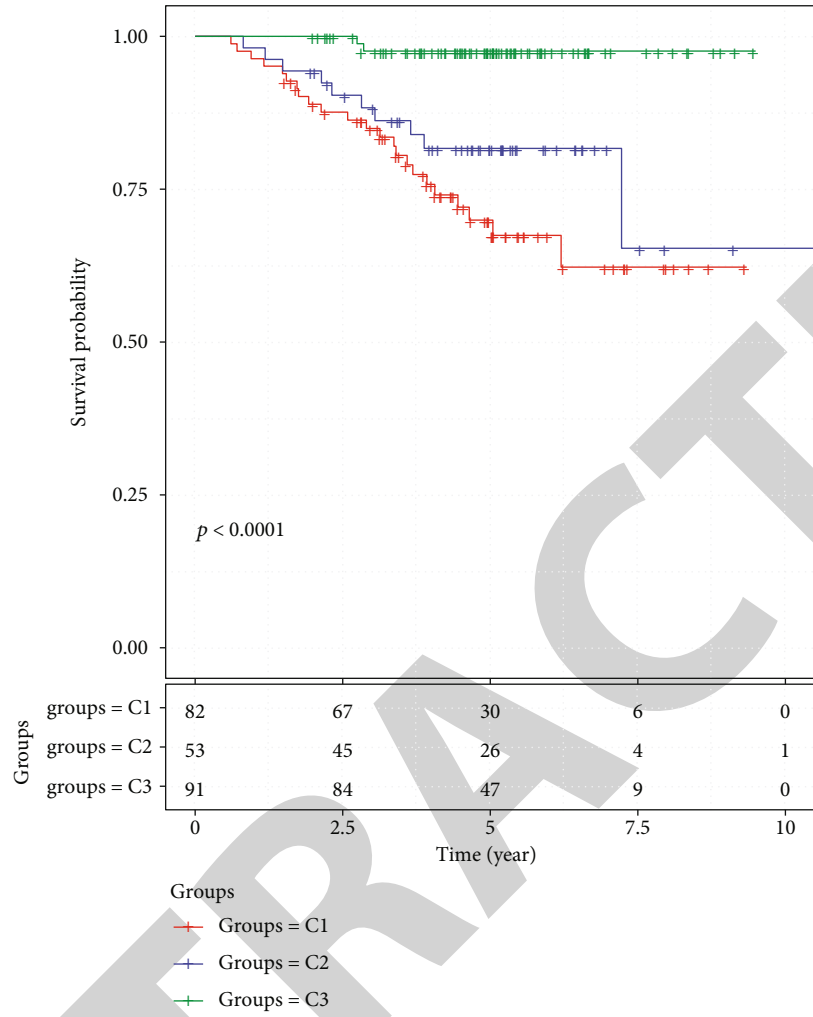
FIGURE 2: Continued.

(g)
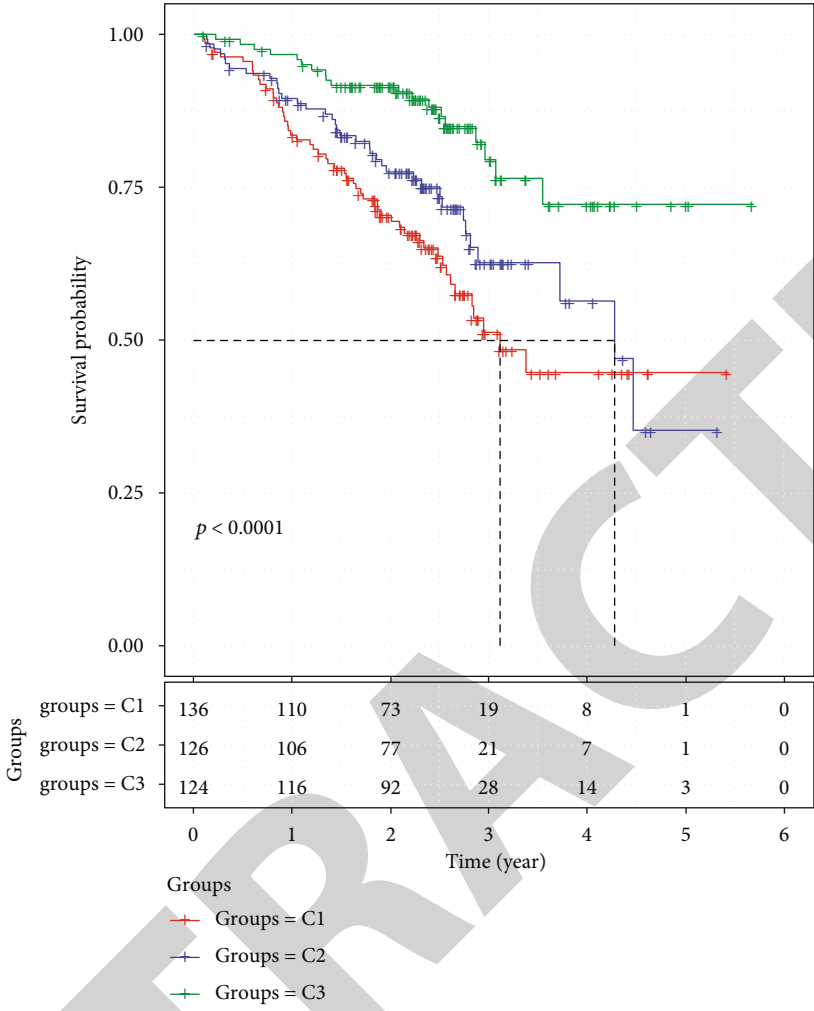
FIGURE 2: Continued.

(h)
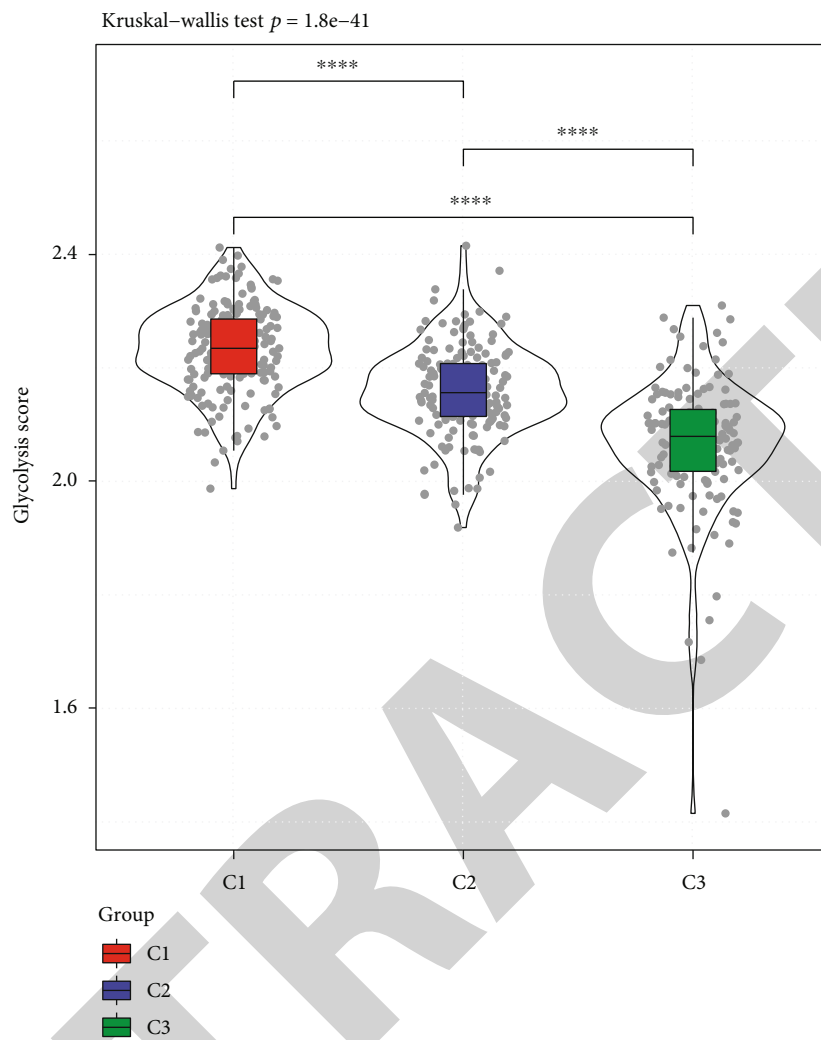
Figure 2: Continued.

(i)

FIGURE 2: Continued.

Kruskal–wallis test $p = 8.3e{-}29$
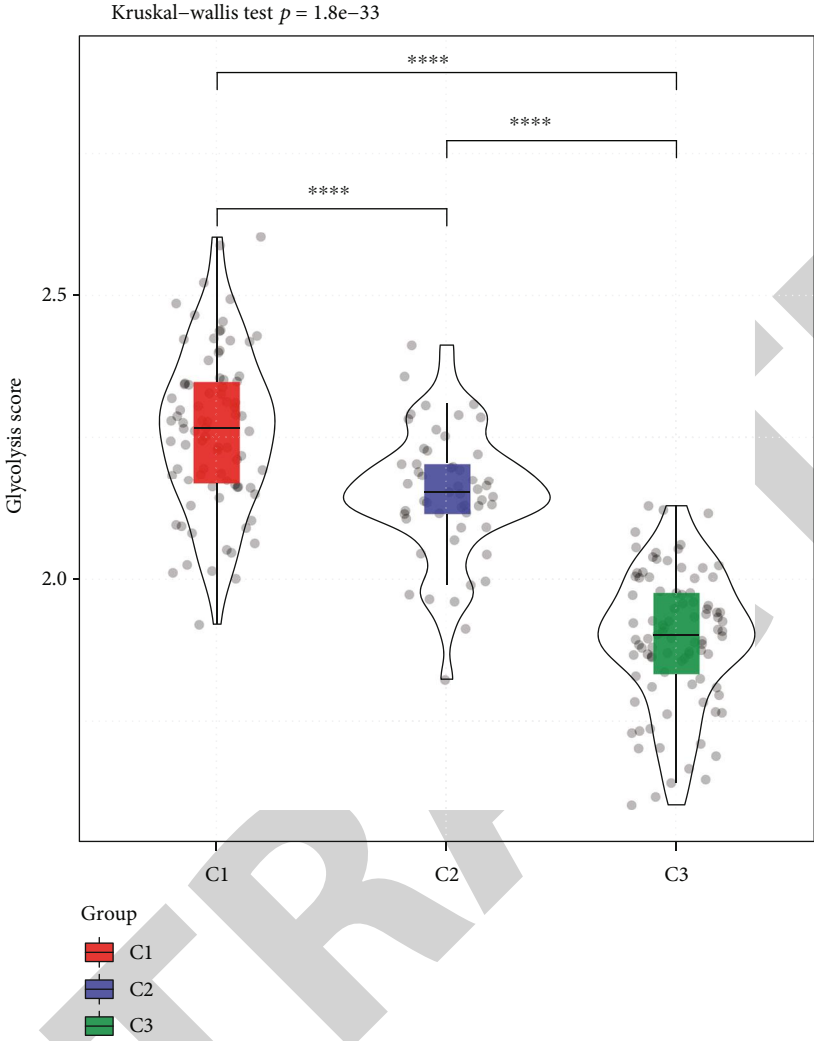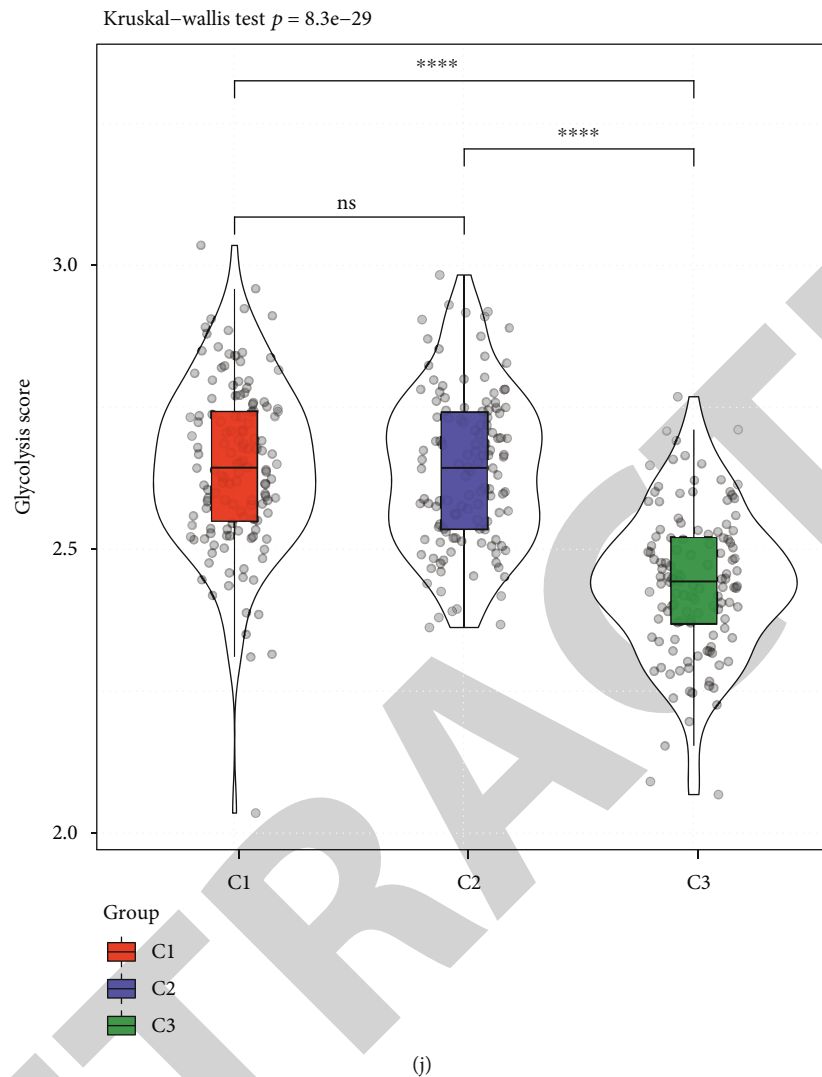
Figure 2: Identification of three subtypes based on glycolysis-related lncRNAs. (a) Venn plot of lncRNAs related to glycolysis in TCGA-LUAD, GSE31210, and GSE72094 datasets. Pos represents lncRNAs that are positively related to glycolysis score, while Neg represents lncRNAs that are negatively related to glycolysis score. (b) CDF curve when cluster number $k = 2$ to 10 in TCGA-LUAD dataset. (c) Relative change in area under CDF curve when $k = 2$ to 10 in TCGA-LUAD dataset. (d) Consensus matrix when $k = 3$ in TCGA-LUAD dataset. (e–g) Kaplan-Meier survival curve of three molecular subtypes (C1, C2, and C3) in TCGA-LUAD (e), GSE31210 (f), and GSE72094 (g) datasets. Log-rank test was performed. (h–j) Glycolysis score of three molecular subtypes in TCGA-LUAD (h), GSE31210 (i), and GSE72094 (j) datasets. Kruskal-Wallis test was performed. ns: no significance. $^{****}p < 0.0001$.

Survival plots showed that three molecular subtypes had distinct OS, with the most favorable OS in C3 group and the worst OS in C1 group across all three datasets (TCGA-LUAD: $p = 0.00039$, GSE31210 and GSE72094: $p < 0.0001$; Figures 2(e)–2(g)). In addition, we calculated glycolysis score based on glycolysis-related genes by ssGSEA in three datasets. Different glycolysis scores in three molecular subtypes were observed, and the C1 group had the highest glycolysis score, but the C3 group had the lowest glycolysis score ($p < 0.0001$, Figures 2(h)–2(j)). The above results proved that the subtyping system could effectively classify LUAD samples into three molecular subtypes significantly associated with prognosis and glycolysis score. Based on the results, we speculated that LUAD prognosis was associated with glycolysis score.

3.2. Three Molecular Subtypes Were Closely Associated with Clinical Stages. Next, we analyzed the relation between molecular subtypes and clinical features. In TCGA-LUAD dataset, the C3 group showed a high proportion of age ≥ 60, and the C1 group had a low proportion of age < 60 (Figure 3(a)). Female patients consisted of a larger percent than male patients in the C3 group, but no significant gender difference was shown among three groups (Figure 3(b)). In relation to stage, mild stages including T1 stage, N0 stage, M0 stage, and stage I accounted for the highest proportion in the C3 group when compared with other two groups (Figures 3(c)–3(f)), which was consistent with the previous result of the most favorable prognosis of the C3 group (Figure 2(e)). For smoking status, current smokers composed the largest proportion in the C3 group, while the proportion of nonsmokers was

(a)

(b)

(c)

(d)

(e)

(f)

Figure 3: Continued.

−log10 (anova *p* value)

(g)
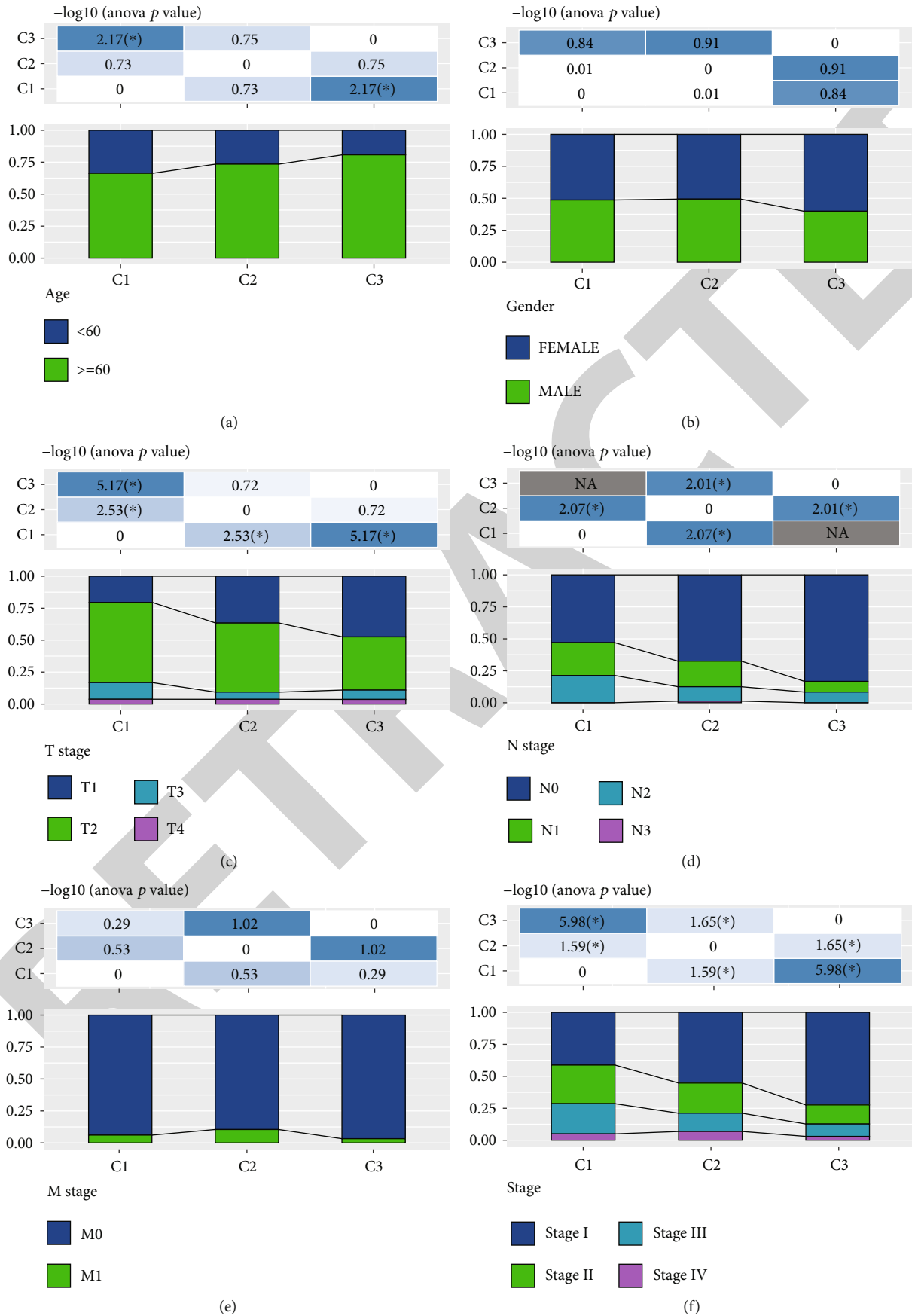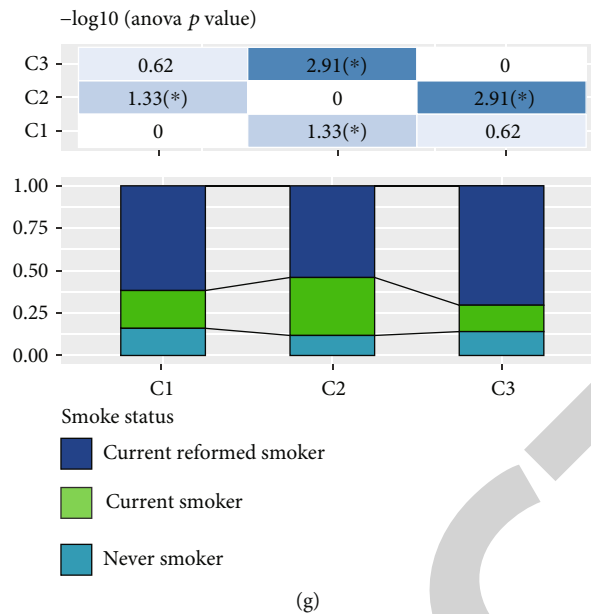
Figure 3: The relation between three molecular subtypes and clinical features including age (a), gender (b), T stage (c), N stage (d), M stage (e), stage (f), and smoke status (g). ANOVA was performed.

similar among the three groups (Figure 3(g)). We also assessed the clinical features in other two datasets, GSE31210 and GSE72094. Age and gender were not significantly related to molecular subtypes, but the tendency of stage distribution was correspondent with the results in TCGA-LUAD dataset (Supplementary Figure S1A-F). However, no significant difference of smoking status was detected in three groups (Supplementary Figure S1G).

3.3. Differences of Genome Variation and Gene Mutation Patterns among Molecular Subtypes.

Genome variations were measured to assess whether there was a correlation between genome stability and molecular subtypes through adopting five dimensionalities including aneuploidy score, homologous recombination defects, fraction altered, number of segments, and tumor mutation burden. C1 and C2 groups showed similar scores of aneuploidy score, fraction altered, number of segments, and tumor mutation burden, but the C2 group had more homologous recombination defects than the C1 group (Figure 4(a)). In all these five aspects, the C3 group obtained the lowest score, suggesting the least genome variations of the C3 group compared with other two groups (Figure 4(a)). Simultaneously, the relation between glycolysis score and genome stability was analyzed by Pearson correlation analysis. The result demonstrated that glycolysis score was positively associated with genome variations, indirectly proving that the C3 group with a high glycolysis score had higher genome variations (Figure 4(b)).

In the case of gene mutations, the C1 group had the largest number of gene mutations, while the C3 group had the smallest number of mutations (Figure 4(c)). The top 10 mutated genes were listed and *TP53*, *TTN*, and *RYR2* accounted for a majority of mutations. Missense mutation, nonsense mutation, and multihit mutation (different combi-

nations of multiple genetic mutations) were common mutation types. Small-scale copy number variations (CNVs) of genes were also evaluated in three groups. Interestingly, the C2 group had obviously high percentage of both gain or loss of CNVs (Figure 4C). *CDKN2A* had the most number of loss of CNVs in all three groups but largely in the C1 group. *ACTRT3* contained about 20% gain of CNVs in the C1 group, while the highest number of CNV amplification in the C2 group was detected in *AGO2*.

3.4. Analyzing Functional Pathways of Molecular Subtypes Based on Hallmark Genes.

Functional pathways of three datasets were enriched based on hallmark genes using GSEA, and FDR < 0.05 was selected to screen differentially enriched pathways between C1 and C3 subtypes. The data revealed that 29 pathways with 27 activated and 2 suppressed were enriched in TCGA-LUAD dataset (Figure 5(a)). In GSE31210 and GSE72094 datasets, 26 and 18 pathways were enriched, respectively. 13 pathways related to cell cycle, immune response, and oncogenesis, including E2F targets, G2M checkpoint, MYC targets, MTORC1, glycolysis, epithelial mesenchymal transition (EMT), unfolded protein response, DNA repair, mitotic spindle, interferon gamma response, hypoxia, and spermatogenesis pathways, were coenriched in all three datasets (Figure 5(a)). Furthermore, enrichment scores of enriched pathways were compared between C1 and C3 groups and C2 and C3 groups in three datasets, as shown in radar plots (Figures 5(b)–5(d)). Obvious high enrichment scores of the pathways were found in the C1 and C2 groups when compared with the C3 group, indicating that the activation of these pathways may be associated with unfavorable prognosis. In addition, the C1 group had relatively higher enrichment score than the C2 group, which further supported our speculation.
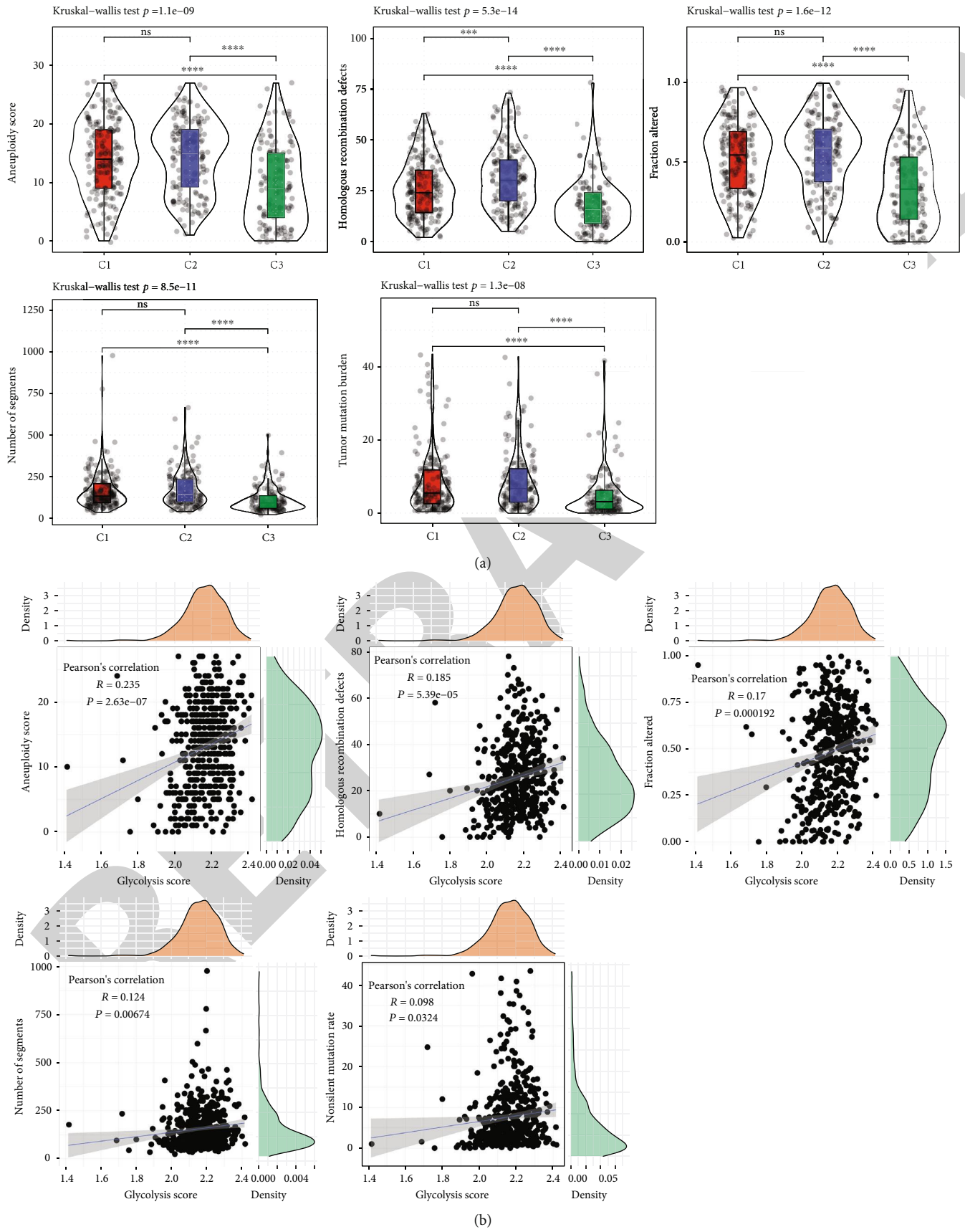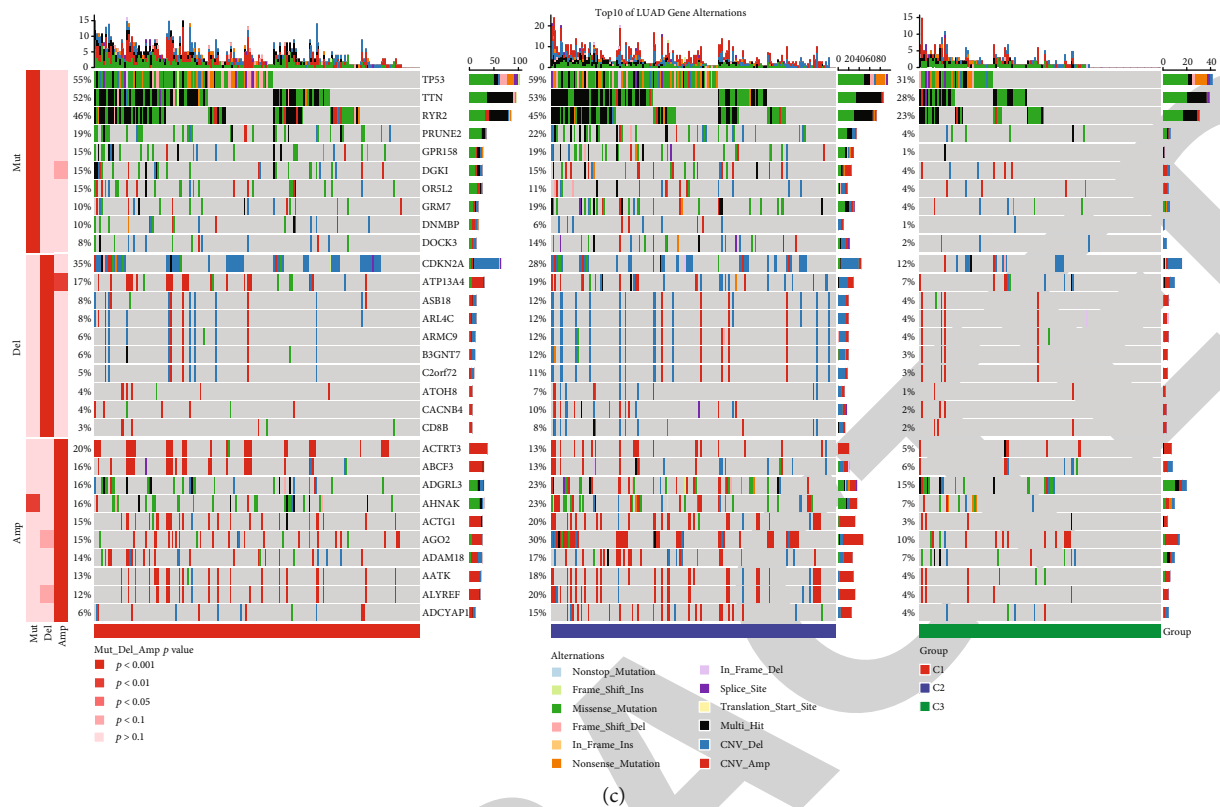
(a)

(b)

Figure 4: Continued.

Figure 4: Genomic variations and mutation patterns of three molecular subtypes in TCGA-LUAD dataset. (a) The difference of aneuploidy score, homologous recombination defects, fraction altered (the fraction of bases pairs present in the copy number profiles deviating from the baseline ploidy), number of segments (the total number of segments present in the copy number profile of each sample), and tumor mutation burden among three subtypes. Kruskal-Wallis test was performed. (b) Pearson correlation analysis between glycolysis score and genomic variations. (c) The difference of mutation patterns of the top 10 altered genes among three subtypes. ns: no significance. $***p < 0.001$, $****p < 0.0001$.

3.5. Differential Immune Infiltration of Three Molecular Subtypes.

To some extent, immune infiltration can decide the degree of tumor progression, and high infiltration of cytotoxic T cells can efficiently kill tumor cells. Therefore, we obtained a series of marker genes related to different types of immune cells from a previous research [32] and calculated enrichment score of LUAD samples grouped by molecular subtypes through ssGSEA in three datasets. Three datasets showed similar distribution of immune cells in three molecular subtypes, and the majority of immune cells were differentially enriched (Figure 6(a)). Notably, the C2 group displayed low immune infiltration than the C1 and C3 groups, while the C3 group had higher infiltration of immune cells, such as cytotoxic cells, T cells, dendritic cells (DCs), and mast cells than the C1 group (Figure 6(a) and Supplementary Figure S2). Moreover, ESTIMATE measurement was applied to further evaluate the immune infiltration of three molecular subtypes. In TCGA-LUAD and GSE72094 datasets, the C2 group presented the lowest enrichment score of stromal score, immune score, and ESTIMATE score (Figure 6(b)), which was in accordance with the result of Figure 6(a). However, the C1 and C3 groups showed comparable enrichment score of the three terms in TCGA-LUAD and GSE72094 datasets, and no significant difference was observed in GSE31210 dataset (Figure 6(b)). To further examine the difference of immune infiltration between C1 and C3 groups, hierarchical clustering was performed to classify the samples into low- and high-immune infiltration. The results demonstrated that the C3 group had a higher immune infiltration than the C1 group, although part of the C1 group also showed a high enrichment of immune cells (Supplementary Figure S3).

3.6. Difference Responses to Immunotherapy of Three Molecular Subtypes.

We then evaluate the prediction ability of three molecular subtypes for guiding immunotherapy based on the expression of immune checkpoints and TIDE analysis. A total of 18 immune checkpoints were screened to be differentially expressed among three subtypes (Figures 7(a)–7(c) and Supplementary Figure S4). A majority of immune checkpoints were high expressed in the C1 group, while the C2 group showed a low expression level of most immune checkpoints. Of 18 differentially expressed immune checkpoints, CD276, HAVCR2, and TNFSF4 were detected in all three datasets, and CD244, CD274, CD80, ICOS, IDO1, LAG3, and VISTA were identified in two datasets, and the rest 8 immune checkpoints were only identified in one dataset (Figure 7(d)). These immune checkpoints, especially CD276, HAVCR2, and TNFSF4 showing similar distribution in three datasets, may serve as potential targets for immunotherapy. In addition, we used TIDE to predict immune response to

(a)

(b)

Figure 5: Continued.

(c)
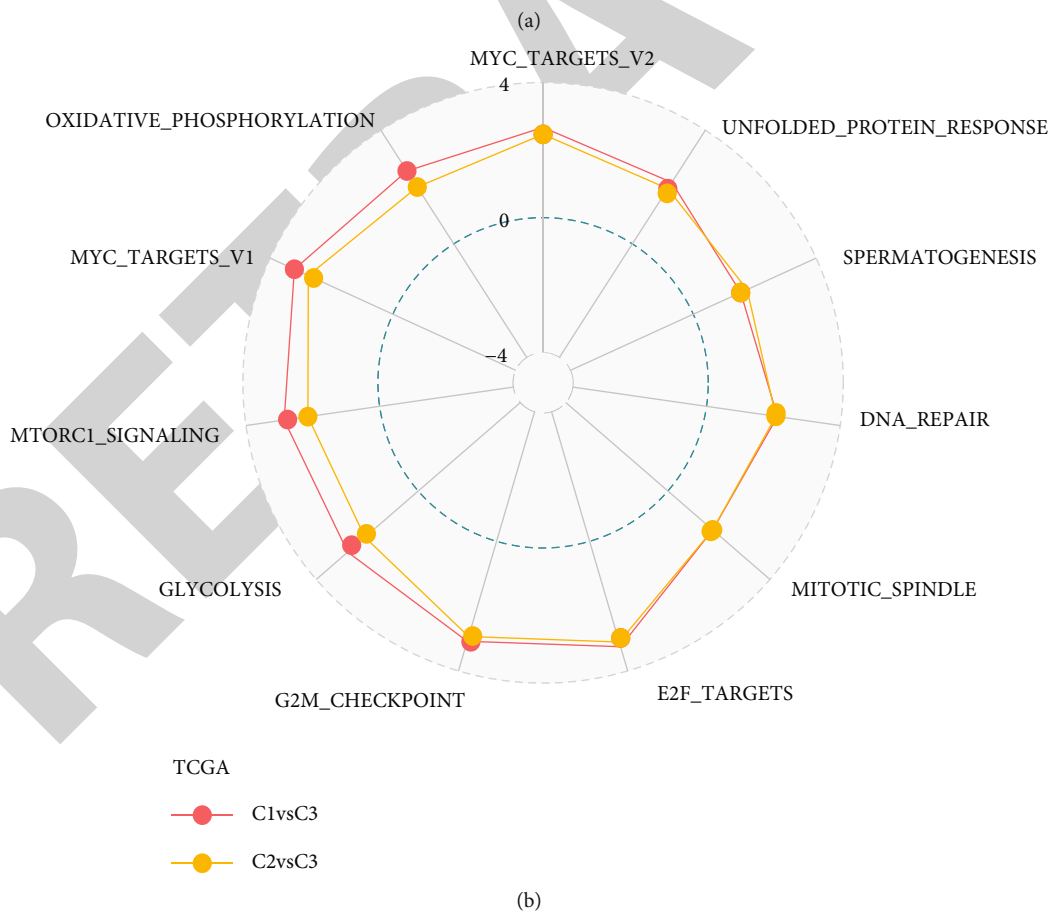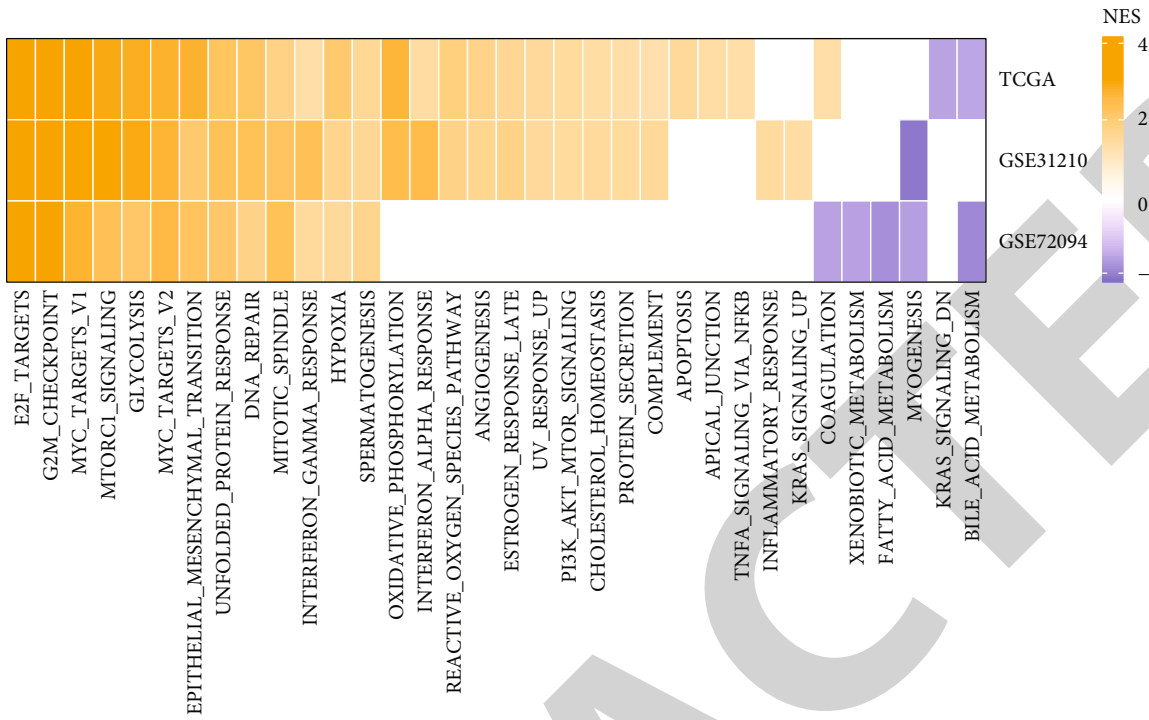
(d)
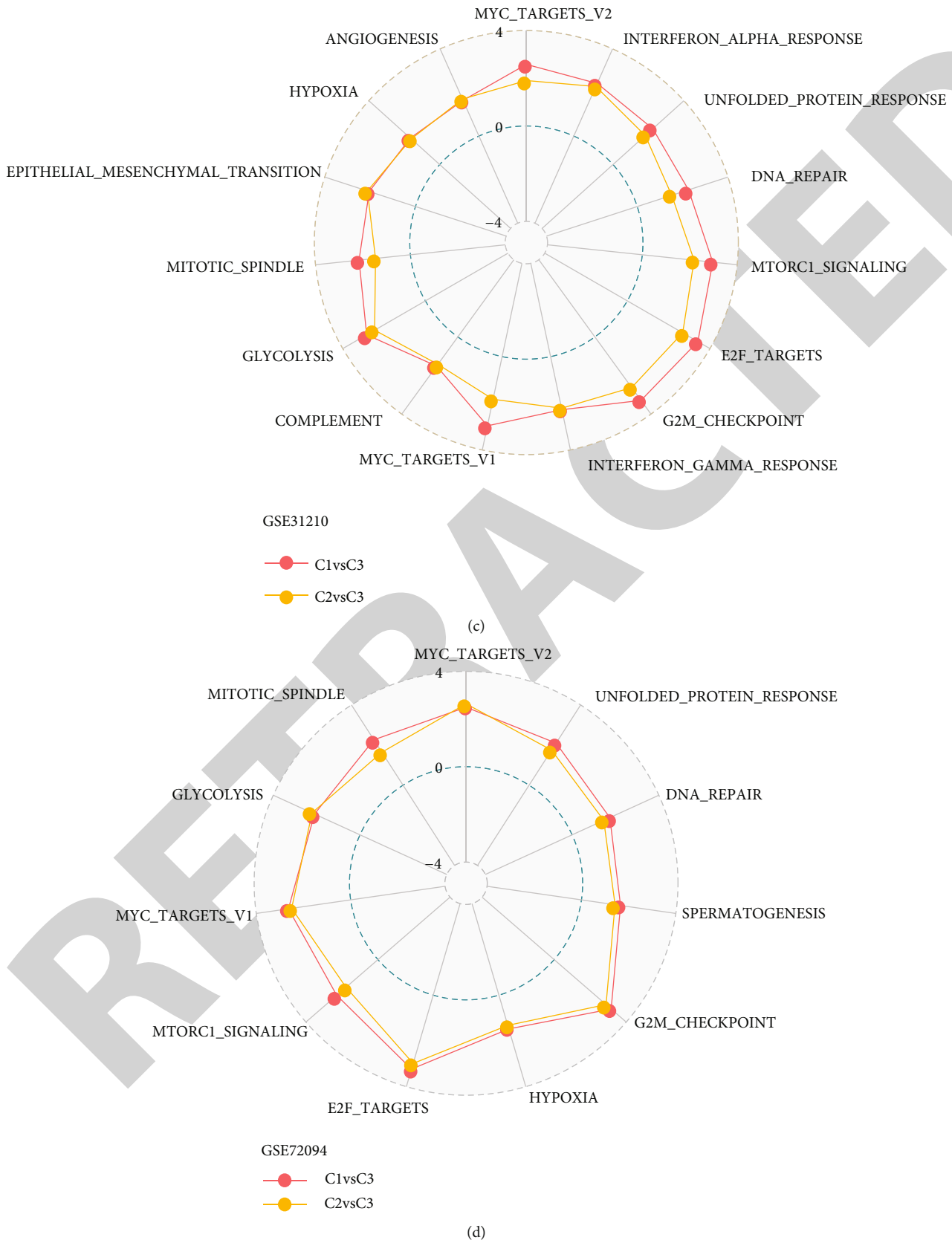
Figure 5: Enrichment analysis of functional pathways based on hallmark genes. (a) A heat map revealing the differentially enriched pathways between C1 and C3 subtypes with FDR < 0.05. NES: normalized enrichment score of C1 vs. C3. (b–d) Radar plots presenting the NES of enriched pathways of C1 vs. C3 and C2 vs. C3 in TCGA-LUAD (b), GSE31210 (c), and GSE72094 (d) datasets.
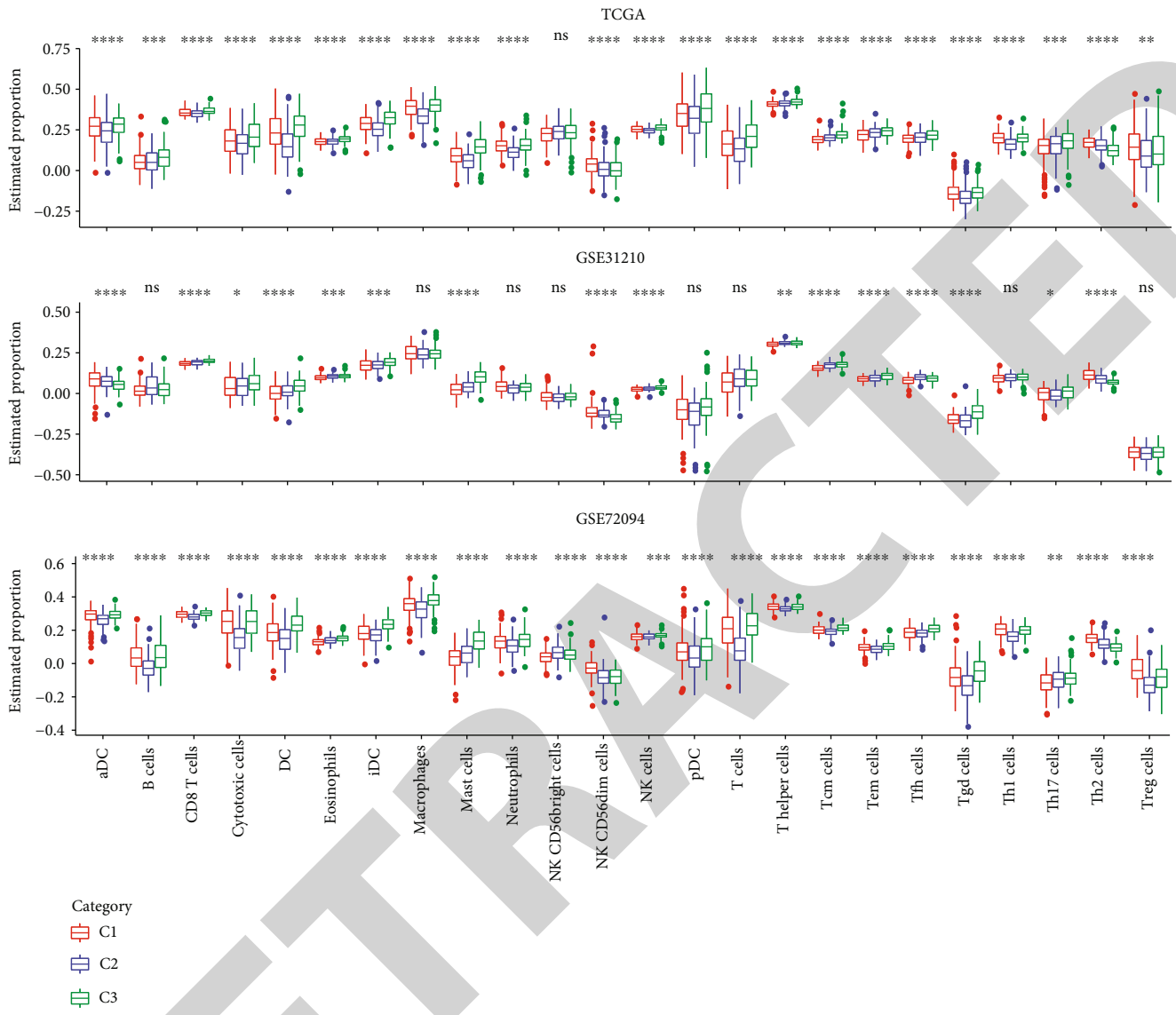
(a)

FIGURE 6: Continued.

(b)
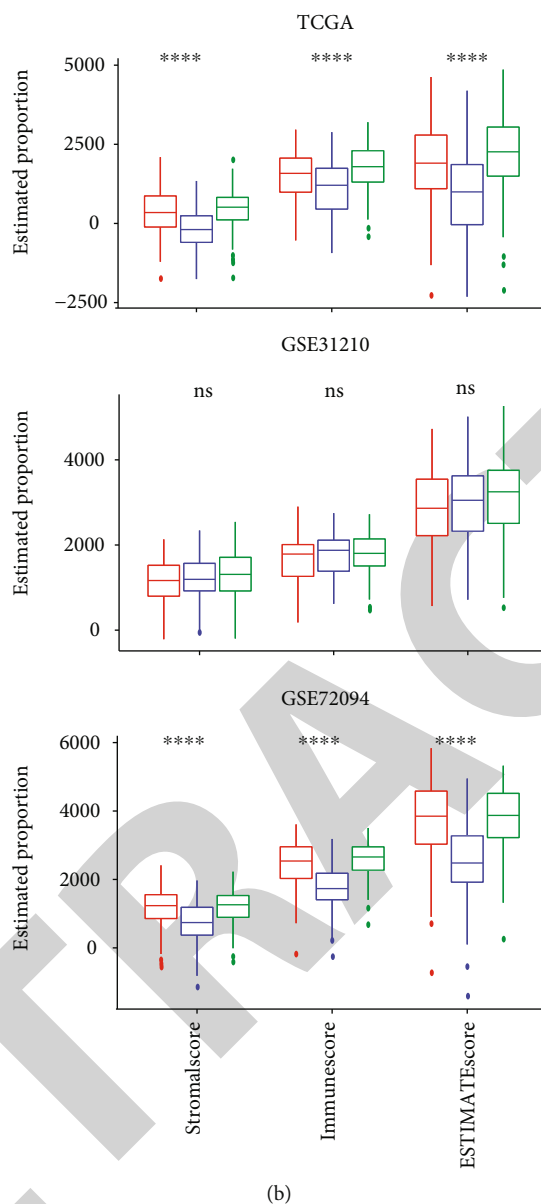
Figure 6: The differential immune infiltration of three molecular subtypes. (a) Estimated proportion of 24 types of immune cells in TCGA-LUAD, GSE31210, and GSE72094 datasets. aDC: active dendritic cells; iDC: immature dendritic cells; NK cells: natural killer cells; pDC: plasmacytoid dendritic cells; Tcm cells: central memory T cells; Tem cells: effector memory T cells; Tfh cells: T follicular helper cells; Tgd cells: gamma delta T cells. (b) Comparison of stromal score, immune score, and ESTIMATE score among three subtypes in TCGA-LUAD, GSE31210, and GSE72094 datasets. ANOVA was performed. ns: no significance. $^*p < 0.05$, $^{**}p < 0.01$, $^{***}p < 0.001$, $^{****}p < 0.0001$.

immunotherapy, with a high TIDE score representing high possibility of immune escape. The result showed that the C3 group had the lowest TIDE score among three molecular subtypes in all three datasets (Figures 7(e)–7(g)), indicating that the C3 group may develop a favorable prognosis after immunotherapy.

3.7. The Aberrant Expression of Transcriptional Factors Was Associated with Glycolysis-Related lncRNAs and Tumor Progression. In the previous sections, we demonstrated that glycolysis-related lncRNAs were associated with prognosis, tumor- and immune-related pathways, and immune infiltra-

tion in LUAD patients, but the role of glycolysis-related lncRNAs play in regulating glycolysis remained unclear. It has been shown that the function of lncRNAs to act in *cis* in the nucleus and *trans* in the nucleus or cytoplasm is dependent on their subcellular localization [33]. lncRNAs can up- or downregulate gene expression level commonly through the interactions with TFs or chromatin-modifying complexes [34]. Therefore, here, we attempted to reveal possible mechanisms of glycolysis-related lncRNAs in tumor development.

A total of 37 glycolysis-related lncRNAs identified in all three datasets were selected for the following analysis. In the
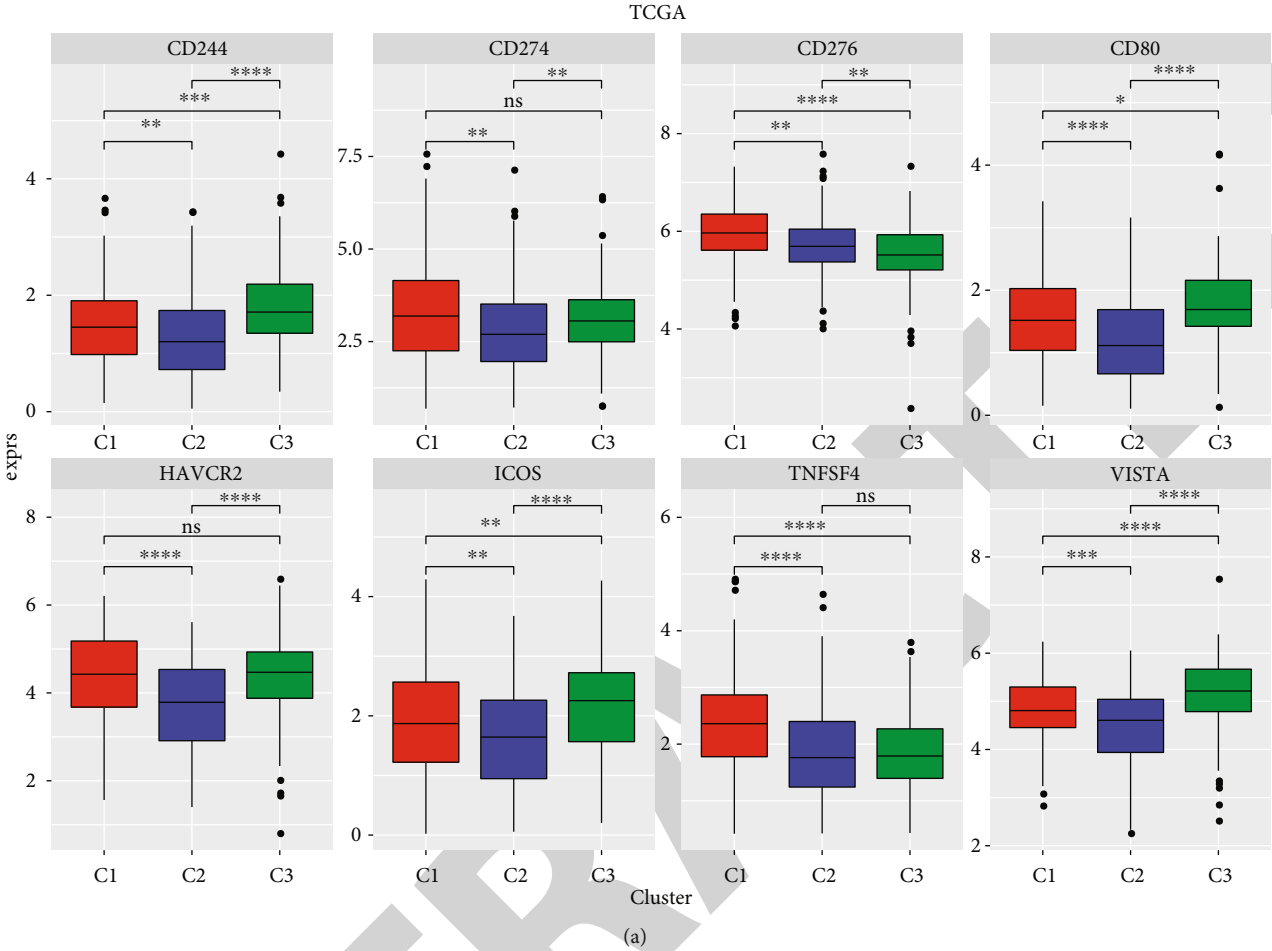
Figure 7: Continued.
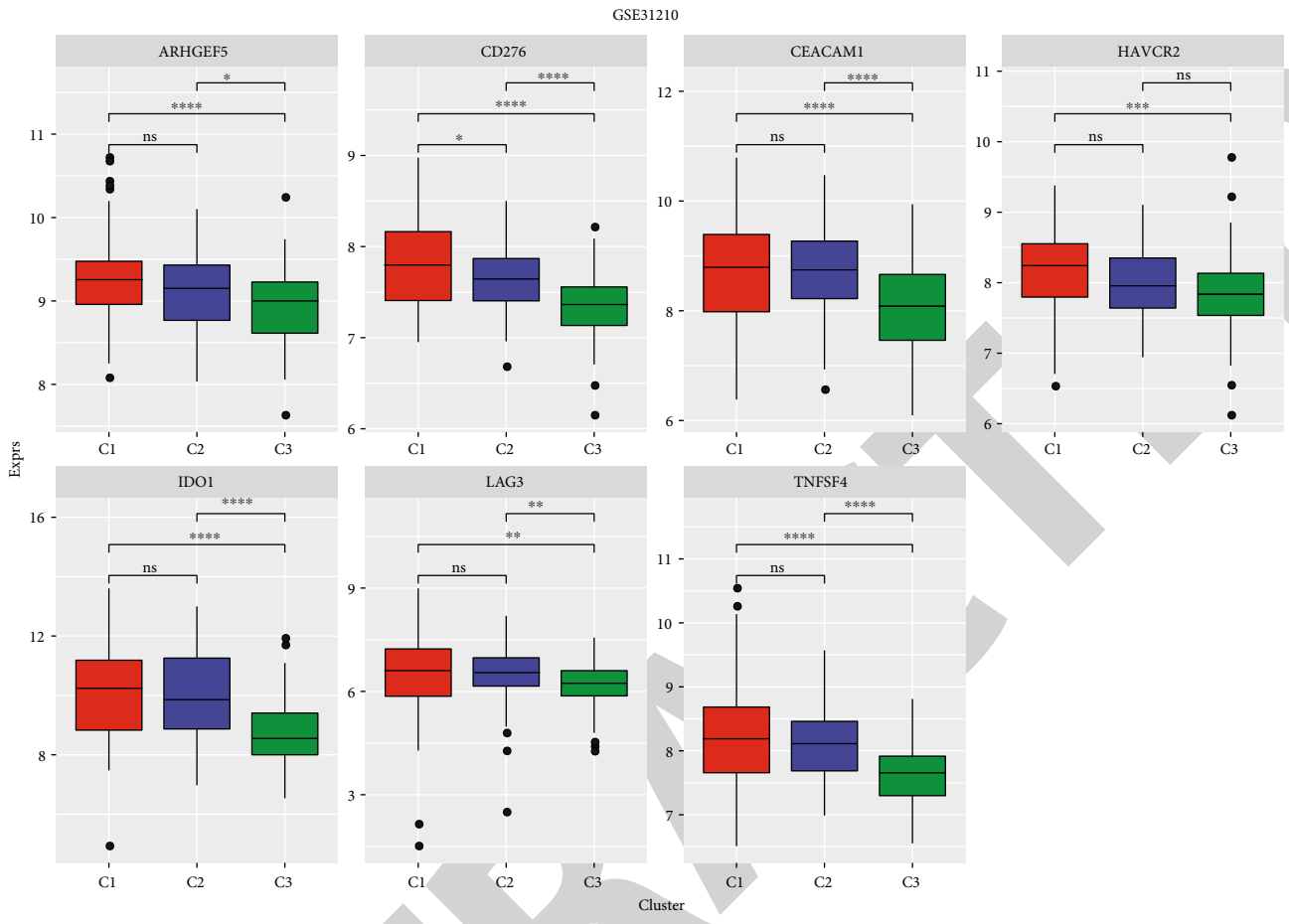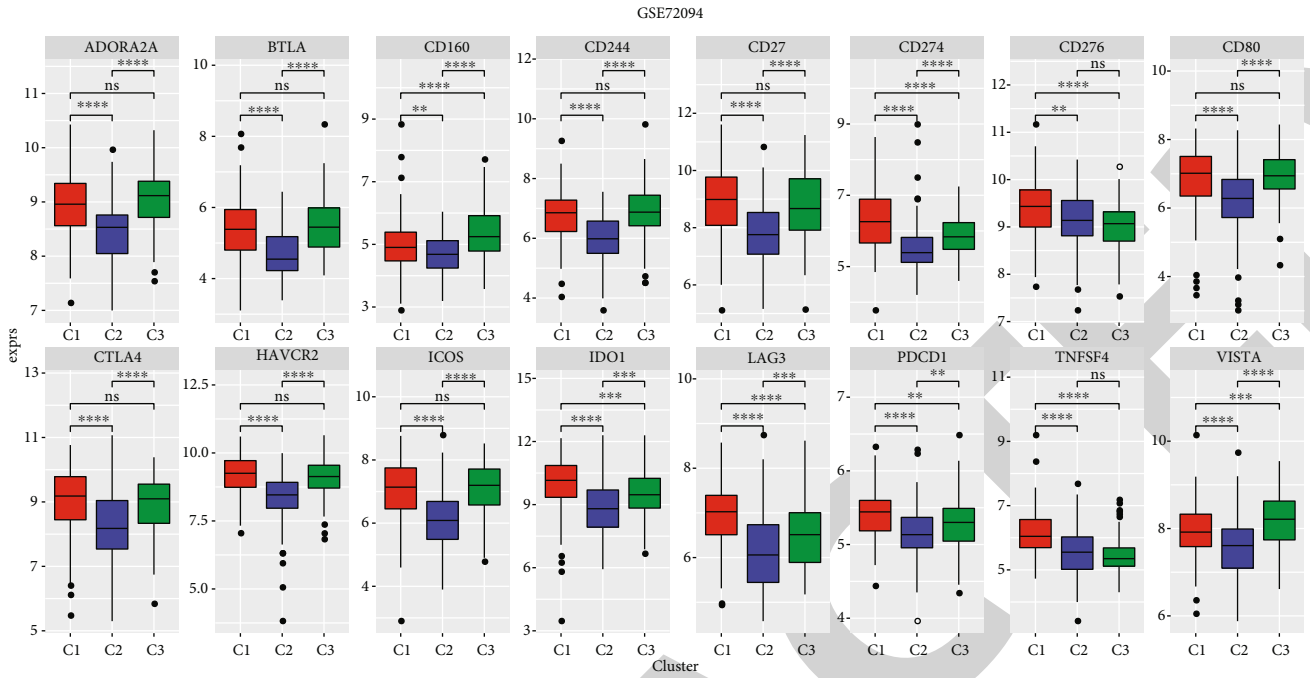
Figure 7: Continued.

(c)

(d)
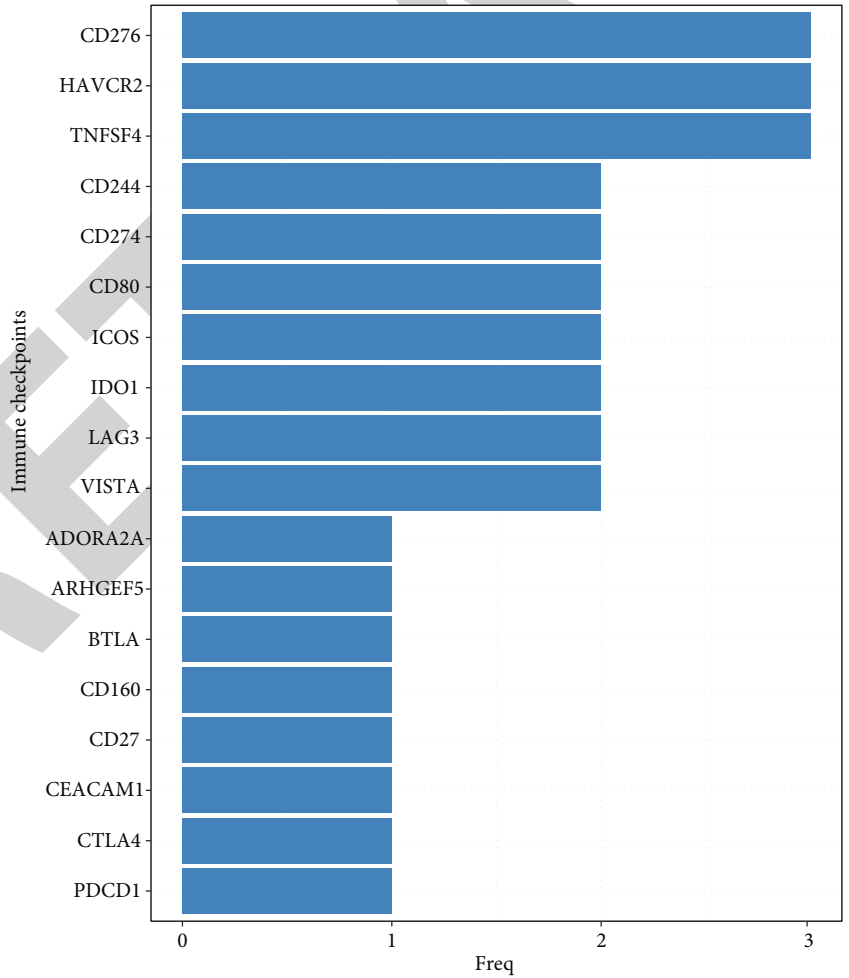
Figure 7: Continued.

(e)
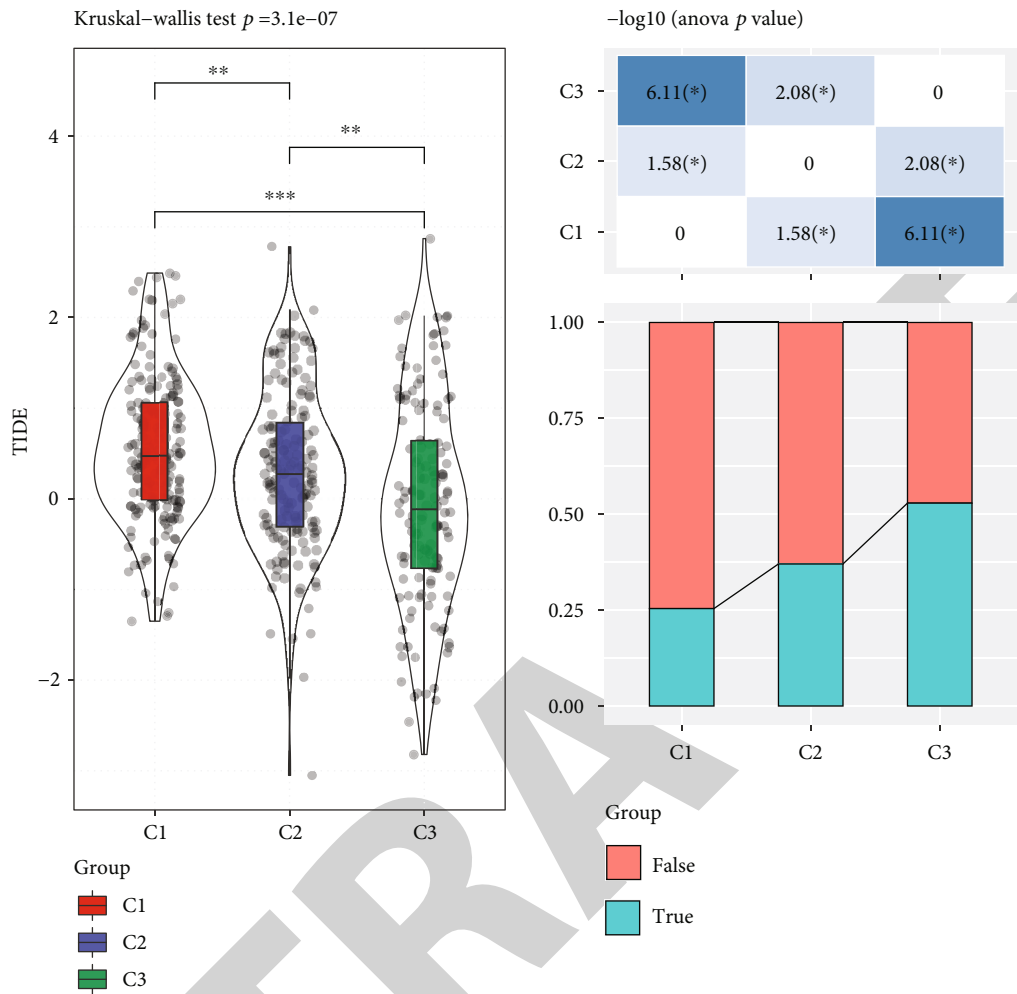
Figure 7: Continued.
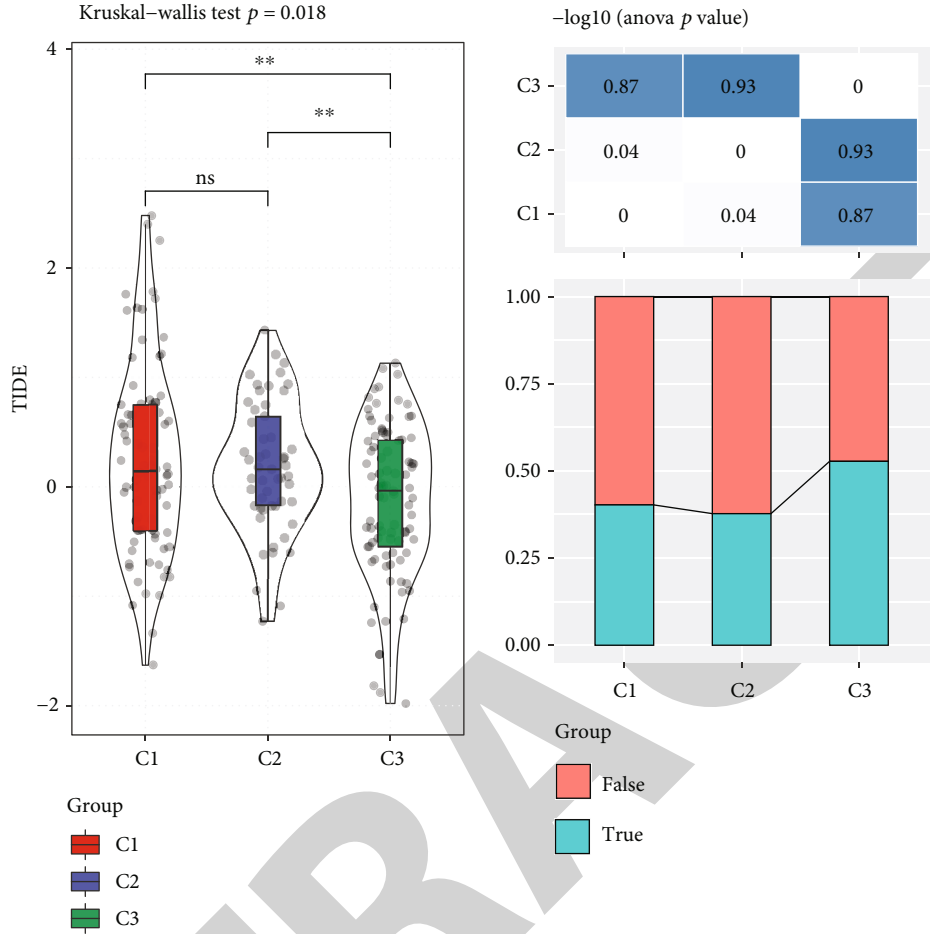
(f)

FIGURE 7: Continued.

(g)
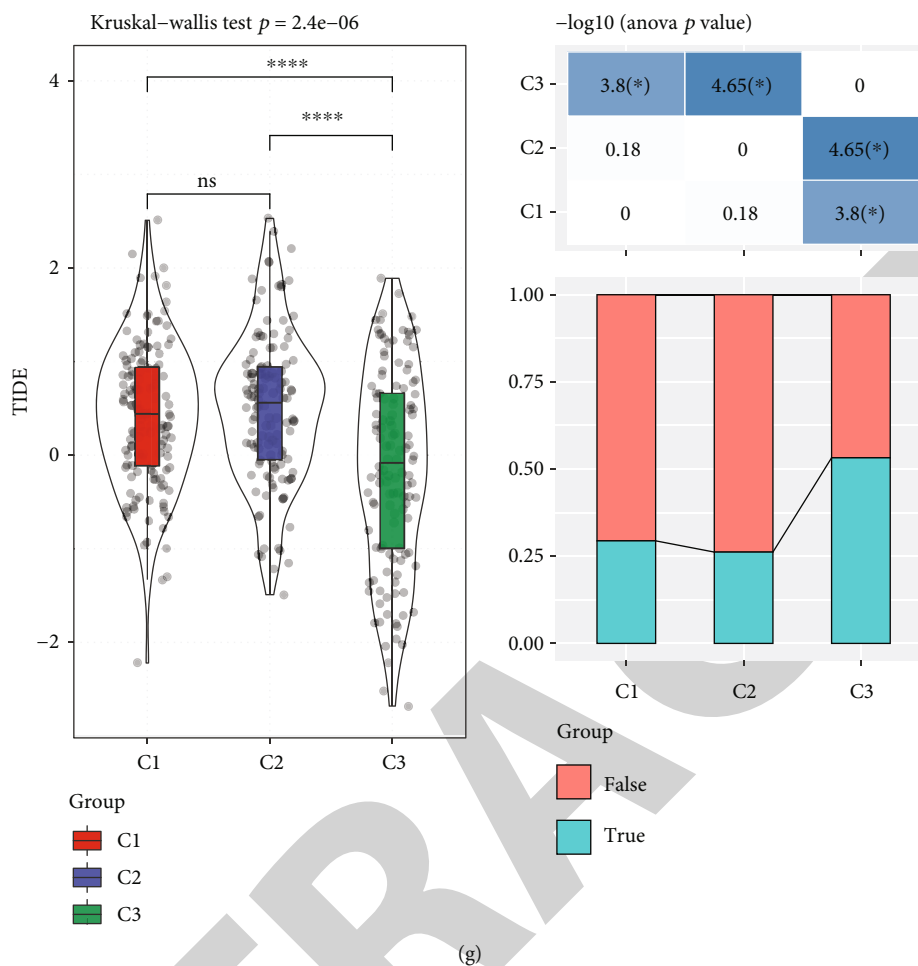
Figure 7: The relation between molecular subtypes and immunotherapy. (a–c) The differential expression of immune checkpoints among three molecular subtypes in TCGA-LUAD (a), GSE31210 (b), and GSE72094 (c) datasets. exprs: expression; ANOVA was performed. (d) The frequency of 18 immune checkpoints present in three datasets. Horizontal axis represents the number of times. Freq: frequency. (e–g) TIDE analysis for predicting the immune response to immunotherapy in three subtypes in TCGA-LUAD (e), GSE31210 (f), and GSE72094 (g) datasets. Kruskal-Wallis test was performed. False represents positive immune response, and true represents negative immune response. ns: no significance. $^{*}p < 0.05$, $^{**}p < 0.01$, $^{***}p < 0.001$, $^{****}p < 0.0001$.

relation between the expression of protein-coding genes (PCGs) related to glycolysis and lncRNAs, we observed that the expressions of most lncRNAs were negatively correlated with that of PCGs (Figure 8(a)), indicating that glycolysis-related lncRNAs were possibly in negative regulation to glycolysis-related PCGs expression. Then, LncATLAS database was employed to study the localization of glycolysis-related lncRNAs, and relative concentration index (RCI) was used to quantify the localization. We found that the majority of lncRNAs localized in nucleus presented as negative (RCI < 0) accounted for 83.28% in TCGA-LUAD dataset, 63.21% in GSE31210 dataset, and 71.29% in GSE72094 dataset (Figure 8(b)). To specifically evaluate the localization of 37 lncRNAs, we included 15 types of cell lines. The data showed that most lncRNAs were highly enriched in the nucleus, which was consistent with the above results (Supplementary Figure S5).

Subsequently, we assessed the activity of TFs in three molecular subtypes according to aREA algorithm, and each sample obtained a score of TF activity. The difference of

TF activity among three subtypes was analyzed in three datasets, and 46, 32, and 46 TFs with differential activity among three subtypes were screened in TCGA-LUAD, GSE31210, and GSE72094 datasets, respectively (Supplementary Table S1). Then, we analyzed the relation between these TFs and the lncRNAs localized in the nucleus. 13 TFs were identified to be negatively associated with the nuclear lncRNAs, and E2F4, FOXM1, MYC, and E2F1 TFs were all present in three datasets (Figure 8(c)). Notably, significantly negative correlation was observed in a number of lncRNA-TF pairs among lncRNAs of FTX, LINC00472, PSMA3-AS1, SNHG14, and TFs of FOXP1, SP1, MYC, FOXM1, HIF1A, and FOS ($R \le -0.3$, Figure 8(d)). The results suggested that the nuclear lncRNAs could interact with TFs, and these lncRNA-TF pairs may function critically in regulating glycolysis.

To analyze whether there was a difference of TF expression among three molecular subtypes, we compared the expression of 13 TFs associated with nuclear lncRNAs in TCGA-LUAD dataset. The C1 group had relatively higher

(a)

(b)

Figure 8: Continued.

(c)
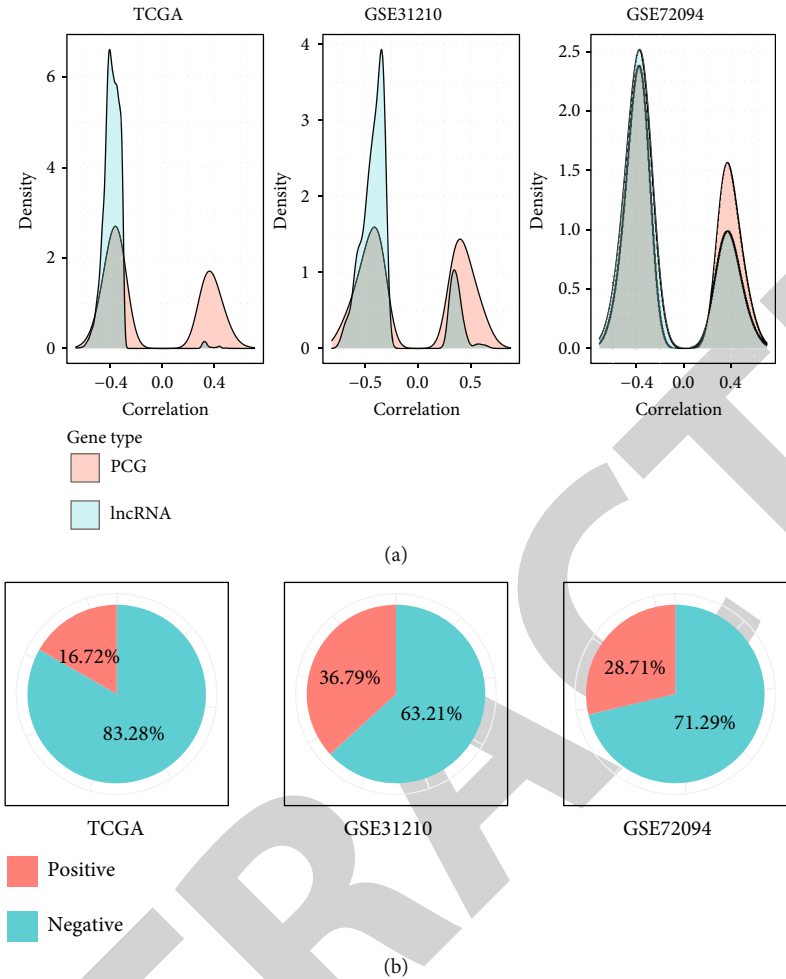
Figure 8: Continued.
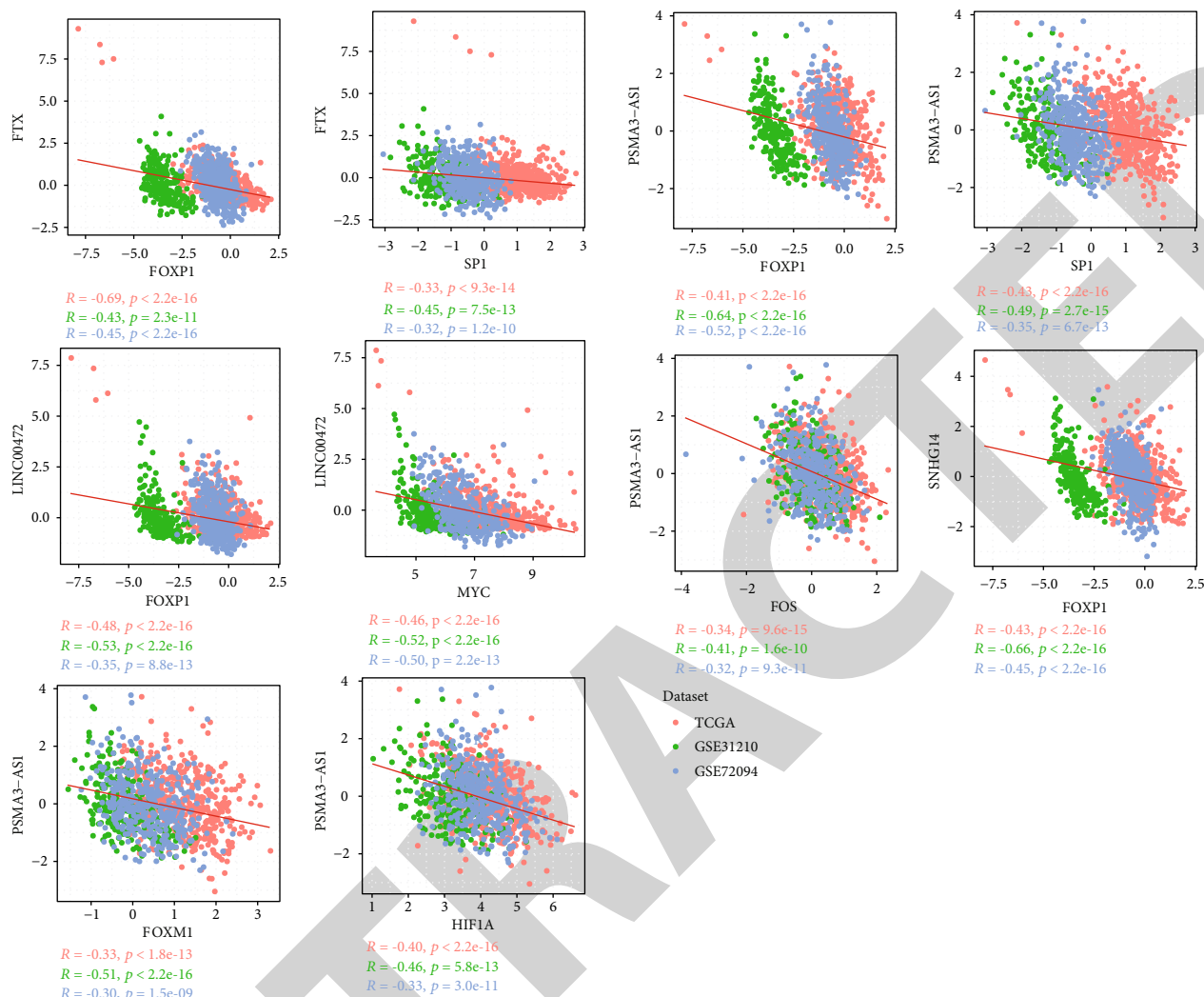
(d)

Figure 8: The relation between glycolysis-related lncRNAs and TFs. (a) The correlation analysis between glycolysis-related lncRNAs and PCGs in TCGA-LUAD, GSE31210, and GSE72094 datasets. Horizontal axis represents correlation coefficients, and vertical axis represents the density of corresponding coefficients. (b) The localization analysis of glycolysis-related lncRNAs based on LncATLAS database. Positive indicates lncRNAs localize in the cytoplasm (RCI > 0), and negative indicates nucleus (RCI < 0). (c) The distribution of upregulated TFs negatively correlated with glycolysis-related lncRNAs in three datasets. Freq: frequency. (d) The Pearson correlation analysis between TFs and glycolysis-related lncRNAs in three datasets. Pairs with coefficient ≤ −0.3 and $p < 0.05$ were presented.

expression of most TFs than other two groups (Figure 9(a)), and we also observed similar results in GSE31210 and GSE72094 datasets (Supplementary Figure S6), indicating that the upregulation of these TFs may be correlated with worse prognosis. Furthermore, we analyzed enriched pathways of these TFs, and a series of tumor-related pathways, such as PI3K-AKT signaling pathway, proteoglycans in cancer, cellular senescence, cell cycle, and small cell lung cancer, were annotated (Figure 9(b)). The above results demonstrated that glycolysis-related lncRNAs may be involved in tumor progression of LUAD through negatively regulating the expression of TFs.

3.8. Identification of Four Central Glycolysis-Related lncRNAs with Prognostic Significance for LUAD. First-order partial correlation was conducted among glycolysis score, the

expression of glycolysis-related lncRNAs, and glycolysis-related genes to examine the key role of glycolysis-related lncRNAs in regulating glycolysis (Figure 10(a)). As a result, four lncRNAs, LINC00511, LINC00472, ADAMTS9-AS2, and LINC00968, showed a strong correlation with glycolysis score and glycolysis-related genes. Moreover, the correlation between glycolysis score and glycolysis-related genes obviously weakened when these four lncRNAs were excluded, indicating that the four lncRNAs were closely involved in glycolysis-related pathways. Then, we identified the corresponding glycolysis-related genes of the four lncRNAs and applied gene enrichment analysis to screen enriched pathways. Several pathways closely associated with tumor development were enriched, for instance, cell cycle, p53 signaling pathway, DNA replication, and mismatch repair pathways (Figure 10(b)). In addition, we compared the expression of

(a)

(b)
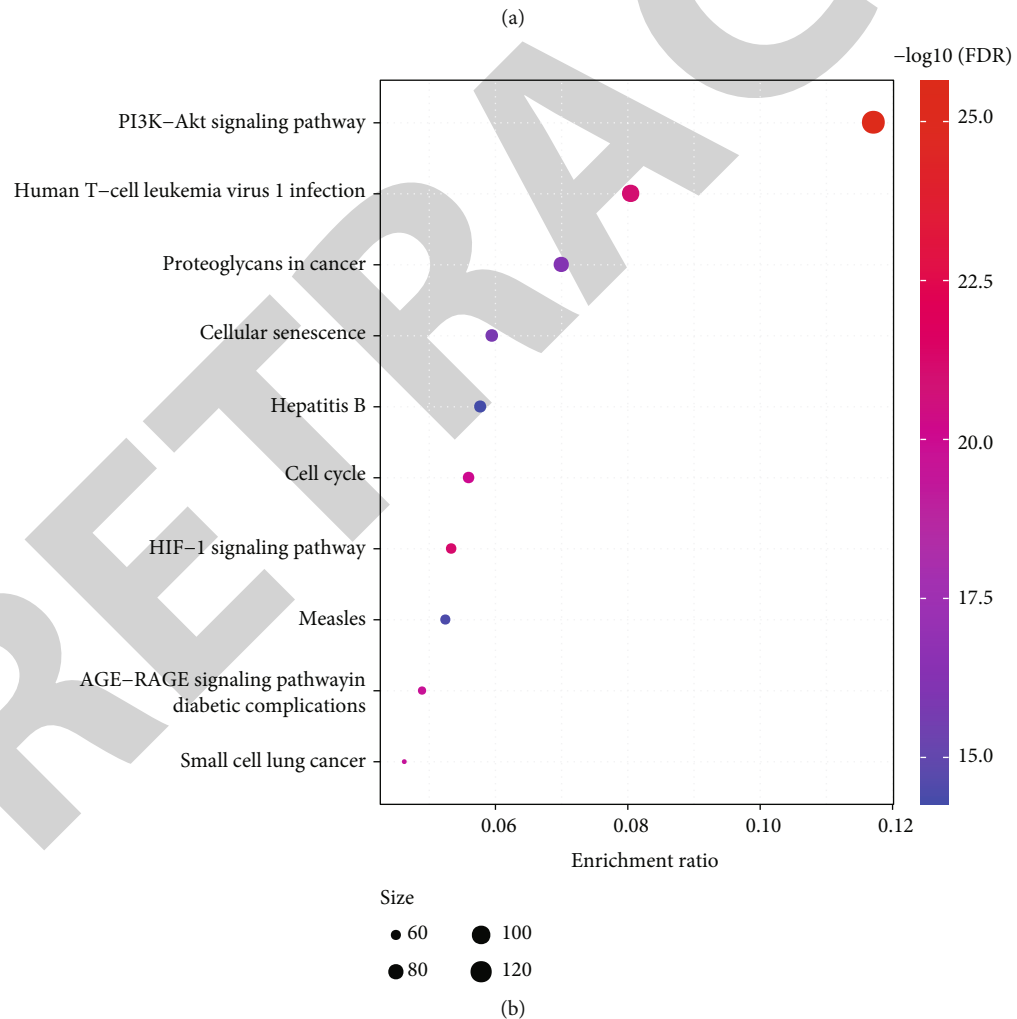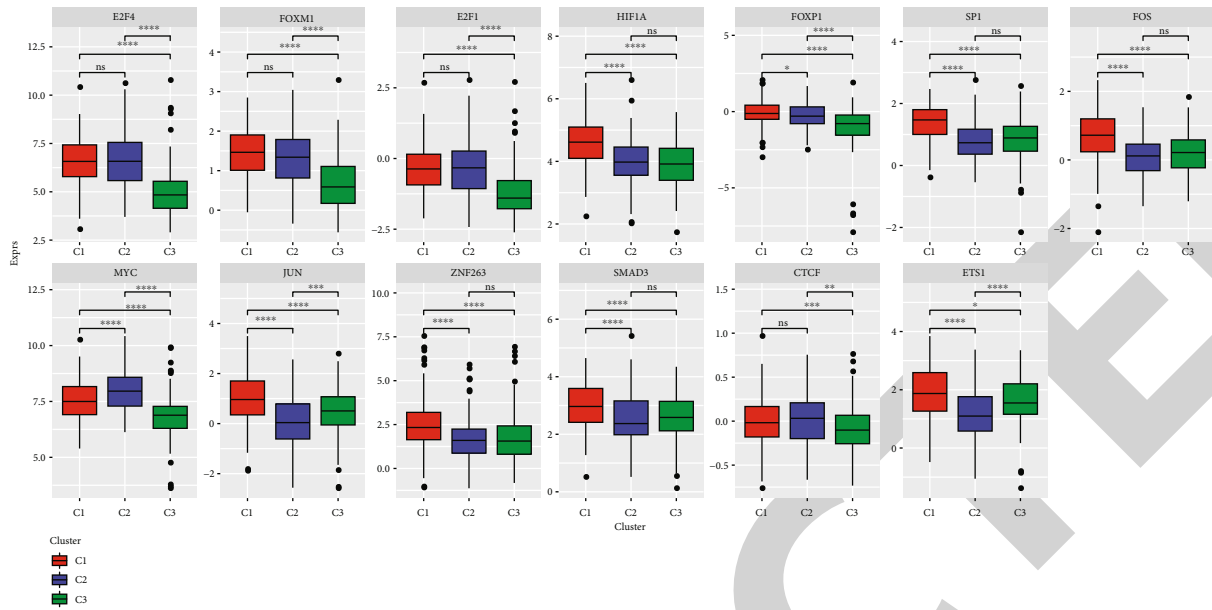
Figure 9: Analysis of possible mechanism of glycolysis-related lncRNAs regulating glycolysis. (a) The differential expression of 13 upregulated TFs negatively correlated with glycolysis-related lncRNAs in TCGA-LUAD dataset. ANOVA was performed. (b) Enriched pathways of TFs upregulated in C1 subtype in TCGA-LUAD dataset. ns: no significance. $^*p < 0.05$, $^{**}p < 0.01$, $^{***}p < 0.001$, $^{****}p < 0.0001$.

DataSet
- TCGA
- GSE31210
- GSE72094

Type
- Cor
- Par_cor
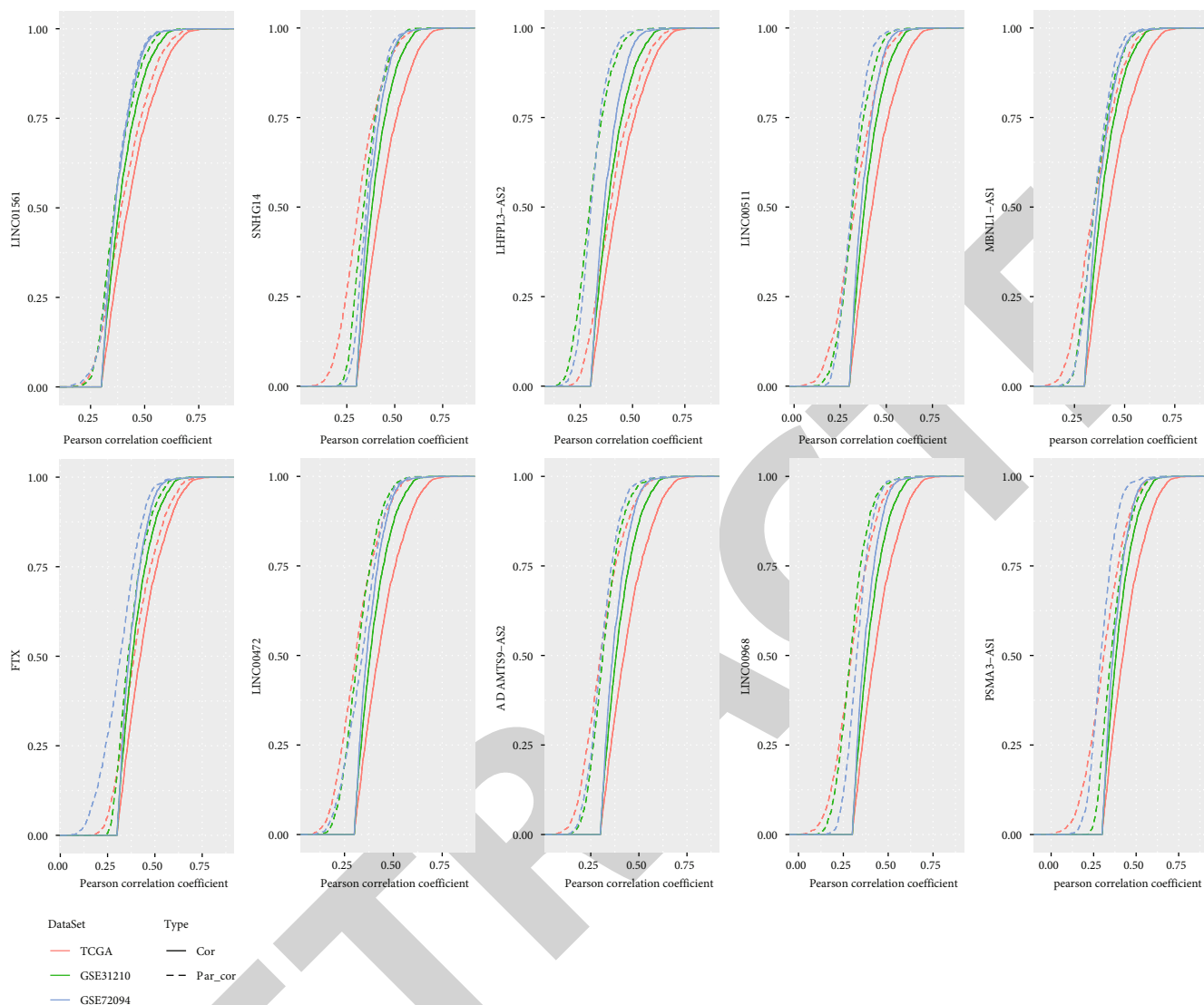
(a)

FIGURE 10: Continued.

(b)

Figure 10: Continued.

(c)

(d)

(e)
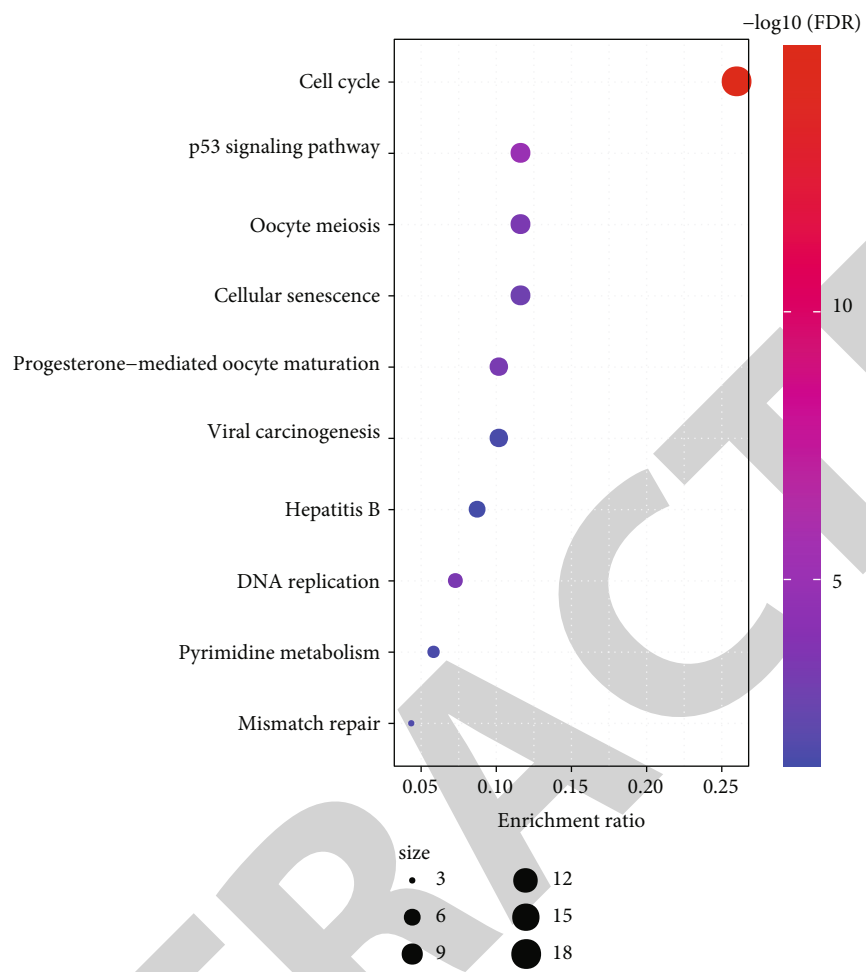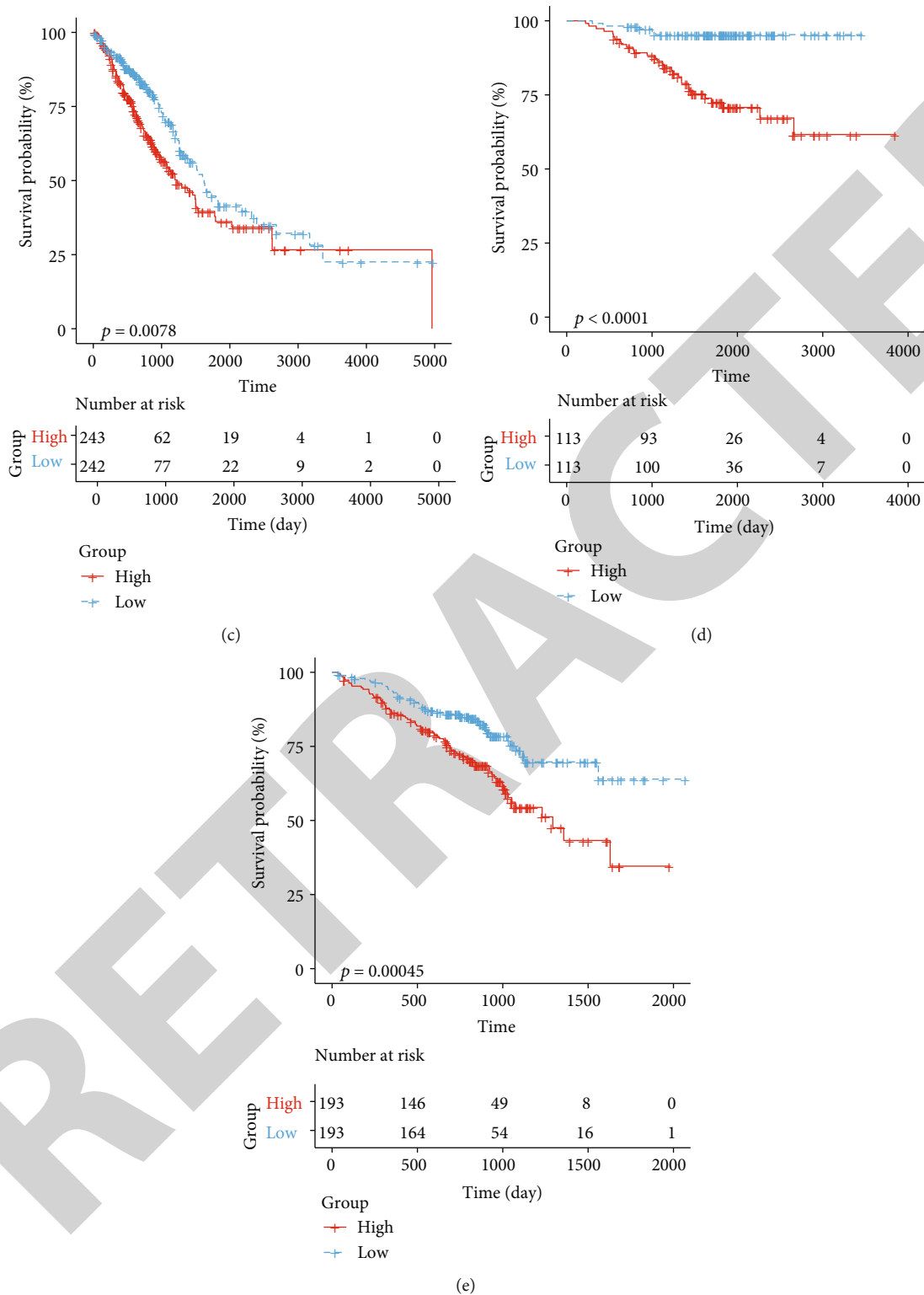
Figure 10: Identification of four glycolysis-related lncRNAs associated with prognosis. (a) A first order partial correlation analysis among glycolysis-related lncRNAs, glycolysis-related genes, and glycolysis score. Solid lines exhibit CDFs of correlation coefficients between glycolysis score and gene expression without adjustment. Dotted lines exhibit CDFs of correlation coefficients between glycolysis score and gene expression adjusted by first-order partial correlation. (b) Function analysis of genes significantly associated with four glycolysis-related lncRNAs in TCGA-LUAD dataset. Size indicates the number of genes. (c–d) Kaplan-Meier survival analysis of high-risk and low-risk groups in TCGA-LUAD (c), GSE31210 (d), and GSE72094 (e) datasets. Log-rank test was performed.

these four key lncRNAs between primary tumor samples and adjacent cancer normal tissue in the TCGA-LUAD cohort. It can be seen that the expression of these four key lncRNAs varied significantly in both tumor and normal samples. Among them, the LINC00511 expression was significantly higher in the tumor samples than in the normal samples. However, LINC00472, ADAMTS9 AS2, and LINC00968 were significantly higher in normal tissues than in tumor samples (Supplementary Figure S7A). Similarly, the four key lncRNAs are differentially expressed in the three molecular subtypes. The expression of LINC00511 in C1 and C2 subtypes is significantly higher than that in C3 subtypes (supplementary figure S7B). Furthermore, whether these four lncRNAs could serve as predictors to evaluate prognosis for LUAD patients was assessed by calculating the correlation coefficients between the four lncRNAs and overall survival, and a prognostic model was constructed. Each sample was calculated by the prognostic model for a risk score, which was converted to z-score for classifying samples into high-risk and low-risk groups. In three datasets, samples were all clearly classified into high-risk and low-risk groups, suggesting that these four lncRNAs could be indicators for predicting prognosis of LUAD (Figures 10(c)–10(e)).

4. Discussion

Previous research has demonstrated that glycolysis is more active in cancer cells than normal cells, and that some lncRNAs have been proven to serve as promoting or suppressing roles in orchestrating glycolysis-related pathways. However, a systematical exploration on relation between lncRNAs and glycolysis has not been studied with LUAD. Therefore, this study focused on examining the possible mechanisms of lncRNAs for coordinating glycolysis in LUAD based on a series of bioinformatics analysis.

We first identified 37 lncRNAs significantly associated with glycolysis score (calculated based on the expression of glycolysis-related genes) and subsequently classified three molecular subtypes according to the expression of these lncRNAs. Three molecular subtypes (C1, C2, and C3) exhibited distinct overall survival and differential glycolysis score in all three datasets, where C1 subtype had the worst prognosis and the highest glycolysis score and C3 was the converse. These molecular subtypes provided a preliminary evidence that glycolysis-related lncRNAs were involved in LUAD development. In the relation between subtypes and clinical features, the proportion of mild stages such as T0, N0, M0, and stage I was higher in C3 subtype. The observation further confirmed the subtyping and critical role of glycolysis-related lncRNAs in LUAD progression.

Following the above findings, the molecular subtypes can be a basis for discovering the functional pathways critically involved in tumor development. Therefore, differentially enriched pathways between C1 and C3 subtypes were screened based on hallmark genes. Apart from glycolysis pathways, other oncogenic pathways such as E2F target, G2M checkpoint, DNA repair, MYC targets, and EMT were also identified to be highly enriched in C1 subtype. E2F target, G2M checkpoint, and DNA

repair pathways are responsible to cell cycle progression and are associated with cancer progression [35–37]. We obtained information on the immune molecular subtypes of TCGA-LUAD from a previous study by Thorsson et al. [38], in which the authors classified lung adenocarcinomas into five immune molecular subtypes based on 160 different immune signatures, with the best prognosis was immune subtype C3. In addition, we compared the relationship between these five immune molecular subtypes and the three molecular subtypes we identified (Supplementary Figure S8), and the analysis showed that the immune subtype C3 subtype occupied more of the C3 molecular subtype we defined, whereas in Vesteinn Thorsson's study the immune molecular subtype C3 (inflammatory) molecularly characterised by elevated Th17 and Th1 genes, low to moderate tumor cell proliferation, lower levels of aneuploidy, and overall somatic cell copy number alterations than the other subtypes, and in terms of prognostic analysis, the C3 subtype has the best prognosis of the five immune subtype molecular subtypes, which is consistent with our molecular subtype C3 having the best prognosis, and we also found a poorer prognosis of the immune molecular subtypes C1, C2, C4, and C6 occupy more of the C1 and C2 subtypes in our study, which is also consistent with the poorer prognosis of C1 and C2.

Studies suggested that E2F target is a potential therapeutic target in lung cancer. The inhibitor HLM006474 of E2F target can reduce the viability of NSCLC cell lines [39]. Park et al. found that lncRNA-EPEL promotes lung cancer cell proliferation through activating E2F target pathway, and EPEL could be a potential target for therapeutic treatments [40]. G2M checkpoint is associated with DNA damage and genome stability, and a less efficient G2M checkpoint was proven to be significantly correlated with lung cancer risk [41]. In addition, through genotype-phenotype correlation analysis, Zheng et el. showed that polymorphisms in cell cycle and DNA repair can modulate the function of G2M checkpoint in lung cancer [41]. Compared with C3 subtype, C1 subtype demonstrated a significantly high level of genetic variations, especially *TP53* gene involved in cell cycle. A large number of copy number variations in C1 subtype will lead to high genome instability. A positive correlation between genome instability and glycolysis score was presented in this study. Apart from the mild correlation, we found a supplementary evidence that genome instability was responsible for aberrant suppression or activation of cell cycle pathways, which therefore contributed to dysregulation of glycolysis-related lncRNAs. EMT is a pivotal process that facilitates cell development and cancer progression, especially when in an active state in aggressive cancers [42]. EMT signatures are considered as indicators of unfavorable prognosis in many cancer types, including lung cancer [43, 44]. Evidence indicates that EMT can promote glycolysis and increases glycolytic dependency [45, 46], which also makes it sensible that C1 subtype with the highest glycolysis activity showed high enrichment of EMT signaling pathway.

As the subtyping was validated to be reliable, we further analyzed whether these subtypes could guide personalized therapy. Immunotherapy as a promising strategy for cancer treatment has been investigated in many cancer types and manifested satisfactory outcomes in partial clinical trials [47,

48]. Lines of immune checkpoint inhibitors (ICIs) have been tested in metastatic NSCLC, and some have been approved by the United States Food and Drug Administration (FDA), for instance, nivolumab [49], pembrolizumab [50], and atezolizumab [51]. Although patients with advanced NSCLC can benefit from these ICIs, still some are not sensitive to these drugs. In the present study, C1 and C3 subtypes showed a higher expression level of ICIs and immune infiltration than C2 subtype. Theoretically, C1 and C3 subtypes are both suitable objects for receiving immune checkpoint blockade (ICB) therapy, but TIDE analysis predicted that only C3 subtype can benefit the most from immunotherapy. We speculated that the possible reason for this result was due to the high activation of EMT in C1 subtype. Apart from the promoting role of EMT in cancer metastasis, drug resistance driven by EMT has also been recognized [52, 53]. As Thompson et al. proposed that responders to ICB in lung cancer have higher EMT signature scores than nonresponders, while higher inflammatory scores is observed in the responders [54], EMT status is a restrictive factor for ICB therapy. Therefore, C3 subtype may be the optimal object for receiving immunotherapy. The subtyping can provide a guidance for deciding personalized therapy for lung cancer patients.

Furthermore, we investigated the possible mechanism of glycolysis-related lncRNAs in modulating glycolysis and found that the majority of glycolysis-related lncRNAs had a negative relation with the expression of protein coding genes related to glycolysis, indicating a negative regulation between lncRNAs and glycolysis genes. These lncRNAs mostly localized in the nucleus, which demonstrated that they functioned the role prior to protein coding or gene transcription. We further examined the relation between lncRNAs and TFs, and significant correlations among four lncRNAs (FTX, LINC00472, PSMA3-AS1, and SNHG14) and six TFs (FOXP1, SP1, MYC, FOXM1, HIF1A, and FOS) were shown by Pearson correlation analysis.

FOXP1 is associated with prognosis of various malignant tumors, and low expression or loss of FOXP1 is predictive of poor prognosis of lung cancer [55, 56]. Hsu et al. proved that overexpression of SP1 can upregulate the expression of E-cadherin, a suppressor of metastasis, and downregulated expression level of SP1 was shown in invasive late-stage LUAD model in mice [57]. In our result, although elevated expression was observed in LUAD patients, higher expression of SP1 was shown in C1 subtypes than other two subtypes. MYC is an oncogene in many cancers and also serve as a metastatic gene in NSCLC [58]. Xu et al. found that FOXM1 can promote tumor progression through EMT, and that knockdown of FOXM1 can suppress the metastatic abilities in NSCLC cells [59]. High FOXM1 expression was also shown in C1 subtype. Overexpression of HIF1A is common in NSCLC, and it is associated with activation of angiogenic factors and a poor prognosis [60]. Consistent with the previous study, C1 subtype exhibited high expression level of HIF1A. The FOS family also plays an important role in tumorgenesis, but its overexpression results in different outcomes depending on different cancer types [61]. Collectively, the aberrant expression of six TFs was all found to be involved in tumorgenesis or tumor progression possibly through the interactions with the four lncRNAs and thus contributed to a worse prognosis of C1 subtype.

Finally, we identified four key glycolysis-related lncRNAs closely involved in oncogenic pathways such as cell cycle and p53 signaling pathway. We also proposed a four-lncRNA prognostic model with clinical significance in classifying LUAD patients into high-risk and low-risk groups. These four lncRNAs could be indicators for early screening of LUAD.

5. Conclusions

In conclusion, this study identified three molecular subtypes with distinct prognosis based on glycolysis-related lncRNAs and confirmed the subtyping through assessing their clinical features and genetic variations. Moreover, the subtyping could guide the personalized therapy, and C3 subtype was supposed to be the optimal group for receiving immunotherapy. The possible mechanism of glycolysis-related lncRNAs involved in tumor progression was possibly realized through interacting with the six critical TFs. Lastly, we constructed a four-lncRNA prognostic model predictive of LUAD prognosis and could serve as an indicator for LUAD patients.

Abbreviations

CDF:	Cumulative distribution function
CNVs:	Copy number variations
DCs:	Dendritic cells
EGFR:	Epidermal growth factor receptor gene
EMT:	Epithelial mesenchymal transition
ESTIMATE:	Estimation of STromal and Immune cells in MAlignant Tumours using Expression data
FDA:	The United States Food and Drug Administration
FDR:	False discovery rate
GEO:	Gene expression omnibus
ICB:	Immune checkpoint blockade
KRAS:	Kirsten rat sarcoma viral oncogene homolog
lncRNAs:	Long noncoding RNAs
LUAD:	Lung adenocarcinoma
MSigDB:	Molecular signatures database
NES:	Normalized enrichment score
NSCLC:	Non-small-cell lung cancer
OS:	Overall survival
PCGs:	Protein-coding genes
RCI:	Relative concentration index
ssGSEA:	Single sample gene set enrichment analysis
TCGA:	The Cancer Genome Atlas
TFs:	Transcription factors.

Data Availability

The data used to support the findings of this study are included within the article.

Conflicts of Interest

The authors declare that they have no competing interest.

Authors' Contributions

Peng Cao, Bo Zhao, and Yajie Xiao contribute equally to this work and are co-first authors.

Acknowledgments

Supplementary Materials

Supplementary 1. Supplementary Figure S1: the relation between molecular subtypes and clinical features in GSE31210 (A-C) and GSE72094 (D-G) datasets. ANOVA was performed.

Supplementary 2. Supplementary Figure S2: the comparison of distribution of 24 immune cells between C1 and C3 subtypes. Student's t-test was performed. ns: no significance. $^*p < 0.05$, $^{**}p < 0.01$, $^{***}p < 0.001$, $^{****}p < 0.0001$.

Supplementary 3. Supplementary Figure S3: unsupervised consensus clustering for immune cell infiltration in C1 and C3 subtypes in TCGA-LUAD (A), GSE31210 (B), and GSE72094 (C) datasets.

Supplementary 4. Supplementary Figure S4: the normalized gene expression of immune checkpoints in three datasets grouped by molecular subtypes. ANOVA was performed. ns: no significance. $^*p < 0.05$, $^{**}p < 0.01$, $^{***}p < 0.001$, $^{****}p < 0.0001$.

Supplementary 5. Supplementary Figure S5: the localization of 37 glycolysis-related lncRNAs in 15 types of cell lines. Blue-green indicates lncRNAs localized in the nucleus, and red indicates in the cytoplasm.

Supplementary 6. Supplementary Table S1: differential TF activity among three subtypes in TCGA-LUAD, GSE72094, and GSE31210 datasets based on aREA algorithm. ANOVA was performed.

Supplementary 7. Supplementary Figure S6: the expression of 13 TFs in GSE31210 (A) and GSE72094 (B) datasets grouped by molecular subtypes. ANOVA was performed. ns: no significance. $^*p < 0.05$, $^{**}p < 0.01$, $^{***}p < 0.001$, $^{****}p < 0.0001$.

Supplementary 8. Supplementary Figure S7: expression difference of four lncRNAs. (A) Differential expression of four lncRNAs in cancer and adjacent tissues. (B) Expression differences of four lncRNAs in different molecular subtypes.

Supplementary 9. Supplementary Figure S8: intersection of the three molecular subtypes with the five immune molecular subtypes previously reported by Vesteinn Thorsson's et al.

References

[1] H. Sung et al., "Global cancer statistics 2020: GLOBOCAN estimates of incidence and mortality worldwide for 36 cancers in 185 countries," *CA: a Cancer Journal for Clinicians*, vol. 71, no. 3, pp. 209–249, 2021.

[2] K. Jao et al., "The prognostic effect of single and multiple cancer-related somatic mutations in resected non-small-cell lung cancer," *Lung cancer (Amsterdam, Netherlands)*, vol. 123, pp. 22–29, 2018.

[3] S. Yang, X. Yu, Y. Fan, X. Shi, and Y. Jin, "Clinicopathologic characteristics and survival outcome in patients with advanced lung adenocarcinoma andKRASmutation," *Journal of Cancer*, vol. 9, no. 16, pp. 2930–2937, 2018.

[4] T. C. Hsia, J. A. Liang, C. C. Li, and C. R. Chien, "Comparative effectiveness of concurrent chemoradiotherapy versus EGFR-tyrosine kinase inhibitors for the treatment of clinical stage IIIb lung adenocarcinoma patients with mutant EGFR," *Thoracic cancer*, vol. 9, no. 11, pp. 1398–1405, 2018.

[5] J. Byun et al., "Genome-wide association study of familial lung cancer," *Carcinogenesis*, vol. 39, no. 9, pp. 1135–1140, 2018.

[6] J. J. Lin et al., "Five-year survival in EGFR-mutant metastatic lung adenocarcinoma treated with EGFR-TKIs," *Journal of Thoracic Oncology: Official Publication of the International Association for the Study of Lung Cancer*, vol. 11, no. 4, pp. 556–565, 2016.

[7] M. C. Jiang, J. J. Ni, W. Y. Cui, B. Y. Wang, and W. Zhuo, "Emerging roles of lncRNA in cancer and therapeutic opportunities," *American Journal of Cancer Research*, vol. 9, no. 7, pp. 1354–1366, 2019.

[8] M. Qiu, Y. Xu, J. Wang et al., "A novel lncRNA, LUADT1, promotes lung adenocarcinoma proliferation via the epigenetic suppression of p27," *Cell Death & Disease*, vol. 6, no. 8, article e1858, 2015.

[9] H. X. Dong, R. Wang, X. Y. Jin, J. Zeng, and J. Pan, "LncRNA DGCR5 promotes lung adenocarcinoma (LUAD) progression via inhibiting hsa-mir-22-3p," *Journal of Cellular Physiology*, vol. 233, no. 5, pp. 4126–4136, 2018.

[10] J. Sui et al., "Integrated analysis of long non-coding RNA-associated ceRNA network reveals potential lncRNA biomarkers in human lung adenocarcinoma," *International Journal of Oncology*, vol. 49, no. 5, pp. 2023–2036, 2016.

[11] J. Wang, X. Yin, Y. Q. Zhang, and X. Ji, "Identification and validation of a novel immune-related four-lncRNA signature for lung adenocarcinoma," *Frontiers in Genetics*, vol. 12, article 639254, 2021.

[12] K. S. Gill, P. Fernandes, T. R. O'Donovan et al., "Glycolysis inhibition as a cancer treatment and its role in an anti-tumour immune response," *Biochimica et Biophysica Acta*, vol. 1866, no. 1, pp. 87–105, 2016.

[13] X. B. Li, J. D. Gu, and Q. H. Zhou, "Review of aerobic glycolysis and its key enzymes - new targets for lung cancer therapy," *Thoracic cancer*, vol. 6, no. 1, pp. 17–24, 2015.

[14] L. Wang et al., "LncRNA LINC00857 regulates lung adenocarcinoma progression, apoptosis and glycolysis by targeting miR-1179/SPAG5 axis," *Human Cell*, vol. 33, no. 1, pp. 195–204, 2020.

[15] Q. Hua et al., "LINC01123, a c-Myc-activated long noncoding RNA, promotes proliferation and aerobic glycolysis of non-small cell lung cancer through miR-199a-5p/c-Myc axis," *Journal of Hematology & Oncology*, vol. 12, no. 1, p. 91, 2019.

[16] W. Gao et al., "Long non-coding RNA NORAD promotes cell proliferation and glycolysis in non-small cell lung cancer by acting as a sponge for miR-136-5p," *Molecular Medicine Reports*, vol. 19, no. 6, pp. 5397–5405, 2019.

[17] M. Yamauchi et al., "Epidermal growth factor receptor tyrosine kinase defines critical prognostic genes of stage I lung adenocarcinoma," *PLoS One*, vol. 7, no. 9, article e43923, 2012.

[18] M. B. Schabath et al., "Differential association of STK11 and TP53 with KRAS mutation-associated gene expression, proliferation and immune surveillance in lung adenocarcinoma," *Oncogene*, vol. 35, no. 24, pp. 3209–3216, 2016.

[19] H. Jiang and W. H. Wong, "SeqMap: mapping massive amount of oligonucleotides to the genome," *Bioinformatics*, vol. 24, no. 20, pp. 2395-2396, 2008.

[20] A. Frankish et al., "Gencode 2021," *Nucleic Acids Research*, vol. 49, no. D1, pp. D916–D923, 2021.

[21] A. Liberzon et al., "The molecular signatures database (MSigDB) hallmark gene set collection," *Cell Systems*, vol. 1, no. 6, pp. 417–425, 2015.

[22] S. Hanzelmann, R. Castelo, and J. Guinney, "GSVA: gene set variation analysis for microarray and RNA-seq data," *BMC Bioinformatics*, vol. 14, no. 1, p. 7, 2013.

[23] M. D. Wilkerson and D. N. Hayes, "ConsensusClusterPlus: a class discovery tool with confidence assessments and item tracking," *Bioinformatics*, vol. 26, no. 12, pp. 1572-1573, 2010.

[24] G. Yu, L. G. Wang, Y. Han, and Q. Y. He, "clusterProfiler: an R package for comparing biological themes among gene clusters," *OMICS*, vol. 16, no. 5, pp. 284–287, 2012.

[25] B. Chen, M. S. Khodadoust, C. L. Liu, A. M. Newman, and A. A. Alizadeh, "Profiling tumor infiltrating immune cells with CIBERSORT," *Methods in Molecular Biology*, vol. 1711, pp. 243–259, 2018.

[26] K. Yoshihara et al., "Inferring tumour purity and stromal and immune cell admixture from expression data," *Nature Communications*, vol. 4, p. 2612, 2013.

[27] P. Jiang et al., "Signatures of T cell dysfunction and exclusion predict cancer immunotherapy response," *Nature Medicine*, vol. 24, no. 10, pp. 1550–1558, 2018.

[28] L. Garcia-Alonso et al., "Transcription factor activities enhance markers of drug sensitivity in cancer," *Cancer Research*, vol. 78, no. 3, pp. 769–780, 2018.

[29] M. J. Alvarez et al., "Functional characterization of somatic mutations in cancer using network-based inference of protein activity," *Nature Genetics*, vol. 48, no. 8, pp. 838–847, 2016.

[30] R. Beroukhim et al., "The landscape of somatic copy-number alteration across human cancers," *Nature*, vol. 463, no. 7283, pp. 899–905, 2010.

[31] A. Mayakonda, D. C. Lin, Y. Assenov, C. Plass, and H. P. Koeffler, "Maftools: efficient and comprehensive analysis of somatic variants in cancer," *Genome Research*, vol. 28, no. 11, pp. 1747–1756, 2018.

[32] Y. Şenbabaoğlu et al., "Tumor immune microenvironment characterization in clear cell renal cell carcinoma identifies prognostic and immunotherapeutically relevant messenger RNA signatures," *Genome Biology*, vol. 17, no. 1, p. 231, 2016.

[33] L. L. Chen, "Linking long noncoding RNA localization and function," *Trends in Biochemical Sciences*, vol. 41, no. 9, pp. 761–772, 2016.

[34] J. J. Quinn and H. Y. Chang, "Unique features of long noncoding RNA biogenesis and function," *Nature Reviews. Genetics*, vol. 17, no. 1, pp. 47–62, 2016.

[35] L. N. Kent and G. Leone, "The broken cycle: E2F dysfunction in cancer," *Nature Reviews. Cancer*, vol. 19, no. 6, pp. 326–338, 2019.

[36] M. Löbrich and P. A. Jeggo, "The impact of a negligent G2/M checkpoint on genomic instability and cancer induction," *Nature Reviews. Cancer*, vol. 7, no. 11, pp. 861–869, 2007.

[37] N. J. Curtin, "DNA repair dysregulation from cancer driver to therapeutic target," *Nature Reviews. Cancer*, vol. 12, no. 12, pp. 801–817, 2012.

[38] V. Thorsson, D. L. Gibbs, S. D. Brown et al., "The immune landscape of cancer," *Immunity*, vol. 48, no. 4, pp. 812–830.e14, 2018.

[39] C. A. Kurtyka, L. Chen, and W. D. Cress, "E2F inhibition synergizes with paclitaxel in lung cancer cell lines," *PLoS One*, vol. 9, no. 5, article e96357, 2014.

[40] S. M. Park et al., "The LncRNA EPEL promotes lung cancer cell proliferation through E2F target activation," *Cellular Physiology and Biochemistry : International Journal of Experimental Cellular Physiology, Biochemistry, and Pharmacology*, vol. 45, no. 3, pp. 1270–1283, 2018.

[41] Y. L. Zheng et al., "Elevated lung cancer risk is associated with deficiencies in cell cycle checkpoints: genotype and phenotype analyses from a case-control study," *International Journal of Cancer*, vol. 126, no. 9, pp. 2199–2210, 2010.

[42] Y. Zhang and R. A. Weinberg, "Epithelial-to-mesenchymal transition in cancer: complexity and opportunities," *Frontiers of medicine*, vol. 12, no. 4, pp. 361–373, 2018.

[43] M. J. Schliekelman et al., "Molecular portraits of epithelial, mesenchymal, and hybrid states in lung adenocarcinoma and their relevance to survival," *Cancer Research*, vol. 75, no. 9, pp. 1789–1800, 2015.

[44] T. Sowa et al., "Association between epithelial-mesenchymal transition and cancer stemness and their effect on the prognosis of lung adenocarcinoma," *Cancer Medicine*, vol. 4, no. 12, pp. 1853–1862, 2015.

[45] Y. Kondaveeti, I. K. Guttilla Reed, and B. A. White, "Epithelial-mesenchymal transition induces similar metabolic alterations in two independent breast cancer cell lines," *Cancer Letters*, vol. 364, no. 1, pp. 44–58, 2015.

[46] H. Kang, H. Kim, S. Lee, H. Youn, and B. Youn, "Role of metabolic reprogramming in epithelial‐mesenchymal transition (EMT)," *International Journal of Molecular Sciences*, vol. 20, no. 8, 2019.

[47] S. Kruger et al., "Advances in cancer immunotherapy 2019 - latest trends," *Journal of experimental & clinical cancer research : CR*, vol. 38, no. 1, p. 268, 2019.

[48] K. Esfahani, L. Roudaia, N. Buhlaiga, S. V. del Rincon, N. Papneja, and W. H. Miller, "A review of cancer immunotherapy: from the past, to the present, to the future," *Current oncology (Toronto, Ont.)*, vol. 27, no. 12, pp. 87–s97, 2020.

[49] D. Kazandjian et al., "FDA approval summary: nivolumab for the treatment of metastatic non-small cell lung cancer with progression on or after platinum-based chemotherapy," *The Oncologist*, vol. 21, no. 5, pp. 634–642, 2016.

[50] R. S. Herbst et al., "Pembrolizumab versus docetaxel for previously treated, PD-L1-positive, advanced non-small-cell lung cancer (KEYNOTE-010): a randomised controlled trial," *Lancet (London, England)*, vol. 387, no. 10027, pp. 1540–1550, 2016.

[51] C. Weinstock, S. Khozin, D. Suzman et al., "U.S. Food and Drug Administration Approval Summary: Atezolizumab for

Retraction

Retracted: Mechanism of Gegen Qinlian Decoction Regulating ABTB1 Expression in Colorectal Cancer Metastasis Based on PI3K/AKT/FOXO1 Pathway

BioMed Research International

This article has been retracted by Hindawi following an investigation undertaken by the publisher [1]. This investigation has uncovered evidence of one or more of the following indicators of systematic manipulation of the publication process:

(1) Discrepancies in scope

(2) Discrepancies in the description of the research reported

(3) Discrepancies between the availability of data and the research described

(4) Inappropriate citations

(5) Incoherent, meaningless and/or irrelevant content included in the article

(6) Manipulated or compromised peer review

The presence of these indicators undermines our confidence in the integrity of the article's content and we cannot, therefore, vouch for its reliability. Please note that this notice is intended solely to alert readers that the content of this article is unreliable. We have not investigated whether authors were aware of or involved in the systematic manipulation of the publication process.

Wiley and Hindawi regrets that the usual quality checks did not identify these issues before publication and have since put additional measures in place to safeguard research integrity.

We wish to credit our own Research Integrity and Research Publishing teams and anonymous and named external researchers and research integrity experts for contributing to this investigation.

The corresponding author, as the representative of all authors, has been given the opportunity to register their agreement or disagreement to this retraction. We have kept a record of any response received.

References

[1] F. Li, L. Chen, J. Zheng et al., "Mechanism of Gegen Qinlian Decoction Regulating ABTB1 Expression in Colorectal Cancer Metastasis Based on PI3K/AKT/FOXO1 Pathway," *BioMed Research International*, vol. 2022, Article ID 8131531, 7 pages, 2022.

Research Article

Mechanism of Gegen Qinlian Decoction Regulating ABTB1 Expression in Colorectal Cancer Metastasis Based on PI3K/AKT/FOXO1 Pathway

Feng Li, Lili Chen, Jinzhou Zheng, Jianfeng Yang, Xiaoyun Song, Yu Wang, and Xiqiu Zhou [ID]

Department of General Surgery, Pudong Branch, Longhua Hospital Affiliated to Shanghai University of Traditional Chinese Medicine, Shanghai 200126, China

Correspondence should be addressed to Xiqiu Zhou; guanzi982842@163.com

It was to investigate the role of Gegen Qinlian decoction (GQD) in the regulation of ABTB1 gene based on PI3K/AKT/FOXO1 signaling pathway in colorectal cancer (CRC) metastasis. In this study, 10 cases of the CRC mouse model were established by inoculating CT26 cells into the spleen of mice, which were divided into the experimental group and the control group, 5 cases in each group; the control group was intragastrically administered with normal saline 0.3 mL/d, and the experimental group was intragastrically administered with GQD 0.2 mL/d at a ratio of 0.2 g medicinal materials/10 g for 10 days and sacrificed, and pathological sections were made. The expression density of signaling pathway PI3K/AKT/FOXO1 as well as gene ABTB1 was detected in the sections of the two groups, and the mechanism of action of this gene in the two groups of mice was studied. It was found that the densities of p-PI3K, p-AKT, and p-FOXO1 in the experimental group of mice were 26.55 g/cm^3, 70.2 g/cm^3, and 24.36 g/cm^3, respectively, which were significantly increased compared with the control group, $P < 0.05$; the density of ABTB1 was 35.4 g/cm^3, which was significantly increased compared with the control group, $P < 0.05$; the proliferation and migration ability of CRC cells in the experimental group were significantly decreased, $P < 0.05$. GQD can promote the expression of ABTB1 by activating the PI3K/AKT/FOXO1 signaling pathway, in order to inhibit the proliferation and growth ability of CRC cells.

1. Introduction

Colorectal cancer (CRC) is a common malignant tumor in the gastrointestinal tract. Globally, the incidence of CRC in males and females ranks the third and second most common malignant tumors, respectively, and its incidence is increasing to varying degrees in most countries in the world [1]. China belongs to a low-incidence area in the world. In recent years, with the continuous improvement of people's living standards and changes in dietary habits, the incidence of CRC in China has shown a significant increase in many areas [2]. The disease is more common in middle-aged men, most common between 40 and 70 years of age, with

an incidence of about 2 : 1 in men and women. It can occur in any part of the colon or rectum, with the rectum and sigmoid colon being the most common, followed by the cecum, ascending colon, descending colon, and transverse colon [3]. It can be diagnosed by clinical manifestations, X-ray barium enema, or fiberoptic colonoscopy. Pathology shows adenocarcinoma, and a few are squamous cell carcinoma and mucinous carcinoma. The modes of CRC metastasis are lymphatic metastasis, blood metastasis, and direct spread, which account for the fourth most common malignant tumor and fatal factor, and recurrence and metastasis are the main causes of death in CRC patients [4, 5]. Early detection, early diagnosis, and radical surgery are the key to

treatment. Although the 5-year survival rate of early CRC is high after operation, the long-term survival rate and prognosis of advanced CRC are still poor [6]. How to improve the therapeutic effect and survival rate of CRC has been the goal of scientists' research.

Gegen Qinlian decoction (GQD) is a classic prescription for the treatment of damp-heat syndrome in *Treatise on Cold-Attack* [7], with the effect of relieving superficies and clearing interior, governing the treatment of body heat, dry mouth, asthma and sweating, red tongue, yellow tongue fur, fast pulse rate, and intermittent stop [8]. Its clinical application has reached more than 2,000 years, the formula contains four kinds of medicinal materials of Gegen (15 g), Zhigancao (6 g), baical skullcap root (9 g), and Huanglian (9 g), which can be used with eight liters of water, first boiling Gegen, remaining six liters of water, and then other herbs are added, and they all are boiled to two liters, filtration to remove dregs, and airing soup until warm [9, 10]. GQD is mainly used for the treatment of type 2 diabetes and ulcerative colitis (UC). Studies showed that PI3K/AKT/FOXO1 signaling pathway is closely related to tumor cell growth, proliferation, survival, apoptosis, metabolism, angiogenesis, invasion and metastasis, tumor resistance, and tumor immune escape [11, 12]. However, in CRC, there are few reports on the gene regulation of ABTB1 (broad complex, tramtrack and bric a brac/poxviruses and zinc finger, BTB/POZ) by GQD based on PI3K/AKT/FOXO1 signaling pathway. It was found that GQD based on PI3K/AKT/FOXO1 signaling pathway plays an important role in the regulation of ABTB1 gene in rectal cancer metastasis [13]. Therefore, in this study, CT26 cells in logarithmic growth phase were inoculated into the spleen of BLACK/C mice to establish a colorectal cancer mouse model. The effect of GQD on the expression of ABTB1 by activating the PI3K/AKT/FOXO1 signaling pathway was studied, which provided certain experimental data for the therapeutic effect of ABTB1 gene in colorectal cancer and new research directions for the treatment of colorectal cancer.

2. Materials and Methods

2.1. Experimental Materials.
In this study, the test animals were mice of BLACK/C strain provided by the Experimental Animal Center, with the number of 10 mice (F: M = 1 : 1) and body weight of 180-220 g. The experiment was completed in the Experimental Animal Center and the Pathology Laboratory. After the completion of animal experiment, the professional personnel restored the original appearance of animal carcass (skin suture, etc.), and the institution recognized by the environmental protection department performed harmless treatment such as incineration.

2.2. Instruments, Equipment, and Main Reagents.
Table 1 is the instruments, equipment, and main reagents required during the experiment.

According to the animal mouse model, this study selected the most suitable and most used instruments and equipment in clinical practice in recent years, which was conducive to our experimental operation and results closer

to clinical practice, and laid a good foundation for the clinical application and promotion of this study in the future.

2.3. Model Preparation and Experimental Method.
Ten black/C mice were divided into two groups according to the random number table: control group and experimental group, with five mice in each group. In both groups, CT26 cells in the logarithmic growth phase were inoculated into the spleen to establish a mouse model of CRC. Mice in the control group: 0.3 mL of normal saline was intragastrically administered per day; mice in the experimental group: 0.2 mL of GQD was intragastrically administered per day at a ratio of 0.2 g of medicinal materials/10 g; both groups were intragastrically administered once a day for 10 days and sacrificed and pathological sections were made. Enzyme-linked immunosorbent assay kit was used for both groups of sections (preparation method: known antigens or antibodies were adsorbed on the surface of solid phase carrier (i.e. polystyrene microreaction plate), so that the enzyme-labeled antigen-antibody reaction was performed here. The free components in the liquid phase were removed by washing method). The expression of PI3K/AKT/FOXO1 signaling pathway was detected, and the expression of the ABTB1 gene was also detected by real-time quantitative PCR (extraction and quality detection of total RNA ⟶ synthesis of cDNA by reverse transcription reaction ⟶ PCR reaction ⟶ result analysis) Finally, the rectal cancer cells in the two groups of mice were subjected to scratch assay and transwell assay (steps: preparation of transwell chamber ⟶ preparation of cell suspension ⟶ inoculation of cells ⟶ statistics of results) to observe the expression of p-PI3K, p-AKT, p-FOXO1, and ABTB1 in mice.

2.4. Statistical Treatment.
All data were statistically analyzed by SPSS17.0 software package. The measurement data of each group were expressed by mean ± standard deviation, the expression level of ABTB1 was compared by t-test, and the mean of two samples was compared by independent sample t-test. The positive rates of p-PI3K, p-AKT, and p-FOXO1were tested by chi-square test and Fisher's exact probability method. When $P < 0.05$, the difference was statistically significant.

3. Results

3.1. General Performance of Mice.
After mice were inoculated with CT26 cells in the spleen, the anorectal temperature measured within 2 days increased to a certain extent, ranging from 37.6°C to 38.0°C, with fluffy hair, crouching and laziness, and loss of appetite, but no other significant changes; on the third day, the anal temperature increased to about 38.5°C, most mice lost weight, some had soft or loose stools, and some had mucopurulent bloody stools. Four days after given GQD by gavage, the anal temperature of experimental group began to decrease, the temperature fluctuated to around 37.8°C, and the symptoms of loose stools, hematochezia, loss of appetite, and sluggish movement were gradually relieved; most of the symptoms of mice

TABLE 1: Instruments, equipment, and main reagents.

Name	Specification	Company
Inverted microscope	DM-IRB type	LEICA, Germany
Transmission electron microscope	JEOE type	Japan
Enzyme-linked immunosorbent assay kit		Shanghai Tongwei industrial Co., Ltd.
ABI 7500 Fluorescence quantitative PCR system		Applied Biosystems (ABI), USA
PCR instrument		Bio-Rad Company, USA

FIGURE 1: Anatomical images of intestinal canals in mice (marked as lesion site).

in the control group given normal saline by gavage were not significantly relieved, of which one died on the 7th day.

3.2. Anatomical Observation of Mice. Almost all black/C mice showed diffuse intestinal mucosal congestion and edema, with a large amount of mucus and fibrin exudation, and some mice had small bleeding spots locally in the intestine. These lesions were obvious in sigmoid colon and rectum, and even more cauliflower-like, protruding into the intestinal cavity, with surface ulceration, bleeding, and necrosis, and the intestinal canal of the control group was more serious than that of the experimental group (Figure 1).

3.3. Expression of PI3K, AKT, and FOXO1 in CRC Mouse Model Tissues. PI3K and FOXO1 were mainly expressed in

cytoplasm and cell membrane, and AKT was mainly expressed in nucleus. After CT26 cells were inoculated into the spleen of mice to establish colorectal cancer mouse model, the positive rates of PI3K, FOXO1, and AKT in CRC tissues were 60% (6/10), 50% (5/10), and 80% (8/10), respectively, as shown in Figures 2 and 3.

By observing Figures 2 and 3, it was found that PI3K, AKT, and FOXO1 were expressed in colorectal cancer tissues, which was of great significance for clinical diagnosis and treatment.

3.4. Relationship between PI3K, AKT, FOXO1, and ABTB1 Expression and Clinicopathological Features in CRC Tissues. The relationship between expression genes and

(a)

(b)

(c)
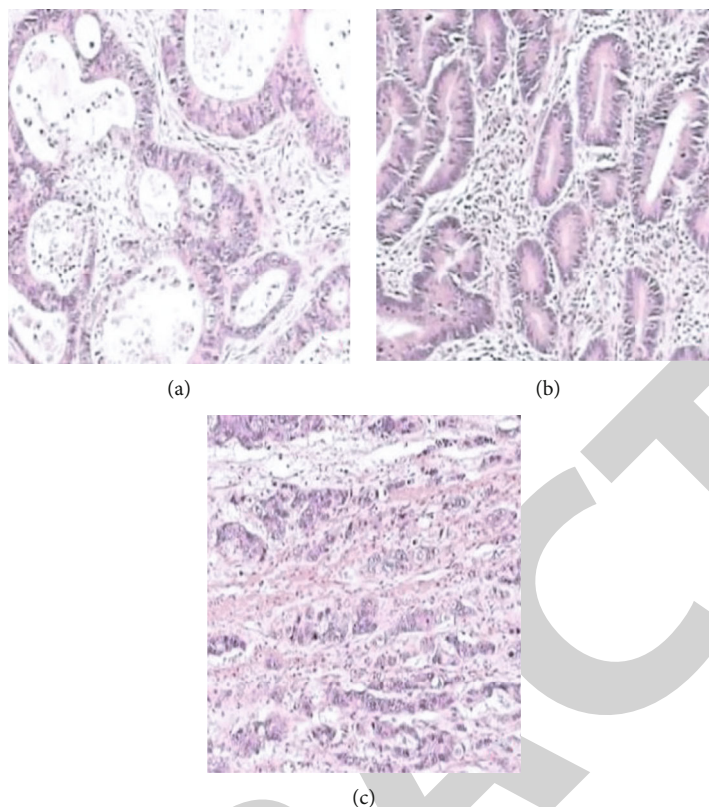
FIGURE 2: Expression in CRC tissues ((a)–(c) are PI3K, AKT, and FOXO1 (SP × 200), respectively).
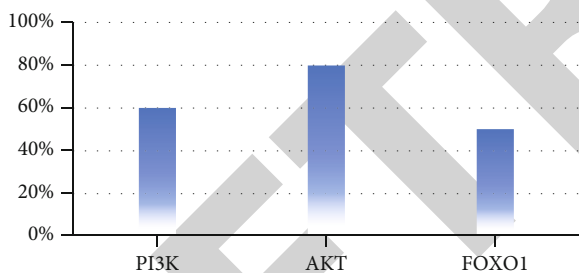
FIGURE 3: Expression rate of PI3K, AKT, and FOXO1 in CRC tissues.
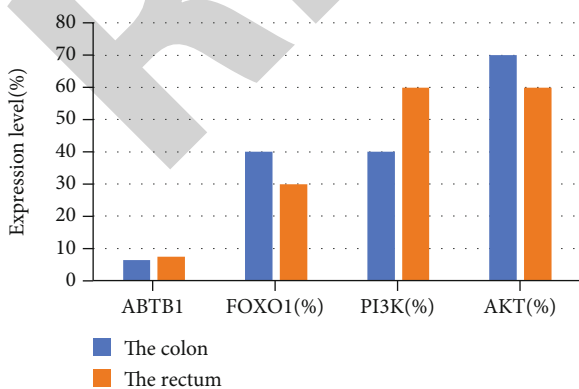
FIGURE 4: Expression levels of PI3K, AKT, FOXO1, and ABTB1 in different tumor sites.

clinicopathological parameters in colorectal cancer tissues is shown in Figures 4–7.

By observing Figures 4–7, it was found that the expressions of PI3K, AKT, FOXO1, and ABTB1 in colon were 40%, 70%, 40%, and 6.35, respectively, and those in rectum were 60%, 60%, 30%, and 7.51, respectively. Their expressions in CRC tissues were not related to the tumor site, $P > 0.05$, and there was no statistical significance. The expression of PI3K, AKT, FOXO1, and ABTB1 under the plasma membrane was 40%, 50%, 80%, and 4.25, respectively, and the expression of submerged plasma membrane was 80%, 90%, 30%, and 7.68, respectively. The expression in high/medium differentiation was 30%, 50%, 90%, and 4.36, in low/undifferentiated that were 80%, 80%, 30%, and 10.51. The expressions without lymph node metastasis were 30%, 70%, 70%, and 4.34, respectively, and those with lymph node metastasis were 70%, 80%, 20%, and 8.71, respectively. Their expression was related to the depth of tumor invasion, differentiation, and lymph node metastasis, $P < 0.05$, and the difference was statistically significant.

3.5. Expression Levels of P-PI3K, P-AKT, P-FOXO1, and ABTB1 in Mice. After the scratch test and transwell test of rectal cancer cells in mice of the two groups, the expression levels of p-PI3K, p-AKT, p-FOXO1, and ABTB1 and the proliferation and migration ability of colorectal cancer cells in mice were determined (Figures 8 and 9).

By observing Figures 8 and 9, it was found that after scratch test and transwell test, the densities of p-PI3K, p-
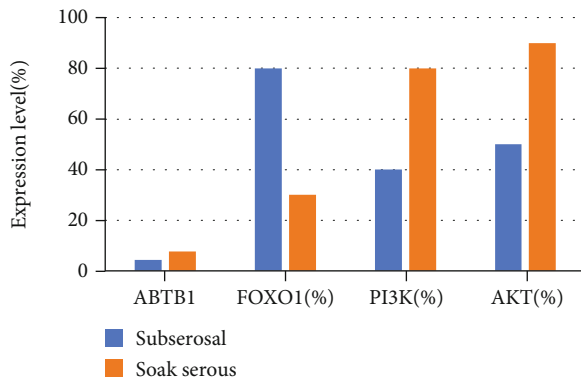
Figure 5: Expression levels of PI3K, AKT, FOXO1, and ABTB1 in different infiltration depths.
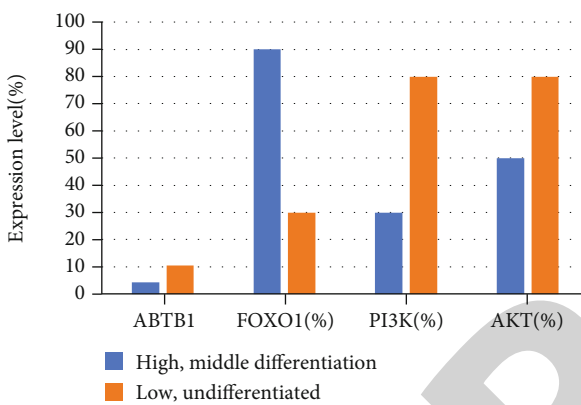
Figure 6: Expression levels of PI3K, AKT, FOXO1, and ABTB1 in different differentiation degrees.
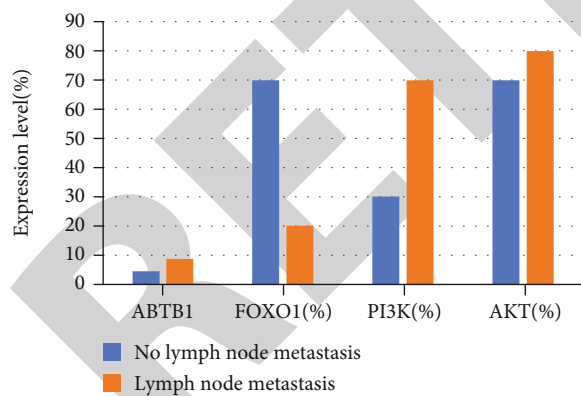
Figure 7: Expression levels of PI3K, AKT, FOXO1, and ABTB1 in patients with and without lymph node metastasis.

AKT, and p-FOXO1 in the experimental group were 26.55 g/cm^3, 70.2 g/cm^3, and 24.36 g/cm^3, respectively, which were significantly higher than those in the control group ($P < 0.05$); the density of ABTB1 was 35.4 g/cm^3, which was significantly higher than that in the control group ($P < 0.05$), the proliferation and migration ability of CRC in the experimental group were significantly decreased ($P < 0.05$), and the differences were statistically significant.
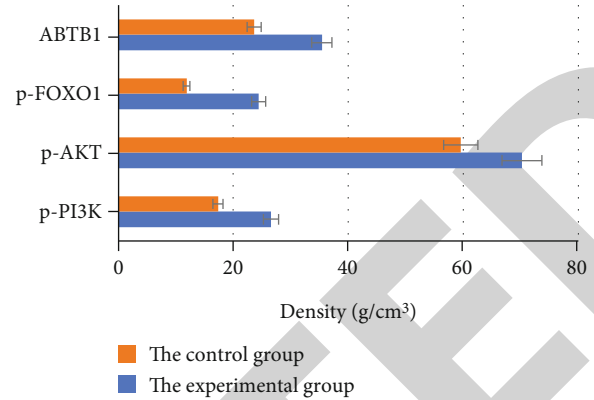
Figure 8: Density of p-PI3K, p-AKT, p-FOXO1, and ABTB1 in mice.

4. Discussion

The occurrence and development of CRC are related to gene regulation. More and more studies have shown that ABTB1 is closely related to the occurrence, development, and metastasis of tumors and is a potential tumor suppressor gene [14]. It was reported in the literature that GQD can successfully express ABTB1 by activating PI3K/AKT/FOXO1 signaling pathway and inhibit the proliferation and growth ability of CRC cells, which is consistent with the results of this study [15]. In this experiment, the levels of P-PI3K/PI3K, P-AKT/AKT, and P-FoxO1/FoxO1 in the experimental group were higher than those in the control group; the positive expression rate of FoxO1 in CRC was 50%, and its expression was significantly correlated with the depth of tumor invasion, differentiation, and lymph node metastasis, which could provide some reference indicators for the occurrence and development of CRC in clinical practice.

Phosphatidylinositol 3-kinase (PI3K), an intracellular phosphatidylinositol kinase discovered by Sugimoto et al. in 1984, has lipokinase activity and protein kinase activity and is responsible for the transduction of stimulating signals such as growth factors from the cell membrane to the cytoplasm [16, 17]. The results of this study showed that the positive expression rate of PI3K in CRC was 60%, and the expression of PI3K was significantly correlated with the depth of tumor invasion, differentiation, and lymph node metastasis. Relevant literature has pointed out that activation of AKT (p-AKT) is key to the role of PI3K/AKT signaling pathway [18, 19]. Lin et al. (2017) [20] reported that p-AKT was significantly higher in CRC than in adenoma, and p-AKT was significantly correlated with the stage of CRC and the level of preoperative serum carcinoembryonic antigen (CEA). The positive rate of AKT in CRC was 80%, and the expression of AKT was significantly correlated with the depth of tumor invasion, differentiation, and lymph node metastasis, which can be used as a reference index to assess the occurrence and development of CRC in clinical practice.

Relevant studies suggested that PI3K/AKT/FOXO1 signaling pathway is widely present in various tumor cells, and activation of this pathway can inhibit apoptosis and
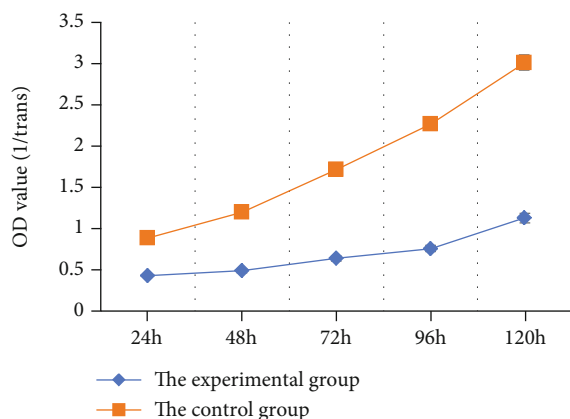
Figure 9: OD value of proliferation and migration of colorectal cancer cells in mice.

promote cell cycle progression, thereby promoting cell growth and proliferation, while participating in tumor angiogenesis, playing an important role in tumor formation, and participating in tumor invasion and metastasis [21, 22]. GQD can successfully express ABTB1 and inhibit the proliferation and growth of tumor cells by positively regulating this signaling pathway. In this study, it was found that GQD can make the ABTB1 expression in CRC positively correlated with the expression of PI3K, p-AKT, and FOXO1, which were involved in the development of CRC while inhibiting the proliferation and metastasis of CRC.

In summary, the combined detection of PI3K, p-AKT, FOXO1, and ABTB1 expression levels can understand its clinical significance, which may play an important role in the early diagnosis of CRC, judging the malignant degree of CRC, estimating the stage of CRC, and judging the prognosis. Understanding the mechanism of occurrence and development of CRC and formulating reasonable therapeutic measures for CRC patients can also provide a theoretical basis for CRC target therapy, which has very important clinical significance.

5. Conclusion

In this study, a mouse model of CRC was established to explore the regulation of GQD on ABTB1 gene expression by activating the PI3K/AKT/FOXO1 signaling pathway, and it was found that compared with the control group, the expressions of p-PI3K, p-AKT, p-FOXO1, and ABTB1 in the experimental group were significantly increased, $P < 0.05$; the expressions of PI3K, AKT, FOXO1, and ABTB1 were related to the depth of tumor invasion, differentiation, and lymph node metastasis, $P < 0.05$, and the proliferation and migration ability of CRC cells in the experimental group were significantly decreased, $P < 0.05$. GQD can promote the expression of ABTB1 by activating the PI3K/AKT/FOXO1 signaling pathway, in order to inhibit the proliferation and growth ability of CRC cells. This study provides some experimental data for the therapeutic role of ABTB1 gene in CRC, but also provides a new research direction for its treatment. However, due to the relatively small sample size in this

study, the experimental results need to be verified by more clinical trials.

Data Availability

The data used to support the findings of this study are included within the article.

Conflicts of Interest

The authors declare that they have no competing interest.

Authors' Contributions

Feng Li and Lili Chen contributed equally to this work as cofirst author.

Acknowledgments

References

[1] E. Picard, C. P. Verschoor, G. W. Ma, and G. Pawelec, "Relationships between immune landscapes, genetic subtypes and responses to immunotherapy in colorectal cancer," *Frontiers in Immunology*, vol. 11, p. 369, 2020.

[2] K. Heinimann, "Erblicher Darmkrebs: Klinik, Diagnostik und management," *Therapeutische Umschau*, vol. 75, no. 10, pp. 601–606, 2018.

[3] I. S. Yu and W. Y. Cheung, "Metastatic colorectal cancer in the Era of personalized medicine: a more tailored approach to systemic therapy," *Canadian Journal of Gastroenterology and Hepatology*, vol. 2018, Article ID 9450754, 11 pages, 2018.

[4] C. Cueva, M. Silva, I. Pinillos, B. Bartolomé, and M. V. Moreno-Arribas, "Interplay between dietary polyphenols and oral and gut microbiota in the development of colorectal cancer," *Nutrients*, vol. 12, no. 3, p. 625, 2020.

[5] L. C. Connell, J. M. Mota, M. I. Braghiroli, and P. M. Hoff, "The rising incidence of younger patients with colorectal cancer: questions about screening, biology, and treatment," *Current Treatment Options in Oncology*, vol. 18, no. 4, p. 23, 2017.

[6] A. Pandey, C. Shen, and S. M. Man, "Inflammasomes in colitis and colorectal cancer: mechanism of action and therapies," *Yale Journal of Biology and Medicine*, vol. 92, no. 3, pp. 481–498, 2019.

[7] J. Lv, Y. Jia, J. Li et al., "Gegen Qinlian decoction enhances the effect of PD-1 blockade in colorectal cancer with microsatellite stability by remodelling the gut microbiota and the tumour microenvironment," *Cell Death & Disease*, vol. 10, no. 6, p. 415, 2019.

[8] Y. Zhao, H. Luan, H. Gao, X. Wu, Y. Zhang, and R. Li, "Gegen Qinlian decoction maintains colonic mucosal homeostasis in acute/chronic ulcerative colitis via bidirectionally modulating dysregulated notch signaling," *Phytomedicine*, vol. 68, article 153182, 2020.

[9] M. Wei, H. Li, Q. Li et al., "Based on network pharmacology to explore the molecular targets and mechanisms of Gegen Qinlian decoction for the treatment of ulcerative colitis," *BioMed*

Retraction

Retracted: Evaluation of Liquid Biopsy in Patients with HER2-Positive Breast Cancer

BioMed Research International

This article has been retracted by Hindawi following an investigation undertaken by the publisher [1]. This investigation has uncovered evidence of one or more of the following indicators of systematic manipulation of the publication process:

(1) Discrepancies in scope

(2) Discrepancies in the description of the research reported

(3) Discrepancies between the availability of data and the research described

(4) Inappropriate citations

(5) Incoherent, meaningless and/or irrelevant content included in the article

(6) Manipulated or compromised peer review

The presence of these indicators undermines our confidence in the integrity of the article's content and we cannot, therefore, vouch for its reliability. Please note that this notice is intended solely to alert readers that the content of this article is unreliable. We have not investigated whether authors were aware of or involved in the systematic manipulation of the publication process.

Wiley and Hindawi regrets that the usual quality checks did not identify these issues before publication and have since put additional measures in place to safeguard research integrity.

We wish to credit our own Research Integrity and Research Publishing teams and anonymous and named external researchers and research integrity experts for contributing to this investigation.

The corresponding author, as the representative of all authors, has been given the opportunity to register their agreement or disagreement to this retraction. We have kept a record of any response received.

References

[1] J. Huai, M. Cao, Y. Jiang et al., "Evaluation of Liquid Biopsy in Patients with HER2-Positive Breast Cancer," *BioMed Research International*, vol. 2021, Article ID 6388492, 5 pages, 2021.

Research Article

Evaluation of Liquid Biopsy in Patients with HER2-Positive Breast Cancer

Jianguo Huai [1] **Ming Cao,**[1] **Yan Jiang,**[1] **Xiaomiao Yang,**[1] **Yanyan Zhu,**[1] **Youyi Si,**[1] **Man Xu,**[1] **Chenxiang Shen,**[1] **Tao Han,**[2] **and Xiaochun Lian**[2]

[1]*Department of Pathology, Wuhu No. 1 People's Hospital, Wuhu 241000, China*
[2]*Department of Breast Surgery, Wuhu No. 1 People's Hospital, Wuhu 241000, China*

Correspondence should be addressed to Jianguo Huai; jianguohuai@163.com

Breast cancer is one of the common malignant tumors, and liquid biopsy has become a hot spot for clinical testing. To clarify the detection effect of liquid biopsy in breast cancer, we collected peripheral blood of HER2-positive (human epidermal growth factor receptor 2-positive) patients. Circulating tumor cells (CTCs) were isolated and analyzed. HER2 expression on CTCs was detected. The results showed that in the 198 HER2-positive samples, the CTC detection rate was 79.8% (158/198), and the mean number of CTCs was 21, ranging from 1 to 63/7.5 mL peripheral blood. Only 41.1% (65/158) of patients had histology and CTC HER2 status consistent with the remaining 58.9% (93/158) of patients, although their histological HER2 was positive, and CTC HER2 was negative. Our study confirmed the value of CTC HER2 real-time status testing in HER2-positive breast cancer patients. The inconsistency in HER2 status between CTCs and histology may be related to the time interval between CTCs and histological HER2 detection, suggesting that real-time HER2 detection is necessary for histological HER2-positive patients.

1. Introduction

Breast cancer is one of the most common female tumors, and GLOBOCAN predicts that there will be 210,000 new cases of breast cancer in China in 2020 [1]. The occurrence and development of breast cancer is regulated by multiple genes. In many markers related to breast cancer, estrogen receptor (ER), progesterone receptor (PR), human epidermal growth factor receptor 2 (HER2), and Ki-67 are considered to be the markers for breast cancer [2, 3]. The expressions of ER, PR, HER2, and Ki-67 directly determine the choice of treatment. HER2 is a very important molecular marker for breast cancer. About 20% of newly diagnosed breast cancer patients are HER2-positive [4, 5]. The main difficulty in tumor treatment is that the cause is complex and constantly changing, and the etiology is complex and constantly changing, and the status of the drug target is not 100% predictive of efficacy [6, 7]. Therefore, for more accurate and effective treatment, it is necessary to evaluate the efficacy in a timely manner and adjust the treatment

strategy in a timely manner. However, traditional evaluation methods do not meet the above requirements [8–10].

Currently, the HER2 status of breast cancer patients is mainly determined by immunohistochemical (IHC) detection and fluorescent in situ hybridization (FISH) on a section of tumor tissue obtained by surgery or needle biopsy. In this context, liquid biopsy has become a hot spot for clinical testing. Liquid biopsy is a diagnostic analysis through body fluid samples. The types of body fluids that have been reported for liquid biopsy include peripheral blood, pleural and ascites fluid and cerebrospinal fluid in disease states, urine, and saliva [11]. CTCs, which can be used for liquid biopsy in peripheral blood, have been widely used in clinics as a biomarker of liquid biopsy, and it is an important marker in the process of tumor metastasis. Moreover, CTCs have been confirmed to be widely present in the peripheral blood of people suffering from breast cancer [12]. The main advantage of liquid biopsy is that it is small in trauma and very convenient for real-time dynamic monitoring. In addition, in the liquid state, the components of various tumor sources are

(a)   (b)
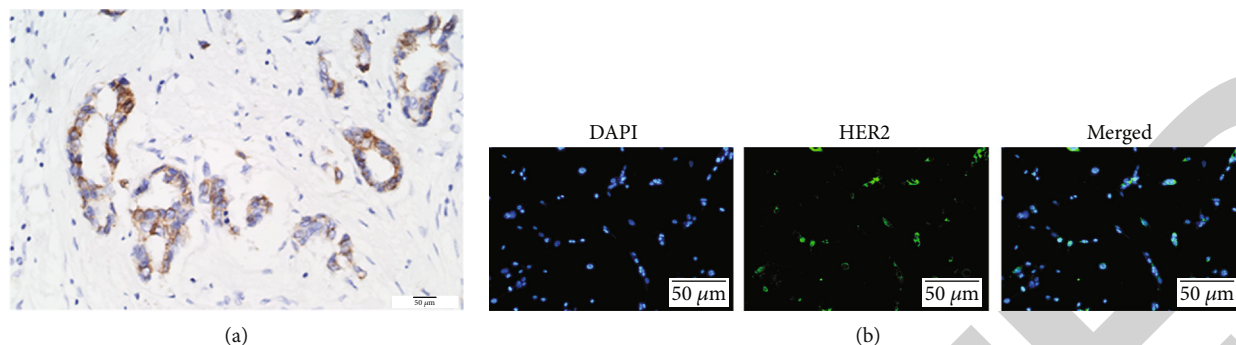
Figure 1: Expression of HER2 protein in breast cancer tissues. (a) Immunohistochemistry and (b) immunofluorescence used to display the HER2 protein expression in breast cancer tissues.

relatively uniform, which can reflect the heterogeneity of the tumor in time and space from a holistic perspective.

In this study, we mainly conducted research on CTCs, collected the peripheral blood of HER2-positive patients, separated and analyzed CTCs, and detected HER2 expression on CTCs, then selected CTCs HER2-positive patients to test the expression of ER, PR, and Ki-67 in order to have a clearer concept of liquid biopsy for its better application in clinic in the future and better guide individualized treatment of such patients.

2. Materials and Methods

2.1. Specimen Source. There are collected breast cancer samples from March 2017 to March 2019 in Wuhu First People's Hospital. Histologically, HER2-positive patients who are defined by the IHC or FISH were enrolled in the present study. The criteria for inclusion were female patients; tumor diameter ≥ 2 cm; no chemotherapy, endocrine therapy, radiotherapy, and targeted therapy [13]. Patients sign a written informed consent form. According to the inclusion criteria, 198 patients with breast cancer were enrolled, aged 29-84 years. We then analyzed 7.5 mL of these samples for CTC content using a Cyttel® (Jiangsu, China) immunofluorescence in situ hybridization (imFISH) approach.

2.2. CTCs Collection and Processing. 7.5 mL peripheral blood was added to the centrifuge tube, 6.5 mL of buffer was added, and the mixture was mixed and centrifuged at 800 g for 10 min. The sample was placed in the AutoPrep system, and the parameters were set according to the instruction manual. After the treatment, the sample was transferred to the MagNest device, incubated for 20 min or more in the dark, and the MagNest was placed in the AnalyZer for fluorescence scanning [14]. The CTC positive standard is CK positive and conforms to cell morphology, DAPI (Sigma-Aldrich, USA) is positive, and the signal is in the range of CK. HER2 expression on CTCs was assessed by staining the cells with a FITC-labeled anti-HER2 antibody (Veridex LLC, USA). For the time when CTCs were positive, its expression was defined as 0 (no expression), 1+ (weak expression), 2+ (moderate expression), and 3+ (strong expression) according to the fluorescence intensity of

Table 1: Clinical characteristics of all patients.

Characteristics	Total	CTC = 0 (%)	CTC ≥ 1 (%)	P
Total n (100%)	198	40 (20.2%)	158 (79.8%)	
Age (years)				
Median	49	49	49	0.546
Range	29-84	29-84	30-79	
ER and/or PR				
Positive	158	32 (20.3%)	126 (79.7%)	0.012
Negative	40	8 (20.0%)	32 (80.0%)	
TNM stage				
II	71	28 (39.4%)	43 (60.6%)	0.036
III	127	12 (9.4%)	115 (90.6%)	
No. of metastasis				
1	38	22 (57.9%)	16 (42.1%)	0.085
≥2	160	18 (11.3%)	142 (88.7%)	
Number of CTCs		21 (1-63/7.5 mL)		

HER2. Those patients with >30% of CTCs overexpressing HER2 (3+) were defined as CTC HER2-positive [15].

2.3. Immunohistochemical Testing. The antibody used was produced by Maixin Co., and the sample was applied to the machine after 1 hour of baking. It was automatically stained with Roche Immunohistochemistry (Roche Diagnostics, Germany). After the procedure was completed, it was washed, dehydrated, and transparently sealed with xylene.

2.4. Immunofluorescence. Frozen tumor tissue slices of 5 mm thickness were fixed with cold acetone for 10 min, washed with PBS, and then, blocked with 10% donkey serum for 45 min at room temperature. Slices were then incubated overnight with pertuzumab (ThermoFisher Scientific, USA) at 4°C [16]. Next, sections were further stained with AlexaFluor488-labeled goat anti-human antibody (ThermoFisher Scientific, USA). A coverglass was applied to each slide using Vectashield mounting medium (Vector Laboratories, Burlingame, CA, USA), and imaging was performed using an A1R confocal microscope (Nikon, Nikon Instruments, Melville, NY, USA).
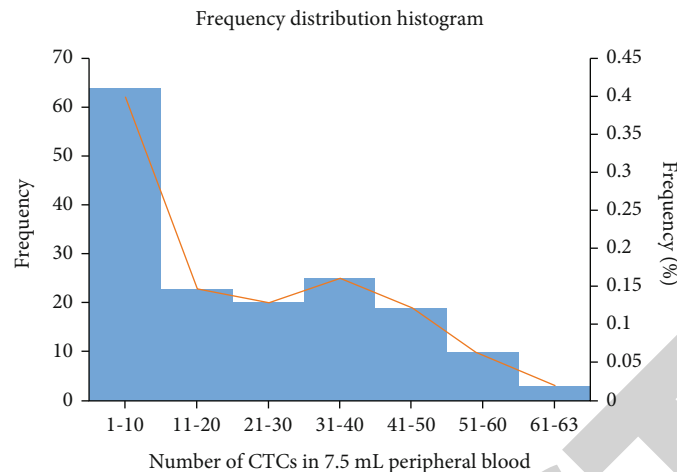
Figure 2: Frequency distribution histogram of CTCs.

2.5. FISH Test. The sample was dewaxed by xylene, dehydrated by 100%, 85%, and 70% alcohol gradient, and then, treated with pretreatment solution for 20 minutes. After digestion with a protease solution, it was naturally air-dried and incubated with a probe. The mixture was heated at 85°C for 5 min in a Thermo Brite hybridization (Abbott Molecular, USA) apparatus and reacted overnight at 37°C. The next day, the unbound probe was washed with a constant temperature buffer, dehydrated by alcohol gradient soaking, air-dried, and DAPI counterstain solution was titrated on a glass slide and sealed.

2.6. Statistical Analysis. Fisher's exact test was used to analyze whether there were differences in clinical features between patients with CTC = 0 and CTC 1 and between patients with CTC HER2-positive and CTC HER2-negative based on histology and time of CTC HER2 testing. Patients were divided into different groups by interval, and differences in HER2 state consistency among different groups were analyzed by chi-square test. *P* values < 0.05 was considered statistically significant, and SPSS 23.0 (IBM Corporation, USA) was used for all analyses.

3. Results

3.1. Patient Characteristics and CTC Detection. From March 2017 to March 2019, a total of 198 HER2-positive breast cancer patients were enrolled, with an average age of 49 years (29-84 years). The results of immunohistochemistry and immunofluorescence showed that the HER2 protein was mainly expressed in the cell membrane of breast cancer, which was brown (Figures 1(a) and 1(b)). According to patient's CTC test value, the patients were divided into CTCs ≥ 1 group and CTCs = 0 group. The clinical characteristics of these two groups of patients are shown in Table 1. The overall CTC detection rate was 79.8% (158/198), and the mean number of CTCs was 21, ranging from 1 to 63/ 7.5 mL peripheral blood. The frequency distribution histogram of CTCs is shown in Figure 2. The lymph node and pathological stage between the CTC detection group and the undetected group were statistically significant (*P* < 0.05).

3.2. HER2 Status on CTCs. The HER2 expression on each CTCs is defined as 0, 1+, 2+, or 3+. 0 is no signal, 1+ is a faint signal, 2+ is ambiguous, and 3+ is a clear and clear signal. Using our CTC HER2 positive criteria, >30% of CTCs were strongly expressed by HER2 (3+), and only 41.1% (65/158) of patients had consistent histology and CTC HER2 status, with the remaining 58.9% (93/158) patients, although their histology HER2 was positive, and CTC HER2 was actually negative (Table 2). In the ER and/or PR positive group, the HER2 inconsistency rate between tissue and CTCs was 74.7% (118/158).

3.3. Expression of ER, PR, and Ki-67 on CTCs. The analysis included a total of 158 CTC-positive patients, estrogen receptor (ER) positive in 98 (62.0%) patients, and progesterone receptor (PR) positive in 75 (47.5%) patients. In 88 (55.7%) patients, the Ki-67 positive rate was greater than 50% (Figure 3). The expression of ER, PR, and Ki-67 can be well detected on CTCs as a real-time dynamic detection, providing guidance for subsequent personalized medication and cancer surveillance.

4. Discussion

There is increasing evidence that HER2 status in breast cancer patients changes during treatment. CTCs can provide a HER2 real-time detection solution with minimally invasive and simple advantages [17, 18]. Although this application is very promising, there are many CTC detection methods and different CTCS HER2-positive standards, which greatly affect the use of CTC HER2 detection in clinical practice to guide HER2-targeted therapy. Histologically, HER2-positive conversion to CTCs-HER2 negative seems to be a very common phenomenon [19, 20]. In this study, this data was 58.9% (93/198), and the results of previous studies were 41.7% (5/12), 45.5% (5/11), and 50% (1/2) [21–23]; the results of this study are similar to those of other literatures. This high degree of inconsistency further underscores the need and urgency of real-time HER2 detection. Especially in developing countries like China, high medical expenses have always been a huge burden for patients. By CTC

Table 2: Comparison of CTCs, primary tumor by HER2 status in patients.

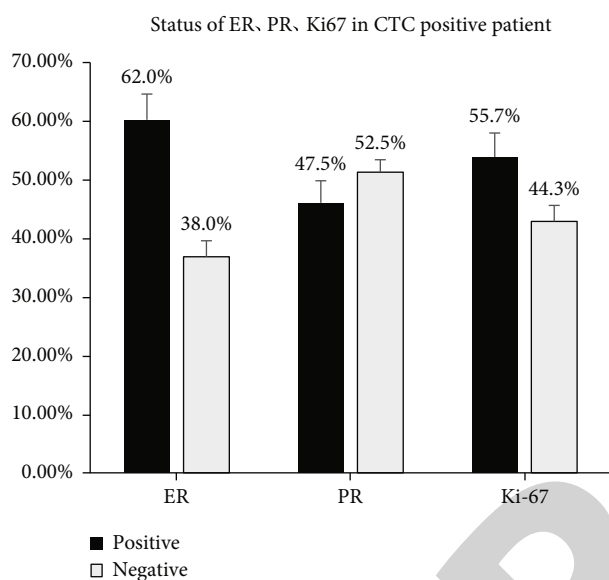|	Total	CTCs-HER2-positive n (%)	CTCs-HER2-negative n (%)
Primary-HER2 status	198	158 (79.8%)	40 (20.2%)
Positive	158	65 (41.1%)	93 (58.9%)
Negative	40	18 (45.0%)	22 (55.0%)

Figure 3: Status of ER, PR, and Ki67 in CTC-positive patient.

testing, patients with histological HER2-positive but CTC HER2-negative patients can avoid overtreatment of HER2-targeted drugs and save costs. One problem with this study was that all CTC data were based on a single-sample test, and no CTC analysis was performed during follow-up of patients. In future studies, CTC analysis during follow-up is necessary because the number of CTCs and the status of HER2 will also change over time.

At present, the detection in breast cancer patients is mainly immunohistochemical technology. The detection of ER, PR, Ki-67, and other expression in breast cancer is very important [24]. The detection of these indicators can not only make the diagnosis of lesions but also choose the basis for personalized treatment. The ER protein is present in the cells of the target organ and can specifically bind to the hormone to form a hormone-receptor complex, so that the hormone exerts its biological effects. ER can bind to its ligand to regulate the proliferation, survival, and invasion of tumor cells and the formation of tumor angiogenesis. PR is a member of the steroid hormone receptor family. Ki-67 is an effective indicator of cell proliferation [6, 25–27]. These three indicators serve as indicators of proliferation and activity of breast cancer cells and are used for the selection of subsequent treatment options. In this study, a total of 158 CTC-positive patients were positive for estrogen receptor (ER) in 98 (62.0%) patients and progesterone

receptor (PR) positive in 75 (47.5%) patients. The Ki-67 positive rate was greater than 50% in 88 (55.7%) patients. The results of this experiment show that CTCs can be used as real-time dynamic detection to provide guidance for subsequent personalized medication and cancer surveillance.

5. Conclusion

In summary, our study demonstrated the value of CTC HER2 real-time status detection in HER2-positive breast cancer patients. The inconsistency of HER2 status between CTCs and histology may be related to the time interval between the detection of CTCs and histological HER2, suggesting that real-time detection of HER2 is very necessary for patients with positive histological HER2.

Data Availability

The data used to support the findings of this study are included within the article.

Ethical Approval

The study complies with the Declaration of Helsinki and was approved by Wuhu No. 1 People's Hospital Ethics Committee.

Conflicts of Interest

The authors declare that there are no conflicts of interest.

References

[1] F. C. Bidard, C. Proudhon, and J. Y. Pierga, "Circulating tumor cells in breast cancer," *Molecular Oncology*, vol. 10, no. 3, pp. 418–430, 2016.

[2] E. F. Cobain, C. Paoletti, J. B. Smerage, and D. F. Hayes, "Clinical applications of circulating tumor cells in breast cancer," *Recent Results in Cancer Research*, vol. 215, pp. 147–160, 2020.

[3] S. Stefanovic, T. M. Deutsch, R. Wirtz et al., "Molecular subtype conversion between primary and metastatic breast cancer corresponding to the dynamics of apoptotic and intact circulating tumor cells," *Cancers*, vol. 11, no. 3, p. 342, 2019.

[4] Y.-H. Cheng, Y.-C. Chen, E. Lin et al., "Hydro-Seq enables contamination-free high-throughput single-cell RNA-sequencing for circulating tumor cells," *Nature Communications*, vol. 10, no. 1, 2019.

[5] M. S. Loeian, S. Mehdi Aghaei, F. Farhadi et al., "Liquid biopsy using the nanotube-CTC-chip: capture of invasive CTCs with high purity using preferential adherence in breast cancer patients," *Lab on a Chip*, vol. 19, no. 11, pp. 1899–1915, 2019.

[6] T. N. Fehm, F. Meier-Stiegen, C. Driemel et al., "Diagnostic leukapheresis for CTC analysis in breast cancer patients: CTC frequency, clinical experiences and recommendations for standardized reporting," *Cytometry. Part A*, vol. 93, no. 12, pp. 1213–1219, 2018.

[7] M. Vishnoi, N. H. Liu, W. Yin et al., "The identification of a TNBC liver metastasis gene signature by sequential CTC-xenograft modeling," *Molecular Oncology*, vol. 13, no. 9, pp. 1913–1926, 2019.

Retraction

Retracted: DNM1: A Prognostic Biomarker Associated with Immune Infiltration in Colon Cancer—A Study Based on TCGA Database

BioMed Research International

This article has been retracted by Hindawi following an investigation undertaken by the publisher [1]. This investigation has uncovered evidence of one or more of the following indicators of systematic manipulation of the publication process:

(1) Discrepancies in scope

(2) Discrepancies in the description of the research reported

(3) Discrepancies between the availability of data and the research described

(4) Inappropriate citations

(5) Incoherent, meaningless and/or irrelevant content included in the article

(6) Manipulated or compromised peer review

The presence of these indicators undermines our confidence in the integrity of the article's content and we cannot, therefore, vouch for its reliability. Please note that this notice is intended solely to alert readers that the content of this article is unreliable. We have not investigated whether authors were aware of or involved in the systematic manipulation of the publication process.

Wiley and Hindawi regrets that the usual quality checks did not identify these issues before publication and have since put additional measures in place to safeguard research integrity.

We wish to credit our own Research Integrity and Research Publishing teams and anonymous and named external researchers and research integrity experts for contributing to this investigation.

The corresponding author, as the representative of all authors, has been given the opportunity to register their agreement or disagreement to this retraction. We have kept a record of any response received.

References

[1] M. Hu, J. Gu, W. Su et al., "DNM1: A Prognostic Biomarker Associated with Immune Infiltration in Colon Cancer—A Study Based on TCGA Database," *BioMed Research International*, vol. 2021, Article ID 4896106, 9 pages, 2021.

Research Article

DNM1: A Prognostic Biomarker Associated with Immune Infiltration in Colon Cancer—A Study Based on TCGA Database

Mingchao Hu [1,2] **Jianchun Gu,** [2] **Wenzhao Su,** [1] **Zhenjie Zhang,** [2] **Baosong Zhu** [3] **Qiang Wang,** [2] **and Chungen Xing** [1]

[1] *Department of Gastrointestinal Surgery, The Second Affiliated Hospital of Soochow University, Suzhou 215000, China*
[2] *Department of General Surgery, The Affiliated Jiangsu Shengze Hospital of Nanjing Medical University, Suzhou 215228, China*
[3] *Department of General Surgery, Suzhou Hospital of Traditional Chinese Medicine, Suzhou 215000, China*

Correspondence should be addressed to Baosong Zhu; soochowzbs@163.com, Qiang Wang; jsszyywq@163.com, and Chungen Xing; xingcg@suda.edu.cn

Aim. The aim of our work was to determine the utility of DNM1 as a biomarker for the diagnosis and prognosis of colon cancer (CC). *Methods.* DNM1 expression variations in CC vs. normal tissues were investigated using The Cancer Genome Atlas (TCGA) database. The association of DNM1 expression levels with the clinicopathological variables in CC prognosis was investigated using logistic regression analyses. Independent prognostic factors for CC were evaluated using univariate and multivariate Cox regression analyses. The correlation between DNM1 expression and immune cell infiltration was estimated using single-sample Gene Set Enrichment Analysis (ssGSEA). *Results.* DNM1 expression in CC tissues was significantly higher than that in normal tissues. High DNM1 expression was significantly correlated with M stage, N stage, perineural invasion and lymphatic invasion and predicted poor prognosis. The univariate analysis highlighted that DNM1 was an independent CC risk factor. Results of ssGSEA showed that DNM1 was linked to several cancer-related pathways, including the neuroactive ligand-receptor interaction, hypertrophic cardiomyopathy, ECM-receptor interaction, dilated cardiomyopathy, and calcium signaling pathway. Moreover, DNM1 expression was positively correlated with the level of infiltration by Neutrophils, Tregs, NK cells, and Macrophages. *Conclusion.* DNM1 has a significant function and has diagnostic and prognostic potential for CC.

1. Introduction

It is estimated that colon cancer (CC) is among the leading cancers globally. Annually, nearly 1.1 million new cases of CC and 551,000 CC deaths occur each year [1]. Colon adenocarcinoma (COAD) is the most common pathological type and accounts for >90% of CC cases [2]. The prognosis of CC always depends on the cancer stage at diagnosis. However, CC is often detected at an advanced stage, after lymph node and distant metastases occurred, resulting in poor overall survival [3]. Colonoscopy is the gold standard for diagnosing CC, but while highly sensitive, it is invasive and may cause serious complications [4, 5]. Additionally, due to high tumor heterogeneity at the single-cell level, local tumor biopsy results often fail to reflect the overall biology of the tumor and its disease

process, which may contribute to the increased incidence of recurrence and metastases of CC [6, 7]. Although serum biomarkers like carbohydrate CA19-9 and CEA are commonly used in cancer diagnosis and prognosis, their sensitivity and specificity are not high [8]. Recently, several studies have pointed to the influence of the immune microenvironment on the development of colon cancer, suggesting that different types of immune cell infiltration may be used as new diagnostic and prognostic biomarkers [9, 10].

Dynamin is a 96 kDa GTPase, and the conventional dynamin family is composed of dynamins 1, 2, and 3 [11]. Of these, dynamin 1 (DNM1; NM_004408) is located on chromosome 9q34.11 and is expressed at different levels in various tissues, where it regulates cell membrane division, cytokinesis, and vesicle secretion [12]. DNM1 is often
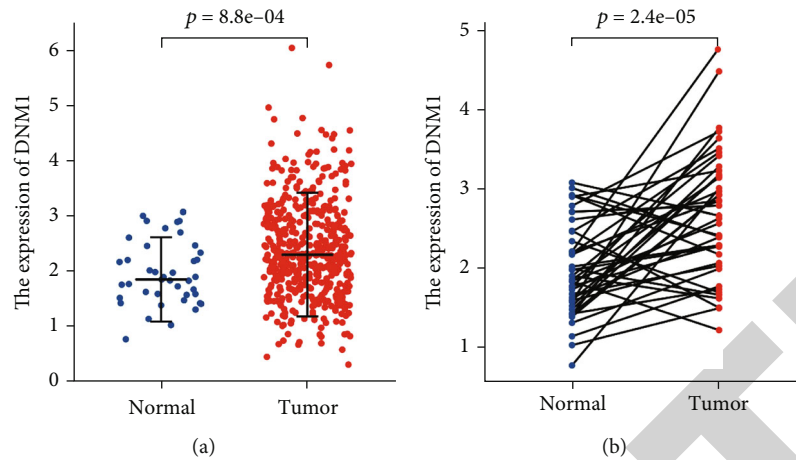
FIGURE 1: (a) Relative to normal tissues, DNM1 expression was elevated in tumor tissues. (b) DNM1 was elevated in tumor tissues compared to normal ones in 41 paired patients.
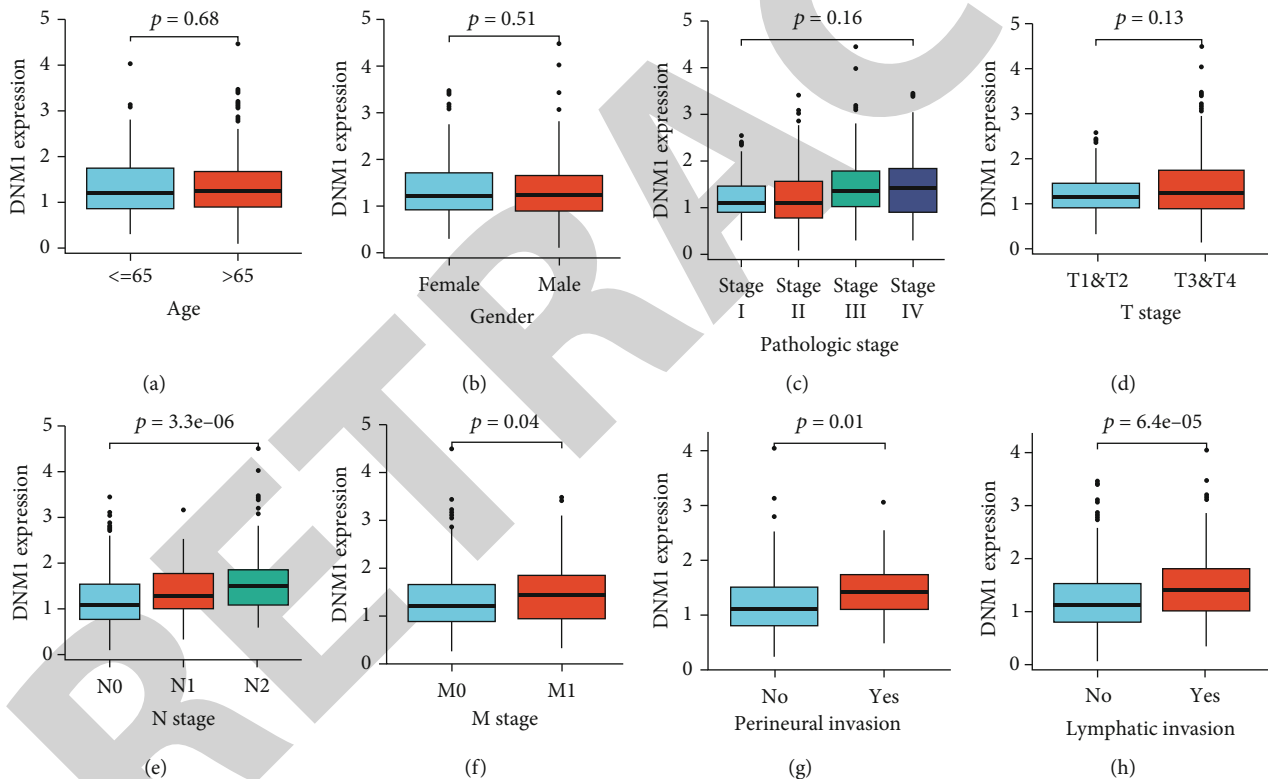
FIGURE 2: Expression patterns of DNM1 in COAD from 478 RNA-Seq data. (a) Age at diagnosis. (b) Gender. (c) Pathologic stage. (d) T stage. (e) N stage. (f) M stage. (g) Perineural invasion. (h) Lymphatic invasion.

thought to be neuron-specific [13], and many studies have implicated it in neurological disorders [14–16]. However, recent studies have implicated DNM1 in the development of various cancers, such as bladder cancer (BC), non-small-cell lung cancer (NSCLC), and hepatocellular carcinoma (HCC) [17–19]. Therefore, the role of DNM1 in CC prognosis is unclear. Here, we investigated DNM1 expression in CC to determine its potential to be a useful biomarker for CC diagnosis and prognosis.

2. Materials and Methods

2.1. Data Collection and Analysis. COAD patients' RNA-Seq data and related clinical records were obtained from TCGA database (https://portal.gdc.cancer.gov) in March 2021 [20]. Upon excluding those lacking clinical information, 455 patients were included in our study. Based on the DNM1 expression level in tumor tissues, patients were classified into low- and high-expression groups.

Table 1: Correlation between DNM1 expression and CC clinicopathological features.

Characteristics	Low DNM1 expression	High DNM1 expression	p
n	239	239	
Age, n (%)			0.402
≤65	102 (21.3%)	92 (19.2%)	
>65	137 (28.7%)	147 (30.8%)	
Gender, n (%)			0.647
Female	116 (24.3%)	110 (23%)	
Male	123 (25.7%)	129 (27%)	
T stage, n (%)			0.540
T1	6 (1.3%)	5 (1%)	
T2	46 (9.6%)	37 (7.8%)	
T3	160 (33.5%)	163 (34.2%)	
T4	26 (5.5%)	34 (7.1%)	
N stage, n (%)			<0.001
N0	163 (34.1%)	121 (25.3%)	
N1	50 (10.5%)	58 (12.1%)	
N2	26 (5.4%)	60 (12.6%)	
M stage, n (%)			0.030
M0	181 (43.6%)	168 (40.5%)	
M1	24 (5.8%)	42 (10.1%)	
Pathologic stage, n (%)			0.002
Stage I	44 (9.4%)	37 (7.9%)	
Stage II	108 (23.1%)	79 (16.9%)	
Stage III	54 (11.6%)	79 (16.9%)	
Stage IV	24 (5.1%)	42 (9%)	
Perineural invasion, n (%)			0.007
No	77 (42.5%)	58 (32%)	
Yes	15 (8.3%)	31 (17.1%)	
Lymphatic invasion, n (%)			<0.001
No	149 (34.3%)	117 (27%)	
Yes	65 (15%)	103 (23.7%)	

2.2. Gene Set Enrichment Analysis (GSEA). GSEA [21] is a genome-wide expression analysis tool that compares genes to a predefined gene collection. Based on the association of DNM1 expression with all genes, GSEA was conducted to create an organized list of genes for our analysis. Next, 1000 gene set alignments were executed for each analysis based on DNM1 levels as the phenotypic marker. Significant enrichment was considered for the normal p value < 0.05 and false discovery rate (FDR) < 0.25. Further, the normalized enrichment score (NES) and adjusted p value were employed to identify pathways enriched in each phenotype.

2.3. Immune Infiltration Analysis. Single-sample GSEA (ssGSEA) was used to determine the infiltration levels of tumor immune cells based on RNA-Seq data [22]. Spearman's correlation was used to examine the relationship between DNM1 and immune cells, and graphs were generated using ggplot2.

2.4. Statistical Analysis. TCGA RNA-Seq gene expression level 3 data and clinical information for all CC patients were analyzed on R version 3.6.3 [23], and $p < 0.05$ was considered statistically significant. Logistic regression (calculation of ORs and 95% CIs) and Wilcoxon signed-rank test were used to determine the correlation between DNM1 expression and CC clinicopathological features. The impact of DNM1 on the prognosis of COAD was evaluated using Kaplan-Meier and Cox regression analyses.

3. Results

3.1. Correlation between DNM1 Expression and Clinicopathological Features. The DNM1 level was substantially elevated in tumor samples than in normal samples (Figure 1(a), $p < 0.0001$). Similar results were found when comparing DNM1 expression in 41 pairs of patients (Figure 1(b), $p < 0.0001$). Wilcoxon signed-rank test analysis of the relationship between DNM1 expression and CC clinicopathological features showed that high DNM1 expression significantly correlated with higher N stage (Figure 2(e), $p = 3.3 * 10^{-6}$), higher M stage (Figure 2(f), $p = 0.04$), more perineural invasion (Figure 2(g), $p = 0.01$), and more lymphatic invasion (Figure 2(h), $p = 6.4 * 10^{-5}$). Similar results were obtained using chi-squared analysis of baseline patient data (Table 1). In the univariate logistic regression analysis, the DNM1 level was found strongly correlated with clinicopathological features (Table 2), including N stage (OR = 2.092, 95% CI: 1.445-3.042, and $p < 0.001$), M stage (OR = 1.885, 95% CI: 1.103-3.287, and $p = 0.022$), pathologic stage (OR = 2.033, 95% CI: 1.402-2.960, and $p < 0.001$), perineural invasion (OR = 2.744, 95% CI: 1.376-5.670, and $p = 0.005$), and lymphatic invasion (OR = 2.018, 95% CI: 1.364-3.001, and $p < 0.001$). However, DNM1 expression did not significantly correlate with age (OR = 1.190, 95% CI: 0.826-1.716, and $p = 0.352$), gender (OR = 1.106, 95% CI: 0.772-1.585, and $p = 0.583$), and T stage (OR = 1.311, 95% CI: 0.835-2.071, and $p = 0.241$). Together, these results suggest that high DNM1 expression predicts poor CC clinicopathological features.

3.2. High DNM1 Expression Affects Colon Cancer Prognosis. Relative to patients with low DNM1 levels, overall survival (OS) was significantly lower in those with high DNM1 levels (HR = 1.72, 95% CI: 1.16-2.56, and $p = 0.007$, Figure 3(a)). Similar results were obtained for disease-specific survival (DSS) (HR = 1.84, 95% CI: 1.11-3.06, and $p = 0.006$, Figure 3(b)) and progression-free interval (PFI) (HR = 1.74, 95% CI: 1.22-2.48, and $p = 0.002$, Figure 3(c)). Univariate analysis of CC prognostic factors revealed that age, T level, lymphatic invasion, M stage, N stage, pathologic stage, and high DNM1 expression are independent prognostic factors for CC (all $p < 0.05$). Multivariate Cox regression analysis showed that age, M stage, and pathologic stage were independent prognostic risk factors for OS in CC patients(all $p < 0.05$, Table 3).

3.3. GSEA Identifies DNM1-Related Signaling Pathways. KEGG pathway analysis identified differentially activated

Table 2: Logistic regression analysis of DNM1 expression associated with clinicopathological features.

| Characteristics	Total (n)	Odds ratio (OR)	p
Age (>65 vs. ≤65)	478	1.190 (0.826-1.716)	0.352
Gender (male vs. female)	478	1.106 (0.772-1.585)	0.583
T stage (T3 & T4 vs. T1 & T2)	477	1.311 (0.835-2.071)	0.241
N stage (N1 & N2 vs. N0)	478	2.092 (1.445-3.042)	<0.001
M stage (M1 vs. M0)	415	1.885 (1.103-3.287)	0.022
Pathologic stage (Stage III & Stage IV vs. Stage I & Stage II)	467	2.033 (1.402-2.960)	<0.001
Perineural invasion (yes vs. no)	181	2.744 (1.376-5.670)	0.005
Lymphatic invasion (yes vs. no)	434	2.018 (1.364-3.001)	<0.001

(a)

(b)

(c)
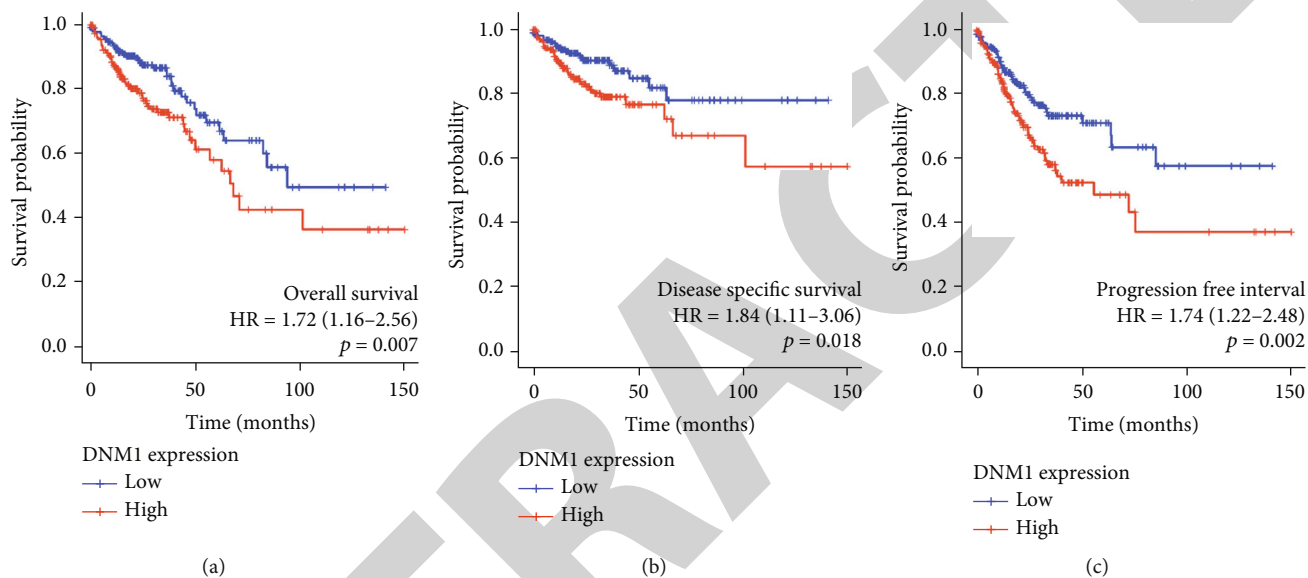
Figure 3: High DNM1 expression predicts poor prognosis of CC. (a) OS in CC patients with differential DNM1 expression ($p = 0.007$). (b) DSS in CC patients with differential DNM1 expression ($p = 0.018$). (c) PFI in CC patients with differential DNM1 expression ($p = 0.002$).

mechanisms and signaling pathways in CC from high DNM1-expression datasets from TCGA (FDR < 0.05, NOM $p < 0.05$). The results of GSEA showed that DNM1-related CC significantly correlated with tumorigenesis and involves various key pathways, including the calcium signaling pathway, dilated cardiomyopathy, neuroactive ligand-receptor interaction, hypertrophic cardiomyopathy (HCM), and ECM-receptor interaction (Figure 4, Table 4).

3.4. Correlation between DNM1 Levels and Immune Cell Infiltration Levels. Tumor-infiltrating lymphocytes can independently reflect cancer survival. Here, we examined if the DNM1 expression level correlated with infiltration of 24 immune cell subpopulations in CC [24] and found that DNM1 expression correlated with Neutrophils, Tregs, NK cells, and Macrophages. We also found a negative correlation between DNM1 levels and T helper cells, Th17 cells, and Th2 cells (Figure 5). Further analysis showed that DNM1 expression had a significant positive correlation with the infiltration level by Neutrophils (Figure 6(a), $r = 0.3$, $p < 0.001$), Tregs (Figure 6(b), $r = 0.310$, $p < 0.001$), NK cells (Figure 6(c), $r = 0.35$, $p < 0.001$), and Macrophages (Figure 6(d), $r = 0.32$, $p < 0.001$).

4. Discussion

Colon cancer has been a challenging clinical condition globally [1]. In recent years, the use of targeted therapies has greatly improved the OS of CC patients [25]. However, the global annual mortality rate remains high, further reinforcing the importance of discovering new biomarkers and using them for early diagnosis, prognosis, and treatment of CC. DNM1 belongs to the dynamin family [11], and numerous studies have implicated DNM1 in encephalopathy [14–16]. Additionally, recent studies indicated that DNM1 is highly expressed in tumor tissues and strongly correlated with cancer prognosis. Tian et al. [19] found that DNM1 was highly expressed in HCC tissues and DNM1 expression significantly correlated with the alpha-fetoprotein (AFP) level, T stage, and TNM stages in HCC. Besides, they found that high DNM1 expression also predicted poor OS in the HCC patients [19]. Schmid [26] recently found that clathrin-mediated endocytosis (CME) in H1299 NSCLC cells is Drp1- (dynamin-related protein 1-) dependent and sensitive to Akt inhibition, indicating its potential as a therapeutic target for NSCLC treatment. Chen et al. [27] showed that isoform-specific upregulation of clathrin light chain B and

TABLE 3: Univariate analysis and multivariate analysis of the correlation of DNM1 expression with OS among CC patients.

| Characteristics	Total (n)	Univariate analysis		Multivariate analysis	
		Hazard ratio (95% CI)	p	Hazard ratio (95% CI)	p
Age (>65 vs. ≤65)	477	1.610 (1.052-2.463)	0.028	2.366 (1.011-5.536)	0.047
Gender (male vs. female)	477	1.101 (0.746-1.625)	0.627		
T stage (T3 & T4 vs. T1 & T2)	476	3.072 (1.423-6.631)	0.004	0.730 (0.134-3.986)	0.716
N stage (N1 & N2 vs. N0)	477	2.592 (1.743-3.855)	<0.001	0.153 (0.014-1.609)	0.118
M stage (M1 vs. M0)	414	4.193 (2.683-6.554)	<0.001	3.022 (1.158-7.887)	0.024
Pathologic stage (Stage III & Stage IV vs. Stage I & Stage II)	466	2.947 (1.942-4.471)	<0.001	17.160 (1.348-218.491)	0.029
Perineural invasion (yes vs. no)	181	1.940 (0.982-3.832)	0.056	0.979 (0.388-2.470)	0.964
Lymphatic invasion (yes vs. no)	433	2.450 (1.614-3.720)	<0.001	1.318 (0.512-3.392)	0.567
DNM1 (high vs. low)	477	1.725 (1.163-2.558)	0.007	2.370 (0.859-6.536)	0.096
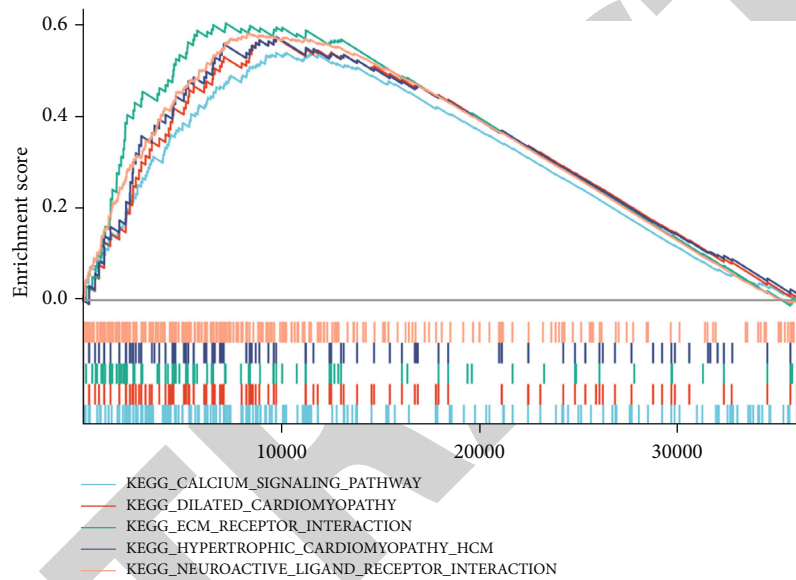
FIGURE 4: Enrichment gene set enrichment analysis (GSEA) plots. DNM1 was differentially enriched in the calcium signaling pathway, dilated cardiomyopathy, ECM-receptor interaction, hypertrophic cardiomyopathy (HCM), and neuroactive ligand-receptor interaction. There are no signaling pathways associated with low DNM1 expression based on the NES, NOM p value, and FDR value. ES: enrichment score; NES: normalized ES; FDR: false discovery rate.

DNM1 in NSCLC cells, combined with the Akt/GSK3β signaling crosstalk, leads to clathrin-mediated adaptive endocytosis, which altered EGFR trafficking and NSCLC metastasis. Reis et al. [28] found that DNM1 overexpression selectively activates tumor necrosis factor- (TNF-) related apoptosis-inducing ligand death receptors to modulate endocytosis, suppress apoptosis, and improve cell migration and survival, indicating that reduced DNM1 expression may sensitize cells to apoptosis induction, while increased DNM1 expression levels may promote apoptosis resistance, thereby enhancing tumorigenesis and cancer progression. DNM1 is highly expressed in various cancers, including acute myeloid leukemia and lung cancer [29], probably due to its effect on apoptosis. Previous studies suggested that DNM1 has the potential to be a biomarker for cancer diagnosis, prognosis, and therapy. Our study showed that DNM1 was highly expressed in CC tissues relative to normal tissues, which also suggested that it may serve an essential role in CC development. Besides, we found high DNM1 expression closely cor-

related with the clinicopathological features of CC and predicted higher N stage, higher M stage, more peripheral invasion and lymphatic invasion. Similar results were obtained by chi-squared analysis of baseline patient data. Moreover, CC patients with higher DNM1 expression had worse OS, DSS, and PFI compared to those with low DNM1 expression. Univariate analysis showed that CC patients with advanced age, higher T stage, N stage, M stage, more advanced pathologic stage, lymphatic invasion, and higher DNM1 expression had significantly lower OS. However, multivariate Cox regression analysis confirmed that age, M stage, and pathologic stage were independent prognostic factors for CC.

To further investigate the function of DNM1 in CC, we performed GSEA on TCGA data, and the results showed that the calcium signaling pathway, ECM-receptor interaction, and neuroactive ligand-receptor interaction in KEGG are differentially enriched in the high DNM1-expression phenotype. Activation of the calcium signaling pathway

TABLE 4: Enrichment plots for gene set enrichment analysis (GSEA).

Description	Set size	Enrichment score	NES	p value	p.adjust	q values	Rank	leading_edge
KEGG_CALCIUM_SIGNALING_ PATHWAY	177	0.5413707	1.39626282	0.000999	0.03299416	0.02839298	9738	Tags = 50%, list = 27 %, signal = 37%
KEGG_DILATED_ CARDIOMYOPATHY	90	0.57422622	1.45061151	0.000999	0.03299416	0.02839298	9738	Tags = 53%, list = 27 %, signal = 39%
KEGG_ECM_RECEPTOR_ INTERACTION	83	0.60605187	1.52489243	0.000999	0.03299416	0.02839298	7196	Tags = 53%, list = 20 %, signal = 43%
KEGG_HYPERTROPHIC_ CARDIOMYOPATHY_HCM	83	0.57650225	1.45054239	0.000999	0.03299416	0.02839298	9738	Tags = 52%, list = 27 %, signal = 38%
KEGG_NEUROACTIVE_LIGAND_ RECEPTOR_INTERACTION	270	0.58383597	1.51792562	0.000999	0.03299416	0.02839298	8274	Tags = 55%, list = 23 %, signal = 43%
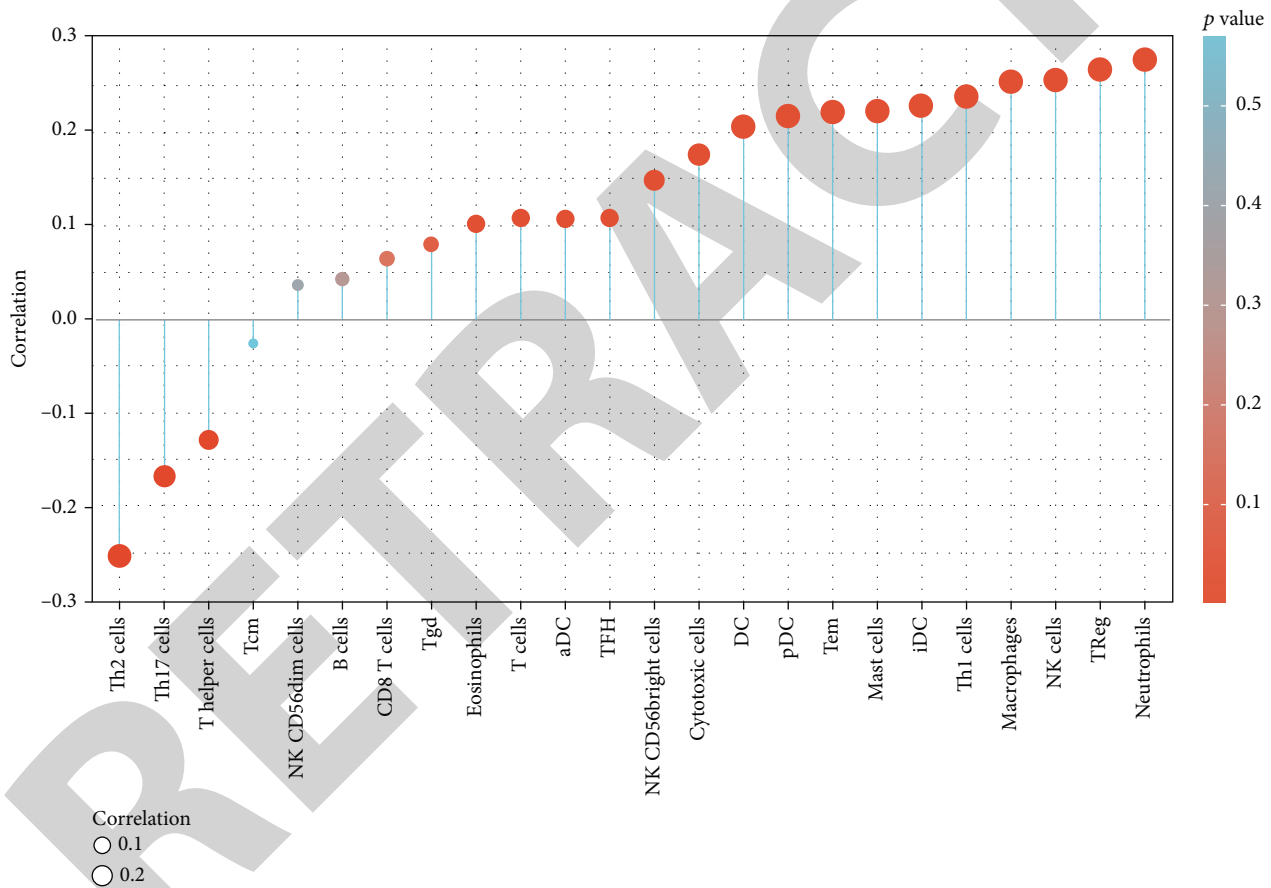
FIGURE 5: Correlation analysis of DNM1 levels and immune cell infiltration.

promotes CC progression [30], suggesting regulation of this pathway as a new avenue for preventing CC development. Cell migration is a highly coordinated process involving the integration of ECM with the actin cytoskeleton across the plasma membrane via receptors [31]. Focal adhesion kinase (FAK) may be activated by the ECM, and its tyrosine phosphorylation facilitates the formation of focal complexes that mature into focal adhesions [32]. Wang et al. [33] found that targeted regulation of miR-17-5p may affect the neuroactive ligand-receptor interaction pathway and promote the

proliferation and apoptosis of gastric cancer cells. CC immunotherapy studies have sought to identify new biomarkers and create rational combination therapy protocols. Thus, drugs targeting these signaling pathways may offer new therapeutic opportunities for CC therapy management.

The tumor microenvironment has a crucial role in tumorigenesis [34]. Our study of the correlation between DNM1 and immune cells found that neutrophils, Tregs, NK cells, and macrophages positively correlate with DNM1 expression, highlighting the importance of DNM1 in
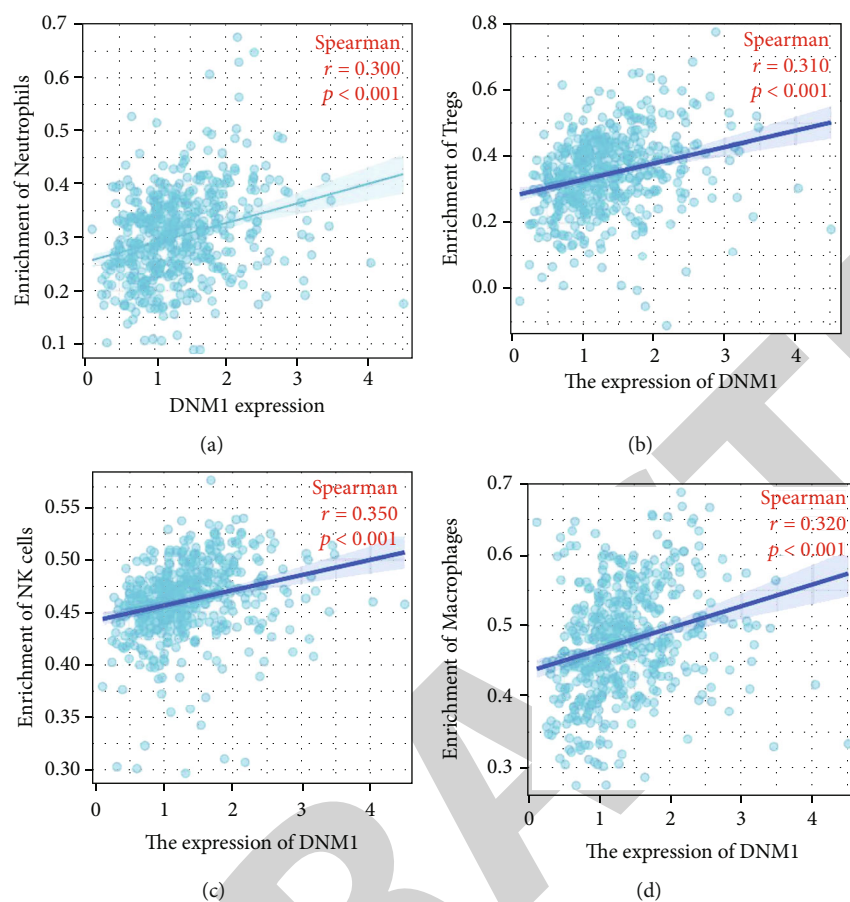
Figure 6: Association analysis between the DNM1 expression and immune cell infiltration levels. (a) Neutrophils. (b) Tregs. (c) NK cells. (d) Macrophages.

regulating the CC tumor immune microenvironment. Neutrophils, the main inflammatory component in tumors, produce cytokines and stimulate tumor progression [35]. Tumor-associated neutrophils (TANs) can recruit immune T cells, which may promote tumor growth, progression, and resistance to chemotherapy [36]. Zhang et al. [37] demonstrated that TANs can independently influence OS and DFS in colorectal cancer. Tregs reduce immunotherapy effectiveness due to their antitumor immune effects [38]. Thus, anti-Treg immunotherapy may be highly effective in CC patients. NK cells are natural lymphocytes that can kill viral infections or cancer cells [39]. Imai et al. [40] found that tumor progression was associated with reduced NK cells' killing capacity in peripheral blood. Thus, NK cells control tumorigenesis and hold great promise as an anti-CC immunotherapeutic target. Macrophages are critical components of the innate immune system [41], and tumor-associated macrophages (TAM) in the tumor microenvironment accelerate angiogenesis, immunosuppression, and cancer cell proliferation, thereby supporting tumor metastasis and growth [42]. Researchers have attempted to restore or enhance the killing ability of macrophages against tumor cells through various approaches, including inhibiting the transformation of TAM to the M1 type and promoting their activation as antigen-presenting cells against other antitumor effector cells, making macrophages an important

member of tumor immunotherapy studies [43–45]. These findings suggest that the effect of DNM1 in CC may be significantly associated with immune infiltration. Our study is the first to clarify the influence of DNM1 expression on CC. Although our results have clinical significance, the study still has some limitations. Firstly, it lacks experimental validation. Secondly, data used in the study were obtained from TCGA only; thus, some biological information may be inevitably overlooked, leading to bias in the final results.

In summary, our findings suggest that high DNM1 expression closely correlates with poor CC prognosis. The key potential DNM1-regulated pathways in CC are neuroactive ligand-receptor interaction, hypertrophic cardiomyopathy (HCM), ECM-receptor interaction, calcium signaling, and dilated cardiomyopathy. Moreover, the DNM1 expression level significantly correlates with infiltration by neutrophils, Tregs, NK cells, and macrophages. Thus, DNM1 has the potential as a biomarker for the diagnosis and prognosis of colon cancer.

Data Availability

Publicly available datasets were analyzed in this study. These data can be found here: https://portal.gdc.cancer.gov. The data from TCGA are publicly available and open-access. Therefore, the local ethics committees did not need to

approve the study because the current research follows TCGA data access policies and publication guidelines.

Ethical Approval

TCGA belongs to public databases. The patients involved in the database have obtained ethical approval. Users can download relevant data for free for research and publication purposes. Our study is based on open-source data, so there are no ethical issues and other conflicts of interest.

Conflicts of Interest

The authors have no conflicts of interest to declare.

Authors' Contributions

Mingchao Hu, Jianchun Gu, and Chungen Xing contributed to the idea for the article. Wenzhao Su, Zhenjie Zhang, and Qiang Wang contributed to the data analysis. Baosong Zhu contributed to the manuscript review. Mingchao Hu and Jianchun Gu contributed equally to this work.

Acknowledgments

References

[1] F. Bray, J. Ferlay, I. Soerjomataram, R. L. Siegel, L. A. Torre, and A. Jemal, "Global cancer statistics 2018: GLOBOCAN estimates of incidence and mortality worldwide for 36 cancers in 185 countries," *CA: a Cancer Journal for Clinicians*, vol. 68, no. 6, pp. 394–424, 2018.

[2] M. Fleming, S. Ravula, S. F. Tatishchev, and H. L. Wang, "Colorectal carcinoma: pathologic aspects," *Journal of Gastrointestinal Oncology*, vol. 3, no. 3, pp. 153–173, 2012.

[3] J. R. Bailey, A. Aggarwal, and T. F. Imperiale, "Colorectal cancer screening: stool DNA and other noninvasive modalities," *Gut and Liver*, vol. 10, no. 2, pp. 204–211, 2016.

[4] K. Garborg, Ø. Holme, M. Løberg, M. Kalager, H. O. Adami, and M. Bretthauer, "Current status of screening for colorectal cancer," *Annals of Oncology : official journal of the European Society for Medical Oncology*, vol. 24, no. 8, pp. 1963–1972, 2013.

[5] C. Chen, E. Läcke, C. Stock, M. Hoffmeister, and H. Brenner, "Colonoscopy and sigmoidoscopy use among older adults in different countries: a systematic review," *Preventive Medicine*, vol. 103, pp. 33–42, 2017.

[6] I. Dagogo-Jack and A. T. Shaw, "Tumour heterogeneity and resistance to cancer therapies," *Nature Reviews Clinical Oncology*, vol. 15, no. 2, pp. 81–94, 2018.

[7] L. Keller and K. Pantel, "Unravelling tumour heterogeneity by single-cell profiling of circulating tumour cells," *Nature Reviews Cancer*, vol. 19, no. 10, pp. 553–567, 2019.

[8] K. A. Heichman, "Blood-based testing for colorectal cancer screening," *Molecular Diagnosis & Therapy*, vol. 18, no. 2, pp. 127–135, 2014.

[9] R. Zhou, J. Zhang, D. Zeng et al., "Immune cell infiltration as a biomarker for the diagnosis and prognosis of stage I-III colon cancer," *Cancer Immunology, Immunotherapy: CII*, vol. 68, no. 3, pp. 433–442, 2019.

[10] X. Li, D. Wen, X. Li, C. Yao, W. Chong, and H. Chen, "Identification of an immune signature predicting prognosis risk and lymphocyte infiltration in colon cancer," *Frontiers in Immunology*, vol. 11, p. 1678, 2020.

[11] G. J. Doherty and H. T. McMahon, "Mechanisms of endocytosis," *Annual Review of Biochemistry*, vol. 78, no. 1, pp. 857–902, 2009.

[12] S. M. Ferguson and P. De Camilli, "Dynamin, a membrane-remodelling GTPase," *Nature Reviews Molecular Cell Biology*, vol. 13, no. 2, pp. 75–88, 2012.

[13] C. R. Reis, P. H. Chen, S. Srinivasan, F. Aguet, M. Mettlen, and S. L. Schmid, "Crosstalk between Akt/GSK3β signaling and dynamin-1 regulates clathrin-mediated endocytosis," *The EMBO Journal*, vol. 34, no. 16, pp. 2132–2146, 2015.

[14] A. N. Sahly, E. Krochmalnek, J. St-Onge, M. Srour, and K. A. Myers, "Severe DNM1 encephalopathy with dysmyelination due to recurrent splice site pathogenic variant," *Human Genetics*, vol. 139, no. 12, pp. 1575–1578, 2020.

[15] S. Appenzeller, R. Balling, N. Barisic et al., "De Novo Mutations in Synaptic Transmission Genes Including _DNM1_ Cause Epileptic Encephalopathies," *American Journal of Human Genetics*, vol. 95, no. 4, pp. 360–370, 2014.

[16] E. Brereton, E. Fassi, G. C. Araujo et al., "Mutations in the PH domain ofDNM1are associated with a nonepileptic phenotype characterized by developmental delay and neurobehavioral abnormalities," *Molecular Genetics & Genomic Medicine*, vol. 6, no. 2, pp. 294–300, 2018.

[17] H. Yamada, T. Takeda, H. Michiue, T. Abe, and K. Takei, "Actin bundling by dynamin 2 and cortactin is implicated in cell migration by stabilizing filopodia in human non-small cell lung carcinoma cells," *International Journal of Oncology*, vol. 49, no. 3, pp. 877–886, 2016.

[18] S. A. Raja, S. Shah, A. Tariq et al., "Caveolin-1 and dynamin-2 overexpression is associated with the progression of bladder cancer," *Oncology Letters*, vol. 18, no. 1, pp. 219–226, 2019.

[19] M. Tian, X. Yang, Y. Li, and S. Guo, "The expression of dynamin 1, 2, and 3 in human hepatocellular carcinoma and patient prognosis," *Medical Science Monitor : international medical journal of experimental and clinical research*, vol. 26, article e923359, 2020.

[20] Cancer Genome Atlas Network, "Comprehensive molecular characterization of human colon and rectal cancer," *Nature*, vol. 487, no. 7407, pp. 330–337, 2012.

[21] A. Subramanian, P. Tamayo, V. K. Mootha et al., "Gene set enrichment analysis: a knowledge-based approach for interpreting genome-wide expression profiles," *Proceedings of the National Academy of Sciences of the United States of America*, vol. 102, no. 43, pp. 15545–15550, 2005.

[22] F. Finotello and Z. Trajanoski, "Quantifying tumor-infiltrating immune cells from transcriptomics data," *Cancer Immunology, Immunotherapy: CII*, vol. 67, no. 7, pp. 1031–1040, 2018.

[23] J. Kruppa and K. Jung, "Automated multigroup outlier identification in molecular high-throughput data using bagplots and gemplots," *BMC Bioinformatics*, vol. 18, no. 1, p. 232, 2017.

Retraction

Retracted: Establishment and Validation of an MTORC1 Signaling-Related Gene Signature to Predict Overall Survival in Patients with Hepatocellular Carcinoma

BioMed Research International

This article has been retracted by Hindawi following an investigation undertaken by the publisher [1]. This investigation has uncovered evidence of one or more of the following indicators of systematic manipulation of the publication process:

(1) Discrepancies in scope

(2) Discrepancies in the description of the research reported

(3) Discrepancies between the availability of data and the research described

(4) Inappropriate citations

(5) Incoherent, meaningless and/or irrelevant content included in the article

(6) Manipulated or compromised peer review

The presence of these indicators undermines our confidence in the integrity of the article's content and we cannot, therefore, vouch for its reliability. Please note that this notice is intended solely to alert readers that the content of this article is unreliable. We have not investigated whether authors were aware of or involved in the systematic manipulation of the publication process.

Wiley and Hindawi regrets that the usual quality checks did not identify these issues before publication and have since put additional measures in place to safeguard research integrity.

We wish to credit our own Research Integrity and Research Publishing teams and anonymous and named external researchers and research integrity experts for contributing to this investigation.

The corresponding author, as the representative of all authors, has been given the opportunity to register their agreement or disagreement to this retraction. We have kept a record of any response received.

References

[1] Z. Yao, S. Wen, J. Luo, W. Hao, W. Liang, and Y. Chen, "Establishment and Validation of an MTORC1 Signaling-Related Gene Signature to Predict Overall Survival in Patients with Hepatocellular Carcinoma," *BioMed Research International*, vol. 2021, Article ID 6299472, 15 pages, 2021.

Research Article

Establishment and Validation of an MTORC1 Signaling-Related Gene Signature to Predict Overall Survival in Patients with Hepatocellular Carcinoma

Zheng Yao, Song Wen, Jun Luo, Weiyuan Hao, Weiren Liang, and Yutang Chen [ID]

Department of Radiology Intervention, Cancer Hospital of the University of Chinese Academy of Sciences (Zhejiang Cancer Hospital), Hangzhou, 310000 Zhejiang, China

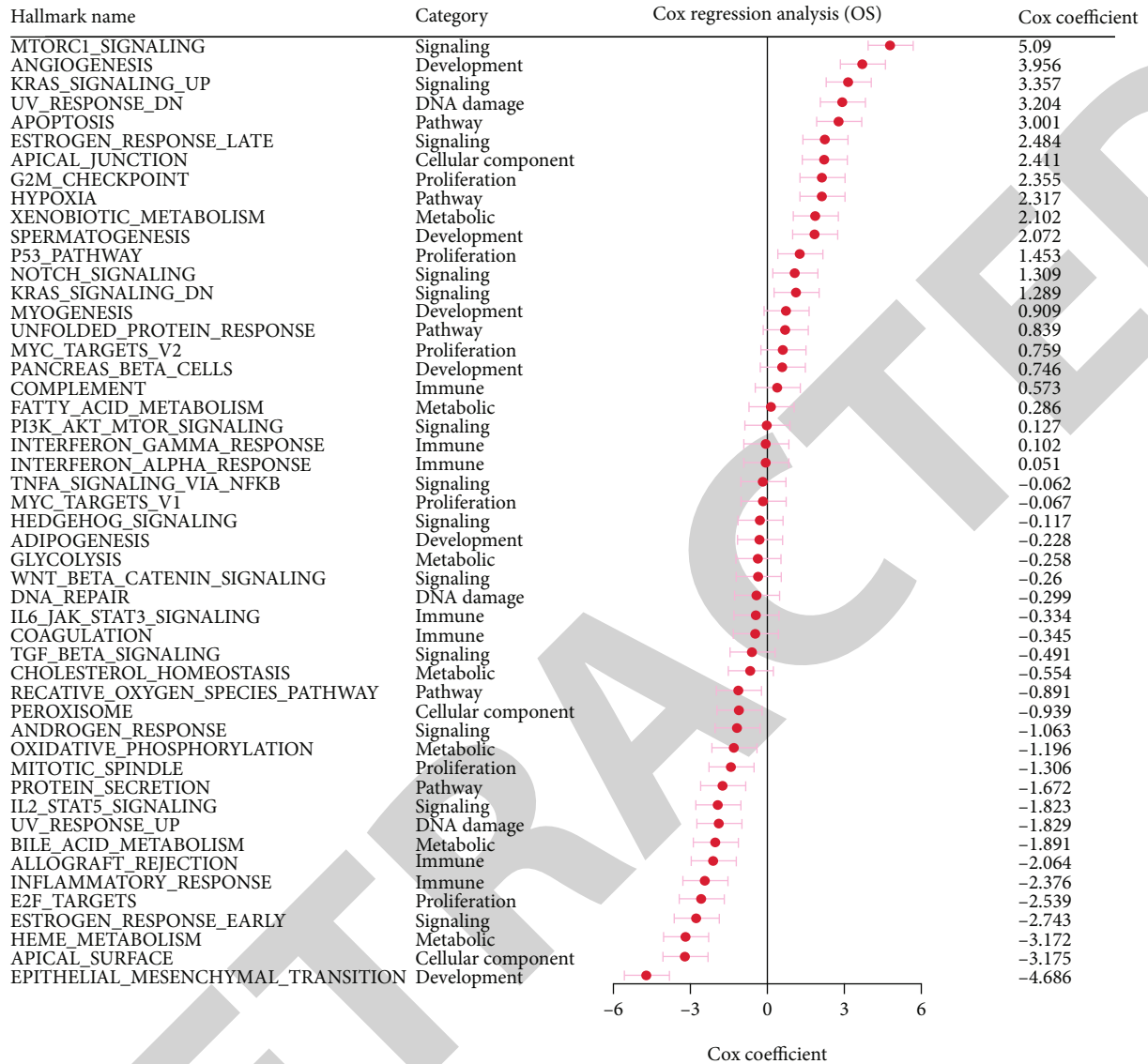Correspondence should be addressed to Yutang Chen; chenyutang@126.com

Background. Accurate and effective biomarkers for the prognosis of patients with hepatocellular carcinoma (HCC) are poorly identified. A network-based gene signature may serve as a valuable biomarker to improve the accuracy of risk discrimination in patients. *Methods*. The expression levels of cancer hallmarks were determined by Cox regression analysis. Various bioinformatic methods, such as GSEA, WGCNA, and LASSO, and statistical approaches were applied to generate an MTORC1 signaling-related gene signature (MSRS). Moreover, a decision tree and nomogram were constructed to aid in the quantification of risk levels for each HCC patient. *Results*. Active MTORC1 signaling was found to be the most vital predictor of overall survival in HCC patients in the training cohort. MSRS was established and proved to hold the capacity to stratify HCC patients with poor outcomes in two validated datasets. Analysis of the patient MSRS levels and patient survival data suggested that the MSRS can be a valuable risk factor in two validated datasets and the integrated cohort. Finally, we constructed a decision tree which allowed to distinguish subclasses of patients at high risk and a nomogram which could accurately predict the survival of individuals. *Conclusions*. The present study may contribute to the improvement of current prognostic systems for patients with HCC.

1. Introduction

Hepatocellular carcinoma (HCC) is the most common form of liver cancer globally and is a leading cause of cancer-related mortality [1, 2]. Currently, the available potentially curative approaches are only suitable for early-stage HCC cases [3], whereas the majority of HCC patients are diagnosed at relatively advanced stages and thus have poor prognosis [1, 4]. Additionally, biomarkers, as emerging tools, play a pivotal role in the diagnosis, prognosis, and prediction of treatment responses, leading to the improvement of patient stratification and clinical outcomes [5]. However, accurate and sufficient biomarkers are still lacking; therefore, there is an urgent need to tackle this limitation by identifying network-based biomarkers for the discrimination of HCC patients with unfavorable outcomes.

MTORC1 signaling belongs to the mTOR pathway, which also includes MTORC2 signaling [6]. It has been proved that aberrant activation of MTORC1 signaling results in tumorigenesis and cancer progression through enhanced cell survival and metastasis [7, 8]. Various research groups have reported that the expression levels of components or modulators of MTORC1 signaling, such as p-AKT and RICTOR, are associated with poor survival in patients with HCC [9]. A recent study reported that a six-gene signature based on MTORC1 signaling can be used for the prognosis of patients with HCC [10]. Nevertheless, a systematic MTORC1 signaling signature based on this coexpression network has yet to be constructed for the application to HCC risk stratification.

In the present study, we found that active MTORC1 signaling was the most predominant predictor of overall survival among a variety of cancer hallmarks. Moreover, by

Hallmark name	Category	Cox regression analysis (OS)	Cox coefficient
MTORC1_SIGNALING	Signaling		5.09
ANGIOGENESIS	Development		3.956
KRAS_SIGNALING_UP	Signaling		3.357
UV_RESPONSE_DN	DNA damage		3.204
APOPTOSIS	Pathway		3.001
ESTROGEN_RESPONSE_LATE	Signaling		2.484
APICAL_JUNCTION	Cellular component		2.411
G2M_CHECKPOINT	Proliferation		2.355
HYPOXIA	Pathway		2.317
XENOBIOTIC_METABOLISM	Metabolic		2.102
SPERMATOGENESIS	Development		2.072
P53_PATHWAY	Proliferation		1.453
NOTCH_SIGNALING	Signaling		1.309
KRAS_SIGNALING_DN	Signaling		1.289
MYOGENESIS	Development		0.909
UNFOLDED_PROTEIN_RESPONSE	Pathway		0.839
MYC_TARGETS_V2	Proliferation		0.759
PANCREAS_BETA_CELLS	Development		0.746
COMPLEMENT	Immune		0.573
FATTY_ACID_METABOLISM	Metabolic		0.286
PI3K_AKT_MTOR_SIGNALING	Signaling		0.127
INTERFERON_GAMMA_RESPONSE	Immune		0.102
INTERFERON_ALPHA_RESPONSE	Immune		0.051
TNFA_SIGNALING_VIA_NFKB	Signaling		−0.062
MYC_TARGETS_V1	Proliferation		−0.067
HEDGEHOG_SIGNALING	Signaling		−0.117
ADIPOGENESIS	Development		−0.228
GLYCOLYSIS	Metabolic		−0.258
WNT_BETA_CATENIN_SIGNALING	Signaling		−0.26
DNA_REPAIR	DNA damage		−0.299
IL6_JAK_STAT3_SIGNALING	Immune		−0.334
COAGULATION	Immune		−0.345
TGF_BETA_SIGNALING	Signaling		−0.491
CHOLESTEROL_HOMEOSTASIS	Metabolic		−0.554
RECATIVE_OXYGEN_SPECIES_PATHWAY	Pathway		−0.891
PEROXISOME	Cellular component		−0.939
ANDROGEN_RESPONSE	Signaling		−1.063
OXIDATIVE_PHOSPHORYLATION	Metabolic		−1.196
MITOTIC_SPINDLE	Proliferation		−1.306
PROTEIN_SECRETION	Pathway		−1.672
IL2_STAT5_SIGNALING	Signaling		−1.823
UV_RESPONSE_UP	DNA damage		−1.829
BILE_ACID_METABOLISM	Metabolic		−1.891
ALLOGRAFT_REJECTION	Immune		−2.064
INFLAMMATORY_RESPONSE	Immune		−2.376
E2F_TARGETS	Proliferation		−2.539
ESTROGEN_RESPONSE_EARLY	Signaling		−2.743
HEME_METABOLISM	Metabolic		−3.172
APICAL_SURFACE	Cellular component		−3.175
EPITHELIAL_MESENCHYMAL_TRANSITION	Development		−4.686

Cox coefficient

−6   −3   0   3   6

(a)

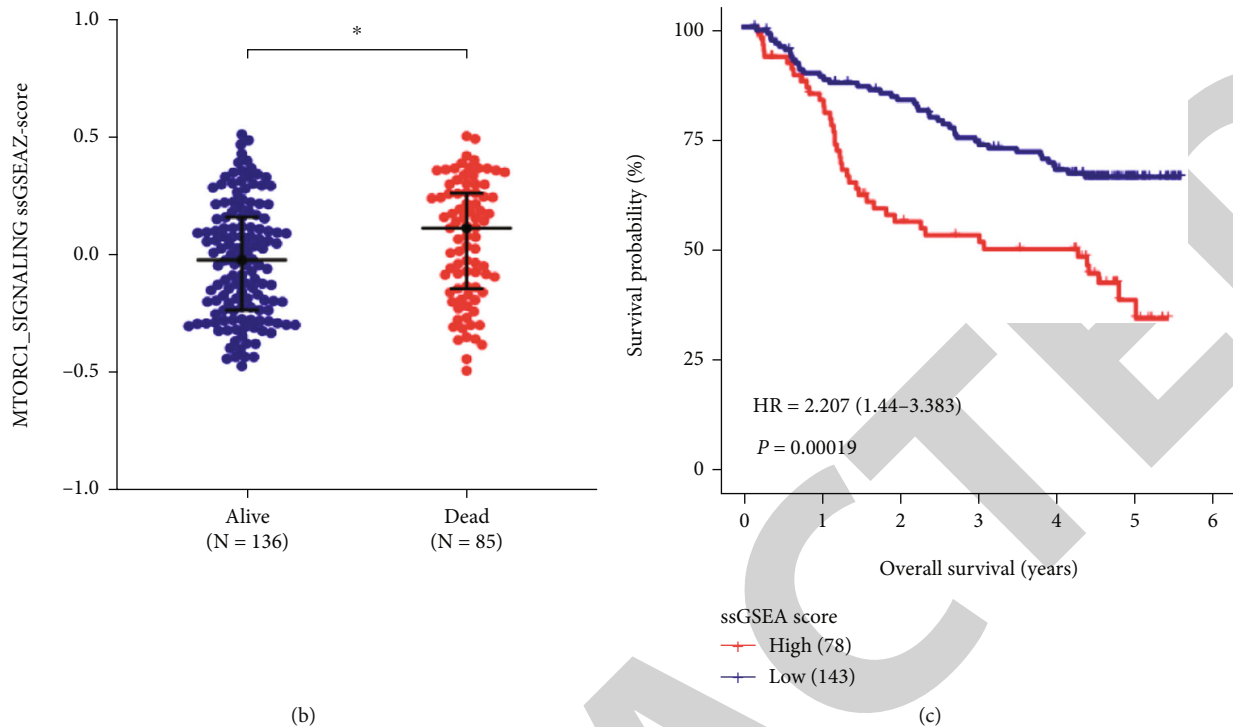Figure 1: Continued.

(b)

(c)

FIGURE 1: MTORC1 signaling is identified as a primary factor for the survival of patients with HCC. (a) Cox regression analysis for the identification of primary factors affecting the overall survival (OS) of HCC patients. (b) Single-sample gene set enrichment analysis (ssGSEA) scores of MTORC1 signaling in patients who were alive or dead during follow-up. (c) Kaplan–Meier plot indicating the survival probabilities of HCC patients stratified by their ssGSEA score of MTORC1 signaling.

applying multiple bioinformatic approaches, an MTORC1 signaling-related gene signature (MSRS) was created; this was found to be robust for risk discrimination via validation in different cohorts. Furthermore, a decision tree and nomogram that integrated multiple clinical parameters were generated to optimize the entire procedure of risk stratification for HCC patients.

2. Material and Methods

2.1. Data Processing. The clinicopathological details and survival data of the training dataset GSE14520 [11] and the validation dataset I GSE76427 [12] were downloaded from the GEO database (http://www.ncbi.nlm.nih.gov/geo/). The same information for the validation cohort II TCGA-LIHC [13] was derived from https://portal.gdc.cancer.gov/projects/TCGA-LIHC. All data used in this study were normalized.

2.2. Pathway Enrichment and Construction of an MTORC1 Signaling-Related Signature. The R package "survival" was applied to perform Cox regression analysis for the assessment of the expression levels of hallmark gene sets [14, 15]. Single-sample gene set enrichment analysis (ssGSEA) scores for each hallmark were determined using the R package "gsva." The construction of a scale-independent coexpression network and module was carried out using the "WGCNA" R package [16]. After the identification of the black module as the one most enriched in genes representing

the MTORC1 gene signature, least absolute shrinkage and selection operator (LASSO) Cox regression analysis was conducted to select the most relevant genes [17]. Finally, an MTORC1 signaling-related signature (MSRS) was constructed by calculating the gene expression levels with the corresponding LASSO Cox coefficients as previously described [18].

2.3. Bioinformatic Analysis. SPSS Statistics (IBM version 20), GraphPad Prism (version 7.0), Stata (version 12), and R software (version 4.1.1,http://www.r-project.org) were used to perform GSEA [19, 20] and generate the plots. The Z-score that is used to estimate the "enrichment" of the entire gene set was applied to calibrate ssGSEA scores [21] and MSRS, and the Kaplan–Meier approach was used to construct patient survival plots. Quantification of predictive power in terms of time-dependent receiver operating characteristic [22] was carried out using the R package "survival-ROC" [23]. A decision tree was generated by recursive partitioning analysis using the R package "rpart" [24]. A nomogram and a correlation curve were constructed using the R package "rms" [25]. Codes for all the algorithms used in this study can be obtained by request to the corresponding author.
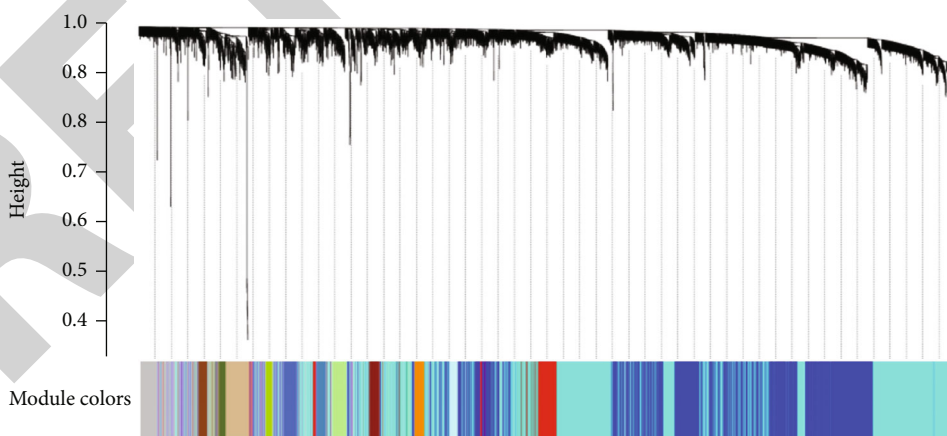
2.4. Statistical Analysis. The log-rank test was used to evaluate differences between the survival of two patient groups. Student's t-test or one-way analysis of variance (ANOVA) was used to determine statistically significant differences between the indicated groups. $p < 0.05$ was considered as
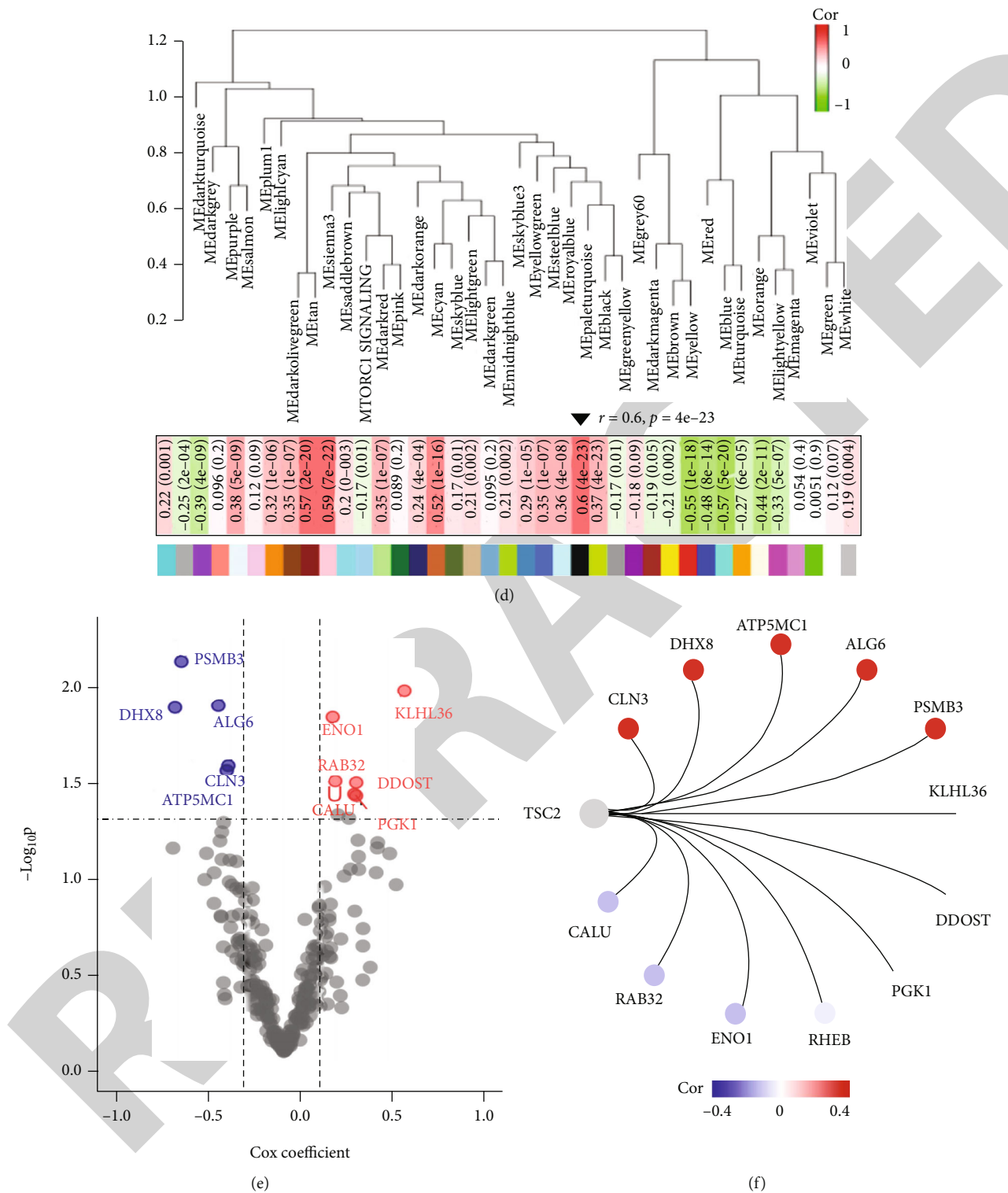
(a)


(b)

(c)
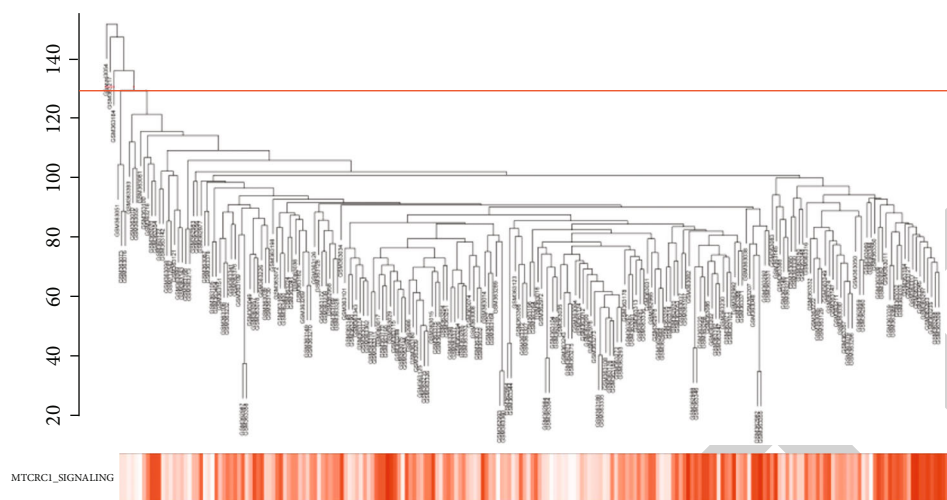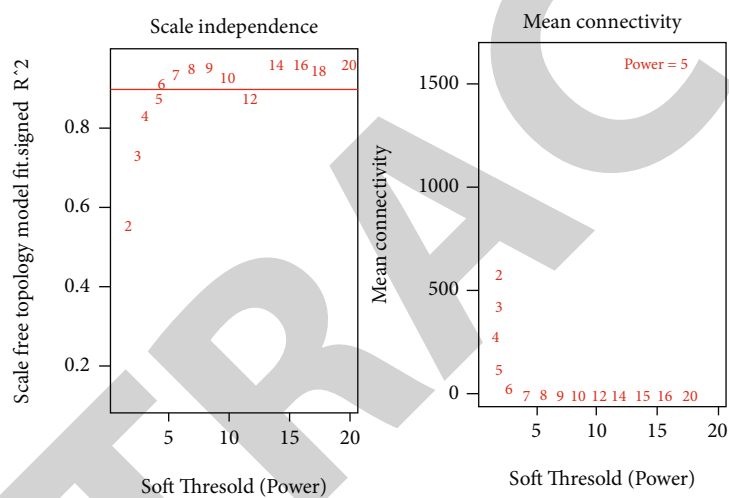
Figure 2: Continued.

FIGURE 2: Construction of an MTORC1 signaling-related signature (MSRS). (a) Cluster analysis of the patients' gene expression data. (b) Plot showing scale-free topology (left) and mean connectivity (right). (c) Results of WGCNA of transcriptomic data and ssGSEA Z-scores of MTORC1 signaling. (d) Correlations between the modules (labeled with different colors) and MTORC1 signaling. The black module, displaying the highest correlation, is highlighted. (e) Plot indicating hub gene candidates derived from the black module. (f) Correlations between *TSC2* expression and that of genes belonging to the MSRS.
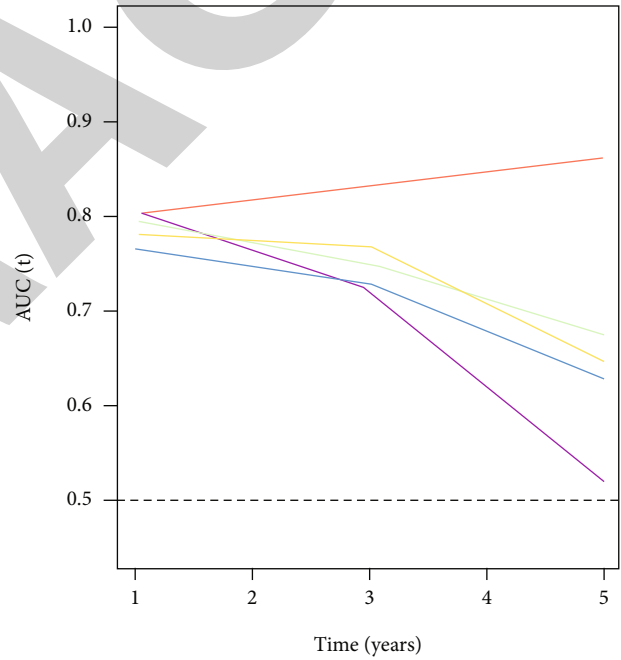
(a)

(b)

HR = 3.522 (2.205−5.624)
P < 0.0001
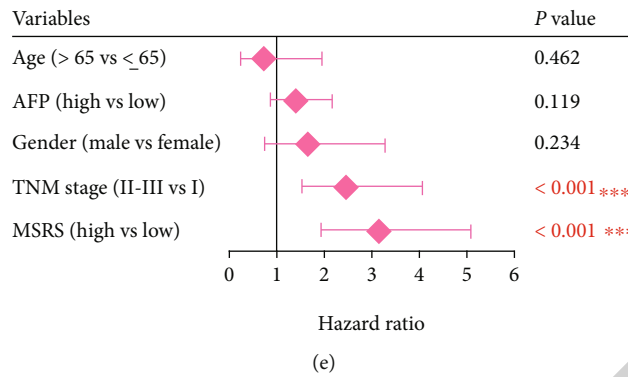
(c)

(d)

Figure 3: Continued.

(e)
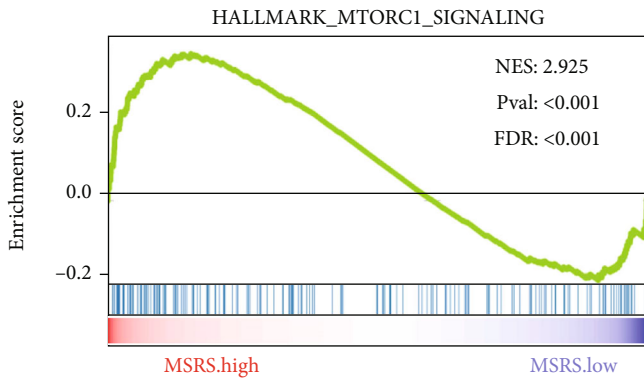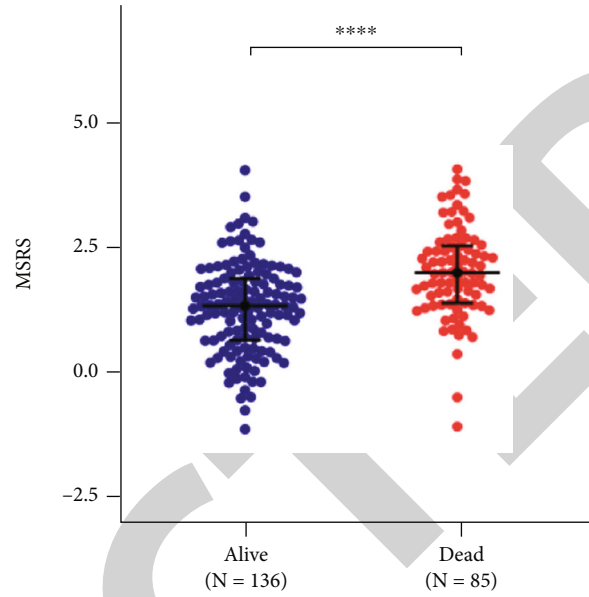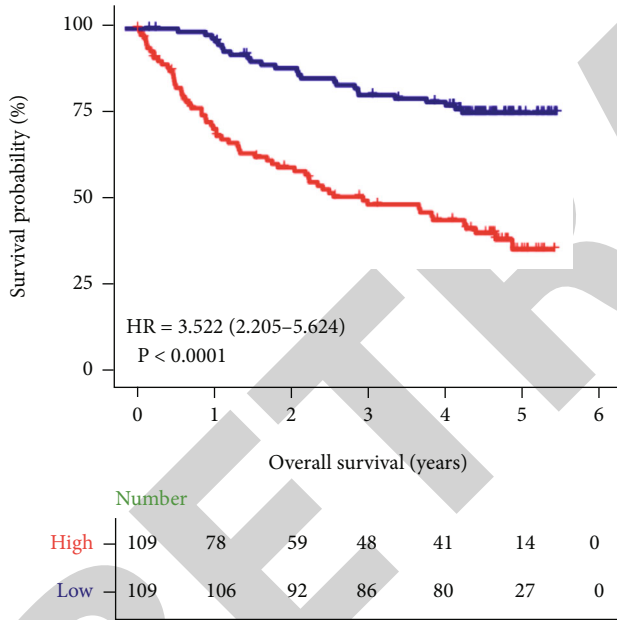
Figure 3: The MSRS enables to predict unfavorable outcome in the training dataset. (a) GSEA results confirming the prognostic robustness of the MSRS. (b) Comparison of MSRS scores between patients who were alive ($N = 138$) or dead ($N = 85$) during follow-up. (c) Kaplan–Meier plot indicating the survival probabilities of HCC patients stratified by their MSRS scores. (d) tROC assessment demonstrating the accuracy of the MSRS for predicting patient survival. (e) Multivariate Cox regression analysis for the validation of the MSRS as a risk factor.

threshold for statistical significance. *, $0.01 < p < 0.05$; **, $0.001 < p < 0.01$; ***, $0.0001 < p < 0.001$; ****$p < 0.0001$; ns: not significant.
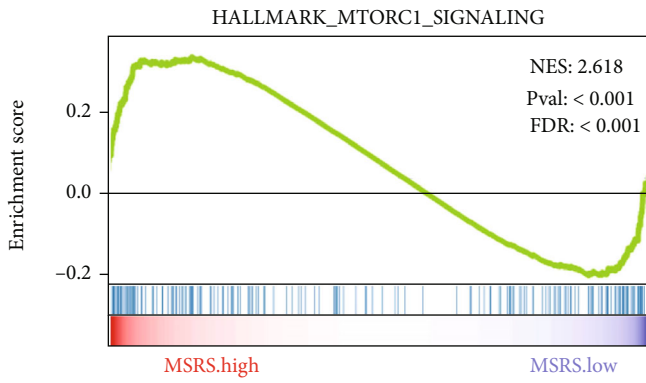
3. Results

3.1. Enriched Expression of MTORC1 Signaling Components Is a Primary Risk Factor for the Survival of Patients with HCC. To identify pathways or cellular processes suitable as novel primary factors for survival prediction in patients with HCC, we calculated the ssGSEA score of each hallmark from the Molecular Signatures Database (MSigDB) in the training cohort GSE14520, which includes transcriptomic data from 221 HCC patients. After ranking the hallmarks according to their Cox coefficients, we observed that MTORC1 signaling was significantly overrepresented with respect to other pathways or processes, including angiogenesis, KRAS signaling, and UV response, thereby becoming the most significant primary factor for predicting the overall survival of patients with HCC (Figure 1(a)). As shown in Figure 1(b), the ssGSEA Z-scores of genes implied in MTORC1 signaling were increased in deceased patients compared to those in patients who were alive during follow-up. Moreover, patient survival was significantly reduced (HR = 2.207, $p = 0.00019$) in patient subgroups exhibiting higher ssGSEA scores for MTORC1 signaling-related genes. Collectively, these results suggest that MTORC1 signaling is a promising primary factor for overall survival prediction in patients with HCC.

3.2. Construction of an MTORC1 Signaling-Related Signature to Predict the Outcome of HCC Patients. Next, we aimed to establish a robust MTORC1 signaling-related signature (MSRS) to better predict the survival outcome of patients with HCC. First, we performed sample clustering on the training dataset, and three samples (above the threshold indicated by the red line) were excluded as outliers in order to carry out more accurate further analysis (Figure 2(a)). After selecting power 5 as the optimal threshold for the scale-independent coexpression network (Figure 2(b)), we carried out weighted gene coexpression network analysis

(WGCNA). This pointed at the black module ($r = 0.6$, $p = 4e^{-23}$) as the module most correlated with MTORC1 signaling (Figures 2(c) and 2(d)). Furthermore, we performed univariate Cox regression analysis using isolated hub genes (with a p value for gene significance < 0.0001) as the input. As a result, 11 candidate markers (six positive and five negative) were identified as the most correlated with MTORC1 signaling (Figure 2(e)). As the tuberous sclerosis (TSC) complex is one of the most crucial negative regulators of MTORC1 signaling [26], we examined the correlations between the expression of *TSC2*, encoding a component of the TSC complex, and that of the 11 identified key hub genes. As expected, we observed strong reverse correlations between the expression levels of *TSC2* and those of risk genes such as *CALU* and positive correlations between *TSC2* expression and that of protective genes such as *CLN3* (Figure 2(f)).

3.3. The MSRS Enables to Predict Poor Survival of Patients in the Training Dataset. We proceeded to investigate whether the MSRS is capable of representing the status of MTORC1 signaling. As expected, GSEA confirmed that the MSRS was significantly correlated with MTORC1 signaling activation in the MSRS-high subgroup (Figure 3(a)). In addition, similar to MTORC1 signaling (Figure 1(b)), the MSRS score was increased in live patients when compared with dead patients in the aforementioned training dataset (Figure 3(b)). Moreover, patient survival analysis showed that HCC patients with high MSRS scores had a poor prognosis (Figure 3(c)). Subsequently, we aimed to test the accuracy of diverse pathological parameters for predicting the overall survival of patients with HCC. Of note, tROC quantification revealed that among all the tested clinical variables, the MSRS was the best prognosis indicator in the training cohort (Figure 3(d)). In line with this result, multivariate Cox regression analysis suggested that the MSRS and TNM stage are two distinct risk factors significantly affecting overall survival (Figure 3(e)). Taken together, our results demonstrated that the MSRS may act as an independent risk factor for overall survival prognosis in patients with HCC.
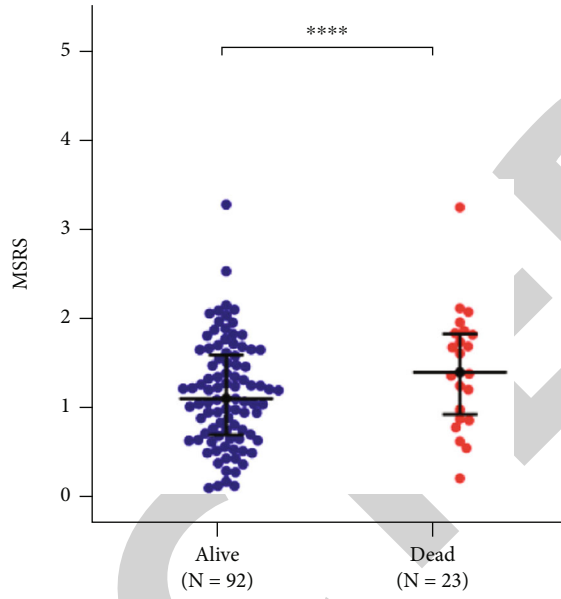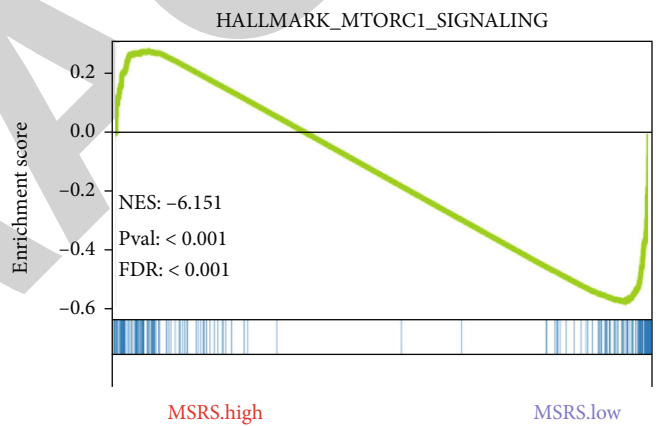
(a)

(b)
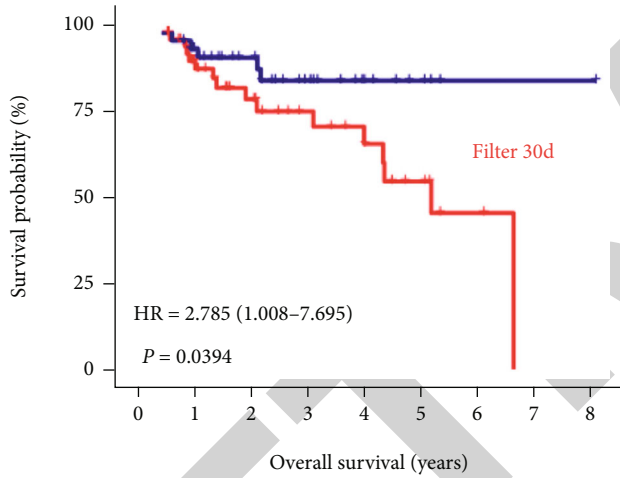
(c)

(d)

Figure 4: Continued.

(e)

(f)

(g)

(h)
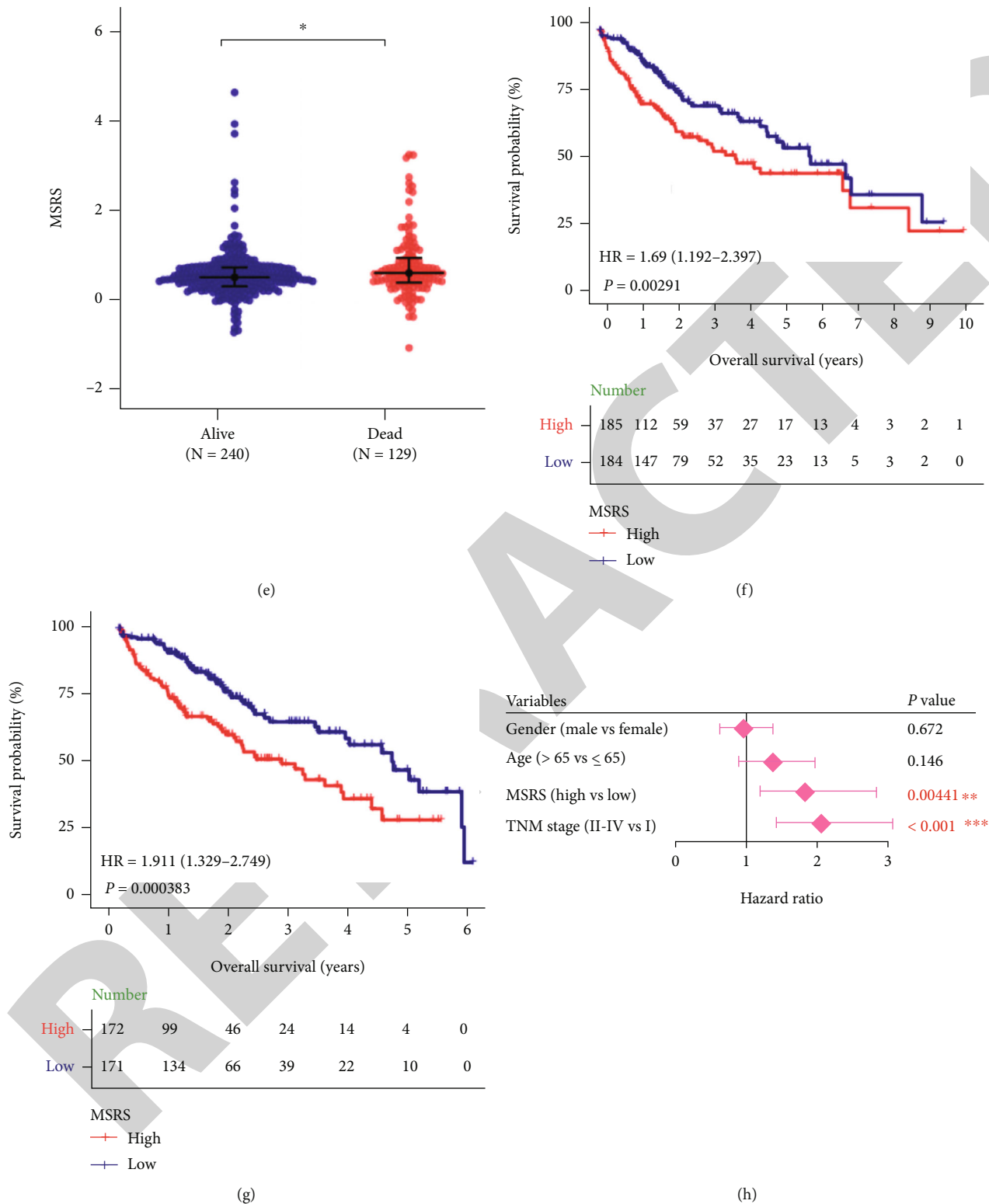
FIGURE 4: Validation of the MSRS as a predicting factor for worse prognosis in two additional datasets. (a) GSEA results confirming the prognostic value of the MSRS in the GSE76427 dataset ($N = 115$). (b) Comparison of MSRS scores between patients of the GSE76427 dataset who were alive ($N = 92$) or dead ($N = 23$) during follow-up. (c) Kaplan–Meier plot indicating the survival probabilities of HCC patients of the GSE76427 dataset stratified by their MSRS scores. (d) GSEA results confirming the prognostic value of the MSRS in TCGA-LIHC dataset ($N = 369$). (e) Comparison of MSRS scores between patients of TCGA-LIHC dataset who were alive ($N = 240$) or dead ($N = 129$) during follow-up. (f) Kaplan–Meier plot indicating the survival probabilities of HCC patients of TCGA-LIHC dataset stratified by their MSRS scores. (g) Kaplan–Meier plot indicating the survival probabilities (<6 years) of HCC patients of TCGA-LIHC dataset stratified by their MSRS scores. (h) Multivariate Cox regression analysis for the validation of the MSRS as a risk factor in TCGA-LIHC dataset (only the parameters relative to the first 6 years were included).

(a)

(b)
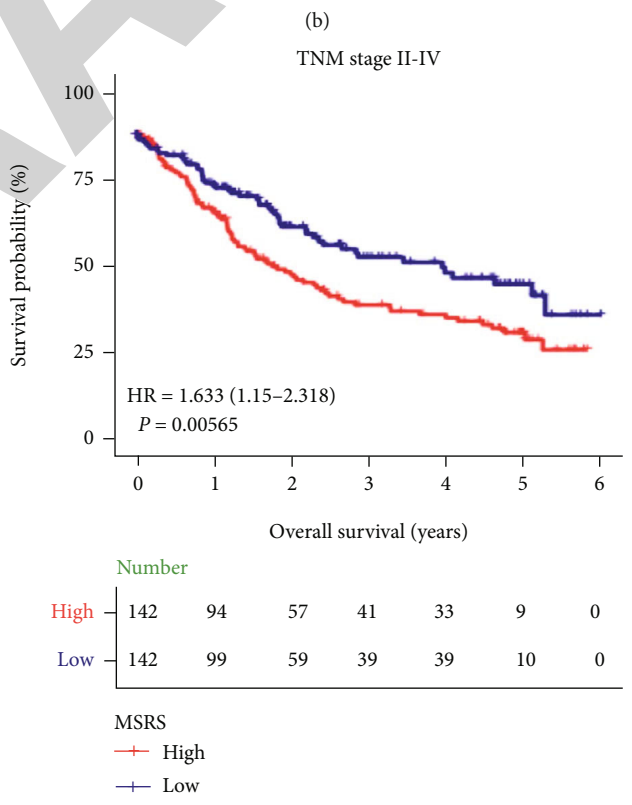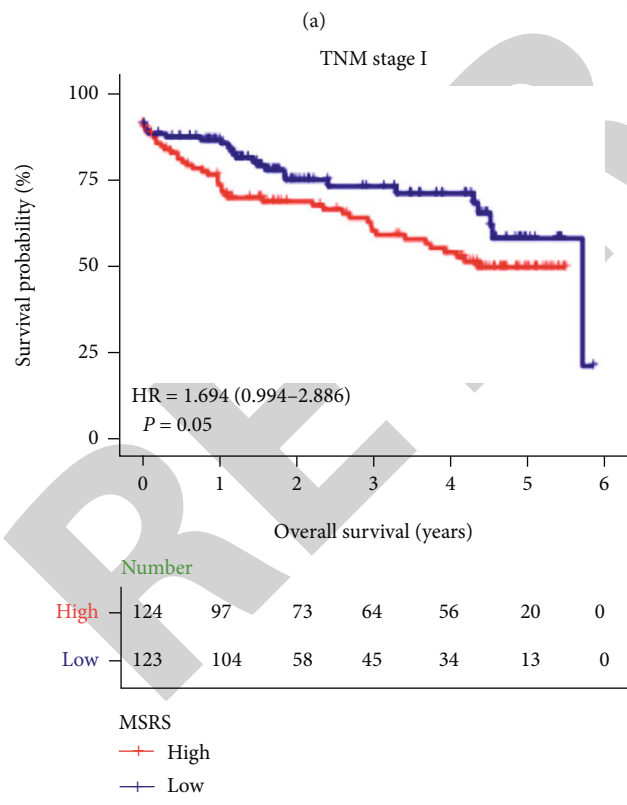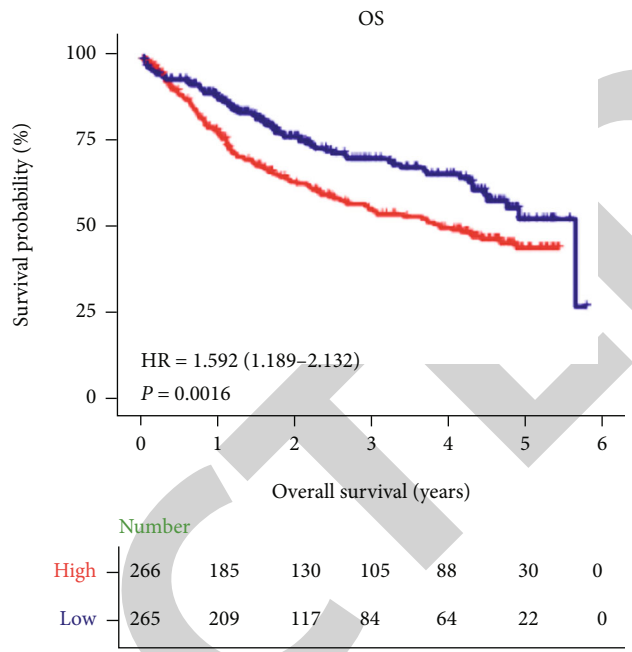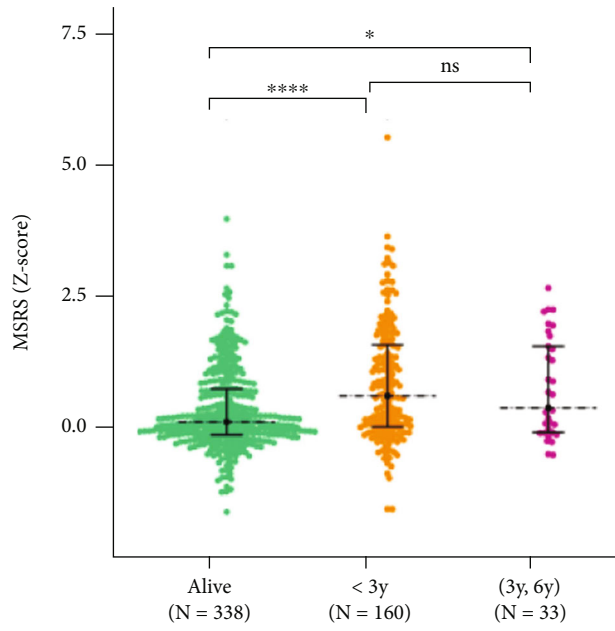
(c)

Figure 5: Continued.

(d)

(e)
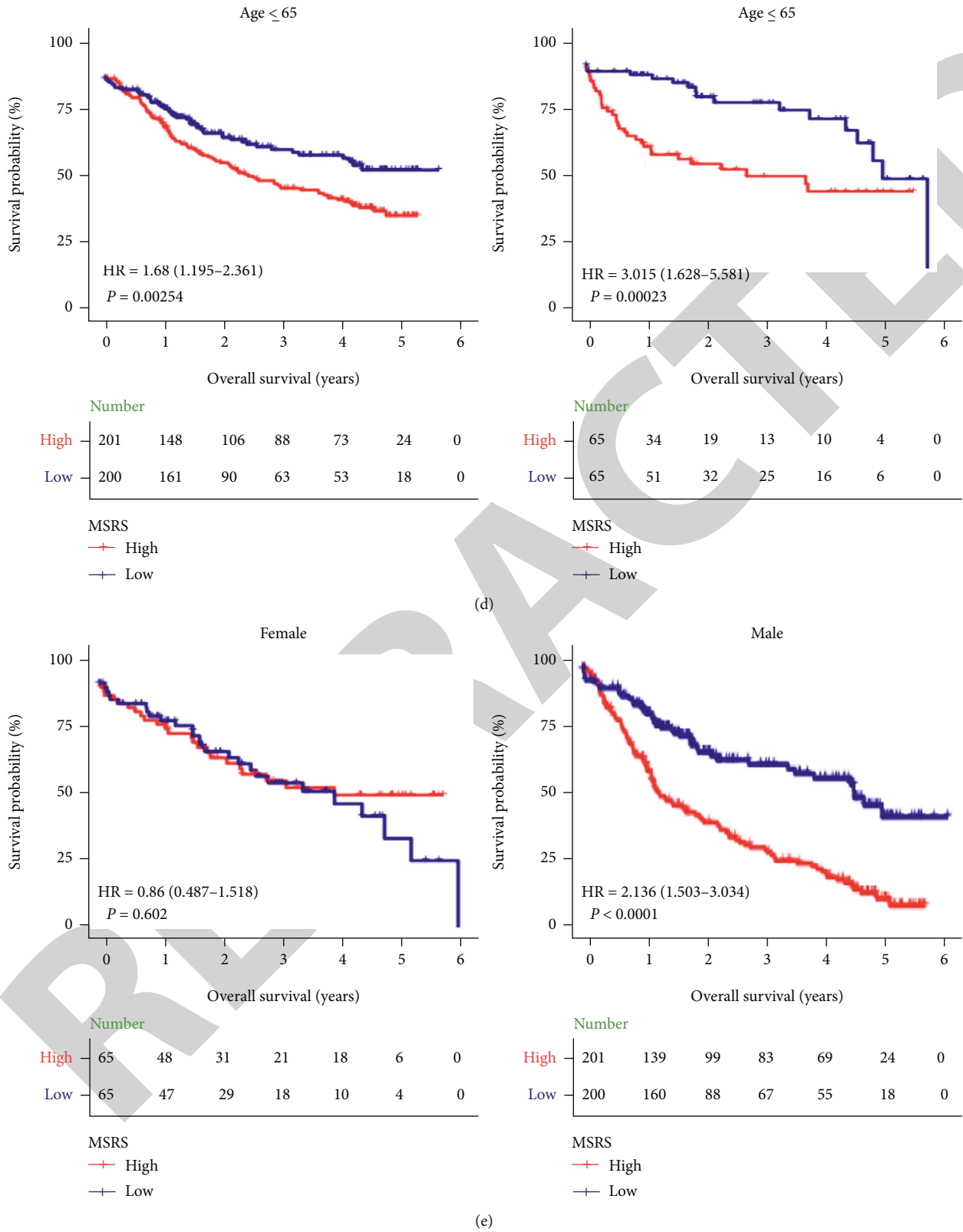
FIGURE 5: The MSRS serves as a prognostic indicator for poor outcome in a combined cohort and subcategories. (a) Comparison of MSRS Z-scores in alive patients ($N = 338$), patients who died within 3 years ($N = 160$), and patients who died between 3 and 6 years ($N = 33$). (b–e) Kaplan–Meier plot indicating the survival probabilities, in terms of overall survival, of HCC patients stratified by their MSRS scores in the (b) whole population or distinguished according to (c) early (left) or (c) late (right) TNM stages, (d) age under 65 (left) or over (d) 65 (right), and (e) gender.

(a)

(b)

(c)

(d)

Figure 6: Continued.

(e)

(f)
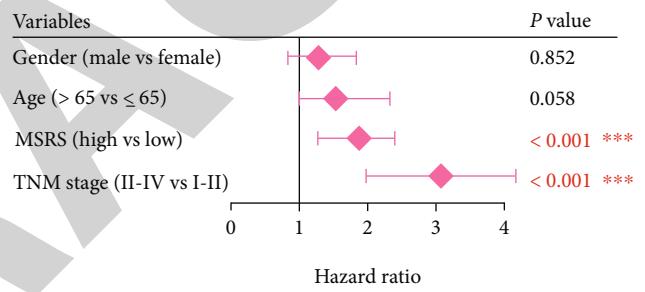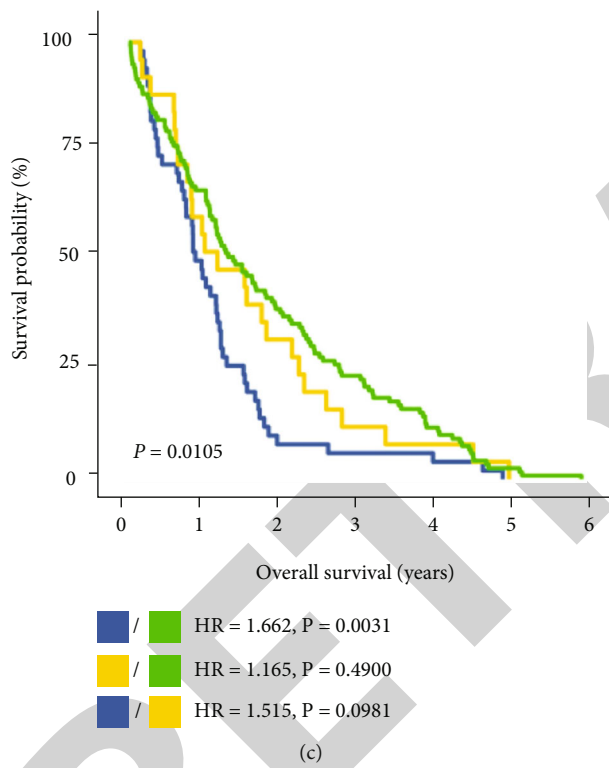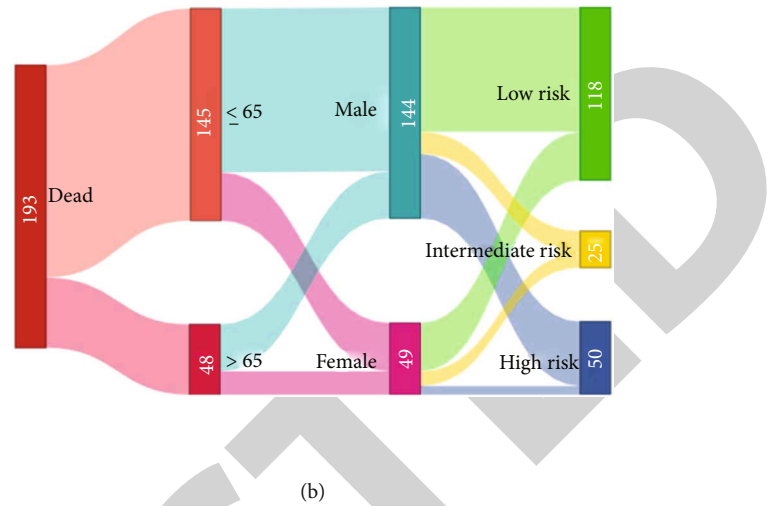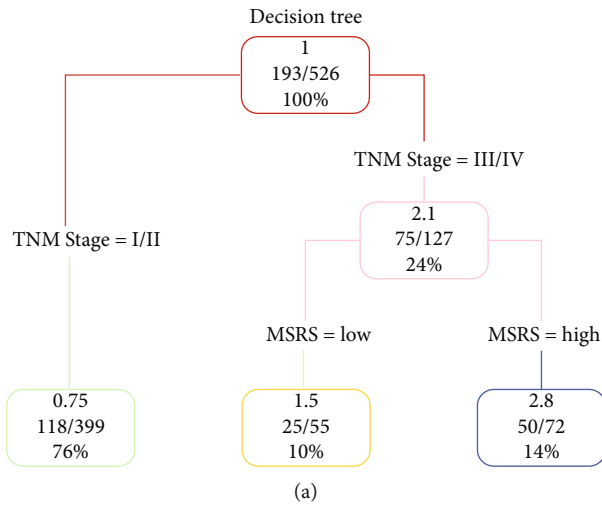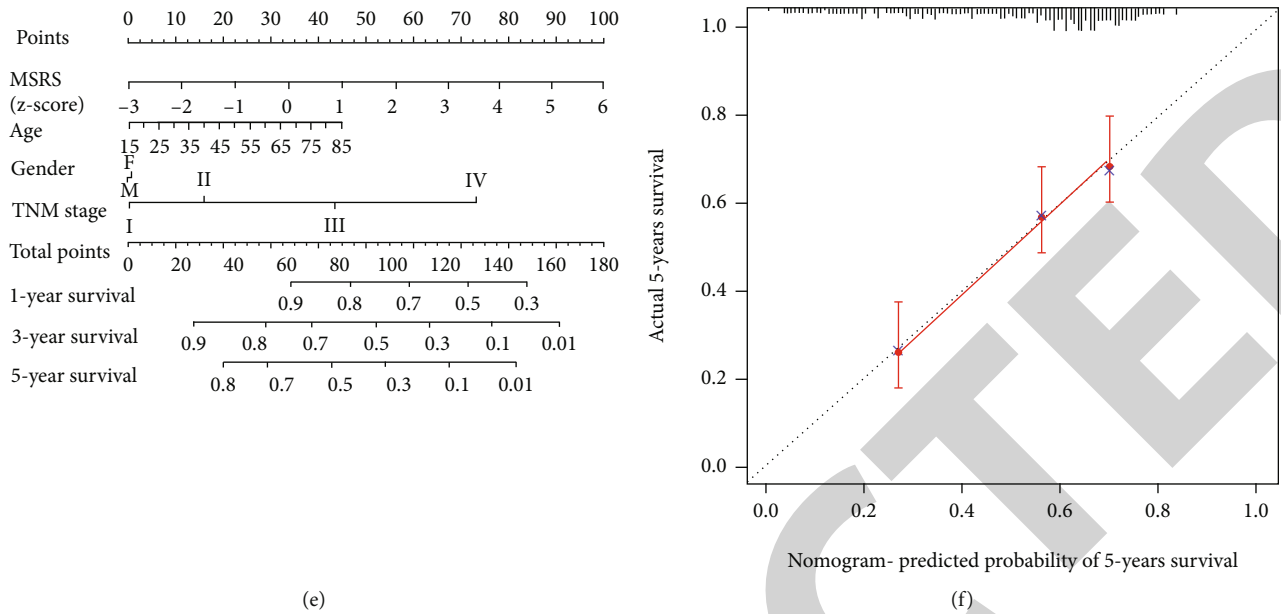
Figure 6: MSRS analysis increases the accuracy of risk stratification and survival prediction when combined with clinical parameters. (a, b) Decision tree for improving the risk stratification process. (c) Kaplan–Meier plot indicating the quality of the decision tree in terms of risk prediction. (d) Multivariate Cox regression analysis demonstrating the significance of diverse variables as primary factors. (e) Nomogram for evaluating the risk for a single patient. (f) Correlation between the actual 5-year survival of patients and that predicted by the nomogram.

3.4. Validation of the MSRS as a Predicting Factor for Worse Prognosis in Two Additional Datasets.

To further evaluate the prognostic robustness of the MSRS, we applied the methodology described above to two other datasets, GSE76427 ($N = 115$) and TCGA-LIHC ($N = 369$). Similar to the training cohort, the MSRS was significantly correlated with MTORC1 signaling in both datasets (Figures 4(a) and 4(d)). Moreover, MSRS scores were higher in deceased patients than in patients who were alive during follow-up (Figures 4(b) and 4(e)). Consistent with this data, survival analysis revealed that the outcomes of MSRS-high patients were worse than those of MSRS-low patients (Figures 4(c) and 4(f)). Since the second dataset consisted of a larger number of patients, we focused on the survival data from the first 6 years of this cohort to test the prediction robustness of the MSRS in relatively early stages of HCC. Interestingly, an even more significant difference between MSRS-high and MSRS-low patients was detected (Figure 4(g)). Furthermore, multivariate Cox regression modeling showed that the MSRS and TNM stage were independent predictors of overall survival in TCGA-LIHC cohort (Figure 4(h)). Therefore, we confirmed that the MSRS can be utilized in various cohorts as a highly effective survival predictor.

3.5. Effectiveness of the MSRS as a Prognostic Indicator of Worse Outcome in a Combined Cohort and Patient Subcategories.

To obtain a better overview of the prognostic value of the MSRS, we combined the training cohort with the two validation cohorts and performed additional analysis including comprehensive clinicopathological information of patients. Notably, we found that the Z-scores of MSRS genes were significantly increased in patients who died within 3 years or between 3 and 6 years from symptom onset in comparison with those of live patients in the pooled cohort (Figure 5(a)). Moreover, the MSRS could also distinguish high-risk HCC patients from the whole population (Figure 5(b)) or within multiple subcategories, such as patients with late TNM stages (stages II–IV, Figure 5(c)), patients of different age groups (Figure 5(d)), and males but not females (Figure 5(e)). In conclusion, we demonstrated that the MSRS is a useful survival predictor in both the whole population and certain subgroups.

3.6. MSRS Analysis Increases the Accuracy of Risk Stratification and Survival Prediction when Combined with Clinical Parameters.

To optimize the process of risk discrimination for overall survival, we generated a decision tree (Figure 6(a)). TNM stage and the MSRS, but not gender or age, were retained in the decision tree to predict the survival of patients who were finally grouped into three subclasses, that is, low risk, intermediate risk, and high risk (Figures 6(a) and 6(b)). Of note, the difference between patients with high and low risk was significant in terms of overall survival probabilities (Figure 6(c)). Moreover, multivariate Cox regression analysis indicated that both the MSRS and TNM stage were robust indicators of overall survival (Figure 6(d)). Ultimately, to determine the risk and predict the survival of patients with HCC, we constructed a nomogram by combining MSRS analysis with that of other valuable clinical parameters (Figure 6(e)). Interestingly, we observed a positive correlation between the predicted 5-year survival and the actual 5-year survival of individuals (Figure 6(f)), suggesting that the generated nomogram holds great potential to support risk assessment and survival prediction of HCC patients.

4. Discussion

MTORC1 signaling is a pivotal pathway triggered by various environmental stimuli, such as growth factors, amino acids, and increased cellular energy levels [6, 8, 27]. As a downstream target of the AKT and RAS-ERK pathways, MTORC1 signaling contributes greatly to the regulation of cell survival and metabolism during cancer progression [28]. Notably, the proactivation of mTOR/MTORC1 signaling has been shown to be correlated with poor outcome in patients with breast cancer, bladder cancer, and HCC [29–32]. In particular, the expression of regulators or components of the MTORC1 or MTORC2 pathways, including p-AKT and RICTOR, is elevated in 40–50% of patients with HCC [33, 34]. Although previous studies have suggested a valuable role of MTORC1 signaling in discriminating high-risk HCC patients, only the expression levels of individual genes in the MTORC1 pathway or upstream modulators or downstream targets of MTORC1 signaling have been considered so far; these may not represent the exact status of this pathway. Hence, an MTORC1-related gene signature based on gene networks was required to optimize its application to the prognosis of HCC patients.

In the present study, MTORC1 signaling was found to be enriched in HCC patients and validated as a key primary risk factor for the overall survival of HCC patients by applying Cox regression analysis to the training dataset. Next, we carried out WGCNA for the selection of MTORC1-related gene modules and LASSO Cox regression analysis for the construction of an MSRS including the most robust candidate genes. Subsequently, the predictive value of the MSRS was validated in the training cohort, two validation cohorts, and in multiple subgroups of the pooled cohort; this strongly suggests that the MSRS can be applied as a reliable predictor for the prognosis of HCC patients. Finally, a decision tree was established to optimize risk discrimination by including information on TNM stages. Also, a nomogram was constructed to integrate the prognostic power of the MSRS with that of other clinical features, for more accurate risk prediction. To improve the research value in the future, we would like to check the importance of MTORC1 signaling using some HCC models such as in vitro genetic approaches or antagonists/agonists for manipulating MTORC1 signaling in HCC cell lines. Mouse model such as Diethylnitrosamine- (DEN-) induced HCC model [35] can also be applied to check the MTORC1 signaling activation in mice and validate the prognostic value of the MSRS.

A recent study showed that an MTORC1 signaling signature involved in six genes was generated and could be utilized for the prognosis of HCC patients [10]. Although they performed analysis on RNA sequencing data from TCGA database, while we applied a diverse cohort, MOTRC1 signaling was enriched in both studies, indicating the prognostic significance of this pathway for patients with HCC. Furthermore, we established a decision tree which can better aid to the prognosis based on the MTORC1 signaling.

Although a few candidate genes have been investigated in multiple cancers, a large proportion of them are still poorly studied in the context of MTORC1 signaling regula-tion. For instance, phosphoglycerate kinase 1 (PGK1), a candidate predictor gene with a high coefficient, has been shown to serve as an indispensable enzyme in the aerobic glycolysis pathway and thus as a promoter of cancer cell survival and chemoradiotherapy resistance in cancer patients [36]. Conversely, enolase-1 (ENO1) promotes the invasion and metastasis of cancer cells by altering a variety of signaling pathways such as the PI3K/AKT pathway [37–39]. Considering the lack of data on the biological effects of the biomarkers included in our MSRS, further functional studies are required to verify the potential links between these and MTORC1 signaling, for a better understanding of their roles as MSRS components.

Moreover, although the constructed MSRS has been demonstrated to be a powerful risk predictor for patients with HCC, its prognostic value should be further tested and validated in cohorts including a larger number of patients; such prospective trials may support the clinical use of this promising novel predictor of HCC outcome.

Data Availability

The data used to support the findings of this study are included within the article.

Conflicts of Interest

The authors declare that they have no competing interest.

References

[1] B. Ruf, B. Heinrich, and T. F. Greten, "Immunobiology and immunotherapy of HCC: spotlight on innate and innate-like immune cells," *Cellular & Molecular Immunology*, vol. 18, no. 1, pp. 112–127, 2021.

[2] J. M. Llovet, R. K. Kelley, A. Villanueva et al., "Hepatocellular carcinoma," *Nature Reviews Disease Primers*, vol. 7, no. 1, p. 6, 2021.

[3] T. Couri and A. Pillai, "Goals and targets for personalized therapy for HCC," *Hepatology International*, vol. 13, no. 2, pp. 125–137, 2019.

[4] D. W. Kim, C. Talati, and R. Kim, "Hepatocellular carcinoma (HCC): beyond sorafenib-chemotherapy," *Journal of Gastrointestinal Oncology*, vol. 8, no. 2, pp. 256–265, 2017.

[5] J. C. Nault and A. Villanueva, "Biomarkers for hepatobiliary cancers," *Hepatology*, vol. 73, Suppl 1, pp. 115–127, 2021.

[6] R. A. Saxton and D. M. Sabatini, "mTOR signaling in growth, metabolism, and disease," *Cell*, vol. 168, no. 6, pp. 960–976, 2017.

[7] C. Magaway, E. Kim, and E. Jacinto, "Targeting mTOR and metabolism in cancer: lessons and innovations," *Cell*, vol. 8, no. 12, p. 1584, 2019.

[8] I. Ben-Sahra and B. D. Manning, "mTORC1 signaling and the metabolic control of cell growth," *Current Opinion in Cell Biology*, vol. 45, pp. 72–82, 2017.

[9] G. Ferrin, M. Guerrero, V. Amado, M. Rodriguez-Peralvarez, and M. De la Mata, "Activation of mTOR signaling pathway in hepatocellular carcinoma," *International Journal of Molecular Sciences*, vol. 21, no. 4, p. 1266, 2020.

Retraction

Retracted: Efficacy of Aidi Injection and Brucea javanica Oil Emulsion Injection in Rectal Cancer during CapeOX Adjuvant Chemotherapy

BioMed Research International

This article has been retracted by Hindawi following an investigation undertaken by the publisher [1]. This investigation has uncovered evidence of one or more of the following indicators of systematic manipulation of the publication process:

(1) Discrepancies in scope

(2) Discrepancies in the description of the research reported

(3) Discrepancies between the availability of data and the research described

(4) Inappropriate citations

(5) Incoherent, meaningless and/or irrelevant content included in the article

(6) Manipulated or compromised peer review

The presence of these indicators undermines our confidence in the integrity of the article's content and we cannot, therefore, vouch for its reliability. Please note that this notice is intended solely to alert readers that the content of this article is unreliable. We have not investigated whether authors were aware of or involved in the systematic manipulation of the publication process.

Wiley and Hindawi regrets that the usual quality checks did not identify these issues before publication and have since put additional measures in place to safeguard research integrity.

We wish to credit our own Research Integrity and Research Publishing teams and anonymous and named external researchers and research integrity experts for contributing to this investigation.

The corresponding author, as the representative of all authors, has been given the opportunity to register their agreement or disagreement to this retraction. We have kept a record of any response received.

References

[1] W. Meng, X. Zeng, Y. Gao, Q. Chen, and L. Bai, "Efficacy of Aidi Injection and Brucea javanica Oil Emulsion Injection in Rectal Cancer during CapeOX Adjuvant Chemotherapy," *BioMed Research International*, vol. 2021, Article ID 2033353, 8 pages, 2021.

Research Article

Efficacy of Aidi Injection and Brucea javanica Oil Emulsion Injection in Rectal Cancer during CapeOX Adjuvant Chemotherapy

Wenjun Meng ⬤,[1] Xiaoge Zeng,[2,3] Yuchen Gao,[1] Qi Chen,[1] and Lian Bai ⬤[1]

[1]*Department of Gastrointestinal Surgery, Yongchuan Hospital, Chongqing Medical University, Chongqing 402160, China*
[2]*College of Acupuncture-Moxibustion and Tuina, Chengdu University of Traditional Chinese Medicine, Chengdu 610075, China*
[3]*Department of Pediatrics, Jinniu Maternity and Child Health Hospital of Chengdu, Chengdu 610081, China*

Correspondence should be addressed to Lian Bai; 19828386708@163.com

Background. Adjuvant chemotherapy with CapeOX regimen is widely used in resected rectal cancer, which brings benefits to patients. But drug-related toxicities are severe during this process; thus, survival outcomes may potentially be affected. This study explored the efficacy of two Chinese herbal injections, Aidi injection (ADI) and Brucea javanica oil emulsion injection (BJOEI), as adjuvant drugs in CapeOX adjuvant chemotherapy on rectal cancer patients. *Methods.* A total of 240 cases were enrolled in this retrospective study. 80 cases received CapeOX with ADI (the ADI group), 80 cases received CapeOX with BJOEI (the BJOEI group), and the rest 80 cases received CapeOX alone (the control group). After four cycles' chemotherapy, adverse reactions (ADRs) and quality of life (QOL) were analyzed. Then, patients received follow-up for at least one year, and the endpoint was disease-free survival (DFS). *Results.* All patients completed at least four cycles' adjuvant chemotherapy. The incidence of leukopenia and thrombocytopenia was significantly lower in the ADI group; the incidence of nausea was significantly lower in the BJOEI group; the incidence of hand-foot syndrome was significantly lower in both the ADI group and BJOEI group. Significant difference was found in the control group regarding the Karnofsky Performance Status (KPS) scores prior and posttreatment. No difference was found among three groups regarding one-year DFS. *Conclusion.* As adjuvant drugs for rectal cancer during CapeOX chemotherapy, ADI shows advantages in decreasing leukopenia and thrombocytopenia, while BJOEI results better in remitting nausea. Both two CHIs had positive impacts on decreasing hand-foot syndrome and the maintenance of patients' QOL. It is worthy of further study and promotion for CHIs.

1. Introduction

Colorectal cancer (CRC) is the most common malignant tumor in the digestive system. Globally, its incidence and mortality rank third and second, respectively [1]. Currently, CRC becomes an increasing cancer burden to Chinese society due to westernization in lifestyles; thus, its incidence has risen to the second [2]. In China, the incidence of rectal cancer is much higher than colon cancer, and the number of which also accounts for nearly half of the total CRC patients [3, 4]. They suffer from a worse quality of life (QOL) and a poorer prognosis. Currently, radical surgery followed by adjuvant chemotherapy is still the standard treatment of

resectable rectal cancer [5]. Unfortunately, quite a few patients are undergoing complications from sphincter excision and chemotherapeutic toxicity. CapeOX (XELOX) is a first-line adjuvant regimen that brings convenient use and lowers toxicity to rectal cancer patients [6]. However, adverse reactions (ADRs) are unavoidable after long-range chemotherapy.

The Chinese herbal injection (CHI) is based on the theories of traditional Chinese medicine (TCM), and the application of which is a symbol of the modernization of TCM. Currently, over a dozen CHIs are frequently used in treating human cancer: Aidi, Astragalus polysaccharides, Brucea javanica oil emulsion, Cinobufacini, compound matrine,

TABLE 1: Karnofsky Performance Status scoring scale.

Score	Definition
100	Normal, no complaints; no evidence of disease
90	Able to carry on normal activity; minor signs or symptoms of disease
80	Normal activity with effort; some signs or symptoms of disease
70	Cares for self; unable to carry on normal activity or to do active work
60	Requires occasional assistance, but is able to care for most personal needs
50	Requires considerable assistance and frequent medical care
40	Disabled; requires special care and assistance
30	Severely disabled; hospital admission is indicated although death not imminent
20	Very sick; hospital admission or active supportive treatment necessary
10	Moribund; fatal processes progressing rapidly
0	Dead

Delisheng, ginseng polysugar, Kangai, Kanglaite, and Shenqifuzheng [7] The majority studies of these anticancer CHIs are related to lung cancer, and it is concluded that CHIs can reduce ADRs during chemotherapy and promote patients' QOL, which has been demonstrated by evidence-based medicine [8]. Most of the reports published in English were reviews or meta-analyses, which were based on similar studies previously published in Chinese. However, among these articles, few researchers directly compared and evaluated different CHIs in one same study. Due to the limitations of current clinical researches and meta-analyses, higher-level evidences are needed.

Aidi injection (ADI) and Brucea javanica oil emulsion injection (BJOEI; Yadanziyouru injection) are both common CHIs for many malignant tumors. It is generally accepted in TCM that CRC, a disease with deficiency of both spleen and kidney, can result better in survival outcome by regulating the immune microenvironment from these TCM drugs [8]. For advanced CRC patients, the two CHIs also show survival benefits as the palliative treatments. But there is a lack of researches concerning their applications after radical surgery. This study focuses on the safety and efficacy of the two CHIs combined with CapeOX adjuvant chemotherapy in patients with resected rectal cancer.

2. Materials and Methods

2.1. Study Design. From August 2017 to May 2020, a total of 240 patients with rectal cancer were enrolled in this study. All patients have undergone laparoscopic radical surgery by our experienced surgeons and received adjuvant chemotherapy. They were divided into three groups: the group with CapeOX regimen plus ADI (the ADI group), the group with CapeOX plus BJOEI (the BJOEI group), and the group with CapeOX alone (the control group).

The inclusion criteria of cases were listed as follows: (I) aged 18 to 75 years; (II) diagnosed as primary rectal adenocarcinoma with clinical-stage I to III; (III) patients have undergone laparoscopic radical surgery (Dixon, Miles or Hartmann) with R0 resection; (IV) diagnosed and confirmed again by postoperative pathological examination; (V) expected survival was longer than three months; and

(VI) Eastern Cooperative Oncology Group (ECOG) score was 0 or 1. The exclusion criteria were listed as follows: (I) history of neoadjuvant therapy; (II) severe cardiac, liver, or renal insufficiency that could not endure postoperative treatment; (III) combined with other primary tumors; and (IV) patients with any contraindication mentioned in the instructions of the two CHIs. The procedures were conducted following the principles of the Declaration of Helsinki (as revised in 2013) and in accordance with the ethical standards of our hospital. All patients have signed informed consent.

Radical surgery was performed among the patients. Three to four weeks after surgery, they started to receive adjuvant chemotherapy with CapeOX regimen, or plus respective CHI. Before the postoperative treatment, patients' QOL was scored using the Karnofsky Performance Status (KPS; scored 100 to 0) scale [9]. KPS scale is commonly applied in cancer patients, which is regarded as an evaluator for the feasibility of chemotherapy, and its detailed criteria are listed in Table 1.

2.2. Treatment Regimen. For the ADI group, 50 mL ADI (Guizhou Yibai Pharmaceutical Co. Ltd., Guizhou, China) diluted into 250 mL normal saline was intravenously infused from day 1 to day 14, once a day. After ADI given on day 1, oxaliplatin (Shandong Xinshidai Pharmaceutical Co. Ltd., Shandong, China) diluted into 500 mL 5% glucose was intravenously infused from day 1 to day 14. The dose of oxaliplatin was calculated on the basis of body surface area (BSA; 130 mg/m^2). Meanwhile, capecitabine (Jiangsu Hengrui Medicine Co. Ltd., Nanjing, China) was taken orally twice a day from day 1 to day 14, and its dose was based on BSA (1000 mg/m^2). Then, drugs were stopped for 7 days. The expected treatment time ranged from three to six months.

For the BJOEI group, 10 mL BJOEI (Shenyang Yaoda Leiyunshang Pharmaceutical Co. Ltd., Shenyang, China) diluted into 250 mL normal saline was intravenously given from day 1 to day 14, once a day. Then, the administration of oxaliplatin and capecitabine was equal to the ADI group. For the control group, only CapeOX regimen was given. The frame of the study is presented in Figure 1.
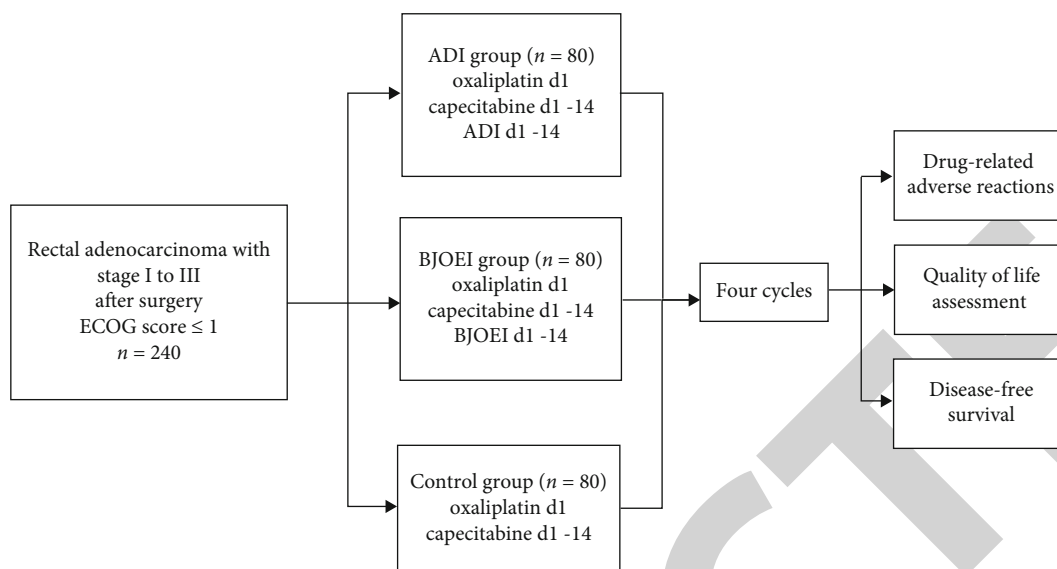
Figure 1: The treatment process and study design. ECOG: Eastern Cooperative Oncology Group; ADI: Aidi injection; BJOEI: Brucea javanica oil emulsion injection.

Table 2: Patient characteristics of the three groups.

	ADI group ($n = 80$)	BJOEI group ($n = 80$)	Control group ($n = 80$)	F/χ^2	P value
Age (years)	59.1 ± 9.0	60.4 ± 9.8	57.9 ± 10.1	1.270	0.283
Gender (%)				0.742	0.690
Male	53 (66.25)	58 (72.50)	55 (68.75)		
Female	27 (33.75)	22 (27.50)	25 (31.25)		
BMI (kg/m^2)	22.12 ± 2.09	21.83 ± 2.40	21.64 ± 1.76	1.060	0.348
Tumor length (cm)	3.69 ± 1.26	3.73 ± 1.20	3.57 ± 0.96	0.393	0.676
Preoperative clinical stage (%)				4.715	0.318
I	2 (2.50)	0 (0.00)	0 (0.00)		
II	22 (27.50)	20 (25.00)	18 (22.50)		
III	56 (70.00)	60 (75.00)	62 (77.50)		
ECOG performance status (%)				0.870	0.647
0	66 (82.50)	70 (87.50)	69 (86.25)		
1	14 (17.50)	10 (12.50)	11 (13.75)		
Baseline CEA level (%)				1.363	0.506
≤4.5 ng/mL	24 (30.00)	19 (23.75)	18 (22.50)		
>4.5 ng/mL	56 (70.00)	61 (76.25)	62 (77.50)		
Surgical method (%)				1.195	0.879
Dixon	60 (75.00)	63 (78.75)	61 (76.25)		
Miles	8 (10.00)	9 (11.25)	10 (12.50)		
Hartmann	12 (15.00)	8 (10.00)	9 (11.25)		
Histological differentiation (%)				2.292	0.682
Well	11 (13.75)	9 (11.25)	13 (16.25)		
Moderate	41 (51.25)	43 (53.75)	46 (57.50)		
Poor	28 (35.00)	28 (35.00)	21 (26.25)		

2.3. Evaluation of Drug-Related Adverse Reactions. Common indicators of drug-related ADRs were graded from 0 to V according to the Common Terminology Criteria for Adverse Events (CTCAE; version 5.0), including leukopenia, anemia, thrombocytopenia, nausea, vomiting, diarrhea, constipation, alanine aminotransferase (ALT), aspartate aminotransferase (AST), creatinine, hand-foot syndrome, and peripheral neuropathy [10].

TABLE 3: Drug-related adverse reactions in the three groups.

|	Grade 0 (%)			Grade 1 + grade 2 (%)			Grade 3 + grade 4 (%)			H	P value
	ADI group	BJOEI group	Control group	ADI group	BJOEI group	Control group	ADI group	BJOEI group	Control group		
Leukopenia	70 (87.50)	61 (76.25)	50 (62.50)	8 (10.00)	15 (18.75)	27 (33.75)	2 (2.50)	4 (5.00)	3 (3.75)	12.645	0.002
Anemia	46 (57.50)	39 (48.75)	36 (45.00)	33 (41.25)	39 (48.75)	44 (55.00)	1 (1.25)	2 (2.50)	0 (0.00)	2.407	0.300
Thrombocytopenia	77 (96.25)	70 (87.50)	65 (81.25)	3 (3.75)	10 (12.50)	14 (17.50)	0 (0.00)	0 (0.00)	1 (1.25)	8.860	0.012
Nausea	44 (55.00)	59 (73.75)	39 (48.75)	35 (43.75)	20 (25.00)	39 (48.75)	1 (1.25)	1 (1.25)	2 (2.50)	11.023	0.004
Vomiting	69 (86.25)	70 (87.50)	64 (80.00)	11 (13.75)	10 (12.50)	14 (17.50)	0 (0.00)	0 (0.00)	2 (2.50)	2.157	0.340
Diarrhea	54 (67.50)	46 (57.50)	42 (52.50)	25 (31.25)	34 (42.50)	35 (43.75)	1 (1.25)	0 (0.00)	3 (3.75)	4.101	0.129
Constipation	64 (80.00)	62 (77.50)	55 (68.75)	13 (16.25)	16 (20.00)	25 (31.25)	3 (3.75)	2 (2.50)	0 (0.00)	2.416	0.299
ALT increase	63 (78.75)	73 (91.25)	66 (82.50)	13 (16.25)	7 (8.75)	12 (15.00)	4 (5.00)	0 (0.00)	2 (2.50)	5.251	0.072
AST increase	67 (83.75)	72 (90.00)	64 (80.00)	12 (15.00)	6 (7.50)	13 (16.25)	1 (1.25)	2 (2.50)	3 (3.75)	3.043	0.218
Creatinine increase	72 (90.00)	68 (85.00)	68 (85.00)	8 (10.00)	12 (15.00)	12 (15.00)	0 (0.00)	0 (0.00)	0 (0.00)	1.149	0.563
Hand-foot syndrome	74 (92.50)	72 (90.00)	58 (72.50)	6 (7.50)	8 (10.00)	21 (26.25)	0 (0.00)	0 (0.00)	1 (1.25)	14.999	0.001
Peripheral neuropathy	70 (87.50)	71 (88.75)	62 (77.50)	10 (12.50)	9 (11.25)	16 (20.00)	0 (0.00)	0 (0.00)	2 (2.50)	4.898	0.086
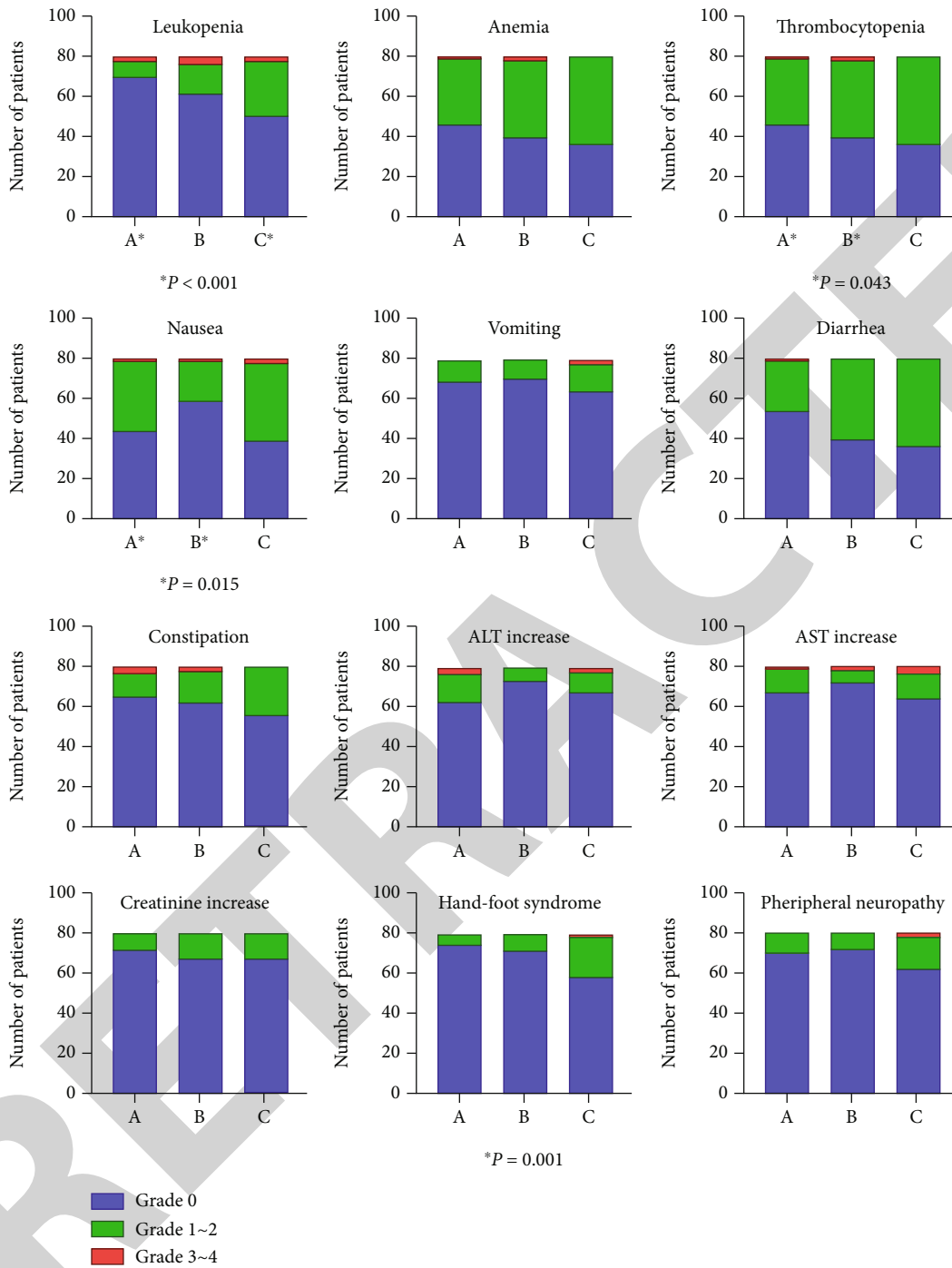
FIGURE 2: The comparison of adverse reactions in the ADI group, the BJOEI group, and the control group. Significant differences were shown concerning leukopenia, thrombocytopenia, nausea, and hand-foot syndrome. (a) The ADI group; (b) the BJOEI group; (c) the control group.

2.4. Quality of Life Assessment. The QOL of the three groups was evaluated three months later by reviewing the QOL score, following the KPS criteria. Comparison of the scores prior and posttreatment can reflect the changes in QOL.

2.5. One-Year Follow-Up. Postoperative follow-up was started after surgical operation. We used telephone and outpatient follow-up to perform data collection. The endpoint of the follow-up was disease-free survival (DFS).

2.6. Statistical Analysis. IBM SPSS Statistics (version 23) software was used for data analysis, and GraphPad Prism (version 8.0.2) for Kaplan-Meier curve drawing. Continuous variables were shown as mean ± standard deviation and analyzed by one-way ANOVA test. Chi-square test was used for enumeration data, Mann-Whitney U test for ranked data between two groups, and Kruskal-Wallis test for ranked data among three groups. When the ranked data were paired, matched samples t-test was performed. Log-rank test was

TABLE 4: Karnofsky Performance Status scoring of the three groups.

|	ADI group ($n = 80$)	BJOEI group ($n = 80$)	Control group ($n = 80$)	F/χ^2	P value
Prior treatment (%)	76.59 ± 8.51	77.35 ± 7.48	78.13 ± 7.48	1.913	0.128
90	10 (12.50)	9 (11.25)	14 (17.50)		
80	36 (45.00)	40 (50.00)	39 (48.75)	8.394	0.211
70	24 (30.00)	26 (32.50)	25 (31.25)		
60	10 (12.50)	5 (6.25)	2 (2.50)		
Posttreatment (%)	76.32 ± 7.81	76.66 ± 6.79	75.00 ± 8.11	0.352	0.788
90	8 (10.00)	6 (7.50)	7 (8.75)		
80	35 (43.75)	39 (48.75)	35 (43.75)	3.681	0.720
70	30 (37.50)	32 (40.00)	29 (36.25)		
60	7 (8.75)	3 (3.75)	9 (11.25)		
t	-0.705	-1.686	5.992		
P value	0.483	0.096	<0.001		
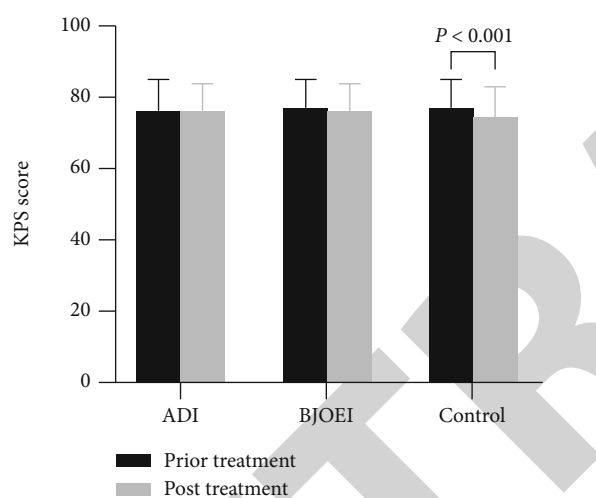
FIGURE 3: The comparison of the mean KPS scores prior and posttreatment in the ADI group, the BJOEI group, and the control group. The mean score in the control group showed a significant reduction after chemotherapy treatment.

used to compare the DFS among the three groups. P values listed in this article were all derived from two-tailed tests. $P < 0.05$ was considered statistically significant.

3. Results

3.1. Patient Characteristics. Patients' characteristics are displayed in Table 2. The mean age of the ADI group, the BJOEI group, and the control group was 59.1 ± 9.0, 60.4 ± 9.8, and 57.9 ± 10.1 years, respectively; and the median age was 59, 60.5, and 58 years, respectively. The number of cases with stoma (permanent or protective) in the three groups was 20, 17, and 19, respectively. There were no statistical significances in demographic and disease characteristics among the three groups (all $P > 0.05$). All patients have finished at least four cycles' adjuvant therapy as planned, and none of them dropped out during this process.

3.2. Adverse Reactions. Drug-related ADRs were compared after four cycles' adjuvant therapy, and the number of which is shown in Table 3. There were a total of 10 cases (12.50%; 8 with grade 1~2, and 2 with grade 3~4) in the ADI group facing leukopenia, while the number in the control group was 30 (37.50%; 27 with grade 1~2, and 3 with grade 3~4), showing a significantly lower incidence after using ADI ($P < 0.001$). As for thrombocytopenia, the number of grade 1~4 in the three groups was 3 (3.75%), 10 (12.5%), and 15 (18.75%), respectively, and the incidence of which in the ADI group was significantly lower than that in the BJOEI group ($P < 0.05$). For the cases of nausea, the BJOEI group (21 cases, 26.25%) was significantly lower than the ADI group (36, 45.00%; $P < 0.05$). Compared with the control group (22 cases, 27.50%), hand-foot syndrome occurred significantly less in the ADI group (6 cases, 7.50%) and the BJOEI group (8 cases, 10.00%; $P < 0.05$). The comparison of each adverse reaction was illustrated with Figure 2.

3.3. Quality of Life. The KPS scores of the three groups prior and posttreatment were shown in Table 4. In the ADI group, the mean KPS scores before and after treatment were 76.59 ± 8.51 and 76.32 ± 7.81, respectively, and no significant difference was found ($t = -0.705$, $P = 0.483$). The scores in the BJOEI group were 77.35 ± 7.48 and 76.66 ± 6.79, respectively, with no significant difference ($t = -1.686$, $P = 0.096$). And the scores in the control group were 78.13 ± 7.48 and 75.00 ± 8.11, respectively, with a significant difference ($t = 5.992$, $P < 0.001$). A histogram is also presented in Figure 3 to show the comparison of the KPS scores prior and posttreatment in each group.

3.4. One-Year Prognosis. All patients received at least one-year follow-up, and the DFS was evaluated by computed tomography examination. Among them, 12, 14, and 17 cases had local recurrence or distant metastasis in the ADI group, the BJOEI group, and the control group, respectively. The DFS rate was 85.0%, 82.5%, and 78.8%, respectively. There was no significant difference among the three groups ($P = 0.289$). The Kaplan-Meier curve of DFS is shown in Figure 4.
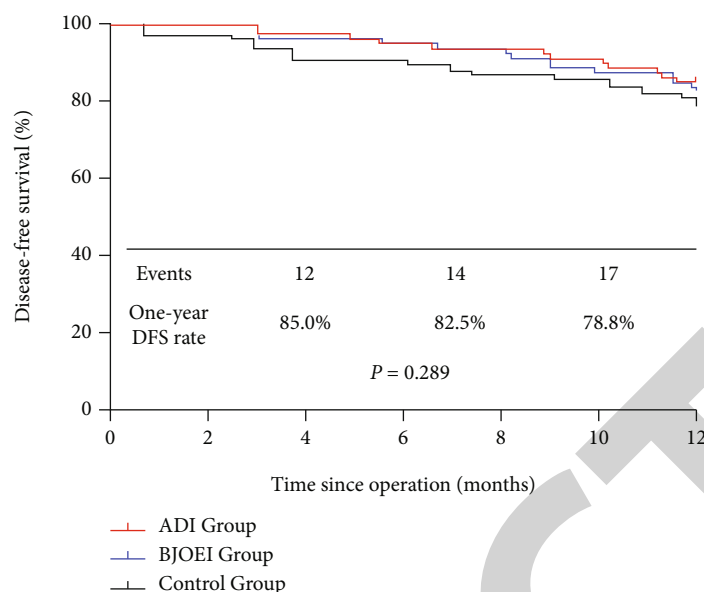
FIGURE 4: The comparison of disease-free survival rate among the three groups. There was no significant difference in disease-free survival rate among them ($P = 0.289$).

4. Discussion

Adjuvant chemotherapy forms an important part in the treatment of rectal cancer. Via systemic administration, long-term benefits are brought to most patients undergone surgical resection [11]. However, drug-related ADRs frequently occur in postoperative treatments; thus, patients' QOL and compliance to adjuvant chemotherapy are accordingly lowered. These negative impacts can potentially limit survival outcomes.

In the theories of TCM, the causes of rectal cancer include excessive fatigue, improper diet, and deficiency of Zheng-Qi (Qi; body energy); thus, the symptom of damp and poison stasis is emerged [12]. Meanwhile, side effects of chemotherapy, especially peripheral neurotoxicity, are also derived from the damage of Qi. The loss of Qi aggravates the imbalance between Yin and Yang, insufficiency of the liver and kidney, and decrease in immunity. As a result, tumor progression is frequently promoted [13]. ADI and BJOEI are both TCM preparations that are extracted and purified from active ingredients of Chinese herbs [14]. Serving as anticancer CHIs, they are generally accepted in TCM hospitals. Multiple studies in China concluded that different CHIs have similar but uneven positive impacts on cancer patients [8]. However, the usage of anticancer CHIs has not been unified, which limits the development of these TCM injections. The compatibility and dosage need to be standardized consequently.

In this study, the efficacy of ADI and BJOEI was directly compared in rectal cancer patients after their surgical operations. Also, the usage of CHIs was in strict accordance with the instructions. The results showed that the two CHIs have respective advantages in preventing different ADRs in CapeOX chemotherapy. There were no significant differences among the three groups including anemia, vomiting, diarrhea, constipation, ALT, AST, creatinine, and peripheral neuropathy ($P > 0.05$). For patients in the ADI group, the risk of leukopenia was much lower than that in the control group ($P < 0.05$), and the risk of thrombocytopenia was much lower than that in the BJOEI group ($P < 0.05$), indicating that ADI may offset the suppressive effect of chemotherapeutic agents on bone marrow to a certain extent; hence, the coagulation function was also sustained. This result can be attributed to cantharides (Banmao), the main component of ADI. As an antitumor agent, cantharides serves for antiangiogenesis, tumor cells apoptosis induction, and multidrug resistance reversal [15, 16]. For the BJOEI group, we found the toxicity grade of nausea was significantly lower compared to the ADI group ($P < 0.05$). Since gastrointestinal reactions are the main side effects during chemotherapy, BJOEI can be commonly used as an adjuvant drug to prevent nausea or vomiting. Also, both ADI and BJOEI showed significant advantages in decreasing the incidence of hand-foot syndrome. Furthermore, the QOL scores posttreatment were compared pairwise with the initial values in respective groups, and neither of groups using CHIs showed significant difference ($P > 0.05$); comparatively, a statistical significance was found in the control group between the scores prior and posttreatment ($P < 0.05$). These results indicated that both two CHIs did not downgrade the living ability; moreover, they may have potential effects on the maintenance of patients' QOL. In addition, we also compared the DFS in the first year, and the results indicated that the one-year prognoses were similar among the three groups. The cases and follow-up time should be expanded.

Some limitations remained in this study. Potential biases were inevitable because of the small sample size, and some of the outcome measures were subjective. Also, there is the absence of more different chemotherapy regimens or CHIs in the study, so the efficacy of CHIs cannot be